



GEOTECHNICAL ASPECTS OF UNDERGROUND CONSTRUCTION IN SOFT GROUND

Wan-Huan Zhou, Zheng Guan and Xue Li, editors



CRC Press
Taylor & Francis Group

GEOTECHNICAL ASPECTS OF UNDERGROUND CONSTRUCTION IN SOFT GROUND

GEOTECHNICAL ASPECTS OF UNDERGROUND CONSTRUCTION IN SOFT GROUND comprises a collection of 68 contributions, including 55 technical papers, 6 General Reports, 5 Keynotes, 1 Fujita Lecture, and 1 Bright Spark Lecture presented at the 11th International Symposium on Geotechnical Aspects of Underground Construction in Soft Ground (IS-Macau 2024), held in Macao SAR, China, on June 14-17, 2024.

The symposium is the latest in a series that began in New Delhi in 1994 and was followed by symposia in London (1996), Tokyo (1999), Toulouse (2002), Amsterdam (2005), Shanghai (2008), Rome (2011), Seoul (2014), Sao Paulo (2017), and Cambridge (2022). This symposium was organized by University of Macau, Civil Engineering Laboratory of Macau, and Macau Association for Geotechnical Engineering under the auspices of TC204 of ISSMGE. The book includes contributions from more than 15 countries on the research, design, and construction of underground works in soft ground. The theme of IS-Macau 2024 is “Tunnelling and Underground Construction for Smart Cities”. The contributions cover the following topics:

- Basic properties and soil improvement in soft ground
- Constitutive and Numerical Modelling
- Innovative analysis and design in tunneling and underground construction
- Smart monitoring and visualization technologies for tunneling and underground construction
- Sustainability and resilience of underground infrastructure
- Field case studies

Similar to the proceedings of the previous series symposia, GEOTECHNICAL ASPECTS OF UNDERGROUND CONSTRUCTION IN SOFT GROUND serves as an invaluable resource offering insights into the contemporary methods of analyzing, designing, and executing tunnels and deep excavations within soft ground environments, crucial for the advancement of smart cities. The book is particularly aimed at academics and professionals interested in geotechnical and underground engineering.



Taylor & Francis

Taylor & Francis Group

<http://taylorandfrancis.com>

PROCEEDINGS OF THE ELEVENTH INTERNATIONAL SYMPOSIUM ON GEOTECHNICAL ASPECTS OF UNDERGROUND CONSTRUCTION IN SOFT GROUND, 14–17 JUNE 2024, MACAO SAR, CHINA

Geotechnical Aspects of Underground Construction in Soft Ground

Edited by

Wan-Huan Zhou, Zheng Guan & Xue Li

University of Macau, SAR, China



CRC Press

Taylor & Francis Group

Boca Raton London New York Leiden

CRC Press is an imprint of the
Taylor & Francis Group, an **informa** business

A BALKEMA BOOK

Designed cover image: Leong Kuong Pui

First published 2024

by CRC Press/Balkema

4 Park Square, Milton Park, Abingdon, Oxon, OX14 4RN

and by CRC Press/Balkema

2385 NW Executive Center Drive, Suite 320, Boca Raton FL 33431

CRC Press/Balkema is an imprint of the Taylor & Francis Group, an informa business

© 2024 selection and editorial matter, Wan-Huan Zhou, Zheng Guan, and Xue Li; individual chapters, the contributors

Typeset by Integra Software Services Pvt. Ltd., Pondicherry, India

The right of Wan-Huan Zhou, Zheng Guan, and Xue Li to be identified as the authors of the editorial material, and of the authors for their individual chapters, has been asserted in accordance with sections 77 and 78 of the Copyright, Designs and Patents Act 1988.

The Open Access version of this book, available at www.taylorfrancis.com, has been made available under a Creative Commons Attribution-Non Commercial-No Derivatives (CC-BY-NC-ND) 4.0 license.

Although all care is taken to ensure integrity and the quality of this publication and the information herein, no responsibility is assumed by the publishers nor the author for any damage to the property or persons as a result of operation or use of this publication and/or the information contained herein.

British Library Cataloguing-in-Publication Data

A catalogue record for this book is available from the British Library

Library of Congress Cataloging-in-Publication Data

A catalog record has been requested for this book

ISBN: 978-1-032-53812-9 (hbk)

ISBN: 978-1-032-53816-7 (pbk)

ISBN: 978-1-003-41379-0 (ebk)

DOI: 10.1201/9781003413790

Table of contents

Preface	xi
Organisation	xiii
Acknowledgements	xv
Editor biographies	xvii
<i>Fujita lecture</i>	
Interactions at the front face of EPB shield when drilling in sand <i>A. Bezuijen</i>	3
<i>Keynote lecture</i>	
Smart monitoring of tunnels <i>W. Broere</i>	19
Deformation of shield tunnel subjected to underlying tunneling <i>R.P. Chen, T. Chen, F.Y. Meng & H.Z. Cheng</i>	30
Exploiting the renewable energy resources of our cities' undergrounds <i>L. Laloui & E. Ravera</i>	39
Three implementations to reduce geotechnical risk on underground projects using information engineering and AI <i>M.A. Mooney, H. Zheng & H. Yu</i>	49
Learning from failure in shallow NATM tunnel <i>W. Wu</i>	60
<i>Bright spark lecture</i>	
Time-dependent fragility assessment of deep circular tunnels in soft soil <i>Z.K. Huang, D.M. Zhang, Y.X. Cheng & X.M. Deng</i>	73
<i>Basic properties of soft soils</i>	
General report for basic properties and soil improvement in soft ground <i>S.Y. Wang</i>	85
Permeability improvement of contaminated soil treated by nano Zero-Valent Iron (nZVI) through a modified slurry-consolidation procedure <i>Y.Z. Chen, C. Fan, Q. Dong & J. Wei</i>	93

Experimental study on non-symmetric polarity reversal for reducing interfacial resistance in electro-osmosis of soft soil	99
<i>Y. Jiang, J. Zhou, C. Xu, Z. Zhu & Q. Gan</i>	
Study on the deformation and strength characteristics of bentonite based on structural fractal features	107
<i>X. Y. Li, Y. F. Xu & W. H. Zhou</i>	
Determination of particle breakage and fractal dimension for marine coral sand	116
<i>X. Li, X. Feng, C. Wang & W. H. Zhou</i>	
Improved determination of the constrained modulus in soft soils using the flat dilatometer test	122
<i>S. Oberhollenzer, L. Hauser, R. Marte, F. Tschuchnigg, H. F. Schweiger & E. J. Lande</i>	
Mechanical strength and resistivity characteristics of activated MgO-carbonated cured Zn ²⁺ contaminated soils	130
<i>Y. Song, S. Ding, S. S. Dong, W. Liu, Y. L. Chen & J. Q. Liu</i>	
Permeability and strength of sand-bentonite mixture stabilized by different binders for construction of two-phase cut-off walls	139
<i>M. Z. Y. Ting, Y. Y. Tan, M. Widjaja & Y. Yi</i>	
Analysis of soil clogging of TBM tunneling in clayey layers and the role of soil compositions	147
<i>G. Wang, L. Yan, X. W. Zhang, X. Y. Liu & H. D. Gao</i>	
Investigation on evolutions of soil arching developed in a pile-supported embankment considering geogrid	154
<i>W. H. Yuan, L. J. Yuan, Y. Chen & L. S. Zhao</i>	
<i>Constitutive and numerical modelling</i>	
General report for “Constitutive and Numerical Modelling” session at IS-Macau 2024	161
<i>Z. Y. Yin</i>	
3D numerical modelling of a compensation grouting field trial in alluvial soils	168
<i>D. Boldini, E. Lusini, C. Spaggiari & S. Fuoco</i>	
Effect of diaphragm wall construction process on the performance of braced excavation	176
<i>Y. P. Dong</i>	
Numerical simulation of lake crossing construction under double-pipe tunnel considering flow-solid coupling	182
<i>Y. J. Liu, K. Wu, Z. Y. Dou, Z. H. Liu, Z. C. Fan & Q. L. Zhang</i>	
Effect of slurry infiltration on trench stability of diaphragm wall	190
<i>J. Ning, J. Yu & M. Huang</i>	
Numerical analysis of ground movement due to shield tunneling at NAPE, Macau	198
<i>W. L. Ung, Y. H. Wang & T. M. H. Lok</i>	
A continuum analysis of piles affected by an advancing tunnel excavation during centrifuge tests with a miniature TBM	206
<i>E. K. L. Wong, A. Franza, A. S. N. Alagha & G. M. B. Viggiani</i>	
Numerical analysis of rectangular tunnel boring machine induced ground settlement	215
<i>J. Yu, H. Li, M. Huang, C. F. Leung & J. Lim</i>	
Effect of infill nonlinearity on frame response to tunnelling	223
<i>Y. Yu, A. Franza, L. Neves & A. M. Marshall</i>	

Surface tension of foam and its influence on tunneling <i>D.Z. Zheng, A. Bezuijen & Q. Zhang</i>	231
Numerical modeling of muck movement and chamber pressure distribution during EPB shield tunneling with auxiliary air pressure balance mode <i>J.Z. Zhong & S.Y. Wang</i>	239
 <i>Innovative analysis and design in tunneling and underground construction</i>	
General Report – Innovative analysis and design in tunneling and underground construction <i>D.M. Zhang & T. Xu</i>	251
Algorithm on setting correction alignment for TBM meandering <i>H.L.C. An, T. Suzuki, M. Sugimoto & H.N. Thi</i>	257
Ground improvement for the shield tunneling in the composite stratum <i>S.H. Cheng, R.K.N. Wong, H.Y. Hsu, I.T.Y. Wong & C.J. Chen</i>	265
Settlement prediction of the Hong Kong-Zhuhai-Macau Bridge tunnel under the effect of typhoon <i>S.Y. He, Y. Yan & W.H. Zhou</i>	273
Delineating the 3D spatial distribution of granite weathering grade from boreholes data <i>K.P. Jeong, P.K. Ao & W.H. Zhou</i>	279
Soil disturbance evaluation in a typical soft clay excavation pit <i>M.Z. Li, Y.G. Zhou, Y. Tian, Y.Z. Li, Y.M. Chen & J.N. Ye</i>	287
Evaluation of landslide susceptibility in Kangding basin based on factor screening <i>Z. Li, F. Xiao, Y. Wang, Y. Zhou, J. Liu & F. Meng</i>	293
Bibliometric data mining of machine learning in tunnel engineering research: A publication trends analysis and visualization <i>Y. Shen, S. Wu, Z. Xia, X. Wang & J. Wang</i>	301
Effects of measurement data size on Bayesian updating of excavation-induced deflection <i>C. Tang, S.Y. He & W.H. Zhou</i>	310
Landslide dam stability analysis using a support vector machine approach <i>X. Xiong, W. Gu, D.Y. Shen & Z.M. Shi</i>	320
Dynamically updating geological uncertainty simulation with the process of tunnel excavation <i>J.Z. Zhang, Q.H. Jiang, D.M. Zhang & H.W. Huang</i>	327
Feature engineering and SHAP correlation analysis for large diameter shield tunneling: A deep data mining approach to explore the core features and mechanism that define the shield attitude <i>S. Zhao & S.M. Liao</i>	333
 <i>Smart monitoring and visualization technologies for tunnelling and underground construction</i>	
General Report – Smart monitoring and visualization technologies for tunnelling and underground construction <i>M.Z.E.B. Elshafie</i>	347
Investigating inherent mechanism of loess adhered to shield machine cutting tools <i>X.D. Bai, W.C. Cheng, B. Wu & D.E.L. Ong</i>	357

Control of grouting in the bedrock and soil in vicinity of tunnels and construction pits, Case study: E18, Oslo, Norway <i>S. Feizi, E. Skretting, T. Sandene, J. Langford, E. Monsås, J.M. Josefsen, F. Karenstuen & H.P. Kristiansen</i>	364
Predicting penetration behavior of foam with different rheology into saturated sand <i>H. Huang, H.M. Wang & W.H. Zhou</i>	371
Development and performance evaluation of a novel FBG-based sensor for measuring positive and negative pore water pressure in soil <i>J. Jing, T. Wang & W. Zhou</i>	378
Research on a CO ₂ Internet of Things online monitoring system for geotechnical engineering construction <i>J.H. Ma, Y.Z. Zhou, W. Cao & J.F. Liu</i>	387
Least squares adjustment approach in real-time monitoring of existing twin tunnels <i>K.H. Phan, B.C.B. Hsiung, J. Huang & A. Chao</i>	396
Coupled centrifuge-numerical modelling of shallow strip foundations <i>C. Tang, S.P. Selvaraj, C.M. Heron & A.M. Marshall</i>	404
Spatial interpolation of sparse SPT values using weighted ellipse nearest neighbors approach <i>W. Yan, C. Yang, W.H. Zhou & P. Shen</i>	413
Study on grouting rehabilitation of asymmetric transverse deformation in an existing shield tunnel <i>Z.W. Ye, D.M. Zhang, J.Z. Zhang, M.L. Zhou, H. Shao & Q. Zhou</i>	421
The relationship between the penetration depth and wavelength of the surface wave in two layers of soil <i>Z. Zhou & T.M.H. Lok</i>	429
 <i>Sustainability and resilience of underground infrastructure</i>	
General Report – sustainability and resilience of underground infrastructure <i>A. Franza</i>	439
Post-tensioned Waler System (PWS) as supporting structure for deep excavations <i>K. Balamonica, A.L.J. Jie, H. Wu, C. Zhengxia & O.K. Won</i>	445
Quantitative vulnerability calculation for existing tunnel affected by under-crossing shield tunnel excavation <i>Y.N. Chen, D.M. Zhang & H.W. Huang</i>	456
Stability assessment of slurry shield tunnel excavation zone <i>Y. Cheng, Y. Wu & W.H. Zhou</i>	464
Flow rate study of geothermal heat exchanger system in north US <i>J. Lin, T.D. Stark & A.J. Stumpf</i>	471
Spatial variability for Deep Cement Mixing in Kallang formation in Singapore. Review of scale of fluctuation and its influence in design <i>G.A. Pittaro & N. Mace</i>	480
Flow and filtration characteristics of bentonite slurry containing silt clay <i>S. Qin, Q.C. Lan & W.H. Zhou</i>	488

Deformation of surrounding soil mass of subway tunnel subjected to traffic loads considering principal stress rotation <i>W. Wu, Y. Yang & J. Wang</i>	494
Structural resilience assessment method for tunnels under seismic hazards <i>C.L. Zhang, D.M. Zhang & Z.K. Huang</i>	502
An ArcGIS toolbox for the probabilistic performance-based assessment of surface building damage in large-scale urban excavations <i>J. Zhao, A.O.K. Lysdahl, E.W. Ánes, L. Piciullo, S. Ritter & M.J. DeJong</i>	511
<i>Field case studies</i>	
General report – field case studies <i>D. Boldini</i>	523
Modelling of large diameter TBM tunnelling beneath new reclamation <i>S.W. Lee, C.O. Leung, K.F. Cheung, T. Wijesooriya & A. Schwob</i>	530
Ground loss and settlement of shield tunnel in tail grouting <i>J. Liang, W. Liu & T. Xu</i>	537
Case study of soil-structure interaction during tunnelling for Barcelona Metro: A comparison between conventional and innovative displacement measurements <i>A.D. Mariano, A. Gens, G.D. Ragione, E. Bilotta, J. Sanchez, B. Royo & S. Cespa</i>	545
A case study on shield cutting reinforced concrete diaphragm walls and piles directly: Key technologies and field investigation <i>J. Sun, S. Liao & Z. Wang</i>	552
Early assessment and mitigation of cracking on concrete tunnel segments – Dubai metro case study <i>V. Tellioglu, E. Delikan, A. Ozturk, A.M. Haimoni & M. Maghazy</i>	564
Investigating transient tunnelling-induced ground surface responses <i>S. Xue & J.R. Standing</i>	577
Author index	587



Taylor & Francis

Taylor & Francis Group

<http://taylorandfrancis.com>

Preface

TC204 of the ISSMGE was originally established in 1989 as TC28 and has since played a significant role in collecting information on the geotechnical aspects of design, construction and analysis of deep excavations, tunnels and large underground structures in urban environments. The inaugural symposium took place in New Delhi in 1994, followed by nine more symposia in London (1996), Tokyo (1999), Toulouse (2002), Amsterdam (2005), Shanghai (2008), Rome (2011), Seoul (2014), Sao Paulo (2017), and Cambridge (2022). Under the current leadership of Prof. Giulia Viggiani, the current Chairman of TC204, the 11th symposium (IS-Macau 2024; Macao SAR, China; 14-17 June 2024) has been organized to foster the exchange of ideas, experiences, and the latest advancements among leading experts in the field of underground construction.

Macao, as the West's first established gateway into China, has played a remarkable role in establishing a series of connections and contacts that have mutually enriched both civilizations across a wide spectrum of human endeavors. While the official languages are Chinese and Portuguese, English is commonly used in trade, tourism and commerce. Having transformed into a vibrant city with a worldwide reputation in entertainment, Macao is also at the heart of the Guangdong-Hong Kong-Macao Greater Bay Area, which has witnessed rapid development in infrastructure and underground construction in recent years. The theme of IS-Macau 2024 is “*Tunnelling and Underground Construction for Smart Cities*”, and the symposium serves as a premier platform for researchers and practitioners to present and discuss new challenges, solutions, and technologies in underground construction and related fields.

This proceedings comprises a total of 68 contributions from over 15 countries, including 48 university and industry companies. It includes written versions of the Fujita Lecture, Keynote Lectures, Bright Spark Lecture and Session Reports, as well as the regular papers in each plenary session. The session topics encompass a wide range of theoretical and experimental research, including basic properties and soil improvement in soft ground, constitutive and numerical modelling, innovative analysis and design in tunneling and underground construction, smart monitoring and visualization technologies for tunneling and underground construction, sustainability and resilience of underground infrastructure, and field case studies.

Seven distinguished speakers were invited to give special lectures during the symposium: Prof. Lyesse Laloui, Prof. Adam Bezuijen (Fujita Lecture), Dr. Zhongkai Huang (Bright Spark Lecture), Prof. Wei Wu, Prof. Michael Mooney, Prof. Ren-Peng Chen, and Prof. Wout Broere. Following tradition, the first two days of the symposium featured six technical sessions, which included a comprehensive general report and a selection of individual papers. To encourage further interaction and discussion on topics not covered in the plenary sessions, the symposium introduced the Best Poster Awards. On the third day, a technical site visit was meticulously organized. Participants had the opportunity to visit the construction site of Macao's 4th Bridge construction site.

We extend our sincere appreciation to all the authors for their exceptional contributions. Despite the tight schedule, we have succeeded in publishing the symposium proceedings as open access for the first time, in time for the conference. We extend special gratitude to Dr. Ao Peng Kong, the President of LECM and the Honorary Chair of IS-Macau 2024. His invaluable support has greatly enhanced the symposium, encouraging active participation and engagement of local engineers with the international professional community.

Hannah, Wan-Huan Zhou
Zheng Guan
Xue Li

Organisation

Honorary Chairs

Ao Peng Kong (Civil Engineering Laboratory of Macau)
Giulia Viggiani (University of Cambridge)

General Chairs

Wan-Huan Zhou (University of Macau)
Tao Xu (Southeast University)

Secretary

Zheng Guan (University of Macau)

CONFERENCE ORGANIZERS

The 11th International Symposium of Geotechnical Aspects of Underground Construction in Soft Ground (IS-Macau 2024) was organized by University of Macau, Civil Engineering Laboratory of Macau, and Macau Association for Geotechnical Engineering under the auspices of TC204 of International Society for Soil Mechanics and Geotechnical Engineering (ISSMGE).

LOCAL ORGANISING COMMITTEE

Professor Wan-Huan Zhou (Chair)

Yang Cheng

Shu-Yu He

Pabodha Maduranga Kannangara

Yan Li

Thomas M. H. Lok

Dian-Jun Sun

Ping Shen

Jia-Zheng Zhong

Zheng Guan

He Huang

Kuong-Pui Ieong

Zhi-Bin Li

Mi Pan

Guo-Xing Sun

Tao Wang

Liang Gao

Jun-Hao Jing

Xiao-Yue Li

Xue Li

Su Qin

Quan Sun

Shi-Lan Wei

INTERNATIONAL SCIENTIFIC COMMITTEE

Adam Bezuijen

Ren-Peng Chen

Bin-Chen Hsiung

Chen-Hui Liu

Duncan Nicholson

Wei Wu

Jing-Min Xu

Ding-Wen Zhang

Ji-Dong Zhao

Dong-Zhu Zheng

Wout Broere

Yong-Zhan Chen

Mandy Korff

Lord Robert Mair

Hua-Fu Pei

Yu Wang

Chungsik Yoo

Dong-Mei Zhang

Li-Min Zhang

Pin Zhang

Xue-Cheng Bian

Zhi-Liang Cheng

Lyesse Laloui

Michael Mooney

Shan-Yong Wang

Wei-Dong Wang

Jian-Hua Yin

Feng Zhang

Jie Zhang

Ankit Garg

Jian Chu

Zhi Ding

Song-Yu Liu

Monika Mitew-Czajewska

Shu-Ying Wang

Yang Xiao

Zhen-Yu Yin

Gang Zheng

Lin-Shuang Zhao



Taylor & Francis

Taylor & Francis Group

<http://taylorandfrancis.com>

Acknowledgements

The successful publication of this proceedings is deeply indebted to the authors of the papers, whose generous sharing of their valuable work has made this endeavor possible. We would also like to express our heartfelt appreciation to the reviewers, whose invaluable technical advice has greatly enhanced the quality of the proceedings.

We would like to express our sincere thanks to the general reporters of the conference, namely Prof. Shuying Wang, Prof. Zhenyu Yin, Prof. Daniela Boldini, Prof. Dongmei Zhang, Prof. Mohammed Zein Elabidin Babiker Elshafie, and Prof. Andrea Franza, for their contributions and unwavering support.

Last but not least, we would like to recognize the outstanding efforts of the team at the University of Macau. In particular, we would like to express our gratitude to Ms. Venus Leong, Dr. Tao Xu, Dr. Jiazheng Zhong, Dr. Quan Sun, Shilan Wei, and Dr. Xiaoyue Li, for their efficiency in ensuring the smooth organization of the conference.



Taylor & Francis

Taylor & Francis Group

<http://taylorandfrancis.com>

Editor biographies

Professor Wanhuan ZHOU currently serves as the Associate Dean of Faculty of Science and Technology and the Head of Department of Civil and Environmental Engineering at University of Macau. She is a core member of the State Key Laboratory of Internet of Things for Smart City, the Vice Director of the Macau Association for Geotechnical Engineering, and a board member in several international geotechnical organizations and societies. Her research mainly focuses on intelligent deformation analysis and monitoring in geotechnical engineering, multiscale modeling of geotechnical materials, and advanced laboratory and field testing. She currently serves as the Associate Editor of the International Journal of Geomechanics and as an editorial board member for several international geotechnical engineering journals such as *Biogeotechnics*, *Transportation Geotechnics*, and *Canadian Geotechnical Journal*. Prof. Zhou has published over 100 papers in top international journals and conferences. She has led more than 10 research projects, funded by the National Natural Science Foundation of China (NSFC), the Department of Science and Technology of Guangdong Province, and the Science and Technology Development Fund (FDCT) of Macau SAR. In 2022 and 2023, she was in the World's Top 2% Scientist of the Civil Engineering discipline-Stanford University Releases List (Career).

Dr. Zheng Guan is a research assistant professor at the University of Macau and a Registered Geotechnical and Structural Engineer in China, with over 5 years of engineering experience in geotechnical site characterization, geotechnical design, and geological hazard mitigation. He obtained his PhD at the City University of Hong Kong (CityU) in 2021, receiving the award for Best PhD Thesis in Geotechnical Studies 2021 from the Hong Kong Institution of Engineers (HKIE). His research interests focus on combining techniques in dimensionality reduction/transforms, sparse sensing, and machine learning for underground digitalization and reliability-based design in geotechnical engineering. He has published more than 20 papers in top international journals.

Dr. Xue Li is a postdoc fellow at the University of Macau. He obtained his PhD at the Sun Yat-sen University in 2022. His research interests focus on mechanical behavior of marine coral sand and soft soil, and the application of machine learning in geotechnical engineering.



Taylor & Francis

Taylor & Francis Group

<http://taylorandfrancis.com>

Fujita lecture



Taylor & Francis

Taylor & Francis Group

<http://taylorandfrancis.com>

Interactions at the front face of EPB shield when drilling in sand

A. Bezuijen

Ghent University, Ghent, Belgium

Bezuijen Consult, Berkel en Rodenrijs, The Netherlands

ABSTRACT: The construction of a tunnel with a tunnel boring machine (TBM) influences the soil in front of the TBM. Excess pore pressures are measured in front of the TBM, which influence the stability of the soil. The magnitude of these pressures depends among others on the soil layering, drilling velocity, permeability of the soil and the pressure in the mixing chamber. The pressure buildup when drilling starts and the decay when drilling stops depends on the plastering properties of the slurry or the foam mixture. This paper describes the interactions between the soil and an earth pressure balance shield (EPB) TBM when drilling in sand. It shows monitoring results and presents theory to describe the results from this monitoring in the field and from laboratory tests. Groundwater flow appears to be of importance on different scales: at the front face, in the foam-water-sand mixture and in the lamella between two foam bubbles.

1 INTRODUCTION

A TBM can drill in soft soil, because a pressure can be applied at the front face that counteracts the soil pressure at the depth of the tunnel and creates a stable soil mass around the tunnel. In the excavation chamber of a TBM there is no effective stress in case of a slurry shield and often hardly any effective stress in case of an EPB (Earth Pressure Balance) shield (Bezuijen et al. 2005). This means that somewhere between the excavation chamber and the soil the pore water pressure that exists in the excavation chamber is transferred to an effective stress in the soil. The two extreme situations for this are: 1) the filter cake forms an ‘impermeable’ layer between the excavation chamber and the soil, the pore water pressure ‘pushes’ against this layer and excess pore water pressure is by this layer transferred to an effective stress. 2) There is no impermeable layer and the water from the excavation chamber flows into the soil. Due to the groundwater flow, the pore water pressure gradually decreases further away from the tunnel and consequently, the effective stress increases. Later in this paper it will be explained when these extremes can be expected and when there is an in between situation, with some pressure transfer at the tunnel face and some in the soil.

Broere (2001) and Bezuijen et al. (2001) have shown that the way the pore pressure from the excavation chamber is transferred to the effective stress in the soil influences the pressure needed to achieve a stable front face. Furthermore, infiltration of foam and bentonite slurry into the soil influences the stability of the front when air pressure is applied. Laboratory tests on slurry and foam infiltration (Talmon et al. 2013; Xu et al. 2019; Zheng et al. 2021; Qin et al. 2023) have increased our understanding of the plastering process. These tests are normally conducted using saturated sand.

The paper starts with a chapter describing the pore pressures in front of a EPB TBM measured in field tests at the Botlek Rail Tunnel. Although the tunnel is constructed more than 20 years ago, some measurements are still unique and worth addressing. The following chapter will describe different laboratory tests and present some theory to analyse these laboratory tests. After that it is analysed what the consequences are for TBM tunneling with and EPB shield. The paper ends with conclusions.

2 PORE PRESSURES IN FRONT OF A TBM

2.1 Theory

A TBM is a large object that moves through the soil when drilling with at the front face a more or less constant pore pressure created by the slurry pressure in a slurry shield or the muck at the face in an EPB shield. Penetration of the slurry or foam into saturated soil is only possible when the removal of pore water in front of the slurry goes as fast as the drilling velocity of the TBM. If this is not the case, the impermeable layer in front of the TBM (caused by penetrating slurry or penetrating foam) cannot move with the same pace as the TBM and will be destroyed during the cutting process. This will lead to excess pore pressures in the soil in front of the TBM. Measurements have shown that this is regularly the case. Measurements were performed for a slurry shield (Bezuijen et al., 2001) and analytical and numerical calculation models have been derived depending on the flow pattern around the TBM (Broere, 2001, Bezuijen 2002; Aime et al.2004, Bezuijen & Xu. 2018, Xu & Bezuijen, 2018). The analytical model, describing the piezometric head in front of a TBM at the tunnel axis when drilling in saturated sand (Bezuijen, 2002) in an unconfined aquifer will be used here:

$$\varphi = \varphi_0 \left(\sqrt{(1 + (x/R)^2} - x/R \right) \quad (1)$$

With φ the piezometric head x m in front of the tunnel at the tunnel axis, φ_0 the piezometric head at the front face, and R the radius of the tunnel. This formula showed good agreement with measurements at the 2nd Heinenoord Tunnel (Bezuijen et al., 2001) for a slurry shield and numerical calculations (Zizka et al., 2018).

For an EPB there were point measurements (Hoefsloot, 2001) from the monitoring at the Botlek Rail Tunnel. Only recently, the time history plots of these measurements became available, Hoefsloot (2022) together with the measurement data from the TBM for the same rings (Joustra, 2022). Results are published by Zheng & Bezuijen (2023). As described by Bezuijen et al. (2016), using Eq. (1), the velocity of the pore water in front of a TBM (v_p) drilling in saturated soil in an unconfined aquifer can be written as:

$$v_p = \frac{k\varphi_0}{nR} \quad (2)$$

Where k is the permeability of the soil, φ_0 the piezometric head at the front face, n the porosity of the soil and R the radius of the tunnel. This formula is valid as long as the velocity (v_p) is smaller than the velocity of the TBM (v_{TBM}). In case $v_{TBM} < v_p$ according to Eq (2), the filter cake or foam layer will not be completely removed during drilling. In equilibrium, the filter cake will move into the soil with equal velocity as the TBM velocity. The piezometric head just in front of the filter cake, or foam layer in the soil (φ_1) will be:

$$\varphi_1 = \frac{nR}{k} v_{TBM} \quad (3)$$

The measurements of the Botlek Rail Tunnel in front of the TBM and in the mixing chamber of the TBM allow verification of these formulas.

2.2 Measurements Botlek Rail Tunnel

The geotechnical profile with the tunnel is shown in Figure 1. Pore pressure transducers (PPTs) were installed at the location of the axis of the tunnel. Consequently, they were ‘eaten’ and destroyed by the TBM during the drilling process. One PPT was installed at location Q1 in fine sand 8 m below mean sea level (MSL), with a d_{50} of 180 μm and a permeability of

between 1×10^{-5} and 3.5×10^{-5} m/s (Hoefsloot, 2001). The second pore pressure transducer was installed at 23 m below mean sea level, location Q4, just after the first river crossing of the tunnel in coarse sand with a d_{50} of 400 μm and a permeability of around 3×10^{-4} m/s. Drilling speed at location Q1 varied between 40 and 60 mm/min and for Q4 this was 20 – 40 mm/min. Both at Q1 and Q4 the ground surface was 5 m above MSL.

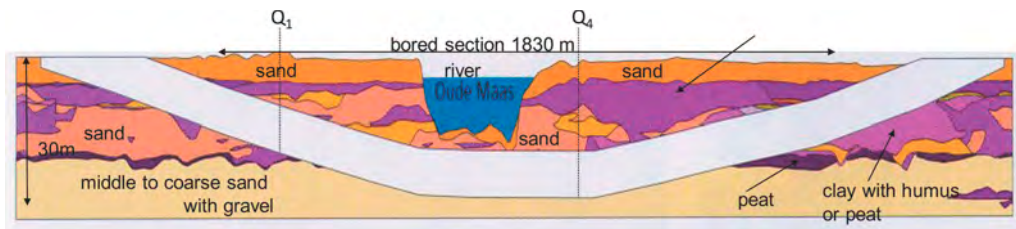


Figure 1. Geotechnical profile Botlek Rail Tunnel.

Foam was used to condition the soil during drilling. Apart from the PPTs in the soil, also the usual data, measured in the TBM, are available (more than 150 measurement channels).

Figure 2 compares the measurement results at Q1 with Eq. (1). The maxima in the measured pore pressure agree well with the theory. The minima in the measured pore pressure were measured during standstill when the foam (partly) blocks the groundwater flow. Both the maxima and minima in the plot have some variation. This is caused because tunnelling was performed in a tidal area.

The influence of the tidal variation was significant in location Q4. At this location the permeability was higher than the drilling velocity, leading to lower excess pore pressures. Furthermore, it is closer to the river, see Figure 1 and therefore, the influence of the tide is dominant in the results, see Figure 3. Correcting for the influence of the tide resulted in a line that has some resemblance to the theoretical curve, but less agreement as shown in Figure 2, see Figure 4.

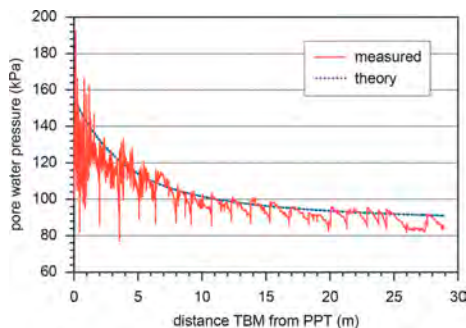


Figure 2. Measured pore pressure compared with theory.

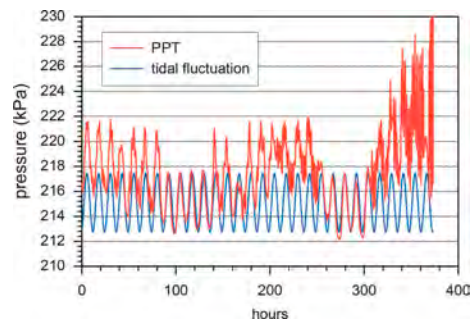


Figure 3. Q4, measured pore pressure (red line) and assumed influence of the tidal fluctuation (blue line).

Of interest is now the relation between the pore pressure in front of the TBM and the pressures measured inside the TBM. For Q1 this is shown in Figure 5, together with the drilling velocity. The time registration shown is during the last rings before the pore pressure gauge in the soil is destroyed by the TBM. In location Q1, the drilling velocity is larger than the pore water velocity (see Zheng & Bezuijen, 2023) and consequently the pore water pressure in the soil is, according to Eq. (2), determined by φ_0 , the pore pressure in the excavation chamber. Figure 5 shows that this is the case. The pore pressure in front of the TBM (PPT) follows during drilling, when the drilling velocity is larger than 0 mm/min, the same course as E1 and

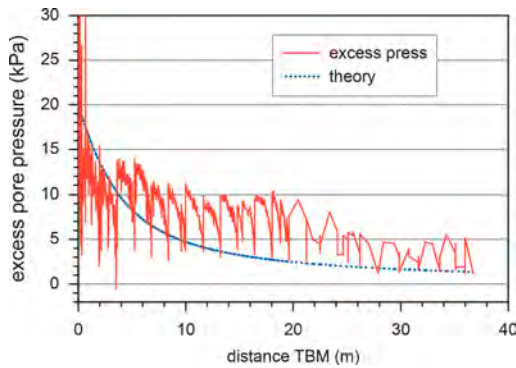


Figure 4. Q4, measured pre pressure compared with theory.

W1. During standstill there are deviations. Since then the foam will penetrate into the sand and make an less permeable layer. In the next drilling phase, the results of the PPT come again in line with the pressure gauges in the excavation chamber until it is destroyed.

In Q4, the drilling velocity is lower than the pore water velocity calculated with Eq. (2) and Eq. (3) is valid. Consequently, the excess pore water pressure is much lower than what is measured in Q1. During drilling the pore pressure should, according to Eq. (3) follow the same line as the drilling velocity. The comparison is shown in

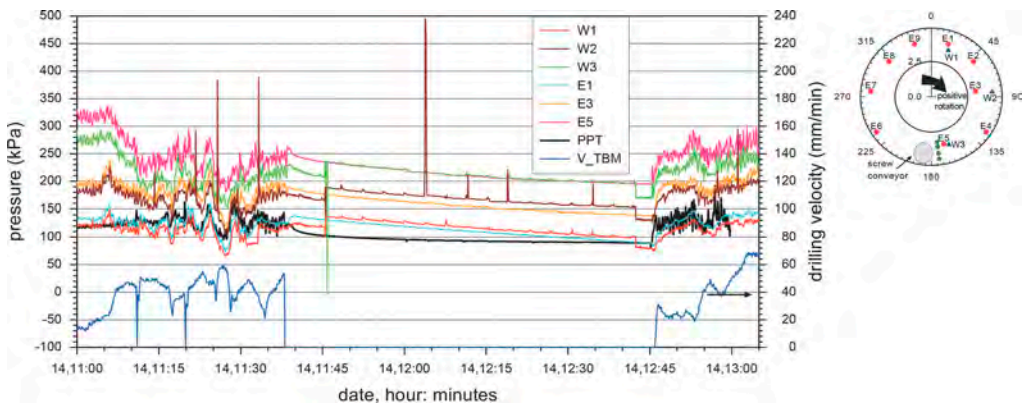


Figure 5. Q1, comparison of measured pore pressure in the soil with pressures at TBM and drilling velocity. The circle right shows the position of the gauges in the pressure bulkhead looking from the tunnel to the tunnel front.

Figure 6. Also here, for the last rings before the destruction of the PPT by the TBM. Clear is that, in agreement with theory, the PPT does not follow the pressure gauges in the excavation chamber. However, the course of the drilling velocity is also not followed precisely. Likely, the infiltration of the foam into the soil in front of the tunnel face goes with the velocity that is the average velocity of the TBM. The type of pressure gauges in the excavation chamber, located at the pressure bulkhead are indicated in the circle right of the plot. The blue triangles represent pore water pressure measurements and the red dots total pressure measurements. Both Figure 5 and Figure 6 show sometimes spikes in the data, especially the pressure gauge W1 that gives the porewater pressure in the top of the excavation chamber in Figure 5. This is caused by an automatic cleaning system (a small jet) that created pressure peaks that should be ignored.

Remarkable is the decrease in pore pressure in the excavation chamber as measured with the pore pressure gauge W1 during drilling. Probably the opening of the valve at the end of the screw conveyor leads to additional ground water flow in the screw conveyer. It is not caused by a groundwater flow through a possible permeable foam layer, as will be elucidated in the next section. Consequence it that there is an effective stress of a 30 kPa in the excavation chamber. This was not found by the less permeable sand during the measurements in Q1 and also not for other rings (Bezuijen et al. 2005).

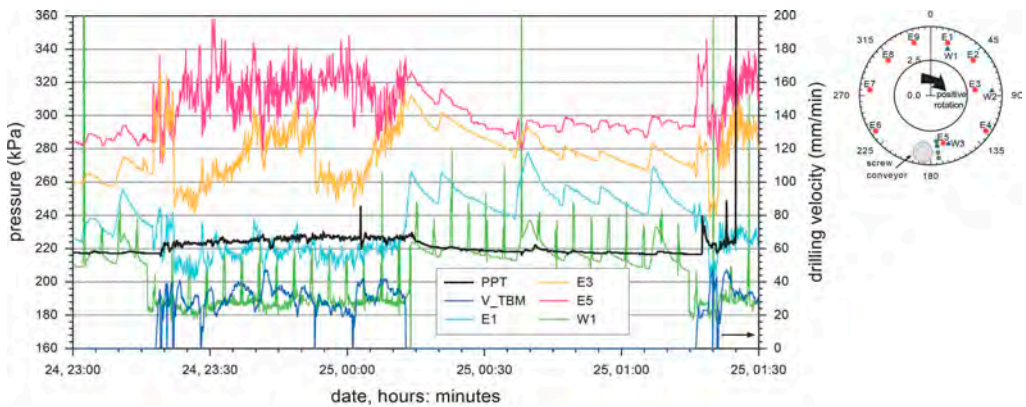


Figure 6. Q4, comparison of measured pore pressure in the soil, with pressures at TBM and drilling velocity.

2.3 Consequences

Eq. (3) is valid for the measurements in Q4. This is elaborated for the rings that were constructed when the TBM was approximately 5.5 to 3.5 m before the PPT in the ground, see Figure 7.

The porosity in the sand is according to COB: K300-W-0055 equal to 0.38. The average tunnel velocity during drilling, see Figure 6, is 20 mm/min thus 0.33 mm/s. The pressure increase as measured with the PPT 3.6 m in front of the tunnel face during drilling is around 10 kPa or approximately 1 m in piezometric head difference. The radius of the tunnel is 5 m. Eq. (1) can be used to calculate the piezometric head just in front of the less permeable layer created by foam that infiltrated into the sand, resulting in a piezometric head of 1.95 m. With Eq. (3) this leads to an average permeability of 3.24×10^{-4} m/s. This value is close to value for the permeability measured during the soil investigation 3×10^{-4} m/s. Indicating that Eq. (3), although derived for a slurry shield, is also valid for an EBP shield. It should be noted that the piezometric head in the excavation chamber is not used to derive the permeability of the soil, only the drilling velocity, the measured piezometric head and the assumption that the porewater velocity is equal to the drilling velocity.

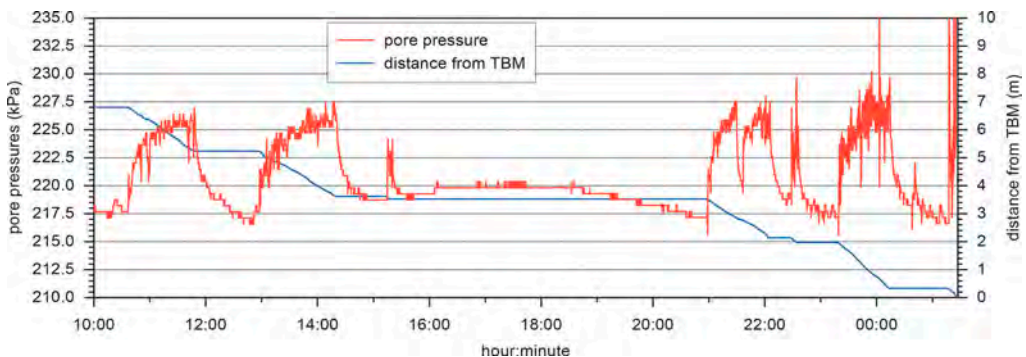


Figure 7. Q4, measured excess pore water pressure and distance of PPT from TBM.

It is also possible to derive from the measurements how far the foam front and the pore-water from the excavation chamber penetrated into the soil during ring building when drilling has stopped. This is of importance because a thicker layer of foam that has penetrated into the sand in front of the TBM indicates a more stable foam layer. To calculate the penetration

of the foam and pore water for Q4, Figure 7 can be used. The figure shows that a bit before 11:00 the drilling for a ring has started. At the end of this drilling, just before 12:00, the excess pore water is more or less constant and 9 kPa higher than the lowest pressure that is measured around 13:00. The moving of the foam front with the velocity of the TBM of 0.33 mm/s results in an excess pore pressure of around 9 kPa. Since this excess pore pressure is caused by the groundwater flow in the soil before the foam front, there is a linear relation between flow and excess pore pressure. Thus an excess pore water pressure of 4.5 kPa corresponds with a movement of the slurry front of 0.165 mm/s. Using the excess pore water pressure as measured from the end of drilling before 12:00 until the drilling of the next ring just before 13:00, the velocity of the foam front can be calculated:

$$v_{foam} = 0.33 \times p(t)/p_i \quad (4)$$

With $p(t)$ the measured excess pressure and p_i the pressure at the moment that drilling stops. Integration results in the movement of the foam front in time, see Figure 10, the red line. The result shows that for this permeable sand there is quite some penetration of the foam into the sand. However, the result gives the movement of the foam and the water in the foam. As shown by Zheng (2021), the infiltrated foam has a certain permeability and when the foam stops moving, the water in the foam can still flow from the excavation chamber into the soil. To get an impression of the foam layer only, another procedure can be followed. During ring building, the foam has penetrated into the soil, as described above. When drilling starts this layer of penetrated foam will be dug away and due to the pressure applied by the TBM the foam will start to move further into the soil. The excess pore water pressure in front of this penetrating foam will again be a linear relation with the penetration velocity. However, since during drilling the pore water pressure W2 at the depth of the tunnel axis is comparable with the pore water pressures measured with the PPT in the soil, see Figure 6, now there will be hardly any pore water penetrating from the foam into the soil. The same procedure can be followed as described before when drilling stopped. However, there is one slight complication. When drilling has stopped there is a constant distance between the TBM and the PPT. During drilling that is not the case. Therefore Eq. (1) was used to calculate the piezometric head close to the TBM from the measured piezometric head during drilling from 13:00 to approximately 14:30. This correction has a significant influence on the piezometric head, see Figure 9.

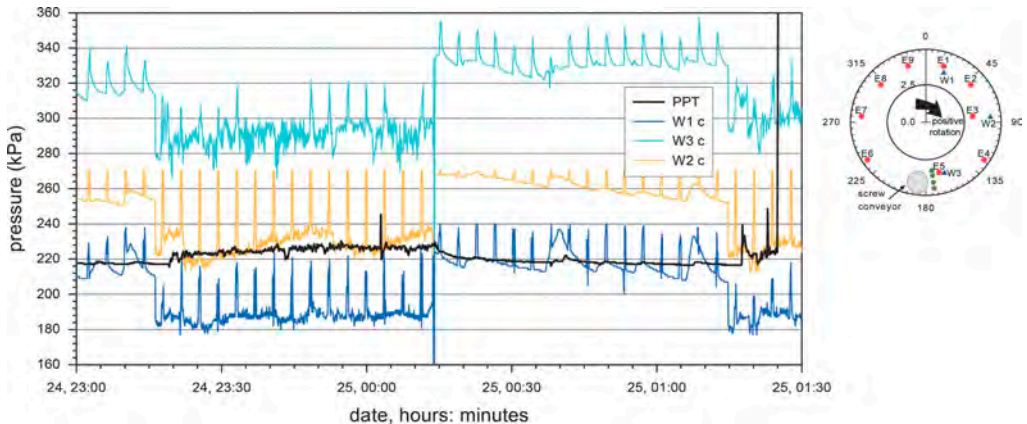


Figure 8. Q4, pore pressures measured in the excavation chamber and in the soil. The peaks in the pressures of the excavation chamber are reduced to see better the course of the pore water pressure. It can be seen that at the tunnel axis the pressure of the PPT during drilling nearly equals W2.

The calculated penetration of the foam is shown in Figure 10. It appears that both methods resulted in a comparable foam thickness of around 0.25 m, indicating that the permeability of

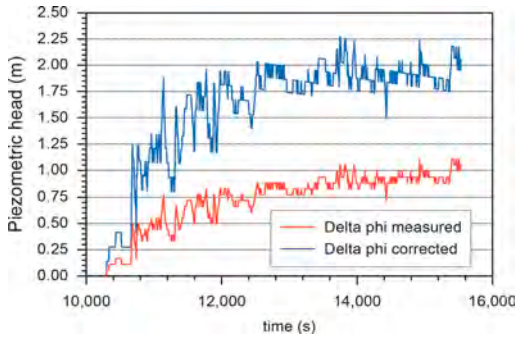


Figure 9. Q4, measured piezometric head and corrected calculated head close to the TBM, using Eq. (1).

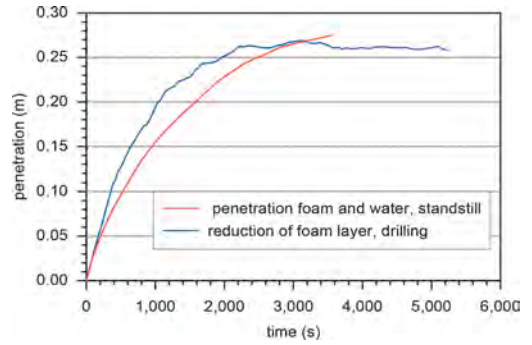


Figure 10. Q4. Foam layer penetrated into sand in front of the TBM. Two different calculation methods, see text.

the foam-sand mixture for water is relatively low. After the drilling, that stops at around 14:20, the stop is only short before there is some further drilling at 15:15. During this short stop the ‘foam cake’ cannot come to the final value. Consequently, the pressure increase when the final drilling starts as 15:15 is much steeper than when the drilling starts at 13:00. Also Q1 results in a steeper pressure rise when drilling starts. See Figure 5 just after the 14th at 12:45. This drilling is performed in finer sand with will result in less penetration of the sand by the foam (Zheng 2021).

3 FOAM PROPERTIES

3.1 Important foam properties

What properties are important for foam as used in an EPB shield. Important properties will be listed here and further elaborated in the following sections of this chapter:

- Create volume. The porosity of the sand has to be increased by the foam to allow the cutting wheel to dig away the soil with reasonable torque.
- Foam should be stable. When foam bubbles collapse, the air is still entrapped into the soil, but air can be collected in the top of the excavation chamber or even escape to the surface. Therefore, it is of importance that the bubbles remain small and equally distributed.

The requirement of stable foam leads to other requirements for its properties:

- the foaming agent must have a low surface tension. It will be explained later that a low surface tension is required for a stable foam.
- low permeability of the lamella between the foam bubbles.
- low permeability in front of the tunnel face.

3.2 Create volume

The sand in front of the TBM will have a certain porosity (n_s). For the TBM to run smoothly a larger porosity in the muck will normally be necessary (n_m). This last porosity is normally on average a bit higher than the maximum porosity of the sand. This means that a relative volume increase $\Delta V/V$ is necessary. From continuity it can be derived that the foam injection ratio (FIR) is:

$$\frac{\Delta V}{V} = FIR = \frac{n_m - n_s}{1 - n_m} \quad (5)$$

To increase, for example, the volume of the muck from a porosity of 40% to 50%, a volume increase of 20% will be necessary, thus the minimum FIR is in that case 20%. However, this is the minimum FIR. In reality the value will be larger. The excess pore water pressure in the mixing chamber will partly remove the pore water at the tunnel face. This will result in a larger FIR. For the situation where the groundwater flow can be described with Eq. (1), the necessary FIR can be calculated with (Bezuijen, 2012):

$$FIR = \frac{k\varphi_0}{v_{TBM}R} + \frac{n_m - n_s}{1 - n_m} \quad (6)$$

In case all the pore water is replaced by foam, because the pore water velocity and thus the foam penetration velocity is equal to the TBM velocity, see also Section 2.1, this equation simplifies to:

$$FIR = \frac{n_m(1 - n_s)}{1 - n_m} \quad (7)$$

The necessary FIR is therefore dependent on the permeability of the soil and the necessary porosity increase.

The influence of the permeability on the necessary FIR, according to these formulas is quite significant. In case the porosity has to be increased from, for example, 40% to 50%. Such an increase will need, as mentioned above, a FIR of 20% in case Eq. (5) is valid, and a FIR of 60% in case of a permeable soil and Eq. (7) has to be used. Consequence is, for the locations Q1 and Q4 for the Botlek Rail Tunnel, see Chapter 2, that the Q4 needs 3 times more foam than Q1.

The theory mentioned above is probably only theory for most of the people involved in tunnelling on the jobsite. As far as I know, they do not make calculations with the Equations (5) to (7). Normally slump tests (Peila et al., 2009; Budach and Thewes, 2015) are performed with different amounts of foam and the result of that slump test determines the FIR to be used. This works reasonably well in most cases and therefore it may be of interest to investigate why.

In case of a saturated low permeable soil, the soil sample will contain most of the original pore water and the necessary FIR can be calculated with Eq. (5). Both in the slump test and in-situ, the pore water will be available, thus the amount of foam that will lead to a good slump value (between 15 and 18 cm) will also be reasonable for the drilling. In case of a permeable sand sample, most of the water will be drained out of the sample and Eq. (7) is valid. Now the situation will be drained for both the slump test and for the in-situ field conditions. In dry soil there is no pore water and also Eq. (7) is valid.

In the situations described above, the slump test can be adequate. This may not be the case for situations with an intermediate permeability or with a large tunnel diameter, see Eq.(6). For these situations, it has to be checked whether the conditions during the slump test are comparable to the in-situ conditions.

Furthermore, the pressure will not be constant at the tunnel face, but higher at the invert compared to the top of the tunnel. Since most of the foam consists of air, it will be compressed at higher pressures and again more foam is necessary to have a minimum porosity at the invert. Measurements (Bezuijen et al., 2005) have shown that normally the porosity of the sand at the invert is comparable to the maximum porosity and the porosity is higher than the maximum porosity when measured more to the top of the tunnel. This influence of the height will increase for larger diameter tunnels.

3.3 Stability of foam

The stability of the foam used in EPB TBM projects is normally measured with the half-life time (*hlt*) test, see Figure 11. 80 g of foam is put in a container with a filter paper and



Figure 11. Sketch half-life time test foam. (Sposetti, 2023).

perforated plate of a synthetic fleece at the bottom and the water that flows through the bottom is collected. The time it takes to collect 40 g of water is the half-life time. Chen (2024) has shown that this test is not very well defined (EFNARC, 2005), since the results are influenced by the height of the sample that is not prescribed, but the test gives an indication of the stability of the foam. In the test the stability of pure foam is measured. This stability can be quite different from the stability of a foam-sand mixture. The stability of a foam-sand mixture can be much higher or lower than the stability, as measured with the hlt for a pure foam mixture. From a theoretical point of view, the hlt can be seen as a permeability test for water through foam. When the water flows out through the fleece or through a filter paper on a perforated plate, the pressure is equal to the atmospheric pressure at the top and the bottom of the foam. This means that the hydraulic gradient in the water is 1 and the filter velocity of the water through the foam will be equal to the permeability of the foam. The results of hlt tests

showed that this permeability is more or less constant until the hlt is reached. For longer times, the filter velocity decreases, because the lamella between the foam bubbles become thinner as a result of the water loss. A permeability test with a hydraulic gradient $i=1$ results in a filter velocity (q) equal to the permeability k . The total discharge is equal to $q \cdot A$ with A the cross-sectional area of the foam container. Therefore, a container with a larger diameter and thus larger cross-sectional area will result in a larger discharge, thus a shorter hlt .

Chen (2024) performed hlt tests not only for pure foam but also for foam-water-sand mixtures with a different FIR and foam injection ratio (FER) and different concentrations of foaming agent. Here only the results of different FIR and FER will be discussed for the usual situation of 3% foaming agent. The tests are performed in a cylinder with a diameter of 0.13 m and a height of 0.1 m. The results are presented in Figure 12.

The results show that the drainage weight after a certain time decreases significantly for pure foam when the FER is changed from 10 to 20. For foam-water-sand mixtures the difference is much smaller. In general the discharge is larger for the mixtures than for the pure foam. To understand the results, some more parameters are necessary. The sand is first fully saturated with a water content (w_c) of 0.25 and then foam is added to achieve the required

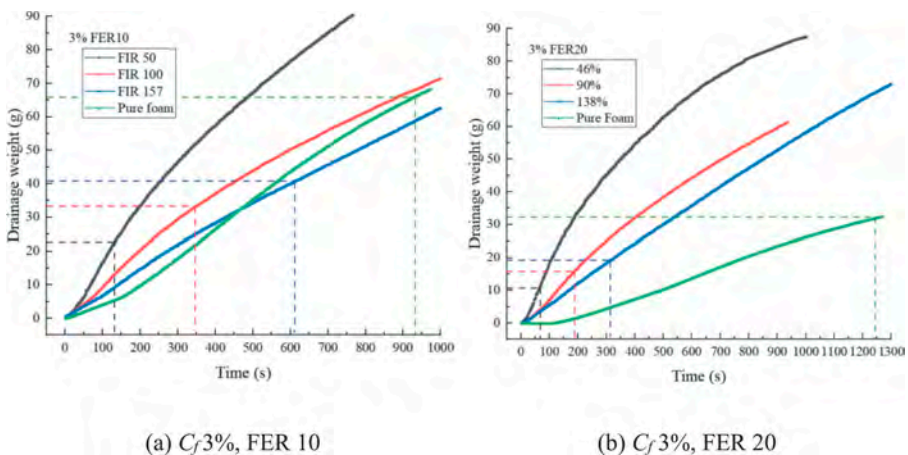


Figure 12. Half-life time tests on foam-sand mixtures for different values of FER. C_f is the concentration of foaming agent (Chen, 2024). The dashed lines indicate the hlt but are not used in the paper.

FIR. For $FER=10$, the black line of the left plot, the porosity of the mixture 60% and the density of the mixture is 1300 kg/m^3 .

The porosity is higher than the maximum porosity of the sand (48%). This means that there is no effective stress in the sample, the total pressure is equal to the pore water pressure. At the beginning of the test the hydraulic gradient will be a bit less than 13 kN/m^2 . When the water can flow through the fleece or filter paper the porosity at the bottom of the foam-water-sand sample will decrease until effective stresses develop in the sand skeleton. After the development of the effective stresses, the test is again a permeability test with a hydraulic gradient of 1, but now through a foam-water-sand mixture.

The results of Chen (2024), see Figure 12, show that when the foam is mixed with saturated sand, the influence of the original FER is limited. The FER of the mixture (FER_m , using the water in the foam + pore water), as defined by Bezuijen (2012) is dominant:

$$FER_m = \frac{n_s - \alpha + FIR}{n_s - \alpha + FIR/FER} \quad (8)$$

In this equation is α the amount of water that is expelled in a field situation due to the excess pressure in the TBM. In this test situation α is zero. The FER of the mixture is only 2 for $FIR = 50\%$ and 3.5 for $FIR = 157\%$. This means that the foam is very 'wet' in all conditions and thus that the permeability of the foam-water-sand mixture is higher than for pure foam with a FER of 10 and 20 respectively. The somewhat higher FER_m for tests with a higher FIR resulted in a lower discharge. Since the difference in FER_m is limited for the tests with a $FER = 10$ and $FER = 20$, the discharge is quite comparable for the foam-water-sand mixtures. For the pure foam the FER does change with a factor of two, resulting in a significant change in discharge (the green line in the plots of Figure 12).

It should be noted that the hlt also depends to a large extent on the boundary conditions. The influence of the diameter was already mentioned, an outflow at the bottom of the container has a significant influence for tests on foam-water-sand mixtures. A hlt test on pure foam can also be performed in a cylinder glass with a closed bottom. 80g foam is poured into the cylinder glass. The hlt is then the time it takes before 40 cc of water (=40 g) is present at the bottom of the cylinder. When foam with a FER of 10 is used, the total pressure at the bottom of the container is then $1 \cdot h \text{ kPa}$, with h the foam height in the container in meters. The effective stress between the foam bubbles cannot be less than zero and this means that the pore pressure at the bottom equals also $1 \times h \text{ kPa}$. This is not a stable static situation, because without flow the pore pressure at the bottom should be $10 \times h \text{ kPa}$ because of the density of the water. This situation can only exist when the bubbles are pushed upwards and the downward directed hydraulic gradient is 0.9. Thus for a FER of 10 in a cylinder glass, the bubbles move upwards and the hydraulic gradient is 0.9. This is close to the hydraulic gradient of 1 for the test setup of Figure 11. Performing this 'cylinder glass' test with a foam-water-sand mixture results in a different outcome. For a FER of 10, a FIR of 50% and an original porosity of 0.4, the specific weight is 13 kN/m^3 . This means that there is in that case an upward directed hydraulic gradient of 0.3 and there will be a water flow to the top of the mixture. The foam bubbles cannot 'escape' from the sand skeleton and as a consequence the mixture is very stable. Experiments (Bezuijen et al., 1999) have shown that this can be stable for days.

3.4 Surface tension of foam

The surface tension determines whether or not a foam can be created. Water has a surface tension of around 72.8 mN/m at $20 \text{ }^\circ\text{C}$ and this is too large to make a stable foam. A commercial foaming agent solution has a surface tension of less than 25 mN/m . The surface tension influences the half-life time of the foam and the behavior of the muck, as will be explained below.

3.4.1 Surface tension and half-life time

The surface tension γ_s , the pressure over the surface of a bubble p and the curvature of the surface influence the pore water pressure according to the following relation:

$$p = \frac{2\gamma_s}{r} \quad (9)$$

Where r is the radius of the curvature. Figure 13 shows that the radius of the curvature at the lamella is larger than at the locations where three lamella meet. Since the pressure in the air bubble is constant, Eq. (9) implies that the pore water pressure at the locations where the lamella meet is lower than in the middle of the lamella. Since water will flow from high pressure to low pressure, there will be a water flow from the middle of the lamella to the corners and the lamella will become thinner.

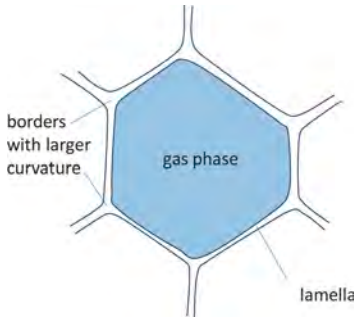


Figure 13. Sketch foam bubble and lamella.

However, this flow is counteracted by the limited permeability of the thin lamella, and by osmotic and electrical forces and most significant by the Marangoni effect (Su Nee et al. 2005). The Marangoni effect is the attraction of liquids to place with a high surface tension. A disturbance in a lamella will lead to temporarily less surfactants on that disturbance and locally a higher surface tension. This causes water to flow in the lamella to the disturbed area, stabilizing the lamella. In any case, Eq. (9) shows that the pressure difference will be smaller when the surface tension is smaller and thus the stability will be higher.

Foam with a relatively large hlt therefore needs:

- A low surface tension of the foaming liquid.
- An increase in surface tension when the lamella are disturbed to have stable lamella.
- Low hydraulic conductivity in the lamella, this can be achieved by polymers or bentonite particles.
- A foam gun that makes bubbles with a constant diameter. An other consequence of Eq. (9) is that the pressure in small bubbles is higher than the pressure in larger bubbles. Due to diffusion of the air through the liquid the small bubbles with high pressure will disappear. The influence of this effect is small when all bubbles have more or less the same diameter.

3.4.2 Influence on muck properties

The influence of the surface tension on the muck properties can be explained using the slump test. In a slump test, a mold, a truncated cone with a height of 0.3 m, an upper diameter of 0.1 m and a bottom diameter of 0.2 m is filled with muck, the mold is removed and the settlement of the muck is measured. The settlement of the top in centimeters is called the slump value. This should be between 15 and 20 cm. Furthermore, the water loss in the muck should be limited. When a test is performed with fine or medium coarse sand, the result will depend on the saturation degree. A cone of fully saturated sand will collapse, because the slopes of the cone are too steep for a stable situation and the slump value will be too high. In case unsaturated sand is used, the capillary pressure in the sand will prevent deformation of the cone, since it creates an effective stress in the sand.

In case foam is added, the capillary pressure will be less, because the surface tension in the foaming agent is only 1/3 of the surface tension of water and thus the maximum capillary pressure of the sample with foam is approximately only 1/3 of the capillary pressure when only water is used. Consequently the sand cone can deform until equilibrium is obtained. The foam also reduces the permeability, lowering water loss. The foam between the sand grains lowers the friction angle (Chen, 2024) and allows volume changes without water flow. When the porosity is higher than the maximum porosity the friction decreases considerably (Bezuijen et al., 1999, Chen, 2024).

3.5 Consequences for an EBP in the field

The *hlt* experiments of Chen (2024) with foam-sand mixtures prove that the FER_m is an important parameter. Variations in the original FER have hardly an influence on the discharge, but variations in the FER_m do have a significant influence.

The muck in the mixing chamber will also dewater through the cutting wheel. In case of a mixture with a low FER_m , the pore water flow can be significantly, leading to pressure losses in the mixing chamber. These pressure losses have been described by Dias and Bezuijen (2017). The relatively wet foam in the mixing chamber prevents the build-up of an impermeable ‘filter cake’ as can be expected for a slurry TBM. This was also found by Zheng (2021) in pressure filtration tests with foam-water-sand mixtures. The pressures in the excavation chamber as shown in Figure 6 when tunnelling in permeable sand, Section Q4, show that the total pressure gauges during standstill regularly have a steep rise and a slower decrease afterwards. This is caused by water flow from the excavation chamber to the soil. The pressure in the excavation chamber should always be higher than the pore pressure in the soil to achieve a stable tunnel face. To keep the pressure in the excavation chamber sufficiently high, regularly small quantities of foam are injected, causing the steep rise. In the less permeable Q1 section this appeared not to be necessary, see Figure 5. These foam injections lead to a decrease in the density of the muck, since in a normal situation water flows out of the excavation chamber and this is replaced by foam.

4 CONCLUSIONS

The monitoring results shown in this study have confirmed the influence of the drilling velocity, tunnel diameter and permeability on the excess pore water pressure in front of the tunnel. The analytical calculation for an unconfined aquifer has been validated for a slurry shield (Bezuijen et al., 2016), and an EPB shield (Zheng & Bezuijen, 2023). The permeability of a filter cake made of bentonite slurry can be very low (Xu, 2018). Such very low permeability was not measured for the foam infiltrated sand in tests simulating the front of an EPB excavation chamber filled with muck (Zheng, 2021). Consequently there is some pressure loss during standstill. The monitoring of the pressures with a PPT in front of the TBM allows to estimate the thickness of the foam infiltrated zone in the sand just in front of the tunnel during standstill.

It is shown that for EPB tunnelling in sand volume and thus porosity increase is an important property of the foam. The amount of foam necessary to achieve the required volume increase can differ a factor of 3, depending on the factor $k\varphi_0/(v_{TBM}R)$. Less foam is needed if this factor is low, the maximum amount of foam is needed when this factor equals or exceeds the porosity n of the soil.

The half-life time test for foam appears to be quite comparable to a standard permeability test. As Chen (2024) has shown, the description of the test setup has to be refined to have comparable results from different laboratories. The test performed with a foam-water-sand mixture shows that the influence of the FER_m on the results is larger than the influence of the original FER .

Up to now the slump test is seen as an empirical test. This paper mentions a more physical explanation for some aspects of this test and shows the limitations of the test. Further research will be needed to quantify this further.

REFERENCES

- Aime R, Aristaghes P, Autuori P. and S.Minec. 2004. 15 m Diameter Tunneling under Netherlands Polders, *Proc. Underground Space for Sustainable Urban Development* (ITA Singapore), Elsevier.
- Bezuijen, A., Schaminée, P.E.L. Kleinjan, J.A. 1999. Additive testing for earth pressure balance shields. *Proc. 12th Eur. Conf. on Soil Mech. and Geotech. Engrg.*, Amsterdam, Balkema, Rotterdam,
- Bezuijen A., Pruiksmá J.P., Meerten H.H. van. 2001. Pore pressures in front of tunnel, measurements, calculations and consequences for stability of tunnel face. *Proc. Symp. Mod. Tun. Science Techn.* Kyoto.

- Bezuijen A. 2002. The influence of soil permeability on the properties of a foam mixture in a TBM. 3rd. *Int. Symp. on Geotech. Aspects of Underground Construction in Soft Ground*, IS-Toulouse
- Bezuijen A, Talmon AM, Joustra JFW, Grote B. 2005. Pressure gradients and muck properties at the face of an EPB. In: 5th international symposium on geotechnical aspects of underground construction in soft ground - Rotterdam. pp 195–201
- Bezuijen, A. 2012. Foam used during EPB tunnelling in saturated sand, parameters determining foam consumption. *Proc. WTC 2012, Bangkok*, Thailand.
- Bezuijen, A., Steeneken, S.P. and Ruigrok, J.A.T. 2016. Monitoring and Analysing Pressures around a TBM. *Proc. 13th Int. Conf. Underground Construction Prague*, Prague, Czech Republic.
- Bezuijen, A. & Dias, T. G. S. 2017. EPB, chamber pressure dissipation during standstill. *Proc. IV Int. Conf. on Computational methods in tunneling and subsurface engineering*, Innsbruck.
- Bezuijen, A. & Xu T. 2018. Excess pore water pressures in front of a tunnel face when drilling in a semiconfined aquifer. *Proc. WTC 2018*, Dubai.
- Bezuijen, A. 2019. Keynote lecture: soil–water–tunnel interaction at the front face of a TBM. In Proceedings of 4th international conference on geotechnics for sustainable infrastructure development (eds D. L. Phung and D. Nguyen), pp. 207–220. Singapore: Springer.
- Broere W. 2001. *Tunnel Face Stability & New CPT Applications*. Ph.D. thesis, Delft University of Technology, Delft University Press.
- Budach, C. & Thewes, M. 2015. Application ranges of EPB shields in coarse ground based on laboratory research. *Tunnelling and Underground Space Technology*, 50, 296–304.
- Chen, Z. 2024. *Soil conditioning with foam: from principle to application*. Ph.D. thesis. Ghent University, Belgium
- COB report. 1999. COB: K300-W-0055 K300 Geotechnical base paper set.
- EFNARC. 2005. *Specification and guidelines for the use of specialist products for soft ground tunnelling*. European Federation for Specialist Construction Chemicals and Concrete Systems, Surry, UK.
- Hoefsloot, F.J.M. 2001. Pore pressures in front of the bore front: A simple hydrological model (in Dutch). *Geotechniek*, October. pp. 26–33.
- Hoefsloot, F.J.M. 2023. Private communication.
- Joustra. J.F.W. 2023. Private communication.
- Peila, D., Oggeri, C., & Borio, L. 2009. Using the slump test to assess the behavior of conditioned soil for EPB tunneling. *Environmental & Engineering Geoscience*, 15(3), 167–174.
- Qin S, Cheng Y, Huang H, Zhou W.H. 2023. *State-of-the-art review on pressure infiltration behavior of bentonite slurry into saturated sand for TBM tunneling*. Smart Construction and Sustainable Cities. <https://doi.org/10.1007/s44268-023-00018-yREV>.
- Sebastiani, D., Vilardi, G., Bavasso, I., Di Palma, L., & Miliziano, S. 2019. *Classification of foam and foaming products for EPB mechanized tunnelling based on half-life time*. *Tunnelling and Underground Space Technology*, 92, 103044.
- Su Nee, T., Fornasiero D., Rossen S., Ralston J., 2005. The role of surfactant structure on foam behaviour. *Colloids and Surfaces A: Physicochemical and Eng. Aspects Vol 263 Is 1-3*. August, pp 233–238
- Sposetti M.A. 2023. New technology of readily biodegradable soil conditioning foaming agents. *Expanding Underground. Knowledge and Passion to Make a Positive Impact on the World – Anagnostou, Benardos & Marinos (Eds) 1462–1469*.
- Talmon, A. M., Mastbergen, D. R. & Huisman, M. 2013. Invasion of pressurized clay suspensions into granular soil. *J. Porous Media* 16, No. 4, 351–365.
- Xu, T. 2018. *Infiltration and excess pore water pressures in front of a TBM, Experiments. Mechanisms and Computational models*, Ph.D. thesis. Ghent University, Belgium.
- Xu, T, Bezuijen, A. 2018. Analytical methods in predicting excess pore water pressure in front of slurry shield in saturated sandy ground. *Tunn Undergr Sp Tech*; 73:203–211. <https://doi.org/10.1016/j.tust.2017.12.011>.
- Xu, T, Bezuijen, A. 2019. Bentonite slurry infiltration into sand: Filter cake formation 512 under various conditions. *Geotechnique* 69(12):1095–1106. 513 <https://doi.org/10.1680/jgeot.18.P.094>.
- Zheng, D. 2021. *Tunnel Boring Machine Excavation Fluids: From Laboratory to Practice*. Ph.D. thesis. Ghent University, Belgium.
- Zheng, D., Bezuijen, A., Thewes, M. 2021. An experimental study on foam infiltration into saturated sand and its consequence for EPB shield tunneling. *Tunn. Undergr. Space Technol.* 111, 103878.
- Zheng D., Bezuijen, A. 2023. Pore pressure measurements in saturated sand in front of an approaching EPB and laboratory investigations. *Acta Geotechnica*. <https://doi.org/10.1007/s11440-023-02139-1>
- Zizka, Z., Schoesser, B., Thewes, M., Schanz, T. 2018. Slurry shield tunneling: new methodology for simplified prediction of increased pore pressures resulting from slurry infiltration at the tunnel face under cyclic excavation processes. *Int. J. Civil Eng.* 15 (4), 387ff.



Taylor & Francis

Taylor & Francis Group

<http://taylorandfrancis.com>

Keynote lecture



Taylor & Francis

Taylor & Francis Group

<http://taylorandfrancis.com>

Smart monitoring of tunnels

W. Broere

Geo-Engineering Section, Delft University of Technology, Delft, The Netherlands

ABSTRACT: Monitoring of tunnels has evolved beyond simple displacement monitoring at a limited number of locations in the tunnel. A multitude of sensor types is available nowadays, making it possible to monitor displacements and deformations as well as material degradation related processes continuously. Automated, online, data collection makes monitoring not only more available, but also allows for continuous monitoring of tunnel locations where in-person access difficult or impossible. The result is a rising number of monitoring applications, not only for construction safety and control or purely for research purposes, but also the long-term use in tunnel operational control and structural health assessment. The increased monitoring offers exciting possibilities in tunnel engineering, but also increases the need to define clearly the needs and purposes of the monitoring solutions before sensor installation.

1 INTRODUCTION

Monitoring of tunnels has evolved over the past decades. Traditionally, monitoring efforts were focused on either the construction phase to control construction processes, or the operational phase to assist with long term management of the tunnel assets, or specifically designed for (often short-term) research projects with specific research goals in mind. The focus and purpose of the monitoring in these different phases can be quite different (Bakker, 2000, van der Poel et al., 2005).

During the construction phase, the focus is quite often limited to short-term deformation monitoring and stability control of the construction processes, with safety during construction and limiting the impact of construction on the surroundings as primary aspects that are be considered. For bored tunnels this could involve, for instance, hourly or daily monitoring of the lining convergence in the period just after lining installation, as well as surface settlement monitoring to assess the impact on existing nearby building (van Tol, 2005). Similar monitoring efforts would be appropriate for sequential excavation methods, where convergence measurements are used in optimising the quality and cost of the temporary lining and the timing of secondary lining installation. Typically, such monitoring efforts are ended once the tunnelling process has progressed sufficiently far beyond the measurement location that no further impact is expected. This point may well lay several tens of meters in space or days to weeks in time after the tunnel has passed a certain location. After that point, the frequency of monitoring is normally decreased or even completely halted (Broere & Festa, 2017).

For the operational phase of such tunnels, long term monitoring at surface is often absent and deformation and convergence measurements start once the tunnel has been completed and transferred to the owner. In most cases, the focus is on operational aspects, which may include visible cracks or leakages in the construction, but the operation and control of the tunnel installations normally gets more attention. Deformation monitoring will often be limited to a small number of monitoring points observed at yearly or multi-year intervals only, although full 3D scans are also increasingly employed (but still at multi-year intervals.) It is only rarely that the monitoring from the construction and operational phases are continuous and at similar locations, and the obtained data sets are often not considered in normal asset management (COB, 2022, 2024).

When monitoring is employed for research projects, this often results in a more extensive use of sensor types, at more detailed and denser sensor grids and higher monitoring

frequencies than would be used for construction control, and the overall monitoring period can be longer than those purely for construction control. But at the same time there are similarities as well in that the overall monitoring is often focused on the construction processes and ends before the operational phase of the tunnel. Again, there is often little connection made with data obtained during the operational phase and even research projects that study the behaviour of existing tunnel structures are often limited in duration.

Advances in sensor types and in data acquisition clearly widen the opportunities to monitor tunnel constructions over longer period and to integrate data from different sources and sensor types. This opens opportunities to study longer term deformation behaviour of tunnels, to study degradation process of the tunnel components or to aid owners in their asset management processes. This will also increase the need to specify what the relevance of possible monitoring solutions is. Below, we will provide an overview of many of the available sensor types for both deformation and degradation monitoring and some of the pitfalls that can be encountered when employing these sensors in actual tunnel projects.

2 SMART MONITORING

As introduced above, the purpose of the monitoring often determines the amount and the location of sensors, as well as monitoring intervals. In the recent past, monitoring during tunnel construction was focused on process control, stability during construction and limiting the impacts on surroundings (Kavvadas, 2005). This implied measuring deformations or pressures in the tunnel boring machine (TBM) or near the excavation phase as well as deformations at the surface, and many research projects studying tunnel construction essentially copied this monitoring strategy with a local denser monitoring campaign. Such research projects generated a significant amount of data in a limited time, and then stopped as construction finished. A reason not to continue such relatively intense monitoring campaigns, apart from cost, was the significant manpower needed for the data collection, processing and interpretation. With the advances in data logging, data communication and algorithm based data processing, this constraint is lessened. Algorithm based processing, sensor fusion and machine learning techniques, combined with automated graphical front-ends for less specialized end-users, now make continuous monitoring also feasible during the operational phase of a tunnel (Glab et al., 2021, 2024, Providakis et al., 2019).

That such novel or advanced monitoring options, sometimes referred to as smart monitoring, have become technically feasible opens up possibilities for extending monitoring during the operational phase and making more accurate structural health monitoring possible.

As an example, in immersed tunnelling, monitoring during the construction phase, and certainly during the immersion phase, can be quite intensive, but focuses on the stability and accurate positioning of the elements during immersion and the short term settlements of the immersed elements after backfilling, in order to assess the optimal time to install shear keys and finalize tunnel construction. Subsequent long term monitoring was often limited to vertical settlements of the tunnel elements obtained by manual leveling measurements of a number of settlement bolts near the tunnel joints at multi-year intervals. As these measurement bolts were only installed after final construction and delivery the tunnels, there was often a gap in time between the short-term settlement and the long-term monitoring. With many of the immersed tunnels, certainly in the Netherlands, getting to the point they are in need of extensive renovations and refurbishments, it becomes clear that the limited settlement monitoring, is not sufficient to accurately assess the structural state of the tunnels and to determine the scope of necessary renovation works. Both a lack of data and the disjoint between construction phase and operational phase have been shown as problematic (Atmakusuma, 2023).

In response, there is a drive to install additional sensors and start more detailed monitoring campaigns, but as budgets remain limited, this also prompted tunnel owners to assess whether the proposed monitoring solutions are SMART, as in the acronym for specific, measurable, achievable, relevant and time-bound. This led to an inventory of what monitoring is available, what sensor types exist, and how a monitoring campaign could be designed to, on one hand, generate sufficient data to help in the asset management and assessment of structural integrity

of the tunnel, and on the other hand generate long-term reliable data that is manageable for specialists and owners alike and will enable us to better predict future reliability and availability of the tunnel, and on the gripping hand remain cost-effective.

3 SENSOR TYPES

3.1 *Deformation monitoring*

The use of *measuring bolts* attached to the structure, from which the settlement of the tunnel is determined using manual precision levelling is probably the most common method to monitor tunnel deformations. Experience shows that measuring bolts can provide reliable results, but only a very limited measuring frequency is possible, as the tunnel needs to be partially or fully closed given that the measurement is mostly done manually. Other issues that exist with this method arise from the limited number of measurement bolts that is normally used, which combined with the low frequency, make it hard to separate periodic effects like seasonal or temperature induced deformations from long term deterioration related effects. Another issue is the often limited reliability of the ‘fixed’ reference points used to correlate subsequent measurement campaigns and the achievable overall accuracy, in the order of 5 to 10 millimeters, which is found not to be sufficient to assess the structural state of the tunnel when assessing the need for renovations in an asset management perspective (COB, 2022).

Even though measurement bolts have drawbacks, it is still recommended that they always be installed and maintained, as they can provide a baseline situation and can be used to combine data from different instruments or period together. The limited cost, structural stability, and the fact that they do not rely on a continuous power supply make them a good reference and backup system.

The use of *robotic total stations (RTS)* can increase the frequency of deformation monitoring. Systems using prisms at specific locations, or prism-free systems both have been employed. When prism are used as reference points there is a higher accuracy possible, in the order of 1 mm, and short-term interference with line of sight can be less problematic than with prism-free systems, but in most tunnels prisms need to be cleaned regularly. As the RTS requires line of sight to the monitoring point, in most tunnels multiple RTS will be needed, which makes the application less cost-effective (van der Poel et al., 2005).

An alternative to RTS is the use of *high resolution cameras* to determine the displacements and deformations of the tunnel. These cameras are more compact and cost-effective than RTS, but still need prisms as reference points to measure. Using automated photogrammetry algorithms, they obviously require line of sight and the achievable accuracy is somewhat lower than laser-based RTS can achieve. Achievable accuracies between 1 and 5 mm are currently listed (Sjölander et al., 2023).

Similar resolutions can be achieved using *3D laser scanning and camera based photogrammetry* systems moving through the tunnel (Lindenbergh et al., 2009). These systems can be vehicle or drone mounted, as to limit the need to fully close a tunnel for a scanning run, but the frequency of monitoring will remain limited. A benefit is the far denser measurement grid these systems provide, allowing the identification of moving or rotation structural elements within the tunnel structure without the need to place sensors at specific locations. Recent advances in automated image manipulation and machine learning allow the comparison between subsequent camera based photogrammetry runs, identifying structural defects at sub-millimeter resolution, although not necessarily providing deformation measurements at the same accuracy.

When higher resolutions for the deformation or displacement of the tunnel structure are needed, sensors at the monitoring location remain the preferred solution. Various *displacement sensors* exist, such as linear variable displacement transducers (LVDT), strain gauges, vibrating wire or laser distance sensors, that can measure the displacements between two fixed ends of the sensor at high accuracy and frequency. LVDT are most common and use a spring loaded pin to measure displacements between two fixed reference ends. Laser distance sensors use optic sensors to detect changes in reflection angle and allow for contact free measurements. Alternatively, magnetic based sensors exist that rely on the Hall effect to measure changes in a local magnetic field, but these require limited distance between the two fixed

reference points. All such sensor types excel in achievable accuracy, at sub-millimeter accuracy, and high monitoring frequencies, compared to measuring bolts and RTS, but they need constant power and provide data on a single location per instrument only (COB, 2022).

Similar constraints exist for *tilt meter* or *inclinometer* based systems. A tilt meter can provide precise angular deflections of a single monitoring point in the tunnel, but will not directly provide settlement data comparable to measuring bolts. Commercial tilt meters, based on MEMS accelerometers, can achieve the required $\mu\text{m}/\text{m}$ accuracy to be of use, and are available in very compact and battery powered models that make them easy to install. Multiple tilt meters and a structural model of the tunnel that translates tilt readings into deformations are needed to get comparable information to traditional measuring bolts, and the extent to which tilt meter results have comparable accuracy as traditional measurements depends highly on the overall accuracy of the assumed structural model.

Differential vertical deformations can be obtained using *liquid leveling systems*. These consist of several pressure sensors mounted to the structure and connected by both liquid line and an air compensation line. If a pressure sensor moves vertically, this will be registered as a pressure change. However, problems are sometimes reported due to drift in the system when the pressure sensors are not more or less horizontally in line to start with, or are subjected to temperature changes.

Accelerometers are primarily used to measure vibrations due to the tunnelling process, running stock during operations, or the impact of external events such as earthquakes. Modern accelerometers, often based on MEMS sensors, can be relatively small and accurate enough to capture tunnelling related processes. The transformation of accelerations to absolute displacements remains problematic, due to the double integration and the impact that measurement error have on the accuracy of the derived displacements.

3.2 Optical fiber based systems

Next to the more traditional use of point based sensors, in recent years there has been an uptake in the use of optical fiber based monitoring systems in tunnels, which offer the possibility of semi-distributed and distributed sensing (Zhang et al., 2024). Systems based on *Fibre Bragg Grating (FBG)* have been available commercially for some time. FBG are constructed by creating local variations in the refractive index of the fiber, such that specific wave lengths of light transmitted through the fiber is reflected at the location of the grating. Straining the fiber at that location will change the wave length the grating is sensitive to, allowing for localized strain measurements (Metje et al., 2006).

Multiple gratings with different refractive indices can be inscribed on a single fiber, allowing strain measurements at multiple locations within a single optical fiber. The number of measurement locations is limited by the accuracy and resolution of the optical analyzer used at the fiber end, but tens of distinct grating locations located in optical fibers of several hundred meters of length are nowadays possible. FBG are somewhat similar to traditional strain gauges, in the sense that only local strains are captured at a specific location in the fiber, but with the benefit that no electrical power is needed at each measurement location as the optical fiber is both the sensor and the optical signal carrier. FBG can capture small local strain at up to kHz frequencies well, but are limited in dealing with large local strains and deformations if the optical fiber is continuously bonded to the structure. Large local strains (roughly over 1% strain) can lead to fiber breakage. Therefore, continuously bonded optical fibers are not suited to monitor crack widths for example, where large deformations occur localized (Zhnag & Broere, 2022b). As a solution, FBG extensometers have been developed, where a short length (1 - 3 m) of FBG fiber is fixed at both ends and unbound between these ends.

More recently *distributed fiber optical sensing (DFOS)* has been used for tunnel monitoring (Gue et al, 2015, Zhang & Broere, 2023a, b). The term DFOS encompasses several related measuring principles, all dependent on the fact that irregularities of the microstructure of the optical fiber core will lead to variations of the refractive index of the fiber, and when light is transmitted through the fiber, a small part of the light wave is backscattered at each point of the fiber.

Due to so-called Raman scattering, light will be backscattered with a shift in the light frequency that depends on the local temperature in the fiber (also referred to as *distributed temperature*

sensing (*DTS*), whereas related Brillouin scattering depends on both the temperature and strain in the fiber (and referred to as *distributed strain sensing (DSS)* (Li & Sun, 2006, López-Higuera et al., 2011). When light pulses of a given wave length are sent through the fiber and the reflected light is monitored for both shift in wave length and arrival time, the spatial temperature and strain distribution along the fiber can be resolved. This allows for the monitoring of strain or temperature along the entire fiber length, where fiber lengths of several to tens of kilometers can be monitored continuously. However, the limitations of the optical interrogators result in averaged strain reading over spatial sampling accuracy of the interrogator, often in the order of tens of centimeters, as well as an averaging over a time integration window of seconds to minutes.

Another DFOS technique relies on Rayleigh scattering and uses *optical frequency domain reflectometry (OFDR)* to determine strain and temperature changes of the optical. OFDR has the benefit of far better spatial resolutions and higher sampling rates, allowing to measure strains at millimeter spatial resolution scales and at better than 1Hz frequencies, but at the cost of shorter possible fiber lengths. Current OFDR interrogators can monitor roughly 100 m fiber lengths reliably, which limits the applications somewhat to controlled laboratory conditions and makes it less suitable for application in long and often harsh tunnel conditions. *Distributed Acoustic Sensing (DAS)* is a related technique that relies on Rayleigh scattering as well, but has a lower spatial resolution in the order of meters, and that monitors the impact of acoustic waves impacting on the fiber. DAS has been used for vibration monitoring in rail and road applications, as well as for seismic monitoring (Zhang et al, 2024).

The benefits of optical fiber based monitoring lie in the long fiber lengths that can be used and, therefore, long tunnel lengths that can be monitored using a single optical interrogator, which can be located even outside the tunnel, whilst the optical fiber in the tunnel has a small cross section and is easily installed (Zhang & Broere, 2022a, b). Other benefits include the fact that the light refraction is not influenced by electro-magnetic interference and the fibers can be located in extremely harsh conditions, as depending on the fiber type used they are not strongly influenced by radiation, chemical or mechanical influenced. This has, for example, allowed their use in the CERN cyclotron tunnels, where traditional electrical signal based sensor could not reliably be used (Di Murro et al., 2019).

The same issues with large strain as for FBG hold for DOFS. The use of fixed points and free unbound spans of fiber in between has been used to monitor deformations over tunnel joints, for example in the London metro to monitor aging cast iron segmented linings. Experience over the years shows that the method used to fixate the ends of the unbound spans has a significant impact on the accuracy of the measurements, as light signals transmitted in a fiber optic line suffer significant signal loss if local bends or kinks are introduced. Early methods using steel hooks and glue points have been superseded by hook and pulley systems or specialized clamp blocks, designed to eliminate local sharp bends and loss of signal quality.

As with both FBG and DOFS the fiber is sensitive to changes in temperature and strain, the temperature of the fiber needs to be recorded independently in order to determine the strain readings. This can be achieved normally by running a second fiber that is not bound to the surface in parallel, but dedicated monitoring cables are also available that contain multiple optical fiber cores, where one or more are loose-buffered inside the cable and free to move unstrained if the outer cable housing is strained.

Another issue with optical fiber is that the fiber only measures strain in the direction of the fiber. Specially designed layouts of the fiber are needed to measure strains or deformations in different perpendicular directions using a single fiber. Whilst this can be achieved, measuring all three axes of movement at a single location can be difficult to achieve.

3.3 Geotechnical monitoring

Whilst not going into extensive detail, monitoring of tunnel construction is often accompanied by geotechnical monitoring at surface (Mair, 2008). Monitoring of surface settlements using settlement plates placed, or prisms fixed to rigid structures, commonly uses manual leveling and RTS similar to those used in the tunnel. To monitor vertical settlements, liquid levelling systems can be used (Bakker, 2000, Kavvadas, 2005, Standing & Selemetas, 2013). More

recently, the use of satellite radar aperture measurements (e.g. INSAR) has been used, although such techniques do offer limited control over the precise location of the monitoring locations obtained (Reinders et al., 2021).

To monitor subsurface deformations around and above the tunnel construction, extensometers and inclinometers installed in boreholes are often used. Boreholes can also be used to install soil stress cells and pore pressure transducers, although proper backfilling is needed to ensure the validity of measurements. Spade cells and self boring piezometers eliminate the need to backfill, but the impact of sensor installation on the soil stress state is never fully eliminated (Broere & Festa, 2017).

3.4 Degradation monitoring

Apart from the sensors used for deformation monitoring of the tunnel, different types of sensors are available to measure physical and chemical parameters involved in the aging process of tunnel structures. Monitoring of these parameters can play a role in the diagnosis of the condition of the tunnel structure, as well as predicting the future evolution of aging and deterioration processes. Combined with deformation monitoring and modelling, information from such sensors can form the basis for predictive maintenance (COB, 2024).

Measuring temperature is often done in order to compensate for temperature effects inherent in different sensors, but can be an object by itself. Temperature development in early age concrete after casting is an indication of maturity and strength, and temperature differences can indicate where risks of cracking exist, with cracks increasing the risk of early deterioration of concrete structures. But temperature development over longer time period (years) could also be beneficial for degradation predictions as well, as some degradation mechanisms are temperature dependent.

Thermocouples are the more common sensor type, and can be incorporated in the concrete structure during casting. Temperature can also be measured using loose-buffered optical fibers. Fiber optic cables are stable even at high temperature, as long as the outer jacket is not impacted. The inner glass core can handle temperatures well over 1000°C, but the most common jacket material is acrylate, which limits the working temperature to 85°C. Higher temperature resistant jacket materials are available.

The relative moisture content of the air in which concrete structures are located determines whether shrinkage or swelling will occur, and thus whether imposed deformations occur. It also influences the ingress rate of carbon dioxide and chlorides, which may speed up degradation process in the concrete. *Relative humidity sensors* are available based on capacitive MEMS sensors, as well as wet-dry bulb psychrometers. MEMS sensors rely on moisture sensitive dielectric layers with often low capacitance, which require accurate amplification. Psychrometers work on the heat extracted by evaporating distilled water from a wet fabric around a thermometer, and are more cumbersome to operate on a continuous basis.

When cracks are present in concrete, this can be an indication that the structure is behaving as intended and the reinforcement has been addressed. If crack patterns differ from expectation, or larger than expected cracks appear, it may be necessary to monitor their development. Many analogue *crack meters* are available, also with integrated loupes in case higher accuracy is needed. These are glued to one side of the crack and need to be read at discrete moments. For continuous measurements, especially with more severe cracks, LVDTs can be used instead.

The quality of the concrete cover, the porosity, and the presence of cracks or delamination, impact the rate at which chlorides or carbon dioxide can ingress and corrode the reinforcement (Dauberschmidt, 2006). The quality of the concrete cover, and the sensitivity to corrosion and degradation of the concrete structure, can be inferred from the electrical resistivity. *Electrical resistivity* of concrete can be measured using multi-ring electrodes or screen-printed sensors (Kamat et al., 2020, Robles et al., 2022). Multi-ring electrode consists of several stainless-steel rings separated by insulating polymer rings. Measuring the resistance to alternating current between adjacent steel rings, a resistivity profile over the multi-ring electrode can be determined (Brameshuber et al., 2003). Screen-printed sensors apply a current over a set of outer electrodes with known spacing, printed on a backer plate, and measure the resulting potential over a set of inner electrodes (Sophocleous et al., 2018). Both types of sensors can be inserted into the

concrete by attaching them to the reinforcement prior to casting, or inserted in holes drilled in existing structures and properly back-filled by non-shrinking mortars. The obtained resistivity profile can be transferred into a moisture profile, but as the resistivity is not only influenced by the moisture, but also by the type of binder and temperature, a calibration curve is needed (Ansuini et al., 2001, Arup et al., 1997, Duffó et al., 2010, Lim et al., 2020).

Alternatively, the electrical resistivity between an anode made out of an (electrically) isolated section of reinforcement steel and a cathode, either the remaining reinforcement mesh or added at the surface of the structure, can be monitored, as an indication of corrosion initiation. If the size of the anode is precisely known, the rate of corrosion could be derived as well. Instead of using the reinforcement mesh inside the structure as the anode, *corrosion monitoring systems* are available that can be mounted externally and contain a steel sample of the same composition and quality as the reinforcement steel used. This sample functions as the anode and is then monitored to get an indication of the corrosion development of the reinforcement or other steel structural components (DGZfP, 2021, van den Hondel & Polder, 2022).

Electrical impedance spectroscopy uses two (temporary) electrodes at the surface of a coated metal structure to measure impedance as a function of varying alternating current frequencies. This measurement can be interpreted as a measure for coating quality (Baboian & Prew, 1993, Lu & Ba, 2010, Raupach, 1996, Xu et al., 2013, Zi, 2009). Similarly, *electrochemical polarisation sensors (EPQ)* add a third reference electrode to the setup, and determine the extended linear polarisation resistance of the metal or coated object. The obtained polarisation resistance is a measure for the electron exchange possible at the surface, which in turn can be translated into a corrosion rate (ASTM, 2018, Faritov et al., 2016, ISO, 2005, Li et al., 2014, OGOS, 2021, Ozkan, 2020, Sadowski, 2010, Song, 2000).

The ingress of chlorides could potentially be measured more directly (compared to multi-electrode potential measurements) using *silver/silver chloride electrodes*, although these sensors are still in a development stage for such use and long-term stability has not been evaluated. Similar silver-chloride or manganese-dioxide sensors are already widely used to monitor the potential of reinforcement steel, where they have been found to properly operate for decades, but the interpretation of the measurement can be difficult as the measured potential difference is hugely impacted by variations in cement type, service conditions or environmental conditions (Climent-Llorca et al., 1996, Du et al., 2022, Seguí Femenias, et al, 2015).

Many deterioration processes of concrete, such as carbonatation, corrosion and acid attacks, are also related to the alkalinity of the concrete. The pH can be measured using embedded *metal/metal-oxide potentiometric electrodes* or pH sensitive fiber optic sensors (Du et al, 2022). Calibration of the metal/metal-oxide sensors is problematic, and although iridium/iridium-oxide based sensors are the most reliable, long-term stability remains an issue (Seguí Femenias, 2017, Seguí Femenias et al., 2017a,b,c). pH sensitive fiber optic sensors are made from a pH sensitive indicator embedded in a solid substrate, which changes color with the pH of the surrounding medium. The optical fiber is used to transmit light and read the luminescence from the sensor. The practical use of these sensors is limited by their long-term chemical stability and the rather low alkalinity levels they can properly detect (pH 9-10), which are often lower than the alkalinity of fresh concrete (pH ranges 13-14) (Behnood et al, 2016, Habel & Krebber, 2011, McPolin, 2005).

So-called *smart aggregates (SA)* provide a novel way to detect (internal) crack formation in concrete, as well as changes in the stress conditions. SA contain piezo-electric sensors in a housing that can be embedded in the concrete, and can function both as an acoustic source as well as a receiver. When multiple SA are embedded, the change in wave velocity due to crack formation or stress change can be detected, but as the technique relies on detecting changes in wave propagation, a reference measurement after installation is needed (Cheng et al., 2023).

4 MONITORING STRATEGIES FOR BORED AND IMMERSED TUNNELS

The myriad of sensors that is available for monitoring creates many possibilities, but also raises questions regarding the optimal and economic use of sensors in different phases of the tunnel.

Tunnels in past decades have had active monitoring during construction, to survey safety, stability and impact on the surroundings. Where scientific research programs were connected with ongoing tunnelling projects, the number of sensors used and the number of intensely monitored locations, was frequently increased beyond what was strictly needed for the construction process, but afterwards monitoring is often limited and only intensified once structural issues have manifested, or large scale renovation is anticipated. Experience shows that this practice of limited monitoring, often limited to visual inspections only, during the operational phase, results in a lack of data needed to assess the structural health of the tunnel later on (DRD, 2019).

Realizing this, tunnel owners increasingly look for more detailed and continuous monitoring solutions, but face limited budgets. For both immersed tunnels and bored tunnels in the Netherlands this has led to the development of a long term monitoring strategy that strikes a balance between the minimum desired information and the options available (COB, 2022, 2024).

For immersed tunnels this strategy is most detailed. Immersed tunnels consist of concrete elements joined by immersion joints, which use so-called GINA and omega rubber gaskets to secure watertightness of the tunnel, and allow a degree of flexibility over the joint. Each element consists of several rigid concrete segments each 20-25 m in length, jointed together and made watertight using rubber-steel water stops, and resulting in a stiffer, but deformable, joint than the immersion joints. To monitor the long term behaviour of the tunnel, the focus can be on the relative deformations between segments over the joints, as this is where for example deformations due to uneven settlement of the tunnel segments are concentrated.

A minimal monitoring program that monitors relative displacements in three axes (x,y,z) over the joint on the two outer walls of the tunnel has been set as the minimum level, but monitoring the joint opening (in the longitudinal direction of the tunnel) at a location near the roof and floor of the tunnel, as well one or more additional monitoring points at the roof, also allow the derive skewing movement of the tunnel. The relative movements over the joints must subsequently be related to a fixed reference point outside the tunnel, as experience has shown that even reference points outside the closed tunnel structure attached to the entrance ramps do not provide stable time series. Given the limited number of joints in most immersed tunnels, this strategy effectively results in a requirement for tens to several hundreds of sensor locations, which is more than the amount of measurement bolts used in the past, but in the end a still manageable number of sensors.

A project to test the capabilities of fiber optic DSS monitoring has further revealed clear daily and seasonal trends in the relative joint deformations. Therefore, the preferred monitoring frequency has been determined at minimally once per hour, to accurately capture daily effects. Advances in data acquisition and storage have made this both technically and economically feasible, but this is a substantial increase in the monitoring frequency compared to the once per year to once per five years that traditionally the measurement bolts were surveyed.

For bored tunnels, the strategy is less detailed. The large number of joints in segmented lining tunnels make it impractical to monitor relative displacements over all joints. Therefore, a number of locations has been identified where during normal conditions the global deformation and ovalisation of the tunnel should be monitored, and only when analysis of deformations measurements raise concerns relative displacements and rotations over individual joints could additionally be monitored.

In general, locations where the cross section of the tunnel should be monitored have been identified as: the entrance and exit of the tunnel where soil cover is lowest (i.e. 5 - 10 m. from the tunnel entrance); near entrance and exit of the tunnel at a position where segments are no longer permanently bolted (i.e. normally 50 - 100 m from the tunnel entrance); next to the cross passage with lowest soil cover, as well as next to the cross passage with most overburden; and at the deepest point of the tunnel with most overburden. Additionally, if the tunnel is located in very soft soils with large overburden, where overburden is largest and very soft soils are present below the crown; if there are locations with large permanent surface loads or multi-story (5+) buildings above or next to the tunnel, or where such loads are foreseen to be added in future, or where deep excavations above the tunnel are foreseen; and finally those locations where during construction incidents like full face collapse or significant lining damage during installation were observed.

In longitudinal direction a number of parameters to monitor has additionally been identified as: the overall displacement between over the entrance portal and a lining ring beyond the permanently bolted section (i.e. the first 50 - 100 m); the displacements between 20 before and after the deepest cross passage; and 20 m before and after those locations identified above where incidents during construction were observed.

Similar to immersed tunnels, daily and seasonal effects have been identified in bored tunnels as well (Zhang & Broere, 2023a,b). Therefore, a monitoring frequency of once per hour or more frequent, preferably once per 10 - 15 minutes, has been proposed. This will result in relatively large data sets compared to those obtained from previous, mostly visual, inspection regimes. The data storage and visualisation of these data sets is another aspects that warrants attention, but beyond the scope of this paper.

5 CONCLUSIONS

Monitoring of tunnels during both the construction phase as well as during the operational phase is needed to get insight in the long term behaviour of tunnels, in order to assess the need and scope for future large scale tunnel renovations and prevent unforeseen calamities during the operational phase. The myriad of sensor types that is available and in development, combined with advancements in data acquisition, data storage and visualisation, has opened such possibilities for tunnel monitoring, but also opens the need for a targeted monitoring strategy that is standardized to the extent it allows data from different phases, from construction to renovation, to be combined, that allows similarities in different tunnels to be compared and analyzed, and that takes available budgets into consideration. Proposals for standard monitoring strategies have been made for Dutch tunnels, and it is clear that the strategy differs strongly depending on the construction method, with different strategies for immersed and bored tunnels now starting to be implemented. The focus of these monitoring strategies is still primarily on deformation monitoring, but an increasing number of sensors becomes available that can directly assess the structural degradation of tunnel materials and components, and the use of these should also be considered in future monitoring strategies. Lastly, recent continuous and frequent monitoring projects in tunnels have indicated the presence of recurring daily and seasonal cyclical deformation effects. This indicates a need to monitor more frequently during the operational phase to fully assess the tunnels' condition, compared to the often only yearly surveying and inspection regimes that have been standard so far.

REFERENCES

- Ansuini, F.J. & Diamond, J.R. 2001. *Long-term field tests of reference electrodes for concrete ten years results*. CORROSION 2001, NACE International, paper No. 01296.
- Arup, H., Klinghoffer, O. & Mietz, J. 1997. *Long term performance of MnO₂-reference electrodes in concrete*. CORROSION 97, NACE International, paper No. 243.
- ASTM G61-86. 2018. Standard Test Method for Conducting Cyclic Potentiodynamic Polarization Measurements for Localized Corrosion Susceptibility of Iron-, Nickel-, or Cobalt-Based Alloys.
- Atmakusuma, P.A. 2023. Settlement Predictions of The Noordtunnel: A Numerical Simulation. MSc Thesis, TU Delft, Delft, The Netherlands.
- Babolian, R. & Prew, P. 1993. *Low-cost electronic devices for corrosion measurements*. Materials Performance 32, No. 7, p. 56–59.
- Bakker, K.J., Boer, F. & Admiraal, J.B.M. 2000. *Monitoring the second Heineoord tunnel and the Botlek Rail tunnel*. Proceedings of the international symposium on geotechnical aspects of underground construction in soft ground, 1999.
- Behnood, A., Van Tittelboom, K. & De Belie, N. 2016. *Methods for measuring pH in concrete: A review*. Construction and Building Materials, 105.
- Brameshuber, W., Raupach, M., Schröder, P., & Dauberschmidt, C. 2003. *Non-destructive Determination of the Water-Content in the Concrete Cover using the Multiring-Electrode*. Non-Destructive Testing in Civil Engineering 2003.
- Broere, W. & Festa, D. 2017. *Correlation between the Kinematics of a Tunnel Boring Machine and the Observed Soil Displacements*. Tunneling and Underground Space Technology 70, pp. 125–147.

- Cheng, H., Weemstra, C., Hendriks, M. A. & Yang, Y. 2023 *Comparing the stretching technique and the wavelet cross-spectrum technique for measuring stress-induced wave-velocity changes in concrete*. Automation in Constructions, 2023.
- Climent-Llorca, M.A., Viqueira-Pérez, E. & López-Atalaya, M.M. 1996. *Embeddable Ag/AgCl sensors for in-situ monitoring chloride contents in concrete*. Cement and Concrete Research 26, p. 1157–1161.
- COB. 2022. Monitoring strategy for immersed tunnels. COB, Delft, The Netherlands.
- COB. 2024. Monitoring material degradation in tunnels. COB, Delft, The Netherlands.
- Dauberschmidt, C. 2006. Untersuchungen zu den Korrosionsmechanismen von Stahlfasern in chloridhaltigem Beton. Dissertation, RWTH Aachen.
- DGZfP Guideline B 12. 2021. Corrosion monitoring in reinforced and prestressed concrete structures.
- Di Murro, V., Soga, K., Fern, E. J., Pelecanos, L., Li, Z. & Scibile, L. 2019. *Distributed fibre optic strain sensing of CERN infrastructures in the molasse region*, Proceedings of the XVII European Conference on Soil Mechanics and Geotechnical Engineering, Reykjavik, Iceland, 1-6 September, pp. 1–7.
- DRD Danish Road Directorate. 2019. Limfjord Tunnel. Assessment and retrofitting. DRD, Denmark.
- Du, Z., Tian, L., Wang, P., Chen, Z., Cui, D., Jin, Z. & Zhang, H. 2022a. *All-solid-state chloride sensor for in-situ monitoring of chloride penetration in concrete*. Construction and Building Materials. 357.
- Du, Z., Wang, P., Chen, Z., Cui, D., Jin, A. & Zhang, H. 2022b. *All-solid-state, long term stable, and embedded pH sensor for corrosion monitoring of concrete*. Journal of Building Materials, 57.
- Duffó, G.S., Farina, S.B. & Giordano, C.M. 2010. *Embeddable reference electrodes for corrosion monitoring of reinforced concrete structures*. Materials and Corrosion 61, p. 480–489.
- Faritov, A. T., Rozhdestvenskii, Y. G., Yamshchikova, S. A., Minnikhanova, E. R. & Tyusenkov, A.S. 2016. *Improvement of the linear polarization resistance method for testing steel corrosion inhibitors*. Russian Metallurgy (Metally), 2016, 1035–1041.
- Gue, C.Y., Wilcock, M., Alhaddad, M.M., Elshafie, M.Z.E.B., Soga, K. & Mair, R.J., 2015. *The monitoring of an existing cast iron tunnel with distributed fibre optic sensing (DFOS)*. Journal of Civil Structural Health Monitoring, 5, 573–586.
- Glab, K., Wehrmeyer, G., Thewes, M. & W. Broere. 2021. *Predictive Machine Learning in EPB TBM Tunnelling for Main Drive Torque Estimation*. EURO-TUN 2021.
- Glab, K., Wehrmeyer, G., Thewes, M. & W. Broere. 2024. Predictive Machine Learning in Earth Pressure Balanced Tunnelling for Main Drive Torque Estimation of Tunnel Boring Machines. Tunnelling and Underground Sapce Technology, 146.
- Habel, W. & Krebber, W. 2011. *Fiber-optic sensor applications in civil and geotechnical engineering*. Photonic Sens. 1, 268–280.
- Van den Hondel, A.W.M. & Polder, R.B., 2022. *Long term performance of reference electrodes for cathodic protection of steel in concrete*. MATEC Web of Conferences 361, Concrete Solutions.ISO 17475:2005. Corrosion of metals and alloys Electrochemical test methods – Guidelines for conducting potentiostatic and potentiodynamic polarization measurements.
- Kamat, A., Abbas, Y., Blagojevi, A., van Casteren, T. & Walraven, J. 2020. *Real-time chloride diffusion in concrete using embedded resistivity sensors*. 4th International RILEM conference on Microstructure Related Durability of Cementitious Composites.
- Kavvasdas, M. 2005. *Monitoring ground deformation in tunnelling: Current practice in transportation tunnels*. Engineering Geology. 79. 93–113.
- Li, C. & Sun, Y. 2006. *Monitoring pressure and thermal strain in the second lining of a tunnel with a Brillouin OTDR*. Smart Materials and Structures 15 (5): N107–N110.
- Li, X.M., Faber, B., Minch, B. & Castaneda, H. 2014. *Analysis of Soft Coating Corrosion Performance on Carbon Steel Using Electrochemical Impedance Spectroscopy*. Corrosion 1 June 2014, 70 (6), 615–626.
- Lim, Y.-C., Kim, T.-S. & Hwang, C.-S.. 2020. *Modelling for apparent resistivity estimation along direction of electrode array above rebar in electrical resistivity measurement*. Journal of Building Engineering, 31.
- Lindenbergh, R.C., Uchanski, L., Bucksch, A. & Van Gosliga, R. 2009. *Structural monitoring of tunnels using terrestrial laser scanning*. Reports on Geodesy, 2 (87).
- López-Higuera, J.M., Rodríguez Cobo, L., Quintela Incera, A., & Cobo, A. 2011. *Fiber optic sensors in structural health monitoring*. Journal of Lightwave Technology, 29, no. 4, 587–608.
- Lu, S. & Ba, H.-J. 2010. *Corrosion sensor for monitoring the service condition of chloride contaminated cement mortar*. Sensors 10, no. 4: 4145–4158.
- Mair, R.J. 2008. *Tunnelling and geotechnics: new horizons*. Géotechnique 58, No. 9, pp. 695–736.
- Metje, M., Chapman, D.N. Rogers, C.D.F., Henderson, P. & Beth, M. 2006. *Optical fibre sensors for remote monitoring of tunnel displacements – Prototype tests in the laboratory*, Tunnelling and Underground Space Technology, Volume 21, Issues 3/4,
- Providakis, S. Rogers, C.D.F., & Chapman, D.N. 2019. *Predictions of settlement risk induced by tunnelling using BIM and 3D visualization tools*. Tunnelling and Underground Space Technology, Volume 92.

- OGOS-210-TRL. 2021. Conditiebepaling Conservering Stalen Objecten (Version 2.0).
- Ozkan, C. 2020. The Role of Phase Combinations on the Corrosion and Passivity Behaviour of High Strength Steels. Master thesis, TU Delft, The Netherlands
- van derPoel, J.T., Gastine, E. & Kaalberg, F.J. 2005. *Monitoring for construction of the North/South metro line in Amsterdam, the Netherlands*. Geotechnical Aspects of Underground Construction in Soft Ground, Amsterdam 2005.
- McPolin, D. 2005. Profiling of Carbonation and Chloride Distributions in Concretes and Development of Novel Fibre Optic Sensors. PhD Thesis, Queen's University Belfast, Northern Ireland.
- Raupach, M. 1996. *Chloride-induced macro-cell corrosion of steel in concrete –Theoretical background and practical consequences*. Cons. Mater. 10, 329–338.
- Reinders, K.J., van Leijen, F.J., Hanssen, R.F. & Korff, M. 2021. *Evaluation of InSAR data for measuring the surface settlement during shield tunnel construction of the North-South Line in Amsterdam*. Geotechnical Aspects of Underground Construction in Soft Ground - Proceedings of the 10th International Symposium on Geotechnical Aspects of Underground Construction in Soft Ground, IS-CAMBRIDGE 2022.
- Robles, K.P.V., Yee, J.-J., & Kee, S.-H. 2022. *Electrical Resistivity Measurements for Nondestructive Evaluation of Chloride-Induced Deterioration of Reinforced Concrete - A Review*. Materials 2022, 15, 2725.
- Sadowski, Ł. 2010. *New non-destructive method for linear polarisation resistance corrosion rate measurement*. Archives of Civil and Mechanical Engineering V10, I2, pages 109–116
- Seguí Femenias, Y., Angst, U. & Elsener, B. 2015. Monitoring chloride concentrations in concrete by means of Ag/AgCl ion-selective Electrodes. ICCRRR.
- Seguí Femenias, Y. 2017. Electrochemical durability monitoring in reinforced concrete. PhD Thesis, ETH Zürich, Switzerland.
- Seguí Femenias, Y., Angst, U. & Elsener, B. 2017a. *Durability monitoring of reinforced concrete*. SMAR.
- Seguí Femenias, Y., Angst, U. & Elsener, B. 2017b. *Monitoring pH in corrosion engineering by means of thermally produced iridium oxide electrodes*. Materials and Corrosion, 69.
- Seguí Femenias, Y., Angst, U., Elsener, B. 2017c. *pH-Monitoring in Mortar With Thermally-Oxidized Iridium Electrodes*. RILEM Tech Lett 2017, 2, 59–66.
- Sjölander, A., Belloni, V., Ansell, A. & Nordström, E.. 2023. *Towards Automated Inspections of Tunnels: A Review of Optical Inspections and Autonomous Assessment of Concrete Tunnel Linings*. Sensors 23, no. 6: 3189.
- Song, G. 2000. *Equivalent circuit model for AC electrochemical impedance spectroscopy of concrete*. Concrete Research 30.
- Sophocleous, M., Savva, P., Petrou, M.F., Atkinson, J.K. & Georgiou, J. 2018. *A Durable, Screen-Printed Sensor for In-Situ and Real-Time Monitoring of Concrete's Electrical Resistivity Suitable for Smart Buildings/Cities and IoT*. IEEE.
- Standing, J.R. & Selemetas, D. 2013. *Greenfield ground response to EPBM tunnelling in London Clay*. Géotechnique 63, No. 12, pp. 989–1007.
- van Tol, A.F. 2005. *The effects of tunnelling on existing structures*. Geotechnical Aspects of Underground Construction in Soft Ground, Amsterdam, 2005.
- Xu, C., Li, Z. & Jin, W. 2013. *A new corrosion sensor to determine the start and development of embedded rebar corrosion process at coastal concrete*. Sensors 2013, 13, 13258–13275.
- Yang, Y.Z. 2009. *Preparation of Ti/MnO₂ reference electrode and its application in concrete structures*. Engineering, Materials Science.
- Zhang, X. & Broere, W. 2022a. *Design of a distributed optical fiber sensor system for measuring immersed tunnel joint deformations*. Tunnelling and Underground Space Technology 131.
- Zhang, X. & Broere, W. 2022b. *Sensing Fiber Selection for Point Displacement Measuring with Distributed Optical Fiber Sensor*. Measurement 197.
- Zhang, X. & Broere, W. 2023a. *Monitoring of Tidal Variation and Temperature Change-Induced Movements of An Immersed Tunnel Using Distributed Optical Fiber Sensors (DOFSs)*. Structural Control and Health Monitoring.
- Zhang, X. & Broere, W. 2023b. *Monitoring seasonal deformation behavior of an immersed tunnel with distributed optical fiber sensors*. Measurement 219.
- Zhang, X., Zhu, H., Jiang, X. & Broere, W. 2024. *Distributed Fiber Optic Sensors for Tunnel Monitoring: A State-of-the-art Review*. Journal of Rock Mechanics and Geotechnical Engineering, 16.

Deformation of shield tunnel subjected to underlying tunneling

R.P. Chen, T. Chen, F.Y. Meng & H.Z. Cheng

Hunan Provincial Engineering Research Center for Advanced Technology and Intelligent Equipment for Underground Space Development, Hunan University, Changsha, China

Research Center for Advanced Underground Space Technologies of Hunan University, Changsha, China

College of Civil Engineering, Hunan University, Changsha, China

ABSTRACT: Shield tunneling beneath existing shield tunnel is a common recurring problem. Excessive settlement and severe disease might occur for the existing tunnel if no appropriate countermeasure is adopted. Evolution of the upward soil arching induced by the shield tunneling is a key factor influencing the responses of the existing tunnel. This research develops a theoretical model to describe the developing upward soil arching associated with the magnitude of ground volume loss. Furthermore, the theory for depicting the interaction between the soil arching and existing shield tunnel is proposed. The nonlinear bending and shearing stiffness of the assembled tunnel is considered. Technologies regarding deformation control for the overlying existing shield tunnels are suggested by mitigating the expansion of the loosened zone and reinforcing the loosened zone. Finally, engineering applications of the technologies are also introduced.

Keywords: Shield tunneling, Soil arching-tunnel interaction, Deformation control

1 INTRODUCTION

During the past few decades, the construction of metro tunnels in China has developed dramatically in urban regions. The assembled shield tunnel is the most dominant structure for metro tunnel. Limited by underground space and the need for transfer, shield tunneling undercrossing the operating shield tunnels becomes quite common. However, shield tunnel undercrossing often causes the large settlement of the existing tunnel and possibly even threatens the safety of tunnel operation. During the construction of the new tunnel, local water seepage occurs in the existing tunnel, decreasing the durability and long-term performance of the tunnel lining (Jin et al., 2018).

In essence, the above-mentioned shield tunnel deformation is determined by the ground deformation and stress change induced by the undercrossing shield tunneling. Soil excavation induced by tunneling leads to uneven ground deformation, and thus to the generation of soil arching effect. The development of soil arching governs the ground stress transfer, deformation propagation and the tunnel response. Soil arching effect is one of the most common phenomena in geotechnical engineering. Terzaghi (1943) proposes an analytical solution for depicting the soil arching above the trapdoor, followed by plenty of studies on the soil arching above the tunnel (Franza et al. 2019; Lin et al. 2022; Chen et al. 2022).

Currently, numerical (Möller and Vermeer, 2008; Zhao et al., 2012; Do et al., 2013; Chen et al., 2016; Meng et al., 2018), empirical (Peck, 1969), and analytical methods (Sagaseta, 1987; Verruijt and Booker, 1996) are primarily used for predicting tunneling-induced ground deformation. The soil arching effect governs the ground stress transfer, and the soil in the

loosened zone experiences relatively larger displacements. However, it is not considered in the earlier empirical and analytical methods. In addition, the current countermeasure for decreasing the existing tunnel settlement mainly include tunneling parameters regulation and ground reinforcement. Among them, it is difficult to effectively control the tunnel deformation in close proximity condition through the regulation of tunneling parameters, while the ground reinforcement is subjected to secondary damage to the existing tunnel due to the difficulty in determining the reinforcement zone and uncontrollable grouting pressure.

Based on the soil arching effect induced by shield tunneling, this study proposes a theoretical model to describe the ground stress and deformation transfer associated with the ground volume loss. Considering the nonlinear characteristics of tunnel bending and shear stiffness, the theoretical model for soil arching-tunnel interaction is proposed to calculate the existing shield tunnel settlement due to the undercrossing shield tunneling. Countermeasures regarding protection of the nearby tunnels are suggested by mitigating the expansion of the loosened zone and reinforcing the loosened zone. Finally, engineering applications of the countermeasures are introduced.

2 SOIL ARCHING MODEL FOR SHIELD TUNNELING

2.1 Description of the model

Ground volume loss is inevitable during shield tunneling because of overbreak, unbalanced face support pressure, and inadequate shield tail grouting. The differential ground deformation induced by the volume loss could cause the occurrence of the soil arching above the tunnel, as shown in Figure 1. To recognize the characteristics of the arching, both experimental and numerical studies have been conducted (Han et al. 2017; Franza et al. 2019; Lin et al. 2019). Lin et al. (2019) find that the shear bands develop obliquely upward from the bottom of the tunnel in sandy ground. Besides, the soil arching develops with the increasing trapdoor displacement (Iglesia et al. 1999), and hence that above the tunnel should develop with the growing ground volume loss.

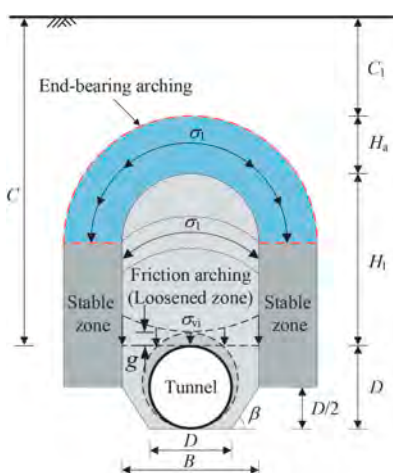


Figure 1. Illustration of the soil arching for shield tunneling (after Lin et al. 2022).

* C is the burial depth of the tunnel crown, B is the width of friction arching zone (loosened zone), H_a is the thickness of end-bearing arching zone, H_1 is the height of friction arching zone, and g is the gap parameter.

2.2 Theoretical model

2.2.1 Determination of the stresses

To predict the earth pressure on the deep circular tunnel, Lin et al. (2022) propose a multi-arching model that integrates earlier theories proposed by Terzaghi (1943) and Hewlett & Randolph (1988). Figure 1 illustrates the concept and framework of the multi-arching model, which consists of the end-bearing arching, frictional arching, and stable zone. The end-bearing arching with a semi-circular ring shape is located on the upper part of the multi-arching model, whose arch feet act on the stable zone. The cover depth and thickness of this zone are C_1 and H_a , respectively. The height and width of the friction arching are H_1 and B , respectively. The transferred load from the end-bearing acting on the top of this zone is partly transferred to the stable zone by the frictional arching effect and the rest of the pressure acts on the top of the tunnel. This zone bears the pressure transferred from the end-bearing arching and frictional arching and provides sufficient support.

To figure out the model, two assumptions are made: (1) the ground loss induced by the tunnel over-excavation is absolutely compensated by the soil mass within the loosened zone, and (2) the frictional arching is composed of a semicircle and a rectangle with two triangles and a circle subtracted. The model geometric parameters include the width and height of the frictional arching and, the thickness of the end-bearing arching, which are determined based upon the earlier researches as listed in Table 1. Based on the geometries of the model, the stress in the end-bearing arching is calculated using the 2D semi-circular ring limit equilibrium model in piled embankments (Hewlett & Randolph 1988). Hence, the vertical earth pressure above the tunnel can be calculated (Equation (1)), which is verified by centrifuge modeling results (Franza et al. 2019). In comparison with the model of Terzaghi (1943), the multi-arching model yields more reasonable predictions for normalized average earth pressure on the tunnel (Lin et al. 2022).

Table 1. Geometric parameters of the soil arching model.

Parameter	Value	Meaning	Literature
B	$D(1+\cot\beta)$	$D =$ tunnel diameter $\beta = 45^\circ + \varphi/2$ $k = \frac{\pi \tan \beta}{4(1+\tan \beta)}$ $b = \frac{(\pi-4)\tan^2\beta+2(1-\pi)\tan\beta+4-\pi}{8 \tan \beta(1+\tan \beta)}$	Stein et al. (1989)
H^1	$D(k(\eta/\alpha)+b)$	$\eta =$ ground volume loss $\alpha =$ rebound coefficient (0.1 to 0.24 and 0 to 0.08 for dense and loose sand)	/
H_a	$C-H_1 > 0.4B, H_a = 0.4B$ $0 < C-H_1 \leq 0.4B, H_a = C-H$ $C-H_1 \leq 0, H_a = 0$	$C =$ tunnel cover depth $B =$ width of frictional arching zone	Lai et al. (2018)

$$\sigma_v = \frac{\gamma B}{2K_{av} \tan \varphi} \left(1 - e^{-\frac{2K_{av} \tan \varphi}{B} z} \right) + q_1 e^{-\frac{2K_{av} \tan \varphi}{B} z} \quad (1)$$

where B is the width of friction arching zone, K_{av} is the lateral stress ratio between the loosened zone and the adjoining soils, q_1 is the stress acting on the crown of the friction arching zone.

2.2.2 Calculation method of subsurface settlement

Based on the multi-arching model (Lin et al. 2022), Chen et al. (2022) propose a novel analytical approach to predict the tunneling-induced subsurface settlement on the tunnel centerline (Figure 2). In addition, the stress-dependent modulus is adopted to consider the soil

mechanical behaviors. This approach assumes that the soil material behaves elastically and isotropically, and the ground movement around the tunnel is oval-shaped. The ground settlement right above the tunnel crown is maximum and equals to the gap parameter g , determined by the physical gap, the over-excavation of the soil around the tunnel, and the 3D elastoplastic deformation of the soil in front of the tunnel face. In engineering practice, the value of g can also be obtained through the back-analysis of the ground volume loss if it is already known. The tunnel excavation leads to the unloading/rebounding deformation within the frictional arching zone u_1 and end-bearing arching zone u_2 . To obtain the ground settlement at a certain depth, g can be used to subtract the rebound deformation of the soil at its location. For instance, the subsurface ground settlement at the top of the end-bearing arching zone is calculated by Equations (2-4).

$$u_z = g - u_1 - u_2 \quad (2)$$

$$u_1 = \int_{B/2}^{B/2+H_a} \frac{1-\mu^2}{E_{ur}^e} \left[(\sigma_{cvi}^e - \sigma_{vi}^e) - \frac{\mu}{1-\mu} (\sigma_{chi}^e - \sigma_{hi}^e) \right] dr \quad (3)$$

$$u_2 = \int_0^{H_1} \frac{1-\mu^2}{E_{ur}^f} \left[(\sigma_{cvi}^f - \sigma_{vi}^f) - \frac{\mu}{1-\mu} (\sigma_{chi}^f - \sigma_{hi}^f) \right] dz \quad (4)$$

where μ is the Poisson's ratio of the soil, E_{ur}^e is unloading/reloading modulus of the soil in end-bearing arching zone, E_{ur}^f is unloading/reloading modulus of the soil in friction arching zone, σ_{cvi}^e , σ_{chi}^e , σ_{cvi}^f , and σ_{chi}^f are the initial stresses, σ_{vi}^e , σ_{hi}^e , σ_{vi}^f , and σ_{hi}^f are the ground stress after tunneling.

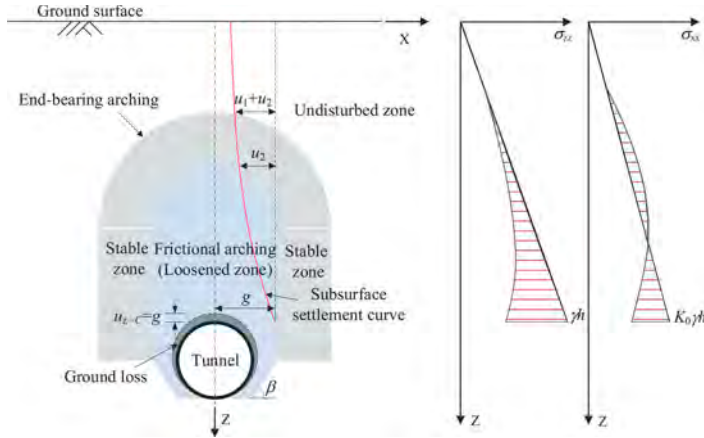


Figure 2. Analytical model for tunneling-induced subsurface ground settlement (after Chen et al. 2022).

The magnitudes of u_1 and u_2 can be calculated by the Hooke's law (Equations (3) and (4)), in which the ground stress change is determined by multi-arching model (Lin et al. 2022) and the stress-dependent elastic unloading modulus (Schanz et al. 1999). The applicability of this methodology is examined by three case histories and one model test, exhibiting satisfying results. Furthermore, the subsurface ground settlement trough can be determined by the calculated settlement at the tunnel centerline and empirical width coefficient of settlement trough.

3 MODEL AND CALCULATION METHOD FOR SOIL ARCHING-TUNNEL INTERACTION

Two-stage method is proposed to predict the tunnel settlement due to nearby construction, which has been widely employed to solve the problem of tunnel-soil interaction. For tunneling underneath the existing tunnel (Figure 3), based on the two-stage method, this study proposes a soil-tunnel interaction model that considers the soil arching effect. The proposed model considers (1) the nonlinearity of the tunnel joint stiffness (Equations (5) and (6)), and (2) the soil stress transfer induced by the soil arching effect.

$$(EI)_{eq} = E_s I_s \frac{l}{l - \lambda l_b \left(1 + \frac{\cos \phi + (\phi + \pi/2) \sin \phi}{\cos^3 \phi} \right)} \quad (5)$$

$$(\kappa GA)_{eq} = \frac{l}{\frac{\varepsilon \lambda l_b}{m \kappa_b G_b A_b} + \frac{l - \lambda l_b}{\kappa_s G_s A_s}} \quad (6)$$

In the first stage, the vertical unloading stress caused by the underlying tunnel is calculated based on the tunneling-induced subsurface settlement trough considering the soil arching. It should be noted herein that the overlying existing tunnel should certainly have an influence on the development of soil arching due to the underlying tunneling, and the calculation does not consider the impacts. The maximum settlement of the trough is obtained by the method proposed by Chen et al. (2022) and the width coefficient of the trough is determined by empirical results. The unloading stress at the level of the tunnel axis is calculated by the corresponding subsurface ground settlement and the coefficient of subgrade reaction. In the second stage, the responses of the existing shield tunnel subjected to the corresponding vertical unloading stress are determined by an analytical model (Equation (7)). In this analytical model, the existing shield tunnel was treated as a Timoshenko beam (Wu et al. 2015; Cheng et al. 2021) resting on a Winkler foundation model. The applicability of this method is validated by several case histories in China, and good agreement is achieved in most cases in which soil improvement between the tunnels is not carried out.

$$\frac{d^4 w(x)}{dx^4} - \frac{k_s(x)}{(\kappa GA)_{eq}} \frac{d^2 w(x)}{dx^2} + \frac{k_s(x)}{(EI)_{eq}} w(x) = \frac{1}{(EI)_{eq}} q(x) - \frac{1}{(\kappa GA)_{eq}} \frac{d^2 q(x)}{dx^2} \quad (7)$$

where $(EI)_{eq}$ and $(\kappa GA)_{eq}$ denote the equivalent flexural stiffness and shear stiffness of the shield tunnel based on Timoshenko beam theory, respectively, ϕ is the neutral axis angle, $q(x)$ is the additional stress distributed along the beam axis after considering soil arching effect, and $k_s(x)$ is the subgrade reaction coefficient.

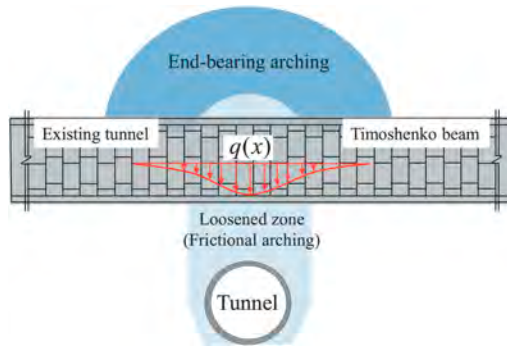


Figure 3. Theoretical model for soil arching-tunnel interaction.

4 VERIFICATION OF THE MODEL

To validate the rationality and effectiveness of the proposed soil arching model and soil arching-tunnel interaction theory, this study carries out calculations and comparisons based on the case of Changsha newly constructed Metro Line 4 undercrossing the existing Metro Line 2. The diameter of the tunnels is 6.2 m. The minimum distance between the newly constructed tunnel and the existing tunnel is 2.9 m. The axial burial depths of the newly constructed tunnel and the existing tunnel are about 20 m and 11.9 m, respectively. For the stiffness of the tunnel structure, the longitudinal equivalent bending stiffness is $1.91 \times 10^8 \text{ kN}\cdot\text{m}^2$ and longitudinal equivalent shear stiffness is $5.14 \times 10^6 \text{ kN}$. The results calculated by the conventional method, in which the subsurface ground settlement is determined by Peck (1969), and the proposed method described in this study are shown in Figure 4. Among them, the ground volume loss and the width coefficient of settlement trough induced by the tunneling in the conventional method are taken as $V_L=1.0\%$ and $K=0.5$, respectively.

From Figure 4, it can be found that the calculated values of this study show a similar trend to those of the conventional method. However, the results calculated by this study are relatively smaller compared to the conventional method. This is mainly attributed that the theory of this study takes into account the stress transfer induced by the soil arching effect and the nonlinearity of the tunnel joint stiffness. It should be noted that the comparison between the calculation and observation is not available because soil improvement before the underlying shield tunneling is carried out in the field condition.

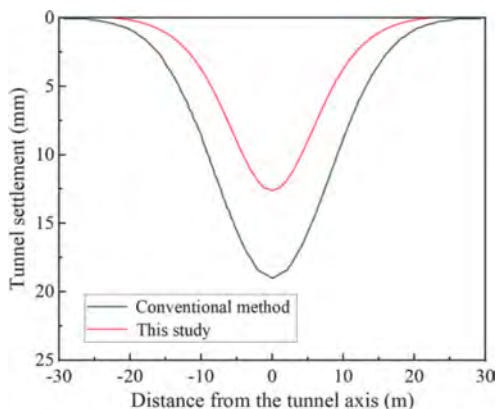


Figure 4. Calculated values of tunnel settlement by theoretical model for soil arching-tunnel interaction and conventional method in which the subsurface ground settlement is determined by Peck (1969).

5 APPLICATION

As aforementioned, nearby tunneling-induced existing tunnel deformation is determined by the ground stress change and soil disturbance degree. The development of the soil arching governs the above two factors. Hence, mitigating the development of the soil arching is an effective alternative for reducing the tunnel deformation. The specific countermeasure for mitigating the tunnel deformation in the cases of shield tunneling is used at the intersection of Metro Line 2 and Line 4 in Changsha, China (Wu et al. 2020).

5.1 Soil improvement method

The overlying existing tunnel deformation is determined by the upward soil arching. Horizontally grouting above the underneath tunnel could reinforce the ground, avoid the underneath tunnel face instability and prevent the loosened zone from developing vertically. Besides,

a key issue involved in this countermeasure is mitigating the disturbance of grouting on the existing tunnel due to the close clear distance between the two tunnels. Spoil discharge jet-grouting (SDJG) technology [S. Nakashima and W. Nakanishi, “All around type reinforcing and consolidating method in the ground and apparatus thereof,” US Patent No. 5,401,121 (1995)] can erode the soil with mixed cement slurry to generate improved columns and also remove the discharging spoil by negative pressure. The spoils can be discharged synchronously during jet-grouting, and the pressure outside the nozzle can be adjusted to a required value by controlling the discharge in light of the measured pressure in front of the injection rod.

5.2 Case history

5.2.1 Site condition

The project studied herein is located at the intersection of Metro Line 2 and Metro Line 4 in Changsha, China. Metro Line 2 has been in operation since 2014, running from west to east. Metro Line 4, a north-south line, is newly constructed. To minimize the tunnel settlement of the operating Metro Line 2 during the tunneling process of Line 4, horizontal SDJG columns are installed to improve the soil layer between the two lines. The soil stratum in the construction site is primarily classified into three layers. The top layer is backfill with a thickness of 2.2 m. It is underlain by a gravel layer with a thickness of about 2.8 m. Under the gravel layer, there is a medium sand layer where the tunnels of Line 4 and SDJG columns were constructed. The relative position between the newly constructed tunnel and the existing tunnel is shown in Figure 5.

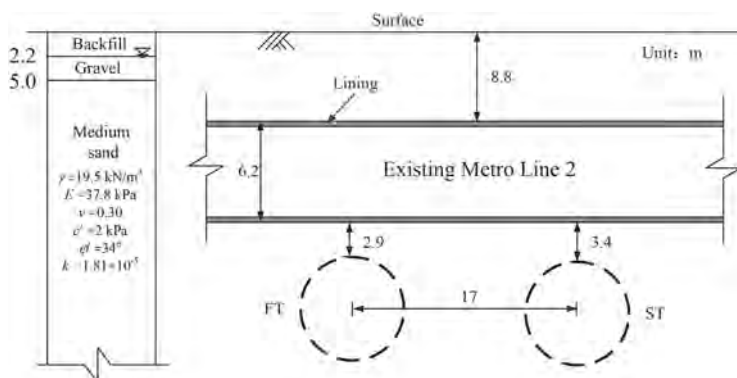


Figure 5. Cross-section view of the relative position between the tunnels.

Based on the soil arching theory described hereinbefore, this study predicts the ground settlement before reinforcement of SDJG technology through calculation, as shown in Figure 6(a). It can be found that the settlement of the ground at the axis location of the existing Metro Line 2 is 19.3 mm, which is far over the control standard (10 mm), so that measures need to be taken to mitigate the tunnel deformation. SDJG is employed in this project to construct 13 horizontal columns to reinforce the soils above Metro Line 4 (Figure 6(b)). The length of the SDJG column is 42.8 m and the radius is 1.0 m. According to the range of the loosened zone, the grouting reinforcement range is determined as $0.2D$ above the newly constructed Metro Line 4 and $0.1D$ at the side. The measured average unconfined compressive strength reaches 3.5 MPa. The measured change in earth pressure near the grouting area ranges from 0.06 to 0.10 MPa.

5.2.2 Deformation response of existing tunnel

The existing tunnels experienced negligible deformation during SDJG construction. The measured vertical displacement of the left tunnel is smaller than 4.0 mm after the shield advancing for Metro Line 4. Overall, the tunneling-induced settlement of the existing tunnel is far smaller than the control value of 20 mm in accordance with MOHURD CJJ/T 202 (MOHURD 2013).

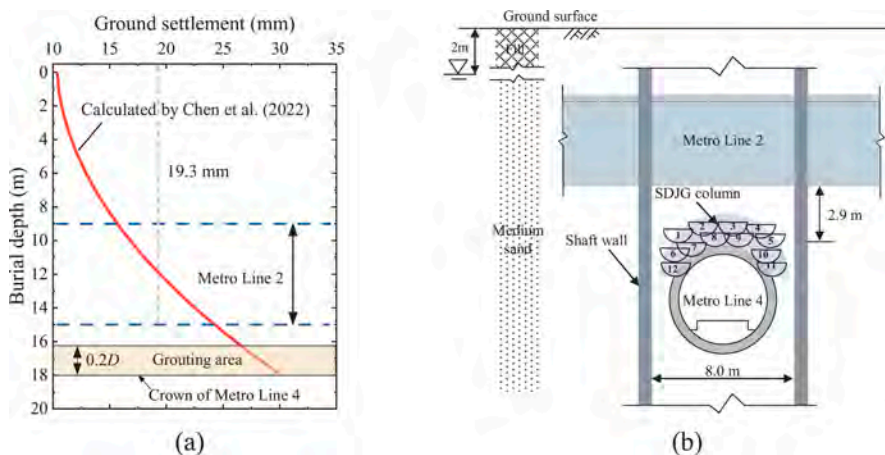


Figure 6. (a) calculated ground surface settlement above the shield tunnel of Metro Line 4 in case of no grouting; (b) SDJG column above Metro Line 4 and relative position between the two metro lines.

6 CONCLUSIONS

This study establishes a theoretical model for soil arching above shield tunnel related to the ground volume loss, as well as a theoretical model for soil arching-tunnel interaction. Emphasis is put on the soil arching effect induced by the undercrossing tunnel and the response of the related existing tunnel. In addition, the corresponding countermeasures for mitigating the tunnel deformation by limiting the development of soil arching are developed and used. The main conclusions can be drawn as follows.

- (1) The arching zone and loosened zone are determined by the ground stress transfer and deformation. The soil arching develops with increasing ground volume loss. Significant ground deformation would occur when the soil arching fully develops. The theoretical model for the tunneling-induced soil arching above the shield tunnel is proposed, as well as the analytical solution for predicting the subsurface ground settlement.
- (2) The theory for soil arching-tunnel interaction is established, which takes into account the nonlinearity of tunnel joint stiffness and the tunneling-induced soil arching effect. It can be used to predict the overlying existing tunnel settlement due to the underlying shield tunneling.
- (3) It is demonstrated through a case history that, limiting the development of soil arching by reinforcing the soils within the loosened zone before the undercrossing shield tunneling is a promising alternative for decreasing the existing tunnel settlement.

ACKNOWLEDGEMENTS

This work was supported by the National Natural Science Foundation of China (grants nos. 52378338; 51938005; 52090082; 52108318). These financial supports are gratefully acknowledged.

REFERENCES

- Chen, R.P., Meng, F.Y., Li, Z.C., Ye, Y.H., Ye, J.N. 2016. Investigation of response of metro tunnels due to adjacent large excavation and protective measures in soft soils. *Tunnelling and Underground Space Technology*. 58: 224–235.
- Chen, R.P., Song, X., Meng, F.Y., Wu, H.N., Lin, X.T. 2022. Analytical approach to predict tunneling-induced subsurface settlement in sand considering soil arching effect. *Computers and Geotechnics*. 141: 104492.

- Cheng, H.Z., Chen, R.P., Wu, H.N., Meng, F.Y., Yi, Y.L. 2021. General solutions for the longitudinal deformation of shield tunnels with multiple discontinuities in strata. *Tunnelling and Underground Space Technology*. 107: 103652.
- Do, N.A., Dias, D., Oreste, P., Maigre, I.D. 2013. Three-dimensional numerical simulation for mechanized tunnelling in soft ground: the influence of the joint pattern. *Acta Geotechnica*. 9: 673–694.
- Franza, A., Marshall, A.M., Zhou, B. 2019. Greenfield tunnelling in sands: the effects of soil density and relative depth. *Géotechnique*, 69(4): 297–307.
- Han, L., Ye, G.L., Chen, J.J., Xia, X.H., Wang, J.H. 2017. Pressures on the lining of a large shield tunnel with a small overburden: a case study. *Tunnelling and Underground Space Technology*. 64: 1–9.
- Hewlett, W.J. & Randolph, M.F. 1988. Analysis of piled embankments. *Ground Engineering*. 21(3): 12–18.
- Iglesia, G.R., Einstein, H.H., Whitman, R.V. 1999. Determination of vertical loading on underground structures based on an arching evolution concept. *Geo-Engineering for Underground Facilities*. ASCE, 495–506.
- Jin, D.L., Yuan, D.J., Li, X.G., Zheng, H.T. 2018. Analysis of the settlement of an existing tunnel induced by shield tunneling underneath. *Tunnelling and Underground Space Technology*. 81: 209–220.
- Lin, X.T., Chen, R.P., Wu, H.N., Cheng, H.Z. 2019. Three-dimensional stress-transfer mechanism and soil arching evolution induced by shield tunneling in sandy ground. *Tunnelling and Underground Space Technology*. 93: 103104.
- Lin, X.T., Chen, R.P., Wu, H.N., Meng, F.Y., Su, D. 2022. Calculation of earth pressure distribution on the deep circular tunnel considering stress-transfer mechanisms in different zones. *Tunnelling and Underground Space Technology*. 119: 104211.
- Meng, F.Y., Chen, R.P., Kang, X. 2018. Effects of tunneling-induced soil disturbance on the post-construction settlement in structured soft soils. *Tunnelling and Underground Space Technology*. 80: 53–63.
- MOHURD (Ministry of Housing and Urban-Rural Development). 2013. Technical code for protection structures of urban rail transit. CJJ/T 202. Beijing: MOHURD.
- Möller, S.C. & Vermeer, P.A. 2008. On numerical simulation of tunnel installation. *Tunnelling and Underground Space Technology*. 23(4): 461–475.
- Peck, R.B. 1969. Deep excavations and tunneling in soft ground. *7th International Conference on Soil Mechanics and Foundation Engineering*. 4: 225–290.
- Sagaseta, C. 1987. Analysis of undrained soil deformation due to ground loss. *Géotechnique*. 37(3): 301–320.
- Schanz, T., Vermeer, P.A., Bonnier, P.G. 1999. The hardening soil model: formulation and verification. *Beyond 2000 in Computational Geotechnics*. 1: 281–290.
- Terzaghi, K., 1943. Theoretical soil mechanics, *John Wiley and Sons*, New York.
- Verruijt, A. & Booker, J.R. 1996. Surface settlements due to deformation of a tunnel in an elastic half plane. *Géotechnique*. 46(4): 753–756.
- Wu, H.N., Shen, S.L., Liao, S.M., Yin, Z.Y. 2015. Longitudinal structural modelling of shield tunnels considering shearing dislocation between segmental rings. *Tunnelling and Underground Space Technology*. 50: 317–323.
- Wu, H.N., Zhang, P., Chen, R.P., Lin, X.T., Liu, Y. 2020. Ground response to horizontal spoil discharge jet grouting with impacts on the existing tunnel. *Journal of Geotechnical and Geoenvironmental Engineering*. 146(7): 05020006.
- Zhao, K., Janutolo, M., Barla, G. 2012. A completely 3D model for the simulation of mechanized tunnel excavation. *Rock mechanics and rock engineering*. 45(4): 475–497.

Exploiting the renewable energy resources of our cities' undergrounds

L. Laloui

Swiss Federal Institute of Technology in Lausanne, EPFL, Laboratory of Soil Mechanics, Lausanne, Switzerland

E. Ravera

GEOEG consulting, Lausanne, Switzerland

ABSTRACT: This paper focuses on innovative technologies that can efficiently and economically tap renewable energy from the urban underground: energy geostructures. These innovative technologies merge geotechnical engineering with energy efficiency, offering both structural support and heating/cooling functions for buildings and infrastructures. The performance of these technologies is governed by multiphysical interactions and phenomena driven by thermal and mechanical loads. Three decades of research have explored the fundamentals of the behavior and performance of energy piles, walls, and tunnels, yielding a variety of tools that can currently serve their analysis and design. This work encompasses this knowledge and bridges the gap between research to practice, showcasing an experimental and computational study that offers valuable insights into the real-world performance of an energy infrastructure installation.

1 INTRODUCTION

1.1 *Energy geostructure technology*

The rapid evolution of digital technology, robotics, and AI is fundamentally reshaping our society while significantly affecting resource consumption. Concurrently, our planet faces climate change due to greenhouse gas emissions and resource depletion. Shifting to a sustainable, low-carbon economy is imperative. Construction consumes 34% of global energy, making the sector a prime target for change. Uncovering the untapped potential of urban subsurface energy resources represents a promising opportunity that could play a pivotal role in decarbonizing the built environment and revolutionizing the construction sector.

Energy geostructures are a new technology that has arisen within the field of shallow geothermal systems over the past three decades. These structures integrate shallow geothermal heat exchangers into the structural elements that directly interface with the ground. Like other shallow geothermal systems, energy geostructures use the low-enthalpy thermal energy present in the earth's surface and exploit the relatively constant temperature field in the shallow subsurface throughout the year (Batini et al., 2015; Laloui and Rotta Loria, 2019).

Heat exchangers can be integrated into various types of foundations and infrastructure (piles, walls, slabs, tunnels, barrettes) and make it possible to harness the renewable thermal energy naturally present in the ground for heating and/or cooling buildings as well as producing domestic hot water and seasonal thermal storage. Alternatively, they can provide heat to prevent icing on the pavements and slabs of structures and infrastructures such as roads, bridges, station platforms, and airport runways or reduce ventilation needs in underground infrastructures. At present, energy geostructures are mainly used in geothermal heat pump

systems. The recent introduction of fifth-generation district heating and cooling networks may pave the way for exploiting energy geostructures as ground-coupled low-temperature energy sources and storage to meet the energy needs of more energy users in neighborhoods rather than individual buildings. Incorporating energy geostructures into fifth-generation district heating and cooling networks can improve the network's sustainability, flexibility, and resilience (Meibodi and Loveridge, 2022).

Energy geostructures are generally made of reinforced concrete. The construction of such geostructures requires the installation of polyethylene heat exchanger tubes to exchange heat with the surrounding ground. These tubes are usually attached to the reinforcing cage of the structure before the concrete is poured (depending on the structural arrangement and the construction provisions) or can be integrated into the drainage paths if, for example, the walls or slabs are insulated from the outside (Figure 1). The pipes can be installed on the reinforcement cage of the energy geostructures either in a factory, in the case of the use of prefabricated piles or prefabricated concrete tunnel segments, or on-site. The dimensions of the heat exchanger tubes and their arrangement in the geostructures are adapted to the latter to minimize the impact on the execution process. A fluid is pumped inside the pipes by electrical equipment and used as a thermal energy carrier. Generally, energy geostructure pipes are of high-density polyethylene, with diameters ranging from 10 to 40 mm and wall thicknesses of 2 to 4 mm. Thermal insulation of the pipes can be considered for the first few meters of the inlet and outlet to limit the influence of climatic conditions on the heat exchange process and optimize energy efficiency. The heat transfer fluid circulating in the pipes is generally water with anti-freeze or a salt solution (Laloui and Rotta Loria, 2019).

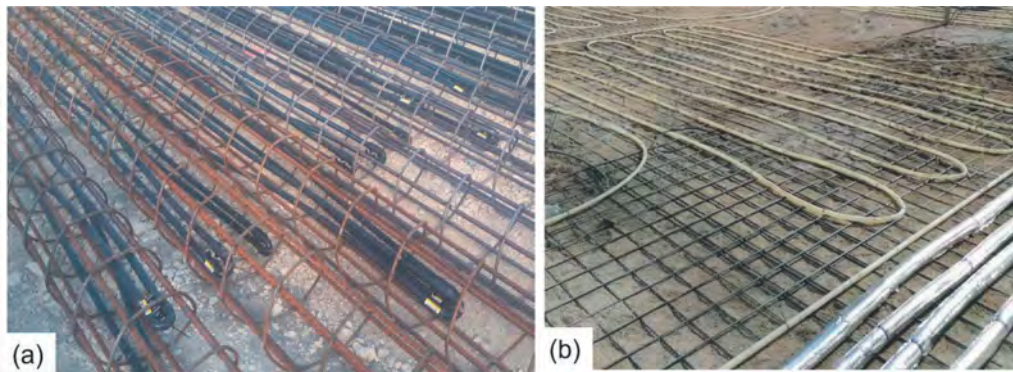


Figure 1. Installation of heat exchanger tubes (a) on the reinforcement cages of foundation structures before the concrete is poured or (b) integrated into drainage channels (image source: GEOEG).

Numerous pipe configurations can be envisaged for energy geostructures. This design variable influences the energy system's installation, operation and running costs. Examples of pipe configurations for different types of energy geostructures are shown in Figure 2. In addition, energy tunnels, walls, and slabs can exchange heat with both the air and the ground. If these characteristics are not properly considered, they can have significant implications for the overall efficiency of the energy system. Depending on the situation, it is possible to seek to promote or limit heat exchange by choosing an appropriate location for the pipes.

2 DESIGN OF ENERGY GEOSTRUCTURES

Analysis of the thermo-hydro-mechanical behavior of energy geostructures requires consideration of the relevant heat transfer, mass transfer and deformation phenomena that characterize the geothermal exploitation and structural support of these technologies. Because of its multidisciplinary nature, the design of a facility with energy geostructures should preferably

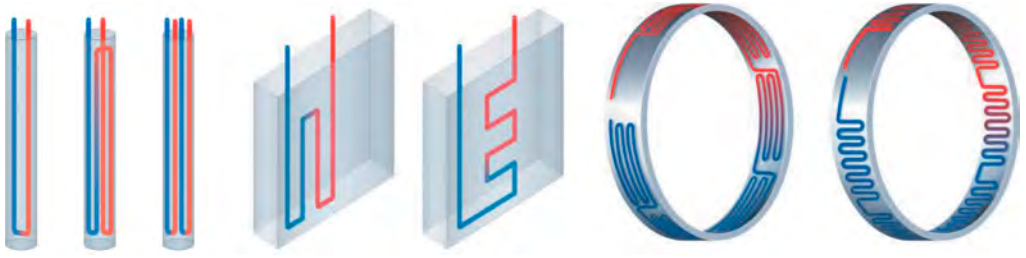


Figure 2. Examples of pipe configurations (modified from Laloui and Rotta Loria, 2019).

be carried out very early on in a project, especially as the geostructures are the first works to be planned and built. Correct dimensioning requires a precise definition of the local hydrogeological context. Energy requirements, both for heating and cooling, also need to be known in advance and as precisely as possible. Different system variants can be considered, evaluated, sized, and compared depending on the geostructures available, their location, their geometry, and their thermal characteristics.

The thermal design of energy geostructures involves analyses to estimate the amount of energy that can be exchanged with the ground or stored in the ground to fully or partially meet the thermal energy loads of buildings or infrastructures. These aspects dictate the outcome of the relative competitiveness between energy geostructures and other energy systems (for example, in terms of performance, return on investment and environmental benefits).

Mechanical design is crucial to ensure the durability and resilience of energy geostructures and superstructures due to the actions involved. Thermal activation of geostructure elements should not be considered detrimental to their geotechnical and structural performance. Nevertheless, the effects (stresses and strains) induced by geothermal exploitation must be considered in the design at service limit states. Verifications must be carried out for this purpose.

2.1 Heat transfer, mass transfer and deformation in the context of energy geostructures

From the point of view of the geothermal heat exchanger role of energy geostructures, the following aspects can be highlighted. In most applications, energy piles are completely delimited by an interface with the soil or rock deposit. On the other hand, energy tunnels and energy walls are additionally characterized by an interface with air flows. The presence of an interface with the air means that aerothermal energy can be harvested in addition to geothermal energy. Figure 3(a) schematically summarizes the heat transfer modes involved in energy geostructures. From the point of view of the structural support role of energy geostructures, the following aspects can be noted. A predominantly axial character typically characterizes the mechanics of energy piles. In contrast, a predominance of bending characterizes the mechanics of energy walls, slabs, and tunnels. Figure 3(b) shows a schematic diagram of the deformation caused by mechanical and thermal loads applied to energy geostructures.

Energy geostructures involve interrelated phenomena where heat transfer induces mass transfer and deformation. In-depth analyses and designs of energy geostructures should consider all these interactions. To model these phenomena, solving relevant balance and constitutive equations is necessary. Through this system of equations, the temperature distributions, the flow fields, the displacement fields, and the stress fields are solved across the finite element mesh.

The continuity and momentum equations are, respectively.

$$\rho_f \nabla \cdot \mathbf{v}_f = 0 \quad (1)$$

$$\rho_f (\mathbf{v}_f \cdot \nabla) \mathbf{v}_f = \nabla \cdot [-p \mathbf{I} + \mathbf{K}] + \mathbf{F} \quad (2)$$

Where ρ_f is the fluid density, \mathbf{v}_f is the velocity vector, p is the pressure, \mathbf{K} is the viscous stress tensor, and \mathbf{F} is the volume force vector.

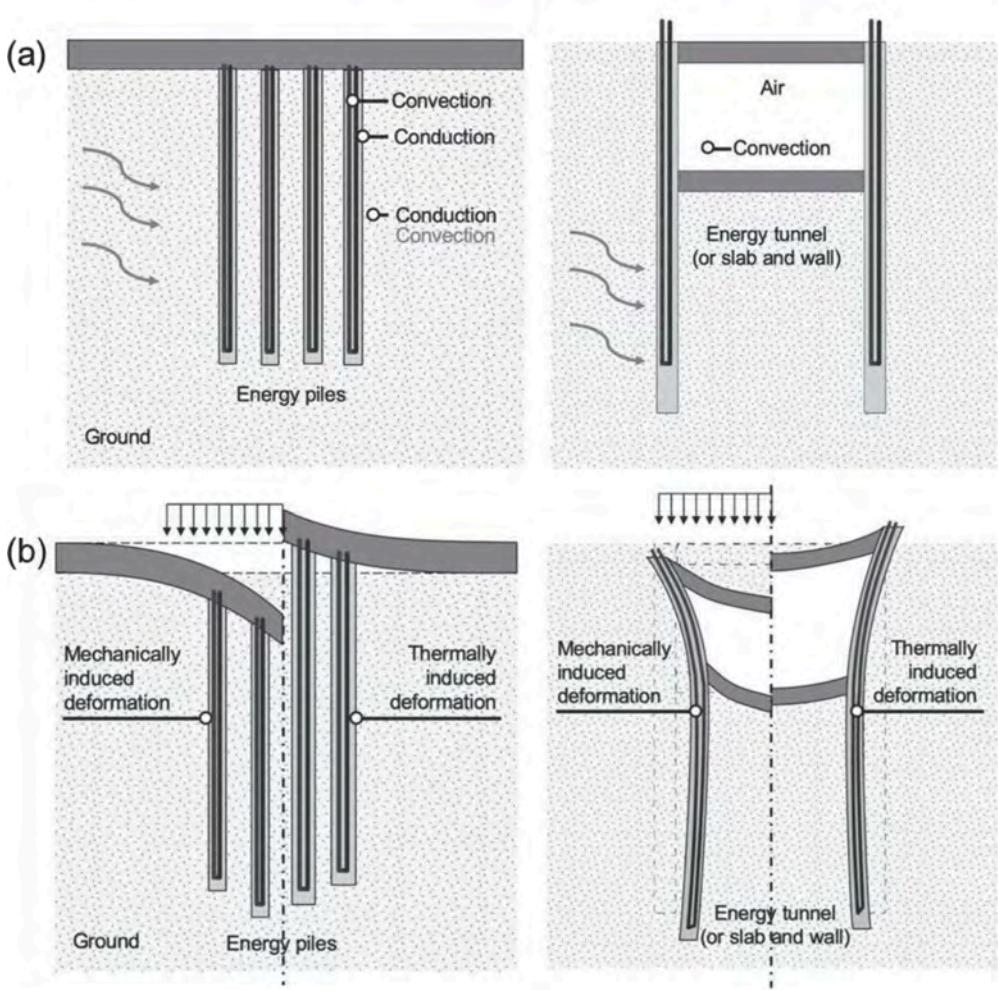


Figure 3. (a) Heat transfer modes in energy geostructures and (b) schematic of deformations characterizing energy geostructures subjected to mechanical and thermal loads. In this case, the schematic refers to positive temperature variations (modified from Rotta Loria, 2020).

When convection and conduction characterize the heat transfer, the energy conservation equation reads:

$$\rho_f c_{p,f} \mathbf{v}_f \cdot \nabla T - \nabla \cdot (\lambda \nabla T) = Q \quad (3)$$

where $c_{p,f}$ is the heat capacity at constant pressure, λ is the thermal conductivity, T is the temperature, and Q is the heat source. Conduction-convection heat transfer problems can be addressed by solving Equation 3 and the mass conservation equation. The previous aspect illustrates the essence of the thermo-hydraulic coupling between heat transfer and mass transfer that occurs as soon as convection is considered.

The momentum conservation equation, written in terms of a simplified indefinite equilibrium equation that neglects the influence of body forces, reads:

$$\nabla \cdot \sigma_{ij} = 0 \quad (4)$$

where ∇ is the divergence operator and σ_{ij} is the total stress tensor. The stress tensor can be expressed as

$$\sigma_{ij} = D_{ijkl}[\varepsilon_{kl} + \beta_{kl}(T - T_0)] \quad (5)$$

where D_{ijkl} is the elastic stiffness tensor, which contains the material parameters (i.e., Young's modulus, E , and Poisson's ratio, ν), ε_{kl} is the total strain tensor, β_{kl} is a vector that comprises the linear thermal expansion coefficient of the material, α , and $T - T_0 = \Delta T$ is the applied temperature variation.

2.2 Thermo-hydro-mechanical behavior of soils and soil-structure interfaces

To address the analysis and design of energy geostructures, it is important to understand the influence of the thermo-hydro-mechanical behavior of soils and soil-structure interfaces on their deformation and load-bearing capacity.

The temperature variations induced in the soil, caused by the operation of energy geostructures, are sufficiently slow to ensure drainage of the water embedded in the soil pores and negligible accumulation of pore water pressure. Therefore, the conditions considered representative for energy geostructures are the drained conditions with respect to thermal loads (Laloui and Rotta Loria, 2019).

Thermally-induced deformation of soils, thermal effects on the strength of soils, soil parameters, and soil-structure interface are the main geomechanics aspects that characterize energy geostructures' behavior. A summary of these aspects is presented below, with particular attention to the application context of energy geostructures.

2.2.1 Thermally-induced deformation

Fine-grained soils have historically received most of the attention in the literature due to their greater sensitivity to temperature changes than coarse-grained soils.

Under normally consolidated (NC) conditions, fine-grained soils contract when heated. Part of this deformation is not entirely recovered upon cooling. Under highly overconsolidated (OC) conditions, fine-grained soils appear to expand when heated, and this deformation recovers upon cooling. The amount of thermally induced deformation also depends on the nature of the soil, through the constituent clay minerals and the plasticity index (Laloui and Rotta Loria, 2019). The cyclic thermal loading of fully saturated fine-grained soils under initially NC or slightly OC conditions can cause further deformation and contraction of these materials, although an accommodating cycle-by-cycle behavior has been observed. For practical ranges of representative temperature variations for energy geostructure applications, very low residual strain changes towards cyclic thermal variations have been observed, and the behavior can be considered mainly reversible (Ravera et al. 2021). No information regarding the cyclic thermal load is currently available in the literature for partially saturated fine-grained soils.

For coarse-grained soils the studies in the literature focus exclusively on coarse-grained soils under saturated or dry conditions, so no information is currently available for these materials under partially saturated conditions. In quantitative terms, these volume changes are about an order of magnitude smaller than in fine-grained soils (Laloui and Rotta Loria, 2019; Rotta Loria and Coulibaly, 2021). It can therefore be summarized that fine-grained soils under normally consolidated conditions show the greatest sensitivity to temperature. Based on the observations considered so far, the temperature sensitivity of the volumetric behavior of fine-grained soils can generally be considered more significant than that of coarse-grained soils. However, based on current observations, the temperature sensitivity for most soils for the practical ranges of application of energy geostructures is limited, and thermally induced deformation is about two/three orders of magnitude lower than mechanically induced deformation. The analysis of these aspects on the design of the foundation over the long term should be considered in case of thermal imbalance. Cycle imbalance can lead to an average ground temperature that deviates from the initial one and thus prolongs the action of temperature in

time (Ravera et al., 2021). Time-dependent effects such as creep may be influenced by temperature variations (Laloui et al., 2008).

2.2.2 *Strength*

Observation on the strength of fine-grained soils under non-isothermal conditions highlighted a global shrinkage of the yield surface along with the decrease of the preconsolidation pressure of fine-grained soils at a constant void ratio with increasing temperature. The effect of temperature on the flow rule is typically neglected in soil constitutive models (Laloui and Rotta Loria, 2019).

2.2.3 *Effects on soil parameters*

The presence of temperature variations resulting from the geothermal operations of energy geostructures can have an influence on the properties of soils, thus determining the need to understand these effects. The literature shows a negligible temperature dependence on elastic moduli, the critical state line CSL slope, and the shear strength angle (Laloui and Rotta Loria, 2019). This last observation is particularly relevant since the mathematical formulations for estimating the capacity of energy geostructures depend, in most cases, on this parameter. An increase with temperature was observed for the primary consolidation coefficient, the secondary compression index, and the hydraulic conductivity. However, from a practical point of view, temperature variations associated with the geothermal operation of energy geostructures do not significantly affect the properties of most soils (Loveridge et al., 2017).

2.2.4 *Soil-structure interface*

In the context of energy geostructures, a characterization of the soil-structure interfaces is essential to address phenomena such as mass transfer, heat transfer, and deformation. The soil-structure interface represents a critical zone for the transfer of loads from structural elements to the ground. Based on current knowledge in the field of energy geostructures, the effect of temperature on the soil-structure interface is absent in the case of concrete interfaces with sand and seems to be minimal (Ravera et al., 2021) or at least on the safety side for interfaces with clay because it increases the interface strength (Di Donna et al., 2016).

3 APPLICATION TO A STATION OF THE CEVA LINE IN GENEVA

An experimental and computational study about the performance of a real-world installation of an underground infrastructure is summarized here concerning a station of the Ceva Line in Geneva (Zannin et al., 2022).

The installation consists of an underground structure with two floors. The walls are 20.5 meters deep and have a 1-meter thickness to support a 13-meter excavation. Heat exchanger pipes are integrated into both the walls and the slab. The upper floor functions as a technical room, while the lower level serves as a train station. A glass wall architectural element is positioned 90 centimeters away from the concrete walls, serving as a separator between the walls and the tunnel, as illustrated in Figure 4(e). Modular elements are used to construct the wall, which are 2.5 meters wide and includes embedded heat exchangers. These modular elements feature two U-loop pipes placed near their edges, with subsequent loops connected in parallel. The inflow and outflow sections for the heat exchangers are situated on the top floor, where a heater is installed and linked to the heat exchangers, as depicted in Figure 4(b).

The testing campaign consisted of two phases. First, a Thermal Response Test (TRT) was conducted in August 2019. The second phase involved testing with the heat pump (HP), which allowed for heating and cooling experiments with a constant inflow temperature, simulating real geothermal operational scenarios. The heating tests occurred in December 2019, while the cooling tests were conducted in March 2020.

A specialized monitoring system was designed to carry out and monitor these experimental tests under various geothermal operation modes. This system was used to track the behavior of the heat carrier fluid (HCF) within the heat exchangers and the air environment at levels -1

and -2. It also recorded deformations on the inner surface of the walls at level -2, as illustrated in Figure 4.

The hydro-thermal monitoring system enabled continuous monitoring (at a rate of one record every 30 seconds) of key parameters, including (i) the temperature of the HCF at the inflow and return ends of the heat exchanger circuit, (ii) the flow rate of the HCF, and (iii) the air temperature at the heat pump ventilator, inside the TRT module, and in the undisturbed air of level -1.

The thermo-mechanical monitoring system facilitated real-time monitoring (with records taken every 5 minutes) of (i) air temperature, (ii) wind speed within the tunnel, and (iii) structural deformations on the wall intrados. Air temperature and velocity were measured using temperature sensors and anemometers, while structural monitoring involved strain gauges (Zannin et al., 2022).

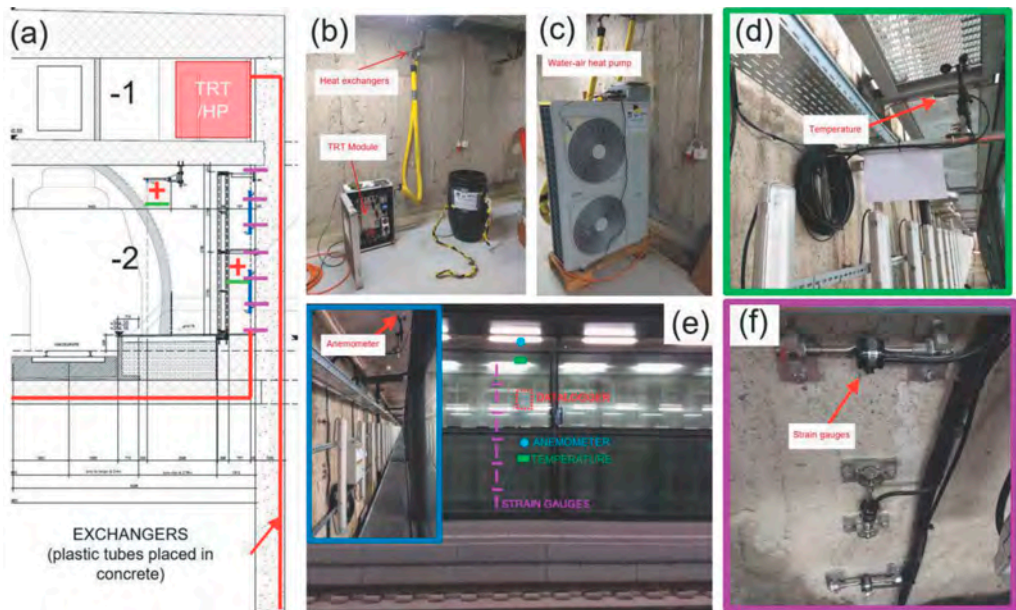


Figure 4. (a) Schematic of the monitoring system setup, (b) details of level -1 with the TRT equipment used to perform the geothermal tests, (c) details of level -1 with the heat pump equipment used to perform the geothermal tests, (d) temperature sensor at level -2, (e) global view of the monitoring system and details of anemometer at level -2 and (f) view of the strain gauges (modified from Zannin et al., 2022).

The monitoring reveals the hydro-thermal behavior and the thermo-mechanical behavior of the infrastructure. Understanding hydro-thermal behavior is essential for understanding the system's energy performance, while monitoring thermo-mechanical behavior helps assess how the structure expands and contracts in response to temperature fluctuations. This information is critical for assessing the structural stability and ensuring that the infrastructure can endure the demands placed on it without experiencing deformation, cracking, or failure.

Figure 5 presents the heating/cooling test profile conducted to achieve the boundary values intended for future representative heating and cooling operations. The figure displays both the observed experimental data and the numerical values employed to replicate the in-situ test, as described in the study by Zannin et al. (2022).

Heating tests are conducted to simulate the summer performance of an underground energy infrastructure system. In these tests, heat is introduced into the ground to generate cool air for use in air conditioning. These heating tests aim to attain high-temperature levels

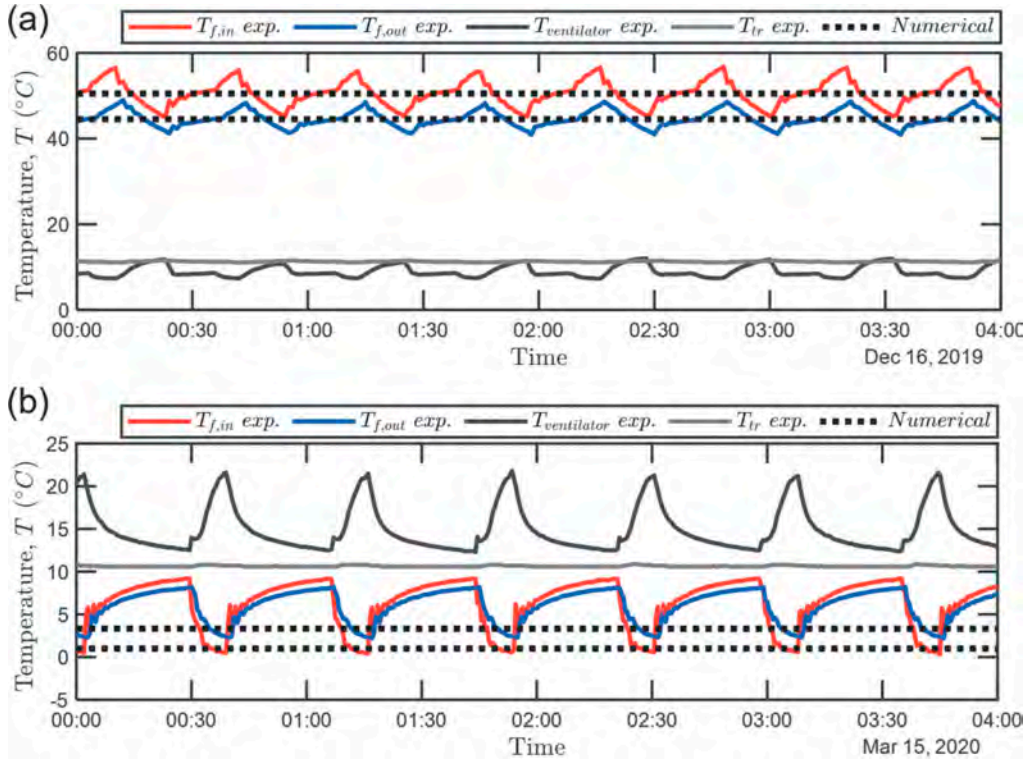


Figure 5. (a) Heating test and (b) cooling test (modified from Zannin et al., 2022).

within the typical range used in low enthalpy geothermal applications and heat storage operations. During these heating tests (which mimic summer operation), the heat carrier fluid is cooled by exchanging heat with the surrounding materials, which are naturally at a lower temperature than that imposed by the heat pump. Consequently, the walls and the surrounding soil get warmed up. Ultimately, the heat pump produces fresh air through its refrigeration cycle.

The cooling test is designed to simulate how an underground energy infrastructure system behaves during the winter season. In this test, the heat carrier fluid absorbs heat from the surroundings, gradually heating the fluid until it reaches the desired outlet temperature. As a result, the pipes, walls, soil, and tunnels experience a cooling effect. The heat pump generates warm air throughout this process to heat the superstructure. The primary objective of this test is to achieve the lowest possible heat carrier fluid temperature that the heat pump can handle, replicating real winter conditions.

To assess the internal forces and ensure the structural stability of the underground energy infrastructure, a comprehensive analysis is conducted, considering both thermal and mechanical load combinations. This involved performing 3D finite element thermo-hydro-mechanical numerical analyses (Zannin et al., 2022).

The initial phase of the analysis involves comparing experimental and numerical results by only considering thermal loads and replicating the heating and cooling tests. Figure 6(a) illustrates this comparison, indicating a close agreement regarding tunnel intrados deformations.

Subsequently, a series of numerical analyses is carried out, focusing on evaluating all potential ultimate (ULS) and serviceability (SLS) limit states while accounting for concurrent thermal and mechanical forces as per Swiss norms (Figure 6(b) and 6(c)). From a thermo-mechanical perspective, the energy infrastructure demonstrates substantial stiffness, allowing

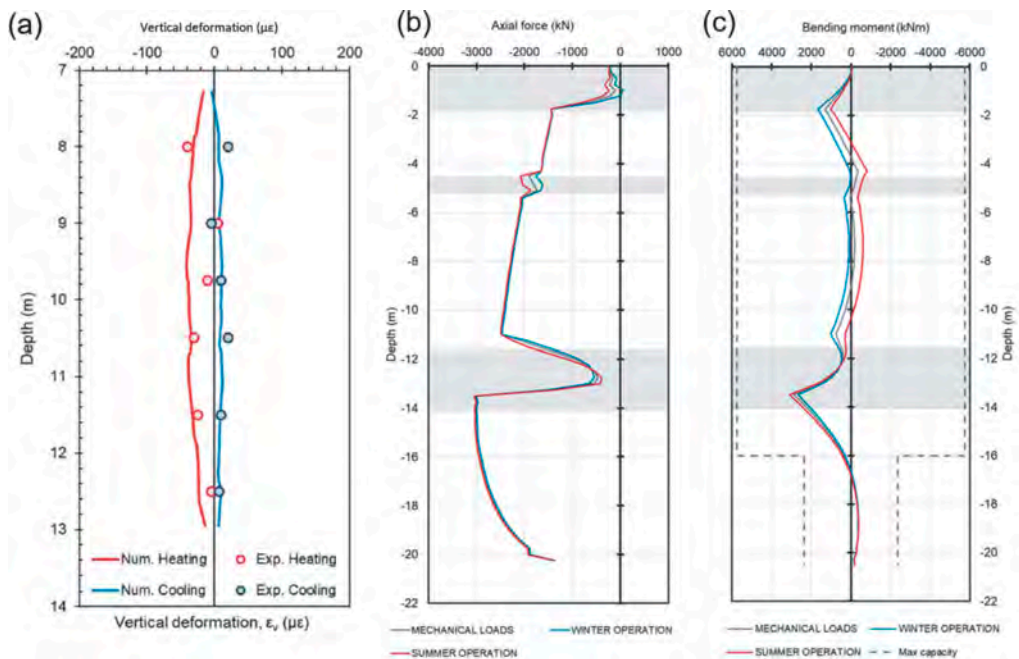


Figure 6. (a) Comparison of the experimental and numerical results for the heating (December 2019) and cooling (March 2020) tests (b) Axial force in the wall at the ultimate limit state: results from 3D numerical thermo-mechanical modeling and (c) Bending moment in the wall at the ultimate limit state: results from 3D numerical thermo-mechanical modeling (modified from Zannin et al., 2022).

it to withstand significant internal forces with minimal displacement and ensuring design limits are effectively met.

4 CONCLUSION

In conclusion, this paper has delved into the field of innovative technology known as energy geotechnical structures, which efficiently and economically harness renewable energy from the urban underground. These technologies combine the principles of geotechnical engineering with energy efficiency, serving the dual purpose of providing structural support and heating/cooling solutions for buildings and infrastructures. The performance of energy geotechnical structures is intricately tied to multiphysical interactions (thermo-hydro-mechanical) and influenced by thermal and mechanical loads.

Over the span of three decades, extensive research has been conducted to unravel the fundamentals of how energy piles, walls, and tunnels behave and perform. This body of work not only encapsulates this wealth of knowledge but also marks the significant transition from theoretical research to practical application. The paper has taken this a step further by presenting an experimental and computational study, which offers invaluable insights into the real-world performance of an energy infrastructure installation.

This study serves as tangible evidence of the viability and practicality of energy geotechnical structures, underlining their potential to deliver sustainable and efficient energy solutions within urban settings.

ACKNOWLEDGMENTS

The authors acknowledge the financial support of SIG (Services Industriels de Genève) through the project “Modélisation des géo-structures énergétiques de la gare CEVA CABA” in the context of the PhD work of J. Zannin.

REFERENCES

- Batini, N., Rotta Loria, A. F., Conti, P., Testi, D., Grassi, W., & Laloui, L. 2015. Energy and geotechnical behaviour of energy piles for different design solutions. *Applied Thermal Engineering*, 86, 199–213.
- Di Donna, A., Ferrari, A. & Laloui, L. 2016. Experimental investigations of the soil–concrete interface: physical mechanisms, cyclic mobilization, and behaviour at different temperatures. *Canadian Geotechnical Journal* 53, 659–672.
- Laloui, L., Leroueil, S. & Chalindar, S. 2008. Modelling the combined effect of strain rate and temperature on one-dimensional compression of soils. *Canadian Geotechnical Journal* 45, 1765–1777.
- Laloui, L., & Rotta Loria, A. F. 2019. Analysis and design of energy geostructures: theoretical essentials and practical application. *Academic Press*.
- Loveridge, F., Low, J., & Powrie, W. 2017. Site investigation for energy geostructures. *Quarterly Journal of Engineering Geology and Hydrogeology*, 50(2), 158–168.
- Meibodi, S. S., & Loveridge, F. 2022. The future role of energy geostructures in fifth generation district heating and cooling networks. *Energy*, 240, 122481.
- Ravera, E., Sutman, M., & Laloui, L. 2021. Cyclic thermomechanical response of fine-grained soil–concrete interface for energy piles applications. *Canadian Geotechnical Journal*, 58(8), 1216–1230
- Rotta Loria, A. F. 2020. Energy geostructures: Theory and application. In *E3S web of conferences* (Vol. 205, p. 01004). *EDP Sciences*.
- Rotta Loria, A. F., & Coulibaly, J. B. 2021. Thermally induced deformation of soils: A critical overview of phenomena, challenges, and opportunities. *Geomechanics for Energy and the Environment*, 25, 100193.
- Zannin, J., Ferrari, A., Kazerani, T., Koliji, A., & Laloui, L. 2022. Experimental analysis of a thermoactive underground railway station. *Geomechanics for Energy and the Environment*, 29, 100275.

Three implementations to reduce geotechnical risk on underground projects using information engineering and AI

M.A. Mooney

Center for Underground, Colorado School of Mines, USA

H. Zheng

Mott MacDonald, USA

H. Yu

Stantec, USA

ABSTRACT: This paper summarizes recent efforts to use continuous monitoring data produced on tunnel boring machine and conventional excavation tunneling projects to estimate tunnel-induced deformation, as-encountered ground conditions and tunnel construction operations. This so-called information engineering approach is aimed at reducing geotechnical risk during construction. The successful implementation of developed approaches is presented herein on three projects in the USA, including the Northeast Boundary tunnel project in Washington DC, the Regional Connector Transit Corridor tunnel project in Los Angeles, and the Northgate Link tunnel project in Seattle.

1 INTRODUCTION

Urban tunneling is complex and challenging. Geotechnical uncertainty is significant due to limited site investigation (typically less than 0.1% of the ground is sampled or tested) and because soil/rock behavior when disturbed by excavation is itself uncertain. Further, allowable deformations of existing infrastructure are relatively small, on order of 10-0 mm. The challenge presented by limited geotechnical site investigation is likely not going to dramatically improve without major innovation. To wit, an entire order of magnitude increase in extent of borings and in-situ testing would be costly and would only raise the sampled/tested ground to 1%.

An alternative approach to reducing geotechnical uncertainty, and therefore geotechnical risk, is to better exploit the real time monitoring data from thousands of sensors on buildings, buried structures, and embedded into the tunnel construction process itself. These data provide valuable information about the actual ground response to tunnel activities. And because tunnel-induced deformation is progressive, i.e., builds over tunneling distances of meters and time periods of hours, using such monitoring data can be useful and is not too late.

This paper documents our recent efforts to use continuous monitoring data produced on tunnel boring machine and conventional excavation tunneling projects to estimate tunnel-induced deformation, as-encountered ground conditions and tunnel construction operations. The objectives of the implementations are divided into two categories. In the first category and addressed via two implementations, the objective is to predict tunnel-induced deformation ahead of the current position such that the contractor could invoke steps to avoid exceeding allowable or alert levels. 3D finite difference method (FDM) modeling is used with advanced constitutive models to accurately capture the complexity of ground response. However, performing 3D FDM modeling and particularly with geotechnical uncertainty measures, is too time intensive to be useful during construction. For this we implemented surrogate modeling. And, given that geotechnical parameters estimated at the beginning of a project are often incorrect, we employ model updating throughout the project. The first implementation

described is for earth pressure balance machine (EPBM) tunneling of the Northeast Boundary tunnel project in Washington DC. The second implementation is for sequential excavation method (SEM) conventional excavation of a crossover cavern as part of the Regional Connector Transit Corridor tunnel project in Los Angeles, California. and the Northgate Link tunnel project in Seattle. The second category objective is to improve tunnel boring machine (TBM) operations via learning from the TBM’s monitored data. One implementation along the Northlink transition extension project in Seattle, Washington is presented and includes characterizing the ground conditions from the EPBM data using machine learning.

2 SURROGATE MODEL UPDATING – TBM INDUCED DEFORMATION

2.1 Northeast boundary tunnel project background

The Northeast boundary tunnel (NEBT) project in Washington, DC is an 8 m diameter tunnel of approximately 8.0 km in length. An extensive geotechnical investigation included 103 boreholes, in-situ testing and laboratory testing was conducted. Soil samples recovered from site investigation were classified in accordance with the Unified Soil Classification System (USCS) and were grouped into engineering soil units (ESUs) depicted in Figure 1 along the alignment with summary descriptions in Table 1. The tunnel tunnel envelope is expected to consist predominantly of G1 and G3 material along with G2 and G4 material in low proportions. G1 and G2 are found to be medium-stiff to hard and over-consolidated, and G3 and G4 are found to be medium dense to very dense with traces of coarse gravels and cobbles. The tunnel was excavated with a 8.0 m diameter earth pressure balance machine (EPBM).

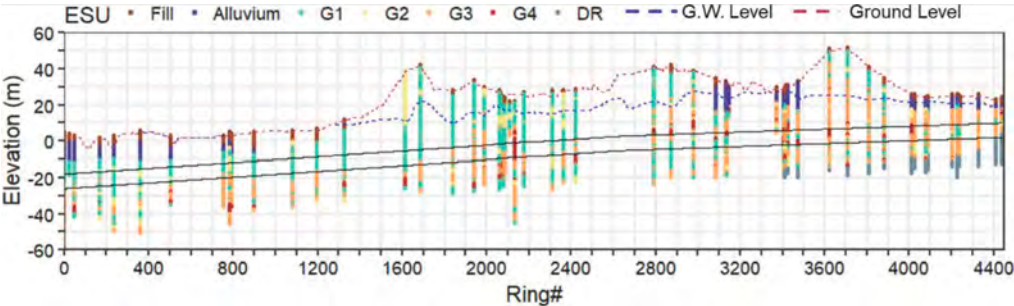


Figure 1. Longitudinal profile of the tunnel, boreholes and ESUs.

Table 1. Description of engineering soil units (ESUs) encountered on the NEBT project.

Engrg Unit	Description
Fill	Fine to coarse-grained soil with fragments of organic material
Alluvium	Inter-layered clay, mixtures of variably dense silt, sand, gravel, and organics
G1	Highly plastic over-consolidated fine-grained soil
G2	Low to medium plastic over-consolidated fine-grained soil
G3	Very dense non-plastic silty/clayey sand, gravel; sand, silt, and low plasticity clay mixes
G4	Fine to coarse sand with trace amounts of coarse gravel, cobbles, and fines

2.2 3D finite difference model calibration

To simulate the EPBM construction, a 3D FDM model was developed using FLAC^{3D}. The general model dimensions and mesh discretization are shown in Figure 2. The EPBM excavation process was modeled by a multi-stage procedure based on Mooney et al. (2016) wherein, for each excavation advance, a length of one segmental ring material is removed. The face pressure is

applied normal to the tunnel face with a gradient distribution based on the recorded average value of EPBM chamber pressure. The shield annulus pressure is uniformly distributed along the length of the shield up to the last ring where it linearly connects to the grouting pressure. The segmental lining is installed five rings behind the face consistent with the distance to the tailshield. Grouting pressure is applied along the last ring installed, and one ring behind the current ring installed, the grout stiffness increases according to a time-dependent modulus increase.

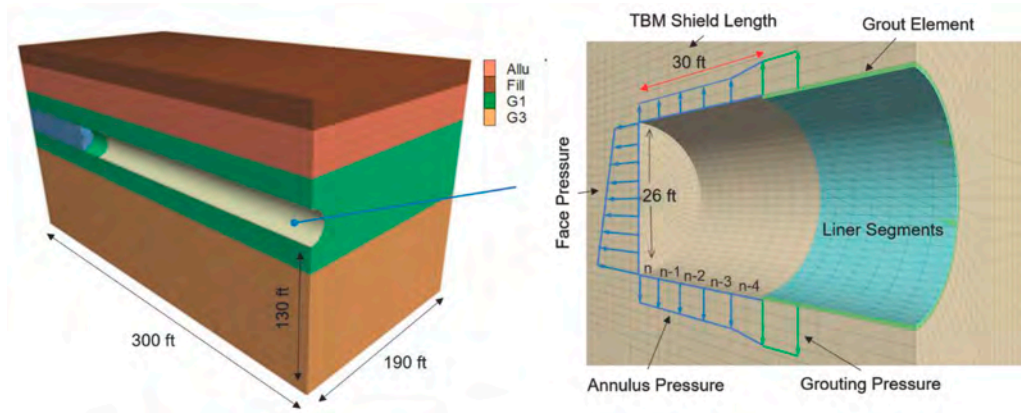


Figure 2. 3D FDM model for NEBT tunneling simulation where face, annulus and grouting pressures from EPBM operations are included in the modeling.

The soil stratigraphy was defined by the most probable ESU conditions from geostatistical modeling (Nebbia et al. 2021). Each ground layer was assumed spatially homogeneous with a constant thickness in order to reduce computing efforts. The hardening soil small-strain (HSS) model was used to represent the ground behavior. For the simulation of mechanized tunneling, the use of a non-linear advanced constitutive model such as the HSS model has significant value as the near field zone is subjected initially to an unloading stress path with unloading-reloading cycles, due to changing confinement conditions from tunnel excavation, chamber/shield pressure changes, and grouting pressure. The HSS model parameters were determined mainly from the results of available lab/field tests, and key parameters were calibrated using measured settlement data during the construction of the initial section. 2 summarizes the parameter used in the FDM model.

Table 2. Input parameters of the HSS model used in FDM model.

Parameter	Fill	Alluvium	G1	G3	G2
p^{ref} (psi)	50	50	50	50	50
m	0.6	0.6	0.85	0.85	0.85
R_f	0.9	0.9	0.9	0.9	0.9
v_{ur}	0.2	0.2	0.2	0.2	0.2
E_{50}^{ref} (psi)	1,450	1,740	4,699	6,947	3,307
E_{oed}^{ref}	1,450	1,740	2,538	6,237	1,414
E_{ur}^{ref} (psi)	4,351	7,252	12,198	20,885	13,793
K_0^{NC}	0.5	0.53	0.63	0.41	0.63
OCR	1	1	7	5	7
ψ' ($^\circ$)	0	0	0	6	0
G_0^{ref} (psi)	-	-	55,114	87,023	60,916
$\gamma_{0.7}$	-	-	3.00E-04	3.00E-04	3.00E-04
c' (psi)	0	0	1.5	0	1.5
ϕ' ($^\circ$)	30	24	22	36	22

2.3 Machine learning surrogate 3D FDM settlement predictor

Given the computational time required to perform 3D FDM modeling during construction, a polynomial-chaos-kriging (PCK) algorithm was applied to predict the 3D FDM-estimated ground settlement induced during EPBM excavation. PCK is a surrogate modeling algorithm that combines two well-established surrogate modeling techniques polynomial chaos expansions (PCE) and kriging (Schobi et al., 2015). PCE approximates the computational model by a basis of orthogonal stochastic polynomials. Kriging is a statistical interpolation method that employs a Gaussian process to represent a sophisticated input and output mapping system. By linking these two methods together, the global behavior of the computational model can be captured by PCE and local approximation can be well represented by kriging interpolation.

The ML model inputs include geological, geotechnical, and EPBM operational parameters as are summarized in Table 3. The geological inputs include the depths of the soil layers (e.g. D_{Fill}), tunnel springline depth (D_{Tsl}), and groundwater table level (D_{GWT}). Nine most influential geotechnical parameters were selected as the geotechnical inputs. The face pressure (P_f) and grouting pressure (P_g) were used as EPBM operational inputs. A total of 800 input parameter combinations were generated to train the PCK model. 3D FDM model simulations were called 800 times to obtain corresponding settlement outputs, which are the longitudinal surface settlement profile and the final surface settlement trough. The split ratio of the dataset for the ML model training/testing was 80/20.

Table 3. Input variables for ML settlement model.

	Parameter	μ	σ	Lower bound	Upper bound	Distribution
Geological condition	D_{Fill} (ft)	16.6	36.4	0.0	39.4	Lognormal
	D_{Allu} (ft)	63.3	984.8	0.0	65.6	Lognormal
	D_{GI} (ft)	81.1	52.6	0.0	196.9	Normal
	D_{Tsl} (ft)	96.0	30.4	55.8	170.6	Lognormal
	D_{GWT} (ft)	87.7	961.1	0.0	105.0	Lognormal
Geotechnical parameters	GI_c (psi)	1.5	0.3	0.6	2.3	Normal
	GI_{ϕ} (°)	22	2.2	18	29	Normal
	GI_{E50} (psi)	4,699	940	1,885	7,513	Normal
	GI_{Eur} (psi)	12,198	3,659	7,542	21,756	Normal
	GI_{E0} (psi)	55,114	11,023	21,756	88,473	Normal
	$G3_{\phi}$ (°)	36	3.6	28	10	Normal
	$G3_{E50}$ (psi)	6,947	1,389	2,756	11,023	Normal
	$G3_{Eur}$ (psi)	20,885	6,266	11,023	39,160	Normal
	$G3_{E0}$ (psi)	87,023	17,405	43,511	139,236	Normal
EPBM parameters	P_f (psi)	44	8	29	73	Normal
	P_g (psi)	58	9	44	87	Normal

2.4 Comparison of model predicted and observed settlement

The surface settlement predicted by the ML model and the FDM model are compared with the field measurements at two monitoring sections in Figure 3. The comparison shows that the ML model performs like the 3D FDM model in successfully predicting ground settlement. Further comparison is presented in Nebbia et al. (2021). The developed ML model was used as a predictor forecasting the settlement as the EPBM advances. To consider the uncertainties from geotechnical parameters and EPBM operational parameters, variations of these variables were included in the analysis. Figure 4 shows the maximum settlement prediction for station 215+00 to 260+00, which includes a range of uncertainty in terms of CI. As shown, the maximum surface settlement has 95% confidence below the 12.5 mm alert level. A wider band at station 220+00 appears mainly due to a shallower cover depth and an increased portion of weak alluvium material, which suggests a better control, is needed within this region. A comparison with measured settlements shows good agreement.

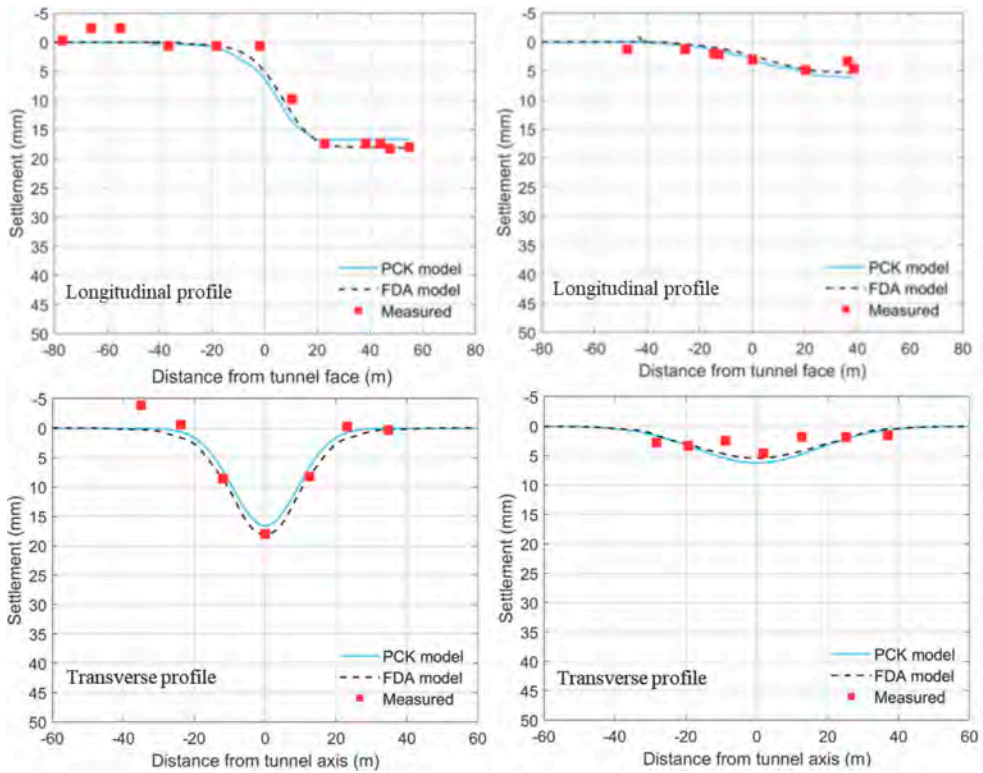


Figure 3. ML settlement prediction compared with the measurements.

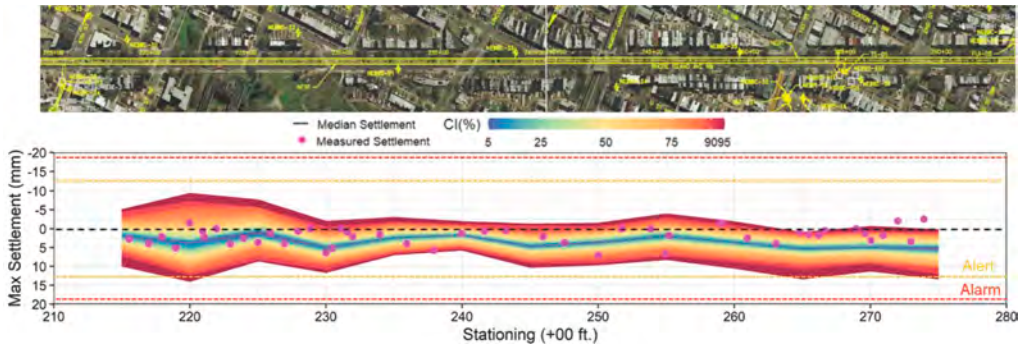


Figure 4. Maximum settlement prediction for station 215+00 to 260+00 considering uncertainties from geotechnical parameters and EPBM parameters.

3 SURROGATE-BASED BAYESIAN PREDICTION – SEM INDUCED DEFORMATION

3.1 Regional Connector Transit Corridor (RCTC) tunnel project

The RCTC project included the sequential excavation method (SEM) construction of a crossover cavern in downtown Los Angeles, USA with dimensions shown in Figure 5. The cavern was excavated in the unweathered Fernando formation (Tf2), a weak clayey siltstone with unconfined compressive strength (UCS) values ranging from 0.2-2.5 MPa (Ulusay,

2014). The Tf2 is overlaid by weathered siltstone (Tf1), coarse-grained alluvial deposits (Qal2) and artificial fill (Af). The groundwater table elevation was approximately 7 m below the ground surface. The Fernando formation has relatively low permeability with hydraulic conductivity ranging from $10e6$ to $10e8$ cm/s. Groundwater inflow into the excavation was not experienced during construction.

Geostatistical modeling was used to capture spatial uncertainty using an approach detailed in Grasmick et al. (2020). The most probable ground profile (Figure 5b) was used in 3D FDM modeling. Extensive instrumentation was employed. Ground surface settlement points (GSSPs) above the left and right drift, multipoint borehole extensometers (MPBXs), and in-tunnel convergence monitoring points (CMPs) close to the center drift and in-tunnel CMPs were used in the back-analysis.

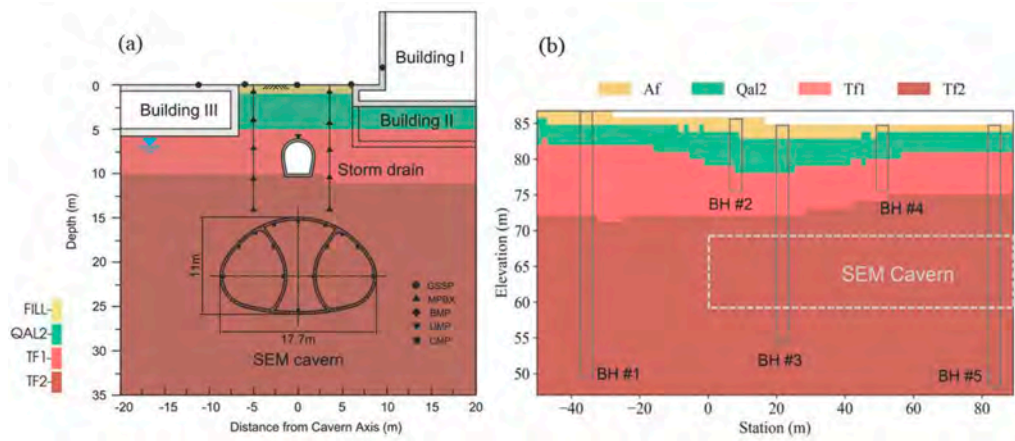


Figure 5. (a) Cross-section of 89 m long RCTC cavern excavated via SEM; (b) Most probable stratigraphy along the cavern's longitudinal profile determined through geostatistical analysis.

3.2 3D finite difference model and PCK Surrogate model

The SEM tunnel construction process was simulated using FLAC^{3D}. Figure 6a shows the dimensions and configuration of the four layer model. Each layer was considered spatially homogeneous but with constitutive parameters modeled as random variables. Explicitly modeling the heterogeneity and spatial variability of the ground properties will increase the computational cost exponentially and thus was not considered here. Undrained response was modeled. The Tf1 and Tf2 layers were represented by the HSS model (Benz 2007) given their significant influence on behavior, while the Af and Qal2 layers were modeled by the elastic-perfectly-plastic Mohr-Coulomb model. Key parameters used in the initial 3D FDM model are detailed in Zheng et al. (2023), where most geotechnical parameters are defined based on all available lab/field tests.

The SEM construction and modeling effort was performed using a three-drift, seven-stage excavation scheme. Stages I through VII involved excavations of LTH, LINV, RTH, RINV, CTH, CBEN and CINV, respectively (Figure 6b). Two temporary walls were demolished in a staggered pattern following the placement of the center invert. The initial support system comprised 300 mm thick fiber-reinforced shotcrete, localised wire mesh and lattice girders. Pre-existing precast concrete tunnel lining (PCTL) segments were removed during excavation (Figure 6c). The left and right drifts had a lag distance of approximately 21 m, and the centre drift was excavated approximately 35 m behind the right drift. Complete information regarding the modeling and excavation procedure can be found in Zheng et al. (2021).

Because the Bayesian approach requires thousands of model evaluations in a short period of time, a PCK surrogate model was constructed to reduce the evaluation time for each input from tens of hours with 3D FDM modeling to seconds. The five most influential parameters on the SEM-induced deformation behavior, and those used as inputs into the surrogate

model, included $Tf2-c'$, $Tf2-E_0^{ref}$, $Tf2-E_{50}^{ref}$, GWT , and $Tf1-E_{50}^{ref}$. Each parameter was treated as a random variable with lognormal distribution, as determined from the geostatistical analysis of the data (Table 4). Hundreds of sample combinations were used to train the surrogate model. For each sample set, the 3D FDM model simulation of the entire SEM construction stage was performed to obtain the corresponding model outputs, comprised of the six deformations shown in Figure 7 after each excavation stage. The normalized RMSE was found to range from 1.8-3.2% for each parameter indicating acceptable error.

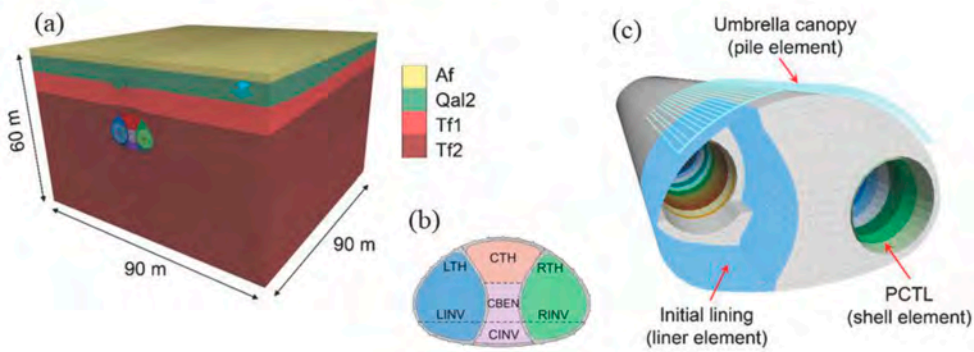


Figure 6. (a) 3D FDM model dimensions; (b) seven stage excavation sequence; (c) 3D FDM image showing modeling of umbrella canopy, pre-existing PCTL and installation of sprayed concrete lining.

Table 4. Summary of parameter ranges used in model development.

Parameter	Mean (μ)	COV (%)	Distribution
$Tf1-E_{50}^{ref}$ [MPa]	48	30	Lognormal
$Tf2-E_{50}^{ref}$ [MPa]	55	50	Lognormal
$Tf2-c'$ [kPa]	170	70	Lognormal
$Tf2-E_0^{ref}$ [MPa]	480	30	Lognormal
GWT [m]	6.8	20	Lognormal

3.3 Bayesian updating of model parameters

Baysian updating was performed on the five parameters identified in Table 4. Six model outputs were compared with field measurements, including the surface settlement at the left and right sides (SL and SR), subsurface settlement (MP) (7.6 m above cavern crown), the convergence of the left drift liner (CM2M3) (3 m above the springline), center crown convergence (CCTH), and center invert convergence (CCINV) as shown in Figure 7.

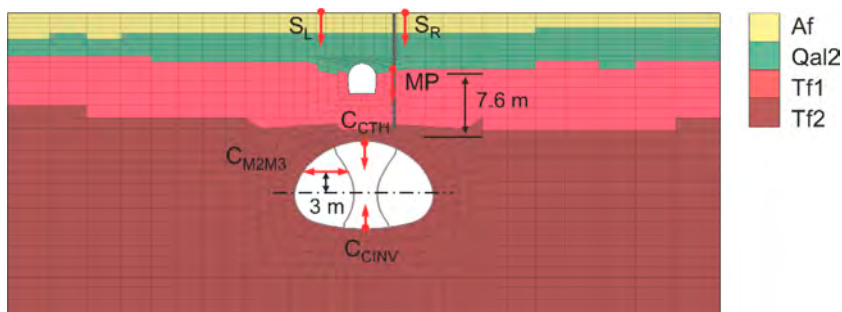


Figure 7. Deformations used in Bayesian updating.

The Bayesian updating of the uncertain parameters began when the LTH was 5 m before arriving beneath the monitoring section. The uncertain parameters were updated progressively with the number of observations growing as the excavation progressed. Since the round length was relatively short and the change of deformation was small, the update interval was set to every four excavation round for the side drifts and center top heading, and two excavation round for the center invert. Five model update phases corresponding to major excavation changes, were defined to visualize the results (Figure 8). At each update stage, all measurements available at that stage were used in the analysis.

Figure 8 presents the revised distributions of the uncertain geotechnical parameters estimated at each major update phase for Sta 0+15. The updated probability distribution functions (PDFs) become narrower as the observed data increases, indicating a reduction in the uncertainty of estimated parameters. The COVs of $Tf1 - E_{50}^{ref}$, $Tf2 - E_{50}^{ref}$, $Tf2 - E_0^{ref}$, $Tf2 - c'$, and GWT reduce from initial values 0.30, 0.45, 0.30, 0.65, 0.20, respectively, to Phase V posterior 0.16, 0.09, 0.06, 0.11, 0.06, respectively. These significantly reduced parameter variances translate into reduced risk simply because prediction uncertainty is far less. Compared to the initial assumption, an obvious increase in mean value can be observed for $Tf2 - E_{50}^{ref}$, $Tf2 - E_0^{ref}$, and $Tf2 - c'$, with mean value increases from initial to post Phase IV of 55 \rightarrow 90 MPa, 480 \rightarrow 550 MPa, and 170 \rightarrow 230 MPa, respectively. The updating results reveal the considerable initial underestimation of the Tf2 modulus and cohesion, e.g. the updated $Tf2 - E_{50}^{ref}$ shifts more than one standard deviation. These findings are consistent with published findings about inaccuracy in estimating HSS parameters from lab test results (e.g. Hsiung et al., 2018, Govindasamy et al., 2019) as well as the importance of back-analysis by comparison to field measurements (e.g. Miro et al., 2015; Zhao et al., 2015).

Another benefit of the Bayesian updating is that the prediction of the responses can also be updated with certain confidence levels. Without the knowledge gained from the field observations, the initial predictions overestimate all observed displacements associated with substantial uncertainties. As the uncertain parameters were updated progressively by Bayesian updating, gradually improved agreement between the final measured displacements and predicted means

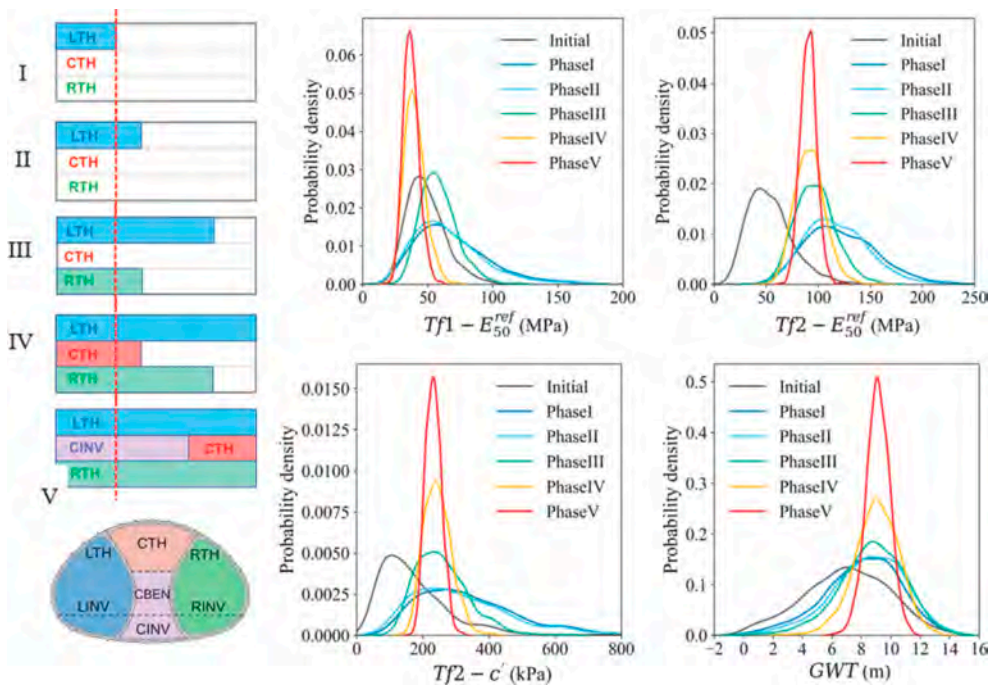


Figure 8. Summary of estimated parameter distributions initially based on geotechnical site investigation data and after Bayesian updating from five phases of excavation.

can be observed. The uncertainty level of predicted displacement also decreases which enables higher confidence that the measurement will be within a specific range.

The operational value of Bayesian updating is illustrated in Figure 9 by the comparison of predicted and observed surface settlement throughout updating. Figure 9 shows the initial estimate of S_L is highly uncertain and with an approximate 0.5 probability that the allowable limit will be exceeded. Upon Phase I Bayesian-updating, this settlement uncertainty and probability of exceeding the allowable limit reduces dramatically. It is worth noting that Bayesian updating does not guarantee that probability of exceedance reduces. Rather, Bayesian updating reduces the uncertainty. As the updating stages continued, observed settlements fell within the estimated ranges.

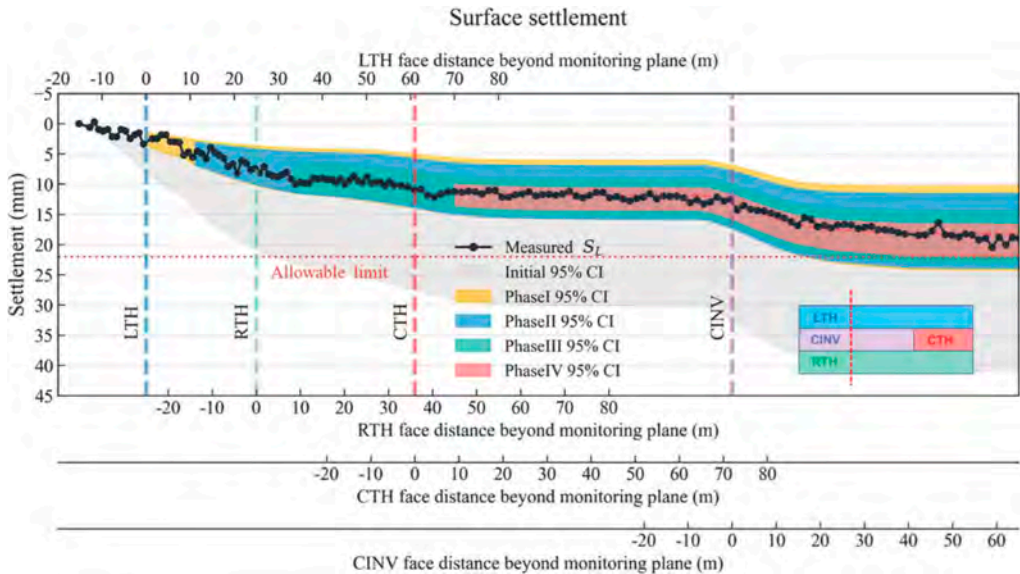


Figure 9. Estimated surface settlement from initial conditions and Bayesian updating compared with measured surface settlement throughout excavation.

4 CHARACTERIZING AS-ENCOUNTERED GROUND FROM EPBM DATA

4.1 Northgate link tunnel project

The Northgate Link tunnel project involved twin 6.4 m diameter EPBM excavated tunnels through 6.4 km of glacial soils as shown in Figure 10. The geotechnical site investigation included 83 boreholes, in-situ testing and laboratory testing. The defined ESUs are shown in

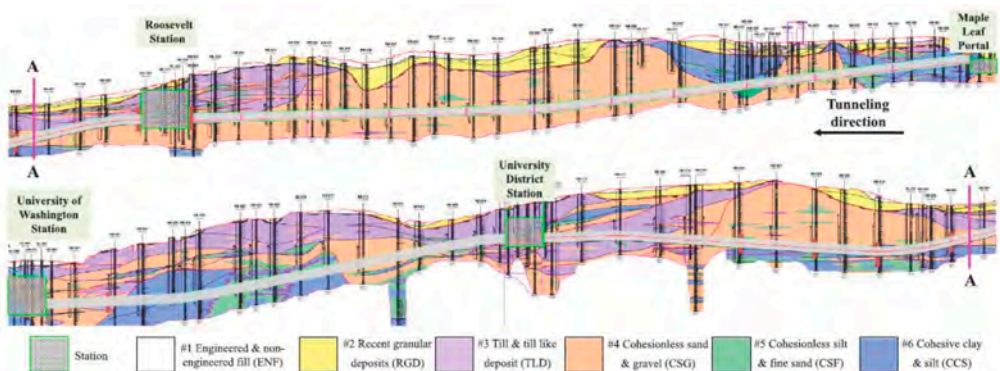


Figure 10. The geological profile for the Northgate Link tunnel project excavated with an EPBM.

Figure 9. The groundwater table was near the ground surface in some locations and below the invert in others. An EPBM was used to excavate the ground. A more detailed explanation of the geotechnical conditions, alignment and EPBM can be found in Yu and Mooney (2023).

4.2 Semi-Supervised Learning (SSL) of ground type

The SSL technique uses supervised learning at the borehole locations where ground truth is available and similarity-based analysis elsewhere (Figure 11). Similarity analysis is based on comparing a quantified similarity measure that quantifies an aggregated difference between EPBM parameters, namely cutterhead contact force, advance rate, cutterhead torque and rotation speed, chamber pressure and its vertical gradient, screw conveyor torque and rotation speed, and excavated soil mass. The SSL model continuously learns as the EPBM passes borehole data along the alignment, and predicts the fractional representation of each ESU within the tunnel envelope. The SSL is not able to localize where the ESUs are within the cross section, e.g. crown, invert, etc.

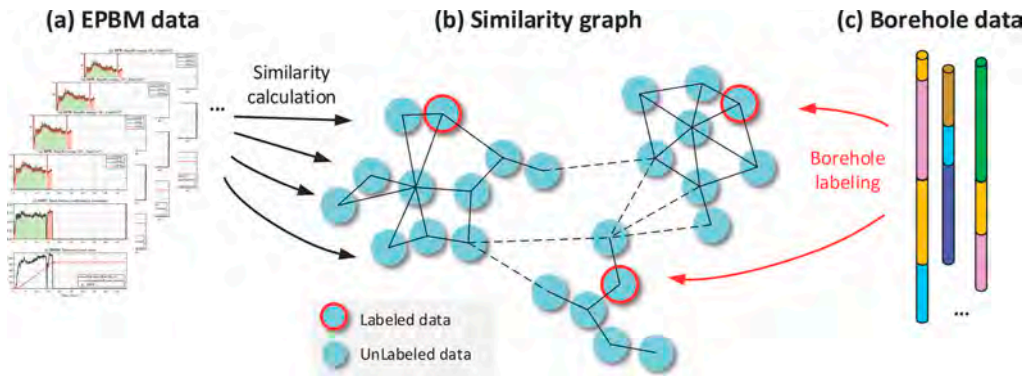


Figure 11. (a) Ring level EPBM data from selected parameters used for similarity analysis; (b) similarity graph where each node represents a ring and its peer similarity is shown by the connecting lines; (c) borehole information used as labeled data.

A comparison of the SSL model-predicted ground types with the geological profile from the geotechnical baseline report (GBR) is shown in Figure 12. The SSL model matches well with the GBR geological profile. One area of disagreement is at the transitions. An investigation of

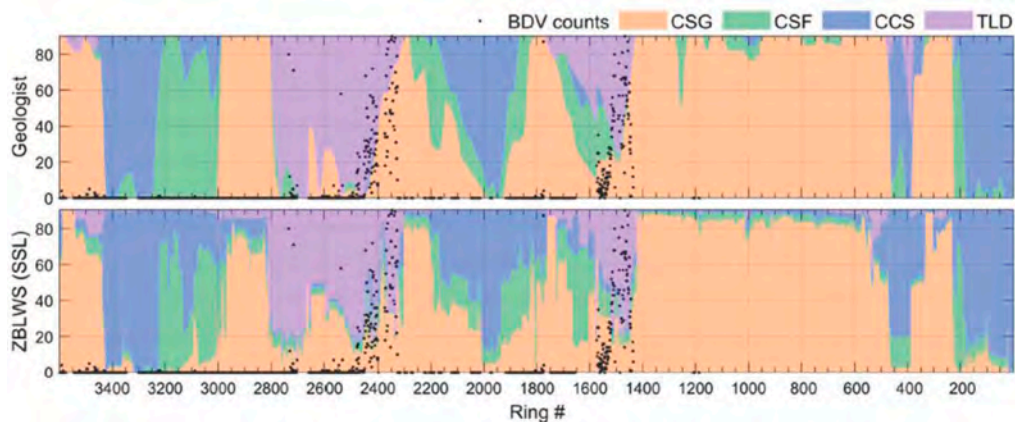


Figure 12. (a) Ring level EPBM data from selected parameters used for similarity analysis; (b) similarity graph where each node represents a ring and its peer similarity is shown by the connecting lines; (c) borehole information used as labeled data.

vibration impacts, shown as boulder detection value (BDV) counts in Figure 12, identifies as ground truth the till deposits (TLD) where boulders and cobbles are known to reside. As observed, the SSL model correctly identifies this ground as TLD whereas the geological profile does not. This indicates that the SSL model is more accurate at transitions. This finding is reasonable because a geologist is interpreting between boreholes spaced 50-100 m apart when drawing transitions while EPBM data is provided every cm.

5 CONCLUDING REMARKS

Uncertainty in geotechnical conditions and behavior leads to considerable geotechnical risk on tunnel projects. The recent adoption of extensive real-time monitoring on tunnel projects provides a vehicle through which geotechnical uncertainty can be reduced in a localized fashion, i.e., during construction and in the near vicinity of the construction activity. Two tunneling-induced deformation implementations were presented herein to demonstrate how geotechnical uncertainty was reduced through the use of monitoring data, forward prediction via 3D FDM models and surrogate ML models, and Bayesian updating of geotechnical parameters during construction. A third implementation showed how EPBM data can be used to provide value, in this case by characterizing the as-encountered ground.

REFERENCES

- Benz, T. 2007. Small-strain stiffness of soils and its numerical consequences, PhD Dissertation, University of Stuttgart. 207 pp.
- Grasmick, J.G, Mooney, MA, Trainor-Guitton, W. and Walton, G. 2020. Global versus local simulation of geotechnical parameters for tunnel projects, *J. Geotechnical & Geoenv. Engineering*, 146(7): 04020048.
- Govindasamy, D., Ismail, M.A.M., Zaki, M.F.M., Abidin, M.H.Z. 2019. Calibration of stiffness parameters for hardening soil model in residual soil from Kenny hill formation. *Bull. Geol. Soc. Malaysia*, 67:131–137.
- Hsiung, B.B., Yang, K., Aila, W., Ge, L. 2018. Evaluation of the wall deflections of a deep excavation in Central Jakarta using three-dimensional modeling. *Tunnelling & Underground Space Technology*, 72: 84–96.
- Miro, S., König, M., Hartmann, D., Schanz, T. 2015. A probabilistic analysis of subsoil parameters uncertainty impacts on tunnel-induced ground movements with a back-analysis study. *Computers and Geotechnics*, 68: 38–53.
- Mooney, M.A., Grasmick, J.G., Kenneally, B. and Yong, F. 2016. The role of slurry TBM parameters on ground deformation: field results and computational modeling. *Tunnelling & Underground Space Technology*, 57(8), 257–264.
- Nebbia, D, Mooney, M, Gangrade, R., Zheng, H, and Smith, J. 2021. NEBT Project: The application of artificial intelligence to improve TBM operations, *Proc. Rapid Excavation and Tunneling*, Las Vegas, NV, June 13-16, 2021.
- Schobi, R., Sudret, B., Wiart, J. 2015. Polynomial-chaos-based kriging, *Int. J. Uncertainty Quantification*, 5(2): 171–193.
- Yu, H and Mooney, MA. 2023. Characterizing the as-encountered ground condition with tunnel boring machine data using semi-supervised learning, *Computers and Geotechnics*, 154:105159.
- Zheng, H., Bragard, C., Calvo, C.H., Mooney, M., Gutierrez, M. 2021. Observed performance and analysis of SEM cavern construction in downtown Los Angeles. *J. Geotech. Geoenvironmental Eng.* 147(11): 05021011.
- Zhao, C., Lavasan, A.A., Barciaga, T., Zarev, V., Datcheva, M., Schanz, T., 2015. Model validation and calibration via back analysis for mechanized tunnel simulations - The Western Scheldt tunnel case. *Computers and Geotechnics*, 69: 601–614.
- Zheng, H, Mooney, MA. 2023. Updating model parameters and predictions in SEM tunneling using a surrogate-based Bayesian approach. *Geotechnique*, <https://doi.org/10.1680/jgeot.22.00299>.

Learning from failure in shallow NATM tunnel

W. Wu

Institute of Geotechnical Engineering, BOKU University, Vienna, Austria

ABSTRACT: We report on the collapse of a shallow tunnel during construction. The tunnel was driven according to the New Austrian Tunneling Method (NATM). This case history brings out several important aspects for tunnel construction. First, it shows the importance of interpretation of instrumentation data and the role of numerical analyses in the decision-making process. Second, it reveals the limitation of the observational method for such processes where spontaneous loss of stability is involved. Moderate or even small deformation does not necessarily mean that sufficient safety is still available. Finally, the provision of a contingency plan as the last resort is indispensable for safe tunnel construction.

1 INTRODUCTION

For short tunnels and those with changing cross sections, e.g. metro stations between running tunnels, the New Austrian Tunneling Method (NATM) often provides a flexible and cost-effective alternative to the mechanised tunnelling method. Developed originally for deep Alpine tunnels in Austria in the 1950s, NATM has been applied for a wide range of ground conditions throughout the world. The application of NATM to shallow tunnels in soft ground was greatly improved by the metro construction in Frankfurt by the end of 1960s and in Munich at the beginning of 1970s, and differs substantially from deep tunnels (Rabcewicz and Golser 1973).

Tunnelling under changing ground conditions poses a formidable challenge to designers, contractors and tunnel experts. The differing geological setting means that each tunnelling project is unique in its own way. Tunnel construction under changing ground conditions means that the designs are to be modified to react to the changing conditions (Muir Wood 2000). On-site decisions on excavation and support are made on a daily or even shift basis. Such decisions have a tangible impact on the safety and economy of the construction. Bad decisions may lead to tunnel failures with casualties. Therefore, it is important to study and learn from the failures in order to avoid similar pitfalls.

Failures are seen as being more instructive than successes. Many laudable civil engineering works completed without incident and giving years of faultless performance do not, as a result of this, receive the attention they deserve. And the quite probably excellent planning that helps predict and plan out risks evidently lacks the drama and excitement of the seat-of-the-pants engineering demanded by a good high-profile crisis. This perception has serious consequences. It seems to be in the nature of man to take a smoothly running project as an indication of an over-conservative design and to question whether the same result could not be achieved more quickly and at less cost. In tunnelling, the pressure to maximise speed and minimise stability measures or, as they say “to optimise”, is the engineer’s constant companion. Often, the most interesting case histories are, to use a euphemism, the “eventful” ones. These do at least grab the attention of the reader and may therefore even fulfil their educational function quite effectively. There is also truth in the saying, that we learn more from our failures than from our successes.

In this paper, we report on the collapse of a shallow tunnel during construction. The tunnel is part of the high-speed rail-link between the cities Hanover and Würzburg, which was constructed some forty years ago (1980s). This failure case was followed by a lengthy litigation and therefore went unnoticed by the public.

2 GENERAL INFORMATION ABOUT TUNNEL

The 1.8 km long Kaiserau Tunnel is located near the town of Melsungen between Kassel and Fulda in the German state of Hesse. It is one of several tunnels built in the mid nineteen eighties through the hilly countryside of middle Germany for a new Hanover - Würzburg high speed rail-link (Figure 1). More than some forty years after its completion the tunnel would not merit much attention, had not an incident occurred during construction, which gave rise to a tunnel collapse to the ground surface. The associated legal dispute went on for several years afterwards.



Figure 1. Tunnel location.

The double track tunnel with a cross-sectional area of around 130 m² was driven according to NATM through arduous underground consisting of water-laden interbedded sandstones and mudstones of the Trias Formation. The regular tunnel cross-section is shown in Figure 2. The overburden varied from 5 m (at the entrances) up to about 100 m. The tunnel support consisted of a primary (initial) shotcrete lining and a final reinforced cast in-situ concrete lining. The waterproofing consisted of a waterproof membrane between the primary and final lining.

Prior to construction, extensive geological and geotechnical investigation was carried out. Despite a comprehensive geotechnical investigation and extensive monitoring programme, however, a major failure occurred during tunnel construction. Six months into the drive and some 150 m from the south entrance an approx. 22 m long tunnel section collapsed just ahead of the bench face, creating a 20 m wide and 5 m deep crater at the ground surface some

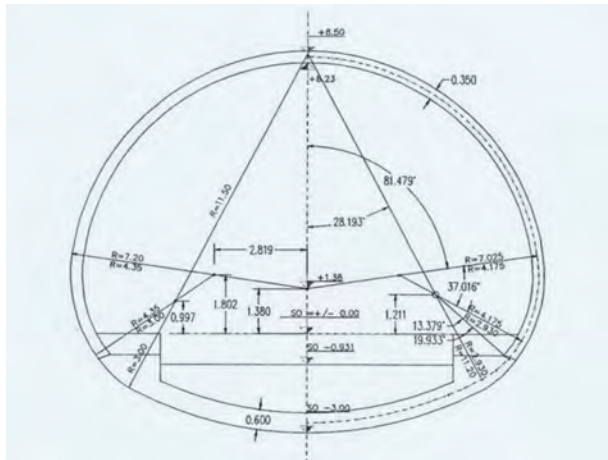


Figure 2. Regular tunnel cross-section.

20-25 m above. Before looking into this tunnel collapse in detail it is worthwhile to look at the geological setting and the construction procedure.

3 GROUND CONDITION AND SUPPORT

The tunnel contract was awarded conventionally, i.e. design-bid-build. Prior to the tendering process, a considerable amount of geotechnical field and laboratory testing had been carried out. The interpretative report enabled the tender documents to reflect fairly accurately the expected range of ground conditions and to provisionally accord appropriate excavation classes to the various tunnel sections. They were also used to define input parameters for the obligatory finite element calculations of the combined rock mass and temporary lining system. The interpreted field and laboratory tests and subsequently defined design parameters and procedure requirements for the tunnel excavation were all set out in the geotechnical report.

The Kaiserau Tunnel lies in Middle and Lower Bunter Sandstone, lower Triassic formations dating back around 230 - 240 million years. The tunnel divides geologically into a northern and southern section. The northern section passes through firm to hard Volpriehausen Sandstone and the underlying Salmünster beds, while in the south weak interstratifications of sandstone, mudstone and siltstone known as the Volpriehausener Interstratifications are to be found (see Figure 3).

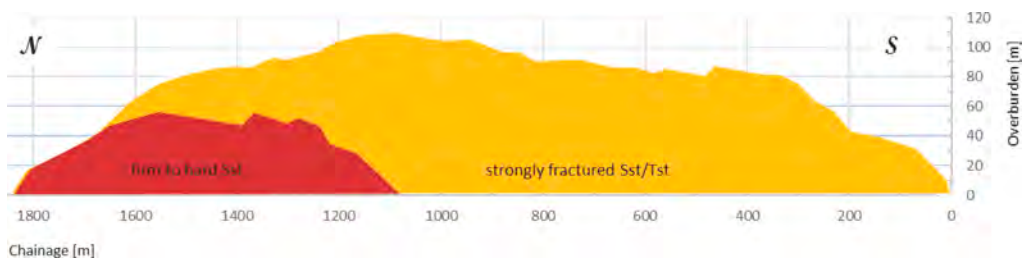


Figure 3. Geological longitudinal section.

The southern formations are characterised by frequent faulting and a high clay fraction. In particular, fault intersections within or just outside the tunnel section made tunnelling arduous and led to significant ground displacements. Water ingress was also a frequent occurrence.

Measurements along the line of the tunnel indicated noticeable lowering of the water table due to the tunnelling operations, while the Volpriehausen Sandstone in the north in contrast presented few tunnelling difficulties.

General permeability was lower than expected. Water ingress of 100 l/s per 100 m for the entire tunnel length had been forecast. The actual maximum measured value of about 20 l/s lay significantly below this value. Most water ingress occurred in the southern tunnel section. The water was generally non-aggressive.

In the southern section, the top heading required additional stabilisation measures at several locations between chainage 150 and 650. In fault zones additional anchors were set, which provided some reinforcement of the immediate surrounding rock mass. At chainage 450, due to the large crown settlement some grouted anchors were also set into the footings of the top-heading lining arch. Furthermore, in very weak rock a canopy of 6 to 8 m long steel pipes was applied as advancing support ahead of the top heading excavation.

Over a length of 40 m around chainage 400 the rock was grouted ahead of the drive using sleeved pipes (manchette tubes). Further along this difficult fault zone the footings of the top-heading arch were grouted to reduce the excessive crown displacements of up to 24 cm.

The tunnel construction was accompanied by an extensive instrumentation program. The general overall settlement was rather large. In the south section in particular settlement of more than 10 cm was normal. The settlement behaviour of the rock mass was found to depend on a number of factors e.g. mudstone fraction, degree of jointing, water saturation, faults, speed of drive etc. The key observations from the collected measurements at tunnel crown were the lasting deformation behaviour in the south section and the relatively constant deformation of about 6 cm in the north section. The highest tunnel crown settlements of around 230 mm were measured in the weak zone around chainage 450.

4 TUNNEL COLLAPSE BETWEEN CHAINAGE 106 AND 132

On August 6th 1985, roughly 8 months into the tunnel drive, the tunnel construction was in full swing. In order to accelerate the construction, the contractor suggested to work simultaneously at the top-heading and the bench/invert. The excavated material was transported via a ramp cut into the bench. A collapse occurred in a roughly 22 m long section of tunnel at and just ahead of the bench face. Some 4000 m³ rock and soil filled the tunnel tube, creating a crater of 20 m wide and up to 5 m deep at the ground surface with an overburden between 22 to 25 m. The miners working at the top-heading were trapped by the collapse. They were evacuated through a steel pipe, which was jacked through the collapse debris. Fortunately, there were no injuries but the collapse delayed tunnel progress for more than half a year and the cost of the delay and associated remedial measures have been estimated at around 3 million € at 1985 prices. This collapse is particularly interesting for a number of reasons: 1. the event was well documented, 2. the ground was relatively homogeneous, 3. numerical analysis carried out before the collapse had highlighted a possible danger with the proposed method of working.

5 SITUATION AT THE TIME OF THE COLLAPSE

The tunnel construction was started in January 1985 with a top-heading from the south tunnel entrance (chainage 0) up to chainage 355. At this point the heading was halted to allow bench and invert excavations to commence and “catch up” the top heading. Note that it was considered as prudent not to allow the gap between opening and ring closure to develop any further since the NATM principles require a fast ring closure in case of need (Austrian National Committee of ITA 1980). From the south portal, the bench and invert were then driven to chainage 89, the invert excavation following closely (never more than 4m) behind the bench excavation, which allowed a fast closure of the shotcrete lining (ring closure).

The status of displacements as of August 5th 1998 between the south entrance and chainage 150 are shown in Figure 4. The following observations can be made. Shortly beyond the

tunnel portal, the displacement increased sharply. For example, for an overburden of about 13 m (chainage 39) the vertical displacements of up to 96 mm were measured. These increased to 126 mm as a result of the subsequent bench/invert drives. At ground-surface settlements of 115 mm (crown drive) and 139 mm (total) were recorded. Unlike the measurements at the ground surface, the measurements at the crown do not capture the entire displacements. The markers in the shotcrete lining are placed after excavation and installation of the shotcrete lining. This part of the displacements at the crown before marker setting is lost before being captured by the measurements.

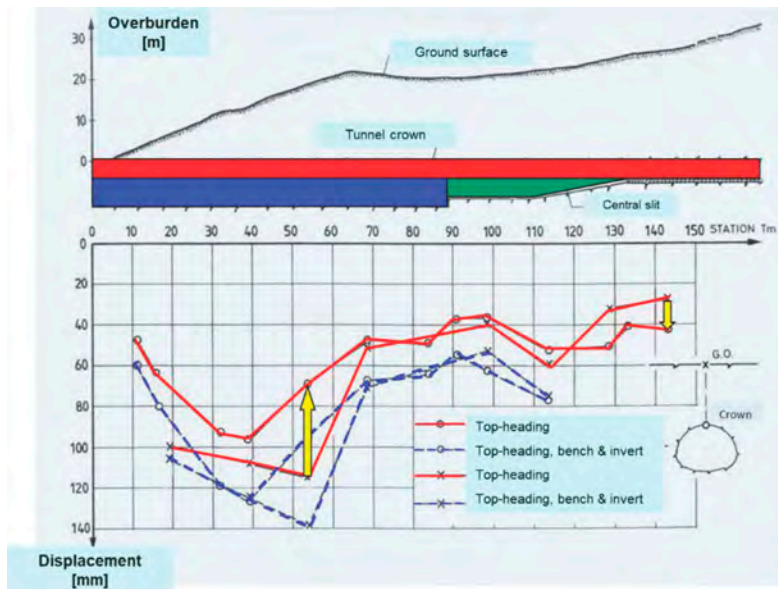


Figure 4. Tunnel long section with measured displacements – chainage 0 – 145.

After chainage 54, despite increasing overburden, the movements dropped significantly. It is interesting to observe the increase in the displacement for the top-heading excavation at chainage 114 and chainage 129 (51 mm at the crown and 61 mm at ground surface respectively). However, these displacements are only half as large as at chainage 39.

To this end, the horizontal measurements were also informative. The measurements were all diverging (i.e. tunnel walls moving apart), as one might expect for shallow tunnels in soft ground. This pointed to weak arching effect i.e. low horizontal stresses, as was predicted in the geotechnical report. The decreasing divergence with increasing chainage indicates too, that the horizontal pressure here was higher than at the start, which also explained the lower vertical movements. This was particularly true for the area of the later collapse. Here the surface settlement was smaller than or roughly as large as the tunnel crown deformation, whereas between chainage 0 and 69 the surface settlement had been significantly larger than the (measured) tunnel deformation.

At chainage 89, in view of the more favourable ground conditions as indicated by the measured settlements, the construction scheme was changed to allow simultaneous driving of the top heading with bench and invert. A vehicular access ramp (gradient 1:10) was cut into the middle of the bench face between bench floor and base of the top heading (the so-called “middle slit”). This would allow mucking and other traffic to freely access both top and bench drives (see Figure 5). As the bench drive progressed the ramp was moved with it. This practice is not uncommon in tunnelling but it can disturb the longitudinal arch in the ground. A filled ramp would be better for the stability but rejected by the contractors for being less efficient.

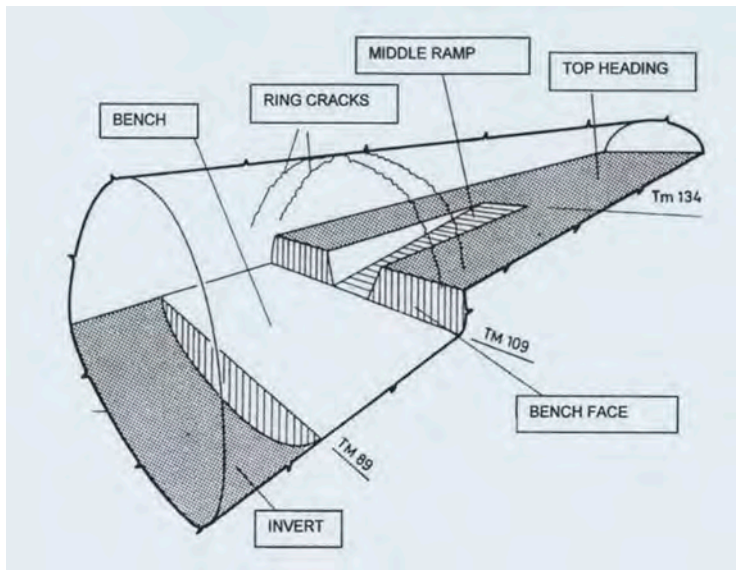


Figure 5. Middle slit ramp allowing simultaneous work at top-heading and bench.

Up to this point the crown heading had been excavated without any unusual incidents with an average speed of 2.5 m/day. The only minor change to the agreed excavation classes had been related to the anchoring. Up to chainage 105 twelve 6 m long anchors per tunnel meter were applied. From chainage 105 m, this had been reduced to six 6m long and six 4 m long anchors with the short anchors set directly overhead and the longer anchors at 10 and 2 o'clock in the tunnel cross section.

The combined bench/invert drive, while the top-heading was halted, achieved rates of ca. 3.6 m/day. However, after restarting the top heading and scaling-down the tunnelling crew on the bench/invert drive, interruptions became frequent and progress slowed down to ca 1.7 m/day. Obviously, the parallel working scheme was rather behind the expectation. The learning curve of the team had taken its toll.

On the morning of the August 6th, the first cracks were registered in the shotcrete lining between chainage 106.5 and 111 (see Figure 6). At this time, the bench face was at chainage 109 and the ramp extended to chainage 134. The deformation in the primary lining increased during the course of the day until some crack development became visible at the top of the ramp as well. The side walls of the ramp started moving inwards and the bench face was being pushed forwards. Efforts were made to stabilise the situation during the course of the morning



Figure 6. Last glimpse into the tunnel before collapse at chainage 109-111.

by installing additional horizontal anchors. However, this remedial action failed when the drilling rod became clamped in the unstable rock mass. A ring closure in shotcrete was also attempted but the fresh shotcrete was too weak to resist the imminent deformations.

Shortly before the tunnel collapse local spalling and destruction of the shotcrete lining could be observed in the tunnel roof between chainage 107 and 115. And rock material started falling into the tunnel before the main collapse occurred. The transition from ever increasing deformations to the fully developed collapse took place in the area of the bench face including the first few meters of ramp. The collapse occurred at about five in the afternoon, creating a huge crater at the surface some 23 m above the crown (Figure 7 and Figure 8). The crater was up to 5 m deep and had an upper radius of around 10 m. The collapse had a funnelling effect like quicksand, drawing down tree roots into the tunnel cross section.

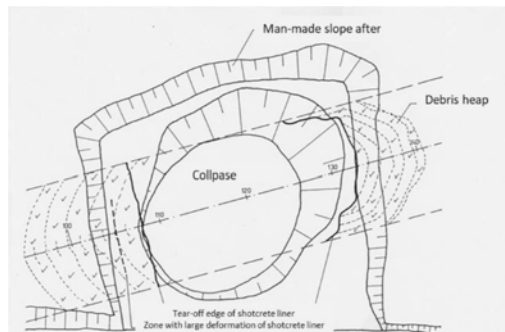


Figure 7. Surface crater caused by tunnel collapse.

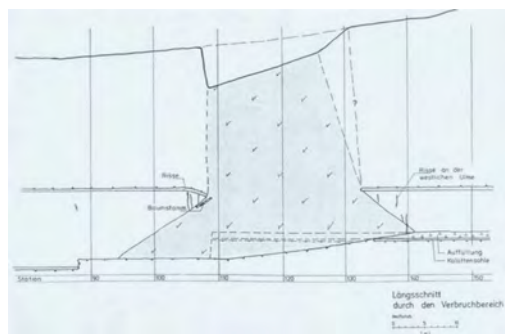


Figure 8. Longitudinal section through the debris heap.

How the tunnel excavation in the collapsed section was secured and later reopened is not the subject of this paper. During the work however, important additional evidence relating to the collapse could be collected. The extent of the cave-in of the rock mass was recorded at chainage 123 and is illustrated in Figure 9. The collapsed shotcrete lining, lying on top of the invert of the original top heading, is clear to see. The circle shown in the middle of the right diagram is the steel pipe used to rescue the team trapped at the top-heading. The abrupt changes in bedding plane can also be seen in Figure 9.

After the collapse, extensive forensic investigation was carried out. The following important facts were recorded:

- There were no apparent construction errors such as insufficient lining thickness, missing reinforcement or fewer anchors.

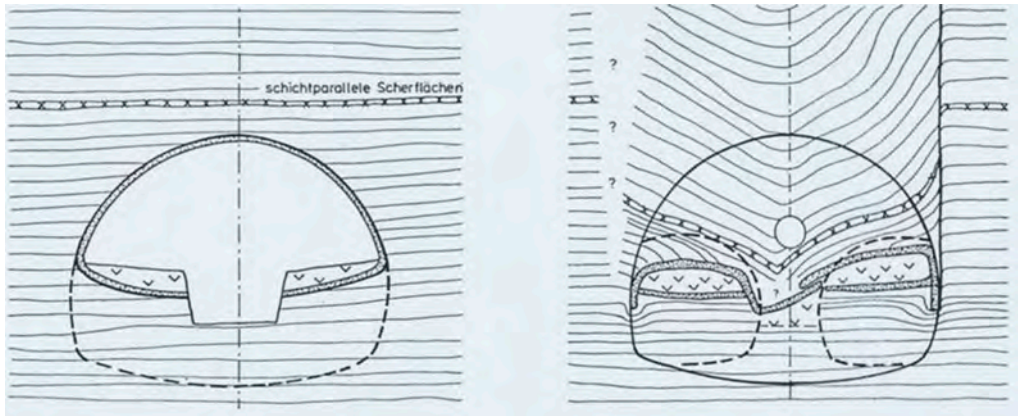


Figure 9. Tunnel cross section and rock strata before (left) and after collapse (right) at chainage 123.

- Whether a possible longitudinal stress redistribution caused by the “hanging” footing in the bench lining from chainage 89 had caused the collapse beyond chainage 109, could not be unambiguously determined, although the crown deformations from the bench excavation measured at chainage 99 and 114 were higher than at chainage 94 and 91.
- The reopening of the excavation showed that the footings of the crown lining had punched down almost 1.3 m and moved up to 0.5 m in towards the middle slit. These movements with concrete bursting into the middle slit can be seen in the photo taken shortly before the fully developed collapse (Figure 6). The photo also showed that the middle slit had been cut too deeply into the bench face. In fact, the lowest 10 m of the ramp were barely sloped at all. This explained also the approx. 5 m longer as planned ramp length (25 m instead of 20 m).

6 STRUCTURAL ANALYSIS BEFORE COLLAPSE

Before the start of the works the contractor carried out a number of FE-analyses of the shotcrete lining. These were based on the representative cross-sections, design parameters and selected excavation classes set by the tunnel consultant (see Table 1). The shotcrete lining had the thickness of 30 cm with two layers of mesh reinforcement (steel mesh Q188 with 1.88 cm²/m in both directions). The shotcrete was C20 with an elastic modulus of 15 GPa. Where field observations differ significantly from the numerical predictions the analysis may no longer be valid for this section. The “pre-designed” excavation class is either under- or overdesigned, with only the former posing a stability problem. Where the excavation class is under-designed it needs to be changed, based on a back-analysis with modified design parameters. This is common practice of decision-making in tunnel construction.

Table 1. Material parameters for rock mass.

Friction angle [°]	Cohesion [kPa]	Elastic modulus [MPa]	Poisson ratio	Earth pressure coefficient at rest	Unit weight [kN/m ³]
25	75	100	0.2	0.35	25

For the load case “lined top-heading and unlined bench” the contractor simulated a temporary construction stage similar to the middle ramp. The calculated max. crown displacement was about 120 mm. The crown footings were calculated as diverging (moving outwards), typical for shallow tunnels with low pressure coefficient. Along the tunnel eaves plastic zones developed which, particularly in the load case with unlined bench, reached the

ground surface. This development highlighted at the very least that the top heading to bench heading transition in weak rock transition could be problematic.

The decision by design checker not to approve the use of a middle slit for bench excavation in poor ground was based on their own FE-analysis of the same tunnel section, which modelled the ramp slit directly. These calculations clearly indicated the unfavourable situation and the tendency for the ramp walls to be pushed up and in towards the ramp middle (Figure 10). Obviously, the simplified calculation of the contractor failed to capture this behaviour. In more favourable ground conditions these effects might be less dramatic and therefore tolerable. So, the deciding weakening factor in tunnel stability was not the slitting of the crown sole itself, but rather the construction of a middle slit combined with comparably weak rock conditions.

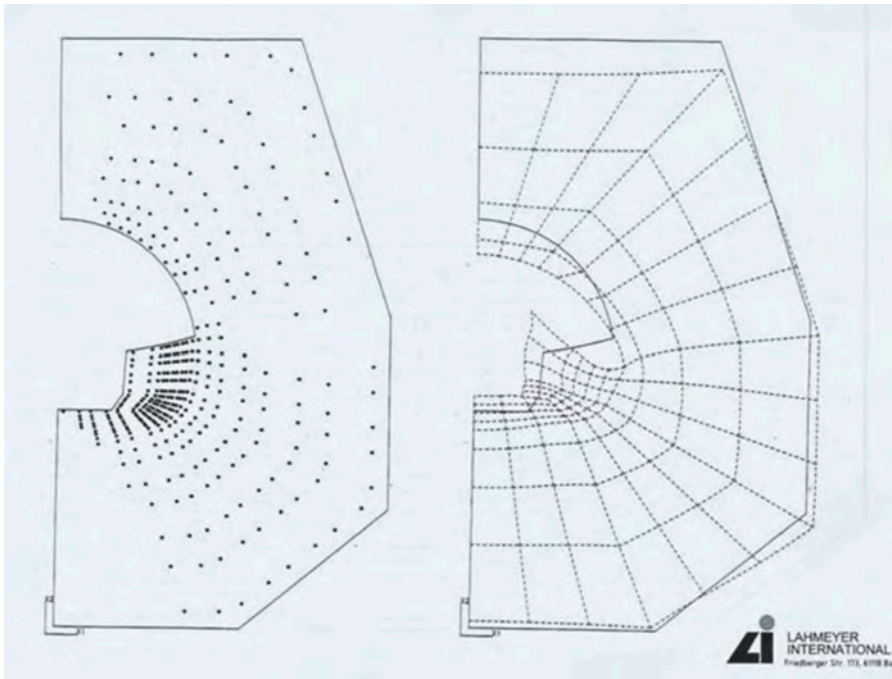


Figure 10. FE analysis for the middle slit by design checker, principal stresses (left) and displacements (right).

Clearly too, the 2D analysis cannot ideally take account of the significant longitudinal arching and load transfer into the hardened lining. However, the checkers conclusion from his own calculations, namely only to allow a middle slit in sound ground conditions, proved with hindsight correct.

What both FE-analyses here could not deliver, in the way familiar from conventional reinforced concrete structures, was to quantify the level of stability of this excavation stage (de Farias et al. 2004). The only guidance is whether equilibrium can be reached during calculation. When after many iterations the out-of-balance forces can still not be taken up elsewhere, the calculation does not reach convergence and indicates a possible stability problem. Even when equilibrium is reached, however, the level of safety above remains mostly unknown. In addition, the extensive monitoring of displacements within and above the tunnel also did not help predict the chain of events that lead to the dramatic collapse. When the large displacements came it was already too late.

7 OBSERVATIONAL METHOD IN TUNNEL DESIGN

The engineering design in tunnelling does not have remotely the status as in structural engineering. Often, the design has to be revised to account for changing ground conditions. This state of affairs gives rise to alternative approaches, e.g. the observational method.

The observational method in geotechnical engineering was proposed by Peck (1969, 2001). In short, the observational method is to modify design in response to measurements. A more recent definition can be found the Eurocode 7, which stipulates the following major requirements for its successful application: (1) establish the limits of behaviour, (2) provide the range of possible behaviour, (3) an extensive monitoring plan, (4) a plan of contingency actions. In tunnelling practice, however, the observational method has been adopted only reluctantly. We are still used to the design practice in structural engineering. An important ingredient of the observational method is the provision of a contingency plan. For the tunnel collapse in this paper, the time from the first sign of critical cracks to the fully developed collapse was only few hours, too short for conventional stabilising measures, e.g. shotcrete and anchors because it takes time for the concrete to harden.

Recently, the immediate support of a shallow tunnel in Germany has become a role model for the contingency plan. The settlements during the top-heading surpassed the alarming limits by far. Neither enhanced shotcrete lining nor more anchors helped reduce the displacement. As the last resort, some tree trunks from the forest nearby placed into the tunnel to bring the displacements to standstill (Figure 11). This unconventional supporting measure is now adopted widely as the last resort for shallow NATM-tunnels and is particularly interesting when the observational method is adopted.



Figure 11. Tree trunks as last resort for shallow NATM tunnel.

The observational method is thought to be particularly suitable for tunnelling construction. However, our failure case shows that the favourable displacements gave no indication of an impending collapse. Rather, the middle slit is thought to be responsible for the collapse. The collapse occurred within relatively short time, which was a clear indication of the loss of stability. The observation method is not well suited for the loss of stability, where small cause may have large effect.

8 CONCLUSIONS

The top heading had given no indication of a possible collapse during the bench/invert drives. The decision to change to a middle-slit concept had been influenced strongly by the construction programme and contractual considerations. The ground conditions (elastic modulus,

stress regime) prevailing at the time of the collapse may have changed as a result of the large deformation by cutting out the middle ramp and letting the tunnel stand too long in partly excavated and unsupported bench excavation with unfavourable longitudinal load transfer. This caused an unfavourable stress redistribution and relaxation.

In addition, the chosen construction sequence led to an increasingly unfavourable take up of load in the tunnel longitudinal direction, which at some stage was no longer able to support the unrestrained, fractured rock mass. Taking the above points into consideration the cause of the collapse can reasonably be said to have been solely due to the middle slit in the bench drive face, which, in the way it was executed, stressed the surrounding rock mass to beyond its load carrying capacity. Had the section been driven without a middle slit - as was the case in the tunnel section between the portal and chainage 89, the collapse would most probably not have occurred.

The New Austrian Tunnelling Method requires that the design shall be modified to account for the changing ground conditions. As such, NATM is believed to epitomise the observational method. However, an important ingredient of the observational method is to provide a contingency plan as the last resort.

REFERENCES

- Austrian National Committee of ITA, The New Austrian Tunnelling Method, Definition and Principles, 1980.
- de Farias, MM, Moraes Jr AH, de Assis, AP, Displacement control in tunnels excavated by the NATM: 3-D numerical simulations, *Tunnelling and Underground Space Technology*, 19(3), 283–293, 2004.
- Golser, J, Keuschnig, M, Weichenberger, FP, NATM – Review and Outlook, *Geomechanik und Tunnelbau*, 13(5), 466–474, 2020.
- Muir Wood, A, *Tunnelling: management by design*, CRC Press, 2000
- Peck, RB, Advantages and limitations of the observational method in applied soil mechanics, *Géotechnique* 19(2), 171–187, 1969.
- Peck, RB, The observational method can be simple, *Proc. Institution Civil Eng. Geotech. Eng.*, 149(2), pp. 71–74, 2001.
- Rabcewicz, L, Golser, J, Principles of dimensioning the supporting system for the “New Austrian Tunnelling Method”, *Water Power*, 25(3), 88–93, 1973.

Bright spark lecture



Taylor & Francis

Taylor & Francis Group

<http://taylorandfrancis.com>

Time-dependent fragility assessment of deep circular tunnels in soft soil

Z.K. Huang*

Assistant Professor, Department of Geotechnical Engineering, Tongji University, Shanghai, China

D.M. Zhang

Professor, Department of Geotechnical Engineering, Tongji University, Shanghai, China

Y.X. Cheng

Postgraduate, Department of Geotechnical Engineering, Tongji University, Shanghai, China

X.M. Deng

Undergraduate, Department of Geotechnical Engineering, Tongji University, Shanghai, China

ABSTRACT: In this research, typical deep circular tunnel sections in soft soils of Shanghai city are used as case studies to reveal the time-dependent fragility functions for deep circular tunnels in soft soils. The seismic performance of the tunnel lining is obtained based on a series of nonlinear dynamic analyses of the soil-tunnel system considering the effect of corrosion on the lining reinforcement. The aging effect due to corrosion of the reinforcement is taken into account by reducing the strength properties of the tunnel lining. Time-dependent fragility curves as a function of free-field Peak Ground Velocity (PGV) and service time t , are developed for minor, moderate and extensive damage states. Results show an overall increase of the seismic fragility for the deep tunnels over time, highlighting the important influence of aging effects on the performance of tunnels. The findings of this study provide an improved understanding of the response of tunnels in soft soils exposed to diverse hazards, and hence, facilitate the life-cycle seismic risk assessment and resilient designs of transport infrastructure.

1 INSTRUCTIONS

The collapse of Dakai station during the Kobe earthquake of 1995 is a rather distinct example, causing the shutdown of the city transportation system and huge economic costs. Therefore, to reduce or even avoid the earthquake-induced damage to tunnel structures, it is of utmost importance to assess their fragility and risk exposure to a range of seismic intensities. Fragility functions constitute a powerful tool to assess the seismic performance and risk of engineering structures. Compared to aboveground structures, the research on the seismic fragility of tunnel structures is limited. Up to now, the seismic fragility analysis of tunnels has mainly relied on observation data (ALA, 2001; Corigliano et al., 2007) and expert elicitation approaches (HAZUS, 2004). More recently, several scholars have proposed a series of fragility functions for different typologies of tunnels and ground conditions using numerical modelling approaches (e.g., Argyroudis and Pitilakis, 2012; Argyroudis et al., 2017). This research contributed to the improved understanding of tunnels' behaviour and reliability under a range of seismic loads, and provided information both for the design process as well as for the risk analysis or stress testing of critical networks subjected to multiple hazards.

*Corresponding authors: huangzhongkai@tongji.edu.cn

The seismic fragility assessment of tunnel structures is commonly carried out assuming that tunnels are optimally maintained during their life span, while the time-dependent degradation mechanisms adversely affecting their performance are commonly ignored. However, tunnel structures are generally designed to operate for over 100 years, and hence, during their long-life span, the materials of concrete, reinforcement and joint bars are expected to deteriorate, and as a result, the strength of the tunnel lining will be decreased (Ai et al., 2016). Particularly, the corrosion of the reinforcing steel is considered as the most common cause of the lining strength deterioration, especially for tunnels located in coastal regions (Gulikers 2003). Moreover, the changing environmental conditions due to global warming and sea-level rise cause an additional increase in the rate of material corrosion (Gao and Wang, 2017).

The above discussion indicates that further research is required to shed light on this aspect aiming to enhance the understanding of life-cycle seismic risk assessment of tunnels. To this end, the probabilistic seismic demand models for the as built and deteriorated conditions of the tunnels considering the impact of lining corrosion are generated. Then, time-dependent fragility curves are proposed for the examined tunnels and corrosion conditions, considering different sources of associated uncertainties. The outcome of this study facilitates more precise and comprehensive life-cycle seismic fragility and risk assessment of tunnels, and hence.

2 NUMERICAL MODELLING

2.1 Tunnel and soil properties

In this study, typical deep circular tunnel sections from Shanghai city, China are selected. The mechanical parameters of the examined tunnel sections are provided in Table 1 and the corresponding cover-to outer diameter ratio h/d is equal to 4.84.

Table 1. Mechanical parameters of the investigated tunnel sections.

Parameters	Adopted value
Embedment depth, h (m)	30.0
Bending reinforcement, A_s (cm ² /m)	58.0
Tunnel outer diameter, d (m)	6.2
Lining thickness, t (m)	0.35
Concrete elastic modulus, E_c (Gpa)	3.55
Concrete Poisson ratio, ν_c	0.2
Steel elastic modulus, E_s (Gpa)	200
Steel Poisson ratio, ν_s	0.2
Concrete cover depth of lining, c (cm)	5.0

This study takes into consideration three typical soil profiles in order to account for the variety of soil conditions in the seismic fragility of tunnels Figure 1 shows the detailed soil properties, namely density ρ , shear wave velocity V_s , cohesion c , and friction angle ϕ for the three soil profiles, represented as D1, D2 and D3, and categorized as soil type D in Eurocode (EC8, 2004) or equivalently site type III or IV based on the Chinese Seismic Design Code (GB50011, 2010). The variation of shear modulus G/G_{\max} and damping ratio D_f with the shear strain level γ for the clay and sand materials are presented in Figure 2, which are obtained from the Shanghai issue code for seismic design of subway structures (DG/TJ08-2064-2009, 2010).

2.2 Soil-tunnel numerical model

The finite element software Abaqus (2012) is employed to numerically analyze the nonlinear dynamic behaviour of the soil-tunnel system. A typical two-dimensional (2D) soil-tunnel numerical model utilized in this research is shown in Figure 3. The x -direction of this

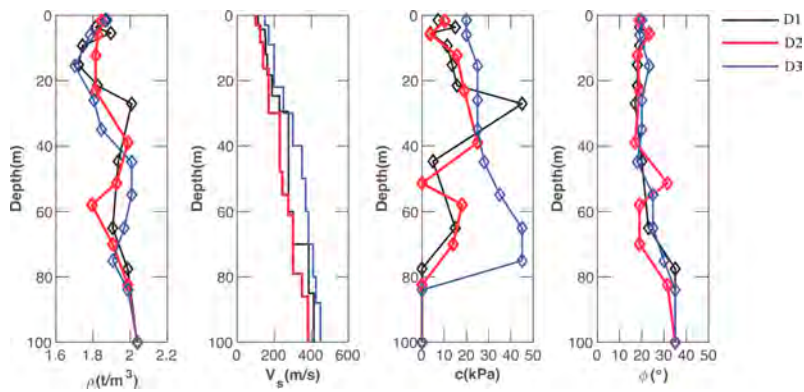


Figure 1. Typical geotechnical properties of the soil profiles.

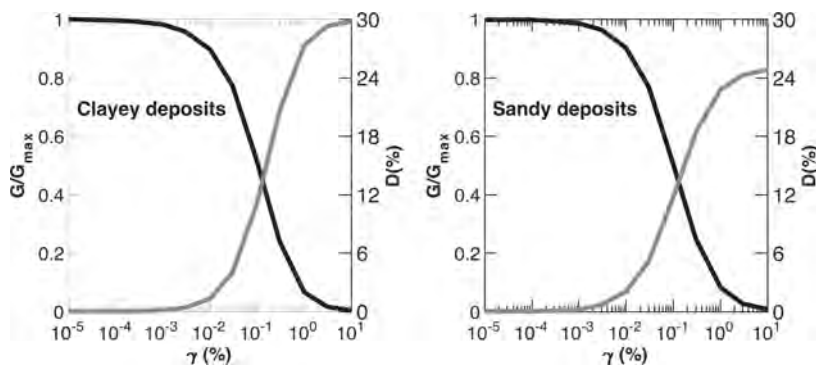


Figure 2. Typical G - γ - D_r curves used for clay and sand in the examined soil deposits.

model (transverse direction) is 400 m, whereas the y -direction (vertical direction) is 100 m. Regarding the modelling of the tunnel lining and to limit the computational cost, two-node beam elements (B21) and a linear elastic model are used. Four node plane strain elements (CPE4R) are adopted for the modelling of soil. A finite-sliding hard contact model is utilized to model the dynamic behavior of the soil-tunnel interface and facilitate the computation efficiency of the potential nonlinear response. The normal and tangential behavior of the interface is simulated by a hard contact formulation and a Coulomb frictional model, respectively.

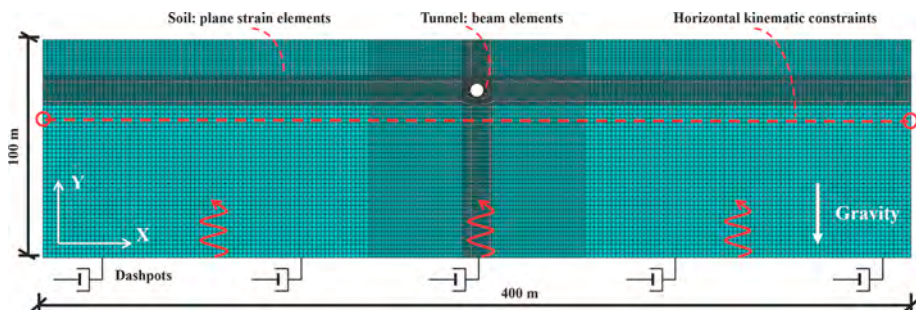


Figure 3. 2D view and the mesh of the numerical model.

For the side boundaries, horizontal kinematic tie constraints, following Tsinidis et al. (2014), are set for the nodes on the opposite vertical sides of the model, to allow them to have the same horizontal deformation. The base of the model is assumed to be the elastic bedrock.

The soil behavior is simulated utilizing the elastoplastic Mohr-Coulomb behavior model. Firstly, the equivalent shear modulus ratio G/G_{\max} and damping ratio are evaluated in the 1D ground response analysis by EERA (Bardet et al., 2000). Then, the equivalent soil properties are integrated with a Mohr-Coulomb yield criterion and are further introduced in the numerical model of the soil-tunnel system.

The numerical analyses, for both the as built and deteriorated conditions of the tunnel, include two steps, i.e. a geostatic step and a dynamic analysis step. To incorporate geostatic stress into the model, the soil-tunnel system is initially analyzed statically while considering the tunnel being in place. The earthquake motion is imposed at the base boundary of the numerical model through the dashpots in the subsequent dynamic analyses.

2.3 Selection of the seismic input motions

For the nonlinear soil-tunnel dynamic analysis, a representative set of earthquake motions is selected to account for the uncertainty in the ground motion and construct a probabilistic seismic demand model for the subsequent fragility analyses of tunnels. The ground motions are selected from the PEER Strong Motion Database (PEER, 2000) using the common spectrum matching method (Iervolino and Manfredi, 2008). Table 2 presents the detail information of 12 real ground motion records that are selected. To ascertain the dynamic response of the tunnel lining under a gradually increasing level of earthquake intensity, the peak ground acceleration values of the selected ground motions are scaled from 0.1g to 1.0g.

Table 2. Lists of records used for the numerical simulations (*PGA*: peak ground acceleration, *Mag.*: Moment magnitude, *R*: epicentral distance).

Earthquake (Year)	Station name	<i>PGA</i> (g)	<i>Mag.</i> (M_w)	<i>R</i> (km)
Tottori, Japan (2000)	TTR008	0.39	6.61	6.86
Northridge USA (1994)	LA - Hollywood Stor FF	0.23	6.69	19.73
Parkfield, USA (1966)	Cholame-Shandon Array	0.24	6.19	12.90
Imperial Valley-07, USA (1979)	El Centro Array #11	0.19	5.01	13.61
Superstition Hills-01, USA (1987)	Imperial Valley W.L. Array	0.13	6.22	17.59
Imperial Valley-02, USA (1940)	El Centro Array #9	0.28	6.95	6.09
Kobe, Japan (1995)	Port Island	0.32	6.90	3.31
Parkfield-02, USA (2004)	Parkfield-Cholame 2WA	0.62	6.00	1.63
Borrego Mtn, USA (1968)	El Centro Array #9	0.16	6.63	45.12
Loma Prieta, USA (1989)	Treasure Island	0.16	6.93	77.32
Kern County, USA (1952)	Taft Lincoln School	0.15	7.36	38.42
San Fernando, USA (1971)	Castaic - Old Ridge Route	0.34	6.61	19.33

3 TIME-DEPENDENT SEISMIC FRAGILITY ANALYSES

3.1 Definition of damage states

The damage measure (*DM*) adopted in this study is determined as the ratio of the actual (*M*) over the capacity (M_{Rd}) bending moment of the tunnel cross-section, as shown in the following equation:

$$DM = M/M_{Rd} \quad (1)$$

According to the previous study by Argyroudis and Pitilakis (2012), five damage states (*ds*) are determined in terms of *DM*, standing for the exceedance of none, minor, moderate, extensive and collapse damage of the tunnels, as shown in Table 3.

Table 3. Definition of damage states for tunnel lining.

Damage state (ds_i)	Range of damage measure (DM)	Central value of DM
ds_0 . None	$DM \leq 1.0$	-
ds_1 . Minor	$1.0 < DM \leq 1.5$	1.25
ds_2 . Moderate	$1.5 < DM \leq 2.5$	2.00
ds_3 . Extensive	$2.5 < DM \leq 3.5$	3.00
ds_4 . Collapse	$DM \geq 3.5$	-

3.2 Definition of fragility curves

The vulnerability of structures is commonly assessed using fragility functions (Shinozuka et al., 2000; Gardoni et al., 2003). The two-parameter lognormal distribution function is widely used in the construction of the fragility curves due to the simple parametric form (Shinozuka et al., 2000; Choi et al., 2004; Cui et al., 2018) and is also adopted in this study. This function can be described by the following equation:

$$P[ds \geq ds_i | IM] = \Phi \left[\frac{\ln(IM) - \ln(IM_{mi})}{\beta_{tot}} \right] \quad (2)$$

where $P(\cdot)$ represents the probability of reaching or exceeding a determined damage state ds_i for a specific intensity IM , which is expressed as peak ground velocity PGV in this study based on the findings of Huang et al. (2021). Φ is the standard normal cumulative distribution function. IM_{mi} is the corresponding median value of PGV at which the tunnels reach the i_{th} damage state. β_{tot} is the total standard deviation and can be further computed as follows in Eq. 3, considering associated uncertainties:

$$\beta_{tot} = \sqrt{\beta_C^2 + \beta_D^2 + \beta_{ds}^2} \quad (3)$$

where β_{ds} represents the epistemic uncertainty associated with the definition of damage state, and is assumed equal to 0.3 (Argyroudis and Pitilakis, 2012). β_C is the aleatory uncertainty associated with the definition of the capacity of the lining of the studied tunnels and is set equal to 0.4 according to HAZUS (2004). The parameter of β_D represents the aleatory uncertainty associated with the earthquake input motions, the frequency content of the seismic input used in the numerical simulation and the corresponding variability in the soil response.

3.3 Consideration of lining corrosion

The chloride-induced corrosion of reinforcement bars is generally recognized as one of the most serious and widespread degradation mechanisms of RC structures. The consideration of lining corrosion in this study follows the modelling employed by Argyroudis et al. (2017). Corrosion initiation time T_0 plays a vital role in the degradation model of lining reinforcement bars based on Fick's second law. Herein, the model introduced by CEB-FIB-Task Group 5.6 (2006) is used to express the corrosion initiation time T_0 :

$$T_0 = \left(\frac{\alpha^2}{4 \times k_e \times k_t \times D_{RCM,0} \times (t_0)^n} \times \left(\text{erf}^{-1} \left(1 - \frac{C_{crit}}{C_s} \right) \right)^{-2} \right)^{\left(\frac{1}{1-n} \right)} \quad (4)$$

where α is the thickness of the concrete (mm), k_e represents an environmental function, k_t is the transfer variable, $D_{RCM,0}$ = chloride migration coefficient (m²/s), t_0 is the reference point of time (years), n is the aging exponent, erf stands for the Gaussian error function, C_{crit} stands for the critical chloride content defined by a percentage by weight of cement ($wt\%$ cement) and C_s is the equilibrium chloride concentration at the concrete surface expressed as a percentage by weight of cement ($wt\%$ cement).

In this study, the corrosion is assumed to grow uniformly along the perimeter of a reinforcement bar. Hence, the time-dependent cross-sectional area $A(t)$ of lining reinforcement bars can be calculated using the following equation (e.g. Ghosh and Padgett, 2010):

$$A(t) = \begin{cases} k \times D_0^2 \times \frac{\pi}{4} & t < T_0 \\ k \times (D(t))^2 \times \frac{\pi}{4} & T_0 \leq t \end{cases} \quad (5)$$

where $A(t)$ is the time-dependent bar cross-sectional area, k is the number of reinforcement bars, D_0 is the original diameter of reinforcement bar, t is the time since the operational start of the tunnel in years, and $D(t)$ represents the diameter of the corroded bar at the end of t , which can be calculated as:

$$D(t) = D_0 - i_{corr} \times \varphi \times (t - T_0) \quad (6)$$

where i_{corr} is the corrosion rate parameter (mA/cm²), φ is the corrosion penetration (μm/year).

Table 4 presents the adopted values of the model parameters describing the chloride-induced corrosion in this study. It is noted that the values of these parameters can refer to the recommendations of FIB-CEB Task Group 5.6 (2006) prescriptions and some relevant research (e.g. Choe et al., 2009; Ghosh and Padgett, 2010).

Table 4. Mean values of parameters affecting the chloride-induced corrosion degradation of RC elements.

Parameters	Value	References
Cover depth \square (cm)	5.0	-
Environmental transfer variable ke	0.325	Choe et al. (2008)
Chloride migration coefficient $D_{RCM,0}$ (m ² /s)	8.9e-12	CEB-FIB Task Group 5.6 (2006)
Aging exponent n	0.3	CEB-FIB Task Group 5.6 (2006)
Critical chloride concentration (C_{cr}) wt% cement	0.6	CEB-FIB Task Group 5.6 (2006)
Surface chloride concentration (C_s) wt% cement	4.5	Choe et al. (2009)
Rate of corrosion (i_{corr}) mA/cm ²	7.0	High corrosion intensity (Stewart, 2004)

Based on the above methodology, the corrosion initiation time can be calculated and is equal to 20.7 years, while the bar area loss is calculated for various tunnel operation years t . For the studied tunnel cases, the bar area loss is defined for three different scenarios, i.e. $t=50, 75, 100$ years, and given in Table 5.

Table 5. Bar area loss (%) for different aging scenarios.

t (year)	50	75	100
Deep tunnel	18.8	33.4	46.5

The DMs for the as built and deteriorated conditions of the tunnel were derived using the following procedures. For the scenario before the corrosion initiation ($t < 20.7$ years), a series of numerical analyses were carried out and the DM is calculated directly based on the dynamical responses of tunnel lining in this case. While for the corrosion scenarios (i.e. $t = 50, 75, 100$ years), firstly, the reinforcement of tunnel lining was modified based on the above-mentioned methodology (Eq. 3), through the modification of bar area for different operation time t . Then, the degradation of the bending moment capacity of tunnel lining can be calculated using section analysis, and thus the time-dependent DM for the considered tunnels can be calculated for the fragility analyses.

3.4 Development of probabilistic seismic demand model

The probabilistic seismic demand model constitutes the basis for the fragility analysis of structures (Gardoni et al., 2003). Generally, it can be obtained through the regression analysis between damage measure (DM) and earthquake intensity (IM) (Freddi et al., 2017). Taking the scenario of initial (as built) conditions ($t=0$ year) and the aging scenario $t= 50$ years as examples, Figure 4 presents the plots (in the natural logarithm scale) of the derived DM - PGV relationships for the examined deep tunnels in soil type D, which represents the sum up of the three soil profiles in a single soil profile.

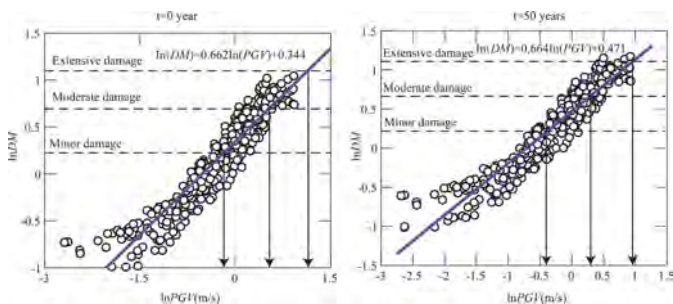


Figure 4. $DM - PGV$ (in m/s) relationship for the examined deep tunnel for initial conditions ($t=0$ year) and for the aging scenario of 50 years.

Following the above approach, for different considered aging scenario $t= 0, 50, 75$ and 100 years, the corresponding fragility function parameters in terms of the median (IM_{mi}) and standard deviation (β_{tot}) can be obtained and they are summarized in Table 6 for deep tunnels.

Table 6. Derived fragility function parameters (PGV in m/s and total standard deviation β_{tot}) for deep tunnel in as built ($t=0$) and different aging scenarios ($t= 50, 75, 100$ years).

t (year)	Minor (m/s)	Moderate (m/s)	Extensive (m/s)	β_{tot}
$t=0$	0.833	1.694	3.124	0.529
$t=50$	0.688	1.397	2.574	0.528
$t=75$	0.582	1.180	2.170	0.530
$t=100$	0.489	0.989	1.817	0.529

3.5 Development of fragility curves

According to the derived fragility function parameters for deep tunnels (Table 6), the computed sets of novel fragility curves in terms of PGV at the surface for different aging scenarios ($t=0, 50, 75$ and 100 years) are given in Figure 5. With the increase of PGV , the damage probability of the tunnel increases for all damage states. Furthermore, the fragility for the deep tunnels will increase significantly as the service time t increases, owing to the aging effects. As an example, for a PGV equal to 1.0 m/s, the exceedance probability of damage for initial conditions ($t= 0$ year) is equal to $0.635, 0.160$ and 0.016 for minor, moderate and extensive damage, respectively. However, for the corrosion scenario of 50 years, the exceedance probability will be increased to $0.846, 0.377$ and 0.072 for minor, moderate and extensive damage, respectively. Thus, for the above three damage states, the exceedance probability for the corrosion scenario of 50 years will be increased on average by 14.4% . Considering the corrosion scenario of 100 years, the exceedance probabilities are equal to $0.912, 0.508$ and 0.130 , for minor, moderate and extensive damage, respectively. This indicates that the exceedance probability will be increased in average by 45.6% for the three damage states. Therefore, it is evident that ignoring the lining corrosion in the design and risk analysis of tunnels will result in an underestimation of structural fragilities. These results highlight the critical effect of lining corrosion on the fragility of tunnels.

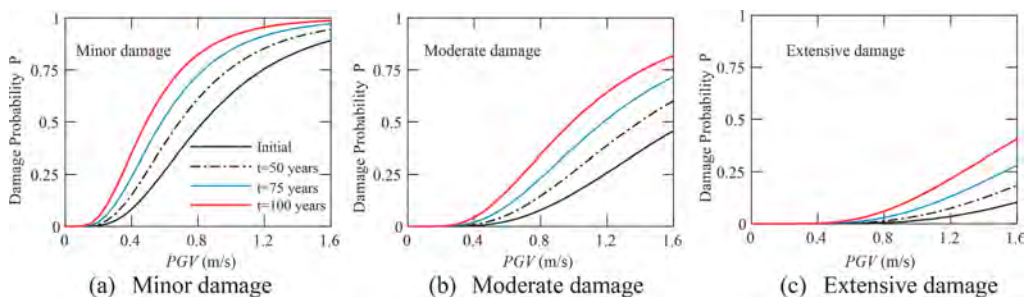


Figure 5. Fragility curves for the deep tunnel in soil type D.

4 CONCLUSIONS

This study developed novel time-dependent fragility functions for deep circular tunnels in soft soils exposed to ground shaking. The influence of aging effect due to lining reinforcement corrosion and earthquake motion characteristics on the seismic response and fragility of tunnels was thoroughly investigated. The seismic performance of the tunnel lining was assessed based on a series of 2D nonlinear dynamic analyses under various levels of seismic intensity. The probabilistic seismic demand models were then generated to estimate the fragility function parameters. The time-dependent fragility curves were proposed for increasing levels of PGV at the ground surface.

From the obtained results, it is evident that the fragility of tunnels is increased with time, due to the degradation of the tunnel lining strength caused by reinforcement corrosion. This highlights the important role of aging effects and earthquake motion characteristics in the fragility of tunnels subjected to seismic loading. The proposed time-dependent fragility curves can be applied in the quantitative life-cycle seismic risk assessment of tunnels in similar soil conditions.

Future studies can include the time-variant corrosion rate in the analysis, accounting for the influential factor of climate change projections, which can exacerbate the water and chloride ingress in concrete structures. More advanced models can be developed to reflect the corrosion mechanisms of underground structures based on laboratory tests, considering the uncertainties in the corrosion process and structural properties, to improve life-cycle fragility assessments.

ACKNOWLEDGEMENTS

The authors would like to thank the support of the National Natural Science Foundation of China (Grant No. 52108381), and Natural Science Foundation of Chongqing, China (No. CSTB2023NSCQ-MSX0808).

REFERENCES

- ABAQUS, 2012. "ABAQUS: Theory and analysis user's manual, version 6.12." Dassault Systèmes SIMULIA, Providence, RI, USA.
- Ai, Q., Y. Yuan, S. Mahadevan, and X. Jiang. 2016. "Probabilistic degradation modelling of circular tunnels assembled from segmental linings." *Struct. Concr.* 17(2): 257–273.
- ALA (American Lifelines Alliance). 2001. *Seismic fragility formulations for water systems part 1 guideline*. Washington, DC.
- Argyroudis, S. A., et al. 2020. "A risk-based multi-level stress test methodology: Application to six critical non-nuclear infrastructures in Europe." *Nat. Hazards* 100(2): 595–633.
- Argyroudis, S., and K. Pitilakis. 2012. "Seismic fragility curves of shallow tunnels in alluvial deposits." *Soil Dyn. Earthq. Eng.* 35: 1–12.
- Argyroudis, S., G. Tsinidis, F. Gatti, and K. Pitilakis. 2017. "Effects of SSI and lining corrosion on the seismic vulnerability of shallow circular tunnels." *Soil Dyn. Earthq. Eng.* 98: 244–256.

- Bardet, J. P., K. Ichii, and C. H. Lin. 2000. EERA. A computer program for Equivalent-linear Earthquake site Response Analyses of layered soil deposits, University of Southern California, Department of Civil Engineering, Los Angeles, Calif.
- CEB-FIB Task Group 5.6. 2006. Model for service life design. *fédération internationale du béton (fib)*.
- Chen, C. H., T. T. Wang, F. S. Jeng, and T. H. Huang. 2012. "Mechanisms causing seismic damage of tunnels at different depths." *Tunn. Undergr. Space Technol.* 28: 31–40.
- Choe, D. E., P. Gardoni, D. Rosowsky, and T. Haukaas. 2008. "Probabilistic capacity models and seismic fragility estimates for RC columns subject to corrosion." *Reliab. Eng. Syst. Safe.* 93(3):383–393.
- Choe, D. E., P. Gardoni, D. Rosowsky, and T. Haukaas. 2009. "Seismic fragility estimates for reinforced concrete bridges subject to corrosion." *Struct. Safety* 31(4):275–283.
- Choi, E., R. DesRoches, and B. Nielson. 2004. "Seismic fragility of typical bridges in moderate seismic zones." *Eng. Struct.* 26(2): 187–199.
- Corigliano, M., C.G. Lai, and G. Barla. (2007). "Seismic vulnerability of rock tunnels using fragility curves." *Proc., 11th Congress of the Intern Society for Rock Mech*, Taylor & Francis, Lisbon, Portugal, 1173–1176.
- DG/TJ08-2064-2009. Tongji University. 2010. Code for Seismic Design of Subway Structures, Shanghai Urban Constructions Communications. Beijing: China Planning Press.
- EC8, 2004. Eurocode 8: Design of Structures for Earthquake Resistance. The European Standard EN 1998-1, Brussels, Belgium.
- Gao, X. J., and X. Y. Wang. 2017. "Impacts of global warming and sea level rise on service life of chloride-exposed concrete structures." *Sustainability*, 9(3): 460.
- GB50011-2010. China Ministry of Housing and Urban-Rural Development. 2016. Code for Seismic Design of Buildings. Beijing: China Architecture and Building Press.
- Gulikers, J. 2003. "Problems encountered in the detection of reinforcement corrosion in concrete tunnel linings—theoretical considerations." *Mater. Corros.* 54(6): 454–459.
- HAZUS-MH. 2003. Multi-hazard loss estimation methodology: Earthquake model. Washington, DC: Dept. of Homeland Security, FEMA
- Pacific Earthquake Engineering Research Center (PEER). 2000. PEER Strong Motion Database. Berkeley, CA: University of California, Berkeley.



Taylor & Francis

Taylor & Francis Group

<http://taylorandfrancis.com>

Basic properties of soft soils



Taylor & Francis

Taylor & Francis Group

<http://taylorandfrancis.com>

General report for basic properties and soil improvement in soft ground

S.Y. Wang

Shenzhen University, Shenzhen, Guangdong, China

ABSTRACT: This general report highlights the papers in the session with the topic of “basic properties and soil improvement in soft ground”. These papers report the recent studies from a wide range of international researchers involving fundamental research on soil properties, soil improvement techniques, and improved material characteristics. Papers related to pile-supported embankment considering geogrid are also included in this topic.

1 INTRODUCTION

There are a total of 9 papers in this session on basic properties and soil improvement in soft ground at IS-Macau 2024, with authors from 4 countries: China, Norway, Austria, and Singapore. The authors of seven papers are from academia, and another two papers are authored by a mixture of academia and industry.

The 9 contributions cover a diversity topics of fundamental aspects of soil properties, soil improvement techniques, and improved material characteristics and applications. For discussion in this General Report, the papers have been grouped into three broad categories:

- Fundamental research on soil properties
- Soil improvement techniques
- Improved material characteristics and applications

Overall, the papers presented several interesting research topics from a wide range of international authors, including some fundamental aspects of soil properties, advanced soil improvement and enhancement techniques, and characteristics and applications of the improved soil materials.

2 FUNDAMENTAL RESEARCH ON SOIL PROPERTIES

The three papers presented in this section are considered to as contributions to the fundamental investigation on soil properties originated from China and Norway.

Wang et al. (2024) performed pull-out tests for the adhesion characteristics of natural and artificial clayey soils to consider the impact of compositional factors, including clay fraction and mineralogy. The findings of the study demonstrate that increasing the clay fraction leads to a proportional increase in adhesion stress. This can be attributed to the larger real contact area at the interface between the soil particles and metal surfaces. Additionally, the presence of montmorillonite, a specific clay mineral, significantly enhances soil adhesion due to its unique microstructural properties.

Wang et al. (2024) also introduced a revised semi-empirical diagram (Figure 1) that allows for qualitative evaluation of compositional factors in relation to clogging potential. The maximum adhesion stresses measured in the experiments align with the region of strong clogging in the diagram, indicating that adhesion stress can serve as an indicative measure for assessing clogging.

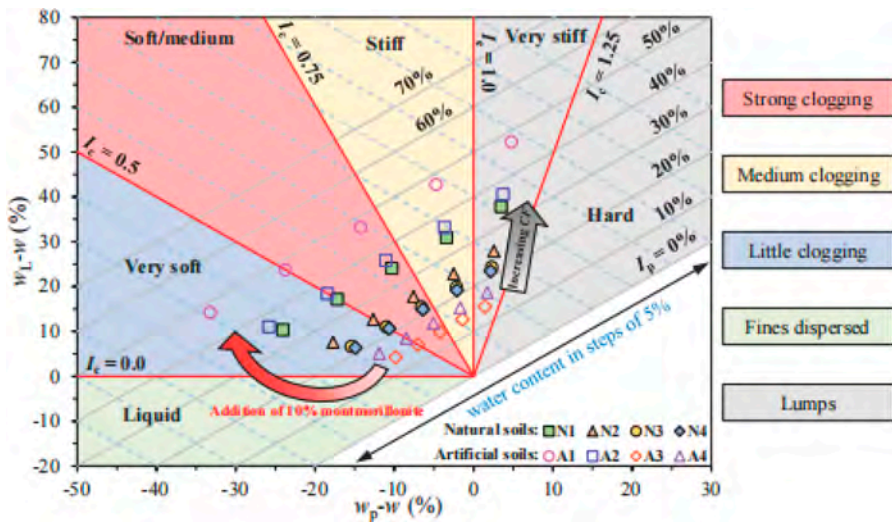


Figure 1. Assessment of the clogging potential of natural and artificial soils using universal diagram updated by considering compositional factors from Wang et al. (2024).

Oberhollenzer et al. (2024) enhanced the characterization of postglacial, fine-grained sediments within the Alpine region through in-situ and laboratory tests conducted at four specific sites. Specifically, the focus was on improving the determination of the in-situ constrained modulus (M) using the Medusa flat dilatometer test (DMT). The researchers initially compared high-quality oedometer results with the correlation proposed by Marchetti (1980) and found that it underestimated the in-situ constrained modulus in Alpine sediments categorized as lean to fat clays according to ASTM D2487-17e1.

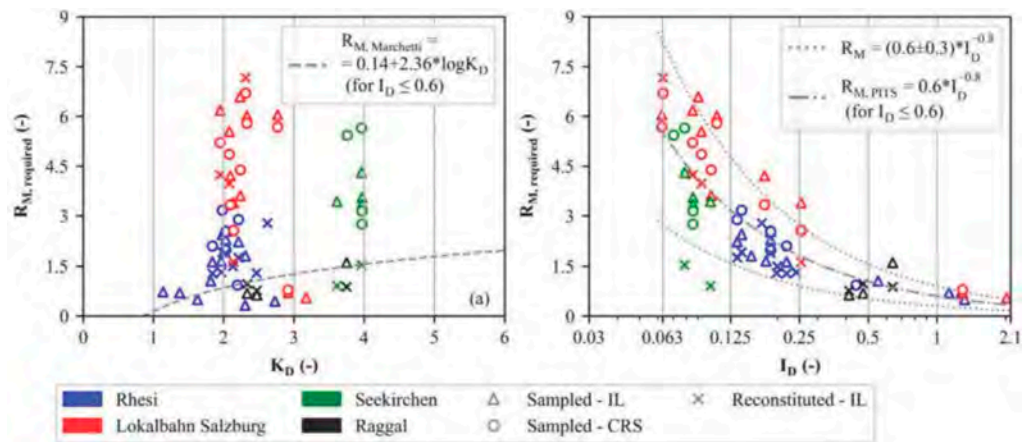


Figure 2. Determination of constrained modulus based on standard DMT-readings (A15/B30) from Oberhollenzer et al. (2024): (a) RM against K_D , (b) RM against I_D .

To address this issue, Oberhollenzer et al. (2024) proposed new correlations for the DMT in order to achieve a better agreement with oedometer tests. The results obtained from the study showed that the agreement between in-situ and laboratory results could be slightly improved by correcting DMT readings for partial drainage. Consequently, new correlations were developed for both uncorrected and corrected DMT readings, leading to an improved agreement with oedometer results. Based on the findings, Oberhollenzer et al. (2024) recommend two

main actions. Firstly, when determining the in-situ constrained modulus from DMT in Alpine fine-grained deposits, it is advisable to use the revised correlations suggested in this study. Secondly, it is crucial to correct DMT readings considering the effects of partial drainage. However, it is important to validate the applicability of these revised correlations in other locations by conducting high-quality laboratory tests.

Li et al. (2024) explored the effects of fines content on particle breakage ratio and fractal dimension in marine coral sand through 1D compression tests (Figure 3(a)). The results demonstrated that coral sand with lower fines content in a loose state is more prone to breakage, while the fractal dimension increases rapidly with higher fines content, followed by a gradual growth. However, higher relative density and larger medium particle size contribute to a reduction in fractal dimension. Li et al. (2024) also propose a relationship between particle breakage ratio and fractal dimension (Figure 3(b)). Additionally, this examines the variations in relative particle breakage ratio and fractal dimension with fines content, relative density, and median particle size, revealing that higher fines content and greater relative density restrain particle breakage. Finally, Li et al. (2024) introduces a logarithmic model for the correlation between particle breakage ratio and fractal dimension.

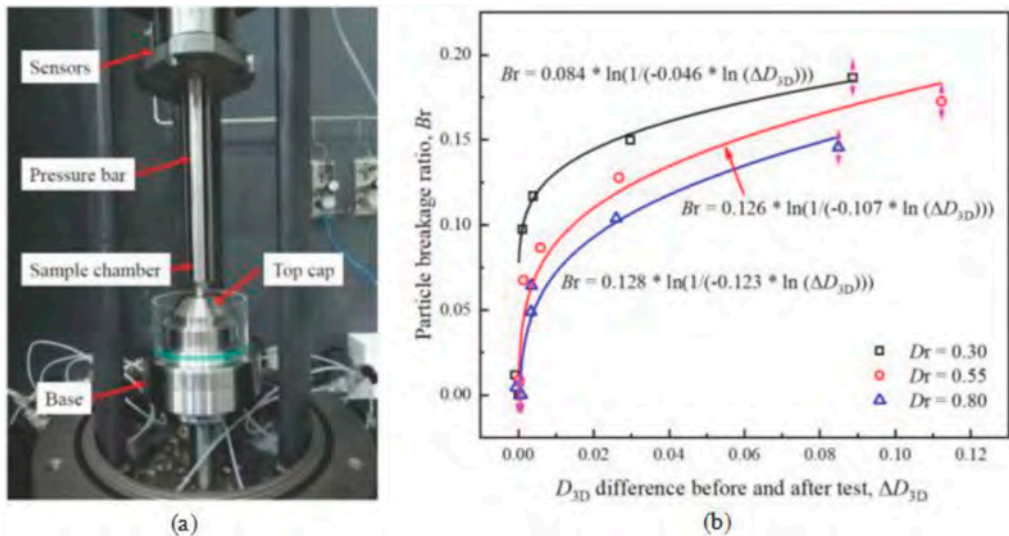


Figure 3. Testing equipment and results from Li et al. (2024): (a) 1D compression test system and (b) Correlation between relative particle breakage ratio with 3D fractal dimension difference.

3 SOIL IMPROVEMENT TECHNOLOGIES

The four papers in this group on soil improvement technologies originate from the Singapore and China. The papers cover the sand-bentonite-binder mixture for construction of two-phase cut-off walls, the contaminated soil treated by nano Zero-Valent Iron (nZVI), the electro-osmosis of soft soil, and the Zn^{2+} -contaminated soils cured by active MgO.

Ting et al. (2024) conducted flexible wall permeability and unconfined compressive strength (UCS) tests on various sand-bentonite-binder mixtures to evaluate their permeability and strength. Furthermore, the effectiveness of MgO-GGBS was compared with other binders including ordinary Portland cement (OPC) and quicklime (CaO)-activated GGBS. The findings indicate that the UCS of MgO-GGBS stabilized soil is 2 to 4 times greater than that of OPC stabilized soil and comparable to that of CaO-GGBS stabilized soil (Figure 4). The hydraulic conductivity of all MgO-GGBS mixtures is well below the permeability requirement of 10^{-9} m/s for the seepage cut-off wall, but OPC mixtures have much higher permeability that

do not meet the requirement. Ting et al. (2024) also identified the hydration products of MgO-GGBS mixtures by the XRD and SEM-EDX. Finally, Ting et al. (2024) highlights the potential application of an effective binder of MgO-GGBS in stabilizing sand-bentonite mixtures for two-phase seepage cut-off walls.

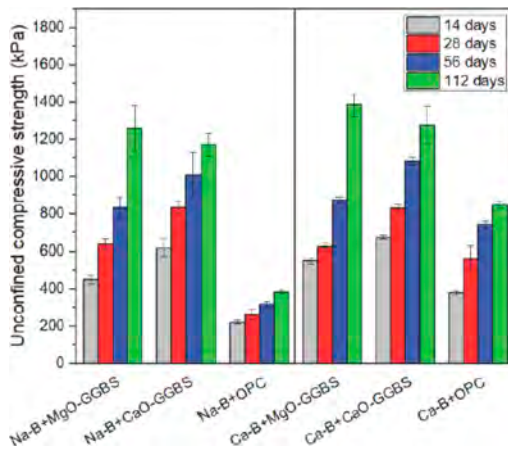


Figure 4. UCS of sand-bentonite-binder soil specimens at 14, 28, 56 and 112 days from Ting et al. (2024).

To address the key issues in pore characteristics and permeability of nZVI treated soil, Chen et al. (2024) investigated the particle size distribution, Atterberg limits, and permeability of lead-contaminated soil when subjected to varying doses of nZVI treatment. As for the special water-oxygen requirement of nZVI reactions, a modified slurry consolidation method was applied for the sample preparation of treated soil. The study indicates that the permeability of nZVI treated soil increases with the increase in nZVI dosage (Figure 5). Additionally, it also proved that the nZVI treatment by the slurry consolidation procedure can lead to better permeability instead of a “blockage effect” by injection-type treatment.

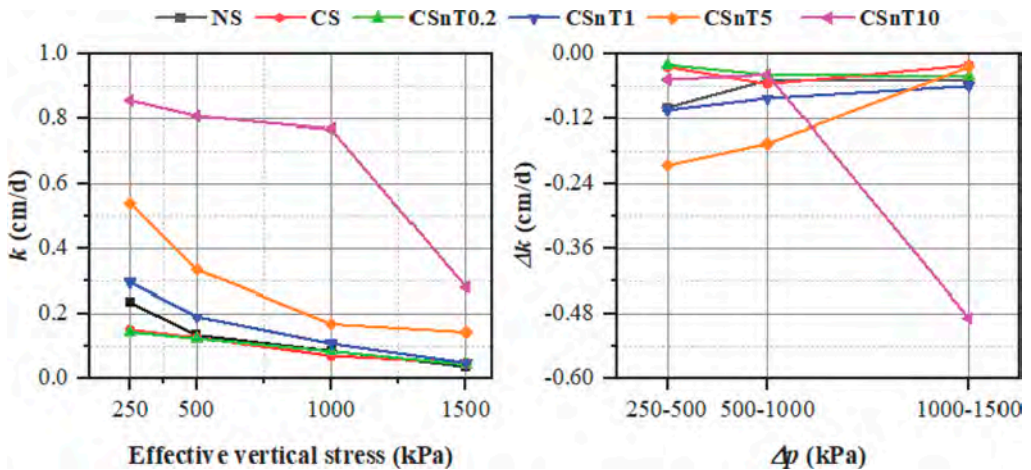


Figure 5. Calculated permeability and the relationship between Δk with stress of samples from Chen et al. (2024).

Jiang et al. (2024) proposed a power supply scheme of non-symmetric electrode polarity reversal (NSPR) from the perspective of interface electrochemical reaction. The influence of the power-on time and current density on the interface resistance was investigated by a constant current mode of electro-osmotic test (Figure 6). The experimental results show that the NSPR mode under certain conditions can effectively alleviate the concentration polarization and reduce the interface resistance. The variation trend of interface resistance corresponds to the power parameters (time and current density), and the method of reversing the external potential can exchange the electrode electrochemical reaction, consume the generated products accumulated on the electrode surface, and improve the utilization efficiency of the power supply scheme.

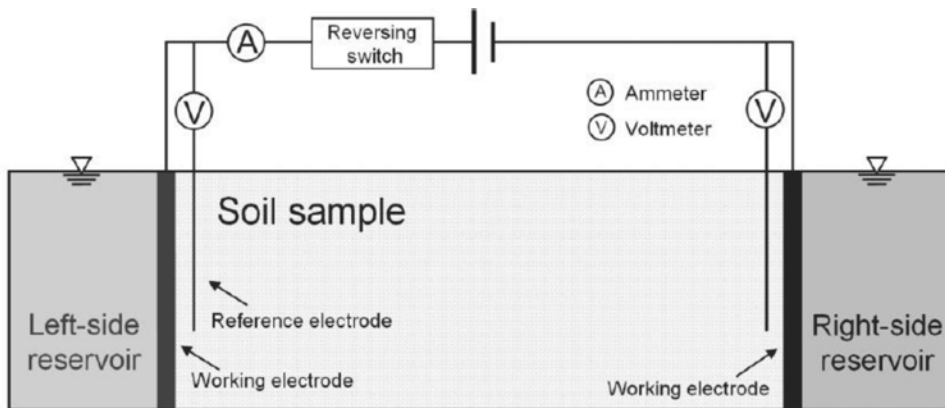


Figure 6. Schematic of the experimental apparatus from Jiang et al. (2024).

Yu et al. (2024) investigated the solidification effect of the polluted soil using active MgO carbonation by conducting unconfined compressive strength and electrical resistivity tests. The findings demonstrate that the unconfined compressive strength of the solidified soil increases with the contamination concentration, while decreases with the increase in the content of active MgO. Moreover, the strength first increases and then decreases with the carbonation time. It is also observed that there exists a basic linear relationship between the unconfined compressive strength and electrical resistivity of the polluted soil (Figure 7). The use of electrical resistivity proves to be effective for evaluating the mechanical strength properties of heavy metal-contaminated soil.

4 IMPROVED MATERIAL CHARACTERISTICS AND APPLICATIONS

The three papers in this group, which focus on improved material characteristics and applications, are from China.

Li et al. (2024) developed structural fractal models for bentonite and derived the effective stresses of saturated bentonite in salt solution and unsaturated bentonite in deionized water. The results indicated that the fractal dimensions can characterize the surface and pore size distribution of bentonite. Based on the fractal structural features, Li et al. (2024) derived the effective stresses for bentonite saturated in saline solutions or unsaturated in deionized water, respectively. Utilizing the proposed effective stress, the swelling deformation and peak shear strength of bentonite can be depicted by a unified expression. Furthermore, Li et al. (2024) verified the feasibility of the expression through tests, and experimental results also showed that the peak shear strength and the effective stress for bentonite saturated in saline solutions or unsaturated in deionized water to comply with the Mohr-Coulomb criterion (Figures 8 and 9). Finally, Li et al. (2024) deduced the unified effective stress for unsaturated soil in salt solution in conjunction with existing studies.

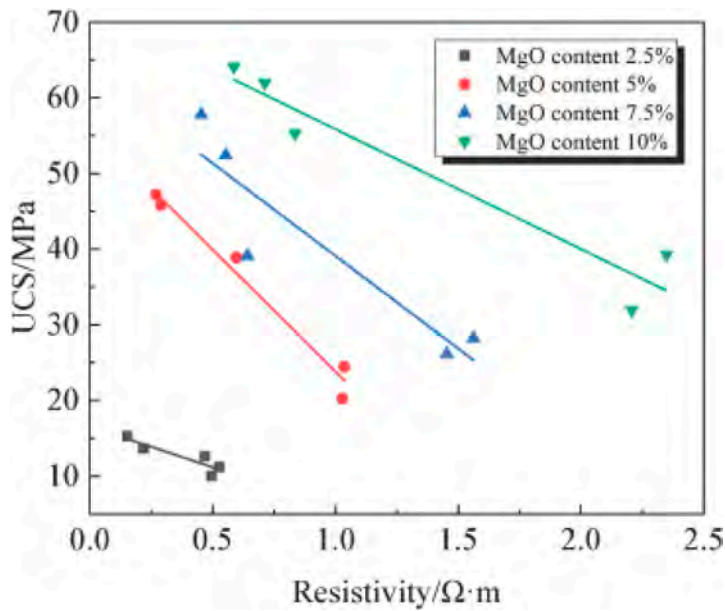


Figure 7. Relationship between resistivity and unconfined compressive strength at carbonation time from Yu et al. (2024).

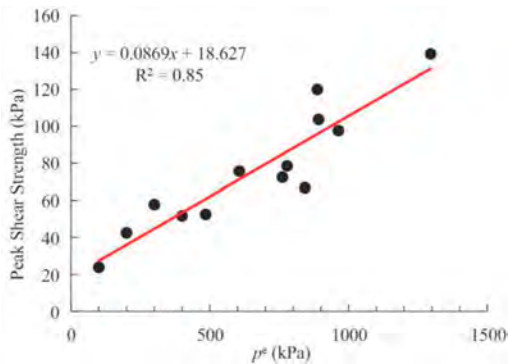


Figure 8. Relationship between peak shear strength and effective stress for unsaturated expansive soil from Li et al. (2024).

Yuan et al. (2024) utilized a series of three-dimensional finite element models to examine the dynamic evolution of soil arching within the PSGR embankment system (Figure 10). The findings indicated that the progression of soil arching predominantly occurred during the embankment construction phase.

Yuan et al. (2024) subsequently reported a slight increase in the stress concentration ratio during the static step-loading process. They also observed uneven stress distribution on the pile-cap, with the lowest stress occurring at the center. This was attributed to the formation of three-dimensional soil arching among adjacent four pile-caps (Figure 11). In addition, Yuan et al. (2024) also found that the critical height for soil arching was determined to be 1.3-1.4 times the net spacing of the pile-cap, with closely similar arching heights observed at both the center and the shoulder of the embankment.

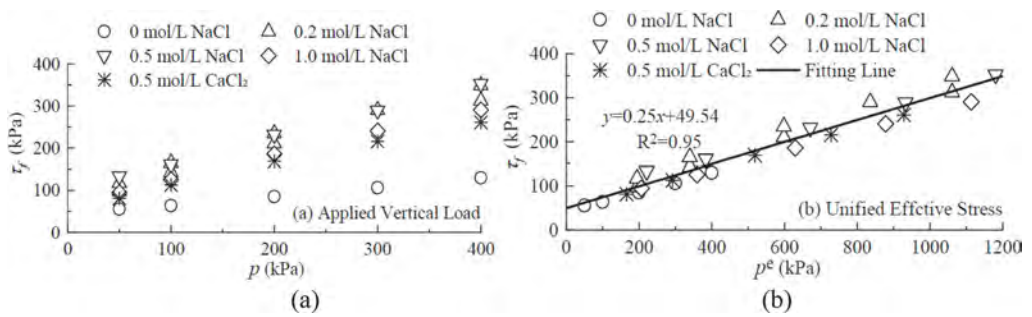


Figure 9. Relationship between peak shear strength and effective stress in Na₂SO₄ solutions from Li et al. (2024).

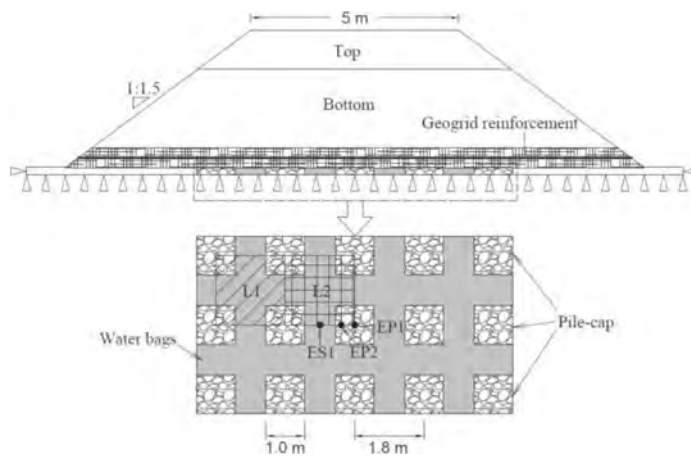


Figure 10. Profile of the embankment model from Yuan et al. (2024).

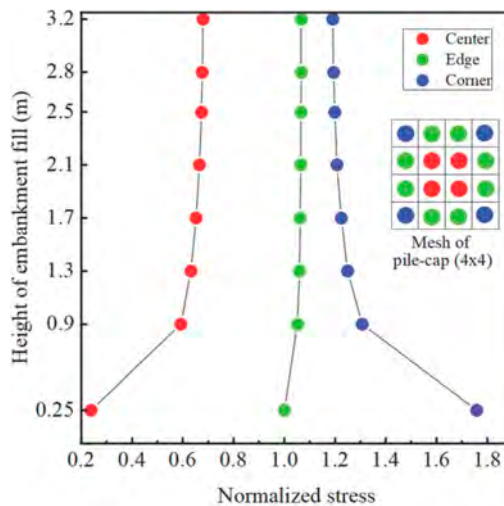


Figure 11. Fluctuations in vertical stress at various positions in the pile cap from Yuan et al. (2024).

5 CONCLUSIONS

This report presents an overview of the papers submitted in this session, and it confirms the intense research activities on basic properties and soil improvement in soft ground at IS-Macau 2024. This report provides the main highlights from all 9 papers relating to soil properties and its advanced improvement techniques for different application proposes. Some improvement and enhancement techniques, such as the technique of stabilization of MgO-GGBS, the remediation of nZVI, the non-symmetric electrode polarity reversal, carbonation solidification using active MgO, and bentonite enhanced with super absorbent polymer, can be beneficial for the improvement of soil behaviour in soft ground.

This paper could only be made thanks to efforts made by the authors of the papers. The validity of the results presented remains the responsibility of the authors of the original papers, while the author of the general report is the sole responsible for all opinions and conclusions derived from them as expressed in this general report.

REFERENCES

- Oberhollenzer, S., Hauser, L., Marte, R., Tschuchnigg, F., and Schweiger, H.F. Im-proved determination of the constrained modulus in soft soils using the flat dilatometer test.
- Ting, M.Z.Y., Tan, Y.Y., Widjaja, M., and Yi, Y. Permeability and strength of sand-bentonite mixture stabilized by different binders for construction of two-phase cut-off walls.
- Chen, Y.Z., Fan, C., Dong, Q.X., and Wei, J. Permeability improvement of contaminated soil treated by nano Zero-Valent Iron (nZVI) through a modified Slurry-Consolidation procedure.
- Jiang, Y.C., Zhou, J., Xu, C.Y., and Zhu, Z.M. Experimental Study on Non-symmetric Polarity Reversal for Reducing Interfacial Resistance in Electro-osmosis of Soft Soil.
- Song, Y., Ding, S., Dong, S.S., Liu, W., Chen, Y.L., and Liu, J.Q. Mechanical strength and resistivity characteristics of activated MgO-carbonated cured Zn^{2+} contaminated soils.
- Li, X.Y., Xu, Y.F., and Zhou, W.H. Study on the deformation and strength characteristics of bentonite based on structural fractal features.
- Yuan, W.H., Yuan, L.J., Chen, Y., and Zhao, L.S. Investigation on Evolutions of Soil Arching developed in a Pile-Supported Embankment Considering Geogrid.
- Wang, G., Yan, L., Zhang, X.W., Liu, X.Y., and Gao, H.D. Analysis of soil clogging of TBM tunneling in clayey layers and the role of soil composition.
- Li, X., Zhou, W.H., and Wang, C. Determination of particle breakage and fractal dimension for marine coral sand.

Permeability improvement of contaminated soil treated by nano Zero-Valent Iron (nZVI) through a modified slurry-consolidation procedure

Y.Z. Chen & C. Fan

School of Civil Engineering and Architecture, Hainan University, Haikou, China

Q. Dong*

School of Civil Engineering and Architecture, Hainan University, Haikou, China

Research and Development Report of Key Laboratory of Equipment Safety and Intelligent Technology for Guangzhou Rail Transit System, Guangzhou, China

J. Wei

School of Civil Engineering and Architecture, Hainan University, Haikou, China

ABSTRACT: Recently, nanoscale Zero-Valent Iron (nZVI) has been extensively applied in treatments of contaminated sites and as key materials of permeable reactive barriers (PRBs), due to its excellent remediation efficiency in both heavy metal and organic contaminants and its environmental friendliness. However, the macro-micro-structural mechanism of nZVI-soil interactions is still unclear. By which, the uncertainty of remediation efficiency and the instability of site engineering properties should be noticed, especially the relationship between “Nanomaterial’s blockage effect” and permeability of target soil. The main objective of this article is to address the key issues in pore characteristics and permeability of nZVI treated soil through a series of macroscopic to microscopic experimental analysis. A modified slurry consolidation method was applied for the sample preparation of treated soil, as for the special water-oxygen requirement of nZVI reactions. Based on the calculated permeability coefficient by oedometer tests, it indicated that the permeability of nZVI treated soil increased with the increase in nZVI dosage. By mercury intrusion pore measurement (MIP), more intra-particle pore distribution and a larger percentage of connectivity pore could prove that the nZVI treatment by the slurry consolidation procedure led to better permeability instead of a “blockage effect” by injection-type treatment. Thus, the article provides an important theoretical and scientific basis for further understanding the macro-microscopic interaction mechanisms of nano-remediation technology on soils and for efficient applications of in-situ nano-remediation engineering.

Keywords: nZVI, permeability, contaminated soil, microstructure, nano-remediation

1 INTRODUCTION

In recent decades, significant releases of non-degradable toxic pollutants, such as heavy metals, have been observed due to rapid industrialization and urbanization. This has resulted in extensive environmental damage. Of particular concern is lead exposure, which poses threats to the human nervous system, kidneys, and blood. The utilization of nanomaterials shows promise in remediating lead contamination and facilitating soil reuse in both water and soil treatment processes (YU et al. 2021; HE et al. 2013). Nanomaterials possess the ability to efficiently degrade lead ions in both water and soil, primarily owing to their NANO-size,

reduction and surface effects, (XI et al., 2010; GIL DÍAZ et al. 2014; VASAREVIČIUS et al. 2019). Among these nanomaterials, nanoscale zero-valent iron (nZVI) stands out for its specific advantages in degrading toxic lead ions. These advantages encompass environmentally friendly attributes, enhanced reactivity, reduction potential, adsorption capacity, and co-/precipitation potential (VITKOVA et al. 2017; LI & ZHANG. 2007; AWANG et al. 2022). Moreover, careful consideration should be given to the geotechnical properties of contaminated soil following treatment with nanomaterials, with particular focus on permeability.

The utilization of nanoparticles in soil remediation has attracted substantial attention due to its ability to affect the permeability. In laboratory-scale experiments, two prevalent methods for sample preparation are the compaction and slurry consolidation. The water and oxygen conditions during the reactions have a significant impact on the reaction between the nanomaterials and soil. The addition of nano-materials (nano-CuO; nano-clay) into clay via compaction leads to a decrease in permeability as the addition of nanomaterials increases, so does the reduction of permeability in permeable reactive barrier (PRB) (NG & COO. 2015; KARUMANCHI et al. 2020). In contrast, treatment with nZVI via the slurry consolidation method results in an increase in soil permeability (CHEN et al., 2019). The “blocking effect” of nanomaterials can be attributed to the specific conditions of sample preparation.

In this study, lead-contaminated soil samples, prepared through a modified slurry consolidation method, were treated by varying dosages of nZVI. The geotechnical properties of samples after nZVI treatment were evaluated by Atterberg limits, particle size distribution analysis and Oedometer tests. Additionally, the impact of soil pore structure on permeability was examined using Mercury intrusion porosimetry (MIP).

2 EXPERIMENTAL PROGRAM

2.1 Sample preparation

The virgin soil was collected from an excavation pit of a construction site in Macau SAR, China. The natural soil (as shown in Table 1) was mixed for a slurry with sieving through 1mm and then mixed with distilled water to the double liquid limit. The slurry was subjected to double-drainage preconsolidation at an effective vertical pressure of 200kPa. After a stable preconsolidation ($\Delta h < 1\text{mm/day}$), the sample was extracted and trimmed using a 50mm diameter ring cutter for Oedometer tests. In preparing treated soil, nZVI underwent two distinct phases in soil slurry: a) water-aerobic process involving addition and stirring in the contaminated slurry, and b) water-anoxic process characterized by consolidation through double drainage of the slurry.

Table 1. Index properties of soil.

Properties of soil	Values
Sand (%)	9.8
Silt (%)	70.1
Clay (%)	20.1
LL (%)	61.7
PL (%)	32.4
PI	29.3

2.2 Contaminant and treat agent

Lead nitrate (99.8AR, $\text{Pb}(\text{NO}_3)_2$), the contaminant, was obtained from Xi-Long Chemical Co. Ltd. in China. nZVI used as the treated agent was synthesized by plasma sputtering and supplied by Xiang-Tian Corp (Shanghai, China). The manufacturer characterized the particles with average particle size of 50 nm, a purity of 99.9%, and BET specific surface area (SSA) of $30 \text{ m}^2/\text{g}$.

The natural soil was artificially contaminated at a concentration of Pb(II) 500 mg/kg dry weight and allowed to equilibrate for more than 48 h. The soil samples were then categorized

into natural soil, lead-contaminated soil, and different treatments with varying percentages of nZVI, such as 0.2%, 1%, 5%, and 10% (NS, CS, CSnT0.2, CSnT1, CSnT5 and CSnT10).

2.3 Atterberg limits of samples

The Atterberg limits, including liquid limit (LL), plastic limit (PL), and plasticity index (PI), are essential properties used in soil classification and the assessment of plasticity characteristics. The cone penetration method described in BS1377 was employed to determine the Atterberg limits of all samples.

2.4 Oedometer tests

To assess the deformation and hydraulic properties of samples, Oedometer tests were conducted on a schedule of 50, 150, 250, 500, 1000, 500U, 250U, 500R, 1000R, 1500kPa. The calculated permeability was obtained from oedometer tests at 250kPa, 500kPa, 1000kPa, and 1500kPa following ASTM D2435. Subsequently, the permeability (k) was calculated according to the equation (1). The coefficient of consolidation (C_v) was obtained using the logarithmic method.

$$k = \frac{aC_v\gamma_w}{1 + e} \quad (1)$$

Where a = the compression coefficient under a certain load level; C_v = the coefficient of consolidation under a certain load level; r_w = Heaviness of water; e = the void ratio under a certain load level.

2.5 Mercury intrusion poroimetry

The pore size distribution of the slurry consolidation samples was analyzed using an Autopore IV 9500 Mercury Pore Sizer (Micromeritics, USA). The measurements covered pressures ranging from 0 to 60,000 psi, corresponding to pore sizes that ranged from 0.003 to 1000 μm .

3 RESULTS

3.1 Particle size distribution and Atterberg limits

As the increasing nZVI dosage, the particle size distribution of treated soil prepared by the modified slurry consolidation method tended more toward larger particles (as Figure 1). Experimental evidence revealed a growth in the proportion of sand particles, with an

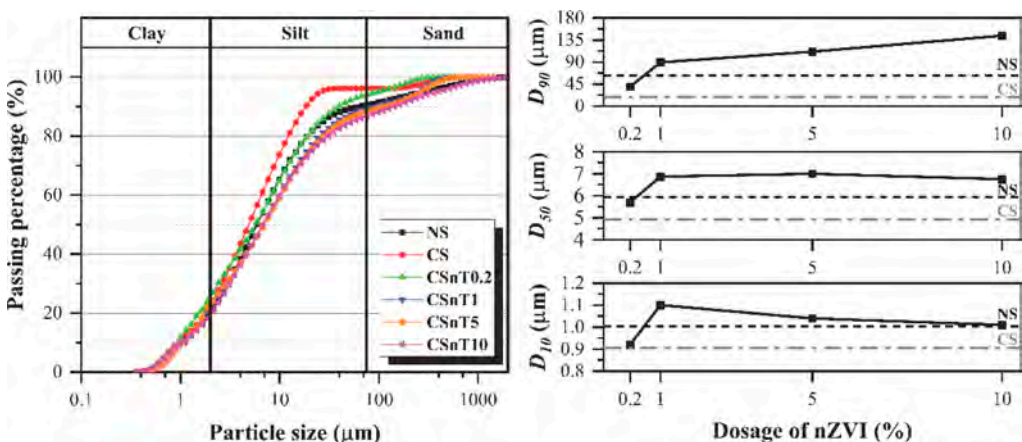


Figure 1. Particle size distribution of samples.

inflection point observed at the introduction of 1% nZVI. Specifically, the D_{10} exhibited an initial increase followed by a gradual decrease, whereas the D_{50} demonstrated an upward trend after the addition of nZVI before attaining stability. Furthermore, the D_{90} indicated a continuous increase. In the presence of water, nZVI presented a higher tendency to interact and aggregate with soil particles, leading to the formation of larger aggregates and consequently influencing the Atterberg limits and permeability.

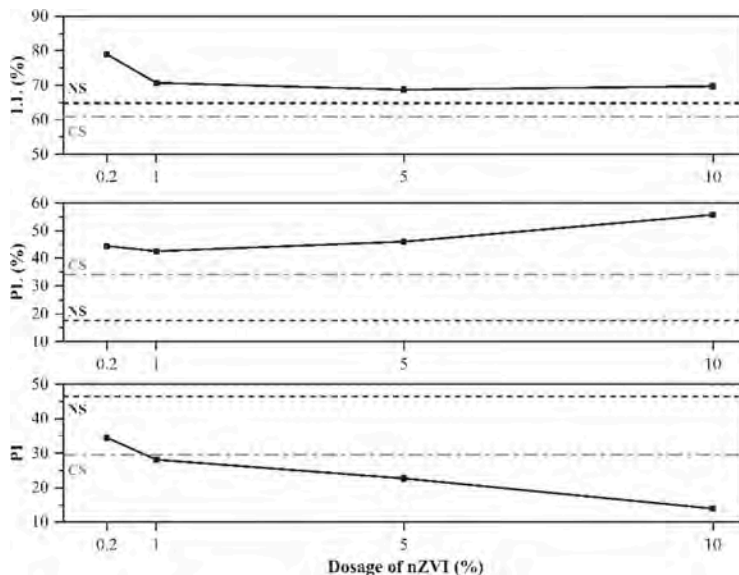


Figure 2. Atterberg limits of samples.

Figure 2 demonstrates a clear inverse relationship between the dosage of nanoscale zero-valent iron (nZVI) and the plasticity index (PI). In lead-contaminated soil, there was a significant reduction in the plastic limit (PL), accompanied by an increase in the liquid limit (LL), resulting in an elevation of the PI. However, the addition of nZVI caused a decreasing trend in PI as the dosage increased. The LL remained relatively constant after an initial decrease, while the PL gradually increased with the nZVI and led to a reduction in the soluble lead ion levels in water, particularly under anaerobic and aqueous conditions. This reduction facilitated the formation of aggregates composed of soil particles and lead compounds. The primary mechanism behind this phenomenon may be related to the thinning of the diffusion double layer around soil particles. The experimental results suggest that the modified slurry consolidation technique used in the preparation of nZVI treated soil modifies the size of soil particles and reduces their water retention capacity. Consequently, this modification affects the permeability of the treated soil.

3.2 Permeability

Figure 3 presents data that illustrates how the permeability of samples, prepared using the modified slurry consolidation method, is influenced by changes in effective vertical stress and nZVI dosage. As the effective vertical stress increased, the soil permeability showed a gradual decrease, eventually stabilizing within the range of 0 to 0.2 cm/d. Notably, soil treated with 10% nZVI exhibited a more pronounced decrease in permeability, with a reduction of 0.48 cm/d observed at a pressure of 1500 kPa. Conversely, increasing the dosage of nZVI had the opposite effect, leading to an increase in permeability for the treated soil under varying stress conditions. The vertical stress served to compact the soil's pore structure progressively, resulting in a gradual decline in permeability. The application of nZVI treatment, particularly under

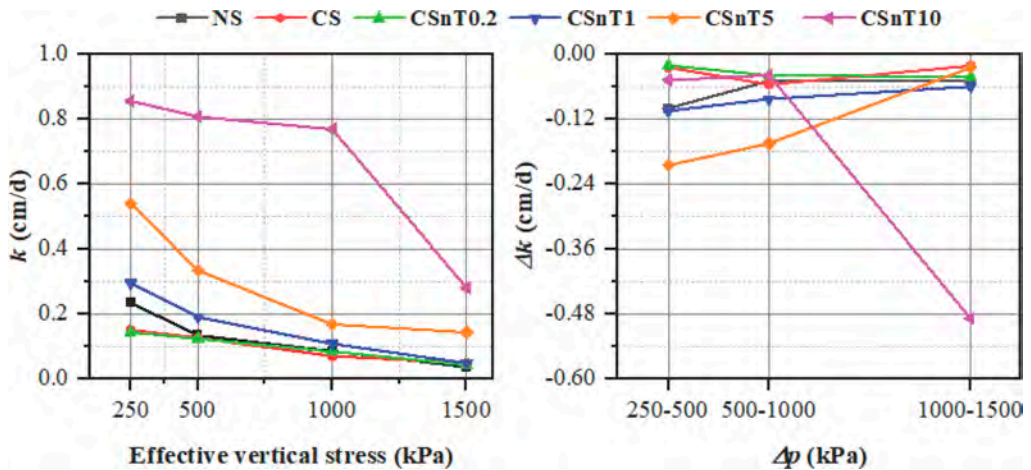


Figure 3. Calculated permeability and the relationship between Δk with stress of samples.

anaerobic and water conditions, led to the formation of larger aggregates with interconnected pore structures. Simultaneously, the water retention capacity of the soil particles decreased, facilitating better water drainage, and contributing to the observed increase in permeability. In light of these findings, it is advisable to conduct further investigations into the pore structure of the soil samples to gain a more comprehensive understanding of these observed effects.

3.3 Pore size distribution

The Mercury Intrusion Porosimetry (MIP) tests conducted on samples prepared using the modified slurry consolidation method have confirmed the previously discussed results (as Figure 4). As the dosage of nanoscale zero-valent iron (nZVI) increased, there was a reduction in the total pore volume within the samples. Simultaneously, there was an increase in the number of well-connected intraparticle pores. This improvement in pore connectivity demonstrated a positive correlation with the dosage of nZVI and reached its peak at a dosage level of 10%. At this 10% dosage, there was also a maximum value in the number of intraparticle pores with sizes smaller than 10 nanometers. However, it's worth noting that an excessive amount of nZVI, specifically 10%, effectively mitigates the accumulation of lead ions in the soil. This mitigation, in turn, enhances the flow of water and solutes within the soil pores. Additionally, the aggregation of particles facilitated by nZVI treatment leads to the formation

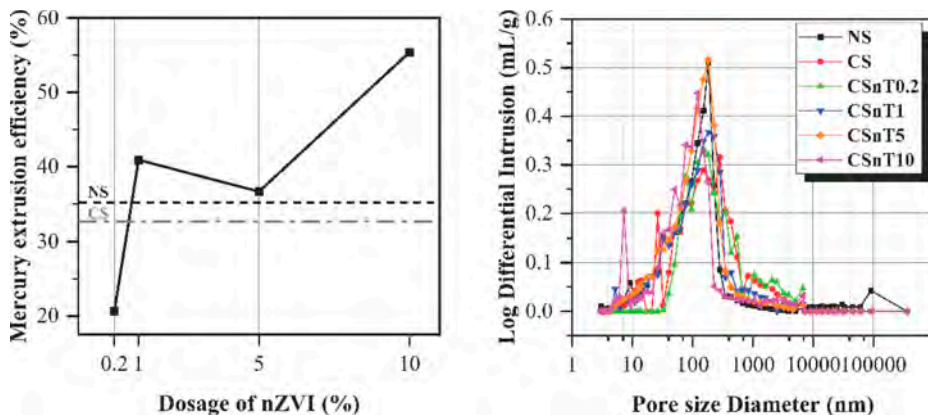


Figure 4. Mercury extrusion efficiency and pore size distribution of samples.

of well-connected intraparticle pores, which further improve the permeability of the soil. In summary, the results of the MIP testing support the previously mentioned observations and phenomena, confirming the positive impact of nZVI treatment on soil pore connectivity, and overall soil permeability.

4 CONCLUSION

This study investigated the particle size distribution, Atterberg limits, and permeability of lead-contaminated soil when subjected to varying doses of nZVI treatment. The results were validated through MIP analysis, yielding the following noteworthy conclusions.

The modified slurry consolidation method, employed in this study, replicates the natural sedimentation of soil under authentic environmental conditions. When nZVI was introduced into lead-contaminated soil in an anaerobic water environment, it exhibited a propensity to form larger aggregates characterized by thinner diffuse double layers and well-connected intraparticle pores. Consequently, this led to a reduction in the soil's water retention capacity while concurrently improving its permeability. This observed phenomenon displayed a positive correlation with the quantity of nZVI utilized.

The experimental results gleaned from this study unequivocally affirm that the judicious application of nZVI can ameliorate soil permeability during the natural sedimentation process, circumventing the undesirable "Nanomaterial's blockage effect." These findings carry substantial implications for the pragmatic implementation of engineering practices.

REFERENCES

- Awang, N. A., Wan Salleh, W.N., Aziz, F., Yusof, N. & Ismail, A. F. 2022. A review on preparation, surface enhancement and adsorption mechanism of biochar-supported nano zero-valent iron adsorbent for hazardous heavy metals. *Journal of Chemical Technology & Biotechnology*, 98, 22–44.
- Chen, Y.Z., Zhou, W.-H., Liu, F. & Yi, S. 2019. Exploring the effects of nanoscale zero-valent iron (nZVI) on the mechanical properties of lead-contaminated clay. *Canadian Geotechnical Journal*, 56, 1395–1405.
- Gil Diaz, M., Ortiz, L.T., Costa, G., Alonso, J., Rodríguez-Membibre, M. L., SáNchez-FortúN, S., Pérez-Sanz, A., MartíN, M. & Lobo, M. C. 2014. Immobilization and Leaching of Pb and Zn in an Acidic Soil Treated with Zerovalent Iron Nanoparticles (nZVI): Physicochemical and Toxicological Analysis of Leachates. *Water, Air, & Soil Pollution*, 225.
- He, M., Shi, H., Zhao, X., Yu, Y. & Qu, B. 2013. Immobilization of Pb and Cd in Contaminated Soil Using Nano-Crystallite Hydroxyapatite. *Procedia Environmental Sciences*, 18, 657–665.
- Karumanchi, M., Avula, G., Pangi, R. & Sirigiri, S. 2020. Improvement of consistency limits, specific gravities, and permeability characteristics of soft soil with nanomaterial: Nanoclay. *Materials Today: Proceedings*, 33, 232–238.
- Li, X. Q. & Zhang, W.-X. 2007. Sequestration of Metal Cations with Zerovalent Iron Nanoparticles A Study with High Resolution X-ray Photoelectron Spectroscopy (HR-XPS). *The Journal of Physical Chemistry C*, 111, 6939–6946.
- Ng, C. W. W. & Co, J. L. 2015. Hydraulic conductivity of clay mixed with nanomaterials. *Canadian Geotechnical Journal*, 52, 808–811.
- Vasarevičius, S., Danila, V. & Paliulis, D. 2019. Application of Stabilized Nano Zero Valent Iron Particles for Immobilization of Available Cd²⁺, Cu²⁺, Ni²⁺, and Pb²⁺ Ions in Soil. *International Journal of Environmental Research*, 13, 465–474.
- Vitkova, M., Rakosova, S., Michalkova, Z. & Komarek, M. 2017. Metal(loid)s behaviour in soils amended with nano zero-valent iron as a function of pH and time. *J Environ Manage*, 186, 268–276.
- Xi, Y., Mallavarapu, M. & Naidu, R. 2010. Reduction and adsorption of Pb²⁺ in aqueous solution by nano-zero-valent iron—A SEM, TEM and XPS study. *Materials Research Bulletin*, 45, 1361–1367.
- Yu, G., Wang, X., Liu, J., Jiang, P., You, S., Ding, N., Guo, Q. & Lin, F. 2021. Applications of Nanomaterials for Heavy Metal Removal from Water and Soil: A Review. *Sustainability*, 13.

Experimental study on non-symmetric polarity reversal for reducing interfacial resistance in electro-osmosis of soft soil

Y. Jiang, J. Zhou*, C. Xu & Z. Zhu

Research Center of Coastal and Urban Geotechnical Engineering, Zhejiang University, Hangzhou, China

Q. Gan

Zhejiang construction investment innovation technology Co., Ltd., Hangzhou, China

ABSTRACT: During the process of electro-osmosis of soft soil, the continuous increase in clay-electrode interfacial resistance has led to the high energy consumption of the electro-osmotic treatment method. To address this issue, this paper proposes a power supply scheme of non-symmetric electrode polarity reversal (NSPR) from the perspective of interface electrochemical reaction. Considering that the change of current density will significantly affect the interface resistance, a constant current mode of electro-osmotic test is designed. Using a self-designed one-dimensional electro-osmotic device, the influence of the power-on time and current density on the interface resistance under the proposed mode is investigated. The experimental results show that the NSPR mode under certain conditions can effectively alleviate the concentration polarization and reduce the interface resistance. The variation trend of interface resistance corresponds to the power parameters (time and current density), and the method of reversing the external potential can exchange the electrode electrochemical reaction, consume the generated products accumulated on the electrode surface, and improve the utilization efficiency of the power supply scheme. The impact of NSPR parameters on the interface resistance can be summarized by the reversal intensity, which reflects the combined effects of reverse current and reverse time. Lower reversal intensities have been found to effectively decrease the interface resistance through the electrode reversal mode.

1 INTRODUCTION

As a method to promote drainage and consolidation of soft soil, electro osmosis(EO) has been extensively studied in various applications such as soft soil foundation reinforcement, dredging sludge treatment, soil heavy metal remediation, and tailings dewatering (Yeung, 2011). However, the traditional electro osmosis is associated with high energy consumption (Ye et al., 2020), electrode corrosion, and poor drainage effect in the later stage, and uneven reinforcement. To address these drawbacks, scholars have proposed an energization method called polarity reversal, which involves changing the positive and negative poles of the external power supply after a period of forward power supply to achieve reverse current of the soil.

The use of polarity reversal in EO in-situ projects is common, but it brings about several challenges. These challenges include the ambiguity of design parameters and the absence of mechanical guidance. Consequently, the desired outcomes are often not achieved, and in some cases, the efficiency of drainage is even reduced. Wan and Mitchell (1976) initially proposed the polarity reversal mode as a solution to address the issue of uneven electroosmotic treatment effects. Shang et al., (1995) discovered that the polarity reversal mode has the ability to counteract the adverse impacts of electrode reactions. As a result, this mode enhances the efficiency of EO and reduces energy

*Corresponding author: zjelim@zju.edu.cn

consumption. Tao et al. (2014) discourage the use of the polarity reversal mode, as indoor tests showed that although it results in more uniform soil consolidation, the average shear strength is lower than conventional EO. In recent years, as the field of electrochemistry has been gradually introduced, scholars have started to focus on the electrode-soil interface electrode reaction. The potential loss at the interface is one of the reasons for the high energy consumption of EO (Sun et al., 2023). Gan et al. (2022) proposed an interface resistance model and suggested that concentration polarization, caused by the continuous accumulation of electrode reaction products at the electrode-soil interface, is a significant factor in the high energy consumption at the interface. Electrodes such as graphite and electro-kinetic geosynthetics (EKG), which are commonly used in EO (Glendinning et al., 2010), undergo oxygen evolution reaction and hydrogen evolution reaction at the anode and cathode, respectively, resulting in the production of hydrogen ions and hydroxyl ions. Polarity reversal can be employed for consuming the accumulated reaction products and mitigating concentration polarization in these electrodes.

In this study, a non-symmetric polarity reversal mode (NSPR) was proposed to consume the accumulated electrode reaction products at the interface, alleviate concentration polarization, and reduce interface potential loss. In contrast to the traditional polarity reversal mode, where the forward and reverse energization durations are equal and the electrodes on both sides are drained, the NSPR mode has a longer forward energization duration and stronger forward current than the reverse. This difference in duration helps prevent the back-and-forth flow of pore water in the soil. This paper investigates the influence of NSPR mode on potential loss in interfaces through indoor experiments. To mitigate the notable influence of variations in current density on interface resistance, a constant current mode for electro-osmotic testing has been developed. A self-designed one-dimensional electro-osmotic device with water replenishing device is used to conduct a comprehensive analysis of the impact of reverse duration and reverse current, and provides recommendations for reversal parameters.

2 MATERIALS AND METHODS

2.1 *Experiment design*

This study investigates the alteration in interface resistance following the application of NSPR. We aim to observe the changes in interface resistance resulting from variations in electrification parameters. Due to the significant impact of current density on interface resistance (Gan et al., 2022), a constant current with water supply method is utilized in this study. While this method differs from the conventional constant voltage drainage method used in traditional experiments, there is no fundamental distinction between controlling voltage and controlling current for electro-osmotic drainage (Hamir, 1997). The constant current method employs an external power supply to ensure a constant current density. At the same time, a water replenishing device was utilized to ensure a constant water level on both sides of the soil sample (Mohamedelhassan and Shang, 2001). By eliminating the influence of hydraulic gradient on soil and replenish the soil with water, it is possible to avoid significant changes in soil water content and conductivity. This allows for a better focus on the soil-electrode interface.

The test device, as shown in Figure 1, consists of a model tank, power supply, voltmeter, ammeter, and electrode system. The model tank, made of organic glass, has dimensions of 260 mm × 100 mm × 80 mm (length × width × height). The model tank includes a main tank with a length of 180 mm, as well as cathode and anode storage tanks with a length of 40 mm. The main tank is used to load the test soil, and it has an internal size of 180 mm × 100 mm × 80 mm. The cathode and anode chambers are used to maintain consistent water heads throughout the test device, and they have a size of 40 mm × 100 mm × 80 mm. The test power supply used in this test capable of providing a maximum output voltage of 60 V. It can be set to operate in constant current or constant voltage mode, and for this test, the constant current power supply mode is used. Additionally, the power supply has the capability of auto polarity reversal, with settings ranging from 10 seconds to 10 hours, and a time control accuracy of 1%. The electrode system comprises a working electrode and a reference electrode, which are utilized to energize the soil and measure

the interface resistance. The working electrode is positioned in the main tank and has small holes to facilitate the free flow of water in the main tank and electrode chamber. Adjacent to the working electrode, a copper rod is selected as the reference electrode. Copper rods are preferred over other metals because of their superior electrical conductivity and resistance to corrosion.

To measure the potential loss at the electrode-clay interface, a voltmeter was inserted between the working and reference electrodes. Simultaneously, an ammeter was used to detect the current in the main circuit in order to determine the normal functioning of the constant current power supply. Both the voltmeter and ammeter have RS485 communication capabilities, allowing for real-time transmission and saving of measured data to the computer. The data collection frequency was set at 2 Hz, with a voltmeter accuracy of 1 mV and an ammeter accuracy of 0.1 mA, ensuring the accuracy of the test data.

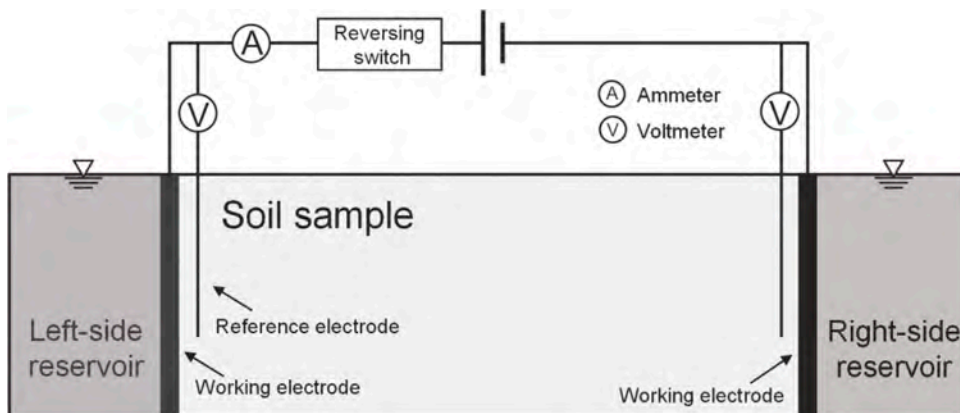


Figure 1. Schematic of the experimental apparatus.

This device effectively replenishes the pore water in the anode area, thereby maintaining a consistent conductivity of the soil. This method keeps the soil resistance stable. Meanwhile, the constant current test also ensures the stability of the electroosmotic coefficient and the changes of activation over potential caused by changes in current density.

In this study, the terms 'left electrode' and 'right electrode' were used to refer to the two working electrodes. The current direction at the beginning of the test (from left electrode to right-side) is referred to as the forward, while the direction after reversing the poles is referred to as the backward direction. During the forward period, the left electrode functions as the anode, the right functions as the cathode. To assess the effectiveness of the NSPR mode, two sets of tests were conducted. The first set included the RT group with reversal time as a variable, and the second set included the RC group with reversal current as the variable. The changes in interface potential loss were compared and verified under two most basic reversal parameters. This analysis helps determine the effectiveness of the NSPR mode. The experiments scheme is shown in Table 1 and Table 2. Each test in the RT test group consists of two consecutive power stages. These stages are used to compare and analyze the impact of two different parameters on the interface potential of the same soil sample.

2.2 Material properties and produce

The soil used in the test was from Hangzhou, China. The relevant parameters of the original soil are presented in Table 3. To ensure the consistency of the test soil samples, the original soil was dried and ground into a powder. To minimize the influence of soil resistance between the reference electrode and the working electrode, and accurately measure the interfacial resistance caused by electrochemical reactions, a remolded soil sample was created by mixing soil powder with a potassium sulfate solution with a mass fraction of 5%. The soil powder and

Table 1. Reversal time group test schemes.

Test number	First Stage				Second Stage			
	Forward time/min	Forward current/A	Backward time/ min	Backward current/ A	Forward time/min	Forward current/A	Backward time/ min	Backward current/ A
RT-1	4.0		4.0		4.0		0.5	
RT-2	4.0	0.1	0.5	0.1	4.0	0.1	1.0	0.1
RT-3	4.0		1.0		4.0		2.0	

Table 2. Reversal current group test schemes.

Test number	Forward time/ min	Forward current/ A	Backward time/ min	Backward current/ A
RC-1				0.1
RC-2	4.0	0.1	3.0	0.025
RC-3				0

solution should be mixed thoroughly several times to ensure even distribution. Stir the mixture until the soil water content reaches approximately 80%. After allowing the remolded soil to rest for 24 hours, it can be put into the model box layer by layer.

Table 3. Physical parameters of original soil.

$w/\%$	G_s	e_0	$w_L/\%$	$w_p/\%$	$\sigma_e/(S/m)$
58.5	2.75	1.47	45.3	23.5	0.16

In the table, w is the water content, G_s is the specific gravity of soil particles, e_0 is the initial void ratio, w_L is the liquid limit, w_p is the plastic limit, and σ_e is the soil electrical conductivity.

The working electrode used in the experiment was a plate-type EKG measuring 5 mm × 75 mm × 90 mm. The EKG were sequentially cleaned with absolute ethanol and distilled water to remove electrode surface stains before insertion into the soil. The left and right reservoirs were filled with potassium sulfate solution having the same mass fraction of 5%, consistent with the solution added to the soil. The reference electrode utilizes a copper rod, which is polished with sandpaper and alumina polishing paste prior to its use.

The experimental procedure consists of the following steps: (1) Insert the working electrodes and reference electrodes into the soil sample and seal the sample with sealing film; (2) Connect the circuit and perform an 8-hour forward pre-energization before commencing the formal test. This step helps minimize the potential variations in soil conductivity and permeability coefficient that may occur during the test; (3) The forward and reverse power-on times should be set according to the test plan. After confirmation, the official energization can be started. The ammeter and voltmeter should record the interfacial potential changes and the actual current at a frequency of 2 Hz. It is also important to monitor the liquid level of the water replenishment reservoir to ensure consistent water head.

3 RESULTS AND ANALYSIS

3.1 Interface voltage loss

Figure 2 illustrates the interfacial voltage loss change of the RT1 group. In the first stage, RT1 follows the conventional polarity reversal mode, where the durations for forward and reverse power-on are equal. It is observed that both the left and right electrodes experience a sudden increase in interface potential loss during the first five energization cycles (known as

the ineffective zone) compared to the end of the previous cycle. The test results show that traditional polarity reversal mode not only causes pore water to move back and forth in the soil, which hinders drainage, but also increases the potential loss at the interface, thus further increasing the energy consumption of EO.

When using the NSPR mode with a shorter reverse time (0.5 minutes) compared to the forward time (4 minutes), it is observed that after a brief transition, the potential loss at the interface between the cathode and anode gradually decreases. In the effective zone shown in Figure 2, the interface potential loss within a single cycle exhibits a different trend. It follows a “T”-shaped trend, initially decreasing rapidly and then gradually increasing. Additionally, the potential loss at the start of each cycle is smaller than the end of the previous cycle. These results show that the NSPR mode effectively reduces interface potential loss, concentrating energy consumption in soil drainage.

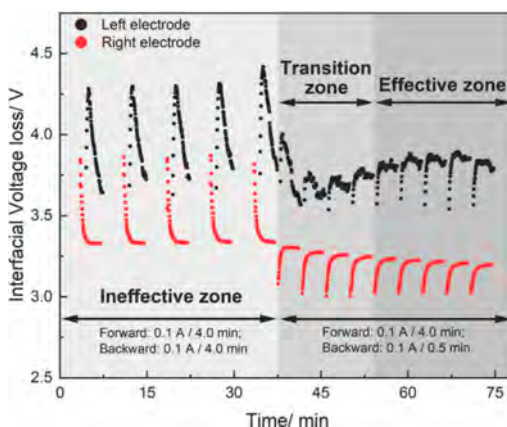


Figure 2. Changes in interfacial voltage loss.

The changes in interface potential loss are analyzed from the perspective of electrochemical reactions. During the forward energization of the left electrode, the oxygen evolution reaction generates hydrogen ions, and during the reverse period, the hydrogen evolution reaction consumes hydrogen ions. In the reversal period, when the forward and backward power-on times are equal, the left electrode both consumes a large amount of hydrogen ions by hydrogen evolution reaction and receives replenishment of hydrogen ions from the soil through electro migration. The interfacial potential loss characterizes the concentration of hydrogen ions at the interface in the case of a constant current test. The ineffective zone in Figure 2 shows that the interfacial potential loss initially increases and then decreases, revealing a decrease and subsequent increase in the hydrogen ion concentration on the left electrode surface. This demonstrates that long-term polarity reversal leads to the replenishment of hydrogen ions, which is caused by electro migration becoming the dominant factor. The consumption of hydrogen ions on the electrode surface is lower than the replenishment amount in the farther soil sample, resulting in a gradual increase in the hydrogen ion concentration on the electrode surface. This concentration gradient is maintained until the reversal ends. After the reversal is completed, forward power starts again, and the left electrode no longer consumes further hydrogen ions. Meanwhile, the hydrogen ions in the solution farther away rapidly diffuse and replenish the surface of the left electrode, leading to an increase in the hydrogen ion concentration on the surface of the left electrode. This results in an obvious sudden rise in the interfacial potential loss of the left electrode. As the forward power proceeds, the hydrogen ions on the left electrode surface gradually decrease due to electro migration and convective migration. Thus, the interfacial potential loss decreases equally slowly.

In the second stage, after shortening the reversal time (adopting the NSPR mode), the interfacial potential loss of the left and right electrodes gradually changed into a “T” shape. This change occurred because, as the reverse power-on time decreased, fewer hydrogen ions electromigrated to

the left electrode during the backward period compared to the hydrogen ions consumed by the left electrode's hydrogen evolution reaction. Once the reversal was completed, the concentration of hydrogen ions on the left electrode decreased and forward power restarts, causing hydrogen ions to gradually accumulate on the surface of the left electrode. Similarly, during the reverse period, fewer hydroxide ions electromigrated to the right electrode compared to the hydroxide ions consumed by the right electrode. Once the reversal ended, the concentration of hydroxide ions on the right electrode decreased and forward energization began, leading to the gradual accumulation of hydroxide ions on the surface of the right electrode. The above explains that under the same forward power condition, when reverse is applied for 4 minutes, the interfacial potential loss does not decrease but instead rises. The use of NSPR has proven to be effective in reducing the interfacial potential loss and improving the efficiency of EO.

3.2 Effect of reversal time on NSPR process

Figure 3 illustrates the interfacial voltage loss change from 0.5min reverse to 1min. The voltage loss of the left electrode decreases gradually as the reverse time increases. Additionally, it can be observed that the amplitude of the sudden drop at the beginning of each cycle increases, illustrating that NSPR is more effective during this power scheme. The changing trend of the right electrode has remained consistent. By appropriately increasing the reverse power time, the growth rate of the interfacial voltage loss can be reduced. The selection of the reverse power time is determined by both the interface electrochemical reaction rate and the ion electromigration rate, and there exists an optimal value.

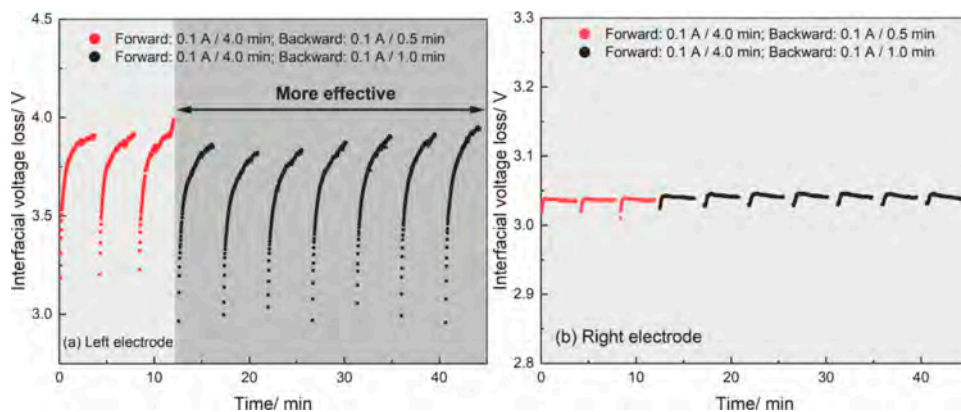


Figure 3. Change in interfacial potential loss for RT-2 (a) left electrode (b) right electrode.

When the reverse time is further extended to 2 min, the interfacial voltage loss of the left electrode gradually increases (Figure 4(a)). These findings show that further increasing the reverse time no longer enhances the alleviation of the anode interface resistance, but instead inhibits its effect and gradually diminishes the reduction of the electrode. In Figure 4(b), the right electrode also exhibits the same trend. As the reverse time is further extended, there is a gradual increase in the interfacial voltage loss.

3.3 Effect of reversal current on NSPR process

Figure 4 presents a comparison of interface voltage loss of RC group, showing the reversal currents of 0.1 A, 0.025 A, and 0 A (representing no reversal current). It can be observed that reverse currents of 0 A and 0.025 A have the most significant positive impact on the Left electrode. The least effective is the reverse current of 0.1 A, which results in an increase rather than a decrease in left. The three different reverse current values have a similar impact on right electrode as they do on the left. This set of experiments demonstrates that an appropriate

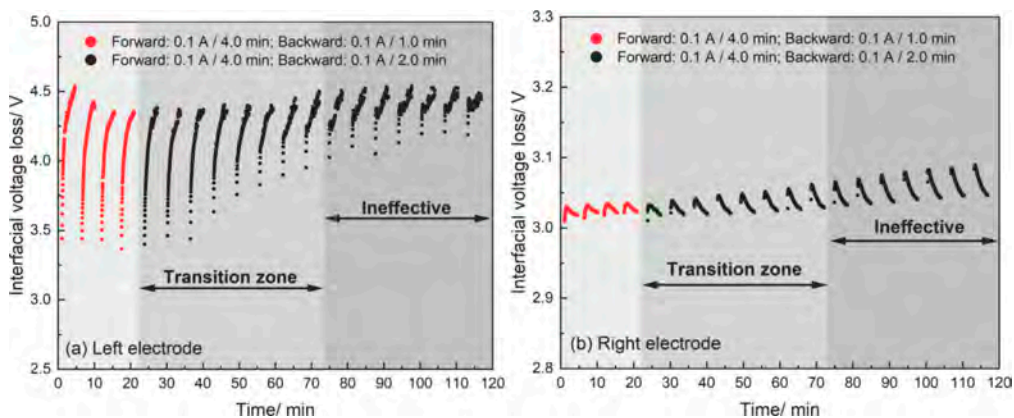


Figure 4. Change in interfacial potential loss for RT-3 (a) left electrode (b) right electrode.

reverse current value can reduce the rate of increase in interfacial voltage loss, while excessively high current values can produce the opposite effect.

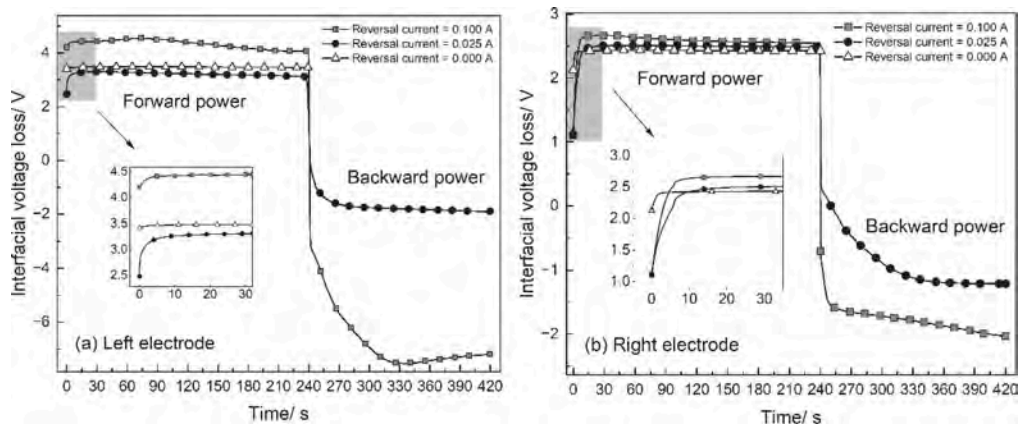


Figure 5. Variation of interfacial potential loss at different currents (a) left electrode (b) right electrode.

With the adoption of the NSPR, the electrochemical reaction of electrodes and the migration of ions in the soil are the main processes. The factors that influence these processes are the reverse current and the reverse time. To describe the design of power, it is recommended to introduce the concept of reversal strength, which is controlled by the reverse current and reverse time. When the reverse current is regulated, there exists an optimal reverse power-on time that minimizes the interfacial voltage loss. Similarly, when the reverse time is regulated, there is an optimal reverse current that minimizes the interfacial voltage loss. The optimal parameters can be determined by analyzing the changes in potential loss at the anode interface during the forward power period. If the change trend follows a “Γ”-shaped pattern, it demonstrates that the parameter is beneficial for EO. Moreover, a larger sudden drop and a slower rise rate means that the power parameter is more effective.

However, if the reverse current and reverse power-on time are equal to or greater than the forward, the polarity reversal mode may lead to an increase in interfacial resistance and hinder the EO effect. Further research is needed to determine the specific effective and ineffective intervals of reverse strength for different soil, as well as the factors that influence them. This research will provide valuable guidance for selecting power parameters in in-situ EO projects.

4 CONCLUSION

In order to minimize the interfacial energy consumption during electroosmotic treatment of soft soil, this study proposes the NSPR energization mode. Indoor experiments were conducted to investigate the effect of this method on interface potential loss. The impact of different reversal times and reversal current strengths was also examined, leading to the following conclusions:

- (1) The use of NSPR mode helps to reduce the potential loss in the interface. During each energization cycle, the potential loss in the interface follows a “T”-shaped trend, initially decreasing rapidly and then slowly rising. In contrast, the traditional polarity reversal mode is not effective in reducing potential loss. Once power is restarted, the potential loss does not decrease but instead continues to rise.
- (2) Experiments involving different backward times and currents demonstrate that the configuration of reversal energization parameters impacts the potential loss at the interface. Both parameters have optimal values that are associated with the efficiency of the electrochemical reaction at the clay-electrode interface. In future investigations, it would be beneficial to explore the correlation between time and current, introduce the concept of reversal intensity, and determine the optimal reversal energization parameters.
- (3) The constant current test with water replenishment in this study improves the consistency of soil sample's moisture content and electrical conductivity, and allows for better monitoring of changes in interface potential loss. The change in potential loss at the clay-electrode interface is controlled by the electrochemical reaction at the interface. By using the NSPR mode, where the backward energization is smaller than the forward, the reaction products accumulated at the interface during forward stage are consumed by the reversed electrode reaction. This helps alleviate concentration polarization and reduce interface energy consumption.

ACKNOWLEDGEMENTS

The research work was funded by the National Science Foundation of China (Grant No. 52078455 and 51478425).

REFERENCES

- Gan, Q., Zhou, J., Tao, Y., Jiang, Y., 2022. Interfacial resistance model for electro-osmotic system. *Géotechnique*.
- Glendinning, S., Mok, C.K., Kalumba, D., Rogers, C.D.F., Hunt, D.V.L., 2010. Design Framework for Electrokinetically Enhanced Dewatering of Sludge. *J. Environ. Eng.* 136, 417–426.
- Hamir, R.B., 1997. Some Aspects and Applications of Electrically Conductive Geosynthetic Materials. University of Newcastle upon Tyne.
- Mohamedelhasan, E., Shang, J.Q., 2001. Effects of electrode materials and current intermittence in electro-osmosis. *Proceedings of the Institution of Civil Engineers - Ground Improvement* 5, 3–11.
- Shang, J.Q., Lo, K.Y., Incullet, I.I., 1995. Polarization and Conduction of Clay-Water-Electrolyte Systems. *Journal of Geotechnical Engineering* 121, 243–248.
- Sun, X., Zhang, R., Wang, Y., Jin, X., Yu, Q., 2023. A novel evaluation method of consolidation efficiency of electro-osmotic system. *Géotechnique*.
- Tao, Y., Zhou, J., Gong, X., Chen, Z., Hu, P.-C., 2014. Influence of Polarity Reversal and Current Intermittence on Electro-Osmosis. pp. 198–208.
- Wan, T.Y., Mitchell, J.K., 1976. Electro-Osmotic Consolidation of Soils. *Journal of the Geotechnical Engineering Division* 102, 473–491.
- Ye, Q., Zhang, Y.H., Liu, J.T., Zhou, K., Feng, T.G., Kong, G.Q., 2020. Study on soft ground reinforcement by electro-osmotic method based on transparent clay. *Chinese Journal of Ground Improvement* 2(3), 187–191. (in Chinese).
- Yeung, A.T., 2011. Milestone developments, myths, and future directions of electrokinetic remediation. *Separation and Purification Technology, Scientific Advances and Innovative Applications in Electrokinetic Remediation* 79, 124–132.

Study on the deformation and strength characteristics of bentonite based on structural fractal features

X.Y. Li

State Key Laboratory of Internet of Things for Smart City & Department of Civil and Environmental Engineering, University of Macau, Macau SAR, China

Y.F. Xu

Department of Civil Engineering, Shanghai Jiao Tong University, Shanghai, China

W.H. Zhou

State Key Laboratory of Internet of Things for Smart City & Department of Civil and Environmental Engineering, University of Macau, Macau SAR, China

ABSTRACT: Mechanical behaviors of bentonite that is widely used in geotechnical engineering, are important for engineering safety. The deformation and strength characteristics of bentonite under unsaturated state or in a salty environment are influenced by osmotic suction and matric suction. A unified quantitative expression of effective stress including the osmotic suction and matric suction terms is required. In this paper, structural fractal models for bentonite were developed and the effective stresses of saturated bentonite in salt solution and unsaturated bentonite in deionized water are derived, respectively. Using the proposed effective stresses, the swelling deformation and the peak shear strength of bentonite can be depicted by a unified expression. Further, the unified effective stress for unsaturated soil in salt solution was deduced in conjunction with existing studies. The results of this study are important for quantifying the mechanical behaviors of bentonite under a complex state.

1 INTRODUCTION

Bentonite, with strong adsorption capacity and low permeability, is widely used in geotechnical engineering. The mechanical properties of bentonite are related to the safety of the project. For example, pressurized bentonite slurry can stabilize the tunnel face for excavation of slurry shield in sandy soils, and thus the study of the mechanical properties of the formed bentonite filter cake is important in analyzing the stability of the tunnel face (Yin et al., 2016; Qin et al., 2023a). The deformation and strength of the soil body are determined by the effective stress carried by the soil skeleton (Mitchell & Soga, 2005), but the effective stress of bentonite in unsaturated as well as salt-containing environments lacks a reasonable expression.

Natural soils involved in engineering usually exist in an unsaturated state and exhibit a larger strength than that in a saturated state due to the action of matrix suction (Fredlund et al., 1996; Guo et al., 2021). Matrix suction, related to the pore structure of the soil is an important part of the effective stress for unsaturated soils. However, the existing classical theory of unsaturated soils contains parameters of unknown meaning and lacks consideration of the structural properties of the soil. In addition, the mechanical properties of soils in offshore areas are also affected by the soluble salts contained in the pore water (Ma et al., 2020; Qin, et al., 2023b; Shen et al., 2023). The effective stresses are governed by the osmotic suction of the pore solution which produces additional stress on the clay similar to the

vertical load, but the complexity of the soil structure makes it difficult to quantify the microscopic osmotic suction effect to a macroscopic strength model (Rao & Thyagaraj, 2007). The swelling deformation and strength properties of bentonite are difficult to describe quantitatively and uniformly due to the existence of osmotic suction and matric suction. In this paper, the expression of effective stress containing the osmotic stress term for bentonite saturated in saline solutions is derived based on the surface fractal model, and that containing the matric suction term for unsaturated bentonite in deionized water is derived based on the pore fractal model. Further, uniform quantitative descriptions for the swelling strain or shear strength of bentonite in different salt solutions or water content are achieved using the proposed effective stress.

2 FRACTAL FEATURES FOR BENTONITE STRUCTURE

The physical and mechanical properties of geomaterial highly depend on the geometric properties of its structure (Li et al., 2023). In classical Euclidean geometry, the study objects are supposed to be perfectly smooth with integer dimensions of points, lines, surfaces, and bodies. However, actual matters are rough. The complexity and hierarchy of the microstructure lead to the inability to accurately describe the structural characteristics of bentonite with classical Euclidean geometry. Therefore, the concept of fractal geometry is introduced here to better characterize the structure of bentonite.

Fractals, originally proposed by Mandelbrot (1967), are figures with self-similarity that exhibit the same or similarity to the whole when the localization is enlarged. The dimension of a fractal may not be an integer but a fraction, making it suitable for analyzing continuous and nondegenerate rough graphs. The dimension used to describe fractal geometry that can be taken without integers is called the fractional dimension, and a simplified formula for calculating the fractional dimension D is given as follows:

$$N(L) \propto L^{-D} \tag{1}$$

where L is the measurement scale and $N(L)$ is the number of cells with dimensions not smaller than L . Take the typical fractal graph, Koch curve in Figure 1 as an example, and the fractional dimension $D = -\ln N(L) / \ln L = 1.26$. Natural substances usually exhibit self-similarity in a certain scale or statistical significance, so the fractal dimension can be used to quantitatively reflect the geometric structural characteristics of the object.

Fractal theory has currently been widely used in geological materials (Brune et al., 1994). The disordered nature of pore structures in soil suggests the existence of a fractal structure formed by both the macro-pores and micro-pores (Yu & Cheng, 2002), and thus clay can be considered a fractal entity. The hierarchical nature of the bentonite structure conforms to the fractal characteristics, and thus its mechanics can be studied by fractal theory.

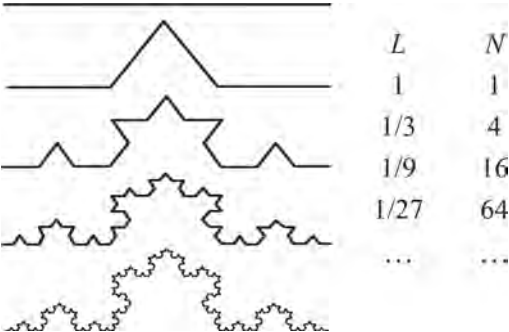


Figure 1. Koch curve.

2.1 Surface

The surface of natural substances on the molecular scale mostly shows fractal features (Burrough, 1981), so the molecular adsorption of surfaces can be utilized to study the fractal surface on the molecular scale using gas molecules as the measuring medium. Avnir et al. (1985) proposed an adsorption isotherm equation for determining the fractal dimension D_s on rough clay surfaces using the nitrogen adsorption test based on the surface adsorption theory:

$$V_{\text{ads}} \propto \left[\ln \left(\frac{P}{P_0} \right) \right]^{D_s - 3} \quad (2)$$

where V_{ads} is the volume of nitrogen adsorbed, P is the equilibrium vapor pressure, and P_0 is the saturation vapor pressure of the pure water surface. The surface fractal dimension of the clay can be obtained by the slope of the linear relationship between the volume of adsorbed nitrogen and the relative vapor pressure in double logarithmic coordinates. In this paper, N_2 adsorption was used to measure the surface fractional dimension of commercial bentonite and GMZ24-200 and GMZ07 bentonite produced in the Gaomiaozi area of the Inner Mongolia Unit, and the test samples were in the form of dry powder.

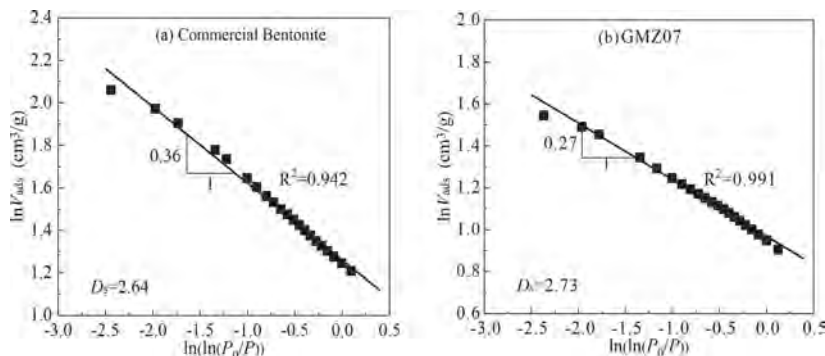


Figure 2. Surface fractal dimension for bentonite.

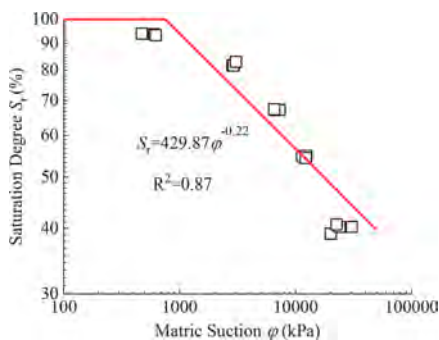


Figure 3. SWCC for expansive soil.

2.2 Pore size distribution

The total volume of pores V_L with sizes less than L can be obtained by integrating as follows:

$$V_L = \int_0^L N 4\pi L^2 dL \quad (3)$$

If the soil pore distribution conforms to the fractal theory, the relationship between the pore volume and pore size can be obtained by combining Eq. (3) with Eq. (1):

$$V_L \propto L^{3-D} \quad (4)$$

Based on this theory, the pore size distribution can be obtained utilizing the mercury intrusion porosimetry (MIP) or soil-water characteristic curve. In MIP experiments, mercury intrudes into pores under pressure to overcome the internal surface tension with the solid. The applied pressure concerning the size of the mercury-filled pores must satisfy the Washburn equation:

$$P = 2\sigma\cos\theta/L \quad (5)$$

where σ is the surface tension of the mercury and θ is the contact angle of the mercury with the solid. In the test, the total pore volume at a given pressure is the volume of mercury injected into the pores. Frieson & Mikulas (1987) have measured the pore volume V_P of a large number of coal and coke samples using the MIP test:

$$\log[dV_P/dP] \sim (D - 4) \log(P) \quad (6)$$

Similarly, the relationship between pore volume and pore size can also be obtained from the soil-water characteristic curve (SWCC) (Tao et al., 2019; Wang et al., 2020). The relationship between matric suction and the effective degree of saturation S_r is obtained from the Young-Laplace equation and is written as follows:

$$S_r = \left(\frac{\varphi}{\varphi_e}\right)^{D-3} \quad (7)$$

where S_r is the degree of saturation, φ is the matric suction and φ_e is the air-entry value. The SWCC was obtained by the filter paper method. The suctions of compacted soil samples with different moisture contents were determined by the calibration curve of filter paper at a closed system with vapor-liquid equilibrium. the relationship between pressure and pore size and the SWCC for expansive soil with more than 20% smectite content is shown in Figure 3 with the fractal dimension D being 2.78.

3 UNIFIED EFFECTIVE STRESS

3.1 *Unsaturated soil in deionized water*

The effective stress of unsaturated soil incorporates the matric suction term and its expression given by Bishop & Blight (1963) is in the following form:

$$p^e = p - u_a + \chi\varphi \quad (8)$$

where p^e is the effective stress, p is the applied external vertical load, u_a is air pressure, and χ is a parameter related to water content. Assuming that χ is equal to the degree of saturation and substituting Eq. (7) into Eq. (8) the fractal expression for the effective stress in unsaturated soil is reached (Xu, 2004):

$$p^e = p - u_a + \varphi^{D-2}\varphi_e^{3-D} \quad (9)$$

Then the shear strength of unsaturated soils can be further obtained by substituting the proposed effective stresses into the equation of the Mohr-Coulomb criterion. It is worth mentioning that the differences between the SWCC and the fitting curve are significant at

both low and high suction ranges, thus an application scope for the proposed theory exists and requires further research.

3.2 Soil saturated by saline solution

Rao & Thyagaraj (2007) suggested that the effect of saline solutions on the mechanical properties of clay is similar to that caused by applying vertical loads. Therefore, the total effective stress on expansive soil in the salt solution can be expressed in the following form:

$$p^e = p + p_\pi \quad (10)$$

where p_π is the osmotic stress related to the osmotic suction π of the solution. Rao & Thyagaraj (2007) found that the osmotic stress is positively proportional to the osmotic suction of the solution with the proportionality factor being less than 1 without giving a quantitative expression for the proportionality factor.

The osmotic suction of the salt solution acts on the microscopic crystalline layers and manifests as osmotic stress on the macroscopic scale. The relationship between osmotic suction and osmotic stress is related to the fractal characteristics of the clay surface. The single crystalline layer surface is smooth relative to the macroscopic soil surface and is set to a size of L , while the rough macroscopic surface is measured on a smaller scale of l . The following relationship between osmotic suction and osmotic stress can be obtained based on the macroscopic and microscopic balance of stresses:

$$\pi L^2 = p_\pi l^2 (L/l)^{D_s} \quad (11)$$

According to the relationship between the vertical stress and the volume of adsorbed water obtained from Eq. (2), macroscopic soils satisfy the following relationship:

$$p^{D_s-3} \propto V_w^L \propto L^{3-D_s} \quad (12)$$

While, the inner intercrystalline layers of clay under the action of osmotic suction satisfy the following relationship:

$$\pi^{D_s-3} \propto V_w^1 \propto l^{3-D_s} \quad (13)$$

The clay is fractal since soil aggregates form a self-similar nested structure. Thus the volume of water absorbed by pores satisfies the fractal adsorption relationship. Substituting Eqs. (12) and (13) into equation (11), the expression of the osmotic stress can be obtained as follows (Li et al., 2020):

$$p_\pi = \pi(\pi/p)^{2-D_s} \quad (14)$$

Then the influence of the osmotic suction in different salt solutions can be uniformly quantified by the osmotic stress term.

3.3 Unsaturated soil in saline solution

For unsaturated soil in saline solution, the effective stress should incorporate both matrix suction and osmotic suction terms (Guo et al., 2021). Wei (2014) proposed a theoretical framework for modeling the chemomechanical behavior of unsaturated soils:

$$\partial p^e = \partial(p - u_a \mathbf{1}) + n^w \cdot \partial(s_M - \Pi_D) \mathbf{1} \quad (15)$$

where s_M is matric suction, n^w is the volume fraction of water and Π_D is the Donnan osmotic suction between the soil and external solution. The partial differential form of the above equation causes difficulties in direct application. Considering the hierarchical nature of the soil structure and combined with Eq. (9) and Eq. (14), the following formula incorporating both matrix suction and osmotic suction terms is proposed:

$$p^e = p - u_a + \chi\varphi + S_r p_\pi \quad (16)$$

Still, this hypothetical formula requires more rigorous derivation and further experimental verification.

4 APPLICATION OF UNIFIED EFFECTIVE STRESS

4.1 Swelling deformation

The swelling properties of bentonite can be explained by the adsorption properties of the mineral surface on water, and the swelling deformation is related to the volume of adsorbed water. According to the conversion principle between work and potential energy, as the soil absorbs water under a constant vertical load, the relationship between the increase in pore surface energy and the work done by the vertical load at the steady state is as follows:

$$\Gamma dS = p dV_w \quad (17)$$

where Γ is the surface free energy per unit area of pore water, dS is the increased pore water surface, p is the applied constant vertical load, and dV_w is the volume of water absorbed. The pore size and the vertical overlying pressure p accord with the Young-Laplace equation and the area S conforms to fractal characteristics so that the relationship between the montmorillonite void ratio of the clay and the external load can be deduced as follows (Xu et al., 2003):

$$e_m = \frac{V_w}{V_m} = K p^{D_s-3} \quad (18)$$

where e_m is the montmorillonite void ratio, V_w is the volume of adsorbed water, V_m is the volume of montmorillonite, and K is the swelling coefficient, which can be determined by the oedometer test for soil in deionized water. Substituting the effective stress on expansive soil in salt solution into Eq. (18), the uniform swelling-deformation relationship of expansive soil in saline solution can be obtained:

$$e_m = \frac{V_w}{V_m} = K (p^e)^{D_s-3} \quad (19)$$

Commercial bentonite and GMZ07 bentonite were selected to conduct the one-dimensional free swelling test to verify the uniform swelling-deformation relationship of bentonite in salt solution. The surface fractal dimensions of the two soils measured by the nitrogen adsorption test were 2.64 and 2.73, respectively, as shown in Figure 2. The soil specimens were made into soil cakes with an initial height of 1 cm and a diameter consistent with the inner diameter of the graduated cylinder and immersed in NaCl (0.1, 0.5, 1, and 2 mol/L), Na₂SO₄ (0.1, 0.5, and 1 mol/L), and CaCl₂ (0.1, 0.5, 1 and 2 mol/L) solutions until the heights no longer change for 48 hours. The test results in Figure 4 show that unified relationships exist between the montmorillonite void ratio and effective stress of the two bentonites used in the test under different immersion conditions, and both conform to the linear relationship in the double logarithmic coordinate with the slope exactly equal to D_s-3 .

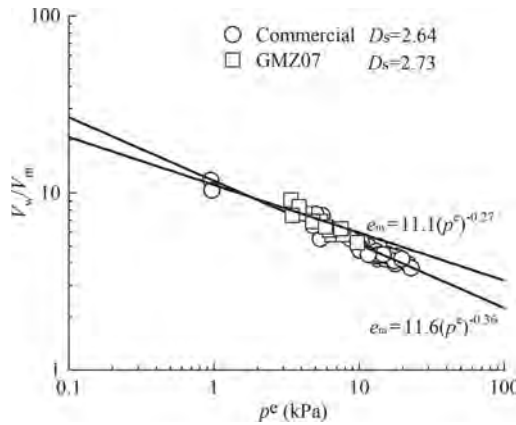


Figure.4. The relationship between p^e and V_w/V_m .

4.2 Shear strength

The direct shear tests were performed on GMZ07 bentonite saturated in different solutions. The GMZ07 bentonite was made into soil cakes with a diameter of 5 cm, a height of 2 cm, and an initial dry density of 1.5 g/cm^3 . The soil specimens were placed in the oedometer and saturated with 0 mol/L, 0.2 mol/L, 0.5 mol/L, 1.0 mol/L Na_2SO_4 solution, and 0.5 mol/L CaSO_4 solution, respectively. The applied vertical loads for each solution condition were 50 kPa, 100 kPa, 200 kPa, 300 kPa, and 400 kPa during the saturation process. After the soil specimens had reached saturation, the applied vertical loads remained unchanged, and a slow-speed direct shear test was carried out to obtain the peak shear strength of the saturated specimens under drained conditions where the total stress was equal to the effective stress. The results in Figure 5a show that the peak shear strength of the bentonite in different salt solutions does not satisfy a uniform linear relationship with the applied vertical loads. Using the surface fractal dimension measured by the nitrogen adsorption test and the unified effective stress of clay in different solutions calculated by Eqs. (10) and (14), the relationship between the unified effective stress and the peak shear strength of bentonite saturated in saline solutions was obtained. The peak shear strength and effective stress of bentonite in different solutions conform to the Mohr-Coulomb criterion with the cohesion being 49.54 kPa and the internal friction angle being 14.3° , as shown in Figure 5b. Thus, a uniform description of the peak shear strength in different salt solutions is achieved using the proposed effective stress on clay in saline solution.

Expansive soil was also conducted to direct shear tests as compacted into soil samples with the same initial dry density being 1.4 g/cm^3 but different initial water contents being 15%, 20%, 25%, and saturation. The matric suctions were also determined by the filter paper method once the shear test had been finished. The relationship between the applied vertical stress and peak shear strength deviates from the Mohr-Coulomb criterion due to the existence of matric suction. The modified effective stress for unsaturated soil in Eq. (9) was calculated with the fractal dimension being 2.78 in Figure 3 and the assumption of the air-entry value being 1 kPa. The peak shear strength exhibits a linear relationship with p^e as shown in Figure 6 which conforms to the Molar Coulomb criterion. The experimental results prove the reliability of Eq. (9).

5 CONCLUSIONS

Determination of the deformation and strength characteristics of bentonite is required for many geotechnical applications. However, a unified quantitative theory of the effective stress of clay in salt solutions or the unsaturated state is lacking. A better estimation of effective

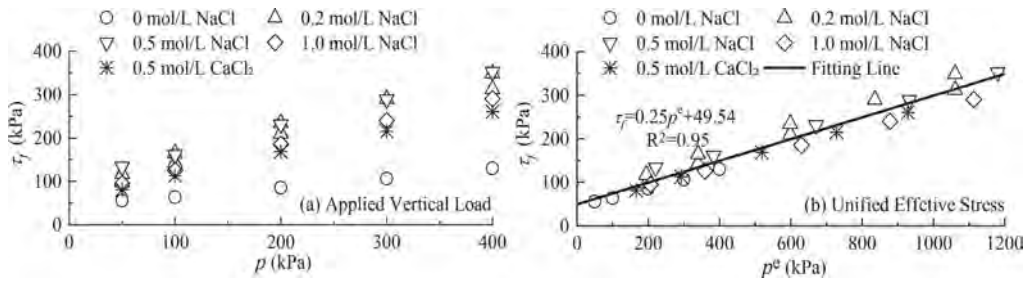


Figure 5. Relationship between peak shear strength and effective stress in Na_2SO_4 solutions.

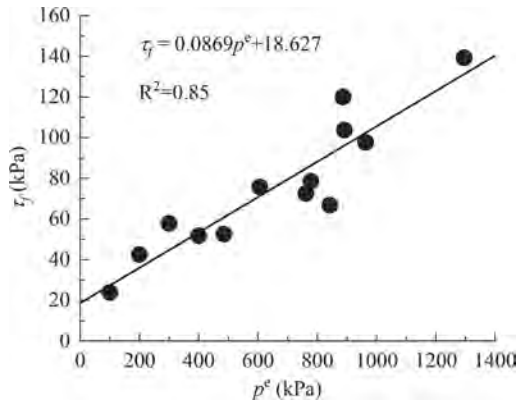


Figure 6. Relationship between peak shear strength and effective stress for unsaturated expansive soil.

stress for bentonite is presented based on its structural fractal features and validated by the good agreement between the prediction and measurement. From the study in this paper, the main conclusions are obtained as follows:

- (1) The surface and pore size distribution of bentonite have fractal characteristics that can be qualified by fractal dimensions. The surface fractal dimension was determined by the nitrogen adsorption test based on surface adsorption theory, while the pore fractal dimension could be reached by the SWCC or MIP test with the relationship between the accumulated volume and corresponding pressure.
- (2) The effective stress for bentonite saturated in saline solutions or unsaturated in deionized water was deduced respectively based on the fractal structure features. Then the volume change for bentonite swelling in different solutions can be uniformly described. The peak shear strength and the effective stress for bentonite saturated in saline solutions or unsaturated in deionized water are proved by tests to comply with the Mohr-Coulomb criterion.
- (3) The effective stress for unsaturated bentonite in saline solution should include the effective terms of both the matric suction and osmotic suction. An expression was proposed by combining the validated forms of effective stresses for bentonite saturated in saline solutions and unsaturated in deionized water. Rigid derivation and further validation by experiments are still required in the next step of research.

ACKNOWLEDGMENTS

The supports from the Science and Technology Development Fund of Macau SAR (File nos. 001/2024/SKL), National Natural Science Foundation of China (Grant No. 52022001) and China Postdoctoral Science Foundation (Certification No.2023M744116) are gratefully acknowledged.

REFERENCES

- Avnir, D., Farin, D. & Pfeifer, P. 1985. Surface geometric irregularity of particulate materials: the fractal approach. *Journal of Colloid and Interface Science* 103(1): 112–123.
- Bishop, A. W. & Blight, G. E. 1963. Some aspects of effective stress in saturated and unsaturated soils. *Geotechnique* 13: 177–197.
- Brune, H., Romainczyk, C., Röder, H. & Kern, K. 1994. Mechanism of the transition from fractal to dendritic growth of surface aggregates. *Nature* 369(6480): 469–471.
- Burrough, P. A. 1981. Fractal dimensions of landscapes and other environmental data. *Nature* 294(5838): 240–242.
- Fredlund, D. G., Xing, A. Q., Fredlund, M. D., & Barbour, S. L. 1996. The relationship of the unsaturated soil shear strength to the soil-water characteristic curve. *Canadian Geotechnical Journal* 33(3): 440–448.
- Frieson, W. I. & Mikula, R. J. 1987. Fractal dimensions of coal particles. *Journal of Colloid and Interface Science* 120(1): 263–271.
- Guo, L., Chen, G., Gao, J. & Li, C. 2021. Micro-scale analysis on shear characteristics of unsaturated soil by considering capillary suction and adsorption suction based on DDA. *Engineering Analysis with Boundary Elements* 132: 321–334.
- Li, B., Li, X. J., Xiao, W., Cheng, Q. & Bao, T. 2023. Quantitative characterization method of 3D roughness of rock mass structural surface considering size effect. *Smart Construction and Sustainable Cities* 1: 9.
- Li, X. Y., Xu, Y. F. & Li, C. Y. 2020. Experimental study on the 1-D free swelling of compacted bentonite. *Acta Geotechnica* 15:1895–1907.
- Ma, T., Wei, C., Yao, C. & Yi, P. 2020. Microstructural evolution of expansive clay during drying-wetting cycle. *Acta Geotechnica* 15: 2355–2366.
- Mandelbrot, B. B. 1967. How long is the coast of Britain? Statistical self-similarity and fractional dimension. *Science* 156(3775): 636–638.
- Mitchell, J. K. & Soga, K. 2005. *Fundamentals of soil behavior*[M]. 3rd ed. New York: Wiley.
- Qin, S., Cheng, Y. & Zhou, W. H. 2023a. State-of-the-art review on pressure infiltration behavior of bentonite slurry into saturated sand for TBM tunneling. *Smart Construction and Sustainable Cities* 1: 14.
- Qin, S., Zhou, W.H., & Xu, T. 2023b. Effects of seawater on the infiltration behavior of bentonite slurry into sand. *Construction and Building Materials* 371: 130759.
- Rao, S. M. & Thyagaraj, T. 2007. Role of direction of salt migration on the swelling behaviour of compacted clays. *Applied Clay Science* 38(1-2): 113–129.
- Shen, P., Wei, S., Shi, H., Gao, L. & Zhou, W. H. 2023. Coastal Flood Risk and Smart Resilience Evaluation under a Changing Climate. *Ocean-Land-Atmosphere Research* 2: 0029.
- Tao, G., Chen, Y., Xiao, H., Chen, Q., & Wan, J. 2019. Determining soil-water characteristic curves from mercury intrusion porosimeter test data using fractal theory. *Energies* 12(4): 752.
- Wang, H., Ni, W., Li, X., Li, L., Yuan, K., & Nie, Y. 2022. Predicting the pore size distribution curve based on the evolution mechanism of soil-water characteristic curve. *Environmental Earth Sciences* 81(1): 23.
- Wei, C. 2014. A theoretical framework for modeling the chemo-mechanical behavior of unsaturated soils. *Vadose Zone Journal* 13(9): 1–21.
- Xu, Y. F. 2004. Fractal approach to unsaturated shear strength. *Journal of Geotechnical and Geoenvironmental Engineering ASCE* 130(3): 264–274.
- Xu, Y. F. & Matsuoka, H. & Sun, D. A. 2003. Swelling characteristics of fractal-textured bentonite and its mixtures. *Applied Clay Science* 22(4): 197–209.
- Yin, X., Chen, R., Li, Y. & Qi, S. 2016. A column system for modeling bentonite slurry infiltration in sands. *Journal of Zhejiang University-SCIENCE A* 17(10): 818–827.
- Yu, B. & Cheng, P. (2002). A fractal permeability model for bi-dispersed porous media. *International Journal of Heat and Mass Transfer* 45(14): 2983–2993.

Determination of particle breakage and fractal dimension for marine coral sand

X. Li

Department of Civil and Environmental Engineering, State Key Laboratory of Internet of Things for Smart City, University of Macau, Macao SAR, People's Republic of China

X. Feng

China Civil Engineering Construction Corporation, Beijing, China

C. Wang

Department of Civil and Environmental Engineering, State Key Laboratory of Internet of Things for Smart City, University of Macau, Macao SAR, People's Republic of China

W.H. Zhou

Department of Civil and Environmental Engineering, State Key Laboratory of Internet of Things for Smart City, University of Macau, Macao SAR, People's Republic of China
Center for Ocean Research in Hong Kong and Macao (CORE), Hong Kong SAR, People's Republic of China

ABSTRACT: A set of 1D compression tests were conducted for marine coral sand with different fines content to investigate the variations of particle breakage ratio, fractal dimension, and the relationship between them. Test results reveal that coral sand with lower fines content in a loose state are more susceptible to breakage. Furthermore, the fractal dimension exhibits a rapid increase with the rising fines content, followed by a gradual growth as the fines content continues to increase. Nevertheless, a combination of high relative density and larger medium particle size contributes to a reduction in fractal dimension. In conclusion, a proposed relationship between particle breakage ratio and fractal dimension is presented.

1 INTRODUCTION

Marine coral sand constitutes a distinctive category of granular marine sediments, distinguished by the prevalence of calcium carbonate and other carbonate-insoluble substances. Abundant in tropical and subtropical regions, it is notably discovered along coral reefs and seashores, encompassing areas such as the South China Sea, Bass Strait, Red Sea, and the western continental platform of Australia (Li and Liu, 2021). In contrast to quartz sand, coral sand exhibits a heightened susceptibility to particle breakage, posing potential engineering challenges. Upon the breakage of larger particles, there is an increase in fines content, consequently altering both the particle breakage ratio and fractal dimension (Qin et., 2023). Over the past few decades, numerous methodologies have emerged for quantifying the particle breakage ratio. Researchers have explored variations in particle size distribution (PSD), particle shape and size, and inputted plastic work as means to assess the particle breakage ratio (Shen et al., 2023). Indeed, there exists a close correlation between fractal dimension and particle breakage ratio, particularly when particles undergo fragmentation. Unfortunately, limited research has been conducted to examine the relationship between particle breakage ratio and fractal dimension.

At current work, a series of one-dimensional (1D) compression tests and PSD experiments were performed to obtain the variations of particle breakage ratio and three-dimensional (3D)

fractal dimension. Based on the test results, relationship between particle breakage ratio and fractal dimension was established.

2 METHODOLOGY

2.1 *Materials properties*

The tested coral sand was collected from South China Sea. The specific gravity of coral sand is 2.81. In fact, coral sand originates and evolves through the accumulation of remains from coral reefs and limestone sediments, primarily composed of CaCO_3 and MgCO_3 . Besides, the Mohs hardness of coral sands measures around 3-4, which is notably lower than that of quartz sand.

2.2 *Testing program*

In the current investigation, the established geotechnical procedure of China (GB/T 50123-2019) was employed for the preparation of coral sand specimens, involving three sequential steps. Initially, the coral sand underwent a 24-hour drying period in an oven to eliminate any moisture effects. Subsequently, it was meticulously mixed with fines to achieve predetermined fines contents of 0%, 10%, 25%, 40%, 70%, and 100% by weight, ensuring a uniform blend. Finally, the desired relative density (D_r), namely 0.30, 0.55, and 0.80, were achieved using the air pluviation method (Dastpak et al., 2021). The tested specimen had dimensions of 20.0 mm in height and 61.8 mm in diameter ($D/H \approx 3$). A one-dimensional (1D) loading system, as shown in Figure 1, was employed for the execution of the 1D compression test. Besides, PSD tests were conducted before and after 1D compression test to quantify the particle breakage ratio and fractal dimension.

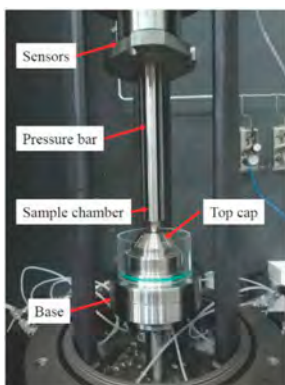


Figure 1. 1D compression test system.

3 TEST RESULTS

3.1 *Particle breakage*

Coral sand exhibits a greater susceptibility to particle breakage in comparison to quartz sand (Li et al., 2022). To date, numerous indices have been developed for assessing the relative particle breakage of granular materials (Einav, 2007a, 2007b; Hardin, 1985; M. R. Coop, 2004). Among them, relative particle breakage ratio B_r , developed by Hardin (1985), has been extensively adopted to quantify particle breakage. As shown in Figure 2, Hardin model assumed that particles with sizes smaller than 0.075 mm would not undergo breakage. Consequently, B_r can be calculated using following expression.

$$B_r = B_t/B_p \quad (1)$$

where B_t is total breakage, defined as the area enclosed by the initial grading curve, current grading curve, and the vertical line at $d = 0.075$ mm; B_p is breakage potential, which is the area surrounded by initial grading curve and the vertical line of $d = 0.075$ mm.

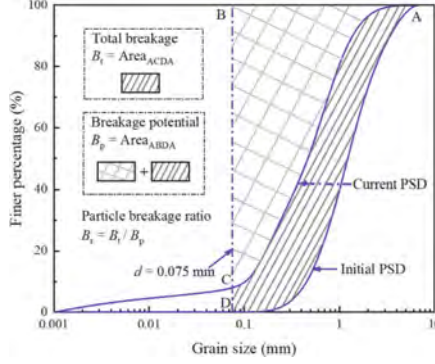


Figure 2. Schematic diagram of relative breakage ratio (Modified after Hardin (1985)).

Figure 3 illustrates the relationships between B_r and fines content, relative density (D_r), and medium grain size (d_{50}). In Figure 3 (a) and (b), it is evident that B_r demonstrates a negative power or linear relationship with fines content and D_r , respectively. Besides, when fines content reaches 70 %, the associated B_r values for D_r of 0.30, 0.55, and 0.80 are 0.012, 0.008, and 0.004, respectively. This behavior suggests that mixtures with a fines content of 70% undergo minimal particle breakage. Larger particles are more prone to breakage than smaller particles, and the presence of smaller particles, in turn, appears to mitigate particle breakage. Combining the findings from Figure 3 (a) and (b), at a given fines content, higher D_r tends to decline B_r . This observation aligns with prior findings reported by Li and Liu (2021). At current study, d_{50} ranges from 0.02 to 0.70 mm, showing a positive correlation with B_r , as shown in Figure 3 (c). It should be noted that there exists a threshold value for d_{50} at 0.61 mm, beyond which B_r increases dramatically. This behavior is different from the results reported by Shen et al., (2023) and Zhu et al., (2022). The differing results can likely be attributed to the fact that B_r is a comprehensive measure influenced by multiple factors. While it was observed in this study that larger particles tend to break more easily than smaller ones, it's essential to emphasize that B_r is influenced by the grain grading conditions.

3.2 Fractal dimension evolution

Granular materials demonstrate a correlation between three-dimensional fractal dimension (D_{3D}) and material mass distribution (Tyler and Wheatcraft, 1992), which can be expressed as Eq. (2)

$$M(\delta > d_i)/M_T \alpha - (d_i/d_{max})^{3-D_{3D}} \quad (2)$$

where $M(\delta > d_i)$ is cumulative mass of material with grain size greater than d_i ; M_T is total mass of particles involved in statistics; d_{max} is maximum particle diameter; D_{3D} is three-dimensional fractal dimension (D_{3D}). From Eq. (2), d_i/d_{max} exhibits a logarithmic relation with $M(\delta > d_i)/M_T$. Defining the slope is k , then $D_{3D} = 3 - k$.

Figure 4 presents the changes in D_{3D} before and after compression test. From Figure 4 (a), D_{3D} experiences a rapid increase before and after the test when fines content is less than 25% (stage 1), followed by a gradual increase (stage 2). When fines content reaches 70 %, the D_{3D} curves before

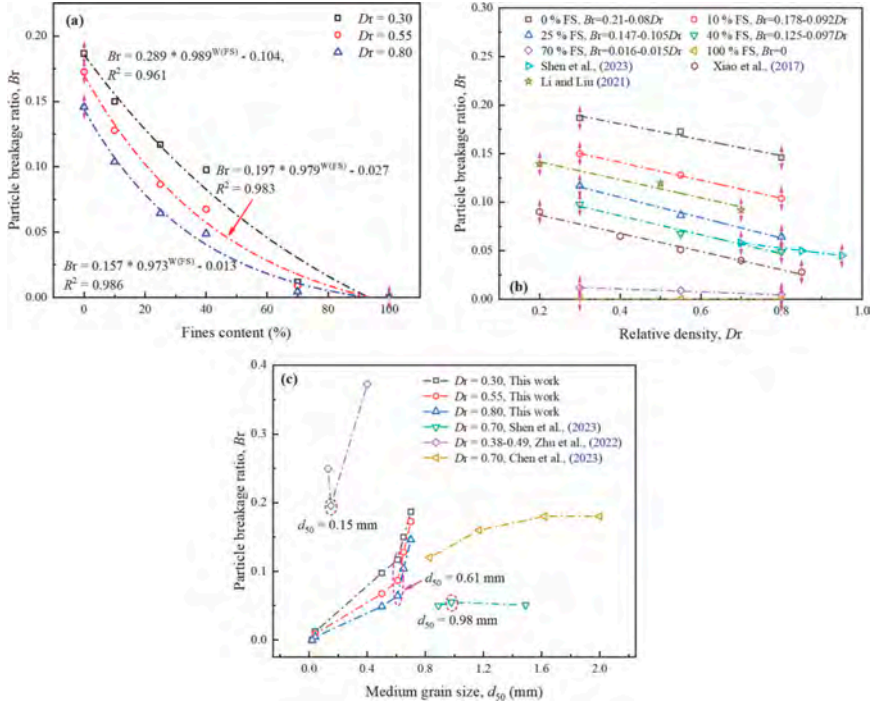


Figure 3. Relationship between particle breakage ratio with (a) fines content, (b) relative density, and (c) d_{50} .

and after test are basically in coincidence, indicating minimal shifting in the PSD curves. Additionally, as demonstrated in Figure 4 (b), consistent with the trend observed in B_r with respect to D_r shown in Figure 3 (b). However, Yu (2018) found that D_{3D} of coral sand decreased (from 1.3068 to 1.2486) as increasing initial void ratio from 0.798 to 0.924 during a consolidated drained triaxial test. The reason for these contradictory results may be attributed to the fact that the fractal dimension quantifies the complexity and space-filling capacity of a pattern. After the larger particles were broken, changes occurred in the shapes of particles, and fines content increased, which collectively influenced the fractal dimension. As d_{50} decreases, the variation in D_{3D} exhibits three distinct stages, as shown in Figure 4 (c). Initially, in stage 1, D_{3D} decreases rapidly when d_{50} is less than 0.04 mm. Subsequently, in stage 2, it continues to decrease at a lower rate. Finally, D_{3D} decline dramatically once again when d_{50} reaches 0.61 mm in the stage 3.

3.3 Correlation between particle breakage ratio with fractal dimension

From Figure 3 and Figure 4, the correlation between B_r and ΔD_{3D} was determined as shown in Figure 5. Overall, the variation in B_r closely fits a logarithmic function with respect to ΔD_{3D} , which can be expressed as follows.

$$B_r = x * \ln(1/(\psi * \ln(\Delta D_{3D}))) \quad (3)$$

where χ and ψ are parameters which can be determined by D_r as Eq. (4) and (5)

$$x = 0.128 - 1.703 * (5.142 * 10^{-6})^{D_r} \quad (4)$$

$$\psi = -0.129 + 0.412 * 0.005^{D_r} \quad (5)$$

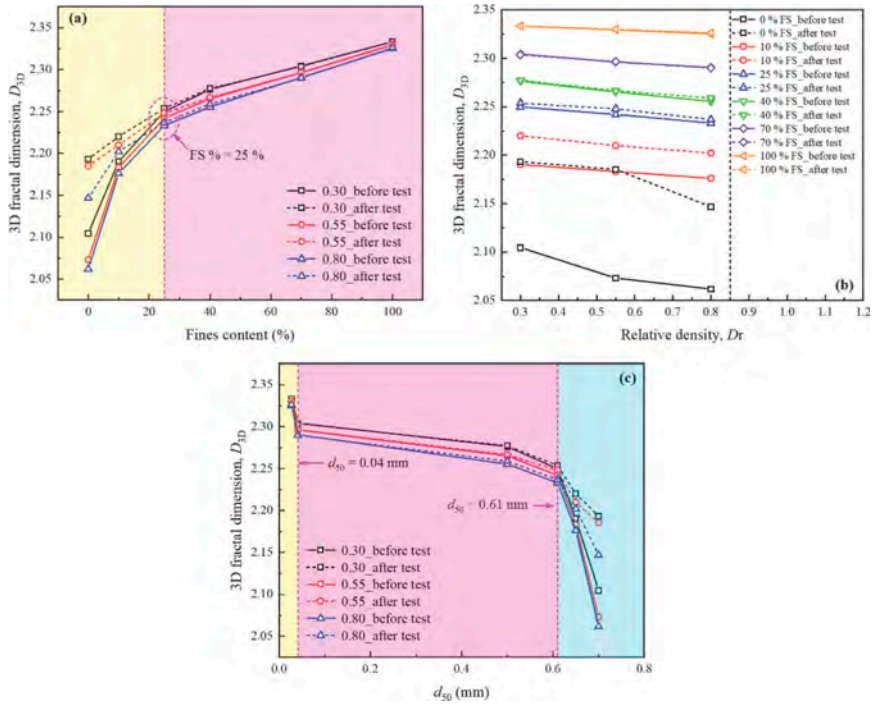


Figure 4. Three-dimensional (3D) fractal dimension variation with (a) fines content, (b) relative density, and (c) d_{50} .

Besides, Yu (2018) have developed a hyperbolic model to correlate B_r and relative fractal dimension during monotonic and cyclic triaxial test as shown in Eq. (6)

$$B_r = (0.048 * D_{r3D}) / (1 - 1.287 * D_{r3D}) \quad (6)$$

where D_{r3D} is relative fractal dimension. Compared with Eq. (6), the logarithmic model proposed in this work considering the relative density effect, which can supplement the existed relations. Indeed, relative density plays a dominant role in particle breakage and should not be overlooked.

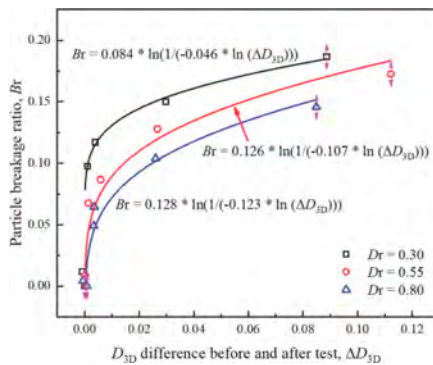


Figure 5. Correlation between relative particle breakage ratio with 3D fractal dimension difference.

4 CONCLUSION REMARK

Variations in relative particle breakage ratio (B_r) and fractal dimension (D_{3D}) with fines content, relative density (D_r), and d_{50} were examined. Higher fines content and greater D_r were found to restrain particle breakage. The fractal dimension experiences a rapid surge with increasing fines content, succeeded by a more gradual expansion as fines content further increases. However, a combination of high D_r and a larger d_{50} contributes to a reduction in the fractal dimension. Furthermore, we have proposed a logarithmic model for the correlation between B_r and ΔD_{3D} .

ACKNOWLEDGEMENTS

This work was funded by the Science and Technology Development Fund of Macau SAR (File Nos. 0056/2023/RIB2, 001/2024/SKL) and the Center for Ocean Research in Hong Kong and Macau (CORE), which is a joint ocean research center established by the Qingdao National Laboratory for Marine Science and Technology and the Hong Kong University of Science and Technology.

DATA AVAILABILITY

The datasets generated during and/or analyzed during the current study are available in the GitHub repository, <https://github.com/umgeotech>.

REFERENCES

- Dastpak, P., Abrishami, S., Rezazadeh Anbarani, M., Dastpak, A., 2021. Effect of Perforated Plates on the Relative Density of Uniformly Graded Reconstituted Sands Using Air Pluviation Method. *Transp. Infrastruct. Geotech.* 8(4), 569–589.
- Einav, I., 2007a. Breakage Mechanics—Part I: Theory. *Journal of the Mechanics and Physics of Solids.* 55(6), 1274–1297.
- Einav, I., 2007b. Breakage Mechanics—Part II: Modelling Granular Materials. *Journal of the Mechanics and Physics of Solids.* 55(6), 1298–1320.
- Hardin, B.O., 1985. Crushing of Soil Particles. *Journal of Geotechnical Engineering.* 111(10), 1177–1192.
- Li, X., Liu, J., 2021. One-Dimensional Compression Feature and Particle Crushability Behavior of Dry Calcareous Sand Considering Fine-Grained Soil Content and Relative Compaction. *Bulletin of Engineering Geology and the Environment.* 80(5), 4049–4065.
- Li, X., Liu, J., Nan, J., 2022. Prediction of Dynamic Pore Water Pressure for Calcareous Sand Mixed with Fine-Grained Soil Under Cyclic Loading. *Soil Dynamics and Earthquake Engineering.* 157, 107276.
- M. R. Coop, K.K.S.T., 2004. Particle Breakage During Shearing of a Carbonate Sand. *Géotechnique.* 54 (3), 157–163.
- Qin, S., Xu, T., Zhou, W., Bezuijen, A., 2023. Infiltration behaviour and microstructure of filter cake from sand-modified bentonite slurry. *Transportation Geotechnics.* 40, 100963.
- Shen, J., Chen, X., Wang, X., Wang, X., Qin, Y., Wu, H., 2023. Compression Responses and Particle Breakage of Calcareous Granular Material in Reclaimed Islands. *Powder Technology.* 418, 118277.
- Tyler, S.W.W.S., 1992. Fractal Scaling of Soil Particle-Size Distributions: Analysis and Limitations. *Soil Science Society of America Journal.* 56(2), 362–369.
- Xiao, Y., Liu, H., Chen, Q., Ma, Q., Xiang, Y., Zheng, Y., 2017. Particle Breakage and Deformation of Carbonate Sands with Wide Range of Densities During Compression Loading Process. *Acta Geotechnica.* 12(5), 1177–1184.
- Yu, F., 2018. Particle Breakage in Triaxial Shear of a Coral Sand. *Soils and Foundations.* 58(4), 866–880.
- Yuan-yi Chen, Y.T.Y.G., 2023. Study On the Mechanical Properties of Coral Sands with Different Particle Gradations. *Marine Georesources & Geotechnology.* 41(3), 327–338.
- Zhu, X., Li, S., Li, Y., Li, T., Yin, J., 2022. Study of the Influence of Particle Breakage on Compression Properties for Carbonate Sand. *Bulletin of Engineering Geology and the Environment.* 81(3).

Improved determination of the constrained modulus in soft soils using the flat dilatometer test

S. Oberhollenzer

Norwegian Geotechnical Institute, Oslo, Norway

Institute of Soil Mechanics, Foundation Engineering and Computational Geotechnics, Graz University of Technology, Graz, Austria

L. Hauser, R. Marte, F. Tschuchnigg & H.F. Schweiger

Institute of Soil Mechanics, Foundation Engineering and Computational Geotechnics, Graz University of Technology, Graz, Austria

E.J. Lande

Norwegian Geotechnical Institute, Oslo, Norway

ABSTRACT: A wide range of geotechnical tasks demand a reliable determination of soil stiffness. Since undisturbed soil sampling is required but difficult for laboratory testing, parameter identification based on in-situ testing in combination with correlations have become more popular. Flat dilatometer testing (DMT) considers the penetration of a steel blade, equipped with a circular, expandable membrane, into the ground. The penetration process is usually stopped in 20 cm intervals for total stress measurements at defined membrane expansions. The present article aims to improve the determination of the in-situ constrained modulus in soft soils by means of DMT. Existing correlations are compared with oedometer results for Alpine deposits. It is shown that constrained moduli, derived from existing correlations, underestimate laboratory results, even when DMT readings are corrected for partial drainage effects. New correlations are developed to reach a better agreement between in-situ and laboratory results in fine-grained soils.

1 INTRODUCTION

Soft soils define the soil layering of various urban areas (e.g., Oslo, Mexico City, Ho Chi Minh) and represent challenging ground conditions due to their moderate stiffness and strength. Alpine regions in Austria are often characterized by several basins, formed during glacial periods and filled by mainly fine-grained sediments after the melting process of glaciers (van Husen 1979). These (geologically) young sediments are usually normally consolidated and high groundwater tables are present. Nowadays, touristic areas like Salzburg, Rosenheim or Bregenz are situated on top of such fine-grained deposits. Recordings confirm that insufficient parameter identification in combination with inappropriate construction measures have often led to building damages (e.g., tilting; cracks along the foundation and walls). Since sampling disturbance can strongly influence the laboratory results, in-situ tests such as the piezocone penetration test (CPTu) and the seismic flat dilatometer test (SDMT) are becoming increasingly popular for identifying soil parameters (Schnaid 2009). However, correlations proposed in literature are usually site-specific and cannot be generally applied. Therefore, Graz University of Technology in cooperation with the Federal Chamber of Architects and Chartered Engineering Consultants initiated the research project PITS (parameter identification using in-situ tests in silty soils) to allow an improved characterization of the stress-strain behavior in postglacial Alpine deposits (Oberhollenzer & Hauser 2022).

The present paper aims to improve the determination of the in-situ constrained modulus (M) in postglacial, Alpine deposits using DMT. Therefore, in-situ testing and soil sampling were performed at four test sites, namely *Rhesi*, *Lokalbahn Salzburg*, *Seekirchen* and *water reservoir Raggal*. Alternative DMT-testing procedures were further executed to consider for partial drainage effects (Oberhollenzer et al. 2023). Constrained moduli, derived from oedometer tests and flat dilatometer results (using corrected and uncorrected in-situ readings) are compared in the first step. Subsequently, new correlations are proposed for DMT to reach an improved agreement between in-situ and laboratory results in Alpine deposits.

2 METHODS

2.1 DMT-equipment and test execution

Piezcone penetration tests (CPTu) and seismic flat dilatometer tests (SDMT) were executed according to ISO 22476-1 and ISO 22476-11 at the test sites *Rhesi*, *Lokalbahn Salzburg*, *Seekirchen* and *water reservoir Raggal*. A steel blade, containing a thin, expandable, circular steel membrane, is pushed into the soil during DMT execution (see Figure 1a). At regular intervals (of usually 20 cm) the penetration is stopped for consecutive pressure readings at defined membrane expansions. The standard procedure, namely DMT-STD, is summarized in the following:

- A-reading: pressure required to lift-off the membrane, approx. 15 seconds after reaching the testing depth.
- B-reading: pressure required to expand the membrane center about 1.1 mm, approx. 15 seconds after the A reading.
- C-reading (optional): pressure reading in A position after slowly deflating the membrane from position B.

When using the DMT-system developed by Marchetti (1980) the membrane is expanded pneumatically by the operator using a control unit. In contrast, the Medusa flat dilatometer test (Medusa DMT) enables a fully automated, hydraulic expansion of the circular membrane using a motorized syringe (Marchetti et al. 2018). The required pressure for expanding the membrane is measured by a high-accuracy transducer. An electric cable, running through the

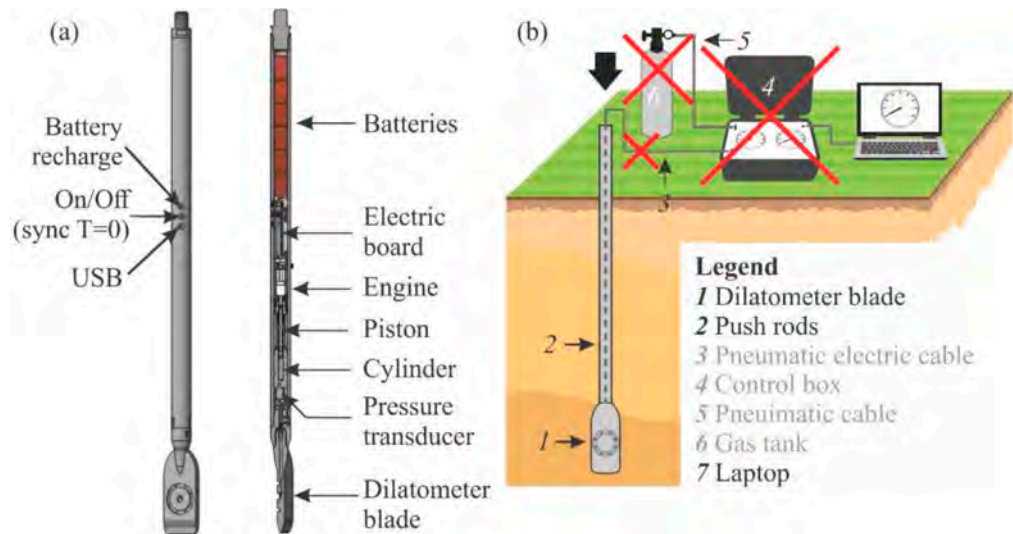


Figure 1. Overview of (a) DMT blade and the (b) components required for medusa test execution (Oberhollenzer et al. 2023).

penetration rods, is used instead of pneumatic cables during Medusa DMT execution connecting the blade with a control unit and the laptop for real-time data interpretation (see Figure 1b). Different membrane expansion rates and repeated A-readings (where the membrane is kept in the same position for repeated pressure readings) can be executed with high accuracy, enabling the enhanced testing procedure DMT-RA. The latter procedure considers repeated A-readings within the first 15 seconds after penetration stop, followed by B and C readings at the time-steps defined for DMT-STD. While DMT-STD was executed at the test sites *Rhesi* (depth: -25 m), *Lokalbahn Salzburg* (depth: 25 m), *Seekirchen* (depth: 12 m) and *water reservoir Raggal* (depth: 17 m), additional *DMT-RA* were considered at *Rhesi* and *Lokalbahn Salzburg*.

2.2 DMT-interpretation

The in-situ readings A, B and C are corrected about the membrane stiffness using the calibration offsets ΔA and ΔB according to Eq. (1), Eq. (2) and Eq. (3) (Marchetti 1980). Subsequently, corrected readings p_0 , p_1 and p_2 are used to derive intermediate parameters, namely material index (I_D , see Eq. (4)), horizontal stress index (K_D , see Eq. (5)), dilatometer modulus (E_D , see Eq. (6)) and pore pressure index (U_D , see Eq. (7)), which represent the foundation for parameter identification according to Marchetti (1980). The in-situ constrained modulus (M) is calculated according to Eq. (8) using the dilatometer modulus (E_D) and the empirical factor R_M . For fine-grained soils characterized by $I_D \leq 0.6$, R_M should be calculated based on Eq. (9) but must be larger than 0.85 (Marchetti 1980).

$$p_0 = 1.05 \cdot (A + \Delta A) - 0.05 \cdot (B - \Delta B) \quad (1)$$

$$p_1 = B - \Delta B \quad (2)$$

$$p_2 = C + \Delta A \quad (3)$$

$$I_D = (p_1 - p_0) / (p_0 - u_0) \quad (4)$$

$$K_D = (p_0 - u_0) / \sigma'_{v0} \quad (5)$$

$$E_D = 34.7(p_1 - p_0) \quad (6)$$

$$U_D = (p_2 - u_0) / (p_0 - u_0) \quad (7)$$

$$M = R_M \cdot E_D \quad (8)$$

$$R_M = 0.14 + 2.36 \cdot \log K_D \quad (\text{for } I_D \leq 0.6) \quad (9)$$

2.3 Correction of DMT-readings about partial drainage effects

Partial drainage effects can occur during DMT execution in a wide range of soil types (e.g., clays and silts) and are further influenced by soil heterogeneity (Oberhollenzer et al. 2023). Different researchers (e.g., Marchetti et al. 2001, Schnaid et al. 2018, Oberhollenzer et al. 2023) proposed test procedures to correct in-situ measurements for partial drainage, enabling a determination of undrained A- and B-readings (A_0 , B_0) in the respective testing depth. It was previously shown that the in-situ readings show an approximately linear decrease over the root of time when keeping the membrane position fixed (see black dashed lines in Figure 2). The inclination of both lines is indicated as k_A and k_B . A- and B-readings, determined by means of DMT-STD, are indicated in Figure 2 by black circles.

It was recommended by Oberhollenzer et al. (2023) to determine undrained readings based on repeated A- and B-readings. The latter procedure is shown in green (see Figure 2) and consists of three main stages: (1) repeated A-reading within the first 15 seconds after penetration

stop (A0 → A15), (2) membrane expansion to position B and (3) repeated B-readings for 15 seconds (B30 → B45). While A0 is measured, B0 can be extrapolated linearly based on k_B and B30.

If repeated B-readings are not available, k_B can be approximated based on the DMT-RA testing procedure (see green line between A0 and B30 in Figure 2). It was shown by Oberhollenzer et al. (2023) that k_B ranges between $k_B \approx 1 \cdot k_A$ and $k_B \approx 2 \cdot k_A$ in postglacial, Alpine deposits. However, the trend is approximated best by $k_B = 1.5 \cdot k_A$. Again, B0 can be determined based on k_B (derived from k_A) and B30.

A third approach was elaborated to roughly estimate A0 and B0 based on DMT-STD. The percentage decrease of A within the first 15 seconds after penetration stop (d_A) is determined based on the material index (I_D , calculated from A15 and B30) (Oberhollenzer et al. 2023). Since the correlation between d_A and I_D is further influenced by the soil heterogeneity - here defined as the change in soil permeability between two consecutive testing depths - two equations (see Eq. (10) and Eq. (11)) were defined empirically based on DMT-RA to approximate the relation between d_A and I_D . If the difference in I_D between two consecutive testing depths is smaller than 80% it is suggested to use Eq. (9), while d_A is derived from Eq. (10) in more heterogeneous soil layers (leading to a difference in I_D between two consecutive testing depths larger than 80%). As described more detail in Oberhollenzer et al. (2023), A0 can be derived from d_A and is further used in combination with A15 to calculate k_A . k_B should be approximated based on $1.5 \cdot k_A$ and used with B30 to determine B0.

$$d_{A \text{ homo}} = -0.012 \cdot I_D^4 + 0.514 \cdot I_D^3 - 3.495 \cdot I_D^2 + 4.619 \cdot I_D + 7.616 \quad (10)$$

$$d_{A \text{ hetero}} = -1.504 \cdot I_D^4 + 18.11 \cdot I_D^3 - 72.02 \cdot I_D^2 + 93.4 \cdot I_D + 4.42 \quad (11)$$

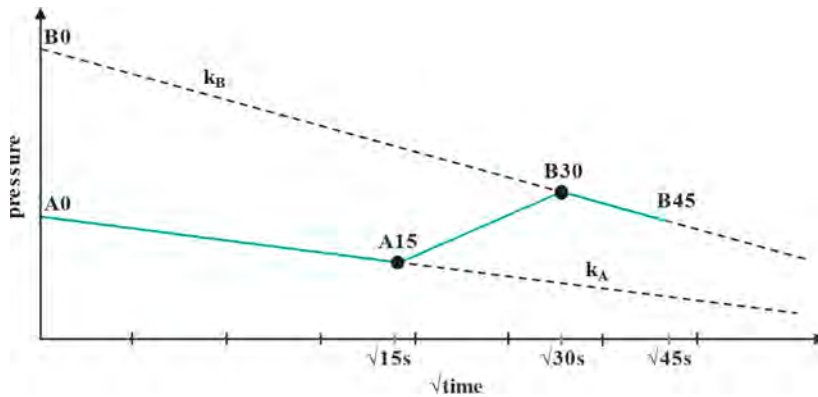


Figure 2. Schematic decrease of DMT readings with the root of time after penetration stop.

2.4 Soil sampling and laboratory testing

Soil specimens were recovered by means of tube sampling (*Rhesi, Lokalbahn Salzburg, water reservoir Raggal*) and block sampling (*Seekirchen*). Sections of highest sample quality were identified based on computer tomography (CT) scans and further used for laboratory testing at Graz University of Technology. Incremental load oedometer tests (IL) and constant rate strain (CRS) oedometer tests were executed on sampled and reconstituted soil specimens according to ISO 17892-5 and ASTM D4186-06, respectively. The soil specimens were loaded from 10 to 960 kPa. Two load steps were considered close to the estimated in-situ effective vertical stress to derive the in-situ constrained modulus (M) (Oberhollenzer 2022).

3 RESULTS

3.1 Characterization of test sites

The ground conditions at the test sites *Rhesi*, *Lokalbahn Salzburg*, *Seekirchen* and *water reservoir Raggal* are described based on DMT-STD. The corrected pressure readings (p_0 , p_1 , p_2), the in-situ pore pressure (u_0) and intermediate parameters (I_D , K_D , E_D , U_D) are shown for individual test sites in Figure 3. In-situ and laboratory investigations are described in more detail in Oberhollenzer (2022).

Test site *Rhesi*, situated in the southeast of lake Constance (47° 28' 03.4924" N/9° 40' 05.4912" E), is composed of three main lithologies (L), namely *L1 silty sand* (0 – 2 m), *L2 sand-silt alternations* (2 – 13 m) and *L3 silty clay* (13 – 25 m). The boundaries between individual layers are indicated by grey, dotted lines in Figure 3 (a-e). The top layer (L1), classified as silt (ML) to silty sand (SM) according to ASTM D2487-17e1, is characterized by a strong variation in I_D ($= 0.2-2$), K_D ($= 5-10$) and E_D ($= 1.5-14$ MPa). The groundwater table was situated 0.8 m below the ground level during test execution. A significant scatter is observed for I_D , E_D , U_D and soil classification (lean clays (CL) to silty, clayey sands (SC-SM) according to ASTM D2487-17e1) within L2. While sections with increased fines-content present high values for U_D , the reverse trend is observed for I_D and E_D . K_D values of around 2 indicate normally consolidated conditions within L2 and L3. Fine-grained deposits within L3 are classified as CL according to ASTM D2487-17e1 and are characterized by $I_D \approx 0.2$, $E_D < 4$ MPa and $U_D \approx 0.7 - 0.8$ (see Figure 3a-e).

Postglacial deposits were investigated in the city of Salzburg at test site *Lokalbahn Salzburg* (47° 48' 58.86" N/13° 2' 42.26" E). Three lithologies, namely *L1 sandy gravel* (0 – 3 m), *L2 sand-silt alternations* (3 – 8.5 m) and *L3 silty clay* (8.5 – 25 m) can be identified based on in-situ and laboratory investigations. As predrilling was required to not damage the membrane, no DMT-STD results are available within L1, classified as silty gravel with sand (GM) based on ASTM D2487-17e1 (see Figure 3f-j). The groundwater table was situated 1.5 m below the ground surface during test execution. Sand-silt alternations (L2) are characterized by a significant scatter of I_D ($= 0.3-4$), K_D ($= 1.5-8$), E_D ($= 2.5-25$ MPa) and U_D ($= 0-0.5$) in Figure 3 (f-j). Soil classifications according to ASTM D2487-17e1 show a clear scatter within L2, ranging from CL to SC. Small material indices ($I_D < 0.2$) and dilatometer moduli ($E_D < 4$) in combination with large pore pressure indices ($U_D \approx 0.6 - 0.8$) were obtained within fine-grained, lacustrine sediments of lithology L3 (CL according to ASTM D2487-17e1).

Test site *Seekirchen* is situated about 2 km south-west of lake Wallersee (47° 53' 27.26" N/13° 7' 29.73" E) and can be subdivided into three lithologies: *L1 silty sand* (0 – 3m), *L2 clay* (3 – 12 m) and *L3 moraine* (12 – 13 m). Alluvial sediments of L1 are heterogeneous with respect to the particle size distribution and lead to a pronounced scatter of DMT-intermediate parameters in Figure 3 (k-n) ($I_D = 0.04 - 1.5$; $K_D = 6 - 15$; $E_D = 0.5 - 14$ MPa). No U_D results are shown in Figure 3 (o) as p_2 was not measured. While I_D and E_D are smaller than 0.1 and 1.5 MPa within L2, respectively, K_D decrease slightly over depth but remains larger than 3. The groundwater table was situated 0.8 m below the ground surface during test execution. Soil specimens - recovered within L2 - were classified as fat clay (CH) according to ASTM D2487-17e1.

Young sediments, characterized by an age smaller than 50 years, were investigated within the *water reservoir Raggal* (47° 13' 11.99" N/9° 50' 27.83" E). In-situ testing and soil sampling were executed from a barge to characterize the sedimentation history within the reservoir (Oberhollenzer et al. 2022). Sand-silt alternations of lithology L1 lead to an erratic distribution of DMT-intermediate parameters ($I_D = 0.4 - 5$, $K_D = 0.5 - 6$, $E_D = 0.5 - 12$ MPa and $U_D = 0 - 0.65$) in Figure 3 (p-t). Fine-grained sections characterized by $I_D < 1.2$ are classified as organic silts (OL, OH) according to ASTM D2487-17e1.

3.2 Determination of in-situ constrained modulus using DMT

Constrained moduli (M) derived from oedometer tests at the estimated in-situ vertical stress are compared with DMT results at the depth of soil sampling. In the first step, the proposed correlation for clays ($I_D < 0.6$, see Eq. (9)) is evaluated based on laboratory results for the test sites *Rhesi*, *Lokalbahn Salzburg*, *Seekirchen* and *water reservoir Raggal*.

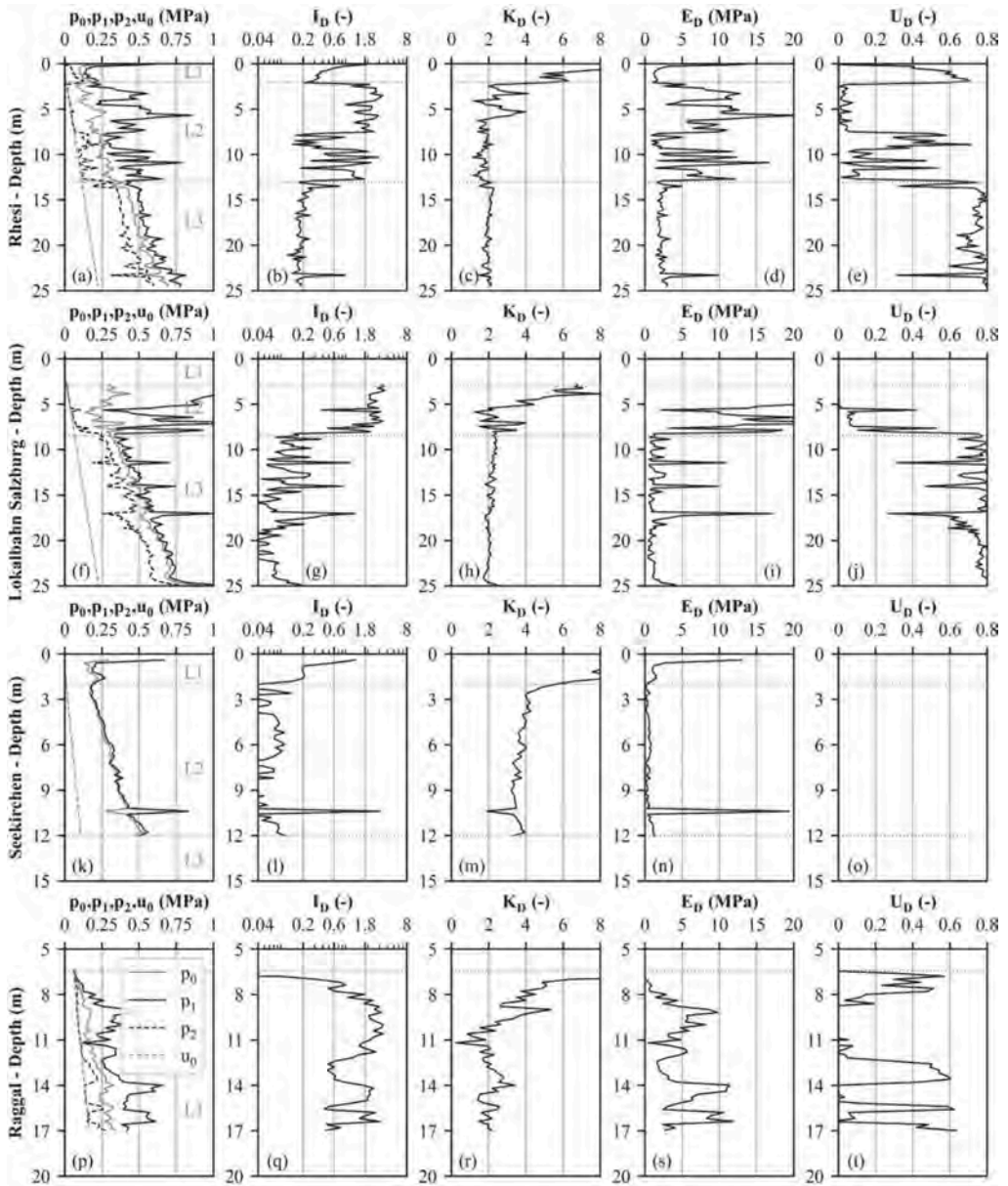


Figure 3. Overview of corrected pressure-readings, in-situ pore water pressure and intermediate parameters at test sites (a-e) Rhesi, (f-j) Lokalbahn Salzburg, (k-o) Seekirchen and (p-t) water reservoir Raggal (the legend for the subplots (a), (f), (k) and (p) is given in Figure 3p).

The constrained modulus (M) derived from oedometer tests, and the dilatometer modulus (E_D) determined at the depth of soil sampling using uncorrected readings (A15, B30) were used according to Eq. (8) to calculate R_M , required to meet the oedometer results (M). The latter R_M values - further declared as $R_{M,required}$ - are compared to I_D and K_D in Figure 4. While individual test sites are indicated by different colors (blue = Rhesi, red = Lokalbahn Salzburg, green = Seekirchen and black = water reservoir Raggal), symbols are used to distinguish between different oedometer testing procedures (see legend of Figure 4). The proposed correlation for deriving R_M in clays (Marchetti, 1980) is indicated by a dashed, grey line in Figure 4a. It is shown that the latter correlation leads to

poor agreement with oedometer results and no clear trend can be derived between K_D and $R_{M,required}$ when using uncorrected DMT readings (A15/B30). A better correlation between oedometer and in-situ results can be observed when comparing $R_{M,required}$ and I_D (see Figure 4b). While the upper and lower bounds of this trend are indicated by grey, dotted lines, the best-fit trend is indicated by a grey, dashed-dotted line. The corresponding (best-fit) function is given by Eq. (12).

$$R_M = 0.6 \cdot I_D^{-0.8} \quad (12)$$

In the second step, DMT-readings corrected about partial drainage (A0/B0) are used in combination with oedometer results to derive $R_{M,required}$ (see Eq. (8)). The latter parameter is compared to I_D and K_D - both calculated based on A0/B0 - in Figure 5.

The data points show a smaller scatter if DMT-readings are corrected about partial drainage. However, the proposed correlation by Marchetti (1980) is still in poor agreement with oedometer results (see Figure 5a). A better trend can be derived between laboratory and in-situ results when using the material index I_D (see Figure 5b). Eq. (13) defines the best-fit trend line which is indicated by a grey, dashed-dotted line in Figure 5b. The upper and lower bounds of the trend line are shown by grey, dotted lines in Figure 5b.

$$R_M = 0.3 \cdot I_D^{-1.1} \quad (13)$$

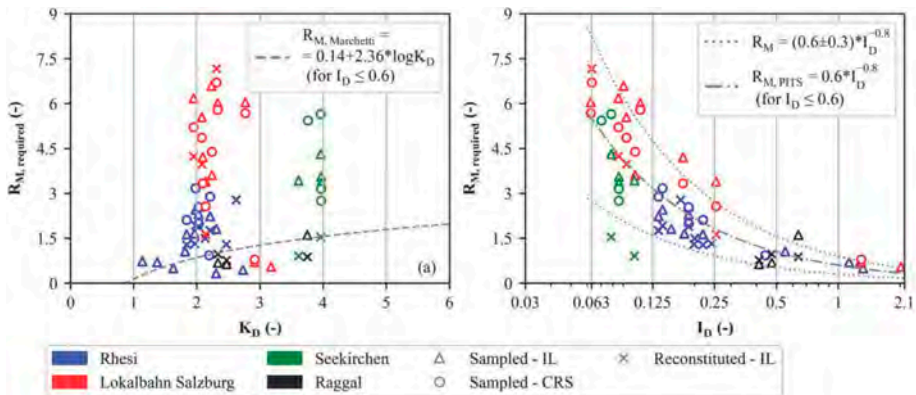


Figure 4. Determination of constrained modulus based on standard DMT-readings (A15/B30): (a) R_M against K_D , (b) R_M against I_D .

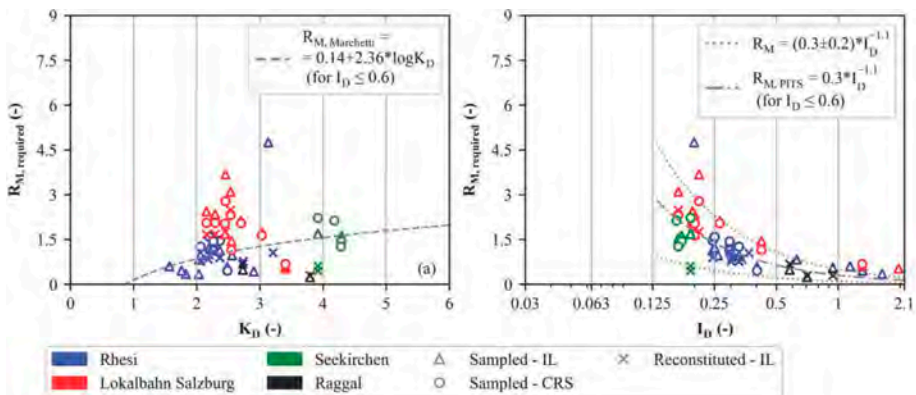


Figure 5. Determination of constrained modulus based on corrected DMT-readings (A0/B0): (a) R_M against K_D , (b) R_M against I_D .

4 CONCLUSION

In-situ and laboratory tests were executed at four test sites (namely *Rhesi*, *Lokalbahn Salzburg*, *Seekri-chen* and *water reservoir Raggal*) within the Alpine region to improve the characterization of postglacial, fine-grained sediments. This article aims to improve the determination of the in-situ constrained modulus (M) using the Medusa flat dilatometer test (DMT). In the first step, high-quality oedometer results were compared to the proposed correlation by Marchetti (1980). Subsequently, new correlations are proposed for the DMT to gain an improved agreement with oedometer tests.

The present results indicate that the correlation proposed by Marchetti (1980) underestimates the in-situ constrained modulus in Alpine sediments, classified as lean to fat clays (ASTM D2487-17e1). The agreement between in-situ and laboratory results can be slightly improved if DMT-readings are corrected about partial drainage. New correlations are elaborated for uncorrected and corrected DMT-readings, leading to a better agreement with oedometer results.

It is recommended to (i) use the revised correlations when deriving the in-situ constrained modulus from DMT in Alpine fine-grained deposits and to (ii) correct DMT-readings about partial drainage effects. The applicability of the revised correlations needs to be validated for other locations based on high-quality laboratory tests.

REFERENCES

- ASTM D2487-17e1. 2017. Practice for Classification of Soils for Engineering Purposes (Unified Soil Classification System). *ASTM International*, West Conshohocken, PA.
- ASTM D4186-06. 2012. Standard Test Method for One-Dimensional Consolidation Properties of Saturated Cohesive Soils Using Controlled-Strain Loading. *ASTM International*, West Conshohocken, PA.
- ISO 22476-1. 2012. Geotechnical investigation and testing — Field testing — Part 1: Electrical cone and piezocone penetration test. *International Organization for Standardization*, Geneva.
- ISO 22476-11. 2017. Geotechnical Investigation and Testing — Field Testing — Part 11: Flat Dilatometer Test. *International Organization for Standardization*, Geneva.
- ISO 17892-5. 2017. Geotechnical investigation and testing — Laboratory testing of soil — Part 5: Incremental loading oedometer test. *International Organization for Standardization*, Geneva.
- Marchetti, S. 1980. In Situ Tests by Flat Dilatometer. *Journal of the Geotechnical Engineering Division* 106, GT3: 299–321.
- Marchetti, S., Monaco P., Totani G. & Calabrese M. 2001. The flat dilatometer test (DMT) In Soil Investigations - a Report by the ISSMGE Committee TC16." In *2nd International Conference on the Flat Dilatometer*, 7–48.
- Marchetti, S. & Monaco P. 2018. Recent Improvements in the Use, Interpretation, and Applications of DMT and SDMT in Practice. *Geotechnical Testing Journal* 41 (5): 20170386.
- Oberhollenzer, S. 2022. Characterization of postglacial, fine-grained sediments by means of in-situ and laboratory testing. *Dissertation*, Institute of Soil Mechanics, Foundation Engineering and Computational Geotechnics, Graz University of Technology.
- Oberhollenzer, S., Hauser, L. 2022. Research project PITS – Parameter identification using in-situ tests in silty soils. *Final report*, Institute of Soil Mechanics, Foundation Engineering and Computational Geotechnics, Graz University of Technology.
- Oberhollenzer, S., Hauser, H., Brand, F., Marte, R. & Schweiger, H.F. 2022. Characterization of young sediments using CPTu and Medusa SDMT. In *Cone Penetration Testing 2022 (CPT22)*: 617–622.
- Oberhollenzer, S., Hauser, H., Brand, F., Marte, R., Tschuchnigg, F., Schweiger, H.F. & Marchetti, D. 2023. Characterization of Partial Drainage during Medusa Flat Dilatometer Testing. *Geotechnical Testing Journal* 46 (5): 731–750.
- Schnaid, F. 2009. In Situ Testing in Geomechanics - the Main Tests. *Taylor & Francis Group*, London.
- Schnaid, F., Belloli, M.V.A., Odebrecht, E. & Marchetti, D. 2018. Interpretation of the DMT in Silts." *Geotechnical Testing Journal* 41 (5): 20170374.
- van Husen, D. 1979. Verbreitung, Ursachen und Füllung glazial übertiefer Talabschnitte an Beispielen in den Ostalpen. *Eiszeitalter und Gegenwart* 29: 9–22.

Mechanical strength and resistivity characteristics of activated MgO-carbonated cured Zn²⁺ contaminated soils

Y. Song, S. Ding, S.S. Dong, W. Liu & Y.L. Chen

School of Civil Engineering, Guilin University of Technology, Guilin, China

Key Laboratory of Karst Dynamics, MNR & Guangxi, Institute of Karst Geology, CAGS, Guilin

J.Q. Liu

Nanning Institute of Technology, Guilin, China

ABSTRACT: With the accelerated urbanization process in China, the reuse of sites contaminated with heavy metals is receiving increasing attention. In this study, the technique of carbonation solidification using active MgO was applied to the stabilization of Zn²⁺-contaminated red clay in the Guilin region. Synchronous tests of unconfined compressive strength and electrical resistivity were conducted to investigate the solidification effect of the polluted soil using active MgO carbonation. The results showed that the unconfined compressive strength of the solidified soil increased with the increase in contamination concentration. However, it exhibited a decreasing trend with the increase in the content of active MgO. Moreover, the strength first increased and then decreased with the extension of carbonation time. The addition of active MgO resulted in strength enhancement ranging from 100% to 349.07%. It was observed that there exists a basic linear relationship between the unconfined compressive strength and electrical resistivity of the polluted soil under three different influencing factors. Furthermore, a set of equations for predicting the strength characteristics of polluted soil based on electrical resistivity was proposed. The use of electrical resistivity proves to be effective for evaluating the mechanical strength properties of heavy metal-contaminated soil.

Keywords: Active MgO, CO₂ carbonation, heavy metal-contaminated soil, prediction model.

1 INTRODUCTION

As a kind of regional special clay, red clay is widely distributed in Yunnan, Guizhou, and Guangdong. The contradictory phenomenon of better engineering mechanical properties (high strength, low compressibility) and poor physical property indexes (high porosity ratio, high water content, high liquid-plastic limit and plasticity index) of red clay in engineering has been widely concerned by scholars at home and abroad (Song,2015 and Zhang,2017). Guangxi Zhuang Autonomous Region is a province rich in non-ferrous metal resources in China. In recent years, the rapid development of the mining and metallurgical industry has resulted in significant soil pollution due to outdated technology, long-term improper mining methods, and improper management, leading to a large number of heavy metal ions in the surrounding water bodies and serious soil contamination (Cheng,2014 and Zhang,2014).

The carbonation solidification of Zn²⁺-contaminated soil using active MgO has become a new type of soil remediation technology, and its mechanical strength and electrical resistivity characteristics have become important research topics of wide concern. The MgO carbonation solidification technology is a pollution soil treatment method based on adsorption and dissolution, known for its high efficiency, low cost, and long-lasting treatment effect. The

Carbonised Mixed Pile technology proposed by Yi Yaolin has been proven to be feasible after indoor tests, which demonstrated that the physical and mechanical properties of the soil were improved after the carbonization treatment (Yi,2013). Li et al. carried out carbonation curing of contaminated soil by MgO and found that MgO carbonation had a good curing effect on Pb^{2+} , Zn^{2+} , Mn, and Cd^{2+} contaminated soil, and the strength of Zn^{2+} curing was significantly higher than that of cement curing (Li,2019 and 2021). Wang Q et al. found through tests that when the concentration of heavy metals (Ni, Cu) increased, the effect of carbonization on the unconfined compressive strength of the specimens was more significant with the increase of carbonization time (Wang,2022). Li et al. found that the higher the reactive MgO content, the higher the unconfined compressive strength and that carbonation contributed more to the strength in the initial period than in the later period (Li,2023). Liang Tong et al. used cement-cured lead-contaminated soil for carbonation tests and found that the strength of the soil had a good power function relationship with porosity after carbonation treatment (Tong,2022). Li M et al. found that steel slag and desulfurization gypsum, as green stabilizers for soil stabilization, improved UCS through carbonation solidification and significantly shortened the solidification time (Li,2021). Zhong Yuqing found that when carbonation was performed on contaminated soil with different proportions of GGBS-active MgO, the unconfined compressive strength of the solidified soil significantly increased when the MgO proportion exceeded 50%(Zhong,2022). Moreover, electrical resistivity is also an important parameter reflecting soil structure characteristics and pollution levels (Yoon,2001, Kibria 2014, Tang,2018 and Lv,2021). Zha F proposed a set of equations for successfully predicting the geotechnical properties of contaminated soil using pore fluid resistivity, and the use of pore fluid resistivity can more effectively predict these effects (Zha,2021).

The active MgO carbonation solidification technology has become an effective method for the remediation of soil contaminated with a large number of heavy metal pollutants. However, a deep understanding of its soil mechanical strength and electrical resistivity characteristics and their influencing factors is crucial for the rational use and effective management of this technology. This study aims to systematically investigate the mechanical strength and electrical resistivity characteristics of active MgO carbonation-solidified Zn^{2+} -contaminated soil and its influencing factors, providing an important theoretical basis and experimental data for future soil remediation technology for contaminated soil.

2 MATERIALS AND METHODS

2.1 Test material

The red clay used in this experiment was sourced from the Yanshan District of Guilin City, Guangxi Zhuang Autonomous Region. It was collected at a depth ranging from 3 to 5 meters and appeared brownish-red in color. Basic geotechnical tests were conducted to obtain the fundamental physical properties of the red clay, as shown in Table 1.

Table 1. Basic physical indicators of Guilin red clay.

Optimum moisture content $\omega/\%$	Maximum dry density $\rho_d/\text{g}\cdot\text{cm}^{-3}$	Specific gravity G_s	Liquid limit $W_L/\%$	Plastic limit $W_P/\%$	Plasticity Index I_P
30.00	1.49	2.73	57.95	31.22	26.73

Based on the geochemical evaluation report of land quality in Guilin City, the set concentrations (i_c) of Zn^{2+} pollution are 0.05%, 0.1%, 0.5%, and 1%, respectively. The heavy metal studied in this experiment is zinc ion. Nitrate ions have good solubility and strong cation activity, making them rapidly soluble in water. Therefore, zinc nitrate ($Zn(NO_3)_2\cdot 6H_2O$) of analytical grade produced by Xilong Scientific Co., Ltd. was used as the indoor pollution source in this study. The experiment employed Magnesium Oxide (MgO) as the solidifying

agent, and the selected MgO used was produced by Hebei Xingtai Magnesium God Chemical Co., Ltd. The MgO content is 93.2%, classified as high-activity Magnesium Oxide.

2.2 Experimental program

This paper selects three different influencing factors, namely, MgO content, carbonation time, and pollution concentration, to study the solidification effect and pattern of Guilin red clay under MgO carbonation. The specific experimental design is presented in Table 2.

According to existing research, the variation in carbonated soil strength is influenced by different factors. The active MgO content is set at 2.5%, 5%, 7.5%, and 10%. Carbonation times of 0.5 h, 1 h, 3 h, 6 h, and 12h are chosen based on the permeability differences among various soil samples. During the experiments, the gas pressure inside the carbonation tank is set at 200 kPa, as it has been found that the physical and chemical properties of the solidified soil are optimized under this pressure condition(Liu,2017).

Table 2. Pilot programme.

MgO doping/% M_c	Carbonation time/h t_h	Zinc ion concentration/% i_c	Water content/%	Gas pressure/kPa
2.5	0.5	0.05		
5	1	0.1	30	200
7.5	3	0.5		
	6			
10	12	1		

2.3 Test methodology

In this test, the static pressure method was used for sample preparation. A predetermined volume of zinc nitrate-contaminated solution is thoroughly mixed with the air-dried red clay until its moisture content reaches the optimal moisture content of the original soil (30%). Three identical samples were also prepared under the same conditions to ensure the reproducibility of sample preparation and test results. The sample is placed in a sealed plexiglass bottle for accelerated carbonization. The carbon dioxide used to accelerate carbonization is 99.9% pure and was purchased from Liuzhou Huao Gas Co., Ltd., China.

3 RESULTS AND DISCUSSION

3.1 Unconfined compressive strength and resistivity-strain curve of carbonized soil under the influence of pollution concentration

Figure 1 shows the variation of unconfined compressive strength under different initial contamination conditions. It can be seen that the unconfined compressive strength of the specimens decreases with the increase of the pollution concentration at different carbonation times. The highest unconfined compressive strength was observed when the concentration of Zn^{2+} was low, which was since Zn^{2+} was less in the soil at low concentration and was easily adsorbed by the minerals and active MgO of red clay. The hydration of active MgO to generate $Mg(OH)_2$ during carbonation will encapsulate part of the Zn^{2+} inside, which will better block the damage of Zn^{2+} to the soil particle cement. With the increase of pollution concentration, the Zn^{2+} adsorbed by activated MgO has been saturated, so that the free Zn^{2+} began to destroy the internal cementing material of the soil, resulting in a gradual decrease in the strength of the carbonated polluted red clay.

Figure 2 shows the variation curve of electrical resistivity for polluted soil with different Zn^{2+} concentrations under the conditions of 10% active MgO content and 1-hour carbonation. From Figure 2, it can be observed that the electrical resistivity variation patterns for

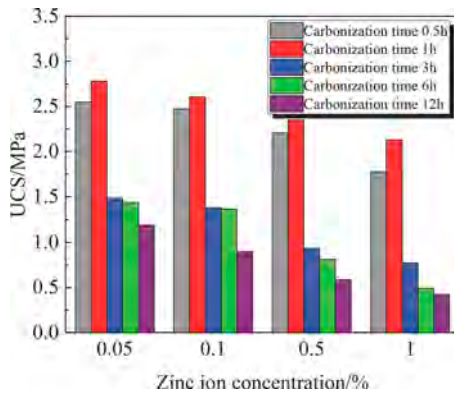


Figure 1. Effect of Zn^{2+} concentration on unconfined compressive strength.

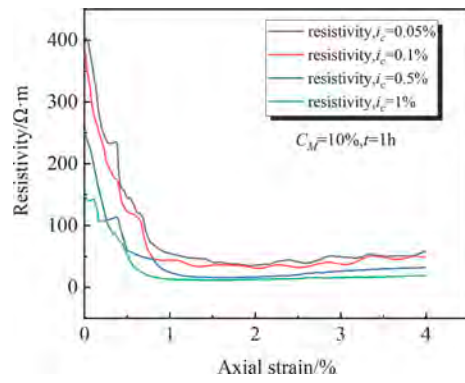


Figure 2. Resistivity-strain curves at different Zn^{2+} concentrations.

polluted soil with different Zn^{2+} concentrations are generally consistent. The curves exhibit a rapid decline, followed by a gradual decrease to a trough, and finally maintain a stable or slow increase. As the Zn^{2+} concentration increases, both the initial resistivity and the failure resistivity of the samples decrease. When the Zn^{2+} concentration reaches 1%, the decrease in resistivity is most pronounced. This is because the increased Zn^{2+} content leads to a greater number of particles in contact and ions in the pore fluid, thereby enhancing the conductivity.

3.2 Unconfined compressive strength and resistivity-strain curves of carbonated soils under the influence of MgO dosing

Figure 3 shows the relationship between the unconfined compressive strength of Zn^{2+} contaminated soil with different active MgO dosing and carbonation times. The results show that the unconfined compressive strength of carbonized contaminated soil with different active MgO treatments varies greatly with the active MgO dosing and carbonation time. When the carbonation time was less than 1h, the unconfined compressive strength of the specimens showed an obvious upward trend with the increase of active MgO dosing. When the active MgO dosing increased from 2.5% to 10%, the unconfined compressive strength of the specimen was enhanced by 345.86%, 345.54%, 100.21%, 270.77%, and 348.37%, respectively. The incorporation of the increase in the dosing of MgO can improve the curing efficiency of Zn^{2+} because MgO is a good adsorbent with a large specific surface area, adsorbable and a wide range of applications.

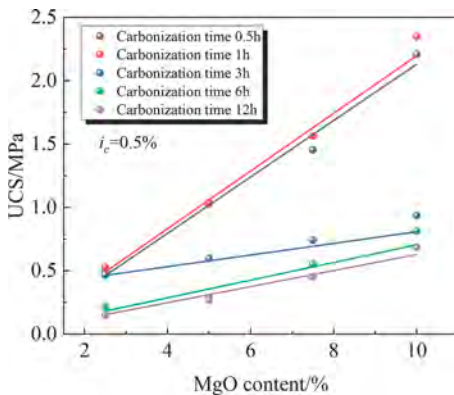


Figure 3. Effect of active MgO dosing on unconfined compressive strength.

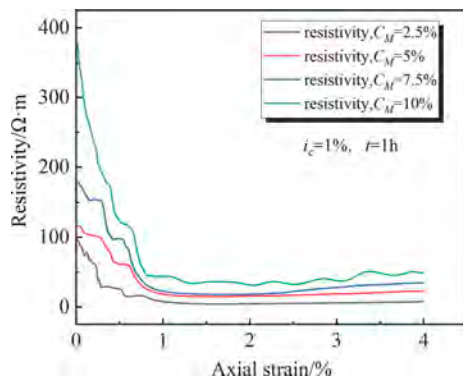


Figure 4. Resistivity-strain curves at different MgO doping levels.

Figure 4 depicts the electrical resistivity-strain variation curves for carbonation-solidified zinc ion-polluted red clay with different levels of active MgO under the conditions of 0.5% Zn^{2+} concentration and 1-hour carbonation. From the graph, it can be observed that the electrical resistivity of the solidified soil with different active MgO contents rapidly decreases until reaching a minimum point, and then stabilizes or slightly increases.

When the active MgO content increases from 2.5% to 5%, the average rate of increase in initial resistivity is 21.67%. As the active MgO content increases from 5% to 7.5%, the average rate of increase in initial resistivity is 51.47%. Similarly, when the active MgO content increases from 7.5% to 10%, the average rate of increase in initial resistivity is 111.65%. This significant increase in initial resistivity indicates that the carbonation solidification process with active MgO has a noticeable improvement effect on the resistivity characteristics of the solidified polluted soil. The carbonation products can fill the pores of the soil and improve the internal structure of the soil.

3.3 Unconfined compressive strength and resistivity-strain curves of carbonized soils under the influence of carbonation time

Figure 5 demonstrates the graph of the variation of the unconfined compressive strength of activated MgO carbonation-cured zinc-ion contaminated red clay with carbonation time, and to prove the similarity of the change rule, the change points under different MgO doping were chosen to be represented. From the graph, it can be observed that the compressive strength of the specimen is positively correlated with the carbonation time in the shorter carbonation time (0.5h, 1h). The maximum values were 0.844 MPa, 1.448 MPa, 2.23 MPa and 3.593 MPa at 1h of carbonization, respectively; when the time of CO_2 gas introduction continued to increase up to 12h, the strength of the specimens first decreased steeply and then leveled off. This shows that the activated MgO-cured contaminated red clay can obtain rapid strength growth (slightly higher than the compressive strength of cement-cured red clay cured at the same dosage for 90 days (Yoon,2001).) in a relatively short carbonation time. Whereas, longer carbonation time leads to loss of strength, which greatly improves the efficiency of the project.

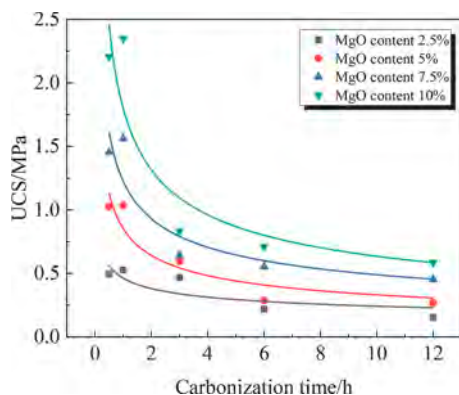


Figure 5. Effect of carbonation time on unconfined compressive strength.

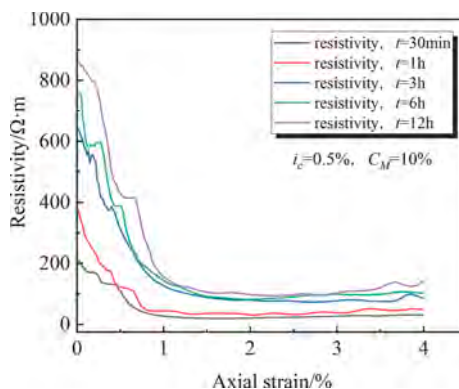


Figure 6. Resistivity-strain curves at different carbonation times.

Figure 6 reflects the resistivity-strain curves of carbonation-cured contaminated red clay at different carbonation times under the conditions of 0.5% Zn^{2+} concentration and 10% active MgO doping. From the figure, it can be seen that the resistivity of the specimens under the conditions of different carbonation times maintains a similar regularity with that of the specimens under the conditions of different active MgO doping. To analyze the reason, the prolongation of carbonation time causes specimen swelling and crack development, which together lead to the blockage of the conductive contact surface, and the transmission of current in the specimen is hindered, which in turn leads to a continuous increase in the resistivity of the specimen.

3.4 Relationship between unconfined compressive strength and resistivity under the influence of pollution concentration

Resistivity and unconfined compressive strength are two inherent properties of soil. Based on the experimental results of unconfined compressive strength and resistivity mentioned earlier, a correlation analysis was conducted, and evaluation models were derived under different influencing factors. It was found that pollution concentration, the dosage of active MgO, and carbonation time significantly affect the resistivity of polluted soil and exhibit consistent patterns.

Figure 7 illustrates the relationship between sample strength and resistivity under different pollution concentrations, including the fitted equations provided in Tables 3, 4, and 5. These fitted equations can be used to predict the relationship between resistivity and the unconfined compressive strength of the soil. It can be observed that there is a positive linear correlation between the strength and resistivity of samples at different pollution concentrations. As the resistivity increases, the strength of the samples also increases. The correlation coefficients of the fitted relationships range from 0.759 to 0.941.

Table 3. Relationship between resistivity and unconfined compressive strength at Zn^{2+} concentration.

Carbonation time (h)	Fitting parameters		Fitting formula	Correlation coefficient
	a	b		
0.5	0.031	1.290	$q_u = 0.031\rho + 1.290$	0.903
1	0.034	1.744	$q_u = 0.034\rho + 1.744$	0.886
3	0.012	0.530	$q_u = 0.012\rho + 0.530$	0.759
6	0.018	-0.187	$q_u = 0.018\rho - 0.187$	0.941
12	0.010	-0.044	$q_u = 0.010\rho - 0.044$	0.929

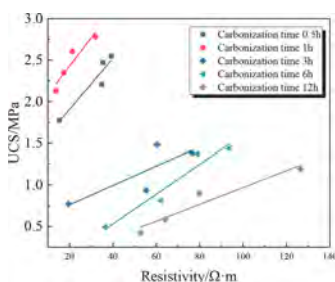


Figure 7. Relationship between resistivity and unconfined compressive strength at Zn^{2+} concentration.

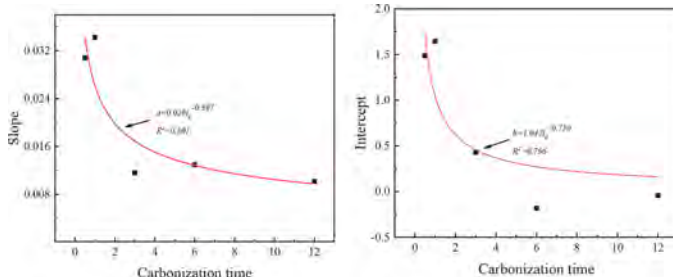


Figure 8. Fitting parameters versus carbonation time.

$$a = 0.026t_c^{-0.397} (R^2 = 0.801) \quad (1)$$

$$b = 1.042t_c^{-0.750} (R^2 = 0.766) \quad (2)$$

$$q_u = 0.026t_c^{-0.397} \rho - 1.042t_c^{-0.750} \quad (3)$$

where q_u = unconfined compressive strength (MPa); ρ = resistivity of the specimen ($\Omega\cdot m$); and t_c = carbonation time (h).

3.5 Relationship between unconfined compressive strength and resistivity under the influence of MgO dosing

The relationship between sample strength and resistivity under different dosages of active MgO is shown in Figure 9. From these graphs, it can be observed that there is also a positive

linear correlation between the strength and resistivity of samples under different dosages of active MgO. As the resistivity increases, the strength of the samples also increases. The correlation coefficients of the fitted relationships range from 0.765 to 0.954.

Table 4. Relationship between resistivity and unconfined compressive strength at active MgO doping.

Carbonation time (h)	Fitting parameters		Fitting formula	Correlation coefficient R^2
	a	b		
0.5	0.075	-0.367	$q_u = 0.075\rho - 0.367$	0.949
1	0.066	-0.328	$q_u = 0.066\rho - 0.328$	0.954
3	0.011	0.182	$q_u = 0.011\rho + 0.182$	0.854
6	0.011	0.021	$q_u = 0.011\rho + 0.021$	0.789
12	0.009	-0.043	$q_u = 0.09\rho - 0.043$	0.765

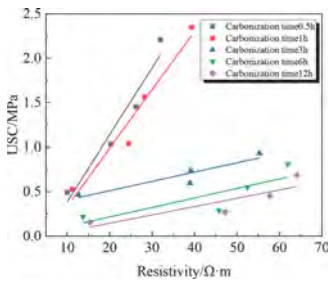
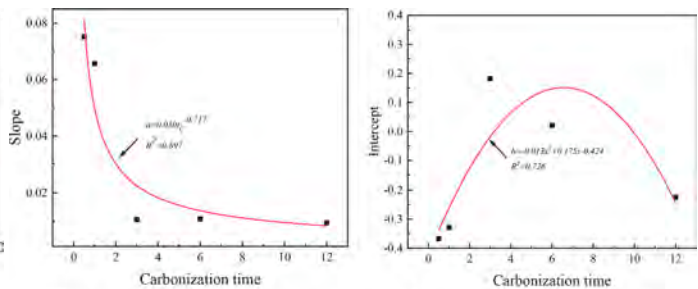


Figure 9. Relationship between resistivity and unconfined compressive strength at active MgO doping.



(a) Slope a versus carbonation time (b) Intercept b versus carbonation time

Figure 10. Fitting parameters versus carbonation time.

$$a = 0.050t_c^{-0.717} (R^2 = 0.897) \quad (4)$$

$$b = 0.0131t_c - 0.424 (R^2 = 0.726) \quad (5)$$

$$q_u = 0.050t_c^{-0.717}p - (0.013t_c^2 + 0.175t_c - 0.424) \quad (6)$$

3.6 Relationship between unconfined compressive strength and resistivity as affected by carbonation time

The relationship between sample strength and resistivity under different carbonization times is shown in Figure 11. It can be observed that there is a stronger correlation between resistivity and carbonization time. Under different carbonization times, there is a negative linear correlation between the strength and resistivity of the samples. As the resistivity increases, the strength of the samples decreases under different dosages of active MgO. The correlation coefficients of the fitted relationships range from 0.810 to 0.974.

Table 5. Relationship between resistivity and unconfined compressive strength at carbonation time.

Carbonation time (h)	Fitting parameters		Fitting formula	Correlation coefficient R^2
	a	b		
0.5	-0.075	1.317	$q_u = -0.075\rho + 1.317$	0.810
1	-0.030	1.711	$q_u = -0.030\rho + 1.711$	0.974
3	-0.035	2.343	$q_u = -0.035\rho + 2.343$	0.847
6	-0.058	4.287	$q_u = -0.058\rho + 4.287$	0.925

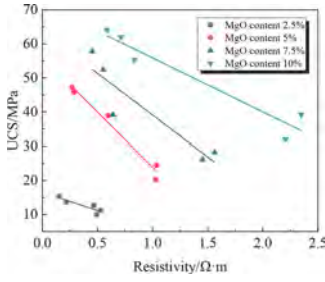
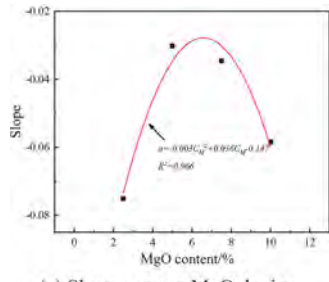
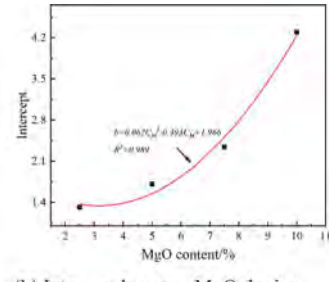


Figure 11. Relationship between resistivity and unconfined compressive strength at carbonation time.



(a) Slope a versus MgO doping



(b) Intercept b versus MgO doping

Figure 12. Fitting parameters versus active MgO doping.

$$a = -0.003C_M^2 + 0.036C_M - 0.147(R^2 = 0.966) \quad (7)$$

$$b = 0.062C_M - 0.393C_M + 1.966(R^2 = 0.989) \quad (8)$$

$$q_u = (-0.003C_M^2 + 0.036C_M - 0.147)p - (0.062C_M^2 - 0.393C_M + 1.966) \quad (9)$$

4 CONCLUSION

1. The unconfined compressive strength of the samples shows a linear increase with the increase in the content of active MgO. With the continuous carbonation time, the overall strength of the samples initially decreases rapidly and then levels off, but when the carbonation time reaches 1 hour, the strength of the samples reaches its maximum value. The influence of Zn^{2+} concentration on the sample strength follows a trend of first increasing and then decreasing, with the maximum strength of the samples observed at a Zn^{2+} concentration of 0.05%.
2. Under different initial conditions, the synchronous variation curves of the electrical resistivity-strain of the samples exhibit a similar trend, presenting a concave-down shape. With longer carbonation time, the minimum point of the electrical resistivity-strain curve increases. The Zn^{2+} concentration causes the wave valley point of the electrical resistivity-strain curve to shift downwards.
3. By comparing the strength and electrical resistivity, it can be observed that there is a linear fit relationship between strength and electrical resistivity under different initial conditions. Except for carbonation time, all other conditions show a positive correlation, and the fitting relationship is quite good. Thus, the electrical resistivity method can be used to evaluate the strength characteristics of carbonated polluted red clay.

REFERENCES

Song, Y., Gao, L., Chen, X., Li, J. 2015 Characteristics of Microstructure and Deformation Mechanism of Red Clay. Geological Hazards and Environmental Protection.

Zhang, Y., Zuo, S., Ji, Y. 2017. Mechanical Property Test Research of Red Clay in Natural and Reshaped States. Chinese Journal of Underground Space and Engineering.

Cheng, F. 2014. Mechanical Properties and Solidification Mechanism of Rock-Soil under Heavy Metal Invasion. Ph.D. Dissertation, Central South University.

Zhang, L., Mo, Z., Qin, J., Chen, Z., Xiong, Y., Wei, Y., Zhang, Z., Zou, Y. 2014. Heavy Metal Pollution in Downstream Rural Soils of the Large Factory Mining Area in Guangxi and Health Risk Assessment for Children. Journal of Environment and Health.

- Yi, Y. 2013. New Technologies and Theories of Stirring Pile Series Based on Sustainable Development. Ph.D. Dissertation, Southeast University.
- Li, W., Yi, Y. 2019. Stabilization/Solidification of Lead- and Zinc-Contaminated Soils Using MgO and CO₂. *Journal of CO₂ Utilization*.
- Li, W., Qin, J., Yi, Y. 2021. Carbonating MgO for Treatment of Manganese- and Cadmium-Contaminated Soils. *Chemosphere*.
- Wang, Q., Guo, X., Li, M., Yang, J., Cui, J., Zhou, W. 2022. Study on Mechanical and Microscopic Properties of Nickel–Copper-Contaminated Soil Solidified by Cement, Fly Ash, and Desulfurization Gypsum Under Carbonization Condition. *Transportation Research Record*.
- Li, M., Cai, G., Wang, Q., et al. 2023. The State of the Art of Carbonation Technology in Geotechnical Engineering: A Comprehensive Review. *Renewable and Sustainable Energy Reviews*.
- Tong, L., Cao, Z., Yang, F. 2022 Influence of Carbonation on Strength Characteristics and Microstructure of Solidified Lead-Contaminated Soil. *Journal of Civil Engineering and Environmental Engineering*.
- Li, M., Wang, Q., Yang, J., et al. 2021. Strength and Mechanism of Carbonated Solidified Clay with Steel Slag Curing Agent. *KSCE Journal of Civil Engineering*.
- Zhong, Y., Cai, G., Wang, J., et al. 2021. Experimental Study on Strength and Conductivity Characteristics of GGBS-Activated MgO Carbonation/Stabilization Zinc-Contaminated Soil. *Chinese Journal of Geotechnical Engineering*.
- Yoon, G. L., Park, J. B. 2001. Sensitivity of Leachate and Fine Contents on Electrical Resistivity Variations of Sandy Soils. *Journal of Hazardous Materials*.
- Kibria, G., Hossain, S., Alam, Z. A Statistical Model Based on Experimental Results: Correlating Electrical Resistivity with Geotechnical Properties of Clayey Soils. In: *Transportation Research Board 93rd Annual Meeting (No 14-1722)*.
- Tang, C. S., Wang, D. Y., Zhu, C., et al. 2018. Characterizing Drying-Induced Clayey Soil Desiccation Cracking Process Using Electrical Resistivity Method. *Applied Clay Science*.
- Liu, S. Y., Du, Y. J., Chen, L., et al. 2010. Application of Electrical Resistivity for Cement Solidified/Stabilized Heavy Metal Contaminated Soils. In: *Advances in Environmental Geotechnics: Proceedings of the International Symposium on Geoenvironmental Engineering in Hangzhou, China, September 8–10, 2009*. Springer Berlin Heidelberg.
- Lv, M., Cao, Z., Zhang, D. 2021 Evaluation Method for Carbonation Depth of Cement Solidified Heavy Metal Contaminated Soil Based on Electrical Resistivity. *Journal of Central South University (Science and Technology)*.
- Zha, F., Zhu, F., Xu, L., et al. 2021. Laboratory Study of Strength, Leaching, and Electrical Resistivity Characteristics of Heavy-Metal Contaminated Soil. *Environmental Earth Sciences*.
- Liu, S. Y., Cai, G., Du, G. Y., Wang, L. 2017. Model Test Research on Carbonated Stirring Pile with Active Magnesium Oxide. *Chinese Journal of Geotechnical Engineering*.

Permeability and strength of sand-bentonite mixture stabilized by different binders for construction of two-phase cut-off walls

M.Z.Y. Ting, Y.Y. Tan, M. Widjaja & Y. Yi*

School of Civil and Environmental Engineering, Nanyang Technological University, Singapore

ABSTRACT: Soil-bentonite-binder cut-off walls have gained popularity as an effective solution for controlling groundwater flow during deep excavation, especially in porous sandy soil. In two-phase cut-off wall construction, the incorporation of binder during the second phase can significantly influence the workability and cause bleeding. The use of reactive magnesia (MgO)-activated ground granulated blast-furnace (GGBS) has been shown to control excessive bleeding. However, the engineering properties of the hardened stabilized sand-bentonite mixtures, particularly in two-phase construction, have not been assessed. In this study, the permeability and strength of various sand-bentonite-binder mixtures were evaluated using flexible wall permeability and unconfined compressive strength (UCS) tests, respectively. The effectiveness of MgO-GGBS was compared with other binder types including ordinary Portland cement (OPC) and quicklime (CaO)-activated GGBS. The result showed that the UCS of MgO-GGBS stabilized soil was 2 to 4 times greater than that of OPC stabilized soil and comparable to that of CaO-GGBS stabilized soil. The hydraulic conductivity of all MgO-GGBS mixtures was well below the permeability requirement of 10^{-9} m/s for seepage cut-off wall, but OPC mixtures had much higher permeability that did not meet the requirement. The hydration products of MgO-GGBS mixture were identified as calcium silicate hydrate, hydrotalcite-like phases, and ettringite, which bonded the soil particles and contributed to the strength and impermeability of cut-off walls. This work highlights the potential application of an effective binder of MgO-GGBS in stabilizing sand-bentonite mixtures for two-phase seepage cut-off walls.

1 INTRODUCTION

Sandy soil has a high permeability ranging from 10^{-3} m/s to 10^{-6} m/s, resulting in high groundwater flow in deep excavation during the construction of structures such as dams and dikes (Elhakim, 2016). Low permeability hydraulic barriers, such as seepage cut-off walls, can therefore be used to minimize the groundwater flow. The seepage cut-off walls are often constructed using a mixture of in-situ sandy soil, bentonite, and cementitious binder that requires low permeability and satisfactory strength. Bentonite is used as a sealing material to reduce the permeability of sandy soil, and binder is incorporated to stabilize the soil mixture.

Trench remixing and deep wall (TRD) method is one of the most recommended cut-off wall construction techniques, particularly in deep depth conditions, due to its benefit to produce homogenous soil mixture (Evans, 2007, Jiang et al., 2020). The TRD method can be executed in two phases. The first phase involves injecting and mixing of bentonite slurry with in-situ soil, while the second phase involves blending cementitious binder with the soil-bentonite mixture. However, in the two-phase construction, the incorporation of binder, in particular ordinary Portland cement (OPC), during the second phase can degrade the properties of bentonite (Cheng et al., 2022, Koch, 2002). The hydration of OPC releases abundant Ca^{2+} ions, which triggers cation exchange reactions with bentonite, reducing its water retention capability. The

*Corresponding author, [yiyalin@ntu.edu.sg](mailto:yiyaolin@ntu.edu.sg)

degradation of bentonite by OPC increases the flowability and bleeding of soil mixture, lowering the soil homogeneity and hence adversely affecting the permeability of seepage cut-off wall. Furthermore, OPC is shown to be less efficient in soil stabilization compared to that in cementitious paste (Li et al., 2022), which may affect the hardened properties of soil mixtures. Therefore, it is essential to look for more effective binders to replace OPC.

Some studies (Yu et al., 2021, Sharma and Sivapullaiah, 2017) indicate that using ground granulated blast-furnace slag (GGBS) binders can alleviate the cation exchange effect on bentonite due to a lower calcium component and hydration rate than OPC. Ting and Yi (2023) further demonstrates that using a reactive magnesia (MgO) activated-GGBS binder is capable of minimizing cation exchange of bentonite, hence preventing increase in workability and excessive bleeding of seepage cut-off walls. A few research have also used MgO-GGBS in stabilizing soil mixtures for cut-off walls (Wu et al., 2019, Wu et al., 2021), and the findings reveal that the MgO-GGBS stabilized soil mixtures could fulfill the permeability requirement ($<10^{-9}$ m/s). However, these studies focus on the one-phase cut-off wall. In two-phase cut-off walls, the interactions between bentonite and binder are more complicated. Although the workability of two-phase cut-off walls can be controlled using MgO-GGBS, the hardened properties, particularly the permeability and strength of the MgO-stabilized soil mixture, have not been investigated.

Therefore, the aim of this study is to investigate the hardened-state properties of sand-bentonite mixture stabilized by MgO-GGBS in two-phase cut-off wall construction. Several laboratory tests have been conducted on the sand-bentonite-binder mixtures, including permeability, unconfined compressive strength (UCS), X-ray diffraction (XRD), and scanning electron microscope with energy dispersive X-ray (SEM-EDX) tests.

2 METHODOLOGY

2.1 Materials

The raw materials used in this work included fine sand, two types of bentonite, and four types of cementitious materials. Table 1 shows some fundamental physical and chemical properties of fine sand and bentonites. The fine sand had a specific gravity of 2.67 and a mean particle size of 0.37 mm. Sodium bentonite (Na-B) and calcium bentonite (Ca-B) are fine clayey soil with mean particle sizes of 0.022 mm and 0.014 mm, respectively. The sodium bentonite had exchangeable Na^+ of 53.14 cmol/kg, Ca^{2+} of 19.25 cmol/kg, Mg^{2+} of 0.29 cmol/kg, and K^+ of 0.43 cmol/kg, whereas the calcium bentonite had 43.63 cmol/kg Na^+ , 37.57 cmol/kg Ca^{2+} , 1.02 cmol/kg Mg^{2+} , and 0.75 cmol/kg K^+ .

In the stabilization of sand-bentonite soil mixtures, the cementitious materials used were GGBS, MgO, CaO, and OPC. The chemical compositions of these cementitious materials were determined as shown in Table 2. To activate the binding properties of GGBS, an MgO to GGBS ratio of 1:9 was used (Yi et al., 2014, Yi et al., 2016). The MgO was a high-reactivity

Table 1. Physical and chemical properties of fine sand and calcium bentonite.

Properties	Fine sand	Sodium bentonite	Calcium bentonite
Specific gravity	2.67	2.69	2.71
Mean particle size (mm)	0.37	0.022	0.014
Liquid limit (%)	-	407	247
Plastic limit (%)	-	58	43
Swelling index (mL/2g)	-	24	17
Exchangeable cations (cmol/kg)			
Na^+	-	53.14	43.63
K^+	-	0.43	0.75
Ca^{2+}	-	19.25	37.57
Mg^{2+}	-	0.29	1.02

MgO with reactivity of 21 s, as determined by the citric acid test in accordance with CFMIS (2006). To compare the stabilizing efficacy of MgO-GGBS, another two binders of CaO-GGBS and OPC were employed.

Table 2. Chemical compositions of cementitious materials.

Components	GGBS (%)	MgO (%)	CaO (%)	OPC (%)
CaO	54.73	0.04	98.77	70.21
SiO ₂	27.29	0.02	0.09	15.63
Al ₂ O ₃	11.92	0.02	0.06	4.83
Fe ₂ O ₃	1.01	N.D.	0.05	3.16
MgO	1.71	99.81	0.92	1.69
K ₂ O	0.39	N.D.	N.D.	0.68
SO ₃	1.55	0.07	N.D.	3
MnO	0.24	N.D.	0.02	N.D.

N.D. = Not detected.

2.2 Specimen preparation

Soil specimens were prepared using a two-phase TRD cut-off wall construction method (Cheng et al., 2022, Evans and Garbin, 2009). In phase one, sand and bentonite were first dry-mixed for 5 min, followed by mixing with distilled water for another 5 min. In phase two, a binder slurry prepared with a water/binder ratio of 1 was added to the sand-bentonite mixtures and mixed for 5 min. Following that, the sand-bentonite-binder mixture was casted into cylindrical molds (50 mm diameter and 100 mm height) in three layers. For each layer, the molds were tapped on the desk 100 times to remove air bubbles. The specimens were cured inside the mold for 28 days in a moist room at a temperature of 26°C. To simulate the in-service condition of a seepage cut-off wall, the specimens were removed from the mold and immersed in freshwater for up to 84 days. Table 3 depicts the proportions (in mass) of sand-bentonite-binder mixture tested in this study.

Table 3. Sand-bentonite-binder mixture proportions (in unit mass).

Mixture	Sand	Bentonite	Water	Binder
Na-B+MgO-GGBS				
Na-B+CaO-GGBS				
Na-B+OPC				
Ca-B+MgO-GGBS	1	0.08	0.5	0.1
Ca-B+CaO-GGBS				
Ca-B+OPC				

2.3 Test methods

To determine the engineering properties of hardened sand-bentonite-binder mixtures, the permeability and strength tests were performed. The permeability of the specimens were determined using a flexible wall permeameter in accordance with the ASTM D5048 standard (ASTM, 2016). The permeability test was conducted on specimens in duplicate at 56 and 112 days. Meanwhile, the UCS of the specimens were determined using a compression machine loaded at 1 mm/min in accordance with the ASTM D1633 standard (ASTM, 2017). The UCS test was conducted on specimens in triplicate at 14, 28, 56 and 112 days. Following the UCS test, the soil specimens were crushed and sieved through a 75- μ m sieve in preparation for microstructural analysis. XRD and SEM-EDX tests were conducted on specimens at 112 days to determine the minerals and hydration products.

3 RESULTS AND DISCUSSION

3.1 Workability

The sand-bentonite-binder mixtures were designed to fulfill the workability requirements, which were studied in the previous work (Ting and Yi, 2023). The flowability and bleeding of freshly stabilized soil mixtures were determined, as shown in Figure 1. Based on the results, the use of MgO-GGBS was able to control the flowability better than OPC and CaO-GGBS. All MgO-GGBS mixtures also exhibited no bleeding after first mixing, demonstrating its ability to minimize cation exchange-induced bentonite degradation. The variation in workability properties of soil mixtures might slightly affect the hardened-state properties, which will be further discussed in the following sections. Nonetheless, all sand-bentonite-binder mixtures had flowability within the recommended range of 150–230 mm and bleeding less than 3% (Evans, 2007).

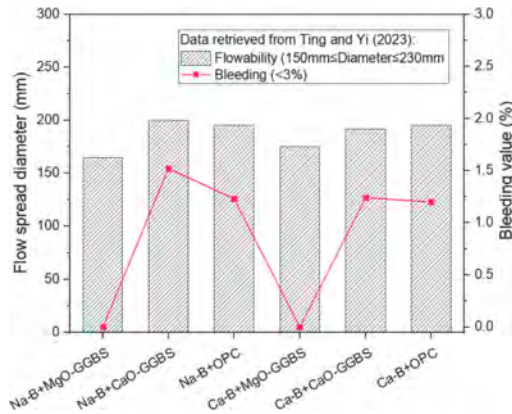


Figure 1. Flowability and bleeding of sand-bentonite-binder mixtures (data adapted from Ting and Yi 2023).

3.2 Permeability

The permeability of various sand-bentonite-binder mixtures at 56 and 112 days were determined, as shown in Figure 2. According to the results, MgO-GGBS stabilized soil exhibited the lowest permeability in both Na-B and Ca-B mixtures, with values ranging between 10^{-10} m/s and 10^{-11} m/s, all of which were well below than the limit of 10^{-9} m/s (Wu et al., 2019). The CaO-GGBS mixtures had a slightly higher but comparable permeability to the MgO-GGBS mixtures, whereas the OPC mixtures had the highest permeability. In comparison to OPC, the permeability of MgO-GGBS mixtures was about 1 to 2 orders of magnitude lower. The negative effect of OPC was the most obvious in the Na-B mixture, where permeability failed to meet the specified requirement. This was because the OPC caused cation exchange reactions to replace exchangeable Na^+ ions of bentonite, degrading its swelling capability and hence increasing the permeability. Besides, all Ca-B mixtures showed permeability slightly less than Na-B mixtures. This was owing to Ca-B having fewer exchangeable Na^+ ions (Table 1) and hence being less influenced by binder-induced cation exchange reactions (Dananaj et al., 2005, Ting and Yi, 2023). Nonetheless, the permeability of all mixtures reduced with the specimen ages due to more complete hydration reactions and hence the formation of more hydration products.

3.3 Unconfined compressive strength

Figure 3 depicts the UCS of sand-bentonite-binder mixtures at 14, 28, 56, and 112 days. In general, the UCS of all soil mixtures increased with the specimen ages. MgO-GGBS and CaO-GGBS gained more strength over time than OPC. This was primarily due to the latent

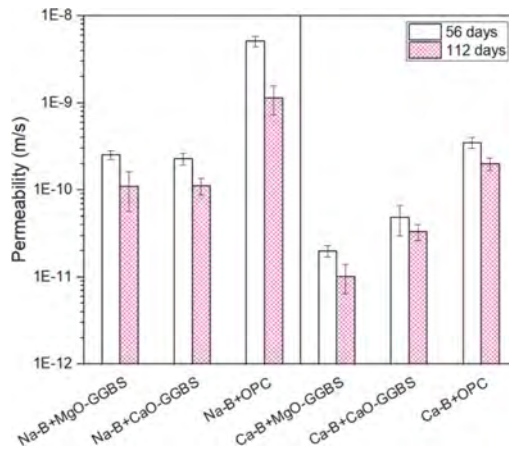


Figure 2. Permeability of sand-bentonite-binder soil specimens at 56 and 112 days.

hydraulic properties of GGBS-based binders to gradually form hydration products with curing durations.

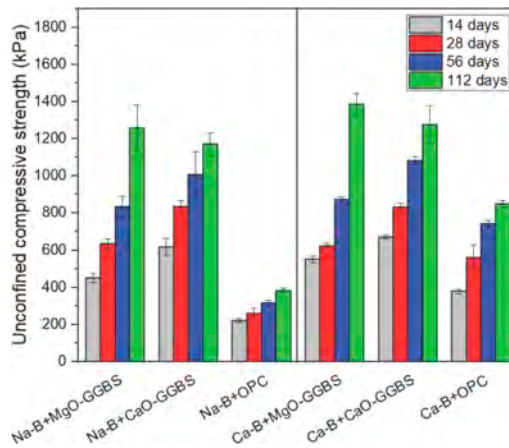


Figure 3. UCS of sand-bentonite-binder soil specimens at 14, 28, 56 and 112 days.

Based on the UCS test results, MgO-GGBS mixtures demonstrated a comparable strength to CaO-GGBS mixtures regardless of the bentonite type. Meanwhile, OPC mixtures had the lowest UCS, which was 2 to 4 times lower than MgO-GGBS mixtures. This was similarly attributed to the degradation of bentonite caused by the OPC-induced cation exchange process. Furthermore, the hydration products of OPC might have a poorer interaction with bentonite clay and sand, which resulted in weaker interlocking particles strength (Li et al., 2022). Nevertheless, the negative effects of OPC in terms of strength was became less noticeable in Ca-B mixtures. In summary, the UCS results were consistent with the permeability results.

3.4 X-ray diffraction

The mineralogy of sand-bentonite-binder mixtures at 112 days was determined by XRD analysis, as shown in Figure 4. The main crystalline phases detected in the soil mixture were quartz from sand and montmorillonite from bentonite. In comparison to MgO-GGBS, both CaO-GGBS and OPC induced a slight shift of montmorillonite peak at 7.2° towards the left side, indicating the occurrence of cation exchange in bentonite. The shift in peak location

suggested a conversion of Na-based montmorillonite to Ca-based montmorillonite (Ting and Yi, 2023). Besides, the main hydration products of MgO-GGBS mixtures included calcium silicate hydrates (CSH), hydrotalcite-like phase and ettringite. The peak intensity (32.9°) of CSH in MgO-GGBS and CaO-GGBS was slightly higher than that in OPC, which was consistent with the permeability and UCS results. The ettringite peaks in CaO-GGBS and OPC mixtures were stronger than those in MgO-GGBS mixtures. This implied an increased formation of ettringite due to a greater calcium components from CaO and OPC hydration, as calcium hydroxide was also identified in CaO-GGBS and OPC mixtures.

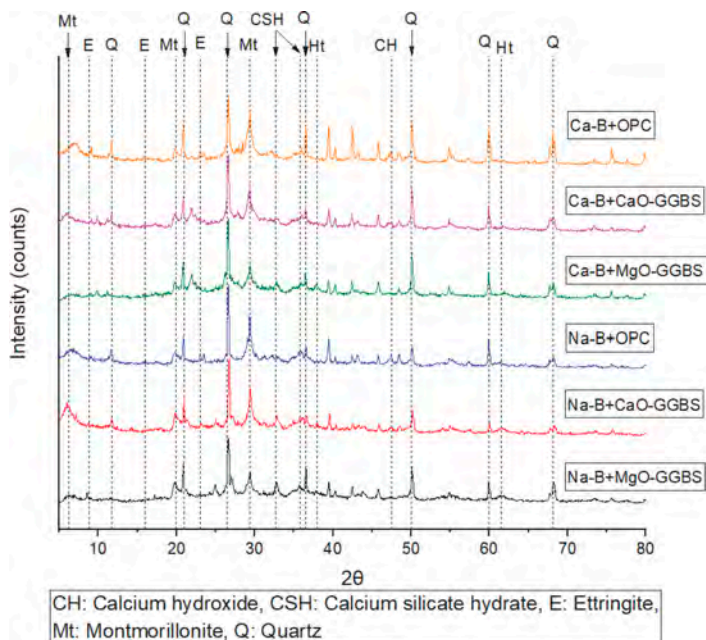


Figure 4. XRD patterns of sand-bentonite-binder mixtures at 112 days.

3.5 Scanning electron microscopy and energy dispersive X-ray

The SEM images with EDX analysis showing the typical morphology of sand-bentonite-binder mixtures at 112 days are provided in Figure 5. The main hydration products of CSH were found in all mixtures, with mesh-like structures that held soil particles together. The CSH was the main binding components that contributed to the strength and impermeability of sand-bentonite-binder mixtures. In addition, another hydration products of ettringite having needle-like crystal were also observed in the soil mixtures. A slight formation of ettringite could densify pore matrix due to its expansive characteristic, but excessive formation could lead to expansion damage. These hydration products were validated with the matching of elements in EDX analysis (Figure 5).

4 CONCLUSION

This study investigates the hardened-state properties of sand-bentonite mixtures stabilized by MgO-GGBS for two-phase cut-off wall construction. The effectiveness of MgO-GGBS is compared to that of CaO-GGBS and OPC. Based on the test results, the main findings are summarized below.

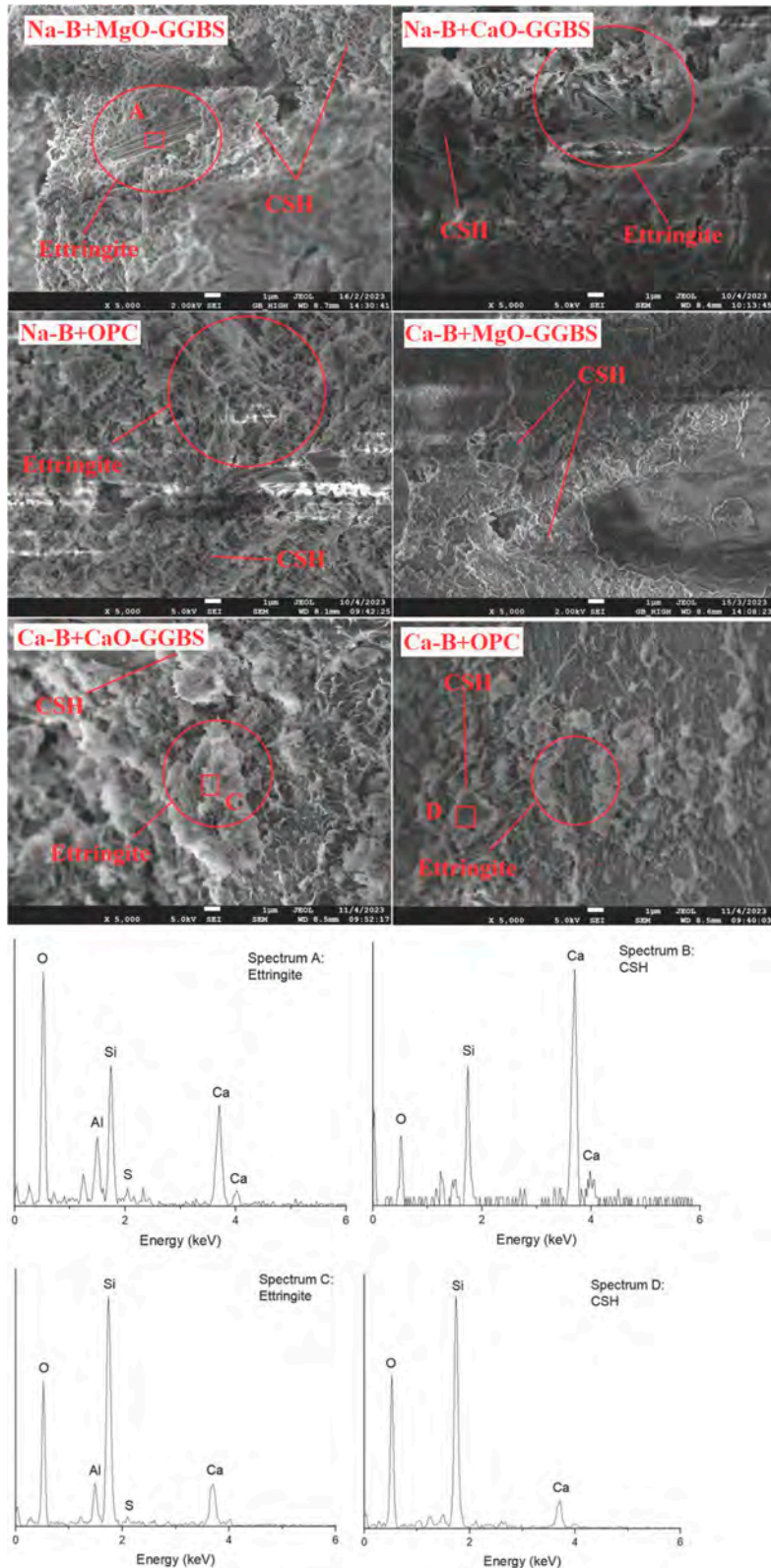


Figure 5. SEM images and EDX analysis of sand-bentonite-binder mixtures at 112 days.

1. The permeability of sand-bentonite mixtures stabilized by MgO-GGBS was one to two orders of magnitude lower than that of OPC-stabilized mixtures, with values far below the specified limit of 10^{-9} m/s.
2. In terms of strength, MgO-GGBS stabilized mixtures had two to four times UCS higher than the OPC stabilized mixtures, demonstrating its excellent effectiveness in stabilizing sand-bentonite mixtures.
3. According to the XRD and SEM-EDX results, the main hydration products of MgO-GGBS stabilized mixtures were CSH and hydrotalcite-like phases, which bonded the sand and bentonite particles, contributing to the strength and impermeability of cut-off walls.
4. By comparing the bentonite type, all Ca-B mixtures had slightly lower permeability and higher UCS than the Na-B mixtures due to their greater resistance to cation exchange processes.

ACKNOWLEDGEMENTS

The authors acknowledge the research grant supported by the Ministry of Education, Singapore, under its Academic Research Fund Tier 2 (MOE-T2EP50220-0004) and China-Singapore International Joint Research Institute (N2052401- A024).

REFERENCES

- ASTM (2016) Standard Test Method for Measurement of Hydraulic Conductivity of Saturated Porous Materials using a Flexible Wall Permeameter. *West Conshohocken, PA:ASTM*, ASTM D5084-16a.
- ASTM (2017) Standard Test Method for Compressive Strength of Molded Soil-Cement Cylinders. *West Conshohocken, PA:ASTM*, ASTM D1633-17.
- CFMIS (2006) Test Methods for Chemical Activity of Caustic Burned Magnesia (YB/T 4019-2006). *China National Development and Reform Commission Press, Beijing*.
- Cheng, H., Li, W., Chen, R. & Yi, Y. (2022) Workability study of sand-bentonite-cement mixtures for construction of two-phase cut-off wall. *Construction and Building Materials*, 345, 128058.
- Dananaj, I., Frankovská, J. & Janotka, I. (2005) The influence of smectite content on microstructure and geotechnical properties of calcium and sodium bentonites. *Applied Clay Science*, 28, 223–232.
- Elhakim, A. F. (2016) Estimation of soil permeability. *Alexandria Engineering Journal*, 55, 2631–2638.
- Evans, J. C. (2007) The TRD method: slag-cement materials for in situ mixed vertical barriers. *Soil Improvement*.
- Evans, J. C. & Garbin, E. J. (2009) The TRD method for in situ mixed vertical barriers. *Advances in Ground Improvement: Research to Practice in the United States and China*.
- Jiang, P., Zhang, Q.-S., Liu, R.-T., Bezuijen, A., Liu, Y.-K. & Li, K.-X. (2020) Development of a trench cutting re-mixing deep wall method model test device. *Tunnelling and Underground Space Technology*, 99, 103385.
- Koch, D. (2002) Bentonites as a basic material for technical base liners and site encapsulation cut-off walls. *Applied clay science*, 21, 1–11.
- Li, W., Yi, Y. & Puppala, A. J. (2022) Comparing carbide sludge-ground granulated blastfurnace slag and ordinary Portland cement: Different findings from binder paste and stabilized clay slurry. *Construction and Building Materials*, 321, 126382.
- Sharma, A. K. & Sivapullaiah, P. V. (2017) Swelling behaviour of expansive soil treated with fly ash-GGBS based binder. *Geomechanics and Geoengineering*, 12, 191–200.
- Ting, M. Z. Y. & Yi, Y. (2023) Influence of short-term binder-bentonite interactions on workability of sand-bentonite-binder mixture for seepage cut-off wall. *Construction and Building Materials*, 383, 131260.
- Wu, H.-L., Jin, F., Ni, J. & Du, Y.-J. (2019) Engineering properties of vertical cutoff walls consisting of reactive magnesia-activated slag and bentonite: workability, strength and hydraulic conductivity. *Journal of Materials in Civil Engineering*, 31.
- Wu, H.-L., Jin, F., Zhou, A.-N. & Du, Y.-J. (2021) The engineering properties and reaction mechanism of MgO-activated slag cement-clayey sand-bentonite (MSB) cutoff wall backfills. *Construction and Building Materials*, 271, 121890.
- Yi, Y., Liska, M. & Al-Tabbaa, A. (2014) Properties and microstructure of GGBS–magnesia pastes. *Advances in Cement Research*, 26, 114–122.
- Yi, Y., Liska, M., Jin, F. & Al-Tabbaa, A. (2016) Mechanism of reactive magnesia–ground granulated blastfurnace slag (GGBS) soil stabilization. *Canadian Geotechnical Journal*, 53, 773–782.
- Yu, H., Yi, Y. & Unluer, C. (2021) Heat of hydration, bleeding, viscosity, setting of Ca (OH) 2-GGBS and MgO-GGBS grouts. *Construction and Building Materials*, 270, 121839.

Analysis of soil clogging of TBM tunneling in clayey layers and the role of soil compositions

G. Wang & L. Yan

State Key Laboratory of Geomechanics and Geotechnical Engineering, Institute of Rock and Soil Mechanics, Chinese Academy of Sciences, Wuhan, China
University of Chinese Academy of Sciences, Beijing, China

X.W. Zhang

State Key Laboratory of Geomechanics and Geotechnical Engineering, Institute of Rock and Soil Mechanics, Chinese Academy of Sciences, Wuhan, China

X.Y. Liu

School of Civil and Hydraulic Engineering, Huazhong University of Science and Technology, Wuhan, China

H.D. Gao

College of Urban Construction, Wuhan University of Science and Technology, Wuhan, China

ABSTRACT: Clogging in tunnel boring machines, particularly in clayey soil layers, is a prevalent problem that could result in decreasing excavation efficiency and elevated project costs. Since clogging is a result of soil adhesion, a comprehensive understanding of this phenomenon is crucial in efforts to mitigate its occurrence. This paper presents the results of pull-out tests for the adhesion characteristics of natural and artificial clayey soils to consider the impact of compositional factors, including clay fraction and mineralogy. The results demonstrate that increasing clay fraction results in a linear increase in adhesion stress, owing to the larger real contact area at the interface between the soil particles and metal, and the results of which were explained theoretically from the mechanism for soil adhesion. The inclusion of montmorillonite led to a significant increase in soil adhesion, due to its distinctive microstructural properties. A revised semi-empirical diagram is proposed, which enables qualitative evaluation of compositional factors on clogging potential. The maximum adhesion stresses measured in the studied samples fall within the region of strong clogging in the semi-empirical diagram, thereby suggesting the feasibility of using adhesion stress as an indicator for clogging assessment.

1 INTRODUCTION

Tunnel boring machines (TBM) are among the safest and most efficient approaches for tunnel excavation. However, when a TBM passes through clayey soil, the most common problem is clogging (Thewes 1999). Clayey soils may adhere to the solid surfaces of a TBM and lead to massive clogging problems in its components or even the entire tunnelling device, which may in turn result in serious engineering accidents. Therefore, it is important to determine the clogging potential of the soil layers before tunnelling begins. Adhesion is widely acknowledged as one of the most important mechanisms for clogging (Thewes 1999). In other words, clogging problems during TBM excavation depend mainly on the adhesion that occurs at the interfaces between clayey soil and metal surfaces.

Different approaches have been proposed for assessing the clogging potential or the adhesion of clayey soils, and these can be categorized roughly as semi-empirical and experimental approaches. Semi-empirical approaches are highly beneficial because they allow clogging

assessment directly via basic soil properties recorded from geotechnical investigations. Meanwhile, experimental measurements have been made in laboratory tests, thereby allowing the clogging potential to be assessed in ways that are closer to the physical drilling process of a TBM. Overall, these experimental methods can themselves be divided into indirect and direct measurements of adhesion (Thewes 1999; Sass & Burbaum 2009). Through numerous trials, researchers have summarized what is required of such adhesion tests, including (i) simple and reproducible test procedure and (ii) accurate test results. Among these test methods, piston pull-out tests are recognized as fulfilling these requirements, which have been used widely to evaluate soil adhesion (Khabbazi et al. 2017).

Previous researchers tended to focus on soil samples from a specific subsoil stratum, thereby considering singular compositional conditions. However, in some engineering projects, a TBM may pass through subsoil layers with different soil compositions. For example, in some tropical areas, the clay fraction of the stratum along the tunnelling driving route varies significantly with the weathering degree of the parent rock, which can result in different clogging potentials. Moreover, the effects of clay mineralogy on the clogging potential have not been studied quantitatively using piston pull-out tests, and their relationships are yet to be established. Therefore, investigations are needed on how soil composition influences the mechanism of adhesion in terms of both adhesion stresses and physical properties. In addition, although semi-empirical diagrams are convenient for assessing clogging potential, they are empirical and derived from different site-specific engineering projects. As such, more analysis combining semi-empirical diagrams with experimental tests is desired to confirm their applicability to different engineering manifestations considering different soil conditions.

In this study, both natural and artificial soil samples were prepared to investigate the compositional effects on clogging potential. The adhesion behaviors of clayey samples with wide range of consistency index were investigated via pull-out tests, and the results of which were explained theoretically from the mechanism for soil adhesion. The risk of TBM clogging was analyzed comprehensively by combining the updated semi-empirical diagram and the experimental results, with the effects of clay fraction and mineralogy being considered.

2 MATERIALS AND METHODS

2.1 *Materials for testing*

The studied site is at the Foshan City, in southeast China, which is dominated by the granite formed during Jurassic period. The warm and humid subtropical climate greatly accelerated the weathering process of the granite. Several tunnelling projects for Line 1 of the Foshan Metro are currently ongoing herein, and four soil samples (labeled N1–N4) were selected from different depths of the foundation pit along the metro line. Natural samples N1–N4 had decreasing clay fraction, representing the typical soils encountered during tunnelling, and the main minerals of which were kaolinite, quartz, and montmorillonite. Based on the mineral compositions of the natural soils, kaolin, montmorillonite, and silica sand were selected as the raw materials for preparation of artificial soils. Those samples were prepared by mixing the oven-dried raw materials in different dry mass ratios. Four artificial soils (labeled A1–A4) were prepared for adhesion tests, and their soil compositions were labeled according to the dry mass ratio of their constituents as given in Table 1.

The basic properties of the studied soils are summarized in Table 1. Generally, the natural and artificial soils had essentially identical specific gravity of $G_s \approx 2.7$. The studied soils could be classified as CL and CH with high plasticity, indicating their strong clogging potential. To investigate further the influence of the clay mineralogy, the chemical indices of the cation exchange capacity (CEC) and specific surface area (SSA) of the artificial soils were also presented in Table 1.

2.2 *Sample preparation*

Samples were prepared with differing water content to cover evenly the range between the liquid limit w_L and the plastic limit w_p . To determine the required water content, we used the consistency

Table 1. Index properties of tested soils.

Index	Natural soils				Artificial soils*					
	N1	N2	N3	N4	A1	A2	A3	A4 (K)	M	S
	Clay	Silty clay	Silt	Clay with sand	90%K 10%M	80%K 10%M 10%S	90%K 10%S	100%K	100%M	100%S
Specific gravity G_s	2.68	2.68	2.7	2.72	2.66	2.64	2.63	2.65	2.68	2.61
Dry density ρ_d (g/cm ³)	1.08	1.22	1.36	1.45	1.25	1.24	1.21	1.18	1.65	1.27
d_{50} (μm)	1.5	6	8	17	0.62	0.69	0.81	0.59	–	123
Liquid limit w_L (%)	63.1	52.2	50.8	47.0	77.6	65.2	36.9	42	312	–
Plastic limit w_p (%)	28.7	26.8	28.7	25.7	30.1	28.3	22.8	25	58	–
Plasticity index I_p (%)	34.4	25.4	22.1	21.3	47.5	36.9	14.1	17	254	–
Kaolinite (%)	82.2	79.7	77.3	72.1						
Quartz (%)	3.4	7.4	9.9	15.1						
Montmorillonite (%)	8.9	7.6	4.0	2.2						
CEC (meq/100g)					15.3	8.6	7.9	9.8	78	–
SSA (m ² /g)					40.8	33.2	26.2	28.3	500	0.7

*K = Kaolin; M = Montmorillonite; S = Silica sand

index I_c , which is an important indicator of how the water content and plasticity index of a soil influence its adhesion. We selected $I_c = 0.3$ to 1.1 within a reasonable range according to historical engineering practices (Hollmann and Thewes 2013). The consistency index correlated with the water content of each mixture was calculated as $I_c = (w_L - w)/(w_L - w_p)$, where w represents water content. For the sample preparation, either the crushed natural soil or the artificial powdery soil was mixed with a predetermined amount of distilled water and then stored in a sealed bag for 24 h to ensure that the moisture was absorbed well by the particles and dispersed uniformly in the soil. Subsequently, the mixed soil was transferred into the sample mold (diameter: 61.8 mm; height: 20 mm) layer by layer to prevent air entrapment. Finally, the soil surface was flattened using the spatula, with any excess soil being carefully scraped off the sample surface.

2.3 Test procedure

The adhesion tests were performed using an Instron 3380 universal testing machine. A computer system for monitoring the force variation in real time was connected to the load cell with a capacity of 5 kN and an accuracy of 0.01 N. The steel piston with a diameter of 50 mm and surface roughness of 2 μm was attached to the load cell to provide a normal force. The prepared sample in the mold was held by the grip fixture and fixed by the base plate. The steel piston was driven at a constant speed of 5 mm/s and pressed vertically onto the soil surface until the required compression stress of 20 kPa was applied, which allowed the piston to sufficiently contact with the soil surface. This process lasted for 1 minute, after which the piston was pulled upwards to separate gradually from the sample surface at a constant rising speed of 5 mm/s for soil–piston separation. During the adhesion tests, the variations of both the adhesion force and stress with elapsed time were recorded. Specifically, the maximum adhesion stress σ_A for soil detachment from the piston was considered as an indicator of adhesion to the steel surface (Barzegari et al. 2020). The tests were repeated five times on duplicate samples, and the average value of σ_A was used for subsequent analysis.

3 RESULTS AND DISCUSSION

3.1 Maximum adhesion stress

Figure 1 shows the results of adhesion-stress test (in terms of the average value of σ_A for each sample) for the natural and artificial samples with different values of I_c . For each type of soil

sample, the maximum adhesion stress increased initially with increasing I_c and then decreased. For relatively high I_c (e.g. $I_c = 1.1$), the soil samples remained solid with low moisture content, and their values of σ_A were generally small. This is consistent with the engineering experience that in tunnelling, clayey soil with higher stiffness in the excavation chamber has comparatively less clogging potential (Hollmann and Thewes 2013). In general, the maximum adhesion stresses of the studied soils were found to peak at $I_c = 0.5\text{--}0.7$, indicating that soils whose water content is slightly biased towards the plastic limit are more likely to stick to steel surfaces.

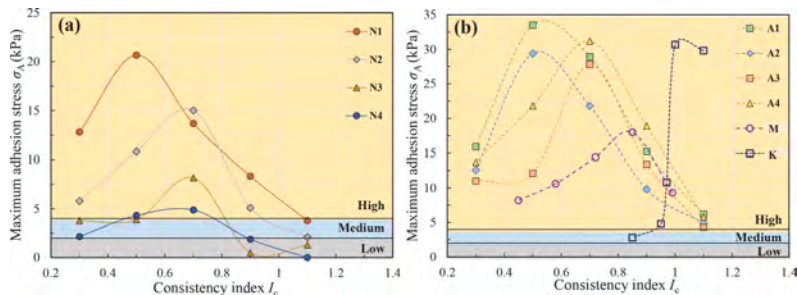


Figure 1. Maximum adhesion stress of (a) natural samples and (b) artificial soils. Data for K and M from Khabbazi et al. (2016a) and Sass & Burbaum (2009).

Khabbazi et al. (2017) conducted piston pull-out tests for the adhesion stresses of different clayey soils, and based on the adhesion values they divided the clogging potential into three degrees from high to low. According to that classification, under differing I_c , the natural samples studied herein have medium to high clogging potential, while the artificial samples have high clogging potential (Figure 1).

For given I_c , the differences in σ_A for different samples can be significant, which means that, in addition to I_c , other factors including the clay fraction and mineralogy also have a major influence on the maximum adhesion stress, as can be seen from the results for the natural samples [Figure 1(a)] and the artificial samples [Figure 1(b)]. Also shown in Figure 1(b) are relevant data from the literature (Khabbazi et al. 2016a; Sass & Burbaum 2009). Although the curves of adhesion versus I_c with the introduction of kaolinite and montmorillonite are both bell-shaped, their peak values and distribution ranges are different, reflecting soil adhesion varies with I_c in response to clay mineralogy.

3.2 Influences of clay fraction and mineralogical composition

Figure 2 shows the correlation between the clay fraction CF and the maximum adhesion stress σ_A of the studied samples according to the complete measurement results. As can be seen, there is a positive correlation between these two parameters, and the best-fit line for both the natural and artificial samples reflects a corresponding ratio of $\sigma_A/CF = 0.36$. Analogously, this essentially linear correlation can also be obtained from the results of Khabbazi et al. (2016b) and Barzegari et al. (2020), with $\sigma_A/CF = 0.19$ and 0.25 , respectively, slightly lower than the present value. The data from Khabbazi et al. (2017) are locally concentrated in the lower right of Figure 2, indicating relatively low adhesion stress for soil samples with different clay fractions. This discrepancy from the positive trend of σ_A and CF may be due to the fact that all the soil samples used by Khabbazi et al. (2017) were illite, which is with low activity, and so soil adhesion is less likely to occur.

Based on the present results, the clay fraction has a significant effect on soil adhesion, and we explain this theoretically from the mechanism for soil adhesion. Understood as a boundary effect, the adhesion of soil to a solid surface depends on the capillary force of a thin water film in the interface between the soil and the solid surface (Burbaum and Sass 2016). Specifically, the capillary force σ can be calculated from Laplace's equation as $\sigma = \gamma(1/R_1 - 1/R_2)$, where γ is the surface tension of water, R_1 is the radius of the meniscus of the water film, and R_2 is its cross-sectional radius; note that R_1 is approximately half the distance from the soil to the solid surface considering the small distance. Accordingly, the above equation suggests that the adhesion stress is proportional to the

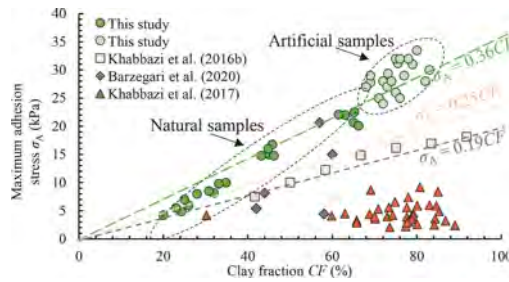


Figure 2. Relationship between clay fraction and maximum adhesion stress of clayey soils.

surface tension of the water and the area of the water film and inversely proportional to the thickness of the water film. Figure 3 shows schematically the water linkage in the interface between a metal surface and different soils. Specifically, the adhesion of soil on metal surface has two specific states, i.e., complete water film and discontinuous water rings, which have also been widely introduced in previous literature (Burbaum and Sass 2016). The water linkage in the fine-grained soil is illustrated in Figure 3(a), where a continuous water film in the soil–metal interface closely connects the metal interface and soil particles. As the soil particles become coarser, a complete water film can no longer form and instead is replaced gradually by a series of discrete small water rings [Figure 3(b)]; the angularity of the soil grains contributes to a single water ring being trapped between the foreign material and the corner of an individual particle. And the soil particle is adhered to the interface of solid face by the discontinuous water ring. Compared with the discontinuous water rings in the interface between metal and coarse soil particles, the intact water film of fine-grained soil has a larger cross-sectional area and so results in higher adhesion stress under the same external conditions.

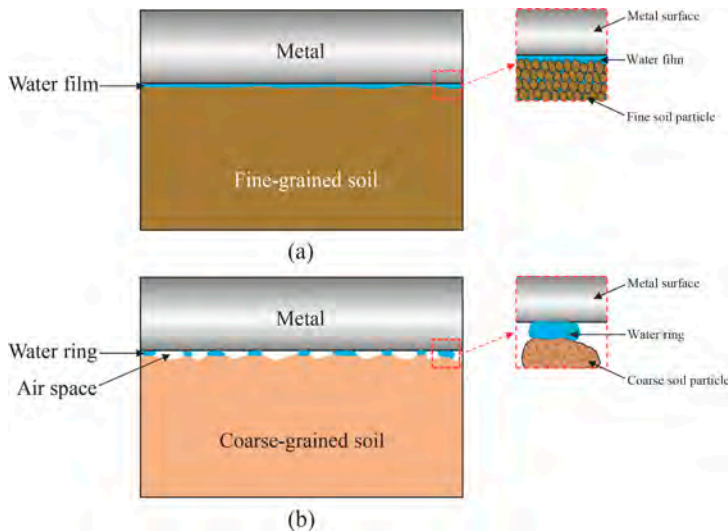


Figure 3. Two different types of water linkage in soils: (a) complete water film; (b) discrete water rings.

Additionally, the mineralogical composition could be another primary factor controlling soil adhesion. The average maximum adhesion stresses for the present artificial samples with and without the addition of montmorillonite are compared in Figure 4. Notably, the soil adhesion of the artificial mixture with montmorillonite is more obvious. Specifically, the maximum adhesion stresses of samples A1 and A4 were improved by 5.8% and 7.4%, respectively, with the addition of only 10% montmorillonite. Furthermore, when montmorillonite dominates the mineralogical composition, the soil adhesion potential is more apparent with sufficiently high adhesion stress. This was the case for the pure montmorillonite samples studied by Khabbazi et al. (2016a), who found

that the maximum adhesion stress of montmorillonite was nine times that for pure kaolinite. A similar phenomenon was also observed by Burbaum and Sass (2016) when measured the values of σ_A of kaolin–illite (K-I) and montmorillonite–illite (M-I) mixtures (Figure 4).

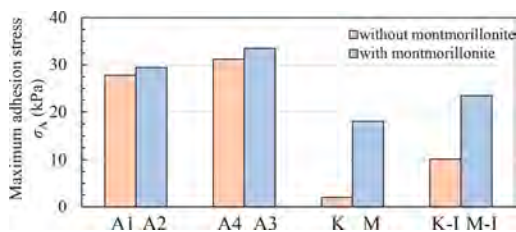


Figure 4. Influence of clay mineralogy on σ_A . Data for K and M from Khabbazi et al. (2016a) and K-I and M-I from Burbaum and Sass (2016).

This significant difference in adhesion mechanism between soil with and without montmorillonite is considered to be both physical and chemical in nature. From a physical perspective, montmorillonite with smaller particles has a larger real contact area with the foreign material, and as noted earlier, small particles contribute to a continuous water film with a larger cross-sectional area, which therefore results in higher capillary forces in the interface zone and thus higher adhesion. Apart from this, the viscosity of the water film increases because of the nature of the hydrogen bonds in the water molecules in the water film in the presence of montmorillonite, thereby producing higher adhesion stress (Khabbazi et al. 2016a).

From a chemical point of view, adhesion also results from the inherent microstructure and properties of the clay minerals. Kaolinite consists of extended tetrahedral and octahedral sheets, and strong hydrogen bonding between these sheets allows no interlayer separation within this clay mineral. Cations are adsorbed on the exterior surface and edges of the particles, consequently resulting in its low CEC (9.8 meq/100 g). In contrast, montmorillonite is a clay mineral consisting of octahedral sheets sandwiched between two tetrahedral sheets, the bonding of which is relatively weak, allowing for not only interlayer separation but also the entering of water molecules. Therefore, montmorillonite has a particularly high CEC (78 meq/100 g). Also, the SSA of kaolinite is much lower than that of montmorillonite (28.3 m²/g versus 500 m²/g). Combining these considerations, montmorillonite has much greater charge deficiency and more exchangeable cations, which means greater plasticity and greater clay adhesion.

3.3 Updated semi-empirical diagram for clogging potential assessment

Hollmann and Thewes (2013) proposed a universal diagram allowing the qualitative assessment of soil clogging potential in conjunction with quantitative adhesion tests. After placing soil in this diagram (Figure 5), the data point of the natural and artificial samples tends to shift downward and to the left with increasing w , indicating that w and I_c serve as the varying parameters. From the experimental results, the adhesion of clayey soil is controlled by its clay fraction and mineralogy, therefore the universal diagram was updated in this study by considering their influences. According to the classification, the samples with $I_c = 0.5$ – 0.75 are prone to strong clogging potential, which agrees well with the region of maximum adhesion stress from the present experimental tests (see Figure 1). As indicated by the grey arrow in Figure 5, the data points for the natural samples move gradually upward and left with increasing CF , which represents the synchronized increase of I_p . With increasing I_p , the zone crossed by the corresponding lines broadens, indicating lower sensitivity to the water content w and that more freely available water is required to transform the clay stiffness. As such, higher I_p is essentially correlated with higher clogging potential. Similarly, as shown by the red arrow in Figure 5, the plasticity index of artificial samples A3 and A4 increased significantly from ca. 15% to more than 35% with the addition of montmorillonite. The contribution of montmorillonite to the clogging potential accords with its influence on soil adhesion, which can be attributed to its intrinsic properties.

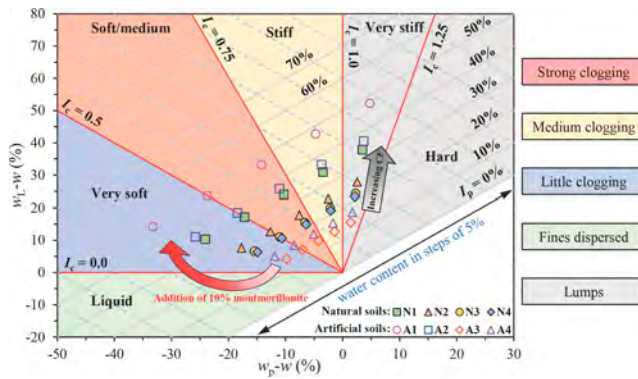


Figure 5. Assessment of the clogging potential of natural and artificial soils using universal diagram updated by considering compositional factors.

4 CONCLUSIONS

The main conclusions are as follows.

- (1) The existence of a threshold water content related to soil adhesion could be observed. Before reaching the thresholding, the interfacial water film expands and adhesion increases with water content; thereafter, adhesion decreases with the thicker water film.
- (2) Under a high clay fraction, the soil–metal interface contains a continuous water film with a large real contact area, whereas with coarser soil particles, discrete water rings trapped between the foreign material and the individual particles give lower soil adhesion.
- (3) The adhesion stresses became more significant when montmorillonite dominated. The smaller particle size of montmorillonite contributes to a larger contact area of the water film, thereby resulting in higher capillary forces and higher adhesion.
- (4) Based on the updated universal diagram considering compositional factors, higher clay fraction and the addition of montmorillonite contribute to higher plasticity, and thus high clogging potential.

REFERENCES

- Barzegari, G., Tirkhooni, M. & Khabbazi, A. 2020. Experimental assessment of clayey layers for clogging of TBM in Tabriz subway lines, Iran. *Tunnelling and Underground Space Technology* 105: 103560.
- Burbaum, U. & Sass, I. 2016. Physics of adhesion of soils to solid surfaces. *Bulletin of Engineering Geology and the Environment* 76(3): 1097–1105.
- Hollmann, F.S. & Thewes, M. 2013. Assessment method for clay clogging and disintegration of fines in mechanized tunnelling. *Tunnelling and Underground Space Technology* 37: 96–106.
- Khabbazi, A., Mirjavan, A., Ghafoori, M. & Cheshomi, A. 2016a. Assessment of the adhesion potential of kaolinite and montmorillonite using a pull-out test device. *Bulletin of Engineering Geology and the Environment* 76: 1507–1519.
- Khabbazi, A., Ghafoori, M., Cheshomi, A. & Azandariani, Y.K. 2016b. Adhesion of clay to metal surface; Normal and tangential measurement. *Geomechanics and Engineering* 10(2): 125–135.
- Khabbazi, A., Ghafoori, M., Tarigh, A.S. & Cheshomi, A. 2017. Experimental and laboratory assessment of clogging potential based on adhesion. *Bulletin of Engineering Geology and the Environment* 78: 605–616.
- Sass, I. & Burbaum, U. 2009. A method for assessing adhesion of clays to tunnelling machines. *Bulletin of Engineering Geology and the Environment* 68: 27–34.
- Thewes, M. 1999. *Adhesion von Tonboden beim Tunnelvortrieb mit Flüssigkeitsschilden*. Ph.D. thesis, Bergische Universität Wuppertal, Germany.

Investigation on evolutions of soil arching developed in a pile-supported embankment considering geogrid

W.H. Yuan

Shantou University, Shantou, Guangdong, China

L.J. Yuan

China Energy Engineering Group Guangxi Electric Power Design Institute, Guangxi, China

Y. Chen

Central Research Institute of Building and Construction (Shenzhen) Co., Ltd, MCC Group, Guangdong, China

L.S. Zhao

Shantou University, Shantou, Guangdong, China

ABSTRACT: This research employs a three-dimensional finite element model to study soil arching evolution in a pile-supported and geogrid-reinforced (PSGR) embankment. Validated against data from a full-scale experiment, the study investigates the dynamics of soil arching during both embankment construction and static step-loading. Findings indicate that the stress concentration ratio, reflecting the average stress on the pile-cap relative to the subsoil, increases with embankment fill height but shows limited variation during static loading. Notably, the arch foot tends to concentrate at the edge and corner of the pile-cap, leading to an uneven stress distribution with higher stress at these locations compared to the center. Additionally, arching heights at different embankment locations are found to be approximately equal. This analysis provides valuable insights into the complex behavior of soil arching in PSGR embankments.

1 INTRODUCTION

In the construction of high-speed railways, precise control of settlement and differential settlement on the embankment surface is essential to mitigate the impact of dynamic traffic loads (Bian et al. 2016). An effective approach to address settlement is the implementation of a pile-supported and geogrid-reinforced (PSGR) embankment, as per the design specifications outlined in BS8006 (1995). Chen et al. (2008) proposed a theoretical solution for pile-supported embankment systems, comparing the results with the BS8006 (1995) design code. Van Eekelen et al. (2013) introduced an analytical model based on a limit-state equilibrium model with concentric arches to explore the load transfer mechanism for PSGR embankments. However, relying solely on theoretical models has limitations due to inherent ideal assumptions.

To capture the genuine characteristics of PSGR embankments, researchers have conducted a series of laboratory and in-situ experiments. Chen et al. (2016) carried out a comprehensive experiment to investigate the load transfer mechanism, while Sloan et al. (2013) utilized expanded polystyrene geofoam to simulate soft soil, implementing a field-scale PSGR embankment. Nevertheless, data obtained are constrained by economic considerations and experimental conditions, particularly in the case of field-scale tests.

Numerical simulation has proven to be an efficient approach for resolving intricate geotechnical challenges. Han & Gabr (2002) employed numerical methods to study the interaction among piles, soil, and geogrid, introducing the concept of the stress concentration ratio. Smith & Filz (2007) focused on an axisymmetric unit cell of a column-supported embankment using FLAC3D. While

most numerical models concentrated on load transfer and employed average stresses to analyze soil arching effects, they often overlooked the uneven stress distribution on the pile cap.

This study constructed a finite element model based on a field-scale experiment, comparing simulation results with data measured from a full-scale test. The evolution of soil arching and the uneven stress distribution at the pile cap were analyzed, followed by an evaluation of load transfer efficiency and arching height.

2 THREE-DIMENSIONAL FINITE ELEMENT MODEL

The numerical model, developed using ABAQUS, is based on a comprehensive full-scale test conducted by Chen et al. (2016) and Bian et al. (2014). Derived from the full-scale test configuration, the model incorporates the embankment fill, 3x5 pile caps, and surrounding water bags (utilized to simulate subsoil). Figure 1 illustrates the profile of the pile-supported embankment, accompanied by a detailed description of the numerical model provided by Zhou et al. (2016a, b). Key parameters in the finite element model include the moduli of the embankment fill and water bags.

To determine the modulus of the embankment fill, obtained through static plate loading tests (PLT) in the full-scale experiment, a series of simulations were conducted to replicate the PLT in the numerical model. The PLT was performed at two different stages (bottom and top of the embankment fill). The deformation modulus of the embankment fill is calculated using $E_{v1} = 1.5r\Delta\sigma/\Delta s_1$ in PLT, where r is the radius of the plate, $\Delta\sigma$ is the increment of extra load, and Δs_1 is the displacement due to the extra loading. Table 1 presents observed displacements from both numerical simulations and real PLT under increasing extra loading, indicating good agreement and reasonable calculated moduli in the numerical model. Model parameters were summarized by Zhou et al. (2016a, b).

In Figure 2, the variation of vertical stress at three locations (EP1, EP2, and ES1) during the embankment construction process is depicted, with measured data closely aligning with numerical results, further verifying the reasonableness of the present numerical simulation.

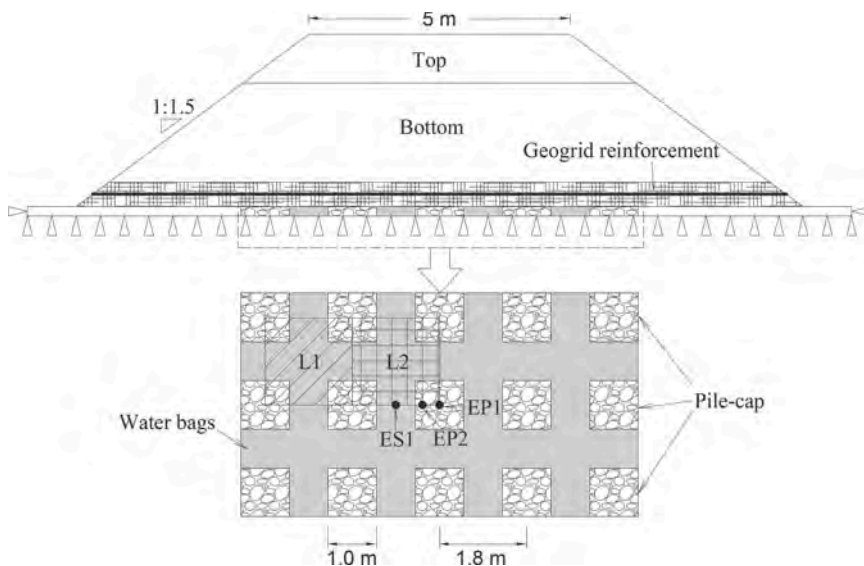


Figure 1. Profile of the embankment model.

Table 1. Parameter calibration for the FE model using the static plate load test.

Load (MPa)	0	0.09	0.16	0.26	0.32	0.39	0.46	0.53	0.62
Bottom layer (test) (mm)	0	0.34	1.76	1.44	1.89	2.49	3.12	3.89	4.88
Bottom layer (FEM) (mm)	0	0.36	0.74	1.21	1.71	2.16	2.81	3.48	4.53
Top layer (FEM) (mm)	0	0.26	0.62	1.03	1.33	1.71	2.11	2.49	2.98

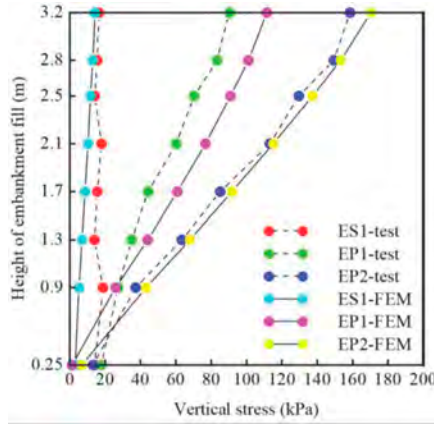


Figure 2. Changes in vertical stress at various points.

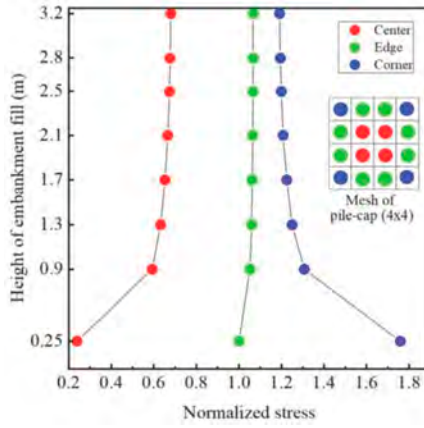


Figure 3. Fluctuations in vertical stress at various positions in the pile cap.

Based on the mesh of the pile-cap as shown in Figure 3, the average stress, σ_{aver} , and the normalized stresses at the corner, $\bar{\sigma}_{corn}$, at the edge, $\bar{\sigma}_{edge}$, and at the center, $\bar{\sigma}_{cent}$, of the pile-cap can be calculated as follows:

$$\sigma_{aver} = \frac{\sum \sigma_{corn} + \sum \sigma_{edge} + \sum \sigma_{cent}}{16} \quad (1)$$

$$\bar{\sigma}_{corn} = \frac{\sum \sigma_{corn}}{4\sigma_{aver}}, \bar{\sigma}_{edge} = \frac{\sum \sigma_{edge}}{8\sigma_{aver}}, \bar{\sigma}_{cent} = \frac{\sum \sigma_{cent}}{4\sigma_{aver}} \quad (2)$$

where $\sum \sigma_{corn}$, $\sum \sigma_{edge}$, and $\sum \sigma_{cent}$ are the summation of the stresses at the corner, the edge, and the center of the pile-cap, respectively.

Figure 3 illustrates the variations in normalized stress at the corner, edge, and center of the pile-cap. The stress distribution on the pile-cap exhibits unevenness, with the minimum stress occurring at the center, attributed to the formation of three-dimensional soil arching among the adjacent four pile-caps. As the height of the embankment fill increases and soil arching evolves, the arch foot gradually shifts towards the center, resulting in a significant increase in stress at the center and a decrease at the corner, especially when the embankment height reaches 0.9 m.

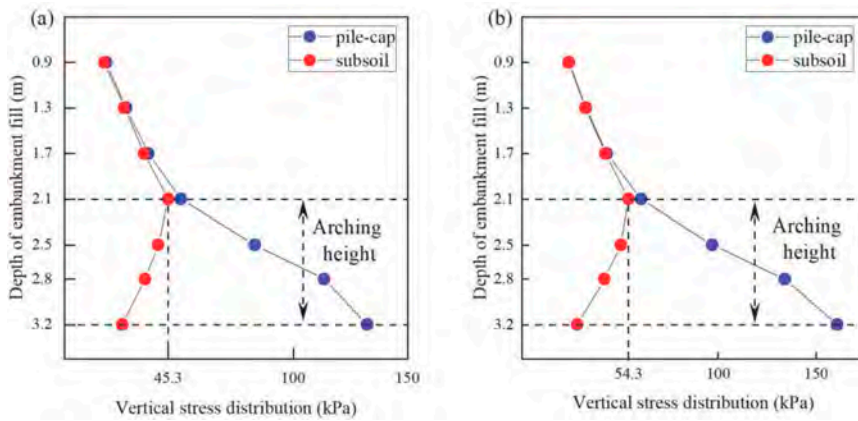


Figure 4. Vertical stress profiles: (a) L1, (b) L2.

In Figure 4, the average vertical stress distribution is depicted concerning the depth of the embankment fill above the pile-caps and the subsoil. From approximately 0.9 m to 2.1 m, earth pressures exhibit an increasing trend with depth. Beyond a depth of 2.1 m, pressures above the pile-cap experience a substantial increase, while those above the subsoil exhibit a decreasing trend, indicating load arching onto adjacent pile-caps due to the soil arching effect. The arching height in this simulation is approximately 1.3-1.4 times the net spacing between the pile-caps. The zone between 2.1 m and 3.2 m is where the load transfer and the evolution of soil arching primarily occur, observed in both regions L1 (the shoulder of the embankment) and L2 (the center of the embankment), with the central region bearing a higher load compared to the shoulder.

The stress concentration ratio, n , representing the average stress on the pile-cap relative to that on the surrounding subsoil, is illustrated in Figure 5. The stress concentration ratio increases with the escalating embankment height. At approximately 2.5 m height, the growth rate of the stress concentration ratio decelerates, surpassing the critical arching height outlined in Figure 4. Notably, the ratio at the center of the embankment slightly exceeds that at the shoulder. In the static loading test, depicted in Figure 5(b), the stress concentration ratio kept growing, but with a very small increment even when reaching 40 kPa. This feature coincided with the later stage (2.5 m ~ 3.2 m) of embankment construction, as illustrated in Figure 5(a), demonstrating that load transfer efficiency cannot be significantly enhanced after reaching the critical arching height.

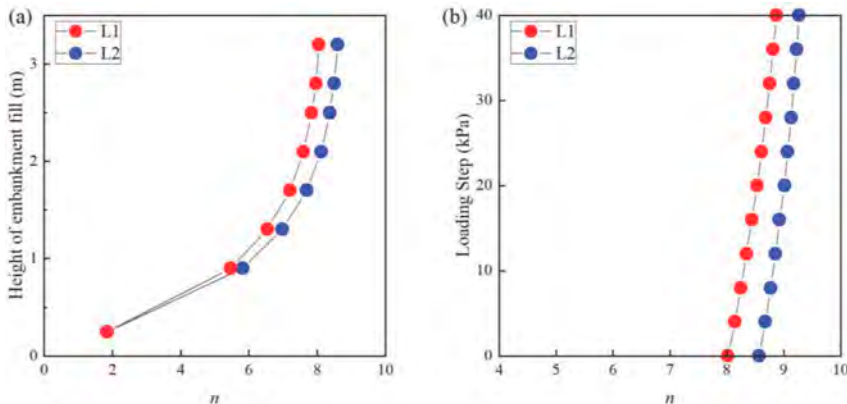


Figure 5. Variations of stress concentration ratio: (a) embankment construction, (b) static step-loading test.

3 CONCLUSIONS

This investigation utilized a series of three-dimensional finite element models to examine the dynamic evolution of soil arching within the PSGR embankment system. The finite element model underwent validation by replicating the static plate loading test (PLT), adjusting parameters used in the simulation. The reasonableness of the simulation results was verified through a comparison with measured data obtained from a full-scale test. The progression of soil arching predominantly occurred during the embankment construction phase. Subsequently, in the static step-loading process, the stress concentration ratio exhibited a slight increase. Throughout the soil arching evolution, the arch foot was observed to be situated at the edge and corner of the pile-cap, leading to higher stresses in these areas compared to the center. In this simulation, the critical height for soil arching was determined to be 1.3-1.4 times the net spacing of the pile-cap, with closely similar arching heights observed at both the center and the shoulder of the embankment.

REFERENCES

- Bian, X., Jiang, H., Cheng, C., Chen, Y., Chen, R., Jiang, J. 2014. Full-scale model testing on a ballastless high-speed railway under simulated train moving loads. *Soil Dynamics and Earthquake Engineering*, 66: 368–384.
- Bian, X., Cheng, C., Jiang, J., Chen, R., Chen, Y. 2016. Numerical analysis of soil vibrations due to trains moving at critical speed. *Acta Geotechnica*, 11: 281–294.
- British Standards Institution. 1995. Code of practice for reinforced soils and other fills. British standard BS8006. London, UK: British Standards Institution.
- Chen, R.P., Chen, Y.M., Han, J., Xu, Z.Z. 2008. A theoretical solution for pile-supported embankments on soft soils under one-dimensional compression. *Canadian Geotechnical Journal*, 45: 611–623.
- Chen, R.P., Wang, Y.W., Ye, X.W., Bian, X.C., Dong, X.P. 2016. Tensile force of geogrids embedded in pile-supported reinforced embankment: A full-scale experimental study. *Geotextiles and Geomembranes*, 44: 157–169.
- Han, J., Gabr, M. 2002. Numerical Analysis of Geosynthetic-Reinforced and Pile-Supported Earth Platforms over Soft Soil. *Journal of Geotechnical and Geoenvironmental Engineering*, 128: 44–53.
- Van Eekelen, S.J.M., Bezuijen, A., Van Tol, A.F. 2013. An analytical model for arching in piled embankments. *Geotextiles and Geomembranes*, 39: 78–102.
- Sloan, J.A., Filz, G.M., Collin, J.G. 2013. Field-scale column-supported embankment test facility. *Geotechnical Testing Journal*, 36(6): 1–12.
- Smith, M., Filz, G. 2007. Axisymmetric numerical modeling of a unit cell in embankments. *Geosynthetics International*, 14(1): 13–22.
- Zhou, W.H., Lao, J.Y., Huang, Y., Chen, R. 2016a. Three-dimensional Finite Element Modelling of Soil Arching in Pile-supported Geogrid-reinforced Embankments. *Procedia Engineering*, 143: 607–614.
- Zhou, W.H., Lao, J.Y., Huang, Y., Chen, R. 2016b. Group effect on soil arching in geogrid-reinforced pile-supported embankments. *Proceeding of International Mini Symposium Chubu (IMS-Chubu)*, May 26-28, 2016, Nagoya, Aichi, Japan.

Constitutive and numerical modelling



Taylor & Francis

Taylor & Francis Group

<http://taylorandfrancis.com>

General report for “Constitutive and Numerical Modelling” session at IS-Macau 2024

Z.Y. Yin

Department of Civil and Environmental Engineering, The Hong Kong Polytechnic University, Hung Hom, Kowloon, Hong Kong

ABSTRACT: This general report overviews twelve papers submitted to the theme of “Constitutive and Numerical Modelling” session at IS-Macau 2024. Seven submitted papers focus on tunneling-related topics and provide insights into subsurface construction effects, ground settlement, etc., while the remaining papers cover other significant topics, including foundation pit support and deep excavation analysis. These submitted works are generally of high quality, contributing new insights into numerical modeling in advancing geotechnical solutions.

1 INTRODUCTION

The “Constitutive and Numerical Modelling” session at IS-Macau 2024 has underscored the pivotal role of numerical modeling in addressing a spectrum of geotechnical challenges. The session featured a predominant focus on tunneling-related topics with seven papers providing insights into the effects of subsurface construction, such as ground settlement. The remaining contributions explored other geotechnical topics, including support systems for foundation pits and the analysis of deep excavations.

2 TUNNELING

The complexities of tunneling operations necessitate sophisticated numerical analyses to predict, design, and control the associated ground movements and structural responses. This section summarizes seven contributed papers that delve into tunneling challenges, covering construction case studies, impact assessments, and new prediction approaches.

2.1 *Case study*

This subsection includes two papers that reported case studies associated with tunnel construction, including ones in Macau SAR and Guangdong, China.

Ung et al. (2024) presented a finite element simulation (using PLAXIS 2D software) of shield tunneling in Macau SAR, Guangdong, China, with a focus on investigating the ground settlement induced by the tunnel construction. The numerical results were compared with field measurements and, despite slight discrepancies due to the limitations of replicating complex site conditions, were considered acceptably accurate. The settlement trough observed was typically normal in distribution but exhibited asymmetry, with the maximum settlement not always centrally located above the tunnel axis.

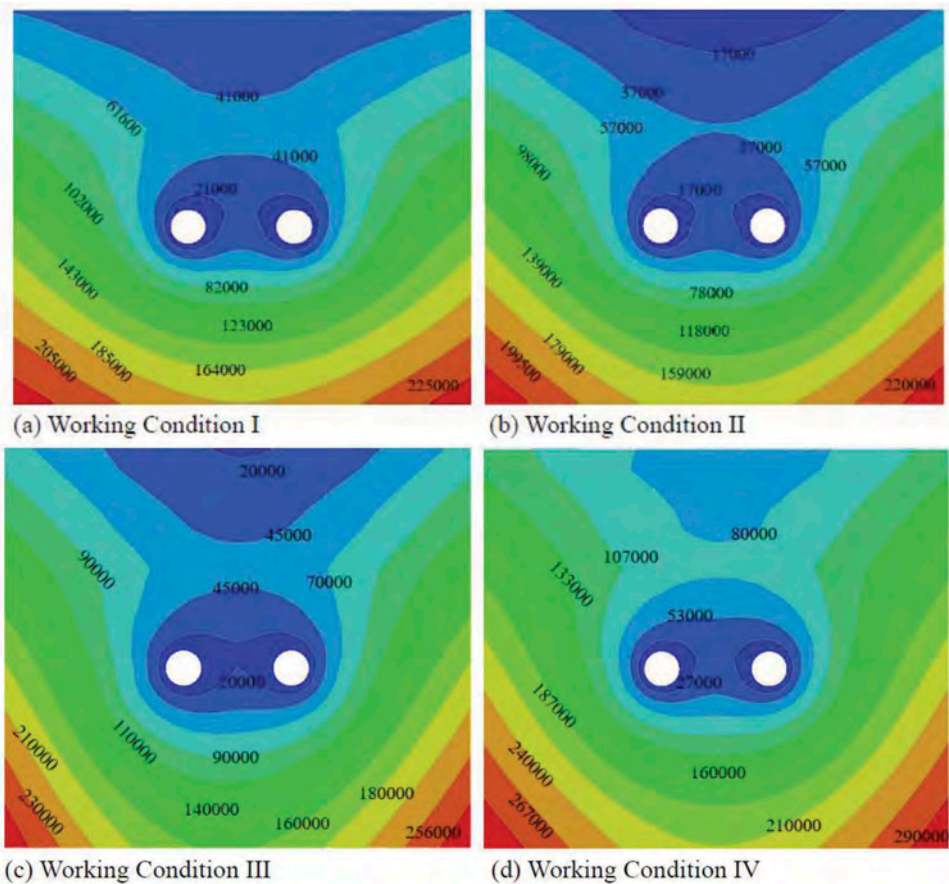


Figure 1. Pore pressure distribution at D=30m section of pipe jacking under different working conditions (from Liu *et al* 2024a).

Similarly, Liu *et al.* (2024a) analyzed the construction of an underwater tunnel as part of the Pearl River Delta Water Resources Allocation Project. Through a three-dimensional finite element method (FEM) simulation, the study highlighted the effects of various jacking methods on surface subsidence, pore water pressure, and seepage velocity, emphasizing the need to consider flow-solid coupling effects and lake depth in construction planning.

2.2 Impact assessment

Two papers in the session investigated the impact of various processes during tunnel construction.

Zheng *et al.* (2024) conducted an experimental study on the influence of dilution of foaming liquid as could be expected in Earth Pressure Balance (EPB) shield tunneling. The study utilized the capillary rise method to measure surface tension at different concentrations, finding that surface tension could increase substantially due to dilution. The implications of increased surface tension for the formation of a low permeability layer, which is crucial for tunnel stability, were theoretically analyzed, suggesting that this change should be factored into the assessment of foam-soil interactions.

The paper by Yu *et al.* (2024b) presented an evaluation of the effect of infill nonlinearity on the response of framed structures to tunneling using a two-stage analysis method (TSAM). The method was validated using experimental data from centrifuge tests and advanced numerical simulations. The study investigated the impact of infill nonlinearity on foundation

displacements and building deformation parameters, particularly in long-frame structures, with an exploration of the impact on frame shear and bending behavior.

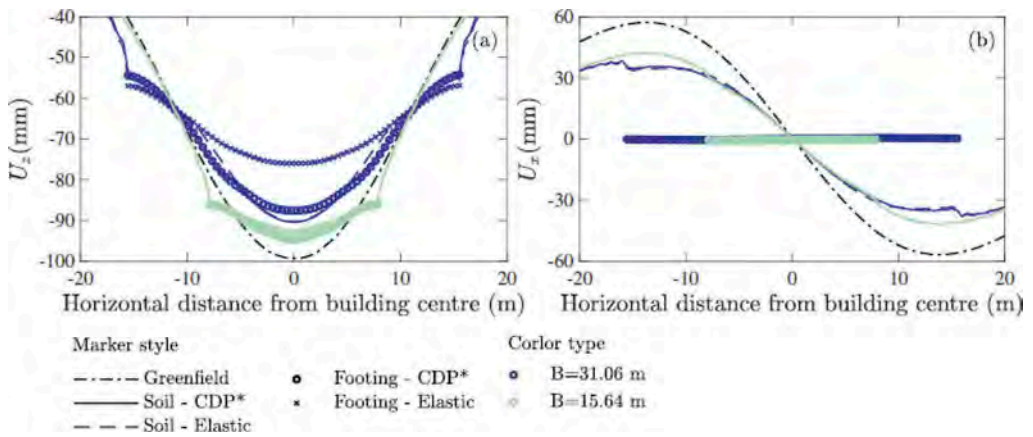


Figure 2. Comparison of footing base and underlying soil displacements with different building transverse widths, (a) vertical displacements and (b) horizontal displacements (upward in vertical and right in horizontal means positive) (from Yu et al 2024b).

2.3 New numerical approaches

Three papers introduced new numerical and analytical methods for assessing tunnel responses.

Yu et al. (2024a) introduced displacement-controlled numerical methods (DCM) based on the gap methods for predicting ground settlement due to rectangular tunnel boring machine (RTBM) operations. The study compared two DCM approaches and found that one method by Ng (2017) was better suited for back-analyzing RTBM drive data from start to end, while the newly proposed DCM was more applicable for analyzing short-term post-drive measurements.

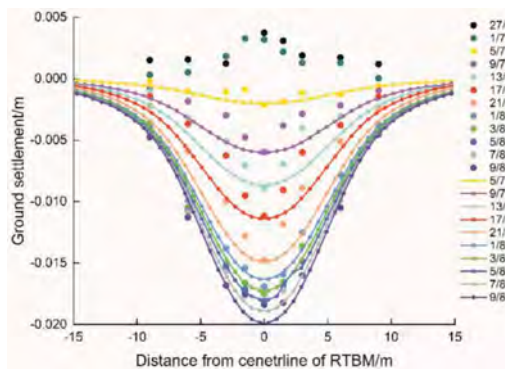


Figure 3. Proposed DCM displacement vs field data (from Yu et al 2024a).

Zhong et al. (2024) employed a two-phase flow model of muck and air using the computational fluid dynamics (CFD) method to simulate the pressure distribution inside the shield chamber during tunneling with an auxiliary air balance mode. This mode is gradually applied to reduce machine loads during earth pressure balance (EPB) shield tunneling. The pressure imbalance observed between the left and right sides of the chamber resulted from the muck's

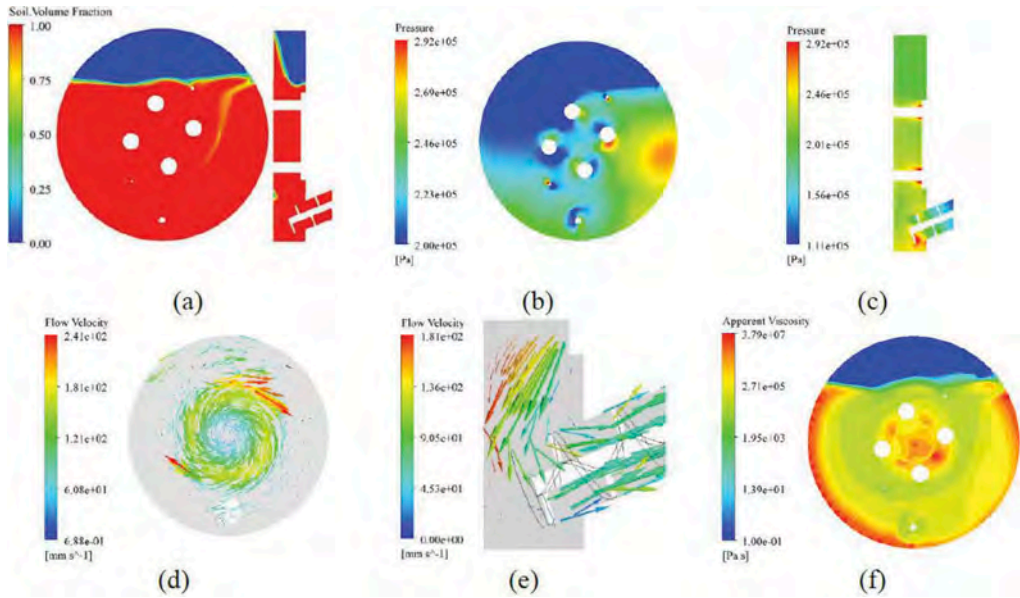


Figure 4. Muck flow field distribution in the chamber during tunneling: (a) volume fraction; (b) pressure in transverse section; (c) pressure in longitudinal section; (d) velocity in transverse section; (e) velocity near the conveyor inlet; (f) apparent viscosity in transverse section (from *Zhong et al.* 2024).

rotating flow. Furthermore, the disturbance of moving shield components led to an evident pressure fluctuation in the muck zones near the components. The supporting pressure increased with growing auxiliary air pressure, accompanied by growing fluctuations and imbalance. In addition, the supporting pressure changed little, but the pressure fluctuation and imbalance decreased with increasing foam injection ratio. The results indicate that face stability and chamber pressure control require a combined adjustment of auxiliary air pressure and foam injection ratio.

Wong et al. (2024) presented a two-stage model based on the elastic continuum approach and nonlinear near-pile stress transfer mechanism to study the three-dimensional behavior of piles under the influence of an advancing TBM. This continuum analysis is compared with the results of centrifuge tests carried out using a novel miniature TBM excavating in clay in the vicinity of piled foundations. The greenfield tunneling-induced movements, a key input for the two-stage model, were estimated empirically by back-analyzing the surface greenfield settlements and pile settlements measured during the centrifuge tests. The predictions of tunneling-induced and post-tunneling pile behavior obtained with the continuum approach are compared with the measured settlements and axial forces for a row of single piles under constant external load. This provides further insights into the effects of TBM advancement on deep foundations. Future work will address pile groups with rigid elevated caps.

3 OTHER TOPICS

Beyond tunneling, the remaining papers submitted explored other geotechnical phenomena using numerical approaches, including the influence of water level fluctuations, seepage behavior, the influence of loading history, and grouting field trials. Since these are not as concentrated as the tunneling-related work, I have grouped them together in this section.

The construction of diaphragm wall panels inevitably changes the initial stress condition and causes movements in the surrounding soil mass, which will also affect the subsequent excavation performance. *Dong* (2024) critically evaluated the conventional ‘wished-in-place’

(WIP) assumption commonly used in the design and analysis of diaphragm wall installations for deep excavations. His study, which utilized a realistic modeling procedure simulating the actual construction sequence, found that the installation of diaphragm wall panels had altered the initial stress conditions and caused movements in the surrounding soil. The research revealed that the WIP assumption could lead to underestimations of potential wall deformation and ground movement, resulting in significant discrepancies between computational predictions and field measurements. It is demonstrated that including the wall installation effects in finite element analysis provided a more accurate assessment of the ground response and was essential for critical projects, challenging the adequacy of simply adjusting the lateral earth pressure coefficient traditionally used to account for these effects.

Boldini et al. (2024) reported on a field trial conducted near the Campo di Marte railway station to assess grouting strategies for ground compensation. A three-dimensional numerical model is presented, incorporating both the grouted volumes and the injection sequence. The model represents the grouted area with non-porous soil bulbs with increased stiffness and simulates expansion through applied volumetric strains. The stepwise activation of injections from tubes-à-manchettes is accurately mirrored in the model. Field-measured displacements validate the effectiveness of the strategy, particularly the application of non-isotropic volumetric strains to replicate observed ground heave.

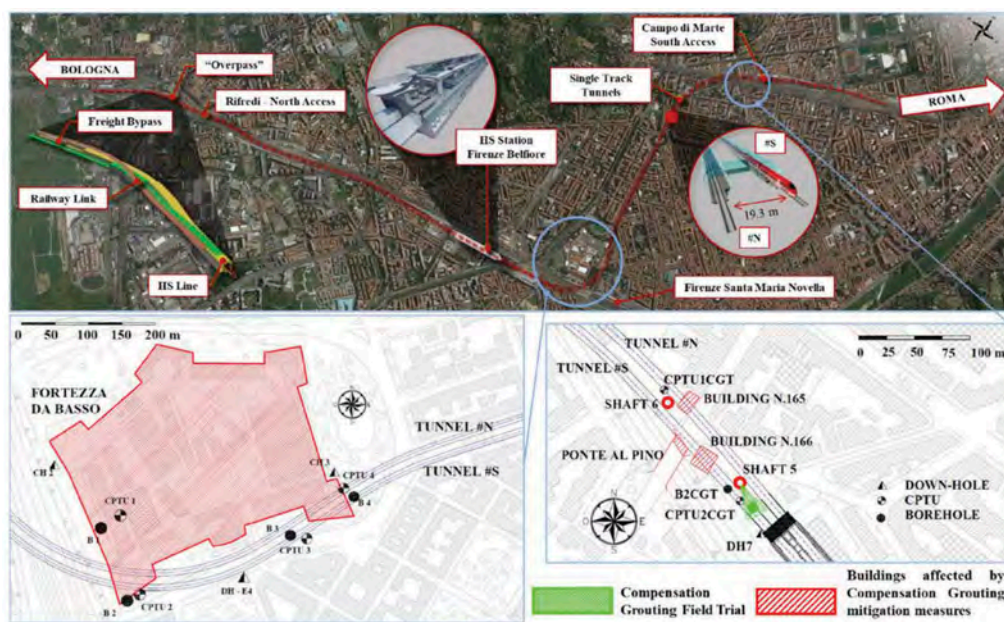


Figure 5. HS/HC Florence bypass project: Fortezza da basso and compensation grouting field trial (from *Boldini et al. (2024)*).

4 DISCUSSION

Although the contributed papers cover a wide range of numerical modeling in geotechnical engineering, those focusing on methodology development are rather limited. Herein, the author wishes to underscore three notable aspects of advancement that merit the readers' attention.

The first area is the particle-based numerical approaches, such as the Material point method (MPM) (*Soga et al., 2016*), Smoothed Particle Hydrodynamics (SPH) (*Bui and Ng, 2017*), and Peridynamics (PD) (*Silling and Lehoucq, 2010*). These approaches have gained

popularity in past years due to the rapid development of computing infrastructure. By representing the problem domain into a large set of particles, they are capable of modeling various challenging scenarios, including large deformation, strong discontinuity, and hydro-mechanical coupling, easing the difficulty of conventional mesh-based approaches.

The second area is multiscale modeling. In contrast to conventional continuum approaches that depend on specific constitutive models to define stress-strain relationships, multiscale modeling employs a representative volume element (RVE) to accurately capture the mechanical behavior of the material being modeled. Various strategies have been explored, including the usage of a micro-mechanical model, e.g., Chang-Hicher model (*Zhao et al., 2018*) and the direct simulation of a DEM packing (*Liang and Zhao, 2019*). Both routes show great success in modeling intricate phenomena of granular media, like anisotropy. Notably, *Liang et al. (2022)* has presents a straightforward implementation and a scalable high-performance computing enhancement for the DEM-based multiscale modeling, which could offer the community an alternative for cross-scale analyses.

Lastly is the boost of the development of Machine Learning (ML), which is poised to revolutionize conventional numerical modeling. By training networks with data derived from advanced constitutive models or physical tests, ML serves as a sophisticated surrogate for traditional constitutive relationships (*Zhang et al., 2024; Guo and YIN, 2024*). Concurrently, through introducing well-known physical constraints or laws into the network to ensure compliance with exact boundary conditions, the resultant Physics-Informed Neural Networks (PINN) could directly solve time-dependent partial differential equations in geotechnical engineering, enabling them to yield highly accurate solutions for boundary value problems (*Wang et al., 2023; Sukumar and Srivastava, 2022*).

5 CONCLUSION

The 12 papers encompassed in the theme of “Constitutive and Numerical Modelling” span a diverse array of topics, ranging from numerical analyses of tunneling projects around the globe to the development of analytical solutions. These contributions compile a significant reference source for the practical implementation of numerical approaches in the field, the insights from these studies will be pivotal in shaping future design and construction strategies.

REFERENCES

- Boldini, D., Lusini, E., Spaggiari, C., & Fuoco, S. (2024). 3D numerical modelling of a compensation grouting field trial in alluvial soils. IS-Macau 2024.
- Bui, H. H., & Nguyen, G. D. (2017). A coupled fluid-solid SPH approach to modelling flow through deformable porous media. *International Journal of Solids and Structures*, 125, 244–264.
- Dong, Y.P. (2024). Effect of diaphragm wall construction process on the performance of braced excavation. IS-Macau 2024.
- Guo H, Yin Z-Y (2024). A novel physics-informed deep learning strategy with local time-updating discrete scheme for multi-dimensional forward and inverse consolidation problems. *Comput. Methods in Appl. Mech. Eng.*, 421: 116819.
- Liang, W., & Zhao, J. (2019). Multiscale modeling of large deformation in geomechanics. *International Journal for Numerical and Analytical Methods in Geomechanics*, 43(5), 1080–1114.
- Liang, W., Wu, H., Zhao, S., Zhou, W., & Zhao, J. (2022). Scalable three-dimensional hybrid continuum-discrete multiscale modeling of granular media. *International Journal for Numerical Methods in Engineering*, 123(12), 2872–2893.
- Liu, Y., Wu, K., Fan, Z., Dou, Z., Liu, Z., & Zhang, Q. (2024a). Numerical simulation of lake crossing construction under double overhead tunnel considering flow-solid coupling. IS-Macau 2024.
- Silling, S. A., & Lehoucq, R. B. (2010). Peridynamic theory of solid mechanics. *Advances in applied mechanics*, 44, 73–168.
- Soga, K., Alonso, E., Yerro, A., Kumar, K., & Bandara, S. (2016). Trends in large-deformation analysis of landslide mass movements with particular emphasis on the material point method. *Géotechnique*, 66(3), 248–273.

- Sukumar, N., & Srivastava, A. (2022). Exact imposition of boundary conditions with distance functions in physics-informed deep neural networks. *Computer Methods in Applied Mechanics and Engineering*, 389, 114333.
- Ung, W.L., Wang, Y-H., & Lok, T.M.H. (2024). Numerical analysis of ground movement due to shield tunneling at NAPE, Macau. IS-Macau 2024.
- Wang, J., Mo, Y. L., Izzuddin, B., & Kim, C. W. (2023). Exact Dirichlet boundary Physics-informed Neural Network EPINN for solid mechanics. *Computer Methods in Applied Mechanics and Engineering*, 414, 116184.
- Yu, J., Li, H., Huang, M., Leung, C. F., & Lim, J. (2024a). Numerical analysis of rectangular tunnel boring machine induced ground settlement. IS-Macau 2024.
- Yu, Y., Franza, A., Neves, L., & Marshall, A. M. (2024b). Effect of infill nonlinearity on frame response to tunnelling. IS-Macau 2024.
- Zhang P, Yin Z-Y*, Sheil B (2024). A physics-informed data-driven approach for consolidation analysis. *Géotechnique*, <https://doi.org/10.1680/jgeot.22.00046>.
- Zhao, C. F., Yin, Z. Y., & Hicher, P. Y. (2018). A multiscale approach for investigating the effect of microstructural instability on global failure in granular materials. *International Journal for Numerical and Analytical Methods in Geomechanics*, 42(17), 2065–2094.
- Zhao, C.-F., Yin, Z.-Y., & Hicher, P.-Y. (2018). A multiscale approach for investigating the effect of microstructural instability on global failure in granular materials. *International Journal for Numerical and Analytical Methods in Geomechanics*, 42(17), 2065–2094.
- Zheng, D., Bezuijen, A., & Zhang, Q. (2024). Surface tension of foam and its influence on tunneling. IS-Macau 2024.
- Zhong, J., Wang, S., & Yuan, X. (2024). Numerical modeling of muck movement and chamber pressure distribution during EPB shield tunneling with auxiliary air pressure balance mode. IS-Macau 2024.

3D numerical modelling of a compensation grouting field trial in alluvial soils

D. Boldini & E. Lusini

DICMA, Sapienza University of Rome, Rome, Italy

C. Spaggiari

DISG, Sapienza University of Rome, Rome, Italy

S. Fuoco

INFRARAIL, Florence, Italy

ABSTRACT: The underground bypass of the new high-speed and high-capacity railway line in Florence (IT) involves the construction of about 7 km of twin tunnels beneath the historic city centre. To minimise the impact of tunnelling works, mitigation measures using the compensation grouting technique were integrated into the design stage with the aim of limiting the induced settlements and the risk of damage to nearby structures. A field trial near the *Campo di Marte* railway station was carried out to assess the efficiency of the compensation measure and establish a successful grouting strategy. This paper presents a three-dimensional numerical model of the field trial, explicitly implementing both the grouted volumes and the injection sequence. The grouted area is represented by non-porous soil bulbs with enhanced stiffness properties and the expansion process is simulated through imposed volumetric strains. The injections from each valve of the sleeved pipes (tubes-à-manchettes) are activated in a stepwise procedure, mirroring the injection sequence. The effectiveness of the proposed strategy is validated against recorded displacements in the field trial, demonstrating that the application of non-isotropic volumetric strains (i.e., vertical strains larger than horizontal ones) is able to accurately reproduce the observed heave.

1 INTRODUCTION

The city of Florence (IT), globally renowned for its cultural and historical significance, is undergoing excavation work to improve national mobility and alleviate its impact on the environment. Started in 2023, the construction of a twin-bore tunnel and modern railway station (*Firenze Belfiore*) aims to enhance train transit and reduce journey times along the existing HS/HC railway system, as part of the Scandinavian-Mediterranean Corridor (TEN-T Network).

Given the project location within the city centre, an extensive assessment was conducted on over 230 buildings to identify any potential interference with existing structures and to develop appropriate mitigation strategies, such as compensation grouting, to keep deformations below acceptable thresholds (Zurlo & Sorbello 2022). Furthermore, the interaction between twin tunnel excavation and the *Fortezza da Basso* (a notable Renaissance fortress in the Historic Centre of Florence, listed as a UNESCO World Heritage site from 1982) was investigated using a comprehensive 3D finite element analysis for class-A prediction of the induced level of damage in an optimal tunnel scenario (i.e. considering a surface volume loss of 0.5%) to exclude any potential induced damage (Boldini et al. 2023). As part of the scheduled interventions utilising the compensation grouting technique, preparative works have been initiated involving a compensation field trial close to the *Campo di Marte* railway station, where *Ponte al Pino* is located (Figure 1).

This paper describes the performed Compensation Grouting Trial (CGT) and the 3D numerical model implemented to simulate the grouting process. The proposed method adopts a novel

formulation based on the grout efficiency factor to assess the appropriate strain magnitude to simulate the grout expansion, and aids in gaining further insight into the complex interaction between the volume of injected grout and soil response in terms of vertical displacements.

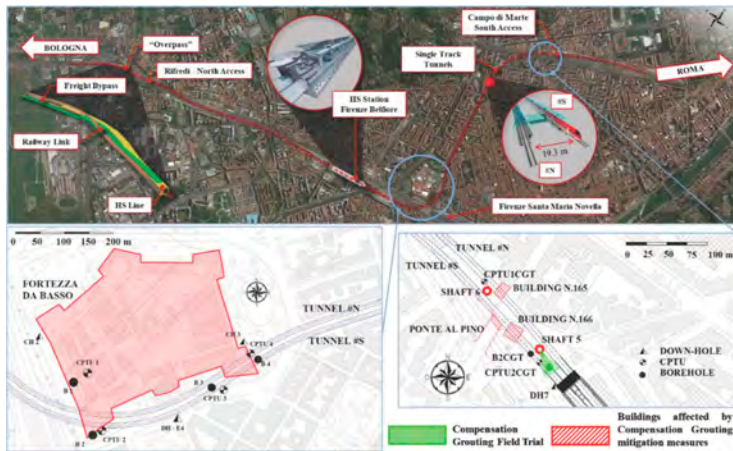


Figure 1. HS/HC Florence bypass project: *Fortezza da Basso* and compensation grouting field trial.

2 THE FIELD TRIAL

2.1 Site conditions

The CGT is located in an area characterised by the presence of made ground, gravels in a sandy matrix from the Arno river Supersystem, and silty clays and clayey silts with lenses and layers of gravel from the Florencia-Prato-Pistoia lake Supersystem.

Geotechnical characterization was conducted based on the results of site investigations and the laboratory tests closest to the CGT carried out during the 1997 and 2007 campaigns (Figure 1). The site investigation included the borehole B2CGT, two cone penetration tests with piezocone (CPTU1CGT and CPTU2CGT) and a downhole seismic test (DH7). Table 1 synthesizes the 6-layer geotechnical model; the piezometric surface is located at 9 m below the ground surface (42 m a.s.l.) and the pore pressure distribution is hydrostatic. Table 2 summarizes the main

Table 1. Site stratigraphy.

Layer	Elevation (m a.s.l.)		Description
	from	to	
R	51.0	47.5	made ground: coarse-grained material in a silty matrix
LA1	47.5	45.0	silty layer with very consistent clay
SL	45.0	43.0	fine silty-sandy and weakly clayey layer
GSL1	43.0	37.5	gravelly layer in a sandy-silty matrix
LA2	37.5	34.0	silty layer with very consistent clay
GSL2	34.0	28.5	gravelly layer in a silty matrix

Table 2. Properties of the soil layers.

Layer	γ_{dry} (kN/m ³)	γ_{sat} (kN/m ³)	ϕ' (°)	c' (kPa)	$K_{0,NC}$ (-)	OCR	$K_{0,OC}$ (-)
R	18.5	18.5	41.5	0	0.337	-	0.337
LA1/2	18.5	20.0	25.0	20.0	0.577	2.25	0.813
SL	17.0	17.0	30.5	5.5	0.494	2.85	0.838
GSL1/2	20.0	20.0	45.0	0	0.293	-	0.293

properties of the soil layers. K_0 values for coarse-grained soils were derived from Jaky's equation (1994), while the equation from Mayne & Kulhawy (1982) was used for overconsolidated strata.

2.2 Methodology and grouting design

Compensation grouting field trials are commonly employed to calibrate the adequate application of compensation injections (e.g. Sciotti et al. 2012). Additionally, numerical studies have been proposed to simulate the grouting process and to assess its impact. They consist in the application of internal pressure or of volumetric strains to interface or solid elements (e.g. Addenbrooke et al. 2002, Schweiger et al. 2004, Wisser et al. 2005).

Even when considering 3D conditions, a plane state of deformation can be assumed around the TAMs. The volumetric strain, ε_{vol} , to be applied to the cylindrical solid elements, representing the pre-treated soil volumes, can be therefore calculated as in Schweiger et al. (2004), modified after Masini et al. (2014) to account for the different sources of grouting inefficiency:

$$\varepsilon_{vol} = \varepsilon_{zz} + \varepsilon_{xx} = \eta_F \frac{V_{inj}}{\pi a^2} = \frac{\xi}{\eta_S \eta_G} \frac{V_{inj}}{\pi a^2} \quad (1)$$

where V_{inj} is the grout injected volume and a is the radius of the cylindrical solid elements. ξ is the grout efficiency factor that represents the ratio between the surface heave volume generated by the grouting and the volume of the injected material. It is composed of three multiplicative factors: the grout filtration (η_F), the soil compaction (η_S) and the geometry effect (η_G).

According to Nicolini & Nova (2000), the single components of the volumetric strain can be obtained as a function of a size parameter, Δ , here made coincident with ε_{vol} from Equation 1, and a shape parameter, α , varying from 0 (i.e., isotropic expansion) to 1 (i.e., vertical expansion only). This approach allows to account for non-isotropic strains and to identify a preferential direction for the grouting diffusion. Differently from the original formulation, the version here applied considers a plane state of deformation around the cylinder: as such, the strain component along the longitudinal axis of the cylinder, ε_{yy} , is considered as always null and the isotropic part is divided by two instead of three:

$$\begin{cases} \varepsilon_{zz} = \frac{1}{2}(1-\alpha)\varepsilon_{vol} + \alpha\varepsilon_{vol} \\ \varepsilon_{xx} = \frac{1}{2}(1-\alpha)\varepsilon_{vol} \end{cases} \quad (2)$$

where z is the vertical direction and x is the perpendicular one transversal to the cylinders (Figure 2).

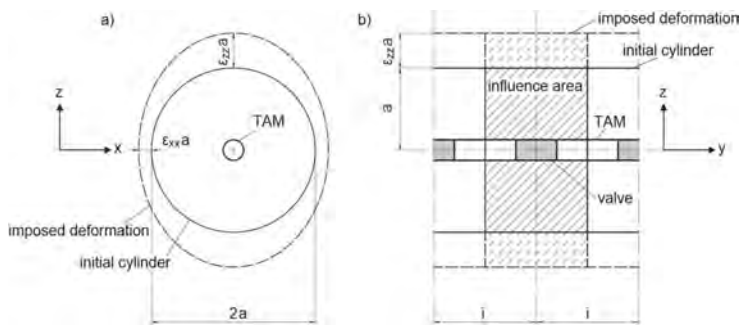


Figure 2. Scheme of the grouting strategy: a) front view (a = radius); b) side view (i = valve inter-axis).

2.3 Observed behaviour

The field trial was carried out near shaft no.5 and consisted of two distinct zones formed by two different reinforced concrete (RC) plates. The present study focuses on one of them (RC plate 2),

with a plan size of 8x8 m and an area of influence equal to 240 m² (Figure 3). Throughout the testing the vertical displacements of the plate were measured at 9 monitoring points.

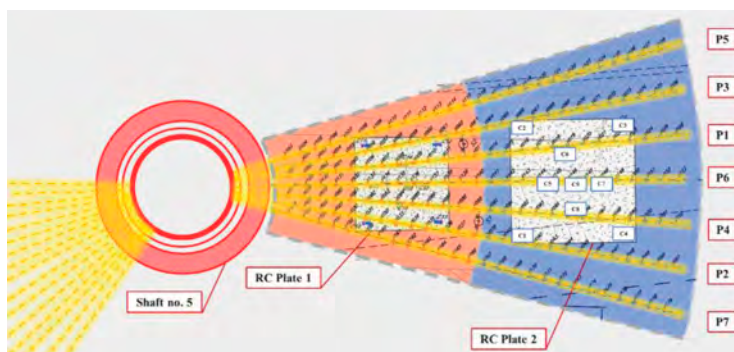


Figure 3. Location of RC plate 2, with TAMs array from shaft no. 5, close to *Campo di Marte*.

The CGT included the following operative phases: installation of tubes-à-manchettes (TAMs), pre-treatment (PT) phase, preliminary (PR) phase, and the proper mitigation phase, subdivided into two further stages (M1 and M2).

The seven TAMs, each with a length of 29.6 m, were installed approximately 7.5 m below the RC plate and arranged in a fan array layout, with each tube containing 26 valves. During the PT phase, a total of 29 m³ were injected during five different sub-stages. The PR phase was carried out with a uniform simultaneous injection with volumes of 100 l/valve (total injected volume of 4.8 m³), allowing the estimation of the initial grout efficiency factor ($\xi = 9.4\%$). This parameter was averaged based on the areas of influence identified around the nine displacement monitoring points on the RC plate.

The subsequent mitigation phase comprised two different stages: a homogeneous one (M1) and a multi-stage phase (M2), involving the application of a differential strategy from different valves depending on the measured heaves. The homogeneous phase resulted in a simultaneous injection of 3.4 m³ and an estimated ξ of 12.4%, providing the target injected volume for the next phase. In the second stage (corresponding to an injected volume of 1.1 m³), excessive heave values were recorded, if compared to those expected, especially at the central control points. In addition, a shifting effect of some parts of the plate was observed and the final estimated $\xi = 21\%$ value has to be considered as overestimated. It turned out that the process was less controllable as the injections were more differentiated.

Figure 4 shows the response of the RC plate to all the described stages, achieved by conducting Kriging interpolation over the recorded heaves of the control points. In general, an inclined heave can be observed during the pre-treatment and preliminary stages, while progressively higher heaves are recorded at the central points during the mitigation stages. Table 3 lists the measured displacements, total injected volumes per phase, and the calculated grout efficiency factor.

3 FINITE ELEMENT MODELLING

3.1 *The geotechnical model*

The finite element analyses were conducted with the PLAXIS 3D[®] software (Brinkgrave et al. 2021). A soil domain 120.0×120.0×22.5 m was chosen for minimizing boundary effects. The model reproduces the 6 soil layers and the local hydraulic conditions.

A concrete plate was placed in the centre of the model, resting on the ground surface, with a uniform thickness of 0.1 m. A simple isotropic linear-elastic material model was assigned to the corresponding solid volume ($\gamma = 27 \text{ kN/m}^3$, $E = 37 \text{ GPa}$, $\nu = 0.2$). A roughness angle equal to that of the underlying soil was considered for the soil-plate interface.

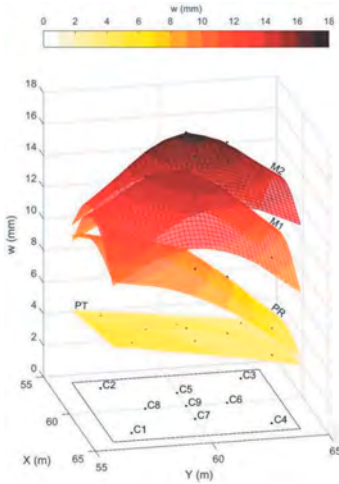


Figure 4. Deformed plate from cumulated control-point (C1–C9) displacements at the end of each injection phase (PT = pre-treatment, PR = preliminary stage, mitigation M1 = 1st stage, M2 = 2nd stage).

All the soil layers were modelled with the Hardening Soil Model with Small Strain Stiffness (HSsmall), an advanced elastoplastic constitutive model (Benz 2007) which could account for the dependency of soil stiffness on the stress level, its progressive decay with increasing strain level, and the early accumulation of hardening plastic deformations. The profile of small shear strain stiffness, G_0 , with depth, z , was determined by calibrating the model parameters G_0^{ref} and $\gamma_{0.7}$ against the down-hole DH7 experimental results (Figure 5). The parameters adopted in HSsmall for different layers are summarised in Table 4. The DH7 experimental profile was slightly adjusted in the vertical direction to align with the soil stratigraphy at the field trial site, which is extremely close to the borehole B2CGT and therefore arguably shares the same stratigraphy.

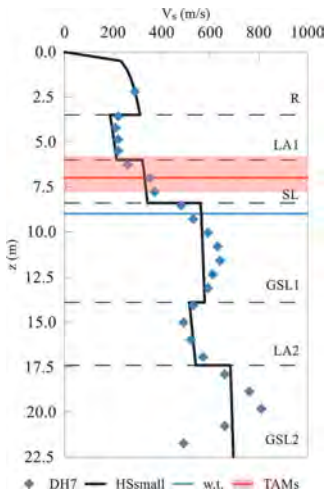


Figure 5. Calibration of HSsmall model from DH7 test results.

Table 3. Incremental vertical displacements per phase and final cumulated displacements at plate control points.

Control points	Vertical displacements (mm)				
	PT	PR	M1	M2	Final
C1	5.7	4.5	1.4	0.9	12.5
C2	4.6	4.9	1.4	1.2	12.1
C3	3.5	1.6	4.8	2.5	12.4
C4	4.3	1.7	4.5	3.7	14.2
C5	4.3	4.7	4.9	2.2	16.1
C6	4.4	3.6	5.5	3.0	16.5
C7	4.9	4.6	4.7	2.4	16.6
C8	5.0	5.5	4.2	1.5	16.2
C9	4.9	5.0	5.0	2.4	17.3
V_{inj} (m ³)	28.9	4.8	3.4	1.1	38.2
ξ (%)	3.0	9.4	12.4	20.9	-

Table 4. Soil parameters for HSsmall.

Parameters	Soil layer			
	R	LA1/2	SL	GSL1/2
ϕ°	41.5	25.0	30.5	45.0
ψ°	0	0	0	0
m (-)	0.3	0.8	0.4	0.2
v_{ur} (-)	0.2	0.25	0.2	0.2
G_0^{ref} (MPa)	286.8	91.3/318.9	188.72	733.9/998.9
E_{ur}^{ref} (MPa)	137.7	45.6/190.9	90.58	352.3/479.5
E_{50}^{ref} (MPa)	45.9	15.2/63.7	30.19	117.4/159.8
E_{oed}^{ref} (MPa)	45.9	15.2/63.7	30.19	117.4/159.8
$\gamma_{0.7}$ (%)	0.01	0.01	0.01	0.01
p^{ref} (kPa)	100	100	100	100
R_f (-)	0.9	0.9	0.9	0.9

3.2 Modelling of compensation grouting

The compensation grouting injections were modelled by introducing cylindrical soil volumes with modified stiffness properties around the TAMs, and concurrently applying volumetric strains in the global vertical (ϵ_{zz}) and x-direction (ϵ_{xx}). Four of the seven cylinders were completely immersed in the SL layer, the remaining three partly affected the LA1 layer. The soil stiffness inside the cylinders was modified as a function of the intensity of grouting, I_g , defined as the ratio between grout volume (i.e., recorded injected volumes of grout) and the grouted soil volume (i.e., initial cylinder volumes). The TAM arrangement in plan view was derived from technical drawings, with the central TAM oriented along the global y-axis of the model, and the other 6 TAMs arranged as spokes of a wheel, owing to the common origin in the access shaft. They were rotated of 5° to one another, resulting in an overall opening angle of 30° (Figure 6). Each cylinder was 13 m long, subdivided into 13 segments representing the influence volume of each valve ($i = 1.0$ m).

Following the actual grouting sequence, the analysis was subdivided into 6 consecutive phases. After the initialisation of initial stresses following the K_0 procedure, the concrete plate was activated at the ground surface in the 2nd phase. In the 3rd phase (i.e., the PT phase), the soil cylinders around the TAMs were activated, and their stiffness was modified according to the chart from Falk (1998), considering $I_g = 15\%$. In addition, the unit weight of the cylinders was increased, according to the injected volume, and the volumetric strains were prescribed. In the next three phases, corresponding to the preliminary and mitigation stages, only volumetric strains were applied, as summarised in Table 5, considering the further stiffening and overloading of the grouted soil body as negligible. The last phase (i.e., the M2 phase) was further subdivided into 8 sub-phases, accounting for the real injection sequence of the different groups of valves, as specified in the field-trial technical report (Passante AV, 2012).

Volumetric strains were separately calculated for each valve according to Equations 1-2, starting from the injected volume data for all phases as reported in the technical papers. The subdivision into the z- and x-direction was determined on the basis of simple considerations: i) in the initial stress condition, $K_0 \approx 0.8$ in the LA1 and SL layers, suggested a nearly isotropic subdivision into vertical and horizontal components in PT phase; ii) in the following phases

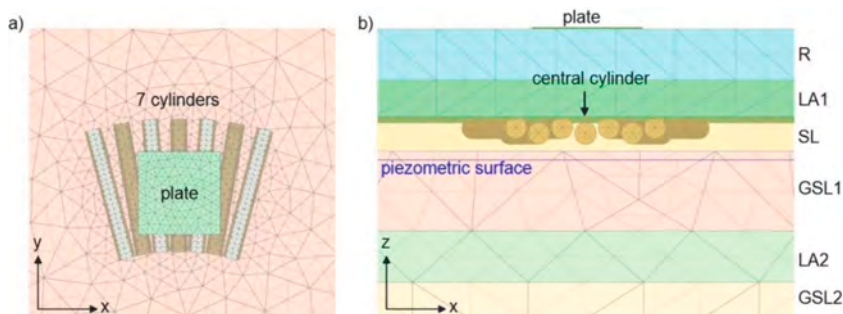


Figure 6. 3D model of the plate and the cylinders: (a) top view, (b) front view.

Table 5. Modifications to the soil parameters inside the cylinders and calibration parameters.

Phase	γ_{unsat} (kN/m ³)		G_0^{ref} ($E_{\text{ocd}}^{\text{ref}}$) (MPa)		ξ (%)	η_F (%)	α (-)
	LA1	SL	LA1	SL			
1 Initial	18.5	17.0	91.3(45.6)	188.7(90.58)	-	-	-
2 Plate activation	18.5	17.0	91.3(45.6)	188.7(90.58)	-	-	-
3 PT	21.5	20.0	456.4(228.2)	754.9(362.3)	3.0	5.6	0.0
4 PR	21.5	20.0	456.4(228.2)	754.9(362.3)	9.4	16.5	0.6
5 M1	21.5	20.0	456.4(228.2)	754.9(362.3)	12.4	21.8	0.6
6 M2	21.5	20.0	456.4(228.2)	754.9(362.3)	20.9	36.7	0.6

the proportion was made varying toward a predominant deformation in the vertical direction. This assumption was based on the idea that repeated injections of grout into the soil would eventually result in a stress state in which the effective horizontal stress exceeds the vertical one and preferential horizontal fractures develop (Bezuijen et al. 2011, Falk 1998).

Parameters α and η_F were treated separately: while the first was defined on the basis of theoretical considerations, the second was calibrated in order to obtain a comparable level of displacements with monitoring data at the control points. Laboratory results in silty soils show a η_F in the range 55-85% (Masini et al. 2014), which are expected to further reduce in sandy soil and in field conditions.

3.3 Results and comparison with field data

The simulated and measured displacements of the plate were in good agreement at the end of the last mitigation phase (Figure 7a), even if a larger curvature was observed in the FE results, as already noticed in Masini et al. (2014). The absolute difference between maximum displacements, $\delta = w_{\text{simulated}} - w_{\text{measured}}$, at the end of phase M2 is shown in Figure 7b: the minimum values were about -3 mm (-18%) along two of the four edges of the plate, while for more than 50% of the surface the difference was less than -9% of the measured values (i.e., reconstructed from control points). In Figure 7c the progressive heaving of the plate during all the grouting phases together with the non-uniform deformation of the central cylinder segments is shown. The maximum heave of the plate at C9 is 17.5 mm, about 1% more than the corresponding recorded value.

The simulation of the single phases was not always able to catch the asymmetry of the displacement field induced on the real plate, despite the accurate modelling of (a) the TAMs arrangement, (b) the grout volumes injected per valve and (c) the differential grouting strategy in phase M2. In particular, the simulation did not reproduce the inclination of the plate during the PT and PR phases, when the edge close to C1 and C2 experienced the largest heave. This may be due to the complex stratigraphy in the vicinity of the field trial site, which can be inferred from the analysis of boreholes, and might cause differential displacements and/or affect the permeability around the TAMs and, consequently, the grout efficiency.

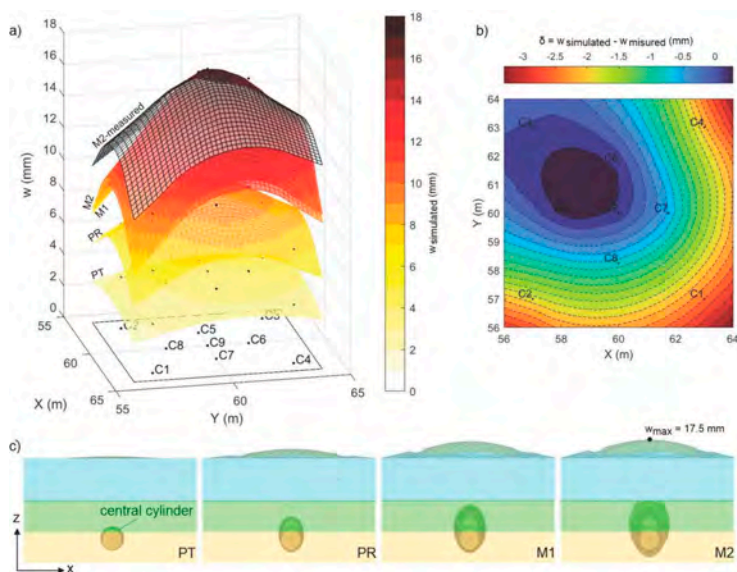


Figure 7. FE results: (a) deformed plate at the end of each injection phase (compared to measured final displacements); (b) difference between simulated and measured displacements (phase M2); (c) deformed mesh of the central cylinder at depth and of the plate at ground surface in all grouting phases.

4 CONCLUSIONS

The paper summarises the numerical modelling of a CG field trial carried out in preparation for the excavation of the high-capacity railway line tunnel below the Florence city centre.

Despite the many practical details of the experimental campaign, the partially simplified numerical procedure was able to capture the displacement field generated by the compensation grouting injections, also thanks to the use of an advanced soil constitutive model properly calibrated in terms of stiffness. While the proposed strategy is highly site-specific and demands careful calibration, it has the potential to assist practitioners in determining the volumes to be injected during full-scale mitigation interventions.

The calibration of injection parameters (i.e. shape factor α and grout filtration efficiency factor η_F) resulting from this study will allow to investigate the effect of compensation grouting in the occurrence of an unlikely critical scenario (i.e. a surface volume loss of 1.5%) during tunnelling below the *Fortezza da Basso*, characterised by similar subsoil conditions. In a unique 3D finite element model, the interaction among tunnelling, soil and structural response, and grouting processes will be simulated, thus permitting a more detailed assessment of the protective effect of the mitigation strategy.

REFERENCES

- Addenbrooke, T.I., Ong, J.C.W. & Potts, D.M. 2002. Finite-element analysis of a compensation grouting field trial in soft clay. *Geotechnical Engineering* 155(1): 47–58. 12546.
- Benz, T. 2007. Small-strain stiffness of soils and its numerical consequences. PhD thesis. Universität Stuttgart.
- Bezuijen, A., te Grotenhuis, R., van Tol, A.F., Bosch, J.W. & Haasnoot, J.K. 2011. Analytical Model for Fracture Grouting in Sand. *American Society of Civil Engineers* 137(6): 611–620
- Boldini, D., Spaggiari, C., Abul, J. K., Fuoco, S. & Lusini, E. 2023. Class A predictions of damage level in a historical fortress induced by twin tunnelling. In *Proc. ITA-AITES World Tunnel Congress 2023 (WTC 2023)*, Athens, 12-18 May 2023. London: CRC Press. DOI:10.1201/9781003348030-215
- Brinkgreve, R.B.J., Kumarswamy, S., Swolfs, W.M., Fonseca, F., Ragi Manoj, N., Zampich, L.M. & Zalamea, N. 2021. *PLAXIS 3D CONNECT* Edition V21.01 Manual. ISBN: 9789076016276
- Falk, E. 1998. *Soil improvement by injection of solid material with hydraulic energy*. Ph.D. Thesis, Institut für Grundbau und Bodenmechanik, Technische Universität Wien (in German).
- Jaki, J. 1944. The coefficient of earth pressure at rest. *Journal of the Society of Hungarian Architects and Engineers*. 355–358
- Nicolini, E. & Nova, R. 2000. Modelling of a tunnel excavation in a non-cohesive soil improved with cement mix injections. *Computers and Geotechnics* 27: 249–272.
- Masini, L., Rampello, S. & Soga, K. 2014. An approach to evaluate the efficiency of compensation grouting. *J. Geotech. Geoenviron. Eng.* 140(12): 04014073. DOI:10.1061/(ASCE)GT.1943-5606.0001180
- Mayne, P. V. & Kulhawy, F. H. 1982. K_0 -OCR relationships in soil. *Journal of the Geotechnical Engineering Division*. 6: 851–872.
- Passante AV, 2012. *Progetto Esecutivo*. Campo prova: relazione di interpretazione finale.
- Schweiger, H.F., Kummerer, C., Otterbein, R. & Falk, E. 2004. Numerical modelling of settlements compensation by means of fracture grouting. *Soil and Foundations* 44(1): 71–86.
- Sciotti, A., Desideri, A., Saggio, G. & Kummerer, C. 2012. Mitigation of the effects induced by shallow tunneling in urban environment: the use of ‘compensation grouting’ in the underground Line B1 works in Rome. In *Proc. 7th Intern. Symp., Rome*, 16-18 May 2011. London: Taylor & Francis Group.
- Wisser, C., Augarde, C.E. & Burd, H.J. 2005. Numerical modelling of compensation grouting above shallow tunnel. *International Journal for Numerical and Analytical Methods in Geomechanics* 29(5): 443–471. DOI:10.1002/nag.421
- Zurlo, R. & Sorbello, R. 2022. Florence high-speed railway underpass – Preservation of the Italian Renaissance pre-existing structures and historical sites. In *Proc. 3rd Intern. ISSMGE TC301 Symp., Napoli*, 22-24 June 2022. London: CRC Press.

Effect of diaphragm wall construction process on the performance of braced excavation

Y.P. Dong

Technical University of Denmark, Kgs Lyngby, Denmark

ABSTRACT: The construction of diaphragm wall panels inevitably changes the initial stress condition and causes movements in the surrounding soil mass, which will also affect the subsequent excavation performance. Majority of current design and analysis of deep excavations assume that the diaphragm wall is ‘wished-in-place’, largely because of the complexities involved to consider detailed wall installation process. Limited analyses suggested that neglecting the wall installation effect would underestimate the ground movement, structure deformation, and strut load during the major excavation stages. This paper develops realistic modelling procedure to simulate the complete construction process of diaphragm wall panels and subsequent excavation, and compares with the analysis assuming the wall ‘wished-in-place’. The ‘wall-installation-modeled’ approach can improve the accuracy of prediction and reduce discrepancy in the back analysis of deep excavations.

1 INTRODUCTION

Reinforced concrete diaphragm walls are widely used in underground constructions as temporary or permanent earth retaining structures. However, the diaphragm wall panel installation process inevitably changes stress conditions within the ground and can also induce significant ground movements (Poh and Wong 1998, Dong and Whittle 2022, Dong 2023b). These changes can become significant in cases where the construction is close to adjacent facilities (Chan and Yap 1992, Thorley and Forth 2002), and will also affect the ground response and structure performance during subsequent excavation process.

Most numerical analyses of excavation performance ignore the effects of wall installation (i.e., the wall is ‘Wished-In-Place’, WIP; e.g., Whittle et al. 1993, Zdravkovic et al. 2005, Dong et al. 2016). There have been a number of studies to simulate stress changes associated with diaphragm wall construction and their impacts (‘Wall Installation Modelled’; WIM) on subsequent predictions of excavation support performance (comparing results for WIM and WIP analyses, Schäfer and Triantafyllidis 2006; Conti et al. 2012). For example, Schäfer and Triantafyllidis (2006) attribute 10-15% of the measured wall deflections and surface settlements during top-down construction of the 17 m deep TNEC basement in Taipei silty clay (Ou et al. 1998) due to effects of diaphragm wall installation. These numerical analyses suggested that modelling the wall installation process can be important to improve the predictive capabilities in the major underground constructions.

This paper develops realistic modelling procedure to simulate the sequential diaphragm wall panel installation process in an idealised deep excavation case, and investigates its interactive effects on the ground response. In addition, braced excavation is conducted subsequently following staged construction sequence. The computed excavation performance are compared with those from WIP analyses to investigate the wall installation effects on the subsequent excavation. The comparison clearly demonstrates that the traditional WIP approach under-predicts the ground movements and wall deformation. It also implies that the WIP

approach can cause large discrepancy between numerical analysis and field measurements in back analysis. Therefore, the WIM approach is suggested in the deep excavation analysis to improve the predictive capabilities.

2 FINITE ELEMENT INVESTIGATION

2.1 Model description

Finite element analyses have been conducted using AbaqusTM (v2020) to simulate the construction process of typical diaphragm wall panels (1.0 m thick, 6.0 m wide, and 30 m deep) and subsequent excavation process, and a quarter-section model is shown in Figure 1. This model is created to represent a moderate size (60m long, 24m wide, and 15m deep) braced-excavation project (with cross-lot steel tube struts) in construction practice, following the typical construction procedure described in Table 1. In brief summary, the whole diaphragm wall is constructed sequentially from primary, secondary, and corner panels, as indicated in Figure 1, and each panel follows the typical installation procedure described in previous sections. The excavation is supported by 3 levels of cross-lot steel tubular struts without preloading, from top to bottom in 4 soil layers. The Two far-field vertical boundaries are free to displace in the vertical direction but constrained against lateral movements, and the bottom is fixed. Excavation of the panels is accomplished by removing elements and imposing a set of boundary tractions along the excavated surface to represent the bentonite slurry and tremie concrete (i.e., the cut surface is assumed impermeable and there is no exchange of fluid with the surrounding soil). Coupled consolidation within the soil mass is simulated in Abaqus/standard using quadratic, hexahedral mixed elements (C3D20RP) with reduced integration.

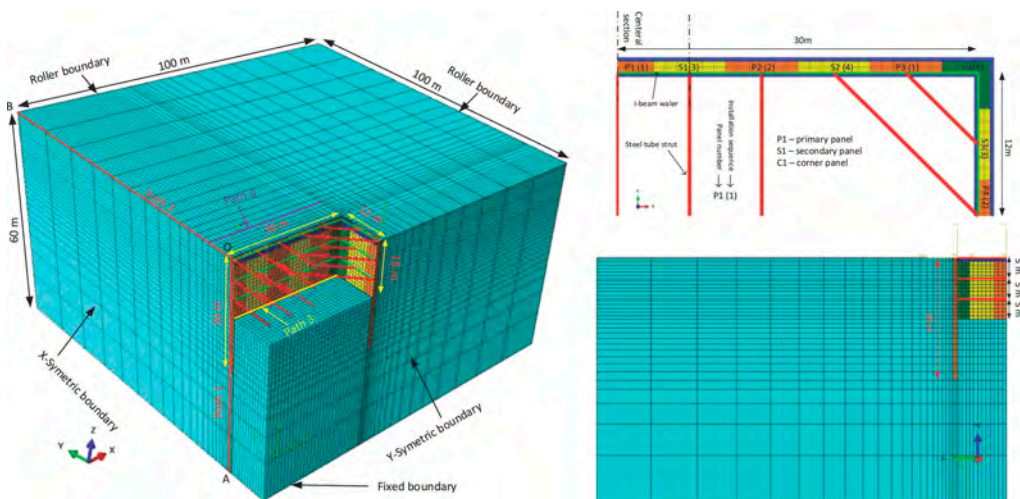


Figure 1. Finite element model of the diaphragm wall installation and braced-excavation.

Effective stress-strain properties of the surrounding ground are represented by the MIT-E3 model (Whittle and Kavvas 1994), using input parameters calibrated for the Boston Blue Clay (Whittle 1993). The MIT-E3 model is a generalized effective stress soil model for predicting the rate-independent behaviour of K_0 normally to moderately overconsolidated clays. The model describes closely the nonlinear and hysteretic nature of the unload-reload process which is related to the diaphragm wall panel installation and major excavation. The MIT-E3 model was implemented into AbaqusTM through a user-specified subroutine (UMAT), using an automatic explicit substepping algorithm with error controls, with details of the integration and verification described in Dong (2023a).

The guidewall is assumed as linear elastic material with the stiffness properties of lean reinforced concrete ($E_v = 20GPa, \nu = 0.2$) for simplicity. The discontinuities between panels is considered by reducing the stiffness of the continuous wall in the wall perimeter direction, and therefore the out-of-plane bending stiffness. The steel tube struts have a diameter of 1000mm and a thickness 15mm. The I-beams waller along the wall have the web and wing size of 500mm and a thickness of 10mm. The steel is assumed to be isotropic linear elastic, with the stiffness properties $E = 200GPa, \nu = 0.2$.

2.2 Analysis procedures

The analysis procedure in the WIM analysis is described in Table 1, which follows the sequence of some typical excavation projects. The trench is excavated under hydrostatic slurry pressure for 48 hours, followed by the concreting process (6 hours for a filling rate of 5m/hour, plus 4 hours for the wet concrete hardening). A rest period of 24 hours is reserved to prepare for the next group of wall installation.

Table 1. Analysis procedures for the panel installation in the base analysis.

Steps	Time (hours)	Description
0		Geostatic step to set up initial stress and pore pressure in the ground.
1	720	Guidewall installation, last for 30 days to consider concrete curing time.
2	48	Trench excavation for primary panels (P1+P2), the slurry level at the trench top, bentonite slurry unit weight $\gamma_b = 10.5 \text{ kN/m}^3$.
3	10	Concreting process using the VP model, with a wet concrete unit weight $\gamma_b = 23 \text{ kN/m}^3$, and filling rate of 5m/hr.
4	24	Post concreting process, concrete hardening
5 - 7	48+10+24	Repeat steps 2-4 to install the primary panels (P3+P4)
8 - 10	48+10+24	Repeat steps 2-4 to install the secondary panels (S1+S2)
11-13	48+10+24	Repeat steps 2-4 to install the secondary and corner panels (S3+C1)
14	24	Excavate the first layer of soils (Exc-1) to elevation -1m
15	240	Install the first level of struts (Strut-1) at elevation 0m
16	72	Excavate the second layer of soils (Exc-2) to elevation -6m
17	240	Install the second level of struts (Strut-2) at elevation -5m
18	72	Excavate the third layer of soils (Exc-3) to elevation -11m
19	240	Install the third level of struts (Strut-3) at elevation -10m
20	72	Excavate the fourth layer of soils (Exc-4) to elevation -15m

In the analysis, the soil is assumed normally consolidated with OCR = 1.0, and the groundwater table is set at 1m below the ground surface. The unit weight of the bentonite slurry is set as 10.5kN/m^3 in the trench excavation, representing an average value of slurry density during the trench excavation (Poh and Wong 1998). The concreting process is simulated by applying a pressure on the trench surface which varies as the wet concrete rises from the trench bottom (the VP model). The VP model was developed by Dong and Whittle (2022) based on analysis of measured data from field and model tests, to address the limitation of the bilinear model in Lings et al. (1994). Figure 2 illustrates the time history of concreting pressures at 6 different depths (for $h_0 = 30\text{m}$ deep trench) as well as the pressure profiles at different time, using selected parameters.

There are 8 wall panels (4 primary panels, 3 secondary panels, and 1 corner panels) in this one quarter excavation analysis, and they are installed sequentially in 4 groups, as shown in Figure 1. This installation sequence is arranged to minimize disturbance to adjacent panels and speed up the construction process, which is normally adopted in practical construction projects.

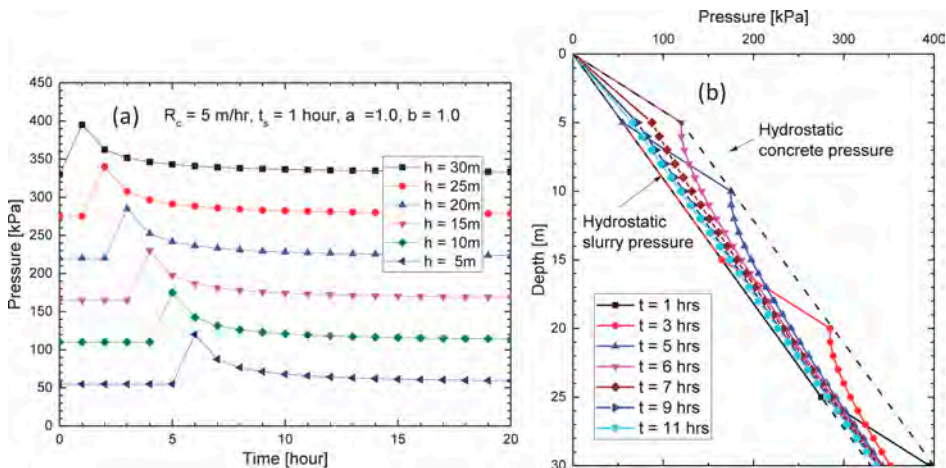


Figure 2. Computed variations of lateral pressures for tremie placement and set-up of wet concrete from the VP model.

Once the whole diaphragm wall construction is completed, the major excavation stages start after 30 days to leave enough time for concrete hardening. The major excavation process, as described in Table 1, is completed in 4 excavation steps and 3 strut installation steps. This is a simplified version based on the practical construction, but detailed process are neglected.

2.3 Strategy of the analysis

The WIM analysis is conducted to (i) find a feasible procedure to incorporate the wall installation process in the braced excavation analysis, (ii) explore the variation of ground response induced by multiple-panel construction prior to the major excavation stage, (iii) investigate the influence of the wall installation on the subsequent excavation performance, and (iv) evaluate the appropriateness of the conventional WIP approach in the design and analysis.

The WIP analysis is conducted as a reference case, in which the whole diaphragm wall are added in one step by switching the material properties. The other steps are the same as the WIM analysis. The comparison is focused on the wall deflection and ground surface settlement, since they are the major concerns in the design process.

3 RESULT INTERPRETATION

3.1 Ground response during the diaphragm wall construction process

The ground response mainly focus on the ground movement, effective lateral stress, pore water pressure at the middle sections of the primary (P1) panel.

Figure 3 illustrates variations of ground response along paths OA and OB at central section of primary panel P1, after each major step of the diaphragm wall construction process (steps 2-14 as described in Table 1). It clearly demonstrates the influence of adjacent panel construction and consolidation effect, especially the neighbouring panel S1. The ground surface settlement increases continuously due to adjacent panel installation, which may cause damage to adjacent facilities. At the end of the diaphragm wall construction, the effective stress and pore water pressure are closer to the initial condition. The pore water pressure may return to initial distribution, depending on the insitu soil permeability and construction duration of the diaphragm wall.

3.2 Diaphragm wall installation effect on the subsequent braced excavation

The current design of braced excavations normally assumes that the wall is wished-in-place (WIP), and the wall is included in the analysis after the geostatic step (by equilibrating the

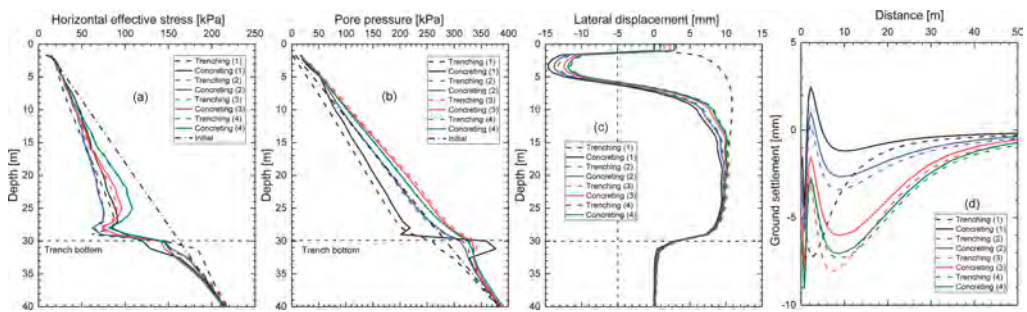


Figure 3. Ground response at the central section of primary panel P1 prior to the major excavation (a) lateral effective stress, (b) pore water pressure, (c) lateral ground movement, and (d) vertical ground movement.

stress with gravity) through switching the material properties from soil to concrete. In this approach, the ground disturbance is quite limited, and the initial ground condition is almost in-situ. The WIP analysis is conducted as a reference case, to investigate the installation effect of diaphragm wall on the braced excavation.

Figure 4 compares the computed excavation performance at the centre of excavation (P1 panel) by the WIM and WIP approaches. It clearly demonstrates that WIP approach significantly underestimates the wall displacement and ground surface settlement, which is consistent with previous preliminary analyses (Schäfer and Triantafyllidis 2006). This is mainly because the WIP approach neglects the change of ground conditions caused by the diaphragm wall installation prior to the major excavation stages. In addition, there are also differences in the earth pressure and pore water pressure changes on the back of the wall after each stage of excavation, which can also explain the differences in the ground and wall movements. This comparison implicates that (i) the WIP assumption widely used in the current design of braced excavations could be unconservative, and (ii) using the WIP approach in back analyses will cause large discrepancies between the computed results and field measurements. Therefore, the WIP approach should be used with caution in some critical projects (e.g. with tight regulations), and the WIM approach can significantly improve the predictive capability.

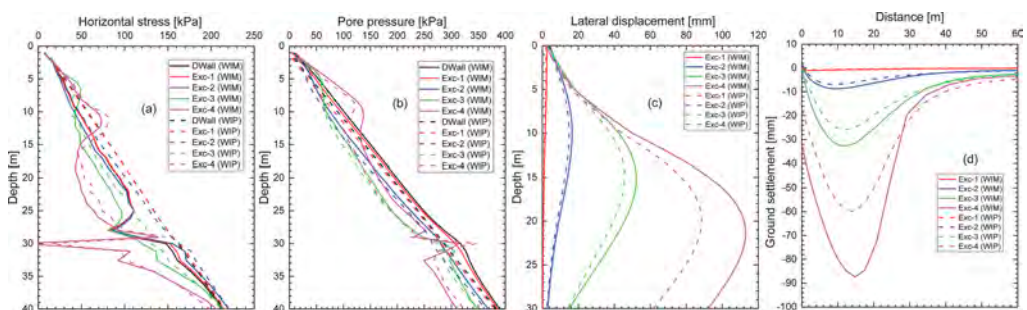


Figure 4. Comparison of ground response at the central section of primary panel P1 between WIP and WIM in braced excavation (a) lateral effective stress, (b) pore water pressure, (c) lateral wall movement, and (d) vertical ground movement.

4 CONCLUSIONS

The construction of diaphragm wall panels will change the initial stress conditions and cause movements in soft clays, which will also affect subsequent excavation performance. Based on these field observation, detailed finite element analyses have been conducted to investigate the installation effects of diaphragm wall panels on the ground response and subsequent excavation performance. General conclusions are drawn for future applications:

- (1) The ground response after single panel installation is further affected by adjacent panel construction, and the ground condition change prior to the major excavation stages can be very complex due to accumulated effects of multiple panel construction.
- (2) The WIP approach can be unconservative in the design, because it tends to underestimate potential wall deformation and ground movement. In addition, the WIP approach will cause large discrepancy between computed results and field measurement in both prediction and back analysis.
- (3) The wall installation effect can be effectively evaluated by the finite element analysis, and should be included in the design for some critical projects (e.g. close to adjacent infrastructure, with tight design regulations). This study has demonstrated a feasible modelling procedure to include the wall installation process in complex analysis. In the literature, the lateral earth pressure coefficient was adjusted to consider the wall installation effect, but this approach can be problematic.

REFERENCES

- Chan, S.F., and Yap, T.F. 1992. Effects of construction of a diaphragm wall very close to a masonry building. ASTM Special Technical Publication, **1129**: 128–139. doi:10.1520/stp19728s.
- Conti, R., de Sanctis, L., and Viggiani, G.M.B. 2012. Numerical modelling of installation effects for diaphragm walls in sand. *Acta Geotechnica*, **7**(3): 219–237.
- Dong, Y. 2023a. Performance of explicit substepping integration scheme for complex constitutive models in finite element analysis. *Computers and Geotechnics*, **162**: 105629.
- Dong, Y., Burd, H.J., and Houslyby, G.T. 2016. Finite-element analysis of a deep excavation case history. *Géotechnique*, **66**(1): 1–15.
- Dong, Y.P. 2023b. Finite element investigation of ground response due to diaphragm wall panel installation. *Canadian Geotechnical Journal*; In print.
- Dong, Y.P., and Whittle, A.J. 2022. Effect of Concreting Pressure on Ground Response Caused by Installation of Diaphragm Wall Panels. *Géotechnique*; ahead of print.
- Lings, M.L., Ng, C.W.W., and Nash, D.F.T. 1994. The lateral pressure of wet concrete in diaphragm wall panels cast under bentonite. *Proceedings - ICE: Geotechnical Engineering*, **107**(3): 163–172.
- Ou, C.Y., Liao, J.T., and Lin, H.D. 1998. Performance of diaphragm wall constructed using top-down method. *Journal of Geotechnical and Geoenvironmental Engineering*, **124**(9): 798–808.
- Poh, T.Y., and Wong, I.H. 1998. Effects of Construction of Diaphragm Wall Panels on Adjacent Ground: Field Trial. *Journal of Geotechnical and Geoenvironmental Engineering*, **124**(8): 749–756. *American Society of Civil Engineers*. doi:10.1061/(ASCE)1090-0241(1998)124:8(749).
- Schäfer, R., and Triantafyllidis, T. 2006. The influence of the construction process on the deformation behaviour of diaphragm walls in soft clayey ground. *International Journal for Numerical and Analytical Methods in Geomechanics*, **30**(7): 563–576.
- Thorley, C.B.B., and Forth, R.A. 2002. Settlement due to diaphragm wall construction in reclaimed land in Hong Kong. *Journal of Geotechnical and Geoenvironmental Engineering*, **128**(6): 473–478. doi:10.1061/(ASCE)1090-0241(2002)128:6(473).
- Whittle, A.J. 1993. Evaluation of a constitutive model for overconsolidated clays. *Géotechnique*, **43**(2): 289–313.
- Whittle, A.J., Hashash, Y.M.A., and Whitman, R. V. 1993. Analysis of deep excavation in Boston. *Journal of Geotechnical Engineering - ASCE*, **119**(1): 69–90.
- Whittle, A.J., and Kavvas, M.J. 1994. Formulation of MIT-E3 constitutive model for overconsolidated clays. *Journal of Geotechnical Engineering - ASCE*, **120**(1): 173–198.
- Zdravkovic, L., Potts, D.M., and St. John, H.D. 2005. Modelling of a 3D excavation in finite element analysis. *Géotechnique*, **55**(7): 497–513.

Numerical simulation of lake crossing construction under double-pipe tunnel considering flow-solid coupling

Y.J. Liu, K. Wu, Z.Y. Dou & Z.H. Liu

School of Civil Engineering, Shandong University, Jinan, Shandong

Z.C. Fan & Q.L. Zhang

STECOL CORPORATION, Tianjin

ABSTRACT: Based on the double-pipe tunnel construction project of the west line of the lake section of the Dongguan supporting pipeline project of the Pearl River Delta water resources allocation project, a three-dimensional fluid-solid coupling calculation model of the double-pipe tunnel under different lake water depths (4 m, 8 m, 12 m) was established using the finite element software ABAQUS. The surface settlement, surrounding rock pore water pressure and seepage velocity distribution of the double-pipe tunnel excavation process under the same lake water depth with different driving methods and under different lake water depths with the same driving method were compared and analyzed. The results show that, under the same lake water depth, the surface settlement of the double-pipe tunnel driven simultaneously is smaller than that of the double-pipe tunnel driven sequentially, the surrounding rock pore water pressure is larger, and the soil seepage velocity is basically consistent; under the same driving method, with the increase of the lake water depth, the surface settlement of the pipe tunnel gradually increases, and the surrounding rock pore water pressure and seepage velocity also increase.

Keywords: ABAQUS, Flow-solid coupling, Surface settlement, Pore water pressure

1 INTRODUCTION

With the rapid development of urbanization in China, the pipe jacking method has been widely used in urban water conservancy pipeline construction, especially when encountering projects crossing urban lakes, rivers, etc. However, the pipe jacking method inevitably causes disturbance and pore water pressure changes in the overlying strata during the construction of crossing rivers and lakes, resulting in surface settlement or uplift and tunnel surrounding rock instability. If these impacts are beyond the controllable range, the risk of environmental hazards will greatly increase. Therefore, it is essential for the project construction to correctly understand and evaluate the impact of pipe jacking tunnel construction on the surrounding environment. In this regard, some scholars have carried out related research work. Bing et al.^[1] studied the deformation law of surface settlement caused by large-diameter pipe jacking in different soils by three-dimensional numerical simulation. Wei et al.^[2] derived the calculation formula of soil vertical deformation caused by the additional thrust at the front of the pipe jacking, the friction between the excavator and the subsequent pipeline and the soil by using the Mindlin solution of elasticity. Li et al.^[3] analyzed the variation and distribution characteristics of ground settlement during the construction of double-line rectangular pipe jacking tunnel under Zhongzhou Avenue in Zhengzhou City by field measurement. Lin et al.^[4] used FLAC3D software and modified Cambridge model to analyze the surface settlement and

lining internal force of shield tunnel under different diving water level and confining water head. Wen et al. [5] combined with practical engineering, adopted the method of combining construction method comparison, numerical simulation and field measurement, and proposed the control measures for surface settlement in gravel stratum. Li et al. [6] proposed a calculation method of stratum displacement for rectangular pipe jacking construction considering the combined effects of three dominant factors: friction, additional stress at excavation face and soil loss. Deng et al. [7] based on the intergranular strain (ICS) small strain stiffness constitutive model, carried out a three-dimensional numerical simulation of the pipe jacking process, and analyzed the stratum deformation response of rectangular pipe jacking construction in soft clay. Liu et al. [8] used a three-dimensional finite element model to analyze the stratum displacement law in large-section rectangular pipe jacking construction. Deng et al. [9] based on the excavation face balance stability principle of slurry shield tunnel and the basic principle of fluid-solid coupling, respectively carried out the micro-mechanism analysis of slurry medium seepage and the calculation analysis of the influence of excavation face slurry seepage on tunnel excavation displacement field. YI et al. [10] analyzed the distribution law of pore water pressure and stratum settlement after shield tunnel excavation by numerical simulation.

In summary, although the pipe jacking method has been widely used in urban street, interchange tunnel, comprehensive pipe gallery and other projects, there are few reports on the impact of long-distance crossing of lakes by double-pipe tunnel. Therefore, based on a typical project, this paper adopts the numerical calculation analysis method, establishes a mechanical model of long-distance crossing of lakes by double-pipe tunnel, and studies the surface settlement, pore water pressure distribution and permeability change law under the disturbance of different water head pressure and driving sequence of pipe jacking across lakes, which provides an important theoretical basis for the design and construction of underground engineering crossing lakes.

2 NUMERICAL COMPUTATIONAL ANALYSIS OF FLOW-SOLID COUPLING

The stress balance equation is expressed in terms of the principle of virtual work. [11,12]

$$\int_V (\sigma' - \chi u_f I) : \delta \varepsilon dV = \int_S \mathbf{t} \cdot \delta \mathbf{v} dS + \int_V (\mathbf{f} \cdot \delta \mathbf{v} dV) + \int_V s n \rho_f g \cdot \delta \mathbf{v} dV \quad (1)$$

Where: $\delta \varepsilon$ is the virtual strain rate; u_f is the fluid average pressure stress; σ' is the Cauchy effective stress; $\delta \mathbf{v}$ is the virtual velocity field; \mathbf{t} is the surface force per element area; \mathbf{f} is the volumetric force per element volume; s is the degree of saturation; n is the porosity; ρ_f is the density of the fluid; g is the gravitational acceleration.

The seepage continuity equation is:

$$\frac{d}{dt} \left(\int_V \frac{\rho_f}{\rho_f^0} s n dV \right) = \int_V \frac{\rho_f}{\rho_f^0} s \mathbf{n} \cdot \mathbf{v}_f dV \quad (2)$$

Where: \mathbf{v}_f is the seepage velocity; \mathbf{n} is the direction normal to the outside of the S-plane, and the equation is dimensionless using the reference density ρ_f^0 of the fluid.

3 ENGINEERING APPLICATIONS

3.1 Overview of the project

This project is the west line of the lake section of the Dongguan supporting pipeline project of the Pearl River Delta water resources allocation project, located at Songshan Lake. The total length of the pipeline of the west line of the lake section is about

1068m, of which the pipeline crossing the Songshan Lake Reservoir is about 540 m, and the water depth of the Songshan Lake Reservoir is about 4 m. Double-pipe jacking is adopted, in which the pipe diameter is 1800mm, the wall thickness is 26 mm, the length is about 504 m, the pipe material is steel pipe, and the center distance between the pipes is 5.4 m. The pipe jacking starts from CJ-B-03 working well, crosses the lake to CJ-B-04 receiving well (as shown in Figure 1). The pipe jacking tunnel is mainly located in completely weathered (rock-like) granite, strongly weathered (soil) granite, and weathered granite is a weakly permeable layer. The overlying soil of the pipe jacking tunnel is mainly silt, silty clay, and sandy clay.



Figure 1. Overview of the top pipe down through the lake.

3.2 Physical modeling

Considering the influence of boundary effects, the calculation range of the numerical simulation model of the pipe jacking tunnel is: the upper part of the vertical direction is the thickness of the overlying rock and soil layer of the tunnel, that is, the length from the crown to the bottom of the lake; the lower part is taken $5D$ (D is the inner diameter of the tunnel) along the center of the tunnel downward, and $5D$ is taken outward in the horizontal direction, and the length of the lake bottom tunnel in the axial direction is 60m, that is, the model length \times width \times height is 60 m \times 23.4 m \times 20 m. The soil adopts the Mohr-Coulomb elasto-plastic model, the pipe jacking adopts the solid element, the soil adopts 8 nodes, and the model is divided into 54024 elements and 71659 nodes. The side and bottom surfaces of the model are displacement boundaries, and the upper surface is a free boundary. The density of the pipe jacking is set to $\rho=1900 \text{ kg/m}^3$, the elastic modulus is $E=210 \text{ Gpa}$, and the Poisson's ratio is $\nu=0.3$.

The pipe jacking tunnel excavation process is shown in Figure 2. The soil excavation in the pipe jacking process adopts the birth-death element method, and the friction coefficient between the soil and the pipe jacking machine and the subsequent pipe jacking is set to 0.3. The grouting pressure is not considered, and the displacement control is used to simulate the pipe jacking. That is, in each analysis step, the soil is controlled to excavate 2 m forward, and the pipe jacking is advanced 2 m (single pipe section) to simulate the pipe jacking process. At the same time, the fluid seepage field is added, and the fluid-solid coupling mode is used to calculate the settlement deformation and pore water pressure of the soil during the excavation time. Repeat the above steps to realize the whole process simulation of pipe jacking.

Table 1. Physical and mechanical parameters of the soil.

Stratigraphic rock sample	H (m)	ρ (kg/m ³)	E_0 (MPa)	ν	K (m/s)	e	C (KPa)	Φ (°)
Sludge	1	1650	7.5	0.32	2.50E-08	1.55	5	3.5
Silty clay	3	1900	15	0.35	2.00E-07	0.721	18	12.5
Sandy clay	2	1850	24	0.3	5.00E-07	0.762	20	18
Fully weathered granite	5	1900	25.5	0.25	2.00E-07	0.837	25	24
Strongly weathered granite	9	2000	135	0.25	3.00E-08	0.897	38	35

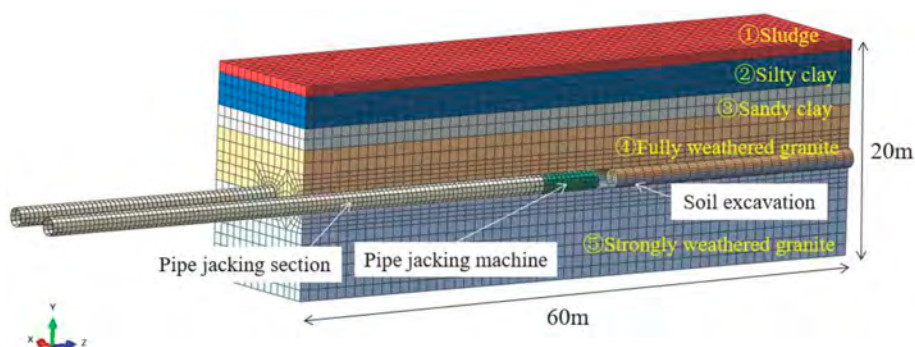


Figure 2. Numerical calculation model.

3.3 Numerical test program

In order to better study the deformation and seepage change law of the surrounding rock in the pipe jacking process under the influence of the driving method and the water head pressure generated by the upper water head, this paper sets up five different working conditions, which are: working condition one: the lake water depth is 4 m, and the double-pipe jacking is carried out simultaneously; working condition two: the lake water depth is 4 m, and the double-pipe jacking is carried out sequentially; working condition three: the lake water depth is 8 m, and the double-pipe jacking is carried out sequentially; working condition four: the lake water depth is 12 m, and the double-pipe jacking is carried out sequentially.

4 ANALYSIS OF SURFACE SETTLEMENT AND PERMEABILITY UNDER CONSTRUCTION DISTURBANCE FOR PIPE JACKING ACROSS LAKES

4.1 Surface settlement for construction of a jacked pipe under a lake

After the pipe jacking is completed, the section with a cover depth of $D=30$ m is selected as the research object, and the surface settlement of the surrounding rock of the pipe jacking under the action of four working conditions is analyzed. The surface settlement data is shown in Figure 3. As can be seen from Figure 3, under the consideration of fluid-solid coupling effect, the vertical surface settlement of the four working conditions is basically consistent, showing a “V” shape distribution, that is, the typical Peck settlement curve. The vertical surface settlement shows a trend of gradually increasing in both directions of the tunnel centerline, the closer to the two tunnel centerlines, the larger the surface settlement, and the farther from the two tunnel centerlines, the smaller the surface settlement on both sides. It can also be seen from the figure that, when the water head pressure is consistent, the vertical surface settlement of the double-pipe jacking simultaneously (Working Condition I) is smaller than that of the double-pipe jacking sequentially (Working Condition II), and with the increase of the water head pressure, the surface settlement and the influence range also increase.

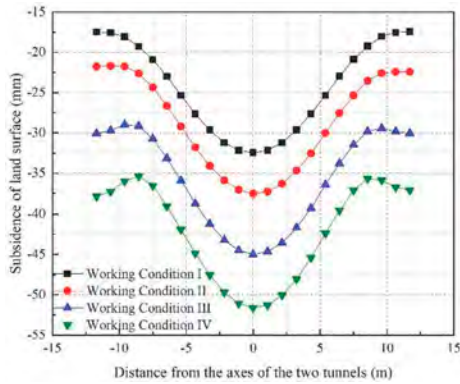


Figure 3. Surface settlement under different operating conditions.

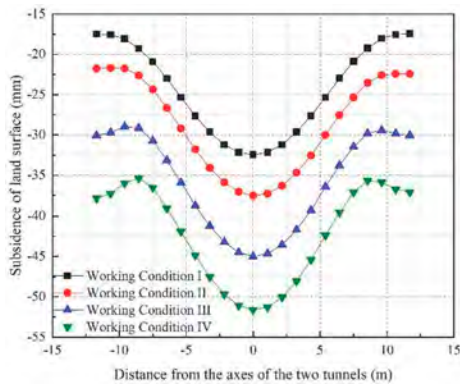


Figure 4. Vertical settlement of surface at D=30 m section of pipe jacking in Working Condition II.

The vertical surface settlement of the section at D=30 m during the whole process of pipe jacking in Working Condition II is shown in Figure 4. As can be seen from Figure 4, with the pipe jacking advancing sequentially, the settlement trough gradually moves to the left, and at the same time widens and deepens, forming a typical Peck settlement curve. When the right pipe jacking advances 10~20 m, the excavation face has not reached the section at D=30 m, and the surface settlement is almost zero at this time. With the increase of the driving distance, the surface settlement becomes more obvious, and the settlement speed is the largest during the pipe jacking of 30~40 m. When the right pipe jacking is completely driven, the maximum surface settlement is 19.78 mm. With the continuous driving of the left pipe jacking, the position of the maximum settlement gradually shifts to the left, and when the pipe jacking advances 40 m, the settlement trough is basically symmetrical, and the position of the maximum settlement is located at the centerline of the two tunnels. When the left and right pipe jacking are completely driven, the maximum vertical surface settlement at the section of D=30 m is 37.53 mm.

4.2 The distribution law of seepage field in the surrounding rock of the tunnel construction of jacking pipe under the lake

The pore pressure distribution of the section at D=30 m under different working conditions is shown in Figure 5. As can be seen from the figure, with the excavation of the pipe jacking tunnel, the pore water pressure of the tunnel surrounding rock decreases, and the groundwater in the distance flows toward the tunnel direction under the action of the water pressure gradient, finally forming a “funnel-shaped” pore water pressure distribution with the centerline of

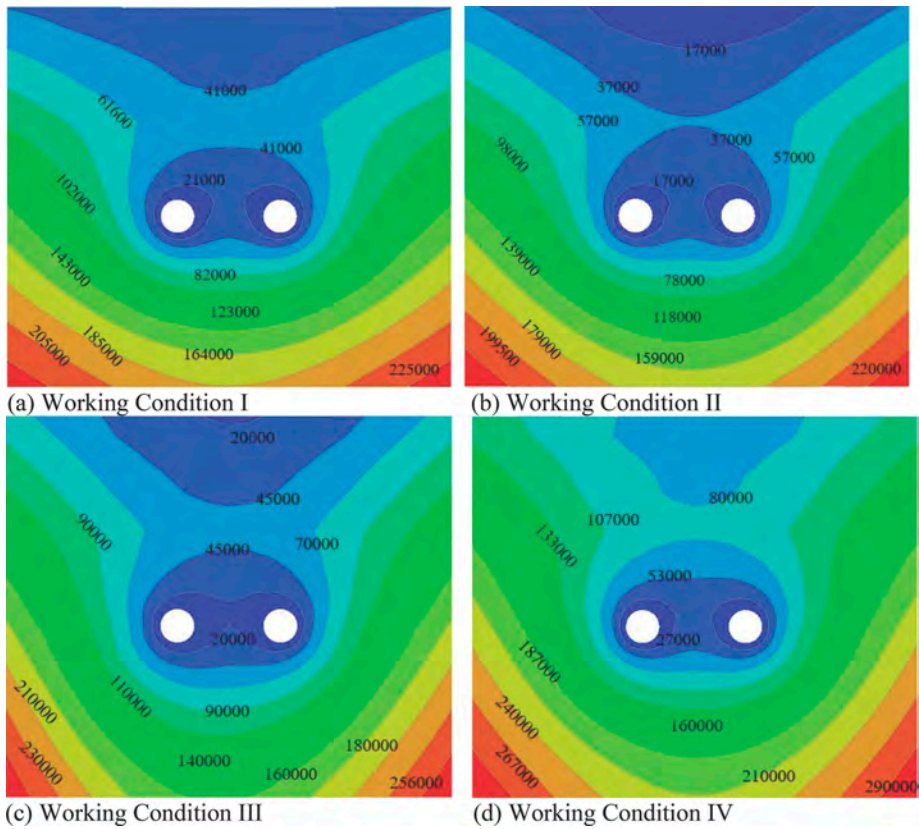


Figure 5. Pore pressure distribution at D=30 m section of pipe jacking under different working conditions.

the two tunnels as the center. As shown in Figure (a) and (b), when the same water head has different pipe jacking tunnel excavation methods, the pore water pressure distribution at the tunnel entrance is different, and the pore water pressure at the tunnel entrance of working condition one and working condition two are 21 kpa and 17 kpa respectively. As shown in Figure (b), (c) and (d), when the water head pressure increases, the pore water pressure also increases.

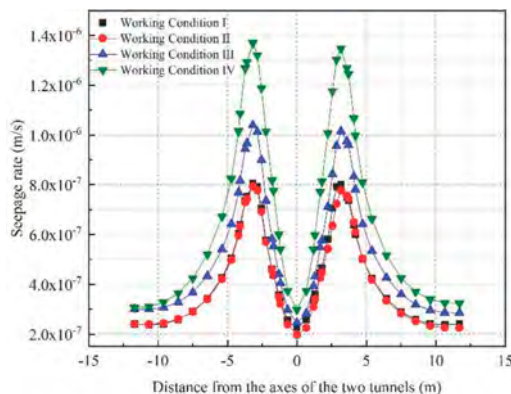


Figure 6. Velocity of seepage under different working conditions.

The seepage velocity distribution of the section at $D=30$ m under different working conditions is shown in Figure 6. As can be seen from the figure, the seepage velocity of the four working conditions at the same section is basically consistent, showing an “M” shape distribution with the centerline of the two tunnels as the center. The seepage velocity above the tunnel entrance on the left and right is the largest, and the seepage velocity away from the centerline of the tunnel entrance on the left and right decreases. It can also be seen from the figure that, under the same water head, the seepage velocity at the tunnel entrance and the left and right sides of different driving methods is basically consistent. This indicates that when the water head is the same, the double-pipe jacking simultaneously (Working Condition I) and sequentially (Working Condition II) have little effect on the soil seepage velocity. In addition, with the increase of the water head, it can be found that the seepage velocity of the soil toward the tunnel entrance gradually increases, which is consistent with the above-mentioned pore water pressure change.

5 CONCLUSIONS

Based on a typical project, this paper adopts the numerical calculation analysis method, establishes a mechanical model of long-distance crossing of lakes by double-pipe tunnel, and studies the surface settlement, pore water pressure distribution and permeability change law under the disturbance of different water head pressure and driving sequence of pipe jacking across lakes. The conclusions are as follows:

- (1) After the pipe jacking is completed, the position of the maximum surface settlement is at the centerline of the two tunnel entrances.
- (2) Under the same lake water depth, the surface settlement of the double-pipe jacking simultaneously is smaller than that of the double-pipe jacking sequentially, the pore water pressure of the surrounding rock is larger, and the seepage velocity of the soil is basically consistent.
- (3) Under the same driving method, the surface settlement of the pipe jacking tunnel gradually increases with the increase of the lake water depth, and the pore water pressure and seepage velocity of the surrounding rock also increase.

6 DECLARATION OF COMPETING INTEREST

The authors declare that they have no known competing financial interests or personal relationships that could have appeared to influence the work reported in this paper.

ACKNOWLEDGMENTS

This research was funded by the National Natural Science Foundation of China (52179106).

REFERENCES

- [1] Bing Fengju, Wang Xin, Xi Ning, et al. 3D numerical simulation of pipe jacking and its soil applicability study [J]. Chinese Journal of Underground Space and Engineering, 2011, 7(6): 1209–1215.
- [2] Wei Gang. Theoretical study on properties of soil and structure during pipe jacking construction [D]. Hangzhou: Zhejiang University, 2003.
- [3] LI Mingyu, WANG Song, ZHANG Weixi, et al. Analysis of ground subsidence caused by construction of large section rectangular pipe jacking tunnel [J]. Railway Engineering, 2019, 59 (5): 81–84.
- [4] Lin Zhibin, Li Yuanhai, Zhao Yaoqiang, Shi Linpo. Numerical Analysis on the Impact of Groundwater on Shield Tunnel Construction under Soft Soil [J]. Chinese Journal of Underground Space and Engineering, 2012, 8(02): 375-381+389.
- [5] Wen Jiwei, Yue Jinshuai, Xiang Tian, et al. Research on ground subsidence control in trenchless pipe jacking in sandy gravel formation [J]. Drilling Engineering, 2022, 49(03): 130–138.

- [6] Li Hui, Yang Guiyang, Song Zhanping, et al. Study on calculation method of soil delamination deformation caused by rectangular pipe jacking construction[J]. Chinese Journal of Underground Space and Engineering, 2019,15(05):1482–1489.
- [7] Deng Ting, Huang Maosong, Shi Zhenhao, et al. Ground deformation response induced by jacking process of deep rectangular tunnel in soft clay [J/OL]. CHINA CIVIL ENGINEERING JOURNAL, 2023, 56(S2):157-162.
- [8] Liu Bo, Zhang Dingwen, Liu Songyu, et al. Numerical simulation and field monitoring on a large cross-section pipe-jacking underpass traversing existing metro tunnels [J]. Chinese Journal of Rock Mechanics and Engineering, 2017, 36(11): 2850–2860 (in Chinese)
- [9] Deng Zongwei, Wu Zhenzhi, Cao Hao, SHEN Pinghuan. Surface deformation of slurry shield tunneling using fluid-solid coupling theory [J]. Journal of Central South University (Science and Technology), 2013 (2): 785–791.
- [10] Yi X, Rowe R K, Lee K M. Observed and calculated pore pressures and deformations induced by an earth balance shield [J]. Canadian Geotechnical Journal, 1993, 30(3): 476–490.
- [11] Zhu Yi-Wen, Cai Yuan-Qi, Xu Han. ABAQUS and Geotechnical Analysis [M]. Hong Kong: CHINA TUSHU PUBLISHING LIMITED, 2005.
- [12] Xu Jin-hua, He Chuan, Xia Wei-yang. Research on coupling seepage field and stress field analyses of underwater shield tunnel [J]. Rock and Soil Mechanics, 2009, 30(11): 3519-3522+3527.

Effect of slurry infiltration on trench stability of diaphragm wall

J. Ning, J. Yu & M. Huang*
Tongji University, Shanghai, China

ABSTRACT: Instability and even collapse of slurry trench may occur during the excavation of diaphragm wall. However, there are few analyses on the stability of slurry trench concerning slurry infiltration. Based on the particle transportation mechanism of convection-dispersion-deposition in porous media, a model for slurry infiltration is established to consider the coupling relationship among the degree of particle transportation, fluid seepage and soil deformation. The model parameters are calibrated by comparing with the existing tests. Plane-strain models are further established to simulate the slurry infiltration after the trench excavation. The formation of mud cake and trench stability are explored based on variation in pore water pressure. The influences of slurry concentration on the trench stability under slurry infiltration are further analyzed by strength reduction technique. It reveals that a proper increase in slurry concentration is beneficial for the trench stability. Finally, the method is applied to a practical engineering for further verification.

1 INTRODUCTION

Underground diaphragm wall is extensively employed in underground engineering due to its advantages of stiffness, integrity, and impermeability. In trench excavation, bentonite slurry is commonly employed to support the wall. However, in highly permeable sand, large amounts of slurry penetrate into the ground, making it difficult for mud cake to form and leading to trench instability or collapse. In addition, slurry proportioning, density and viscosity also impact the effectiveness of wall support. Therefore, the slurry infiltration plays a crucial role in ensuring the trench safety.

Existing analyses of trench stability mostly assume that the impermeable mud cake is formed immediately and slurry pressure acts entirely on the soil grains through the mud cake (Lei et al. 2019). It leads to an overestimation of the stability of the slurry trench. Before the formation of the mud cake, the pore water pressure increases, reducing the effectiveness stress of soil. Therefore, it is necessary to establish a model for slurry infiltration in soil and determine the variation of pore water pressure. This study utilizes the strength reduction technique to evaluate the stability of slurry trenches based on the slurry infiltration.

2 SLURRY INFILTRATION IN SATURATED SOIL

2.1 *Slurry infiltration model*

A large number of previous slurry infiltration tests have investigated the transport behavior of slurry in soil. The laboratory test results provide great insights into the physical mechanisms of slurry infiltration. Figure 1 depicts the physical process of slurry infiltration in soil, which includes the transportation of slurry particles and the seepage of slurry flow. The transportation of slurry particles consists of three parts: convection, which is related to the flow velocity,

*Corresponding author: mshuang@tongji.edu.cn

dispersion, which is related to the concentration gradient, and deposition, which is related to the concentration (Lu et al. 2022). Slurry particles infiltrate into the soil under the slurry pressure. Some slurry particles are deposited in soil by physical filtration and adsorption of the soil skeleton. The deposition can block pores and affect the seepage of fluid. A mud cake with low permeability can only be formed when the blockage reaches a certain extent. The excess pore fluid pressure in the stratum gradually transforms into an effective slurry pressure that acts on the soil grains upon the establishment of the mud cake. The research indicates that the slurry infiltration in soil is influenced by various factors, including hydraulic properties of soil, soil porosity, slurry concentration, slurry pressure. The soil deformation caused by flow affects the distribution of permeability (hydro-mechanic coupling). Therefore, it is necessary to establish a model of slurry infiltration in soil that can account for the aforementioned factors.

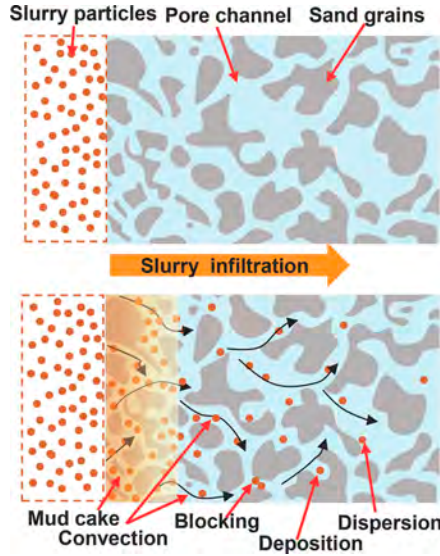


Figure 1. Physical process of particle transport in saturated porous media.

Based on the mass conservation of the slurry and soil, the governing equations for slurry infiltration is expressed as follow:

$$\frac{\partial[(1-n)\rho_s]}{\partial t} + \nabla \cdot [(1-n)\rho_s \mathbf{u}] + \rho_s \dot{m} = 0 \quad (1)$$

$$\frac{\partial[(1-c)n\rho_w]}{\partial t} + \nabla \cdot [(1-c)n\rho_w \mathbf{u}] + \nabla \cdot [(1-c)\rho_w(-\bar{k}\nabla p + \bar{k}\rho_{sus} \mathbf{b})] = 0 \quad (2)$$

$$\frac{\partial(c\rho_s n)}{\partial t} + \nabla \cdot (c\rho_s n \mathbf{u}_w) - D_L \nabla^T \nabla c \rho_s - \rho_s \dot{m} = 0 \quad (3)$$

$$\nabla(\boldsymbol{\sigma}' - \mathbf{m}p) + \rho \mathbf{b} = 0 \quad (4)$$

Equation (1) is the soil skeleton mass conservation equation, where n is the porosity of the infiltrated soil; ρ_s is the density of solid particles; \mathbf{u} is the absolute velocity of solid phase; \dot{m} describes the deposition rate of particle per unit volume of porous media. Equation (2) is the fluid phase mass conservation equation, where c is the volume concentration of particles; ρ_w is the density of water; $-\bar{k}\nabla p + \bar{k}\rho_{sus} \mathbf{b}$ is the relative velocity of fluid phase according to Darcy's

law; ρ_{sus} is the density of suspension, which can be determined as $n\rho_s + n(1-c)\rho_w$; Equation (3) is particle mass conservation equation, where $D_L(\text{kg}/\text{m}^2/\text{s})$ is the dispersion coefficient of slurry particles in porous media. This equation states that the change of particles mass in a porous media is determined by convection, dispersion, and deposition. Equation (4) is the momentum balance equation, where σ' is the effective stress, $\mathbf{m}^T = \{1,1,0\}$ for 2D problems; ρ is the total density of infiltrated soil, which can be determined as $n\rho_s + n(1-c)\rho_w + (1-n)\rho_s$.

Equations (1), (2), (3), and (4) constitute the governing equations for the slurry convection-dispersion-deposition in soil. The governing equations can be solved numerically by COMSOL Multiphysics. For some physical quantities in the governing equations, the following equations need to be supplemented:

$$\dot{m} = -\frac{1}{\rho_s} \frac{d(nc_T)}{dt} = -hmc - \frac{nc_T}{\rho_s} \quad (5)$$

$$n = n_0 - \frac{c_T n}{\rho_s} + \varepsilon_v \quad (6)$$

$$k = k_0 \left(\frac{1-n}{1-n_0} \right)^{-4} \left(\frac{n}{n_0} \right)^5 \left(\frac{\mu_0}{\mu} \right) \quad (7)$$

Equation (5) is the deposition rule of particle (Herzig et al. 1970). nc_T is the deposition mass per unit volume of the porous media. c_T is the mass of deposited slurry particles per unit volume of suspension; h is the deposition coefficient. The value of h depends on the pore properties of soil, and the type and size of transported particles. h can be calibrated based on one-dimensional slurry infiltration tests. The influence of deposition and porous media deformation on the soil porosity can be expressed as Equation (6), in which n_0 is the initial porosity of clean soil that does not contain suspension particles; ε_v is the volume strain of porous media. Equation (7) depicts the variation of permeability coefficient in slurry infiltration, in which k_0 is the permeability coefficient of clean soil; k is the permeability coefficient after the particle deposition; μ_0 is the initial viscosity coefficient of fluid phase (without slurry particle); μ is the state viscosity of fluid phase in voids of the soil (with slurry particle). The relationship between slurry viscosity and concentration can be expressed as $\mu = \mu_0 e^{bc}$, where b is a parameter that affects the viscosity change rate (Lu et al. 2022).

2.2 Simulation of slurry infiltration tests

Xu and Bezuijen (2019) performed a series of column tests to study the slurry infiltration in sand. The experimental setup consisted of a plexiglass column test system, a pneumatic loading system and a monitoring system, as shown in Figure 2(a). The upper part of the apparatus filled with 13 cm of fine sand and 10 cm of slurry. The small diameter cylinder at the bottom contained 4 cm of fine sand to reproduce a hydraulic gradient comparable to that in engineering. The pore water pressure transducers (k1, k2, k3, and k4) were placed on the test column. During the infiltration process, the time variation of the water discharge is recorded.

The axisymmetric slurry infiltration model is established to simulate the test, as illustrated in Figure 2(b). The dimensions of the model are consistent with the test setup. The parameters used in the model are listed in Table 1.

The numerical simulation most accurately reflects the experimental data when the deposition coefficient (h) is set to 0.4, as shown in Figure 3. The calculated discharged volumes and permeability coefficients agree well with the corresponding experimental results, indicating that the model effectively captures the phenomenon of sand pore blockage and the subsequent reduction in permeability caused by slurry infiltration.

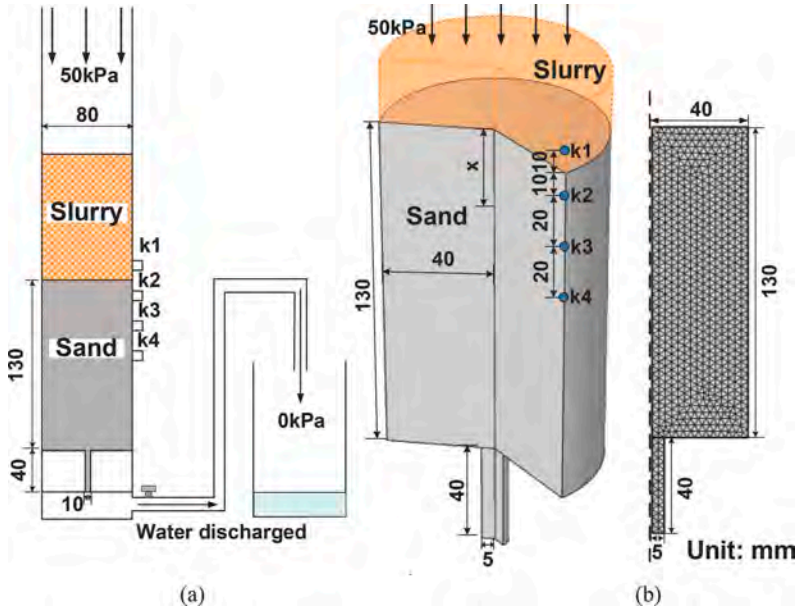


Figure 2. One-dimensional slurry infiltration model: (a) Test set-up; (b) Numerical model and finite element mesh.

Table 1. Model parameters.

$c_0/(\text{kg}\cdot\text{m}^{-3})$	n_0	$h/(\text{s}^{-1})$	$k_0/(10^{-4}\text{m}\cdot\text{s}^{-1})$	$D_L/(10^{-4}\text{m}^2\cdot\text{s}^{-1})$	$\rho_s/(\text{g}\cdot\text{cm}^{-3})$	b
40/50/60	0.37	0.4	4.4/4.4/4.2	2	2.65	0.0338

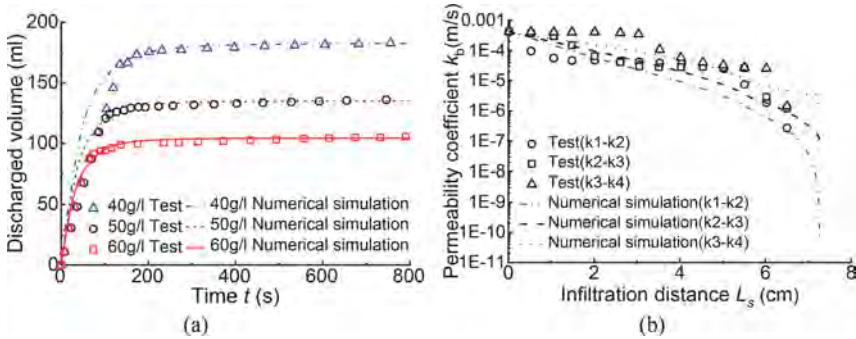


Figure 3. Comparison of infiltration behavior between model and test: (a) Discharged volume; (b) Permeability coefficient of slurry ($c_0=50\text{g/l}$).

3 STABILITY OF SLURRY TRENCH

3.1 Slurry infiltration in the trench

To simulate the slurry infiltration in the vertical excavation face of a trench, a 2D plane-strain model is established as depicted in Figure 4. The trench excavation depth is 20m. A model with dimensions of 60 m in width and 40 m in height is developed to ensure that slurry infiltration and deposition occur within the boundaries of the model. Since AB represents the vertical excavation face, the boundary condition for AB is defined by setting with the concentration of

c_0 and the slurry pressure. The mesh near the AB boundary is refined, where is the main region of particle dispersion and deposition. The model parameters are presented in Table 2.

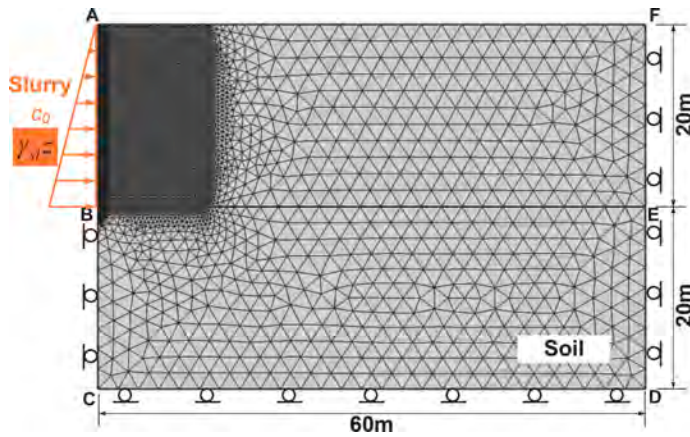


Figure 4. Model geometry and mesh division of slurry trench.

Table 2. Model parameters of slurry trench.

$c_0/(\text{kg}\cdot\text{m}^{-3})$	n_0	$h(\text{s}^{-1})$	$k_0/(10^{-4} \text{ m}\cdot\text{s}^{-1})$	$E/(\text{MPa})$	$D_L/(10^{-4} \text{ m}^2\cdot\text{s}^{-1})$	$\rho_{sl}/(\text{g}\cdot\text{cm}^{-3})$	$\gamma/(\text{kN}\cdot\text{m}^{-3})$
80	0.37	0.4	4.4	10	2.0	1.17	18

Figure 5 illustrates the variation of excess pore water pressure in the soil behind the excavation face during slurry infiltration. Initially, the pore water pressure exceeds the hydrostatic pressure due to high slurry pressure outside the excavation face. The excess pore water pressure increases with depth. According to the effective stress theory, the excess pore water pressure reduces the effective stress of the soil, thereby diminishing the trench stability. As slurry infiltration and deposition continue, a mud cake slowly forms, wherein the excess pore water pressure within the soil gradually transforms into effective slurry pressure acting upon the soil skeleton. This imparts a retaining wall effect.

Wei et al. (2014) proposed a method to estimate the period of mud cake formation based on the pore water pressure. The effective stress conversion ratio is defined as $\omega = (p_{sl} - p)/(p_{sl} - p_0)$, where p_{sl} is the initial slurry pressure and p_0 is the hydrostatic pressure. ω is the function of p/p_0 . The initial point of inflection on the $\omega - \log(t)$ curve indicates the onset of mud cake formation. Prior to this point, a significant volume of slurry had already infiltrated into the soil. After this point, the mud cake begins to form, and excess pore water pressure gradually dissipates. The onset time of the mud cake formation is 20 s in this model as depicted in Figure 6. The second point of inflection on the curve is identified as the time when the mud cake is primarily formed and the particle infiltration into the soil ceases. At this point, the water pressure has reached a relatively stable state, which corresponds to a time point of 81s.

The initial slurry concentration is adjusted to 40, 80, and 120 g/l, corresponding to slurry densities of 1.05, 1.17, and 1.21 g/cm^3 , respectively. As depicted in Table 3, the time of the mud cake formation significantly reduces with the increase in the initial slurry concentration. Increasing the initial slurry density intensifies the particle convection and dispersion effect. As a result, the pore clogging accelerates, shortening the time of the mud cake formation. large amounts of slurry penetrate into the coarse sand due to its high permeability, which prevents the particle deposition. As a result, the formation of mud cake is delayed or may not occur at all.

When the initial soil porosity is increased, it leads to a prolongation in the formation time of mud cake. Due to the correlation between soil porosity and permeability, large amounts of slurry are lost in highly permeable soil, such as coarse sand. Consequently,

the slurry particles cannot be deposited in the soil, resulting in slow or even non-formation of mud cake.

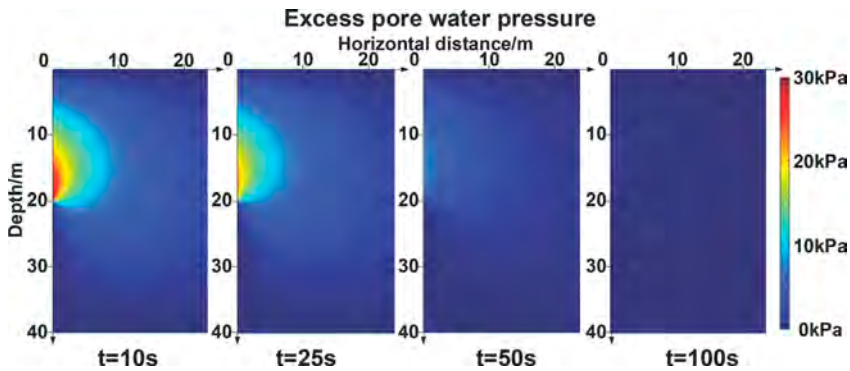


Figure 5. Excess pore water pressure in soil at different times.

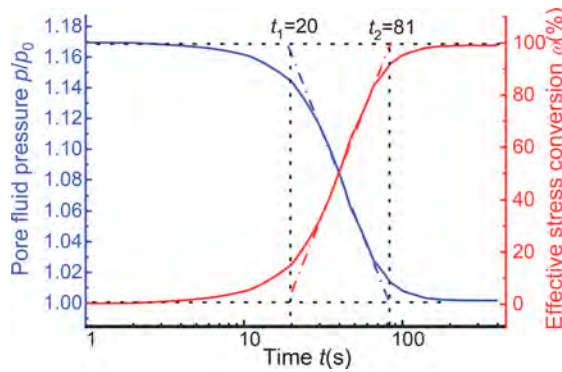


Figure 6. Pore water pressure and effective stress conversion rate along logarithm of time.

Table 3. Time of mud cake formation at different initial concentrations.

Initial slurry concentration/(g·l ⁻¹)	Initial formation time /s	Final formation time /s
40	54	220
80	20	81
120	8	43

3.2 Stability assessment with slurry infiltration

Based on the calculations of the slurry infiltration, stability analysis of the mud trench is performed using shear strength reduction technique in finite element model (SSRFEM). The strength parameters of the soil after strength reduction are expressed as $c'_F = c'/F_t$ (kPa), $\varphi'_F = \arctan(\tan \varphi'/F_t)$. The initial friction angle of sand is set as $\varphi' = 35^\circ$. The strength reduction factor F_t increases incrementally until collapse occurs. At this instant, the strength reduction factor comes to safety factor defined in the limit equilibrium method.

The safety factors are computed for three types of slurry concentrations, as shown in Figure 7. When the slurry concentration is 40 g/L, the safety factor remains consistently below 1, indicating an unsafe trench condition. With the elevation of slurry concentration, the corresponding rise in slurry pressure contributes to the enhancement of trench stability. It is worth noting that the safety factor of the trench gradually increases with the duration of slurry infiltration.

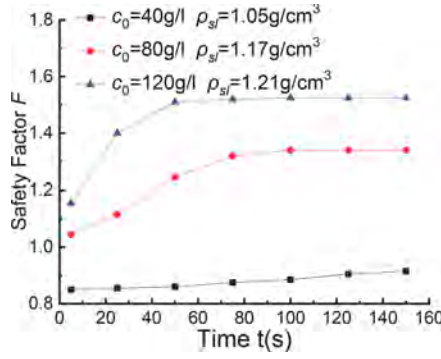


Figure 7. Safety factors with time under different initial concentrations.

Based on the wedge stability model, the wedge is influenced by four forces: the buoyant weight of soil (W'), the effective slurry pressure (P), the normal force (N') and the shear force (T) on the slanted failure plane, as depicted in Figure 8. The equilibrium equations for the wedge are express as Equations (8), (9). As slurry permeates, the effective slurry pressure (P) gradually increases due to the reduction in pore water pressure. The safety factor (F_s) gradually increases according to Equation (11). Upon the formation of mud cake, the pore water pressure in soil reverts to the hydrostatic pressure, and the safety factor of the trench reaches a stable value.

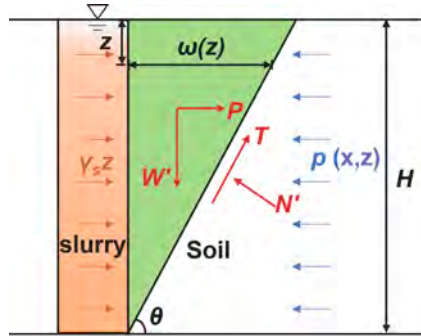


Figure 8. Wedge model under slurry infiltration.

$$T = W' \sin \theta - P \cos \theta \quad (8)$$

$$N' = P \sin \theta + W' \cos \theta \quad (9)$$

$$P = \iint_A i \gamma_w dS = \frac{1}{2} \gamma_{st} H^2 - H_0 p(\omega(z), z) dz \quad (10)$$

$$F_s = \frac{N' \tan \varphi}{T} \quad (11)$$

3.3 Trench excavation case

Tsai et al. (2000) conducted a full-scale stability experiment on a diaphragm wall trench. The geotechnical site characterization is depicted in Figure 9. The groundwater table is at 3 m below the grade. The excavation depth of the trench is 15m. The density of slurry is 1.05 g/cm³. The trench collapsed and the adjacent ground subsided when the slurry level was 2 m below the ground. Considering the low permeability of the soil above the groundwater table, it is assumed

that there is no slurry infiltration in the soil above the groundwater table and that the slurry pressure directly acts on the soil above the groundwater table. Based on the slurry infiltration model, strength reduction technique is conducted to evaluate the trench stability. The safety factor is 0.545 and indicates an unsafe condition of the trench wall, aligning with the actual observations. Figure 9 illustrates the potential failure mechanism of the trench wall.

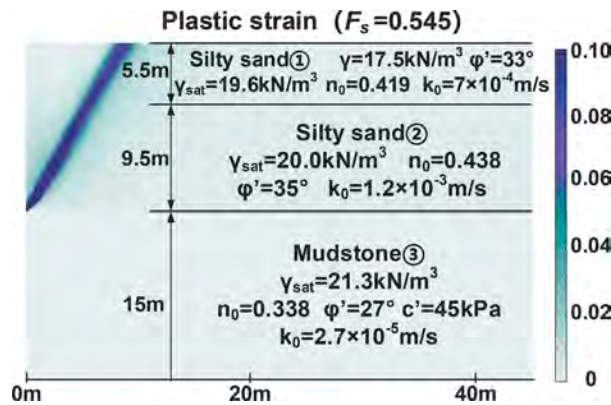


Figure 9. Calculation of Tainan area engineering example.

4 CONCLUSIONS

The slurry infiltration model is developed to consider the coupling relationship among the degree of particle transportation, fluid seepage and soil deformation. The model parameters are calibrated by comparing with the existing infiltration tests. The influence of slurry infiltration on the time of mud cake formation and the variations in pore water pressure is explored in this study. The slurry trench stability is analyzed using the strength reduction technique. It reveals that a proper increase in slurry concentration is beneficial for the trench stability. The safety factor of the trench gradually increases with the duration of slurry infiltration, which is theoretically explained using the wedge stability model. The method is applied to a practical engineering for further verification.

ACKNOWLEDGEMENTS

The authors acknowledge the financial support from the National Natural Science Foundation of China (Grant Nos. 42372311 and 51738010).

REFERENCES

- Herzig, J. & Leclerc, D. & Le Goff, P. 1970. Flow of suspensions through porous media: application to deep filtration. *Ind Eng Chem* 62: 8–35.
- Lei, M. & Liu, L. & Lin, Y. & Shi, C. & Yang, W. & Cao, C. & Liu, Y. 2019. Research progress on stability of slurry wall trench of underground diaphragm wall and design method of slurry unit weight. *Adv Civ Eng* 2019: 1–19.
- Lu, Z. & Zhou, W. & Yin, Z. & Yang, J. 2022. Numerical modeling of viscous slurry infiltration in sand. *Comput Geotech* 146: 104745.
- Tsai, J.S. & Jou, L.D. & Hsieh, H.S. 2000. A full-scale stability experiment on a diaphragm wall trench. *Can Geotech J* 37: 379–392.
- Wei, D. & Zhu, W. & Min, F. 2014. Experimental study of forming time of filter cake and conversion rate of slurry pressure in slurry shield in sand stratum. *Rock Soil Mech* 35(2): 423–428.
- Xu, T. & Bezuijen, A. 2019. Pressure infiltration characteristics of bentonite slurry. *Géotechnique* 69(4): 364–368.

Numerical analysis of ground movement due to shield tunneling at NAPE, Macau

W.L. Ung, Y.H. Wang & T.M.H. Lok

Department of Civil and Environmental Engineering, University of Macau, Macau SAR, China

ABSTRACT: With intensive underground infrastructures accompanying the rapid development and urbanization worldwide, the shield tunneling method has been widely adopted for fast and safe construction where traditional methods cannot be implemented. However, the occurrence of ground movements during tunnel construction is inevitable. In this study, a finite element model simulating a shield tunnel in Macau is established by the software PLAXIS 2D to investigate the ground settlement induced by tunnel construction. After a series of analyses, the numerical results obtained from the software are compared with the field measurements. Though a slight difference exists between the results due to the limitations of simulating the intricate conditions of the actual site, the numerical simulation is considered to be acceptable. The analysis reveals that the settlement trough observed in the field exhibits a distribution resembling a normal curve; however, it demonstrates asymmetrical characteristics. The maximum settlement trough might not always lie on the center of the tunnel axis.

1 INTRODUCTION

With the speedy growth worldwide, conventional construction techniques cannot be applied smoothly due to the crowded environment of the city. Thus, engineers shifted to the underground space for additional infrastructure. With the advancement of tunneling technology, shield tunneling is one of the most significant methods of tunnel construction nowadays. It has been widely adopted on account of being fast and safe. The first shield tunnel in Macau was recently constructed in the NAPE area, which will be investigated in this study.

An accurate prediction of the ground settlement is essential in shield tunneling construction design. Numerous works and research have been done to estimate the ground surface settlement. The empirical solution was proposed by Peck in 1969. A Gaussian distribution function is generated by fitting the deformation trough shape to estimate the ground movement above the tunnel (Peck 1969). Moreover, Sagaesta (1987) has proposed a closed-form analytical solution to approximate the ground settlement in terms of ground loss. The model of the removed soil is simulated as a point sink at a certain depth below the ground surface. The ground loss is assumed to be concentrated at the axis (Sagaesta 1987). On the other hand, Pinto & Whittle (2014) proposed another closed-form analytical solution to predict the shield tunneling ground movements in soft ground in 2014. Ground settlement is obtained through the superposition of uniform convergence, ovalization, and vertical translation.

Besides empirical and analytical methods, many construction cases have been simulated via different numerical simulation software for analysis. Chen (2017) analyzed the shield tunnel of the north extension line of the Paris Metro Line 14 by using the software PLAXIS 2D. It is concluded that the difference between the maximum ground settlement simulated and that measured in the field is 1.6 mm. In addition, the maximum settlement obtained from the software is located near the tunnel axis, which is consistent with the monitoring result (Chen 2017). Furthermore, Lei-Kilany et. al (2017) simulated the ground movement induced by the tunneling

of Cairo Metro-Line III in Egypt. More than 8 layers of different soils are involved in the analysis. Two and three-dimensional numerical analyses of PLAXIS are utilized. It is concluded that the result of both dimensional analyses matches the field measurement. Besides, the paper compares the results obtained from 2D and 3D finite element programs. It suggests that the result of 3D is more accurate than that of 2D. However, most research works use 2D-finite elements more as it is faster, cheaper, and more efficient. (Lei-Kilany et. al, 2017)

2 METHODOLOGY

An accurate forecast of the tunneling effects is crucial for shield tunnel construction, for both the safety and feasibility of the project. This study will establish a finite element model using the software PLAXIS 2D to investigate the ground movement induced by shield tunneling. The tunnel being simulated is the first shield tunnel of Macau in the NAPE area which has been recently constructed. The resulting ground movement obtained from the numerical method will be compared with the field monitoring data.

To simulate the mechanical behavior of the soils, the Mohr-Coulomb model is used in this study for soil close to the tunnel, while the linear elastic model is used for soil away from the tunnel. The input parameters for the different soil layers are described in the following section.

The construction sequence of the shield tunnel is the cutter head cuts the upper soil body and continues to push forward until the distance reaches a segment width value. At this time, the shield machine stops, and the shield tail segment is assembled and grouted into the shield tail building gap. In this way, cutter head excavation and segment assembly are carried out alternately until all excavation and lining works of the tunnel are completed.

In the numerical simulation, the construction sequences are divided into 5 phases: (1) initial phase, (2) tunneling, (3) contraction, (4) grouting, and (5) final lining. The initial phase is the initial soil condition before any action. Tunneling is the excavation of soil and putting the shield. Contraction means the contraction of the tunnel lining resulting from ground loss. Grouting is the pouring of concrete to fill the gaps created during tunneling. The final lining is the final condition of the tunnel constructed.

3 SHIELD TUNNEL MODELLING

3.1 Soil profile and cross-section

The distribution of the SPT N-value with depth is shown in Figure 1. The SPT N-value generally increases with depth. It reveals that the deeper the soil is, the denser and harder the soil is. From the SPT N-value and the historical geological condition of Macau, it is determined that the soil profile includes the fill layer, the marine deposit clay layer, the alluvium layer, and the CDG layer.

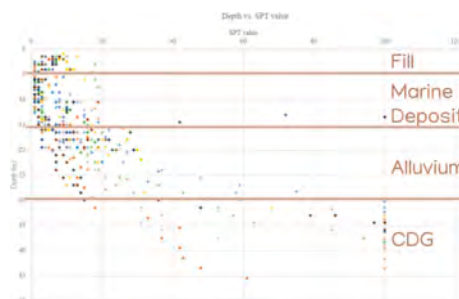


Figure 1. Depth vs. SPT N-Value.

With the stratigraphic statistics based on all the borehole data, the typical soil profile includes the most frequently occurred layer and its average soil height in each category of soil. Moreover, the typical groundwater table level of -1 meter was adopted in this analysis. The typical soil profile generated is shown in Figure 2. In addition, as CDG is an impermeable soil layer, it is ignored in this analysis.

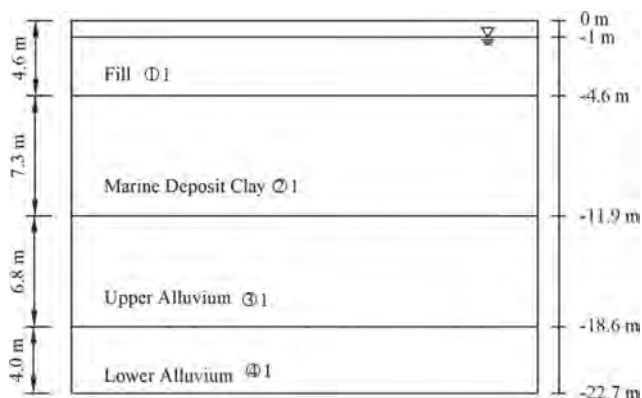


Figure 2. Soil profile of the typical cross-section.

3.2 Material parameters

In terms of material parameters, most of them are obtained from the data provided by the construction company. After calibrating by the SPT N-value, the soil and lining materials used are shown in Table 1 and 2, respectively.

Table 1. Soil material properties in numerical simulation (MBEC-CRTG-MS CONSORTIUM, 2021).

Index	Soil Type	Natural Unit Weight (kN/m ³)	c' (kPa)	ϕ (°)	ν	E_s (Mpa)	SPT value
11	Fill	19			0.25	9	8.8
21	Clay	16.5	7.5	28.8	0.42	2	1.8
31	Mucky soil, silty soil	19.1			0.35	7.5	9.6
32	Medium coarse sand	20			0.28	20	20.2

Table 2. Lining material properties in numerical simulation (MBEC-CRTG-MS CONSORTIUM, 2021).

Material type	Elastic
Unit weight, w (kN/m/m)	8.4
Prevent punching	No
Isotropic	Yes
Axial stiffness, EA_1 (kN/m)	7.5×10^6
Bending stiffness, EI (kNm ² /m)	56.3×10^3
Poisson's ratio	0.15

3.3 Model geometry and boundary conditions

In this case, the tunnel depth is estimated to be 10 meters below the ground surface. The thickness of the lining segment simulated is 200 mm while the tunnel diameter is 3200 mm. For the mesh dimension and boundary condition, according to Möller (2006), the width of the symmetrical half model should be 23 meters. Figure 3 illustrates the numerical model applied in PLAXIS 2D. For the boundaries in the vertical direction, the displacement is set to be free vertically while restrained

horizontally. The bottom boundary is fixed for both the vertical and the horizontal directions because deeper ground layers tend to have higher stiffness and are hard to deform. Therefore, this condition is made to let both normal stress and shear stress appear. The upper horizontal boundary is left free to displace to determine the surface settlement.

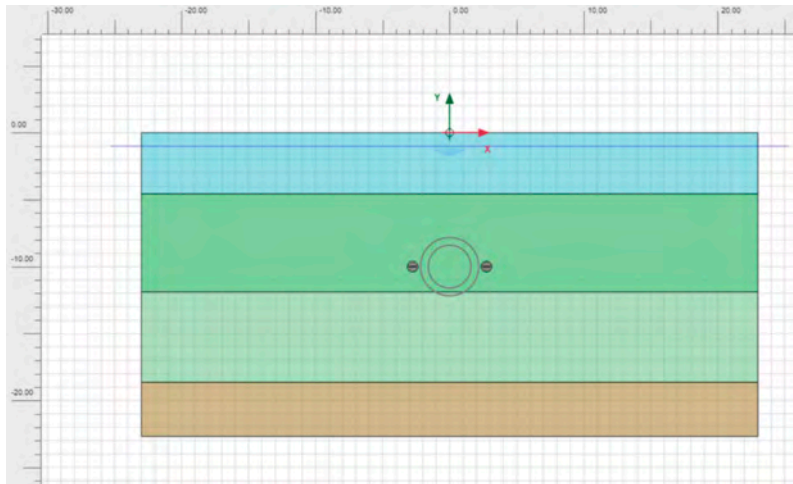


Figure 3. The numerical model simulated with dimensions.

4 RESULTS AND DISCUSSION

4.1 Results from the numerical simulation

After inputting the data into the software, the numerical analysis is carried out and the result is discussed.

Figure 4 shows the deformed mesh of the model. The mesh size and distribution of the soil body are the same in both models. As the soil deformation is most significant around the tunnel body, the closer the mesh towards the tunnel, the smaller the mesh size to increase the accuracy of determining the soil deformation. On the other hand, the deformed shape of the tunnel is related to the absolute total displacement of the model (Figure 5). It is observed that the upper part of the tunnel is flatter than the bottom part. From the absolute total displacement graph, the top part of the tunnel displaces more as the red color appears, which matches the flat deformed shape of the top tunnel. Meanwhile, the absolute total displacement of the tunnel bottom is relatively small, so it has no obvious displacement in the deformed shape shown in the software.

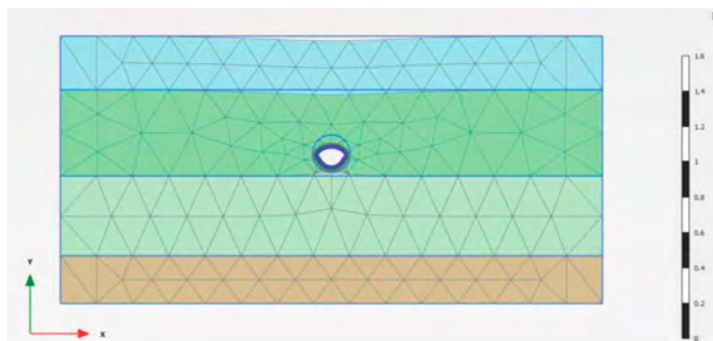


Figure 4. Deformed mesh of the model.

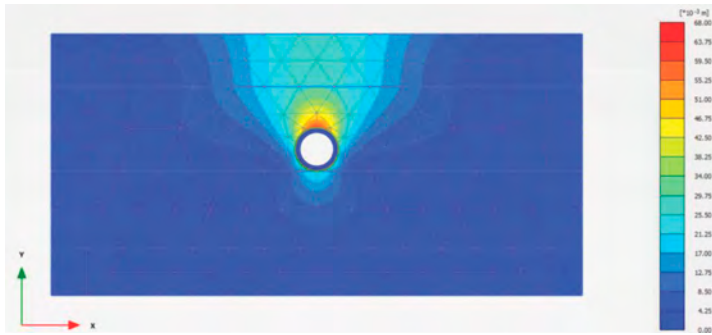


Figure 5. Absolute total displacement distribution.

The plastic points of the soil body are presented in Figure 6. Some plastic points exist on the soil near two sides of the tunnel body. It also implies that the two sides of the tunnel have a high chance of instability. Also, from the deformed mesh, the two sides of the tunnel body have more significant deformation.

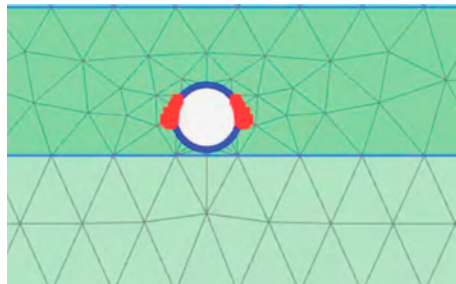


Figure 6. Plastic point around the tunnel (in red color).

Next, the surface settlement is obtained in Figure 7. The maximum surface settlement obtained is 27 mm. Moreover, the deformed shape of the surface is analyzed. A cross-section is selected exactly on the model's top surface and deformation curves of the cross-section at

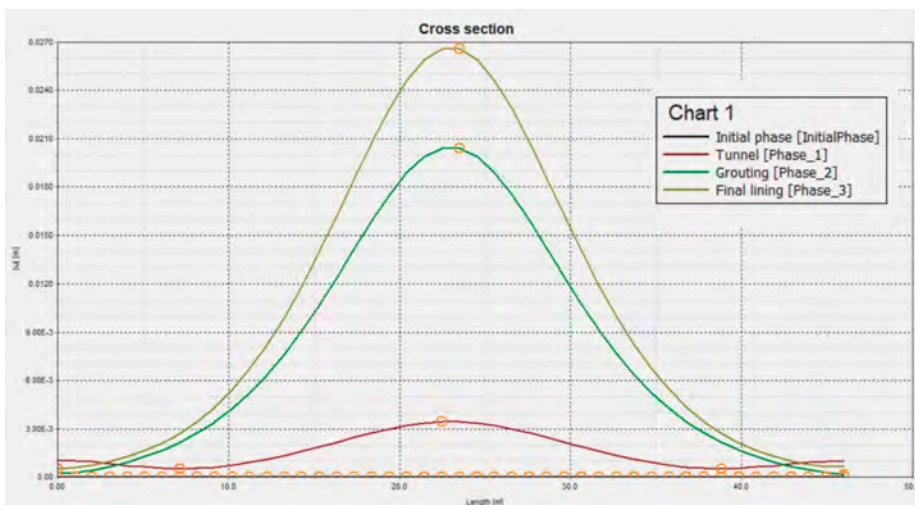


Figure 7. Deformation curve from the top surface.

every stage are generated. At the initial stage, there is no displacement on the surface. After the tunnel excavation stage, a small deformation occurs near the center of the tunnel axis. After the grouting stage, the deformation of the surface increases sharply because of the grouting pressure. There is a little increase in deformation after the final lining stage. Aside from the curves at the initial stage, all other curves exist in bell shape.

4.2 Comparison with field measurement data

In this section, the result obtained from the numerical analysis is used to compare with the field measurement data provided by the construction company. The field measurement data regarding the ground settlement was completed in March 2023, before the submission of this paper. For this construction project, the field measurement data is huge, and more than 200 monitoring spots and 20 cross-sections are included. To simplify the data, a cross-section from the field data is selected to compare with the numerical results.

As shown in Figure 8, a monitoring section with measurement points is located at Avenida da Amizade near the car park of Artyzen Grand Lapa Macau. It is located on one of the busiest roadways in Macau. Table 3 shows the monitoring data of the cross-section selected including the final cumulative settlement and maximum cumulative settlement recorded of each monitoring point.

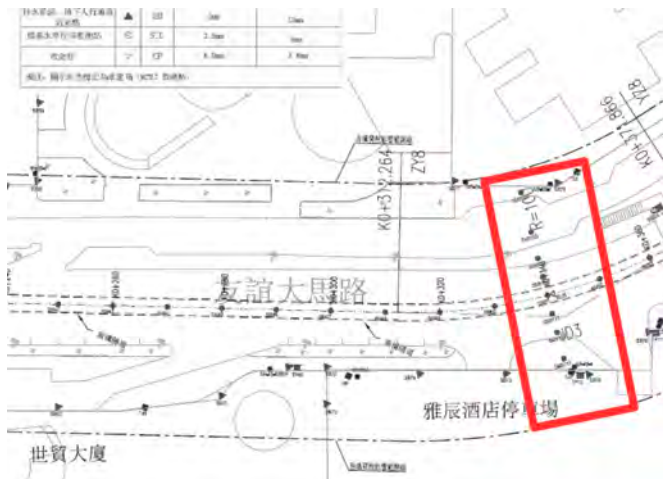


Figure 8. Location of the first monitoring cross-section selected. (MBEC-CRTG-MS CONSORTIUM, 2021).

Table 3. Monitoring data of the first cross-section selected (MBEC-CRTG-MS CONSORTIUM, 2021).

Monitoring point	SM 5104	SM 5103	SM 5102	SM 5101	SM 51	SM 5111	SM 5112	SM 5113
Final Cumulative Settlement, Δh , (mm)	4.9	-1.7	-12.1	-16.0	-17.0	-20.7	-17.1	-7.0
Maximum Cumulative Settlement recorded $\Sigma\Delta h$, (mm)	-0.6	-5.0	-15.1	-18.6	-19.7	-22.9	-18.4	-7.4

From Table 3, the maximum cumulative settlement recorded is 22.9 mm at the monitoring spot SM 5111. It is slightly smaller than the numerical analysis from the model (26.6 mm). The percentage error between the results is around 15%. It is believed that this difference is due to the complexity of the geological condition, the effect of the building and the traffic condition on

the ground surface, etc., which is unable to be simulated using the software. Moreover, some dynamic processes such as grouting and the change in water pressure will be greatly affected by external factors, which cannot be completely considered in PLAXIS 2D. As the field data are measured manually and the value of the measured value is tiny (in mm), some possible errors might exist during the measuring procedures. Therefore, this percentage error is acceptable.

On the other hand, the settlement curve is plotted in Figure 5.4 using the final cumulative settlements of the monitoring points selected. According to Peck (1969) and the numerical simulation, the settlement trough is normally distributed and symmetrical. However, the settlement trough measured from the field is unsymmetrical. It might result from external factors, leading to the shifting of the transverse trough. The maximum settlement trough might not lie above the center tunnel axis.

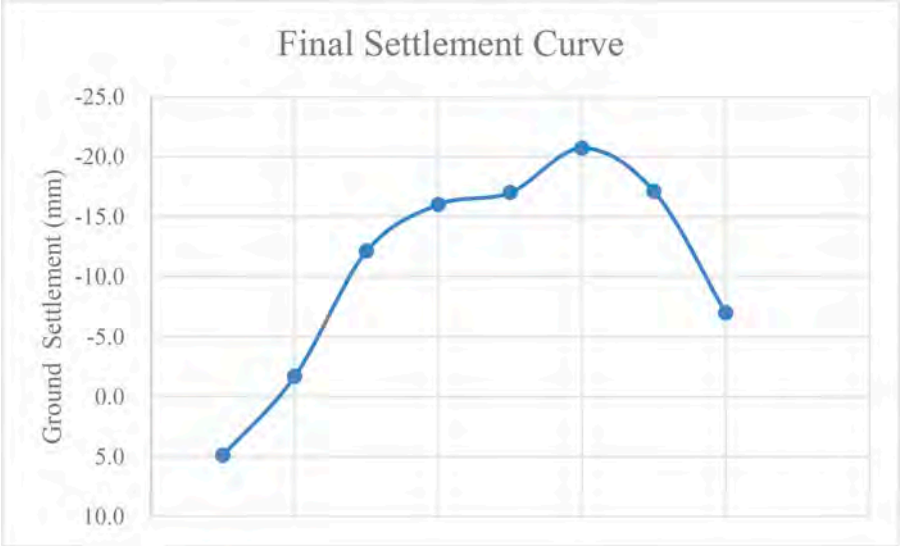


Figure 9. Final settlement curve of the first cross-section selected.

5 CONCLUSION

In this study, PLAXIS 2D was adopted to analyze the shield tunnel constructed in the NAPE area in Macau. After the simulation, the results obtained are discussed and compared with the field monitoring data.

From the result of PLAXIS 2D, the maximum surface settlement is obtained to be 27mm. Moreover, the deformed mesh matches the absolute total displacement distribution, where a larger deformation exists around the top part of the tunnel. Furthermore, plastic point checking has been carried out. It was found that plastic conditions occurred around the two sides of the tunnel, which matched with the deformed mesh.

On the other hand, the results obtained from the model were used to compare with the field measurement data provided by the construction company. The conclusions of the study have been summarised:

- There is a small but acceptable difference between the ground settlement obtained from PLAXIS 2D and the field measurement data. This difference is due to the complexity of the real geological condition and the part of the dynamic processes of the tunnel construction.
- The settlement trough measured from the field is unsymmetrical. It might be affected by external factors. Therefore, the maximum settlement is not necessarily at the position directly above the tunnel.

REFERENCES

- Bentley. 2020. *PLAXIS CONNECT Edition V21.00*.
- Chen, B. 2019. *Numerical Simulation of Soil Displacement in Shield Tunnel Construction Stages*. Master Thesis. Hefei University of Technology, China.
- Chen, X. 2017. *Study in ground settlement caused by metro shield construction – A case study of north extension line of Paris metro line 14*. Nanjing University of Science and Technology, China.
- Chow, Lily. 1994. *The prediction of surface settlements due to tunneling in soft ground*. Master Thesis. University of Oxford, the United Kingdom.
- Dhatt, G., Lefrançois, E., & Touzot, G. 2012. *Finite element method*. John Wiley & Sons.
- Lei-Kilany, M. E., El-Sayed, T.A., Mohab, R. A. 2017. Numerical analysis of tunnel boring machine in the soft ground. *Jokull Journal*. Vol. 67: No.5.
- MBEC-CRTG-MS CONSORTIUM (2021). “完善新口岸區污水截流管設計連建造承包工程 – 附件06: 現地調查報告”. 附件04: 岩土工程勘察報告.
- MBEC-CRTG-MS CONSORTIUM (2021). “地表沉降監測點數據一覽表”. 報告編號: SMM-041
- Möller S.C. 2006. *Tunnel induced settlements and structural forces in linings*. PhD thesis. University of Stuttgart–Institute of Geotechnical Engineering, Stuttgart, Germany.
- Peck, R.B. 1969. Deep excavations and tunnels in soft ground. *Proc., 7th Int. Conf. on Soil Mechanics and Foundation Engineering*. Mexico City, Mexico. pp. 225–290.
- Pinto, F., & Whittle, A.J. 2014. Ground Movements due to Shallow Tunnels in Soft Ground. I: Analytical Solution. *Journal of Geotechnical and Geoenvironmental Engineering*. ASCE. Vol. 140: No. 4, pp. 04013040–04013040.
- Sagaesta, C. 1987. Analysis of undrained soil deformation due to ground loss. *Geotechnique*. Vol. 37: No.3, pp.301–320.
- Zhu, C., Li, N. 2017. Prediction and analysis of surface settlement due to shield tunneling for Xi'an Metro. *Canadian Geotechnical Journal*. cgi-2016-0199.R2.

A continuum analysis of piles affected by an advancing tunnel excavation during centrifuge tests with a miniature TBM

E.K.L. Wong

Department of Engineering, University of Cambridge, UK

A. Franza

Department of Civil and Architectural Engineering, Aarhus University, Denmark

A.S.N. Alagha & G.M.B. Viggiani

Department of Engineering, University of Cambridge, UK

ABSTRACT: A two-stage model based on the elastic continuum approach and nonlinear near-pile stress transfer mechanism is used to study the three-dimensional behaviour of piles under the influence of an advancing tunnel boring machine (TBM). In particular, this continuum analysis is compared with the results of centrifuge tests carried out using a novel miniature TBM excavating in clay in the vicinity of piled foundations. The greenfield tunnelling-induced movements, a key input for the two-stage model, were estimated empirically by back-analysing the surface greenfield settlements and pile settlements measured during the centrifuge tests. The predictions of tunnelling-induced and post-tunnelling pile behaviour obtained with the continuum approach are compared with the measured settlements and axial forces for a row of single piles under constant external load. This provides further insights into the effects of TBM advancement on deep foundations. Future work will address pile groups with rigid elevated caps.

1 INSTRUCTION

Underground infrastructure can improve the environment and enable the sustainable development of urban areas (Parker 2004). The construction of tunnels and underground stations is often carried out near existing buildings, infrastructure and their foundations. Thus, it is important to conduct reliable impact assessments in the preliminary design stages for these works to take place safely.

The analysis of tunnel-soil-structure interaction with 3D finite element modelling involving sophisticated constitutive soil models requires careful calibration of model parameters, often difficult to define at an early stage. Also, the effort required for refined 3D finite element modelling may not be commensurate with the need to explore a large number of possible configurations efficiently. As an alternative, simplified, reduced-order interaction methods that capture the response of existing foundations to tunnelling are often useful. However, before their use in practice, it is necessary to validate these simplified methods against experimental or field data.

While centrifuge modelling for piles subjected to tunnelling effects has been carried out for tunnelling in plane strain (e.g. Loganathan et al. 2000; Jacobsz et al. 2004; Marshall & Mair 2011; Williamson et al. 2017) or in pseudo 3D by applying a staged volume loss (e.g. Ng et al. 2015; Soomro et al. 2018), previous studies do not capture in sufficient detail the mechanisms resulting from the advancement of a tunnel boring machine (TBM). To this end, Alagha (2024) developed a novel mini-TBM which can realistically simulate mechanised excavation of tunnels in the centrifuge and the 3D tunnelling-induced effects on piles.

In this paper, the experimental results of Alagha (2024), for a TBM advancing in clay in the vicinity of a row of single piles, are compared with those of a two-stage interaction model

(based on the elastic continuum approach and nonlinear near-pile stress transfer mechanism) to validate the model and provide insights into the modelling of tunnel advancement.

2 TWO-STAGE INTERACTION MODEL

The two-stage method is based on the beam theory for the piles, the half-space theory for the soil continuum, and nonlinear (linear elastic - perfectly plastic or hyperbolic) local stress transfer mechanism for the soil-pile interface. This enables the consideration of both active (self-weight and external) and passive (tunnelling-induced) loads, the latter defined as a function of input greenfield movements, thus bypassing the need to model the excavation process directly. In stage 1, active loads are applied to the foundation to obtain the pre-tunnelling conditions. In stage 2, in addition to active loads, the system is subjected to tunnelling-induced passive loads, which is represented by the greenfield displacements, to compute tunnelling-induced results. Tunnelling-induced effects are obtained from the difference between stages 2 and 1.

The equilibrium equation detailed by Franza et al. (2021) was modified from Klar et al. (2007) for the tunnelling case. The behaviour of a piled foundation is analysed by solving

$$(\mathbf{S} + \mathbf{K}^*)\mathbf{u} = \mathbf{P} + \mathbf{K}^*\lambda_s^* \mathbf{f} + \mathbf{K}^* \mathbf{u}^{\text{CAT}} + \mathbf{K}^* \mathbf{u}^{\text{IP}} \quad (1)$$

$$\mathbf{K}^* = \mathbf{R}(\lambda_s - \lambda_s^*)^{-1} \quad (2)$$

in which \mathbf{u} is the displacement of the pile nodes, \mathbf{P} is the active load vector (given by head load and self-weight distributed along a pile), \mathbf{S} is the stiffness matrix of the pile group, λ_s is the soil flexibility matrix, λ_s^* controls the interaction between pile nodes and is obtained by setting diagonal terms of λ_s to zero, \mathbf{K}^* is the local stiffness matrix defined as the inverse of the diagonal of λ_s , to which the diagonal reduction matrix \mathbf{R} (Franza et al. 2021) is applied to model the local hyperbolic local stress transfer mechanism using a hyperbolic soil stiffness degradation term $R_f = 0.8$, \mathbf{u}^{CAT} is the tunnelling-induced greenfield displacement, and \mathbf{u}^{IP} is the displacement of plastic sliders between the pile and the continuum, which model soil yielding when the mobilised resistance reaches the soil strength (as $R_f < 1$). This paper considers soil nonlinearities of the stress transfer mechanism only for the vertical degrees of freedom, while the horizontal soil-pile interaction is assumed to be linear elastic. Thus, the vertical sliders limit the vertical components of the soil reaction vector \mathbf{f} acting on the pile by the soil according to the available shaft friction and end-bearing resistance as follows:

$$-\{f_{\text{lim}}^{\text{up}}\}_i < \mathbf{f}_{z,i} = (\mathbf{S}\mathbf{u} - \mathbf{P})_{z,i} < \{f_{\text{lim}}^{\text{down}}\}_i \quad (3)$$

where $\{f_{\text{lim}}^{\text{up}}\}$ and $\{f_{\text{lim}}^{\text{down}}\}$ are upwards and downwards soil resistance vectors (obtained by intergrating shaft friction resistance and ultimate base pressure, while assuming tension cut-off at the base). This paper presents nonlinear hyperbolic - perfectly plastic results (denoted NP, where $R_f = 0.8$), while linear elastic - perfectly plastic analyses (denoted EP, i.e. $R_f = 0$) are also briefly discussed (results omitted for brevity).

To compare with centrifuge results, the soil flexibility matrix (λ_s) considers the presence of a bottom rigid boundary and the increase in stiffness of the undrained continuum layer. The flexibility matrix is first obtained from the solution of the linear elastic half-space. A modification factor is introduced based on influence coefficients (Steinbrenner 1934) which takes into account the relative dimensions of the pile cross-section and the thickness of the compressible layer. To consider the variation of stiffness with depth, the diagonal (local) terms of the flexibility matrix are computed from the values of the Young's modulus at the relevant depth while the off-diagonal terms, which describe the interaction between nodes, are computed using the average value of Young's moduli at the depths of the two nodes (Chow 1986). This implementation of the flexibility matrix has been compared with literature results for pile groups in an elastic continuum under external load and tunnelling-induced ground movements (e.g. Poulos 1989; Kitiyodom et al. 2005).

Tunnelling-induced greenfield settlements are key to the two-stage analysis; however, in this case there are uncertainties because, as discussed later, only surface displacements were measured during centrifuge testing. In this study, the centre-line surface settlement $W_{\max,0}^*$ measured for different locations of the TBM is used to generate an empirical 3D tunnelling-induced settlement field with Equation 4 which considers a standard Gaussian settlement trough in the transverse direction (Peck 1969; Attewell & Woodman 1982). In particular, the settlement troughs are inferred from the surface profile considering undrained conditions and a linear relationship with depth for the transverse distance i of the inflection point of the settlement trough from the tunnel axis (see Equation 5).

$$w(x, y, z) = w_{\max}(y, z) \exp\left(-\frac{x^2}{2i^2}\right) \quad w_{\max}(y, z) = \sqrt{\frac{\pi}{32}} \frac{V_L D_t^2}{i} \quad (4)$$

$$\frac{i}{z_t} = A + B \left(1 - \frac{z}{z_t}\right) \quad (5)$$

where x , y , and z are spatial coordinates, D_t is the tunnel diameter, V_L is the tunnel volume loss (expressed as a percentage of the nominal tunnel face area and constant for all horizons above the tunnel under undrained conditions) and z_t is the tunnel axis depth. While Mair et al. (1993) suggested $A = 0.175$ and $B = 0.325$ for Equation 5, in this paper A and B are back-analysed from the surface inflection distance i_0 and the settlement of the pile at the centre-line, as detailed below). Note that A and B are physically related to the focus of the vectors of tunnelling-induced displacements, which is at the intersection between the tangent di/dz and the tunnel centre-line (Grant & Taylor 2000).

3 CENTRIFUGE SET-UP AND MODEL PREPARATION

Two centrifuge tests are considered in this paper, one in greenfield conditions and one for tunnelling in the vicinity of a row of single piles. The internal usable dimensions of the centrifuge strong box were 780 mm width, 460 mm depth and 620 mm height (Figure 1). In these experiments, the thickness of the clay layer was 375 mm; the depth of the tunnel axis was 235 mm; the cutterhead diameter of the mini-TBM was 78 mm which gave a cover-to-diameter ratio of 2.5. The development of the mini-TBM has been documented in Viggiani et al. (2022) and Alagha (2024). At 50 g, the setup simulates a 4 m diameter TBM excavating at a depth of 11.75 m in clay.

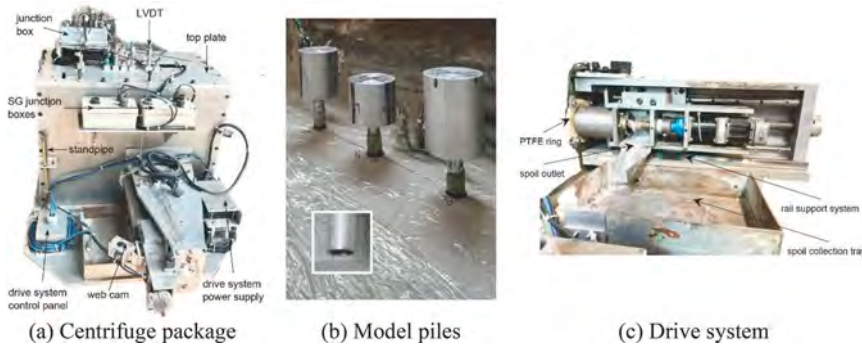


Figure 1. Centrifuge setup.

The clay was consolidated by applying a compressive load at the surface and suction at the base to achieve a lightly over-consolidated sample. Speswhite Kaolin clay was used to model an undrained tunnelling process, with critical state parameters $M = 0.8$, $N = 3.14$, $\lambda = 0.14$, $\kappa = 0.033$, $\phi_{\text{crit}} = 21^\circ$ and plasticity index $PI = 24\%$. The following linear variations (from top to bottom of clay) of properties were estimated from the pre-consolidation phase: specific

volume $v = 2.89 - 2.86$, pre-consolidation pressure $\sigma'_{v,max} = 85 - 165$ kPa, while the vertical effective stress was constant at $\sigma'_v = 75$ kPa. For further details, refer to Alagha (2024). Considering the dependency of the undrained shear strength on plasticity index, overconsolidation ratio and vertical effective stress (Wroth 1984), across the depth of the model, the undrained S_u increased linearly between 16.1 – 23.9 kPa. These values agree with the results of T-bar penetration tests performed in-flight (omitted for brevity, see Alagha 2024). From the critical state parameters and mean effective stress after consolidation, a profile of linearly increasing small-strain undrained Young's modulus $E_u = 7.1 - 8.1$ MPa is obtained.

Close-ended hollow aluminium tubes of 10 mm outer diameter and 1 mm thickness were used to simulate concrete piles (Figure 1b). The corresponding prototype piles are 0.5 m diameter reinforced concrete piles with Young's modulus of 30 GPa. The three model piles P1, P2 and P3 have a length of 175 mm, 235 mm and 275 mm, respectively. During preparation, the piles were pushed into pre-drilled holes which were smaller and shallower than the piles; this ensured that shaft friction and base resistance could be mobilised. In flight, constant head loads of approx. mately 50% the capacity of each pile were applied before the TBM drive. The pile capacity was estimated from the shaft friction while ignoring the base resistance, using the alpha method with an adhesion factor $\alpha = 1$. Accordingly, in the two-stage numerical model, the estimated profile of S_u with depth is used to derive the limiting shaft friction (αS_u) and the base compressive resistance is taken as $9S_u$ to compute f_{lim}^{up} and f_{lim}^{down} .

4 CENTRIFUGE GREENFIELD RESULTS

In the greenfield centrifuge test, the cross-section monitored was located at a TBM drive distance of half the tunnel diameter from the starting position, as shown in Figure 2a. Surface settlements were measured at five locations L1 to L5.

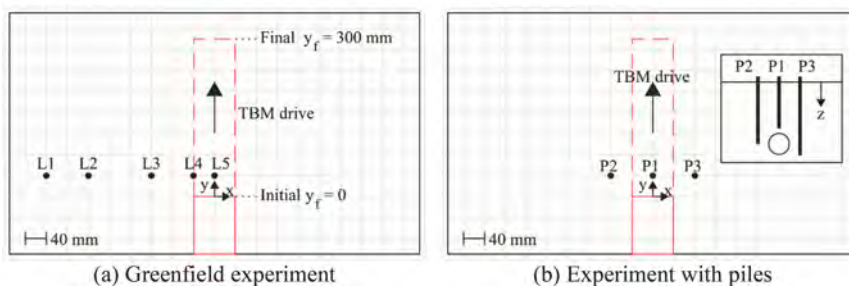


Figure 2. Layout of centrifuge tests.

Figure 3 shows the fitted greenfield settlement profiles. Figure 3a shows that the measured transverse settlement troughs w_0^* for different TBM positions are consistent with a Gaussian profile, with an average value of surface inflection distance $i_0 = 0.56z_t$. In Figure 3b, the centre-line settlement at L5 ($w_{max,0}^*$) is fitted with an empirical function of the tunnelling distance $w_{max,0}^* \approx 0.4018 - 0.3994 \exp(-0.648yf / Dt)$. This is then combined with $i_0 = 0.56 z_t$ to obtain the greenfield surface profiles at L1 to L4 using Equation 4. As the steady-state condition was not reached at the end of the tunnel excavation, this empirical fit is used for the two-stage analysis instead of the traditional approach of estimating longitudinal settlement using a cumulative probability function.

Finally, Figure 4 shows the adopted i/z_t profile and its comparison with other expressions available in the literature; i/z_t associated with $A = 0.067$ and $B = 0.497$ is estimated from surface $i_0/z_t = 0.56$ and the ‘neutral point’ of central pile P1, which is the location at which the shaft friction changes sign. The ‘interaction level’, where subsurface greenfield soil settlement is equal to the tunnelling-induced pile settlement, is assumed to match the location of the neutral point (Franza et al. 2021). The assumed empirical profile implies that the focus of the

displacement vectors is at a depth $z = 1.13zt$, which is between the tunnel axis and the depth of $1.54zt$ from the expression by Mair et al. (1993). Further work will involve a sensitivity study of the depth of the focus on the results.

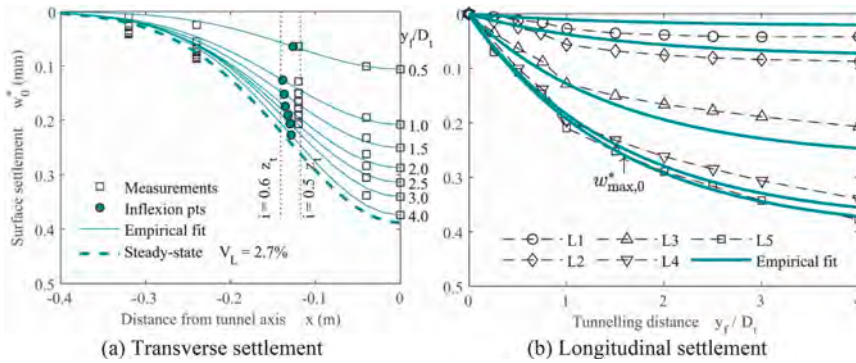


Figure 3. Greenfield settlement at model scale.

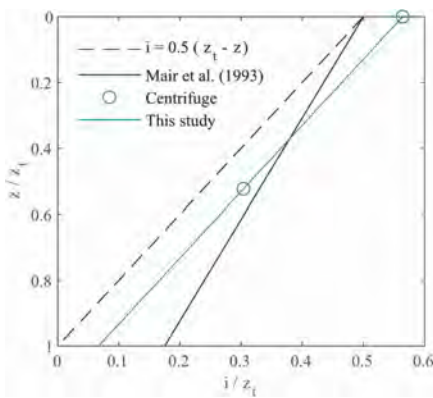


Figure 4. Settlement trough width.

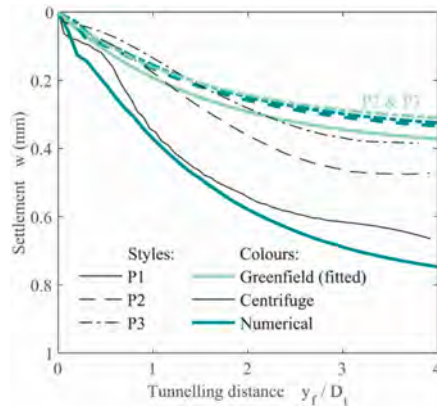


Figure 5. Tunnelling-induced pile settlements.

5 RESULTS FOR TUNNELLING NEAR PILES

Figure 2b shows the layout of the centrifuge experiment in which the TBM advanced close to the three model piles: pile P1 directly above the tunnel at a clearance of $0.26Dt$ from the tunnel crown; piles P2 and P3 extending to the levels of the axis and invert of the tunnel respectively, both at an offset of $|x| = Dt$ from the centre-line. The comparison between predicted and measured settlements of the piles is shown in Figure 5. The TBM crossed underneath the transverse sections with the piles at $y_f/Dt = 0.5$. The cutterhead and brass shield collar were 110 mm in length in total, i.e. they had completely passed the pile location when $y_f/Dt = 2$. The pile settlements continued to develop and had not completely stabilised at the end of the tunnel drive. The final settlement of pile P1 exceeded the greenfield surface settlement at L5 by 76%. Likewise, the settlements of P2 and P3 were larger than the corresponding measured greenfield settlements.

In the following, numerical estimates of the pile response to tunnelling are presented. In this paper, two values of the soil's stiffness were in the nonlinear elastic - perfectly plastic model, namely 30% and 100% of the small-strain value, E_u . This is meant to account in a simplified manner for the likely reduction of stiffness due to pile installation and tunnelling-induced

shearing. The corresponding results are labelled as NP 30 and NP 100. Given the relatively large tunnel volume loss, a reduction of about 2/3 of Young's modulus is reasonable.

Figure 5 reports the pile settlement obtained from the nonlinear elastoplastic (NP) analyses. Elastic perfectly plastic (EP) simulations return very similar pile settlements and are not shown for clarity; the effect of the adopted soil stiffness, whether 100% or 30% of the small-strain value, on tunnelling-induced pile settlements is also minor and thus only NP 100 results are presented.

The agreement between the simulated and measured settlements of P1 is very good, particularly up to a TBM position of $y_f = 2Dt$. For $y_f > 2Dt$, the external piles P2 and P3 settled in the experiment more than the centre-line surface greenfield value (which is not consistent with the observations by Selemetas & Standing 2017). Focusing on the central pile P1 only, the good agreement is attributed to the fact that the measured greenfield settlement at L5 is used to derive the input greenfield settlements in the numerical analysis. The final settlement at the end of the test is close to the measured value, with a difference of 14%. Consistently with other results in the literature, the numerical pile settlement is greater (approximately double) than the maximum greenfield surface settlement, also shown in Figure 5 for comparison; this is due to greenfield settlements increasing with depth along the pile (see Figure 6d) as the result of decreasing i with depth z . Piles P2 and P3 were located at an offset of one tunnel diameter from the tunnel axis. Surprisingly, the experimental results for $y_f > 2Dt$ indicate that the piles settled more than the soil at the tunnel centre-line in greenfield conditions. As discussed by Alagha (2024), this may be due to the tunnel linings advancing with the TBM and thus unrealistically shearing the soil.

The final pile settlement of pile P2 in the centrifuge test was 0.47 mm, while the final settlement of pile P3, which extended to a deeper level, was 0.38 mm; both are larger than the centreline greenfield settlement of $w_{\max,0}^* = 0.37$ mm. In contrast, the final simulated settlements at $y_f = 4Dt$ of the two piles were similar (≈ 0.33 mm and smaller than the measured values by 30% and 16%, respectively) and both lower than $w_{\max,0}^*$ (consistent with evidence from literature). Therefore, the subsequent detailed analyses of interaction results focus on a maximum tunnel advancement up to $y_f = 2Dt$.

The average shaft friction mobilised along the central pile (P1) was calculated from strain gauge measurements. Figure 6a shows the distribution of shear stress τ_{mob} mobilised under the applied external load only (pre-tunnelling) and after the passage of the tail of the shield ($y_f = 2Dt$). Note that, in the centrifuge test, the pile head mass was in place from the start of the test (Figure 1b). Its weight increased during the spin-up until the full service load was achieved at 50 g. As a result of this procedure, the pre-tunnelling pile forces and mobilised shear stress along the shaft did not correspond exactly to the behaviour of an initially unloaded pile under the application of external load, which the numerical analysis simulates. When considering pre-tunnelling results, the numerical mobilised shear stress along the shaft τ_{mob} is consistent with but slightly larger than the centrifuge measurements. After the passage of the TBM shield, the measurements indicate that further positive (upwards) shear stresses were mobilised along the shaft down to the middle portion of the pile in the test while, near the pile base, a stress reduction (and reversal) was induced by the excavation. These trends are captured by the NP numerical model, although both numerical models with small-strain (NP 100) and reduced stiffness (NP 30) overestimate the stress reversal and negative (downwards) shaft friction in the bottom portion of the pile. Comparing the two numerical analyses, NP 30 is in closer agreement with experimental results than NP 100, as confirmed by the axial force profiles in Figure 6e. If the profiles of measured axial forces in Figure 6e are extrapolated linearly to the case of the pile, it can be observed that a significant base resistance was mobilised in the centrifuge model before tunnelling, which reduced to essentially zero after the passage of the TBM. In contrast, the numerical analyses predict relatively small pile base pressures prior to tunnelling, and relatively large tunnelling-induced negative friction associated with tensile (negative) axial forces in the lower part of the pile. These differences may be partially explained by the experimental pile installation process, in which the piles were installed in pre-drilled holes which were 30 mm shallower than the piles and thus resulting in greater stiffness of the pile base with respect to the shaft than what is being modelled in this paper.

Note that, in continuum analysis, the spin-up process of the centrifuge test with increasing g level is not modelled. Thus, it is of interest to consider the tunnelling-induced shaft friction ($\Delta\tau_{mob}$) and axial force (ΔN) of the pile, and the neutral point associated with the variation in shaft friction, to isolate (albeit only partly) the influence of the spin-up. Figure 6b shows the measured and simulated change in shaft friction $\Delta\tau_{mob}$ induced by tunnelling. From the numerical analyses, a neutral point occurs at $z/L_p = 0.76$ (Point ‘A’ in Figure 6b) above which $\Delta\tau_{mob} > 0$ as the pile settles more than the greenfield soil due to the down-drag exerted by the subsurface tunnelling-induced settlements close to the tip. Below Point ‘A’, because the soil movement is greater at depth but the pile is relatively rigid, the soil settles more than the pile and negative shear stresses develop ($\Delta\tau_{mob} < 0$). In other words, in Figures 6c and 6d, $\tau_{mob} > 0$ when the pile settlement w (due to both active and passive loads) exceeds approximately the greenfield soil.

Settlement and $\Delta\tau_{mob} > 0$ when the tunnelling-induced pile settlement Δw (due to passive loads only) exceeds the greenfield soil settlement. Similarly, the neutral point from the centrifuge test was also at about $z/L_p = 0.70$ (Point ‘B’ in Figure 6b and 6d), as pile settlements due to active loads are relatively small compared to tunnelling-induced greenfield movements. In both the numerical analyses and centrifuge test, the maximum reduction in pile axial force ΔN occurred near a depth z/L_p of 0.7 - 0.8, which is close to the neutral point of the pile. As stated previously, the empirical subsurface greenfield settlement profile adopted in the two-stage analysis was backcalculated from the depth of the neutral point ‘B’ in Figure 6b, hence the same depth of point ‘B’ in Figure 6d.

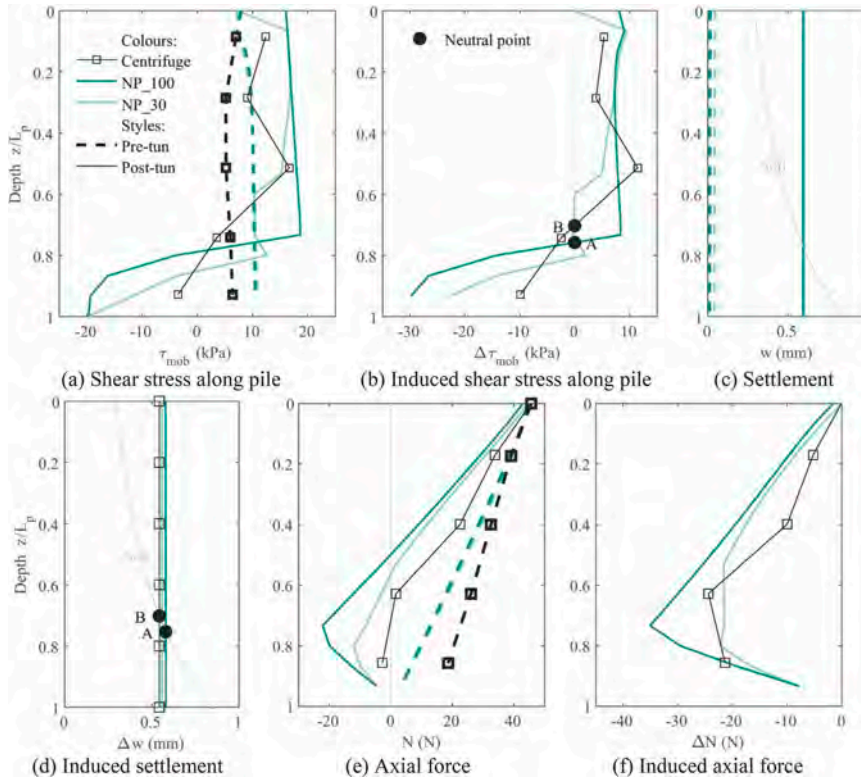


Figure 6. Tunnelling-induced effects on Pile P1 (TBM at $y_f = 2D_t$).

6 CONCLUSION AND PERSPECTIVE

This paper presents the back analysis of centrifuge test results of piles subjected to advancing mechanised tunnelling effects using a nonlinear two-stage continuum interaction model. It addresses pile settlement and the development of shaft friction and internal forces during the

excavation. Despite differences, the proposed numerical approach has reproduced the salient features of pile response to an advancing tunnel excavation. Differences are partly due to uncertainties in the greenfield displacement field arising from the lack of direct subsurface settlement measurements; this model has enabled a quick sensitivity study which shows the importance of considering an appropriate secant stiffness in the prediction of tunnelling-induced effects. Future work will involve further characterising subsurface greenfield movements and their impact on piles.

Algha (2024) performed additional centrifuge tests to investigate the effects of pile length, pile location and pile arrangement (e.g. single piles vs pile groups). Research work is currently ongoing, to compare experimental and reduced-order modelling results in the case of pile groups to demonstrate the reliability of continuum analysis for 3D assessment of tunnelling underneath piled foundations.

ACKNOWLEDGEMENT

The first author gratefully acknowledges the support of the Hong Kong Institution of Engineers

Arthur & Louise May Memorial Scholarship.

REFERENCES

- Algha, A.S.N. 2024. Centrifuge modelling of the impact of mechanised tunnelling on piled foundations using a miniature TBM. PhD thesis, Department of Engineering, University of Cambridge.
- Attewell, P. B. & Woodman, J. P. 1982. Predicting the dynamics of ground settlement and its derivative caused by tunnelling in soil. *Ground Engineering*, 15:13–22.
- Chow, Y. K. 1986. Analysis of vertically loaded pile groups. *International Journal for Numerical and Analytical Methods in Geomechanics*, 10(1):59–72.
- Franza, A., Marshall, A. M. & Jimenez, R. 2021. Non-linear soil–pile interaction induced by ground settlements: pile displacements and internal forces *Geotechnique* , 71(3):239–249.
- Jacobsz, S. W., Standing, J. R., Mair, R. J., Hagiwara, T. & Sugiyama, T. 2004. Centrifuge modelling of tunnelling near driven piles *Soils and Foundations*, 44(1):49–56.
- Grant, R. J. & Taylor, R. N. 2000. Tunnelling-induced ground movements in clay. *Proceedings of the Institution of Civil Engineers - Geotechnical Engineering*, 143(1):43–55.
- Kitiyodom, P., Matsumoto, T., and Kawaguchi, K. 2005. A simplified analysis method for piled raft foundations subjected to ground movements induced by tunnelling. *International Journal for Numerical and Analytical Methods in Geomechanics*, 29(15):1485–1507.
- Klar, A., Vorster, T. E., Soga, K., & Mair, R. J. 2007. Elastoplastic Solution for Soil-Pipe-Tunnel Interaction. *Journal of Geotechnical and Geoenvironmental Engineering*, 133(7):782–792.
- Loganathan, N., Poulos, H., & Stewart, D. 2000. Centrifuge model testing of tunnelling-induced ground and pile deformations. *Geotechnique* , 50(3):283–294.
- Mair, R. J. & Taylor, R. N. 1997. Bored tunnelling in the urban environment. In *Proceedings of the 14th International Conference on Soil Mechanics and Foundation Engineering*, Hamburg, 2353–2385.
- Mair, R. J., Taylor, R. N. & Bracegirdle, A. 1993. Subsurface settlement profiles above tunnels in clays. *Geotechnique* , 43(2):315–320.
- Marshall, A. & Mair, R. J. 2011. Tunneling beneath driven or jacked end-bearing piles in sand. *Canadian Geotechnical Journal*, 48(12):1757–1771.
- Ng, C. W. W., Hong, Y., and Soomro, M. A. 2015. Effects of piggyback twin tunnelling on a pile group: 3d centrifuge tests and numerical modelling. *Geotechnique* , 65(1):38–51.
- O'Reilly, M. P. & New, B. M. 1982. Settlements above tunnels in the United Kingdom - their magnitude and prediction. In *Proceedings of the Tunnelling '82 Symposium*, London, 173–181.
- Parker, H. W. 2004. Underground Space: Good for Sustainable Development, and Vice Versa. In *International Tunnelling Association Open Session, World Tunnel Congress*, Singapore.
- Peck, R. B. 1969. Deep excavations and tunneling in soft ground. In *State of the Art Volume of the 7th International Conference on Soil Mechanics and Foundation Engineering*, Mexico, 225–258.
- Poulos, H. G. 1989. Pile behaviour - theory and application. *Geotechnique* , 39(3):365–415.
- Selemetas, D. & Standing, J. R. 2017. Response of full-scale piles to EPBM tunnelling in London Clay. *Geotechnique* , 67(9): 823–836.

- Soomro, M. A., Ng, C. W. W., Memon, N. A., & Bhanbhro, R. 2018. Lateral behaviour of a pile group due to side-by-side twin tunnelling in dry sand: 3d centrifuge tests and numerical modelling. *Computers and Geotechnics*, 101:48–64.
- Steinbrenner, W. 1934. Tafeln zur Setzungsberechnung. *Die Strasse*, 1:121–124.
- Viggiani, G., Algha, A.S.N. & Haigh, S.K. 2022. Reduced scale modelling of mechanised tunnelling - challenges and perspectives. In *Proceedings of the 10th International Conference on Physical Modelling in Geotechnics*.
- Wan, M. S. P., Standing, J. R., Potts, D. M. & Burland, J. B. 2017. Measured short-term ground surface response to EPBM tunnelling in London Clay. *Geotechnique* ', 67(5):420–445.
- Williamson, M. G., Elshafie, M. Z. E. B., Mair, R. J., & Devriendt, M. D. 2017. Open-face tunnelling effects on non-displacement piles in clay. *Geotechnique* ', 67(11):983–1000.
- Wroth, C. P. 1984. The interpretation of in situ soil tests. *Geotechnique* ', 34(4):449–489.

Numerical analysis of rectangular tunnel boring machine induced ground settlement

J. Yu, H. Li & M. Huang
Tongji University, Shanghai, China

C.F. Leung & J. Lim
National University of Singapore, Singapore

ABSTRACT: A method to be able to simulate induced ground settlement by Rectangular Tunnel Boring Machines (RTBMs) will allow engineers to predict possible ground deformations and put in place measures to mitigate the risk of settlements. In this paper, displacement controlled numerical methods (DCM) based on the gap methods proposed by this study and Ng (2017) are used to predict the ground settlement caused by RTBM. The former assumes that the deformed tunnel shape is similar to the original excavated shape, while the latter assumes that the four corners of the rectangle segment is considered to be fixed. The trend and the magnitude of the settlement will be used as a basis of comparison to see whether the two DCMs are suitable to back analyse the transverse settlement. The DCM by Ng (2017) is more applicable to back analysing the RTBM drive from before it approaches towards the end of the drive whereas the proposed DCM in this study is more applicable to back analysing measurements that have been taken at a short time frame after the drive has been completed.

1 INTRODUCTION

With urban population ever on the rise, the increase in demand for space has been one of the top priorities for cities to deal with. With such close proximity to live traffic flow on the roads and nearby buildings in such dense areas, new underpass or subway projects face the tough challenge of needing to minimize disturbance and displacements in the ground. Any excessive movement in the ground could lead to dire consequences. Rectangular Tunnel Boring Machine (RTBM) is a typical choice when it comes to the construction of these tunnels. With the ability to minimize the damage to the surface and change the various sizes of the rectangular box segment, the application of RTBM in underground space becomes extremely relevant. Hence, a method to be able to simulate induced ground settlement by RTBM will allow engineers to predict possible ground deformations and put in place measures to mitigate the risk of settlements.

The analytical and displacement control numerical methods were often used to simulate tunnelling-induced ground settlement (Sagaseta, 1987; Loganathan and Poulous, 1998; Cheng et al., 2007). However, these methods have only been able to be applied to conventional circular TBM tunnelling and PJ projects. It is notable to see that there have been no established empirical relationships to predict ground deformations that arise from RTBM projects. In this paper, two different displacement controlled numerical methods (DCM) based on the gap method are used to predict the ground settlement caused by RTBM. The two novel methods will be used to back analyse field data from a case study in a bid to validate the methods.

2 DISPLACEMENT CONTROLLED NUMERICAL METHODS

2.1 *Displacement controlled method 1 – The proposed DCM*

This paper suggested a method based on the gap method to back analyse the data from RTBM projects. The gap method, GAP, has the advantage of taking into account effects of

construction depending on the site conditions and the modelling input. It can also assume plane strain analysis and this will allow 2D Finite Element Modelling (FEM) software to be used. The intention of the method is to simulate the closing of the physical gap between the RTBM segment lining and annular space. The main concept of this method proposed is that it follows the mechanism similar to that of DCM with the same assumptions and a change to the in shape from circular to rectangular.

The first assumption of Proposed DCM is that there is minimal to none displacement at the invert of the tunnel. Any displacement at the invert will considered to contribute to the magnitude of displacement at the top of the rectangular tunnel. The second assumption was that the deformed tunnel shape is similar to the original excavated shape. In addition, we assume that the area of the final tunnel shape is equal to the inner area of the segment lining, disregarding the thickness of the segment lining. The third assumption is that the volume of the annular space is the same volume as the volume of the settlement trough of the field data. In this paper, since we are only looking at the trailing settlement of the RTBM, the time at which we are analysing the data is considered to be immediately after the construction of the RTBM segment lining. Thus, it can be assumed that the conditions under which we are back analysing the data are short term and that the excess pore water pressure has not dissipated.

The Schematic diagram of Proposed DCM is shown in Figure 1, where, W is the width of theoretical excavated tunnel, H is Height of theoretical excavated tunnel, δW is the prescribed displacement for width, δH is the prescribed displacement for height, W_f is the Width of final excavated tunnel H_f is the height of final excavated tunnel. The nodes of the tunnel boundary will be pulled from the original position to a final position.

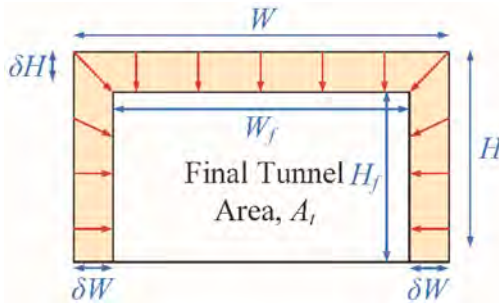


Figure 1. Schematic diagram of the proposed DCM.

With the assumptions in place, the steps below will show the calculation method is arrived at for the proposed DCM.

Step 1: Assume that the deformed tunnel shape is similar to the original excavated shape, we obtain a geometric ratio called α

$$\frac{W}{W_f} = \frac{H}{H_f} = \alpha \quad (1)$$

Step 2: Under the assumption that the volume of the annular gap is equal to the volume of the settlement trough, we can take the subtract the area of the final shape away from the area of the initial excavated shape. Using this relation, we are able to obtain the equation for theoretical volume loss VL,

$$VL = \frac{V_t}{V_t + A_t} = \frac{HW - H_f W_f}{HW} \quad (2)$$

Step 3: With the value of the final and initial excavated height obtained, we are able to get the necessary values of the displacement required to be prescribed.

Prescribed Displacement for height,

$$\delta H = H - H_f \quad (3)$$

Prescribed Displacement for width,

$$\delta W = W - W_f \quad (4)$$

2.2 Displacement controlled method 2 – NG DCM

The second method put forward is proposed by Dr Ng (Ng, 2017). It will be referred to as NG DCM for this paper. The first assumption of NG DCM is that there is minimal to none displacement at the invert of the tunnel. Any displacement at the invert will be considered to contribute to the magnitude of displacement at the top of the rectangular tunnel. The second assumption of NG DCM is that the area of the final tunnel area shape is equivalent to the inner area of the segment lining, disregarding the thickness of the segment lining. The third assumption of NG DCM is that the four corners of the rectangle segment are considered to be fixed. Hence, by converting the volume loss around the four sides of the rectangle tunnel and converting it to prescribed displacements, it gives rise to 3 triangular shaped displacements at the top and the two sides of the tunnel. The deformed tunnel shape is not the same as the original shape of the rectangular tunnel.

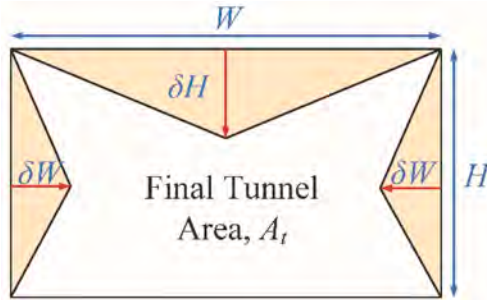


Figure 2. Schematic diagram of NG DCM (Ng, 2017).

With the assumptions of NG DCM in place, the steps below will show the calculation method is arrived at for NG DCM.

Step 1: Under the assumption that the volume of the annular gap is equal to the volume of the settlement trough, the volume loss is taken as the area of prescribed displacements over the total excavated area per unit metre. Using this relation, we are able to obtain the equation for theoretical volume loss VL ,

$$VL = \frac{0.5\delta HW + \delta WH}{WH} \quad (5)$$

Step 2: With the equation of the volume loss, the prescribed displacements, δW and δH are going to be varied in Microsoft Excel. The magnitude of the Final Tunnel Area, A_t , will be used as a check to ensure that the amount of prescribed displacements does not cause the magnitude of A_t to be lesser than the magnitude of the inner area of the segment lining.

$$A_t = WH - (0.5\delta HW + \delta WH) \quad (6)$$

3 CASE STUDY

In this section, the proposed DCM in this study and NG DCM will be used to back analyse the field data from a case studies. The trend and the magnitude of the settlement will be used as a basis of comparison to see whether the 2 DCMs put forward is a suitable method to back analyse the transverse settlement trough at selected sections. The results of the back analysis will then be compared with the field data and the findings will be discussed subsequently.

FEM software Plaxis 2D has been used to model the ground conditions and the prescribed displacement methods, and Mohr-Coulomb (MC) model is selected to model the materials.

The modelling of DCM process can be split into three main stages

Table 1. Modelling of DCM process.

Sequence	Modelling sequence
Step1	Generation of initial effective stress, state parameters and pore pressures
Step2	Rectangular tunnel is wished in place, line displacements are set to fixed to ensure that there is no movement of soil, and displacements and small strain are reset to zero
Step3	Line displacements used to pull nodes of tunnel boundary pulled to simulate the closing of the annular gap around the rectangular tunnel

The case study is the construction of a long pedestrian underpass with the use of the RTBM. The project is the Jiangdong Underground Walkway along Line 2 of Nanjing Metro. As can be seen in Figure 3, the pedestrian underpass was jacked under two roads and over two existing metro tunnels. The length of the pedestrian walkway is 94.5 m. The dimensions of the RTBM used was 7.02 by 4.32 m. The overburden of the ground from the top of the pedestrian walkway to the ground is in the range of 6.0 to 6.2 m. Reinforced (RC) precast segments were used with dimensions of 7.0 by 4.3 m of width and height; 1.5 m in length and 500 mm in thickness. There was a total of 63 precast RC segments being used for the total length of the pedestrian walkway. The RTBM was selected for the project as it was the most economical and fastest way to construct an underground pedestrian walkway without having to resort to an open cut method that would be extremely disruptive to the activities and the traffic in the area. (Dingwen Zhang B. L., 2016). The monitored data was taken from the nine monitoring points along monitoring section over the period of 23rd June to 9th August.

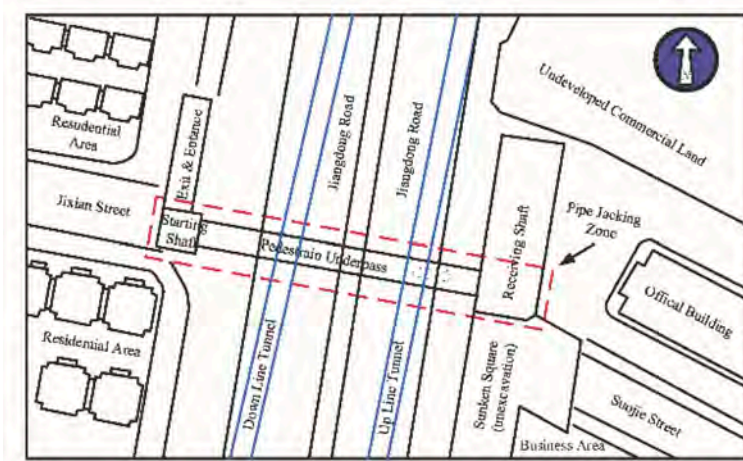


Figure 3. Overview of Nanjing Pedestrian Underpass.

3.1 The proposed DCM

Table 2 shows the ground properties which will be used for FEM back analysis in later sections. Plaxis 2D was utilized to carry out the back analysis. The proposed DCM in this study is used first. The FEM model as seen in Figure 4 was 700 m wide (x -direction transverse to the tunnel). 80 m deep (y -direction) as shown in the figure below. The model was modelled using 15-noded elements. The width of the model was made large enough such that any boundary effects of the model will be eliminated. a 40 m by 22 m rectangular area demarcated around

the rectangular tunnel where the mesh was refined to the highest settings possible. The mesh was then generated on settings of ‘Very Fine’. This was done with the intention of being able to obtain the displacements around the tunnel as accurately as possible.

Table 2. Nanjing case study ground properties.

Material	Fill	Muddy Silty Clay	Silty Clay	Silty Fine Sand 1	Silty Fine Sand 2	Medium Coarse Sand	Highly Weathered Siltstone	Moderate Weathered Siltstone
Drainage Type	Drained	Undrained	Undrained	Drained	Drained	Drained	Undrained	Undrained
Depth (m)	0-4	4-22	22-29	29-43	43-58	58-60	60-62.5	62.5-80
Unit Weight	18.00	17.90	18.20	18.10	18.50	20.00	21.00	23.00
γ (kN/m ³)								
Cohesion c' (kPa)	17.50	15.40	17.70	9.00	8.50	8.00	30.00	200.00
Friction Angle ϕ' (°)	13.40	14.70	15.00	36.00	36.30	35.00	30.00	30.00
Elastic Modulus E' (MPa)	15.00	18.00	23.00	55.00	60.00	100.00	150.00	200.00
Poisson's ratio ν	0.35	0.39	0.37	0.35	0.35	0.35	0.30	0.30

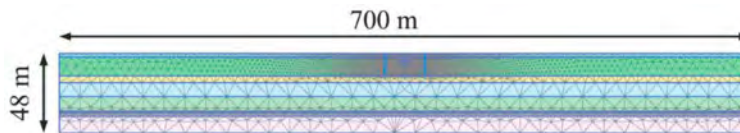


Figure 4. Dimensions of 2D finite element mesh model used in Plaxis.

From the field data obtained, the trapezoidal rule was utilized to calculate the volume of the settlement trough, this is, evaluates the volume of the settlement trough by dividing it into smaller trapezoids. Once that is done, the volume loss for every date monitored is taken, the prescribed displacements δW and δH of different magnitudes were input into Excel and a check was done to ensure that the equivalent volume loss would be the same. After many trial and error runs of changing δW and δH , the prescribed displacements are applied for ten different phases in Plaxis. The data from Plaxis output is then extracted. The trapezoidal rule was again used to calculate the volume of the settlement troughs from Plaxis and the volume losses were compared against the field data and the excel input. This can be shown in Table 3.

Figure 5 shows the graph of Plaxis Output against Field Data. The overall graph is able to fit the S_{max} at the first 5 points of measurement which is during the phase at which RTBM is driving past the monitoring section. The last 5 points are exceeding S_{max} by a little bit. Overall, the trend of the settlement trough during construction and post construction was matched well by the back calculation. However, the width of the settlement trough is wider than those of the discrete data points of the first 5 measurements. For the last 5 measurements which was taken during secondary grouting, the proposed DCM in this study is able to fit the width of the settlement

Table 3. Proposed DCM equivalent volume loss data.

Material	Measured Data		Excel Input		Plaxis Output		Proposed DCM Parameters	
	Vol	VL %	Vol	VL %	Vol	VL %	δW	δH
5-Jul	0.0187	0.0619	0.0187	0.0619	0.0262	0.0869	0.0005	0.0024
9-Jul	0.0494	0.1640	0.0494	0.1640	0.0699	0.2316	0.0008	0.0070
13-Jul	0.0772	0.2560	0.0772	0.2560	0.0980	0.3247	0.0010	0.0100
17-Jul	0.0983	0.3256	0.0983	0.3256	0.1240	0.4104	0.0010	0.0130
21-Jul	0.1411	0.4667	0.1411	0.4667	0.1630	0.5388	0.0015	0.0170
1-Aug	0.1961	0.6473	0.1961	0.6473	0.1886	0.6227	0.0025	0.0190
3-Aug	0.2121	0.6998	0.2121	0.6998	0.1978	0.6529	0.0025	0.0200
5-Aug	0.2189	0.7221	0.2189	0.7221	0.2109	0.6959	0.0030	0.0210
7-Aug	0.2268	0.7478	0.2268	0.7478	0.2193	0.7232	0.0030	0.0220
9-Aug	0.2338	0.7707	0.2338	0.7707	0.2275	0.7502	0.0030	0.0230

trough well enough. This suggests that the δW induced by the sides during the last 5 measurements. In Figure 6 and 7, the values of δH were much higher in magnitude than δW against time. In Figure 7, the change of displacements with respect to time showed that towards the end of the drive on 21st July, δW had an increase in trend of change in magnitude while δH had a decrease in trend in the change of magnitude. In addition, even though δH shows a higher magnitude than δW , δH has an overall decreasing trend in change as compared to δW .

The trial runs for the different magnitudes of displacement for top and both sides in volume loss have been prescribed. In all the runs, the magnitude of the total excavated shape used was the same throughout to ensure that the only parameter changed are the displacements being prescribed. From the equation and calculations in Section 2.1, the total excavated shape was scaled up by $\alpha = 1.0038$.

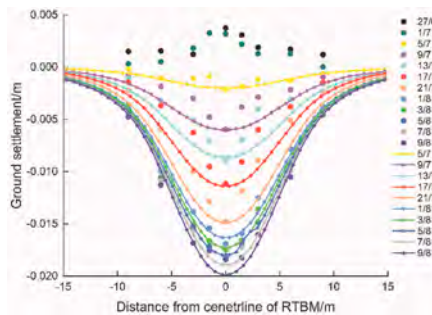


Figure 5. Proposed DCM displacement vs field data.

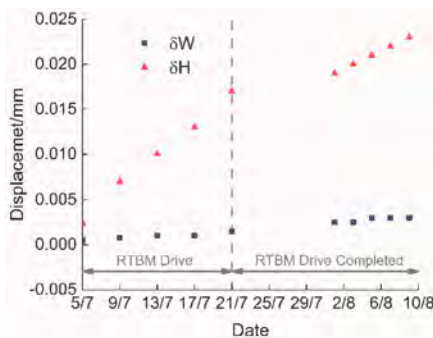


Figure 6. Proposed DCM displacements against duration of RTBM drive.

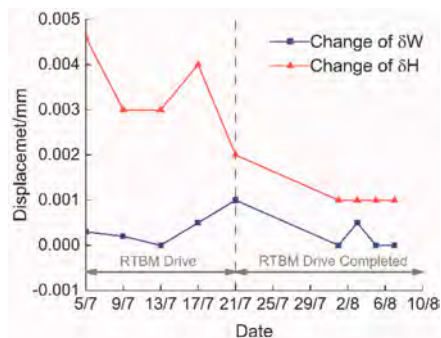


Figure 7. Change in proposed DCM displacements against duration of RTBM drive.

3.2 Ng Dcm

The modelling of NG DCM process is split into the same main three stages as the Proposed DCM. After many trial and error runs of changing δW and δH , the volume losses were compared against the field data and the excel input are shown in Table 4.

Table 4. NG DCM equivalent volume loss data.

Material	Measured Data		Excel Input		Plaxis Output		NG DCM Parameters	
	Vol	VL %	Vol	VL %	Vol	VL %	δW	δH
5-Jul	0.0187	0.0619	0.0173	0.0570	0.0190	0.0625	0.0001	0.0048
9-Jul	0.0494	0.1640	0.0483	0.1592	0.0570	0.1672	0.0002	0.0135
13-Jul	0.0772	0.2560	0.0780	0.2573	0.0817	0.2693	0.0018	0.0200
17-Jul	0.0983	0.3256	0.0965	0.3180	0.1014	0.3344	0.0020	0.0250
21-Jul	0.1411	0.4667	0.1405	0.4632	0.1477	0.4869	0.0065	0.0320
1-Aug	0.1961	0.6473	0.1948	0.6420	0.2032	0.6697	0.0150	0.0370
3-Aug	0.2121	0.6998	0.2126	0.7008	0.2212	0.7291	0.0175	0.0390
5-Aug	0.2189	0.7221	0.2181	0.7195	0.2271	0.7484	0.0180	0.0400
7-Aug	0.2268	0.7478	0.2226	0.7337	0.2312	0.7621	0.0190	0.0400
9-Aug	0.2338	0.7707	0.2304	0.7595	0.2391	0.7880	0.020	0.0420

As shown in Figure 8, the overall graph is able to fit the S_{max} at all 10 points of measurement. It is also able to follow the overall trend of the trailing settlement. In addition, the shape of the settlement trough in Plaxis is able to match the ‘triangular’ shape of the field data settlement trough. However, this can only be shown for the first 5 measurements which is the duration at which the RTBM passes by monitoring section. For the last 5 measurements which was taken while secondary grouting was carried out, NG DCM was not able to fit the width of the settlement trough well enough. All these was done where the equivalent volume loss was carried out. This suggests that the δW induced by the sides during the last 5 measurements is higher. In Figure 9 and 10, the values of δH were much higher in magnitude than δW against time. In Figure 10, the change of displacements with respect to time showed that towards the end of the drive on 21st July, δW had an increase in trend of change in magnitude while δH had a decrease in trend in the change of magnitude. This shows that the closing of the annular gap at the sides start to occur only towards the end of the drive, after the RTBM has passed by the monitoring section.

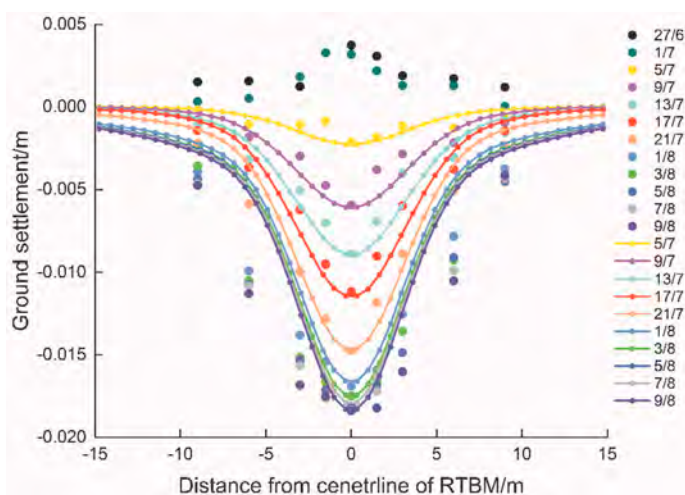


Figure 8. NG DCM displacement vs field data.

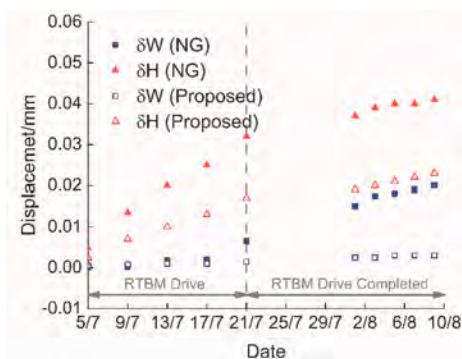


Figure 9. NG DCM displacements against duration of RTBM drive.

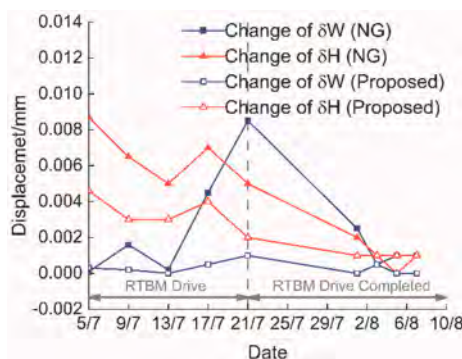


Figure 10. Change in NG DCM displacements against duration of RTBM drive.

In all the runs for NG DCM, the magnitude of the total excavated shape used was the same throughout to ensure that the only parameter changed are the displacements being prescribed. From the equation and calculations in Section 2.2, the total excavated shape was scaled up by $\alpha = 1.0038$.

4 CONCLUSIONS

Using the numerical method of displacement control based on gap method proposed by this study and Ng, the ground settlement caused by rectangular tunnel boring machine (RTBM) is studied. The two Numerical analysis on a RTBM case study were carried out to back analyze field data. Comparison of numerical simulation results and field data shows that the DCM by Ng (2017) may be more applicable to back analysing the RTBM drive from before it approaches towards the end of the drive whereas the proposed DCM may be more applicable to back analysing measurements that have been taken at a short time frame after the drive has been completed. Due to the limited case study, further research is needed. In addition, Mohr-Coulomb model adopted in this paper can not perfectly simulate the mechanical properties of soil, especially the small strain stiffness. More advanced soil constitutive model, such as HSS model, can be considered to explore this problem.

REFERENCES

- Cheng, C. Y., Dasari, G. R., Chow, Y. K., & Leung, C. F. 2007. Finite element analysis of tunnel-soil-pile interaction using displacement controlled model. *Tunnelling and Underground Space Technology* 22(4), 450–466.
- Loganathan N. & Poulos H. G. 1998. Analytical prediction for tunneling-induced ground movements in clays. *Journal of Geotechnical and geoenvironmental engineering* 124(9): 846–856.
- Ng, T. G. 2017. *Havelock Station Rectangular TBM*. Singapore: Golder Associates.
- Sagaseta, C. 1987. Analysis of undrained soil deformation due to ground loss. *Geotechnique* 37(3): 301–320.
- Zhang, D., Liu, B., & Qin, Y. 2016. Construction of a large-section long pedestrian underpass using pipe jacking in muddy silty clay: A case study. *Tunnelling and Underground Space Technology* 60, 151–164.

Effect of infill nonlinearity on frame response to tunnelling

Y. Yu

College of Civil Engineering, Qilu Institute of Technology, Jinan, China

A. Franza

Department of Civil and Architectural Engineering, Aarhus University, Aarhus, Denmark

L. Neves & A.M. Marshall

Department of Civil Engineering, University of Nottingham, Nottingham, UK

ABSTRACT: Tunnel construction is needed for infrastructure development in urban areas. However, underground excavation can detrimentally influence adjacent buildings; in particular, for framed structures with shallow foundations, damage would localise in the infill walls. This paper uses a two-stage analysis method (TSAM) to evaluate the effect of infill nonlinearity on the frame response to tunnelling. First, TSAM results are validated using centrifuge experimental and advanced numerical results. Then, the influence of the infill nonlinearity on the foundation displacements and building deformation parameters are analysed, considering both long and short structures. During this stage, the reinforced concrete (RC) frame and the endwall are modelled as elastic, while both elastic and advanced constitutive models are adopted for the masonry infills. Finally, the role of infill nonlinearity in frame shear and bending behaviours is investigated.

Keywords: Finite element modelling, infilled frame, tunnelling, soil-structure interaction, two-stage analysis method

1 INSTRUCTION

Rapid urbanisation has resulted in the increased demand for constructing underground transport systems. An increasing number of tunnels are excavated around or beneath existing surface structures and buried foundations. The excavation of the soil will cause ground movements as well as stress relief, which may adversely affect the surrounding structures. Inevitably, the tunnel, soil and the existing structure will interact with each other, which is known as tunnel-soil-structure interaction (TSSI).

Reinforced concrete (RC) frame structures are recognised as one of the most common structural forms of buildings worldwide. In practice, frame response to tunnelling is generally analysed by simplifying it as an equivalent elastic beam or plate (Franzius et al. 2006; Pickhaver et al. 2010; Farrell et al. 2014), although the structural characteristics have been shown to significantly affect the frame response to tunnelling (Boldini et al., 2018; Elkayam and Klar, 2019; Franza and DeJong, 2019). The response of bare frames to tunnelling while considering structural details has been investigated through numerical modelling (Boldini et al., 2018; Boldini et al., 2021; Goh and Mair, 2014) and experimental methods (Xu et al., 2020). In addition, Son (2015) adopted elastic bricks and inelastic brick-mortar joints in the 2-D Universal Distinct Element Code. Franza et al. (2022) investigated the response of frame structures with elastic infills to tunnelling. However, the nonlinear behaviour of infills has received limited attention in previous studies (Fu et al., 2018).

Various researchers have employed a two-stage analysis method (TSAM) to investigate the TSSI problem (Deck and Singh, 2012; Franza et al., 2022; Selby, 1999; Elkayam and Klar, 2019; Haji et al., 2018; Franza and DeJong, 2019). In the first stage, greenfield displacements, acquired either empirically or through analytical means, are applied to an elastic soil model in the absence of the structure to calculate the reaction forces of the soil caused by tunnelling; in the second stage, the computed reaction forces are applied to the soil with the structure in place. This method allows for the efficient and acceptably accurate simulation of tunnelling-induced building response without considering the complex soil nonlinear behaviour and advanced constitutive models.

The aim of this paper is to investigate the effect of the nonlinearity of infills on the global behaviour of infilled frame structures subjected to tunnelling, adopting the TSAM analysis method within the Finite Element Method (FEM) software Abaqus (Simulia, 2010). First, the tunnelling-induced bare frame response obtained using the TSAM are validated by comparison against published experimental (Xu. et al., 2020) and numerical results (Boldini et al., 2021). The TSAM approach is then used to investigate the effect of infill nonlinearity on the soil-structure interactions, for both short and long frames. Results indicate the significant underestimation in terms of building shear response and vertical displacements of the foundation when adopting an elastic model for the frame infills compared to a more realistic nonlinear model.

2 BUILDING DEFORMATION PARAMETERS

Building deformation parameters were reported by Son and Cording (2005), Ritter et al. (2020) and Xu et al. (2020) to evaluate the building distortions under the shear, bending and axial modes caused by tunnelling. Figure 1 shows the parameter definitions using four corner points of a single unit of the frame building.

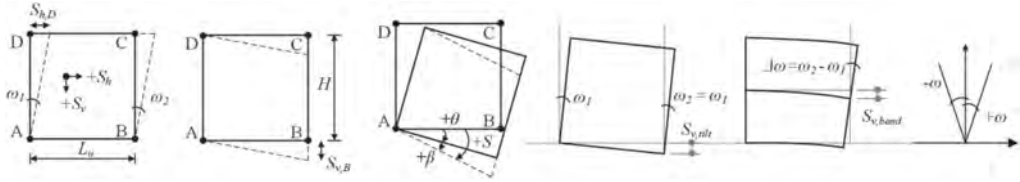


Figure 1. Building deformation parameters in bays and sign convention (after Ritter et al., 2020).

The building response to tunnelling was quantified based on the horizontal S_h and vertical S_v displacements of the corner points, the building unit height H , and the building unit length L_u .

Base horizontal strain:

$$\varepsilon_{h,base} = \frac{S_{h,B} - S_{h,A}}{L_u} \quad (1)$$

Top horizontal strain:

$$\varepsilon_{h,top} = \frac{S_{h,C} - S_{h,D}}{L_u} \quad (2)$$

The angular distortion β was expressed by the subtraction of tilt θ from slope S :

$$\beta = S - \theta = S - \frac{\omega_1 + \omega_2}{2} = \frac{S_{v,B} - S_{v,A}}{L_u} - \frac{(S_{h,C} - S_{h,B}) + (S_{h,D} - S_{h,A})}{2H} \quad (3)$$

where ω_1 and ω_2 are in radians. The angular distortion β , which is equal to shear strain when using the method of Son and Cording (2005); Ritter et al. (2020); Xu et al. (2020), relates to the level of building shear distortion and its shear response, whereas the curvature relates to the bending contribution of the building response (Ritter et al., 2020).

In addition, as done by Ritter et al. (2020), it can be informative to decompose the total vertical displacements of each building bay as:

$$S_{v,total} = S_{v,B} - S_{v,A} \quad (4)$$

where A and B are the nodes at the bottom corners of a given bay, into those caused by tilt $S_{v,tilt}$, shear $S_{v,shear}$, and bending $S_{v,bend}$, so as to distinguish the role of each mechanism. The value of $S_{v,tilt}$ is defined as:

$$S_{v,tilt} = \omega_1 L_u \quad (5)$$

The value of $S_{v,bend}$ is defined as:

$$S_{v,bend} = \chi \frac{L_u^2}{2} = \Delta\omega \frac{L_u}{2} \quad (6)$$

where χ is the average curvature and $\Delta\omega = \omega_2 - \omega_1$. Positive values imply a hogging mode. The sum of $S_{v,tilt}$, $S_{v,shear}$ and $S_{v,bend}$ gives total vertical displacement:

$$S_{v,total} = S_{v,tilt} + S_{v,shear} + S_{v,bend} \quad (7)$$

It should be noted that the parameters β and $S_{v,shear}$ represent the building shear response while χ and $S_{v,bend}$ mainly indicate the building bending behaviour.

3 TSAM VALIDATION - BARE FRAME SCENARIO

The TSAM results in modelling the bare frame response to tunnelling are validated using the centrifuge tests conducted by Xu et al. (2020), as well as numerical modelling results by Boldini et al. (2021) and Franza et al. (2022) for the same scenario; the advanced SANISAND model was used to replicate soil behaviour and implemented within Abaqus and Plaxis 3D, respectively. The experiments were performed using Leighton Buzzard Fraction E silica sand with a soil relative density of $I_d = 90\%$. A plane strain setup was used, incorporating a flexible cylindrical membrane tunnel filled with water. The centrifuge test labelled as F2t3b6L is considered as the validation case. The layout of the bare frame building is plotted in Figure 2. In the prototype scale of the centrifuge tests, the tunnel has a diameter of $D_t = 6.1\text{m}$, and a cover depth of $C = 8\text{m}$ ($C/D_t = 1.3$). The entire frame structure has a transverse width of $B = 31.3\text{m}$, with each bay having a width of $b_{bay} = 5.2\text{m}$. The height of each storey is $h_{storey} = 2.7\text{m}$, and the thickness of each floor and foundation is equivalent to $t = 0.22\text{m}$. All the TSAM simulations consider the structure standard weight case.

According to the numerical model parameters from Boldini et al. (2021) and Franza et al. (2022), the TSAM model adopted an elastic frame with Young's modulus of $E = 53.8\text{GPa}$, a Poisson's ratio of $\nu = 0.334$, and a unit weight of $\gamma = 27 \text{ kN/m}^3$. Franza et al. (2022) also adopted an analytical two-stage method (results omitted), assuming for the elastic continuum a Young's modulus of $E_s = 45\text{MPa}$ and a Poisson's ratio of $\nu = 0.3$. To simulate the soil-frame interaction, a friction coefficient of $\mu_{soil} = 0.625$, corresponding to the critical state friction of the soil, was used. The soil was assumed to have zero tensile strength. The greenfield vertical and horizontal displacements provided by Boldini et al. (2021) at the soil surface were fitted as input data in the TSAM model. These displacements were obtained at tunnel volume losses of $V_{L,t} = 1\%$ and 2% .

Figures 3a to d show the vertical and horizontal displacements at the foundation base and the underlying soil from the centrifuge tests, advanced numerical results, and the TSAM results, all with tunnel volume loss of $V_{L,t} = 1\%$ and 2% . The TSAM model demonstrates a satisfactory replication of the foundation and underlying soil displacements observed in the centrifuge tests and advanced numerical simulations, both in the vertical and horizontal

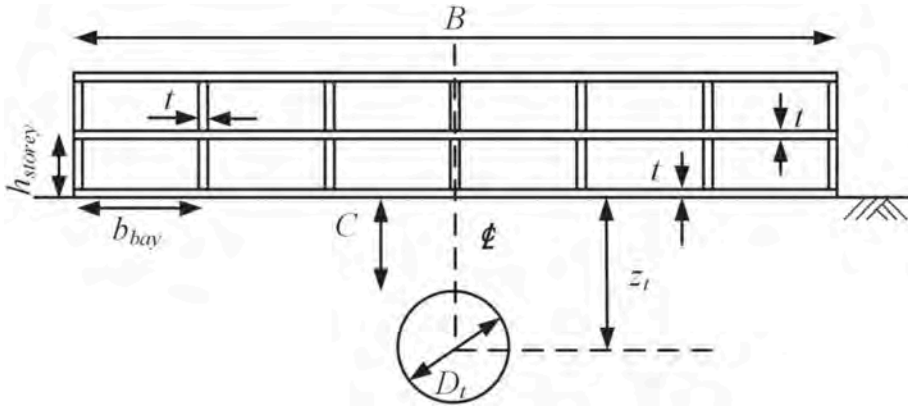


Figure 2. Layout of bare frame building in validation case.

directions. However, the numerical data, including both results from Boldini et al. (2021), Franza et al. (2022) and the TSAM analysis, slightly underestimate the vertical deformations of the foundation observed in the centrifuge tests at $V_{l,t} = 1\%$ and overestimate the vertical displacements of the frame at $V_{l,t} = 2\%$. In the meantime, the horizontal displacements predicted at the foundation base are negligible in both centrifuge and numerical results; the level of slippage between the foundation and the soil is well captured in the TSAM. The comparison of the maximum angular distortion β_{max} (sign was not considered) is shown in Figure 3e. The numerical results, including both the advanced numerical model and the TSAM model, show a tendency to underestimate β_{max} at $V_{l,t} = 1\%$. The TSAM results exhibit good agreement with experimental results at $V_{l,t} = 2\%$, when the formation of a gap influences the induced distortions. Overall, the TSAM modelling satisfactorily replicates the frame response to tunnelling. Interestingly, there is a difference in predicted settlements of the building (as well as greenfield conditions) by Boldini et al. (2021) and Franza et al. (2022), despite the fact that they used a identical advanced soil constitutive model. This indicates that a simple

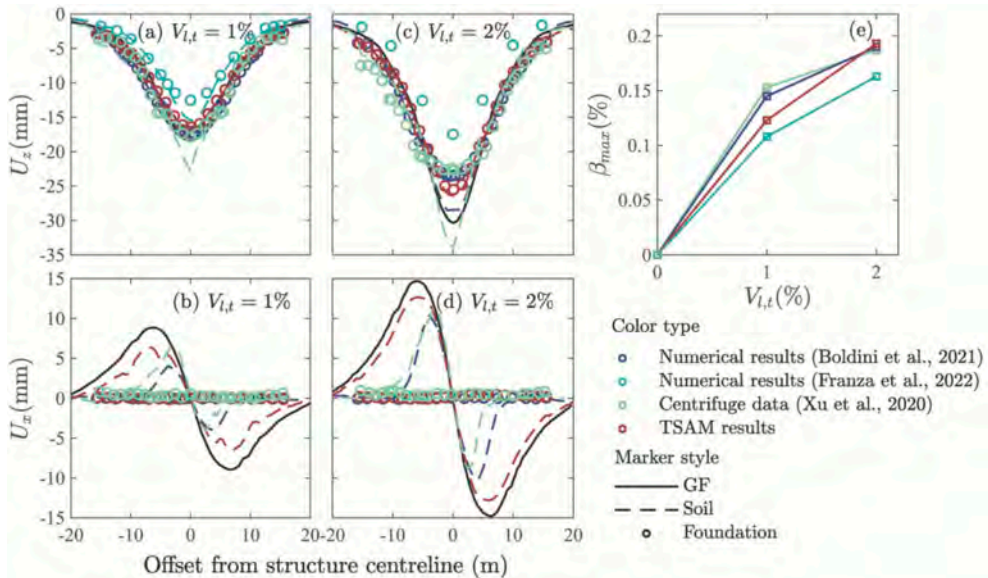


Figure 3. Validation of TSAM results on (a)-(d): vertical U_z and horizontal U_x displacements, and (e): maximum frame distortion.

TSAM may, in certain cases, benefit the analysis of tunnelling-induced soil-structure interaction since it provides a unique input (greenfield displacements), ensuring the focus is on the effect of structural features.

4 RESPONSE OF INFILLED FRAMES TO TUNNELLING

4.1 Model details

The frame structure in this study is based on the prototype-scale model of in-plane centrifuge tests conducted by Xu et al. (2020) and includes the masonry infills, focusing on assessing the impact of infill nonlinearity on the frame response to tunnelling. The short building consists of three bays with a transverse length (B) of 15.64 m, while the long building has six bays with $B = 31.06$ m. Both buildings have a height above ground level (H) of 5.46 m, a raft foundation, a slab, and column thickness of 0.22 m, and a building width (L) of 8.66 m. Each bay is divided by a column and has a length (b) of 5.19 m. All the scenarios considered in this study have the same dimension for the openings with a width of 1 m and height of 1.4 m. For the case where the tunnel is constructed directly beneath the structure with $e = 0$, the entire short frame scenario is located in the sagging zone; the sagging length (B_{sag}) equals the building transverse length of 15.64 m. In contrast, the long frame building has a sagging length (B_{sag}) of 25.1 m and a hogging length (B_{hog}) of 5.96 m. To reduce computational cost and focus on the in-plane strain behaviour, only half of the structure is modelled along the longitudinal direction of the tunnel.

The greenfield with a tunnel volume loss of $V_{lt} = 3\%$, represented by a Gaussian curve, is obtained by doubling greenfield profiles corresponding to $V_{lt} = 1.5\%$ from Yiu et al. (2017) (Figure 4). The whole soil-structure system (soil, frame, lintel and endwalls) is assumed elastic except for the masonry infill walls. The elastic properties of different components in the soil-frame system are presented in Table 1. The masonry infills are simulated as isotropic linear elastic within the yield surface, with a perfectly plastic post-yield response. A modified Concrete Damaged Plasticity (CDP) model (CDP model with infinite compressive strength) is adopted for the infill simulation (Yiu et al., 2017). This CDP* model is defined by $\sigma_c = \text{infinite}$, $\sigma_t = 0.5$ MPa, $\psi = 36.9^\circ$, the flow potential eccentricity ε (Abaqus default value of 0.1 adopted here), ratio of initial equi-biaxial compressive yield stress to initial uniaxial compressive yield stress σ_{b0}/σ_{c0} (Abaqus default value of 1.16 adopted here), and dimensionless parameter K that controls the shape of the yield surface (Abaqus default value of 0.67 adopted here) (Kupfer and Gerstle, 1973; Richart et al., 1928).

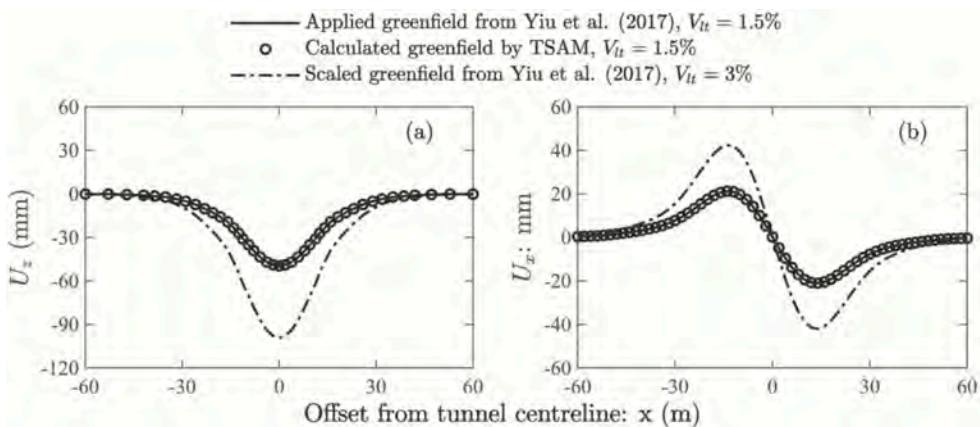


Figure 4. Validation of TSAM results on maximum frame distortion.

Table 1. Elastic properties of soil-frame structure system.

Elements	γ (kN/m ³)	E (GPa)	ν (-)
Soil	19.5	0.02	0.35
Frame	27	53.8	0.33
Lintel	13	9	0.2
Endwall	13	4	0.2
Infill wall	13	4	0.2

Notes: γ = density; E = Young's modulus; μ = Poisson's ratio.

A three-dimensional ten-node quadratic tetrahedron continuum element (C3D10) is employed to model the entire soil-frame system. The displacements of the soil bottom boundary are fixed in all directions, while displacements are restrained perpendicular to the vertical planes at the sides of the model. Additionally, this study utilises a frictional interface implemented as a surface-to-surface contact with finite sliding formulation in ABAQUS. The shear behaviour at these interfaces follows the basic isotropic Coulomb friction model, with the soil-frame interface adopting a frictional coefficient $\mu_{soil} = 0.3$ (Fu et al., 2018) and the frame-infill contact using $\mu_{infill} = 0.7$ (Wu et al., 2022). The structure is positioned at the tunnel centreline with zero eccentricity.

4.2 Effect of infill nonlinearity

Figure 5 compares vertical (U_z) and horizontal (U_x) displacements of the frame foundations and the soil for short and long frames. In both CDP * and elastic models: (i) notable changes in soil deformation slopes occur at foundation edges for both U_z and U_x in both frame scenarios due to the higher stiffness of the structure compared to the soil; (ii) long structures exhibit considerably smaller vertical displacements (Figure 5a) compared to short structures, indicating that increased transverse width reduces maximum settlements for structures with zero eccentricity; (iii) the gap between the foundation and underlying soil is more pronounced in long frames; (iv) sliding occurs in both short and long buildings, but horizontal displacements at the foundation base are negligible, demonstrating the raft foundation's effectiveness in resisting horizontal ground movements due to high axial stiffness. These findings align with prior studies by Xu et al. (2020), Boldini et al. (2021), and Goh and Mair (2011). Additionally, the elastic model yields smaller vertical displacements and larger soil-foundation gaps compared to the CDP * model, particularly in long frames (Figure 5a). The difference in horizontal displacements between the elastic and CDP * models is negligible (Figure 5b). These

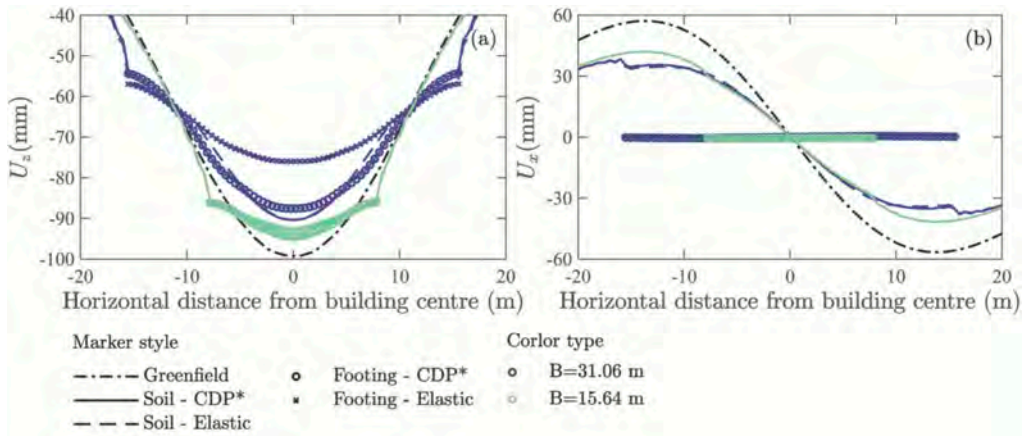


Figure 5. Comparison of footing base and underlying soil displacements with different building transverse widths, (a) vertical displacements and (b) horizontal displacements (upward in vertical and right in horizontal means positive).

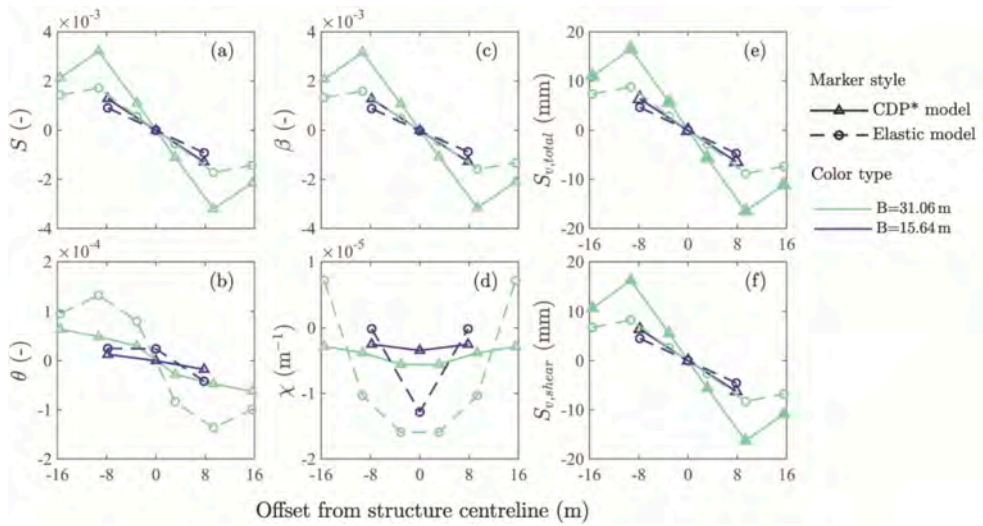


Figure 6. Building deformation parameters along building bays with different building transverse widths when $e = 0$: (a) slope, (b) tilt, (c) angular distortion, (d) curvature, (e) total vertical deflection and (f) vertical deflection caused by shear.

observations highlight the importance of accounting for infill nonlinearity when assessing building responses to tunnelling (when tunnelling induces relatively large settlements).

The comparison of building deformation parameters between short and long frames is illustrated in Figure 6. When the building eccentricity is zero, tilt ($S_{v,tilt}$) is minimal and the bending response for a frame structure is negligible, the vertical deflections primarily result from shear ($S_{v,total} \approx S_{v,shear}$). (i) The slope (S) and angular distortion (β) trends caused by the CDP* model are similar in both buildings, with the long building showing higher magnitudes, especially near inflection points. (ii) The largest tilt (θ) occurs at frame edges for both models in both scenarios, with the long frame showing higher values near inflection points. (iii) The long frame exhibits greater building curvature (χ) when using the elastic model, with the highest values near the building centre. (iv) The elastic model results in larger building tilt and curvature but underestimates building slope and angular distortion compared to the CDP* model. (v) Figure 6e and f reveal that vertical settlements in the infilled frame building are primarily due to shear deformation, with bending contributing negligibly. (vi) For the long building in sagging and hogging areas, the largest $S_{v,total}$ and $S_{v,shear}$ magnitudes occur near inflection points. Figure 6 shows that wider building transverse width leads to the increased shear response whereas the elastic model significantly underestimates the overall deflection (mainly caused by shear) caused by tunnelling. These results highlight the importance of considering infill nonlinearity for accurately assess the building behaviour during tunnelling.

5 CONCLUSIONS

This study numerically investigated the effect of infill nonlinearity on the frame response to tunnelling, taking into account the structure's transverse length. A two-stage analysis method (TSAM) was implemented in ABAQUS, adopting the elastic model for soil and the reinforced concrete frame, and both elastic and CDP* models for the infills. Tunnelling-induced foundation displacements and building deformation parameters along frame bays were analysed. It was demonstrated that the elastic model underestimates the shear and total vertical displacements of the building. Results highlight the significant influence of infill nonlinearity on the behaviour of the frame structure, particularly for relatively long frames spanning across both sagging and hogging regions.

REFERENCES

- Boldini, D., Losacco, N., Bertolin, S., & Amorosi, A. 2018. *Finite Element modelling of tunnelling-induced displacements on framed structures*. Tunnelling and Underground Space Technology, 80 (April):222–231.3
- Boldini, D., Losacco, N., Franza, A., DeJong, M., Xu, J., & Marshall, A. 2021. *Tunneling-induced deformation of bare frame structures on sand: Numerical study of building deformations*. Journal of Geotechnical and Geoenvironmental Engineering, 147(11).
- Boscardin, M. D. & Cording, E. J. 1989. *Building response to excavation-induced settlement*. Journal of Geotechnical Engineering, 115(1):1–21.
- Deck, O. Singh, A. 2012. *Analytical model for the prediction of building deflections induced by ground movements*. International Journal for Numerical and Analytical Methods in Geomechanics, 36(1):62–84.
- Elkayam, I. & Klar, A. 2019. *Nonlinear elastoplastic formulation for tunneling effects on superstructures*. Canadian Geotechnical Journal, 56(7):956–969.
- Farrell, R., Mair, R., Sciotti, A., & Pigorini, A. 2014. *Building response to tunnelling*. Soils and Foundations, 54(3):269–279.
- Franza, A. DeJong, M. J. 2019. *Elastoplastic solutions to predict tunneling-induced load redistribution and deformation of surface structures*. Journal of Geotechnical and Geoenvironmental Engineering, 145(4):04019007.
- Franza, A., Miraei, S., Boldini, D., Losacco, N. 2022. *An equivalent beam approach for assessing tunnelling-induced distortions of frames with infills*. Tunnelling and Underground Space Technology, 129:104686.
- Franzius, J. N., Potts, D. M., & Burland, J. B. 2006. *The response of surface structures to tunnel construction*. Proceedings of the Institution of Civil Engineers-Geotechnical Engineering, 159(1):3–17.
- Goh, K. H. & Mair, R. J. 2014. *Response of framed buildings to excavation-induced movements*. Soils and Foundations, 54(3):250–268.
- Goh, K. & Mair, R. J. 2011. *Building damage assessment for deep excavations in Singapore and the influence of building stiffness*. Geotechnical Engineering, 42:1–12.
- Haji, T. K. et al. 2018. *Mixed empirical-numerical method for investigating tunnelling effects on structures*. Tunnelling and Underground Space Technology, 73:92–104.
- Kupfer, H. B. & Gerstle, K. H. 1973. *Behavior of concrete under biaxial stresses*. Journal of the engineering mechanics division, 99(4):853–866.
- Pickhaver, J. & Pickhaver, J. 2006. *Numerical modelling of building response to tunnelling*. PhD thesis, Oxford University, UK.
- Richart, F. E., Brandtzaeg, A., & Brown, R. L. 1928. *A study of the failure of concrete under combined compressive stresses*. Technical report, University of Illinois. Engineering Experiment Station. Bulletin; no. 185.
- Ritter, S. et al. 2020. *Building deformation caused by tunneling: Centrifuge modeling*. Journal of Geotechnical and Geoenvironmental Engineering, 146(5):04020017.
- Selby, A. 1999. *Tunnelling in soils—ground movements, and damage to buildings in Workington, Uk*. Geotechnical & Geological Engineering, 17(3-4):351–371.
- Simulia, D. S. 2010. *Abaqus analysis user's manual*. Dassault Systemes, Pawtucket, USA.
- Son, M. (2015). *Response analysis of nearby structures to tunneling-induced ground movements in sandy soils*. Tunnelling and Underground Space Technology, 48:156–169.
- Son, M. Cording, E. J. (2005). *Estimation of building damage due to excavation-induced ground movements*. Journal of geotechnical and geoenvironmental engineering, 131(2):162–177.
- Wu, J.-R., Di Sarno, L., Freddi, F., & D'Aniello, M. 2022. *Modelling of masonry infills in existing steel moment-resisting frames: Nonlinear force displacement relationship*. Engineering Structures, 267:114699.
- Xu, J., Franza, A., & Marshall, A. M. 2020. *The response of framed buildings on raft foundations to tunneling*. Journal of Geotechnical and Geoenvironmental Engineering.
- Yiu, W. N., Burd, H. J., Martin, C. M. 2017. *Finite-element modelling for the assessment of tunnel-induced damage to a masonry building*. Geotechnique, 67(9):780–794.

Surface tension of foam and its influence on tunneling

D.Z. Zheng

School of Civil Engineering, Shandong University, Jinan, China

Department of Civil Engineering, Ghent University, Ghent, Belgium

A. Bezuijen

Department of Civil Engineering, Ghent University, Ghent, Belgium

Deltares, Delft, The Netherlands

Q. Zhang

School of Civil Engineering, Shandong University, Jinan, China

ABSTRACT: Foam is produced in a predetermined concentration of foaming agent and water and injected to the excavation chamber for soil conditioning in Earth Pressure Balance (EPB) shield tunneling. This mixing process will induce the dilution of the foaming liquid and thus influence its surface tension. This paper presents an experimental study on the influence of dilution of foaming liquid as could be expected in EPB shield tunneling. The capillary rise method is employed for the measurement of surface tension at different concentrations. It is shown that in a typical tunnel application the surface tension can be twice as high as that in the original foam. Consequences from the increase in surface tension are theoretically analyzed. Volume change and compressibility of the foam bubbles are hardly influenced by the increased surface tension for the foam used in tunneling. While the influence of a higher surface tension is negative for the formation of a low permeable layer that is anticipated by engineers. The study suggests that the change in surface tension due to dilution in tunneling should be incorporated in the inspection of foam-soil interactions.

1 INTRODUCTION

Foam as an additive for soil conditioning has been widely used in EPB shield tunneling. While only limited research could be found regarding its properties (Wu et al., 2018; Thewes et al., 2012). Conventional tests put more emphasis on the integral properties of such a foam-soil-mixture including its rheology (Peila et al., 2009; Quebaud et al, 1998), shear behavior (Pena, 2007; Psomas, 2001), compressibility (Bezuijen, 2013; Pena, 2007) and permeability (Borio & Peila, 2010; Bezuijen & Schaminée, 1999). These properties are critical in engineering applications and have greatly contributed to the application range of the EPB shield TBM.

Some recent research (Wu et al., 2020; Xu, 2018; Galli, 2016; Psomas, 2001; Bezuijen & Schaminée, 1999; Quebaud et al, 1998) focus on the interaction between foam and soil that is anticipated in the excavation chamber. However, the macro behavior (such as the infiltration behavior of foam bubbles) of such a mixture sometimes is difficult to be explained due to the lack of knowledge on the foam-soil interaction at micro scale level (Zheng et al., 2023; Wu et al., 2020; Xu, 2018; Bezuijen, 2013). One of the important parameters related to the foam bubbles is the surface tension, while it is seldom investigated in previous studies.

The role of surfactant is to lower the surface tension of the target liquid, making it possible to produce foam. The pressure difference between the inside and outside of a bubble in liquid is:

$$P_a - P_w = \frac{2\gamma}{R} \quad (1)$$

With P_a the pressure inside the bubble, P_w the liquid pressure outside the bubble, γ the surface tension and R the radius of the bubble.

The principle of a foam generator is to mix an air flow and a liquid flow through a porous medium such as a bed of glass beads (Psomas, 2001). With a given air pressure difference, the size of the generated bubbles will be smaller at a lower γ according to Equation (1).

Foam is usually pre-generated at a certain concentration of foaming agent and water and injected into the excavated soils. It is mixed in the excavation chamber together with the excavated soils. Under the groundwater table, the remaining pore water in the excavated soils will induce the dilution of the foaming liquid surrounding the foam bubbles, resulting in a potential change in its surface tension.

To this end, surface tension of foaming liquid at different concentrations is measured with the capillary rise method. A theoretical study is implemented to convey the influence from the increment of surface tension on the micro behavior of the foam such as volume change, compressibility and mobility. Consequences for tunneling are discussed.

2 MATERIALS AND PROCEDURE

2.1 Foaming liquid and capillary tube

Foaming agent Condat CLB F5/TM is used for this study. The foaming liquid is created by adding foaming agent to water with a predetermined ratio to get different concentrations and mixed manually. The concentration (C.%) of the foaming liquid is calculated:

$$C.\% = \frac{V_s}{V_w + V_s} \quad (2)$$

With V_s the volume quantity of the foaming agent and V_w the quantity of water.

A commercial glass capillary tube (CM Scientific, CV1525 Borosilicate Glass Round Capillaries) is used for the measurements. The capillary tube has an inner diameter of 0.15 mm and an outer diameter of 0.25 mm and a length of 300 mm.

2.2 Procedure

The capillary tube with a black background is placed on a ruler that is supported with a stick hold vertically by a stand. Because the inner diameter of the capillary tube is only 0.15 mm, a camera with magnification is used for the recognition on the capillary rise in the tube. The container has a diameter of 10 cm and a depth of 3 cm. The capillary end is put 1 cm into the liquid. The

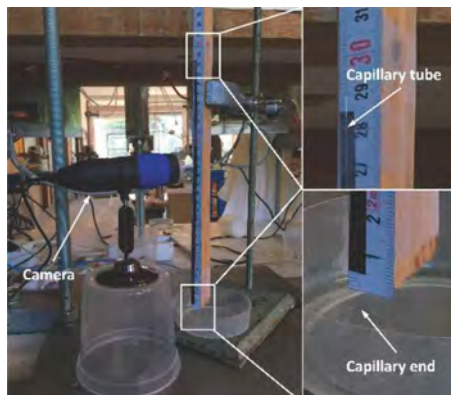


Figure 1. Picture of the testing system.

measurement is also conducted with water as a reference. All measurements are carried out at a room temperature of 20 °C and each measurement takes 24 hours to get a stable capillary rise. In case there is liquid loss due to vaporization, new liquid is slowly injected with a syringe to achieve a comparable initial liquid level. The whole measuring system is shown in Figure 1.

3 RESULTS AND DISCUSSION

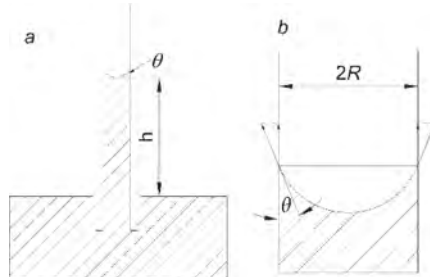


Figure 2. Capillary rise in a tube with a small diameter.

Inserting a capillary tube vertically into a liquid will result in a capillary rise due to the surface tension of the liquid (Figure 2a). By balancing the pressures between the capillary liquid (under the meniscus) and the atmosphere (Figure 2b), the following relation can be obtained:

$$\frac{2\gamma \cos \theta}{R} = (\rho_w - \rho_a)gh \quad (3)$$

The surface tension (γ) can be calculated with the measured capillary rise in the tube.

$$\gamma = \frac{(\rho_w - \rho_a)hgR}{2 \cos \theta} \quad (4)$$

With ρ_w the density of water, ρ_a the density of air, h the capillary rise in the tube, g the acceleration of gravity, R the radius of the tube and θ the contact angle between the wall and the liquid, which is 0 here as the same to that of water.

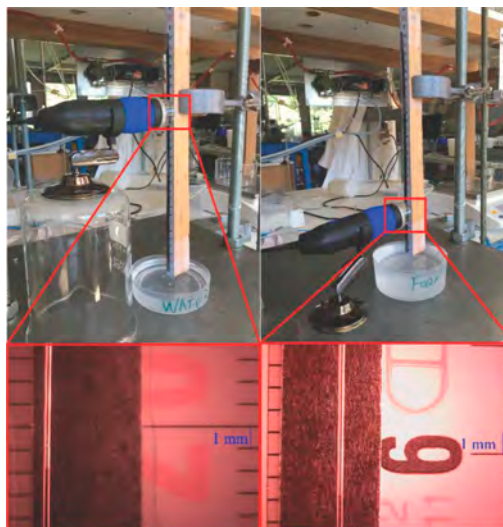


Figure 3. Capillary rise at the end of each test (left: water; right: foaming liquid 3%).

Figure 3 shows that the measured capillary rise at the end of the test for water and foaming liquid is 19.82 cm and 5.83 cm, respectively. With Equation (4), the measured surface tension of water is 0.0728 N/m, very close to the standard value of 0.07275 N/m (Vargaftik et al., 1983), indicating the accuracy of the capillary rise method.

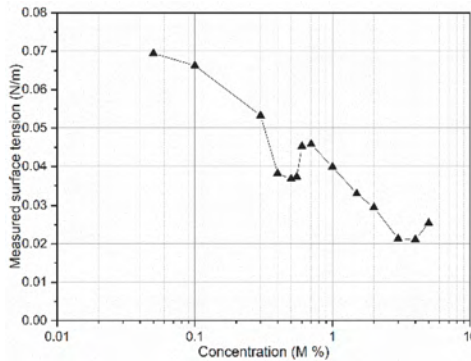


Figure 4. Measured surface tension at different concentrations.

Figure 4 shows the measured surface tension as a function of concentration for the foaming liquid. It shows that with a concentration of 3 M % foaming liquid, the surface tension can be lowered effectively to around 0.0214 N/m, smaller than one third of the surface tension for water. Barely any reduction on it can be achieved by further increasing the concentration. On the contrary, increasing the concentration to 5 M % results in an increase in its surface tension. This may explain the reason why 3 M % is preferred in field use because it is cost effective and it has a small surface tension.

It should be noted that below 3 M %, the surface tension increases with decreasing concentration as is expected. However, results show that this is not a monotonic relation. Instead, there is a U curve in the range between the concentration of 0.3-0.7 %. Inside this range, the surface tension first decreases with decreasing concentration until 0.5 M %, after which it increases again. After this U curve, the increase will continue as the concentration decreases. At the concentration of 0.05 M %, the surface tension is almost 0.07 N/m, close to the value of water.

Normally the results shown in Figure 4 match the initial purpose in the engineering application. Because the foam bubbles produced at the concentration of 3 M % have a low surface tension. However, as mentioned in the beginning, mixing the foam with the excavated soils results in the dilution of the foaming liquid, which will induce the increase in its surface tension.

The increase in surface tension will depend on the ratio between the FIR and the porosity (n_s) of the excavated soils. In this way, the concentration of the foaming liquid in the foam-soil-mixture ($C.'\%$) can be calculated as follows:

$$C.'\% = \frac{FIR}{FERn_s(1 - \frac{2}{n_s}) + FIR} C.\% \quad (5)$$

It should be noted that the groundwater flow is not considered in Equation (5). Because with continuous drilling the concentration of the foam in the mixture will be closer to the original foam. This dynamic condition will complicate the current study that here it is only discussed without the influence of the groundwater flow.

The surface tension of the liquid in this foam-soil-mixture should then be determined with the new concentration calculated with Equation (5). Assuming the FIR is 40 Vol % and the porosity of the soils is 0.4. For fine sand there is no foam infiltration at the tunnel face and all pore water is taken into the excavation chamber, which is a reasonable assumption as is found by Bezuijen and Dias (2017). The resulting concentration of the foaming liquid in the excavation chamber according to Equation (5) is 0.27 M %. The surface tension of the liquid is then 0.054 N/m, twice the value of the initial foam.

A bubble usually becomes smaller when its surface tension increases. As illustrated in Figure 5, when its surface tension increases from γ to γ' , the radius of the bubble decreases from S to s . And the pressure inside the bubble changes from P_a to P_a' .

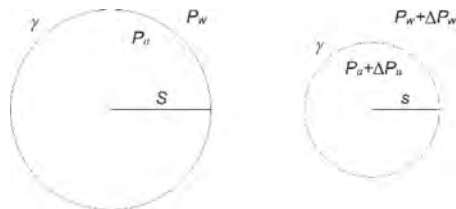


Figure 5. Definition sketch of a foam bubble being compressed when its surface tension increases.

By the definition of surface tension (γ), the following relations can be obtained:

$$P_a - P_w = \frac{2\gamma}{S} \quad (6)$$

$$P_a' - P_w = \frac{2\gamma'}{s} \quad (7)$$

With P_w the pore water pressure.
Combining these two yields:

$$P_a' - P_a = \frac{2\gamma}{s} - \frac{2\gamma'}{S} \quad (8)$$

Also, according to Boyle's Law

$$\frac{P_a' - P_a}{P + P_a} = \left(\frac{S}{s}\right)^3 - 1 \quad (9)$$

With P the atmospheric pressure (1 bar).

With Equations (8) and (9), the volume change of the bubble can be obtained when its surface tension increases.

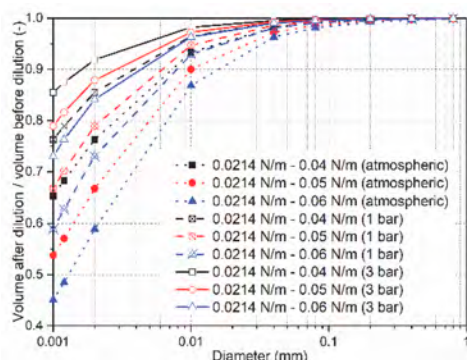


Figure 6. Normalized volume ratio between bubble volumes after and before surface tension increases. The different lines represent different γ' for the foam after dilution. Value of γ for the initial foam is 0.0214 N/m.

Figure 6 shows that when surface tension increases, the volume of a foam bubble will decrease. With a smaller diameter, the change in volume will be more significant because the surface tension will be dominant. The volume also decreases more with more increment in

surface tension. With a higher pore pressure, the influence on volume change due to the increasing surface tension will be smaller. It shows that for bubbles bigger than 0.02 mm, the volume ratio is still larger than 0.95 when the surface tension increases to 0.6 N/m at a pore pressure of 3 bar, which is a possible scenario in tunneling application.

The diameter of the foam bubbles used in EPB shield tunneling is usually larger than 0.02 mm, as is shown in Zheng et al. (2021), Wu et al. (2018) and Wang et al. (2021). When the diameter of the foam bubble is larger than 0.02 mm, the volume ratio after the decrease is still larger than 0.95, indicating that the volume change can be negligible when the foam is mixed with the excavated soils.

Sand grains and liquid are usually treated as incompressible media compared with gaseous phase in a foam-soil-mixture. Assume a foam bubble with an initial radius S , the surrounding pore pressure is P_w and the air pressure inside the bubble is P_a . After applying an excess pore pressure of ΔP_w , the bubble will be compressed and the radius will become s . The situation is illustrated in Figure 7.

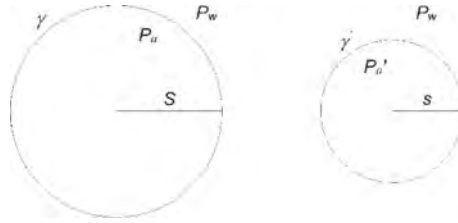


Figure 7. Sketch of a foam bubble being compressed when applying an excess pore pressure.

By the definition of surface tension (γ), the following relations can be obtained:

$$P_a - P_w = \frac{2\gamma}{S} \quad (10)$$

$$(P_a + \Delta P_a) - (P_w + \Delta P_w) = \frac{2\gamma}{s} \quad (11)$$

With ΔP_a the increase in air pressure inside the bubble. Combining these two equations yields:

$$\Delta P_a - \Delta P_w = 2\gamma \left(\frac{1}{s} - \frac{1}{S} \right) \quad (12)$$

Resulting in, according to Boyle's law

$$\frac{\Delta P_a}{P + P_a} = \left(\frac{S}{s} \right)^3 - 1 \quad (13)$$

Equations (12) and (13) enable the calculation of the volume ratio between the original volume and after being compressed at an excess pressure of 50 kPa (the ratio is 1.5 for ideal gas).

Figure 8 shows the normalized volume ratio between original foam and after being compressed at different surface tensions under various pore pressures. The situation simulates the volume ratio between the original volume and after being compressed at an excess pressure of 50 kPa (the ratio is 1.5 for ideal gas at atmospheric pressure and 1.25 and 1.125 at 1 bar and 3 bar of pore water pressure, respectively). Results suggest the influence on compressibility is not so obvious in tunneling at a high pore pressure (3 bar) as the compressibility is almost the same to ideal gas even at a larger surface tension (0.6 N/m). While for a smaller pore pressure (for example, atmospheric pressure), the compressibility can be influenced by surface tension, which should be taken into account when conducting experiments at atmospheric pressure.

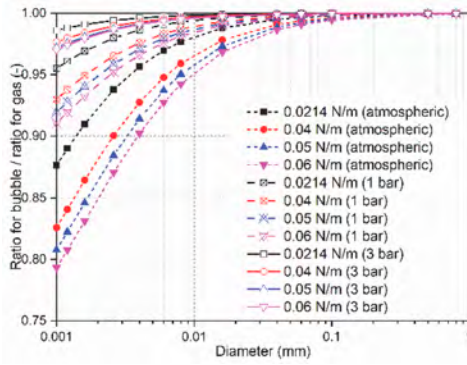


Figure 8. Normalized volume ratio between original foam and after being compressed at different surface tensions under various pore pressures. Different lines represent different γ' for the foam after dilution.

The above discussions indicate that the influence from the increase in surface tension on volume change and compressibility can be negligible for foams used in tunneling practice. However, the influence from the increase in surface tension can be significant with respect to the mobility of foam bubbles. In the micro stability model presented in Zheng et al. (2022), the minimum pressure drop required to for an individual bubble to penetrate is:

$$P_{w1} - P_{w2} = 4\gamma \left(\frac{1}{d} - \frac{1}{D} \right) \quad (14)$$

Equation (14) shows that the required pressure drop to initiate the penetration process is proportional to the surface tension of the bubbles. The increase in surface tension makes it more difficult for a foam bubble to squeeze through the pore throat. The consequence is the lowered potential of a low permeable layer at the tunnel face which is preferred in tunneling.

4 CONCLUSIONS

An experimental study on surface tension of foaming liquid at different concentrations was conducted with the capillary rise method. Injecting foam into the excavated soils induces the dilution of the foaming liquid surrounding the foam bubbles and consequently results in an increase in surface tension. Up till now, works on foam research failed to incorporate this influence. This work suggests that the surface tension after the foam being mixed with the excavated soils can be twice the value before mixing. Volume change and compressibility for the foam used in tunneling can be negligible within the range of increment in surface tension. While the ability for foam to penetrate the grain skeleton is lowered as a result. Results suggest that the increase in surface tension due to dilution will lower the penetration potential. The influence on the stability of the foam-sand mixture should be further investigated.

ACKNOWLEDGEMENT

The first author acknowledges the support from China Postdoctoral Science Foundation (No. 2022M721945).

REFERENCES

Bezuijen, A., Schaminée, P.E.L. & Kleinjan, J.A., 1999. Additive testing for earth pressure balance shields. Proc. 12th Eur. Conf. on Soil Mech. and Geotech. Engrg., Amsterdam, Balkema, Rotterdam, pp. 1991–1996.

- Bezuijen, A., 2013. Foam parameters in saturated sand, theory and model tests. Proc. WTC, Geneva.
- Bezuijen, A. & Dias, T.G.S., 2017. EPB, chamber pressure dissipation during standstill. EURO: TUN 2017, Innsbruck University, Austria.
- Borio, L. & Peila, D., 2010. Study of the Permeability of Foam Conditioned Soils with Laboratory Tests. American Journal of Environmental Sciences 6 (4): 365–370.
- Galli, M., 2016. Bochum Rheological characterisation of Earth-Pressure-Balance (EPB) support medium composed of non-cohesive soils and foam. Doctoral thesis. Ruhr-Universität, Germany.
- Peila, D., Oggeri, C. & Borio, L., 2009. Using the slump test to assess the behaviour of conditioned soil for EPB tunnelling. Environmental & Engineering Geoscience XV (3): 167–174.
- Pena, M., 2007. Foam as a Soil Conditioner in Tunnelling: Physical and Mechanical Properties of Conditioned Sands, Doctoral thesis. Oxford.
- Psomas, S., 2001. Properties of foam/sand mixtures for tunneling applications. Master's thesis, Oxford.
- Quebaud, S., Sibai, M. & Henry, J.P., 1998. Use of chemical foam for improvements in drilling by earth pressure balance shields in granular soils. Tunnelling and Underground Space Technology 13 (2): 173–180.
- Thewes, M., Budach, C. & Bezuijen, A., 2012. Foam conditioning in EPB tunneling. Geotechnical Aspects of Underground Construction in Soft Ground. London.
- Wang, S., Hu, Q., Wang, H., Thewes, M., Ge, L., Yang, J. & Liu, P., 2021. Permeability Characteristics of Poorly Graded Sand Conditioned with Foam in Different Conditioning States. Journal of Testing and Evaluation. Published ahead of print, September 01, 2021, <https://doi.org/10.1520/JTE20190539>.
- Wu, Y., Mooney, M.A. & Cha, M., 2018. An experimental examination of foam stability under pressure for EPB TBM tunneling. Tunnelling and Underground Space Technology 77 (2018): 80–93.
- Wu, Y., Nazem, A., Meng, F. and Mooney, M.A., 2020. Experimental study on the stability of foam-conditioned sand under pressure in the EPBM chamber. Tunnelling and Underground Space Technology 106 (2020): 103590.
- Vargaftik, N.M., Volkov, B.N. and Voljak, L.D., 1983 International Tables of the Surface Tension of Water. Journal of Physical and Chemical Reference Data 12 (3): 817–820.
- Xu, T., 2018. Infiltration and excess pore water pressures in front of a TBM, Experiments, Mechanisms and Computational models, Doctoral thesis. Ghent University, Belgium.
- Zheng, D., Bezuijen, A. & Thewes, M. 2021. An experimental study on foam infiltration into saturated sand and its consequence for EPB shield tunneling. Tunnelling and Underground Space Technology 111 (2021): 103878.
- Zheng, D., Bezuijen, A. & Thewes, M., 2022. Modelling the infiltration behavior of foam into saturated sand considering capillary resistance for EPB shield tunneling. Géotechnique. doi.org/10.1680/jgeot.21.00146.
- Zheng, D., Bezuijen, A. & Thewes, M., 2022. Experimental study of foam infiltration from foam-sand mixture into saturated sand for EPB shield tunnelling: A mechanism study. Tunnelling and Underground Space Technology 138(2023): 105206.

Numerical modeling of muck movement and chamber pressure distribution during EPB shield tunneling with auxiliary air pressure balance mode

J.Z. Zhong

Central South University, Changsha, China

State Key Laboratory of Internet of Things for Smart City & Department of Civil and Environmental Engineering, University of Macau, China

S.Y. Wang

Shenzhen University, Shenzhen, China

Central South University, Changsha, China

ABSTRACT: To reduce machine loads during Earth Pressure Balance (EPB) shield tunneling, the auxiliary air pressure balance mode is gradually applied. However, the improper control of auxiliary air balance mode may cause inadequate support pressure, leading to higher risk of tunnel face instability. This study employs a two-phase flow model of muck and air using Computational Fluid Dynamics (CFD) method to simulate the pressure distribution inside shield chamber during tunneling with auxiliary air balance mode. The pressure unbalance is observed between the left and right sides of the chamber resulting from the muck rotating flow. Furthermore, the disturbance of moving shield components leads to an obvious pressure fluctuation in the muck zones near components. The growing supporting pressure is accompanied by growing fluctuation and unbalance with increasing auxiliary air pressure. In addition, the supporting pressure has little change but the pressure fluctuation and unbalance decrease with increasing foam injection ratio. The results indicate that face stability and chamber pressure control require a combined adjustment of auxiliary air pressure and foam injection ratio.

Keywords: EPB shield tunneling, Auxiliary air pressure balance mode, Computational fluid dynamics, Two-phase flow, Chamber pressure

1 INTRODUCTION

The muck behavior during earth pressure balance (EPB) shield tunneling significantly affects the characteristics of muck pressure inside the chamber, and thus improper control would cause excessive strata deformation. Scholars have conducted relevant studies on the dynamic control of chamber pressure or muck discharge efficiency by using field tests (Bezuijen et al. 2006), physical model tests (Li et al. 2020), numerical simulations (Jin et al. 2023), etc. These studies aimed to optimize cutterhead selection and chamber pressure control. Among them, the engineering-scale numerical simulation of shield tunneling based on computational fluid dynamics can comprehensively and visually investigate the muck flow characteristics during tunneling and discharge and then reveal the variation and mechanisms of muck behavior influenced by various tunneling parameters. However, existing numerical studies have not specifically addressed the increasingly popular use of auxiliary air pressure balance mode in EPB shield tunneling, where the chamber is not filled with muck. The tunnel face is stabilized by air pressure on the upper part of the chamber and muck pressure on the lower part, as illustrated in

Figure 1. The air pressure is provided by air compressor. Zhu et al. (2017) used auxiliary air pressure balance mode in the actual tunneling case for the first time to reduce the cutter wear and the machine load including thrust and torque. As a result, this mode can effectively prevent the muck spewing and enhance the tunneling efficiency. Successful shield tunneling cases have been reported in areas that are insensitive to ground subsidence (Wang et al. 2022).

The maintenance of chamber pressure and regulation of muck discharge pose greater challenges in the auxiliary air pressure mode compared to the full muck pressure mode, thus limiting the widespread adoption of the auxiliary air pressure mode in shield tunnels (Zhou 2012). Currently, no research has attempted to investigate the effect of active tunneling parameters on muck pressure characteristics in the auxiliary air pressure mode. Consequently, there is still a lack of scientific understanding regarding the mechanism of chamber pressure maintenance.

This study introduces the Volume of Fluid (VOF) method to calculate the two-phase flow problem of air and muck in the chamber and screw conveyor. It is assumed that the first phase of simulated muck is immiscible with the second phase of air, and there is no material exchange between them. The numerical simulation of two-phase flow is utilized to explore the effect of auxiliary air pressure and the foam injection ratio (FIR) of muck on the chamber pressure characteristics, and thus guide the control strategy of chamber pressure in auxiliary air pressure mode.

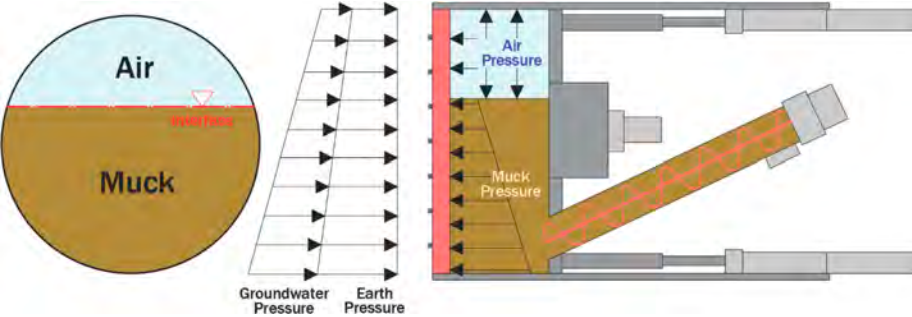


Figure 1. Internal and outer pressure balance of tunnel face during shield tunneling using auxiliary air pressure mode.

2 MUCK FLOW MODEL DURING EPB SHIELD TUNNELLING USING CFD

2.1 Computational method

The VOF algorithm is an interface-tracking method applied to an Eulerian computational domain for flow problems with two or more immiscible phases. The proportions of each fluid phase within a grid cell are characterized by the phase volume fractions, which are the continuous functions of time and space. The sum of the volume fractions of all phases within the cell is 1 and all physical quantities are shared by the phases. In the VOF two-phase flow model, two fluid phases share a set of momentum equations. The volume fraction of each fluid within each cell can be solved and tracked throughout the computational domain, thereby obtaining the interfaces between immiscible fluids. The application scenarios of the VOF method include the dam break problem, the free-surface flow problem, and the liquid sloshing problem. However, the VOF method also has the potential advantages of tracking the muck-air interface and obtaining the muck flow characteristics in the chamber filled with air and muck. This method can be extended to simulate the behavior of air and muck during shield tunneling with auxiliary air pressure mode.

2.2 Computational model for EPB shield

According to the R155 EPB shield machine used in a shield tunnel project in Kunming metro, an engineering-scale geometric model of the shield machine is established, as shown in

Figure 2. The geometric model consists of the cutterhead with its four supporting shafts, two mixing rods, a chamber, and a screw conveyor. The screw in the model is extended into the chamber by 0.5 m to enable the muck inside the chamber to be discharged along the screw conveyor. In addition, the simulation focuses on the muck flow behavior in the chamber and screw conveyor without considering the effect of cutters on the stratum and the interaction of soil particles, water, foam, and other substances within the muck. It is assumed that the excavated muck flows into the chamber directly from the opening of cutterhead, which is similar to the simplified setup of the existing literature (Dang and Meschke 2020).

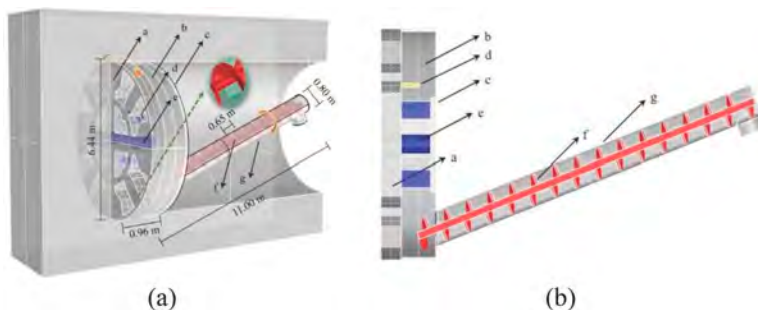


Figure 2. Geometric model of shield machine: (a) main view; (b) cross-section (a. cutterhead, b. chamber, c. bulkhead, d. mixing rod, e. support shaft, f. screw, g. the shell of conveyor).

The internal region of the shield geometry model shown in Figure 2 is extracted as the computational fluid domain of muck flow. Considering the influence of rotating parts such as cutterhead, support shafts, mixing rods, and screw blade on the muck “fluid”. The computational fluid domain is divided into several partitions. Each partition is discretized into a number of grid cells. As shown in Figure 3, the computational partitions near the rotating components are defined as the moving domains (green domains in Figure 3), while the rest are defined as the static domains (gray domains in Figure 3). In order to realize the continuous flow of muck in the computational domain, adjacent partitions need to set up a pair of interfaces to transfer the physical information of grid nodes. Fluent adopts the Mesh Motion method to simulate the disturbance of the shield components wall to the muck “fluid” and then calculate the transient flow field. Based on the equations of solid motion, the grid nodes in the moving domain are set to rotate or translate. The interface nodes are updated in time with the grid motion. In addition, the inlet and outlet of the CFD model are set up with expansion zones respectively for the convergence of computation.

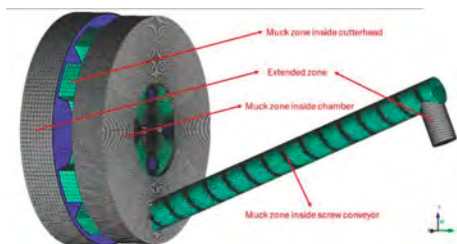


Figure 3. Discretization of the computational domain of muck fluid.

The model inlet adopts the mass flow inlet boundary, which only allows the inflow of muck. The muck inflow rate is related to the tunneling speed and its direction is parallel to the axis of EPB shield. The inlet mass flow rate is calculated by Equation (1):

$$M_{in} = \rho_f \bar{v}_f \cdot \pi D_c^2 / 4 \quad (1)$$

where M_{in} is the inlet mass flow rate, kg/s, ρ_f is the muck density in front of the cutterhead, kg/m³, v_f is the average inflow rate of muck, m/s, which is equal to the average value of tunneling speed, D_e is the excavation diameter of EPB shield, m.

In the auxiliary air pressure mode, a pressurized air channel above the chamber is connected to the air compressor (Zhu et al. 2017) to ensure a stable auxiliary pressure. The numerical model simplifies the scenario by assuming the presence of an air inflow inlet above the chamber. This inlet is assigned as a total pressure boundary, with the total pressure matching the specified auxiliary air pressure. Furthermore, the model outlet is simulated with a static pressure outlet boundary, where the pressure is equal to atmospheric pressure. The outlet allows the muck phase to flow out while allowing the air phase to flow out or reflux. The moving speed of the walls of shield rotating components should be consistent with the rotational speed of the belonging components.

The iterative computation is conducted using an adaptive time step, ensuring that the global Courant number remains below 1 throughout the iteration. The computation is considered converged when the residual values of the variables reach a value lower than 10^{-4} . Then, the current time step iteration computation is terminated, and the subsequent time step computation begins.

2.3 Compressibility and rheological model of muck

2.3.1 Compressibility model of muck flow

Due to the compressible foam, the foam-conditioned soil undergoes undrained one-dimensional compression under pressure. The relationship between the apparent density of soil and applied pressure can be fitted by the simplified form of Tait's semi-empirical formula provided by the Fluent Materials Library. The Tait's formula can be characterized by Equations (2) to (4):

$$\left(\frac{\rho}{\rho_0}\right)^n = \frac{K}{K_0} \quad (2)$$

$$K = K_0 + n\Delta p, \Delta p = p - p_0 \quad (3)$$

$$\rho_{r,\min} \leq \frac{\rho}{\rho_0} \leq \rho_{r,\max} \quad (4)$$

where p_0 is the atmospheric pressure, kPa, ρ_0 is the apparent density of foam-conditioned soil at atmospheric pressure, kg/m³, n is the density index, reflecting the sensitivity of the density change to the pressure change, K_0 is the bulk modulus of foam-conditioned soil at atmospheric pressure, kPa, K is the bulk modulus at specific pressure p , kPa; $\rho_{r,\max}$ and $\rho_{r,\min}$ are the maximum and minimum density ratios, respectively, defined as the ratio of maximum or minimum density to the density reference value ρ_0 .

2.3.2 Pressure-dependent rheological model of muck flow

The apparent viscosity η of a Herschel-Bulkley (H-B) fluid is determined by its intrinsic parameters, such as yield stress τ_0 , plastic viscosity μ , and power-law exponent m . To address the difficulties in the numerical realization of the H-B model, i.e., the discontinuity in the apparent viscosity at the yield point and the uncertainty in the shear stress below the yield point, Fluent modified the constitutive equations of classical H-B fluid by expressing the apparent viscosity η as a two-stage function bounded by the critical value of the shear rate as shown in Equation (5).

$$\begin{cases} \eta = \frac{\tau_0}{\dot{\gamma}} + \mu\dot{\gamma}^{m-1} & \dot{\gamma} > \dot{\gamma}_c \\ \eta = \frac{\tau_0 \left(2 - \frac{\dot{\gamma}}{\dot{\gamma}_c}\right)}{\dot{\gamma}_c} + \mu(\dot{\gamma}_c)^{m-1} \left[\left(2 - m\right) + (m - 1) \frac{\dot{\gamma}}{\dot{\gamma}_c} \right] & \dot{\gamma} < \dot{\gamma}_c \end{cases} \quad (5)$$

where $\dot{\gamma}_c$ is the critical value of shear rate, s⁻¹, which is generally set to 1×10^{-7} s⁻¹.

Since the fluidity of the foam-conditioned soil is pressure-dependent, the effect of pressure on the rheological parameters needs to be taken into account to modify the apparent viscosity

equation. Thus, a program of user-defined functions is utilized to customize the apparent viscosity model to be embedded in the CFD model.

3 VARIATION OF MUCK FLOW AND PRESSURE PROFILE INSIDE EPB CHAMBER

The face stability for shield tunneling with auxiliary air pressure mode requires a dynamic balance between the strata pressure and the support pressure provided by the air above the soil chamber and the muck below. In this study, it is assumed that initially 25% of the space above the chamber is air and 75% of the space below is muck. The tunneling speed is fixed at 40 mm/min, and the rotation speeds of the cutterhead and screw conveyor are set at 1.4 rev/min and 6 rev/min, respectively. To investigate the effects of the auxiliary air pressure and FIR on the muck flow and pressure profile inside the chamber, a series of working conditions are designed for comparison, as illustrated in Table 1.

Table 1. Case parameters in CFD models.

Case	Auxiliary air pressure (kPa)	Foam injection ratio (%)	Fixed parameters
1 (Reference)	200	30	• Tunneling speed is 40 mm/min
2-1	200	20	• Rotation speed of cutterhead is 1.4 rev/min
2-2	200	40	• Rotation speed of cutterhead is 6 rev/min
3-1	150	30	
3-2	100	30	

The FIR affects the compression and rheological parameters of muck. According to the experimental results from Zhong et al. (2023), it was found that the shear behavior of foam-conditioned soil after large deformation behaved similarly to shear-thinning fluids with yield stresses. Therefore, the modified H-B model was used to fit the curves of residual shear strength versus the shear rate of the foam-conditioned soil to obtain the rheological

Table 2. Compressibility and rheological parameters of foam-conditioned soil in various FIRs.

FIR/%	Tait model parameters			Modified H-B model parameters
	$\rho_0/(\text{kg}/\text{m}^3)$	K_0/kPa	$m/(-)$	
20	1616.63	176.58	28.09	τ_0/Pa $1.56 \times 10^{-7} \times \sigma_v^2 + 6.14 \times 10^{-2} \times \sigma_v + 1471.48$ $\mu/(\text{Pa} \cdot \text{s}^n)$ $7.55 \times 10^{-9} \times \sigma_v^2 + 4.13 \times 10^{-3} \times \sigma_v + 557.73$ $n/(-)$ $1.98 \times 10^{-7} \times \sigma_v + 0.194$
30	1518.43	189.80	16.25	τ_0/Pa $1.56 \times 10^{-7} \times \sigma_v^2 + 1.89 \times 10^{-2} \times \sigma_v + 1261.01$ $\mu/(\text{Pa} \cdot \text{s}^n)$ $6.43 \times 10^{-9} \times \sigma_v^2 + 4.11 \times 10^{-3} \times \sigma_v + 433.10$ $n/(-)$ $1.55 \times 10^{-7} \times \sigma_v + 0.216$
40	1400.70	188.18	10.35	τ_0/Pa $1.60 \times 10^{-7} \times \sigma_v^2 + 5.07 \times 10^{-4} \times \sigma_v + 896.70$ $\mu/(\text{Pa} \cdot \text{s}^n)$ $3.73 \times 10^{-9} \times \sigma_v^2 + 2.26 \times 10^{-3} \times \sigma_v + 434.78$ $n/(-)$ $1.97 \times 10^{-7} \times \sigma_v + 0.266$

parameters. The correlations between the rheological parameters and pressure were fitted by polynomial equations. In addition, the Tait model was used to fit the apparent density versus pressure curve of the foam-conditioned soil. The compression and rheological parameters of the soil corresponding to various FIRs are shown in Table 2. The relevant parameters were applied to the two-phase flow model to characterize the compressibility and rheological properties of the muck.

3.1 Local pressure fluctuation induced by muck flow

The profile of the muck volume fraction, pressure, and velocity in the transverse section (parallel to cutterhead surface) and the longitudinal section (normal to cutterhead surface) inside chamber was obtained from the simulation results, as shown in Figure 4. Figure 4 (a) shows the volume fraction distribution of muck and air in the transverse and longitudinal sections. The muck almost fills up the domain of the screw conveyor, whereas the air above the chamber maintains an obvious interface with the muck below it. Figure 4(b) shows the pressure contour in the transverse section. On the one hand, the pressure of the muck zones near the shield components fluctuates severely. On the other hand, the muck zone in the lower part of the chamber exists an obvious pressure imbalance phenomenon between the left and right sides. Figure 4(c) reveals the pressure contour in the longitudinal section. It is found that localized low pressure occurs near the conveyor inlet and the muck pressure is high in front of the screw blade along the discharge direction.

Figure 4 (d) shows the flow velocity vector profile in the transverse section inside chamber. The muck mainly flows with the rotation of the supporting shafts and mixing bars. The area with higher flow velocity is consistent with the area with significant pressure fluctuation. The muck flows in a clockwise direction, so the muck on the right side of the chamber is compressed and the corresponding pressure is higher. Furthermore, as shown in the local flow velocity vector profile at the chamber outlet in Figure 4(e), the muck rotates and flows to the chamber outlet and discharges along the screw conveyor. Therefore, the muck near the chamber outlet is loose and the corresponding pressure is low. It is also found that the muck flow mainly along the axis of the conveyor is driven by the screw blade. The phenomenon of the high muck pressure in front of the screw blade proves that the rotating screw can promote muck discharge. Figure 4(f) shows the apparent viscosity profile in the transverse section. The greater apparent

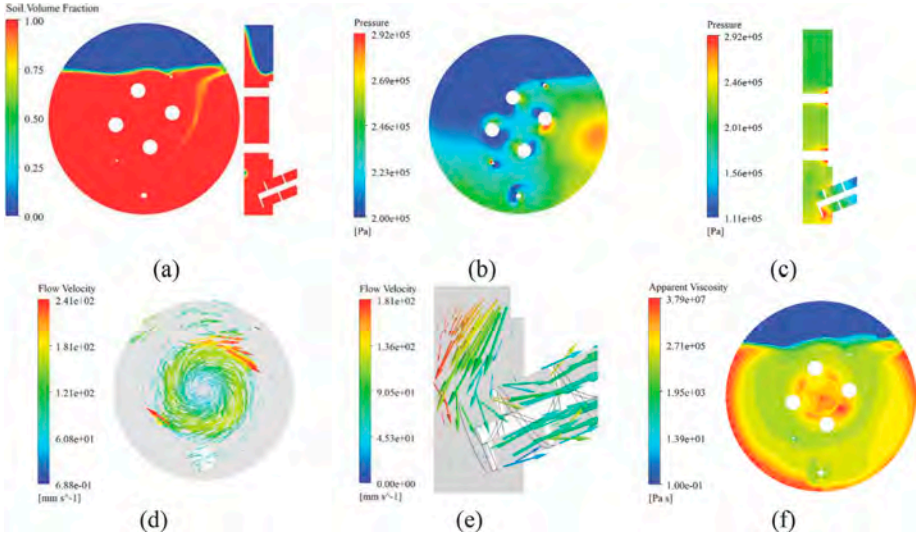


Figure 4. Muck flow field distribution in the chamber during tunneling: (a) volume fraction; (b) pressure in transverse section; (c) pressure in longitudinal section; (d) velocity in transverse section; (e) velocity near the conveyor inlet; (f) apparent viscosity in transverse section.

viscosity reflects the poorer fluidity of muck. Combined with Figure 4(d), it can be seen that the muck near the left edge of the chamber has a small velocity and high viscosity. This zone can be defined as the stagnant zone. In addition, the muck in the center of the chamber has a high viscosity and large velocity, indicating that the overall muck in that zone rotates with the supporting shafts, leading to easy muck accumulation and clogging in the center of the chamber. Therefore, the observed stagnant zone should be raised the attention of the optimization of the nozzle design of soil conditioning.

3.2 Influence of foam injection ratio

Figure 5 demonstrates the pressure distribution pattern in the central line of the cutterhead and bulkhead in various FIRs. It can be seen that the muck pressure in the chamber bulkhead is lower than that in front of the cutterhead, but the air pressure in the upper part of the chamber is higher than the support pressure of the same height in front of the cutterhead. Therefore, the auxiliary air pressure is required to be higher than the same-height pressure in front of the cutterhead to support the tunnel face efficiently and maintain a constant tunneling speed. Moreover, the bulkhead pressure fluctuates severely close to the position of the supporting shafts and the screw blade. The fluctuation is significantly reduced with the increase of FIR, indicating that foam conditioning is beneficial in reducing the degree of local pressure fluctuation.

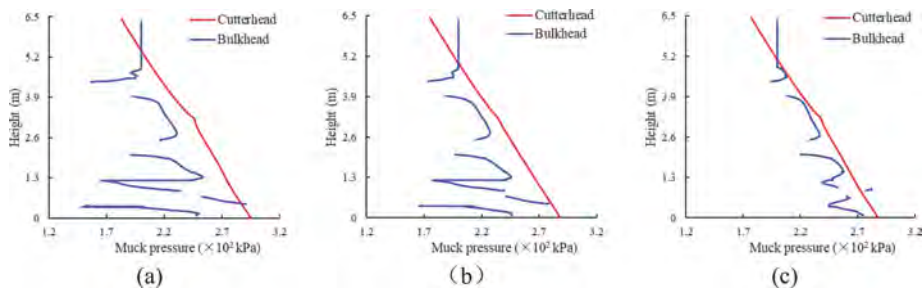


Figure 5. Pressure distribution patterns in the central line of the cutterhead and bulkhead in various FIRs: (a) 20%; (b) 30%; (c) 40%.

Figure 6 demonstrates the pressure unbalance phenomenon in the chamber under various FIRs. The degree of pressure unbalance decreases with the increase of the FIR. Although the FIR can increase the muck compressibility, which is not conducive to the pressure equilibrium of the right and left sides, it can also reduce the rheological parameters, which is conducive to the pressure equilibrium (Dang and Meschke 2020). The simulation observation shows that the rheological properties of muck have a more significant effect on the pressure unbalance characteristics.

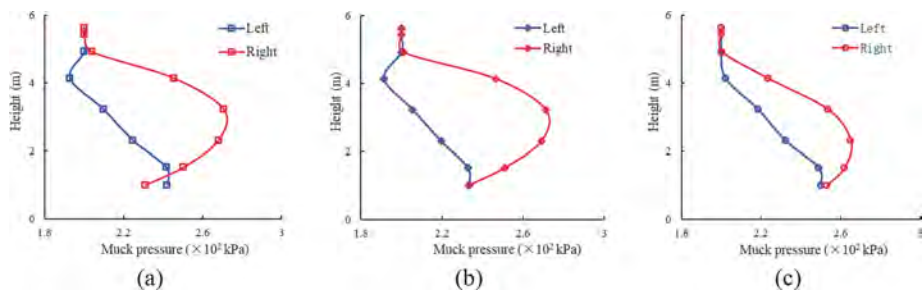


Figure 6. Pressure unbalance characteristics of the left and right sides in the chamber in various FIRs: (a) 20%; (b) 30%; (c) 40%.

3.3 Influence of auxiliary air pressure

The air at the upper part of the chamber is another support for the tunnel face other than muck. The magnitude of auxiliary air pressure above the soil chamber also affects shield tunneling. Figure 7 demonstrates the pressure distribution patterns in the central line of the cutterhead and bulkhead in various auxiliary air pressures. It is found that the chamber pressure is higher with the increase of auxiliary air pressure. The pressure fluctuation due to the disturbance of rotating components is also larger.

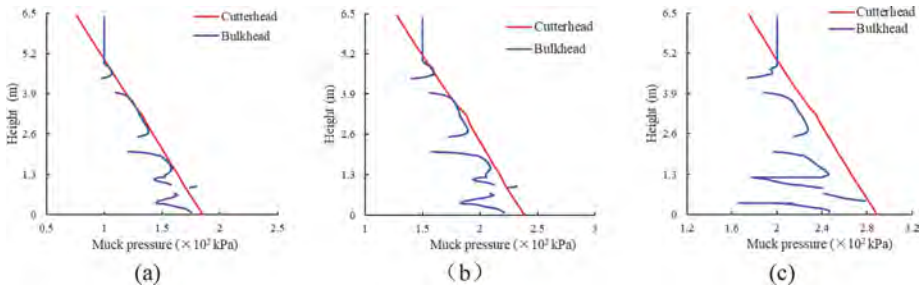


Figure 7. Pressure distribution patterns in the central line of the cutterhead and bulkhead in various auxiliary air pressures: (a) 100 kPa; (b) 150 kPa; (c) 200 kPa; (d) Comparison of pressure in front of the cutterhead.

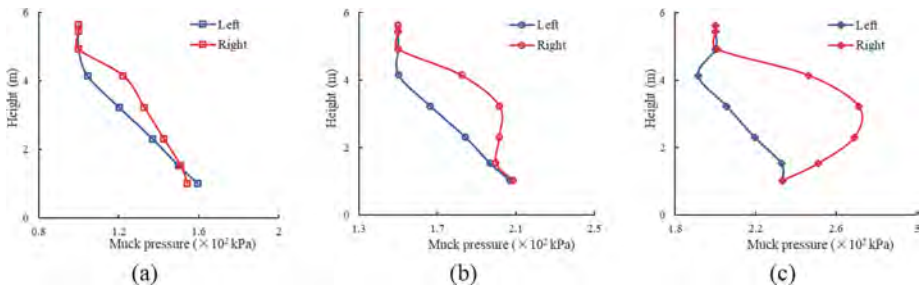


Figure 8. Pressure unbalance characteristics of the left and right sides in the chamber in various auxiliary air pressures: (a) 100 kPa; (b) 150 kPa; (c) 200 kPa.

Furthermore, the pressure unbalance of the chamber in different auxiliary air pressures is shown in Figure 8. The pressure unbalance phenomenon mainly occurs in the center of the chamber. The degree of pressure unbalance increases significantly with increasing the auxiliary air pressure. The auxiliary air pressure would compress the muck and weaken its fluidity, so the poorer fluidity of muck is accompanied by the larger pressure unbalance, which is similar to the observation from Figure 6.

4 CONCLUSION

In this paper, the two-phase flow model using CFD method is innovatively used to investigate the pressure distribution variation inside the EPB shield chamber with auxiliary air pressure mode. A series of engineering-scale two-phase flow CFD simulations is then performed to analyze the variation of auxiliary air pressure and foam injection ratio on the pressure fluctuation and unbalance inside chamber. The main findings of the study are as follows:

- (1) The muck pressure in the lower area of chamber is higher than the support pressure in front of the cutterhead at the same height. However, the air pressure in the upper area of chamber is higher than the support pressure in front of the cutterhead at the same height.

- (2) Due to the rotating flow of the muck, there is an obvious pressure unbalance between the left and right sides of the chamber. Meanwhile, the zones near moving shield components have obvious pressure fluctuation, resulting from the disturbance of moving components. Near the chamber outlet, the pressure drop promotes the muck discharge along the screw conveyor. The pressure increase locally is attributed to the push effect of the rotating screw.
- (3) As an increase in auxiliary air pressure, the growing supporting pressure is accompanied by growing fluctuation and unbalance. As an increase in FIR, the supporting pressure has little change but the pressure fluctuation and unbalance decrease. Face stability and chamber pressure control require a combined adjustment of auxiliary air pressure and FIR. However, it should be noted that excessively foam-conditioned muck may lead to muck spewing. Therefore, it is suggested that shield tunneling should adjust FIR and auxiliary air pressure simultaneously to guarantee the face stability.

ACKNOWLEDGEMENTS

The financial support from the National Natural Science Foundation of China, China (No. 52022112) are acknowledged and appreciated.

REFERENCES

- [1] Bezuijen, A., Talmon, A. M., Joustra, J. F. W., et al. 2006. Pressure gradients and muck properties at the face of an EPB. *Symp. on Geotechnical Aspects of Underground Construction in Soft Ground*, Rotterdam. 43–49.
- [2] Li, X., Yang, Y., Jin, D., et al. 2020. Theoretical analysis and experiment of pressure distribution and pressure gradient of shield screw conveyor: Taking sandy soil as an example. *Scientific Reports*, 10, 7831.
- [3] Jin, D., Guo, Y., Li, X., et al. 2023. Numerical study on the muck flow behavior in the screw conveyor during EPB shield tunneling. *Tunnelling and Underground Space Technology*, 134.
- [4] Zhu W., Zhong C., Huang W., et al. 2017. Key techniques for the auxiliary air pressure balance mode for shield tunnelling. *Modern Tunnelling Technology*, 54, 1–8.
- [5] Wang, S., Liu, P., Gong, Z., et al. 2022. Auxiliary air pressure balance mode for EPB shield tunneling in water-rich gravelly sand strata Feasibility and soil conditioning. *Case Studies in Construction Materials*, 16, e00799.
- [6] Zhou G. 2012. Analysis on earth conveying and pressure maintaining of screw conveyors of EPB shields. *Tunnel Construction*, 32, 302–308.
- [7] Dang, T. S. & Meschke, G. 2020. Influence of muck properties and chamber design on pressure distribution in EPB pressure chambers – Insights from computational flow simulations. *Tunnelling and Underground Space Technology*, 99, 103333.
- [8] Zhong J., Wang S., Qu T. 2023. Undrained vane shear strength of sand-foam mixtures subjected to different shear rates. *Journal of Rock Mechanics and Geotechnical Engineering*, 15(6), 1591–1602.



Taylor & Francis

Taylor & Francis Group

<http://taylorandfrancis.com>

*Innovative analysis and design in tunneling
and underground construction*



Taylor & Francis

Taylor & Francis Group

<http://taylorandfrancis.com>

General Report – Innovative analysis and design in tunneling and underground construction

D.M. Zhang

Department of Geotechnical Engineering, Tongji University, Shanghai, China

T. Xu

School of Transportation, Southeast University, Nanjing, China

ABSTRACT: This General Report presents an overview of the papers submitted for the Symposium session dedicated to “Innovative analysis and design in tunnelling and underground construction”. These papers address studies related to shield tunnelling, underground construction and landslide projects in Asia. The main focuses are on the ground and structure response to excavation, as well as on operation quality during project construction. Many of the contributions cover the use of innovative analysis and design methods, including AI, machine learning, or real-uncertainty analysis during the construction process.

1 OVERVIEW

A total of eleven papers were submitted to the session dedicated to innovative analysis and design. Among these, seven contributions were authored by individuals from Asia, primarily from China mainland (six), with additional representatives from China Macao SAR (two), China Taiwan (one), Japan (two), Vietnam (one). No contributions were received from other continents. In terms of affiliation, all the submissions are from academia and two with joint academia-industry cooperation.

The content of the papers predominantly focuses on innovative analysis method in tunneling and underground construction, such as AI, machine learning, and uncertainty analysis for shield or TBM tunnelling and deep excavation. Only one paper addresses immersed tunnel. Additionally, two paper describes geotechnical problems about landslides.

The following discussion is organised into three sections. The first session provides an overview of papers primarily dedicated to ground and structure responses to shield or TBM tunnelling. The second session delves into contributions addressing problems encountered during underground construction, along with the strategies employed to finalise solutions. Finally, the third section is dedicated to papers focused on susceptibility and stability of landslide based on field data analysis.

2 SHIELD TUNNELLING

Cheng et al. (2024) employed the jet grouting (Rapidjet Method) and Tube-a-Manchette (TAM) with chemical grouting to address composite strata with varying properties, ensuring the necessary strength and waterproofing for TBM tunneling. Jet grouting enhances the grouting zone above the soil-rock interface, preventing the shield machine from shifting upward or causing ground collapse during excavation. TAM grouting around the jet-grouted bodies serves both for structural support and reducing soil permeability. The TBM launch and arrival in the study case proceeded smoothly, with a settlement of approximately 10 mm recorded 160 days after the shield passed through the improved composite strata by jet grouting. Therefore, meticulous planning of grouting methods can significantly reduce construction time and costs.

An et al. (2024) proposed a method for setting up a correction alignment for TBM meandering that takes into account the trajectory of the shield machine at the correction beginning point RB and correction end point RE. We analyze the deviation of position and the direction of the shield machine from DTA, and categorize the type of modified alignments separately on horizontal and vertical planes for all combination cases that arise in practice. This correction algorithm for TBM meandering can identify the optimal correction alignment that meets the requirement of geometric condition between RB and RE, and find the range of correction curve for each case. The research aims to enhance the precision of the shield tunneling method by providing an effective approach for correcting deviations and directions from the planned alignment.

Zhao & Liao (2024) The control mechanism for tunnel construction is highly intricate and becomes even more challenging with the shield radius increases. Identifying the key features of shield attitude changes under the combined influence of multiple parameters is essential in the posture prediction and deviation adjustment. Therefore, this study utilizes methods such as feature engineering, ensemble tree algorithms, SHAP correlation analysis, and big data analysis to thoroughly explore combinations of features that significantly impact posture changes. The results indicate that synthetic features comprise a high portion of the key features. Six primary patterns of SHAP bee swarm plot are proposed to reflect the working conditions of shield attitude control. In the context of the water supply tunnel project in Hangzhou, unfavorable working conditions that should be avoided have been identified. These include extremes in values such as excessively high or low of $n \times TD$, n , RD , Tch , $n \times TB$, $Tch \times FD$, $v \times T$. Also, parameters that consistently and reliably influence variations in the targets are demonstrated. Through feature engineering and SHAP correlation analysis, crucial features have been identified. This is crucial and indispensable for comprehending shield tunneling posture changes and subsequently conducting attitude prediction and deviation correction.

In shield construction, it is inevitable to induce ground loss and thereby cause surface settlement, as shown in Figure 1. Tail grouting is regarded as an efficient method for reducing ground loss during shield tunnelling. The grout will inevitably be compressed under earth pressure (see Figure 2), resulting in ground loss and surface settlement that have not been accurately estimated. Liang et al. (2024) investigated the compressed deformation of tail grouts subjected to earth pressure in different types of soils using a lab device. The lab test results reveal that compressed deformation rises with increased pressure and soil permeability. As the pressure increases, the increase rate of ultimate compressed deformation becomes smaller. Based on test results, analysis was conducted to determine how ground loss and surface settlement were affected by various parameters, including tail gap, tunnel radius, pressure, burial depth and soil permeability.

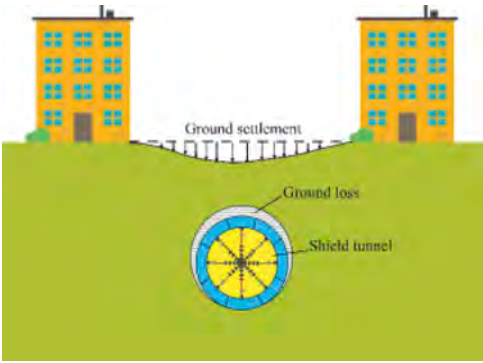


Figure 1. Tunnelling-induced ground settlement.

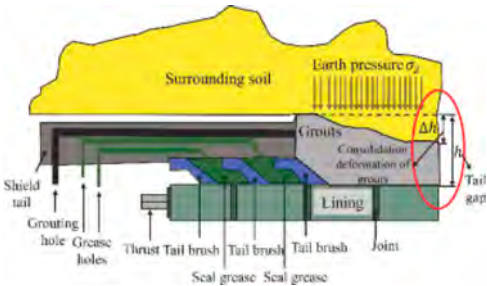


Figure 2. Tail grouting.

3 UNDERGROUND CONSTRUCTION

Settlement monitoring and prediction are among the most concerning problems for an immersed tunnel. However, settlement monitoring usually relies on manual surveys with low

frequency, while the settlement prediction for the entire tunnel is usually based on the assumption of an elastic foundation. Therefore, determining the impact of short-term events on the settlement of an immersed tunnel is difficult. He et al. (2024) combines a physics-informed machine learning algorithm with the Kelvin-Voigt model, introducing a retardation time factor to express the delayed response to an applied force. This framework is further used in the Hong Kong-Zhuhai-Macau Bridge tunnel (Figure 1), and the effect of an extreme water level caused by a typhoon on this tunnel is analyzed.

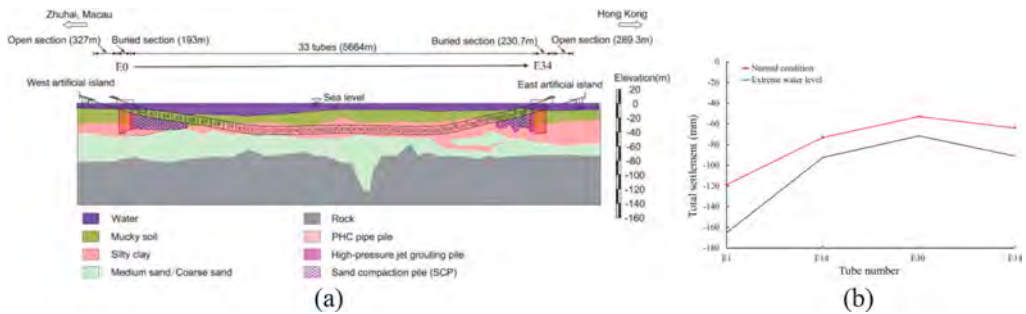


Figure 3. (a) Geological profile of the HZMB tunnel; (b) Settlement prediction of the HZMB tunnel at 2026/12/8 with the elastic foundation assumption.

Geological uncertainty is common due to complex depositional processes as one layer appears to be randomly embedded in neighbouring layers. The geo-structures could be significantly affected by geological uncertainty, such as tunnels. Borehole data obtained during the geological survey is the most commonly used information to simulate geological uncertainty. However, borehole data is usually sparse and inadequate. With the process of tunnel excavation, a large amount of new formation information will be continuously revealed. How to effectively use this disclosed geological information to update previously modelled formations? In other words, the geological cross-section along the planned tunnel trajectory can be used as additional information to incorporate with the original borehole data to update the simulated stratum dynamically. Zhang et al. (2024) developed a dynamically updating geological simulation framework incorporating the original borehole data and geological cross-section revealed from continuous tunnel excavation. The coupled Markov chain (CMC) model is a popular method to simulate geological uncertainty. Firstly, the initial stratum is obtained using the coupled Markov chain model based on limited borehole data. Then, the geological formation of the tunnel cross-section will be given with the process of tunnel excavation. Next, adding the additional information to the coupled Markov chain model to update the whole stratum simulation. The dynamic update of the whole stratum simulation can be realized along the tunnel trajectory by repeating the above process. The proposed framework can provide a dynamic formation modelling with tunnel excavation. It continuously updates the whole simulated stratum through the formation information revealed by the tunnel cross-section. It can also be used to forecast geological cross-sections ahead of the tunnel face, which will be helpful for tunnel construction. Results show that the proposed method can adequately use the original borehole data and revealed geological information to update the simulated stratum with the tunnel excavation dynamically.

Li et al. (2024a) introduced a dimensionless soil structural parameter, S_{vh} , derived by normalizing the effective stresses and the void ratio in Hardin equation for small-strain shear modulus, G_{max} , as the indicator for characterizing the degree of soil structure disturbance during construction. Based on field measurements of shear wave velocities before and after excavation, laboratory tests and numerical analysis, a procedure is proposed to evaluate the soil disturbance behind the retaining walls during excavation in a typical soft clay ground. All field measuring instruments are positioned on the southeast side of the excavation pit. Settlement meters, inclinometers and shear wave velocity testing boreholes are distributed at certain distances from the

retaining walls in the perpendicular direction (see Figure 4). As shown in Figure 5, when the excavation reaches 16.7 m, the peak disturbance degree with a value between 40-50% occurs in the area adjacent to diaphragm walls and underneath the excavation surface.

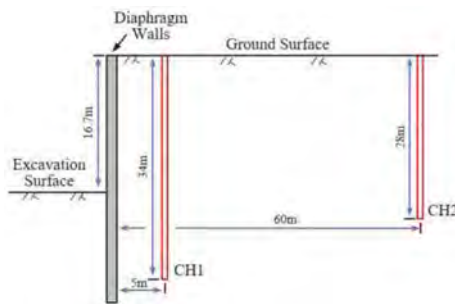


Figure 4. Plan view of the construction site for borehole testing.

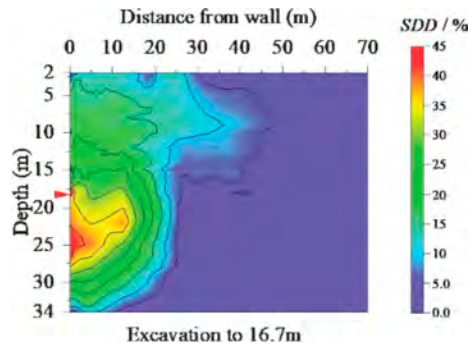


Figure 5. Soil structure disturbance field behind the retaining walls.

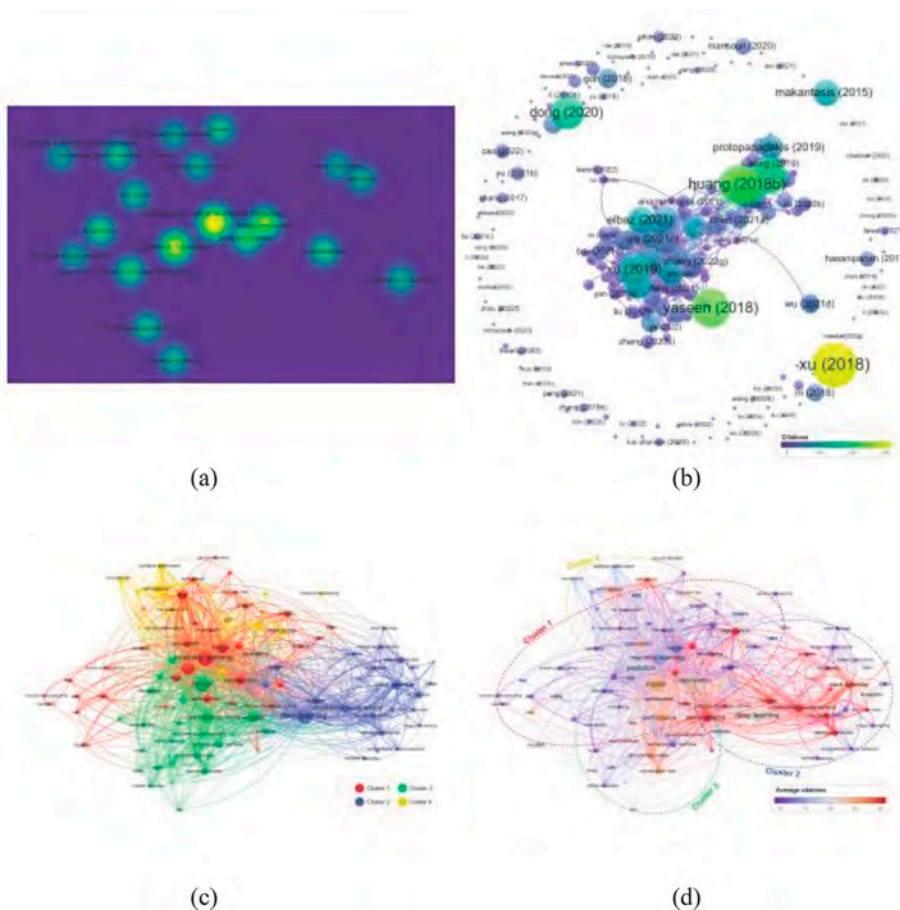


Figure 6. (a) Citation density visualization of source in fields of “AI + Tunnel”; (b) The most frequently citation publications; (c) Keywords co-occurrence analysis of “AI + Tunnel” publications; (d) Keywords co-occurrence analysis of “AI + Tunnel” publications with avg. citations information.

Quantifying uncertainty is crucial for enhancing the reliability of geotechnical engineering designs and reducing potential risks. Bayesian inference is commonly used for this purpose, yet the impact of measurement data size on updating results remains underexplored. Tang et al. (2024) took the excavation-induced wall deflection as a research demonstration, analyzing the influence of measured data size on Bayesian updates in the context of the TNEC excavation. Results demonstrate that utilizing five or more measured points yields satisfactory predictive outcomes ($R^2 > 0.90$). The variation in MPI values quantitatively reflects decreasing uncertainty with an increasing number of measurement points, while changes in PICP indicate the combined influence of predictive performance and confidence interval width on the probability of measured points falling within the predicted range. This research provides insights into using suitable measurement data sizes for robust parameter calibration and effective predictive performance in Bayesian updating for geotechnical engineering.

In recent years, machine learning technology has rapidly advanced and found widespread application in various domains. To further explore its potential in tunnel engineering, as Figure 6 shows, Shen et al. (2024) employed bibliometric data mining to systematically review machine learning research in the context of tunnel engineering and their interconnections. Using specific search terms, relevant information was extracted from the Web of Science Core database and analyzed with VOSviewer, a bibliometric mapping analysis software, to visualize the network of recently published literature and investigate interactions between machine learning and tunnel engineering research through citation networks. The analysis identified four distinct categories of machine learning research in tunnel engineering. Moreover, an examination of the connection and keyword co-occurrence networks in these two fields revealed challenges such as limited samples of actual engineering data and the constrained applicability of conventional machine learning models in tunnel engineering. These findings provide valuable insights for prospective research in this area.

4 LANDSLIDES

The main urban area of Kangding City and its surrounding watershed were taken as the study area. Sixteen environmental factors were selected. In Li et al. (2024b), factor combinations used to input a random forest (RF) model are screened by using the Apriori algorithm. The comparison of the evaluation results using frequency ratio accuracy and receiver operating characteristic curve (ROC) shows that the prediction results of the random forest model after factor screening are highly consistent with the actual landslide hazard distribution, and can better predict the spatial distribution characteristics of landslide susceptibility in the study area, which provides a more appropriate method for eliminating redundancy and noise factors in the environmental factors of landslide disasters.

Landslide dam (LD) is a kind of natural hazards that occurs worldwide. Typically, LDs are structurally weak and prone to failure in a short time after formation, posing a threat to downstream areas. Therefore, it is crucial to have a method for quickly determining the stability of an LD. However, traditional research methods, such as model testing and numerical calculations, are time-consuming and may not meet this requirement. Xiong et al. (2024) trained a support vector machine (SVM) based prediction/classification model to analyze the stability of LDs. Since the success of data-driven AI approaches highly depends on the number and type of data, we discuss the selection of training datasets and input parameters by utilizing a real-world LD dataset. Experimental results demonstrated that the prediction accuracy of LD stability can be improved by incorporating hydraulic information along with geometric information, compared to using geometric information alone.

5 CONCLUSIONS

This general report analysed eleven papers dedicated to innovative analysis and design in tunneling, underground construction and landslides. Most of them were very interesting, presenting innovative applications in terms of data analysis, design concept, construction techniques, and

field data interpretation and approaches. It is evident that the contexts in which tunnels and underground infrastructures are built are becoming increasingly demanding over time, thus requiring new construction technologies as well as innovative analysis and design methods. However, significant progress would also rely on deep mining of the monitored data from the jobsites. In this respect, these contributions give researchers and engineer some new insights to field data and during tunnelling and underground construction.

REFERENCES

- An, H. L. C, Suzuki, T., Sugimoto, M. & Thi, H. N. 2024. Algorithm on setting correction alignment for TBM meandering. *Proceedings of 11th International Conference on Geotechnical Aspects of Underground Construction in Soft Ground, Macao SAR, 14-17 June 2024.*
- Cheng, S. H., Wong, R. K. N., Hsu, H. Y., Wong, I. T. Y. & Chen, C. J. 2024. Ground improvement for the shield tunneling in the composite stratum. *Proceedings of 11th International Conference on Geotechnical Aspects of Underground Construction in Soft Ground, Macao SAR, 14-17 June 2024.*
- He, S. Y. & Zhou, W. H. 2024. Settlement Prediction of the Hong Kong-Zhuhai-Macau Bridge Tunnel Under the Effect of Typhoon. *Proceedings of 11th International Conference on Geotechnical Aspects of Underground Construction in Soft Ground, Macao SAR, 14-17 June 2024.*
- Li, M. Z., Zhou, Y. G., Tian, Y., Li, Y. Z. & Chen, Y. M. 2024a. Soil disturbance evaluation in a typical soft clay excavation pit. *Proceedings of 11th International Conference on Geotechnical Aspects of Underground Construction in Soft Ground, Macao SAR, 14-17 June 2024.*
- Li, Z. X., Xiao, F., Wang, Y., Zhou, Y. Z., Liu, J. F. & Meng, F. B. 2024b. Paper evaluation of landslide susceptibility in Kangding basin based on factor screening. *Proceedings of 11th International Conference on Geotechnical Aspects of Underground Construction in Soft Ground, Macao SAR, 14-17 June 2024.*
- Liang, J. X., Liu, W. & Xu, T. 2024. Ground loss and settlement of shield tunnel in tail grouting. *Proceedings of 11th International Conference on Geotechnical Aspects of Underground Construction in Soft Ground, Macao SAR, 14-17 June 2024.*
- Shen, Y., X., Wu, S. C., Xia, Z. Y., Wang, X. L. & Wang, J. X. 2024. Bibliometric data mining of machine learning in tunnel engineering research: A publication trends analysis and visualization. *Proceedings of 11th International Conference on Geotechnical Aspects of Underground Construction in Soft Ground, Macao SAR, 14-17 June 2024.*
- Tang, C., He, S. Y. & Zhou, W. H. 2024. Effects of measurement data size on Bayesian updating of excavation-induced deflection. *Proceedings of 11th International Conference on Geotechnical Aspects of Underground Construction in Soft Ground, Macao SAR, 14-17 June 2024.*
- Xiong, X., Gu, M., Shen, D.Y. & Shi, Z. M. 2024. Landslide dam stability analysis using a support vector machine approach. 2024. *Proceedings of 11th International Conference on Geotechnical Aspects of Underground Construction in Soft Ground, Macao SAR, 14-17 June 2024.*
- Zhang, J. Z., Jiang, Q. H., Zhang, D. M. & Huang, H. W. 2024. Dynamically updating geological uncertainty simulation with the process of tunnel excavation. *Proceedings of 11th International Conference on Geotechnical Aspects of Underground Construction in Soft Ground, Macao SAR, 14-17 June 2024.*
- Zhao, S. & Liao, S. M. 2024. Feature Engineering and SHAP Correlation Analysis for Large Diameter Shield Tunneling: a Deep Data Mining Approach to Explore the Core Features and Mechanism that Define the Shield Attitude. *Proceedings of 11th International Conference on Geotechnical Aspects of Underground Construction in Soft Ground, Macao SAR, 14-17 June 2024.*

Algorithm on setting correction alignment for TBM meandering

H.L.C. An, T. Suzuki & M. Sugimoto

Nagaoka University of Technology, Nagaoka, Japan

H.N. Thi

Vietnam National University Ho Chi Minh City-University of Technology, Ho Chi Minh, Viet Nam

ABSTRACT: In construction processes, the tunnel boring machine (TBM) can deviate from the planned alignment due to unpredictable factors, which can negatively affect the construction quality. This paper proposes a method for setting up a correction alignment for TBM meandering that takes into account the trajectory of the shield machine at the correction beginning point RB and correction end point RE. We analyze the deviation of position and the direction of the shield machine from DTA, and categorize the type of modified alignments separately on horizontal and vertical planes for all combination cases that arise in practice. This correction algorithm for TBM meandering can identify the optimal correction alignment that meets the requirement of geometric condition between RB and RE, and find the range of correction curve for each case. The research aims to enhance the precision of the shield tunneling method by providing an effective approach for correcting deviations and directions from the planned alignment.

1 INTRODUCTION

Shield machine, or tunnel boring machine (TBM), excavates tunnel according to a predetermined alignment plan that takes into consideration the purpose of the tunnel, the ground conditions, and the construction requirements. In practical construction processes, TBM inevitably deviates from the design alignment (Wang et al. 2023) and tends to follow a snake-like path as it attempts to realign with the planned alignment (Sugimoto et al. 2002). Excessive deviations can lead to notable issues, such as inaccurate segment installation and alignment deviations (Liu et al. 2018). Hence, it's imperative to promptly correct the alignment of TBM back to its planned alignment. (Zhou et al. 2018, Li et al. 2021, Zhou et al. 2018).

Recent advancements have seen the incorporation of technologies, primarily driven by artificial intelligence (Guo et al. 2022) and correction models (Wang et al. 2019, Sramoon et al. 2002), to rectify these deviations. These models, rooted in mathematical principles, facilitate the development of automatic control and trajectory systems. Consequently, shield machines can maintain a more accurate excavation path, minimizing under- or over-excavation. However, when the deviation of the TBM position exceeds an acceptable limit, the guidance system should employ rectification techniques to redirect the TBM back to planned alignment (Saracin et al. 2014). Notably, Xie (2012) sets up a set of scientific strategies that the machine turns left or right with its minimum turning radius until the shield axis runs parallel with the tunnel design axis. The inequality relationship to determine the condition of position and angle deviation is proposed to divide the strategy into the combined forms applied in the practical projects. Nevertheless, these strategies primarily focus on the DTA and lack a comprehensive theoretical foundation for the correction curve, failing to account for the position of correction end point. Tang (2022) used the inverse curve including two consecutive circular arcs with fixed correction beginning and end points, as well as the direction of the TBM at these points. While advantageous in pre-calculating coordinates on the curve, this approach is not universally applicable, as evidenced by some limitations. Two consecutive circular arcs cannot be applied in some exceptional cases, such as Type 1-2 and Type 2-2 in Table 1; because the chosen radius curve does not satisfy the geometric relationship

between the radius of the curve and the shape of the segment, or creates an extremely sharp curve that affects the construction quality.

Considering the highlighted challenges, it is essential to explore methods that offer optimal rectification controls for shield machines, especially in complex tunneling conditions. This research presents an innovative approach focusing on both the deviations from planned alignment and the TBM direction. The study aims to make a correction alignment to redirect the shield machine towards the planned path. By examining the relationship between the shield's trajectory at the correction beginning and end points, effective rectification strategies are identified. The efficacy of this model is underscored by its application to Takaogawa project.

2 METHODOLOGY

2.1 Coordinate system

In setting the correction alignment, the following coordinate systems shown in Figure 1 were used.

- 1) $C^T(x, y, z)$: Total coordinate system in three dimensional space
 The origin O is arbitrarily fixed to a point on the earth's surface
 The x -axis is the vertical downward direction
 The z -axis is the north toward direction
 The y -axis is orthogonal to the z - and x -axes with the right-hand rule
 - 2) $C^{T'}(x', y', z')$: Local coordinate system in three dimensional space
 The origin O' is the correction beginning point RB
 The x' -axis is the vertical downward direction
 The z' -axis is the projection of the shield axis on the y - z horizontal plane
 The y' -axis is orthogonal to the z' -axis with the right-hand rule on the y - z horizontal plane
 - 3) $C^H(y', z')$: Local coordinate system in two dimensional space for horizontal alignments
 The origin O' is the correction beginning point RB
 The z' -axis is the projection of the shield axis on the y - z horizontal plane
 The y' -axis is orthogonal to the z' -axis with the right-hand rule on the y - z horizontal plane
 - 4) $C^V(-x', L)$: Local coordinate system in two dimensional space for displaying modified vertical alignments
 The origin O' is the correction beginning point RB
 The L -axis is the projection of the shield trace on the y - z horizontal plane
 The x' -axis is the vertical downward direction
- where r_B^T = position vector at RB; r_E^T = position vector at RE
 θ_B^T = direction angle at RB; θ_E^T = direction angle at RE
 k_B^T = tangent vector at RB; k_E^T = tangent vector at RE
 θ_B^T : Rotation angle from z -axis to z' -axis around x -axis at RB

When the above defined C^H and C^V are used, replacing L and $(-x)$ -axes in C^H with z' and y' axes in C^V respectively; and third coordinates is always 0 since 2D space considering that the same calculation method in 3D space can be applied.

2.2 Horizontal correction alignment

$r_B^L = [0, 0, 0]$, $k_B^L = [0, 0, 1]$, $|\theta_E^L - \theta_B^L| < \pi/2$ are assumed.

2.2.1 Classification of correction alignment

The correction alignment is classified into four types according to the combination of changes in position and direction angle at RB and RE.

The position change of TBM can be determined by Equation 1. $a = +1$ indicates that RB shifts to the right side from z' -axis, while $a = -1$ indicates that RB shifts to the left side from z' -axis. When $a = 0$, the TBM remains on k_B^L .

$$a = \text{sign} \left[(\mathbf{k}_B^L \times (\mathbf{r}_E^L - \mathbf{r}_B^L))^T \mathbf{e}_x^L \right] \begin{cases} = -1 & \text{change to the left side} \\ = 0 & \text{no change} \\ = +1 & \text{change to the right side} \end{cases} \quad (1)$$

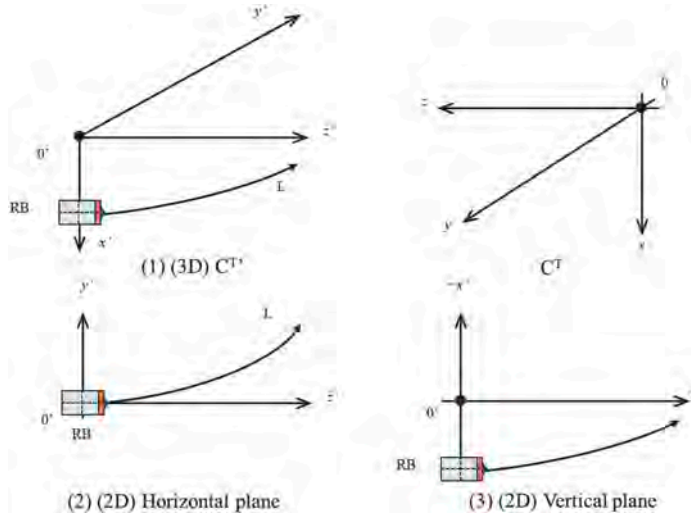


Figure 1. Co-ordinate system.

Similarly, the direction change of the TBM can be determined by Equation 2. $b = +1$ indicates the TBM rotates clockwise, while $b = -1$ indicates a counterclockwise rotation. If $b = 0$, the direction angle of the TBM is same at both RB and RE.

$$b = \text{sign} \left[(\mathbf{k}_B^L \times \mathbf{k}_E^L)^T \mathbf{e}_x^L \right] \begin{cases} = -1 & \text{counterclockwise rotation} \\ = 0 & \text{no change} \\ = +1 & \text{clockwise rotation} \end{cases} \quad (2)$$

The meandering types are categorized based on position change a and direction change b , as detailed in Table 1.

Table 1. Type of correction alignment.

		Position change a		
		Left(-1)	No change (0)	Right (+1)
Direction change b	Counterclockwise (-1)	Type1	Type4	Type3
	No change (0)	Type2	-	Type2
	Clockwise (+1)	Type3	Type4	Type1

2.2.2 Type 1

At first, if RE satisfies the following equation

$$(\mathbf{r}_{RE}^H - \mathbf{r}_{IP}^H)^T \mathbf{k}_E^H < R_{\min} \tan|\alpha/2| \quad (3)$$

where IP = intersection point between \mathbf{k}_B^L at RB and \mathbf{k}_E^L at RE; α = intersection angle; and R_{\min} = minimum radius of the correction alignment

Since the distance between RE and IP is too short to set a correction alignment, RE should move forward. When RE satisfies Equation 3, Type 1 shown in Figure 2 can be categorized as follows

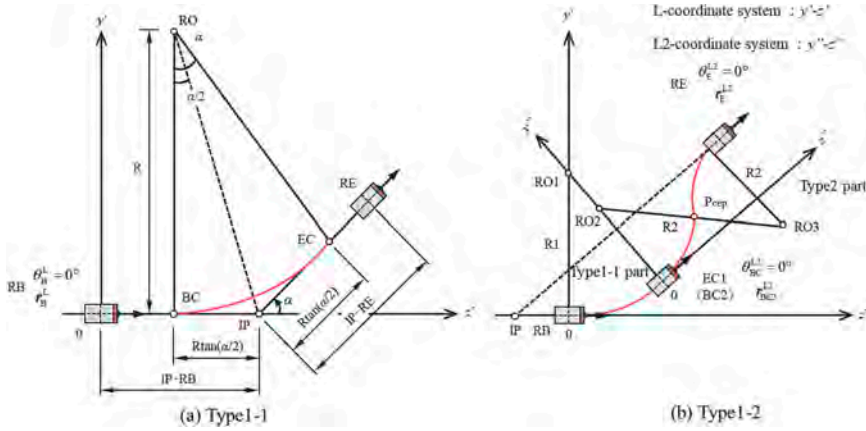


Figure 2. Type1 correction alignment.

$$\begin{aligned} (r_{IP}^H - r_{RB}^H)^T k_B^H &\geq R_{\min} \tan|\alpha/2| && \text{Type1 - 1} \\ &< R_{\min} \tan|\alpha/2| && \text{Type1 - 2} \end{aligned} \quad (4)$$

In case of Type1-1, the correction alignment consists of a single arc and straight line. In case of Type1-2, the intersection point IP is too close to RB. In that case, the correction alignment needs two circular curve. Type1-2 will be explained later in “2.2.4 Type3”.

The intersection angle α is obtained as

$$\alpha = \tan^{-1} \left(\frac{(k_B^L \times k_E^L)^T e_x^L}{k_B^L \cdot k_E^L} \right) \left(|\alpha| < \frac{\pi}{2} \right) \quad (5)$$

The intersection point IP can be represented by

$$r_{IP}^L = r_B^L + t_B k_B^L = r_E^L + t_E k_E^L \quad (6)$$

where t_E = Distance from r_B^L to r_{IP}^L in the k_B^L direction; t_B = Distance from r_E^L to r_{IP}^L in the k_E^L direction

The radius of curvature R_{\min} should be set to ensure that the TBM passes the curvature R_{\min} based on the TBM dimension. On the other hand, the maximum curve radius R_{\max} must satisfy the below conditions.

$$\begin{aligned} |r_{IP}^L - r_B^L| &\geq R \tan|\alpha/2|, \quad |r_{IP}^L - r_E^L| \geq R \tan|\alpha/2| \\ R_{\max} &= \min \left(\frac{|r_{IP}^L - r_B^L|}{\tan|\alpha/2|}, \frac{|r_{IP}^L - r_E^L|}{\tan|\alpha/2|} \right) \end{aligned} \quad (7)$$

The position vector r_{BC}^L of beginning point of curve BC and r_{EC}^L of end point of curve EC can be solved as follows

$$\begin{aligned} r_{BC}^L &= r_B^L + (|r_{IP}^L - r_B^L| - R \tan|\alpha/2|) k_B^L \\ r_{EC}^L &= r_E^L + (|r_{IP}^L - r_E^L| - R \tan|\alpha/2|) k_E^L \end{aligned} \quad (8)$$

The position vector r_o^L of the arc center RO is obtained as

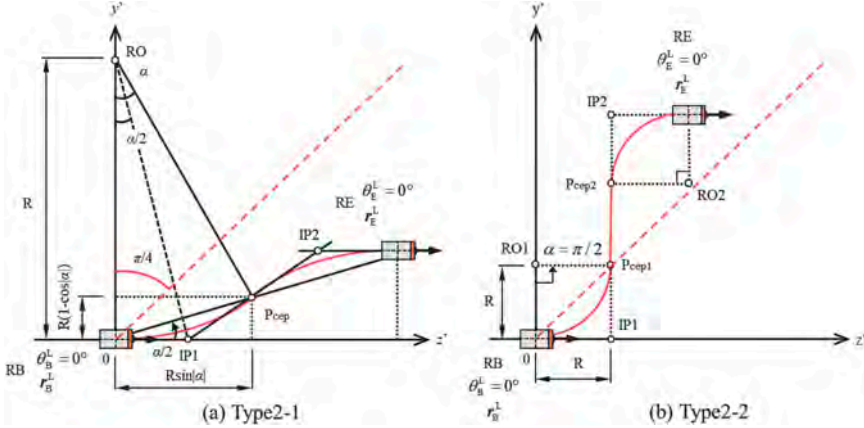


Figure 3. Type2 correction alignment.

$$r_o^L = r_{BC}^L - aRk_{By}^L \quad (9)$$

where $k_{By}^L = [0, 1, 0]^T$ is the unit vector in the y' -axis direction; a = position change of the TBM in Equation 1.

2.2.3 Type 2

In Type2, the correction alignment is categorized into two types by Equation 10 as shown in Figure 3.

$$\begin{aligned} z'_E + ay'_E &\geq 0 && \text{Type2 - 1} \\ &< 0 && \text{Type2 - 2} \end{aligned} \quad (10)$$

where, a = position change of the TBM in Equation 1; and y'_E, z'_E = component of r_E^L

In Type2-1, the correction alignment comprises of two symmetrical arcs, while the Type2-2 alignment includes two symmetrical arcs and a straight line.

Rotation angle from the RB to the P in Figure 3 of the first arc, α , can be obtained by

$$\alpha = \begin{cases} -2\tan^{-1}\left(\frac{y'_E}{z'_E}\right) & \text{Type2 - 1} \\ a\frac{\pi}{2} & \text{Type2 - 2} \end{cases} \quad (11)$$

The radius of curvature R in Type2-1 can be obtained as

$$R = \begin{cases} a\frac{z'_E}{2\sin\alpha} & |\alpha| \leq \pi/4 \\ -a\frac{y'_E}{2(1-\cos\alpha)} & |\alpha| > \pi/4 \end{cases} \quad (12)$$

Similarly, the radius R in Type2-2 can be calculated as

$$R = \frac{z'_E}{2} \quad (13)$$

When the R is less than R_{\min} , the RE should move forward to find out the required condition to set correction alignment.

In Type2, the point RB and RE are positioned at the beginning of curve BC and correction end EC respectively. The position vector at the center of the arc on RB side r_{o1}^L and at the center of the arc on RE side r_{o2}^L are obtained as follows

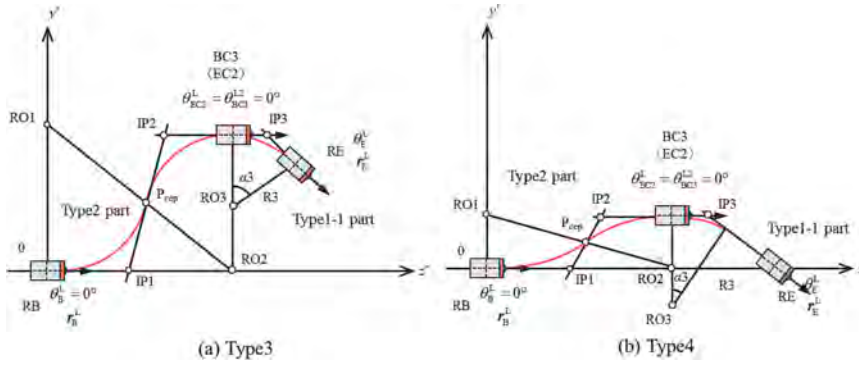


Figure 4. Type3 and Type4 correction alignment.

$$\begin{aligned} r_{o1}^L &= r_B^L - aRk_{By}^L \\ r_{o2}^L &= r_E^L - aRk_{By}^L \end{aligned} \quad (14)$$

The position vector at the inflection point P_{cep} in Type2-1, r_{cep}^L , is obtained as

$$r_{cep}^L = r_E^L/2 \quad (15)$$

On the other hand, in case of Type2-2, position vector at the inflection point on RB side P_{cep1} and RE side P_{cep2} , r_{cep1}^L and r_{cep2}^L , are obtained as

$$\begin{aligned} r_{cep1}^L &= [0, -aR, R]^T \\ r_{cep2}^L &= [0, y'_E + aR, R]^T \end{aligned} \quad (16)$$

The Type 2 correction alignment has two intersection points on RB side IP1 and on RE side IP2 as shown in Figure 3. The position vectors of IP1 and IP2, r_{IP1}^L and r_{IP2}^L , are obtained by

$$\begin{aligned} r_{IP1}^L &= r_B^L + aR \tan\left(\frac{\alpha}{2}\right) k_B^L \\ r_{IP2}^L &= r_E^L - aR \tan\left(\frac{\alpha}{2}\right) k_B^L \end{aligned} \quad (17)$$

2.2.4 Type3 and Type 4

The correction alignment of Type3 and Type 4 comprise three arcs that is the correction alignment of Type2 is positioned on the RB side and that of Type1-1 is located on RE side as illustrated in Figure 4. On the other hand, the correction alignment of Type1-2 is also similar alignment of Type3 but the correction alignments of Type1-1 and Type 2 appear reversely.

3 APPLICATION

3.1 Site description

The target site in this study is Takao River discharging tunnel. The target section includes the curve radius $R = 16m$ and constant downward slope 0.333%. Figure 5 shows the planned and the correction alignment on horizontal plane and vertical plane.

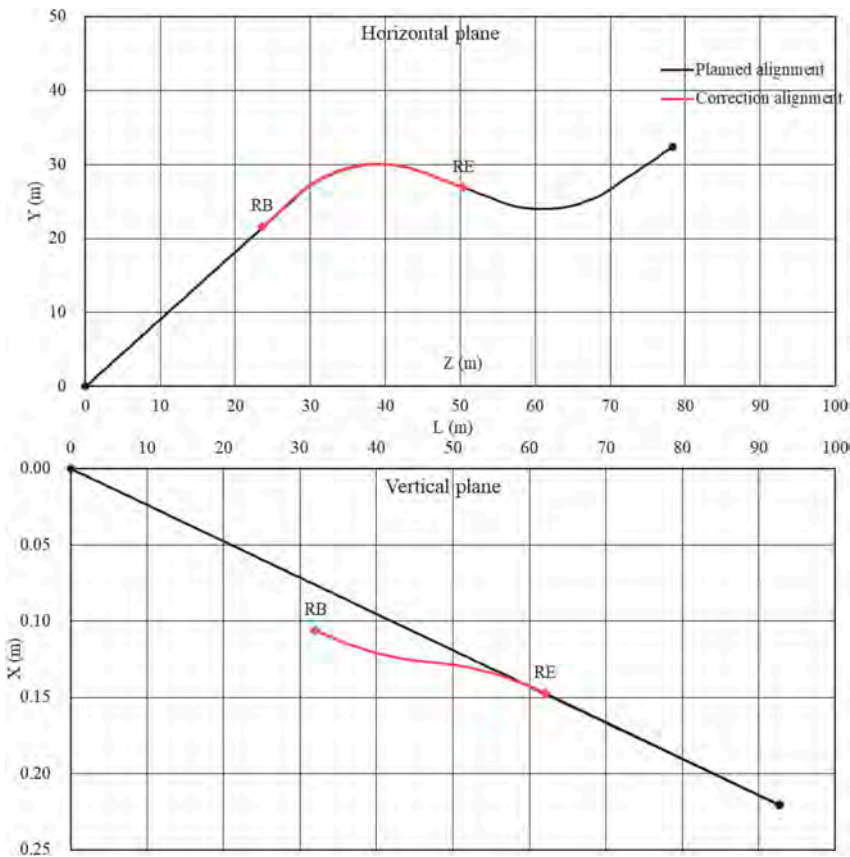


Figure 5. Planned and correction alignment.

3.2 Setting deviation

It is assumed that the horizontal deviation is 100 mm to the outside of the curve, the yawing angle deviation is 0.5° to the outside of the curve on the horizontal alignment, the vertical deviation is 30 mm to the downward, and the pitching angle deviation is 0° on the vertical alignment at the beginning correction point. In addition, it was assumed that the distance L increased by 50mm due to the meandering of the shield machine.

3.3 Correction alignment

To obtain the correction alignment in Figure 5, for the horizontal correction, Type1-1 is employed, whereas for the vertical correction Type2-1 is in use.

Table 2. Comparison of planned and correction alignment.

		Distance	Coordinate			Yawing angle	Pitching angle	
		L(m)	x(m)	y(m)	z(m)	θ_x (deg)	θ_y (deg)	
Begin point	Planned_alignment	RB	7.000	0.016	5.970	3.655	-58.53	0.14
	Correction_alignment	RB'	7.050	0.046	6.022	3.570	-59.03	0.14
End point	Planned_alignment	RE	37.000	0.088	18.902	28.228	3.41	0.14
	Correction_alignment	RE'	37.120	0.088	18.902	28.228	3.40	0.14

Table 2 represents both the position vector and direction angle for the planned and correction alignment. From the Table 2, the followings were found: 1) At the RE, the position vector of the planned and correction alignment are identical; and 2) The TBM's orientation at the RE is closely aligned with the yawing and pitching angles of the planned alignment, that is the TBM can adjust to the planned alignment.

4 CONCLUSION

This research developed the algorithm on setting correction alignment for TBM meandering. The key contributions are as follows:

- 1) three dimensional correction alignment separates to both horizontal and vertical alignments, then the correction alignment can be obtained by independent 2D calculation;
- 2) the meandering types were classified systematically, based on position and direction changes; and
- 3) the methods to set the correction alignment for each meandering Type were proposed.

To validate the efficacy of our approach, a case study assuming the deviation on the horizontal and vertical planes was carried out. The obtained correction alignment by applying the developed method shows the reasonable results along the transition part between RB and RE and at RE not only for the position but also for the direction of the alignment.

As a future research, to validate the developed method, it is necessary to carry out more case studies.

REFERENCES

- Guo, D., Li, J., Jiang, S.-H., Li, X. & Chen, Z. (2022) Intelligent assistant driving method for tunnel boring machine based on big data. *Acta Geotechnica*, 17, 1019–1030.
- Li, X., Di, H., Zhou, S., Huo, P. & Huang, Q. (2021) Effective method for adjusting the uplifting of shield machine tunneling in upper-soft lower-hard strata. *Tunnelling and Underground Space Technology*, 115, 104040.
- Liu, W., Zhao, T., Zhou, W. & Tang, J. (2018) Safety risk factors of metro tunnel construction in China: An integrated study with EFA and SEM. *Safety Science*, 105, 98–113.
- Saracin, A., Cosarca, C., Savu, A. & Negrila, A. (2014) TBM (Tunnel Boring Machine) guidance systems for tunnel construction. *RevCAD Journal of Geodesy and Cadastre*, 106–113.
- Sramoon, A., Sugimoto, M. & Kayukawa, K. (2002) Theoretical Model of Shield Behavior During Excavation. II: Application. *Journal of Geotechnical and Geoenvironmental Engineering - J GEOTECH GEOENVIRON ENG*, 128.
- Sugimoto, M. & Sramoon, A. (2002) Theoretical Model of Shield Behavior During Excavation. I: Theory. *Journal of Geotechnical and Geoenvironmental Engineering - J GEOTECH GEOENVIRON ENG*, 128.
- Tang, L., Kong, X., Ling, X., Zhao, Y., Tang, W. & Zhang, Y. (2022) Deviation correction strategy for the earth pressure balance shield based on shield-soil interactions. *Frontiers of Mechanical Engineering*, 17, 20.
- Wang, P., kong, X., Guo, Z. & Hu, L. (2019) Prediction of Axis Attitude Deviation and Deviation Correction Method Based on Data Driven During Shield Tunneling. *IEEE Access*, 7, 163487–163501.
- Wang, R. & Zhang, L. (2023) A Theoretical Method and Model for TBM Tunnelling Trajectory Adjustment. *Applied Sciences*.
- Xie, H., Duan, X., Yang, H. & Liu, Z. (2012) Automatic trajectory tracking control of shield tunneling machine under complex stratum working condition. *Tunnelling and Underground Space Technology*, 32, 87–97.
- Zhou, S., Xiao, J., Di, H. & Zhu, Y. (2018) Differential settlement remediation for new shield metro tunnel in soft soils using corrective grouting method: case study. *Canadian Geotechnical Journal*, 55, 1877–1887.

Ground improvement for the shield tunneling in the composite stratum

S.H. Cheng

National Taiwan University of Science and Technology, Taipei, Taiwan

R.K.N. Wong, H.Y. Hsu & I.T.Y. Wong

SANSHIN CORPORATION, Taipei, Taiwan

C.J. Chen

Department of Rapid Transit Systems, Taipei, Taiwan

ABSTRACT: The composite stratum encountered in Tunnel Boring Machine (TBM) tunneling presents great challenges and may be caused by potential hazards because of ground heave or ground settlements. In this study, the jet grouting (Rapidjet Method) and Tube-a-Manchette (TAM) with chemical grouting are employed to address composite stratum with varying properties, ensuring the necessary strength and waterproofing for TBM tunneling. Jet grouting enhances the grouting zone above the soil-rock interface, preventing the shield machine from shifting upward or causing ground collapse during excavation. TAM grouting around the jet-grouted bodies serves both for structural support and reducing soil permeability. The TBM launch and arrival in the study case proceeded smoothly, with a settlement of approximately 10 mm recorded 160 days after the shield passed through the improved composite strata by jet grouting. Therefore, meticulous planning of grouting methods can significantly reduce construction time and costs.

1 INTRODUCTION

Various ground improvement techniques have been widely used outside the tunnel-shaft interface for tunnel boring machine (TBM) launching and arrival works. In this study, ground improvement works for the Taipei Mass Rapid Transit (MRT) Xinyi-East extension line are reported. As shown in Figure 1, the TBM tunneling departure at the R03 station arrives at the R03 ventilation shaft and passes through the composite stratum on the east side between the R03 station and the R03 ventilation shaft. The soft soils outside of the tunnel-shaft interface require jet grouting to increase strength and decrease permeability. When tunneling passes through the composite ground, it needs jet grouting in the soft soils to increase strength and homogenize the TBM tunneling face. However, the hard rock cannot be improved by jet grouting, so chemical grouting was combined in the ground improvement work to decrease permeability. In this study, the Rapidjet Method for jet grouting and Tube-a-Manchette (TAM) with chemical grouting are used to address the composite strata with various properties, meeting the strength and waterproofing requirements for TBM tunneling. The ground treatment shows that the total core recovery, compression strength (q), and permeability coefficient (k) in the jet grouting zone meet the design requirements. In addition, in-situ permeability tests were carried out in the TAM grouting zone and also met the specifications. A settlement of 10 mm was recorded 160 days after the passing of the shield at the composite strata. The performance and results of jet grouting and TAM grouting are presented in the following.

2 SITE CONDITIONS OF STUDY CASE

The location and route layout for the study case are shown in Figure 1. The Xinyi-East extension line consists of the R05 tail shaft, R03 station, and R03 tail shaft. Cut-and-cover and TBM tunneling were employed to construct the shield tunnel. The shield tunnel in this study adopts a circular section with an inner diameter of 5.6 m and an outer diameter of 6.1 m. The shield machine operates on the earth pressure balance critical, where the total length of the shield machine is 8.5 m with an outer diameter of 6.24 m, as shown in Figure 2 (Chen et al., 2020). The lengths of the shield tunnels from the east side of the R03 station to the R03 tail rail ventilation shaft are about 524 m, and the overburden depth is approximately 20.8 m to 22.0 m. The shield tunnel primarily traverses through composite strata, consisting of alluvial deposits, colluvial deposits, and rock formations.



Figure 1. Location and route layout of the Taipei MRT-Xinyi East extension line.

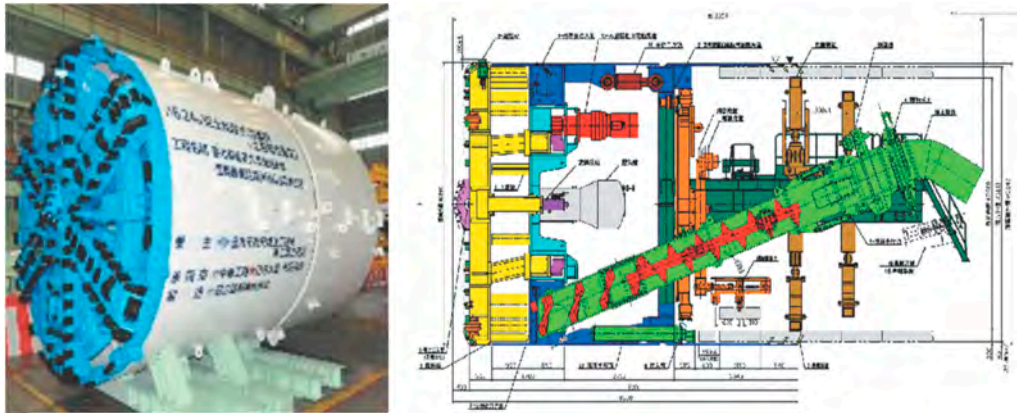


Figure 2. The TBM shield machine used for this study case (Chen et al., 2020).

The soil condition near the ground surface mainly consists of fill material (SF), alluvial deposits (CL/CH/ML/SM) with a thickness of 10-20 m and a very soft to weak consistency, and underneath is soft to medium-hard, moderately weathered to fresh sandstone (SS), and shale (SH). The soil-rock interface is occasionally mixed with colluvial deposits, the main components of which are gravel and rock blocks. The physical properties of the soil near the east side/west side of the R03 station and R03 tail shaft are shown in Table 1. Additionally, the soil and rock properties along the R03 station to the R03 tail rail ventilation shaft are depicted in Figure 3. It indicates that the q_u value of the rock formation is greater than 1000 kgf/cm², and the RQD of the rock formation ranges between 0 and 100. The groundwater level is approximately 0 to 1.8 m below the ground surface.

3 GROUTING FOR THE INTERFACE OF COMPOSITE STRATUM

In this study case, the jet grouting (Rapidjet Method) and TAM grouting are utilized to overcome the strata with a soil and rock interface to meet the design strength and reduce the permeability of the ground. The layout of the improved zone for the launching and arrival shield of the study case is depicted in Figure 4 and detailed in Table 2. When the TBM drills through the interface of the soil and rock formation, the stratum located on the cutting face of the TBM is soft at the top and hard at the bottom. This makes the TBM susceptible to offset during drilling and digging, increasing the possibility of over-excavation. The strength of the composite strata varies greatly in some areas of the study area. To minimize the impact of drilling on the surrounding area, ground improvement is carried out for these specific areas. The grouting method of the soil-rock interface is situated on the east side of the R03 station, as illustrated in Figure 4. The grouting zone above the soil-rock interface is enhanced by jet grouting to ensure that the shield machine does not shift upward or cause the ground to collapse due to improper digging. TAM grouting around the jet-grouted bodies is employed for building protection and decreases soil permeability. Figure 5 shows the position of the soil-rock interface, the grouting range, and the grouting method used.

Table 1. The soil properties at the west side, east side, and tail rail ventilation shaft of R03 station.

West side of R03 station					
Soil Layer	Depth (m)	Soil Type	SPT-N (avg.)	Unit Weight (kN/m ³)	Water Content (%)
1	1.6	SF	-	-	-
2	16.5	CH-CL	2.2	15.89~17.85	41~52
3	21.4	CL	4.5	18.05~18.34	31~37
4	22.8	SM	53	17.95~18.25	29~32
5	35.0	SS/SH	100	-	-
East side of R03 station					
Soil layer	Depth (m)	Soil type	SPT-N (avg.)	Unit weight (kN/m ³)	Water content (%)
1	1.6	SF	-	-	-
2	8.3	CH	2.5	16.30	61
3	15.0	ML-SM	8.8	18.24~19.72	24~34
4	23.3	CL	6.7	16.38~17.10	42~49
5	33.5	SS	100	-	-
R03 tail shaft					
Soil layer	Depth (m)	Soil type	SPT-N (avg.)	Unit weight (kN/m ³)	Water content (%)
1	1.6	SF	-	-	-
2	11.8	CH~CL	5.1	16.48~18.25	28~43
3	20.0	SM-CL-ML	65	19.32~21.29	16~23
4	35.0	SS/SH	100	-	-

Table 2. Grouting method and improved zone for launching and arrival shield of the study case.

Location	Center of tunnel EL (m)	Grouting method	Improved range (m)										
			L ₁	L ₂	H ₁	H ₂	H ₃	W ₁	W ₂	W ₃	W ₄		
East Tunnel	Launching	85.6	R-Jet/TAM Grout	TAM Grout	7.8	2.2	4	2	6.5	2	2	2.7	0.5*
	Arrival	84.6	R-Jet/TAM Grout	TAM Grout	8.8	2.2	2.5	2	5.5	2	2	2.7	2.7
West Tunnel	Launching	85.6	R-Jet/TAM Grout	TAM Grout	8.8	2.2	2.5	2	4.4	2	2	2	2
	Arrival	89.9	JSG **		-	10.5	2.5	2	10.8	-	-	2	2

Noted: *Close to D-Wall of Entrance C; **Not included in this report

3.1 Jet grouting method (R-Jet method)

In this study, jet grouting was performed using a double-fluid jet grouting system, commercially known as the R-Jet method. The construction procedures and applicable operating parameter range used were identical to those recommended by Burke (2004) and Lunardi (1997). However, two nozzles were mounted on the opposite side of the monitor with a 25 mm difference in elevation. This setup increases the cutting and mixing efficiency of the jetting fluid. The grout jet was shrouded with compressed air ($p_a = 0.9$ MPa) to enhance its cutting ability and cutting distance while also enhancing the mixing of cement grout with the in-situ soil. Two nozzles were mounted on the opposite side of the monitor with a 25 mm difference in elevation. The grouting parameters used for this study case are listed in Table 3. The jetting pressure (p_g) and flow rate (q_g) of the jet grouting test were 35 MPa and 360 liters/min, respectively; the nozzle diameters (d_o) were 4.24 mm. The revolution rate (R_s) was 0.52 rad/sec, and the lift-up rate (v_s) of the nozzle was 1.19×10^{-3} m/sec. The lift-up step (ΔS_s) was set to 2.5 cm/step (Cheng et al., 2017, 2020, 2023).

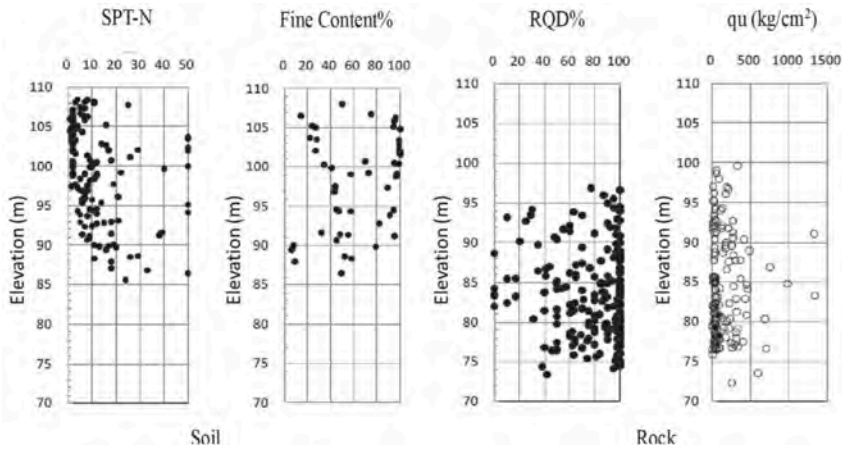


Figure 3. Soil and rock properties along R03 station to R03 tail shaft (Chen et al., 2020).

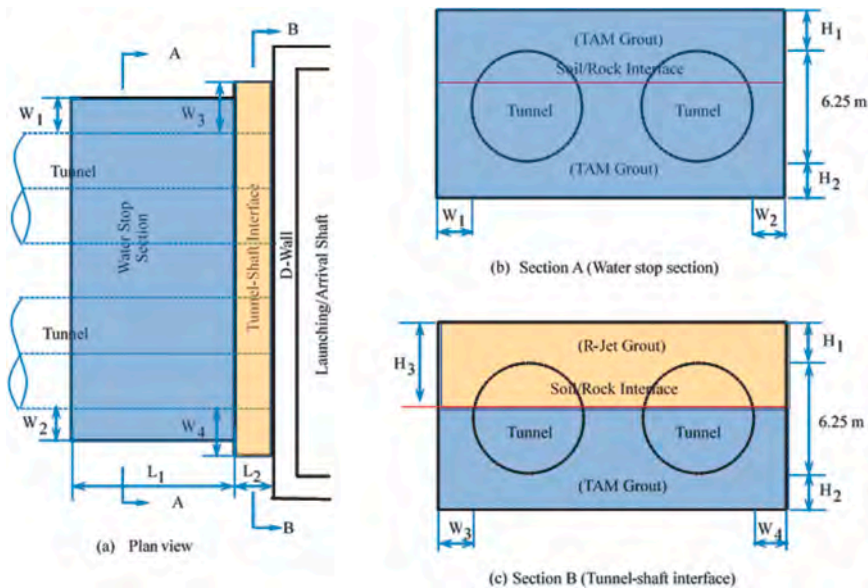


Figure 4. Grouting plan and profile for launching and arrival shield of the study case (Chen et al., 2020).

Table 3. Jet grouting parameters used in the Rapidjet grouting.

Parameter	Value
Water cement ratio, W/C	1.4
Jetting pressure of air, p_a (MPa)	0.9
Jetting pressure of grout, p_g (MPa)	$35 \pm 10\%$
Flow rate of grout, q_g (liters/min)	180 per nozzle
Nozzle diameter, d_o (mm)	4.24
Number of nozzles on the monitor	2
Rotation speed of the rod, R_r (rad/s)	0.52
Lift up or withdrawal rate of rod, v_s (m/s)	1.19×10^{-3}
Lift up step, ΔS_i (cm/step)	2.5

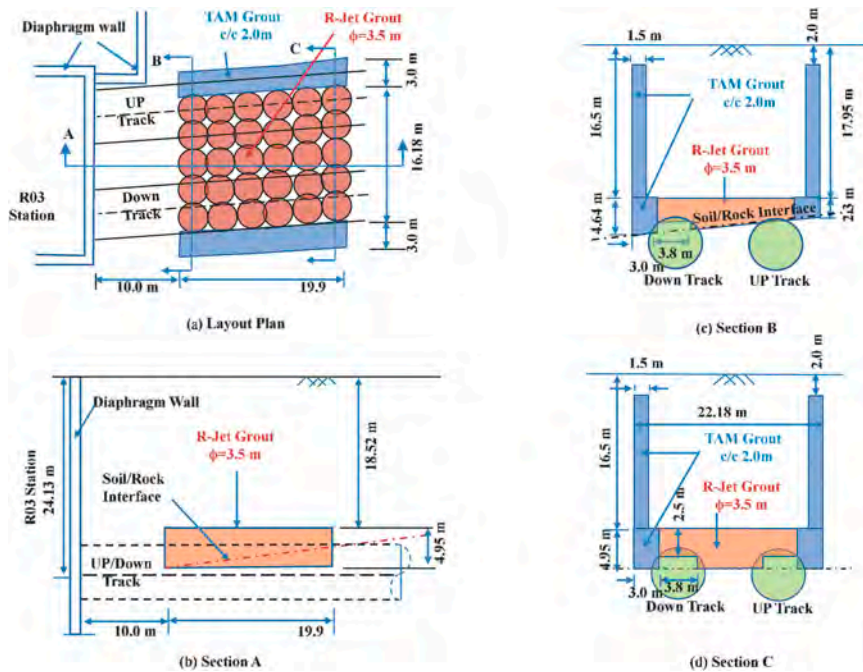


Figure 5. The soil-rock interface, grouting zone, and adopted grouting method the at east side of R03 station.

3.2 Chemical grouting method (TAM grouting method)

The TAM grouting method was adopted for waterproofing in this study case. The grout volume control method was chosen as the quality assurance measure for this grouting work. Grouting pressure at each injection port was recorded while a given amount of grout was injected from the port. For each grout hole, grouting started from the soil-rock interface and then proceeded upward step-by-step (0.33 m per step). Once the injection volume and injection ratio of a port reached the refusal criteria, grouting was terminated at that port. The applied grouting pressure to meet the refusal criteria was recorded. Two stages of grouting were used in the grouting work: the first-stage CB grouting aimed to fill and compact the voids in the ground. Grouting did not stop until the design grouting quantity was reached. Such grout intrusions compress the sandy soil and homogenize the improved zone. In comparison, the injection of MK grout into the soil-rock interface was for low-permeability purposes and increased its overall strength. TAM grout mix proportions and grout ratio for the study case are shown in Table 4 to Table 5.

4 QUALITY CONTROL AND MONITORED RECORDED

The main focus of this case is on the grouting above the soil-rock interface to ensure that the shield machine does not shift up or cause the ground to collapse due to improper digging. Meanwhile, grouting is also employed for building protection and to decrease soil permeability in order to mitigate construction risks. Relevant methods for ensuring construction quality are outlined as follows:

4.1 *Quality of jet grout zone*

According to the design specifications, 28 days after the completion of grouting, 2 grout piles were randomly chosen from all jet-grouted columns for quality checks. Cored samples were taken from the columns and inspected following the evaluation method for jet grout mixing columns proposed by the Japan Society of Civil Engineers (Takashi et al., 2003). The total core recovery (TCR) of sampling should be $\geq 90\%$, the 28-day uniaxial compressive strength (UCS) of each sample should be ≥ 2.0 MPa for sandy soil and ≥ 1.2 MPa for clayey(silty) soil, and the permeability coefficient k should be $\leq 1 \times 10^{-5}$ cm/sec. All test results meet the design requirements.

Table 4. Summary of mix proportions for CB grout and MK grout.

CB grout	Mix proportion	MK grout	Mix proportion
Cement binder	150~250 kg	Sodium silicate	250 L
bentonite	40 ~ 80 kg	MK reaction	35 ~ 65 L
Water	888~937 L	Water	685~715 L
Total	1000 L	Total	1000 L

Table 5. TAM grouting ratio.

Grouting zone	Soil type	Grout ratio %		
		1 st Grout	2 nd Grout	Total
Tunnel-shaft interface	SS/SH	5	10	15
Water-stop section	CL/ML	10	10	20
	SM	15	20	35
East side of R03 station (Soil-Rock Interface)	SS/SH	5	10	15
	CL/ML	10	15	25

Remark: If the filling is completed according to the grouting rate but the pressure is low, the MK material will be used to inject about 3 to 5% of the inspection and supplement grouting.

4.2 *Quality of TAM grout zone*

Although the value of grouting pressure observed at each step may not be individually meaningful, the relative change itself is important. It proves useful to record the primary and secondary grouting pressure at the injection hole in each step (33 cm) and compare them with each other to evaluate the grouting effects and detect insufficiently-improved areas (Hayashi and Matsubayashi, 1996). Therefore, the average TAM grout pressure recorded for the first grout, second grout, and supplemental grout on the clayey layer, sandy layer, and sandstone/shale ranges from 0.64 to 0.80, 1.18 to 1.30, and 0.70 to 1.33 MPa, respectively. According to the TRTS specification, every 100 grout holes should be tested with at least 3 holes, and the permeability coefficient k should be $\leq 1 \times 10^{-5}$ cm/sec.

4.3 *Horizontal leakage test*

Before breaking the mirror-face on the diaphragm wall for the TBM to enter or from the shaft, it is of critical importance to conduct leakage tests for the grout zone behind the wall.

Normally, horizontal boreholes are drilled at the mirror-face location, through the wall into the grouted zone to the desired length. Then the valve attached to the horizontal borehole is opened to measure the rate of groundwater inflow through the grouted zone into the working shaft. The supplement of the grout will, according to the test results, achieve the purpose of safely breaking the mirror. According to the TRTS specification, with five holes within the mirror frame and nine holes outside the mirror frame, the depth is at least 2 m into the grout zone. The depth of at least one hole must reach the front edge of the outermost row of the grout zone, or the position 1 m before the grout zone. After drilling, the leaking amount of each test hole is measured by the measuring cup with the meter after the water leakage is stable. The field permeable test uses a spherical flow method to determine the permeability coefficient. The design permeability coefficient k should be $\leq 1 \times 10^{-5}$ cm/sec.

The horizontal leakage tests of the up track and down track at the west side of the R03 station for launching are shown in Figure 6. The depth of the center hole was 8.6 m into the grout zone, and the depth of the other holes was 2 m. There were 5 holes inside the mirror frame that were equally distributed in the center diameter of 4.4 m, and the 9 holes outside the mirror frame distributed the hole positions evenly within the center diameter of 7.2 m. A total of 28 horizontal leakage tests were carried out in the up and down track grout zone, with test results of permeability k ranging from 0.0 to 9.2×10^{-7} cm/sec, and the maximum quantity of water was 20 c.c./min at the center hole. All tests meet the design requirements without supplementary grouting.

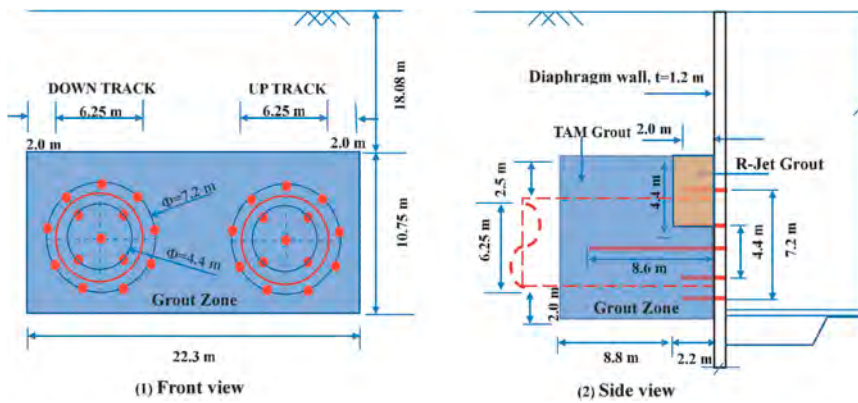


Figure 6. Horizontal leakage tests at the west side of the R03 station for launching.

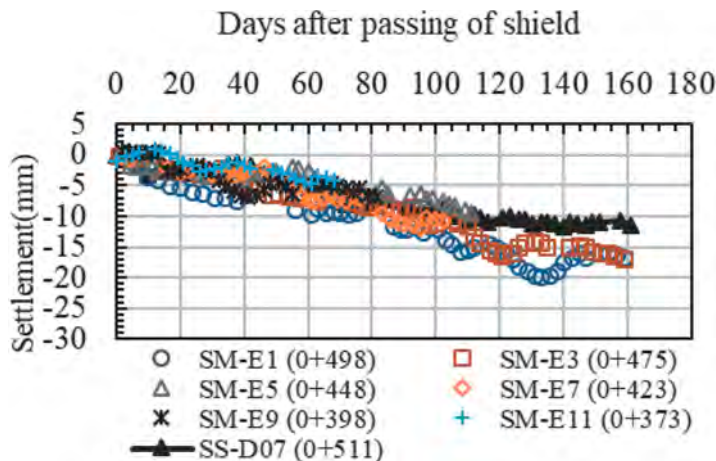


Figure 7. Monitoring results at soil-rock interface.

4.4 Settlement monitored recorded when TBM pass through the soil-rock interface

Figure 7 shows the monitoring results of ground settlement in the east tunnel at the soil-rock interface composite zone caused by TBM tunneling. The settlement point SS-D07 is located in the composite zone that has been improved by jet grouting. From the monitoring results, a settlement of 10 mm was recorded after the passing of the shield at SS-D07, which is lower than at other locations. This indicates that the use of the jet grouting method to enhance the strength of the alluvial layer in the composite layer at the soil-rock interface can indeed prevent shield machine deviation, collapse, and reduce surface subsidence.

5 CONCLUSIONS REMARKS

This study reports on the grouting works for the TBM tunneling passing through the soil-rock interface of the Taipei MRT. The upper treatment zone consists of a soft clayey layer, and the hard rock (sandstone or shale) is in the lower layer. Jet grouting and TAM grouting were utilized to overcome the strata with various ground conditions and reduce construction risks. The following conclusions were drawn from the findings of this study case:

- (1) All quality assurance tests conducted in the jet grout and TAM grout zones met the design requirements. The 28-day compression strength of jet-grouted areas was ≥ 2.0 MPa for sandy-soil and ≥ 1.2 MPa for clayey (silty) soil, with a permeability coefficient k of $\leq 1 \times 10^{-5}$ cm/sec. Additionally, the permeability coefficient of the TAM grouted zone is smaller than 1×10^{-5} cm/sec.
- (2) The TBM launch and arrival for the study case proceeded smoothly. Therefore, careful planning of grouting works can significantly shorten construction time and reduce construction costs.
- (3) Construction of the diaphragm wall for TBM launching and arrival works may have an adverse effect on grouting works (such as the verticality of the grout holes, the impermeability of grouting, etc.). A row of low-pressure inspection grout (TAM grout) can be added at the interface between the diaphragm wall and the ground, improving the effectiveness of the grouting works.
- (4) A settlement of 10 mm was recorded from the subsidence gauge 160 days after the TBM passed through the soil-rock interface. This value was lower than in other tunneling routes. It indicates that the use of jet grouting to enhance the strength of the alluvial soil at the soil-rock interface can indeed prevent shield machine deviation, collapse, and reduce surface subsidence.

REFERENCES

- Burke, G.K. (2004). "Jet grouting systems: Advantages and disadvantages." In Proceedings of Drilled shafts, Micropiling, Deep mixing, Remedial method, and Specialty foundation systems, Orlando, Florida, 29-31 January 2004. American Society of Civil Engineers, New York, pp. 218–234.
- Chen J. R., Zhang Z. L., Yang G. R., Guo J. W. (2020). "Design consideration and construction plan of shield tunneling through composite stratum in edge of Taipei basin." *Rapid Transit Systems and Technology*, N0.55. (In Chinese).
- Cheng, S.H., Liao, H.J., Yamazaki, J., and Wong, Ricky K.N. (2017). "Evaluation of Jet Grout Column Diameters by Acoustic Monitoring", *Canadian Geotechnical Journal*, Vol. 54, No. 12., pp. 1781–1789.
- Cheng, S.H., Liao, H.J., Yamazaki, J., Wong, Ricky K.N., and Iwakubo, T. (2020). "Alignment of Vertical and Inclined Jet Grout Columns for Waterproofing", *Geotechnical Testing Journal*, Vol. 43, No. 2., pp. 325–338. (doi:10.1520/GTJ20180324).
- Cheng, S.H., Chao, K.C., Wong, Ricky K.N., and Wang, Morris I.M. (2023). "Control of jet grouting process induced ground displacement in clayey soil", *Transportation Geotechnics*, Vol. 40, pp100983, May, 2023. <https://doi.org/10.1016/j.trgeo.2023.100983>.
- Hayashi K. and Matsubayashi Y. (1996). "Chemical grouting contributed to the urban development in Hiroshima city", *Proceedings of Grouting and Deep Mixing, Japan*, pp. 299–302.2.
- Lunardi, P. (1997). "Ground improvement by mean of jet grouting." *Proceedings of Institution of Civil Engineers—Ground Improvement*, 1 (2), 65–85. doi: 10.1680/gi.1997.010201.
- Takashi, M., Ikeda, A., Akira, Y., Yuukiti, T. and Nakagawa, K. (2003). "Evaluation method of soil improvement effect of high-pressure injection mixing method." *Japan Society of Civil Engineers*, No. 735 (VI-59): 215–220.

Settlement prediction of the Hong Kong-Zhuhai-Macau Bridge tunnel under the effect of typhoon

S.Y. He

State Key Laboratory of Internet of Things for Smart City and Department of Civil and Environmental Engineering, University of Macau, Macau, China

Y. Yan

Hong Kong-Zhuhai-Macao Bridge Authority, Zhuhai, China

W.H. Zhou

State Key Laboratory of Internet of Things for Smart City and Department of Civil and Environmental Engineering, University of Macau, Macau, China

ABSTRACT: Settlement monitoring and prediction are among the most concerning problems for an immersed tunnel. However, settlement monitoring usually relies on manual surveys with low frequency, while the settlement prediction for the entire tunnel is usually based on the assumption of an elastic foundation. Therefore, determining the impact of short-term events on the settlement of an immersed tunnel is difficult. This paper combines a physics-informed machine learning algorithm with the Kelvin-Voigt model, introducing a retardation time factor to express the delayed response to an applied force. This framework is further used in the Hong Kong-Zhuhai-Macau Bridge tunnel, and the effect of an extreme water level caused by a typhoon on this tunnel is analyzed.

1 INTRODUCTION

Immersed tunnels are usually used for road crossings of rivers, estuaries, and sea channels. This kind of tunnel has been widely used in different countries since the mid-twentieth century, especially in the Netherlands, the USA, Japan, China, etc. (Lunniss and Baber, 2013). One of the challenges for such a tunnel is the need for careful waterproofing since it is in direct contact with water. However, many real cases show large settlement variations during their service period, leading to concrete cracks or water leakage. These issues could damage the metal walls, electrical systems, and shorten the service life of the tunnel (Grantz, 2001). Therefore, settlement monitoring and prediction are important during the service period of an immersed tunnel.

The statistics on immersed tunnels by Lunniss and Baber (2013) showed that the length of immersed tunnels is usually larger than 500 m, and there is a trend for longer tunnels with the development of technology. Considering the difficulties in the analysis of such a large and complex structure, much research tends to analyze it with a simplified model, and one of the most popular models is the beam on elastic foundation model (Liu et al., 2020; Tang et al., 2022; He et al., 2024a). Previous research has proved that this kind of model can be used in different analysis systems and provide accurate settlement predictions of immersed tunnels under the effect of long-term events, such as back silting accumulation, sunken ship, etc. However, an important problem for such a model is a significant overestimation of settlement that will be predicted under the effect of short-term events, since an elastic model will react

immediately when a load is applied, and those short-term events, such as extreme water level, only exist from a few hours to a few days. For an immersed tunnel in a coastal area, the impact of extreme water level caused by typhoon cannot be ignored. However, current settlement monitoring usually relies on manual work using a level gauge, and it is impossible to do the measurement during the passage of a typhoon.

The objective of this study is to combine the physics-informed machine learning (PIML) framework with a viscoelastic model for predicting the settlement of an immersed tunnel under the effect of a typhoon. The framework is verified through a case study of the Hong Kong-Zhuhai-Macau Bridge (HZMB) tunnel. The next section introduces the PIML algorithm and Kelvin-Voigt model used in this paper. The third section describes the application of the proposed framework in the HZMB tunnel. Finally, the conclusion is presented.

2 METHODOLOGY

2.1 Multi-beam model

An immersed tunnel is composed of several tubes connected by joints, therefore, it can be simplified as a series of beams lying on an elastic foundation, which is named the multi-beam model, as shown in Figure 1. In this model, each beam is used to represent a tube, and they are supported by N Winkler foundations with different moduli ($k_i, i=0, 1, \dots, N$). The tunnel joint is represented by a shear spring with shear stiffness k_s .

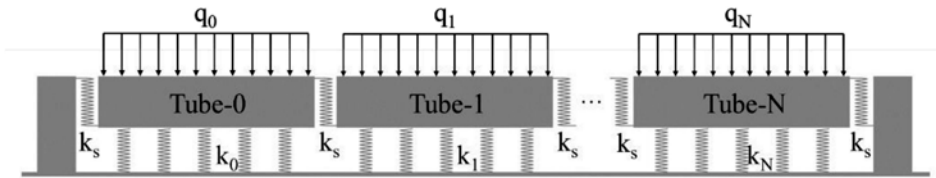


Figure 1. Multi-beam model for the HZMB tunnel.

The governing equation of tube i of the multi-beam model is:

$$EI \frac{d^4 y}{dx^4} + k_i b y = q_i b \quad (1)$$

where E is the Young's modulus of the tube, I is the moment of inertia, k_i is the foundation modulus under tube i , q_i is the distributed load on tube i , b is the width of the tube and y is the settlement.

The distributed load on different tubes is calculated based on data from design documents, relevant research, and monitoring data. This includes the self-weight of the structure, back-fill, back silting, etc. Further details can be found in He et al. (2024a).

2.2 Physics-informed machine learning algorithm

Machine learning is a widely used strategy in solving scientific problem (Cheng et al., 2022; Kannangara et al., 2022; Yan et al., 2023). However, such method usually required large amount of data, and the physical meaning of the results is usually difficult to explain. In this case, physics-informed machine learning algorithm becomes popular in different areas (Cheng et al., 2023; Tang et al., 2023; Tang et al., 2024). In He et al. (2024a, 2024b), we proposed a PIML algorithm to predict the settlement of an immersed tunnel. This algorithm can incorporate a physical model with machine learning, providing efficient inverse analysis of unknown parameters in the physical model with very limited monitoring data. The framework of the algorithm is shown in Figure 2, the neural network composed of one hidden layer with 20 neurons, and the input is the coordinates of each beam.

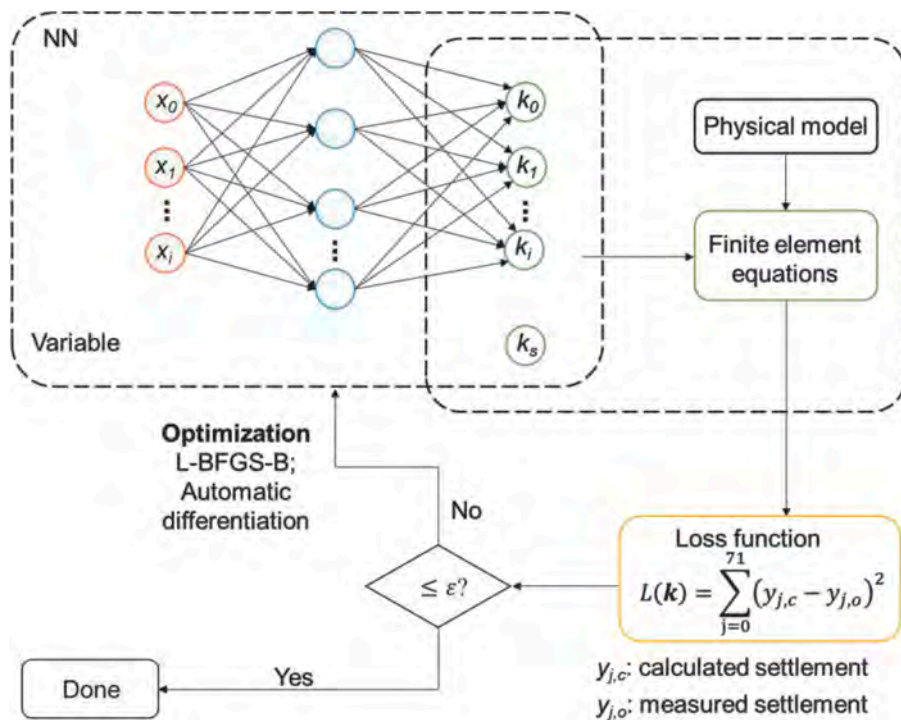


Figure 2. Framework of the PIML algorithm.

2.3 Kelvin-Voigt model

As introduced, the multi-beam model cannot be used for the settlement prediction under the effect of short-term events. In this case, the deformation formula of Kelvin-Voigt model is introduced, where a retardation time is used to express the delayed response to an applied force (Dey and Basudhar, 2010).

Kelvin-Voigt model:

$$y(t) = \frac{q_i}{k_i} \left(1 - e^{-t/\tau_R} \right) \quad (2)$$

where t is the time, τ_R is the retardation time.

3 APPLICATIONS IN THE HZMB TUNNEL

The HZMB tunnel is part of the HZMB link in China, with a total length of 6087.3 m, composed of 33 tubes (E1-E33) and 2 buried sections (E0, E34). The geological profile of the tunnel is shown in Figure 3. This tunnel will be simplified with a multi-beam model composed of 35 tube elements and 36 joint elements. Therefore, there are a total of 36 unknown parameters in the system, consisting of 35 unknown foundation moduli (k_i) and 1 unknown joint shear stiffness (k_s). These unknown parameters will be inversely analyzed with the proposed PIML algorithm, and the settlement of the tunnel under different conditions can be accurately predicted. The details for the usage of PIML algorithm in the settlement prediction can be found in He et al. (2024a).

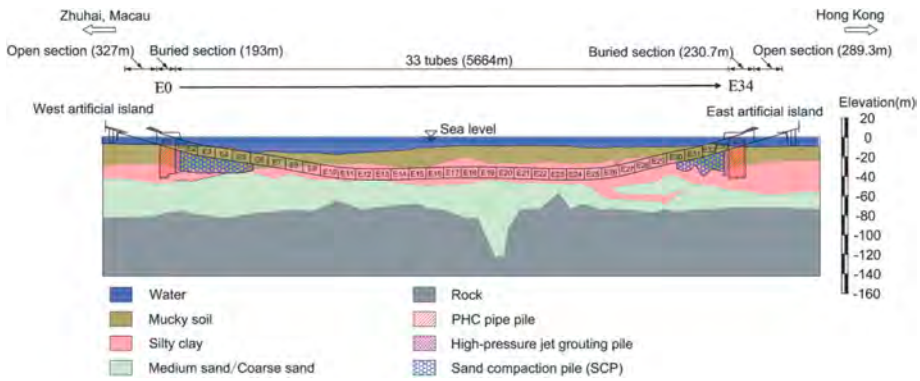


Figure 3. Geological profile of the HZMB tunnel.

As emphasized by Su et al. (2022), the mean sea level in the area of HZMB is 0.54 m, and the extreme water level in a 300-year return period is 3.82 m. In this case, the difference between the extreme water level and the mean sea level will be defined as the extra load on the immersed tunnel. Note that this water pressure load is caused by the short-term changes in sea level and the low permeability of the back silting on the tunnel, which prevents the water pressure from dissipating immediately (Zhou et al., 2021). Figure 4 partially shows the predicted settlement of the HZMB tunnel on 2026/12/8 with only the elastic foundation assumption. For cases in normal conditions and extreme water levels, the difference in settlement can be over 40 mm. However, the effect of the extreme water level is much different from the long-term events, as introduced earlier. According to public data from the Hong Kong Observatory, the high-water level caused by Typhoon Hato in 2017 lasted less than two days. Other research on tidal load also proved that the displacement caused by tidal level variation at a joint is only 3.9 mm for the Yongjiang tunnel (Wei et al., 2018). In this case, the predicted settlement can be concluded to be extremely overestimated.

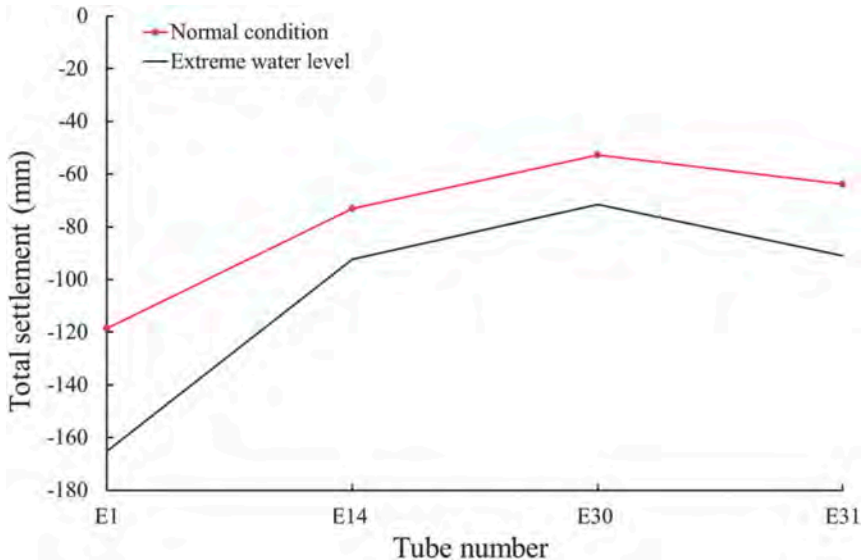


Figure 4. Settlement prediction of the HZMB tunnel at 2026/12/8 with the elastic foundation assumption.

To solve the problem of overestimation, this paper introduces the Kelvin-Voigt model for the consideration of retardation time (τ_R), as shown in Eq. 3. To calculate the value of τ_R , the monitoring settlement data after the installation of each tube is collected, with Figure 5 illustrating an example for E5. Additionally, the load on each tube after installation is calculated, and the foundation is inversely analyzed, as introduced in He et al. (2024a). For instance, the load on E5 is calculated as 45.3 kN/m^2 , and the foundation modulus is analyzed as 567.82 kPa/m . Then, we attempt to use the Kelvin-Voigt model to fit the monitoring data, the τ_R is analyzed as 180.45 for E5, and the curve fitting results are shown in Figure 5.

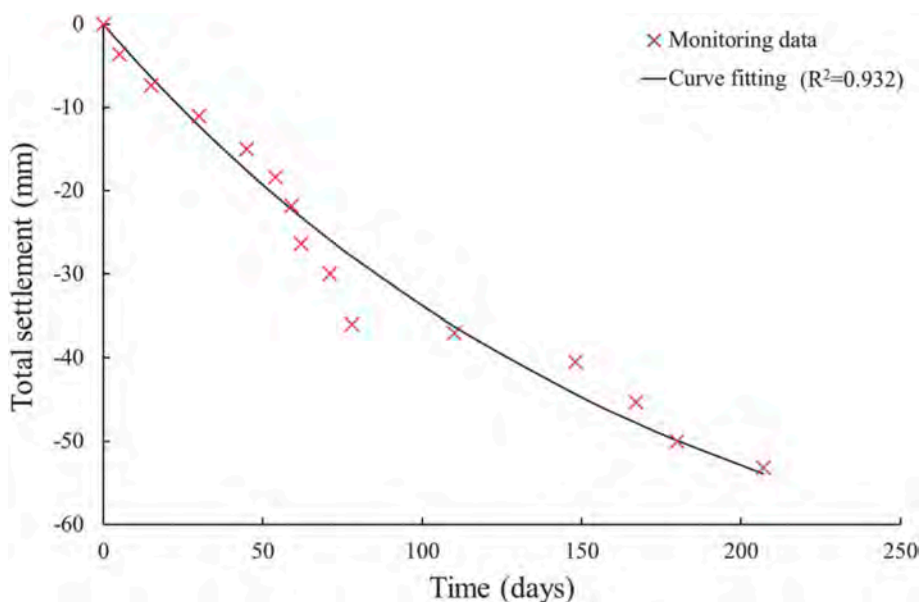


Figure 5. Fitting of settlement data of E5 with the Kelvin-Voigt model.

In He et al. (2024c), we have considered the time-dependent effect on the foundation modulus, and the foundation modulus of E5 is defined as 527 kPa/m at the end of 2026. Moreover, the extra load caused by the extreme water level is 32.144 kN/m^2 , and the duration of the extreme water level caused by the typhoon is defined as two days, according to the data from the Hong Kong Observatory. Therefore, it is predicted that the settlement caused by the extreme water level at E5 is 0.58 mm . The prediction results show that the short-term effect will not cause significant settlement of the HZMB tunnel. And the small settlement caused by the extreme water level is assumed to be a benefit from its deep-buried design.

4 CONCLUSIONS

This paper has combined the physics-informed machine learning algorithm with the Kelvin-Voigt model to predict the settlement of the HZMB tunnel under the effect of a typhoon. The analysis shows that the extreme water level won't induce significant settlement variation for this tunnel, with only 0.58 mm for tube E5 benefiting from deep-buried design. The results prove that the settlement caused by short-term events is not applicable to the research about safety problems caused by large settlements; it can be further used for the research of fatigue damage caused by events such as daily tide level variation.

ACKNOWLEDGEMENTS

The authors greatly acknowledge the financial support from the Ministry of Science and Technology of the People's Republic of China (Grant No. 2019YFB1600700), Guangdong Provincial Department of Science and Technology (Grant No. 2019B111106001), Science and Technology Development Fund, Macau SAR (001/2024/SKL). The field monitoring data was partially supported by the National Observation and Research Station for Material Corrosion and Engineering Safety of Hong Kong-Zhuhai-Macao Bridge.

REFERENCES

- Cheng, Y., Zhou, W.H., Xu, T. 2022. Tunneling-induced settlement prediction using the hybrid feature selection method for feature optimization. *Transportation Geotechnics*, 36: 100808.
- Cheng, Z.L., Kannangara, K.K.P.M., Su, L.J., Zhou, W.H. 2023. Physics-guided genetic programming for predicting field-monitored suction variation with effects of vegetation and atmosphere. *Engineering Geology*, 315: 107031.
- Dey, A., Basudhar, P.K. 2010. Applicability of Burger model in predicting the response of viscoelastic soil beds. *GeoFlorida 2010: Advances in Analysis, Modeling & Design*. 2611–2620.
- Grantz, W.C. 2001. Immersed tunnel settlements Part 1: Nature of settlements. *Tunnelling and Underground Space Technology*, 16(3): 195–201.
- He, S.Y., Zhou, W.H., Tang, C. 2024a. Physics-informed neural networks for settlement analysis of the immersed tunnel of Hong Kong-Zhuhai-Macau bridge. *International Journal of Geomechanics*, 24(1): 04023241.
- He, S.Y., Kuok S.C., Tang, C., Zhou, W.H. 2024b. Efficient Bayesian model updating for settlement prediction of the immersed tunnel of HZMB. *Transportation Geotechnics*, 44: 101179.
- He, S.Y., Tang, C., Zhou, W.H. 2024c. Settlement prediction of immersed tunnel considering time-dependent foundation modulus. *Tunnelling and Underground Space Technology*, 144: 105562.
- Kannangara, K.K.P.M., Zhou, W.H., Ding, Z., Hong, Z.H. 2022. Investigation of feature contribution to shield tunneling-induced settlement using Shapley additive explanations method. *Journal of Rock Mechanics and Geotechnical Engineering*, 14(4): 1052–1063.
- Liu, P., Chen, J., Chen, Y.H., Yang, J.X., Tang, Q. 2020. Mechanical Model for Joints of Immersed Tunnel Considering the Influence of Joint Differential Settlement. *International Journal of Geosynthetics and Ground Engineering*, 6: 1–10.
- Lunniss, R., Baber, J. 2013. *Immersed tunnels*. CRC Press, Boca Raton.
- Su, Q.K., Zhu, Y.L., Chen, Y., Fang, L., Yan, Y., Su, Z.X., Hans, D.W., Li, Y. 2022. Hong Kong Zhuhai Macao Bridge-Tunnel project immersed tunnel and artificial islands – From an Owners' perspective. *Tunnelling and Underground Space Technology*, 121, 104308.
- Tang, C., He, S.Y., Zhou, W.H. 2022. Settlement-based framework for long-term serviceability assessment of immersed tunnels. *Reliability Engineering & System Safety*, 228: 108801.
- Tang, C., He, S.Y., Guan, Z., Zhou, W.H., Yin, Z.Y. 2023. Enhanced elastic beam model with BADS integrated for settlement assessment of immersed tunnels. *Underground Space*, 12: 79–88.
- Tang, C., He, S.Y., Zhou, W.H. 2024. An efficient physics-guided bayesian framework for predicting ground settlement profile during excavations in clay. *Journal of Rock Mechanics and Geotechnical Engineering*.
- Wei, G., Lu, S.J., Wang, Z., Huang, X. 2018. A theoretical model for the circumferential strain of immersed tunnel elements under tidal load. *Geotechnical and Geological Engineering*, 36: 1633–1645 (in Chinese).
- Yan, W., Yan, Y., Shen, P., Zhou, W.H. 2023. A hybrid physical data informed DNN in axial displacement prediction of immersed tunnel joint. *Georisk: Assessment and Management of Risk for Engineered Systems and Geohazards*, 17(1): 169–180.
- Zhou, H.Z., Wang, Y.N., Kou, X.Q. 2021. Calculation of vertical displacement of immersed tube tunnel under tidal load. *Journal of Railway Science and Engineering*, 19(3):790–797 (in Chinese).

Delineating the 3D spatial distribution of granite weathering grade from boreholes data

K.P. Jeong

*Civil Engineering Laboratory of Macau, State Key Laboratory of Internet of Things for Smart City
Department of Civil and Environmental Engineering, University of Macau, Macao SAR, China*

P.K. Ao

Civil Engineering Laboratory of Macau, Macao SAR, China

W.H. Zhou

*State Key Laboratory of Internet of Things for Smart City, Department of Civil and Environmental
Engineering, University of Macau, Macao SAR, China*

ABSTRACT: Evaluation of the bearing capacity of bedrock is a long-lasting challenge to geotechnical engineering. However, identifying the rock layer distribution using boreholes is usually time-consuming and costly, particularly in areas with a significant depth of overburden soils. The Weathering Grade (WG) of bedrock is critical for identifying bearing capacity, yet the spatial distribution of WG is often overlooked in current studies. This study employs the K-Nearest Neighbors (KNN) method to predict the spatial distribution of WG using data from 127 boreholes in a Macau construction project. The proposed classification model could generate the distribution of WG in 3D space. Validated by the test dataset, the root mean square errors for predicting surfaces of grade III and grade II are only 1.76m and 2.21m, respectively. Moreover, the model achieved an F1 score exceeding 70% in classifying the WG of bedrock. The classification of various WG and elevation of rock layer provide geotechnical engineers with valuable insights into bedrock quality assessment.

1 INTRODUCTION

The bearing capacity of bedrock plays a crucial role in the design of deep foundations. In Hong Kong and Macau, geotechnical engineers typically follow the “Code of Practice of Foundation” for defining the allowable bearing capacity from various characteristics of rock quality, as listed in Table 1. Only the bearing and frictional resistance of bedrock are considered in the design of the bored pile according to this guideline.





According to Table 1, the weathering grade (WG) of bedrock is an essential index in the determination of allowable vertical bearing pressure. The method for classification of WG is described in Table 2. In Hong Kong and Macau, many engineering projects encounter substantial thicknesses of weathered rock, with WG that may vary significantly over relatively short distances. While boreholes can effectively identify the distribution of WG in practical engineering projects, predicting the WG distribution still presents challenges. On the one hand, the penetration depth of boreholes is limited to around 5 meters into the rock layers. On the other hand, boreholes are costly and time-consuming, leading to a limitation in their number.

Machine learning is employed as an efficient methodology for the prediction and analysis of intricate issues in geotechnical engineering, such as tunnel induced settlement(Kannangara et al, 2022 & He et al, 2024), soil suction(Cheng et al, 2023), borehole planning(Yan et al, 2023), etc. Besides, simulation of geological interfaces from borehole data utilizing statistical and machine learning methodologies has gained widespread acceptance. The prediction

Table 1. Presumed allowable vertical bearing pressure under foundations on horizontal ground/bedrock (Code of practice of foundation, 2017).

Description of Rock	Presumed Allowable Bearing Pressure (kPa)
Fresh strong to very strong rock of weathering grade I, with 100% TCR, and UCS strength of rock material not less than 75 MPa	10,000
Fresh to slightly decomposed strong rock of weathering grade II or better, TCR more than 95% and UCS strength not less than 50 MPa	7,500
Slightly to moderately decomposed moderately strong rock of weathering grade III or better, TCR more than 85%, UCS strength not less than 25 MPa	5,000
Moderately decomposed, moderately strong to moderately weak rock of material weathering grade better than IV, with a total core recovery of more than 50% of the grade.	3,000

Table 2. Classification of rock material decomposition grades of Hong Kong (excerpted from Geoguide 3, 2017).

Descriptive Term	Grade Symbol	Plate Photo	General characteristics of granite and volcanic rocks
		(Coarse-grained Granite)	
Highly decomposed	IV		Can be broken by hand into small pieces. Makes a dull sound when struck by geological hammer. Completely discoloured compared with fresh rock
Moderately decomposed	III		Cannot usually be broken by hand; easily broken by geological hammer. Makes a dull or slight ringing sound when struck by geological hammer. Completely stained throughout.
Slightly decomposed	II		Not broken easily by geological hammer. Makes a ringing sound when struck by geological hammer. Fresh rock colours are generally retained but stained near joint surfaces.
Fresh	I		Not broken easily by geological hammer. Makes a ringing sound when struck by geological hammer. No visible sign of decomposition.

models such as the random field (Yan et al, 2023), conditional random field (Han et al, 2022), the Kriging method (Dasaka and Zhang, 2012), support vector machine (Ji et al, 2022), and eXtreme Gradient Boosting method (Zhu et al, 2021) are established for generating rock head surface. However, the prediction of spatial distribution of WG of bedrock is often ignored in current studies. This study aims to address the problem by employing the KNN model to delineate the spatial distribution of WG in 3D space.

2 STUDY SITE

The borehole logging data obtained from a site investigation report in a Macau construction project is used in this study. The site was designed as a public building with the foundation proposed using bored piles. Following the design requirement, a borehole should be drilled for each pile to

obtain the elevation of the bearing bedrock layer. Totally, 127 boreholes were drilled, and their locations and bedrock elevation are shown in Figure 1. The elevation is measured in Macau Mean Sea Level (MSL). Profile A and B are arranged to evaluate the accuracy of prediction. All boreholes have reached grade II weathered granite, with 32% of them reaching grade III layer above grade II layer. In this study, the rock head at a specific location is defined as the top elevation of the stronger WG layer. Summary of the site investigation is listed in Table 3. Boreholes were positioned with an average distribution density of 46.2 square meters. The elevation of the rock head exhibited variation, ranging from -18.42m to -44.15m MSL. Notably, the head elevation of Grade II granite was observed from -18.42m to -52.37m MSL. The histogram in Figure 2 illustrates a wide range and non-uniform distribution of elevations for both interfaces.

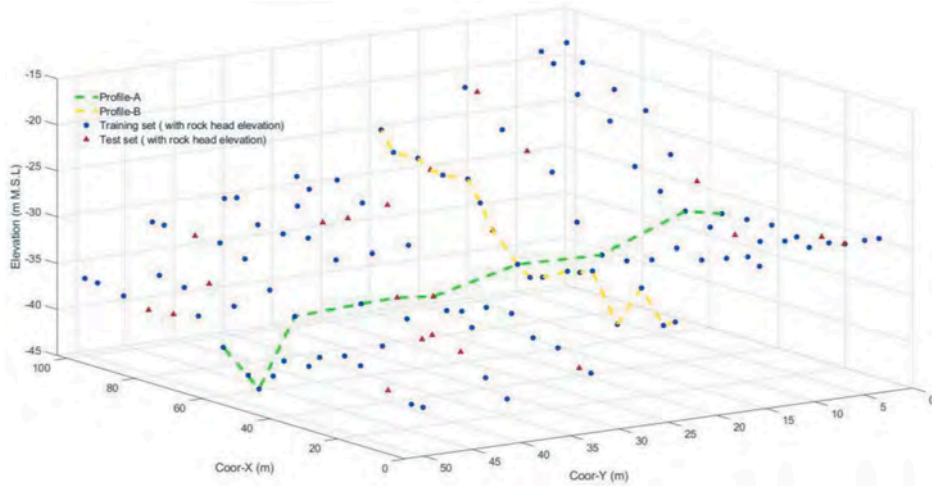


Figure 1. Layout of the 127 boreholes with elevation of their rock head, two profiles are labelled.

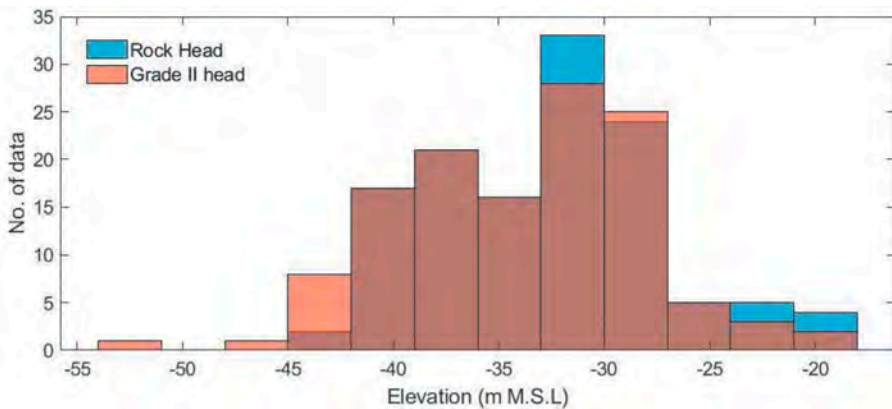


Figure 2. Histogram of interfaces elevation.

Table 3. Summary of site investigation reports with 127 boreholes.

Site feature			Rock head elevation (MSL)			Grade II head elevation (MSL)		
Length	Width	Borehole density	Max.	Min.	Median	Max.	Min.	Median
102m	53m	42.6m ² @	-18.42m	-44.15m	-32.01m	-18.42m	-52.37m	-33.05m

The semivariogram is used to characterize the dependence existing between variables (z values) at different points in space (Zhang and Dasaka, 2010). At a given spatial distance (h), the semivariance ($\gamma(h)$) is defined as the average squared difference in the z -values of pairs of input samples that are spaced by the lag distance. The equation of semivariance at lag distance h is defined by Equation 2.1:

$$\gamma(h) = \frac{1}{2} E\{X(t+h) - X(t)\}^2 \quad (1)$$

where t denotes a specific location; $X(t)$ represents the z value at location t , and h denotes lag describing the separation between two locations t and $t+h$; $E\{\}$ represents the symbol of mean function.

If the semivariogram does not level off for large values of separation distance, it indicates that the data set is nonstationary (Kulatilake and Ghosh, 1988). Figure 3(a) and (b) show the semivariograms of rockhead and head of grade II, respectively. It is evident that both semivariograms increase linearly until approximately 50m, after which they display a disorder trend with increasing the separation distance. This implies the complexity of geological characteristics in this site.

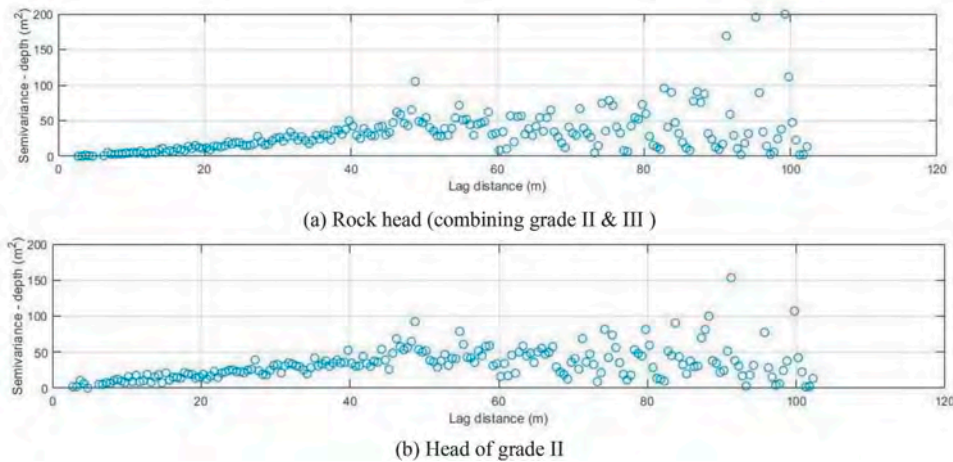


Figure 3. Semivariograms of (a) rock head and (b) grade II rock head from borehole data.

3 METHODOLOGY FOR PREDICTING WEATHERING GRADE

K-nearest neighbor (KNN), which is a multi-classification machine learning technique, is proposed to predict the 3D spatial distribution of WG. KNN has demonstrated its capability for classifying sedimentary layers (Bullejos et al, 2022) and has been successfully applied to delineate faults and other stratigraphic features (Martín-Martín et al., 2023), making it suitable for adoption in this study.

KNN algorithm aims to identify the closest neighboring points in relation to a specific query point, find the k nearest training samples based on some distance metric, and then use these k “neighbors” to make predictions (Zhou, 2016). It operates in both regression and classification problems. In the KNN classification model, the algorithm groups data points into clusters based on their similarity, which is measured by Euclidean distance $d(x_i, x_j)$:

$$d(x_i, x_j) = \sqrt{\sum_{k=1}^n (x_{ik} - x_{jk})^2} \quad (2)$$

where n represents the dimension of space; x_i and x_j are two points in n -dimensional space. Then, the label of the query point is determined based on the majority class among its ‘ k ’ nearest neighbors. The mathematical expression is shown as follows:

$$\hat{y} = \text{mode}\{y_i | x \in N_k(q)\} \quad (3)$$

where \hat{y} is the predicted class label for the query point q ; $N_k(q)$ represents the set of ‘ k ’ nearest neighbors of q in data points; y_i means the class labels the ‘ k ’ nearest neighbors. If ‘ k ’ is set to 5, the query point will be classified according to the majority class among its 5 closest neighbors.

Figure 4 illustrates the framework of this study, consisting of data preparation, machine learning model training, and validation and evaluation of prediction results. The training data is classified as ‘soil’, ‘III’, and ‘II’ categories, corresponding to residual soil, Grade III and Grade II rock, respectively. The prediction area is constructed as a rectangular cuboid, assuming WG under Grade II head are all ‘II’. The predicted data will be reshaped into a 3D model to illustrate the distribution of bedrock WG. The predicted data is then validated with the test set to evaluate its reliability.

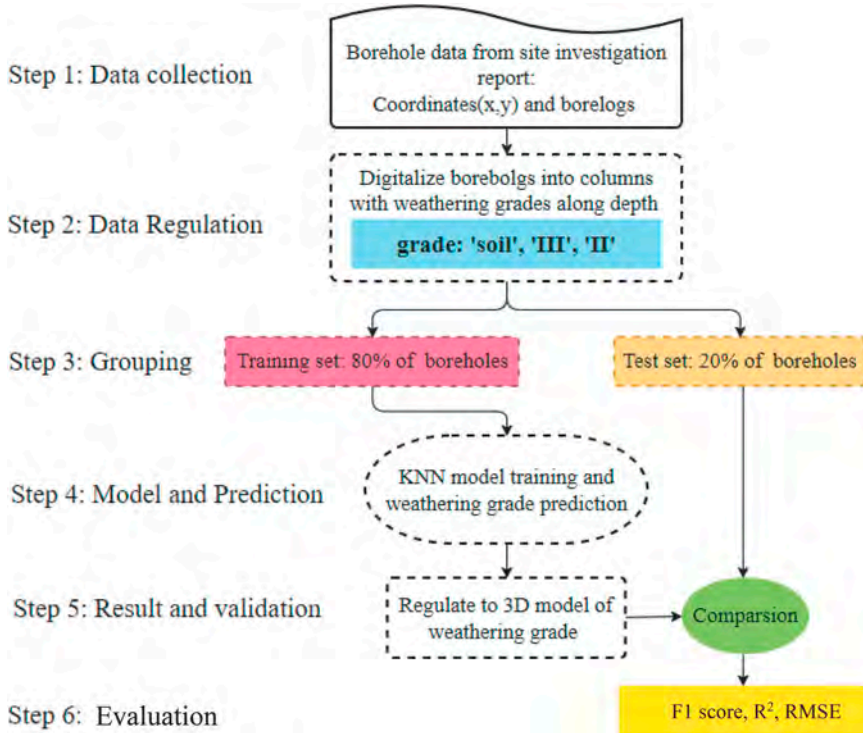


Figure 4. Procedure for 3D spatial modeling of rock weathering grade.

4 RESULT AND DISCUSSION

The performance of the prediction in this study is evaluated based on the classification of WG and the elevation of interfaces. To better illustrate the WG prediction results, Figure 5 depicts the predicted rock surface with overlaid measured borehole data. The green and yellow lines correspond to those in Figure 1. It is obvious that the WG discovered in borehole data well aligns with the prediction. Excluding the predictions around the 30m region in Profile A (Figure 6(a)), the remaining prediction points display good performance. The accuracy of predicted WG is measured by the F1 score, which consists of True Positive (TP), True

Negative (TN), False Positive (FP) and False Negative (FN). The higher F1 score indicates better performance of the classifier. Moreover, root mean square error (RMSE) is employed to illustrate the performance of predicted elevation for rock head and grade II head.

With only 6 mistaken observations of WG among 127 datasets, the model demonstrates a high F1 score of 0.946, as shown in Figure 7(a). After excluding the training set, the F1 score declines to 0.702, as illustrated in Figure 7(b). Nevertheless, this score indicates that the method is effective in such complex geological conditions.

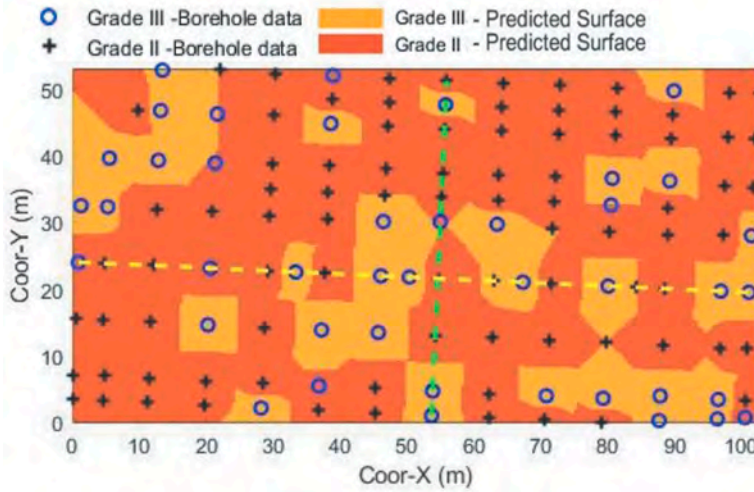


Figure 5. Predict rockhead surface with weathering grade distribution.

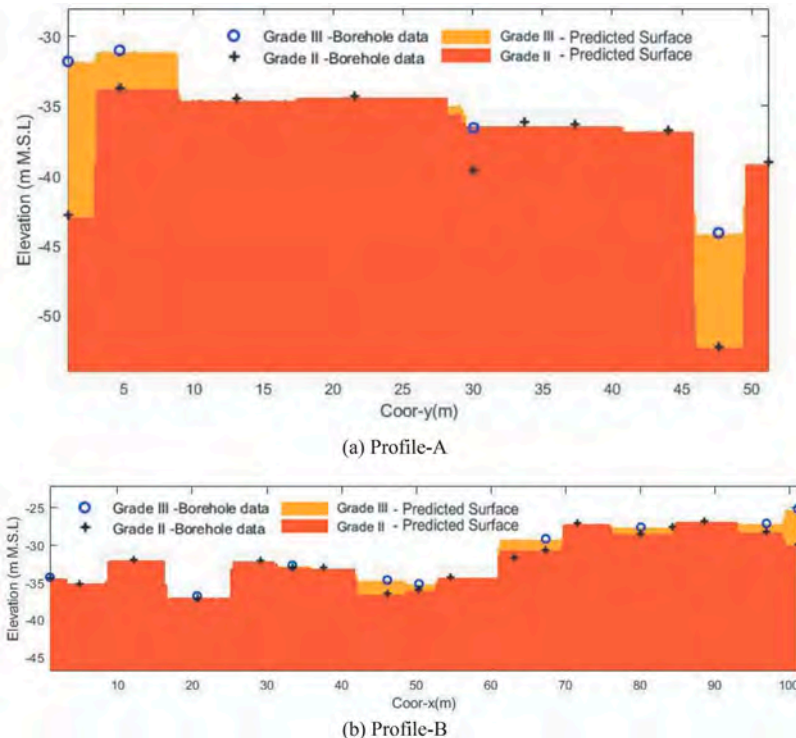


Figure 6. Simulated geological profile of grade II & III weathered granite (a) Profile-A (b) Profile-B.

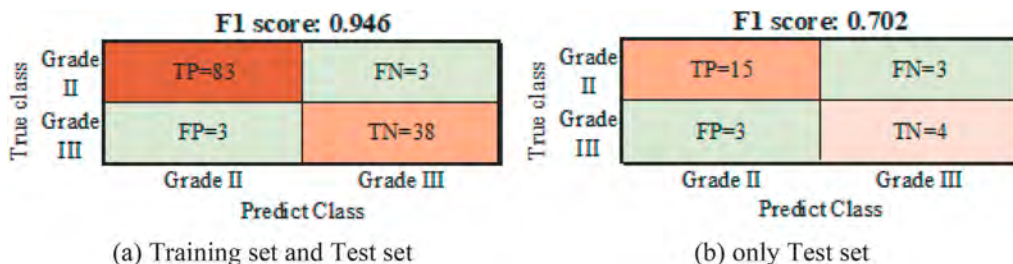


Figure 7. F1 score of classifying grade II and III rock in (a) Training set and Test set (b) only Test set.

The performance of interface elevation prediction is illustrated in Figure 8, using 20% of 127 borehole data for validation. Although the spatial variation of grade II head is complicated, the prediction still indicates high R^2 (0.887 and 0.843 for rock head and grade II head, respectively) and acceptable RMSE (1.76m and 2.21m for rock head and grade II head, respectively), as shown in Figure 8(a) and (b).

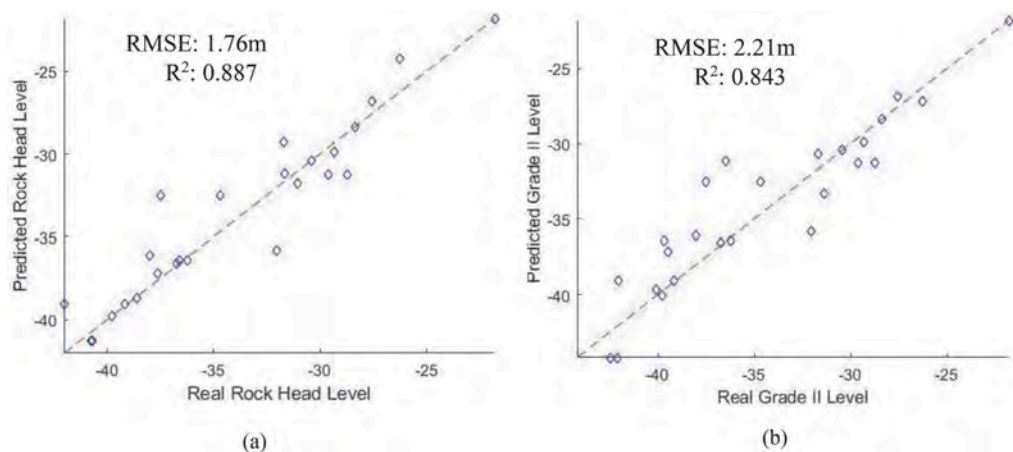


Figure 8. Evaluation of predicted elevation for interface using test set: (a) Rock head (b) Grade II rock head.

5 CONCLUSION

Characterization of rockhead and its weathered grades (WG) is essential to geotechnical design, which determines the financial cost, construction time and safety of the whole building project. This paper introduces KNN methodology to simulate 3D spatial distribution of granite weathering grade in a pile foundation site. Three weathering grades of granite material are fed into the KNN model, which could predict the head elevation of grade II and grade III granite.

In this study, 127 boreholes from a site in Macau are collected, 80% of them are used to train KNN model, while the remaining 20% is reserved for validating the predictions. Evaluated by the validation set, the outcomes reveal an R^2 of 0.887 for predicting the rock head and 0.843 for the grade II head, respectively. Additionally, the model achieved an RMSE of 1.76m for the rock head and 2.21m for the grade II head, respectively. Besides, only 6 mistaken observations in predicting granite weathering grade indicate reliable weathering grade prediction. The paper demonstrates the effectiveness of KNN in delineating the 3D spatial distribution of WG in complex geological conditions. It can be considered a valuable tool for addressing limitations associated with limited boreholes and holds the potential to reduce investigation costs and time in construction projects.

ACKNOWLEDGEMENT

The authors greatly acknowledge the financial support from Guangdong Provincial Department of Science and Technology (Grant No. 2019B111106001), Science and Technology Development Fund, Macao SAR (Grant Nos. 001/2024/SKL). The data was supported by the Civil Engineering Laboratory of Macau (LECM).

REFERENCES

- Bullejos, M., Cabezas, D., Martín-Martín, M., & Alcalá, F. 2022. A K-Nearest Neighbors Algorithm in Python for Visualizing the 3D Stratigraphic Architecture of the Llobregat River Delta in NE Spain. *Journal of Marine Science and Engineering*, 10986.
- Cheng, Z.-L., Kannangara, K. K. P. M., Su, L.-J., Zhou, W.-H., & Tian, C. (2023). Physics-guided genetic programming for predicting field-monitored suction variation with effects of vegetation and atmosphere. *Engineering Geology*, 315, 107031.
- Code of Practice for Foundations. 2017. Hong Kong: The Buildings Department, HK SARS.
- Dasaka, S. M., & Zhang, L. M. 2012. Spatial variability of in situ weathered soil. *Geotechnique*, 62(5), 375–384.
- Geoguide 3, Guide to Rock and Soil Descriptions. 2017. Hong Kong: Geotechnical Engineering Office, Civil Engineering and Development Department, HK SAR.
- Han, L., Wang, L., Zhang, W., Geng, B., & Li, S. 2022. Rockhead profile simulation using an improved generation method of conditional random field. *Journal of Rock Mechanics and Geotechnical Engineering*, 14(3), 896–908.
- He, S., Kuok, S., Tang, C., Zhou W. 2024 Efficient Bayesian model updating for settlement prediction of the immersed tunnel of HZMB. *Transportation Geotechnics*, 44, 101179
- Ji, X., Lu, X., Guo, C., Pei, W., & Xu, H. 2022. Predictions of Geological Interface Using Relevant Vector Machine with Borehole Data. *Sustainability*, 14(16), 10122.
- Kulatilake, P. H. S., & Ghosh, A. 1988. An investigation into accuracy of spatial variation estimation using static cone penetrometer data. *In International Symposium on penetration testing*; 815–821.
- Kannangara, K. K. P. M., Zhou, W., Ding, Z., & Hong, Z. (2022). Investigation of feature contribution to shield tunneling-induced settlement using Shapley additive explanations method. *Journal of Rock Mechanics and Geotechnical Engineering*, 14(4), 1052–1063.
- Martín-Martín, M., Bullejos, M., Cabezas, D., & Alcalá, F. J. 2023. Using Python libraries and k-Nearest neighbors algorithms to delineate syn-sedimentary faults in sedimentary porous media. *Marine and Petroleum Geology*, 153, 106283.
- Yan, W., Shen, P., Zhou, W. H., & Ma, G. 2023. A rigorous random field-based framework for 3D stratigraphic uncertainty modelling. *Engineering Geology*, 323, 107235.
- Yan, W., Zhou, W.-H., & Shen, P. (2023). An Uncertainty-driven Peak-integration (UP) Strategy for 3D Borehole Layout Planning. *Computers and Geotechnics*, 156, 105280
- Zhang, L. M. & Dasaka, S. M. 2010. Uncertainties in Geologic Profiles versus Variability in Pile Founding Depth. *Journal of Geotechnical and Geoenvironmental*. 11, 1475–1488.
- Zhu, X., Chu, J., Wang, K., Wu, S., Yan, W., & Chiam, K. 2021. Prediction of rockhead using a hybrid N-XGBoost machine learning framework. *Journal of Rock Mechanics and Geotechnical Engineering*, 13(6), 1231–1245.
- Zhou, Z. H. (2016). *Machine learning*. Springer Nature.

Soil disturbance evaluation in a typical soft clay excavation pit

M.Z. Li, Y.G. Zhou*, Y. Tian, Y.Z. Li & Y.M. Chen

MOE Key Laboratory of Soft Soils and Geoenvironmental Engineering, Institute of Geotechnical Engineering, Center for Hypergravity Experiment and Interdisciplinary Research, Zhejiang University, Hangzhou, P. R. China

J.N. Ye

Ningbo Rail Transit Group Co., Ltd., Ningbo, P. R. China

ABSTRACT: **ABSTRACT:** This study introduces a dimensionless soil structural parameter, S_{vh} , derived by normalizing the effective stresses and the void ratio in Hardin equation for small-strain shear modulus, G_{max} , as the indicator of soil structure disturbance during construction. Different from the large strain shear strength or other field testing indices which will introduce extra soil disturbance, S_{vh} represents the soil mineral, particle and fabric at initial state and could fully characterize micro-structure of soil skeleton. Based on field measurements of shear wave velocities before and after excavation, and the relevant laboratory tests and numerical analysis, a well-defined procedure is proposed to evaluate the soil disturbance behind the retaining walls during excavation in a typical soft clay ground.

1 INTRODUCTION

Soil disturbance assessment primarily relies on in-situ testing indices, complemented by laboratory tests and numerical analysis. In-situ testing indices can be categorized into two types: one is large-strain strength parameter, such as the undrained shear strength S_u , the other is small-strain stiffness parameter, like the shear wave velocity V_s . These physical-mechanical parameters are influenced by both the stress state and soil structure, facilitating them for the quantitative description of soil disturbance.

Excavation or construction induces disturbance in the soil medium, accompanied by stress state change and structural damage. Macroscopic changes often trigger microstructural disturbance, such as particle rearrangement or bonding break (Kempfert & Gebreselassie, 2006). Therefore, excavation disturbance induces a simultaneous change in both the stress state and microscopic structure. The existing soil disturbance evaluation methods based on large strain strength parameters integrate the initial physical state and the shear- or compression-induced extra soil structure damage, which makes it difficult to distinguish the construction-induced disturbance from its initial state.

The dimensionless structure parameter, denoted as S_{vh} , which is obtained by normalizing the effective stresses and the void ratio in Hardin equation for small-strain shear modulus (Hardin et al., 1989), is employed as a quantitative soil structure disturbance evaluation parameter in this study. A case study of a soft clay excavation pit in Ningbo, Zhejiang Province, P. R. China is conducted, and the excavation-induced soil disturbance behind the retaining walls is evaluated.

2 PRINCIPLES OF SOIL DISTURBANCE EVALUATION

The small-strain shear modulus, G_{max} , representing the maximum shear modulus at very small strain level about 1×10^{-6} , serves as a comprehensive characterization parameter for soil

states. Determination of G_{\max} is accomplished via field or laboratory shear wave velocity measurements according to the principles of elastic waves in solid:

$$G_{\max} = \rho V_s^2 \quad (1)$$

where ρ is soil density, and V_s is the shear wave velocity.

Existing research indicates that the small-strain shear modulus is primarily influenced by soil structure, stress state, void ratio and stress history (Hardin & Blandford, 1989; Santagata et al., 2005). This study adopts the Hardin formula recommended by Jamiolkowski (1995), where G_{\max} or shear wave velocity is measured in the vertical plane as follows:

$$G_{\max} = S_{\text{vh}} F(e) p_a^{(1-n_v-n_h)} (\sigma'_v)^{n_v} (\sigma'_h)^{n_h} \quad (2)$$

where S_{vh} is a dimensionless parameter characterizing the structure in vertical plane; $F(e)$ is the void ratio function and in the form of $F(e) = e^{-x}$; p_a is atmospheric pressure which equals to 100 kPa; σ'_v and σ'_h are effective vertical and horizontal stress respectively. Exponents x , n_v and n_h are all fitting parameters that can be obtained by multi-stage consolidation tests. Previous research by Jamiolkowski et al. (1995) and Shibuya (2000) demonstrated that, for a specific type of soil, stress exponents n_v and n_h can be assumed as constant regardless of any changes in the microscopic structure or stress state, as well as void exponent x . Hence, the soil structure can be uniquely characterized by the dimensionless parameter S_{vh} :

$$S_{\text{vh}} = G_{\max} / \left[F(e) p_a^{(1-2n)} (\sigma'_v \sigma'_h)^n \right] \quad (3)$$

where $n = n_v = n_h$.

To quantitatively characterize the soil disturbance degree, this study incorporates the concept of disturbance states introduced by Desai & Gens (2000). Assuming that natural deposits represent the initial “relatively intact” state without any structure disturbance, remolded soil represents the “fully adjusted” state with a disturbance degree of 100 %. Zhou et al. (2023) suggested the expression for calculating the soil structure disturbance degree (*SDD*) as follows:

$$SDD = \frac{S_{\text{vh},i} - S_{\text{vh},d}}{S_{\text{vh},i} - S_{\text{vh},r}} \times 100\% \quad (4)$$

where subscripts i , d and r denote the intact, disturbed, and fully remolded states, respectively.

3 EXCAVATION-INDUCED SOIL DISTURBANCE

As mentioned above, soil disturbance evaluation demands small-strain shear modulus, effective stresses, void ratio and the corresponding exponents in Hardin equation. Therefore, the evaluation process involves the field testing, numerical analysis and laboratory experiments.

3.1 Site condition and field measurement of shear wave velocity

The construction site locates in the alluvial plain of Ningbo, Zhejiang Province, P. R. China. The site is filled with normal-consolidated soft clay, and its physical properties are provided in Figure 1. The ground water table is 1.5 meters below the ground surface. This excavation pit has a dimension of 152 m in length, 20 m in width and a designed depth of 16.7 m. The enclosure structure comprises 0.8 m thick concrete diaphragm walls equipped with internal bracing.

All field measuring instruments are positioned on the southeast side of the excavation pit. Settlement meters, inclinometers and shear wave velocity testing boreholes are distributed at certain distances from the retaining walls in the perpendicular direction (see Figure 2). Cross-hole shear wave velocity measurements were conducted before excavation and done again when the excavation depth reached 16.7 m, where the boreholes are located at 5 m and 60 m away from the diaphragm wall respectively, and the testing interval in the borehole is 1 m. The compiled results are illustrated in Figure 3. At the excavation depth of 16.7 m, a significant reduction in shear wave velocity is observed in the borehole located 5 m away from the diaphragm wall. Shear wave velocity above the excavation depth undergoes a slight decrease, while a remarkable reduction

happens in the deeper soil layers underneath the excavation elevation. Almost no reduction of shear wave velocity is observed in the borehole located at distance of 60 m. These phenomena suggest that excavation has a more pronounced impact on the stiffness of the deeper soil layers than the shallower ones, especially in the vicinity of retaining walls.

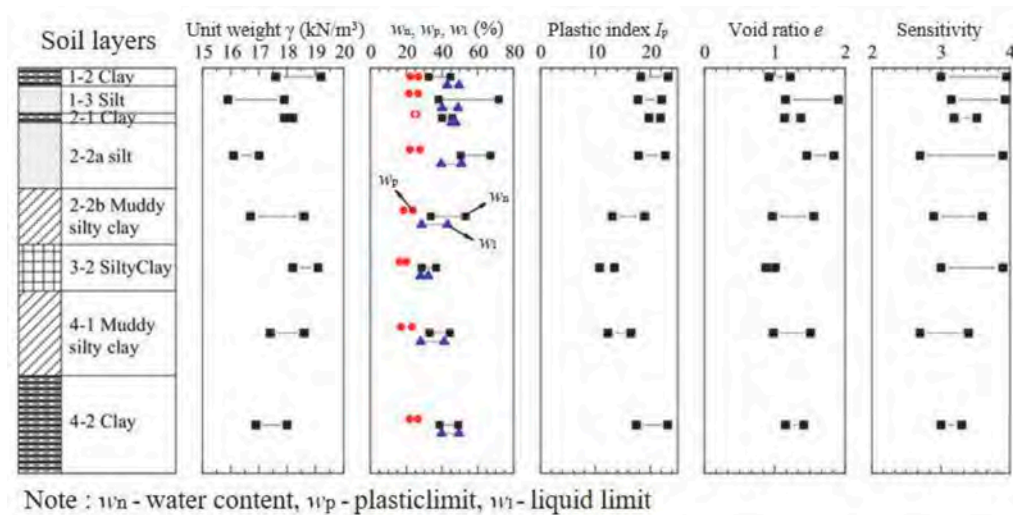


Figure 1. Soil physical properties in the excavation layer.

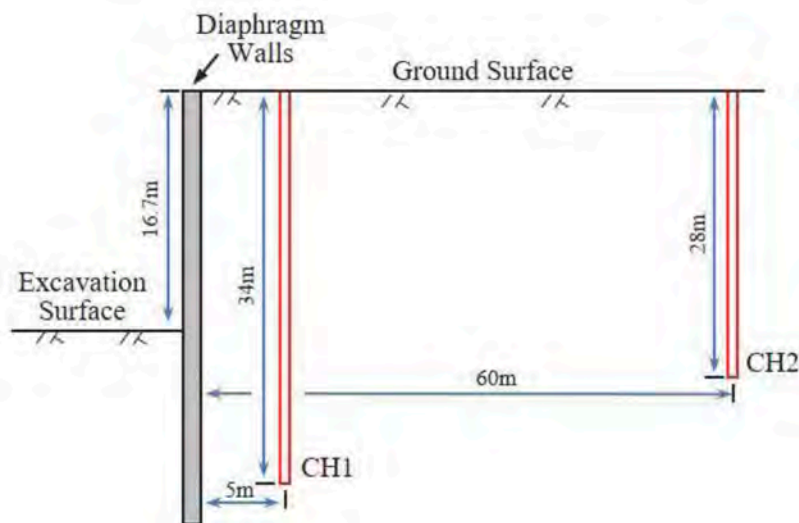


Figure 2. Plan view of the construction site for borehole testing.

3.2 Soil disturbance evaluation behind the wall

Firstly, the parameters mentioned in Equation 3 need to be fitted through multi-stage consolidation tests, which were conducted on a GDS triaxial apparatus equipped with a pair of bender elements. The confining pressure ranges from 25 to 400 kPa. After each consolidation stage, drainage volume was recorded and shear wave velocity was measured. The corresponding parameters can be obtained by taking the logarithm of both sides of Equation 2, which are summarized in Table 1.

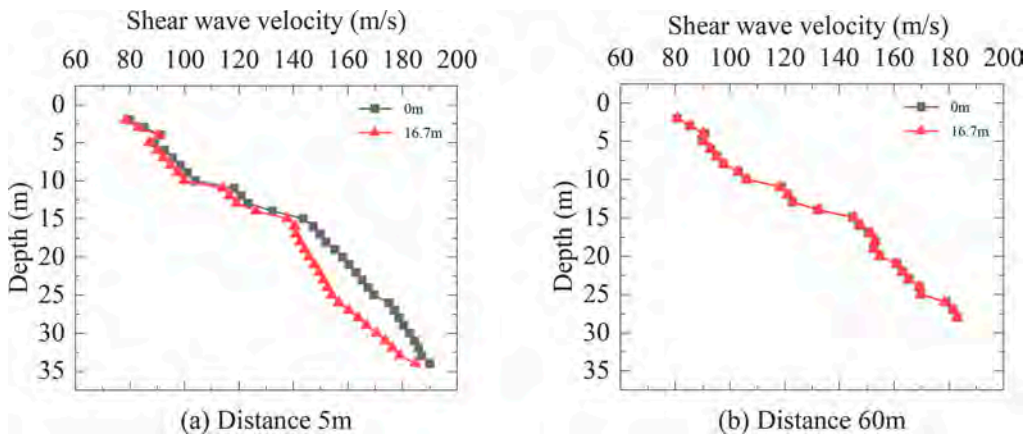


Figure 3. Measurements of shear wave velocity at different distances behind the diaphragm wall.

Table 1. Parameters obtained from laboratory tests.

Soil layer		n	x	$S_{v,h,r}$
2-2a	Silt	0.231	2.120	353
3-2	Silty clay	0.269	1.819	301
4-1	Muddy silty clay	0.257	1.710	337
4-2	Clay	0.268	1.714	331

Secondly, the effective stresses at each borehole of shear wave velocity measurement should be determined for Equation (3). The two-dimensional plane strain model at the monitored cross-section is established using Plaxis 2D software to calculate the effective stress fields. The small-strain hardening model (Benz, 2007) is used to describe soil behaviors under undrained condition. The numerical calculations of effective stress at the excavation depth of 16.7 m are shown in Figure 4. There are negligible variations in vertical effective stress near the diaphragm walls before and after excavation, while considerable changes in horizontal effective stress within the range of 20 m away from the wall. Influenced by internal bracing, horizontal effective stress near the wall experiences local enhancement, but in distant areas, unloading phenomena predominate, as shown in Figure 4(b).

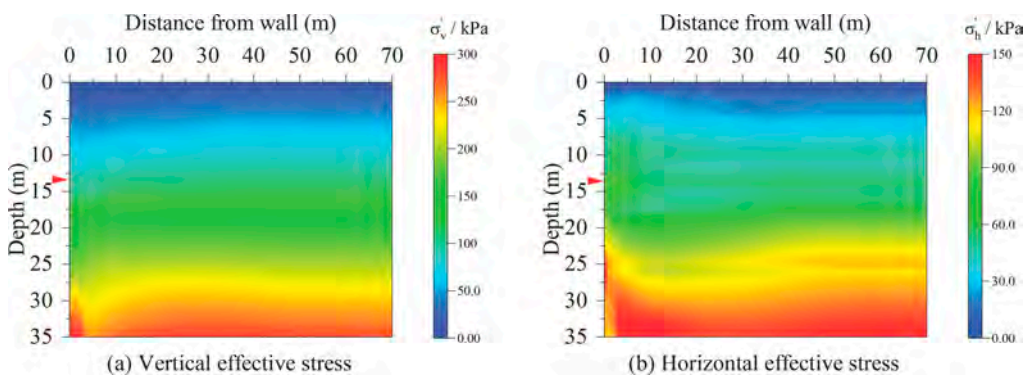


Figure 4. Effective stresses behind the walls at excavation depth of 16.7m.

As the field measurement of shear wave velocity were conducted right after excavation, it is assumed that the void ratio of soft clay remains unchanged despite the generation of excess pore pressure during excavation, which is equal to the void ratio before construction. Combining the effective stress field calculated from the Plaxis 2D model and the fitting parameters obtained from multi-stage consolidation tests, dimensionless structure parameters of intact soil, disturbed soil and remodeled soil can be calculated respectively. Finally, the soil disturbance field behind the walls at the excavation depth of 16.7 m, as shown in Figure 5, is determined through the above-mentioned procedure. When the excavation reaches 16.7 m, the peak disturbance degree with a value between 40-50% occurs in the area adjacent to diaphragm walls and underneath the excavation surface. By comparing Figure 5 with Figure 4, it can be found that the zone of soil structure disturbance is approximately consistent with the zone of stress state change. It implies that the construction process will change the stress state of the soil adjacent the diaphragm wall, which result in plastic strain and micro-structure damage.

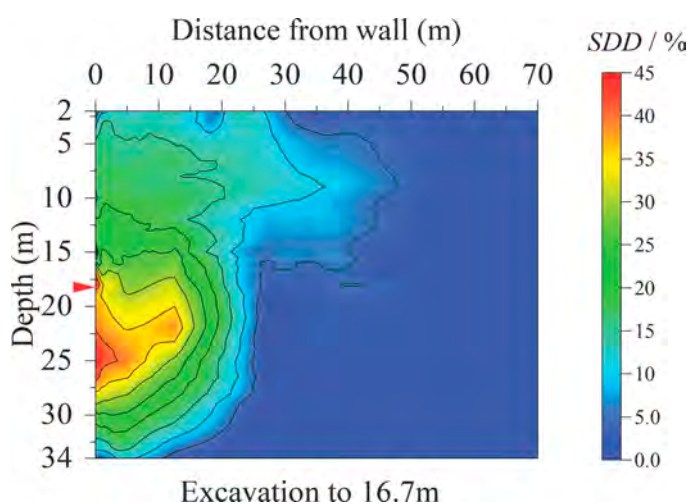


Figure 5. Soil structure disturbance field behind the retaining walls.

4 CONCLUSIONS

This study proposes an approach for evaluating soil disturbance in soft clay ground by combining the disturbance state concept and dimensionless structural parameters. Soil disturbance behind retaining walls at an excavation pit in Ningbo is evaluated based on field measurement of shear wave velocity, laboratory tests and numerical analysis. When the excavation depth reaches 16.7 m, soil disturbance about $SDD=40-50\%$ occurs in the area adjacent to the diaphragm wall, especially in the elevation underneath the excavation surface.

ACKNOWLEDGEMENTS

This work was partly supported by the National Natural Science Foundation of China (Nos. 51978613 and 52278374). Dr. Zhuo-Feng Li of Guangxi University and Dr. Fei Gao of Zhejiang University are greatly appreciated for their helps for conducting the field measurements.

REFERENCES

- Benz, T. 2007. *Small-strain stiffness of soils and its numerical consequences*. Stuttgart: University of Stuttgart.
- Desai, C. S. & Gens, A. 2000. Mechanics of materials and interfaces: The disturbed state concept. *Journal of Electronic Packaging*. 123(4):406.
- Hardin, B. O. & Blandford, G. E. 1989. Elasticity of particulate materials. *Journal of Geotechnical Engineering*. 115(6): 788–805.
- Jamiolkowski, H., Lancellotta, R. H., Lo Presti, D. C. F. 1995. Remarks on the stiffness at small strains of six Italian clays. *Proc. of I Int. Symp. on Prefailure Deformation Characteristics of Geomaterials*. IS-Hokkaido.
- Kempfert, H. G. & Gebreselassie, B. 2006. *Excavations and foundations in soft soils*. Berlin, Heidelberg: Springer.
- Santagata, M., Germaine, J. T., Ladd, C. C. 2005. Factors affecting the initial stiffness of cohesive soils. *Journal of Geotechnical and Geoenvironmental Engineering*. 131(4): 430–441.
- Shibuya, S. 2000. Assessing structure of aged natural sedimentary clays. *Soils and Foundation*. 40(3): 1–16.
- Zhou Y. G., Tian Y., Ye, J. N., Bian X. C., Chen Y. M. 2023. Soil disturbance evaluation of soft clay based on stress-normalized small-strain stiffness. *Journal of Rock Mechanics and Geotechnical Engineering*. <https://doi.org/10.1016/j.jrmge.2023.08.019>.

Evaluation of landslide susceptibility in Kangding basin based on factor screening

Z. Li

School of Earth Science and Engineering, Sun Yat-sen University, Guangzhou, China
Southern Marine Science and Engineering Guangdong Lab. (Zhuhai), Zhuhai, China
Guangdong Provincial Key Lab. of Geodynamics and Geohazards, Zhuhai, China

F. Xiao

School of Earth Science and Engineering, Sun Yat-sen University, Guangzhou, China
Guangdong Provincial Key Lab. of Geodynamics and Geohazards, Zhuhai, China

Y. Wang

School of Earth Science and Engineering, Sun Yat-sen University, Guangzhou, China
Southern Marine Science and Engineering Guangdong Lab. (Zhuhai), Zhuhai, China
Guangdong Provincial Key Lab. of Geodynamics and Geohazards, Zhuhai, China

Y. Zhou

School of Earth Science and Engineering, Sun Yat-sen University, Guangzhou, China
Guangdong Provincial Key Lab. of Geodynamics and Geohazards, Zhuhai, China

J. Liu

School of Earth Science and Engineering, Sun Yat-sen University, Guangzhou, China
Southern Marine Science and Engineering Guangdong Lab. (Zhuhai), Zhuhai, China
Guangdong Provincial Key Lab. of Geodynamics and Geohazards Zhuhai, China

F. Meng

School of Earth Science and Engineering, Sun Yat-sen University, Guangzhou, China
Southern Marine Science and Engineering Guangdong Lab. (Zhuhai), Zhuhai, China
Earth & Environmental Science, Faculty of Science, The Chinese University of Hong Kong, Hong Kong SAR, China

ABSTRACT: The main urban area of Kangding City and its surrounding watershed were taken as the study area. Sixteen environmental factors that can potentially cause landslides were identified and selected. The Apriori algorithm was used to screen out the combination of environmental factors. Put this combination into a random forest (RF) model for prediction. The results of the factor-screened model were compared with that of the original random forest model. The comparison of the results evaluated by frequency ratio accuracy and receiver operating characteristic curve (ROC) shows that the prediction results of the random forest model after factor screening are highly consistent with the actual landslide hazard distribution, and can make better predictions in the spatial distribution of landslide susceptibility of the study area. This study provides a more appropriate method for eliminating redundancy and noise factors in the environmental factors of landslide disasters.

Landslide susceptibility assessment refers to the probability of landslides occurring in a specific area with mountain slopes, and is influenced by various environmental factors. In the past few decades, various studies have been carried out on landslide susceptibility assessment and risk

assessment all over the world. There are two types of models for susceptibility evaluation: qualitative evaluation and quantitative evaluation. In recent years, researchers have increasingly preferred machine learning methods (Renchenbach et al., 2018), which have also been widely used in landslide susceptibility assessment. As a widely used ensemble learning algorithm based on a tree model, the Random Forest (RF) algorithm boasts numerous advantages, such as the ability to evaluate variables with minimal restrictions, disregard data scale or distribution, deliver high computational efficiency, and accurate predictions, etc (Guo et al., 2023). Additionally, compared to neural networks and deep learning, RF's hyperparameter debugging requires less expense (Chen et al., 2023). To evaluate landslide susceptibility, creating an evaluation index system is essential. A crucial aspect of this is screening environmental factor combinations to eliminate redundancy. Selecting a significant number of influencing factors based on the development mechanism of landslide disasters can help reduce interference (Sun et al., 2020). The Association Rule Algorithm can detect previously unknown rule patterns, which may be proved useful when working with large amounts of data (Cui and Bao, 2016). Incorporating association rules into landslide susceptibility evaluation can make the selection of evaluation indices more rational.

1 STUDY AREA AND DATA SOURCE

The parameters of the study area are chiefly defined by the 8-level watershed boundary present in the HydroBASINS database (Lehner and Grill, 2013). In the context of this paper, the study area encompasses the watershed boundary that encompasses the key urban region of Kangding, and also intersects with the administrative boundary of Kangding City. Therefore, the study area is identified as the Kangding Basin (KB) throughout this paper.

The research data in this study include both landslide data and landslide influencing factors. Among them, the remote sensing image data comes from the Landsat image data satellite of the United States Geological Survey, with a spatial resolution of 30 m and a revisit period of 16 days. The landslide disaster investigation data were collected from the Kangding Municipal Bureau of Land and Resources and the Resource and Environmental Science and Data Center of the Chinese Academy of Sciences. The elevation data comes from the high-precision global digital surface model data released by JAXA in Japan, with a horizontal resolution of 30m and an elevation accuracy of 5m. Rainfall data is from the National Earth System Science Data Center. Land use data are from the global 30m fine land cover products in 2020 (GLC_FCS30-2020). Road data is sourced from the OpenStreetMap website. Fault data is from the Kangding 1:5,000 geological map.

2 MODEL METHODOLOGY

Association rules were first proposed by Professor R. Agrawal in 1993 and measure the relevance of things. Association rules are described in terms of support and confidence (Papi et al., 2022). It is one of the most important and popular data mining techniques for discovering unknown knowledge from transactional databases. Support (Supp) indicates the probability that itemsets A and B will occur at the same time in a transactional database. It is defined as follows:

$$Supp(AR : X \Rightarrow Y) = P(X \cup Y) \approx \frac{Count(X \cup Y)}{|T|} \times 100\% \quad (1)$$

Random forest (RF) was proposed by American scholar Breiman in 2001 as an ensemble algorithm for binary decision trees trained separately, which belongs to a supervised classification algorithm (Breiman, 2001). Several studies have shown that it has a relatively high tolerance to outliers and noise, and is not prone to overfitting (Emrehan et al., 2020), with high prediction accuracy and stability. In this method, multiple decision trees are established through different data subsets, and then n feature subsets are randomly selected in each sample, from which the optimal features are selected to grow the nodes. Finally, the final result is obtained through the voting of each decision tree, as shown in the equation:

$$H(x) = \arg\max_z \sum_{i=1}^k I(h_i(x) = Z) \quad (2)$$

where $H(x)$ denotes the random forest model, h_i is a single decision tree model, Z is the output variable, and $I(\cdot)$ is an indication function.

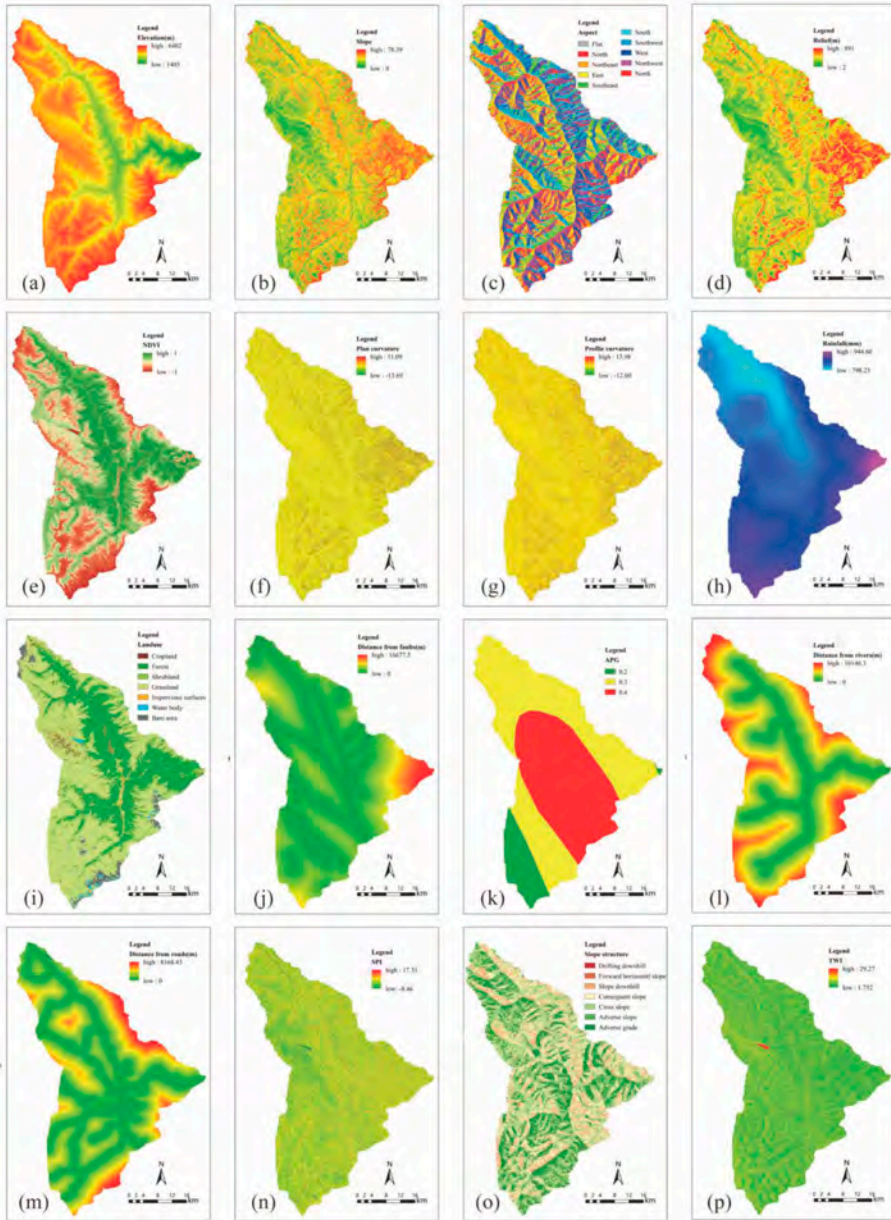


Figure 1. The environmental factors used for landslide susceptibility assessment.

The steps to construct a random forest model are as follows: (1) construct a subset from the original dataset; (2) Generate a training set for each decision tree sample. The bag sampling technique was used to set N training subsets in the playback, and the number of training subsets was less than the total number of training samples; (3) Vote on multiple decision trees.

3 SELECT AND SCREEN OUT ENVIRONMENTAL FACTORS

Landslide disasters occur as a result of a combination of internal and external factors (Li et al., 2022; Li et al., 2023). The influencing factors of the geological environment determine the geological conditions of the region, while factors such as rainfall and earthquakes are the external factors that can induce landslide disasters. Referring to the relevant literature of the KB and similar studies, the objectivity of relevant environmental factors and data availability were considered. A total of 16 environmental factors were selected from four aspects: topography, geological environment, meteorology and hydrology, as well as human activities for landslide susceptibility evaluation. All the selected environmental factors, including elevation, slope, aspect, relief, rainfall, distance from rivers, distance from roads, distance from faults, Normalized Difference Vegetation Index(NDVI), Acceleration of Peak Ground(APG), landuse, plan curvature, profile curvature, Stream Power Index(SPI), Topographic Wetness Index(TWI), as well as slope structure are shown in Figure 1. The original classification of all the discrete environmental factors was used, including aspect, APG, landuse, and slope structure etc. Continuous factors were classified by the natural break point grading method (Jenks) of ArcGIS.

16 environmental factors were extracted by ArcGIS based on the point features in the study area, along with an equal number of random points. These attributes were then used as a sample dataset for association rule data mining. The environmental factors were classified and assigned numbers before constructing the dataset for rule mining. Partial data is shown in Table 1. The Apriori algorithm was used to mine frequent itemsets, and then the rules with a strong correlation with the development of landslide disasters are generated. ArcGIS and Excel were used to preprocess the collected data. Then the Apriori association rule model was constructed to realize the strong association analysis between environmental factors and landslides, and the environmental factors were screened, optimized, and combined. Landslide is taken as the consequence of Apriori algorithm mining. 16 environmental factors were used as the antecedent to predict the relationship between themselves and landslide occurrence. By setting parameters such as support degree,

Table 1. Association rule datasets (only partial data are shown).

Factors	Samples									
Landslide	T0	T0	T0	T0	T1	T1	T1	T1	...	T1
SPI	A2	A2	A4	A4	A2	A5	A2	A2	...	A3
TWI	B1	B1	B3	B4	B1	B3	B1	B2	...	B3
Plan curvature	C4	C5	C4	C4	C4	C3	C4	C4	...	C3
Profile curvature	D3	D2	D3	D3	D3	D3	D2	D4	...	D4
Relief	E3	E2	E3	E2	E2	E4	E3	E3	...	E5
Slope	F4	F4	F3	F2	F3	F6	F5	F2	...	F3
Rainfall	G3	G4	G2	G5	G2	G6	G3	G2	...	G2
NDVI	H3	H1	H5	H1	H6	H6	H6	H5	...	H6
Elevation	I5	I6	I4	I6	I1	I1	I2	I2	...	I2
Faults	J6	J6	J6	J6	J1	J6	J4	J3	...	J3
Distance from rivers	K6	K6	K6	K6	K2	K3	K4	K5	...	K6
Distance from roads	L6	L6	L6	L6	L2	L3	L5	L4	...	L2
Landuse	M4	M4	M2	M7	M2	M2	M2	M4	...	M2
APG	N3	N3	N2	N3	N3	N2	N3	N3	...	N3
Slope structure	O3	O6	O5	O3	O6	O5	O6	O6	...	O5
Aspect	P5	P9	P8	P7	P3	P2	P3	P4	...	P9

landslide association rules were generated based on frequent item sets. Environmental factors in the rules may have a greater impact on landslides. A combination of factors for landslide susceptibility is then constructed, which is considered to have higher predictive power.

According to the findings presented in Table 2, seven environmental factors demonstrate strong correlations with the occurrence of landslide disasters. These factors are landuse, rainfall, elevation, plan curvature, distance from faults, NDVI, and APG. The confidence degree of these correlations is greater than 60%.

Table 2. Association rules.

antecedent	consequent	support	confidence	lift	leverage
N3, I1	frozenset({'T1'})	0.2593	1.0000	2.0000	0.1296
J1, N3	frozenset({'T1'})	0.2037	0.9565	1.9130	0.0972
I1	frozenset({'T1'})	0.3241	0.9459	1.8919	0.1528
G2, N3	frozenset({'T1'})	0.2500	0.9000	1.8000	0.1111
H6, N3	frozenset({'T1'})	0.2037	0.8148	1.6296	0.0787
J1	frozenset({'T1'})	0.2037	0.7857	1.5714	0.0741
G2	frozenset({'T1'})	0.2500	0.7714	1.5429	0.0880
C4, N3	frozenset({'T1'})	0.2130	0.7667	1.5333	0.0741
H6	frozenset({'T1'})	0.2407	0.7429	1.4857	0.0787
N3	frozenset({'T1'})	0.4352	0.6714	1.3429	0.1111
M4, N3	frozenset({'T1'})	0.2500	0.6585	1.3171	0.0602
C4	frozenset({'T1'})	0.2407	0.6047	1.2093	0.0417

4 ASSESSMENT OF LANDSLIDE SUSCEPTIBILITY

4.1 Evaluation results of random forest model

To train a landslide disaster prediction model, 54 locations with landslide disasters were identified as positive samples and assigned a value of 1. Negative samples were randomly generated within the study area using ArcGIS, assigning a value of 0. The ratio of positive to negative samples was 1:3, and the distance between random points was set to 500m. Using ArcGIS, the 30m x 30m raster of the study area was converted into point feature data. The attribute values of 16 environmental factors were then extracted using the multi-value extraction to-point tool (Liu, Li and Chen, 2018; Şahin, Çölkesen & Kavzoğlu, 2018). The sample dataset was randomly divided into a training set and a validation set according to a ratio of 7:3, and the random forest model was trained. The data of 16 environmental conditions were collected from all the grid points in the KB. The data was then analyzed using a model to predict the susceptibility of each point to landslides. The feature importance of the RF result is shown in Figure 2. The result is

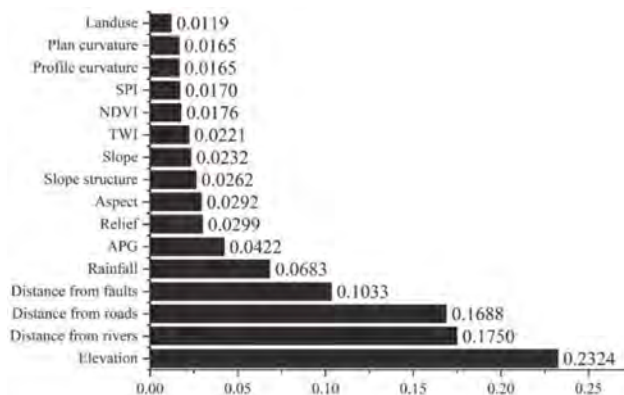


Figure 2. Feature importance of random forest model.

assigned to each grid point, and a raster layer is created. The raster layer is then divided into five categories using the natural break point grading method (Figure 3).

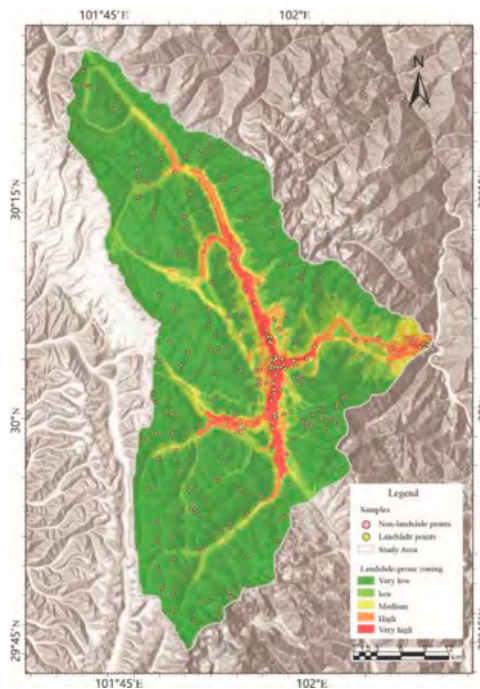


Figure 3. Landslide susceptibility based on random forest.

5 ASSOCIATION RULES - RANDOM FOREST MODEL EVALUATION RESULTS

The occurrence of landslide has a variety of influencing factors. In the landslide susceptibility, different environmental factors are used to characterize the impact of various aspects. When the input environmental factors are too many, the prediction results of the model may not achieve the best performance (Huang et al., 2021). A combination of environmental factors was screened out by the data mining method. Using this combination to input the random forest model can effectively reduce the negative effects of redundancy factors. Therefore, the Apriori algorithm was used to mine the data of environmental factors. Landslide susceptibility in KB based on factor screening is shown below (Figure 5). The feature importance of the RF result is shown in Figure 4.

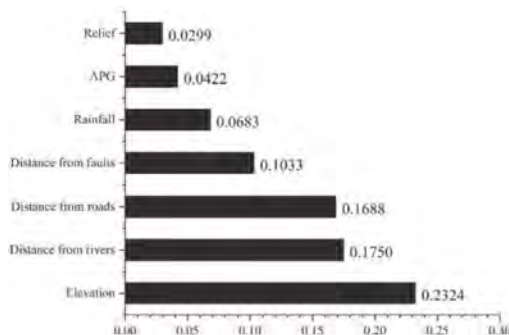


Figure 4. Feature importance of random forest model based on factor screening.

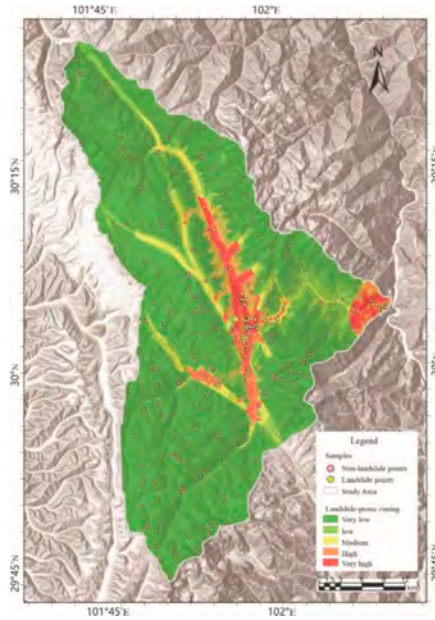


Figure 5. Landslide susceptibility of RF based on factor screening.

6 EVALUATE METRICS

The concept of frequency ratio accuracy is the ratio of the sum of the frequency ratios of extremely high and high-prone areas to the sum of all frequency ratios. The frequency ratio can characterize the nonlinear relationship between landslide and environmental factors, and can reflect the linkage of each attribute interval of the factor to the landslide susceptibility. The quantitative statistical frequency ratio formula is as follows:

$$FR = \frac{N_j/N}{S_j/S} \quad (3)$$

where N is the total area/number of landslides in the study area, N_j is the total area/number of landslides in the study area, S is the total area of the evaluation unit, and S_j is the area of the evaluation unit under the classification of the environmental factor. According to the statistical results, the accuracy of the random forest model is 0.969, and the accuracy of the association rule-random forest model is 0.950.

Cross-validation is a way to evaluate model performance by dividing a data set into a training set and a validation set. It can help to evaluate the generalization ability of the model. After cross-validation, the RF achieved a score of 0.899. The RF based on factor screening achieved a score of 0.904. The ROC curve provides a simple and intuitive approach for assessing the performance of a model. It is a commonly used accuracy test method in evaluating landslide susceptibility. The AUC of the area under the ROC curve ranged from [0.5, 1], and the model accuracy was particularly high when the AUC was higher than 0.9 (Li et al., 2021). The AUC values of the two models are 0.933 and 0.974, respectively. It shows that the accuracy of the model is higher, and the AUC value predicted by the environmental factors screened by association rules is higher. The ROC curve shows that the performance of the model based on factor screening is better.

7 CONCLUSIONS

The areas with the highest susceptibility are mostly located in the valleys of the Yala River and the Zheduo River, as well as near faults. These areas are primarily concentrated in urban

built-up areas that have experienced a lot of human engineering activities. This indicates that landslides occur in specific geological environments under particular conditions and are greatly influenced by human activities.

By using association rules and random forest models, the interference of redundant factors after optimizing the environmental factors for landslides can be eliminated. Additionally, when compared to the feature importance of random forests, association rules can make better identification of the nonlinear association among feature attributes.

The accuracy of both models was relatively high, but the RF based on factor screening showed better results with a higher AUC value and a better score of cross-validation. Therefore, it is recommended to use the association rule algorithm for screening environmental factors during the evaluation of landslide susceptibility.

ACKNOWLEDGEMENT

This study was supported financially by the Key Program of National Natural Science Foundation of China (Project No.: U1911202), the Key-Area Research and Development Program of Guangdong Province (Project No.: 2020B1111370001), the National Key Research and Development Program of China (Project No.: 2022YFF0801201).

We thank the anonymous reviewers for their valuable comments and suggestions to improve our manuscript.

REFERENCES

- Breiman, L. 2001. Random Forests. *Machine Learning* (45): 5–32.
- Chen, D., Sun, D., Wen, H. & Gu, Q. 2023. A study on landslide susceptibility of LightGBM-SHAP based on different factor screening methods. *Journal of Beijing Normal University (Natural Science)* 59(5):1–11.
- Cui, Y. & Bao, Z. 2016. Survey of association rule mining. *Application Research of Computers* 33(02): 330–334.
- Huang, F., Ye, Z., Jiang, S., Huang, J., Chang, Z. & Chen, J. 2021. Uncertainty study of landslide susceptibility prediction considering the different attribute interval numbers of environmental factors and different data-based models[J]. *CATENA*. 202: 105250.
- Şahin, E.K., Çölkesen, İ. & Kavzoğlu, T. 2018. A comparative assessment of canonical correlation forest, random forest, rotation forest and logistic regression methods for landslide susceptibility mapping. *Geocarto International* 35(4): 341–363.
- Guo, F., Lai, P., Huang F., Liu, L., Wang, X. & He, Z. 2023. Literature review and research progress of landslide susceptibility mapping based on knowledge graph. *Earth science*: 1–33.
- Lehner, B. & Grill, G. 2013. Global river hydrography and network routing: baseline data and new approaches to study the world's large river systems. *Hydrological Processes* 27(15): 2171–2186.
- Li, C., Li, X., Guo, C., Zhang, X. & Yang, Z. 2022. Seismic landslide hazards assessment along the Xianshuihe fault zone, Tibetan Plateau, China. *Geological Bulletin of China* 41(08): 1473–1486.
- Li, W.B., Fa, X., Huang, F., Wu, X., Yin, K. & Chang, Z. 2021. Uncertainties of landslide susceptibility modeling under different environmental factor connections and prediction models. *Earth Science* 46(10): 3777–3795.
- Li, Y., Xu, L., Zhang, L., Li, Z. & Su, N. 2023. Study on development patterns and susceptibility evaluation of coseismic landslides within mountainous regions influenced by strong earthquakes. *Earth science* 48(05): 1960–1976.
- Liu, J., Li, S., & Chen, T. 2018. Landslide susceptibility assesment based on optimized random forest model. *Geomatics and Information Science of Wuhan* 43(7): 1085–1091.
- Papi, R., Attarchi, S., Darvishi, B.A. & Neysani, S.N. 2022. Knowledge discovery of middle east dust sources using apriori spatial data mining algorithm. *Ecological Informatics* 72: 101867.
- Reichenbach, P., Rossi, M., Malamud, B.D., Mihir, M. & Guzzetti, F. 2018. A review of statistical-ly-based landslide susceptibility models. *Earth-Science Reviews* 180: 60–91.
- Sun, D., Wen, H., Wang, D & Xu, J. 2020. A random forest model of landslide susceptibility mapping based on hyperparameter optimization using the Bayes algorithm. *Geomorphology* 362: 107201.

Bibliometric data mining of machine learning in tunnel engineering research: A publication trends analysis and visualization

Y. Shen

Faculty of Public Safety and Emergency Management, Kunming University of Science and Technology, Kunming, China

S. Wu, Z. Xia, X. Wang & J. Wang

Faculty of Land Resources Engineering, Kunming University of Science and Technology, Kunming, China

ABSTRACT: In recent years, machine learning technology has rapidly advanced and found widespread application in various domains. To further explore its potential in tunnel engineering, this study employs bibliometric data mining to systematically review machine learning research in the context of tunnel engineering and their interconnections. Using specific search terms, relevant information was extracted from the Web of Science Core database and analyzed with VOSviewer, a bibliometric mapping analysis software, to visualize the network of recently published literatures and investigate interactions between machine learning and tunnel engineering research through citation networks. The analysis identified four distinct categories of machine learning research in tunnel engineering. Moreover, an examination of the connection and keyword co-occurrence networks in these two fields revealed challenges such as limited samples of actual engineering data and the constrained applicability of conventional machine learning models in tunnel engineering. These findings provide valuable insights for prospective research in this area.

1 INTRODUCTION

Tunneling has long played a vital role in modern infrastructure development. With the extensive construction of tunnels, there's an increasing emphasis on risk management in tunnel construction. Given the intricate technology, construction complexities, and elevated risks involved, tunnel projects are particularly susceptible to accidents that can disrupt construction timelines or, worse, lead to casualties. Consequently, the tunneling industry grapples with a multitude of intricate challenges. Inadequate handling of these issues can gravely jeopardize the safety of engineering personnel and property, and impede construction progress. In response to these challenges, engineers and researchers have been seeking innovative solutions.

In recent years, machine learning techniques have gained significant prominence and are being widely applied across various fields (Shen et al., 2023, Sun et al., 2023). In the realm of tunnel engineering, Luo et al. (2023) introduced a two-step rockburst prediction method, which integrates the stacking ensemble algorithm, a combined prediction model, and normal cloud theory. This method was utilized for predicting rockburst during the construction of the Grand Canyon tunnel. The results demonstrate that this machine learning approach effectively addresses the randomness and uncertainty associated with rockburst, rendering rockburst prediction more objective and reliable. Furthermore, the changes in rockburst risk within each section of the tunnel are visually represented through visualization techniques. Zhou et al. (2022a) presented a WOA-SVM model for predicting rock squeezing by enhancing the support vector machine model using the whale optimization algorithm, enabling accurate classification of rock squeezing types. Similarly, visual analysis and temporal prediction based

on deep learning have found widespread application in tunneling projects. Brien et al. (2023) devised a tunnel crack detection method for tunnel facility environments. They employed convolutional neural networks and transfer learning to automatically identify and classify tunnel cracks, providing a robust model. Wu et al. (2021) combined a graph theory spectral clustering algorithm with a deep neural network to propose a method that automatically identifies rock parameters in the TBM excavation process. This method dynamically adjusts the excavation parameters of the TBM according to the rock state, enabling interaction-aware prediction. This approach proves to be significantly more effective in real-time excavation parameter prediction when compared to traditional machine learning models, can predict the state of the rock and soil in front of the excavation tunnel in real time.

The application of machine learning in the field of tunneling is relatively new, and there are still numerous challenges that can be addressed through machine learning techniques. Scientometrics plays a crucial role in examining the research output of individual authors, literature, or collections of related works and institutions (Bapte and Kherde, 2020). This approach employs mathematical methods and visualizations to track published research results, enabling the identification of trends over specific time periods, thus, offering a comprehensive perspective of a particular field and creates a knowledge map of the scientific landscape.

This study aims to explore the research related to machine learning in tunneling using a scientometric approach. It seeks to provide a macro-level overview of the field, outlining its key characteristics, developmental trajectory, and delving into the potential advantages and limitations of machine learning applications within the tunneling domain. Section 2 address the research objectives, data sources, analysis software, and bibliometric methodologies employed. Section 3 present the findings of the analysis. Sections 4 and 5 provide discussion and conclusion, respectively.

2 METHODOLOGY

2.1 *Data source and search strategy*

Research data were covering the years 2000-2023 and obtained from Web of Science Core (WoSC). The WoSC database contains a large number of literature records covering a time span of up to several decades. This provides a rich source of data that can be used for bibliometric analysis, including trend analysis, partnership studies, author analysis, and citation network analysis, possessing high research value. Advanced search terms were used: “(TI = (“machine learning” OR “deep learning” OR “AI”) OR AB = (“machine learning” OR “deep learning” OR “AI”)) AND (TI = (tunnel) OR AB = (tunnel))”, the statistical data is up to October 13, 2023. Excluding the inclusion of terms such as “HTTP tunneling”, “DNA tunneling”, “cubital tunnel”, “ferroelectric tunnel”, and “wind tunnel” (which are only relevant to the fields of communication, medicine, physics, and meteorology), a total of 466 valid records were retrieved from the research publications on “AI + Tunnel”, and the researcher profiles with complete information were exported as plain text files.

2.2 *Bibliometric analysis*

VOSviewer is an analysis software developed by van Eck from Leiden University, the Netherlands, based on the JAVA platform for constructing visual bibliometric maps. Through its excellent image display capability, it presents large-scale sample data in the form of co-occurrence maps, year labeling maps, and density maps using keyword co-occurrence analysis, citation analysis, and other clustering methods.

There are others existing bibliometric mapping software such as Bibexcel and Citespace. However, Bibexcel can only construct a social relationship matrix and cannot create network clustering data, and its operation steps are extremely complex. Citespace cannot be used to distinguish the form of the grid in English data, whether singular or plural, leading to overlapping node label problems when forming a clustered network. In comparison to Citespace and Bibexcel,

VOSviewer offers the advantage of visualizing knowledge units in the literature with strong graphical presentation capabilities (Chen et al., 2023), making it suitable for analyzing large sample data (van Eck and Waltman, 2010). In this study, the open-access software VOSviewer was chosen to analyze the literature records obtained between 2000 and 2023 to explore the “AI + Tunnel” research hotspots and trends. Plain text files were imported into VOSviewer (version v1.6.19) to visualize high-frequency keywords, countries, journals, and relationships among authors, respectively.

3 RESULTS

3.1 The growth and output of publication

The statistical data is up to October 13, 2023, and a total of 466 documents have been retrieved from WoSC. The number of publications over the years is shown in Figure 1 and can be roughly divided into two phases. The first study to enter the WoSC database was conducted by Ince et al. (2010), who extracted features from rock cracks in tunnels and used SVM classifiers with fused probabilistic outputs to identify P-wave arrivals in noisy environments. Subsequently, machine learning research in tunneling remained in the first phase of near-stagnant development. The second stage is the development stage. Since the beginning of 2018, the number of related research publications has been growing rapidly, from 12 articles per year in 2018 to 149 articles per year in 2022. The number of publications for the year 2023 has also reached 116 literatures as of now, indicating a general trend of rapid development.

3.2 Source of publications

3.2.1 Countries or regions distribution of publications

Table 1 displays the distribution of the top 10 countries issuing “AI + Tunnel” publications from 2000 to 2023. The statistical approach considers any author’s affiliation with a specific country. China (330) leads in the number of publications, surpassing all other countries. Following China are the USA (41), Australia (29), Iran (29), and Singapore (22), with China notably having a significantly higher publication count than the other countries.

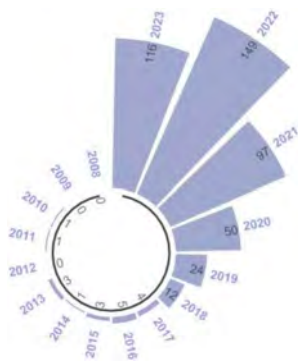


Figure 1. Number of the “AI + Tunnel” publications over the years.

Table 1. The top 10 countries distribution of the literature.

Rank.	Countries	No. of literature
1	China	330
2	USA	41
3	Australia	29
4	Iran	29
5	Singapore	22
6	Iraq	20
7	South Korea	19
8	Vietnam	15
9	Japan	14
10	England	13

3.2.2 Most preferred source

Figure 2 presents the citation density plot for various sources containing “AI + Tunnel”. Citations are displayed using labels, similar with the network visualization and coverage visualization. Each point in the citation density visualization represents a source, and the color

surrounding it indicates the citation density of that point. The colors range from blue to green to yellow. The point and its surrounding color are closer to yellow, the more citations are near that point, indicating the highest total number of citations.

Figure 2 shows the articles related to “AI + Tunnel” published in the top international journal *Tunnelling and Underground Space Technology (TUST)* have the highest total number of citations (1438 citations), followed by *Automation in Construction* (551 citations), *IEEE Transactions on Geoscience and Remote Sensing* (379 citations), *Computer-aided Civil and Infrastructure Engineering* (290 citations), and *Applied Sciences-base* (244 citations), and *Journal of Rock Mechanics and Geotechnical Engineering* (230 citations). It is worth noting that all of the mentioned journals belong to the top journals in ranking Q1 following the division by the Chinese Academy of Sciences, with the exception of *Applied Sciences-base*. *Applied Sciences-base* is an open-access journal that has gradually developed in recent years, and open-access journals enable authors to swiftly disseminate their articles through open access, thus enhancing the impact of the articles.

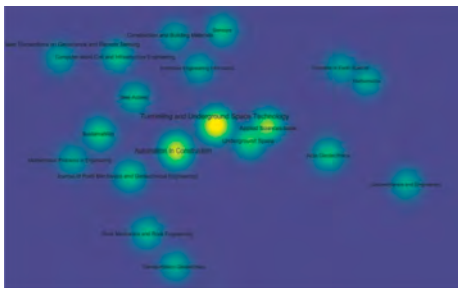


Figure 2. Citation density visualization of source in fields of “AI + Tunnel”.

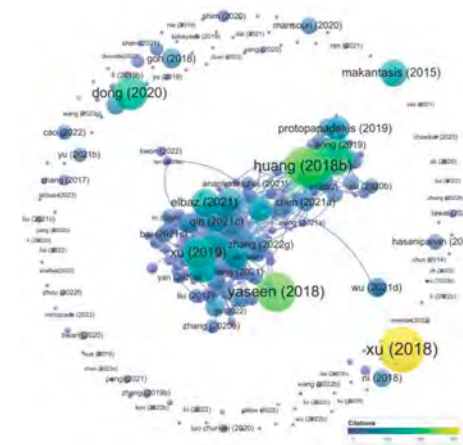


Figure 3. The most frequently citation publications.



Figure 4. Keywords co-occurrence analysis of “AI + Tunnel” publications.

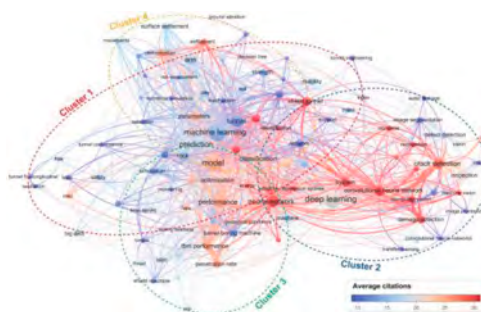


Figure 5. Keywords co-occurrence analysis of “AI + Tunnel” publications with avg. citations information.

3.2.3 Citation analysis

Citation analysis, as an effective method for assessing the impact and performance of academic publications, plays a crucial role in reflecting a paper's impact by counting the number of cited by other works. Figure 3 displays the most frequently cited publications in the field of "AI + Tunnel" during the period 2000-2023. To provide a concise representation, only the first author's last name and the year of publication are shown. The most cited paper is titled "Multisource Remote Sensing Data Classification Based on Convolutional Neural Network" by Xu et al. (2018) in the "IEEE Transactions on Geoscience and Remote Sensing", was cited 306 times. "Predicting Compressive Strength of Lightweight Foamed Concrete using an Extreme Learning Machine Model" by Yaseen et al. (2018) in the "Advances in Engineering Software" and "Deep Learning Based Image Recognition for Crack and Leakage Defects of Metro Shield Tunnel" by Huang et al. (2018) in the "Tunnelling and Underground Space Technology", which were collectively cited 226 and 224 times, respectively. Independent literature represents publications that are not cited within the collected literature. Therefore, it's worth noting that despite the high number of citations for the paper by Xu et al. (2018), it is not cited within the collected literature.

3.2.4 Keywords co-occurrence analysis

Keywords are closely associated with the specific content of literature, making the exploration of keyword relationships highly valuable for identifying key topics in the field of "AI + Tunnel". Utilizing text mining techniques, one can extract keywords and significant terminology from article titles, author-provided keywords, database-indexed keywords, and keyword co-occurrences in multiple documents.

Keywords with a co-occurrence frequency greater than 5 times are selected, synonymous keywords are merged, and meaningless keywords are eliminated. A keyword co-occurrence graph is then plotted, resulting in a total of 101 eligible keywords. Based on the color of keyword nodes in Figure 4, keywords can be categorized into four types. The size of the connecting dots in the graph indicates the frequency of keyword occurrence, and the thickness of the line between the keywords indicates the frequency of their co-occurrence in the same literatures. As depicted in Figure 4, there are four distinct clusters of terms, referred to as cluster 1 (red network), cluster 2 (blue network), cluster 3 (green network), and cluster 4 (yellow network).

Cluster 1 contains 38 keywords. It can be inferred that the primary focus of this literature is the utilization of conventional machine learning techniques to address issues such as regression or classification within the field of geotechnics. Cluster 2 includes 27 keywords. These pieces of literature lies in leveraging the capabilities of deep learning to process images, addressing issues related to crack detection and water leakage detection in tunneling engineering. This is predominantly approached from a visual analysis perspective to resolve tunneling engineering challenges. Cluster 3 comprises 24 keywords. These pieces of literature lies in utilizing machine learning models to address issues like predicting TBM boring behavior or time-series forecasting of boring efficiency in tunneling engineering. Cluster 4 comprises 12 keywords. It can be inferred that these pieces of literature are primarily concerned with topics such as feature selection and sensitivity analysis in the context of machine learning applied to tunneling.

Figure 5 displays the average citation rate of keywords in the field of "AI + Tunnel". The average citation rate for these terms is represented by the color changes. As seen in the figure, it is evident that cluster 2, which concentrates on addressing tunnel engineering through visual analytics, exhibits the highest average citation rate. This suggests that research based on deep learning in the context of tunnel engineering offers valuable insights and contributes significantly to solving real-world issues and exploring critical domains. Furthermore, the application of machine learning models to conduct research related to tunnel boring machine (TBM) has garnered interest and attention from other scholars.

4 DISCUSSION

4.1 *Summary of main research of machine learning in tunnelling engineering*

A comprehensive evaluation of the literature in the field of “AI + Tunnel” was conducted using bibliometric analysis. Overall, various “AI + Tunnel” studies have garnered increasing attention over the past two decades. China leads with the highest number of publications, followed by the United States and Australia. In contrast, some developing countries, including those in Africa (e.g., Tunisia, Sudan) and the Middle East (e.g., United Arab Emirates), have made limited contributions to research in this field. Furthermore, there has been a significant increase in the number of publications in this field after 2017. This growth can be attributed to the rapid development of deep learning and big data during this period, as well as the development and deployment of machine learning models facilitated by open-access deep learning frameworks and tools like TensorFlow 1.0 and PyTorch, which were released in 2017. The widespread use of these tools has reduced the barriers to entry for the development of machine learning applications, thereby contributing to the advancement of research in machine learning within tunnel engineering.

In terms of journal analysis, the majority of “AI + Tunnel” articles originate from “Tunnelling and Underground Space Technology”. This journal holds a prominent position in the field of underground engineering. Its articles are widely cited, and its impact factor signifies its importance in the academic world. The journal encompasses original research and case studies on the advancement of tunnelling technology, underground space utilization, and trenchless technology. As a result, it is widely acknowledged as a significant academic journal within the field of underground engineering. The inclusion of research articles related to “AI + Tunnel” in this journal underscores the attention and recognition that the field of “AI + Tunnel” has garnered from experts and scholars.

In terms of citation analysis, the content most frequently referenced in the relationship network with cross-references (the central position in Figure 3) pertains to deep learning-based tunnel crack identification and the use of deep learning technology for predicting TBM boring efficiency. These concepts offer new insights for tunnel engineering research and technical professionals. Simultaneously, several scholars have pointed out that one of the impediments to the application of deep learning in tunnel engineering is the currently insufficient amount of available data (Protopapadakis et al., 2019, Zhou et al., 2022b, Zhang et al., 2022). Presently, there aren't enough real cases to adequately train deep learning models, often resulting in sub-optimal prediction performance. Instead, models with advantages in handling small sample sizes (support vector machine, random forest, etc.) are more commonly utilized.

4.2 *Association and difference of keywords cluster*

Figure 4 displays the four clusters of “AI + Tunnel” are interconnected rather than isolated from each other. There is a relatively close connection among these clusters. Cluster 1, for instance, indicates that current research often employs conventional machine learning to address regression or classification problems in tunnel engineering. Regression analysis is frequently used for tasks like tunnel convergence prediction and rock uniaxial compressive strength prediction. Classification analysis is often applied to predict rockburst intensity and surrounding rock grade. In Cluster 3, many scholars tend to collect extensive field data from a single engineering example or create time-series samples through long-term monitoring. They then apply deep learning techniques to make predictions. For instance, Gao et al. (2021) gathered 2570 sets of data from the water conveyance tunnel of the Hangzhou Second Water Source project, divided the data in a 9:1 ratio, and used a long short-term memory neural network model to predict the penetration rate of the TBM for the project. The proposed model achieved mean squared error and mean absolute error values of 4.733 and 3.204, respectively. Cluster 2 suggests that the application of deep learning in visual analytics surpasses that of traditional machine learning. Deep learning models possess a multi-level representation capability for extracting information, mapping from low-level features to high-level abstract

features. This enables deep learning models to better understand the hierarchical structure in an image and excel at visual tasks such as tunnel crack recognition (Daneshgaran et al., 2019, Zhou et al., 2023). Furthermore, feature selection in Cluster 1 tends to have closer to conventional machine learning in Cluster 2. This is because conventional machine learning typically requires manual feature screening, and feature selection can eliminate irrelevant or redundant features, and reduces the number of features, thus enhancing model accuracy and reducing runtime.

Additionally, as observed from Figure 5, it is noticeable that studies based on the application of conventional machine learning in tunnel engineering have a relatively low average citation rate, despite having a higher number of publications. When considering these published articles, two primary reasons contribute to this issue. Firstly, some studies lack practical applicability. They only employ test samples with distributions similar to the training set for assessing the model's predictive performance, and lacking practical application. Without ample experiments to establish the generalizability of their models, they often struggle to gain widespread recognition. Secondly, the model's lack of interpretability serves as another crucial factor in the limited recognition of such studies. Some studies fail to provide explanations for the model-building and prediction processes. Models lacking interpretability may encounter difficulties in gaining trust and adoption by decision-makers. This issue is particularly significant in critical application areas like tunneling, which involve substantial risk and safety requirements. The "black-box" problem inherent to predictive modeling significantly hinders the adoption of machine learning models in tunneling (Phoon and Zhang, 2023).

4.3 *The research limitations*

It's important to acknowledge certain limitations in interpreting the results of this study. Firstly, this study only conducted searches within the WoSC database. While WoSC is one of the largest databases globally, it does not encompass all research on "AI + Tunnel". Complementary databases such as PubMed and Scopus could be used in conjunction for a more comprehensive analysis. Moreover, despite using a reasonably comprehensive set of keywords to retrieve relevant literature, it is important to note that it is impossible to completely eliminate the possibility of missing a small number of pertinent articles using only those specific keywords.

Considering the limitations of this paper, it is advisable to perform a more in-depth content analysis, possibly by manually examining the references of "AI + Tunnel" studies to consider those that are reasonably relevant. Nevertheless, this task cannot guarantee the inclusion of all relevant literature. It may not be essential to account for every individual study when analyzing research trends in the field of "AI + Tunnel", as the co-citation relationships among most of the literatures can be employed to summarize the prevailing patterns in existing studies.

4.4 *Future research of machine learning in tunnelling engineering*

The results of the bibliometric analysis yield several positive aspects and offer the following outlook for research related to "AI + tunnel":

- Considering the analysis of the citation density graph, the rise of open-access journals and the shift from subscription-based journals will collectively propel the "AI + tunnel" field towards increased openness, collaboration, and transparency, which can facilitate knowledge sharing and foster scientific research progress on a global scale.
- The scarcity of datasets in the field of tunnel engineering is undoubtedly a challenge, and it is imperative to actively encourage governments, academic institutions, and industry groups to promote the openness and sharing of as many available datasets as possible. Despite the current limitations in tunnel engineering datasets, with the ongoing development of technology and collaboration, it can be anticipated that more datasets will become accessible for machine learning research and application in the future. For instance, the "TBM

Tunneling Parameter Data Sharing and Machine Learning Competition”, organized by the Chinese Society of Rock Mechanics and Engineering (CSRME), has enhanced China’s TBM big data mining and construction intelligence through open datasets (Li et al., 2023).

5 CONCLUSION

A scientometrics of the publications and distribution of “AI + tunnel” was conducted, covering aspects such as the year of publication, country, journal of publication, citation network, keyword co-citation network, and other relevant information.

In summary, from 2018 to 2023, the total number of “AI + tunnel” studies showed a steady increase year by year. China, the United States, and Australia are the top three countries with the highest publication rates of “AI + tunnel” literatures.

The most cited journals publishing articles related to the field of “AI + tunnel” include “Tunnelling and Underground Space Technology”, “Automation in Construction”, and “IEEE Transactions on Geoscience and Remote Sensing”. Additionally, “Applied Sciences-basel”, representing open-access journals that have gained prominence in recent years, also exhibits a relatively high citation rate owing to its open-access advantages. Currently, research topics with high citation rates predominantly revolve around the identification of tunnel cracks and the prediction of TBM boring efficiency, signaling their significant attention in those field.

Keyword analysis reveals that the “AI + tunnel” field can be categorized into four main areas. These categories are interrelated. It should be emphasized that the application of conventional machine learning in tunnel engineering exhibiting a relatively lower average citation rate, despite having a higher number of publications.

The application of deep learning in tunnel engineering is hindered by the insufficient amount of data. In the traditional machine learning field, the limited practicality of predictive models obtained from training and the “black-box” problem significantly impede the practical adoption of machine learning models in tunnel engineering. This raises controversy regarding their practical applicability in the field. Efforts should be made to promote the openness and sharing of more available datasets. Simultaneously, promoting the development of machine learning model interpretability will facilitate the practical implementation of machine learning in real engineering scenarios, which will contribute to achieving the digital transformation of tunnel engineering.

REFERENCES

- Bapte, V. D. & Kherde, M. R. (2020) The research output of State Universities in Vidarbha Region of Maharashtra: A scientometrics study. *International Journal of Information Dissemination and Technology*, 10, 141–147.
- Brien, D. O., Osborne, J. A., Perez-Duenas, E., Cunningham, R. & Li, Z. L. (2023) Automated crack classification for the CERN underground tunnel infrastructure using deep learning. *Tunnelling and Underground Space Technology*, 131, 15.
- Chen, X., Zhang, Y., Xu, S. & Dong, F. (2023) Bibliometric analysis for research trends and hotspots in heat and mass transfer and its management of proton exchange membrane fuel cells. *Applied Energy*, 333, 15.
- Daneshgaran, F., Zacheo, L., DI Stasio, F. & Mondin, M. (2019) Use of Deep Learning for Automatic Detection of Cracks in Tunnels: Prototype-2 Developed in the 2017-2018 Time Period. *Transportation Research Record*, 2673, 44–50.
- Gao, B. Y., Wang, R. R., Lin, C. J., Guo, X., Liu, B. & Zhang, W. G. (2021) TBM penetration rate prediction based on the long short-term memory neural network. *Underground Space*, 6, 718–731.
- Huang, H. W., Li, Q. T. & Zhang, D. M. (2018) Deep learning based image recognition for crack and leakage defects of metro shield tunnel. *Tunnelling and Underground Space Technology*, 77, 166–176.
- Ince, N. F., Kao, C. S., Kaveh, M., Tewfik, A. & Labuz, J. F. (2010) A Machine Learning Approach for Locating Acoustic Emission. *Eurasip Journal on Advances in Signal Processing*, 14.

- Li, J. B., Chen, Z. Y., Li, X., Jing, L. J., Zhangf, Y. P., Xiao, H. H., Wang, S. J., Yang, W. K., Wu, L. J., Li, P. Y., Li, H. B., Yao, M. & Fan, L. T. (2023) Feedback on a shared big dataset for intelligent TBM Part I: Feature extraction and machine learning methods. *Underground Space*, 11, 1–25.
- Luo, H., Fang, Y., Wang, J. F., Wang, Y. B., Liao, H., Yu, T. & Yao, Z. G. (2023) Combined prediction of rockburst based on multiple factors and stacking ensemble algorithm. *Underground Space*, 13, 241–261.
- Phoon, K. K. & Zhang, W. G. (2023) Future of machine learning in geotechnics. *Georisk-Assessment and Management of Risk for Engineered Systems and Geohazards*, 17, 7–22.
- Protopapadakis, E., Voulodimos, A., Doulamis, A., Doulamis, N. & Stathaki, T. (2019) Automatic crack detection for tunnel inspection using deep learning and heuristic image post-processing. *Applied Intelligence*, 49, 2793–2806.
- Shen, Y., Wu, S., Cheng, H., Zhang, H., Wang, J., Yang, Z., An, H. & Song, X. (2023) Uncertainty analysis method of slope safety factor based on quantile-based ensemble learning. *Bulletin of Engineering Geology and the Environment*, 82, 87.
- Sun, J. L., Wu, S. C., Wang, H., Wang, T., Geng, X. J. & Zhang, Y. J. (2023) Inversion of Surrounding Rock Mechanical Parameters in a Soft Rock Tunnel Based on a Hybrid Model EO-LightGBM. *Rock Mechanics and Rock Engineering*, 17.
- Van Eck, N. J. & Waltman, L. (2010) Software survey: VOSviewer, a computer program for bibliometric mapping. *Scientometrics*, 84, 523–538.
- Wu, Z. J., Wei, R. L., Chu, Z. F. & Liu, Q. S. (2021) Real-time rock mass condition prediction with TBM tunneling big data using a novel rock-machine mutual feedback perception method. *Journal of Rock Mechanics and Geotechnical Engineering*, 13, 1311–1325.
- Xu, X. D., Li, W., Ran, Q., Du, Q., Gao, L. R. & Zhang, B. (2018) Multisource Remote Sensing Data Classification Based on Convolutional Neural Network. *Ieee Transactions on Geoscience and Remote Sensing*, 56, 937–949.
- Yaseen, Z. M., Deo, R. C., Hilal, A., Abd, A. M., Bueno, L. C., Salcedo-Sanz, S. & Nehdi, M. L. (2018) Predicting compressive strength of lightweight foamed concrete using extreme learning machine model. *Advances in Engineering Software*, 115, 112–125.
- Zhang, D. M., Shen, Y. M., Huang, Z. K. & Xie, X. C. (2022) Auto machine learning-based modelling and prediction of excavation-induced tunnel displacement. *Journal of Rock Mechanics and Geotechnical Engineering*, 14, 1100–1114.
- Zhou, J., Zhu, S., Qiu, Y., Armaghani, D. J., Zhou, A. & Yong, W. (2022a) Predicting tunnel squeezing using support vector machine optimized by whale optimization algorithm. *Acta Geotechnica*, 17, 1343–1366.
- Zhou, Q., Qu, Z., Li, Y. X. & Ju, F. R. (2022b) Tunnel Crack Detection With Linear Seam Based on Mixed Attention and Multiscale Feature Fusion. *Ieee Transactions on Instrumentation and Measurement*, 71, 11.
- Zhou, Z., Zhang, J. J., Gong, C. J. & Wu, W. (2023) Automatic tunnel lining crack detection via deep learning with generative adversarial network-based data augmentation. *Underground Space*, 9, 140–154.

Effects of measurement data size on Bayesian updating of excavation-induced deflection

C. Tang, S.Y. He & W.H. Zhou

State Key Laboratory of Internet of Things for Smart City and Department of Civil and Environmental Engineering, University of Macau, Macau SAR, China

ABSTRACT: Quantifying uncertainty is crucial for enhancing the reliability of geotechnical engineering designs and reducing potential risks. Bayesian inference is commonly used for this purpose, yet the impact of measurement data size on updating results remains underexplored. This study takes the excavation-induced wall deflection as a research demonstration, analyzing the influence of measured data size on Bayesian updates in the context of the TNEC excavation. Results demonstrate that utilizing five or more measured points yields satisfactory predictive outcomes ($R^2 > 0.90$). The variation in MPI values quantitatively reflects decreasing uncertainty with an increasing number of measurement points, while changes in PICP indicate the combined influence of predictive performance and confidence interval width on the probability of measured points falling within the predicted range. This research provides insights into using suitable measurement data sizes for robust parameter calibration and effective predictive performance in Bayesian updating for geotechnical engineering.

Keywords: Bayesian updating, measurement data size, deflection, uncertainty

1 INTRODUCTION

The construction of urban infrastructures, such as high-rise buildings and subway stations, requires deep excavation as an essential step. Wall deflection is a primary concern during excavations, as excessive deformation has the potential to inflict damage on both retaining structures and adjacent infrastructures (Ou et al., 2000; Goh et al., 2017; Jin et al., 2019a). To avoid such potential risks, it is crucial to accurately assess the excavations-induced deflection.

In practice, excavation is an intricate process encompassing numerous uncertainties stemming from soil properties, model bias, measurement error, construction quality, and various environmental factors, among others (Juang et al., 2013; Qi and Zhou, 2017; Jin et al., 2021). Consequently, the assessment of wall deflection may diverge considerably from on-site observations. A practical approach to address associated uncertainties and enhance assessment accuracy involves employing Bayesian updating methods to incorporate information gained from field observations for refining the initial design (e.g., Jin et al., 2021; Yang et al., 2021). Juang et al. (2013) initially introduced a Bayesian framework for predicting the maximum wall deflection in braced excavations, employing the KJHH model as the assessment model. Qi and Zhou (2017) aimed to enhance updating efficiency in predicting the maximum wall deflection by using field deflection data at multiple points. They concluded that integrating observations from multiple points into the Bayesian updating framework resulted in more accurate predictions with reduced uncertainties. Tang et al. (2023) incorporated a beam on elastic foundation model (BEFM) into the Bayesian framework for evaluating wall deflection. They included all observed deflection data within this framework, revealing that the BEFM exhibited strong predictive performance at the initial updating stage, benefitting from the utilization of all points in the observed deflection dataset in the Bayesian updating process. The

aforementioned studies suggest that the size of measurement data utilized in the Bayesian updating process significantly influences the updating outcomes.

In theory, the integration of more observational data into the Bayesian framework is expected to empower the likelihood function progressively within the posterior distribution. Insufficient measurement data may not be adequate to effectively update uncertain parameters and yield unsatisfactory prediction results. This raises the question of how much measured information can provide effective parameter calibration in geotechnical engineering. Additionally, the uncertainty in updating parameters tends to decrease as more measurement data points are used. However, the relationship between the degree of uncertainty reduction and the size of the measurement data used has not been investigated. Therefore, a study on the impact of the measurement data size on updating outcomes would be meaningful.

This study aims to primarily explore the influence of different measurement data size on Bayesian updating outcomes within the field of geotechnical engineering, using excavation-induced deflection as an illustrative example. The research will utilize the BEFM proposed by Tang et al. (2023) as the model for deflection estimations, incorporating considerations for both measurement error and model bias in the Bayesian updating process.

2 METHODOLOGY

2.1 BEFM for deflection estimations

In this study, the BEFM proposed by Tang et al. (2023) is employed to assess excavation-induced wall deflection. The basic idea of the BEFM is to simulate soil-structure interactions through a series of individual springs. The soil spring constant, also referred to as the foundation modulus, is the ratio of stress to displacement based on the assumptions of the Winkler model (Ou, 2006; Liu and Wang, 2009; MOHURD, 2012; SMCHURD, 2018; Tang et al., 2023). In this model, the retaining wall is simulated as a vertically placed continuous beam of a unit width under plane strain conditions (Liu and Wang, 2009; Guo et al., 2019). The struts are simplified as spring supports, with the soil below the excavation bottom modeled as soil springs. A schematic diagram of the BEFM can be seen in Figure 1. The governing equation can be expressed as follows (Ou, 2006; Liu and Wang, 2009; MOHURD, 2012; SMCHURD, 2018):

$$EI \frac{d^4 y}{dz^4} + cf(z) \cdot y \cdot b_0 - e_a(z)b_0 = 0 \quad (1)$$

where b_0 is the calculation width, usually set to 1m (i.e., unit width) for the retaining wall, and E and I are Young's modulus and area moment of inertia of the wall, respectively. Thus, EI denotes the bending stiffness of the wall per unit width. y is the lateral wall deflection, z is the

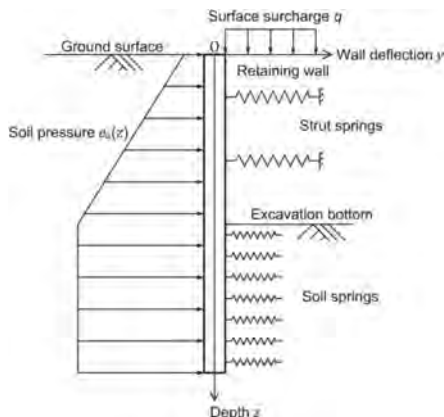


Figure 1. BEFM for wall deflection estimations.

depth below the ground surface, $e_a(z)$ is the Rankine active earth pressure at depth z , and $cf(z)$ is the soil spring constant at depth z .

Based on engineering experience, the soil spring constant (soil resistance) is commonly assumed to increase linearly with the depth below the excavation surface (Liu and Wang, 2009; Gong and Hou, 2017), and can be expressed as follows:

$$cf(z) = \begin{cases} 0 & (0 \leq z < h_r) \\ k_s z_b & (z \geq h_r) \end{cases} \quad (2)$$

where k_s is the slope of soil spring constant, z_b is depth below the excavation bottom (i.e., $z_b = z - h_r$), and h_r denotes the excavation depth at the r th stage.

In the BEFM, the soil pressure is calculated using the Rankine active earth pressure theory above the excavation bottom but remains constant below the excavation bottom. In this study, $e_a(z)$ is simplified as trapezoidal distribution above the excavation bottom and can be expressed as follows:

$$e_a(z) = \begin{cases} k_a(z + \frac{q}{\gamma_{wei}})(0 \leq z < h_r) \\ k_a(h_r + \frac{q}{\gamma_{wei}}) & (z \geq h_r) \end{cases} \quad (3)$$

where k_a is the slope of soil pressure above the excavation surface, q is the surface surcharge around the excavation, and γ_{wei} represents the weighted unit weight of soil layers based on their respective thickness.

The struts (or slab floors) are regarded as elastic supports, bearing only axial forces. The reactions of struts are computed by (MOHURD, 2012; SMCHURD, 2018):

$$T^{(u)} = K_{strut}^{(u)}(y_{now}^{(u)} - y_0^{(u)}) - P_{pre}b_0 \quad (4)$$

where $K_{strut}^{(u)}$ is the axial stiffness of the u th strut; $y_{now}^{(u)}$ is the current deflection at the depth of the u th strut; $y_0^{(u)}$ is the initial deflection at the depth of the u th strut before the strut has been installed; P_{pre} is the preload of steel struts per calculation width.

The axial stiffness of struts is computed by (MOHURD, 2012):

$$K_{strut} = \frac{\alpha_R b_0 E_{strut} A_{strut}}{\lambda_0 S_{strut} L_{strut}} \quad (5)$$

where α_R is the relaxation coefficient of struts, $\alpha_R=1.0$ is for concrete struts (slab floors) or steel struts with preload, and $\alpha_R=0.8-1.0$ is for steel struts without preload. E_{strut} , A_{strut} , S_{strut} , and L_{strut} are Young's modulus, equivalent cross-section area, average horizontal spacing, and length of struts, respectively. λ_0 is the adjustment factor of the fixed point to consider the unsymmetrical load effect from two sides of the excavation. For symmetrical excavations, λ_0 is set to 0.5. If floor slabs are used as supports in an excavation constructed using the top-down method, S_{strut} should be set to 1 m.

It is noteworthy that the slope of the soil spring constant k_s and the slope of soil pressure k_a are considered as uncertain parameters, since their values mainly depend on highly variable soil properties. For simplicity, hereafter k_s and k_a are referenced as the soil resistance factor and the soil pressure factor, respectively.

The wall deflection is calculated by solving the BEFM, as described by Eq. (1), using a finite element algorithm (Reddy, 2006). The details of this algorithm can be found in Tang et al., (2023).

2.2 Bayesian probabilistic method

In this study, the Bayesian method is adopted as the probabilistic framework to integrate prior and observed information in a systematic manner to improve prediction accuracy. In

order to account for both model bias and measurement error, the implementation of the Bayesian method is initiated by expressing the observations as follows (Li et al., 2021; Wang et al., 2022):

$$Y = c \cdot \eta(\boldsymbol{\theta}_m) + \varepsilon = \delta(\boldsymbol{\theta}) + \varepsilon \quad (6)$$

where Y denotes field observations (i.e., observed wall deflection or ground settlement), and $\delta(\boldsymbol{\theta}) = c \cdot \eta(\boldsymbol{\theta}_m)$ represents corresponding predictions considering model bias. $\boldsymbol{\theta}_m$ denotes the vector of uncertain model parameters. c represents the model bias factor that is adopted for characterizing the model uncertainty, which is often assumed to follow a normal or lognormal distribution with a mean of 1.0. ε is the measurement error that is assumed to be a zero-mean normal random variable with a standard deviation (SD) of σ_ε . Notably, c is another uncertain parameter beyond $\boldsymbol{\theta}_m$. Accordingly, the uncertain parameters vector $\boldsymbol{\theta}$ that includes the uncertain model parameters and the model bias can be expressed as $\boldsymbol{\theta} = [\boldsymbol{\theta}_m, c]$.

Specifically, the vector of uncertain parameters $\boldsymbol{\theta}$ in the proposed method can be summarized as $[k_s, k_a, c]^T$, with c represented the model bias factor for assessments of deflection.

The vector $\boldsymbol{\theta}$ and its uncertainty can be derived from a posterior probability density function (PDF) based on Bayes' theorem, which is expressed as follows (Yuen, 2010; Zhou et al., 2018, 2021; Jin et al., 2019b; He et al., 2024):

$$f(\boldsymbol{\theta}|Y) = f(\boldsymbol{\theta})f(Y|\boldsymbol{\theta})/f(Y) \quad (7)$$

where $f(\boldsymbol{\theta})$ is the prior PDF of $\boldsymbol{\theta}$ which represents the user's judgments or previous knowledge before the data Y are observed. $f(Y)$ is a normalization factor that guarantees a unity for the cumulative probability over the entire range of $\boldsymbol{\theta}$. $f(Y|\boldsymbol{\theta})$ is the likelihood function that expresses the degree to which the observed data Y fit the model predictions given the values of the parameters $\boldsymbol{\theta}$. If the measurement errors at different observed points are assumed to be statistically independent, the likelihood function can be expressed as:

$$f(Y|\boldsymbol{\theta}) = (2\pi\sigma_\varepsilon^2)^{-\frac{N}{2}} \exp\left\{-\frac{\sum_{n=1}^N [y_n - \delta_n(\boldsymbol{\theta})]^2}{2\sigma_\varepsilon^2}\right\} \quad (8)$$

where y_n and $\delta_n(\boldsymbol{\theta})$ are observations and predictions at the n th observed point. N denotes the total number of observed points.

In this study, the posterior PDF is obtained by using the differential evolution Markov chain Monte Carlo (DE-MCMC) algorithm (Braak, 2006; Nelson et al., 2013). The implementation of the DE-MCMC algorithm is conducted by the emcee package developed by Foreman-Mackey et al. (2013).

3 FIELD CASE STUDY OF TNEC EXCAVATION

The proposed method is first validated through a case study of the Taipei National Enterprise Center (TNEC) excavation, which has well-documented and high-quality observed data (Ou et al., 1998, 2000; Jin et al., 2019a; Fan et al., 2021). Figure 2 depicts the soil profile and cross-section of the TNEC excavation. The excavation was carried out in seven stages using the top-down construction method and was supported by a 0.9 m-thick diaphragm wall and horizontal struts (i.e., concrete slabs and steel struts). The maximum excavation depth and width were 19.7 m and 41.2 m, respectively. The subsoil at the TNEC site consisted of six alternating layers of silty clay and fine sand, overlying a dense gravel soil hard stratum layer. The groundwater table was located 2.0 meters below the ground surface prior to excavation. Further information about the TNEC excavation can be found in Ou et al. (1998, 2000).

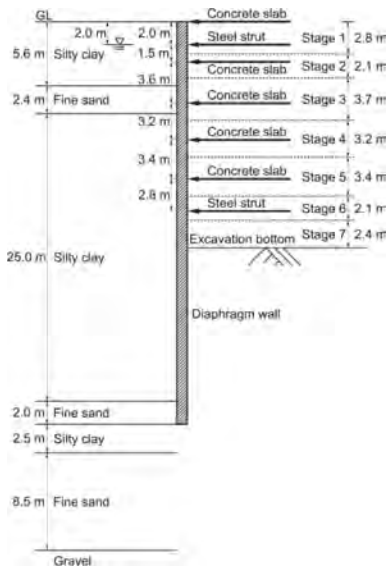


Figure 2. Soil profile and cross-section of the TNEC excavation.

3.1 Parameters setting

The prior PDFs must be determined before conducting the calculations. As there is no established method for determining the exact value of the soil resistance factor k_s (Ou, 2006; Liu and Wang, 2009), this parameter is assumed to follow an uninformative distribution (i.e., the uniform distribution). The prior PDFs for the remaining parameters are assumed to be log-normal distributions, thereby ensuring that the parameter values remain positive (Juang et al., 2013; Wang et al., 2012; Zheng et al., 2018). Notably, the coefficients of variation (COVs) for these normal distributions are uniformly set to 0.30, following the recommendations of pertinent studies concerning geotechnical variability and Bayesian updating (Phoon and Kulhawy, 1999; Zhang et al., 2009; Qi and Zhou, 2017; Jin et al., 2021). Furthermore, the SD of the

Table 1. Summary of prior knowledge for uncertain parameters.

Uncertain parameters	Distributions	Mean (Lower bound)	COV (Upper bound)
k_s (kN/m ⁴)	Uniform	0	1.00×10^4
k_a (kN/m ³)	Lognormal	1.17×10^1	0.30
c	Lognormal	1.00	0.30

Note: The lower and upper bounds in parentheses denote the bounds for the uniform prior PDF.

Table 2. Different numbers of measurement points used in the Bayesian updating.

Number of measurement points	Corresponding depth coordinates (m)	Coordinates spacing (m)
35	1, 2, 3,, 35	1
18	1, 3, 5,, 35	2
12	1, 4, 7,, 34	3
9	1, 5, 9,, 33	4
7	1, 6, 11,, 31	5
6	1, 7, 13,, 31	6
5	1, 9, 17,, 33	8
4	1, 12, 23, 34	11
3	1, 18, 35	17

measurement error, denoted as σ_{ϵ_s} , is assumed to be 2 mm based on the previous studies and practical experiences (Ou et al, 1998, 2000; Calvello, 2002; Kelly and Huang, 2015; Qi and Zhou, 2017). Table 1 summarizes the prior PDFs used in this case.

In this study, the updating procedure commences from stage 3, as observations from earlier stages often exhibit larger relative measurement errors and undergo inevitable changes in the deformation pattern (Juang et al., 2013; Qi and Zhou, 2017). Tang et al. (2023) highlighted the favorable predictive performance of BEFM in the initial updating stage (i.e., stage 3), leveraging the utilization of all available measurement data in Bayesian updating. This study succinctly explores the influence of measurement data size on Bayesian updates, employing the deflection measured exclusively in the third stage as an illustrative example. The measurement data for stage 3 comprises 35 points, covering depths from 1m to 35m, with adjacent monitoring points spaced at 1m intervals. To analyze the impact of measurement data size, updates are conducted using varying numbers of measurement points, as outlined in Table 2.

In DE-MCMC, each chain is configured to generate 3000 samples, with the initial burn-in stage set to produce 1000 samples. Additionally, 20 chains are employed for each uncertain parameter. To ensure effective sampling, the potential scale reduction factor (PSRF), is calculated and found to be very close to 1.0, indicating the Markov chains have converged (Gelman et al., 2013; Roy, 2020; Li et al., 2021).

3.2 Effects of measurement data sizes

In this study, different amounts of information from observations are incorporated into the Bayesian framework to refine the prior knowledge of the uncertain parameters. Figure 3 compares prior distributions and posterior distributions updated by different sizes of field observations for three uncertain parameters. The distributions exhibit diminishing variability as more measured information is introduced, underscoring the refinement of our understanding with increased observational input. As the quantity of measured information employed in the Bayesian update increases, the posterior distributions of k_s and k_a undergo a transition from lognormal to normal distributions. In contrast, the distribution of c consistently maintains a normal form throughout. This is likely attributed to the fact that model bias c is more significantly influenced by measured information (i.e., likelihood function) compared to k_s and k_a , as illustrated in Eq. (6).

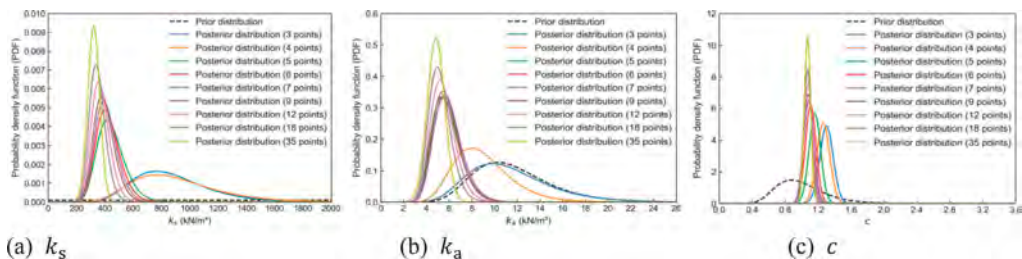


Figure 3. Prior and posterior distributions of uncertain parameters.

Deflection predictions for subsequent stages are derived through Monte Carlo simulations employing the updated parameters. Figure 4 provides a comparative analysis of measured and predicted deflections at stages 4 to 7, utilizing posterior distributions updated at stage 3. This illustration specifically examines a scenario where only 35 measurement points were used for the update, serving as a representative example. The shaded region in the figure represents the 95% confidence interval (CI) of the predictions. The results demonstrate a significant concordance between the predicted curves and observed data, indicating effective calibration of the prediction model with field information through the Bayesian framework.

To explore the impact of the measured data size on predictive performance, Figure 5 depicts the variation in the coefficient of determination (R^2) between predictions and observations with

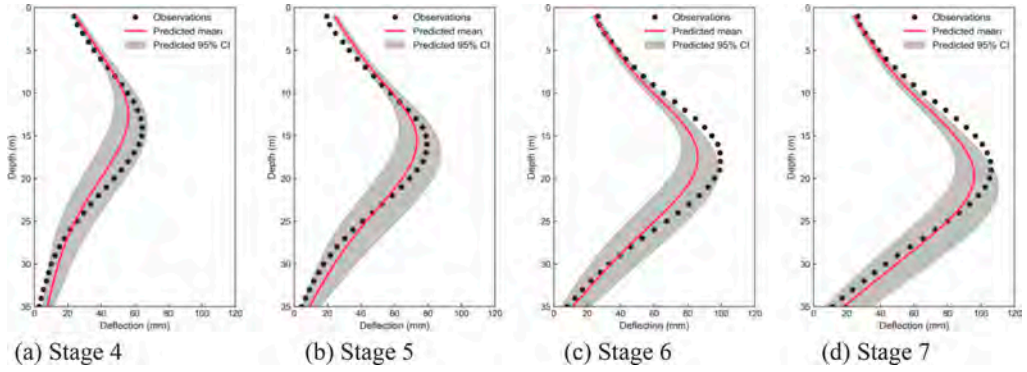


Figure 4. Measured and predicted wall deflection based on posterior distributions (35 points).

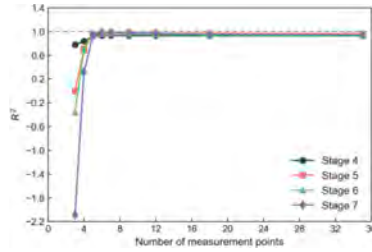


Figure 5. Variations of R^2 values with number of measurement points.

changes in the number of measured points. The R^2 values exhibit a significant increase until 5 points of measurement data are utilized, and consistently exceed 0.90 for stages 4 to 7 when employing measured data comprising 5 points or more. This observation suggests that the information obtained from 5 points is sufficient to attain a high level of prediction performance.

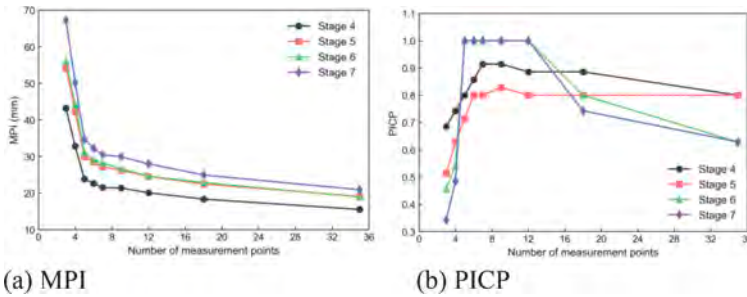


Figure 6. Variations of MPI and PICP values with number of measurement points.

To further investigate the effects of the measured data size on the uncertainties of the predictions, two statistics, mean prediction interval (MPI) and prediction interval coverage probability (PICP), are used. MPI represents the mean width of the prediction interval, with lower values indicating less uncertainty. On the other hand, PICP quantifies the percentage of observed values that fall within the prediction interval (Shrestha and Solomatine, 2006; Rahmati et al., 2019; Cheng et al., 2023). The calculations for MPI and PICP are as follows:

$$\text{MPI} = \frac{1}{N} \sum_{n=1}^N (PL_n^{\text{upper}} - PL_n^{\text{lower}}) \quad (9)$$

$$\text{PICP} = \frac{1}{N} \sum_{n=1}^N C, C = \begin{cases} 1, PL_n^{\text{lower}} \leq y_n \leq PL_n^{\text{upper}} \\ 0, \text{otherwise} \end{cases} \quad (10)$$

where y_n is the observed deflection; PL_n^{lower} and PL_n^{upper} are the lower and upper prediction limits, respectively.

Figure 6 illustrates the variations in MPI and PICP values with the number of measurement points, where the 95% CI boundaries are considered as prediction limits. The MPI values gradually decrease with an increase in the number of measurement points, particularly exhibiting a significant reduction when the measurement points increase from 3 to 5. Specifically, the decrease in MPI values from 3 to 5 measured points constitutes 67% to 70% of the overall reduction when the number of measured points increases from 3 to 35. This intuitively indicates that with the increasing integration of measurement information into the Bayesian framework, the uncertainty in predicting deflection gradually diminishes. In contrast, the PICP values exhibit an initial increase followed by a decrease. The initially smaller PICP values result from an inferior match between predicted and measured deflection when using fewer measurement data points. This leads to a significant portion of measured deflection points falling outside the 95% predicted CI. As data points increase, predictions get closer to observations, leading to an initial PICP increase. Further data point increases result in minimal changes in predicted performance (as illustrated in Figure 5) but decreased prediction uncertainty, narrowing the interval and decreasing PICP values.

4 CONCLUSIONS

This study takes the excavation-induced wall deflection as a research demonstration and quantitatively analyzes the influence of the size of measured data used in Bayesian updates on parameter calibration and predicted performance. The study reveals that the more measured data utilized, the smaller the uncertainty in updating parameters and the narrower the predictive confidence interval for obtained values. The variation in MPI values indicates a significant uncertainty change in the initial stages of increasing the number of measurement points. Moreover, it was found that employing five or more measured points leads to satisfactory predictive outcomes, specifically with an R^2 exceeding 0.90. Similar analyses can be conducted for other geotechnical structures and can offer some insights for optimizing on-site monitoring plans in geotechnical engineering.

The variation in PICP values indicates that the probability of measured points falling within the predicted CI is influenced by both predictive performance and the confidence interval width. From the perspective of predictive accuracy, a higher PICP value signifies better predictive outcomes, as we always aspire for all measured values to fall within the prediction interval (i.e., PICP equals 1). In this context, utilizing an appropriate number of measured points contributes to achieving higher PICP values, as an excess of measured information can foster overconfidence in predictions, leading to excessively narrow confidence intervals. This may be attributed to the fact that the Bayesian approach typically addresses parameter uncertainty, measurement errors and model errors, but may not simultaneously incorporate other uncertainties such as construction impacts, environmental factors, and spatial variability in soil properties. This study only provides an initial analysis of the impact of measurement information on predictive performance and uncertainty using a specific case. Further efforts are needed to consider diverse sources of uncertainties when conducting uncertainty quantification in geotechnical engineering.

ACKNOWLEDGMENTS

The authors greatly acknowledge the financial support from the Guangdong Provincial Department of Science and Technology (2022A0505030019), and Science and Technology Development Fund, Macau SAR (File nos. 0056/2023/RIB2, 001/2024/SKL).

REFERENCES

- Braak, C. J. T. 2006. A Markov Chain Monte Carlo version of the genetic algorithm Differential Evolution: easy Bayesian computing for real parameter spaces. *Statistics and Computing* 16: 239–249.
- Calvello, M. 2002. Inverse analysis of a supported excavation through Chicago glacial clays. PhD thesis. Northwestern University, Evanston.
- Cheng, Z. L., Kannangara, K. P. M., Su, L. J., Zhou, W. H., & Tian, C. 2023. Physics-guided genetic programming for predicting field-monitored suction variation with effects of vegetation and atmosphere. *Engineering Geology* 315: 107031.
- Fan, X. Z., Phoon, K. K., Xu, C. J., Tang, C. 2021. Closed-form solution for excavation-induced ground settlement profile in clay. *Computers and Geotechnics* 137: 104266.
- Foreman-Mackey, D., Hogg, D. W., Lang, D., & Goodman, J. 2013. emcee: the MCMC hammer. *Publications of the Astronomical Society of the Pacific* 125(925): 306.
- Gelman, A., Carlin, J. B., Stern, H. S., Dunson, D. B., Vehtari, A., Rubin, D. B. 2013. Bayesian data analysis. Florida: CRC Press.
- Goh, A. T. C., Zhang, F., Zhang, W. G., Zhang, Y. M., Liu, H. L. 2017. A simple estimation model for 3D braced excavation wall deflection. *Computers and Geotechnics* 83: 106–113.
- Gong, X. N., Hou, W. S. 2017. Design and construction manual for deep excavation engineering. Beijing: China Architecture & Building Press.
- Guo, P. P., Gong, X. N., Wang, Y. X. 2019. Displacement and force analyses of braced structure of deep excavation considering unsymmetrical surcharge effect. *Computers and Geotechnics* 113: 103102.
- He, S. Y., Kuok, S. C., Tang, C., Zhou, W. H. 2024. Efficient Bayesian model updating for settlement prediction of the immersed tunnel of HZMB. *Transportation Geotechnics* 44: 101179.
- Jin, Y. F., Yin, Z. Y., Zhou, W. H., Huang, H. W. 2019a. Multi-objective optimization-based updating of predictions during excavation. *Engineering Applications of Artificial Intelligence* 78: 102–123.
- Jin, Y. F., Yin, Z. Y., Zhou, W. H., Horpibulsuk, S. 2019b. Identifying parameters of advanced soil models using an enhanced Transitional Markov chain Monte Carlo method. *Acta Geotechnica* 14(6): 1925–1947.
- Jin, Y. Y., Biscontin, G., Gardoni, P. 2021. Adaptive prediction of wall movement during excavation using Bayesian inference. *Computers and Geotechnics* 137: 104249.
- Juang, C. H., Luo, Z., Atamturktur, S., Huang, H. W. 2013. Bayesian updating of soil parameters for braced excavations using field observations. *Journal of Geotechnical and Geoenvironmental Engineering* 139(3): 395–406.
- Kelly, R., Huang, J. S. 2015. Bayesian updating for one-dimensional consolidation measurements. *Canadian Geotechnical Journal* 52(9): 1318–1330.
- Li, Z. B., Gong, W. P., Li, T. Z., Juang, C. H., Chen, J., Wang, L. 2021. Probabilistic back analysis for improved reliability of geotechnical predictions considering parameters uncertainty, model bias, and observation error. *Tunnelling and Underground Space Technology* 115: 104051.
- Liu, G. B., Wang, W. D. 2009. Excavation engineering manual. Beijing: China Architecture & Building Press.
- Ministry of Housing and Urban-Rural Development of China (MOHURD). 2012. Technical specification for retaining and protection of building foundation excavations (JGJ120-2012). Beijing: China Architecture & Building Press.
- Nelson, B., Ford, E. B., & Payne, M. J. 2013. Run dmc: an efficient, parallel code for analyzing radial velocity observations using n-body integrations and differential evolution markov chain monte carlo. *The Astrophysical Journal Supplement Series* 210(1): 11.
- Ou, C. Y. 2006. Deep excavation: theory and practice. London: Taylor & Francis Group.
- Ou, C. Y., Liao, J. T., Lin, H. D. 1998. Performance of diaphragm wall constructed using top-down method. *Journal of Geotechnical and Geoenvironmental Engineering*. 124: 798–808.
- Ou, C. Y., Liao, J. T., Cheng, W. L. 2000. Building response and ground movements induced by a deep excavation. *Geotechnique* 50(3): 209–220.
- Qi, X. H., Zhou, W. H. 2017. An efficient probabilistic back-analysis method for braced excavations using wall deflection data at multiple points. *Computers and Geotechnics* 85: 186–198.
- Rahmati, O., Choubin, B., Fathabadi, A., Coulon, F., Soltani, E., Shahabi, H., Bui, D. T. 2019. Predicting uncertainty of machine learning models for modelling nitrate pollution of groundwater using quantile regression and UNEEC methods. *Science of the Total Environment* 688: 855–866.
- Reddy, J. N. 2006. An introduction to the finite element method. Singapore: Mc Graw Hill.
- Roy, V. 2020. Convergence diagnostics for Markov chain Monte Carlo. *Annual Review of Statistics and Its Application* 7: 387–412.
- Shanghai Municipal Commission of Housing and Urban-Rural Development (SMCHURD). 2018. Technical code for excavation engineering (DG/TJ 08-61-2018). Shanghai: Tongji University Press.

- Shrestha, D. L., Solomatine, D. P. 2006. Machine learning approaches for estimation of prediction interval for the model output. *Neural Networks* 19(2): 225–235.
- Tang, C., He, S. Y., Zhou, W. H. 2023. A beam on elastic foundation method for predicting deflection of braced excavations considering uncertainties. *International Journal for Numerical and Analytical Methods in Geomechanics* 47(4): 533–548.
- Wang, C. H., Wang, K., Tang, D. F., Hu, B. L., Kelata, Y. 2022. Spatial random fields-based Bayesian method for calibrating geotechnical parameters with ground surface settlements induced by shield tunneling. *Acta Geotechnica* 17(4): 1503–1519.
- Wang, L., Ravichandran, N., Juang, C. H. 2012. Bayesian updating of KJHH model for prediction of maximum ground settlement in braced excavations using centrifuge data. *Computers and Geotechnics* 44: 1–8.
- Yang, J., Liu, Y. J., Yagiz, S., Laouafa, F. 2021. An intelligent procedure for updating deformation prediction of braced excavation in clay using gated recurrent unit neural networks. *Journal of Rock Mechanics and Geotechnical Engineering* 13(6): 1485–1499.
- Yuen, K. V. 2010. Bayesian methods for structural dynamics and civil engineering. Singapore: John Wiley & Sons.
- Zhang, J., Zhang, L. M., Tang, W. H. 2009. Bayesian framework for characterizing geotechnical model uncertainty. *Journal of Geotechnical and Geoenvironmental Engineering* 135(7): 932–940.
- Zheng, D., Huang, J. S., Li, D. Q., Kelly, R., Sloan, S. W. 2018. Embankment prediction using testing data and monitored behaviour: a Bayesian updating approach. *Computers and Geotechnics*. 93: 150–162.
- Zhou, W. H., Tan, F., Yuen, K. V. 2018. Model updating and uncertainty analysis for creep behavior of soft soil. *Computers and Geotechnics*. 100: 135–143.
- Zhou, W. H., Yin, Z. Y., Yuen, K. V. 2021. Practice of Bayesian probability theory in geotechnical engineering. Singapore: Springer.

Landslide dam stability analysis using a support vector machine approach

X. Xiong

Kanazawa University, Ishikawa, Japan

W. Gu

Japan Advanced Institute of Science and Technology, Ishikawa, Japan

D.Y. Shen

Zhejiang University, Hangzhou, China

Z.M. Shi

Tongji University, Shanghai, China

ABSTRACT: Landslide Dam (LD) is a kind of natural hazards that occurs worldwide. Typically, LDs are structurally weak and prone to failure in a short time after formation, posing a threat to downstream areas. Therefore, it is crucial to have a method for quickly determining the stability of an LD. However, traditional research methods, such as model testing and numerical calculations, are time-consuming and may not meet this requirement. In this paper, we trained a Support Vector Machine (SVM) based prediction/classification model to analyze the stability of LDs. Since the success of data-driven AI approaches highly depends on the number and type of data, we discuss the selection of training datasets and input parameters by utilizing a real-world LD dataset. Experimental results demonstrated that the prediction accuracy of LD stability can be improved by incorporating hydraulic information along with geometric information, compared to using geometric information alone.

1 INTRODUCTION

Landslide dam (LD) is a kind of natural dam that forms worldwide when the body of a landslide partially or completely blocks a river channel, mostly triggered by rainfall and earthquake. Once LDs formed, upstream water will result in landslide dammed lakes (LD lake). Due to rapid packing of natural geomaterials, LD is normally weak in structure, which can lead to LD failure with the increase of LD lake water level in short time after its forming. The flooding caused by LD failure threatens downstream people and property. As a result, to prevent disaster and risk decision-making, a method for quickly determining the stability of a LD after its formation is undoubtedly necessary.

Since LDs are formed in mountainous areas and are caused by natural hazards, it is generally difficult to conduct field tests. Model tests and numerical calculations have become main methods to study the stability of LDs. Although it can be known from many current studies that these two methods are effective approaches for studying the stability of LDs, there are still some deficiencies. Different from the artificial dam, LD materials usually have a wide grain size distribution from millimeters to meters and its geometric dimensions are various. The lack of site survey data makes it difficult to establish physical and numerical models for model tests and numerical calculations. Another more important thing is that both model tests and numerical calculations require a quantity of time. As a result, these two approaches cannot meet the requirement of quickly determining the stability of LDs.

Though current codes in many countries provide empirical methods for determining the stability of LDs, these methods only consider single or a few influence factors. The stability of LDs is a very complex problem, which is affected by the geometric dimensions, material composition, geological structure and environmental conditions. Thus, the abovementioned empirical methods lack sufficient reliability.

In recent decades, artificial intelligence (AI) methods have been developed and implemented in the field of geotechnical engineering (Baghbani et al., 2022). Samui (2008) used support vector machines (SVMs), a type of machine learning algorithms, to successfully predict the stability of slopes, which was modeled as a classification problem. Based on SVMs, prediction models of the stability of slopes were developed by Cheng et al. (2012) and Cheng and Hoang (2015). They found that SVM prediction models have more advantages to slope stability evaluation over ANN models under the condition of limited data. Therefore, in this paper, the stability of LDs was also regarded as a classification problem. SVM and a LD dataset (Shen et al., 2020) were used to analyze the stability of LDs. Since the accuracy of machine learning applications depends on the number and type of datasets and selection of input parameters, the selection of training datasets and input parameters was also discussed.

2 SUPPORT VECTOR MACHINE

SVM is firmly based on the theory of statistical learning used for classification, regression, and outlier detection. It was first introduced in 1963 and developed by Vapnik (1995). In SVM, using supervised learning, a training dataset is used to train a model to obtain some parameters. The dataset includes a set of n -dimensional training vectors $x \in R^n$ and the corresponding class label y . The problem of LD stability inference is a binary classification problem with target variable $y \in \{-1, 1\}$. The main aim is to find a generalized classifier that can distinguish the two classes (0, 1) from the set of the training vectors. A commonly used form of the function classifier can be noted as

$$f(x) = w \cdot x + b = 0 \quad (1)$$

where $w \in R^n$ determines the orientation of a discriminating hyperplane, $b \in R$ is a bias. Figure 1 shows an example of SVM classifier. For the linearly separable case, a separating hyperplane can be defined for the two classes as

$$\begin{cases} w \cdot x_i + b \geq 1 \text{ for } y_i = 1, \text{ LD failure} \\ w \cdot x_i + b \leq -1 \text{ for } y_i = -1, \text{ non-failure} \end{cases} \Rightarrow y_i(w \cdot x_i + b) \geq 1, \text{ for } i = 1, \dots, m \quad (2)$$

To find a generalized classifier, some misclassification is allowed and variables ξ_i , called slack variables, are used to consider the training error (Figure 1). Hence, the Equation 2 can be revised as

$$y_i(w \cdot x_i + b) \geq 1 - \xi_i, \quad \xi_i \geq 0, \text{ for } i = 1, \dots, m \quad (3)$$

The perpendicular distance between the two planes is called margin,

$$M(w, b) \geq \frac{2}{\|w\|} \quad (4)$$

The optimal hyperplane is defined as the margin between two classes is maximized and the error is minimized. The maximization of this margin leads to the following constrained optimization problem

$$\begin{aligned} & \text{Minimize : } \frac{1}{2} \|w\|^2 + C \sum_{i=1}^m \xi_i \\ & \text{Subjected to : } y_i(w \cdot x_i + b) \geq 1 - \xi_i, \xi_i \geq 0, \text{ for } i = 1, \dots, m \end{aligned} \quad (5)$$

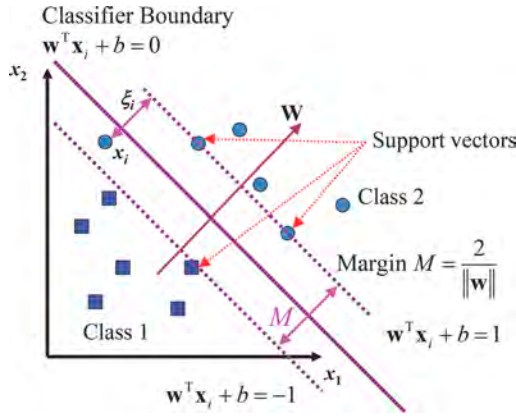


Figure 1. An example of SVM classifier.

where C is a parameter for the trade-off between the number of misclassifications in the training data and the maximization of margin. A smaller C encourages a wider margin by allowing some training points to be misclassified if it results in a larger separation, which can help generalize better to unseen data and mitigate overfitting. On the other hand, a larger C aims to minimize the training error, potentially leading to a narrower margin and increased sensitivity to outliers.

In order to solve the above optimization problem (Equation 5), the method of Lagrange multipliers was applied and the dual problem of the original optimization problem becomes

$$\begin{aligned} \text{Maximize : } L(\alpha) &= \sum_{i=1}^m \alpha_i - \frac{1}{2} \sum_{i=1}^m \sum_{j=1}^m \alpha_i \alpha_j y_i y_j (x_i \cdot x_j) \\ \text{Subjected to : } \sum_{i=1}^m \alpha_i y_i &= 0, \quad 0 \leq \alpha_i \leq C, \text{ for } i = 1, \dots, m \end{aligned} \quad (6)$$

where α is the Lagrange multiplier. Solving Equation 6 with constraints determines the Lagrange multipliers. According to the Karush–Kuhn–Tucker (KKT) optimality condition, some of the multipliers will be zero. The non-zero multipliers are called support vectors (Figure 1). The value of w can be calculated from $w = \sum_{i=1}^m y_i \alpha_i x_i$ and b can be calculated from w and support vectors using Equation 1. Then, the classifier can be constructed as:

$$f(x) = \text{sgn}(w \cdot x + b) \quad (7)$$

where $\text{sgn}(x)$ is the signum function. If $w \cdot x_i + b \geq 0$, it gives 1, otherwise -1.

For some complex classification problems, the classifier becomes non-linear. Training vectors x are transformed into a high-dimensional feature space $\phi(x)$ and classification can become easier with a proper transformation (Figure 2). The optimization problem of Equation 6 becomes

$$\begin{aligned} \text{Maximize : } L(\alpha) &= \sum_{i=1}^m \alpha_i - \frac{1}{2} \sum_{i=1}^m \sum_{j=1}^m \alpha_i \alpha_j y_i y_j (\phi(x_i) \cdot \phi(x_j)) \\ \text{Subjected to : } \sum_{i=1}^m \alpha_i y_i &= 0, \quad 0 \leq \alpha_i \leq C, \text{ for } i = 1, \dots, m \end{aligned} \quad (8)$$

Kernel function $K(x_i, x_j) = \phi(x_i) \cdot \phi(x_j)$ has been used to calculate the inner product in the feature space directly. Radial basis functions (RBF), sigmoid functions and polynomial were used as kernel functions in this study as the follows

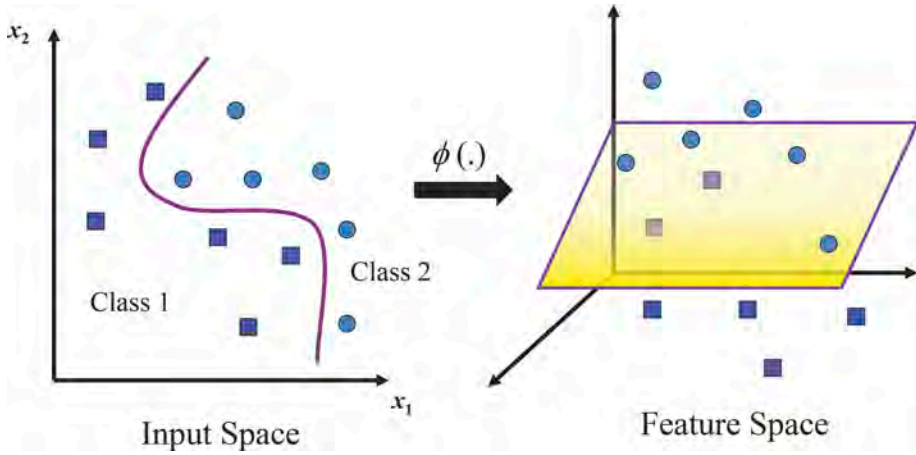


Figure 2. Concept of non-linear SVM for classification problem.

$$\begin{aligned}
 \text{RBF kernel : } K(x_i, x_j) &= \exp(-\gamma \|x_i - x_j\|^2) \\
 \text{Sigmoid kernel : } K(x_i, x_j) &= \tanh(\gamma x_i^\top x_j + r) \\
 \text{Polynomial kernel : } K(x_i, x_j) &= (\gamma x_i^\top x_j + r)^d
 \end{aligned} \tag{9}$$

Where γ , r and d are parameters of corresponding kernel functions.

To summarize, in supervised learning, the values of C and kernel function parameters should be properly determined to obtain a generalized classifier. In this study, cross-validation on the training data was utilized to determine their values.

3 LANDSLIDE DAM DATA

A LD dataset proposed by Shen et al. (2020) was used in this study. This dataset collected the geometric/hydrological information of LD from 1737 cases. The geometric information such as dam height, dam width and dam length are most easily obtained within a short period of time after the LD formation and thus they were used in the analyses. Moreover, hydrological information like LD lake volume and length are related to LD failure, which can be quickly estimated from geographic information after the LD formation. Hence, they were also considered in this study. However, due to the missing of some data, only 126 cases containing complete geometric information were selected. For partially missing hydrological information, it was simply resolved by filling in the value 0.0, which means data is missing for these features. Though most LDs failed after formation, for better learning the characteristics of stable LD, the ratio of failed and non-failed LD was set at 1:1 in the dataset.

Figure 3 shows LD information used in this study. It can be found that LD lake volume and length generally increase with the increasing in LD scale. Nevertheless, it is clear that the stability of LD cannot be predicted by one or two influencing factors since it is affected by multiple factors.

4 RESULTS AND DISCUSSIONS

The main scope of this work is to establish SVM model for predicting the status of stability in the case of LDs. In this study, 100 out of the 126 selected cases of LD were considered for training dataset, and the remaining 26 data was considered as testing dataset. The data was first normalized by subtracting their mean values and dividing by their standard deviation values. Then the training dataset was randomly divided into 4 groups for cross-validation.

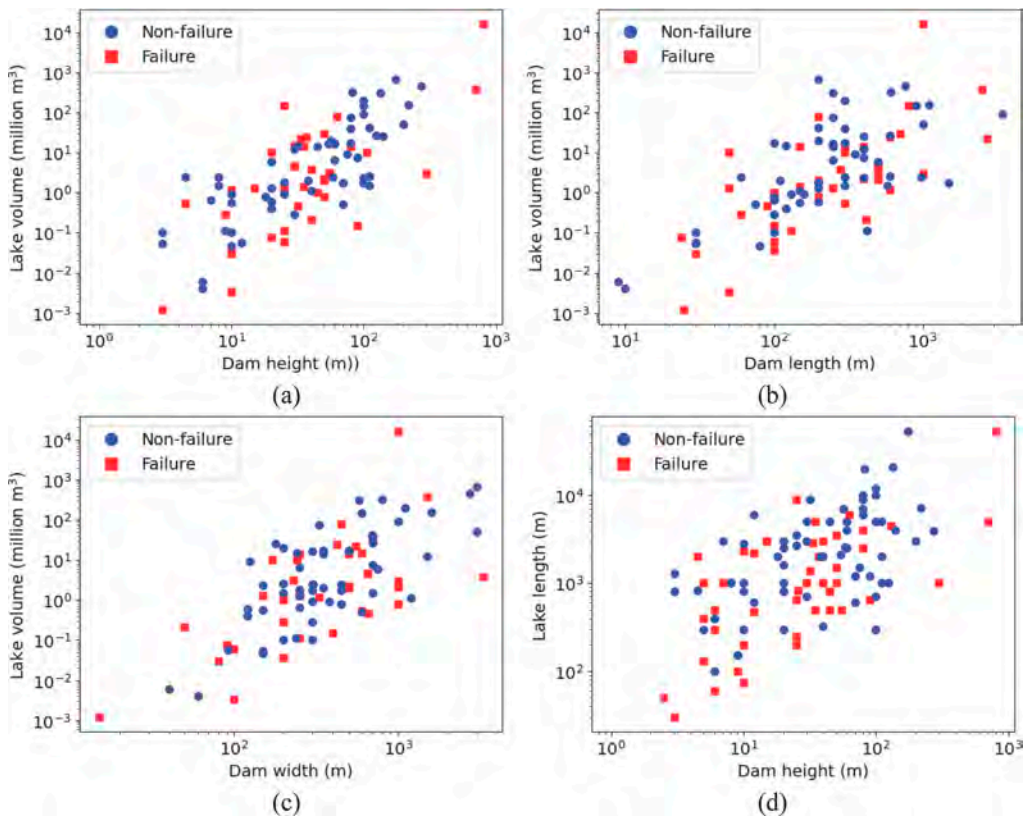


Figure 3. Landslide dam information used in this study.

To evaluate testing performance, accuracy, precision, recall and false failure rate were calculated. The accuracy is the percentage of all cases that were correctly predicted. The precision is the percentage of cases predicted as failure that are predicted correctly, while the recall is the probability of a failure test result, conditioned on the case truly being failure. The false failure rate is the probability of being incorrectly predicted as non-failure.

4.1 Kernel function

The choice of kernel functions is discussed first. Abovementioned RBF, sigmoid functions and polynomial were used as kernel functions in this study. To find a generalized classifier, the values of C and kernel functions parameters were set to range values and determined by trial-and-error method.

The best accuracy results for three kernel functions are shown in Case 1, 2 and 4 in Table 1 and Figure 4. Polynomial kernels performed best with an accuracy of 0.81, while the accuracy using RBF kernels was only 0.65. Though the accuracy and precision using sigmoid kernels were better than those of RBF kernels, the results of calculations using RBF kernels were extremely sensitive to the parameters. Even only a slight change in the parameters can lead to failure in building the classifier. Therefore, polynomial kernels were considered to be the most suitable for solving the problem of LD stability prediction.

4.2 Optimal classifier

The influence of parameters values for polynomial kernels were investigated. Comparing the results of Case 3, 4 and 5 in Table 1, the accuracy did not vary linearly with the changes in C , and there existed the C with the highest accuracy. Moreover, comparing the results of

Case 5, 6 and 7, when the value of C was constant, the changes in parameters of polynomial kernels can also lead to different results.

Though the performance of Case 3 and 6 was almost the same, a smaller C can help generalize better to unseen data and mitigate overfitting. Hence, the classifier obtained in Case 3 was considered superior to that of Case 6. In addition, the false failure rate of Case 4 was slightly greater than that of Case 3. Although the accuracy and recall of Case 3 were lower, it can be considered as a conservative solution. Therefore, both Case 3 and Case 4 are evaluated as the optimal classifier for the problem of LD stability prediction.

Table 1. Performance of SVM model using testing dataset.

Case	Kernel function	Parameter	Accuracy	Precision	Recall	False failure rate
1	RBF	$\gamma=3, C=15$	0.65	0.63	0.77	0.46
2	Sigmoid	$\gamma=2, C=100$	0.73	0.80	0.62	0.15
3	Polynomial	$d=4, \gamma=1, C=15$	0.77	1.0	0.54	0.0
4	Polynomial	$d=4, \gamma=1, C=25$	0.81	0.90	0.69	0.08
5	Polynomial	$d=4, \gamma=1, C=40$	0.65	1.0	0.31	0.0
6	Polynomial	$d=4, \gamma=2, C=40$	0.77	1.0	0.54	0.0
7	Polynomial	$d=2, \gamma=1, C=40$	0.69	0.77	0.54	0.15
8*	Polynomial	$d=2, \gamma=1, C=40$	0.58	0.56	0.77	0.62

*Only geometric information of the LDs was used.

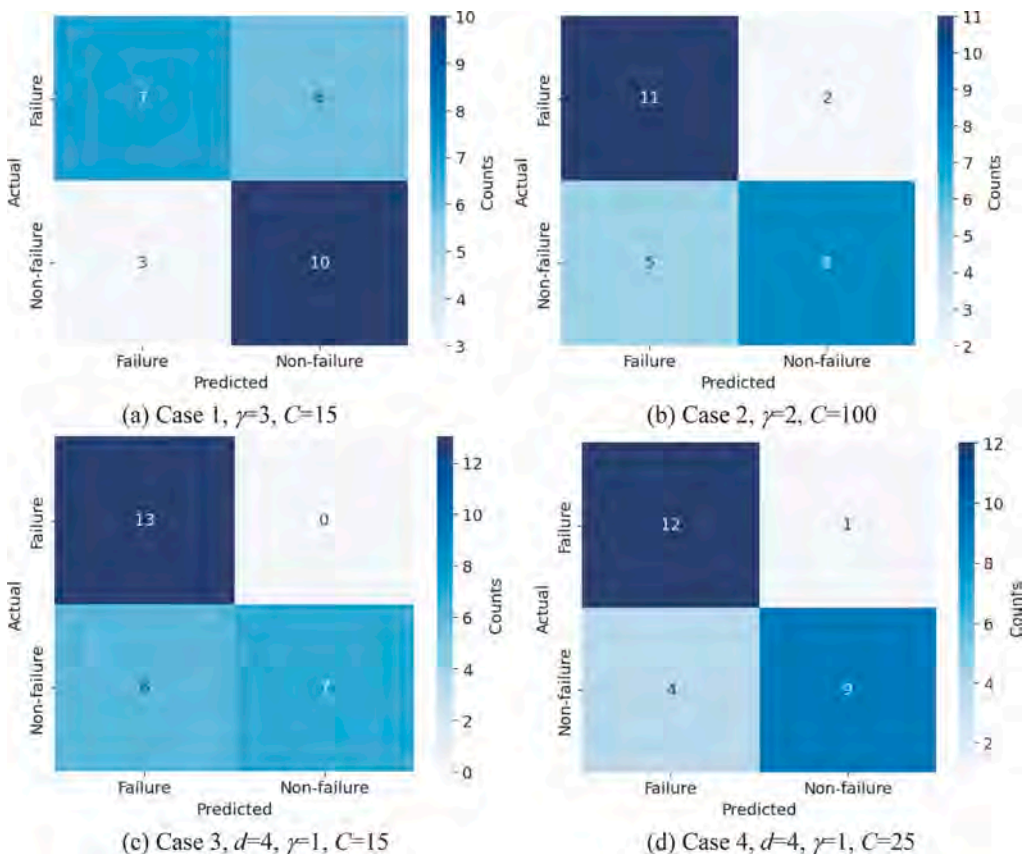


Figure 4. Performance of SVM model for testing dataset using polynomial kernel.

4.3 Influence of training dataset

Comparing Case 7 and 8, the prediction accuracy of LD stability can be improved significantly by incorporating hydraulic information along with geometric information, compared to using geometric information alone. It can be noted that quickly obtaining hydrological information is crucial to the prediction of LD stability.

5 CONCLUSION

The stability of LDs was regarded as a classification problem in this study. A type of machine learning algorithms SVM and a LD database (Shen et al., 2020) were used to analyze the stability of LDs. The following conclusions were obtained:

- (1) Among three types of kernel functions, Polynomial kernels were found to be the most suitable for solving this problem. Though the accuracy and precision using sigmoid kernels were better than those of RBF kernels, the results of calculations using RBF kernels were extremely sensitive to the parameters.
- (2) Two optimal classifiers with higher accuracy and lower false failure rate were obtained. Although the accuracy and recall of Case 3 were lower than those of Case 4, it can be considered as a conservative solution.
- (3) The prediction accuracy of LD stability can be improved significantly by incorporating hydraulic information along with geometric information, compared to using geometric information alone.

REFERENCES

- Baghbani, A., Choudhury, T., Costa, S., & Reiner, J. 2022. Application of artificial intelligence in geotechnical engineering: A state-of-the-art review. *Earth-Science Reviews* 228: 103991.
- Cheng, M. Y., Roy, A. F., & Chen, K. L. 2012. Evolutionary risk preference inference model using fuzzy support vector machine for road slope collapse prediction. *Expert systems with applications* 39(2): 1737–1746.
- Cheng, M. Y., & Hoang, N. D. 2015. Typhoon-induced slope collapse assessment using a novel bee colony optimized support vector classifier. *Natural Hazards* 78: 1961–1978.
- Vapnik V. 1995. *The nature of statistical learning theory*. New York: Springer.
- Samui, P. 2008. Slope stability analysis: a support vector machine approach. *Environmental Geology* 56: 255–267.
- Shen, D., Shi, Z., Peng, M., Zhang, L., & Jiang, M. 2020. Longevity analysis of landslide dams. *Landslides* 17: 1797–1821.

Dynamically updating geological uncertainty simulation with the process of tunnel excavation

J.Z. Zhang, Q.H. Jiang, D.M. Zhang & H.W. Huang
Department of Geotechnical Engineering, Tongji University, China

ABSTRACT: Geological uncertainty is common due to complex depositional processes as one layer appears to be randomly embedded in neighbouring layers. The geo-structures could be significantly affected by geological uncertainty, such as tunnels. Borehole data obtained during the geological survey is the most commonly used information to simulate geological uncertainty. However, borehole data is usually sparse and inadequate. With the process of tunnel excavation, a large amount of new formation information will be continuously revealed. How to effectively use this disclosed geological information to update previously modeled formations? In other words, the geological cross-section along the planned tunnel trajectory can be used as additional information to incorporate with the original borehole data to update the simulated stratum dynamically. This study aims to develop a dynamically updating geological simulation framework incorporating the original borehole data and geological cross-section revealed from continuous tunnel excavation. The coupled Markov chain (CMC) model is a popular method to simulate geological uncertainty. Firstly, the initial stratum is obtained using the coupled Markov chain model based on limited borehole data. Then, the geological formation of the tunnel cross-section will be given with the process of tunnel excavation. Next, adding the additional information to the coupled Markov chain model to update the whole stratum simulation. The dynamic update of the whole stratum simulation can be realized along the tunnel trajectory by repeating the above process. The proposed framework can provide a dynamic formation modelling with tunnel excavation. It continuously updates the whole simulated stratum through the formation information revealed by the tunnel cross-section. It can also be used to forecast geological cross-sections ahead of the tunnel face, which will be helpful for tunnel construction. Results show that the proposed method can adequately use the original borehole data and revealed geological information to update the simulated stratum with the tunnel excavation dynamically.

Keywords: Dynamically updating, geological uncertainty, tunnel excavation

1 INTRODUCTION

The construction and operational environment of underground shield tunneling are concealed, with significant spatial variability in the surrounding soil parameters (Shuku, T. & Phoon, K. K. 2023). Moreover, in the longitudinal alignment design of tunnels, to meet energy-saving and drainage requirements, tunnel routes are often designed with certain slopes, leading to the inevitable crossing of multiple layers of heterogeneous strata (Zhang et al. 2021; Wei et al., 2022). The objectively complex hazardous environment poses numerous disadvantages for risk control in tunnel and underground engineering.

Meanwhile, under uncertain geological conditions, the occurrence and development of risks in shield tunneling follow unique evolutionary patterns. The uncertain and unclear operational environment significantly increases the structural safety risks in operating tunnels. For

instance, in 2007, a major accident occurred during the construction of Pinheiros Station on Line 4 of the São Paulo Metro in Brazil. An approximately 80-meter diameter collapse resulted in 7 casualties, delaying the start of metro operations for nearly 2 years. The accident was attributed to the inaccurate estimation of the geological conditions, with significant discrepancies between the anticipated and actual geological profiles (Mylius 2007).

Site exploration stands as the sole means for geotechnical engineers to understand uncertain geological information. However, due to tight schedules and high costs, there is usually a scarcity of on-site data. Therefore, researching methods to accurately and dynamically characterize the uncertainty of geological strata using limited on-site exploration data and tunnel construction data becomes particularly crucial.

2 METHODOLOGY

Coupled Markov chain model has the ability to characterize the heterogeneity of geological formations (Elfeki & Dekking 2001). It is easy to explain, has few parameters, and high applicability (Elfeki & Dekking 2005; Qi et al. 2016). The two-dimensional CMC model is more suitable for simulating the geological uncertainty than the one-dimensional CMC model, which can only characterize one direction. As shown in Figure 1, the domain is divided into $N_x \times N_y$ cells of the same size, and each cell corresponds to its state. The basic idea of the CMC model is that the state of the current step depends only on the state in the previous step. This means that the state X_{ij} of the cell (i, j) depends on states $X_{i-1, j}$ and $X_{i, j-1}$ of the cells on the left $(i-1, j)$ and on the top $(i, j-1)$ of the current cell in the domain. For simplicity, let the state of cells (i, j) , $(i-1, j)$, $(i, j-1)$ and (N_x, N_y) is S_q, S_b, S_m, S_o , respectively. The conditioning formula can be expressed by

$$\begin{aligned} & \Pr\{Z_{i,j} = S_q | Z_{i-1,j} = S_l, Z_{i,j-1} = S_m, Z_{N_x, N_y} = S_o\} \\ &= C' P_q^x P_m^y \Pr\{Z_{i,j} = S_q | Z_{N_x, N_y} = S_o\} \\ &= \frac{P_{lq}^x P_{mq}^y (P^x)^{(N_x-i)} (P^y)^{(N_y-j)}}{\sum_f P_{lf}^x P_{mf}^y (P^x)^{(N_x-i)} (P^y)^{(N_y-j)}} \end{aligned} \quad (1)$$

Where $p_{qo}^{x(N_x-i)}$ is the (N_x-i) -step horizontal transition probability from S_o to S_q , p_{mq}^y is the vertical transition probability from S_m to S_q .

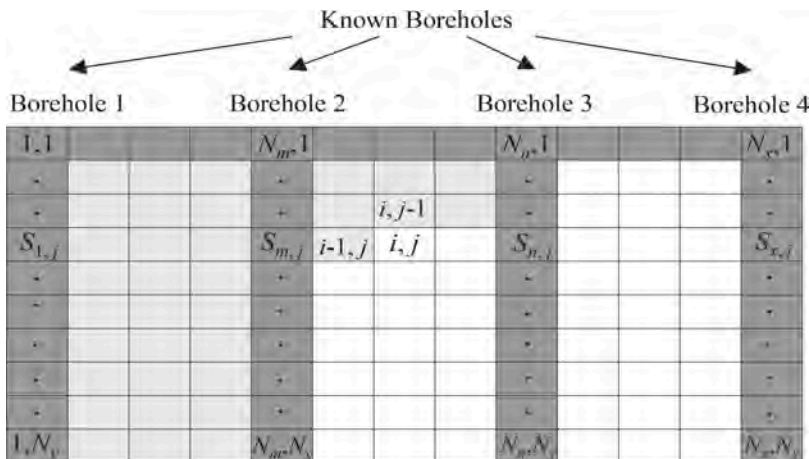


Figure 1. The schematic of using coupled Markov chain to simulate two-dimensional domain.

After incorporating tunnel simulation, to better utilize this dataset, additional conditional probability constraints are introduced for predicting the geological layers above the tunnel. The green area in Figure 2 is simulated using Equation 2. The yellow area represents the exposed geological layers due to tunnel excavation, while the simulation in the blue area continues to employ Equation 1. The specific modified formula is as follows:

$$\begin{aligned}
 & \Pr\{Z_{i,j} = S_q | Z_{i-1,j} = S_l, Z_{i,j-1} = S_m, Z_{N_x,j} = S_o\} \\
 &= C' \Pr\{Z_{i,j} = S_q | Z_{i-1,j} = S_l, Z_{N_x,j} = S_o\} \Pr\{Z_{i,j} = S_q | Z_{i,j-1} = S_m\} \\
 &= \frac{P_{lq}^{x_i} (P_{qo}^{x_i})^{(N_x-i)} P_{mq}^{z_j}}{\sum_f P_{lf}^{x_i} (P_{fo}^{x_i})^{(N_x-i)} P_{mf}^{z_j}}
 \end{aligned} \tag{2}$$

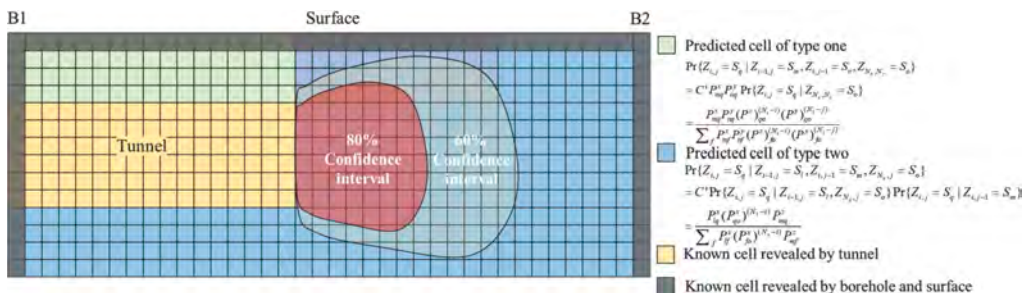


Figure 2. Coupling Markov chain simulation diagram.

3 CASE STUDY

The boreholes, labeled from left to right as B1 to B3, provide the stratigraphic information depicted in Figure 3. Four distinct soil types have been identified: topsoil, clay, quick clay, and sand, respectively, in Figure 3. The x and z coordinates correspond to the horizontal and vertical directions, respectively. It's important to note that the x-axis aligns with the direction of borehole extension shown in Figure 3. This study focuses on the strata between 0 m and -30 m depth at a 70 m long and 30 m deep geological profile.

The initial step in simulating stratum uncertainty involves discretizing the geological profile into cells. In the CMC model, the cell size should not exceed the minimum thickness of the

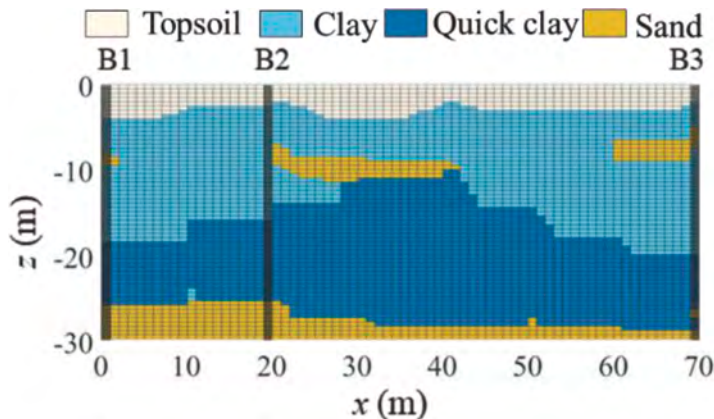


Figure 3. Hypothetical real strata.

geologic unit in the respective direction. The thinnest revealed strata measure 0.5 m, a thin sand layer. Consequently, the vertical sampling interval for this study is set at 0.5 m.

Horizontal sedimentation scales typically surpass vertical scales, allowing for larger horizontal sampling intervals. To optimize computational efficiency, a horizontal sampling interval of 1 m is utilized in this study, maintaining a balanced approach. Figure 3 shows a hypothetical stratum.

In this study, the tunnel excavation strata will be dynamically updated using the known parameters as depicted in Figure 4.

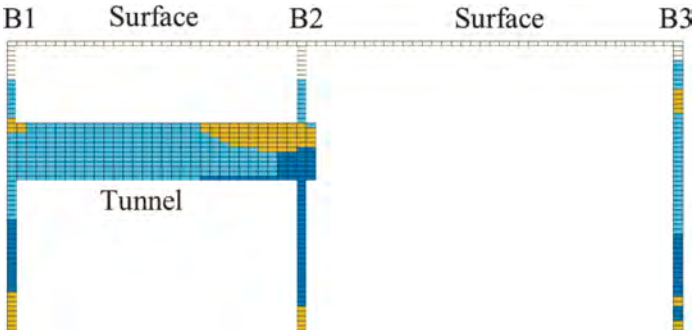


Figure 4. A schematic of the strata exposed by the borehole and tunnel.

The strata simulated based on the exposure from only three boreholes, as depicted in Figure 5, resulted in an accuracy rate of only 73.5% in the geological stratum simulation.

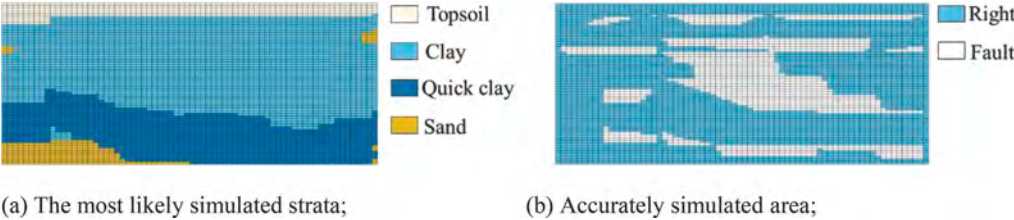


Figure 5. The simulated strata generated from 3 boreholes.

After incorporating tunnel information and updating the simulation of the entire geological stratum, the accuracy of the site simulation increased to 86.45%, as shown in Figure 6. The tunnel excavation progressed by 32 meters during this process.

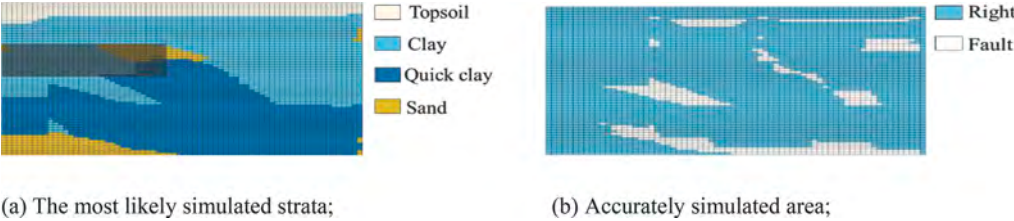


Figure 6. The simulated strata generated from 3 boreholes and tunnel.

As the tunnel excavation progresses, the accuracy of the entire site's geological stratum simulation exhibits some fluctuations but generally improves over time, showing a consistent trend of increasing accuracy, as shown in Figure 7.

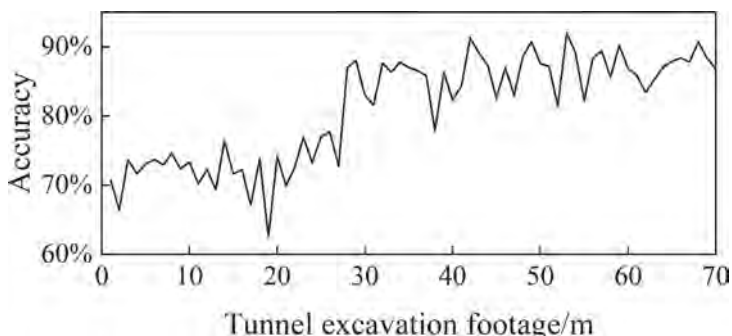


Figure 7. The accuracy of stratigraphic updates throughout the site as the tunnel driving.

As the tunnel progresses, the accuracy of predicting the forward geological layers varies due to the differences in the geological formations ahead. Overall, however, it's generally observed that areas closer to the tunnel face have more accurate geological predictions, as shown in Figure 8.

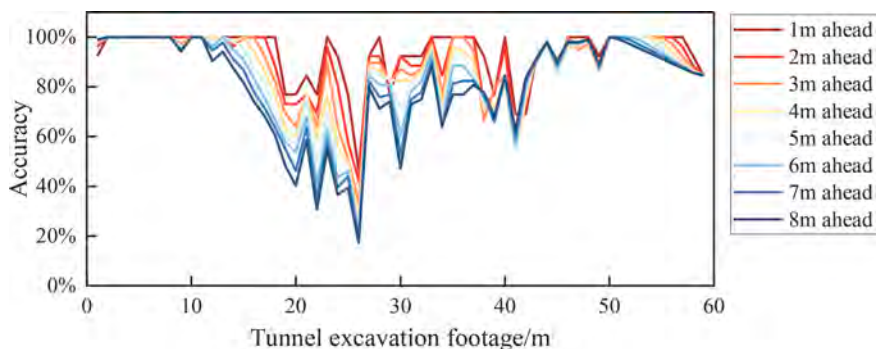


Figure 8. Prediction accuracy of strata in front of tunneling.

4 CONCLUSION

In conclusion, the method's dynamic ability to continuously update simulated strata in real-time, reacting promptly to tunnel excavation progress, highlights its efficacy in forecasting geological conditions ahead of tunnel faces. This proactive approach not only enhances the efficiency of tunnel construction processes but also mitigates potential risks associated with unforeseen geological complexities. By seamlessly adapting to evolving geological formations, this innovative methodology offers a robust solution for effectively managing uncertainties encountered during tunneling activities. Its capacity to provide timely and comprehensive geological insights empowers project managers and engineers to make informed decisions, thereby optimizing construction timelines and ensuring the safety and success of tunneling endeavors.

REFERENCES

- Shuku, T., & Phoon, K.K. 2023. Comparison of data-driven site characterization methods through benchmarking: Methodological and application aspects. *ASCE-ASME Journal of Risk and Uncertainty in Engineering Systems, Part A: Civil Engineering*, 9, 04023006.
- Zhang, J.Z., Huang, H.W., Zhang, D.M., Phoon, K.K., Liu, Z.Q., & Tang, C. 2021. Quantitative evaluation of geological uncertainty and its influence on tunnel structural performance using improved coupled Markov chain. *Acta Geotechnica*, 16, 3709–3724.
- Wei, X.X., & Wang, H. 2022. Stochastic stratigraphic modeling using Bayesian machine learning. *Engineering Geology*, 307, 106789.
- Mylius, A. Sao Paulo collapse: NATM used despite failure history. *New Civil Engineer International*, 2007.
- Elfeki, A.M.M., & Dekking, F.M. 2005. Modelling subsurface heterogeneity by coupled Markov chains: directional dependency, Walther's law and entropy. *Geotechnical and Geological Engineering*, 23, 721–756.
- Qi, X.H., Li, D.Q., Phoon, K.K., Cao, Z.J., & Tang, X.S. 2016. Simulation of geologic uncertainty using coupled Markov chain. *Engineering Geology*, 207, 129–140.
- Elkateb, T., Chalaturnyk, R., & Robertson, P.K. 2003. An overview of soil heterogeneity: quantification and implications on geotechnical field problems. *Canadian Geotechnical Journal*, 40, 1–15.

Feature engineering and SHAP correlation analysis for large diameter shield tunneling: A deep data mining approach to explore the core features and mechanism that define the shield attitude

S. Zhao & S.M. Liao

Department of Geotechnical Engineering, Tongji University, Shanghai, China

ABSTRACT: The control mechanism for tunnel construction is highly intricate and becomes even more challenging as the shield radius increases. Identifying the key features of shield attitude changes under the combined influence of multiple parameters is essential in posture prediction and deviation adjustment. Therefore, this study utilizes methods such as feature engineering, ensemble tree algorithms, Shapley Additive Explanations (SHAP) correlation analysis, and big data analysis to thoroughly explore combinations of features that significantly impact posture changes. The results indicate that synthetic features comprise a high portion of the key features. Six primary patterns of the SHAP plot are proposed to reflect the working conditions of shield attitude control. In the context of the water supply tunnel project in Hangzhou, unfavorable working conditions that should be avoided have been identified. Also, parameters that consistently and reliably influence variations in the targets are concluded and demonstrated. Through feature engineering and SHAP correlation analysis, crucial features have been identified. This is crucial and indispensable for comprehending shield tunneling posture changes and subsequently conducting attitude prediction and deviation correction.

Keywords: Shield attitude control, Feature engineering, SHAP correlation analysis

1 INTRODUCTION

Tunnel boring machines (TBMs) are among the most commonly used equipment in tunnel construction. During the advancement process, the TBM is susceptible to various factors such as complex geological conditions, thrust from the hydraulic jacks, cutterhead rotation speed, earth pressure in the chamber, grouting pressure, and more (Liao *et al.*, 2009). These factors can lead to deviations in the TBMs from the designated tunnel alignment (DTA), which can lead to misalignment and damage to the tunnel segments, further impacting the overall quality of the tunnel (Mo and Chen, 2008; Liu *et al.*, 2018). In this context, the prediction of the shield tunnel's attitude has become a hot topic of research for numerous scholars.

The attitude and position of the shield tunneling can primarily be divided into four components: *HDM* (Horizontal Deviation of shield Machine, unit: mm), *VDM* (Vertical Deviation of shield Machine, unit: mm), *PAA* (Pitch Attitude Angle, unit: degree), *SRA* (Shield Rolling Angle, unit: degree). Many scholars also categorize the *HDM* and *VDM* of the shield head deviations (*HDSH*, *VDSH*) and shield tail deviations (*HDST*, *VDST*).

Over the years, scholars have proposed numerous theoretical analyses and empirical formula prediction models. They are established using data derived from laboratory tests and on-site investigations. These models offer regression analyses between uniaxial compressive

strength, Brazilian tensile strength, rock quality designation, thrust force, cutterhead torque, and rock mass rating, providing insights into the compressive strength relationships among these variables(BARTON, 1999; Yagiz, 2008). These models are characterized by interpretability and have shown good predictive performance in certain engineering applications(Festa, Broere, and Bosch, 2015). However, they also come with some drawbacks, such as high computational complexity, limited consideration of factors, and the inability to perform dynamic real-time calculations and analyses. These limitations result in a lower accuracy of tunnel boring machine orientation analysis and prediction.

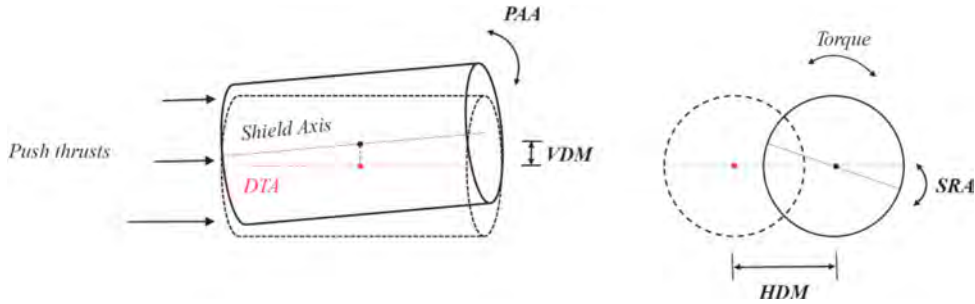


Figure 1. Diagram of the parameters that signify the attitude and position of the tunnel shield machine.

In recent years, the rapid development of deep learning, represented by artificial intelligence neural networks, has introduced many powerful learning-capable network models, including CNN (Convolutional Neural Network)(Lecun *et al.*, 1998; He *et al.*, 2015), RNN (Recurrent Neural Network) and others. RNN demonstrates promising predictive capabilities when applied to time series data, such as stock prices. The robust predictive capabilities of these networks have prompted numerous researchers to apply them in predicting variations in tunneling parameters(Salehi and Burgueño, 2018). Zhou *et al.* (2019) proposed a hybrid deep learning model, using a Wavelet filter to denoise the input data and apply a CNN-LSTM network for the prediction of attitude and position.

However, a notable drawback of neural networks is their susceptibility to the black box effect (Wang *et al.*, 2019). Despite our ability to train neural networks for various tasks, the intricate nonlinear relationships between the hidden layers and weights in the network often prove hard to interpret. Therefore, even though we can predict changes in the tunnel boring machine's posture, adjusting the shield operational parameters to simultaneously correct multiple posture deviations remains challenging, especially when dealing with a large number of input features. Traditional machine learning methods have made progress over the years, giving rise to ensemble algorithms such as Random Forest(Biau and Scornet, 2016), XGBoost(Chen and Guestrin, 2016), and LGBM(Ke *et al.*, 2017a). These models may not match the predictive accuracy of deep learning methods, but they offer the advantage of interpretability. Specifically, tree models like LGBM can rank the importance of input features about output targets. Wang *et al.* (2019) proposed a shield deviation correction method, using XGBoost to analyze feature importance and provided recommended parameters for various deviation intervals. Additionally, some researchers(Wang *et al.*, 2021) leveraged shield tunneling operational and positional parameters to predict the performance of the shield tunneling process. They initially applied wavelet denoising to preprocess the data and built a Bi-LSTM model to predict. Before feeding the data into the model, an LGBM model was utilized to filter out important parameters. The results of the algorithm application and the statistical summary of predicted targets are as follows:

Notation: CNN, Convolutional Neural Network; **RF**, Random Forest; **LSTM**, Long Short-Term Memory; **LGBM**, Light Gradient Boosting Machine; **GRU**, Gated Recurrent Unit; **RNN**, Recurrent Neural Network; **SVR**, Support Vector Regression; **XGBoost**, Extreme Gradient Boosting; **HDM**, Horizontal Deviation of shield Machine; **VDM**, Vertical Deviation of shield Machine; **PAA**, Pitch Attitude Angle; **SRA**, Shield Rolling Angle; v , Propulsion Speed; T , Cutterhead Torque; T_h , Total Thrust.

Table 1. Literature review.

Authors	Based model	Shield diameter(m)	Main predicting targets
Zhou <i>et al.</i> , 2019	CNN-LSTM	15.2	<i>HDM, VDM</i>
Xu <i>et al.</i> , 2023	CNN-LSTM	6.28	<i>HDM, VDM, PAA, SRA</i>
Wang <i>et al.</i> , 2021	LGBM, Bi-LSTM	12.07	<i>v, T</i>
Wang <i>et al.</i> , 2019	RF, XGBoost	-	<i>HDM, VDM</i>
Zhang <i>et al.</i> , 2022	GRU	9.15	<i>HDM, VDM</i>
Chen <i>et al.</i> , 2023	LGBM	6.2	<i>HDM, VDM, PAA, SRA</i>
Shen <i>et al.</i> , 2022	LSTM	-	<i>HDM, VDM, PAA, SRA</i>
Li <i>et al.</i> , 2021	LSTM, RF	7.9	T_h
Shi <i>et al.</i> , 2021	RF, LSTM, CNN, RNN	6.68	T
Gao <i>et al.</i> , 2019	RNN, RF, SVR, Lasso	6.3	T_h, T, v

Existing research predominantly focuses on enhancing and comparing models to improve predictive accuracy. However, there is limited investigation into data mining and exploring the relationships between input features, reflecting complex operational conditions to variations in shield tunneling deviation.

2 METHODOLOGY

2.1 Feature engineering

To unearth features that more accurately reflect the patterns of attitude changes, feature engineering is an efficient, comprehensive, and scientific approach. Feature engineering is the process in machine learning and data mining where the original data is transformed, combined, or selected to extract features that are more valuable and better represent the characteristics of the data. Effective feature engineering can significantly enhance the performance of a model, as the training effectiveness of a model relies heavily on the quality of its input features. There are several methods for feature engineering, such as automatically deriving features (Wang *et al.*, 2023) and batch-generating features through cross-combination, second cross-combination, and polynomial derivation.

However, our primary goal is to obtain features that contain practical engineering or physical significance, facilitating targeted adjustments and preventing adverse working conditions. Specifically, the combination of features can reflect the working conditions in the tunneling process. For example, we can analyze the on shield tunneling by examining the imbalance between various features, such as variances in stroke and thrust among symmetrical hydraulic cylinders. Additionally, this study takes into account the impact of other scholars' assessments of shield tunneling parameters on postural changes, such as excavation efficiency. Meanwhile, the multiplication of the propulsion speed and total thrust can illustrate the combined effect on the variation of the shield tunneling attitude, such as when the tunneling speed of the shield is slowed along with a high overall thrust force. Certainly, we can further combine and derive features from the ones obtained, allowing for the assessment of a broader range of working conditions. The specific content and methods of feature engineering will be detailed in **Chapter 4**.

Feature engineering, especially the cross-combination, tends to result in an exponential increase in the number of features. Excessive input dimensions in a predictive model can result in increased memory usage, and longer computation times, and may even lead to a decline in predictive accuracy. Therefore, it is often advisable to employ feature filtering methods after feature engineering, such as principal component analysis (PCA) (Yang, Liao, and Liu, 2023), correlation analysis, and machine learning filters (Chen *et al.*, 2023), to eliminate less relevant features.

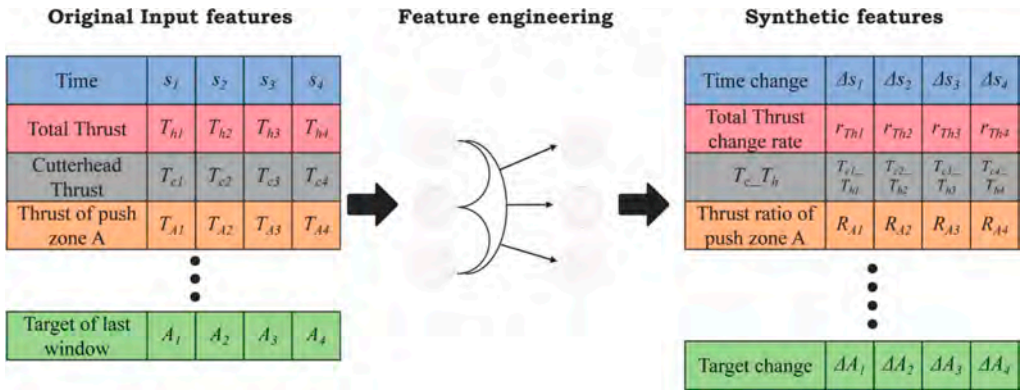


Figure 2. Examples of some synthesized features.

2.2 LGBM algorithm and SHAP values

Light Gradient Boosting Machine (LGBM) (Ke *et al.*, 2017b) stands out as a gradient-boosting framework known for its efficiency and rapid training of predictive models. LGBM excels in extracting feature importance by employing a leaf-wise tree growth strategy and gradient-based one-side sampling.

Unlike other gradient tree models, such as XGBoost, LGBM adopts histogram-based learning, efficiently handling continuous and categorical features and eliminating the need for one-hot encoding. With parallel and distributed training support, LGBM is optimal for large-scale datasets.

In the current era dominated by the formidable performance of deep learning neural networks, LGBM distinguishes itself in predictive algorithms by its fast computational speed and interpretability. SHAP (Shapley Additive Explanations) values stem from the concept of Shapley values in cooperative game theory. In machine learning, SHAP values calculate the importance of features to explain the contribution of each feature to that prediction (Kannan-gara *et al.*, 2022). By calculating the marginal contribution when a feature is introduced to the model, considering the different marginal contributions of that feature in all possible feature sequences, and taking the average, we obtain the SHAP baseline value for that particular feature. SHAP belongs to post-interpretability methods, whose core idea involves calculating the marginal contribution of features to the model output and explaining “black-box models” from both global and local perspectives.

Using the LGBM tree model allows for an initial prediction of shield attitude, but the predictive accuracy of pure machine learning methods falls short compared to deep learning approaches. However, LGBM can filter key features that are advantageous for prediction by calculating SHAP values, thereby reducing the dimensionality of inputs into the deep learning network. By leveraging the merits of both machine learning and deep learning, a balanced approach can be achieved, optimizing the trade-off between predictive accuracy and speed in model performance. Most importantly, through the analysis and adjustment of key parameters using SHAP values to achieve precise, efficient, and scientific correction of the attitude deviation.

After the model predicts each window’s dataset, the model is refined and upgraded by calculating the differences with the real measure value. Meanwhile, newly measured data can be incorporated into the dataset and predict the next time step’s posture changes by the updated model. By maintaining a fixed window size, the input data quantity is constrained while effectively utilizing recent parameter changes. This balance allows the model to achieve a favorable trade-off between accuracy and computation time, playing an important role in dynamically predicting shield tunneling deviations.

3 DATA PREPROCESSING

3.1 Project overview

The project involves a water supply tunnel project in Hangzhou, China, with a total length of 5,620 meters from 1#shaft to 3#shaft. The project utilizes an extra-large-diameter shield tunnel construction with an internal diameter of 13.3 meters and an external diameter of 14.5 meters. The tunnel is buried under approximately 6.7 to 15.6 meters of soil, traversing primarily through layers of silty sand and silty sand interspersed with sandy loam. Each ring is propelled by the jacking system of 28 hydraulic cylinders in total. The jacking system can be roughly divided into six push zones, labeled A-F. This study focuses only on the analysis of the six advancing zones.

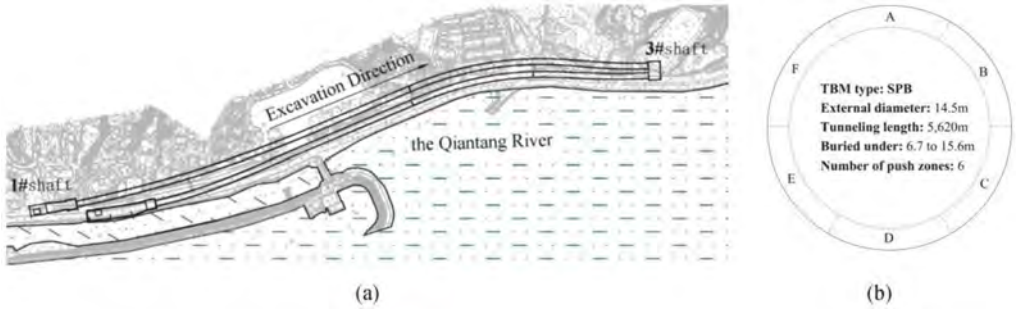


Figure 3. Project overview. (a) Project geographical location. (b) Basic information of TBM.

The data is derived from the monitoring records within the shield's VMT system over two months, with a monitoring frequency of once every 5 seconds. After removing the periods of the TBM's downtime from the raw monitoring data, the dataset contains 238,489 records, 18 input features, and 4 target features. The input features include advancement speed, cutterhead thrust, cutterhead torque, cutterhead rotation speed, thrust in each advancement zone, travel in each advancement zone, and time. The target features include *HDM*, *VDM*, *PAA*, and *SRA*.

3.2 Data preprocessing

Before conducting feature engineering, data preprocessing is essential, which includes outlier detection and wavelet transform denoising. The purpose of data preprocessing is to enhance the performance, robustness, and generalization capability of the algorithm, mitigating the impact of noise and unnecessary interference.

3.2.1 Outlier detection

During the period of tunneling, situations such as signal distortion in monitoring devices and machine downtime for maintenance are inevitable. Consequently, the data obtained may contain outliers, which are detrimental to the model's ability to learn patterns and generalization capabilities. There are several statistical methods for handling outliers, including Mahalanobis distance filtering (Gao *et al.*, 2022) and Z-score filtering (Dai *et al.*, 2023).

Mahalanobis Distance is a distance metric that takes into account the covariance matrix of the data. Widely utilized in multivariate statistical analysis. It quantifies the deviation of a data point from the center of the dataset. When the Mahalanobis Distance of a data point exceeds a specific threshold in the dataset, it is considered an outlier. Subsequently, the data associated with this outlier is removed. The formula for Mahalanobis Distance is:

$$D_M(\mathbf{x}) = (\mathbf{x} - \boldsymbol{\mu})^T S^{-1} (\mathbf{x} - \boldsymbol{\mu}) \quad (1)$$

Where $D_M(\mathbf{x})$ is the Mahalanobis Distance of the data point. $\boldsymbol{\mu}$ denotes the mean vector of the dataset. S^{-1} is the inverse matrix of the covariance matrix.

In a normal distribution, approximately 99.7% of data points fall within a Z-score range of 3. By computing the Z-score, we can assess the extent to which a data point deviates from the mean of the dataset, measured in standard deviations. If the absolute value of the Z-score exceeds a certain threshold (often 3), the data point is regarded as an outlier. This method is particularly effective for datasets exhibiting a normal distribution pattern. Z-score can be calculated:

$$Z = (X - \mu) / \sigma \tag{2}$$

This study employs two filtering methods to evaluate and filter parameter outliers from two perspectives. The study determines the indices of outliers identified by the two methods and takes their intersection as the final set of sample indices for removal. Meanwhile, the threshold values should not be too high to avoid removing normal data. The chosen filtering of Z-score and Mahalanobis Distance thresholds for this study are 3 and 5.

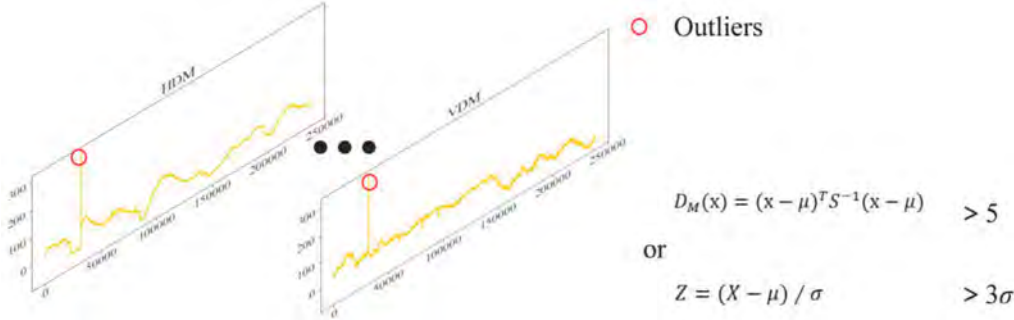


Figure 4. Outliers detection.

3.2.2 Wavelet transform denoising

Despite the removal of outliers, the data still contains a significant amount of noise, which is highly detrimental to accurate predictions. This noise often originates from construction disturbances and fluctuations in sensor signals. Wavelet transformation is a mathematical technique that decomposes a signal into different frequency components, making it useful for separating signal and noise. The Daubechies wavelet, specifically the db4 wavelet, was selected for the denoising process in this study. The wavelet transformation involved an eight-layer decomposition of the shield parameters, which means that the original signal was decomposed into approximation coefficients and detail coefficients across eight different scales or levels. The **Figure 5** illustrates the application effect of wavelet denoising.

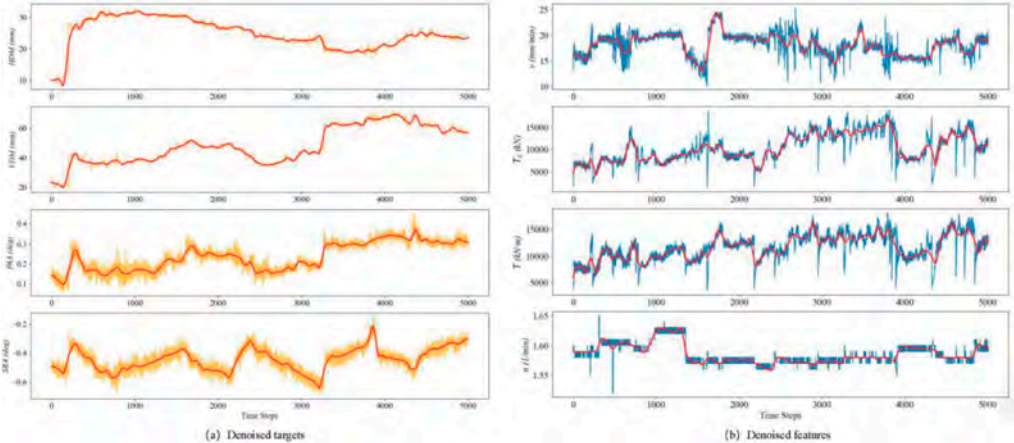


Figure 5. Part of the Wavelet transform denoised data. (a) Denoised targets. (b) Denoised features.

4 FEATURE ENGINEERING

Concerning the attitude control of the shield, our primary focus is to assess the impact of various controllable parameters, such as jacking force and cutterhead rotation speed. This evaluation is crucial for making informed adjustments in the event of deviations. The correction process not only involves ensuring the appropriate values of the parameters but also demands the appropriate rate and magnitude of parameter changes. Simultaneously, feature engineering through cross-combination enables the assessment of the combined impact of two parameters on predicting the targets.

4.1 Synthetic features

Considering the above, the synthesized feature employed in this study is as follows:

- 1. Time change:** Due to the removal of anomalies, such as the periods of shield downtime or sensor damage, the time steps between adjacent points in the dataset may be different. We want to improve the model's ability to predict attitude variance after a shutdown by adding a time change feature.

Table 2. Overview of original and synthesized feature.

Type (208)	Parameter	Abbr.	Unit	Statistical indicators		
				Mean	Min	Max
Output (4)	Horizontal deviation	HDM	mm	-5.2	-69.94	68.80
	Vertical deviation	VDM	mm	8.59	-65.70	67.94
	Pitch attitude angle	PAA	deg	0.57	0.04	1.04
	Shield rolling angle	SRA	deg	-0.47	-1.20	0.25
Original Input (18)	Propulsion speed	v	mml min	18.98	12.88	23.71
	Cutterhead Thrust	T_c	kN	8973.63	2304.06	18828.75
	Cutterhead torque	T	$kN \cdot m$	11779.30	5340.71	17957.85
	The rotational speed of the cutterhead	n	l/min	1.60	0	1.74
	Forward of push zone A	F_A	mm	7.07	-11	37
	Forward of push zone B	F_B	mm	15.01	-11	63
	Forward of push zone C	F_C	mm	15.32	-4	53
	Forward of push zone D	F_D	mm	11.18	-9	42
	Forward of push zone E	F_E	mm	2.16	-6	29
	Forward of push zone F	F_F	mm	1.40	-4	88
	Thrust of all push zones	T_h	kN	58775.93	28829.68	78473.78
	Thrust of push zone A	T_A	kN	7426.07	352.11	18899.94
	Thrust of push zone B	T_B	kN	13622.71	391.82	18229.20
	Thrust of push zone C	T_C	kN	14004.01	356.38	21409.04
	Thrust of push zone D	T_D	kN	13194.31	371.15	18250.19
	Thrust of push zone E	T_E	kN	6625.50	60.71	15047.69
	Thrust of push zone F	T_F	kN	3903.34	103.7	10812.16
	Time feature	s	sec	566141.94	1	983550
Synthetic Input (186)	Time change (1)	$\Delta s = s_i - s_{i-1}$	1	31.16	3	201105
	Boring efficiency (1)	$P = Fv + 2\Pi nT$	kW	289103.83	106052.48	524560.08
	Thrust ratio of zone X (6)	$R_X = T_X/T_h$	1	0.12	0.08	0.19
	X change (21)	$\Delta X = X_i - X_{i-1}$	-	X includes all original parameters besides time, including targets		
	X change rate (21)	$r_X = \Delta X/\Delta s$	-	X includes all original parameters besides time, including targets		
	Cross Combinations (136)	$CX_c = X_a \cdot X_b$	-	X includes all original input parameters besides time		

2. **Boring efficiency:** A parameter that comprehensively considers cutterhead torque, cutterhead rotation speed, total thrust, and propulsion speed.
3. **Thrust ratio of zone X:** The proportion of total thrust allocated to each thrust zone, used to gauge the degree of thrust imbalance.
4. **Change and change rate of X:** Reflecting the temporal variations of controllable parameters such as the change rate of jacking force, as well as predicted targets like the change rate of HDM and PAA.
5. **Cross-combination features:** Multiplying each pair of original features to reflect the combined impact of parameters on predicted targets.

The input features were initially 18, and after feature derivation, they expanded to 204. The original and synthetic features, as well as the statistical indicators, are all listed in **Table 2**.

Certainly, we can continue with second-feature engineering based on the derived features. However, the performance improvement becomes marginal, and it significantly adds computational costs, making it unsuitable for the dynamic prediction of shield attitudes. Therefore, this paper does not engage in secondary feature derivation.

4.2 Feature correlations analysis

After synthesizing features, we can calculate SHAP values by LGBM to find key features of each target. It is essential to note that the historical data of the prediction target and time-related features are parameters beyond our control, such as ΔHDM , Δs , only synthesized for enhancing prediction accuracy. Therefore, during the feature correlations analysis, these related features are excluded to highlight the key features that can be actively controlled. Before training, standardization is recommended to minimize scale differences among data. After removing uncontrollable features and standardization, the number of features inputted into the LGBM model is 198.

Although we may not be able to explain the reasons for changes in attitude under various engineering conditions, we can take proactive measures to avoid the unfavorable working conditions revealed by big data analysis. In the bee swarm chart, the closer the color of the scattered points is to red, the higher the corresponding feature values. The positive or negative SHAP values indicate whether a feature has a positive or negative impact on the model output. Specifically, if the feature value increases, the model's predicted output will also increase. Each feature is arranged in descending order by average SHAP values.

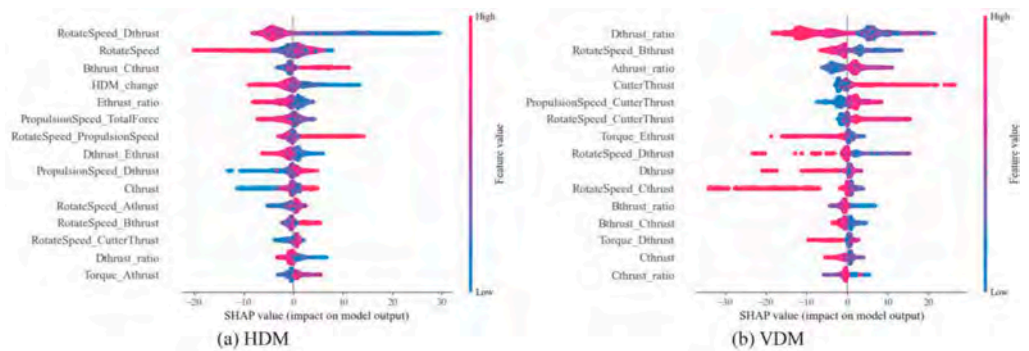


Figure 6. SHAP bee swarm plot of HDM and VDM.

Figure 6 lists the top 15 features with the most substantial impact on each target from top to bottom. From **Figure 6(a)**, it is evident that the product of “rotational speed of the cutterhead (n)” and “Thrust of push zone D (T_D)” has the most significant impact on HDM . The blue scattered points on the right side of the first line with higher SHAP values, indicating that a smaller of $n \times T_D$ can significantly increase the predicted value of HDM . The second line

represents the impact of n on the HDM . In contrast to $n \times T_D$, the smaller red SHAP values are distributed on the left side of this line, indicating that an increase in n will decrease the predicted values of HDM . However, our goal is to maintain a stable HDM around zero, and it is undesirable for it to either increase or decrease too fast. Above all, working conditions with excessively large SHAP values, like the “tail of a tadpole”, should be avoided. A longer tail indicates a greater magnitude of change, while a purer color and wider tail signify a higher confidence level in the occurrence of the change.

Another crucial piece of information on the SHAP plot is the stacking position of the scattered points in each row, like the “head of the tadpole”, representing the stable impact relationship. On the right side of the first line, there is a “head of tadpole” around SHAP values from -3 to -7. The head contains multiple red and purple spots with small SHAP negative values, indicating that a high or medium value for $n \times T_D$ can stably decrease HDM . This gives us insight into rectifying the attitude deviation for different targets. When in the “tadpole head” region with relatively pure colors and small non-zero SHAP values, it signifies a slow and confidently predicted change in posture. For example, under this engineering condition, when HDM deviates significantly in the positive direction, consider moderately increasing $n \times T_D$, while avoiding excessively high values of n .

Similarly, we can conclude the impact of features on the other three targets. For VDM in **Figure 6(b)**, the crucial factor is the proportion of thrust in zones A and D to the total propulsive force. In the first line, the thrust ratio of zone D (R_D) has two “heads of a tadpole”. The relatively purer red head has a negative -15~-10 SHAP value, while the head with a mix of blue and purple has a small positive SHAP value, around 3~6. This indicates that a substantial number of larger data points in R_D show a decreasing trend in VDM prediction, with the reduction around -15~-10. On the other hand, smaller values in R_D show an increasing impact on VDM prediction. Meanwhile, we should also avoid bad working conditions with the “long tadpole tail,” which include: excessively small R_D , overly large T , and high values of $n \times T_C$.

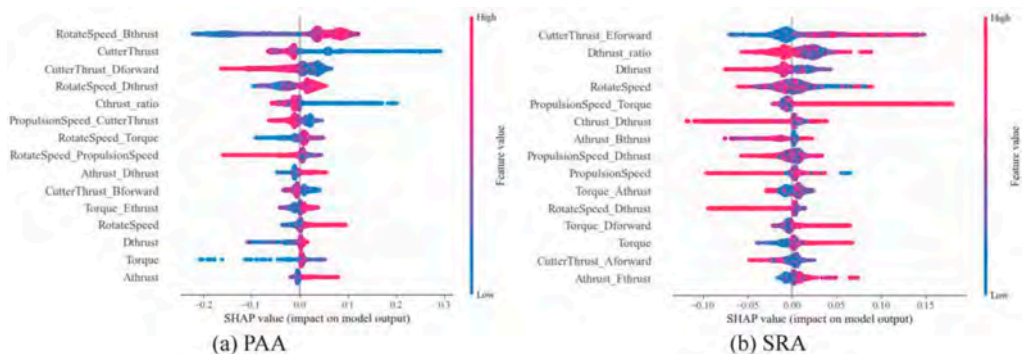


Figure 7. SHAP bee swarm plot of PAA and SRA.

The occurrences of the “long tadpole tail” situations are more frequent for changes in the angles of PAA and SRA compared to changes in position. In **Figure 7(a)**, among the 198 input features, $n \times T_B$, Cutterhead thrust (T_{ch}), and Cutterhead thrust \times Forward of push zone D ($T_{ch} \times F_D$) have the most significant impact on PAA . Working conditions to avoid include excessively small values for $n \times T_B$ and T_{ch} , overly large for $T_{ch} \times F_D$ and small for R_C . In **Figure 7(b)**, most important features for SRA include: $T_{ch} \times F_E$, R_D , T_D , n , et al. For the SRA target, a significant number of “red tadpole tails” indicate that, during construction, a combination of key features with high values is not advisable. Additionally, we can draw some adjustment suggestions from the “small SHAP pure-color tadpole heads.” Specifically, when SRA is excessively high, consider using a smaller value for $T_{ch} \times F_E$.

In summary, **Table 3** outlines six key patterns for posture control objectives. The “long blue tadpole tail” indicates that parameter values should be avoided being too small, while the

“long red tadpole tail” suggests avoiding excessively large parameter values. The “pure tadpole head” indicates that a large number of data points consistently demonstrate the same impact of that feature on the target. **Figure 8** illustrates the meaning of six key patterns in the SHAP figure.

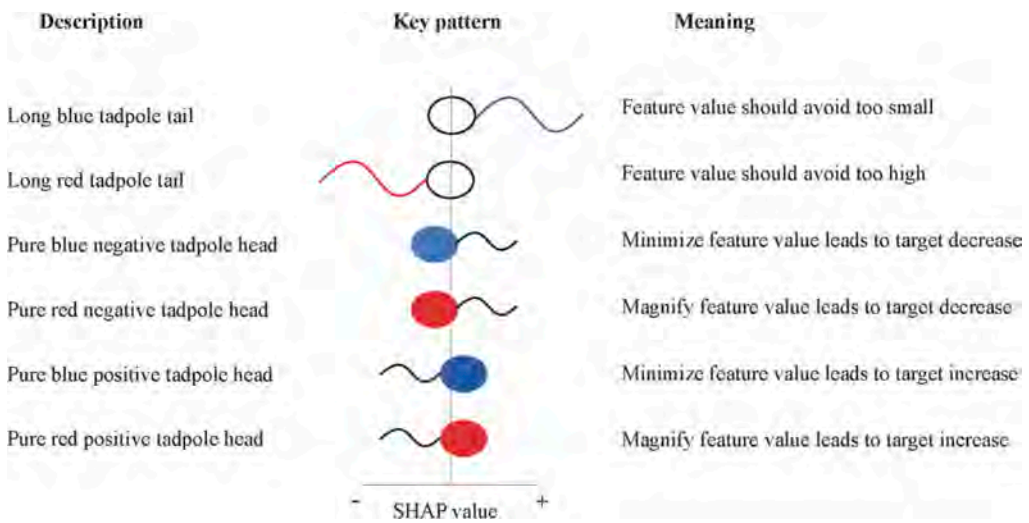


Figure 8. Meaning of key patterns in SHAP bee swarm figure.

Table 3. Key patterns for shield attitude control.

Key patterns in the SHAP figure	HDM	VDM	PAA	SRA
“Long blue tadpole tail”	$n \times T_D$	R_D	$n \times T_B$	-
“Long red tadpole tail”	n	T_{ch}	$T_{ch} \times F_D$	$v \times T$
“Pure blue negative tadpole head”	-	R_A	-	$T_{ch} \times F_E$
“Pure red negative tadpole head”	$n \times T_D$	R_D	R_C	-
“Pure blue positive tadpole head”	R_E	-	$T_{ch} \times F_D$	R_D
“Pure red positive tadpole head”	-	R_A	$n \times T_D$	-

5 CONCLUSION

The framework of this study can be divided into three main parts: data preprocessing, feature derivation, and parameter correlation analysis. Through feature engineering, this study has derived composite features that reflect a more comprehensive set of operational information, such as feature change rates, thrust imbalances, and combinations of parameters. The LGBM algorithm is applied to calculate SHAP values for each synthetic feature. Bee swarm plots are subsequently utilized to identify unfavorable operational conditions in shield control and to recognize key patterns suitable for adjustment.

The results indicate that synthetic features comprise a significant portion of the key features. This suggests that the synthesized features play a crucial role in the model’s prediction of shield attitude changes. By analyzing the SHAP plots for each parameter feature, six key patterns of shield tunneling posture changes have been summarized. In this project, the working conditions to be avoided are: excessively high or low of $n \times T_D$, n , R_D , T_{ch} , $n \times T_B$, $T_{ch} \times F_D$, $v \times T$. The features filtered out through key patterns have a significant impact on shield tunneling posture. They can serve as crucial control parameters for posture prediction and

correction, contributing positively to the realization of autonomous steering control for tunnel boring machines.

REFERENCES

- Barton, N. (1999) 'TBM performance estimation in rock using QTBM', *TBM performance estimation in rock using QTBM*, 31(9), pp. 30–34.
- Biau, G. and Scornet, E. (2016) 'A random forest guided tour', *TEST*, 25(2), pp. 197–227. Available at: <https://doi.org/10.1007/s11749-016-0481-7>.
- Chen, H. *et al.* (2023) 'Shield attitude prediction based on Bayesian-LGBM machine learning', *Information Sciences*, 632, pp. 105–129. Available at: <https://doi.org/10.1016/j.ins.2023.03.004>.
- Chen, T. and Guestrin, C. (2016) 'XGBoost: A Scalable Tree Boosting System', in *Proceedings of the 22nd ACM SIGKDD International Conference on Knowledge Discovery and Data Mining*. New York, NY, USA: Association for Computing Machinery (KDD '16), pp. 785–794. Available at: <https://doi.org/10.1145/2939672.2939785>.
- Dai, Z. *et al.* (2023) 'Dynamic prediction for attitude and position of shield machine in tunneling: A hybrid deep learning method considering dual attention', *Advanced Engineering Informatics*, 57, p. 102032. Available at: <https://doi.org/10.1016/j.aei.2023.102032>.
- Festa, D., Broere, W. and Bosch, J.W. (2015) 'Kinematic behaviour of a Tunnel Boring Machine in soft soil: Theory and observations', *Tunnelling and Underground Space Technology*, 49, pp. 208–217. Available at: <https://doi.org/10.1016/j.tust.2015.03.007>.
- Gao, B. *et al.* (2022) 'Mahalanobis distance-based fading cubature Kalman filter with augmented mechanism for hypersonic vehicle INS/CNS autonomous integration', *Chinese Journal of Aeronautics*, 35(5), pp. 114–128. Available at: <https://doi.org/10.1016/j.cja.2021.08.035>.
- Gao, X. *et al.* (2019) 'Recurrent neural networks for real-time prediction of TBM operating parameters', *Automation in Construction*, 98, pp. 225–235. Available at: <https://doi.org/10.1016/j.autcon.2018.11.013>.
- He, K. *et al.* (2015) 'Deep Residual Learning for Image Recognition'. arXiv. Available at: <http://arxiv.org/abs/1512.03385> (Accessed: 8 March 2023).
- Kannangara, K.K.P.M. *et al.* (2022) 'Investigation of feature contribution to shield tunneling-induced settlement using Shapley additive explanations method', *Journal of Rock Mechanics and Geotechnical Engineering*, 14(4), pp. 1052–1063. Available at: <https://doi.org/10.1016/j.jrmge.2022.01.002>.
- Ke, G. *et al.* (2017a) 'LightGBM: A Highly Efficient Gradient Boosting Decision Tree', in *Advances in Neural Information Processing Systems*. Curran Associates, Inc. Available at: <https://proceedings.neurips.cc/paper/2017/hash/6449f44a102fde848669bdd9eb6b76fa-Abstract.html> (Accessed: 20 November 2023).
- Ke, G. *et al.* (2017b) 'LightGBM: A Highly Efficient Gradient Boosting Decision Tree', in *Advances in Neural Information Processing Systems*. Curran Associates, Inc. Available at: https://papers.nips.cc/paper_files/paper/2017/hash/6449f44a102fde848669bdd9eb6b76fa-Abstract.html (Accessed: 27 November 2023).
- Lecun, Y. *et al.* (1998) 'Gradient-based learning applied to document recognition', *Proceedings of the IEEE*, 86(11), pp. 2278–2324. Available at: <https://doi.org/10.1109/5.726791>.
- Li, J. *et al.* (2021) 'Advanced prediction of tunnel boring machine performance based on big data', *Geoscience Frontiers*, 12(1), pp. 331–338. Available at: <https://doi.org/10.1016/j.gsf.2020.02.011>.
- Liao, S.-M. *et al.* (2009) 'Shield tunneling and environment protection in Shanghai soft ground', *Tunnelling and Underground Space Technology*, 24(4), pp. 454–465. Available at: <https://doi.org/10.1016/j.tust.2008.12.005>.
- Liu, X.-X. *et al.* (2018) 'Analytical approach for time-dependent groundwater inflow into shield tunnel face in confined aquifer', *International Journal for Numerical and Analytical Methods in Geomechanics*, 42(4), pp. 655–673. Available at: <https://doi.org/10.1002/nag.2760>.
- Mo, H.H. and Chen, J.S. (2008) 'Study on inner force and dislocation of segments caused by shield machine attitude', *Tunnelling and Underground Space Technology*, 23(3), pp. 281–291. Available at: <https://doi.org/10.1016/j.tust.2007.06.007>.
- Salehi, H. and Burgueño, R. (2018) 'Emerging artificial intelligence methods in structural engineering', *Engineering Structures*, 171, pp. 170–189. Available at: <https://doi.org/10.1016/j.engstruct.2018.05.084>.
- Shen, S.-L. *et al.* (2022) 'Real-time prediction of shield moving trajectory during tunnelling', *Acta Geotechnica*, 17(4), pp. 1533–1549. Available at: <https://doi.org/10.1007/s11440-022-01461-4>.
- Shi, G. *et al.* (2021) 'A VMD-EWT-LSTM-based multi-step prediction approach for shield tunneling machine cutterhead torque', *Knowledge-Based Systems*, 228, p. 107213. Available at: <https://doi.org/10.1016/j.knsys.2021.107213>.

- Wang, P. *et al.* (2019) 'Prediction of Axis Attitude Deviation and Deviation Correction Method Based on Data Driven During Shield Tunneling', *IEEE Access*, 7, pp. 163487–163501. Available at: <https://doi.org/10.1109/ACCESS.2019.2952649>.
- Wang, R. *et al.* (2021) 'Dynamic prediction of mechanized shield tunneling performance', *Automation in Construction*, 132, p. 103958. Available at: <https://doi.org/10.1016/j.autcon.2021.103958>.
- Wang, Y.-Q. *et al.* (2023) 'Machine learning framework for intelligent aeration control in wastewater treatment plants: Automatic feature engineering based on variation sliding layer', *Water Research*, 246, p. 120676. Available at: <https://doi.org/10.1016/j.watres.2023.120676>.
- Xu, J. *et al.* (2023) 'Predicting shield position deviation based on double-path hybrid deep neural networks', *Automation in Construction*, 148, p. 104775. Available at: <https://doi.org/10.1016/j.autcon.2023.104775>.
- Yagiz, S. (2008) 'Utilizing rock mass properties for predicting TBM performance in hard rock condition', *Tunnelling and Underground Space Technology*, 23(3), pp. 326–339. Available at: <https://doi.org/10.1016/j.tust.2007.04.011>.
- Yang, Y.-F., Liao, S.-M. and Liu, M.-B. (2023) 'Dynamic prediction of moving trajectory in pipe jacking: GRU-based deep learning framework', *Frontiers of Structural and Civil Engineering*, 17(7), pp. 994–1010. Available at: <https://doi.org/10.1007/s11709-023-0942-5>.
- Zhang, Nan *et al.* (2022) 'Real-time prediction of shield moving trajectory during tunnelling using GRU deep neural network', *Acta Geotechnica*, 17(4), pp. 1167–1182. Available at: <https://doi.org/10.1007/s11440-021-01319-1>.
- Zhou, C. *et al.* (2019) 'Dynamic prediction for attitude and position in shield tunneling: A deep learning method', *Automation in Construction*, 105, p. 102840. Available at: <https://doi.org/10.1016/j.autcon.2019.102840>.

*Smart monitoring and visualization technologies for tunnelling
and underground construction*



Taylor & Francis

Taylor & Francis Group

<http://taylorandfrancis.com>

General Report – Smart monitoring and visualization technologies for tunnelling and underground construction

M.Z.E.B. Elshafie

College of Engineering, Qatar University, Doha, Qatar

ABSTRACT: This General Report presents an overview of the papers featured at the Symposium in the session “Smart Monitoring and Visualization Technologies for Tunnelling and Underground Construction.” Three papers in this session cover various aspects, including case studies on international projects involving tunnelling and deep excavations, with a focus on monitoring and data interpretation. Additionally, two papers delve into technology advancements in underground construction applications, such as the development of FBG pore water pressure sensors and the utilisation of IoT monitoring systems in geotechnical engineering. The effects of tunnel excavation processes, such as the penetration of foam into saturated sand and the behaviour of loess under cutting tools, are investigated in two papers in this session. Furthermore, the session includes contributions on site ground characterization and interpolation of geotechnical properties. A noteworthy inclusion is a paper presenting advancements in hybrid centrifuge and numerical modelling for addressing soil-structure interaction problems within the geotechnical centrifuge.

1 INTRODUCTION

There are ten papers in total in this session on “Smart Monitoring and Visualization Technologies for Tunneling and Underground Construction” with authors from Macau, Shanghai, Xi’an, Zhuhai, Guangdong, Taipei, Oslo, Queensland and Nottingham. Seven of the papers are authored by researchers affiliated to academic/research institutions with the remaining three authored by a mixture of both academics/researchers and industry professionals.

The papers present a wide range of topics that have been grouped into five categories:

- Advancements in underground construction, tunnel rehabilitation, and monitoring technologies
- Technology development in underground construction applications.
- Enhancing the efficiency of excavation and tunnelling processes.
- Developments in site ground characterization
- Other papers

Overall, the papers present a wide range of topics with interesting case studies (albeit a small number in total) that included, among others, the design and execution of hydrogeological barriers for open excavation pits and tunnels, the use of finite element (FE) simulations to investigate the use of grouting for the rehabilitation of existing tunnels and the use of the least squares theory for the real-time monitoring of existing tunnel movements due to adjacent diaphragm wall construction. These case studies not only offer valuable insights for upcoming projects, but also present a valuable repository of reference material illustrating the application of innovative design, analyses and monitoring methods.

2 ADVANCEMENTS IN UNDERGROUND CONSTRUCTION, TUNNEL REHABILITATION AND MONITORING TECHNOLOGIES

The three papers in this group originate from Oslo, Shanghai and Taipei. The papers cover the control of groundwater during the construction of new tunnels and deep excavations in Oslo, the use of FE simulations to investigate the use of grouting for the rehabilitation of the existing Shanghai Metro tunnels and the use of the least square theory to report reliable measurements of the movements of existing tunnels due to adjacent construction activity in Taipei.

Feizi *et al* present a case study in connection with the development of the E18 West Corridor highway, near the capital of Norway, Oslo. The E18 highway is one of Norway's busiest roads, with an average of 90,000 vehicles using the highway daily. The E18 Western Corridor comprises a road system from Lysaker in the east, to Asker and beyond in the western direction; the first stage being Lysaker to Ramstadsletta (where a deep excavation was being constructed). The vicinity of the Ramstadsletta deep excavation exhibits prominent rock outcrops interspersed with intermediate depression zones. Typically, soft marine clay accumulates within these depressions. Beneath the clay, above the bedrock, layers of more permeable moraine material can be identified. The excavation pit at Ramstadsletta, and the surrounding areas filled with clay depressions are shown in Figure 1.

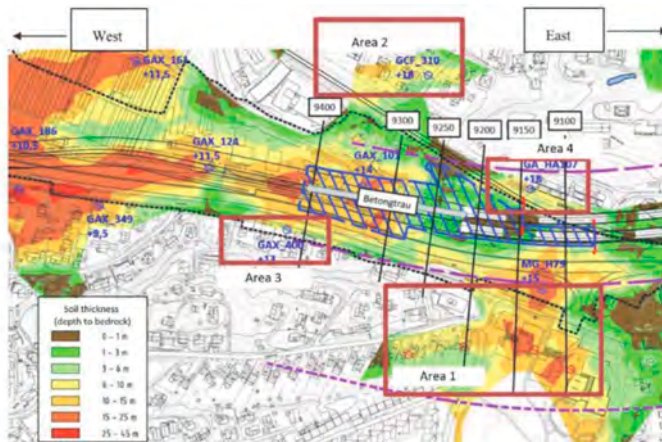


Figure 1. Map of Ramstadsletta, soil thickness to bedrock, areas susceptible to settlement marked with red. The deep excavation is highlighted with the blue hatchet (from Feizi *et al*).

Previous experience indicated that even minimal leakage could lead to a significant drop in pore pressures at the bedrock level which, in turn, triggers settlements in the surrounding areas. As such, a groundwater barrier was designed as follows:

- Steel sheet pile walls to bedrock
- Concrete beam/jet grouted columns at the sheet pile toe
- Continuous cement grouting curtain in bedrock below the sheet pile wall

The paper presents the design and construction details of installing a rock grouting curtain using over 700 grouting holes employing a “split spacing” technique, as depicted in Figure 2. Initially, A holes were drilled and grouted at 3m c/c spacing, followed by the drilling and grouting of B holes at the same spacing. Drilling additional holes was determined based on the analysis of grouting field data looking at parameters including volume grouting and grouting pressures obtained from operating A and B holes. The drilling extended to a depth of 10 m below the bottom level of the excavation in the relevant profile, reaching a minimum depth of 10 m into the rock.

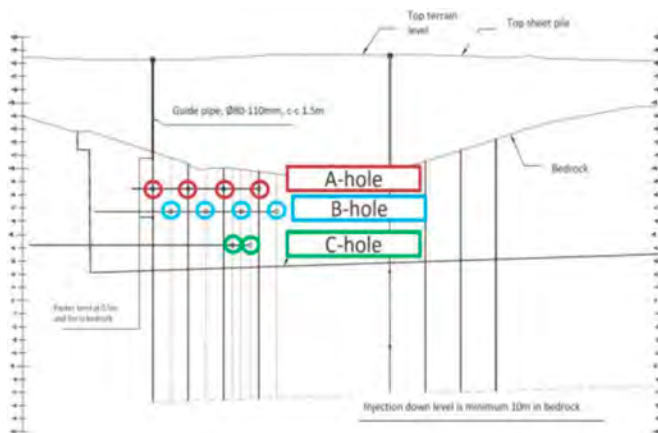


Figure 2. Illustration showing grouting holes with split-spacing procedure and photo of drilled casings for grout holes (from Feizi *et al.*).

The authors note that minimal seepage was observed across the majority of the designated region, demonstrating the effective implementation and performance of the grouting work and groundwater barriers. Predominantly, instances of seepage were identified in association with the sheet pile anchors and rock bolt holes. The principal factor contributing to these notable instances of seepage was the perforation of the grout curtain by the anchors, creating conduits for the flow of water. The case study emphasizes the importance of systematizing drilling and grouting data before initiating grouting works. It also underscores the significance of accurate transmission and sequencing of drilling and grouting data to avoid time-consuming errors during quality control work. Additionally, the need for regular site inspections by designers and the identification of grouting holes is highlighted for improved communication between designers and contractors.

Ye *et al* investigate the maintenance challenges faced by shield tunnels in metro lines as their operational service life extends. The focus is on the rehabilitation of the transverse deformation caused by complex surrounding construction activities, impacting tunnel linings and potentially leading to structural defects. In recent years, the deployment of two-fluid light-disturbance grouting technology has emerged as a prevalent methodology for rehabilitating tunnels experiencing substantial deformations. The authors posit that while the prevailing practice relies on horizontal transverse convergence as the singular evaluation index for grouting efficacy, the rehabilitation of joint behaviour within the tunnel under asymmetric deformation is not comprehensively considered. Consequently, the paper endeavors to bridge this gap by establishing a finite difference model utilizing FLAC 3D. This model enables the simulation of the impact of light-disturbance grouting technology through the application of expansion stress. The simulations are used to explore the combined variations in transverse convergence and joint behavior within tunnels undergoing both symmetric and asymmetric deformation under the influence of grouting action.

The 2D numerical model (Figure 3) involved detailed considerations, including a grid mesh configuration incorporating the soil layers (and associated soil properties) for a typical section of the Shanghai metro. The concrete segments (six prefabricated segments in total per ring) of the metro tunnel which were modelled using solid elements, adhered to a linear elastic model; the joint behaviour was simulated through interface elements to strike a balance between computational efficiency and simulation precision. The grouting process is simulated in good detail, accounting for sequential grouting on both sides of the tunnel to mitigate disturbances effectively.

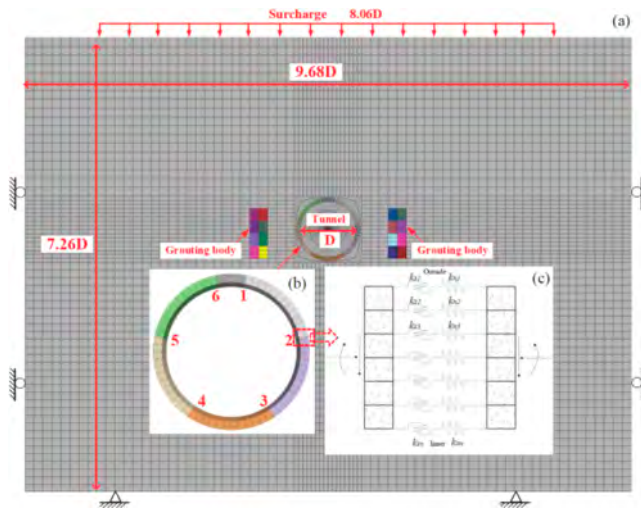


Figure 3. Finite difference model and boundary conditions (from Ye *et al.*).

The authors present results showing variations in transverse convergence, joint opening and dislocation at different stages of the grouting process. Notably, as shown in Figure 4, the study distinguishes between symmetric and asymmetric deformations unraveling valuable insights into the efficacy of grouting for different joint positions and deformation scenarios. The findings underscore the importance of considering the spatial and symmetrical attributes of tunnel deformations when evaluating the effectiveness of grouting interventions.

The paper provides valuable contributions to the understanding of the coupled variations in tunnel behaviour during grouting, offering insights that extend beyond conventional assessments. It serves as a good resource for researchers, practitioners, and stakeholders involved in the realm of tunnel rehabilitation.

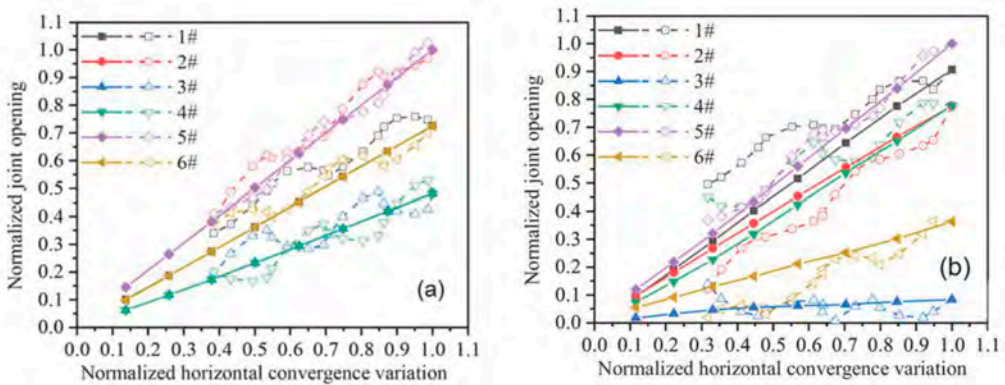


Figure 4. Coupled variations of transverse convergence and joint behaviour during the surcharge and grouting process with (a) symmetric deformation (b) asymmetric deformation.

Phan *et al* discuss the implementation of real-time monitoring, using robotic total stations (RTSs) and objective prisms (OP), to observe the movements of tunnel structures during their operational lifespan. Real-time monitoring is crucial for observing tunnel deformations during their operation, especially in the presence of ongoing construction activities nearby. The authors advocate for the use of robotic total stations (RTSs) and objective prisms (OP) as efficient measurement sensors for tunnel deformation monitoring. However, acknowledging the complexity of metro tunnel structures and the necessity for a large number of monitoring points,

the study emphasizes the challenges associated with using multiple RTSs. In order to overcome potential measurement errors arising from an increased number of stations, the authors propose the integration of the least squares adjustment method into real-time data acquisition systems (GeoAuto was used as an example). The least squares adjustment technique, a well-established method in deformation surveying, relies on statistical analysis to estimate the most probable coordinates of measurement points within a network, thereby mitigating errors. This was illustrated by the case study of the Aozidi Metro Station (R13) and its existing twin tunnels (LUR22 and LUR23) in Kaohsiung City, Taiwan. An automatic monitoring system utilizing four total stations, four 360° prisms and 160 OPs instruments was employed. The system was implemented to observe the movement of tunnel structures and the track bed during adjacent deep excavation construction activities. The least squares adjustment method, facilitated by STAR*NET software, was applied to refine real-time data collected from the observation system. The authors used the error factor and the Chi-Square test to showcase the reliability of the adjustment process which highlights its potential as a valuable tool for ensuring the safety and stability of tunnel structures amidst dynamic construction activities.

3 TECHNOLOGY DEVELOPMENT IN UNDERGROUND CONSTRUCTION APPLICATIONS

The authors of the two papers (from Macau and Zhuhai) in this section on technology development in underground construction applications describe the development of sensors and sensor systems that could be used for underground construction applications.

Jing *et al* introduce a highly sensitive fiber Bragg grating (FBG) sensor designed for measuring both positive and negative pore water pressures, discussing its design, manufacturing and calibration. Understanding the hydraulic properties of soil is imperative for assessing the long-term stability of geotechnical structures. Pore water pressure and matrix suction are critical parameters for this purpose. The electronic pressure sensors commonly used in practice face some limitations including susceptibility to electromagnetic interference and poor stability, hence the authors propose the use of an FBG-based sensor. The sensor employs a cylindrical structure made up of five shells connected via threads and sealed with epoxy glue. The sensor features a permeable stone, an elastic diaphragm, two fibre Bragg gratings (FBG1 and FBG2), a semi-circular groove, a rigid plate, a shell, and fiber tail as shown in Figure 5. The elastic diaphragm and FBG1 are the core sensing devices while FBG2 is encapsulated in the temperature chamber for measuring temperature (and hence enable temperature compensation) and is connected in series with FBG1.

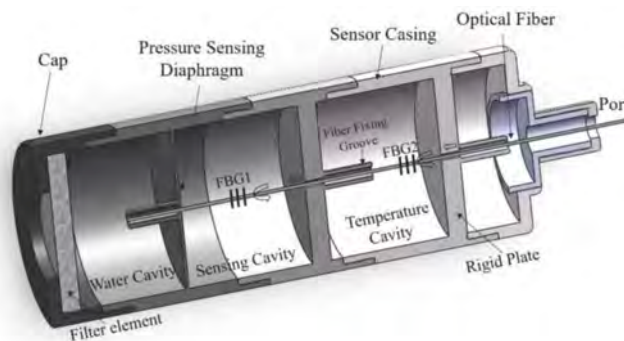


Figure 5. A half-sectional structure of the FBG pore water pressure sensor (from Jing *et al*).

The authors elucidate the elastic diaphragm deformation model, deriving equations governing the relationship between hydraulic pressure, strain and FBG wavelength changes. Theoretical models for both positive and negative hydraulic pressures are presented. A comprehensive

numerical model is then developed using Abaqus software; the simulations that followed carefully analysed the displacement distribution and strain values under positive and negative hydraulic pressures, affirming a linear relationship between strain and pressure. The paper establishes the feasibility and effectiveness of the proposed pore water pressure sensor based on FBG technology. The sensor exhibits high sensitivity, effectively measuring both positive and negative pressures. Following the theoretical analyses and the finite element simulations, calibration experiments were presented validating the sensor's design and indicating its potential for geotechnical monitoring in underground space engineering. The sensor's robustness positions it as a promising tool for future geotechnical applications.

Ma *et al* emphasize the pivotal role of Internet of Things (IoT)-based online monitoring in addressing monitoring demands in construction sites. Geotechnical engineering activities disturb carbon reservoirs, necessitating effective monitoring. While satellite monitoring and power consumption-based methods are limited, the study advocates for IoT online monitoring due to its real-time precision and applicability in geotechnical engineering. The authors argue that advancements in sensing, computing, and communication technology enable low-cost, low-power sensors in Wireless Sensor Networks (WSN) forming IoT Online Monitoring systems. The study then delves into the components of these systems, emphasising their advantages like adjustable measurement ranges and unattended, remote-control capabilities. The study also outlines the team's efforts in creating an IoT platform for monitoring carbon emissions; combining regional energy consumption and CO₂ emissions data, the platform provides real-time monitoring, early warnings, and comprehensive data analysis, offering valuable insights for carbon neutrality management. The authors provide a comprehensive exploration of monitoring carbon emissions in geotechnical engineering, offering insights into the principles, technologies and design frameworks of IoT-based online monitoring systems.

4 ENHANCING THE EFFICIENCY OF EXCAVATION AND TUNNELLING PROCESSES

Two papers are reviewed under this section; the first from Xian investigates the mechanisms of loess adhesion to shield machine cutting tools and the second from Macau studies the penetration behaviour of foam into saturated sand. Both papers present studies aiming to enhance the efficiency of excavation and tunnelling processes.

Bai *et al* address a prevalent issue encountered during tunneling operations in Northwest China, where cohesive soils, specifically loess, adhere to the cutting tools of shield machines, causing operational disruptions and additional costs. According to the authors, despite existing theories on soil-metal interface adhesion, a comprehensive exploration of the inherent mechanisms affecting loess adhesion is lacking. The study seeks to address this knowledge gap and proposes strategic countermeasures to mitigate adhesion-related challenges. Loess, classified as low plasticity clay, was studied with additives such as sand, kaolin, and montmorillonite. Laboratory tests included mixing, fluidity, and atomic force microscopy (AFM). Adhesion potential was determined through the adhesion ratio in mixing tests, fluidity was measured by changes in specimen diameter before and after vibrations and AFM tests provided insights into surface morphology. The results presented in the paper enhance the understanding of loess adhesion mechanisms and provide valuable insights for practical countermeasures. The utilization of sand emerges as a promising strategy to mitigate adhesion-related challenges, thereby contributing to the optimization of tunnelling processes in loess-rich geological contexts.

The utilisation of foam as a soil conditioner in Earth Pressure Balance (EPB) shield tunneling operations to mitigate the permeability of highly porous soil layers like sand, has been a subject of particular interest in tunnelling engineering. Injected ahead of the cutter head, foam displaces water within saturated sand, thus altering soil properties during excavation (Figure 6). While previous studies have investigated foam penetration characteristics, limitations exist regarding the influence of different foam parameters on penetration behaviour.

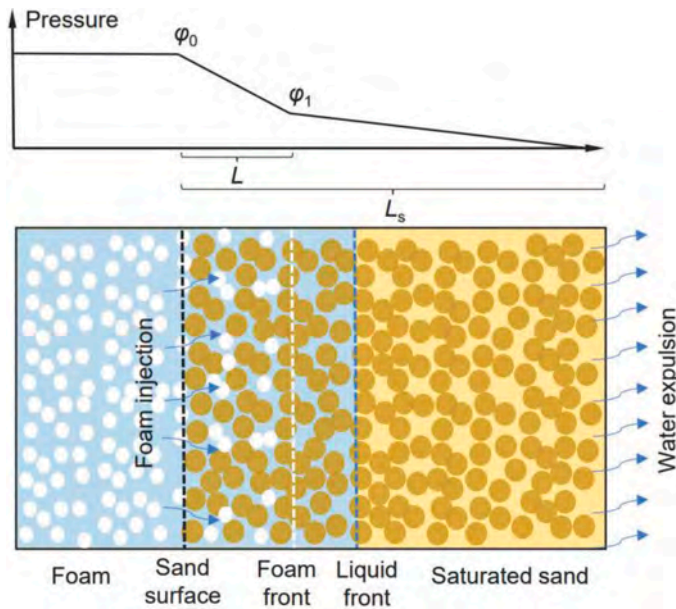


Figure 6. Schematic diagram of foam penetration process on site (from Huang and Zhou).

In response, Huang and Zhou present a simplified one-dimensional foam penetration model capable of predicting foam penetration processes in saturated sandy soil under diverse conditions. Incorporating equations derived from Darcy's law and a power-law fluid model to describe foam rheology, the study delves into the penetration behaviour of various rheological foams, elucidating the influence of foam rheological indices on penetration characteristics. Predictions of foam penetration behaviour were made by manipulating rheological parameters within the model. Results indicated that foams with lower flow behaviour indices and higher flow consistency indices exhibited more desirable characteristics for shield tunnelling, forming low-permeability layers swiftly within sand. Conversely, foams with higher flow behaviour indices and lower flow consistency indices demonstrated prolonged penetration velocities, potentially hindering effective soil conditioning. The study offers insights into foam penetration behaviour and its implications for EPB shield tunnelling operations. By providing a predictive framework for foam penetration, engineers can make informed decisions regarding foam selection to optimise tunnelling efficiency and soil conditioning effectiveness.

5 DEVELOPMENTS IN SITE GROUND CHARACTERIZATION

There are two papers under this section. The first paper from Macau investigates, numerically, the relationship between the penetration depth and wavelength of the surface wave in two layers of soil while the second paper from Zhuhai studies the spatial interpolation of SPT values using the Weighed Ellipse Nearest Neighbors (WENN) approach. Both papers provide useful insights that help practitioners in understanding the ground characteristics.

Zhou and Lok challenge the conventional assumption concerning penetration depth in surface wave methods by quantifying the relationship between penetration depth and wavelength. Surface wave methods have gained prominence as non-invasive testing methodologies, offering cost-effectiveness, convenience, and environmental sustainability. Widely employed in civil engineering, geophysics, and earthquake engineering, these methods utilize the dispersive nature of surface waves in layered media, particularly through techniques like Multichannel Analysis of Surface Waves (MASW), to deduce soil stiffness profiles. However, a critical

assumption in MASW’s inversion analysis – specifying the penetration depth within 0.5 to 1.0 wavelength – warrants a nuanced investigation, especially when the maximum wavelength is smaller than the interface depth. An investigation of the penetration depth and wavelength assumption was conducted using a numerical model for a two-layered soil. The study focused on dispersive phenomena, varying the thickness of the upper soil layer. The stiffness matrix method facilitated theoretical calculations, defining the relationship between external forces, displacements, and material properties. The results from Zhou and Lok’s analyses indicate that the penetration depth can exceed previous assumptions, approximating a constant value of around 1.67. Such findings hold significant implications for inversion analysis, enabling the use of a smaller wavelength to accurately infer deeper soil stiffness profiles. The study offers valuable insights for refining and optimising surface wave methods in geotechnical investigations.

Yan *et al* paper addresses challenges in geotechnical engineering arising from limited and sparse data obtained through site investigations due to cost and scheduling constraints. In particular, the study focuses on the Standard Penetration Test (SPT) N-values. The authors argue that traditional interpolation methods like Inversed Distance Weighted (IDW) and Ordinary Kriging (OK) have limitations in efficiently handling complex natural heterogeneity and providing sufficient interpretation for subsurface visualization. The authors also highlight the efforts of previous studies in proposing advanced interpolation methods, such as Glasso, sparse Bayesian learning and machine learning, but note the ongoing challenges in achieving efficient modelling with engineering interpretation. In response, the study introduces a novel method, the Weight Ellipse Nearest Neighbors (WENN), as an alternative solution for interpolating geotechnical properties.

The method, presented as an improved version of IDW, incorporates an ellipse function to consider geological anisotropy, providing a mathematical formulation for the modified distance between sampled and unsampled elements. The paper details the estimation of the spatial mean and standard deviation using WENN, introducing a novel approach for quantifying uncertainty associated with the weighted mean. In order to validate the proposed method, the authors include a simulated example featuring a non-stationary SPT profile and a real-world application using data from Kaiapoi, New Zealand. The data from five unequal-spaced boreholes in a 140m-long profile (Figure 7a) was acquired from the New Zealand Geotechnical Database (NZGD). The measurements as well as the spatial interpolation results are illustrated in Figure 7b.

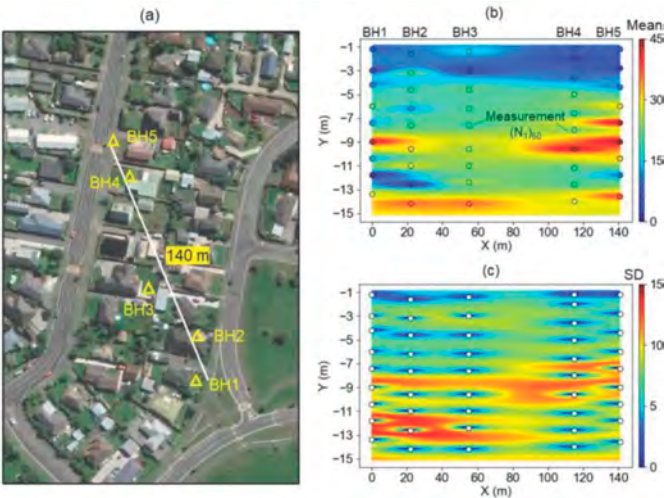


Figure 7. (a) Layout of borehole distribution (NZGD, 2023); profile of (b) interpolated mean and (c) standard deviation (from Yan *et al*).

The proposed WENN method is a valuable tool for geotechnical engineers, providing a simplified and efficient solution for interpolating geotechnical properties, especially SPT N-values. The method's rapid processing time further emphasizes its potential for practical engineering applications.

6 OTHER PAPERS

Tang *et al* paper explores the challenges associated with tunnel excavation beneath masonry buildings featuring shallow foundations, a scenario that could have significant implications for structural integrity of the buildings. The traditional investigative methodologies, primarily relying on small-scale physical models and full-scale numerical simulations, come under scrutiny due to their limited ability to accurately replicate realistic stress conditions. Recognizing this gap, the paper introduces an innovative hybrid testing approach, CCNM (coupled centrifuge-numerical modelling) presented in Figure 8. Unlike conventional methods, CCNM combines the strengths of both physical and numerical models, with a specific focus on masonry buildings supported by shallow strip foundations.

The authors present the methodological intricacies of CCNM, emphasizing the incorporation of concrete damage plasticity constitutive models in finite element numerical simulations (using Abaqus software) for the representation of masonry buildings. The centrifuge models, on the other hand, encompass the soil, tunnel, and strip foundation components. A key emphasis is placed on the data transfer protocols between the experimental and numerical domains, highlighting the crucial role of LabVIEW in controlling and manipulating the shared data.

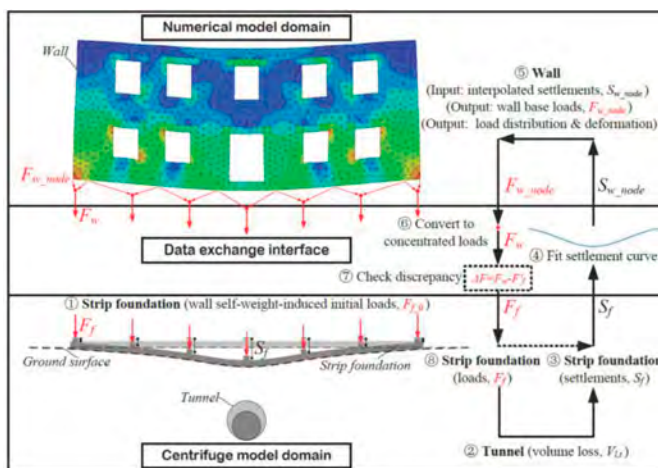


Figure 8. Diagram of the coupled centrifuge-numerical modelling of shallow foundations (from Tang *et al*).

The paper underscores the necessity of considering load redistribution within the building during the data transfer process for accurate assessments of deformations and potential damage.

Preliminary results from CCNM experiments are presented, demonstrating its efficacy in providing realistic insights into the dynamic interactions between tunnelling activities and structures with shallow foundations. Notably, the paper discusses the impact of load redistribution within the building on foundation settlements, offering valuable implications for understanding the structural behaviour under tunnel-induced ground movements.

The authors advocate for future research endeavors aimed at expanding the CCNM application to three-dimensional scenarios. This extension is seen as a crucial step towards a more comprehensive understanding of the complex interplay between geological conditions, construction contexts, and the structural response of buildings with shallow foundations during tunnel excavation. The paper contributes significantly to the advancement of methodologies for investigating the impacts of tunnelling on structures, advocating for integrated testing approaches that better reflect real-world conditions.

The session on “Smart Monitoring and Visualization Technologies for Tunnelling and Underground Construction” incorporates 10 papers addressing a diverse array of topics derived from underground construction projects spanning 9 different cities worldwide. This compilation of papers serve as a valuable academic and professional resource, providing comprehensive references for the exploration, design, construction and monitoring aspects of underground construction particularly those involving deep excavations and tunnelling. The case studies presented within these papers offer valuable insights into various projects, employing distinct construction and monitoring methodologies across diverse ground conditions and project scenarios. The accumulated knowledge from these studies offers valuable perspectives and experiences that can inform and guide the development and execution of future projects and research endeavours in this domain.

ACKNOWLEDGEMENT

The support provided to the author from Qatar University to attend this conference is acknowledged.

REFERENCES

- Chuanjin Tang, Senthil Prakash Selvaraj, Charles M. Heron, & Alec M. Marshall. Coupled centrifuge-numerical modelling of shallow strip foundations.
- Feizi, E. Skretting, T. Sandene, J. Langford, E. Monsås, J.M Josefsen, F. Karenstuen, and H. P Kristiansen. Control of grouting in the bedrock and soil in vicinity of tunnels and construction pits, Case study: E18, Oslo, Norway.
- He Huang and Wan-Huan Zhou. Predicting penetration behaviour of foam with different rheology into saturated sand
- Jian-Hua Ma, Yong-Zhang Zhou, Wei Cao & Jin-Feng Liu. Research on a CO2 Internet of Things online monitoring system for geotechnical engineering construction.
- Junhao Jing, Tao Wang and Wanhuan Zhou. Development and Performance Evaluation of a novel FBG-based Sensor for Measuring Positive and Negative Pore Water Pressure in soil.
- K.H. Phan, B.C.B. and J. Huang. Least Squares Adjustment Approach in Real-time Monitoring of Existing Twin Tunnels.
- Wei Yan, Wan-Huan Zhou and Ping Shen. Spatial Interpolation of Sparse SPT values using Weighted Ellipse Nearest Neighbors Approach.
- Xue-Dong Bai, Wen-Chieh Cheng, Bin Wu Xi'an and Dominic E.L. Ong. Investigating inherent mechanism of loess adhered to shield machine cutting tools.
- Z. Zhou and T.M.H. Lok. The relationship between the penetration depth and wavelength of the surface wave in two layers of soil.
- Z.W. Ye, D.M. Zhang, J.Z. Zhang, M.L. Zhou, H. Shao & Q. Zhou. Study on grouting rehabilitation of asymmetric transverse deformation in an existing shield tunnel.

Investigating inherent mechanism of loess adhered to shield machine cutting tools

X.D. Bai, W.C. Cheng & B. Wu

Xi'an University of Architecture and Technology, Xi'an, China

D.E.L. Ong

Griffith University, Queensland, Australia

ABSTRACT: Soils adhered to cutting tools or clumped to each other could not only cause a low advance rate in tunneling but also a difficulty in spoil discharging. These results especially hold true while tunneling in the loess containing primarily silt particles. The above remains to be addressed toward preventing unplanned downtimes and additional project costs. In addition to the mixing and fluidity tests, the atomic force microscopy (AFM) test is applied in the present work to explore the inherent mechanism affecting their adhesion properties when sand, kaolinite, and montmorillonite are introduced as adhesion reduction materials. The adhesion ratio is in a negative relation with the fluidity. The latter two are deemed poor adhesion reduction materials despite the higher adhesion force of the sand-loess mixture than the kaolinite-loess mixture. The intermolecular force plays a key role in promoting such a phenomenon. The highest adhesion force of 52.5 nN is attained by the montmorillonite-loess mixture due to the development of capillary force.

1 INTRODUCTION

Cohesive soils often adhere to cutting tools of a shield machine, increasing the clogging potential [1-2]. Based on existing theories, the adhesion formed at soil-metal interface can be divided into three categories [3]. The intermolecular force controls the adhesion force when a small amount of water is present at the soil-metal interface. With the increase of moisture content, water rings are formed between soil particles and metal, and the physical interaction represented by capillary tension controls the adhesion force. When water rings penetrate with increasing moisture content and form a water film, the water film (capillary) tension is considered to be the key factor affecting the adhesion force [4-5]. Loess which is an aeolian sediment is widespread in Northwest China and contains mainly silt particles. Although previous studies have largely improved our understanding of the development of the adhesion force, the inherent mechanism affecting the loess adhered to cutting tools has not been explored yet. The above reveals some research gaps and shortcomings. The main objectives of this study are to: (1) explore the inherent mechanism affecting the loess adhered to cutting tools; and (2) propose countermeasures applied to reducing the adhesion force toward preventing unplanned downtimes and additional costs while tunnelling in Northwest China.

2 MATERIALS AND METHODS

The loess containing a higher than 85% silt fraction was classified as low plasticity clay according to the Unified Soil Classification System (USCS). Kaolinite and montmorillonite are the main components of the bentonite slurry applied to counterbalance chamber pressures

exerted during shield tunneling. By contrast, the mechanical properties of sand are not governed by Van der Waals forces but by gravity forces. To this end, it is applied accentuating their relative merits. In the present work, sand, kaolin, and montmorillonite are used as additives to explore their effect on the adhesion force and fluidity of the soil mixtures. Laboratory tests applied to the present work mainly included mixing, fluidity, and atomic force microscopy (AFM) tests. The mixing test aimed to determine the adhesion potential through the adhesion ratio. Soil specimens at different additive proportions and moisture contents were first mixed using an agitator and stood still. When it started falling from the agitator, the remaining was weighed. The measurement was repeated 7 times and 5 out of the readings were applied to determine the adhesion ratio (see Equation 1).

$$\lambda = \frac{1}{5} \sum_{x \in \{0,1,2,3,7\}} \frac{G_{MTx}}{G_{TOT}} \quad (1)$$

where G_{MTx} is the adhesion mass of soil after x numbers of drops; G_{TOT} is the total mass of soil; λ is the average adhesion ratio obtained. Furthermore, the fluidity of soil specimens was determined by the difference in specimen diameter before and after vibrations (see Equation 2).

$$Flow_{25} = \frac{d_{25} - d_0}{d_0} \times 100\% \quad (2)$$

3 RESULTS AND DISCUSSION

3.1 Results of sand-loess mixture

The maximum adhesion ratio of the sand-loess mixture decreases with the increasing sand fraction (see Figure 1). The reduction in adhesion starts taking effect as the sand fraction is in excess of 30%. The soil consistency I_c of the sand-loess mixture remains in a 0.2-0.4 range when subjected either to a high sand fraction or a low sand fraction (see Figure 4). Further, results from the AFM tests show that the surface morphology varies notably with the highest difference in elevation being 20 nm toward reducing the contact between the loess and the metal probe and then the adhesion force (see Figure 3). Moreover, results also show that the fluidity of the sand-loess mixture increases with increasing sand fraction and that the fluidity against the soil consistency I_c of 0.2 is rather close to that against the soil consistency I_c of 0 (corresponding to the liquid limit of the sand-loess mixture) (see Figure 2). The higher the fluidity, the lower the potential for the spoils to clump together, and the smaller the difficulty for spoil discharging. On the whole, the sand addition can effectively reduce the adhesion between the loess and the metal, preventing difficulties in cutting. The increase in fluidity by the sand addition can also prevent clogging in spoil discharging. In light of the above, the sand addition is considered as a good adhesion reduction material, preventing unplanned downtimes and additional project costs.

3.2 Results of kaolinite-loess mixture

The maximum adhesion ratio of the kaolinite-loess mixture remains above 0.4 when subjected either to a low kaolinite fraction or a high kaolinite fraction, indicating a high potential of adhesion to cutting tools (see Figure 5). Under this circumstance, the soil consistency falls within a 0.5-0.75 range (see Figure 8). Results from the AFM test show that the surface topography does not vary as significantly as that of the sand-loess mixture, with the highest difference in surface elevation of 3 nm, corresponding to a larger contact area (see Figure 7). The adhesion force is supposed to be higher under this circumstance. However, the adhesion force is higher in the sand-loess mixture (31.4 nN) than in the kaolinite-loess mixture (25.8 nN).

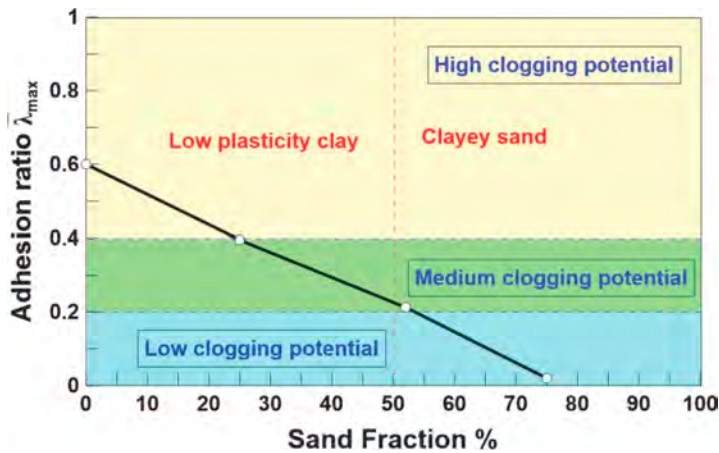


Figure 1. Mixing test results applied to the sand-loess mixture.

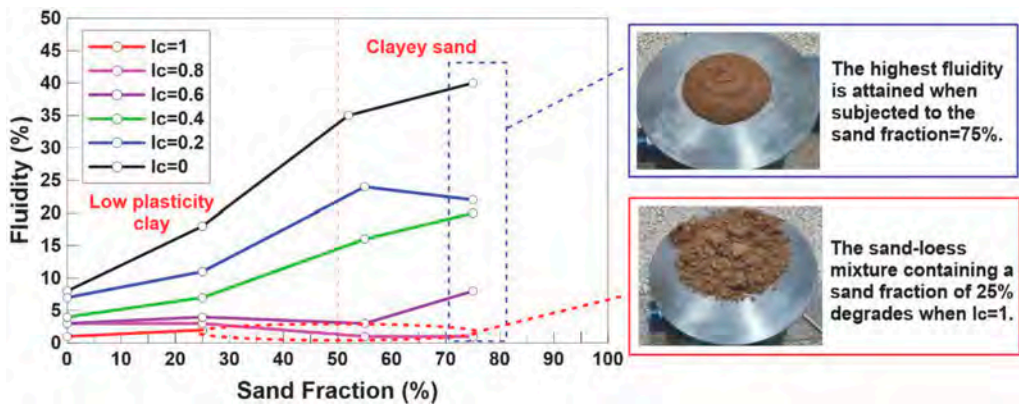


Figure 2. Fluidity test results applied to the sand-loess mixture.

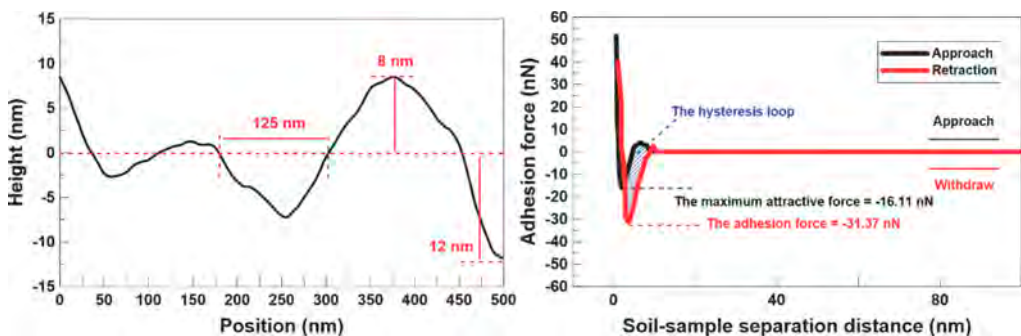


Figure 3. AFM test results applied to the sand-loess mixture.

This is mainly attributed to the non-swelling nature of the kaolinite, preventing water intrusion. The adhesion cannot be developed until water intrudes the DDL (diffuse double layer). As to the sand-loess mixture, its adhesion is not dominated by the capillary tension but by the inter-molecular force. Apart from that, the fluidity of the kaolinite-loess mixture against $I_c = 0.6$ (which is within a 0.5-0.75 range) is rather low, meaning that the kaolinite-loess mixture not

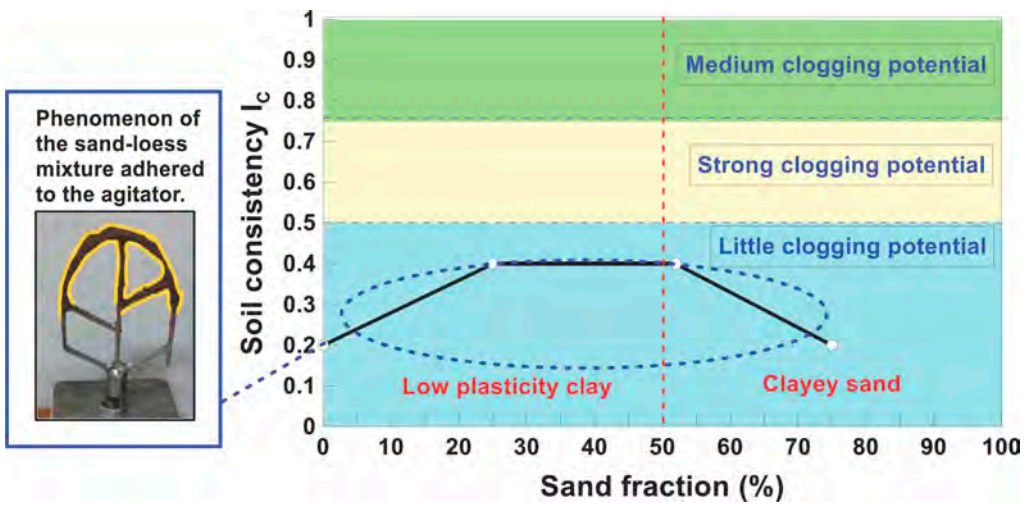


Figure 4. Relationship of consistency index versus sand fraction applied to the sand-loess mixture.

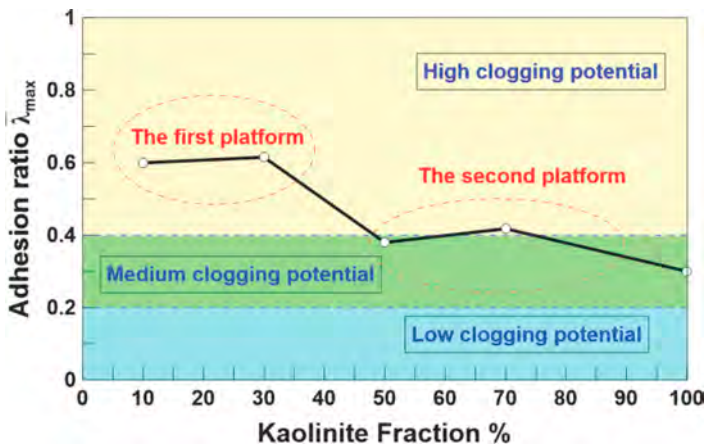


Figure 5. Mixing test results applied to the kaolinite-loess mixture.

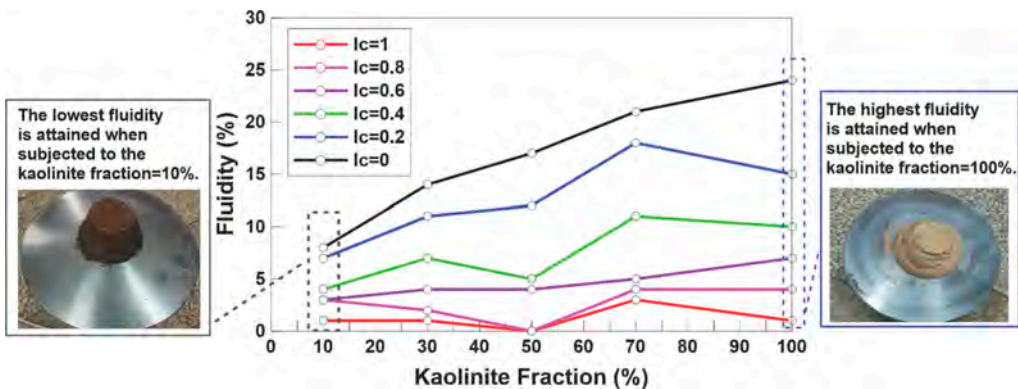


Figure 6. Fluidity test results applied to the kaolinite-loess mixture.

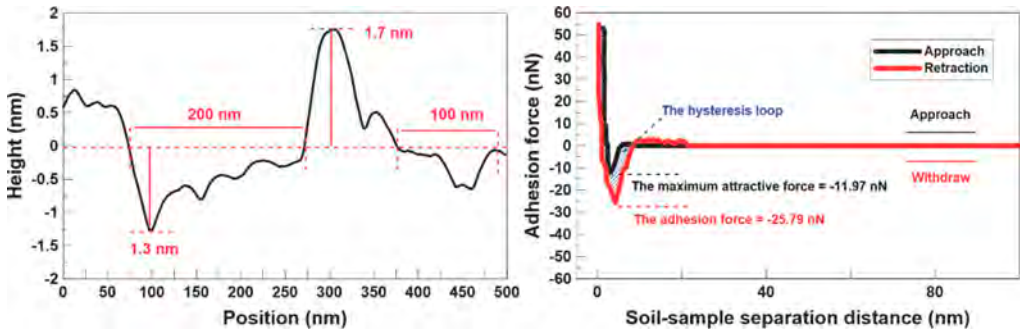


Figure 7. AFM test results applied to the kaolinite-loess mixture.

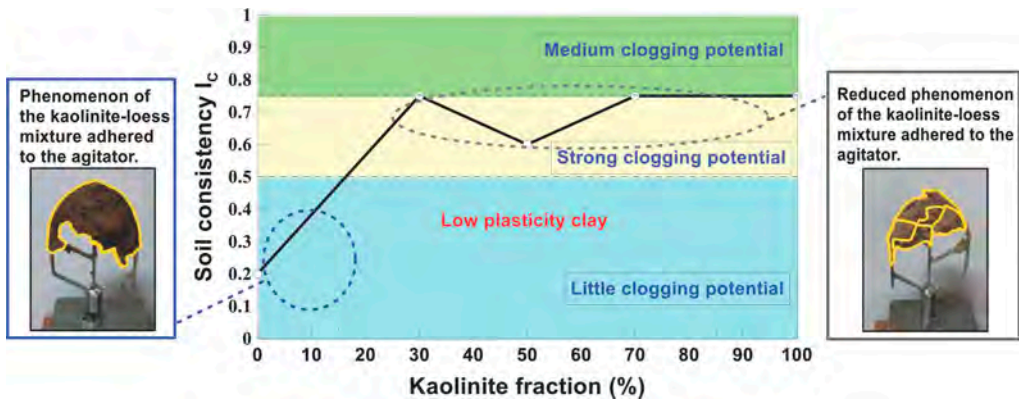


Figure 8. Relationship of consistency index versus sand fraction applied to the kaolinite-loess mixture.

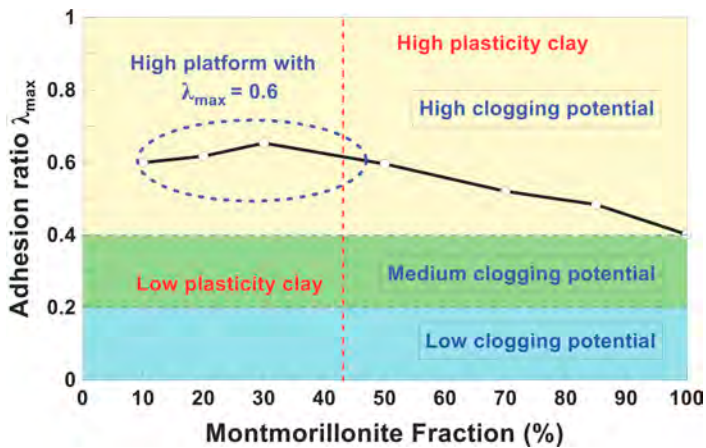


Figure 9. Mixing test results applied to the montmorillonite-loess mixture.

only has a high potential to adhere to cutting tools but can easily clump together, causing a clogging problem in spoil discharging (see Figure 6). In short, the kaolinite addition cannot be considered a good adhesion reduction material.

3.3 Results of montmorillonite-loess mixture

The maximum adhesion ratio of the montmorillonite-loess mixture is way higher than that of the kaolinite-loess mixture, corresponding to a maximum adhesion ratio of above 0.6 (see Figure 9). Under this circumstance, the soil consistency falls also within a 0.5-0.75 range (see Figure 12). Results from the AFM test indicate that the montmorillonite-loess mixture has the lowest roughness (smallest difference in surface elevation) and the adhesion force being 52.5

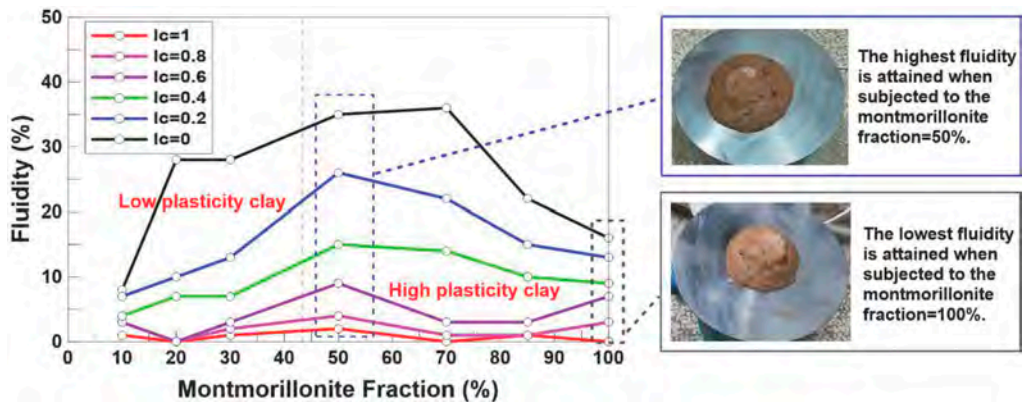


Figure 10. Fluidity test results applied to the montmorillonite-loess mixture.

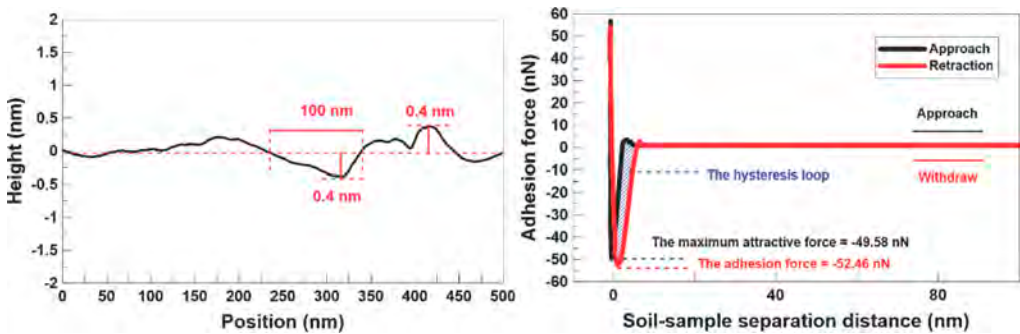


Figure 11. AFM test results applied to the montmorillonite-loess mixture.

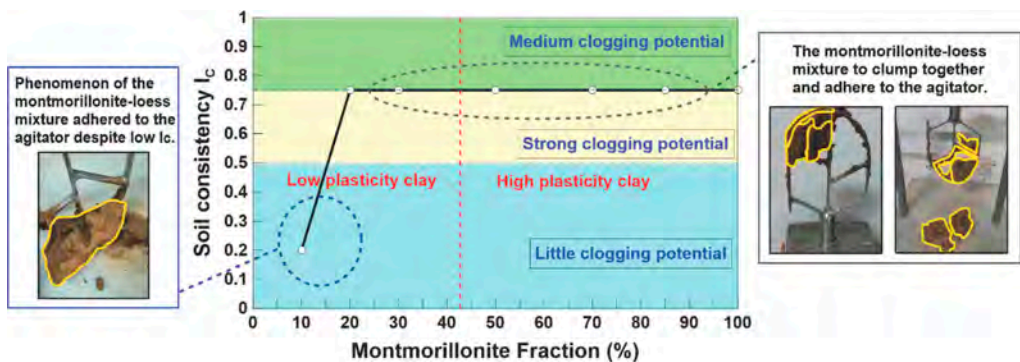


Figure 12. Relationship of consistency index versus sand fraction applied to the montmorillonite-loess mixture.

nN (the highest in the present work) (see Figure 11). On the other hand, the fluidity of the montmorillonite-loess mixture against $I_c = 0.6$ (which is within a 0.5-0.75 range) is extremely low. These results correspond to a high potential for it to clump together and also a significant clogging phenomenon in spoil discharging (see Figure 10).

4 CONCLUSIONS

Based on the results and discussion, some main conclusions can be drawn as follows. The higher the adhesion ratio, the lower the fluidity. The use of kaolinite and montmorillonite are not deemed as good adhesion reduction materials despite the higher adhesion force of the sand-loess mixture than that of the kaolinite-loess mixture. The intermolecular force plays a leading role in triggering such a phenomenon. The highest adhesion force of 52.5 nN is attained by the montmorillonite-loess mixture, most likely due to the development of the capillary force.

REFERENCES

- Zumsteg, R., Puzrin, A. 2012. Stickiness and adhesion of conditioned clay pastes. *Tunnelling & Underground Space Technology* 31: 86–96.
- Wang, S., Liu, P., Hu, Q., Zhong, J. 2020. Effect of dispersant on the tangential adhesion strength between clay and metal for EPB shield tunnelling. *Tunnelling & Underground Space Technology* 95: 103144.
- Fountaine, E.R. 1954. Investigations into the mechanism of soil adhesion. *European Journal of Soil Science* 5(2): 251–263.
- Wan, Z., Li, S., Yuan, C. 2021. Soil conditioning for EPB shield tunneling in silty clay and weathered mudstone. *International journal of geomechanics* 21(9): 06021020.
- de Oliveira, D.G.G., Thewes, M., Diederichs, M.S. 2019. Clogging and flow assessment of cohesive soils for EPB tunnelling: Proposed laboratory tests for soil characterisation. *Tunnelling & Underground Space Technology* 94: 103110.

Control of grouting in the bedrock and soil in vicinity of tunnels and construction pits, Case study: E18, Oslo, Norway

S. Feizi, E. Skretting, T. Sandene, J. Langford, E. Monsås & J.M. Josefsen
Norwegian geotechnical Institute (NGI), Norway

F. Karenstuen
The Norwegian Public Roads Administration (NPRÅ), Norway

H.P. Kristiansen
Dr. Ing. A. Aas Jakobsen AS (AAJ), Norway

ABSTRACT: Construction of open excavation pits and tunnels below groundwater level in urban areas are continuous geotechnical challenges. Reducing the water ingress to excavations is vital, to limit drawdown of the groundwater head at bedrock level and consequent consolidation settlements in soft clays deposits, which potentially can cause damage to nearby buildings and infrastructure. In connection with the development of the E18 highway near the city of Oslo in Norway, a hydrogeological barrier consisting of sheet pile walls, rock mass pre-grouting and jet column grouting have been designed and executed for a deep excavation in soil and rock. This paper presents the design of the barrier and control of pre-grouting execution which was required to optimize the barrier construction with respect to local ground conditions.

1 INTRODUCTION

Dealing with groundwater during the execution of deep excavations is vital to avoid or reduce damage to nearby buildings and infrastructure. Many studies have been done with respect to rock mass-grouting technology. In some research for example from Rombough et al. (2006); Lombardi (2008); Shuttle et al. (2008); El Tani (2009), the propagation behavior of cement grouting in planar fractures is investigated in detail while other groups such Bremen (1997); Rombough et al. (2006) are more focused on the rheological properties and stability characteristics of cement grout mixed with additives. Besides, safe and sustainable design as highlighted in the Tann (2022 and 2023) paper is key that should be considered in all geotechnical and geological aspects.

Despite many theoretical studies, there are however not many available practical documents showing control documentation, composition and quality of pre-grouting from case studies. In connection with the development of the E18-west corridor highway, near the capital of Norway, Oslo, NGI is engaged to design and quality control of: *a)* The sealing works with rock grouting curtain around the Ramstadsletta deep excavation pit where the abutment for the Høvik-tunnel is going to be established, and *b)* The jet column installation works along the southern area as a sealing measure at the sheet pile toe where the toe is not to be excavated.

This study focuses mainly on the practical process of controlling the rock grouting and jet column installation works. The goal is to avoid or reduce groundwater head draw down of the surrounding areas which may affect the nearby buildings and infrastructure.

2 BACKGROUND

The first stage of the E18 West Corridor highway is being developed west of Oslo. The location of the project is shown in Figure 1. As is the case with many urbanized areas in Norway, the area around the Ramstadsletta deep excavation is characterized by rock outcrops with intermediary depression zones. Soft marine clay is commonly deposited in these depressions. Layers of more permeable moraine material may be found below the clay above bedrock.



Figure 1. Location of the E18 project in world map and highlighted with red in the local map.

Experience from tunnels and ground water pumping (Langford et al 2016), shows that even small amounts of leakage can result in substantial decrease in pore pressures at bedrock level where the pore pressure reduction triggers settlements on the surrounding areas. During early stages of the design the clay filled depression zones were mapped by ground investigations. Figure 2 shows the extent of the Ramstadsletta excavation pit with the surrounding clay filled depressions.

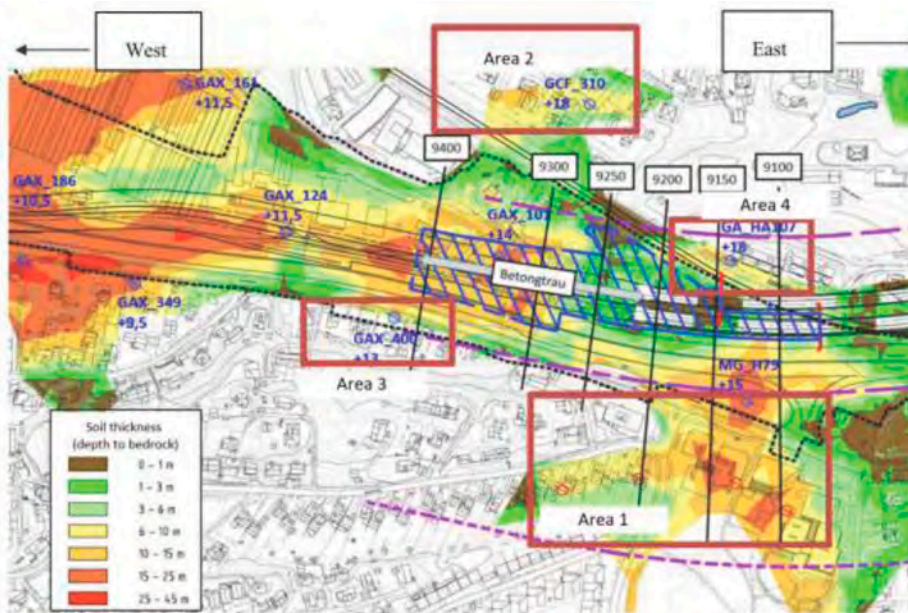


Figure 2. Map of Ramstadsletta, soil thickness to bedrock, areas susceptible to settlement marked with red. The deep excavation is highlighted with the blue hatchet.

As well as investigating depth to bedrock and soil deformation characteristics, the in situ pore pressures were logged over several years prior to the construction work, to determine effects of natural seasonal variations. Based on the thickness of the clay layer and soil deformation characteristics a risk assessment was performed identifying the potential settlements for different groundwater drawdown scenarios in different depression zones. A groundwater barrier as shown in Figure 3 was designed to maintain two different scenarios; *i)* The temporary full drainage of the excavation pit for up to 4 years and *ii)* The permanent drainage level within the excavation when construction is completed and water levels are reestablished around the water tight concrete structures. The complete groundwater barrier design consists of:

- Steel sheet pile walls to bedrock, including watertight interlocks, corners and anchors
- Concrete beam or jet grouted columns at the sheet pile toe, to seal potential groundwater ingress in the gap between rock and sheet pile through permeable moraine material
- Continuous cement grouting curtain in bedrock below the sheet pile wall down to 10 m under the lowest excavation level and minimum 10m in bedrock.

Figure 3 illustrates the location of the sealing barrier, as well as the recorded level of pore pressure at the rock before the start of construction.

In addition to the groundwater barrier, several water infiltration wells were located in strategic locations around the deep excavation. Wells, where water can be infiltrated into bedrock to counter groundwater head drawdown, temporarily during the construction phase. Furthermore, a large number of piezometers were installed, which all had automatic logging of pore pressures with set limits connected to acceptance criterion for drawdown which would cause damaging settlements. Figure 4 illustrates pore the pressure versus time from one of the closet piezometers to the construction area. This piezometer is installed in the bedrock. Variation on pore pressure is mainly either due to the precipitation (which is plotted in red) or construction activities.

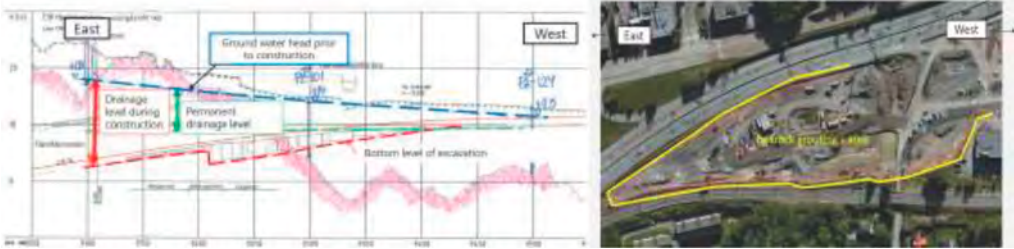


Figure 3. Location of the sealing barrier, as well as the recorded level of pore pressure at the rock before and after the start of construction.

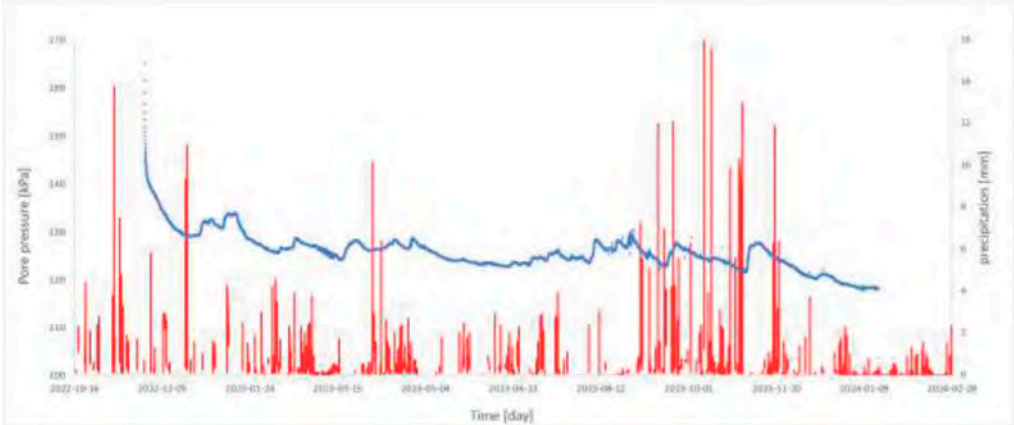


Figure 4. Pore pressure versus time. The left vertical axis shows the amount of rain in mm.

3 ROCK GROUTING CURTAIN

Drilling of grouting holes was performed with a steel casing through soils and typically 0.5 to 1.0 m into rock. In areas where the rock surface was uncovered, the rock hole was drilled directly without any casing. The drilling and pre-grouting works were carried out as a form of “split spacing” as shown in Figure 5. A-holes (center to center- c/c 3.0 m) were first drilled and grouted, then B-holes (c/c 3.0 m). The need for additional drilling C-holes (c/c 1.5 m) between the A- and B-holes was assessed based on reported grouting documentation (volume grouting and grouting pressures) from A- and B-holes.

The holes were drilled to 10 m below the bottom level of the excavation in the relevant profile, and a minimum of 10 m down into the rock. Grouting was performed with packer placement first at approx. 5 m into the rock hole, then at approx. 0.5 m depth in rock, see Figure 5. A grouting procedure with stop criterion for grouting volumes pressure for packer placement 5 m and 0.5 m was suggested. A grouting pressure of 10 bar and 5 bar were used for the packers at 5 m and 0,5 m depth. If the grouting pressure was not achieved, the instruction was to gradually reduce the w/c ratio (water to cement ratio) of the grout and then stop at given volumes injected into the bedrock. The amount stop limits were specified accordingly:

- w/c ratio 1.0: 100 liters
- w/c ratio 0.7: 200 liters
- w/c ratio 0.5: 200 liters

Grouting was terminated at a total grot-take of 500 liters of grouting if pressure build up was not achieved.

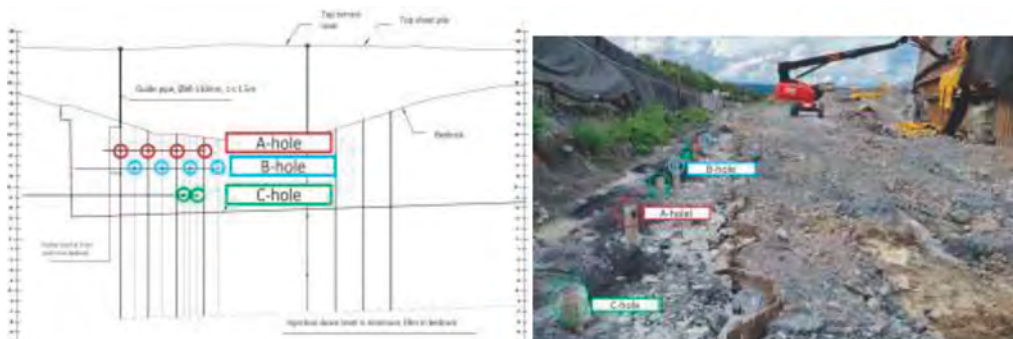


Figure 5. Illustration showing grouting holes with split-spacing procedure and photo of drilled casings for grout holes.

To ensure good progress and rational operation, the contractor was interested to get a specified distance between A-holes where grouting was undergoing, and drilling and grouting of subsequent B-holes. For that reason two criteria were set, both of which must be met. Firstly the distance between ongoing grouting in A-hole and simultaneous drilling of B-hole

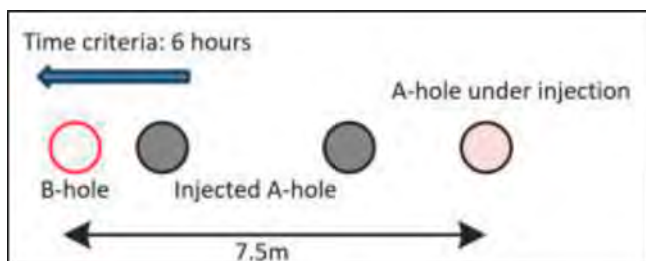


Figure 6. Outline of criteria in relation to distance and time between injected A, and drilling of B holes.

must be large enough to reduce the interaction effects (communication) between holes. The minimum distance from ongoing grouting in A-hole to drilling of B-hole was set to 7.5 m. The second criteria was the time since the nearest A-hole was grouted and drilling of B-hole. It was specified a minimum 6-hour time interval between the nearest A-hole that has been grouted and drilling of B-hole, see Figure 6. Based on following up works in the site, the introduced measures seemed to be working.

4 VISUALIZATION OF DRILLING DATA

All documentation of drilling and injection data was collated through a shared portal with the contractor, NPRA and consulting engineers. With a total of over 700 grouted holes, there was a need to systematize the data. A separate Excel spreadsheet was created where drilling and grouting protocols were systematized and visualized (see Figure 7). The data were sorted based on location coordinates from drilling data. Grouting data was entered and visualized with a color scale based on the completed grouting quantity against set maximum quantities for each w/c ratio. The Excel sheet was used as support for deciding on the need for supplementary grouting holes (C-holes).

In areas where grouting amount is below the stop criteria on volume (liters) on any of the w/c numbers, a color code “green” has been used. In areas where the stop criteria on volume (liters) of grouting was met, or where back pressure had not been achieved on any of the w/c numbers on either “A holes” or neighboring “B holes”, a color code “red” has been assigned and it was deemed necessary to introduce C holes. In any other conditions and depending on amount of grouting compared to the stop criteria, a color shift between lower estimate of “green” to upper estimate of “red” has been assigned. On a few occasions it also became necessary to introduce D-holes because back pressure was not reached on C-holes. The drilling and grouting data was also visualized in an longitudinal section of the grouting line. This was done both to get an overview of the injection quantities that have passed along the injection line, but also to assess the location of the injection holes against the assumed groundwater level and planned construction bottom, which is visualized in “Grapher” and “bokeh.plotting” (python), see Figure 8.

BOREHULL	Packer location (kote)	Packer at 5 m			Packer at 0.5 m			
		w/c=1	w/c=0.7	w/c=0.5	w/c=1	w/c=0.7	w/c=0.5	
L2_A90	10.0	5	0	0	14.5	1	0	0
L2_B89	-4.8	11	102	0	-0.3	7	0	0
L2_A89	-3.2	6	0	0	1.3	3	0	0
L2_C88.1	9.8				14.3	31	0	0
L2_B88	-2.8	130	109	0	1.7			
L2_C88	9.8				14.3			
L2_A88	-3.2	9	0	0	1.3	4	0	0
L2_B87	-2.8	19	0	0	1.8	20	0	0
L2-A87	-2.5	4	0	0	2.0	4	0	0
L2_B86	-2.2	49	0	0	2.3	34	0	0
L2_A86	-1.6	11	0	0	2.9	3	0	0
L2_B85	0.1	34	0	0	4.6	29	0	0
L2_A85	1.4	120	200	200	5.9	10	52	0
L2_B84	3.7	19	0	0	8.2	6	0	0
L2_A84	4.4	26	0	0	8.9	3	0	0
L2_B83	4.4	21	0	0	8.9	10	0	0
L2_A83	4.4	120	200	200	8.9	10	10	100

Figure 7. An example view of the excel sheet with injection data visualized by color scale.

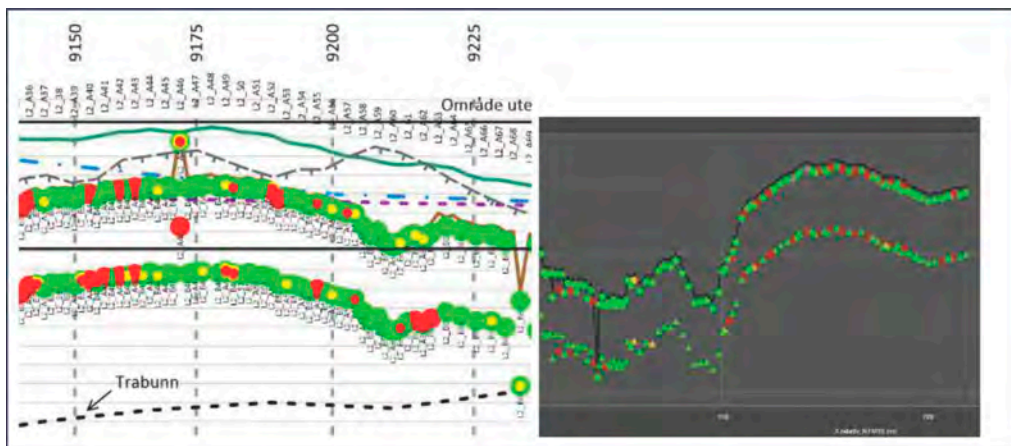


Figure 8. An example of injection data. Left from Grapher, right using bokeh.plotting (python).

5 PERFORMANCE OF GROUNDWATER BARRIER

The risk of obtaining pore pressure decrease due to leakage into an excavation can be reduced by mitigating measures. Combined solutions of sheet pile, grouting in bedrock and jet-grouting are amongst those measures for this project. After finishing the grouting work, very limited leakage (waterproof) was observed in most of the target area which proves a good execution and performance of the grouting work and groundwater barriers. The most leakages observed are through anchors in the sheet pile wall and rock bolt holes. The main reason for such significant leakage was that the anchors were puncturing the grout curtain and opened paths for flow. The introduced measure to stop this leakage is to grout with cement suspension and polyurethane in casings which is still under process.

6 DISCUSSION AND CONCLUSIONS

The following experiences and aspects are gained through the rock grouting work in the project:

i) Systematization of data

Drilling data provides important information regarding the level of the bedrock surface and how high the impermeable barrier ends up in relation to the groundwater level. This is critical information when assessing whether the sealing barrier is acceptable with regard to the requirements in the design. There were cases where the actual rock surface was lower than assumed, so that the sealing barrier ended up at a lower level than designed. This is only recognized when drilling data is post-processed and visualized. It should therefore be specified to the contractor that drilling data should preferably be submitted before the associated injection data.

In other places, it was unclear what level the rock surface actually was, and whether or not casing had been drilled further into the rock than the agreed requirement. For this project, it was agreed that injection data would be sent twice a week, while drilling data would be sent once a week. It is therefore very important that before starting the grouting works, one should investigate the possibilities of achieving a more seamless systematization of drilling and grouting data, by e.g. create a code that acquires data automatically and sorts it, to avoid manual entering of data in spread sheets. Preferably a template could be made for the contractor to use for data documentation and systematization.

- ii) Transmission and content of drilling data
During quality control work, rock grouting data were often sent before drilling data. Reentering the correct drilling data (depth to bedrock, length of hole in bedrock etc) afterwards turned out to be time-consuming and a source of error. For example, the rock surface sometimes was discovered to be lower than assumed, and this would affect the intended function of the grouting curtain. Again, a commonly adapted protocol template, improved lines of communication and perhaps utilization of coding for data handling would have benefited the process, reducing hours and errors.
- iii) Documentation of w/c numbers and back pressure
It is important that documentation of grouting mass is done according to the w/c number. For grouting work carried out, all mass of w/c=1.0 has been recorded for several holes, with the assumption that quantity criteria for the various w/c numbers have been followed. 500 liters registered at w/c=1.0 means that 100 liters have been grouted for w/c=1.0, 200 liters for w/c=0.7 and 200 liters for w/c=0.5. Data management should then be carried out properly from the start point.
- i) Regular site inspection
Regular site visit should always be undertaken by designers if possible. This will help both the designer and the contractor in mutual understanding of different issues which may occur during execution of the drilling and grouting works.
- ii) Identification of grouting holes
Hole identification must be consistent through the different manual and electronically kept protocols.

REFERENCES

- Bremen R. 1997. The use of additives in cement grouts. *Int Journal of Hydropower Dams*, 4: pp 71–76.
- El Tani M. 2009. Grout-time to break through the SL dispute, *Geotech News* 27(3), pp 41–49.
- Langford J., Baardvik G. and Karlsrud K. 2016. Pore pressure reduction and settlements induced by deep supported excavations in soft clay, *Proceedings of ISSMGG*, Iceland.
- Lombardi G. 2008. Misunderstanding of GIN confirmed. *Geotech News*, 26(2): pp 57–63.
- L. von der Tann, IF Størdal, Ritter S. and Feizi S. 2022, First steps in the development of standardized process for life cycle assessments of geotechnical works, *IOP Conference Series: Earth and Environmental Science*, DOI 10.1088/1755-1315/1122/1/012046
- L. von der Tann, Baardvik G., Mortensen O., Monsås E. and Feizi S. 2023, Cost and carbon implications of different foundation solutions-Desk study of foundation design for a bridge and a building in Norway, *1st Conference on Foundation Decarbonization and Re-use*, DOI 10.5281/zenodo.8172004
- Rombough V., Bonin D., Shuttle D. 2006. Penetrability control of the GIN mixes during fractured rock grouting, sea to sky geotechnique. *Proceedings of the 59th Canadian geotechnical conference*, Vancouver, Canada, pp 528–535.
- Shuttle D, Rombough V, Bonin G. 2008. An alternative viewpoint on GIN. *Geotech News*, 26 (2): pp 64–66.
- NGI report number V-539, 2020. Drainage conditions and sealing measures at Ramstadsetta, *NGI report*, Norway.

Predicting penetration behavior of foam with different rheology into saturated sand

H. Huang

State Key Laboratory of Internet of Things for Smart City & Department of Civil and Environmental Engineering, University of Macau, Macau, China

H.M. Wang

China Civil Engineering Construction Corporation, Beijing, China

W.H. Zhou

State Key Laboratory of Internet of Things for Smart City & Department of Civil and Environmental Engineering, University of Macau, Macau, China

ABSTRACT: Foam, an instrumental soil conditioner in Earth Pressure Balance (EPB) shield tunneling, serves to reduce soil permeability. This study employs a simplified one-dimensional foam penetration model to predict the penetration behavior of foams with distinct rheological properties in saturated sand. The rheological behavior of various foams is described using power-law fluid model. The foam penetration characteristics are represented through the temporal curves depicting foam penetration distance. Results indicate that the flow behavior index of foam governs its penetration characteristic. A smaller flow behavior index facilitates rapid injection of foam into the sand, forming a low-permeability layer. Moreover, while maintaining a constant flow behavior index of foam, increased foam flow consistency index decreases the foam penetration distance. From an engineering perspective with anti-permeability, foams characterized by lower flow behavior indices and higher flow consistency indices exhibit pronounced advantages in EPB shield tunneling. The outcomes of this study provide valuable insights for the selection of foams in facilitating EPB shield tunneling.

1 INTRODUCTION

The EPB shield machine often needs to use foam as a soil conditioner to reduce the permeability of highly permeable soil layers (such as sand layers) during tunneling (Herrenknecht et al., 2011; Hu et al., 2020). Besides, in soil layers with high coarse content, additional polymers and bentonite slurry are needed as additives. Those soil conditioners are injected into the soil through conditioning tools placed in the cutter head and excavation chamber (see Figure 1). Galli et al. (2021) suggest that injecting foam ahead of the cutter head can lead to water displacement in saturated sand soil, thereby affecting the properties of the excavated soil. Thus, studying the foam penetration characteristics in saturated soil is crucial for understanding its role in EPB shield tunneling.

Xu et al. (2022a&b) conducted studies on foam penetration characteristics using a model test setup, delineating the penetration process into four distinct stages. Building on this, Zhang et al. (2022) conducted further model experiments and proposed a micro-model for foam penetration, explaining the mechanism behind foam penetration. However, existing experimental setups, despite simulating hydraulic gradients similar to field conditions (Qin et al., 2023a&b; Xu et al., 2022a,b&c), are limited by soil columns only tens of centimeters in height, restricting deeper foam penetration studies. Additionally, due to the limited types of foam available, a comprehensive study of foam parameters' influence on the penetration process is unfeasible.

This study presents a simplified one-dimensional foam penetration model capable of predicting foam penetration processes in saturated sandy soil under various conditions. The

model utilizes a power-law fluid model to describe foam rheology and investigates the penetration characteristics of different rheological foams, elucidating the impact of foam rheological indices on penetration characteristics.

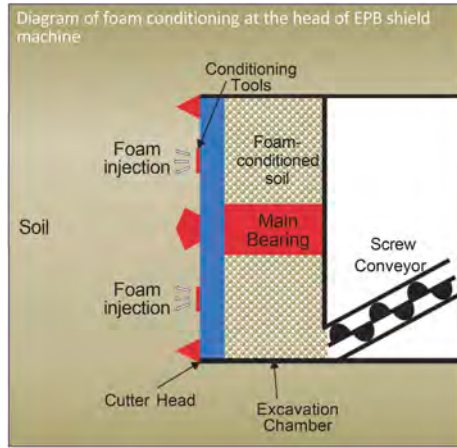


Figure 1. Diagram of foam conditioning at the head of EPB shield machine.

2 METHODOLOGY

2.1 Simplified one-dimensional foam penetration model

The foam penetration ahead of the tunnel face can be simplified as illustrated in Figure 2. Foam injection divides the soil into two regions with different pressure gradients. This distinction arises due to the rheological differences between foam and water. Previous studies (Jing et al., 2017; Bashir et al, 2022) have confirmed that the rheology of foam can be described using a power-law model:

$$\tau = \gamma \dot{\gamma}^x \quad (1)$$

where γ is the flow consistency index ($\text{Pa}\cdot\text{s}^x$), x is the flow behavior index (-), τ is the shear stress (Pa), and $\dot{\gamma}$ is the shear rate (s^{-1}).

The fluid flow velocity in the saturated sand region can be described by Darcy's law:

$$v = ki = \frac{K\rho g \Delta h}{u L} \quad (2)$$

where u represents the dynamic viscosity ($\text{Pa}\cdot\text{s}$) of water, ρ is the density (kg/m^3) of water, g is the acceleration of gravity (m/s^2), K is the intrinsic permeability (m^2), $k=K\rho g/u$ is the permeability coefficient (m/s), $i=\Delta h/L$ is the hydraulic gradient (-).

The fluid flow velocity in the foam injection area can be described as the velocity of power-law fluids in porous media (Ejezie et al., 2021):

$$v = Ci^{1/x} = \frac{nx}{3x+1} \left(\frac{8K}{n}\right)^{(x+1)/2x} \left(\frac{\rho g}{2\gamma}\right)^{1/x} \left(\frac{\Delta h}{L}\right)^{1/x} \quad (3)$$

where n is the porosity (-), C is defined as the generalized permeability coefficient (m/s):

$$C = \frac{nx}{3x+1} \left(\frac{8K}{n}\right)^{(x+1)/2x} \left(\frac{\rho g}{2\gamma}\right)^{1/x} \quad (4)$$

According to Figure 2, the simplified one-dimensional foam penetration model can be established as the following equations:

$$v = Ci_f^{1/x} = C \left(\frac{\varphi_0 - \varphi_1}{\rho_f g L} \right)^{1/x} \quad (5)$$

$$v = ki_w = k \frac{\varphi_1}{\rho_w g (L_s - L)} \quad (6)$$

$$v = n \frac{dL}{dt} \quad (7)$$

where i_f is the hydraulic gradient on the foam-penetrated region, φ_0 is the initial pressure (kPa) applied in the tests, φ_1 is the pressure (kPa) at the foam front, ρ_f is the density (kg/m^3) of foam, L is the foam penetration distance (m), i_w is the hydraulic gradient on the saturated sand region, ρ_w is the density (kg/m^3) of water, L_s is the total length of the sand (m). Assume that the Darcy velocities in Equations 5 to 7 as equal. By solving these equations with initial conditions at $t=0$ and $L=0$, numerical solutions for $L-t$ can be computed.

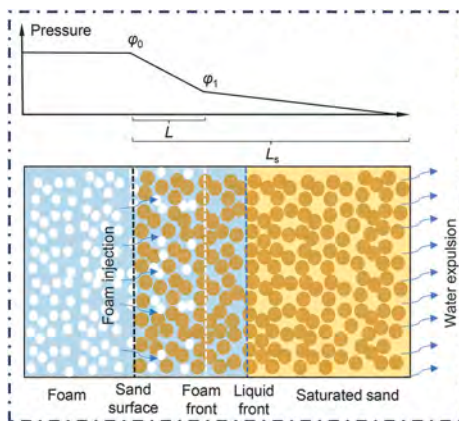


Figure 2. Schematic diagram of foam penetration process (referring zhang et al., 2022).

2.2 Obtain parameters through model experiment

This study conducted model experiments following the methods proposed by Xu et al. (2022 a & b) to validate the accuracy of the model and obtain the relevant parameters. The experimental details are in line with the previous works of the authors (Huang et al., 2023). The initial pressure was set as 50 kPa and L_s was set as 5 m in the experiment. Coarse sand with particle sizes ranging from 0.6 to 1.43 mm was used as the sand bed in the experiments. The foam utilized was CLB F5/M solvent produced by Condat (France), with an expansion ratio of 15. According to the model and theory presented in Section 2.1, the parameters involved can be analyzed as shown in Table 1.

The parameters from Table 1 were incorporated into the model described in Section 2.1. Utilizing MATLAB, the relationship between the penetration distance and time can be computed. Figure 3 compares the model's calculated values with the measured data. The results indicate that the model can accurately depict the actual penetration process.

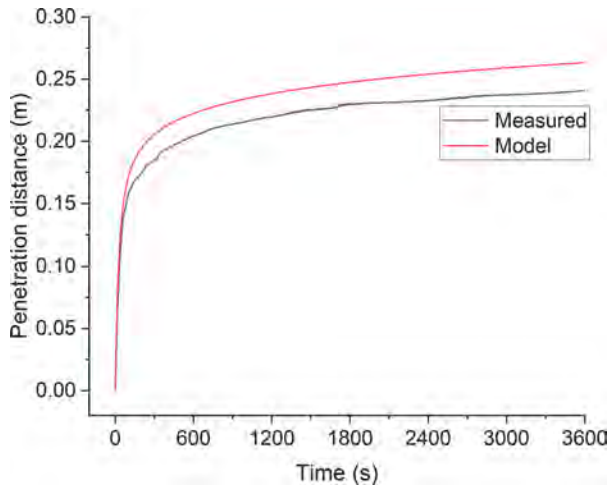


Figure 3. Comparison of the measured values and computed values of foam penetration.

Table 1. Summary of parameters.

k (m/s)	u (Pa·s)	ρ_w (kg/m ³)	K (m ²)	C (m/s)	n	x	ρ_f (kg/m ³)	y (Pa·s ^{0.09})
0.0026	0.00101	1000	2.6×10^{-10}	3.2×10^{-32}	0.38	0.09	97	7.6

2.3 Predicting penetration behavior of foam with different rheology

As shown in Table 1, the flow behavior index (x) of foam used in the model experiments was 0.09, and the flow consistency index of foam was 7.6. To predict the penetration behavior of different foams, the study manipulated the values of x and y in the calculations. Initially, y was set to 1, while x was increased gradually from 0.1 to 1 in increments of 0.1, to investigate the impact of the flow behavior index on foam penetration. Then, keeping x at 0.1, y was increased gradually from 1 to 10 in increments of 1, to study the effect of the flow consistency index on foam penetration.

3 RESULTS AND DISCUSSION

3.1 Impact of the flow behavior index on foam penetration

Figure 4 illustrates the rheological profiles of foam with varying flow behavior indices. It is observed from Figure 4 that at low shear rates (below 1), the foam viscosity decreases gradually as x increases. However, at shear rates above 1, the foam viscosity increases with the gradual increase of x .

Figure 5 illustrates the curves depicting the penetration distance over time for foams with different x values. Foams with smaller x values rapidly penetrate into the sand, followed by a significant reduction in the penetration velocity to approximately zero. This is advantageous in EPB shield tunneling as it aids in swiftly forming a low-permeability layer. Although foams with larger x values start with a slower penetration

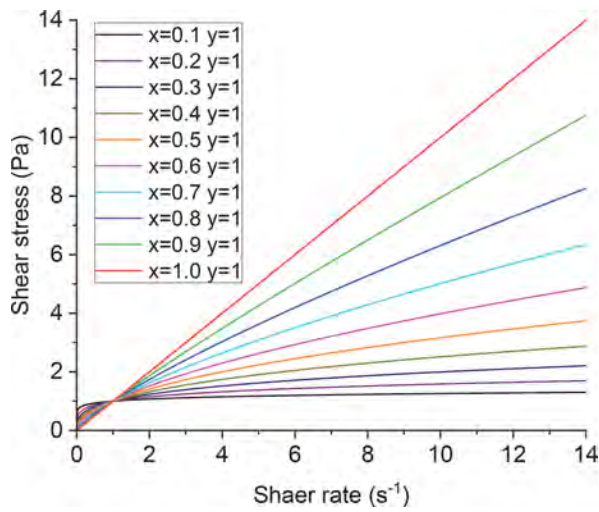


Figure 4. Rheological profiles of foams with varying x .

velocity, they maintain this velocity almost until the end. This characteristic hinders its effectiveness as a sealing agent. Hence, from an engineering perspective, foams with smaller x values prove more beneficial in shield tunneling.

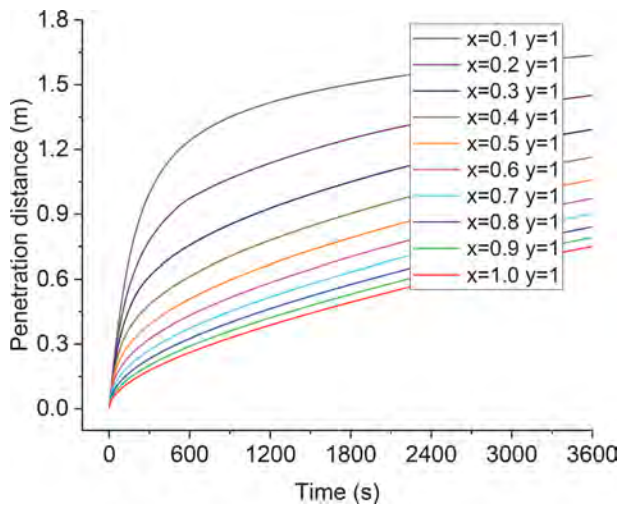


Figure 5. Penetration distance over time of foams with varying x .

3.2 Effects of the flow consistency index on foam penetration

Figure 6 illustrates the rheological profiles of foams with varying flow consistency indices. It is noticeable that all curves share a similar trend. However, with the gradual increase in y , there is a corresponding rise in foam viscosity across all curves.

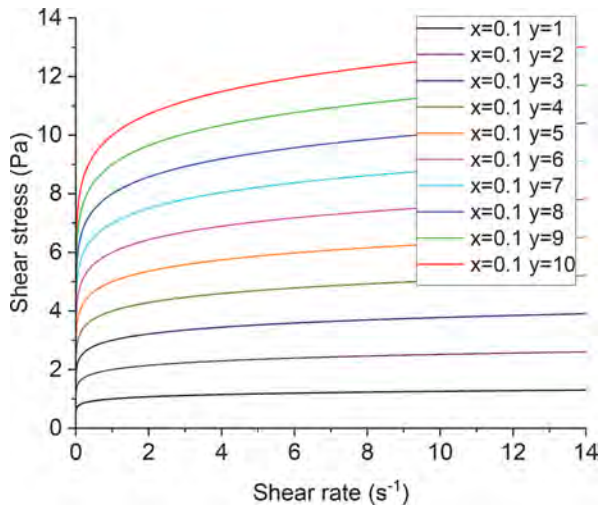


Figure 6. Rheological profiles of foams with varying y .

Figure 7 demonstrates the curves depicting the variation of penetration distance over time for foams with different y values. The trends of penetration distance over time for all foams are similar. Foams with larger y exhibit smaller penetration distances. This is attributed to higher viscosity under the same conditions when y is larger. Therefore, from an engineering perspective, foams with higher y are more beneficial for EPB shield tunneling.

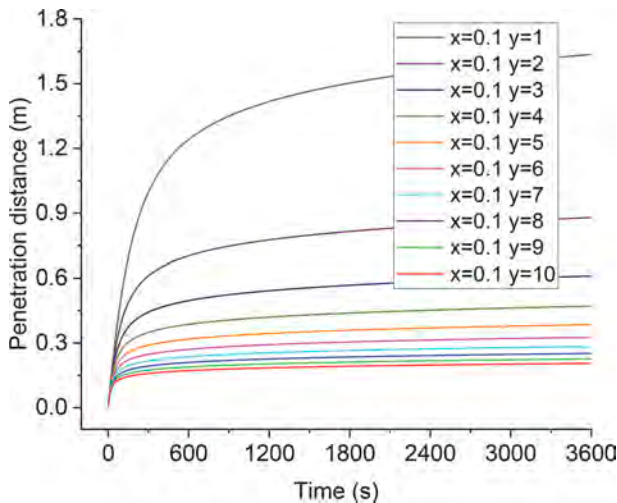


Figure 7. Penetration distance over time of foams with varying y .

3.3 Discussion

From the model predictions, it is evident that foams with lower flow behavior indices are more effective in reducing infiltration velocity during penetration, thereby forming effective seals. Additionally, foams with higher flow consistency indices exhibit relatively higher viscosity, also contributing to reduced infiltration velocity. Hence, for the practical engineering perspective of reducing permeability in highly permeable soil layers, selecting foams with lower flow behavior indices and higher flow consistency indices can achieve the desired improvement effects.

However, for less permeable soil layers where reducing permeability is not required, selecting foams with higher flow behavior indices and lower flow consistency indices may facilitate easier mixing with the soil and enhance soil fluidity. In summary, selecting foams with different characteristics is necessary depending on the specific requirements of practical engineering projects.

This study only employed a simplified one-dimensional model to investigate foam penetration characteristics in saturated soil. The model is based on numerous simplifications of actual penetration processes. Therefore, the results of this study only provide basic theoretical foundations. Further research into the intricate penetration processes encountered in practical engineering may necessitate alternative methods, such as large-scale model experiments and numerical simulations.

4 CONCLUSION

The foam penetration behavior can be described using a simplified one-dimensional flow model. Based on this model, the penetration behavior of foams with different rheological profiles was predicted. Furthermore, an analysis was conducted on the impact of the flow behavior index and flow consistency index on foam penetration behavior. Foams with a lower flow behavior index and higher flow consistency index theoretically align more with the anti-permeability demands of practical engineering. Such foams are more adept at swiftly forming a low-permeability layer within the sand. The outcomes of this study hold significance in guiding the selection of foam during EPB shield tunneling.

ACKNOWLEDGEMENTS

The research was funded by the Guangdong Provincial Department of Science and Technology (Grant No. 2019B111106001), the Science and Technology Development Fund, Macau SAR (File nos. 0056/2023/RIB2, 001/2024/SKL), and the National Natural Science Foundation of China (Grant No. 52022001).

REFERENCE

- Bashir, A., Haddad, A. S., & Rafati, R. (2022). An experimental investigation of dynamic viscosity of foam at different temperatures. *Chemical Engineering Science*, 248, 117262.
- Galli, M., Thewes, M., Freimann, S., & Schröer, M. (2021). Residual water content of excavated soil in EPB tunnelling. *Tunnelling and Underground Space Technology*, 114, 103991.
- Herrenknecht, M., Thewes, M., & Budach, C. (2011). The development of earth pressure shields: from the beginning to the present/Entwicklung der Erddruckschilde: Von den Anfängen bis zur Gegenwart. *Geomechanics and Tunnelling*, 4(1), 11–35.
- Hu, Q., Wang, S., Qu, T., Xu, T., Huang, S., & Wang, H. (2020). Effect of hydraulic gradient on the permeability characteristics of foam-conditioned sand for mechanized tunnelling. *Tunnelling and Underground Space Technology*, 99, 103377.
- Huang, H., Sun, Q., Xu, T., & Zhou, W.H. (2023). Mechanism analysis of foam penetration in EPB shield tunnelling with a focus on FER and soil particle size. *Underground Space*, in press.
- Jing, J., Sun, J., Zhang, M., Wang, C., Xiong, X., & Hu, K. (2017). Preparation and rheological properties of a stable aqueous foam system. *RSC advances*, 7(62), 39258–39269.
- Qin, S., Cheng, Y., & Zhou, W. H. (2023a). State-of-the-art review on pressure infiltration behavior of bentonite slurry into saturated sand for TBM tunneling. *Smart Construction and Sustainable Cities*, 1(1), 14.
- Qin, S., Cheng, Y., Huang, H., & Zhou, W. H. (2023b). Pressure infiltration behavior and fluid loss of bentonite slurry: a comparative study of two bentonite slurries. *Canadian Geotechnical Journal*, (ja).
- Xu, T., Bezuijen, A., & Thewes, M. (2022a). Pressure infiltration characteristics of foam for EPB shield tunnelling in saturated sand—part 1: ‘clean’ foam. *Géotechnique*, 72(4), 283–294.
- Xu, T., Bezuijen, A., & Thewes, M. (2022b). Pressure infiltration characteristics of foam for EPB shield tunnelling in saturated sand—part 2: soil–foam mixture. *Géotechnique*, 72(4), 295–308.
- Xu, T., Zhou, W. H., Bezuijen, A., & Qin, S. (2022c). Effects of sand and slurry characteristics on pressure infiltration of bentonite slurry into sand. *Géotechnique*, 1–12.
- Zheng, D., Bezuijen, A., & Thewes, M. (2022). Modelling the infiltration behaviour of foam into saturated sand considering capillary resistance for EPB shield tunnelling. *Géotechnique*, 1–11.

Development and performance evaluation of a novel FBG-based sensor for measuring positive and negative pore water pressure in soil

J. Jing & T. Wang

State Key Laboratory of Internet of Things for Smart City and Department of Civil and Environmental Engineering, University of Macau, Macao SAR, People's Republic of China.

W. Zhou

State Key Laboratory of Internet of Things for Smart City and Department of Civil and Environmental Engineering, University of Macau, Macao SAR, People's Republic of China.

Center for Ocean Research in Hong Kong and Macao (CORE), Hong Kong SAR, People's Republic of China

ABSTRACT: Pore water pressure sensors are essential instruments for geotechnical testing in the development of underground spaces. We report on a high-sensitivity pore water pressure sensor, incorporating a femtosecond fiber Bragg grating (Fs-FBG) embedded in an elastic diaphragm. The FBG is axially fixed at the center hole of the elastic diaphragm and sealed on the other end to a rigid plate, forming the core sensing component. An additional FBG compensates for temperature cross-sensitivity effects. A mathematical theoretical model suitable for measuring both positive and negative pore water pressures was proposed and simulated. The simulation results demonstrate the sensor's pressure sensitivity under positive and negative pressure conditions as 33.8586 pm/kPa and 32.136 pm/kPa, respectively. Calibration tests under positive pressure indicate that the sensor's sensitivity within a range of 100 kPa is 21.403 pm/kPa, with excellent linearity and a linear fit coefficient of 0.999. This confirms the sensor's capability for effective pore pressure measurement in the complex environments of geotechnical engineering.

Keywords: pore water pressure sensor, femtosecond fiber Bragg grating, elastic diaphragm, geotechnical engineering

1 INTRODUCTION

In the development of underground spaces, it is necessary to monitor the hydraulic properties of the soil to understand the long-term stability of the geotechnical body. Pore water pressure sensors and matrix suction sensors are two key instruments. (Huang H et al. 2024; Qin S et al. 2023, 2021; Correia R et al. 2009; Pei H F et al. 2014) The pore water pressure sensor measures the water pressure in the soil, while the matrix suction sensor focuses on measuring the suction between soil particles, used for accurately measuring and monitoring the water content in the soil. Electronic pressure sensors are a common type of instrument in engineering, but they have some limitations. For example, electronic sensors are susceptible to electromagnetic interference, and they have poor long-term stability and corrosion resistance. (Guo Y X et al. 2021; Xiong L et al. 2021; Pei H F et al. 2020)

To overcome these limitations, sensors based on fiber Bragg grating (FBG) sensing technology have emerged in large numbers and are gradually being applied in underground space engineering tests, demonstrating advantages of high sensitivity and good electrical insulation. (Hong C Y et al. 2016; Leng J et al. 2003; Song H et al. 2021) The sensitivity of fiber Bragg gratings themselves for pressure measurement is relatively low and easily affected by surrounding temperatures, making them unsuitable for direct measurement of pore water pressure. Often, mechanical structures are required to amplify the sensitivity. For instance, the

fiber Bragg grating can be radially adhered to a highly elastic membrane to increase the pressure sensitivity of the FBG at low pressure ranges (Allwood G et al. 2015; Jiang Q et al. 2011; Liang M et al. 2018; Huang J et al. 2013). However, this method can lead to uneven stress distribution in the fiber, causing non-uniform changes in the grating period.

Compared to silica fibers, polymer fibers have the advantage of being more flexible and having better tensile strength. The point-by-point writing method with femtosecond lasers makes it convenient to inscribe gratings in polymer fibers. Due to the low Young's modulus of polymer fibers, Bragg gratings etched in them can withstand greater pressure (Laarossi I et al.2019).

Given the advantages of FS-FBG sensors, this article introduces a highly sensitive fiber Bragg grating sensor for measuring both positive and negative pore water pressures, and discusses its design, manufacturing, and calibration. The feasibility and performance of the sensor are analyzed based on numerical models and laboratory tests. The research results show that the fiber optic pore water pressure sensor has good sensitivity in the low-pressure range.

2 SENSOR STRUCTURE AND THEORETICAL ANALYSIS

2.1 FBG sensor structure

The half-sectional structure of the fiber Bragg grating (FBG) pore water pressure sensor along its axis is shown in Figure 1 and can be used for measuring both positive and negative pore water pressures in geotechnical bodies. Five shells are connected via threads and sealed with epoxy AB glue. The sensor mainly includes a permeable stone, an elastic diaphragm, a fiber Bragg grating, a semi-circular groove, a rigid plate, a shell, and a fiber tail. The elastic diaphragm and FBG1 are the core sensing devices. FBG1 is pre-stretched by 10nm and encapsulated in the semi-circular groove of the sensing cavity using epoxy resin. The temperature-compensating FBG2 is encapsulated in the temperature chamber for measuring temperature and is connected in series with FBG1. The fiber is led out from the tail-end outlet hole and is protected by a sheath.

When the water inflow increases, the elastic diaphragm deforms inward under the action of water pressure, driving FBG1 to compress and causing the Bragg wavelength to shift towards the blue. Conversely, when the water inflow decreases or is subjected to suction, the elastic diaphragm deforms outward, causing FBG1 to stretch and the wavelength to shift towards the red. Therefore, the pore water pressure is calculated based on the change in the central wavelength of FBG1.

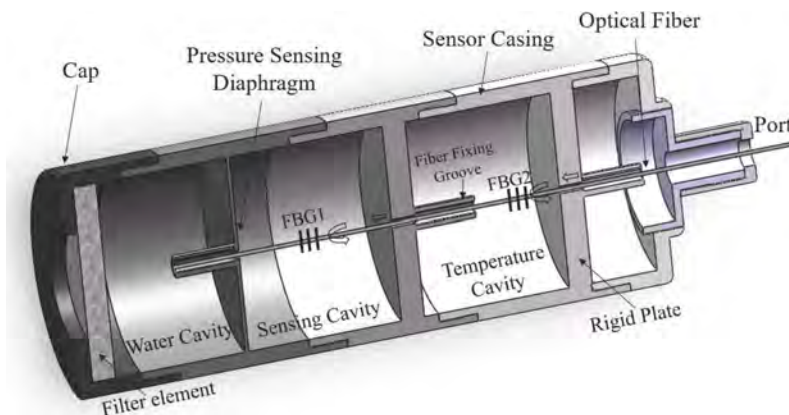


Figure 1. Schematic diagram of the proposed sensor.

2.2 Mechanical properties of sensors

The Fiber Bragg Grating (FBG) is fabricated through the induction of a periodic alteration in the refractive index within the fiber core, a process achieved through substantial exposure to ultraviolet light. Coupling Mode Theory theory explains that upon the incidence of light from

a broadband source onto the grating, the central wavelength of the FBG, which is a critical parameter in its functional efficacy, can be mathematically represented by the grating equation(A. Othonos et al. 2000; A. Kersey et al. 1997).

$$\lambda_B = 2n_{eff}\Lambda \quad (1)$$

In this context, λ_B represents the central wavelength inherent to the Fiber Bragg Grating, while n indicates the refractive index of the optical fiber core. Furthermore, Λ is indicative of the grating's periodicity. The correlation between variations in the FBG wavelength and changes in temperature or strain is quantitatively described by the subsequent equation:

$$\frac{\Delta\lambda_B}{\lambda_B} = (\alpha_f + \xi)\Delta T + (1 - P_e)\Delta\varepsilon \quad (2)$$

Where ΔT is the temperature change, $\Delta\varepsilon$ is the strain change: $\Delta\lambda_B$ is the FBG central wavelength change: α_f is the thermal expansion coefficient, ξ is the thermo-optic coefficient, P_e is the effective photoelastic coefficient (approximately 0.22 at room temperature)(K. O. Hill et al. 1993; G. Meltz et al.1989).

The elastic diaphragm deformation model of the pore water pressure sensor is shown in Figure 2. In accordance with the design of this study, the pre-tensioned fiber is encapsulated at the center of the diaphragm, exerting a concentrated force F on the diaphragm. When the diaphragm is subjected to external pressure P , it undergoes two instances of deflection. Thus, the deflection at any point on the diaphragm, located at a distance r from the center, can be represented as follows:

$$\omega_F = \frac{3F(1 - \nu^2)}{4\pi E_d h^3} [(R^2 - r^2) - 2r^2 \ln \frac{R}{r}] \quad (3)$$

$$\omega_p = \frac{3P(1 - \nu^2)}{16E_d h^3} (R^2 - r^2)^2 \quad (4)$$

In the formula, ν represents the Poisson's ratio, E_d is the Young's modulus, h denotes the thickness, R is the radius of the diaphragm, and r is the distance from a point on the diaphragm to the center. Under the influence of forces F and P , the deflection at the center point of the diaphragm can be expressed as follows:

$$\omega_F = \frac{3FR^2(1 - \nu^2)}{4\pi E_d h^3} \quad (5)$$

$$\omega_p = \frac{3PR^4(1 - \nu^2)}{16E_d h^3} \quad (6)$$

For the fiber Bragg grating, the prestress force $F = \varepsilon_0 E_f A$, ε_0 、 A 、 E_f are the initial tensile strain, cross-sectional area, and Young's modulus of the optical fiber, respectively. The axial strain of the Fiber Bragg Grating (FBG) can be defined as $\Delta\varepsilon = \frac{\Delta w}{L_f}$, where L_f is the length of the fiber within the sensing cavity. When the sensor is subjected to positive hydraulic pressure, its deformation model conforms to Figure 2(a). The final deformation of the diaphragm can be considered as the combined result of the forces F and P :

$$\Delta w = \omega_{F,r=0} + \omega_{p,r=0} = \frac{(12\varepsilon_0 E_f A + 3\pi P R^2)(1 - \nu^2) R^2}{16\pi E_d h^3} \quad (7)$$

The mathematical expression linking the hydraulic pressure sensed by the sensor and the strain of FBG1 can be derived as follows:

$$P = \frac{16E_d h^3 L_f}{3(1 - \nu^2) R^4} \Delta\varepsilon - \frac{4\varepsilon_0 E_f A}{\pi R^2} \quad (8)$$

Integrating the analyses from equations (2) and (8), define k_1 and k_2 as $(\alpha_1 + \xi_1)$ and $(\alpha_2 + \xi_2)$ respectively. The relationship between the hydraulic pressure P and the central wavelength of the Fiber Bragg Grating can be formulated as:

$$P = \frac{16E_d h^3 L_f}{3(1 - \nu^2)R^4} \left(\frac{\Delta\lambda_{B1}}{\lambda_{B1}} - \frac{k_1 \Delta\lambda_{B2}}{k_2 \lambda_{B2}} \right) \frac{1}{(1 - P_e)} - \frac{4\epsilon_0 E_f A}{\pi R^2} \quad (9)$$

Conversely, when the sensor is subjected to negative hydraulic pressure or suction, its deformation relationship transforms as illustrated in Figure 4(b). In this scenario, the directions of forces P and F are opposite, resulting in an altered computation for the diaphragm's deflection:

$$\Delta w = \omega_{F,r=0} - \omega_{P,r=0} = \frac{(12\epsilon_0 E_f A - 3\pi P R^2)(1 - \nu^2)R^2}{16\pi E_d h^3} \quad (10)$$

Therefore, the relationship between negative hydraulic pressure and the strain in the optical fiber is as follows:

$$P = \frac{4\epsilon_0 E_f A}{\pi R^2} - \frac{16E_d h^3 L_f}{3(1 - \nu^2)R^4} \Delta\epsilon \quad (11)$$

Integrating equations (2) and (11), the final mathematical model relating negative hydraulic pressure to wavelength is derived as:

$$P = \frac{4\epsilon_0 E_f A}{\pi R^2} - \frac{16E_d h^3 L_f}{3(1 - \nu^2)R^4} \left(\frac{\Delta\lambda_{B1}}{\lambda_{B1}} - \frac{k_1 \Delta\lambda_{B2}}{k_2 \lambda_{B2}} \right) \frac{1}{(1 - P_e)} \quad (12)$$

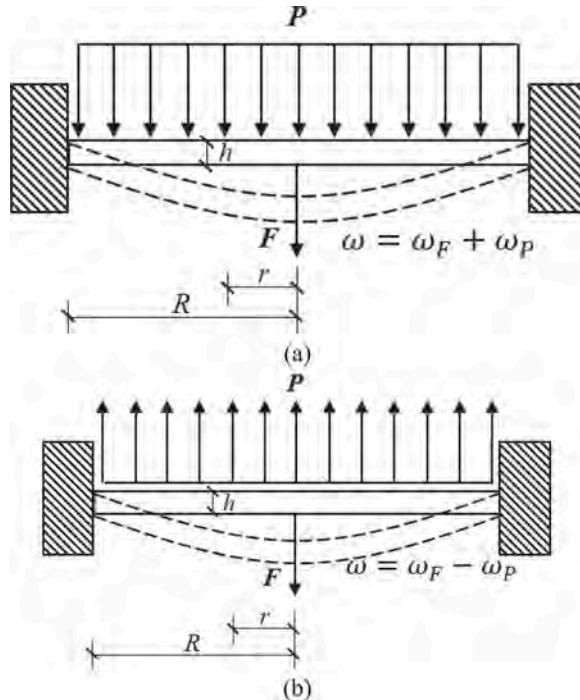


Figure 2. Schematic diagram of the force model of the elastic diaphragm.

3 THE FINITE ELEMENT ANALYSIS OF THE SENSOR

To validate the feasibility of the sensor, a numerical model of the sensor was established using the Abaqus software. In the simulation analysis, the displacement distribution on the surfaces of the diaphragm has been calculated, and Table 1 lists the material parameters employed in the simulation.

Table 1. Parameter of the sensor model.

Parameter	Value
R/mm	13
h/mm	0.5
E_d/Mpa	71000
ν	0.33
Diameter of optic fiber/mm	0.5
Pre-strain of FBG1/ $\mu\epsilon$	10000
Length of the sensing cavity/mm	20
Length of the temperature cavity/mm	20
Young's modulus of the sensor casing/Mpa	193000
Young's modulus of the optic fiber/Mpa	80000
Young's modulus of the epoxy adhesive/Mpa	10000

The sensor's model, as depicted in Figure 3, comprises two independently established models, each simulating different load conditions to analyze the sensor's performance under both positive and negative hydraulic pressures. All components are assembled using rigid body constraints. Notably, a line element is created at the end of the optical fiber, to which connection properties are assigned. Pre-stress is applied to the fiber by setting stiffness coefficients and reference lengths. The 3D model is subjected to a high-density mesh division using C3D8R hexahedral elements and C3D6 wedge elements, resulting in a total of 118,107 mesh elements and 145,609 nodes. Boundary conditions at both ends of the sensor are fixed, and the diaphragm region is subjected to perpendicular surface liquid pressure. Two analysis steps are established: in the first step, pre-stress is applied to the optical fiber, and in the second step, pressure is applied to the diaphragm.

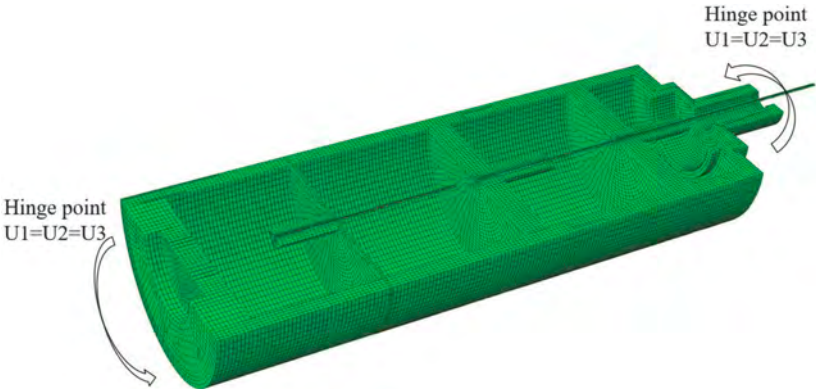


Figure 3. Finite element model of the pore water pressure sensor.

Through finite element simulation analysis, the axial displacement distribution of the sensor at 100 kPa and -100 kPa is illustrated in Figure 4. The elastic diaphragm undergoes inward flexural deformation due to the pre-stress applied to the optical fiber. Under the influence of

100 kPa, the displacement at the center of the diaphragm further increases, showing an increment of 0.0564 mm compared to the initial stage of the second analysis step. Conversely, under -100 kPa, the diaphragm moves in the opposite direction, with the central point's displacement change amounting to -0.05357 mm.

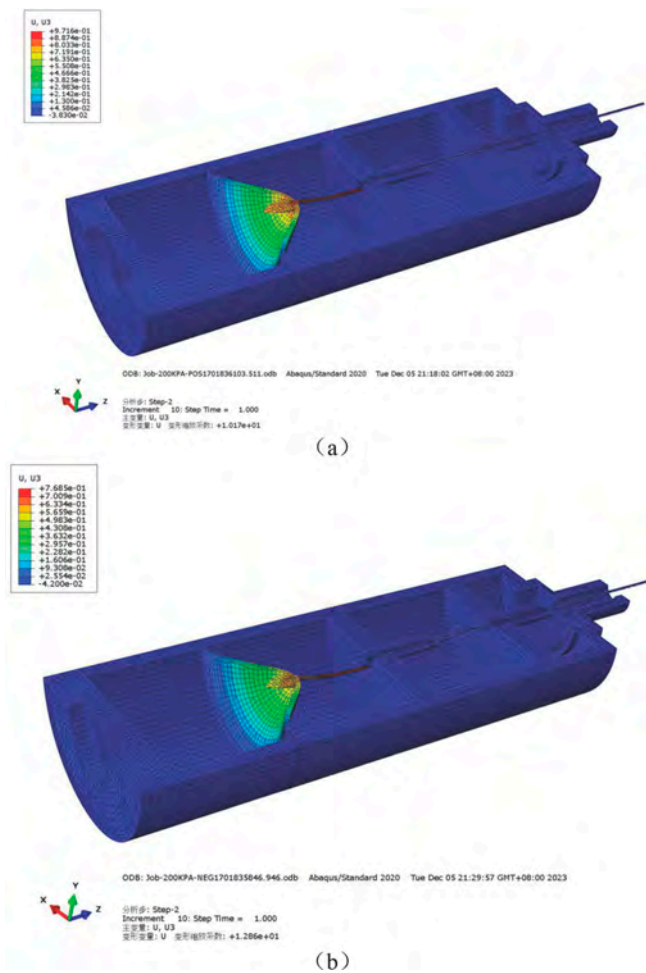


Figure 4. Displacement cloud diagrams of the sensor model: (a) Positive loading of 100kPa; (b) Negative loading of 100kPa.

The variation in the strain values of FBG1 is depicted in Figure 5. The results indicate a clear linear relationship between the strain values and the hydraulic pressure, which aligns well with the theoretical analysis. The fitting curves for FBG1 in relation to positive and negative pressures are respectively as follows:

$$\Delta\varepsilon = 28.2155P \quad (13)$$

$$\Delta\varepsilon = -26.78P \quad (14)$$

Utilizing the standard Fiber Bragg Grating sensitivity of 1.2 pm/ $\mu\varepsilon$ for strain calculations, the sensor exhibits pressure sensitivities of 33.8586 pm/kPa and 32.136 pm/kPa under positive and negative pressure conditions, respectively. Consequently, the proposed pore water pressure sensor demonstrates effective sensitivity enhancement.

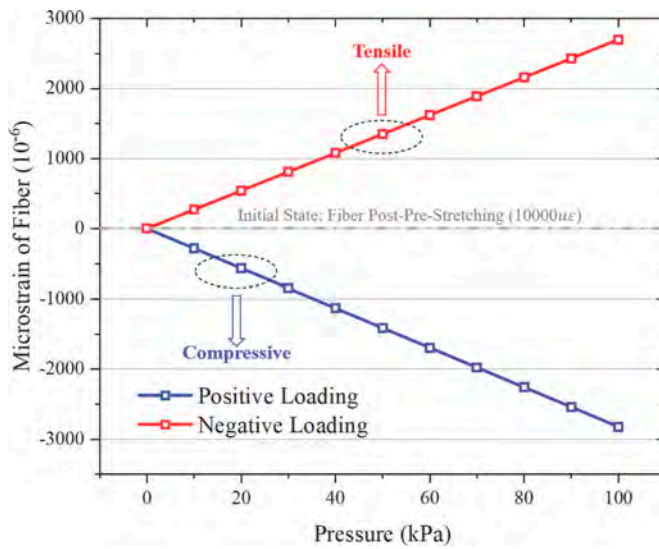


Figure 5. The relationship between strain of fiber and water pressure in the FEM model.

4 SENSOR CALIBRATION EXPERIMENT AND RESULT ANALYSIS

Consistency of style is very important.

The experimental setup and instrumentation are schematically represented in Figure 6. One end of the FBG pore water pressure sensor is connected to a piston pressure pump, which is capable of directly applying high-pressure liquid onto the surface of the sensor's diaphragm. A pressure control module is utilized for the precise control of pressure exerted on the sensor. The Bragg wavelength shifts of the two FBGs inside the sensor under varying pressures are demodulated using an FBG interrogator with a minimum resolution of 1 pm. During the experiment, pressure is applied to the sensor using the pressure control module in increments of 10 kPa, ranging from 0 to 100 kPa, followed by a gradual release of pressure to decrease it. This test is repeated three times, with the temperature maintained at room conditions.

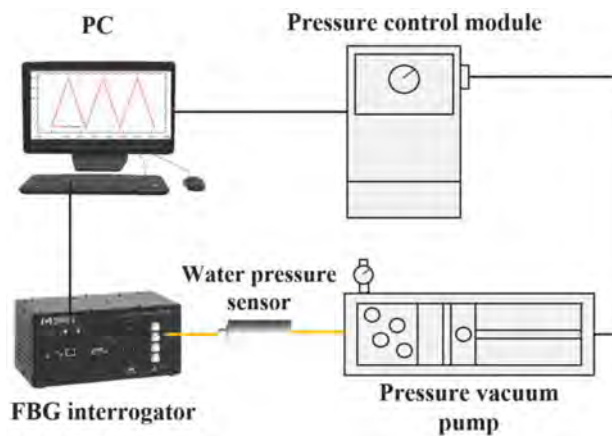


Figure 6. Sensor pressure calibration experimental setup.

The data results, as shown in Figure 7(a), reveal that the central wavelength of FBG1 exhibits a blue shift, indicating compression and negative strain sensed by FBG1. The wavelength

drift of the FBG displays a linear relationship with changes in pressure. After conducting the experiment three times, the average values from these trials were analyzed. The fitting results, presented in Figure 7(b), lead to the derivation of the sensor's fitting equation: $y = 1547.087x - 0.019$. The fitting linear correlation coefficient is 0.999, indicating a pressure sensitivity of 21.403 pm/kPa. Compared to the results of numerical simulation, the sensitivity of the sensor obtained from the experiment has been slightly reduced, mainly due to the following reasons:

Differences in boundary conditions: In the simulation, both ends of the sensor housing were completely constrained, while in the experiment, only the inlet part of the sensor was constrained.

Errors in the machining process of the sensor components led to thicker dimensions of the diaphragm, resulting in reduced deformation.

Epoxy resin sealing was used at both ends of the optical fiber, but the strain transfer efficiency could not reach 100%.

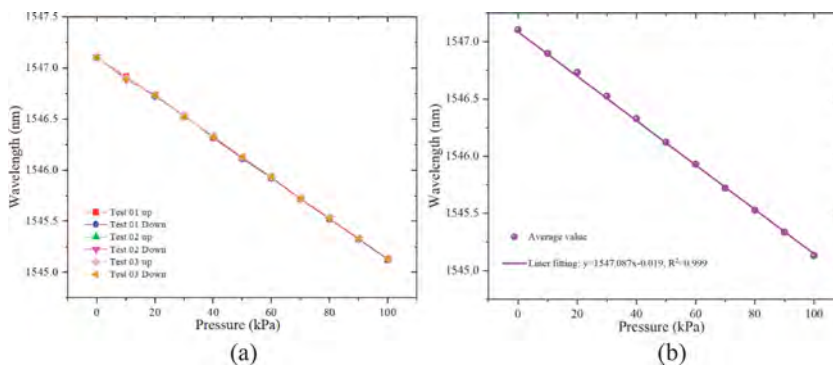


Figure 7. Sensor pressure calibration test results: (a) 3 cycle test results; (b) Average value of 3 cycle tests.

5 CONCLUSION

The research successfully demonstrates the feasibility and efficacy of a novel pore water pressure sensor based on FS-FBG technology. The sensor exhibits good sensitivity in low-pressure ranges and effectively measures both positive and negative pressures. Theoretical analyses and finite element simulations confirm the sensor's design and operational principles, highlighting its potential in geotechnical monitoring. Calibration experiments further validate the sensor's linear response to pressure changes in the range of 100kPa, with high sensitivity of 21.403pm/kPa. The sensor's robust design makes it a promising tool for underground space engineering and geotechnical studies.

ACKNOWLEDGMENT

This research was supported by the Guangdong Provincial Department of Science and Technology (2019B111106001, 2022A0505030019), and the Science and Technology Development Fund of Macau Special Administrative Region (Approval No. 001/2024/SKL). The authors also acknowledge the financial support from CORE, which is a joint research center for ocean research between Laoshan Laboratory and HKUST.

REFERENCES

- Huang H, Sun Q, Xu T, et al. Mechanism analysis of foam penetration in EPB shield tunnelling with a focus on FER and soil particle size[J]. *Underground Space*, 2024.
- Qin S, Cheng Y, Zhou W H. State-of-the-art review on pressure infiltration behavior of bentonite slurry into saturated sand for TBM tunneling[J]. *Smart Construction and Sustainable Cities*, 2023, 1(1): 14.

- Qin S, Xu T, Zhou W H. Predicting pore-water pressure in front of a TBM using a deep learning approach[J]. *International Journal of Geomechanics*, 2021, 21(8): 04021140.
- Shen P, Wei S, Shi H, et al. Coastal Flood Risk and Smart Resilience Evaluation under a Changing Climate[J]. *Ocean-Land-Atmosphere Research*, 2023, 2: 0029.
- Pei H F, Teng J, Yin J H, et al. A review of previous studies on the applications of optical fiber sensors in geotechnical health monitoring[J]. *Measurement*, 2014, 58: 207–214.
- Correia R, Li J, Staines S, et al. Fibre Bragg grating based effective soil pressure sensor for geotechnical applications[C]//20th International Conference on Optical Fibre Sensors. SPIE, 2009, 7503: 74–77.
- Guo Y, Xiong L, Wu H, et al. A FBG inclinometer for simultaneous measurement of horizontal deformation and sudden deformation[J]. *IEEE Transactions on Instrumentation and Measurement*, 2021, 70: 1–10.
- Guo Y, Zhou W, Xiong L, et al. A fiber Bragg grating sensor for positive and negative displacement measurement[J]. *IEEE Sensors Journal*, 2021, 21(19): 21564–21571.
- Xiong L, Guo Y, Zhou W, et al. Fiber Bragg grating-based three-axis vibration sensor[J]. *IEEE Sensors Journal*, 2021, 21(22): 25749–25757.
- Pei H, Jing J, Zhang S. Experimental study on a new FBG-based and Terfenol-D inclinometer for slope displacement monitoring[J]. *Measurement*, 2020, 151: 107172.
- Hong C Y, Zhang Y F, Zhang M X, et al. Application of FBG sensors for geotechnical health monitoring, a review of sensor design, implementation methods and packaging techniques[J]. *Sensors and Actuators A: Physical*, 2016, 244: 184–197.
- Leng J, Asundi A. Structural health monitoring of smart composite materials by using EFPI and FBG sensors[J]. *Sensors and Actuators A: Physical*, 2003, 103(3): 330–340.
- Song H, Pei H, Zhu H. Monitoring of tunnel excavation based on the fiber Bragg grating sensing technology[J]. *Measurement*, 2021, 169: 108334.
- Allwood G, Wild G, Lubansky A, et al. A highly sensitive fiber Bragg grating diaphragm pressure transducer[J]. *Optical Fiber Technology*, 2015, 25: 25–32.
- Jiang Q, Du H, Hu D, et al. Hydraulic pressure sensor based on fiber Bragg grating[J]. *Optical engineering*, 2011, 50(6): 064401-064401-4.
- Liang M, Fang X, Ning Y. Temperature compensation fiber Bragg grating pressure sensor based on plane diaphragm[J]. *Photonic Sensors*, 2018, 8: 157–167.
- Huang J, Zhou Z, Wen X, et al. A diaphragm-type fiber Bragg grating pressure sensor with temperature compensation[J]. *Measurement*, 2013, 46(3): 1041–1046.
- Laarossi I, Roldán-Varona P, Quintela-Incera M A, et al. Ultrahigh temperature and strain hybrid integrated sensor system based on Raman and femtosecond FBG inscription in a multimode gold-coated fiber[J]. *Optics Express*, 2019, 27(26): 37122–37130.
- Othonos, K. Kalli, and G. E. Kohnke, “Fiber Bragg gratings: Fundamentals and applications in telecommunications and sensing,” *Phys. Today*, vol. 53, no. 5, pp. 61–62, May 2000.
- Kersey et al., “Fiber grating sensors,” *J. Lightw. Technol.*, vol. 15, no. 8, pp. 1442–1463, Aug. 1997.
- K. O. Hill, B. Malo, F. Bilodeau, D. C. Johnson, and J. Albert, “Bragg gratings fabricated in monomode photosensitive optical fiber by UV exposure through a phase mask,” *Appl. Phys. Lett.*, vol. 62, no. 10, pp. 1035–1037, Mar. 1993.
- G. Meltz, W. Morey, and W. Glenn, “Formation of Bragg gratings in optical fibers by a transverse holographic method,” *Opt. Lett.*, vol. 14, no. 15, pp. 823–825, Jul. 1989.

Research on a CO₂ Internet of Things online monitoring system for geotechnical engineering construction

J.H. Ma, Y.Z. Zhou, W. Cao & J.F. Liu

School of Earth Sciences & Engineering, Sun Yat-sen University, Zhuhai, China

ABSTRACT: The construction industry contributes significantly to global carbon emissions, releasing substantial amounts of CO₂. To effectively evaluate and reduce these emissions, it is crucial to create corresponding reduction plans by monitoring carbon emissions throughout the construction process. However, current carbon emission monitoring methods mainly focus on material and electricity consumption, lacking actual field data that could precisely portray the project's scale. This paper presents a design methodology for online monitoring technology in geotechnical engineering based on the Internet of Things (IoT). The methodology emphasizes sensing technology, criteria for sensor selection, and analysis of sensor node deployment. This results in an online monitoring system that accurately measures atmospheric CO₂ concentration parameters and integrates electricity usage data to compute carbon emissions during construction. This system facilitates future trend analyses and strategic planning for carbon reduction.

1 INTRODUCTION

The concentration of CO₂ in the atmosphere has surged significantly since the Industrial Revolution. It has increased from 280 ppm in the mid-19th century to 413 ppm in 2020, with a continued annual increase of 2~3 ppm (International Energy Agency, 2017). This massive increase in CO₂ and other greenhouse gas emissions has resulted in an approximately 1.11 (± 0.13) °C increase in the global average temperature above pre-industrial levels (World Meteorological Organization, 2022). The effects of global warming have gone beyond ecological impacts and have affected other areas such as politics and economies. Many countries across the globe have started to adopt stricter regulations on CO₂ emissions, and the European Union and the United States will levy carbon taxes on products that exceed the baseline carbon emissions.

The construction industry was responsible for a massive 11.7 billion tons of CO₂ emissions globally in 2020, with 3.16 billion tons produced during construction, accounting for 10% of the world's total emissions (United Nations Environment Programme, 2021). China contributed approximately 5.09 billion tons to the overall carbon emissions. While building material production and construction operations were once the main contributors to emissions, the recent adoption of low-carbon building materials and carbon life cycle management has helped to reduce them. However, energy consumption and emissions during construction have increased substantially, making it a critical area to focus on reducing carbon emissions (Cai et al., 2022). Geotechnical engineering construction activities disturb carbon reservoirs and emit greenhouse gases, posing challenges for carbon monitoring.

Since CO₂ moves around in the air, it is crucial to have continuous and responsive monitoring to manage carbon emissions effectively. Satellite monitoring scales are too broad to accurately reflect specific project emissions. Similarly, carbon assessment methods based on power consumption are unable to monitor other sources of carbon emissions at construction sites. However, online monitoring technology utilizing the Internet of Things (IoT) provides real-time monitoring of CO₂ concentration with high accuracy and broad applicability in

geotechnical engineering carbon emission monitoring. The IoT online monitoring system can monitor atmospheric CO₂ concentrations for extended periods, establishing regional gas concentration baselines. Changes in gas concentration and composition during construction enable the analysis of carbon emission sources and scales at different stages.

This study outlines the principles and key technologies behind IoT-based online monitoring and provides a design framework for underlying sensor technology in geotechnical engineering carbon emissions monitoring. It includes detailed analyses of sensor selection and sensor node design and an introduction to the completed CO₂ IoT online monitoring system. The findings of this research offer valuable insights and serve as a useful reference for the future implementation of monitoring systems on construction sites.

2 INTERNET OF THINGS ONLINE MONITORING PRINCIPLE

In recent years, advances in sensing, computing, and communication technology have enabled low-cost, low-power sensors to integrate with computing, communication, and processing functions in sensor systems. This has led to the development of Internet of Things Online Monitoring (IoT Online Monitoring), which organizes diverse sensors into Wireless Sensor Networks (WSN) using wired or wireless communication technologies. WSN facilitates data transmission and remote access through the Internet, making it possible to monitor various parameters, such as temperature, humidity, pressure, and spatial positioning in real-time. The essence of IoT's online monitoring technology lies in the WSN's perception and monitoring of the physical world, which enables real-time remote control and data collection through networking. (Weimer et al., 2008).

IoT online monitoring systems consist of sensors, communication modules, control systems or gateways, cloud platforms, and clients (Gulati et al., 2022). Collected data are transmitted to central storage or cloud platforms for processing, allowing users to conduct trend analysis, anomaly monitoring, predictions, and early warnings on visual interfaces. This enables remote management and control of monitoring sites. Sensor nodes usually feature precise positioning capabilities, which, when strategically placed, achieve comprehensive coverage and high-precision monitoring within construction areas, finding widespread applications in various fields (Plaza et al., 2019; Wang et al., 2023; Zhang et al., 2019). Compared to other monitoring methods, IoT online monitoring technology offers several advantages. Firstly, it boasts adjustable measurement ranges and multiple measurement parameters. Secondly, it has unattended, remote control capabilities, fulfilling the requirements of long-term, cost-effective monitoring and control within construction areas. Lastly, sensor nodes can analyze gas concentration changes, especially in CO₂ and other pollutants, using algorithms, that enable timely intelligent monitoring (Yang et al., 2023).

The structural framework of IoT online monitoring technology comprises the perception layer, the transmission layer, and the application layer, which handle data acquisition and transformation, information transmission and processing, and data storage and analysis, respectively (Figure 1). The fundamental technological components include sensing technology, communication technology, data management, and analytical tools. While the data management and communication technologies in the transport and application layers have achieved maturity through practical applications, the sensing layer remains critical for obtaining site-specific information. However, the applicability of key sensing technologies in construction sites is still unclear, necessitating further design according to construction site requirements.

Sensor technology relies on the design of sensors and sensor nodes. Sensors can detect changes in physical and chemical parameters in real-time, and convert them into electrical signals. Sensor nodes perform data acquisition, processing, communication, and network connections, and respond to emergencies and abnormal situations promptly, ensuring the reliability of monitoring. Therefore, the selection and design of sensors and sensor nodes have a significant impact on the stability and accuracy of data collection, as well as the communication capabilities and performance of the monitoring network. These factors are crucial for determining the applicability and feasibility of IoT online monitoring in real-world scenarios.

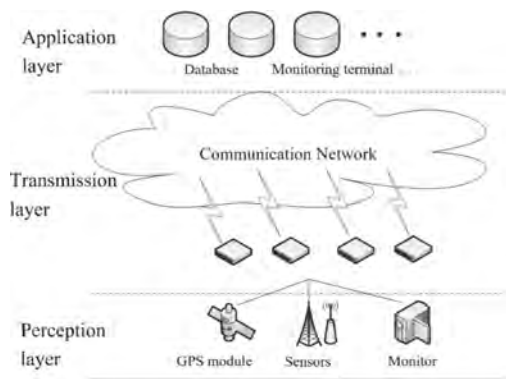


Figure 1. The structural framework of online monitoring of the Internet of Things.

3 SELECTION OF CO₂ SENSOR

Sensors play a pivotal role in gathering environmental data, including CO₂ concentration. Infrared CO₂ sensors are the most commonly utilized sensor type, due to their superior sensitivity, energy efficiency, and affordability. They operate by measuring the absorption rate of infrared light by CO₂ gas in particular bands of infrared light, which helps determine the CO₂ concentration. In contrast, laser CO₂ sensors depend on the specific absorption of CO₂ to laser light waves, resulting in superior intensity, resolution, and sensitivity. Fourier Transform Infrared Spectrometers (FT-IR) allow for the qualitative and quantitative analysis of low-concentration gas mixtures. They selectively absorb electromagnetic radiation in the infrared region, providing precise measurements. FT-IR equipment is costly and bulky but is valuable for regional monitoring in complex environments such as high-temperature, high-humidity, and mixed flue gases. Photoacoustic Spectroscopy (PAS) is another emerging monitoring technology that determines CO₂ concentration by monitoring the CO₂ absorption of acoustic signals generated by laser beams. PAS is ideal for online CO₂ monitoring due to its high sensitivity in monitoring multi-component gas mixtures.

To ensure ongoing monitoring with consideration for both cost-effectiveness and accuracy, the primary use is made of infrared CO₂ sensors, with laser CO₂ sensors used for specific key areas. For comprehensive coverage of the monitoring area, FT-IR is employed on regular patrols along fixed routes. To enhance the stability and reliability of the data sources, re-measurements are performed whenever there are significant fluctuations or deviations in the CO₂ concentration.

Nevertheless, most sensors are significantly affected by environmental factors. For example, the ambient temperature can adversely affect light sources and filters in infrared detectors, whereas the temperature and atmospheric pressure can impact the absorption line broadening and wavelength modulation coefficient of laser detectors (Liu et al., 2023). To minimize the influence of these environmental parameters on the monitoring outcomes, a two-fold strategy is employed. The design process considers environmental factors such as temperature, humidity, and pressure. The values initially measured are calibrated using particular algorithms or compensation mechanisms, and the error can be controlled in a small range (Figure 2). To ensure precision, multiple CO₂ concentration sensors are utilized, and the results are amalgamated through extensive monitoring techniques. Algorithms are employed to determine and produce reliable data based on specific environmental conditions. Surface sensor measurements are enhanced and adjusted by data obtained from satellites or global atmospheric observation networks to provide a comprehensive understanding of regional alterations in CO₂ concentrations. The sensor node incorporates all of these elements.

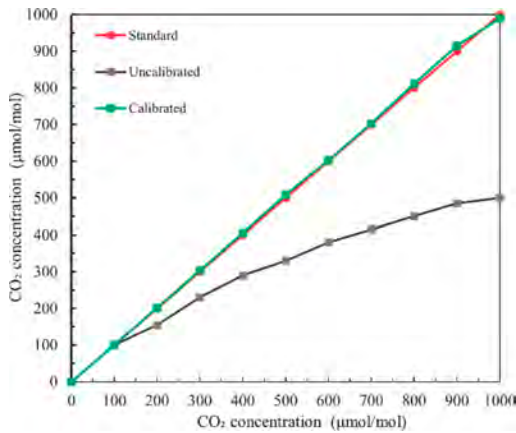


Figure 2. Temperature correction diagram of the infrared spectrum sensor (Liu et al., 2023).

4 SENSOR NODE DEPLOYMENT DESIGN

A sensor node is a compact apparatus that incorporates an assortment of components including sensors, microprocessors, communication modules, and power supplies. The primary function of such nodes is to amass and supervise sensory data, as well as manipulate, transmit, and interconnect with networks. Consequently, they are recognized as the fundamental element of online monitoring in the Internet of Things (IoT). Typically, these miniature systems are measured in millimetres or centimetres. Whilst a singular sensor node may have limited coverage, deploying multiple nodes strategically within a monitoring area and transmitting the data via communication modules enables extensive coverage and collaborative operation. This achieves the objective of large-scale and high-precision online monitoring.

Due to the vast expanse of construction sites, a multitude of sensors must be deployed across the area. Consequently, sensor node design must meet three critical conditions. Firstly, to enhance monitoring efficiency, the monitoring range should cover the whole construction area to detect CO₂ emissions and abnormal events (Li & Liu, 2022). Secondly, online monitoring systems must ensure data continuity because of the complex construction environments. Even if certain nodes fail, the system should retain data transmission to improve reliability and robustness. Finally, it is crucial to reduce the system's energy consumption to minimize operating costs and enhance the monitoring network's durability. To achieve this, the sensor node design process must meticulously deliberate deployment modes and network topologies.

4.1 Sensor node deployment design

Three primary strategies are utilized when deploying sensor nodes: fixed deployment, random deployment, and mobile deployment. Figure 3 shows the different types of distributions for deploying sensor nodes. Fixed deployment involves strategically placing sensors in specific locations. This can be accomplished through methods such as uniform distribution or specific grid shapes (Figure 3a). On the other hand, random deployment disperses sensors in batches from aircraft or other aerial means to cover inaccessible areas or difficult environments (Figure 3b). Mobile deployment, the third approach, enables the sensors to be relocated or reprogrammed according to fluctuating environmental conditions (Figure 3c). Figure 3 illustrates that the fixed deployment method can cover the monitoring area, but it lacks robustness and cannot meet monitoring requirements if sensor nodes get damaged. On the other hand, random deployment cannot ensure full coverage of the monitoring area and has certain security risks. The mobile deployment method allows for the adjustment of monitoring range, but long-distance movement may drain the energy of the sensor nodes.

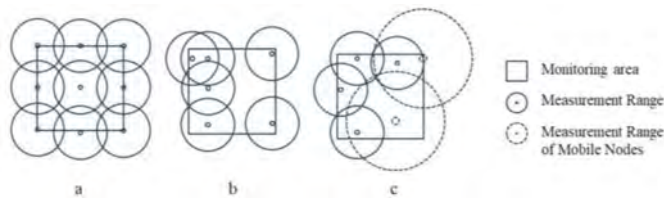


Figure 3. (a) Fixed distribution; (b) random distribution; (c) mobile distribution.

To guarantee full coverage and promote high-quality communication at a construction site, a combination of deployment methods is utilized. Fixed deployment is initially designated for critical zones to ensure comprehensive coverage. The primary deployment mode integrates regular hexagonal and quadrilateral grids. Regular hexagonal deployment effectively reduces energy loss and eliminates overlapping monitoring areas. Quadrilateral deployment decreases the number of monitoring nodes within the same transmission range (Sun et al., 2011). Combining these tactics enables the efficient allocation of monitoring resources.

Once fixed deployments are completed in crucial areas, the monitoring area expands through random deployment, concentrating on encrypting important monitoring zones. Random deployment can result in certain areas being unmonitored, therefore full coverage through this method may necessitate a greater number of sensor nodes. This could lead to redundant coverage in specific regions and an increase in initial deployment costs. Nevertheless, random deployment is a quick approach, and energy consumption can be minimized by optimizing sensor node sleep and communication mechanisms, which extends the operational lifespan of the monitoring network (Sun et al., 2011). In the event of node failures, any remaining redundant nodes are capable of self-organization, leading to improved system robustness. Consequently, random deployment is utilized for encryption and expansion, building on top of the foundation of fixed deployment. This allows for fast deployment whilst ensuring continuity in data measurement.

To tackle issues related to resource wastage and monitoring gaps that arise due to random deployment, a mobile deployment mode has been introduced to further optimize the topology. This approach enlarges coverage areas by leveraging sensor node mobility or adjusting node density based on measurement requirements. Nevertheless, mobile deployment results in higher sensor node energy consumption. To mitigate this, repeater-assisted sensor nodes have been introduced, which reduce energy consumption during mobile node communication. Furthermore, remote charging of mobile nodes is made possible through radio frequency wireless charging technology, which enhances the service life of monitoring nodes (Qu et al., 2015).

The implementation of multiple sensor node deployment methods has led to reduced monitoring costs, continuous transmission of monitoring data, and improved real-time monitoring capabilities of online Internet of Things monitoring systems. This integration aligns with the dynamic monitoring requirements of construction sites, ensuring a reliable and efficient monitoring system.

4.2 Network topology design

The design of a sensor node network topology is crucial because it determines how nodes are integrated to meet specific requirements. The topology significantly impacts the deployment, communication, and collaboration among sensor nodes, which affects the efficiency and reliability of online monitoring. During online monitoring, sensor nodes exchange data through wireless communication technology. However, the fluctuating number of sensor nodes in the monitoring process due to environmental changes or power depletion may cause nodes to fail, while new or migrated nodes may join. To adapt to varying monitoring demands or project progress, the network topology needs real-time adjustment, resulting in dynamic changes within the sensor node structure.

Star topology, mesh topology, tree topology, ring topology, and cluster topology are the most commonly used network topologies. Figure 4 shows a diagram representing the structure of various network types. The star topology utilizes a single central node, or multiple backup

nodes, to establish communication with all sensor nodes, providing a simple and easy-to-deploy topology (Figure 4a). Meanwhile, the mesh topology makes use of redundant paths, allowing data transmission through multiple routes, and enabling multi-hop communication between nodes (Figure 4b). Lastly, the cluster topology divides sensor nodes into multiple clusters, with select nodes serving as cluster heads responsible for data aggregation and transmission (Figure 4c). Similar to the cluster topology, the tree topology displays a hierarchical structure where monitoring data are transmitted uniformly from child nodes to the root node, and then to the base station, enabling data aggregation during transmission (Figure 4d). Overall, both star and tree topologies have a single central node or root node that is connected to all other nodes, making it easy to manage. However, there is a risk of a single point of failure, which could cause the entire network to fail. On the other hand, mesh and cluster topologies have direct connections between all nodes, which reduces the risk of a single point of failure. However, this may increase the complexity and cost of the network.

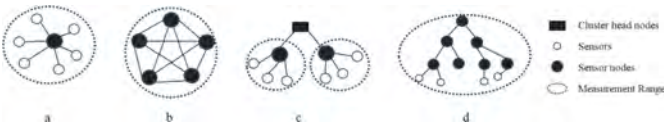


Figure 4. (a) Star topology; (b) network topology; (c) cluster topology; (d) tree topology.

When designing the network topology, it is essential to consider geological and environmental conditions, coverage, monitoring demands, communication distance, data transmission, and site extensibility. The topology must meet the requirements of cost-effectiveness, low-power normal monitoring, and emergency monitoring. To achieve these objectives, real-time optimization of the topology based on changes in demand and the environment is necessary. Therefore, it is essential to incorporate the benefits of different topologies and implement varying topologies for different regions.

In areas with high emissions, a hybrid combination of cluster and network topology is utilized to expand the coverage area and improve the stability of the system. Cluster head nodes are carefully placed in pivotal emission zones and are surrounded by an array of sensor nodes. Nodes can be added, removed, hibernated, or activated based on real-time monitoring conditions to efficiently manage limited energy resources and prolong the system’s lifespan. To mitigate the confined distribution range of cluster head nodes, additional nodes are deployed in nearby areas to expand coverage or serve as standby nodes, enhancing system stability. However, in cases of significant CO₂ emissions, monitoring nodes situated far from the emission site may face difficulties in participating in data transmission due to the large volume of data that needs uploading. Fixed and isolated nodes do not suffice to meet the monitoring demands. By deploying numerous sensor nodes in key zones, connecting them with the primary nodes of the cluster structure, and establishing multiple redundant channels for extensive communication, integrating the mesh topology addresses this issue. This combination of the network topology and the cluster topology guarantees the continuous transmission of monitoring data in vital regions (Wu et al., 2020). However, for peripheral areas or locations with low monitoring intensity, it is preferable to use simpler topological structures such as limited-range star topology or tree topology that connects to the primary region for data summarization.

5 COMPLETED WORK

Our team has created IoT platforms for monitoring carbon emissions based on discussed sensor design principles. To evaluate regional carbon emissions, we combine data on regional energy consumption and CO₂ emissions. The electricity meter data from the power monitoring unit is utilized to establish the energy consumption, which is combined with the emission

factor provided by power enterprises (0.5810 t CO₂/MWh) for calculating the carbon emissions (Figure 5a). We analyze changes in CO₂ concentration resulting from carbon emissions originating from fossil fuels or other sources and compare them to long-term monitoring data (Figure 5b). The monitoring data are preprocessed and uploaded to the cloud in real time to be displayed in the user interface.

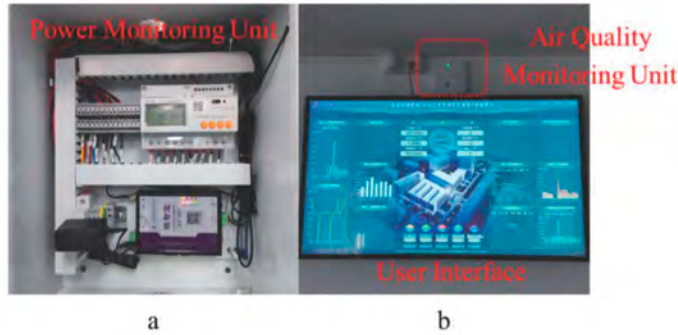


Figure 5. (a) Power monitoring unit; (b) air quality monitoring unit and user interface.

Carbon emission data are stored in the database to record emissions at various time scales (1 day to 1 year). Early warnings are issued when monitoring data exceeds alarm thresholds. To ensure the reliability of the monitoring data, repeated measurements follow (Figure 6a, b). The platform analyzes carbon emissions over different time scales and derives emission trends from long-term monitoring data. The monitoring results are compared to targeted values to predict future trends in carbon neutrality. This includes recommendations for managing regional carbon emissions in the future (Figure 6b). Furthermore, our air quality monitoring unit is equipped with a sensor that enables real-time monitoring of changes in the concentrations of different pollutants. These data are analyzed by examining the changes in gas concentration and composition over time through the user interface (Figure 6c).

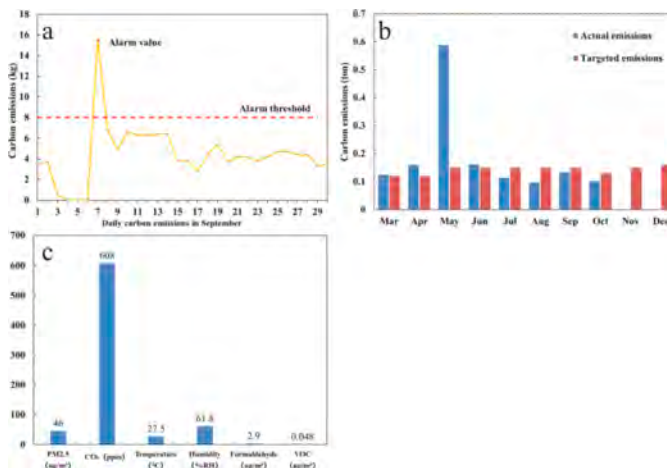


Figure 6. (a) Carbon emissions in September 2023; (b) actual and targeted carbon emissions in 2023; (c) real air quality monitoring data.

The IoT online monitoring platform is being extensively used to monitor carbon emissions in industrial parks and estates. It can also be an effective and cost-efficient method to monitor carbon emissions during construction. By analyzing carbon emissions and pollutant

concentrations, along with the region's power and energy consumption, we can ensure construction safety. It is important to note that although the IoT online monitoring technology has been widely adopted for large-scale industrial parks, it is not yet commonly used in geotechnical engineering construction. The core sensor technology design requires further study and improvement. However, the monitoring technology employed in large-scale industrial parks has the potential to be modified for on-site monitoring in engineering sites.

First of all, the special environment of the geotechnical construction site, including dusty, irregular terrain, and large temperature and humidity changes, may affect the performance of infrared CO₂ sensors and laser CO₂ sensors. Therefore, it is necessary to improve the housing and dust filter to enhance the ability to resist environmental effects. Additionally, modify the initial measurement value according to a specific temperature, humidity, pressure compensation mechanism or algorithm to ensure its stability and accuracy. Secondly, the deployment design of sensor nodes should consider the frequent changes in the topography and construction activities of the geotechnical construction site. Random deployment may be more flexible to accommodate irregular construction sites. In key monitoring areas, based on fixed deployment, encryption monitoring should be more intensive to ensure comprehensive monitoring of key areas. Since continuous power supply is often lacking on construction sites, energy management needs to be optimized, considering solutions such as low-power technology, solar power, or portable power supplies. Lastly, in terms of network topology design, signal interference and communication instability issues may exist in geotechnical engineering construction sites. Therefore, it is necessary to address signal interference, network instability, and other problems and adopt multi-channel communication, reliable communication protocols, local cache, and data redundancy to ensure the stability of data transmission. The mesh topology is the main topology. When the star topology or tree topology is used for data summary in the edge area, the layout of nodes may need to be optimized to adapt to terrain changes due to the complex terrain of the geotechnical construction site. The combination of real-time alarm systems and data visualization technology ensures the effective application of IoT online monitoring technology in the geotechnical engineering construction process.

6 CONCLUSION AND PROSPECT

Monitoring technology is crucial for analyzing carbon emissions and reducing carbon footprints. The Internet of Things (IoT) offers online monitoring technology, which is a pivotal solution for construction sites. It comes with unattended operation, high precision, extensive coverage, continuous monitoring, and intelligent processing abilities, making it suitable for addressing the dynamic monitoring demands of construction sites. This technology also enables prolonged, cost-effective monitoring in construction areas, providing valuable insights to inform targeted carbon emission reduction policies in subsequent development phases.

Looking ahead, the continuous evolution and enhancement of online monitoring technology, coupled with the expansive growth of engineering monitoring projects, is set to bring transformative changes. With the miniaturization and mass production of sensors and their auxiliary equipment, the material costs associated with online monitoring are expected to decrease significantly. Furthermore, the continuous drive toward large-scale networking connections will catalyze the standardization of sensor node distribution designs and networking protocols, resulting in reduced management costs for implementing IoT-based online monitoring systems. This will enhance the feasibility and accessibility of this state-of-the-art technology.

REFERENCES

- Cai, W.G., Wu, Y., Ni, J.B. & Yu, Y.H. 2022. *2022 Research Report of China Building Energy Consumption and Carbon Emissions*. Chong Qing: China Building Energy Efficiency Association Building Energy Consumption and carbon emission data committee (in Chinese).
- Gulati, K., Boddu, R.S.K., Kapila, D., Bangare, S.L., Chandnani, N. & Saravanan, G. 2022. A review paper on wireless sensor network techniques in Internet of Things (IoT). *Materials Today: Proceedings*, 51:161–165.

- International Energy Agency. 2017. *Energy Technology Perspectives 2017*. Paris: International Energy Agency.
- Li, Q.Y. & Liu, N.Z. 2022. Coverage optimization algorithm based on control nodes position in wireless sensor networks. *International Journal of Communication Systems*, 35(5):1–20.
- Liu, Q., Wang, L., Zhu, X.B. & Liu, Y. 2023. Temperature Compensation for Infrared Detection of Carbon Dioxide Concentration. *Infrared Technology*, 45(6):671–677(in Chinese).
- Plaza E.G., López, P.J.N. & González, E.M.B. 2019. Efficiency of vibration signal feature extraction for surface finish monitoring in CNC machining. *Journal of Manufacturing Processes*, 44:145–157.
- Qu, Y., Xu, K., Liu, J.C. & Chen, W.L. 2015. Toward a Practical Energy Conservation Mechanism With Assistance of Resourceful Mules. *IEEE Internet of Things Journal*, 2(2):145–158.
- Sun, Y.W., Shen, M.X., Xiong, Y.J., Lu, M.Z., Liu, L.S. & Kong, X.L. 2011. Design on the System of Collection, Storage and Release for Field Information. *Advanced Materials Research*, 347-353:252–257.
- United Nations Environment Programme. 2021. *2021 Global Status Report for Buildings and Construction: Towards a Zero-emission, Efficient and Resilient Buildings and Construction Sector*. Nairobi: United Nations Environment Programme.
- Wang, H.Q., Zhou, J.T., Li, X., Ling, Q., Wei, H.Y., Gao, L., He, Y., Zhu, M., Xiao, X., Liu, Y.J., Li, S., Chen, C.L., Duan, G.T., Peng, Z.M., Zhou, P.L., Duan, Y.F., Wang, J.B., Yu, T.Z., Yang, Y. X., Wang, J.G., Zhou, Z., Gui, H.Q. & Ding, Y.J. 2023. Review on recent progress in on-line monitoring technology for atmospheric pollution source emissions in China. *Journal of Environmental Sciences*, 123:367–386.
- Weimer, J.E., Sinopoli, B. & Krogh, B.H. 2008. A Relaxation Approach to Dynamic Sensor Selection in Large-Scale Wireless Networks. *The 28th International Conference on Distributed Computing Systems Workshops*, Beijing, IEEE.
- World Meteorological Organization. 2022. *State of the Global Climate in 2022*. Geneva: World Meteorological Organization.
- Wu, Y.B., Niu, R.Q., Wang, Y. & Chen, T. 2020. A Fast Deploying Monitoring and Real-Time Early Warning System for the Baige Landslide in Tibet, China. *Sensors*, 20(22):6619.
- Yang, H., Fang, H.W., Wang, W.F. & Zhang, Y.H. 2023. Air-ground Integrated Monitoring Method of Leakage Risk during Geological Carbon Sequestration. *Journal of Engineering Geology*, 26(1):1–7 (in Chinese).
- Zhang, L., Gray, H., Ye, X.J., Collins, L. & Allinson, N. 2019. Automatic Individual Pig Detection and Tracking in Pig Farms. *Sensors*, 19(5):1187–1207.

Least squares adjustment approach in real-time monitoring of existing twin tunnels

K.H. Phan

Geotech-Science Co., Ltd, New Taipei City Taiwan

B.C.B. Hsiung

Department of Civil Engineering, National Chung-Hsing University, Taichung, Taiwan

J. Huang & A. Chao

Geotech-Science Co., Ltd, New Taipei City Taiwan

ABSTRACT: The paper presents the application using least squares theory to adjust tunnel movements measured from real-time monitoring. It is aware that existing tunnels in use may move due to construction activities nearby or ground and structure natures so nowadays real-time monitoring using total station with objective prism (OP) is recognized as one of the most effective solutions in measuring said displacements. However, considering the reliability which the equipment could achieve as well as the relative distances between total stations as well as total station and OP, the monitoring results may need to be further adjusted to eliminate the measurement error. Thus, the real-time GEOAUTO and the least squares adjustment START*NET software were adopted to present and analyze the monitoring data from measurements of total station. Associated with the advanced least squares techniques using the free network adjustment solution, two total stations could be installed in the influence zone of each tunnel (i.e. upward and downward tunnels) without further concern about the impact from instability of the equipment and could still possibly obtain reliable monitoring results. In order to improve the accurate measurements of the whole system for each tunnel, the two 360° prisms were installed in the deformation zone while the four benchmark (BM) points were set outside the movement zone. The initial results of real-time monitoring for the existing twin tunnels movements are also presented herein to further confirm that this reliable and cost-competitive monitoring method using least squares adjustment could be highly recommended to apply in engineering practice.

1 INTRODUCTION

Real-time monitoring such as cross-sectional convergence, crown settlement, and track bed deformation for existing tunnel structures is one of the most effective methods to observe the movements of the structures during its operating time since the trains run almost the time of the day. The measuring sensors using robotic total stations (RTSs) and objective prisms (OP) are recognized as one of the simplest and the most convenient automatic measurements for deformation monitoring for structures (Bird (2009), Luo et al. (2016), da Silva et al. (2018), Zhou et al. (2020), Fan et al. (2020)). The tunnel structure is relatively long so it requires a large number of monitoring points to be installed to adequately observe the structure movements. In general, the multiple RTSs that work simultaneously would be used to reduce the time-consuming of monitoring. However, the challenge of using multiple RTSs is that measurement errors would increase if the number of RTSs increases (Fan et al. (2020)). To eclipse this issue, the least squares adjustment is recommended to be used for the real-time monitoring system. This paper introduces the least squares adjustment theories, supported by STAR*NET software, integrated

into the real-time data acquisition system GeoAuto to enhance coordination adjustments and minimize errors associated with the operation of multiple RTSs.

2 METHODOLOGIES

2.1 Least squared adjustment

The application of the least squares technique has a well-established history in deformation surveying, spanning several decades (Atkinson et al. (1988), Setan and Ibrahim (2003), Tong et al. (2010), Ghazali et al. (2012), Okiemute et al. (2020)). This method relies on statistical analysis to estimate the most probable coordinates of measurement points within a network, thereby mitigating errors. The observation method, an indirect approach, is widely recognized as one of the most powerful techniques for adjustment computations in geomatics. The observation equation typically derives from a single observed quantity, such as distance, angle, or azimuth direction, and it can be linear or nonlinear, depending on the problem at hand. The least squares adjustment method for observations offers post-analysis capabilities and enables the estimation of accuracy measures after adjustment. Furthermore, it can be readily programmed, integrated into other software tools, and applied to a wide range of traverse types, with the added benefit of appropriately weighting observations of varying precisions (Yusoff et al. (2013)).

2.2 Measurement schematic

The proposed three-dimensional measurement network, which employs the least squares adjustment to determine the unknown coordinates of each point, is illustrated in Figure 1. This schematic comprises two stations (total stations), two common points represented by 360° prisms, four fixed benchmark points (BM), and various measurement points. As the total stations are strategically positioned in the deformation zone, the network adjustment incorporates a free network adjustment solution and an indirect method utilizing station transformation (Ghilani (2017)). Key observations involve angles (horizontal and vertical), distances (slope, horizontal, and vertical), and zenith observations. This schematic is highly effective in boosting the precisions of the monitoring due to the increased observation redundancies. Furthermore, its design minimizes the number of total stations required leading to the cost-effectiveness monitoring solution compared to the traditional methods where the total stations

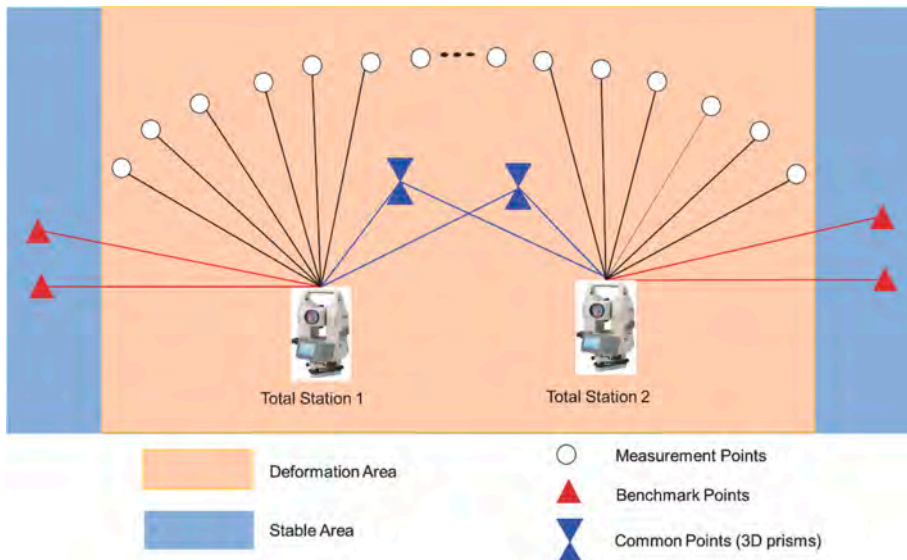


Figure 1. Measurement schematic method.

are placed outside the deformation zone. Thanks to the least squares adjustment technique, the monitoring achieves greater accuracy, even in the face of significant changes within the long tunnel. This capability addresses a critical need that many other deformation monitoring methods, as noted by Fan et al. (2020), may not adequately fulfill.

3 CASE STUDY AND ANALYSES

3.1 Project description

Existing twin tunnels and their associated station in the Kaohsiung City, Taiwan have been selected for this project to showcase the application of the least squared adjustment method in real-time monitoring. The automatic monitoring system aims to observe the movement of tunnel structures and the track bed during adjacent deep excavation construction activities. Based on the instrument placement mentioned in Figure 1, Figure 2 provides a plan view of the instruments, featuring 4 total stations, 4 360° - prisms, and 160 OP. Specifically, the total stations and 360° - prisms are strategically placed in the deformation zone, while BM points (i.e., D533, U33, D65, and U65) are positioned outside the movement zone. Notably, each tunnel incorporates 2 360° - prisms, observed by both total stations, enhancing the overall measurement accuracy of the system. To refine the real-time data collected from the observation system, the least squares adjustment method, facilitated by commercial STAR*NET software version 8, has been employed.

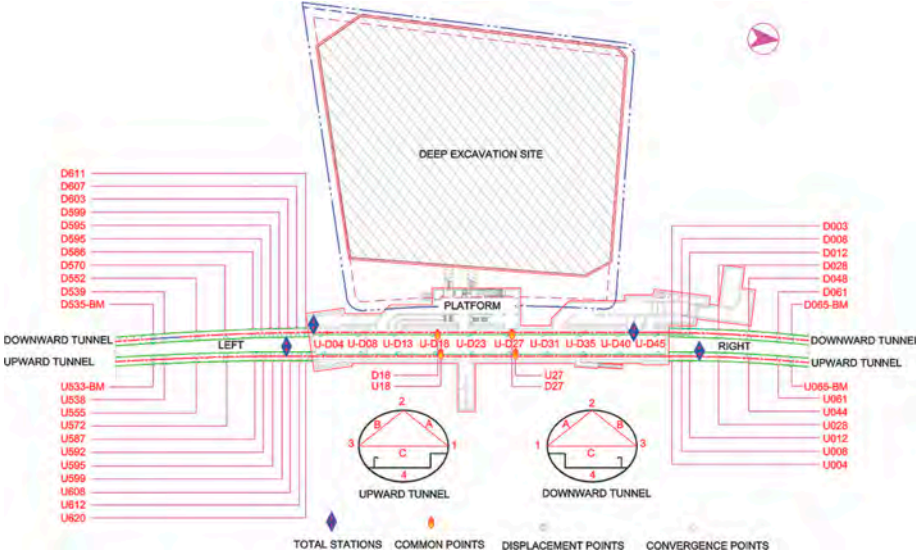


Figure 2. The layout of instruments installation for real-time observation in the tunnels.

3.2 Analysis software

The central control room houses the main server, where computers undertake the critical roles of managing and analyzing field data gathered from the total station. Wireless transmission through the general packet radio service (GPRS) facilitates the transfer of data from the total station to the main server. The GeoAuto, a built window software operating on the main server, serves as a comprehensive tool for automated data collection, storage, and display. Running parallel with the GeoAuto on the main server, the STAR*NET software functions to refine and adjust the raw data obtained from the server database. It excels in handling least squares analysis and adjustments for three-dimensional observation consisting of angles and distances. Combining GeoAuto and STAR*NET gives the efficiency and accuracy of surveying operations, making it a powerful solution for deformation monitoring applications. Figure 3 illustrates the real-time monitoring structure upon receiving data from the total

station. The main server then shares data with the web platform and various stakeholders such as consultants, contractors, and project users engaged in monitoring efforts.

As previously mentioned, STAR*NET software is employed to refine measurement results from the total station through the least square adjustment method. A notable

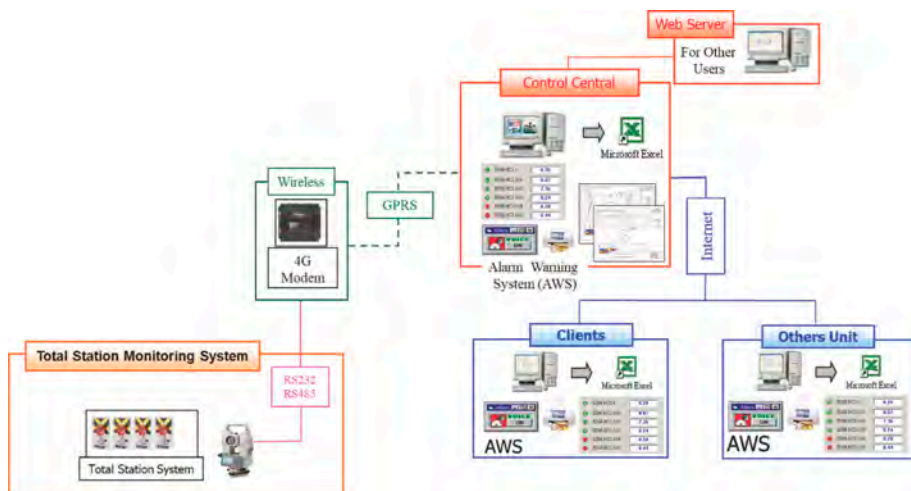


Figure 3. Structure of the real-time monitoring server.

Table 1. Select input parameters for STAR*NET software.

Options	Types		Values	Units
Adjustment	Adjustment type		3D	
	Units		m	
	Angular		DMS	
General	Coordinate system		Local	
	Adjustment solution	Convergence Limit	0.01	
		Max Iterations	10	
		Chi-Square significance level	5	%
		Fixed Std Error	Default	
		Angular	Default	
		Input/Output coordinate order	North-Earth	
Instrument	Error propagation	Confidence level	95	%
	Angle data station order		At-from-to	
	Earth radius		Default	
	Conventional	Distance constant	0.001	m
		Distance PPM	2	
		Angle	1.414214	Sec
		Direction	1	Sec
		Azimuth/bearing	1	Sec
		Zenith	2	Sec
		Elev. diff constant	0.0000001	M
		Elev. diff PPM	9.696	M
	Centering errors	Horizontal instrument	0.001	M
		Horizontal target	0.0022	M
		Vertical	0.0025	M
	Levelling (default by choosing length option)		0.001	m/km

feature of STAR*NET is its ability to assign weights to input data, either independently or by category. This enables more weight to be assigned to accurately known measurements in the adjustment process compared to less accurate measurements. By incorporating the standard errors derived from observation data weighting, the software allows users to input instrument standard errors for various conventional and leveling observations in the adjustment. Table 1 presents input parameters for STAR*NET calculation in this project which are determined based on the guidelines of the STAR*NET team support (available online here <https://support.microsurvey.com/convert/instrumentsettings.html>).

3.3 Benchmark points

The benchmark points for each measurement in the tunnels are interpreted by using the two manual survey methods measurement namely intersection and closure traverse. These BM points are converted from known global reference points provided by the project's owners. Table 2 shows the lists of BM points that come from the upward tunnel and the downward tunnel.

Table 2. The coordinates of BM points are calculated by using local reference points.

(a) Upward Tunnel			
Points	N (m)	E (m)	Z (m)
U533_BM_1	2506472.11788	177590.01364	89.71092
U533_BM_3	2506472.46595	177595.27891	90.51557
U65_BM_3	2506890.03165	177553.11136	90.54653
U66_BM_1	2506891.06463	177547.89258	89.51413
(b) Downward Tunnel			
Points	N (m)	E (m)	Z (m)
D533_BM_1	2506474.8289	177580.3100	89.4404
D533_BM_3	2506473.9990	177575.2815	89.4111
D65_BM_1	2506889.1509	177538.1728	89.6116
D65_BM_3	2506888.6149	177532.9252	90.4423

4 RESULTS AND DISCUSSIONS

4.1 Case evaluations

Figure 4 illustrates the results of the least squares adjustment using STAR*NET software for the downward tunnel. It is important to note that partially fixed coordinates are employed in the adjustment process, treating the BM points as observations akin to entered angles or distances. This approach allows all BM points to have maximum standard errors of 1 mm in the north, east, and elevation directions. To assess the adjustment process for case studies, the error factor and the Chi-Square test are crucial factors for examination. As depicted in Figure 4, the Chi-Square test for observations passes, signifying the optimal fit of adjustment results derived from real-time measurements. Across various data types such as coordinates, directions, distances, and zeniths, these error factors remain consistently within a range of 0.5 to 1.5, aligning with STAR*NET recommendations (Sawyer (2001)). Similarly, for the upward tunnel, the Chi-Square test is successful, and the error factors fall within the appropriate range mentioned earlier.

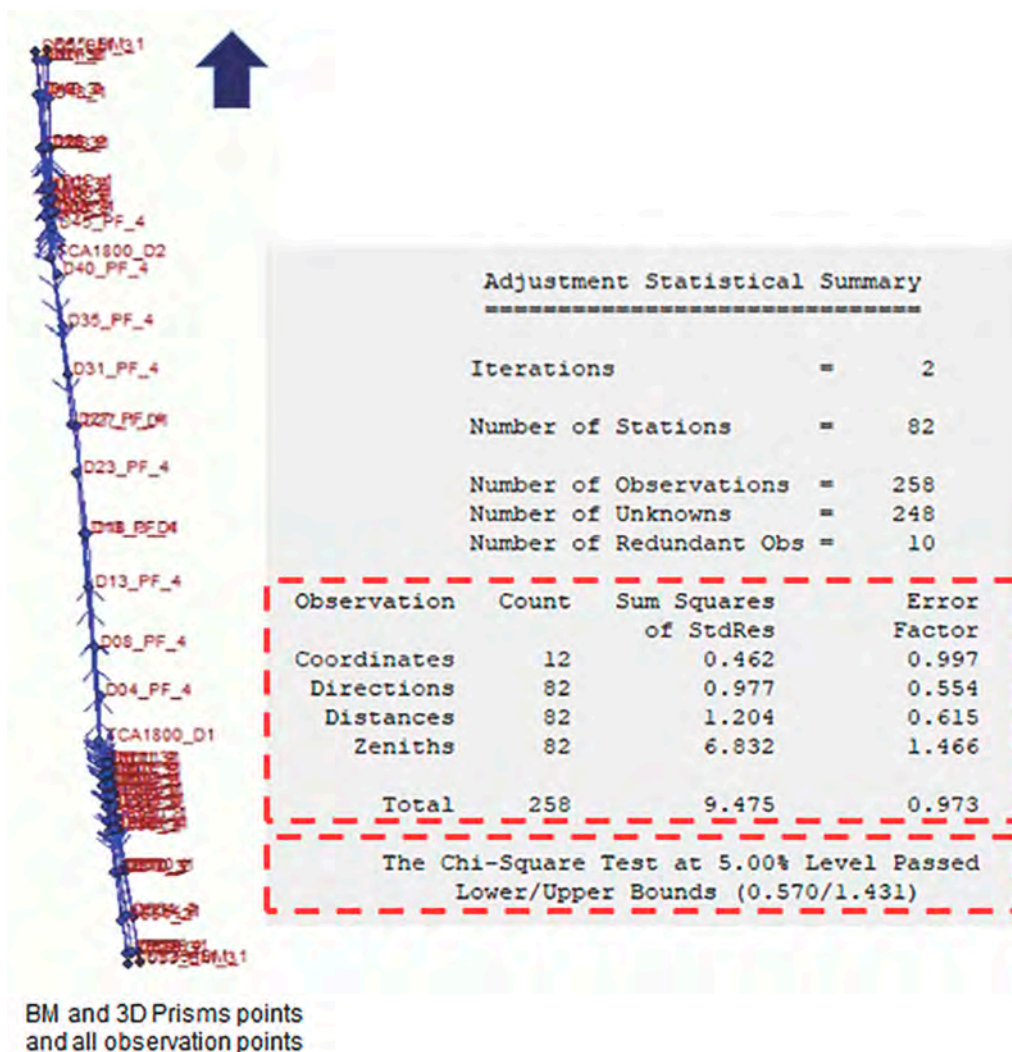


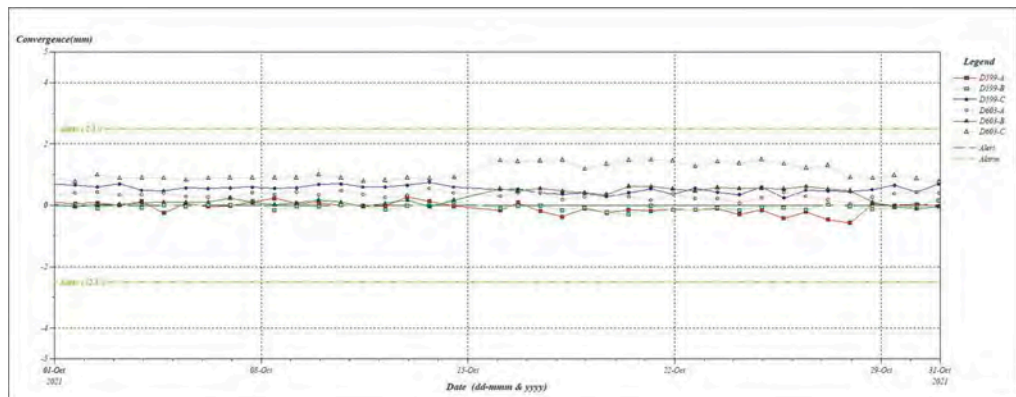
Figure 4. Adjustment output from STAR*NET.

4.2 Observations

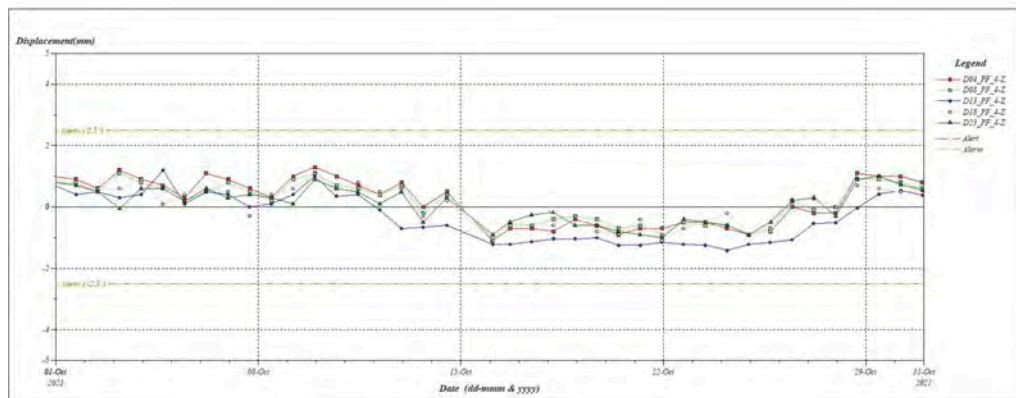
GeoAuto serves as the primary software responsible for presenting data from the real-time tunnel deformation monitoring system in this project. The data is segmented into three main observation areas: left downward and upward (i.e. D535~D611, U533~U620), right downward and upward (i.e. D003~D065, U04~U45), and downward and upward station platform (i.e. D04~D45, U04~U45). GeoAuto showcases two key observation outputs: tunnel cross-sectional convergence and track bed deformation. It is important to note that an alert and alarm system will be triggered if data observations exceed 2.5 mm.

This paper presents the 30-day monitoring results from October 2021 to showcase the effectiveness of the real-time tunnel deformation monitoring system. During this period, the data primarily reflects the behavior of the existing twin tunnel and station platform influenced by the installation of the diaphragm wall for adjacent deep excavation. Since the upward tunnel and station platform were minimally impacted by the adjacent construction during this timeframe, the selected output focuses on convergence and track bed vertical settlement for the downward tunnel and station platform, as illustrated in Figures 5a and 5b. The cross-

section convergence monitoring, represented by the time-history graph of two rings (D599 and D603) in Figure 5a, consistently indicates values less than 1 mm throughout October, with a slight increase to 1.5 mm for D603C from mid-October to 28th October, likely due to the proximity of diaphragm wall installation. Figure 5b depicts the settlement of the track bed over time through five selected observation points (i.e. D04_PF_Z, D08_PF_Z, D13_PF_Z, D018_PF_Z, D23_PF_Z). The data analysis system demonstrated effective functionality during the observation period, with minimal impact from dynamic loads generated by train operations. As mentioned earlier, significant settlements were observed from mid-October to 28th October 2021 due to the construction of the diaphragm wall near the station platform.



(a)



(b)

Figure 5. Tunnel convergence and track bed settlement time - history represented by GeoAuto: (a) cross-sectional convergence in tunnel on the left side; and (b) track bed settlement in the downward station platform.

5 CONCLUSION

The paper effectively demonstrates the application of the least squares theory to refine tunnel movements observed in real-time monitoring. The following conclusions can be drawn from this study:

1. To achieve both reliable and cost-effective tunnel deformation monitoring, an effective monitoring schematic is proposed in this study. The use of two total stations and two common 360° prisms are placed in the influence zone for each tunnel (i.e. upward and

downward tunnels) while the BM points are set outside the movement area for comprehensive monitoring.

2. The integration of real-time GEOAUTO and the least squares adjustment STAR*NET software emerges as a robust solution for presenting and analyzing monitoring data obtained from total station surveys. The selected input data for adjustment using STAR*NET meets stringent criteria, as evidenced by passing the Chi-Square Test value and maintaining error factors consistently within the recommended range of 0.5 to 1.5.
3. Short-term monitoring results presented in this study demonstrate the efficacy of the proposed approach using the least squares adjustment in real-time tunnel deformation monitoring. Additionally, data visualization using GEOAUTO highlights its potential as a valuable tool for ensuring the safety and stability of tunnel structures during construction activities. Future research could explore more case studies and longer timeframes of monitoring to enhance confidence in the proposed methodology for engineering practice.

REFERENCES

- Atkinson, K., Duncan, A. & Green, J. J. I. O. N. A. 1988. The application of a least squares adjustment program to underwater survey. 17, 119–131.
- Bird, B. J. B. C. I. O. T. 2009. Analysis of survey point displacements using total station measurements.
- Da Silva, I., Ibanez, W. & Poleszuk, G. Experience of using total station and GNSS technologies for tall building construction monitoring. Facing the Challenges in Structural Engineering: Proceedings of the 1st GeoMEast International Congress and Exhibition, Egypt 2017 on Sustainable Civil Infrastructures 1, 2018. Springer, 471–486.
- Fan, W., Pan, G., Wang, I. J. J. O. G. & Analysis, S. 2020. Development and application of a networked automatic deformation monitoring system. 4, 1–10.
- Ghazali, R., Adzmi, M. F. & Abd Latif, Z. The evaluation of 3D traverses of three different distance lengths toward the quality of the network for Deformation Survey. 2012 IEEE 8th International Colloquium on Signal Processing and its Applications, 2012. IEEE, 419–425.
- Ghilani, C. D. 2017. *Adjustment computations: spatial data analysis*, John Wiley & Sons.
- Luo, Y., Chen, J., Xi, W., Zhao, P., Qiao, X., Deng, X. & Liu, Q. J. M. 2016. Analysis of tunnel displacement accuracy with total station. 83, 29–37.
- Okiemute, Eteje Sylvester, Detailed Geodetic Technique Procedures for Structural Deformation Monitoring and Analysis (May 30, 2020). Eteje, S. O. (2020). Detailed Geodetic Technique Procedures for Structural Deformation Monitoring and Analysis. 6, 7–23.
- Sawyer, R. J. O., CA 2001. STAR* NET-PRO V6 least squares survey network adjustment program reference manual.
- Setan, H. & Ibrahim, M. S. 2003. *Deformation Detection Using Starnet, Trimble Geomatic Office and GPSAD2000*, Universiti Teknologi Malaysia.
- Tong, X., Meng, X. & Ding, K. J. S. R. 2010. Estimating geometric parameters of highways and railways using least-squares adjustment. 42, 359–374.
- Yusoff, M. Y. M., Jamil, H., Halim, N. Z. A., Yusof, N. M. & Zain, M. M. Ekadaster: A Learning Experience for Malaysia. FIG Pacific Small Island Developing States Symposium Policies and Practices for Responsible Governance Suva, 2013. 18–20.
- Zhou, J., Xiao, H., Jiang, W., Bai, W. & Liu, G. J. M. 2020. Automatic subway tunnel displacement monitoring using robotic total station. 151, 107251.

Coupled centrifuge-numerical modelling of shallow strip foundations

C. Tang, S.P. Selvaraj, C.M. Heron & A.M. Marshall

Department of Civil Engineering, University of Nottingham, Nottingham, UK

ABSTRACT: Hybrid modelling within geotechnical centrifuge tests is capable of combining the advantages of centrifuge models (providing soil stress/deformation data) with those of numerical models (capturing structural details along with associated load distributions and deformations), resulting in more accurate and reliable data of full-scale soil-structure interaction scenarios. This paper discusses a new version of the coupled centrifuge-numerical modelling (CCNM) method developed at the University of Nottingham Centre for Geomechanics (NCG) that is designed to test a continuous interface representing a shallow foundation. Specifically, the displacements of a strip foundation affected by tunnelling measured in a centrifuge model are transferred to an Abaqus numerical model of a masonry wall, with revised structural loads (from load redistribution within the building) from the numerical model then fed back to the loading of the strip foundation in the centrifuge model. This hybrid modelling approach provides a more realistic global interaction analysis compared to “traditional” approaches where a constant load is applied to the foundation. The paper provides details of the adopted equipment and methodologies, including rules for selecting and transferring displacement data from the centrifuge model and how the data is conditioned during the transfer processes. Preliminary test results are provided to demonstrate the effectiveness of the new CCNM method for data transfer at the continuous interface between the centrifuge and numerical models. The new CCNM method provides novel avenues for studying tunnel-building interactions with shallow strip foundations.

Keywords: centrifuge, Abaqus, hybrid modelling, tunnel-building interaction

1 INTRODUCTION

Tunnel excavation often occurs beneath low-rise masonry buildings with shallow foundations. The resulting ground movements can cause deformations and stress redistribution in overlying structures. Therefore, it is crucial to investigate the impacts of tunnelling on masonry buildings with shallow foundations.

Researchers have typically investigated the tunnel-masonry building interaction problem using small-scale physical models and full-scale numerical models, aiming to provide a reference or specific predictions for actual construction projects. Physical models at 1 g (where g is gravity) can provide indications of the important relationships and trends in tunnel-masonry building interactions, however the direct applicability of results to the full-scale is questionable because of the mismatch in stress conditions (where the 1 g model stresses are much less than the full-scale) (Giardina et al., 2012; Al Heib et al., 2020). Centrifuge models at elevated gravity are capable of reproducing full-scale stress conditions more realistically, while still benefiting from the reduced dimensions and controlled laboratory environment of a physical model. Centrifuge models necessarily involve the simplification of structures, varying from beams and plates that reproduce certain aspects of a building’s behaviour (Farrell et al., 2014), to the use of 3D printed miniature buildings (Ritter et al., 2018). Numerical models are able to reproduce, in

detail, many aspects of the construction and material complexities involved in real tunnelling projects (Burd et al., 2000; Yiu et al., 2017), however the reliability/fidelity of results is difficult to verify unless corresponding experimental/full-scale data are available.

Hybrid tests can be used to combine the strengths of physical and numerical modelling by analysing, within the respective physical/numerical domain, the part of the problem that is best suited to that domain, with data being transferred between models at a shared boundary. For the tunnel-building interaction problem, a real-time hybrid modelling method referred to as coupled centrifuge-numerical modelling (CCNM) was developed at the University of Nottingham Centre for Geomechanics (NCG) (Idinyang et al., 2018, 2019). This technique has been applied for the study of weightless elastic framed buildings on piled foundations, where the tunnel, soil, and piles were modelled in the centrifuge, and the framed building was modelled numerically, with data of pile vertical displacements/loading being shared between the physical (centrifuge) and numerical models representing pile-frame connections (Franza and Marshall, 2019; Song and Marshall, 2020).

The aim of this paper is to present developments in the CCNM testing methods that enable the testing of buildings on shallow strip foundations. In the new CCNM method, masonry buildings are simulated using a concrete damage plasticity (CDP) constitutive model in the finite element (FE) numerical simulation software Abaqus (Simulia, 2014), while the centrifuge model includes the soil, tunnel, and strip foundation. The emphasis of this paper is on lessons learned regarding the treatment of data shared between the experimental domain (controlled by Labview) and the numerical domain (Abaqus). The paper first provides an overview of the new CCNM method and its applications, followed by an explanation of the data transfer protocols between the centrifuge and numerical model domains. Preliminary test results are provided, as well as discussions regarding the advantages and applications of the advanced CCNM method.

2 CCNM OVERVIEW

The new CCNM application aims to model the scenario illustrated in Figure 1(a) (a wall with openings is illustrated, however other scenarios are also considered). Small-scale (1/70th) models of the strip foundation, tunnel, and soil are included in the centrifuge, while a masonry wall is simulated in Abaqus at a full (prototype) scale (see Figure 2). The initial foundation loads are first applied to the foundation based on a geostatic Abaqus analysis. A small increment of tunnel volume loss (0.1-0.2%) is then initiated in the centrifuge and vertical footing displacement data are transferred to Abaqus, which calculates revised foundation loads based on the level of distortion caused to the building. These revised loads are then applied within the centrifuge, which may result in displacement changes, which are then transferred again to Abaqus, and the cycle is repeated. Upon reaching a stable state where loads and displacements no longer change, additional increments of tunnel volume loss are applied. The “data exchange interface” between the centrifuge and numerical domains is done by LabVIEW, allowing the manipulation of data transferred at the interface (e.g. adjusting parameters between model and prototype scales) and the control of various test conditions, such as the activation of the numerical model (handing control of load actuation over to Abaqus), and the initiation of tunnel volume loss.

2.1 Centrifuge model

Figures 1(b)-(d) show the configuration of the centrifuge model. The strong box has internal dimensions of 700mm × 150mm × 500mm, with a front wall made of transparent acrylic that facilitates soil movement visualisation/measurement using two Dalsa Genie Nano-M4020 12.4 megapixel cameras and the GeoPIV-RG technique (Stanier et al., 2016). The soil is dry Leighton Buzzard Fraction E silica sand, characterised by a typical average diameter D_{50} of 0.14 mm, a uniformity coefficient U_c of 1.58, a specific gravity G_s of 2.65, a maximum void ratio e_{max} of 1.01, and a minimum void e_{min} of 0.61 (Lanzano et al., 2016). The uniform dense sand ($I_d \approx 90\%$) was prepared using an automatic sand pourer. An eccentric rigid boundary mechanical model tunnel with a diameter D_t of 90 mm developed by Song and Marshall (2020) was used to achieve tunnel volume loss (maximum of 3.5%). The tunnel was

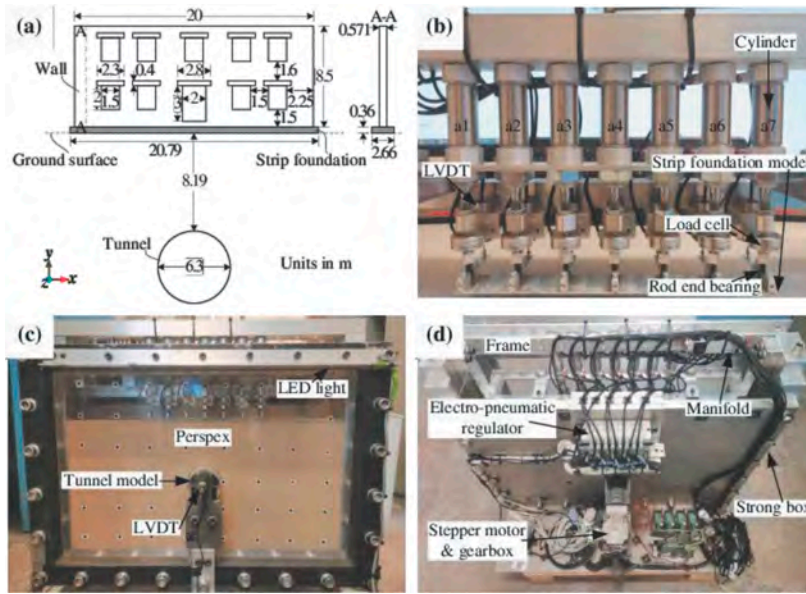


Figure 1. (a) Layout of prototype-scaled tunnel-strip foundation-wall, (b) loading system for strip foundation, and (c) front and (d) top views of centrifuge model.

buried with a cover depth (from the surface to the tunnel crown)-to-tunnel diameter ratio C/D_c of 1.3, which represents a typical scenario for shallow buried tunnels.

The centrifuge tests were conducted at a gravitational acceleration of 70 g. An aluminium strip foundation model (297mm \times 38mm \times 1.8mm, Young's modulus $E_a = 70$ GPa) was located on the soil surface (directly above the tunnel) to simulate a prototype-scale masonry strip foundation (20.79m \times 2.66m \times 0.36m, Young's modulus $E_m = 3$ GPa); the model foundation has the same scaled bending stiffness as the prototype foundation ($E_I = 31$ MN.m²). The minimum width (in the direction of the tunnel) of the foundation was 38mm to give sufficient space for the pneumatic cylinders used to apply loads. The strip foundation is subjected to loading at seven predetermined positions at a spacing of 47.5 mm (see Figure 1(b)) within raised beams along the foundation (the raised beams ensure load is applied evenly across the width of the foundation). The beams are loaded via rod end bearings (ensuring no bending action is applied) and 3 mm diameter steel rods inserted through the beams (a 6 mm length at the central position of the raised beams was removed to accommodate the rod end bearings).

The loading system consists of a frame, seven pneumatic cylinders (25 mm bore, 25 mm stroke, C85 series, double acting, maximum 1 MPa), a manifold, and eight compact electro-pneumatic regulators (ITV0050-3ML-Q, maximum 1 MPa pressure supply). The pressure within the lower chamber of each cylinder is connected to a unique regulator using 4mm diameter pipe, while the pressure within the top chamber of all cylinders is linked to a common regulator using a manifold. A dedicated air compressor is used that supplies compressed air at approximately 950 kPa to the regulators. The frame, positioned on top of the strongbox, securely holds the manifold, cylinders, and 10 mm stroke linear variable differential transformers (LVDTs). Load cells with a 500 N range are connected in-line with the cylinder rods and the rod end bearings, enabling the application/measurement of loads onto the strip foundation.

2.2 Numerical model

The masonry wall (20 m long and 8.5 m high) with openings, labelled H8.5O19, where H is wall height and the number following O indicates the percentage of door and window opening areas within the entire wall, as shown in Figure 1(a), is modelled at prototype scale using 3D

shell elements (S3) in Abaqus based on construction and dimensions derived from previous studies (Burd et al., 2000; Pickhaver et al., 2010; Yiu et al., 2017). According to Yiu et al. (2017), the CDP constitutive model of the masonry buildings is characterised by a mass density of 2423.5 kg/m³, a Poisson's ratio of 0.3, a Young's modulus E_m of 3 GPa, infinite compressive strength, and post-failure tensile stress that increases with a positive gradient of 0.01 E_m after reaching a tensile strength of 50 kPa (hardening failure), while Young's modulus of the linear elastic lintel in the facade model is 9 GPa. In Yiu et al. (2017), a 215 mm thick masonry wall rested on a 1 m wide strip foundation, resulting in a nominal stress of 33.7 kPa under plane strain conditions. In the centrifuge, the prototype scale foundation width had to be increased to 2.66 m (as mentioned in the previous section, the minimum model foundation width was 38 mm due to experimental constraints); to achieve the same nominal bearing stress of 33.7 kPa, the prototype wall thickness from the centrifuge tests was therefore scaled by the ratio of foundation widths (2.66) to 571 mm.

To establish a plane strain condition, the numerical models impose global constraints on the displacement degrees of freedom in the z direction and the rotational degrees of freedom about the x and y axes. The boundary conditions applied to the 50 nodes along the base of the wall allow for horizontal movement in the x-direction and rotation about the z-axis; vertical displacements (in the y-direction) are controlled through a connection to the data exchange interface using a FORTRAN subroutine. The experimental equipment has a limitation in that it does not allow measurement or control of the rotation of the model foundation about the z-axis; this may result in some disparity between centrifuge and numerical models, however this disparity can be considered a secondary factor in the overall interaction behaviour.

Two analysis steps are implemented: the first involves the rapid application of a gravity load to the walls within a single increment, while the second step is the subsequent coupled simulation with the centrifuge model through the data exchange interface, necessitating a substantial number of increments to cover the entire testing duration.

2.3 Coupled modelling

Firstly, the centrifuge undergoes three spin up/down/up "stabilisation cycles" (1-70-10-70-10-70 g), with the aim of reducing localised soil stress concentrations and improve test repeatability; the strip foundation is suspended from the load actuators during these cycles and is not in contact with the soil. The foundation is then lowered slowly onto the soil and a preliminary load of 2 N is simultaneously applied to the seven loading positions on the strip foundation using a LabVIEW load-control program, thereby ensuring the establishment of full contact between the bottom of the strip foundation and the soil surface. The test progresses as follows, as illustrated in Figure 2:

1. Initial loads from the wall self-weight (F_{f_0}) are simultaneously applied to the foundation in increments of 25% of final load. Soil surface settlements are then initialised to 0. The data exchange interface is activated and control of the foundation load is passed to Abaqus.
2. An increment of tunnel volume loss ($\Delta V_{1,t} \approx 0.1-0.2\%$) is manually initiated, causing settlements of both the surrounding soil and the strip foundation.
3. The seven LVDT measurements of foundation settlements (S_f) are transferred to the data exchange interface when the stabilisation criteria are met and displacement threshold is reached.
4. The strip foundation settlements (S_f) are fitted using the modified Gaussian curve (Vorster et al., 2005) to get the input of settlement (S_{w_node}), after scaling to prototype scale and interpolating, of the 50 nodes along the base of the wall in the numerical model.
5. The node loads at the wall base (F_{w_node}) are calculated in the numerical model according to the input wall base settlements (S_{w_node}); the change in settlement along the base of the wall in the numerical model is always from a 'reference' state corresponding to the final settlement profile at the end of the preceding volume loss increment ($S_{w_node_ref}$).
6. The revised node loads at the wall base (F_{w_node}) are transferred to the data exchange interface and distributed, after scaling to model scale, to the 7 concentrated (actuator) loads (F_w)

according to the following: n1-3[3]:a1, n4-13[10]:a2, n14-21[8]:a3, n22-29[8]:a4, n30-37[8]:a5, n38-47[10]:a6, n48-50[3]:a7, where n#-# indicates the node number in Abaqus, [#] is the number of nodes, and a# is the actuator number in the centrifuge (see Figure 1(b)).

- The data exchange interface assesses whether loads are balanced ($F_f = F_w$). If yes, continue with step 8, and wait for the next tunnel volume loss (i.e. step 2, which is manually initiated; as long as the displacement threshold is not reached ($|S_{f,tot}| < 15\mu\text{m}$) and the stabilisation criteria are met). If not, continue with step 8 and repeat steps 3-8 (this process, i.e. steps 3-8, repeat automatically until a stable and balanced condition is achieved).

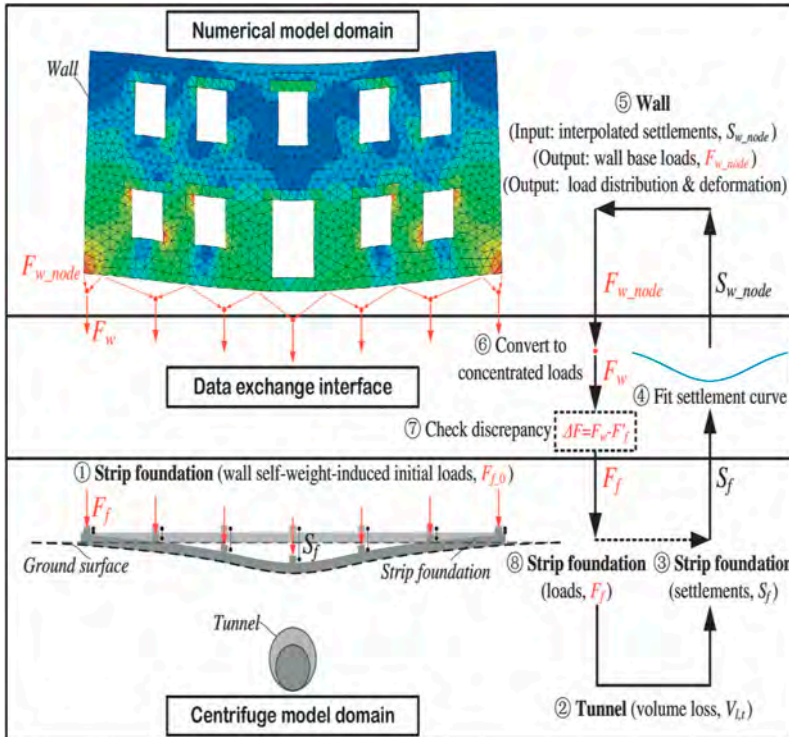


Figure 2. Diagram of the coupled centrifuge-numerical modelling of shallow foundations.

- The new loads (F_f) from the data exchange interface are applied to the strip foundation, resulting in new settlements of both the strip foundation and the underlying soil.

3 CCNM DATA TRANSFER PRINCIPLES

The following provides additional details relating to certain aspects of the control system and how data was managed in the data exchange interface.

Pneumatic cylinder air pressure control (load control): The bottom chamber of the pneumatic cylinders is controlled via the pressure regulators using a Proportional-Integral-Derivative (PID) algorithm within LabVIEW. Using the target load F_f (either manually input or obtained from Abaqus) and the load cell data, the PID algorithm adjusts the input voltage to the pressure regulator (i.e. the bottom chamber pressure) until the required target load is achieved. The test load range is typically set from -20 N (an upwards force of approximately 1/6 the foundation self-weight, representing the force needed to lift the (local) foundation off the surface) to half of the wall self-weight.

Settlement data transfer rules for centrifuge model (steps 3–4): The prerequisite for sending settlement data from the centrifuge to Abaqus is that the foundation system reaches a stable state and that displacements are above a certain threshold (such that insignificant changes in readings are not continually passed across the data exchange interface). The stabilisation criteria require ① the load tolerance $|F_{f,tot}| = |F_f - F_{f,cur}| \leq 5 \text{ N}$, where F_f is the target load and $F_{f,cur}$ is the current load cell reading, ② the maximum fluctuation of the foundation load cell readings $|F_{f,fluc}| \leq 3 \text{ N}$, and ③ the settlement fluctuation of the strip foundation $|S_{f,fluc}| \leq 5 \mu\text{m}$; the displacement threshold condition is represented by the foundation settlement tolerance $|S_{f,tot}| = |S_{f,cur} - S'_f| \geq 15 \mu\text{m}$, where $S_{f,cur}$ is the current LVDT reading and S'_f is the previous target from Abaqus (i.e. the settlement change is sufficiently large to be passed to Abaqus). Once these criteria are met for a time window of $ST = 5\text{ s}$, the average of foundation settlement S_f over the preceding 1 s are transferred to the data exchange interface for fitting the modified Gaussian curves.

Settlement input rules for Abaqus (steps 4-5): The difference (ΔS) between the current target settlement ($S_{w,node}$) and the reference settlement for the wall base nodes after settlement curve fitting (i.e. the initialised soil/foundation settlement or the stable settlement at the end of the last tunnel volume loss process, $S_{w,node,ref}$) is applied in Abaqus in 10 increments to ensure the convergence of the Abaqus analysis of each increment. For the CDP masonry wall model, this process takes $\approx 4\text{ s}$, with each increment taking $\approx 400\text{ ms}$; the exact timing depends on the convergence time of the Abaqus analysis.

Load output rules for Abaqus (steps 5-6): According to the input foundation displacements, the Abaqus analysis provides a new load distribution along the building base ($F_{w,node}$ for each of the 50 nodes). These are transferred to the data exchange interface after each assignment of nodal settlements in steps 4-5. The distributed loads at the complete settlement curve ($S_{w,node}$) are grouped into seven discrete loading points based on their proximity to the load actuation points in the centrifuge (see Figure 2); the vertical loads from each node within a group are added together (F_w) to obtain the target actuator load (F_f).

Load application rules for centrifuge model (steps 6-8): The application of the target loads F_w from Abaqus directly to the centrifuge model caused stability issues, especially at the outset of tests where settlement magnitudes were low and building stiffness was greatest. Prior to the onset of yielding within the wall, fluctuations in foundation settlements caused relatively large variations in foundation load (and subsequently settlement) changes, ultimately preventing the overall system from stabilising. To overcome these issues, the loads from Abaqus were essentially ‘damped’ according to the following rules. If the load increment at a given actuation point $|\Delta F| = |F_w - F'_f| > 3 \text{ N}$, where F'_f is the previous target load, the target load $F_f = 50\% \Delta F + F'_f$ is applied; if $|\Delta F| \leq 3 \text{ N}$, the target loads are applied directly ($F_f = F_w$, i.e. load is balanced). If the application of ΔF causes settlements that satisfy the ‘Settlement data transfer rules for centrifuge model (steps 3-4)’ criteria, then a new cycle (steps 3-8) is initiated; if the stabilisation criteria are satisfied and the displacement threshold is not exceeded (i.e. the whole model is stable and balanced), the next tunnel volume loss trigger can be activated.

4 CCNM RESULTS

Figure 3 presents preliminary test results (in model scale) of masonry walls with strip foundations at a tunnel volume loss $V_{l,t} = 2.2\%$, including (a) the load distribution along the foundation, and (b) the settlement of the foundation; greenfield (GF) settlements from a separate centrifuge test are also included for reference. The CCNM method was used for the masonry wall (H8.5O19), effectively capturing the load redistribution within the building caused by foundation settlements. For comparison, an equivalent test was conducted with constant dead loads applied to the foundation, labelled as H8.5O19*.

Note that in Figure 3(a), the 7 centrifuge load magnitudes are much larger than the 50 Abaqus loads because the centrifuge values are obtained by summing up loads from nodes close to the centrifuge load actuation points. A distributed load beneath the model foundation in the centrifuge that is similar to the load profile from Abaqus should be obtained due to the

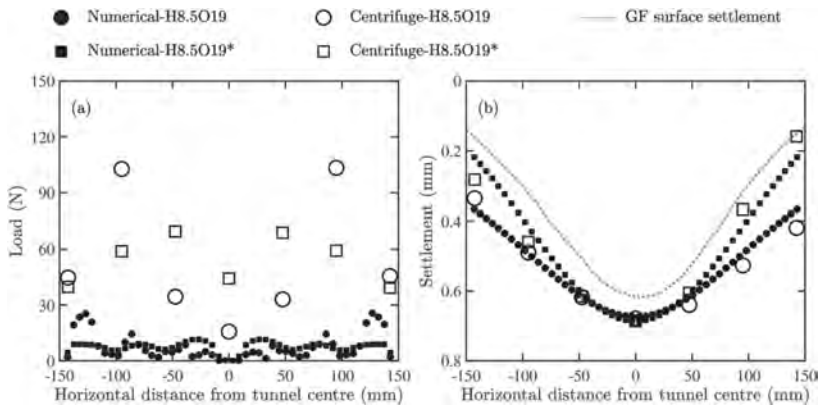


Figure 3. Comparison of model-scaled (a) load and (b) settlement (downwards positive) at the interface between centrifuge model domain (7 positions), numerical model domain (50 nodes), and the corresponding greenfield settlement profiles at $V_{Lt} = 2.2\%$.

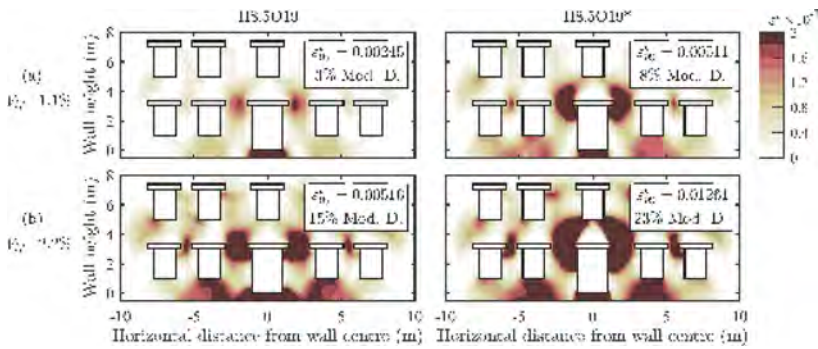


Figure 4. Changes in max principal strain (tensile strain) of H8.5O19 and hypothetical changes of H8.5O19* during tunnel volume loss.

stiffness of the foundation in the centrifuge model; the settlement profile in Figure 3(b), to some degree, gives confidence that this is the case. The load data in Figure 3(a), noting that the initial loading in the CCNM test (H8.5O19) is the same as the data plotted for the constant load test (H8.5O19*), shows that, as a result of building distortions caused by tunnelling ground movements, building load is transferred from the centre of the foundation towards its ends. This load redistribution has a notable effect on the foundation settlements, as shown in Figure 3(b), where relative displacements between the foundation centre and ends is reduced as a result of the load transfer mechanism. Figure 3(b) also demonstrates that the modified Gaussian curve fitted to the seven data points of centrifuge settlement gives a sensible input of settlements at the 50 nodes along the base of the wall in the Abaqus model. There is some asymmetry of settlements to the left and right side of the tunnel, however this level of variability is typical for these types of centrifuge tests.

The tunnelling-induced building tensile strain ϵ^t is provided in Figure 4. The values of ϵ^t for test H8.5O19* (where constant loads were applied and therefore an Abaqus simulation was not done alongside the centrifuge test) were obtained by applying the measured foundation settlements to the Abaqus model of the wall after the test. The regions of high magnitude tensile strains are observed to be near the building centre (directly above the tunnel); these areas are notably greater in size for the constant load test H8.5O19* compared to the CCNM test H8.5O19. Comparing the values of characteristic strain ϵ_{99}^t (the strain that is not exceeded in 99% of the total volume of the masonry wall, as adopted by Yiu et al. (2017)) and the areas of

at least moderate damage (Mod. D., defined as $\epsilon^f > 0.0015$ according to Mair et al. (1996)) in Figure 4, the outcome demonstrates that the use of constant dead loads in these types of tests will overestimate the extent and severity of damage in masonry buildings.

5 CONCLUSIONS

This paper presented an overview of a new development of the coupled centrifuge-numerical modelling (CCNM) method which enables the testing of shallow foundations and masonry walls. The paper described the equipment, the application, and the adopted data transfer rules. The new CCNM application successfully established a data exchange at a continuous interface between the model foundation within the centrifuge model domain and the base of the masonry wall in the numerical model domain under plane strain conditions. Results demonstrated the effectiveness of the CCNM approach and the importance of including load redistribution within the building to obtain accurate assessments of building distortions and damage. Future work will focus on extending the application to 3D scenarios, allowing for a more comprehensive understanding of the behaviour and response of buildings with shallow foundations in complex geological and construction contexts.

ACKNOWLEDGEMENTS

The first author recognises the financial support provided by the China Scholarship Council (CSC) and the University of Nottingham, UK.

REFERENCES

- Al Heib, M., F. Emeriault, & H.-L. Nghiem (2020). On the use of 1g physical models for ground movements and soil-structure interaction problems. *Journal of Rock Mechanics and Geotechnical Engineering* 12(1), 197–211.
- Burd, H., G. Housby, C. Augarde, & G. Liu (2000). Modelling tunnelling-induced settlement of masonry buildings. *Proceedings of the institution of civil engineers-geotechnical engineering* 143(1), 17–29.
- Farrell, R., R. Mair, A. Sciotti, & A. Pigorini (2014). Building response to tunnelling. *Soils and foundations* 54(3), 269–279.
- Franza, A. & A. M. Marshall (2019). Centrifuge and real-time hybrid testing of tunneling beneath piles and piled buildings. *Journal of Geotechnical and Geoenvironmental Engineering* 145(3), 04018110.
- Giardina, G., A. Marini, M. A. Hendriks, J. G. Rots, F. Rizzardini, & E. Giuriani (2012). Experimental analysis of a masonry façade subject to tunnelling-induced settlement. *Engineering Structures* 45, 421–434.
- Idinyang, S., A. Franza, C. Heron, & A. Marshall (2018). Millisecond interfacing of physical models with abaqus. In *9th Int. Conf. Phys. Modelling in Geotechnics, London*, pp. 209–214.
- Idinyang, S., A. Franza, C. M. Heron, & A. M. Marshall (2019). Real-time data coupling for hybrid testing in a geotechnical centrifuge. *International Journal of Physical Modelling in Geotechnics* 19(4), 208–220.
- Lanzano, G., C. Visone, E. Bilotta, & F. Santucci de Magistris (2016). Experimental assessment of the stress-strain behaviour of leighton buzzard sand for the calibration of a constitutive model. *Geotechnical and Geological Engineering* 34, 991–1012.
- Mair, R., R. Taylor, & J. Burland (1996). Prediction of ground movements and assessment of risk of building damage due to bored tunnelling. In *Geotechnical aspects of underground construction in soft ground*, pp. 713–718.
- Pickhaver, J., H. Burd, & G. Housby (2010). An equivalent beam method to model masonry buildings in 3d finite element analysis. *Computers & structures* 88(19-20), 1049–1063.
- Ritter, S., G. Giardina, M. J. DeJong, & R. J. Mair (2018). Centrifuge modelling of building response to tunnel excavation. *International Journal of Physical Modelling in Geotechnics* 18(3), 146–161.
- Simulia, D. S. (2014). Abaqus 6.14. Providence, RI, USA.

- Song, G. & A. M. Marshall (2020). Centrifuge study on the influence of tunnel excavation on piles in sand. *Journal of Geotechnical and Geoenvironmental Engineering* 146(12).
- Stanier, S. A., J. Blaber, W. A. Take, & D. White (2016). Improved image-based deformation measurement for geotechnical applications. *Canadian Geotechnical Journal* 53(5), 727–739.
- Vorster, T. E. B., A. Klar, K. Soga, & R. J. Mair (2005). Estimating the effects of tunneling on existing pipelines. *Journal of Geotechnical and Geoenvironmental engineering* 131(11), 1399–1410.
- Yiu, W., H. Burd, & C. Martin (2017). Finite-element modelling for the assessment of tunnel-induced damage to a masonry building. *Géotechnique* 67(9), 780–794.

Spatial interpolation of sparse SPT values using weighted ellipse nearest neighbors approach

W. Yan

State Key Laboratory of Internet of Things for Smart City, Department of Civil and Environmental Engineering, University of Macau, Macao SAR, China
Zhuhai UM Science & Technology Research Institute, Zhuhai, China

C. Yang

CCCC-FHDI MACAU CO., LTD., Macao SAR, China

W.H. Zhou

State Key Laboratory of Internet of Things for Smart City, Department of Civil and Environmental Engineering, University of Macau, Macao SAR, China
Zhuhai UM Science & Technology Research Institute, Zhuhai, China

P. Shen

State Key Laboratory of Internet of Things for Smart City, Department of Ocean Science and Technology, University of Macau, Macao SAR, China

ABSTRACT: The interpolation of geotechnical properties, such as the N-value in the standard penetration test, plays a crucial role in site characterization and subsurface visualization. However, the sparsity of data often poses challenges in characterizing their spatial distribution and variability. In this study, a Weight Ellipse Nearest Neighbors (WENN) is proposed as a novel interpolation method for sparse geotechnical properties. The method can estimate the spatial mean with standard deviation for uncertainty quantification. The parameters of WENN are data-driven by site-specific measurements using leave-one-borehole-out approach. WENN is applied to a simulated non-stationary SPT example and the effect of number of measurements is discussed in detail. Furthermore, WENN is applied to a field example from New Zealand Geotechnical Database, and its capability is validated by cross-validation tests and comparative results with traditional methods. The outcomes indicate that WENN can capture the overall trend of measurements with acceptable errors, reasonable uncertainty, and sufficient interpretation.

1 INSTRUCTION

The geotechnical properties obtained through site investigations are invaluable for engineering design. However, constrained by cost and scheduling limitations, geotechnical data often remains sparse and limited (Yan et al., 2023a), presenting challenges in reducing geotechnical risks and impeding the progress toward smart city development (Shen, 2023). For example, the N-value in the standard penetration test (SPT) is often available at specified intervals, while the gaps still exist in significant uncertainty. In such cases, employing an interpolation method with sparse geotechnical data becomes crucial for site characterization (He et al., 2024) and the visualization of subsurface areas.

The interpolation of geotechnical properties has been extensively explored in prior studies. The inversed distance weighted (IDW) (Karkush et al., 2023) and Ordinary Kriging (OK)

(Samui and Thallak, 2010) stand out as widely adopted techniques, but their robustness is still constrained due to complex natural heterogeneity and limited observed data. To enhance spatial interpolation of geotechnical properties, advanced methods such as Glasso (Shuku and Phoon, 2021), sparse Bayesian learning (Ching et al., 2020), Bayesian compressive sampling (Wang and Zhao, 2017, Lyu et al., 2023), machine learning methods (Xie et al., 2022), etc., have been proposed. Despite these significant efforts, current studies face challenges in achieving efficient modeling with sufficient engineering interpretation (Yan et al., 2023b), which is crucial for subsurface visualization and forms the bedrock for decision-making in engineering applications.

To offer an alternative solution for interpolating geotechnical properties, such as SPT N-values, this study proposes a simplified and efficient method, namely Weight Ellipse Nearest Neighbors (WENN), as an improved version of IDW. WENN introduces an ellipse function to consider geotechnical anisotropy and overcome the limitations of traditional IDW. Additionally, WENN can provide uncertainty estimations for unsampled locations that align with engineering intuition and interpretation. In this study, the effectiveness of WENN is verified in 2D profiles, including a simulated non-stationary SPT example and a real-world SPT example.

2 WEIGHT ELLIPSE NEAREST NEIGHBORS (WENN)

2.1 Estimation of the spatial mean

The fundamental concept of IDW involves estimating values for unsampled locations by considering the available values at sampled locations, incorporating the inverse of the distance as a weighting factor. WENN could be regarded as an improved version of the IDW approach for two key distinctions: introducing an ellipse function to consider the geological anisotropic and providing uncertainty estimation. WENN is able to interpolate the geotechnical properties (such as N-value in SPT) between sparse measurements. Specifically, the ellipse function can be formulated mathematically as follows (Liu and Leung, 2018):

$$U(i, j) = (\mathbf{x}_j - \mathbf{x}_i) \mathbf{D}^T \mathbf{A} \mathbf{D} (\mathbf{x}_j - \mathbf{x}_i)^T \quad (1)$$

$$\mathbf{A} = \begin{bmatrix} \frac{1}{R_x^2} & 0 \\ 0 & \frac{1}{R_y^2} \end{bmatrix} \quad (2)$$

$$\mathbf{D}(\theta_i) = \begin{bmatrix} \cos\theta_i & -\sin\theta_i \\ \sin\theta_i & \cos\theta_i \end{bmatrix} \quad (3)$$

where \mathbf{x}_i and \mathbf{x}_j represent the spatial coordinates of the unsampled element i and the borehole element j , respectively; R_x and R_y are the lengths of the major and minor axis of the ellipse; θ_i is the dip angles of the unsampled element i . In this study, as a typical situation when dip angles are not available, θ_i could be set to zero. Essentially, $U(i, j)$ is a modified distance between sampled and unsampled elements, which is controlled by tuning parameters R_x and R_y that indicate the level of spatial correlation in horizontal and vertical directions. According to IDW, the reciprocal of $U(i, j)$ represents the weight of the measurements, and the mean of the unsampled element could be estimated by the weighted method:

$$\mu(i) = \frac{\sum_{j=1}^{n_j} \frac{1}{U(i,j)} V(j)}{\sum_{j=1}^{n_j} \frac{1}{U(i,j)}} \quad (4)$$

where $V(j)$ is the geotechnical property of sampled element j ; n_j is the total number of sampled elements in space.

2.2 Estimation of the spatial standard deviation

It is well acknowledged that quantifying uncertainty for the weighted mean is always challenging due to the sparsity of measurements. Previous studies have proposed empirical equations for estimating weighted standard deviation for weighted mean (Gatz and Smith, 1995), but their suitability in geotechnical problems remains unknown. In this study, we adopt a simplified form of weighted standard deviation (SD), which is widely used in statistical software like Statistical Product and Service Solution (Madansky and Alexander, 2017):

$$SD(i) = \sqrt{\frac{\sum_{j=1}^{n_j} \frac{1}{U(i,j)} (V(j) - \mu(i))^2}{\sum_{j=1}^{n_j} \frac{1}{U(i,j)} - 1}} \quad (5)$$

In this case, each unsampled element is assumed to be assigned with a normal distribution with a weighted mean $\mu(i)$ and standard deviation $SD(i)$.

2.3 Parameter determination based on ellipse search

The combination of R_x and R_y in WENN determines the shape of the ellipse, and it should be data-driven by site-specific measurements. Traditional IDW often employs a leave-one-out strategy for parameter optimization using sampled points that are randomly distributed in space (Liu et al., 2019). Since each borehole could be treated as a one-time sampling, in this study, a leave-one-borehole-out strategy is employed, which is a common approach in geotechnical studies (Lyu et al., 2023, Wei and Wang, 2022).

Specifically, in each trial with a specified combination of R_x and R_y , the geotechnical properties of each leave-out borehole are treated as unsampled elements and are to be estimated using sampled elements from other boreholes lying within the ellipse (refer to Equation 1 where $U \leq 1$). The performance of each trial is quantified by Mean Absolute Error (MAE):

$$MAE = \frac{\sum_{j=1}^{n_j} |V(j) - \mu(j)|}{n_j} \quad (6)$$

where $\mu(j)$ is the estimated mean for the sampled element j . Through several trials, the optimal combination of R_x and R_y could be determined which minimized MAE.

3 METHOD VERIFICATION IN A SIMULATED EXAMPLE

3.1 Simulated example and results

To verify the proposed WENN, a profile of non-stationary data ($(N_1)_{60}$) is generated using a random field with the addition of a linear trend (see Figure 1a). The random field is constructed using the Covariance Matrix Decomposition method, with the autocorrelation function expressed as:

$$\rho(\Delta x_1, \Delta x_2) = \exp\left(-2\sqrt{\frac{\Delta x_1^2}{I_H^2} + \frac{\Delta x_2^2}{I_V^2}}\right) \quad (7)$$

where I_H and I_V are horizontal and vertical scales of fluctuation; Δx_1 and Δx_2 are horizontal and vertical distances of any two elements in the field. In this study, the parameters of the random field are set within the reasonable ranges (Phoon and Kulhawy, 1999) for SPT data (i.e., $I_H = 20$, $I_V = 3$, Mean = 10, coefficient of variation = 0.3, probability distribution = log-normal). Additionally, a linear trend $f(x_1, x_2) = 2 + 0.05x_1 + 0.2x_2$ is introduced into the above

random field, where x_1 and x_2 are the horizontal and vertical coordinates. The dimensions of the profile are 100 m \times 50 m with a resolution of 1 m in both directions. Six equally distributed boreholes with SPT sampling intervals of 4 m along depth are assumed.

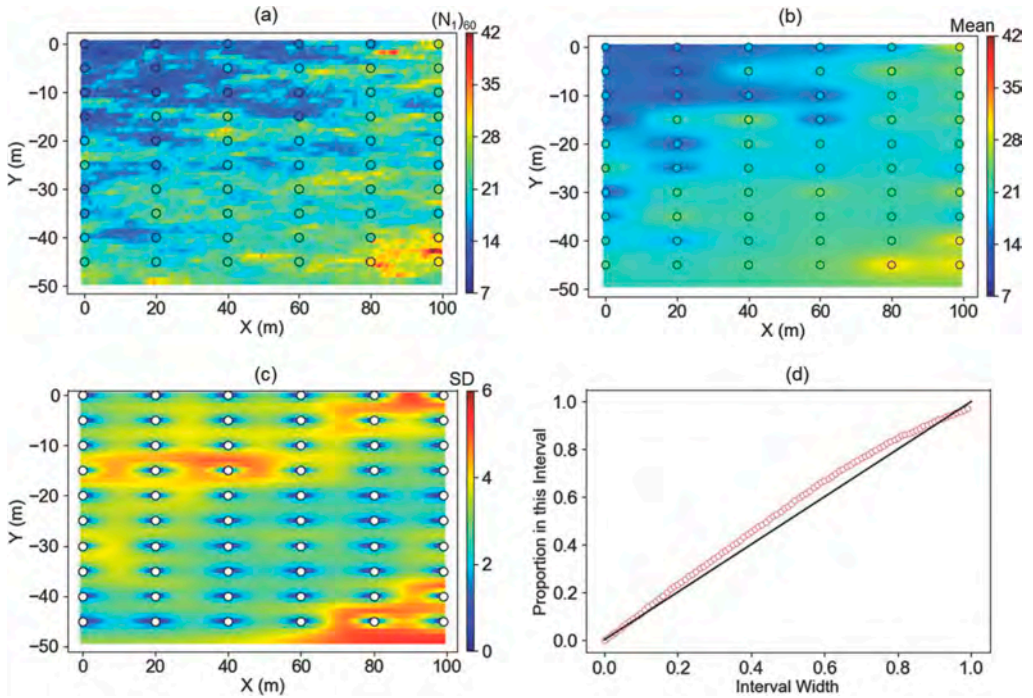


Figure 1. Interpolation results of a simulated example: (a) simulated non-stationary $(N_1)_{60}$ profile; (b) visualization of interpolated mean and (c) standard deviation (SD); (d) uncertainty evaluation based on P-P plot.

The optimal combination of parameters is 40 m and 7.5 m for R_x and R_y , respectively. The running time of WENN is 3.5 s. The estimated mean of $(N_1)_{60}$ using the proposed WENN is plotted in Figure 1b. Notably, the estimated mean is able to capture the overall trend using limited sampled data which agrees well with the original profile. The estimated standard deviation of $(N_1)_{60}$ in Figure 1c represents the uncertainty within the gaps. High uncertainty regions are primarily distributed in areas where adjacent measurements exhibit significant differences, which is consistent with the general knowledge of the site characterization. To further evaluate the uncertainty, the probability-probability plot (P-P plot) is shown in Figure 1d, which is widely used to illustrate the predicted cumulative distribution functions against the true one (Takoutsing and Heuvelink, 2022). The results indicate that the prediction curve only slightly deviates above the 1:1 line, signifying a reasonable prediction in uncertainty.

3.2 Effect of number of measurements

To investigate the effect of the number of measurements, different numbers of boreholes (i.e., 1, 3, and 5) and SPT sampling numbers (i.e., 6, 13, 25, 50 per borehole) are adopted using the simulated profile as ground true. The boreholes and SPT samples are equally and symmetrically distributed in the profile (refer to Figure 3). The parameters remain unchanged and are consistent with the previous section. Figure 2a illustrates the overall decrease trend of the entire profile with an increase in the number of measurements, thus validating the effectiveness of the proposed method. In addition, the 1D data in $X = 50$ is selected to manifest the contribution of measurement to the local effect. As shown in

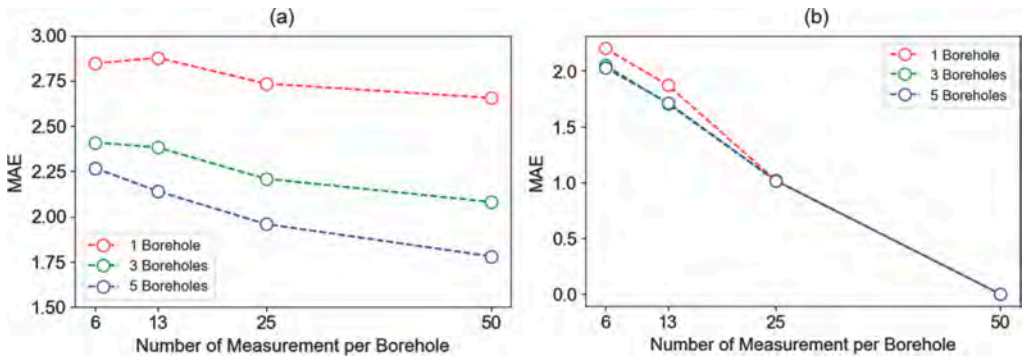


Figure 2. MAE of (a) 2D profile and (b) borehole ($X = 50$) under different number of measurements.

Figure 2b, the increase in borehole number from 1 to 3 results in a decrease in MAE, especially when only sparse measurements (6 to 13 per borehole) are available. This improvement is attributed to WENN's effectiveness in capturing and interpreting spatial variability using surrounding borehole data.

The detailed illustrations of the 2D profiles and interpolation results at $X = 50$ using one and five boreholes are depicted in Figure 3. Generally, the details of the simulated profile improve as the SPT sampling interval becomes denser. The interpolation at $X = 50$ aligns well with the original trend of the true data and indicates a reasonable range of uncertainty (the grey area represents twice the standard deviation). However, a slight underestimation of uncertainty is observable around $Y = 9$ and $Y = 45$ in Figure 3b, which is caused by insufficient measurements. This limitation could be addressed by employing more surrounding boreholes, as validated in Figure 3h.

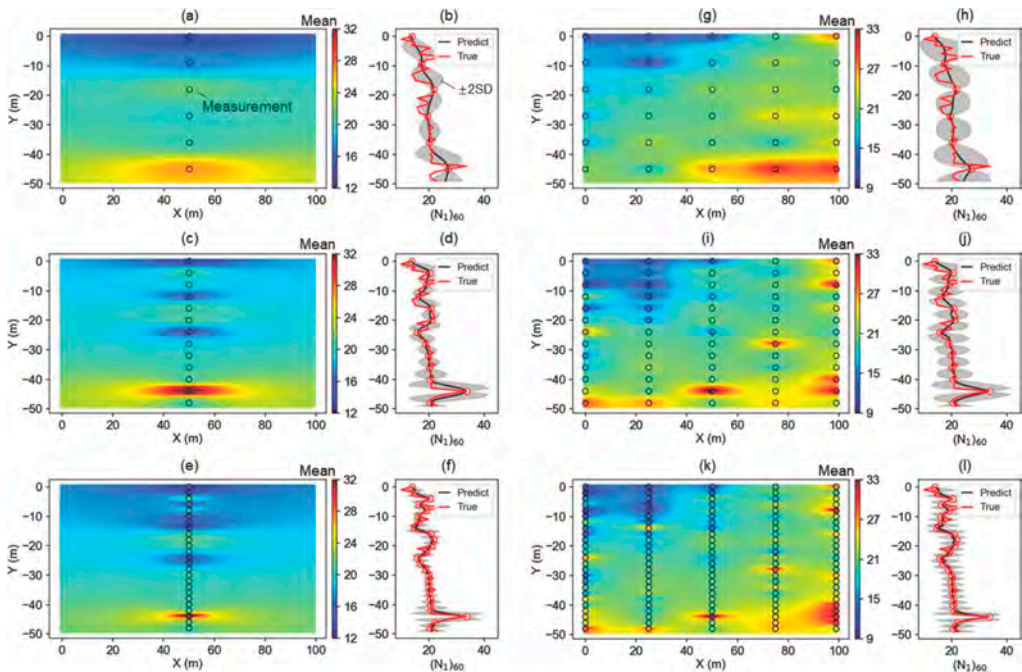


Figure 3. (a) (c) (e) 2D profile and (b) (d) (f) interpolation results at $X = 50$ using single borehole; (g) (i) (k) 2D profile and (h) (j) (l) interpolation results at $X = 50$ using five boreholes.

4 REAL SPT DATA EXAMPLE

4.1 Geological settings and simulated results

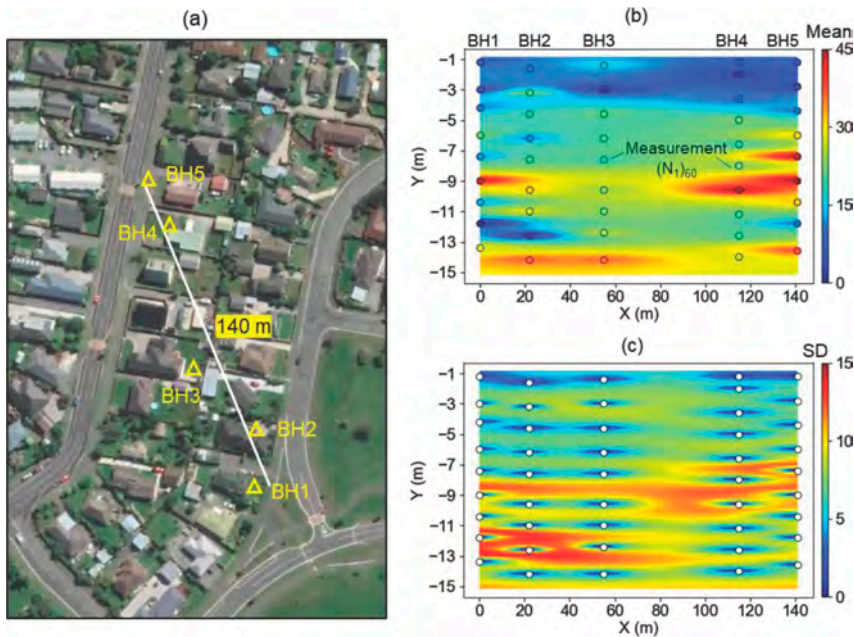


Figure 4. (a) Layout of borehole distribution (NZGD, 2023); profile of (b) interpolated mean and (c) standard deviation.

In this section, WENN is applied to a real-world example in Kaiapoi, New Zealand. The data can be found in New Zealand Geotechnical Database (NZGD). The 140m-long profile and the layout of five unequal-spaced boreholes are illustrated in Figure 4a. The SPT N-values recorded in borehole logging are calibrated to $(N_1)_{60}$ values according to the geotechnical information of the site. The measurements as well as the spatial interpolation results are illustrated in Figure 4b. The optimal parameter combination for R_x and R_y is determined as 90 m and 1.5 m, respectively. The dimensions of the profile are 140 m \times 15 m with a resolution of 1 m and 0.2 m for horizontal and vertical directions, respectively. The running time is 6.4s. As confirmed by records, the shallow area and depth around -12 exhibit low values which is attributed to the silty sand. The area with relatively large values indicates the presence of coarse gravel. Figure 4c displays the uncertainty distribution estimated by WENN. The uncertainty drops significantly around the measurements. The region with high uncertainty is predominantly observed at the interbed of low and large values, indicating potential interfaces between two strata. Overall, the results are deemed reasonable and interpretable.

4.2 Cross-validation

To validate the proposed WENN in a real-world scenario, leave-one-borehole-out cross-validation is performed. The measurements and predictions at corresponding locations are visually represented using black and red circles, respectively. The error bars, denoting uncertainty and indicated by twice the standard deviation, accompany the predictions. It is observed from Figure 5a-e that the predictions generally align with the measured values. Most of the measurements fall within the estimated error bars, indicating that the predicted uncertainty falls within a reasonable range.

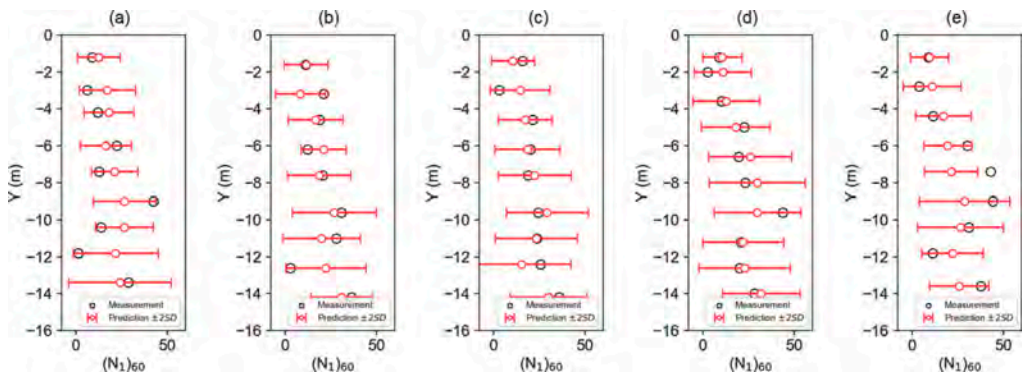


Figure 5. Results of cross-validation: (a) BH1; (b) BH2; (c) BH3; (d) BH4; (e) BH5.

However, certain critical points, particularly in the depth range of -10 to -12 m in BH1 and -7 to -10 m in BH5, exhibit considerable errors attributed to interlayers. These errors are caused by the presence of interlayers in neighboring boreholes and limited SPT data. Consequently, incorporating the stratigraphic information revealed in boreholes is one of the solutions to improve the performance further.

Additionally, OK and IDW were employed in this field example using the same cross-validation tests for comparative purposes. The average MAE is 7.8 and 9.5 for OK and IDW, respectively, while that for WENN is 7.4. Although the result of OK is similar to WENN, five points are lying outside the error bars, whereas WENN only has one. This indicates that WENN could estimate the uncertainty more accurately than OK in this example.

5 CONCLUSION

This study introduces a novel Weight Ellipse Nearest Neighbors (WENN) approach for interpolating the SPT values of a 2D profile with high efficiency. WENN could effectively estimate the spatial mean and standard deviation at the unsampled locations using sparse measurements in boreholes. WENN is applied to a non-stationary simulated profile and the results presented have demonstrated the effectiveness of the model. The effect of the number of measurements is discussed in detail through 1D and 2D illustrations. In addition, the study validates WENN using data from five boreholes in the NZGD database, assessing its capability to address real-world scenarios. Compared to the traditional methods, WENN outperforms OK and IDW in cross-validation in the field example. The modeling process for both simulated and field examples only takes less than 7s. The results reveal that WENN could efficiently capture the overall trend of the measurements with acceptable errors and reasonable uncertainty with sufficient interpretation. Regions with high uncertainty could be identified, attributed to large differences in adjacent measurements or the presence of interlayers. Lastly, the field example emphasizes the significance of incorporating stratigraphic information to enhance performance. To offer robust solutions, future investigations will focus on exploring the capability of WENN in stratigraphic uncertainty. The coupled probability analysis using both stratigraphic data and geotechnical properties for site characterization will be a pivotal aspect in advancing geotechnical engineering practices.

ACKNOWLEDGMENTS

The authors greatly acknowledge the financial support from Guangdong Provincial Department of Science and Technology (Grant No. 2022A0505030019 and 2019B111106001) and Science and Technology Development Fund, Macau SAR (File nos. 001/2024/SKL).

REFERENCES

- Ching, J., Huang, W. H. & Phoon, K. K. 2020. 3D Probabilistic Site Characterization by Sparse Bayesian Learning. *Journal of Engineering Mechanics*, 146.
- Gatz, D. F. & Smith, L. 1995. The Standard Error of a Weighted Mean Concentration—I. Bootstrapping vs Other Methods. *Atmospheric Environment*, 29, 1185–1193.
- He, S. Y., Kuok, S. C., Tang, C. & Zhou, W. H. 2024. Efficient Bayesian model updating for settlement prediction of the immersed tunnel of HZMB. *Transportation Geotechnics*, 44.
- Karkush, M., Ibrahim, M. O., Raheem, A. M., Naser, I. J., Omar, N. Q. & Najmadeen, K. T. 2023. Correlating Standard Penetration Test (SPT) with Various Soil Properties in Different Kirkuk City Locations: A Case Study Utilizing Inverse Distance Weighted (IDW) for Assessment and Prediction. *E3S Web of Conferences*, 427.
- Liu, H., Chen, S., Hou, M. & He, L. 2019. Improved inverse distance weighting method application considering spatial autocorrelation in 3D geological modeling. *Earth Science Informatics*, 13, 619–632.
- Liu, W. F. & Leung, Y. F. 2018. Characterising three-dimensional anisotropic spatial correlation of soil properties through in situ test results. *Géotechnique*, 68, 805–819.
- Lyu, B., Hu, Y. & Wang, Y. 2023. Data-driven development of three-dimensional subsurface models from sparse measurements using bayesian compressive sampling: a benchmarking study. *ASCE-ASME Journal of Risk and Uncertainty in Engineering Systems, Part A: Civil Engineering*, 9.
- Madansky, A. & Alexander, H. 2017. Weighted standard error and its impact on significance testing. In The Analytical Group, Inc. (ed.).
- NZGD. 2023. *New Zealand Geotechnical Database (NZGD)*. <https://www.nzgd.org.nz>.
- Phoon, K. K. & Kulhawy, F. H. 1999. Characterization of geotechnical variability. *Canadian Geotechnical Journal*, 36, 612–624.
- Samui, P. & Thallak, S. 2010. Site characterization model using artificial neural network and kriging. *International Journal of Geomechanics*, 10, 171–180.
- Shen, S. L. 2023. Research attitudes at a crossroads: advancing research on smart and sustainable cities. *Smart Construction and Sustainable Cities*, 1.
- Shuku, T. & Phoon, K. K. 2021. Three-dimensional Subsurface Modeling using Geotechnical Lasso. *Computers and Geotechnics*, 133.
- Takoutsing, B. & Heuvelink, G. B. M. 2022. Comparing the prediction performance, uncertainty quantification and extrapolation potential of regression kriging and random forest while accounting for soil measurement errors. *Geoderma*, 428.
- Wang, Y. & Zhao, T. 2017. Statistical interpretation of soil property profiles from sparse data using Bayesian compressive sampling. *Géotechnique*, 67, 523–536.
- Wei, X. & Wang, H. 2022. Stochastic stratigraphic modeling using Bayesian machine learning. *Engineering Geology*, 307.
- Xie, J., Huang, J., Zeng, C., Huang, S. & Burton, G. J. 2022. A generic framework for geotechnical subsurface modeling with machine learning. *Journal of Rock Mechanics and Geotechnical Engineering*, 14, 1366–1379.
- Yan, W., Shen, P., Zhou, W. H. & Ma, G. W. 2023a. A rigorous random field-based framework for 3D stratigraphic uncertainty modelling. *Engineering Geology*, 323, 107235.
- Yan, W., Zhou, W. H. & Shen, P. 2023b. An Uncertainty-driven Peak-integration (UP) Strategy for 3D Borehole Layout Planning. *Computers and Geotechnics*, 156.

Study on grouting rehabilitation of asymmetric transverse deformation in an existing shield tunnel

Z.W. Ye, D.M. Zhang, J.Z. Zhang & M.L. Zhou

Department of Geotechnical Engineering, Tongji University and Laboratory of Geotechnical and Underground Engineering of Ministry of Education, Shanghai, China

H. Shao & Q. Zhou

Shanghai Rail Transit Maintenance Support Co., Ltd. Engineering Affairs Branch, Shanghai, China

ABSTRACT: The control technology of double-fluid light-disturbance grouting on both sides of existing tunnels with large transverse deformation for rehabilitation has been widely used. Horizontal transverse convergence is commonly used in practice as a single index to measure the effect of grouting treatment, without considering the joint behavior. In this paper, numerical simulation is used to simulate the effect of grouting rehabilitation in two cases of the shield tunnels with symmetric and asymmetric deformation. In this paper, the development path and recovery path are used to characterize the variation of joint behavior with decreasing transverse convergence during the whole process of grouting. Studies have shown that the final rehabilitation of joints within the direct action of grouting is better. The grouting treatment of joints in tunnels with asymmetric deformations is weaker compared to those with symmetric deformations. During the grouting process on one side of the tunnel, the joints on the grouting side are subjected to greater disturbance, which requires strict control of the grouting parameters in practice.

1 INTRODUCTION

As the operational service life of existing metro lines increases, the structural problems of shield tunnels and their maintenance are receiving increasing attention. Complex surrounding construction activities cause the tunnel structure to be affected by various types of loading and unloading activities, including foundation pit engineering (Zhang et al. 2023), resulting in varying degrees of transverse deformation. As of 2007, 70%, 49.5%, and 37.5% of the lining of Shanghai's three metro lines exceeded the 0.5% D control standard (Shen et al. 2014). When the transverse deformation exceeds a certain degree, a series of structural diseases will develop on the shield tunnel structure, such as lining cracking, joint opening, water seepage, and leakage (Zhang et al. 2019b). If not treated in time, the structural diseases will further aggravate the overall deformation of the tunnel.

In recent years, the control technology of double-fluid light-disturbance grouting on both sides of existing tunnels with large deformation for rehabilitation has been widely used in practice (Zhang et al. 2019a). The grouting action on both sides of the tunnel creates lateral additional loads on the tunnel structure, causing the convergence deformation that occurs to be further controlled or even reduced (Fu et al. 2023). The tunnel undergoes asymmetric deformation under the disturbance of the surrounding environment in practice, which means that the joints behaviour at different locations are not consistent. The performance of segmental lining in transverse section largely depends on the joint performance (Arnau and Molins, 2011). For simplicity and convenience, horizontal transverse convergence is usually adopted as a single evaluation index of the grouting effect, and the rehabilitation of joint behavior within the tunnel under asymmetric deformation is not fully considered. However, the

excessive grouting-induced joint dislocation would deteriorate the working condition of the joint and consequently affect waterproof performance (Zhang et al. 2019a). It means that the convergence reduction alone is not enough to show that the grouting achieved good results.

Therefore, this paper establishes a finite difference model by FLAC 3D and simulates the effect of the light-disturbance grouting technology by applying expansion stress (Soga et al. 1999). The combined variation of transverse convergence and joint behavior in tunnels with symmetric and asymmetric deformation under grouting action is explored. Based on the simulation results, the development path and recovery path of tunnel deformation are proposed to evaluate the grouting effect.

2 FINITE DIFFERENCE ANALYSIS

2.1 Numerical modeling and Verification

A typical numerical grid mesh in FLAC 3D is illustrated in Figure 1. As shown in Figure 1, the interested soil domain is set as $9.68 D$ in width and $7.26 D$ in depth (i.e., D is the outer diameter of the tunnel) to avoid the boundary effects. A shield tunnel embedded into the mucky clay with its outer diameter $D = 6.2$ m, the width of a ring $b = 1.2$ m, lining thickness $t = 0.35$ m, and the cover depth $C = 16$ m is considered. The cover depth and size of the shield tunnel discussed here is the typical grouting case for the Shanghai metro shield tunnel (Huang et al. 2017a). The plane strain condition is assumed given in this paper. This paper focuses on the deformation behavior of the tunnel structure during the grouting process. Due to the short grouting time of a single lining ring in practice, the soil is considered in this model under undrained conditions, and the long-term behavior of additional stress dissipation after grouting is not considered.

The concrete segments are modeled by solid elements with the linear elastic model. For material parameters of the concrete lining, Young's modulus is 34.5 GPa, the unit weight is 25 kN/m^3 and the Poisson's ratio is 0.2 (Huang et al. 2017b). As shown in Figure 1b, a typical metro tunnel consists of 6 prefabricated segments, including one top block, one bottom block, two standard blocks, and two adjacent blocks. The joint between two adjacent segments is connected by two steel bolts, rubber mats, and a waterstop. Meanwhile, all the joints in the numerical model are numbered. To gain a balance between the computational time and simulation accuracy, the interface elements in FLAC 3D are employed to simulate the normal and tangential behavior of joints shown in Figure 1c. Figure 1c is a detailed interface mesh with seven rows of nodes to model the tunnel joint. Each row of interface nodes can be regarded as a surface spring assigned with a different normal stiffness k_n and shear stiffness k_s to represent different joint components (Zhang et al. 2019a). The input normal stiffness and shear stiffness of each row (From rows 1 to 7) are consistent with the model of previous literature (Zhang et al. 2021). The specifics of interface mesh will not be covered here. The soil in this model is modeled as an elastic-plastic medium (Mohr-Coulomb yield criterion), divided into six layers. With a typical grouting case, the soil parameters refer to the relevant literature (Huang et al. 2023) and the engineering case (Zhang et al. 2019a) are shown in Table 1.

In practice, the grouting, which is about 3m away from the tunnel, began at a depth equivalent to the bottom of the tunnel invert and gently lifted up by 5 m in total. After the slurry sets, each grouted soil (grouting body) is shaped like a column, with a diameter of 1.0 m and a length of 5 m. Therefore, the grouting body on both sides of the tunnel in the numerical model is covered by different colors in Figure 1a. In this paper, applying the isotropic and constant expansive stress on the meshes in the grouting body is used to simulate the grouting effect (Soga et al. 1999), and the volumetric strain increment is used to characterize the grouting volume. Although the expansion stress is not equal to the real grouting pressure, the previous study shows that both have the same variation trend (Zhang et al. 2022). Considering that not all slurry from ejection to solidification will produce expansion effect, the volumetric strain increment needs to be reduced based on the actual grouting volume. Figure 2 shows the flow chart of the grouting simulation. When the mesh of the grouting body begins to expand, the expansion effect will produce lateral loads on the tunnel model, thus reducing the transverse convergence of the tunnel.

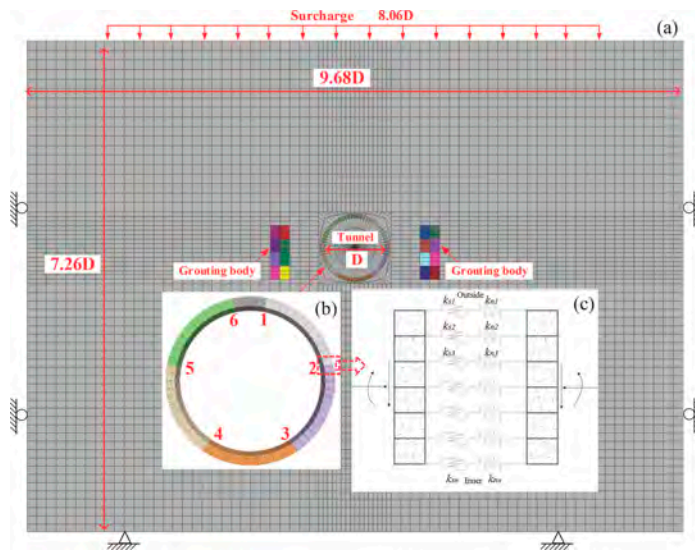


Figure 1. Finite difference model and boundary conditions: (a) Global model; (b) Number of lining blocks; (c) Joint simulation.

Table 1. Parameter of soil mechanics.

Soil	Thickness h (m)	Unit weight γ (kN/m ³)	Friction angle ψ (°)	Cohesion c (kPa)	Poisson's ratio ν	Compression modulus E_s (MPa)
① Fill	2.2	18.0	/	/	0.4	5.0
② Silty clay	1.7	18.5	25.0	10.0	0.35	4.3
③ ₁ Mucky Silty clay	9.6	17.6	20.0	10.0	0.4	3.3
④ Silty clay	9.1	16.7	27.0	3.0	0.4	2.3
⑤ ₁ Silty clay	6.0	17.3	26.7	16.0	0.3	2.9
⑤ ₁ Mixed silt and clay	16.4	17.9	25.0	17.0	0.3	4.4

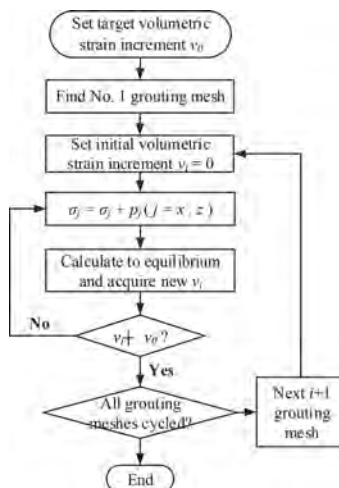


Figure 2. Flow chart of grouting simulation.

2.2 Calculation case setting

Figure 3 illustrates the basic process of grouting and the case setup of the numerical model. In practice, double rows of grouting are usually performed on both sides of a ring, such as R1 and R2 in Figure 3a. Meanwhile, it is usual for the outer rows (R1) to be grouted first, followed by the inner ones (R2). To balance the effect of grouting and the disturbance of the tunnel, grouting is not carried out on both sides of the tunnel at the same time.

To realize the lifting grouting process in practice and to simulate the grouting of the double rows in the determined sequence. The meshes of the grouting body (Figure 1a) are divided into 16 sections and numbered as shown in Figure 3b. Therefore, in this paper, the grouting is simulated according to the numbering of the grouted body from smallest to largest. To investigate the grouting effect under the asymmetric deformation of the shield tunnel, two calculation cases of grouting to rehabilitate the tunnel with symmetric and asymmetric deformation are selected for simulation and analysis in this paper. In this model, symmetric and asymmetric transverse deformations of the tunnel are induced by applying surface surcharge at different locations. The surcharge in Case 1 is located directly above the tunnel. On this basis, the surcharge in Case 1 is translated 10m to the right to get Case 2. The magnitude of the overload and its induced deformation of the tunnel is within the range of the previous literature (Zhang et al. 2021). Meanwhile, to make the effect of grouting more obvious, the volume expansion set in this paper is larger than that in the literature (Zhang et al. 2019b). This means that the disturbance of the tunnel during the entire grouting process is more significant.

The calculation process of the numerical model includes the equilibrium of the earth stresses, tunnel excavation, application of surcharge, and grouting. Huang et al. (2017a) statistics the transverse convergence of normal tunnels and tunnels that need to be rehabilitated for this typical grouting case (Zhang et al. 2019b). Before calculating Case 1 and Case 2 of this paper, the rationality of the model is verified by applying an extreme surcharge from the real case.

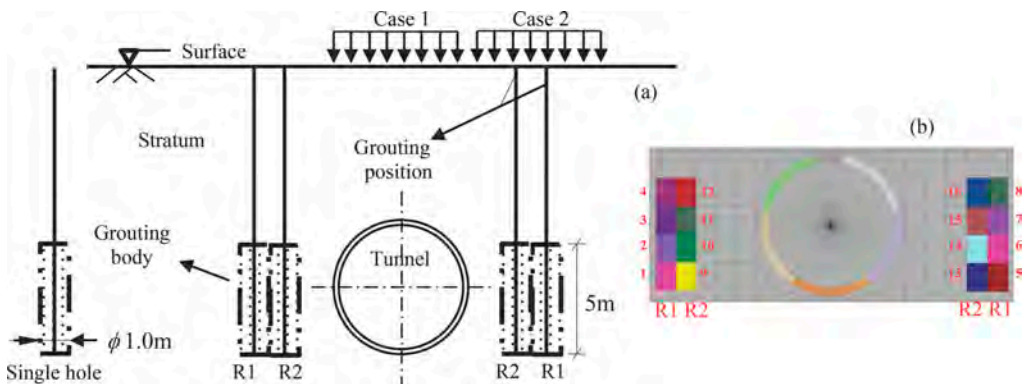


Figure 3. (a) Actual grouting engineering; (b) Case setup of the numerical model.

3 RESULTS AND DISCUSSIONS

As the grouting body is divided into 16 sections, the amount of transverse convergence, joint opening, and dislocation of the tunnel at this point is extracted as soon as grouting is completed in each section. In this way, the variations in the mechanical behavior of the tunnel structure during the entire grouting process can be obtained. To investigate the coupled variations of transverse convergence and joint behavior during the grouting process, the variation curves of joint behavior with the development of convergence are plotted for the whole process of the tunnel from surcharge to subsequent grouting. In addition, normalization is required due to the large difference in the quantities of horizontal convergence and joint deformation.

3.1 Grouting to rehabilitate the symmetric deformation

Figure 4 shows the coupled variations of transverse convergence and joint behavior during the surcharge and grouting process under symmetric deformation. Specifically, Figure 4a shows the variation relationship between the convergence and joint opening under external action. Figure 4b shows the variation relationship between the convergence and joint dislocation under external action. Figure 4c shows the symmetrical deformation of the tunnel before grouting (magnification factor of 30).

In Figure 4, the solid line represents the development curve of each joint with increasing convergence due to surcharge, while the dashed line represents the development curve of each joint with decreasing convergence due to grouting. Here, the solid line is referred to as the development path while the dashed line is referred to as the recovery path for subsequent comparative analysis. Simultaneously, the rehabilitation of the tunnel structure is more effective if the rehabilitation path is located below the development path.

From Figure 4a, 4b, when the tunnel gradually undergoes symmetric deformation, the development paths of the joints at the symmetrical location basically overlap. Joint opening and dislocation increase linearly with growing convergence.

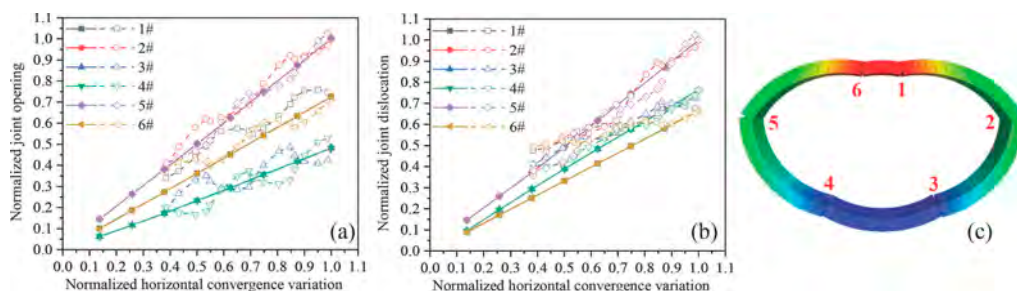


Figure 4. Coupled variations of transverse convergence and joint behavior during the surcharge and grouting process with symmetric deformation: (a) Joint opening; (b) Joint dislocation; (c) Symmetrical deformation of the tunnel before grouting.

To further analyze the grouting effect of each joint, Figure 4 is divided into Figure 5 and Figure 6, and the joints at each symmetrical position are put together for analysis. The right side of the red dotted line indicates the completion of the R1 part of the grouting, and the left side indicates the completion of the R2 part of the grouting.

As shown in Figure 5a and Figure 6a, the recovery paths of joints 1# and 6# are located above the development path, suggesting that their recovery is weak. In conjunction with Figure 3, joints 1# and 6# at the top of the tunnel are located outside the direct action of the grouting and are not directly affected by the action of the grouting relative to the other joints. The behavioral variations of the joints are mainly caused indirectly by the variations of the other segments.

Figure 5 and Figure 6 show that the recovery paths of joints 2# and 5# basically fluctuate and develop near the development paths, reflecting their better recovery effects. The degree of fluctuation in the joint opening recovery curves of joints 3# and 4# is significantly greater than that of joints 2# and 5#, while the recovery effect of their dislocations gradually becomes weaker as grouting proceeds. This suggests that light-disturbance grouting for rehabilitation of shield tunnels with symmetrical deformations has the best recovery results for joints 2# and 5#, where their locations are completely within the direct action of the grouting, and the worst recovery results for joints 1# and 6#.

Furthermore, in the process of single-hole grouting on one side, the recovery paths of symmetrically located joints within the direct-action range of grouting show a fluctuating trend with the development path as the symmetry axis. The joints located on this grouted side have a weaker recovery than the non-grouted side, as shown in Figure 5 and Figure 6.

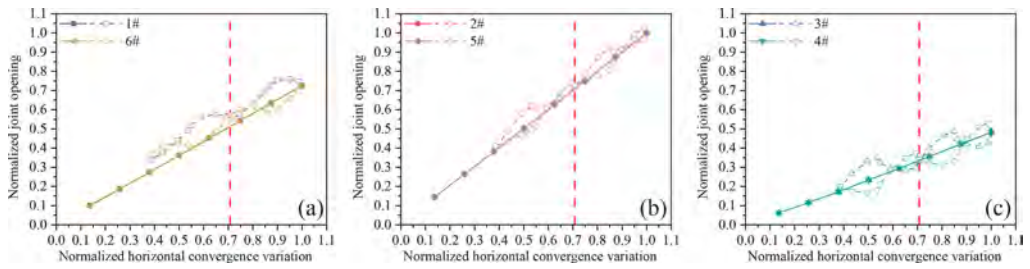


Figure 5. Development and recovery paths for the joint opening of each joint: (a) Joint 1# and 6#; (b) Joint 2# and 5#; (c) Joint 3# and 4#.

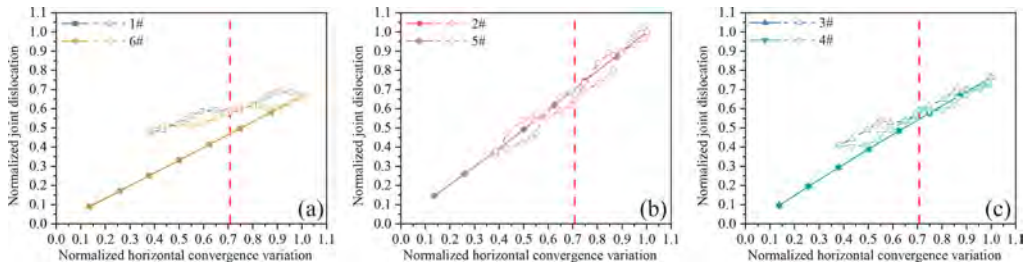


Figure 6. Development and recovery paths for the joint dislocation of each joint: (a) Joint 1# and 6#; (b) Joint 2# and 5#; (c) Joint 3# and 4#.

3.2 Grouting to rehabilitate the asymmetric deformation

Figure 7 shows the coupled variations of transverse convergence and joint behavior during the surcharge and grouting process under asymmetric deformation. Specifically, Figure 7a shows the variation relationship between the convergence and joint opening under external action. Figure 7b shows the relationship between the convergence and joint dislocation under external action. Figure 7c shows the asymmetrical deformation of the tunnel before grouting (magnification factor of 30).

From Figure 7a, 7b, when the tunnel gradually undergoes asymmetric deformation, the development path of each joint is different but it is also a straight line. To further analyze the grouting effect of each joint, Figure 7 is divided into Figure 8 and Figure 9, and the joints at each symmetrical position are put together for analysis.

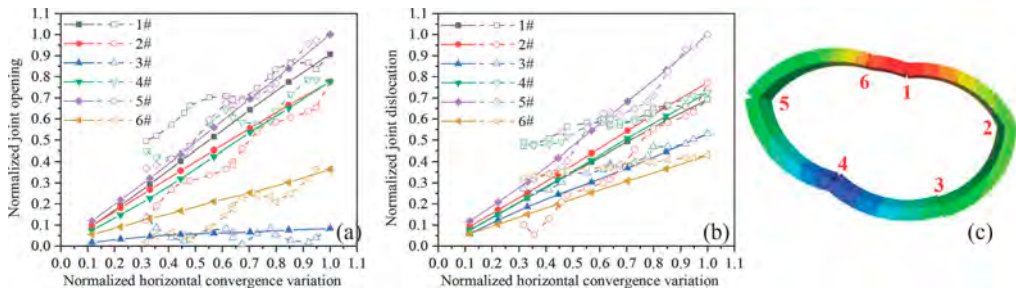


Figure 7. Coupled variations of transverse convergence and joint behavior during the surcharge and grouting process with asymmetric deformation: (a) Joint opening; (b) Joint dislocation; (c) Asymmetrical deformation of the tunnel before grouting.

As can be seen from Figure 8, the recovery paths of joints 6# and 2# are located below the development path. Meanwhile, the recovery path of joint 5# is basically coincident with the

development path, indicating that the grouting effect of these three joints is better and the rest of the joints are poorly recovered from the perspective of joint opening.

Figure 9 shows that the recovery path of joint 2# is located below the development path, and the recovery path of joint 5# basically fluctuates along the development path, which indicates that the grouting effect of the two joints is better. In contrast, the rest of the joints showed poor recovery effect of the dislocation. This indicates that for the tunnel with asymmetric deformation, the degree of joint dislocation has also increased compared to the original tunnel. For this type of asymmetric deformation occurring in the tunnels in this paper, the best recovery is achieved in joints 2# and 5# within the direct action of grouting, and the recovery of joint openings is better than that of dislocations.

Like the findings in Section 3.1, the recovery paths of symmetrically located joints within the direct action of grouting during single-hole grouting on one side of the tunnel show opposite fluctuating development trends, as shown in Figure 8b, 8c, and Figure 9b, 9c. This reflects a weaker grouting effect of the joints on that grouting side compared to the other side. In difference, the degree of joint opening and dislocation varies considerably among the joints of the tunnel with the asymmetrical deformation. The degree of fluctuation in the recovery paths of the joints with less deformation is smaller.

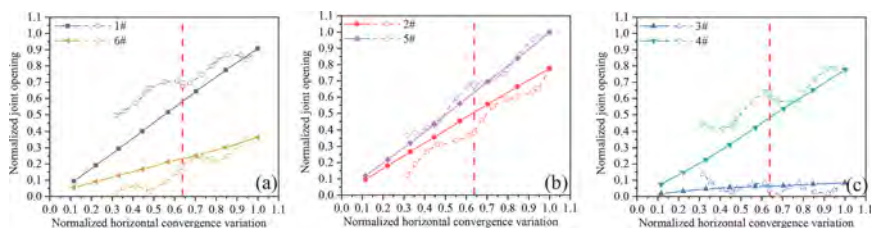


Figure 8. Development and recovery paths for the joint opening of each joint: (a) Joint 1# and 6#; (b) Joint 2# and 5#; (c) Joint 3# and 4#.

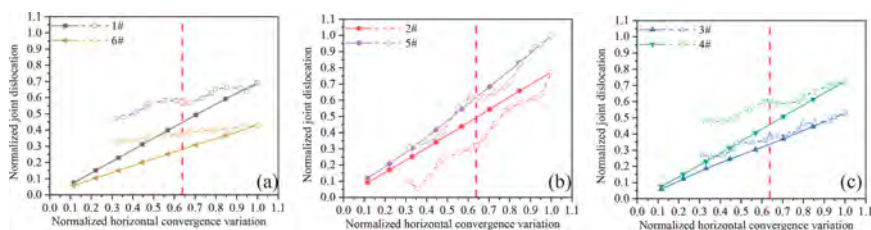


Figure 9. Development and recovery paths for the joint dislocation of each joint: (a) Joint 1# and 6#; (b) Joint 2# and 5#; (c) Joint 3# and 4#.

4 CONCLUSION

Based on a typical grouting case, this paper focuses on the analysis of the variation of transverse convergence and joint behavior in tunnels with symmetric and asymmetric deformation under grouting action. The following conclusions are obtained:

- (1) The use of the development path and recovery path can better describe the variation relationship between the mechanical behavior of joints and tunnel convergence during the whole process of grouting. The recovery paths above development paths indicate weaker grouting effects.
- (2) For tunnels with symmetrical and asymmetrical deformations in this paper, the joints within the direct action of grouting are better rehabilitated eventually (mainly the joints at the waist of the tunnel).

- (3) Compared to tunnels with symmetrical deformation, joint recovery is weaker in tunnels with asymmetrical deformation, and particularly poor in joint dislocation.
- (4) During single-side grouting, the recovery effect of joints on the grouted side is weaker than that on the non-grouted side. Therefore, it is necessary to strictly control the grouting parameters to reduce the structural disturbance of the tunnel.

This paper portrays the development path and recovery path of the tunnel to evaluate the grouting effect, which provides a new idea for the subsequent improvement of the evaluation system of grouting rehabilitation. In the numerical model, contact surfaces are used to model the joints, which are still somewhat different from the actual bolted joints. Meanwhile, the soil spatial variability is not considered. The computational time for a single case is about half an hour for this numerical model. If the uncertainty is to be considered subsequently, this computational time is unacceptable and the model needs to be optimized to improve computational efficiency.

ACKNOWLEDGMENTS

This work is substantially supported by the National Natural Science Foundation of China (No. 52022070 and 51978516), China National Postdoctoral Program for Innovative Talents (BX20220234), Shanghai Shentong Metro Group Co., Ltd. Research Program Project (JS-KY22R005-3) and Shanghai Municipal Science and Technology Innovation Action Plan Technical Standards Project (22DZ2206200). The financial support is gratefully acknowledged.

REFERENCES

- Arnau, O. & Molins, C. 2011. Experimental and analytical study of the structural response of segmental tunnel linings based on an in situ loading test. Part 2: Numerical simulation. *Tunn. Undergr. Space Technol.* 26, 778–788.
- Fu, Y., Wang, B., Wu, H., Chen, X., Sun, X., Bian, Y. & Shen, X. 2023. Theoretical analysis on horizontal rectification of tunnel near deep foundation pit by grouting. *Tunn. Undergr. Space Technol.* 133, 104977.
- Huang, H. W., Hua, Y. S., Zhang, D. M., Wang, L. J. & Yan, J. Y. 2023. Recovery of longitudinal deformational performance of shield tunnel lining by soil Grouting: A case study in Shanghai. *Tunn. Undergr. Space Technol.* 134, 104929.
- Huang, H.W., Shao, H., Zhang, D.M. & Wang, F. 2017a. Deformational responses of operated shield tunnel to extreme surcharge: a case study. *Struct. Infrastruct. Eng.* 13(3), 345–360.
- Huang, H. W., Xiao, L., Zhang, D. M. & Zhang, J. 2017b. Influence of spatial variability of soil Young's modulus on tunnel convergence in soft soils. *Eng. Geol.*, 228, 357–370.
- Shen, S. L., Wu, H. N., Cui, Y. J. & Yin, Z. Y. 2014. Long-term settlement behaviour of metro tunnels in the soft deposits of Shanghai. *Tunn. Undergr. Space Technol.* 40, 309–323.
- Soga, K., Bolton, M. & Au, S. 1999. Development of compensation grouting modelling and control system. *In Proc. Int. Symp. on Geotechnical Aspects of Underground Construction in Soft Ground*, (Tokyo) pp. 425–430.
- Zhang, D. M., Liu, Z. S., Wang, R. L. & Zhang, D. M. 2019a. Influence of grouting on rehabilitation of an over-deformed operating shield tunnel lining in soft clay. *Acta Geotech.* 14(4), 1227–1247.
- Zhang, D. M., Zhai, W. Z., Huang, H. W. & Chapman, D. 2019b. Robust retrofitting design for rehabilitation of segmental tunnel linings: Using the example of steel plates. *Tunn. Undergr. Space Technol.* 83, 231–242.
- Zhang, D. M., Ye, Z. W., Zhang, J. Z., Li, J. P. & Jia, J. W. 2022. Influence of grouting on rehabilitation of an over-deformed shield tunnel lining in spatially variable soil. *Comput. Geotech.* 152, 104999.
- Zhang, D. M., Zhang, D. M., Soga, K., Huang, H. W. & Wang, F. 2019c. Rehabilitation of overdeformed metro tunnel in Shanghai by multiple repair measures. *J. Geotech. Geoenviron. Eng.* 145(11), 04019101.
- Zhang, J.Z., Huang, H.W., Zhang, D.M. & Phoon, K.K., 2023. Experimental study of the coupling effect on segmental shield tunnel lining under surcharge loading and excavation unloading. *Tunn. Undergr. Space Technol.* 140, 105199.
- Zhang, J. Z., Huang, H. W., Zhang, D. M., Zhou, M. L., Tang, C. & Liu, D. J. 2021. Effect of ground surface surcharge on deformational performance of tunnel in spatially variable soil. *Comput. Geotech.* 136, 104229.

The relationship between the penetration depth and wavelength of the surface wave in two layers of soil

Z. Zhou & T.M.H. Lok

Department of Civil and Environmental Engineering, Faculty of Science and Technology, University of Macau, Macau, China

ABSTRACT: The surface wave method is a promising non-invasive test technique, which is cost-saving, convenient, and environmentally friendly. However, some fundamental issues still require further improvements. For the relationship between the penetration depth and wavelength of the surface wave, some researchers adopted an assumption that the penetration depth is within the range of 0.5 to 1.0 wavelength. In this study, to evaluate this assumption quantitatively, a numerical model for two layers of soil was established. A series of dispersion curves were obtained by varying the thickness of the upper layer. According to the results, when the ratio between the thickness with the wavelength equals a constant value, the dispersion phenomenon happens. The results of a parametric analysis on the minimum dispersive wavelength in different thicknesses show that this constant ratio is close to 1.67 which is much larger than the previous assumption. This result implies that the dispersion curve can be used to infer a deeper soil stiffness profile.

1 INTRODUCTION

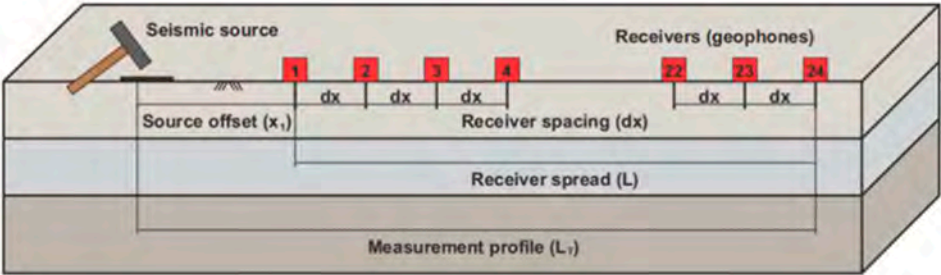
The surface wave methods are promising non-invasive test methods, which are cost-saving, convenient, and environmentally friendly (Olafsdottir et al., 2018). Because of the above advantages, the surface wave methods have a wide application in civil engineering (Olafsdottir et al., 2018 & 2020), geophysics (Ben-Zion et al., 2020), and earthquake engineering (Lin et al., 2021b). The surface wave methods mainly use the dispersive characters of surface waves in a layered medium, then from the dispersion curve to infer the soil stiffness profile (Lin et al., 2021c).

The most commonly employed surface wave method is the multichannel analysis of surface waves (MASW) (Park et al., 1998). It requires a series of geophones (usually 24) to capture the response of the ground from an impact loading, as shown in Figure 1. When MASW is carried out, three steps should be finished, including, field measurements, dispersion analysis, and inversion analysis (Olafsdottir et al., 2018). Inversion analysis is a challenging problem and has attracted a lot of researchers' attention in recent times. Plenty of inversion methods applied in surface wave inversion have been proposed, such as genetic-simulated annealing optimization (Lin et al., 2023), transitional Markov Chain Monte Carlo (Yang and Yuen, 2021), Monte Carlo search technique (Olafsdottir et al., 2020), and so on.

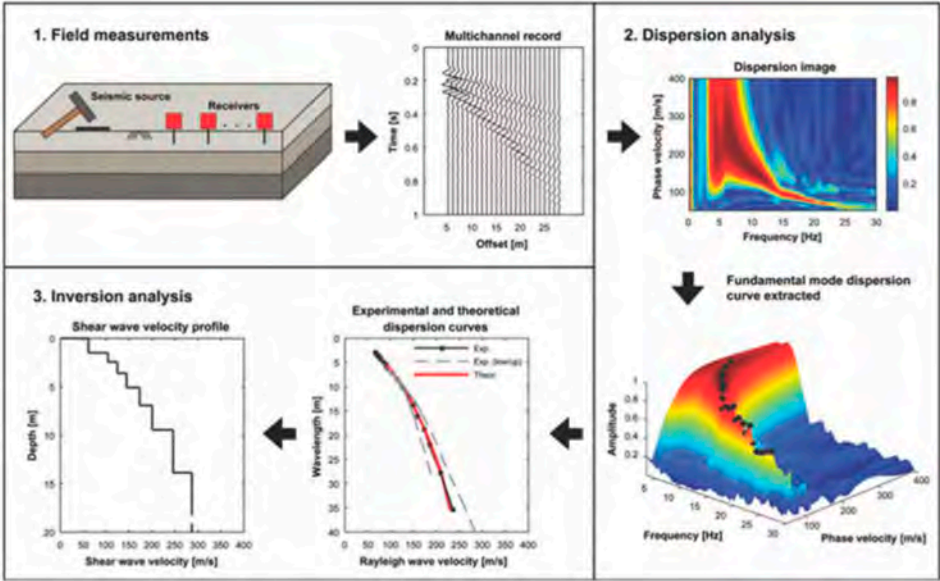
In the inversion analysis, some basic assumptions are adopted. Among them, a key assumption is that the penetration depth is within the range of 0.5 to 1.0 wavelength (Lin et al., 2021a, Olafsdottir et al., 2018). However, in some cases, the maximum wavelength is smaller than the interface depth, which means this extracted dispersion curve can not be used to infer the soil stiffness profile correctly. These situations lead to the limitation of some advanced methods, for example, artificial neural networks (Zhou and Lok, 2022), to be used to do inversion analysis.

In this study, to investigate the above assumption quantitatively, a numerical model for two layers of soil was established, in which the thickness of the lower layer of soil is infinite, and that

of the upper layer of soil is finite. In the analysis, keeping the other soil parameters unchanged and only changing the thickness of the upper layer, a series of dispersion curves can be obtained. According to the analysis results, when the thickness of the upper soil layer is much larger than the wavelength, the dispersive phenomenon would not happen. But when the ratio between the thickness with the wavelength equals a constant value, the dispersion phenomenon happens. With increasing thickness, the wavelength decreases correspondingly. The study was carried out by conducting a parametric analysis by varying the thickness of the soil layer and collecting the minimum dispersive wavelength. With the results, a more suitable ratio would be proposed.



(a)



(b)

Figure 1. (a) The setup of a MASM test (b) Three steps in a MASM test.

2 METHODOLOGY

For a layered medium, as shown in Figure 1(a), the dispersive phenomena will happen. If the properties of each layer are determined, the dispersion curve can be calculated by several theoretical methods, such as the transfer matrix method (Haskell, 1953, Thomson, 1950), global matrix method (Lowe, 1995, Nazarian, 1984), stiffness matrix method (Ganji et al., 1998, Gucunski and Woods, 1992, Kausel and Roësset, 1981), and so on. In general, the differences

between the dispersion curves from different methods are not significant. In this study, the stiffness matrix method is used, so this method is described here in detail (Olafsdottir et al., 2018, Lin, 2014).

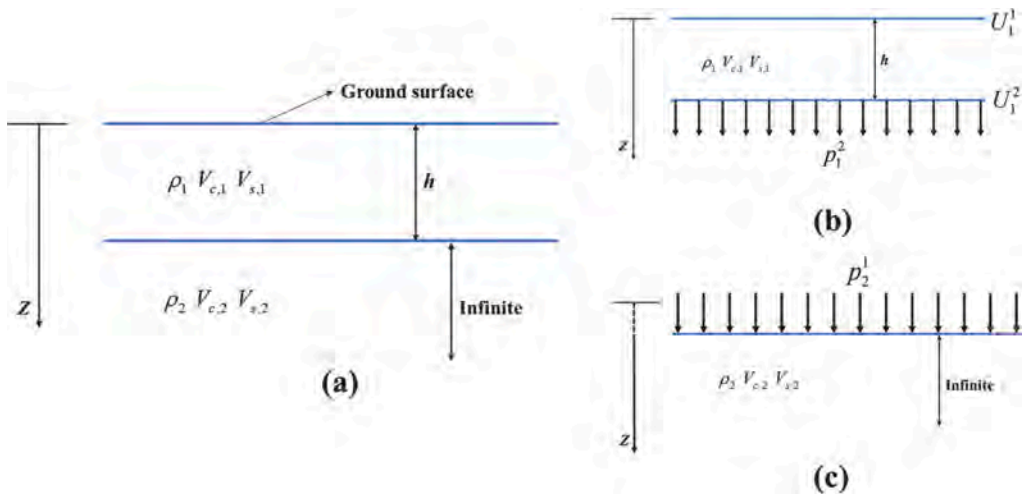


Figure 2. (a) Notation for a two-layered soil model. (b) Notation for layer 1 with external forces and displacements. (c) Notation for the last layer with external forces and displacements.

For a two-layered soil model shown in Figure 2(a), the external forces applied to the top and bottom surfaces of layer 1 are shown in Figure 2(b). Displacements will occur due to the external forces and the corresponding relationship between the displacements and the external forces can be described by the following equation.

$$\begin{pmatrix} p_1^1 \\ p_1^2 \end{pmatrix} = \begin{pmatrix} 0 \\ p_1^2 \end{pmatrix} = \begin{bmatrix} K_{11}^1 & K_{12}^1 \\ K_{21}^1 & K_{22}^1 \end{bmatrix} \begin{pmatrix} U_1^1 \\ U_1^2 \end{pmatrix} = K_e^1 \begin{pmatrix} U_1^1 \\ U_1^2 \end{pmatrix} \quad (1)$$

Where K , p and U represent the stiffness matrix, external load vector, and vertical displacement vector, respectively.

Because the second layer is infinite, as shown in Figure 2(c), the corresponding relationship between the external force and displacement can be depicted in the following equation.

$$p_2^1 = K^2 U_2^1 \quad (2)$$

By considering the entire external force and ignoring the known displacement, $U_2^2=0$, for the last layer, the global stiffness matrix for the two-layered model can be assembled as the following equation.

$$P = KU \quad (3)$$

Where the K is the global stiffness matrix, and its definition is shown in the following equation.

$$K = \begin{bmatrix} K_{11}^1 & K_{12}^1 \\ K_{21}^1 & K_{22}^1 + K^2 \end{bmatrix} \quad (4)$$

For the plane surface wave propagation, without the external force, the non-trivial solution of displacement still exists, which means:

$$f(\omega, k_R) = |K| = 0 \quad (5)$$

Equation 5 describes the dispersive property in the wavenumber–velocity domain, which can be converted to the previously defined wavelength–velocity domain, of the surface wave in a layered continuum.

3 MODEL DETAILS AND ANALYSIS RESULTS

3.1 Model description

In the two-layered soil model, as shown in Figure 2 (a), there are three material properties for each layer, namely, density (ρ), shear wave velocity (V_s), and compressive wave velocity (V_c), so a total of six material properties for the two-layered model. In addition, there is another variable, namely, the thickness (h) of the top layer. By varying the thickness, the dispersive characteristic in the wavelength-phase velocity domain is investigated. The material properties of the model are shown in Table 1.

Table 1. The material properties in the two-layer soil model.

Layer number	Constant name	Value
First layer	ρ_1	18.5 (kg/m ³)
	$V_{s,1}$	100 (m/s)
	$V_{c,1}$	1440 (m/s)
Second layer	ρ_2	18.5 (kg/m ³)
	$V_{s,2}$	300 (m/s)
	$V_{c,2}$	1440 (m/s)

3.2 Analysis results

The dispersion curves for various thicknesses of the top layer, h equal to 80m, 60m, 50m, 40m, and 30m are plotted in Figure 3. For the case with $h=80m$, the dispersion curve is a vertical line and no dispersive phenomena occur. The reason is that although dispersion phenomena

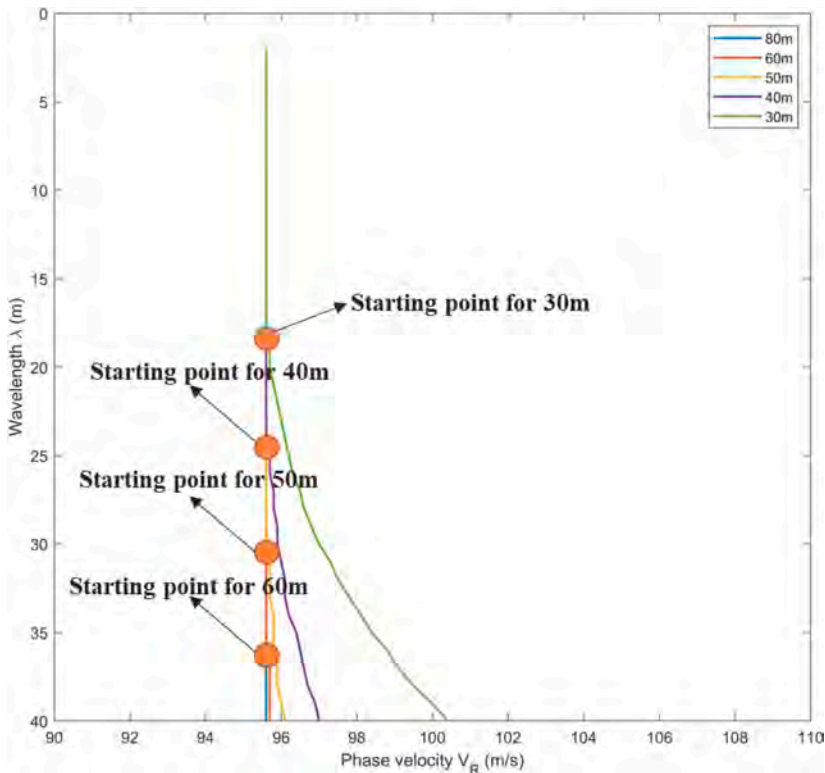


Figure 3. Dispersion curves for different thicknesses of the top layer (h).

occur in the two-layer soil model, they cannot be detected in the range with wavelength (λ) from 0 to 40m. With decreasing h , the dispersion phenomena occur gradually. For the case with $h=60, 40,$ and 30m , the dispersion phenomena appear at λ equal to about $36\text{m}, 24\text{m},$ and 18m , respectively.

By plotting the starting point in Figure 4, a straight line can be obtained, with a slope of about 1.67. These results imply that the ratio between the penetration depth and wavelength of the surface wave is a constant of about 1.67, which is different from that of previous assumptions that the penetration depth is within the range of 0.5 to 1.0 wavelength.

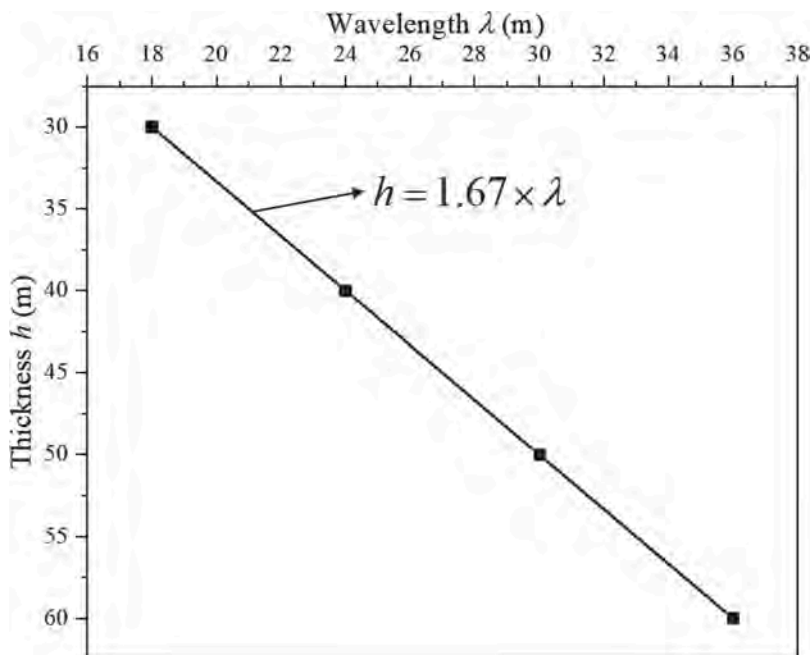


Figure 4. The scatterplot of the starting points of dispersive phenomena.

3.3 Discussion

For the surface wave propagating in a homogeneous medium, the penetration depth for a certain surface wave with a specific wavelength is shown in Figure 5. According to this figure, the normalized amplitude will first increase, then decrease. When approximately equal to twice the wavelength of the surface wave, the energy transferred by the surface wave is close to zero. This phenomenon also reveals that the penetration depth of surface waves is much greater than one wavelength. However, in the layered medium, the penetration depth of the surface wave will decrease, but the penetration depth is still larger than the common assumption that the penetration depth is within the range of 0.5 to 1.0 times wavelength.

4 CONCLUSION

In this article, to study the relationship between the penetration depth and wavelength of surface waves, a numerical model for two layers of soil is established. By changing the thickness

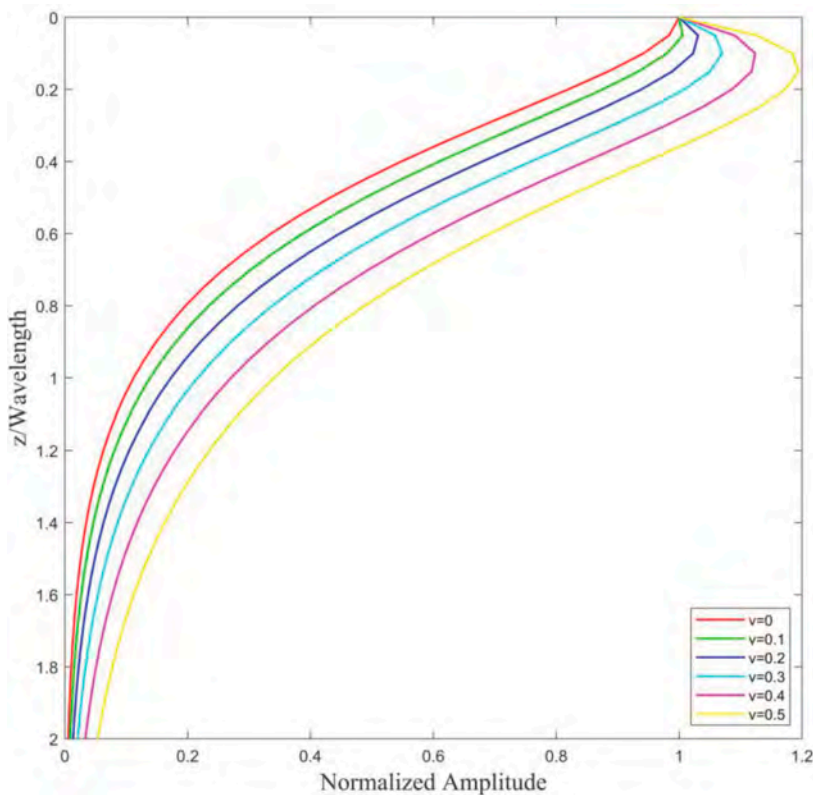


Figure 5. The penetration depth for a certain surface wave with a specific wavelength in the homogeneous medium with different Poisson ratios ν .

of the first layer, the relationship between the penetration depth and wavelength of the surface wave is obtained.

The common assumption was that the penetration depth was within the range of 0.5 to 1.0 wavelength. This study carried out a series of quantitative studies to prove that the penetration depth is much larger than the previous value and can approach a value of about 1.67. Compared with the penetration depth in the homogeneous medium, the penetration depth in the layered medium may decrease, but it is still larger than the previous assumption. This result implies that a smaller wavelength can be used to infer the deeper soil stiffness profile in inversion analysis.

REFERENCES

- Ben-Zion, Y., Zhang, H., Qiu, H. & Hu, J. 2020. Using Deep Learning to Derive Shear-Wave Velocity Models from Surface-Wave Dispersion Data. *Seismological Research Letters*, 91, 1738–1751.
- Ganji, V., Gucunski, N. & Nazarian, S. 1998. Automated inversion procedure for spectral analysis of surface waves. *Journal of geotechnical and geoenvironmental engineering*, 124, 757–770.
- Gucunski, N. & Woods, R. D. 1992. Numerical simulation of the SASW test. *Soil Dynamics and Earthquake Engineering*, 11, 213–227.
- Haskell, N. A. 1953. The dispersion of surface waves on multilayered media*. *Bulletin of the Seismological Society of America*, 43, 17–34.
- Kausel, E. & Roësset, J. M. 1981. Stiffness matrices for layered soils. *Bulletin of the seismological Society of America*, 71, 1743–1761.

- Lin, S. 2014. *Advancements in active surface wave methods: modeling, testing, and inversion*. Ph.D, Iowa State University.
- Lin, S., Ashlock, J. & Li, B. O. 2021a. Direct estimation of shear-wave velocity profiles from surface wave investigation of geotechnical sites. *Géotechnique*, 1–9.
- Lin, S., Ashlock, J. C., Zhao, G., Lai, Q., Xu, L. & Zhai, C. 2023. Genetic-simulated annealing optimization for surface wave inversion of shear-wave velocity profiles of geotechnical sites. *Computers and Geotechnics*, 160.
- Lin, S., Gucunski, N., Shams, S. & Wang, Y. 2021b. Seismic Site Classification from Surface Wave Data to $V_{s,30}$ without Inversion. *Journal of Geotechnical and Geoenvironmental Engineering*, 147, 04021029.
- Lin, S., Yi, T. H., Ashlock, J. & Gucunski, N. 2021c. Forward modeling of Rayleigh surface waves for analytical characterization of dominant dispersion trends. *Earthquake Engineering & Structural Dynamics*, 51, 240–255.
- Lowe, M. J. S. 1995. Matrix techniques for modeling ultrasonic waves in multilayered media. *IEEE Transactions on Ultrasonics, Ferroelectrics, and Frequency Control*, 42, 525–542.
- Nazarian, S. 1984. *In situ determination of elastic moduli of soil deposits and pavement systems by spectral-analysis-of-surface-waves method*. The University of Texas at Austin.
- Olafsdottir, E. A., Erlingsson, S. & Bessason, B. 2018. Tool for analysis of multichannel analysis of surface waves (MASW) field data and evaluation of shear wave velocity profiles of soils. *Canadian Geotechnical Journal*, 55, 217–233.
- Olafsdottir, E. A., Erlingsson, S. & Bessason, B. 2020. Open-Source MASW Inversion Tool Aimed at Shear Wave Velocity Profiling for Soil Site Explorations. *Geosciences*, 10.
- Park, C. B., Miller, R. D. & Xia, J. 1998. Imaging dispersion curves of surface waves on multi-channel record. *SEG Technical Program Expanded Abstracts 1998*. Society of Exploration Geophysicists.
- Thomson, W. T. 1950. Transmission of Elastic Waves through a Stratified Solid Medium. *Journal of Applied Physics*, 21, 89–93.
- Yang, X.-H. & Yuen, K.-V. 2021. All-parameters Rayleigh wave inversion. *Earthquake Engineering and Engineering Vibration*, 20, 517–534.
- Zhou, Z. & Lok, T. M. H. 2022. Neural Network Modeling of Shear Wave Velocity of Macau Soils Using SPT and CPT Data. *In: Huynh, D. V. K., Tang, A. M., Doan, D. H. & Watson, P., eds. Proceedings of the 2nd Vietnam Symposium on Advances in Offshore Engineering, 2022//2022 Singapore*. Springer Singapore, 164–171.



Taylor & Francis

Taylor & Francis Group

<http://taylorandfrancis.com>

Sustainability and resilience of underground infrastructure



Taylor & Francis

Taylor & Francis Group

<http://taylorandfrancis.com>

General Report – sustainability and resilience of underground infrastructure

A. Franza

Department of Civil and Architectural Engineering, Aarhus University, Aarhus, Denmark

ABSTRACT: This General Report highlights key aspects of the papers included in the session on ‘Sustainability and resilience of underground infrastructure’. A variety of topics can be found in this session (e.g., excavations and geothermal systems), with contributions focusing on the design and construction aspects of deep excavations and tunnels. This indicates that civil engineers face the challenge of reducing over-engineering of underground infrastructure.

1 INTRODUCTION

There are a total of nine papers in this session with Authors from four countries (China, Norway, Singapore, and the USA), with the majority submitted by Authors with a Chinese affiliation. Most manuscripts are the outcome of academic research, although there are also submissions from both practitioners as well as collaborations between academia and industry.

This session gives the opportunity to identify current trends in the research that aim to impact the sustainability and resilience of underground space and infrastructure. Most contributions address challenges for tunnels and excavation projects using analytical methods, numerical modelling, and laboratory testing. A single contribution is within the area of geothermal energy. For the sake of facilitating an overview and the discussion of results, this General Report groups papers into three broad themes: *risk and resilience assessments; stability and deformations; energy geotechnics*. The following sections discuss these main themes.

2 RISK AND RESILIENCE ASSESSMENTS

Four papers address risk assessments during deep excavations and tunnel construction, while there is a contribution to the reliability estimates under seismic hazards.

The assessment of detrimental distortions induced by deep excavations in urban areas is deterministically carried out in routine design. To demonstrate the feasibility of probabilistic risk assessment at the district level, Zhao et al. present an extension of the REMEDY GIS RiskTool, a geoprocessing toolbox in the GIS software ArcGIS, for the probabilistic performance-based assessment (PPBA) of multiple buildings affected by deep excavations. The extended tool models excavation-soil-building interaction employing a two-stage approach (using greenfield movements and an equivalent beam on the half-space) with Monte Carlo simulation to quantify the probability of damage exceeding a target category of damage; in this way, it is possible to assess the impact of uncertainties in excavation-induced ground displacements and building parameters. Interestingly, this model implements semi-empirical expressions for a probabilistic estimate of excavation-induced movements and their effect on buildings; however, only short-term greenfield displacements were accounted for in this work. To showcase the potential of PPBA to improve engineering decision-making in complex urban deep excavations, PPBA’s

capabilities are demonstrated through a case study of a foundation excavation in Oslo, Norway. Results in Figure 1 illustrate how probabilistic assessment can complement conventional deterministic methods, to ensure conservative risk assessments while considering the practical implications of uncertainties. Future developments may include automating building detection procedures. Finally, Zhao et al. discuss the feasibility of multi-building PPBA analysis thanks to parallel and cloud computing of the Monte Carlo simulation.



Figure 1. Excavation-induced deformations: (left) deterministic and (middle) mean maximum principal strain; probability of maximum principal strain greater than 0.05% (Zhao et al.).

Chen et al. investigate, with a quantitative calculation model, the vulnerability of existing tunnels affected by under-crossing shield tunnel excavation. Also this study employs the two-stage interaction analysis method (combining half-space theory, simplified ground model, and equivalent beam), which enables the input of multiple shield construction parameters to compute resulting stress and settlements. A vulnerability analysis is carried out to evaluate the influence of construction parameters on the disturbance intensity (I) and the resistance ability (R). In particular, as the disturbance intensity and the resistance ability can be obtained as a product of individual element contributions, the interlink between the disturbance intensity I and resistance ability R is studied as a function of tunnelling parameters (thrust, friction, the rate of soil loss, and crossing angle), and relative stiffness (equivalent bending stiffness, buried depth of tunnel, soil stiffness). This could enable to identify the implications of design decisions on the vulnerability assessment.

Finally, Zhang et al. propose a resilience assessment framework to assess urban tunnels in the case of seismic disasters. In this context, the concept of resilience is illustrated in Figure 2 as a combination of the robustness and the rapid recovery capability of the infrastructure,

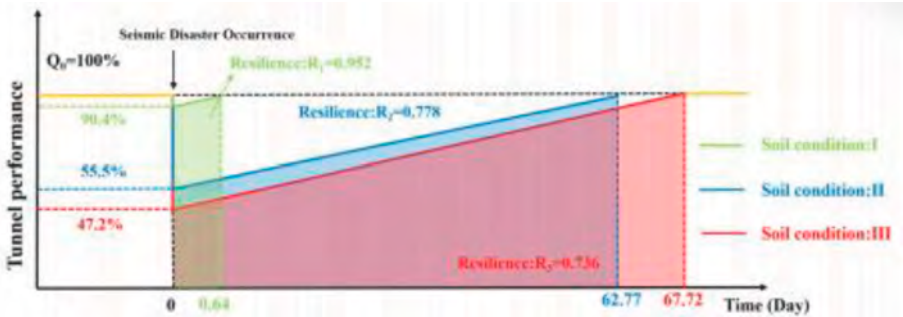


Figure 2. Results of resilience of tunnel under different soil condition (Zhang et al.).

which for a given tunnel typology is a function of ground conditions and hazard intensity, among other aspects. Using a finite element model to assess the tunnel ovalization, a vulnerability function is established describing the probability of damage category for a given seismic intensity. The proposed framework integrates vulnerability and recoverability indicators to provide a quantitative estimate of resilience. As resilience is affected by both the seismic intensity and soil conditions, design and construction of tunnels with a target resilience may combine adequate seismic resistance and recovery capabilities. The proposed framework is also illustrated through a case study.

3 STABILITY AND DEFORMATIONS

Five papers address issues related to ground deformations, soil strength, and stability under deep excavations and tunnelling scenarios.

Balamonica et al. present an innovative Post-tensioned Waler System (PWS) for braced excavations, shown in Figure 3. This system integrates prestressing elements into trussed walers, facilitating access to larger free work areas compared with traditional propping methods. The manuscript comprehensively addresses the load transfer mechanisms and modeling procedures specific to PWSs. Through a detailed soil-structure interaction analysis of a deep excavation, the paper illustrates potential cost savings of approximately 10 to 15% when implementing PWS, despite a slight increase in wall deflection and bending moments compared to the standard strut and waler system. Balamonica et al. emphasize PWS as a cost-effective alternative, highlighting reductions in steel quantities and the expedited bottom-up construction process. A future carbon footprint assessment could enhance the argument for adopting the PWS over conventional prop techniques.

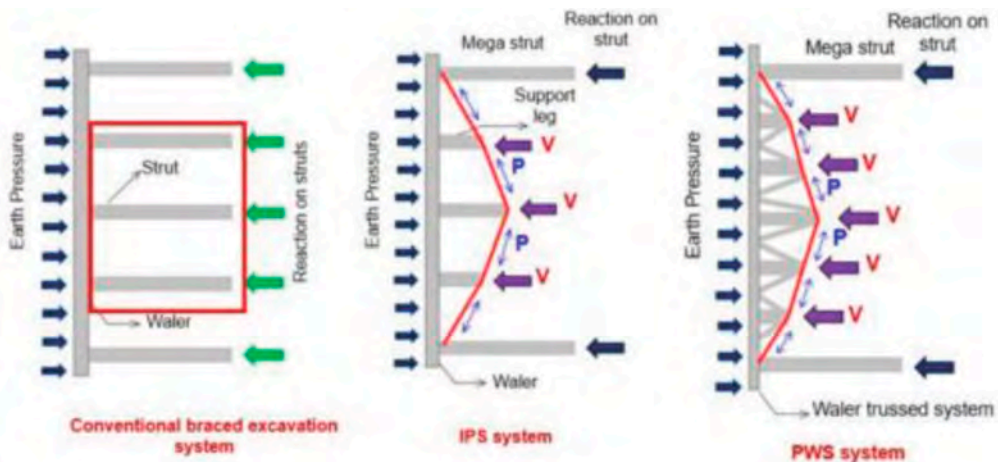


Figure 3. Braced, IPS and PWS excavation support systems (Balamonica et al.).

Pittaro & Mace investigate, through spatial variability analyses, the strength of Deep Cement Mixing (DCM) for the ground improvement of soft marine clay deposits. To quantify the vertical and horizontal spatial variability, this paper presents the scale of fluctuation SoF (in the vertical and horizontal directions) estimated from 5500 unconfined compressive tests carried out from over 700.000 m³ of a construction site in south-central part of Singapore. Figure 4 shows the analysis of the autocorrelation function that gave mean values for the vertical and horizontal SoF of 1.5 m and 10 m; these values differ in the horizontal direction from literature indications for deep cement mixing, confirming the dependence of the spatial variability on the type of soil and the construction techniques. Integrating SoF into design

methodologies may lead to more efficient parameter selections compared to current practices, with implications on optimal design. In particular, Pittaro & Mace discuss the benefit of relating the characteristic values of cement-treated ground to the ratio between the average dimension of the governing limit state and the scale of fluctuation (I/SoF) for more rational design: contrarily to current practice (that selects the characteristic parameter between the 0 and 20th fractile), lower I/SoF would result in a higher characteristic value up to 50th fractile (the mean value).

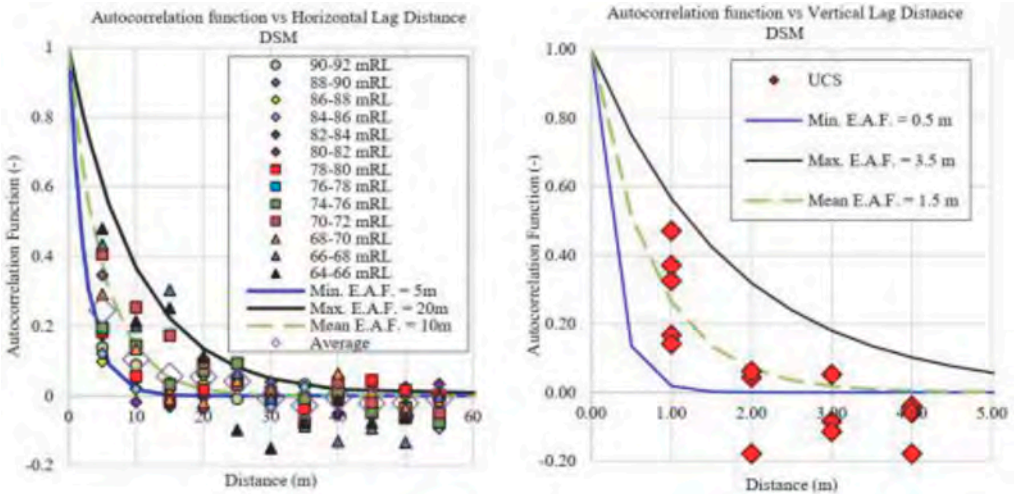


Figure 4. Estimated autocorrelation function vs distance obtained in (left) horizontal and (right) vertical direction (Pittaro & Mane).

Bentonite slurry is extensively adopted for temporary support and the transport of cuttings of soils and rock fragments. On site, fine-grained particles are difficult to eliminate from the slurry, with implications for excavations in soft soils. For this, Qin & Zhou characterised the rheological and hydraulic properties of bentonite-kaolin slurry at varying kaolin content with rheometer tests and modified fluid-loss tests. Figure 5 shows obtained rheological parameters. Measurements indicate that high content of non-swelling kaolin can increase the yield point,

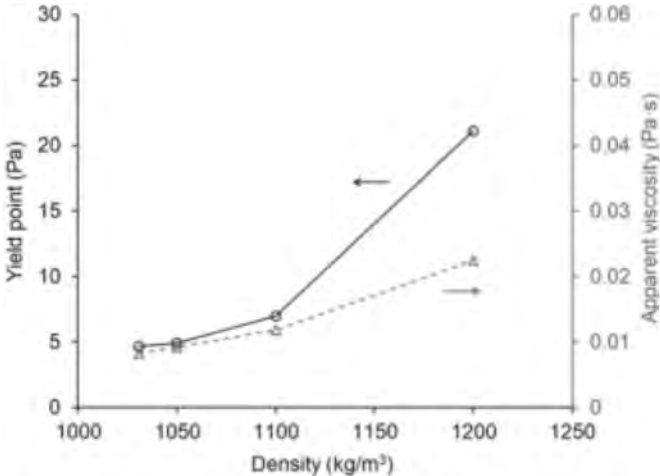


Figure 5. Rheological parameters of water-bentonite-kaolin slurries with varying densities (Cheng & Zhou).

viscosity, and thickness of filter cakes, with benefits on the slurry stabilising action and the filter cake resistance against cutting tools; on the other hand, low kaolin content had minimal influence on the rheological parameters. Therefore, this study provides valuable indications for slurry management and its treatment in the presence of fines.

An application of slurry to tunnel excavations is presented by Cheng & Zhou that propose an analytical method for the face stability analysis of slurry shield tunnelling. The upper bound solution accounts for the coupling of slurry infiltration and groundwater seepage in front of the slurry shield; namely, 2D translational multi-block is adopted for the failure mechanism, whereas the piezometric head field accounts for the effect of the slurry infiltration on pore water pressure (at depths comprised between tunnel crown and invert) through a rate of transfer α of the piezometric head of the slurry. The analytical study quantified for an example application how the safety factor slightly decreases as the transfer rate α increases.

Finally, dynamic element testing is reported in Wu et al. to study the cyclic deformations of soil under the influence of subway traffic. To investigate the influence of soil principal stress rotation (PSR) under subway loads, first linear elastic 3D finite element analysis was employed to compute realistic stress paths underneath the tunnel invert for a dynamic load. Subsequently, cyclic laboratory tests for such stress paths were carried out on sand using the hollow cylinder apparatus (at 1 Hz, up to 1000 cycles). At the element scale, the heart-shaped stress paths below the tunnel inverter resulted in increased vertical (axial) deformation for greater principal stress rotation, while the influence on the shear strains was limited. Also, the amplitude of the stress rotation affected both radial and vertical strains. Further experiments may evaluate soil behaviour at different locations relative to the tunnel, so that advanced constitutive models could be calibrated for study this problem.

4 ENERGY GEOTECHNICS

The session hosts a single contribution on storage and exchange of thermal energy in the ground. The numerical study of Lin et al. investigate the feasibility of a shallow-depth geothermal heat exchange system as a heating and cooling source for a building of the University of Illinois at Urbana-Champaign; this is framed within the University's plan towards an environmentally sustainable campus. To calibrate the model parameters, the thermal capacity and conductivity of the ground were estimated. The geothermal exchange system consists of forty boreholes, including a geothermal monitoring well (U-bend geothermal loop of high-density polyethylene pipe instrumented with a fibre-optic cable). The numerical model was first validated with field data. Next, parametric analyses for summer and winter scenarios indicated that the designed system can effectively store heat during summer for winter use and that the reduction in the flow rate in winter can result in higher temperature gains.

5 CONCLUSIONS

The papers in this session show the growing interest on analytics and modelling for risk and resilience assessments of underground infrastructure, which closely connect to the need to optimize the design and construction of excavations and tunnels. Concurrently, presented results confirmed the pivotal role that the laboratory experiments (of the ground or soil-structure interface) as well as innovative design have in the advancement of ground engineering for underground infrastructure. This suggests that civil engineers face the challenge of reducing over-engineering of underground infrastructure. However, considering the role that underground infrastructure can play in the green transition, future research could benefit from an integrated approach that combines mechanics for ground engineering, probabilistic methods, and embodied carbon analysis. This paper was possible thanks to the research of all Authors who participated in this session.

REFERENCES

- Balamonica, K., Jie, A. L. J., Wu, H., Zhengxia, C. & Won, O. K. Post-tensioned Waler System (PWS) as supporting structures for braced excavations. In *Geotechnical Aspects of Underground Construction in Soft Ground; Proc. intern. symp., Macao SAR, 14-17 June 2024*.
- Chen, Y. N., Zhang, D. M. & Huang, H. W. Quantitative vulnerability calculation for existing tunnel affected by under-crossing shield tunnel excavation. In *Geotechnical Aspects of Underground Construction in Soft Ground; Proc. intern. symp., Macao SAR, 14-17 June 2024*.
- Cheng, Y. & Zhou, W.-H. Stability assessment of slurry shield tunnel excavation zone. In *Geotechnical Aspects of Underground Construction in Soft Ground; Proc. intern. symp., Macao SAR, 14-17 June 2024*.
- Lin, J., Stark, T. D. & Stumpf, A. J. Flow rate study of geothermal heat exchanger system in north US. In *Geotechnical Aspects of Underground Construction in Soft Ground; Proc. intern. symp., Macao SAR, 14-17 June 2024*.
- Pittaro, G. A. & Mace, N. Spatial variability for deep cement mixing in kallang formation in singapore. Review of scale of fluctuation and its influence in design. In *Geotechnical Aspects of Underground Construction in Soft Ground; Proc. intern. symp., Macao SAR, 14-17 June 2024*.
- Qin, S. & Zhou, W.-H. Flow and filtration characteristics of bentonite slurry containing silt clay. In *Geotechnical Aspects of Underground Construction in Soft Ground; Proc. intern. symp., Macao SAR, 14-17 June 2024*.
- Wu, W., Yang, Y. & Wang, J. Deformation of surrounding soil mass of subway tunnel subjected to traffic loads considering principal stress rotation. In *Geotechnical Aspects of Underground Construction in Soft Ground; Proc. intern. symp., Macao SAR, 14-17 June 2024*.
- Zhang, C. L., Zhang, D. M. & Huang, Z. K. Structural resilience assessment method for tunnels under seismic hazards. In *Geotechnical Aspects of Underground Construction in Soft Ground; Proc. intern. symp., Macao SAR, 14-17 June 2024*.
- Zhao, J., Lysdahl, A. O. K., A nes, E. W., Piciullo, L., Ritter, S. & DeJong, M. J. An ArcGIS toolbox for the probabilistic performance-based assessment of surface building damage in large-scale urban excavations. In *Geotechnical Aspects of Underground Construction in Soft Ground; Proc. intern. symp., Macao SAR, 14-17 June 2024*.

Post-tensioned Waler System (PWS) as supporting structure for deep excavations

K. Balamonica, A.L.J. Jie & H. Wu
Singapore Institute of Technology, Singapore

C. Zhengxia
Woh Hup (private) limited, Singapore

O.K. Won
SENSG Pte. Ltd, Singapore

ABSTRACT: Deep excavations are often built utilising a conventional braced excavation system that includes steel struts, walers, king posts, and runner beams. When used for a project site with a significantly wide excavation, traditional braced excavation may not be economical and can create a limited working area that hinders the construction of permanent structures. In order to address this limitation, the present study introduces a novel Post-Tensioned Waler system (PWS) as an alternative to conventional strut and waler excavation systems. The proposed system improves the walers flexural stiffness by incorporating prestressing elements into trussed waler. This enables greater spacing between struts, a larger work area, and increased productivity. This study discusses the principles, load transfer mechanisms, and modelling procedures of the PWS system, and presents the advantages of using the PWS system over conventional strutting systems.

1 INTRODUCTION

The spatial constraints in Singapore have necessitated the building of underground and high-rise structures, many of which require the usage of Earth Retaining and Stabilising Structures (ERSS) to control ground movements and wall deflections during construction phase. The conventional ERSS system consists of several components, such as walers, struts, king posts, and runner beams. This ERSS system also referred to as the strut and waler system, is a robust and commonly used supporting system in Singapore. However, the placement of multiple struts intersecting with each other can create a cumbersome construction site and provide challenges during bottom-up construction, especially when dealing with wider excavations.

Kim et al. (2004) introduced the Innovative Prestressed Support System (IPS), with an aim to maximise the excavation space by reducing the number of struts in the site. The IPS system uses post-tensioning principles to enhance the flexural rigidity of the waler, which helps to increase the distance between the struts thereby reducing the number of struts required in an excavation. This innovation, not only expands construction space but also allows control over wall deflection through prestressed forces in the tendon (Kim et al. 2005). However, waler is the crucial member in this system and in situations where tendon failure occurs, the waler's flexural rigidity decreases, resulting in a possible instability of the system.

The present work proposes Post-Tensioned Waler System (PWS) as an alternative to traditional braced excavation and the IPS system, to further enhance the waler redundancy by using prestressing technology for earth-retaining structures. A double-waler structure with

a basic truss design and a prestressed element is used in the PWS, which is similar to Zeng's work (2016) used for a long-span structural system. The paper explains the fundamental principles and force transfer mechanisms of the PWS system, showcasing its suitability for modern construction projects. Furthermore, a case study comparing the effectiveness of the PWS to the conventional strut system is presented, highlighting scenarios where the PWS proves advantageous.

2 INNOVATIVE PRE-STRESSED SUPPORT SYSTEM

Innovative Prestressed System (IPS) as an alternative to strut and waler system (Figure 1) is proposed by Kim et al. 2005 by using prestressed tendons to apply an active force to the waler. This prestressed force distribution mechanism effectively resists the lateral earth pressure of the retained soil, offering distinct advantages over conventional methods. Notably, the IPS provides larger unsupported waler lengths, resulting in a reduction in steel cost and increase in the functional space (Feng et al. 2017; Kim et al. 2005; Park et al. 2009).

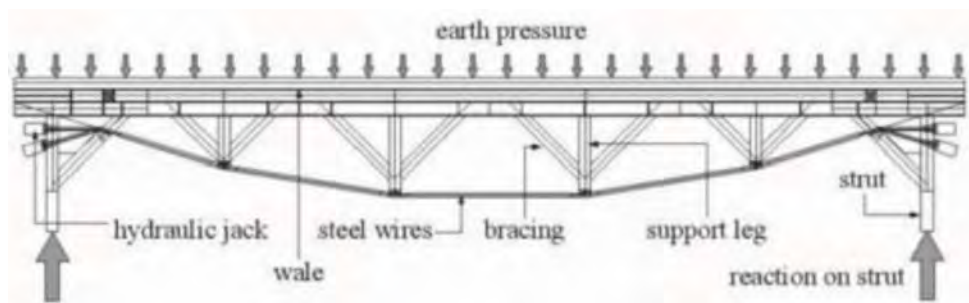


Figure 1. Typical IPS system in 3D view (Kim et al. 2005).

Though the IPS system seems advantageous over the braced excavation, the practical implementation of the system seems to have some drawbacks. Firstly, the absence of redundancy in the design of the IPS raises concerns, as failure in a steel tendon might potentially result in the instability of the excavation. Secondly, due to the nature of ERSS as a soil-structure interaction problem, there is currently a lack of developed approaches for incorporating IPS into geotechnical modelling tools. This limits the ability to accurately study the impact of IPS on retaining walls.

3 POST-TENSIONED WALER SYSTEM (PWS)

The Post-Tensioned Waler System (PWS) has been conceived as an innovative solution aimed at addressing the limitations inherent in the IPS system, while leveraging the distinctive advantage of incorporating a prestress tendon in the waler beams. The PWS also utilizes prestressed forces from the tendons to minimise wall deflection and increase flexural rigidity of the system. Moreover, the PWS further improves waler redundancy by introducing a double waler system with elements arranged in a truss configuration, as depicted in Figure 2.

A PWS system comprises two waler beams, with one serving as a straight beam running along the excavation's perimeter and the other adopting a curved profile positioned between the mega struts (struts are referred to as mega struts in the IPS/PWS system). The prestress tendon follows the curvature of the beam, as illustrated in Figure 2. Connecting the two walers are supporting legs and truss elements, collectively enhancing the flexural rigidity of the entire system.

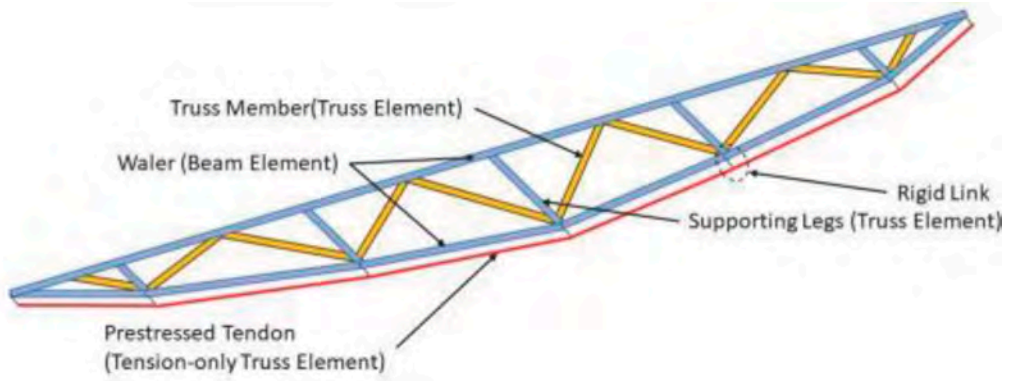


Figure 2. Typical PWS system in 3D view.

Several noteworthy advantages distinguish the PWS system. Firstly, similar to the IPS system, it facilitates increased spacing between the struts by enhancing the flexural rigidity of the waler beam. Secondly, the incorporation of an curved waler in the proposed configuration enhances the system's redundancy, ensuring that tendon failure does not cause an instability in the system. Furthermore, the integration of the prestress tendon allows for the regulation of wall deflections, with adjustments tailored to on-site measurements.

The PWS system also presents economic advantages, reducing the quantity of steel required in the Earth Retention Support System (ERSS) and thereby contributing to a more cost-effective excavation. Additionally, the increased space availability not only expedites the bottom-up construction process but also leads to reductions in project duration, further highlighting the benefits of the PWS system.

4 COMPARISON OF BRACED EXCAVATION, IPS AND PWS SYSTEM

4.1 Load transfer mechanism

Figure 3 shows a schematic layout comparing the load transfer mechanisms between the conventional braced excavation support system, IPS, and PWS. In braced excavations, the

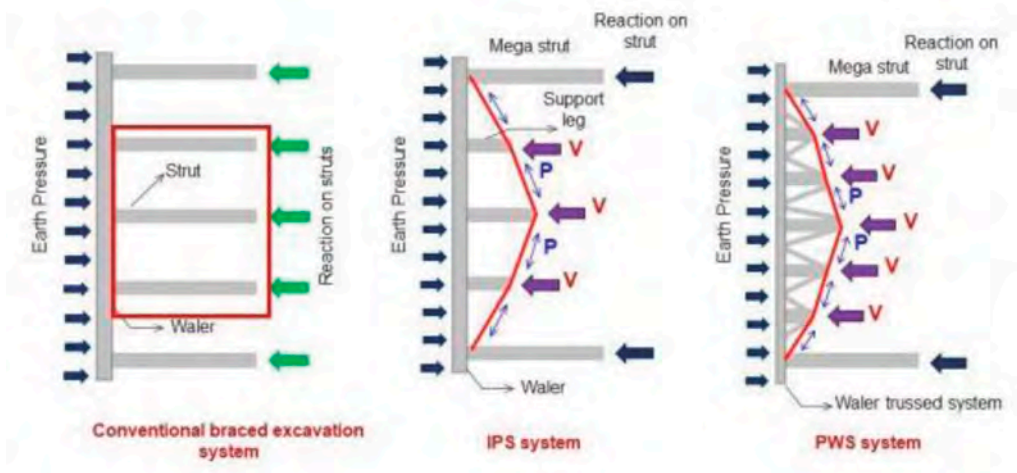


Figure 3. Load transfer mechanism in braced excavation support system, IPS system and PWS system.

arrangement involves struts spaced at regular 5 – 6 meter intervals in plan, with earth pressures evenly distributed across the waler beam spanning between these struts. Acting as primary compression support, the struts provides essential reaction force necessary for the waler beam in supporting the retaining wall.

In the IPS system, mega struts, covering a typical spacing of 20 to 50 meters (Park et al., 2009), provide the required reaction to the waler beam. As the struts are placed at 20-50 meters distance, the unsupported waler length increases which intensifies deflection at the beam centre. This increase in deflection is mitigated by increasing the flexural rigidity of the beam by a system of prestressed tendons running parallel to the waler beam and supported by the supporting legs (see Figure 3). The resultant prestressed force, coupled with cable tension arising from beam bending, transfers as point loads through the supporting legs which effectively counterbalances the lateral earth pressures.

The load transfer mechanism in the PWS system resembles that of the IPS (see Figure 3). The tendon’s prestress, resting on the curved waler, generates a uniform force as a reaction on the curved beam. This uniform force is then transmitted through the supporting legs and truss elements as a counteracting force to the applied earth pressure. The integration of a truss configuration into the IPS system introduces an additional layer of safety and stability, enhancing the overall load distribution and structural integrity of the PWS system.

4.2 Stiffness comparison

To compare the PWS and IPS systems, a 20-meter span of waler with five supporting legs is analysed (Figure 2). The structural components, including the beam and supporting legs, were assumed to be constructed from a UB 610x305x238 steel section of Grade S355. Both systems, modelled in a structural analysis software Staad Pro, incorporated a prestressed tendon with a diameter of 0.1 m. Notably, the PWS system featured a double waler with truss elements constructed from an H300x300x10 steel section of Grade S355.

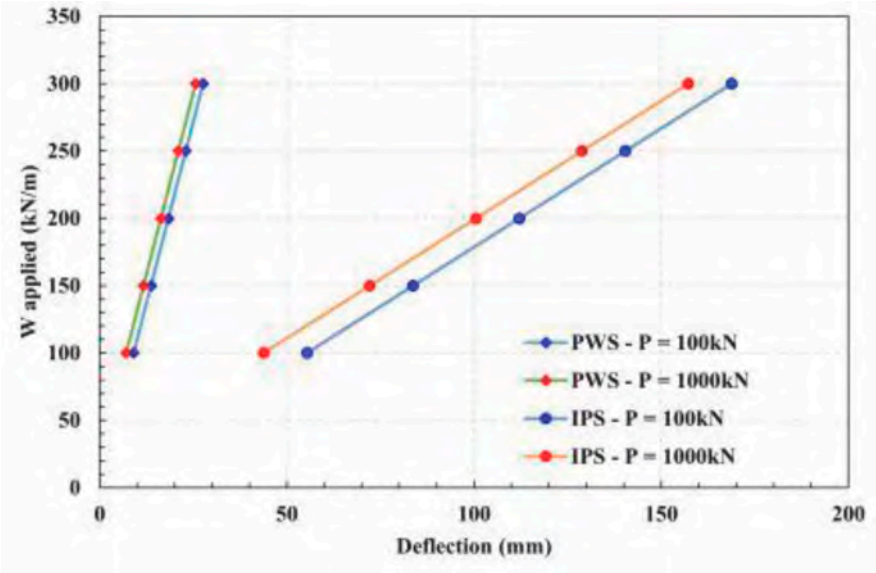


Figure 4. Comparison of load deflection behaviour for IPS and PWS system.

In the structural modelling, the waler is represented as a beam element, while the truss member and supporting legs are modelled as truss elements. The prestressed tendon, crucial to both systems, was simulated as a tension-only truss element. To properly capture the effect of

the tendon attached to the curved waler in the PWS system, rigid links were employed to connect the corresponding nodes between the tendons and the curved beams, as depicted in Figure 2. The waler beam was subjected to a uniformly distributed load of varying intensities, and maximum displacements at the beam's centre were recorded for analysis.

Figure 4 illustrates the relationship between the applied force and measured displacement for the PWS and IPS systems, considering two different tendon pretension levels. The system's apparent stiffness, indicative of its structural integrity, is derived from the gradient of the curves. The findings from Figure 4 reveal that the waler beam with the PWS system exhibits greater bending stiffness compared to an equivalent IPS system. Furthermore, the rigidity of the waler beam in both systems remains unaffected by the prestressing force applied to the tendon. External prestressing in tendons tends to reduce the overall displacement of the beam in both the PWS and IPS systems.

4.3 Steel tonnage comparison

In this study, a comparative analysis is conducted on the performance of the Post-Tensioned Waler System (PWS), braced excavation and the Innovative Prestressed System (IPS) in a deep excavation scenario. The ground condition is assumed to comprise of Bukit Timah Granite residual soils as illustrated in Figure 5. The excavation depth is 12.5 m, supported by a 0.8m diameter secant bored piles (SBP) wall and three levels of steel struts (see Figure 5). The geotechnical analysis follows Eurocode 7, considering DA1-C1 and DA1-C2 loading combinations and also one strut failure (OSF) scenario.

Geotechnical finite element (FE) analyses with soil model using the Mohr-Coulomb constitutive model was carried out to simulate the excavation analysis in stages. The strut loads at each level during various construction stages are compared, and critical loads for all relevant scenarios are summarized in Table 1. This load is used in the subsequent section, where comparisons are made between various system designed to withstand the identified critical loads.

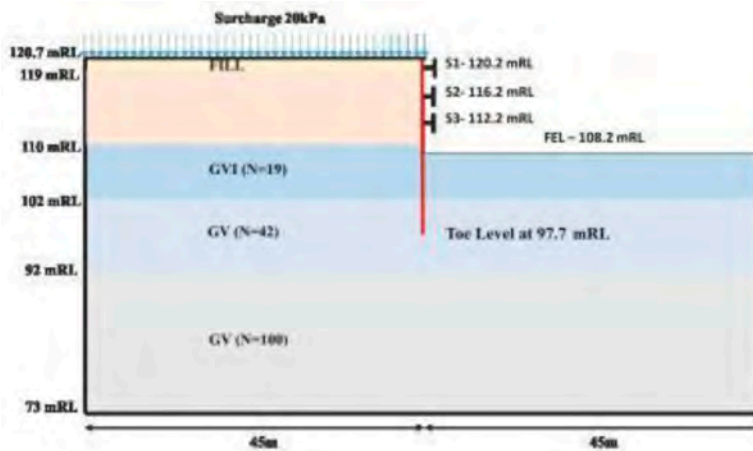


Figure 5. PLAXIS 2D model of the excavation.

For 90 m x 90 m excavation site, the ERSS systems is divided into sections of 25m, 40m, and 25m. Diagonal struts support the 25m sections near the corners, while the 40m span is supported by one of the conventional strut and waler system, Innovative Prestressed System (IPS), or the Post-Tensioned Waler System (PWS). This comparative evaluation aims to provide insights into the relative performance and suitability of these systems.

Table 1. Maximum strut loads for various limit states.

Design Approach	S1 kN/m	S2 kN/m	S3 kN/m
SLS	179	245	247
ULS-DA1C1	242	331	333
ULS-DA1C2	199	325	390
OSF	253	365	370

4.3.1 Braced excavation system

Figure 6 shows the design layout plan for the braced excavation system. The layout incorporates struts that span the excavation at intervals of 6 metres in both directions, accompanied by strategically positioned king posts along the braced excavations. The longest of the five corner struts is constructed as a laced strut in order to enhance the overall structural strength. The entire system, including struts, walers, king posts, and runner beams, is designed to align with the criteria of Eurocode 3 and 7, based on predicted strut loads. The whole configuration requires 1,903 tonnes of steel, accounting for all three layers of struts, king posts, walers, lacings, and cross beams.

4.3.2 IPS system

Figure 6 also depicts the configuration of the IPS system for the same location. Although the corner strut configuration remains identical, the IPS system replaces the traditional struts that extend across the whole width of the excavation. A 20-meter span of IPS system, consisting of five supporting legs with central supporting leg spanning 3m in length is used. The lengths of the remaining supporting legs are determined in a manner that ensures the cable profile maintains its parabolic shape.

Kim et al. (2004) suggests selecting a prestress force that matches the cable tension determined from a study of the IPS system without any prestress. However, for consistent comparison with the PWS system, the tendons in the IPS system are assumed to have a prestress of 2000 kN. The design is simulated and evaluated using a structural analysis software, where the walers are subjected to the earth pressure loadings determined in a geotechnical analysis. The structural elements are designed to withstand the highest shear force and bending moments experienced by the members. The prestressed tendons are built to accommodate the cable tension derived from the analysis, together with the applied prestress force.

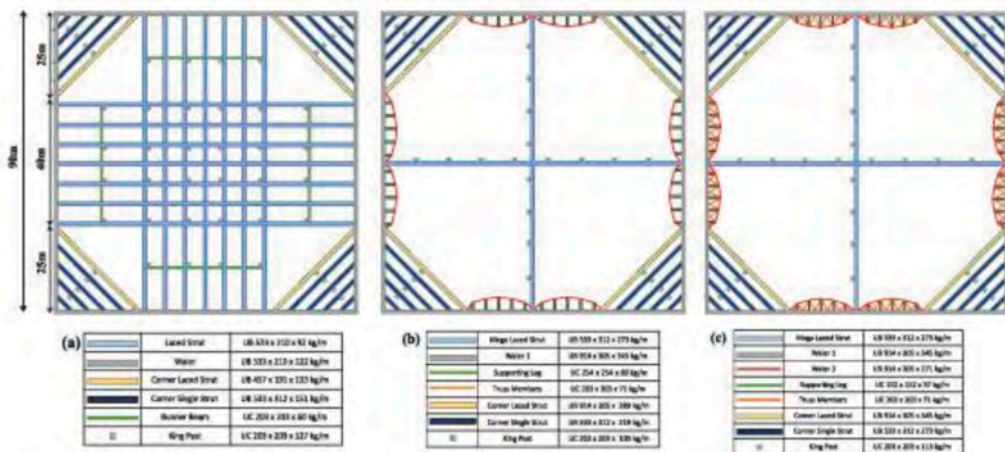


Figure 6. Layout of 90 mx 90 m site supported by (a) Conventional Strut and Waler (b) IPS system (c) PWS system.

When comparing the waler sections for the braced excavation and IPS system, it is observed that the IPS layout necessitates thicker waler sections because of the longer unsupported

length and greater moments in the waler beam. The layout involves the presence of two mega struts that span the breadth of the excavation. These struts are essential components that provide crucial support to the excavation. Due to the critical role of the mega struts in preventing the collapse of the excavation, they are intentionally designed to operate at only 60% of their maximum capacity. The total steel tonnage required for the IPS is 1550 tonnes, which is considerably lower than that of the braced excavation system, when accounting for all members across three levels of struts.

4.3.3 PWS system

The 20mPWS system comprises five supporting legs, with the middle leg measuring 3min length. This design closely resembles the IPS system and is intended for use at the same location (see Figure 6). In the PWS system, the five supporting legs are evenly distributed and their lengths are selected to maintain the parabolic form of the cable/curved waler. The PWS system, like the IPS system, is simulated using a structural analysis software and the members of the PWS system are designed to withstand the critical forces in accordance with Eurocode 7.

In the PWS system, the prestress cable rests on the curved beam in actuality and to reproduce this effect in the model, the curved beam and the tendon are defined independently, with a small gap between them. The connecting nodes are made as rigid links, allowing axial movement in the members. Utilising double-waler enhances the beam's resistance to bending and the flexural stiffness of the PWS systems is not exclusively reliant on the tendons. The prestressed tendons, supporting legs, and mega struts are designed to closely mimic the IPS system and the mega strut's capacity is restricted to 60% in this scenario also. The total amount of steel needed is determined to be 1657 tonnes.

The PWS technology offers a steel tonnage savings of approximately 10% compared to the braced excavation method. Although the weight of steel needed for the proposed PWS system is slightly greater than that of the IPS system, the PWS system is more durable and robust in comparison to the IPS system.

5 SOIL-STRUCTURE INTERACTION

Excavation analysis is a soil-structure interaction problem in which the forces acting on a structural element are determined by the earth pressure mobilised and the earth pressure mobilised, in turn, is influenced by the movement of the structural elements. This section outlines the modelling approach used to represent the recently developed PWS system in PLAXIS 3D. Three dimensional modelling is necessary because waler beams cannot be clearly modelled in two dimensional modelling.

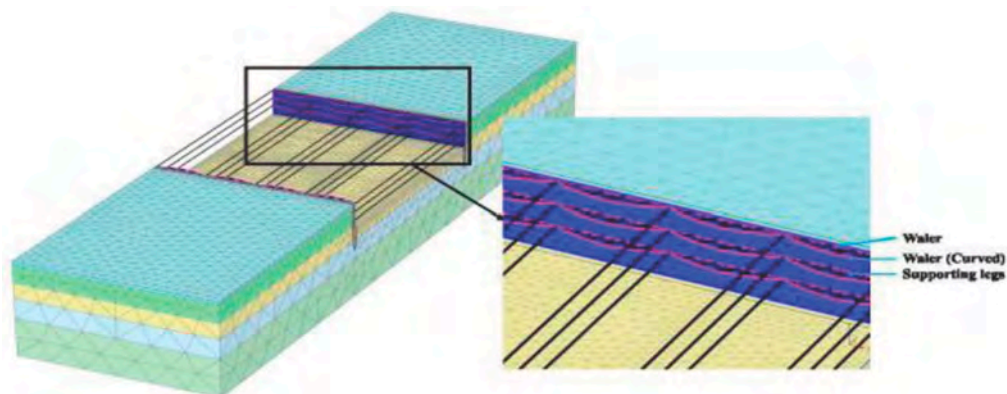


Figure 7. ERSS model with a PWS system.

The present analysis utilizes the 3D finite element programme PLAXIS. The soil layers, like the 2D analysis, are simulated using quadratic tetrahedral components and the Mohr-Coulomb constitutive relationships are used. The soil boundaries are modelled to be approximately 8 times the width of the excavation, which is 90m, in order to prevent any boundary impacts from affecting the predictions. The complete square-shaped arrangement measuring 90m x 90m is not represented in the model. Instead, four bays of PWS system is modelled as shown in the Figure 7 as the deflection and forces in the wall at the location of the PWS is of interest.

The comparison of results is limited to the middle two PWS systems in the model due to the anticipated presence of boundary effects in the PWS system at the edges. The walers, including both the straight and curved ones, are represented as beam elements in the model and the supporting legs, struts, and truss components are represented as node to node anchors. PLAXIS, unlike other structural analysis software, does not offer explicit choices for defining curved beams and cables as independent entities connected by rigid links. In order to overcome this challenge, the cable or prestress within the cable element of the PWS is not explicitly simulated. Instead, the predicted forces exerted by the cable prestress on the supporting legs and truss members are considered as prestress forces on the respective member that counteract the movement of the wall. In order to assess the effectiveness of the PWS system in comparison to the strut and waler excavation method, a separate excavation model with conventional strut and waler system is used.

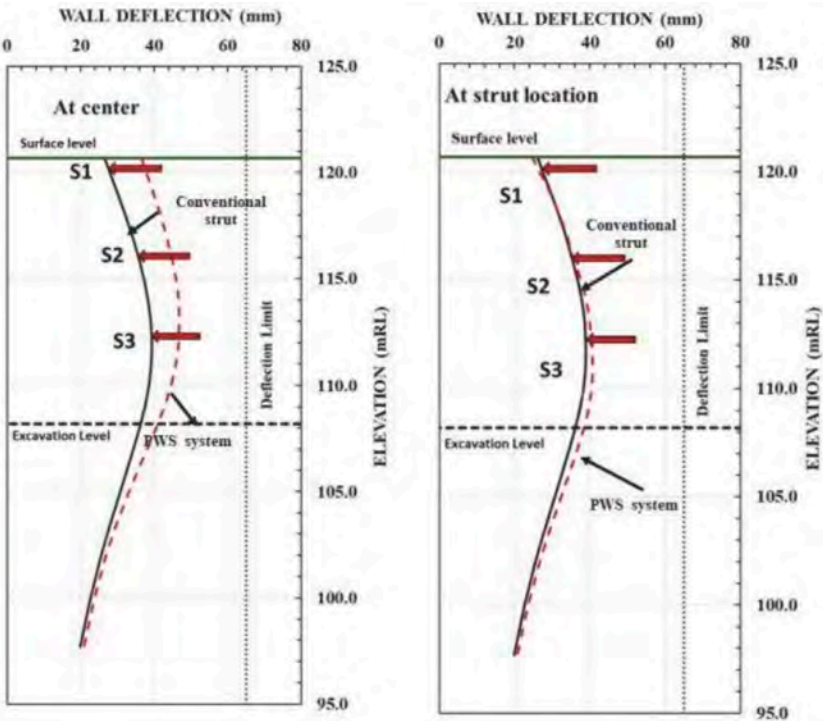


Figure 8. Wall deflection comparison between conventional strut and waler system and PWS system.

This model represents the strut and waler excavation by simulating the struts as node to node anchors and the waler as beam elements. Both the versions employing the strut and waler system, as well as the PWS system, apply a preload of around 100kN/m to the struts.

Deflection measurements are taken at two specific locations: at the point where the strut meets the wall, and at the midpoint of the unsupported waler that spans between two struts.

Figure 8 displays the displacement of the wall, as measured at the final excavation depth. The displacement of the wall at the strut location is similar between the PWS waler system and a traditional braced excavation.

At the centre of the waler the PWS system deflects around 47mm which is higher than the strut and waler system that deflects by 39mm. Although the deflection of the PWS is slightly more than that of the strut and waler system, it still falls within the acceptable limit set by LTA CDC, which is 0.5% of the excavation depth. Looking at the overall displacement (Figure 9), the wall with the strut and waler system undergoes similar displacement at the strut location as well as at the centre of the waler beam. Whereas, the wall with PWS system undergoes differential displacements with higher displacement at the waler centre.



Figure 9. Deflected shape of the retaining wall (a) Conventional strut and waler system (b) PWS system.

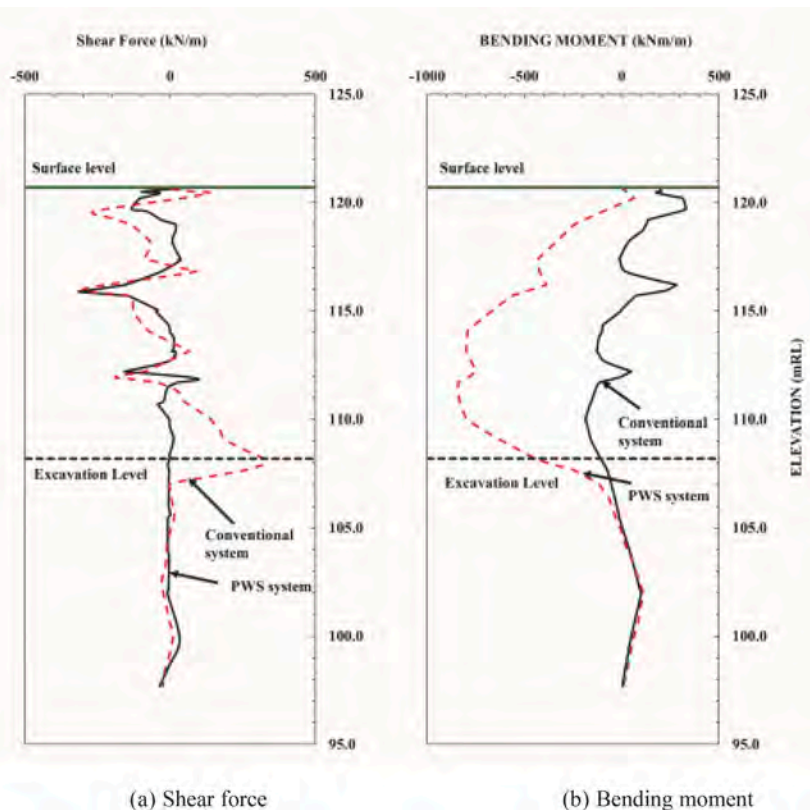


Figure 10. Shear force and bending moment comparison between conventional strut and waler system and PWS system.

A comparison of the shear force and bending moment between the PWS and the strut and waler system is depicted in Figure 10. The presence of the PWS leads to an increase in the bending moment and the shear force in the wall, which can be attributed to the longer unsupported length of the waler. An increase in unsupported length of the waler increases the strut loadings, which in turn will cause higher moments in the wall. Comparing the ground surface settlement as a result of excavation incorporating the PWS and conventional system, the former induces a maximum settlement of 35mm, higher than the latter.

whose settlement is 30mm (Figure 11). In general, the PWS system results in greater wall deflection, settlement, and bending moment compared to the standard strut and waler system. However, these values remain within the acceptable limits specified by the codal regulations.

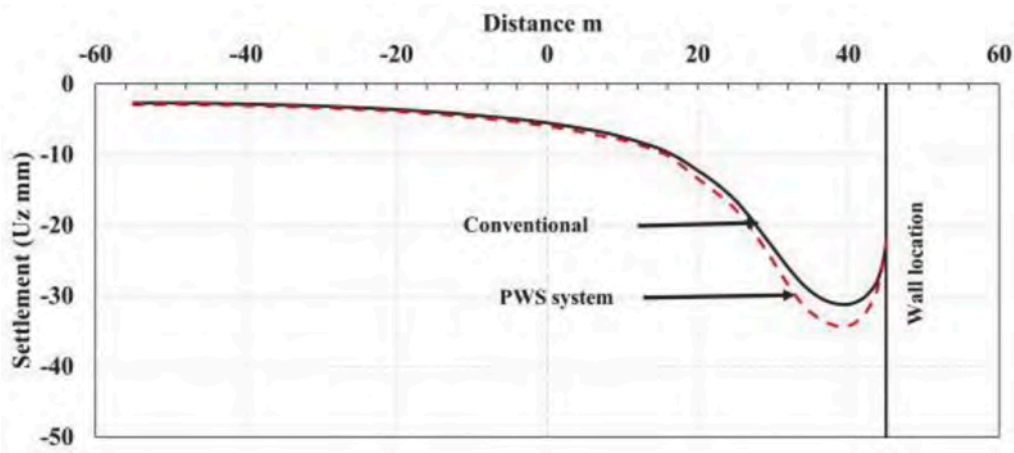


Figure 11. Settlement at the ground level behind the wall.

6 CONCLUSION

In conclusion, the Post-Tensioned Waler System is a viable alternative to conventional ERSS techniques, as it offers a cost-effective, and adaptable solution for earth retention in urban construction. Similar to the IPS system, prestressing technology significantly improves the bending rigidity of the PWS beam, thereby increasing the distance between the struts. In addition, the PWS system offers redundancy due to its double-waler design, which provides comparable steel tonnage reductions to that of the IPS system while eliminating the risk of instability induced due to tendon failure. In addition to reductions in steel tonnage, this expedites the bottom-up construction process, resulting in additional cost savings. Using the proposed PWS system, which is demonstrated through a case study, it is possible to obtain cost savings of approximately 10 to 15%. Soil-structure interaction study performed reveals that the PWS system produces larger deformation and bending moments compared to the conventional strut and waler system, but the obtained values are well within the threshold values given in the code provisions.

ACKNOWLEDGEMENT

This work is supported by Construction Technology Innovation Laboratory (CTIL) in SIT, Woh Hup Pte. Ltd., SEN SG Pte. Ltd, National Research Foundation, Singapore, and Building and Construction Authority (BCA) under its Built Environment Technology Alliance (BETA) Catalyst Funding Grant (Award No: BETA-20211111001).

DISCLAIMER

This research project is partly funded by National Research Foundation, Singapore and Building and Construction Authority (BCA) Singapore under its Built Environment Technology Alliance (BETA) Catalyst Funding Grant (Award No. BETA-20211111001). Any opinions, findings and conclusions or recommendations expressed in this material are those of the authors and do not reflect the views of the National Research Foundation, Singapore and the Building and Construction Authority (BCA) Singapore.

REFERENCES

- BCA (2009) Advisory Note on Earth Retaining or Stabilising Structures (ERSS).
- Brinkgreve, J., Shen, R.B.J. 2011. 'Structural Elements & Modelling Excavations in Plaxis', Delft, the Netherlands.
- BSI. BS EN 1997: Eurocode 7: Geotechnical design – Part 1: General rules, 2004a, BSI, London, UK
- BSI. BS EN 1990: Eurocode: Basis of structural design, 2002, BSI, London, UK.
- CIRIA C760 Guidance on Embedded Retaining Wall Design, 2017.
- Feng, T., Liu, L., Tong, T., and Zhou, M. 2017. 'Numerical Study on Lateral Wall Displacement of Deep Excavation Supported by IPS Earth Retention System'. *Underground Space (China)* 2 (4):259–71. doi: 10.1016/j.undsp.2017.09.001.
- Kim, N. K., Park, J.S., Jang, H.J., Kim, M.Y., Han, M.Y., and Kim, S.B. 2005. 'A New IPS Earth Retention System'. Pp. 1369–72 in *Proceedings of the 16th International Conference on Soil Mechanics and Geotechnical Engineering*.
- Kim, N.K., Park, J.S., Han, M.Y., Kim, M.Y., and Kim, S.B. 2004. 'Development of Innovative Prestressed Support Earth Retention System'. *Journal of the Korean Geotechnical Society* 20(2):107–13.
- Kim, S.B., Han, M.Y., Kim, M.Y., Kim, N.K., and Ji, T.S. 2005. 'Analysis and Design of Walerin Innovative Prestressed Support System (IPS)'. *Journal of Korean Society of Computational Structural Engineering* 18(1):79–91.
- NA to SS EN 1997-1: 2010 Geotechnical Design – General Rules.
- Park, J.S., Yong S.J., and Kim, N.K. 2009. 'New Earth Retention System with Prestressed Wales in an Urban Excavation'. *Journal of Geotechnical and Geoenvironmental Engineering* 135(11).
- Zeng, P. 2016. 'Influence of External Post-Tensioning on the Behaviour of Long-Span Steel Mega Trusses'. Nanyang Technological University, Singapore.

Quantitative vulnerability calculation for existing tunnel affected by under-crossing shield tunnel excavation

Y.N. Chen, D.M. Zhang & H.W. Huang

Laboratory of Geotechnical and Underground Engineering of Ministry of Education and Department of Geotechnical Engineering, Tongji University, Shanghai, China

ABSTRACT: Within the civil engineering profession, vulnerability is a fundamental component in the evaluation of risk, and is often used to assess the level of potential damage or degree of loss of structures when they are affected by disasters. Based on the two-stage method, this paper uses mindlin solution, Pasternak foundation model and Timoshenko beam theory to obtain the mechanical and displacement responses of the existing tunnels above the shield tunnel. Then, the parameter values of the standard condition are specified, and the influence of the parameter on excavation disturbance intensity and structural resistance ability in shield under-crossing existing tunnels is analyzed. Finally, based on the quantitative vulnerability calculation model, considering the disturbance intensity (I) of shield tunneling and the resistance ability (R) of the existing tunnel, the vulnerability evaluation model of the existing tunnel under the influence of the under-crossing shield tunnel is established.

1 INTRODUCTION

In recent years, the density of subway lines has been increasing, and the underground space network has gradually formed, which brings some challenges to the construction of new shield tunnels. The new shield tunnels inevitably cross existing tunnels, which will cause the longitudinal non-uniform settlement of existing tunnels, and even cause the serious deformation and structure destruction. Hence, engineers are paying attention to risk evaluation and protection of existing structures in crossing engineering.

Vulnerability is a fundamental component in the evaluation of risk (Einstein 1988; Leone et al. 1996), it is defined as the level of potential damage or degree of loss of an element at risk in some literature (AGS 2000). The application of vulnerability in the field of civil engineering mainly focuses on the risk analysis of earthquake, debris flow and landslide, and mainly applied to building or bridge structures (Remondo 2008). Vulnerability evaluation of shield tunnel still needs further development, and most of the existing methods rely on subjective evaluation for qualitative description, lacking accurate quantitative analysis (Dai 2002). Li (2010) proposed a vulnerability calculation model, which defined vulnerability as a function of the hazard intensity associated with exposed elements at risk and the resistance ability (R) of the elements to withstand a threat.

In this paper, the two-stage method is used to calculate the settlement and maximum curvature of the existing tunnel in the shield crossing process, and the main factors affecting the maximum curvature value are analyzed. Then, based on the previous research result on vulnerability, a quantitative vulnerability model based on disturbance intensity of shield tunneling and resistance ability of existing tunnel is proposed.

2 SETTLEMENT CALCULATION OF EXISTING TUNNEL

2.1 Calculation model

The simplified mechanical model of a shield tunnel under-crossing through an existing tunnel is established, as shown in Figure 1. The shield tunnel is parallel to the y axis. α is the angle between the shield and the existing tunnel in the xoy plane. z and z_0 are the buried depth of

the existing tunnel and the shield center axis, respectively. L is the length of the shield. L_s is the horizontal distance between the shield excavation face and the xoz plane, which is positive when the shield is not reached. D is the diameter of the existing tunnel. m is the width of a ring segment. l is the spreading length of the slurry.

To obtain the vertical additional stress of the soil under the coordinate system xyz , the results under the coordinate system $x_e y_e z_e$ need to be transformed as follows: $x = x_e \sin \alpha$, $y = -x_e \cos \alpha$, $z = z_e$.

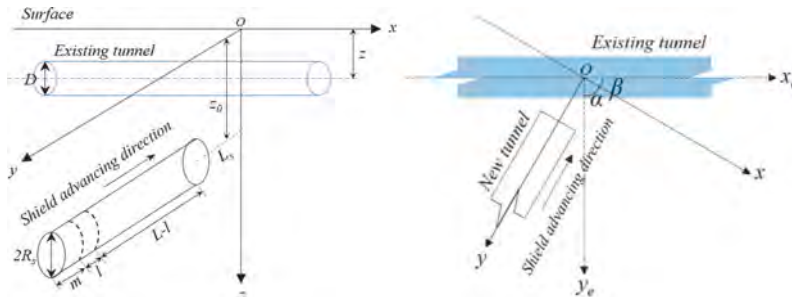


Figure 1. Calculation model of a shield tunnel under-crossing an existing tunnel.

In this paper, the two-stage analysis method is used to analyze the existing tunnel responses to construction of a new tunnel under. The Pasternak foundation is used to consider the tunnel-ground interaction, and the Timoshenko beam model is adopted to model the behaviors of the existing tunnel caused by shield excavation.

In order to obtain the final settlement value of the tunnel, first, the excavation-induced loads exerted on the existing shield tunnel are calculation using the Mindlin's solution (Mindlin 1936). Second, the deformation of the existing tunnel is calculated by the finite difference method.

2.2 Additional stress

Based on Mindlin's solution, a vertical concentrated force (F_v) exerts on the xoy plane, so the vertical additional stress σ_{zv} at an arbitrary point (x, y, z) of the soil induced by this force are as follows:

$$\sigma_{zv} = -\frac{F_v}{8\pi(1-u)} \left[-\frac{(1-2u)(z-h)}{R_1^3} + \frac{(1-2u)(z+h)}{R_2^3} - \frac{3(z-h)^3}{R_1^5} - \frac{3(3-4u)z(z+h)^2 - 3h(z+h)(5z-h)}{R_2^5} - \frac{30hz(z+h)^3}{R_2^7} \right] \quad (1)$$

Where $R_1 = \sqrt{x^2 + y^2 + (z-h)^2}$, $R_2 = \sqrt{x^2 + y^2 + (z+h)^2}$, (x, y, z) is the coordinate of the calculation point; u is the Poisson's ratio of soil; h is the depth of the point where the concentrated force exerts.

Analogously, a horizontal concentrated force (F_h) exerts on the xoz plane, so the vertical additional stress σ_{zh} at an arbitrary point (x, y, z) of the soil induced by this force are as follows:

$$\sigma_{zh} = \frac{F_h}{8\pi(1-u)} \left[\frac{1-2u}{R_1^3} - \frac{1-2u}{R_2^3} - \frac{3(z-h)^2}{R_1^5} - \frac{3(3-4u)(z+h)^2}{R_2^5} + \frac{6h}{R_2^5} \left(h + (1-2u)(z+h) + \frac{5z(z+h)^2}{R_2^2} \right) \right] \quad (2)$$

Based on the above basic theory, the vertical additional stress caused by various factors of shield crossing is calculated in this paper, such as additional thrust on the shield excavation face, friction of the shield shell, grouting pressure of the shield tail and soil loss.

2.2.1 Additional thrust on the shield excavation face

Additional thrust on the shield excavation face is usually simplified as the difference between the cutter pressure and the frontal water and soil pressure. The additional thrust q is evenly distributed on the excavation face (Lin et al., 2013) and exerts on the soil in front of the excavation face.

Analyzing a random micro-element at the excavation face, the concentrated force is $dF_h = q r d r d \theta$. Substituting it into Equation (2), and integrating the equation, the vertical additional stress at a certain point (x, y, z) induced by additional thrust q can be calculated as:

$$\sigma_{z-q} = \int_0^{2\pi} \int_0^{R_s} d\sigma_{z-q} \quad (3)$$

The transformation relation between coordinate system xyz and coordinate system $x'y'z$ shall comply with the following equation: $x' = x - r \cos \theta$, $y' = y - L s$, $z' = z$, and $h = z_0 - r \sin \theta$.

2.2.2 Friction of the shield shell

The friction f is assumed that uniformly distributed on the shell of the shield and also exerts on the soil around the shield. Analyzing a random micro-element on the surface of the shield shell, the concentrated force is $dF_h = f R_s d s d \theta$. Substituting it into Equation (2), and integrating the equation, the vertical additional stress at a certain point (x, y, z) induced by friction f can be calculated as:

$$\sigma_{z-f} = \int_0^{2\pi} \int_0^{L-l} d\sigma_{z-f} + \lambda \int_0^{2\pi} \int_{L-l}^L d\sigma_{z-f} \quad (4)$$

Where λ is a reduction factor of shield friction, λ is taken as 0.5; l is taken as 2.2 m. The transformation relation between coordinate system xyz and coordinate system $x'y'z$ shall comply with the following equation: $x' = x - R_s \cos \theta$, $y' = y - L s - L s$, $z' = z$, and $h = z_0 - R_s \sin \theta$.

2.2.3 Grouting pressure of the shield tail

With the distribution range is assumed to be the width of one ring segment, the grouting pressure p is uniformly distributed along the annular direction of the segment at the tunnel shield tail.

Analyzing a random micro-element at the grouting site of the shield tail, the concentrated force is $dF = p R_s d s d \theta$. The grouting pressure is decomposed in vertical and horizontal directions, the decomposed forces are $dF_v = -p R_s \sin \theta d s d \theta$ and $dF_h = p R_s \cos \theta d s d \theta$, respectively. Substituting it into Equation (1) and Equation (2), and integrating the equations, the vertical additional stress at a certain point (x, y, z) induced by grouping pressure can be obtained as:

$$\sigma_{z-pv} = \int_0^{2\pi} \int_0^m d\sigma_{z-pv} \quad (5)$$

$$\sigma_{z-ph} = \int_0^{2\pi} \int_0^m d\sigma_{z-ph} \quad (6)$$

The transformation relation between coordinate system xyz and coordinate system $x'y'z$ shall comply with the following equation: $x' = x - R_s \cos \theta$, $y' = y - L s - L s$, $z' = z$, and $h = z_0 - R_s \sin \theta$.

2.2.4 Soil loss

Due to shield tail gap, attitude adjustment in shield construction, and other reasons, the excavation boundary is always larger than the occupied space of the tunnel, resulting in soil loss and deformation of the surrounding soil (Yin, 2018). The vertical deformation U_z of the surrounding soil at a certain point (x, y, z) caused by soil loss is calculated as (Loganathan 1998):

$$U_z = \frac{B \eta R_s^2}{4} \left\{ \frac{z_0 - z}{x^2 + (z_0 - z)^2} + \frac{z_0 + z}{x^2 + (z_0 + z)^2} - \frac{2z [x^2 - (z_0 + z)^2]}{[x^2 + (z_0 + z)^2]^2} \right\} \cdot \left(1 + \frac{y}{\sqrt{y^2 + z_0^2}} \right) \cdot \exp \left[\frac{x^2 \ln \lambda}{(z_0 + R_s)^2} + \frac{z^2 (\ln \lambda - \ln \delta)}{(z_0 + d)^2} \right] \quad (7)$$

$$\eta(y) = \frac{\eta}{2} \left(1 + \frac{y}{\sqrt{y^2 + z_0^2}} \right) \quad (8)$$

$$B = \frac{4z_0 \left[z_0 + d - \sqrt{(z_0 + d)^2 - \eta(y)(R_s + d)^2} \right]}{R_s \eta(y)(R_s + d)} \quad (9)$$

$$\delta = \frac{1}{2} - \frac{1}{\pi} \arcsin \left[\frac{2d}{R_s(1 + \sqrt{1 - \eta(y)})} \right] \quad (10)$$

$$\lambda = \frac{1}{4} - \frac{2(1 - \sqrt{1 - \eta(y)})}{\pi \eta(y)} \left[\arcsin \left(\frac{d}{R_s \sqrt{1 - \eta(y)}} \right) + \sqrt{1 - \left(\frac{d}{R_s \sqrt{1 - \eta(y)}} \right)^2} - 1 \right] \quad (11)$$

Where x is the horizontal distance from the shield center axis; y is the horizontal distance from the shield excavation face; d is the distance from the moving focus of the soil to the center of the tunnel, $d=0.4R_s$; η is the rate of soil loss. The transformation relation between coordinate system $x y z$ and coordinate system $x' y' z'$ shall comply with the following equation: $x'=x$, $y'=y-L_s$, $z'=z$. The vertical additional stress induced by soil loss can be obtained as:

$$\sigma_{z-s} = k U_z \quad (12)$$

Where k is the coefficient of the subgrade.

2.2.5 The total vertical additional stress

In summary, the total vertical additional stress at an arbitrary position caused by shield crossing excavation is derived from additional thrust q , friction force f , grouting pressure p and soil loss, the calculation formula is as follows:

$$\sigma_z = \sigma_{z-q} + \sigma_{z-f} + \sigma_{z-pz} + \sigma_{z-ph} + \sigma_{z-s} \quad (13)$$

The final settlement value can be obtained by treating the existing tunnel as a Timoshenko beam of the Pasternak foundation model and applying the calculated stress to it.

3 QUANTITATIVE VULNERABILITY MODEL

3.1 The vulnerability calculation model

Vulnerability (V) is defined as a function of the hazard intensity (I) associated with exposed elements at risk and the resistance ability (R) of the elements to withstand a threat. The Vulnerability model as follows:

$$V = f(I, R) = \begin{cases} \frac{I^2}{R^2} & \frac{I}{R} \\ 1.0 - \frac{2(R-I)^2}{R^2} & 0.5 < \frac{I}{R} \leq 1.0 \\ 1.0 & \frac{I}{R} > 1.0 \end{cases} \quad (14)$$

In this study, the hazard is the disturbance of shield excavation and the exposed element is the existing tunnel. So, I is the disturbance intensity, and R is the resistance ability of the existing tunnel. Both intensity and resistance ability are expressed in nondimensional terms.

3.2 Vulnerability evaluation index

The maximum curvature, that is, the minimum curvature radius of the tunnel after longitudinal deformation, is used as the vulnerability evaluation index.

Through the above calculation method, the longitudinal settlement of each point of the existing tunnel is obtained. By connecting the settlement points along the longitudinal

direction of the existing tunnel and using cubic B-spline curve fitting method, then the bending curvature at any point of the tunnel longitudinal can be calculated.

3.3 The standard condition

In order to achieve dimensionless parameters, it is necessary to determine the standard condition, that is, when the values of the I and R parameters are 1. The selection of standard condition does not affect the results of vulnerability evaluation.

Through the analysis of the characteristics of the crossing engineering, to be specific, the disturbance intensity (I) mainly involves the following factors: additional thrust, friction, grouting pressure, soil loss, diameter of shield tunnel, angle and vertical distance between the existing tunnel and the shield tunnel, and the Poisson ratio of soil.

The resistance ability (R) mainly involves the following factors: equivalent bending stiffness, buried depth of the existing tunnel, and elastic modulus of soil. Combined with the shield crossing case in Shanghai area, the parameters of the standard condition are determined as Table 1.

Table 1. Calculation parameters of the standard condition.

Parameters	Value	Parameters	Value
Additional trust q /kPa	40	Poisson ratio of soil u	0.3
Friction f /kPa	120	Length of shield L /m	9
Grouping pressure p /kPa	400	Rate of soil loss η	0.0025
Radius of shield R_s /m	3.3	Diameter of the existing tunnel D /m	6.2
Angle α /°	60	Equivalent bending stiffness EI /kN·m ²	5.88e6
Buried depth of the existing tunnel z /m	15	Equivalent stiffness κGA /kN·m ⁻¹	2.1e6
Buried depth of shield tunnel z_0 /m	25.4	Elastic modulus of soil E_s /MPa	30
Horizontal distance between the shield excavation face and the xOz plane L_s			3

3.4 The standard coefficient δ

In order to make the selected standard condition feasible, the value of I/R needs to be corrected by using the standard coefficient δ before calculating the vulnerability (V).

$$\delta = \frac{\kappa_{sc}}{\kappa_{lim}} \quad (15)$$

where κ_{sc} is the maximum longitudinal curvature of the tunnel in the standard condition, and κ_{lim} is the maximum curvature corresponding to the longitudinal deformation limit state of the existing tunnel.

Referring to previous studies, when the longitudinal deformation curvature of a tunnel in Shanghai reaches $1.145E^{-4}$, the vulnerability value is 1. According to the standard condition set in this paper, the standard coefficient δ is 0.100.

4 PARAMETERS IN THE VULNERABILITY CALCULATION

4.1 Disturbance intensity (I)

Based on the above theory, the function between the disturbance intensity (I) and the parameters are fitted by changing the different values of the influencing parameters. Fitting functions of each parameter can be obtained, as shown in Figure 2.

Except for the grouting pressure, the disturbance intensity of shield excavation increases with the increase of other parameters. The change of the additional thrust and the Poisson ratio of the soil has little influence on the disturbance strength parameter.

By multiplying the disturbance intensity values corresponding to each parameter, the overall disturbance intensity can be obtained, as follows:

$$I = f(I_q, I_p, I_f, I_\eta, I_a, I_v, I_u, I_d) = I_q \times I_p \times I_f \times I_\eta \times I_a \times I_v \times I_u \times I_d \quad (16)$$

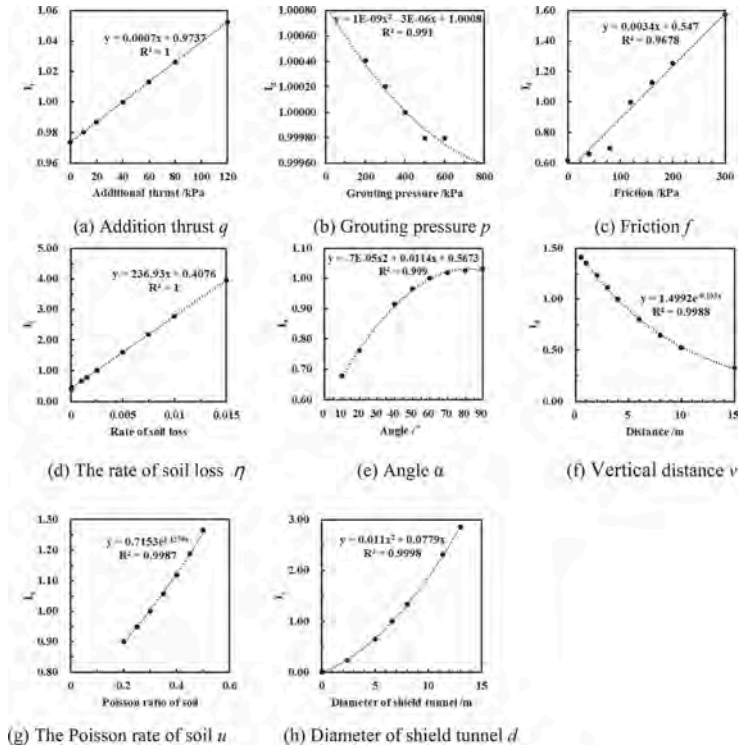


Figure 2. Fitting curve of disturbance intensity (I) of each parameter.

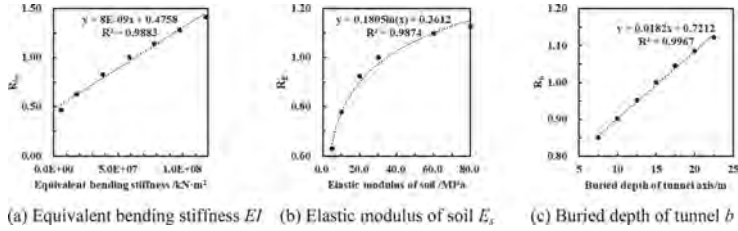


Figure 3. Fitting curve of resistance ability (R) of each parameter.

4.2 Resistance ability (R)

Analogously, the function between the resistance ability (R) and the parameters are fitted by changing the different values of the influencing parameters. Fitting functions of each parameter can be obtained, as shown in Figure 3.

The resistance ability increases with the increase of all the parameters. For the existing tunnel itself, the larger the equivalent bending stiffness and the deeper the buried depth, the stronger the resistance ability, and the less the impact in the shield crossing process. By multiplying the resistance ability values corresponding to each parameter, the overall resistance ability can be obtained, as follows:

$$R = f(R_{bs}, R_E, R_b) = R_{bs} \times R_E \times R_b \quad (17)$$

4.3 The vulnerability of the existing tunnel

When calculating the vulnerability value of an existing tunnel in a shield crossing project, the values of various parameters in the project are obtained first, and then substituted into the parameter fitting formula obtained above to obtain the resistance ability values and disturbance intensity values.

After calculating the values of I and R using Equation (16) and Equation (17), multiplying by the standard coefficient δ and bringing into the vulnerability calculation formula Equation (14), the vulnerability value of the existing tunnel in the crossing project can be obtained.

5 CASE APPLICATION

In order to apply the proposed vulnerability calculation method and verify its feasibility, a project is selected for calculation. The case is a large-diameter shield tunnel crossing over Shanghai Metro Line 8.

The excavation diameter of the cross-river tunnel is 11.58m, the outer diameter is 11.36m, and its buried depth of is about 30.6 m, the vertical distance from the existing tunnel is about 3.2m. The shield mainly crosses through straw yellow sandy silt and grayish yellow silt, and the existing tunnel is mainly buried in gray silt clay and dark green silty clay. The parameters value of the case condition is shown in Table 2.

Table 2. Calculation parameters of the case condition.

Parameters	Value	Parameters	Value
Additional thrust q/kPa	50	The Poisson ratio of soil u	0.5
Friction f/kPa	145	Length of shield L/m	11.245
Grouping pressure p/kPa	445	Rate of soil loss η	0.0035
The radius of shield R_s/m	5.79	The diameter of the existing tunnel D/m	6.2
Angle $\alpha/^\circ$	56	Equivalent bending stiffness $EI/kN \cdot m^2$	5.88e7
Buried depth of the existing tunnel z/m	19.12	Equivalent stiffness $\kappa GA/kN \cdot m^{-1}$	2.1e6
Buried depth of shield tunnel z_0/m	30.6	Elastic modulus of soil E_s/MPa	20
the horizontal distance between the shield excavation face and the xoz plane L_s			3

According to the parameter fitting curves of I and R obtained above, the disturbance intensity values corresponding to additional thrust (I_q), grouting pressure (I_p), friction (I_f), the soil loss rate (I_η), angle (I_α), distance (I_v), soil Poisson's ratio (I_u) and shield diameter (I_d) are 1.0087, 0.9997, 1.0400, 1.2369, 0.9862, 1.0782, 1.2572 and 2.3045, respectively.

The resistance ability values corresponding to equivalent bending stiffness (R_{bs}), elastic modulus of soil (R_E) and the buried depth of existing tunnel axis (R_b) are 1.0000, 0.9019 and 1.0692.

Therefore, the overall values of I and R are 3.996 and 0.9643, respectively. The final vulnerability value is 0.3435.

Reference to the risk management code for underground engineering (China, M. 2011), the risk of the shield crossing project is acceptable, but daily management and monitoring should be strengthened, and protective measures should be taken in time to reduce the vulnerability value.

Since the values of each calculation parameter in this method are related to the variation range in the actual situation, the vulnerability calculation method can be applied to most of the projects when the shield tunnel under-crossing through the existing tunnel. According to the setting of the standard condition, when the sum of the radius of the existing tunnel, the radius of the new tunnel and the vertical distance between the two tunnels does not exceed 15m, the vulnerability value can be calculated by this method.

6 CONCLUSION

In this study, based on the two-stage method and vulnerability function, a calculation method for the vulnerability value of the existing tunnel during shield tunneling is proposed, and the influence of various construction and structure parameters is analyzed.

Compared with the existing vulnerability evaluation methods, the two-stage method in this paper considers multiple parameters in the shield construction process, the existing structural characteristics and spatial location are considered, more accurately calculates the maximum settlement and maximum curvature of the existing tunnel, and obtains more accurate disturbance intensity (I) and resistance ability (R) value.

In addition, the calculation of the vulnerability function in this paper is relatively simple, and the reference coefficient is used to calculate the correction. All these makes the vulnerability calculation in this paper more effective.

The following conclusions are obtained:

- (a) The parametric analysis of disturbance intensity (I) shows that the increase of additional thrust, friction, the rate of soil loss, crossing angle and other parameters will increase the maximum curvature of the existing tunnel and increase the disturbance intensity value. The rate of soil loss, vertical distance and excavation diameter of shield tunnel have great influence on disturbance intensity
- (b) The parametric analysis of resistance ability (R) shows that the increase of soil elastic modulus of soil, equivalent bending stiffness and buried depth of tunnel will reduce the maximum curvature of the existing tunnel and increase the resistance ability value, and the equivalent bending stiffness has the greatest influence on the resistance ability.
- (c) This method can be applied to most of the projects when the shield tunnel under-crossing through the existing tunnel. When the sum of the radius of the existing tunnel, the radius of the new shield tunnel and the vertical distance between the two tunnels does not exceed 15m, the vulnerability value can be calculated by this method.
- (d) A vulnerability evaluation model based on disturbance intensity and resistance ability is initially established, it can be used to evaluate the potential damage degree of the existing tunnel. Further, it provides a reference for ensuring the structural safety of the existing tunnels in shield crossing projects.

ACKNOWLEDGMENTS

This work is substantially supported by the National Natural Science Foundation of China (No. 52130805) and the Scientific Research Project of Shanghai Science and Technology Commission (No.20dz1202200). The financial support is gratefully acknowledged.

REFERENCES

- Australian Geomechanics Society. 2000. Landslide risk management concepts and guidelines. *Aust Geomech* 35:49–92
- China, M. 2011. Code for risk management of underground works in urban rail transit.
- Dai, F.C., Lee, C.F. & Ngai, Y.Y. 2002. Landslide risk assessment and management: an overview. *Eng Geol* 64:65–87.
- Einstein, H.H. 1988. Landslide risk assessment procedure. In proceeding of International Symposium On landslides. Lausanne 2:1075–1090.
- Leone, F., Asté, J.P. & Leroi, E. 1996. Vulnerability assessment of elements exposed to mass-movements: working toward a better risk perception. In: Senneset K (ed) *Landslides-Glissements de Terrain*. Balkema, Rotterdam, pp 263–270.
- Li, Z.H., Nadim, F., Huang, H.W., Uzielli, M. & Lacasse, S. 2010. Quantitative vulnerability estimation for scenario-based landslide hazards. *Landslides*, 7: 125–134.
- Lin, C.G., Zhang, Z.M., Wu, S.M., & Yu, F. 2013. Key techniques and important issues for slurry shield under-passing embankments: a case study of Hangzhou Qiantang River Tunnel. *Tunn. Undergr. Space Technol.* 38, 306–325.
- Loganathan, N. & Poulos, H.G. 1998. Analytical prediction for tunneling-induced ground movements in clays. *J. Geotech. Geoenviron. Eng.* 124 (9), 846–856.
- Mindlin, R.D. 1936. Force at a point in the interior of a semi-infinite solid. *Physics* 7 (5), 195–202.
- Remondo, J. 2008. Quantitative landslide risk assessment and mapping on the basis of recent occurrences. *Geomorphology* 94:496–507.
- Yin, M.L., Jiang, H., Jiang, Y.S., Sun, Z.Y. & Wu, Q.L. 2018. Effect of the excavation clearance of an under-crossing shield tunnel on existing shield tunnels. *Tunn. Undergr. Space Technol.* 78, 245–258.

Stability assessment of slurry shield tunnel excavation zone

Y. Cheng

State Key Laboratory of Internet of Things for Smart City and Department of Civil and Environmental Engineering, University of Macau, Macau SAR, China
Department of Civil and Environmental Engineering, The Hong Kong Polytechnic University, Hung Hom, Hong Kong SAR, China

Y. Wu

China Civil Engineering Construction Corporation, Beijing, China

W.H. Zhou

State Key Laboratory of Internet of Things for Smart City and Department of Civil and Environmental Engineering, University of Macau, Macau SAR, China

ABSTRACT: Tunneling in complex geotechnical conditions and in built-up urban areas is becoming widespread. The stability of the tunnel excavation zone is closely related to the construction process and the safety of adjacent buildings. For the stability of slurry shield tunneling face, an attempt is made to propose an analytical solution with pore pressure distribution field and to assess the stability of the excavation zone of shield tunnel based on upper bound solution. The proposed method incorporates the coupling effect of slurry infiltration while considering groundwater seepage. The safety factors and the support pressure that influenced by the slurry transform rate are analyzed.

Keywords: Excavation zone, Upper bound limit, Slurry infiltration, Pore water pressure

1 BACKGROUND

With the development of cities, Shield tunnelling technology is abundantly used, greatly enriching the expansion of underground space. During the construction process, the stability of the excavation face, which can be critical for the safety of the tunnel and adjacent buildings. The stability of the tunnel excavation area is closely related to the ground conditions, hydrological condition, support force and support method, etc. Generally, due to insufficient support, especially under the influence of water (He, S. Y., et.al. 2024, Tang, C, et.al. 2023), the characteristics of the soil change and its own stability decreases, the soil in front of the tunnel tends to move through the tunnel excavation face towards the interior of the tunnel, causing tragedies such as failure of the excavation surface. Because active failure mode is more common in practice than passive mode, the active failure mode is our focus in this study (Zhao et al., 2019). It means that the soil in front of the tunnel excavation has a tendency to move inside the tunnel through the excavation face under the action of self-weight and other loads, causing accidents such as sudden surges and collapses.

Starting in the 1950s, limit analysis theory was introduced into the analysis of geotechnical stability problems (Drucke and Prager, 1952). The limit analysis includes the upper bound method and lower bound method. Derived on the basis of plastic theory, assumes that the soil is an ideal rigid-plastic body, using the principle of virtual work, the solution to the upper bound and lower bound can be obtained. For the upper bound solution can be state as the

work rate of internal dissipation is no less than the work rate of external loads, the mechanism is satisfied in a kinematically admissible displacement velocity field. In case that the upper bound solution only considers the dynamic requirement and not the static case, so the limit solution obtained is always greater than the real load, which is safer for the using. The limit analysis takes the material stress-strain relationship into account, and the solution derived under the condition the work done by the self-weight and external load in the limit state is equal to the work dissipation on the failure mechanism can be considered as a rigorous theoretical solution.

As for the stability analysis of the soil with the presence of water, theoretically one can directly use the seepage force and buoyancy force to calculate the work rate of the water, but in practice it is difficult to realize this process. After a rigorous derivation, (Michalowski et al., 2013) considered the emergence of water as an external work superimposed on the original governing equation, and represent the work done by seepage and buoyancy force with the work done by pore water pressure, the stability of slopes under submerged surfaces and under precipitation was analyzed. (Mollon et al., 2011) proposed some modified translational model and used spatial discretization technique to generate rotation failure model, developing the practicality of limit analysis for tunnel stability. And (Pan and Dias, 2016) based on the model proposed by Mollon analysis the factor of safety for shield tunnel face subjected to underground water seepage.

Consider the pore pressure distribution under the influence of groundwater level only, it is important to know the pore pressure at any point (Qin et.al. 2021). (Bishop and Morgenstern, 1960) proposed a coefficient $\gamma_u = u/\gamma h$ stands for pore-pressure ratio to describe the pore water distribution, where γ is the density of soil and h is the depth of the point in the soil mass below the soil surface. Due to the uncertainty of the value of γ_u , only a rough description of the situation can be achieved. Another way is using the flow net or based on the Navier-Stokes equations and Darcy's law to directly calculate the pore pressure distribution inside the soil mass, obviously, it is very difficult to get the true results. Therefore, a more general way in the previous studies to calculate the pore water distribution in the soil mass is used the numerical simulation, although the problem of parameter taking has been the focus and difficulty of numerical simulation. As for the pore pressure distribution in front of the slurry shield tunnel affected by both slurry infiltration and groundwater, through pore water pressure measurements in real projects and comprehensive analysis of seepage influencing factors, one dimensional analytical solution was proposed by (Xu and Bezuijen, 2018) to describe the excess pore pressure distribution. Therefore, it is important to establish a reasonable analytical flow field and use it to evaluate the stability of the excavation area under the special support form of the slurry shield tunnel.

In this study, a rigorous analytical solution based on the upper bound limit analysis theory to assess the stability of excavation zone is proposed, and the excess slurry pressure transform rate is integrate into the calculation. A close form hydraulic water head solution is used to simulate the pore pressure distribution ahead of the excavation surface by the slurry shield machine. Then the support pressure and safety factor under the effect of transform rate is obtained.

2 LIMIT ANALYSIS AND FAILURE MECHANISM

The upper bound method considers the kinetically admissible velocity field, can be expressed as the work rate of internal dissipation is no less the work rate of external loads. The governing equation is shown in Eq. 1.

$$\int_V D(\dot{\epsilon}_{ij}^k) \geq \int_S T_i v_i^k dS + \int_V X_i v_i^k dV \quad (1)$$

Where, T_i is a true traction vector on boundary S , X_i is the distributed load, V is the volume of the mechanism, v_i^k is the velocity field vector in a kinematically admissible mechanism, $\dot{\epsilon}_{ij}^k$ is the strain rate tensor in a kinematically admissible velocity field.

Different types of failure mechanism models of the excavation zone have been established to analysis of the stability of the excavation surface. Considering practicality and computational expandability, a 2D multi-block translational failure mechanism is employed in this study to describe the collapse in the excavation zone. Shown in the Figure 1. Assuming that the failure mode of the excavation surface has n blocks in total, the n-th block is an irregular quadrilateral or triangle. The angles of the first n-1 triangular blocks at point A are α_i ($i = 1, 2, \dots, n-1$), the angle of the i-th block at D_i point is β_i ($i = 1, 2, \dots, n$), v_i and $v_{r(i)}$ represent the absolute and relative velocities of rigid triangle blocks, respectively. According to the associate flow law, the angle between them and the speed discontinuity line is the internal friction angle ϕ .

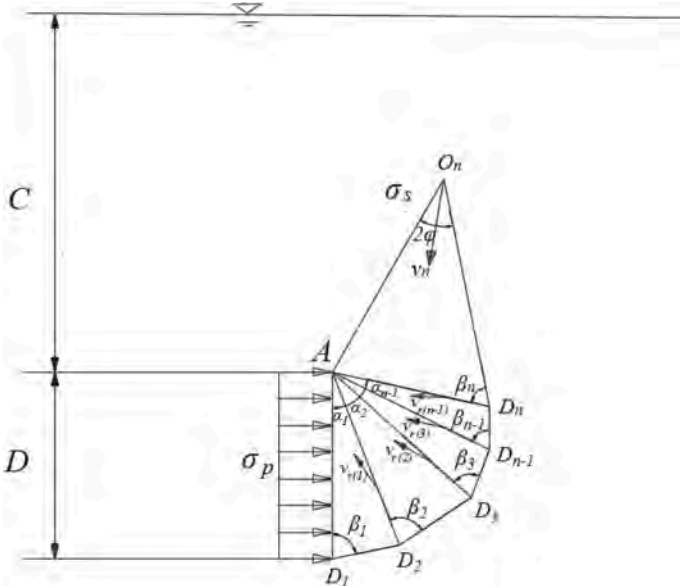


Figure 1. 2D Multi-block failure mechanism.

3 PORE PRESSURE DISTRIBUTION

For the consideration of the slurry shield tunnel, the special form of support for slurry infiltration is not fully considered in the stability analysis. A reasonable face stability analysis model should be based on the combined understandings of the support force and pore pressure distribution.

Considering the influence of water on the stability of the tunnel excavation area limit analysis, (Michalowski et al., 2013) after a rigorous derivation, the influence of water including buoyancy force and seepage force was replaced by the work done by pore water pressure, and then, the work rate of the pore water pressure is added to the control equation as an external force.

$$\dot{W}_u = - \int_V u \dot{\epsilon}_{ii} dV - \int_S u n_i v_i dS \tag{2}$$

$$\int_V D(\dot{\epsilon}_{ij}) dV \geq \int_S T_i v_i dS + \int_V X_i v_i dV - \int_V u \dot{\epsilon}_{ii} dV - \int_S u n_i v_i dS \tag{3}$$

In case that pore pressure distribution suffered the influence not only by the ground water but also the slurry infiltration. Rigorous derivation through mathematical formulas will become very difficult. The use of numerical simulation also has the shortcomings of low computational efficiency, difficult selection of parameters, and only one-way extraction of pore

water pressure to the analytical solution for calculation, which is not possible to make adjustments in the back calculation in the support pressure design. In this study, an analytical approach is proposed to describe a model that considers the effects of groundwater and slurry infiltration. The area in front of the excavation is divided into two zones, bounded by the upper surface of the tunnel, shown in the Figure 2, The pore water pressure distribution in Zone1 is influenced by both slurry infiltration and groundwater.

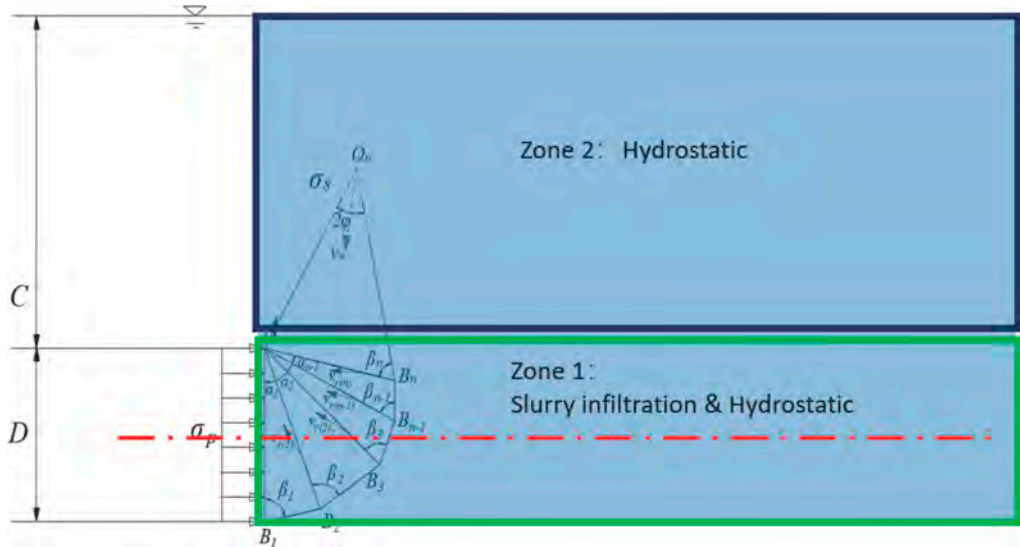


Figure 2. Proposed hydraulic impact model.

In the slurry infiltration process, part of the support pressure is not transformed to effective stress, but is present as an excess pore water pressure in the soil. According to (Bezuijen, 2002; Xu and Bezuijen, 2018), the piezometer head along the tunnel axis can be expressed as Eq. 4.

$$\phi_{distribution} = \alpha \times \phi_{excess} \left(\sqrt{1 + (x/R)^2} - x/R \right) + \phi_{static} \quad (4)$$

Where, ϕ_{slurry} is piezometric head of slurry, ϕ_{static} is hydrostatic water head at tunnel axis, ϕ_{excess} is difference between ϕ_{slurry} and ϕ_{static} , $\phi_{distribution}$ is piezometric head in front of the tunnel face along the tunnel axis, α is transform rate.

In case that the piezometer head at the tunnel axis is influenced by the concentration of the entire seepage surface, and the piezometer head generated by the influence of slurry infiltration at the tunnel crown or tunnel invert drop faster as the distance from the excavation surface gets farther. Using the same pressure drop mechanism to describe the change in piezometric head will slightly overestimate the pore pressure distribution in front of the excavation surface. Considering that the work done by the pore pressure in the limit analysis is negative, therefore, the calculation results will towards to safety side. And similar to the pore pressure distribution method proposed by (Bishop and Morgenstern, 1960), the pore pressure distribution in zone1 is considered only suffer the influence by the ground water. The ϕ_{static} only related to the depth of calculation point to the ground water table. The pore pressure distribution simulates by the proposed analytical method are shown in Figure 3.

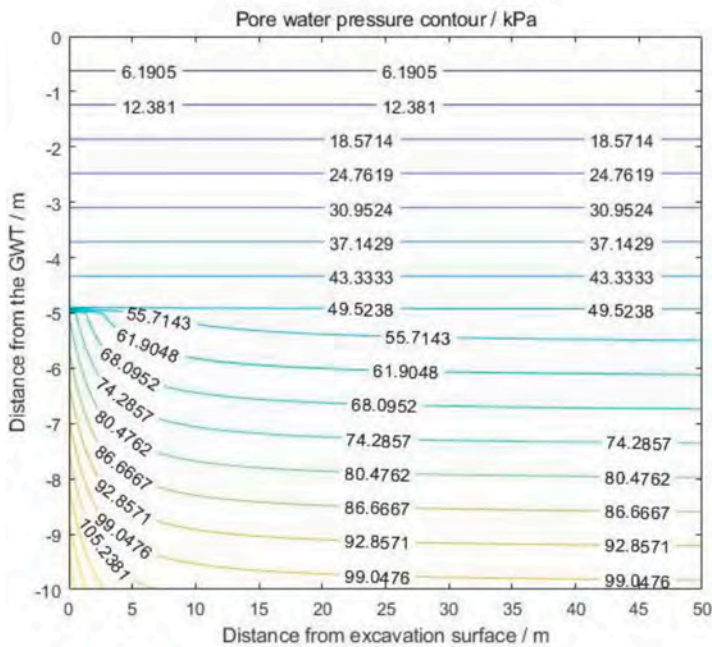
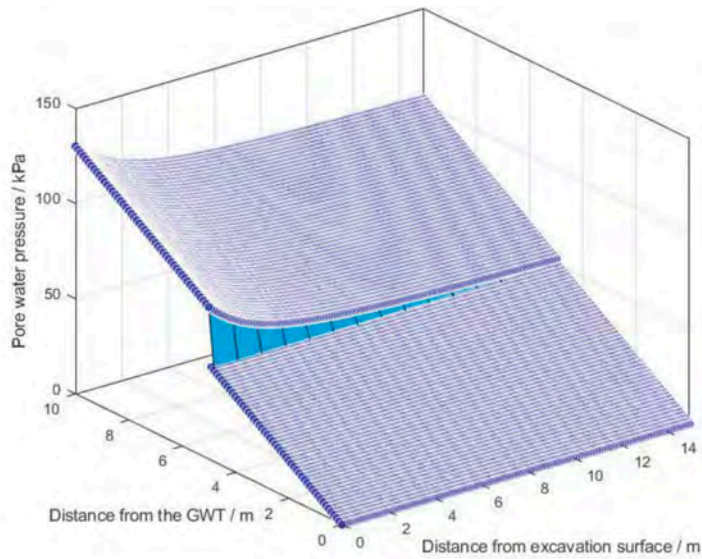


Figure 3. Pore pressure distribution by the proposed model.

4 SAFETY FACTOR AND PARAMETER ANALYSIS

Based on the upper bound limit analysis theory and with the pore pressure distribution field proposed in this study, the number of blocks in failure mechanism was determined first. Consider the soil properties, tunnel geometry and hydraulic condition shown in Table 1, without any normalize operations, the safety factor is obtained by the effective support force and the upper bound solution. As shown in Figure 4, with increase of the excess slurry transfer rate, the effective support force gradually decreases at the same time, which also means that the excess pore pressure in

front of the excavation gradually increases. Due to the pore pressure distribution is affected by slurry infiltration, therefore, the upper bound solution obtained also gradually increases. The safety factor is affected by the superposition effect of both, which gradually decreases as the excess slurry pressure transfer rate increases.

Table 1. Parameters list.

Parameter	Unit	Value
Diameter	m	10
Ground water	m	10
Excess slurry pressure	m	5
Density of soil	10^{23}kg/m^3	20
Cover depth	m	10
Friction angle	$^\circ$	25
Cohesion Force	kPa	0

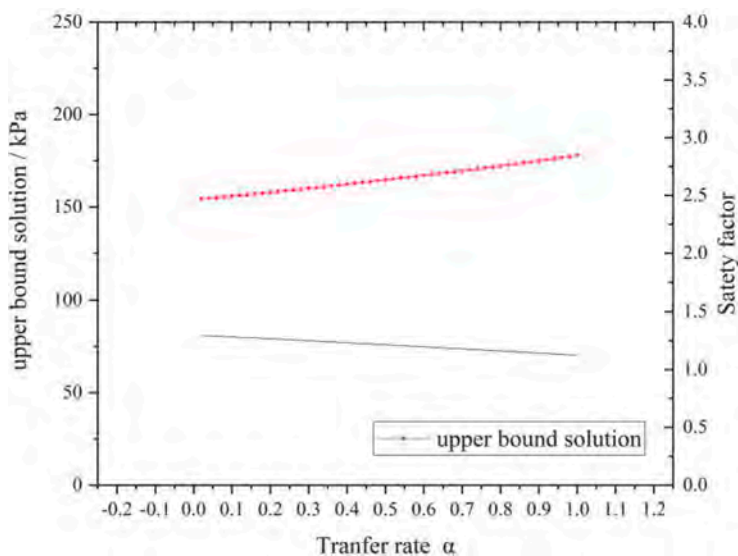


Figure 4. Safety factor influenced by excess slurry transfer rate.

5 CONCLUSION

In this study, the stability of the tunnel excavation zone is analyzed. Based on the limit analysis upper limit theorem, combined with the damage criterion and the associated flow law, a two-dimensional multi block failure mechanism at the exaction zone under slurry shield conditions is conduct. By establishing an analytical solution to describe the flow field, the analytical solution of the support force and safety factor of the slurry shield tunnel support has been derived. With the increase of the transfer rate, the effective support pressure required to stabilize the tunnel face will be increase and the safety factor will be decrease.

ACKNOWLEDGMENTS

The authors greatly acknowledge the financial support from the Science and Technology Development Fund of Macau SAR (File nos. 0056/2023/RIB2, 001/2024/SKL), National Natural Science Foundation of China (Grant No. 52022001), and Guangdong Provincial Department of Science and Technology (Grant No.2019B111106001).

CONFLICT OF INTEREST STATEMENT

We declare that we have no known competing financial interests or personal relationships that could have appeared to influence the work reported in this article.

REFERENCES

- Bishop, A.W., Morgenstern, N., 1960. Stability Coefficients for Earth Slopes. *Géotechnique* 10, 129–153. <https://doi.org/10.1680/geot.1960.10.4.129>
- Drucker, D.C., Prager, W., 1952. Soil mechanics and plastic analysis of limit design. *Q. Appl. Math.* 10, 157–165
- He, S. Y., Zhou, W. H. & Tang, C. (2024). Physics-Informed Neural Networks for Settlement Analysis of the Immersed Tunnel of the Hong Kong–Zhuhai–Macau Bridge. *International Journal of Geomechanics*, 24(1), 04023241.
- Michalowski, R.L., Asce, F., Nadukuru, S.S., Asce, S.M., 2013. Three-Dimensional Limit Analysis of Slopes with Pore Pressure 139, 1604–1610. [https://doi.org/10.1061/\(ASCE\)GT.1943-5606.0000867](https://doi.org/10.1061/(ASCE)GT.1943-5606.0000867)
- Mollon, G., Phoon, K.K., Dias, D., Soubra, A., 2011. Validation of a New 2D Failure Mechanism for the Stability Analysis of a Pressurized Tunnel Face in a Spatially Varying Sand 137, 8–21. [https://doi.org/10.1061/\(ASCE\)EM.1943-7889.0000196](https://doi.org/10.1061/(ASCE)EM.1943-7889.0000196)
- Pan, Q., Dias, D., 2016. The effect of pore water pressure on tunnel face stability 2123–2136. <https://doi.org/10.1002/nag>
- Qin, Su, Xu, Tao, Zhou, Wan-Huan. 2021. Predicting Pore-Water Pressure in Front of a TBM Using a Deep Learning Approach. *International Journal of Geomechanics*. 21. 04021140. [10.1061/\(ASCE\)GM.1943-5622.0002064](https://doi.org/10.1061/(ASCE)GM.1943-5622.0002064).
- Tang, C., He, S. Y., Guan, Z., Zhou, W. H., & Yin, Z. Y. (2023). Enhanced elastic beam model with BADS integrated for settlement assessment of immersed tunnels. *Underground Space*.
- Xu, T., Bezuijen, A., 2018. Analytical methods in predicting excess pore water pressure in front of slurry shield in saturated sandy ground. *Tunn. Undergr. Sp. Technol.* 73, 203–211. <https://doi.org/10.1016/j.tust.2017.12.011>
- Zhao, L., Li, D., Yang, F., Li, L., Cheng, X., 2019. Dimensionless Parameter Diagrams for the Active and Passive Stability of a Shallow 3D Tunnel Face 23, 866–878. <https://doi.org/10.1007/s12205-018-5835-0>

Flow rate study of geothermal heat exchanger system in north US

J. Lin

University of Macau, Macau, China

Department of Civil and Environmental Engineering & State Key Laboratory of Internet of Things for Smart City, University of Macau, China

T.D. Stark

University of Illinois at Urbana-Champaign, Champaign, IL, USA

A.J. Stumpf

Illinois State Geological Survey, Prairie Research Institute, University of Illinois at Urbana-Champaign, Champaign, IL, USA

ABSTRACT: A feasibility study of installing multiple wellbores geothermal heat exchange system in the Badeen Quad with a complex heating steam tunnel and pipe underground in the University of Illinois at Urbana-Champaign (U of IL) to serve as an additional cooling and heating system for the Campus Instructional Facility (CIF) Building. The initial field condition was simulated before running the numerical simulation for the geothermal heat exchange system. Numerical modeling is conducted on multiple wellbore groups to study the effects of flow rate in heating and cooling the underground space and its ability on the heat storage of the geothermal system. This preliminary study provides a feasibility analysis for running the shallow-depth geothermal heat exchange system.

1 INTRODUCTION

Energy consumption is a major topic in the global economy all the time (Liu et al., 2023). Traditional fossil-based energy supplies 84.5% of the global energy consumption. The usage of fossil energy causes the increment of carbon dioxide (CO₂) and global warming. Renewable energy is promising because it can generate energy without additional carbon emission (Wang et al., 2018; Ellabban et al., 2014; Manzano-Agugliaro et al., 2013) and reduce the significant lost due to sea level rise (Shen et al., 2023). Geothermal energy is a renewable resource that harnesses the heat from within the earth for various purposes. It can be used for heating, cooling, or converted into electricity. Geothermal energy has several advantages, including low cost, year-round operation, and the ability to provide firm and dispatchable electricity. (IRENA, 2023). Stumpf et al. (2021) shows that academic campuses are actively working towards achieving ambitious goals of reducing their carbon footprints and improving operational resiliency. They are taking proactive measures and implementing strategies to minimize their environmental impact and increase their ability to withstand and recover from disturbances or disruptions. Shallow-depth geothermal heat exchange systems offer high efficiency in heating and cooling buildings (Sofia et al., 2023; Wang et al., 2023). These systems utilize the stable temperature of the earth just a few meters below the surface to extract heat during the winter and release heat during the summer. This makes them a sustainable and cost-effective solution for maintaining the desired indoor temperature.

The University of Illinois is advancing toward an environmentally sustainable campus by achieving the goals set in the Illinois Climate Action Plan (iCAP). This pledge to environmental

stewardship follows the university's 2008 commitment to the American College and University Presidents' Climate Commitment, which sets a goal for the campus to reach carbon neutrality at the earliest possible time, but no later than 2050, either by eradicating or balancing out greenhouse gas emissions. Since the initial formulation of iCAP in 2010 and its subsequent reaffirmations in 2015 and 2020 (iCAP, 2020), there has been an increasing recognition that solar and wind power alone will not suffice to achieve the ambitious goal of zero carbon emissions. Consequently, the University of Illinois is increasingly interested in sourcing its energy from additional renewable and eco-friendly options such as geothermal exchange systems. This study is a feasibility analysis of a shallow-depth geothermal heat exchange system to serve as an additional heating and cooling source to a new Campus Instructional Facility (CIF) Building in the University of Illinois at Urbana-Champaign (U of IL) (Stumpf et al. 2021).

2 INSTALLATION OF SHALLOW-DEPTH GEOTHERMAL HEAT EXCHANGE SYSTEM

2.1 Site location

The CIF is located on the U of I campus in Urbana, Illinois, which is located ~220 km (135 miles) south of the City of Chicago, 290 km (180 miles) northeast of the City of St. Louis, and ~195 km (120 miles) west of the City of Indianapolis. The geothermal borefield is located in the northern part of campus just west of Grainger Library in the northwest corner of the John Bardeen Quad, and southeast of the intersection of Springfield Avenue and Wright Street (Figure 1). A geothermal monitoring well CHAM-18-01 was constructed in the northwestern part of the geothermal borefield. This well was constructed with a U-bend geothermal loop of high-density polyethylene (HDPE) pipe, with a fiber-optic cable secured along the axis of the pipe. To measure the representative subsurface temperatures and heat flow, parameters used as boundary conditions for determining the intrinsic permeability and hydraulic conductivity, a distributed temperature sensing (DTS) system was deployed and distributed thermal response (DTRT) performed to identify the thermal transport processes in monitoring well CHAM-18-01. The temperature is periodically measured in the well to detect changes in the ambient ground conditions.



Figure 1. Location of CIF and geothermal borefield at the U of I. The geothermal monitoring well is at latitude N40.112094° and longitude W88.227469°.

2.2 Installation of the geothermal exchange system

Forty boreholes were drilled in a grid pattern in two areas of the John Bardeen Quadrangle (Figure 2). The wells are spaced 6.1 m apart and drilled to a depth of 137.2 m. The geothermal

monitoring well (CHAM-18-01) where ongoing field measurements are being made is also identified. Figure 2 is the installation design of wells in the geothermal borefield. The diagram includes placement of grout respective to the well depth and casing diameter, and position of the U-bend pipe.

The soil properties for the numerical simulation are shown in Table 1. The details of the soil information are shown in Okwen et al., 2020. The thermal conductivity and heat capacity are measured with a Hot Disk TPS 1500 thermal constants analyzer using Kapton® plastic-coated sensors with radii of 6.403 mm, 9.868 mm, and 14.61 mm (Hot Disk AB, 2018). The Hot Disk sensor is an electrically conducting metallic double spiral (nickel), covered by two thin layers of insulating material as shown in Stumpf et al. (2021). The Hot Disk equipment relies on the transient plane source method (Gustafsson 1991; Gustafsson and Gustafsson 2005), according to the Dansk Standard (2015) DS/EN ISO 22007-2.

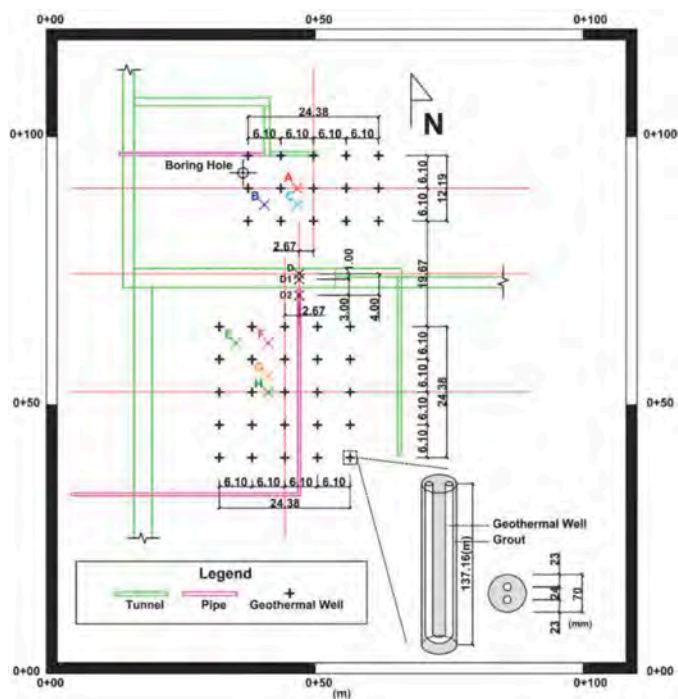


Figure 2. Borefield diagram with location of simulation positions (A to H).

Table 1. Thermal capacity and conductivity of the soil samples.

Unit	Thickness (m)	Density (g/cm ³)	Porosity	Permeability (mD)	Heat Capacity (J/kgK)	Thermal Conductivity (W/mK)
Soil	1.82	1.085	0.4	50	2530	1.57
Quaternary 1	24.38	2.4	0.25	2	545	2.21
Quaternary 2	31.34	1.635	0.38	9000	2380	2.31
Pennsylvanian	52.99	2.48	0.12	5	1010	1.84
Mississippian	77.82	2.66	0.15	10	820	3.5

3 MODEL SET UP

3.1 Initial condition

The COMSOL numerical model was initially run to simulate the natural ground conditions. Different model size was run to determine the boundary effect and model efficiency. The final dimension of the model is 50 m in width, 50 m in length, and 140 m in depth. The model was set up without any impacts from the adjacent steam tunnels, heat pipes, or wellbores in the subsurface to establish the pre-existing surface temperature conditions. The surface temperature was set at 5°C for the average surface temperature of the Illinois area (Stumpf et al., 2020; Okwen et al., 2020), while the bottom temperature was set at 15°C based on physical measurements to perform an initial or steady-state analysis (Stumpf et al., 2020). The temperature at each depth interval changed linearly, extrapolated from the temperature at the top (ground surface) and bottom (glacial till) boundaries. The boundaries serve as the heat source in the initial or steady-state analysis. The side boundaries of the COMSOL model were set to be thermally insulative, meaning there is no heat exchange across the side boundaries due to the same temperature in and outside the boundary. The initial or steady-state analysis returned a temperature profile that is the natural site conditions before well installation.

Once the initial conditions were calculated, the numerical model was adjusted to include the positions of the heat tunnels and pipes that run parallel to Talbot Laboratory which is on the left of the borefield in Figure 1. The outer surface of the heat tunnel and pipes were set to 40.6 °C, and served as a secondary heat source into the bore field. The simulation with the heat tunnels and pipe was run for around 100 years to achieve a steady-state or equilibrium subsurface thermal condition to represent the quad before geothermal heat exchange well installation.

The DTS temperature profiles from January 6, 2021, and March 6, 2019 (See Figure 3) are shown with the predicted summer, fall, and winter temperature profiles in Figure 3. The predicted ground conditions are based on simulated field measurements with changing ambient air temperature without impacts from the geothermal wells. It is clear that at depths >20 m, the ground temperature is no longer affected by the ambient air temperature.

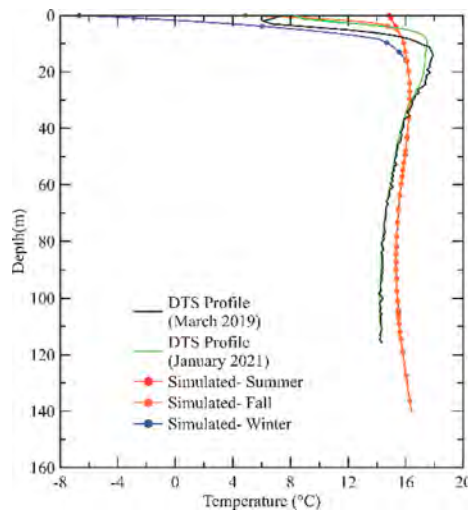


Figure 3. Measured and simulated ground temperature profiles after three seasons of operation.

3.2 Operation cycle and environment

The geothermal borefield will operate throughout the year but during the summer and winter months, the fluid leaving the CIF building and being circulated will have different temperatures. In summer, the fluid leaving the building and entering the geothermal loop system will be at a higher temperature than the ground temperature and will heat the ground surrounding

the closed U-shaped wells but cool the water inside the U-shaped well. This cooled water will flow back to the CIF building to cool the building. In winter, the fluid will flow in the same direction exiting the building and entering the loop system at a lower temperature than the ground and will cool the surrounding ground but heat the water inside the wells. The anticipated ambient air and fluid temperatures are shown in Table 2 for all four seasons.

Table 2. Ambient air and circulating fluid temperatures.

	Summer	Fall	Winter	Spring
	(°C)	(°C)	(°C)	(°C)
Air Temperature	14.9	4.6	-6.7	4.9
Inlet Fluid Temperature	32	nd	10	nd

4 RESULTS

4.1 Summer scenario

In summer, the impacts of circulating heated fluid from the CIF into the geothermal borefield are emphasized in this scenario. To determine the impacts on the existing ground temperature, the temperature profiles at positions A to C and E to H (see Figure 2) are compared with the measured ground temperatures in the geothermal monitoring well (see Figure 4). The geothermal wells are uniformly impacted by circulating heated fluid within the borefield because the measured temperature profiles at positions A to C and E to H are similar. Figure 4 shows that there is no significant change in the pre-existing temperature profiles from March 2019 to January 2021 because the geothermal system had not started operation, i.e., no additional heat source for the borefield. After running the geothermal heat exchange system, the borefield is heated by around 6 °C underground in the borefield because the hot water flows into the pipe and heats the ground.

Figure 5 shows the decrease in outflow temperature in the U-bend pipe and temperature increase in the surrounding ground due to the circulation of fluid from the CIF that is hotter than the ground temperature. With fluid circulating through the borefield having an elevated

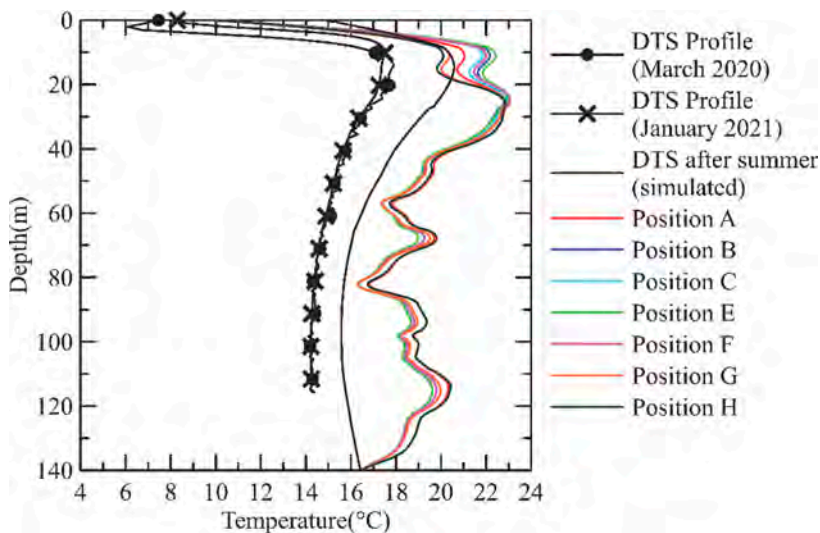


Figure 4. Simulated temperature profiles at positions A to C and E to H at the end of summer are compared with the DTS measurements collected in 2019 and 2021.

temperature of 32°C (90°F) during the summer months (see solid blue line in Figure 22), the computed ground temperatures increase by ~5.6°C (10°F) over the 4-month period (See solid black line in Figure 22). This needs to be investigated after the system becomes operational to determine if the analysis is accurate. The borefield will increase in temperature because the energy from inflow is conducted to the ground. The simulated temperature profiles at positions A to C and E to H at the end of the four summer months also show a significant increase in subsurface temperature (Figure 21).

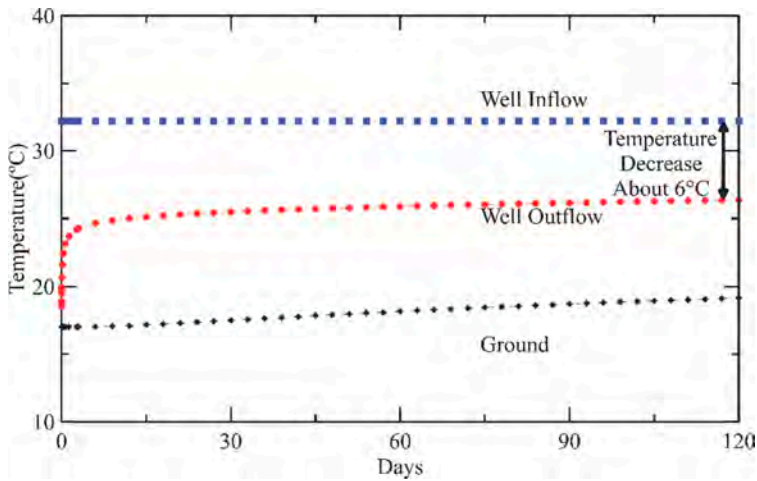


Figure 5. Simulated ground heating during the summer. Estimated temperatures of fluid flowing in and out of at 0.82 m³/hour of each pipe in the geothermal borefield.

4.2 Winter scenario

The autumn scenario was run after summer scenario with ambient temperature decreasing from 14.85 °C to 4.85 °C without any fluid injection. Analysis for winter scenario was followed autumn scenario with ambient temperature of -6.67 °C with the same injected flow at 10 °C at injection rate 0.82 m³/hour as summer.

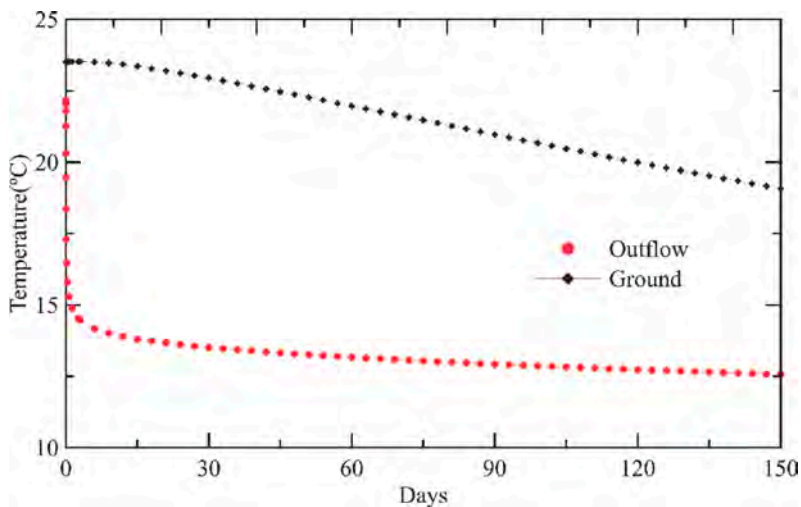


Figure 6. Simulated ground cooling during the winter. Estimated temperatures of fluid flowing in and out of at 0.82 m³/hour of each pipe in the geothermal borefield.

The surroundings on the geothermal well group is cooled in winter. Based on the COMSOL results, all geothermal wells have outflows with almost the same temperature regardless of location. Outflow temperature changes along with time after injection is plotted in Figure 6. The largest stable outflow temperature can reach 14.4 °C which is 4.4 °C higher than injection temperature (10°C). However, outflow temperature will decrease with time and at the end of the winter, only about 2.5°C increase can be obtained from the geothermal energy.

4.3 Flow rate analysis

The previous simulations assume a circulation rate of 0.82 m³/hour. To increase the efficiency of the borefield, additional simulations were performed to investigate adjusting fluid rates into the borefield based on the principle that fluid being circulation at a slower rate in the U-bend pipe will lead to more heat transfer into the surrounding ground.

In these simulations, the rate of circulating fluid entering the borefield varied between 0.082 m³/hour and 8.2 m³/hour. The temperatures at the well outlet estimated from the numerical simulation are plotted in Figure 7. The final outflow temperatures at different circulation rates are shown in Table 3. This comparison illustrates that a slower circulating fluid rate leads to a higher rate of temperature from the borefield to the U-bend pipe because the less flow has more time to allow heat transfer. The results are also summarized in Table 3. Conversely, the higher the circulation rate, the temperature increment during circulation in the flow are less and the lower the temperature gain at the well outlet into the building because of less contact time between the flow and the surrounding ground. However, when the flow rate increases, more energy is gained in the flow because the total volume and temperature gain are equally important in the energy gain as shown in equation (1). For example, the flow rate of 8.2 m³/hours is 100 times of flow rate of 0.082 m³/h, but the temperature gain at a higher flow rate of 8.2 m³/hours is about one-sixth of that in the lower flow rate. Thus, more energy in the higher flow rate. The actual flow rate is dependent on the building energy consumption.

$$Q_u = \rho V_u c_p (T_{outflow} - T_{inlet}) / 3600000 \tag{1}$$

where Q_u means the heat gain, kW. V_u represents the flow rate on the customer side, m³/h. c_p is the heat capacity of water, 4.18 J/(g × °C). $T_{outflow}$ and T_{inflow} indicate the outflow and inlet water temperature on the customer side, °C.

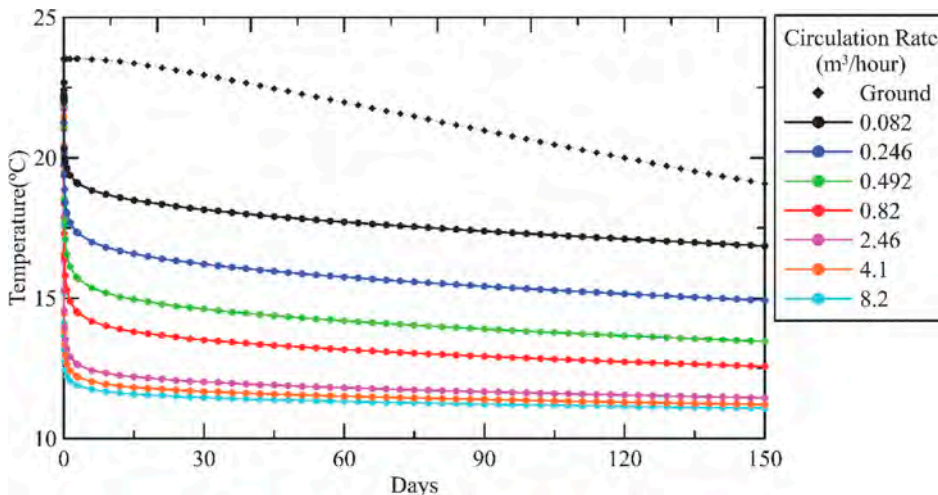


Figure 7. Well outflow temperature with different winter circulation rates.

Table 3. Outlet fluid temperatures under different flow rates.

Circulation Rate for One Well (m ³ /hour)	Terminal Outflow Temperature (°C)	Total energy gain (kW)
0.08	16.8	258.4
0.25	14.9	558.7
0.49	13.4	775.3
0.82	12.6	988.1
2.45	11.4	1596.2
4.09	11.2	2280.3
8.18	11.1	4180.6

5 SUMMARY

The following conclusions are made after running the flow simulations:

- 1) the geothermal exchange system can fulfill the thermal energy requirements by storing heat during summer in the borefield, which can be fully utilized during the subsequent winter.
- 2) By decreasing the flow rate in winter, the exiting fluid from the shallow geothermal exchange system can achieve a higher temperature gain, resulting in reduced energy consumption.
- 3) Increasing the flow rate enhances the overall energy output, leading to lower energy consumption in the building. Given the expected lifespan of at least 30 years, significant energy savings can be achieved with this geothermal exchange system.

ACKNOWLEDGEMENTS

Funding for the research was provided through the “Campus as a Living Lab” program at the Institute for Sustainability, Energy, and Environment and the U of I Carbon Credit Sales Fund.

The authors greatly appreciate the in-kind support provided by the ISGS and F&S. The ISGS drilling crew and Kandi Herzog from Durbin Geothermal Incorporated are recognized for their professional work installing the geothermal monitoring well.

The authors also greatly acknowledge the support from Guangdong Provincial Department of Science and Technology (Grant No.2019B111106001), Science and Technology Development Fund, Macau SAR (001/2024/SKL).

REFERENCES

- Dansk Standard DS/EN ISO 22007-2, 2015, Plastics: Determination of the thermal conductivity and thermal diffusivity, Part 2: Transient plane heat source (hot disc) method: Nordhavn, Denmark, Danish Standards Foundation, 34 p., <https://webshop.ds.dk/en-gb/search/83-080-01-plastgenerelt/ds-en-iso-22007-22015>.
- Ellabban, O. & Abu-Rub, H. & Blaabjerg, F. 2014. Renewable energy resources: current status, future prospects and their enabling technology, *Renew. Sustain. Energy Rev.* (39): 748–764.
- Gustafsson, S.E., 1991, Transient plane source techniques for thermal conductivity and thermal diffusivity measurements of solid materials: Review of Scientific Instruments, v. 62, no. 3, p. 797–804, <https://doi.org/10.1063/1.1142087>.
- Gustavsson, M. & S.E. Gustafsson, 2005, On the use of transient plane source sensors for studying materials with direction dependent properties, in R. Dinwiddie, ed., Proceedings of the 26th International Thermal Conductivity Conference and the 14th International Thermal Expansion Symposium: Lancaster, Pennsylvania, DEStech Publications, Incorporated, p.367–377.
- Illinois Climate Action Plan. 2020. University of Illinois at Urbana-Champaign. <https://sustainability.illinois.edu/campus-sustainability/icap/>

- IRENA, 2023. Geothermal Energy Data. Retrieved from. <https://www.irena.org/geothermal>. (Accessed 1 May 2023).
- Liu, W.& Yao, J.& Jia,T. et al. 2023. The long-term operation and thermal disturbance investigation on a four-borehole-heat-exchanger residential heating system, *Appl. Therm. Eng.* (219): 119–129.
- Manzano-Agugliaro, F. & Alcayde, A. & Montoya, F. et al., 2013. Scientific production of renewable energies worldwide: an overview, *Renew. Sustain. Energy Rev.* (18): 134–143.
- Okwen, R. & Yang, F. & Lin, Z. et al. 2020. Assessment of Geothermal Energy Extraction from the Mt. Simon Sandstone at University of Illinois at Urbana-Champaign Using a Doublet Well System, *Proceedings, Forty-Fifth Workshop on Geothermal Reservoir Engineering*, Stanford University, Stanford, CA (2020), this volume.
- Shen, P., Wei, S., Shi, H., Gao, L., Zhou, W. (2023) Coastal Flood Risk and Smart Resilience Evaluation under a Changing Climate. *Ocean-Land-Atmos Res.* 2:Article 0029, DOI:10.34133/olar.0029
- Sofia, V.& Cecilia I. & Nicolás H. 2023.Social and cultural aspects in the adoption of geothermal heat pump systems to replace wood-burning heaters in educational spaces: The Chilean Patagonian case, *Journal of South American Earth Sciences*, (128):104426
- Stumpf, A. J. & Frailey, S.M. & Okwen, R.T. et al. 2020. Feasibility of Deep Direct-Use for District-Scale Applications in a Low-Temperature Sedimentary Basin. *PROCEEDINGS, 45th Workshop on Geothermal Reservoir Engineering*, Stanford University, Stanford, California, February 10-12.
- Stumpf, A.J.& Lin, Y-F & Stark, T.D. 2021. Sub surface Monitoring and Modeling of a Geoexchange Borefield for the Campus Instructional Facility at the University of Illinois Urbana-Champaign: Illinois State Geological Survey, Circular 66
- Wang, X. & Zhan, T. & Liu, G. & Ni, L. 2023. A field test of medium-depth geothermal heat pump system for heating in severely cold region. *Case Studies in Thermal Engineering.* (48): 103125
- Wang, Z.& Song, M. & Wang, F. et al. 2018. Experimental investigation and seasonal performance assessment of a frost-free ASHP system with radiant floor heating, *Energy Build.* (179):200–212.

Spatial variability for Deep Cement Mixing in Kallang formation in Singapore. Review of scale of fluctuation and its influence in design

G.A. Pittaro & N. Mace
Mott MacDonald, Singapore

ABSTRACT: Ground Improvement using Deep Cement Mixing (DCM) is commonly used to enhance properties of in-situ soft clays. Properties of DCM are often highly variable in intensity and in spatial distribution, posing significant challenges in the analysis and design of geosystems when these man-made admixtures are used. This paper presents spatial variability results obtained from laboratory tests carried out from samples acquired from in situ DCM. A project in Singapore where over 700.000 m³ of DCM was installed is first introduced following by the results of the horizontal and vertical scale of fluctuation. Finally, some recommendations are drafted based on the results of the DCM's scale of fluctuation presented in this paper for a more comprehensive and sustainable design.

1 INTRODUCTION

The properties of soils and cement treated soils can vary in both intensity and spatial distribution. Spatial variability is typically characterized using the scale of fluctuation, usually denoted as SoF or δ . The scale of fluctuation is defined as the distance over which the property of a soil, cement treated soil or rock mass are correlated (Cami et al., 2020). Figure 1 below shows a scheme of a soil property and vertical trend with the schematic vertical scale of fluctuation.

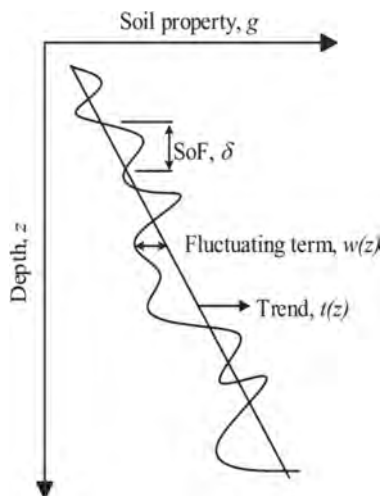


Figure 1. Illustration of the soil inherent variability (from Nie et al, 2015).

The spatial variability of cement treated soils (from now on called as deep cement mixing or DCM) is often anisotropic, where the horizontal SoF (δ_x) and vertical SoF (δ_y) are often used to describe the spatial variability in the two principal directions. The spatial variability has been recognized as one of the major sources of uncertainties that can influence the performance of geotechnical engineering systems (Phoon & Kulhawy, 1999; Kasama et al., 2012; Pan et al., 2018). The below equation has been proposed to account the SoF in the coefficient of variability of a property:

$$\text{CoV}_{\text{Total}} = \sqrt{\Gamma^2 \text{CoV}_{\text{inher}}^2} \quad (1)$$

Where Γ^2 is the variance reduction function (Vanmarcke, 1977) which considers the extent of the governing failure mechanism and the SoF; and $\text{CoV}_{\text{inher}}$ is the coefficient of variation of the inherent variability. Vanmarcke (1983) proposed to use the following form to calculate Γ^2 :

$$\Gamma^2 = \frac{\text{SoF}}{l} \times \left(1 - \frac{\text{SoF}}{3l}\right), \text{ for } \frac{l}{\delta} > 1 \quad (2)$$

$$\Gamma^2 = \left(1 - \frac{l}{3\text{SoF}}\right), \text{ for } \frac{l}{\delta} < 1 \quad (3)$$

Where l is the average dimension of the governing limit state and SoF is the scale of fluctuation in the l direction.

The SoF is also used when performing advanced numerical analysis using, for example, random finite element method (RFEM). Such analyses are carried out by incorporating the inherent and spatial variability of the property and are used to study the influence of the spatial variability of the soil or DCM on the geosystem under analysis. For example, the below figure, obtained from Pittaro (2022), present a cross section of a deep excavation where DCM is used as stabilization method below the final excavation level (Figure 2a). Figure 2b shows two contour plots of the DCM's strength where random realizations were carried out using different values of SoF in horizontal and vertical direction.

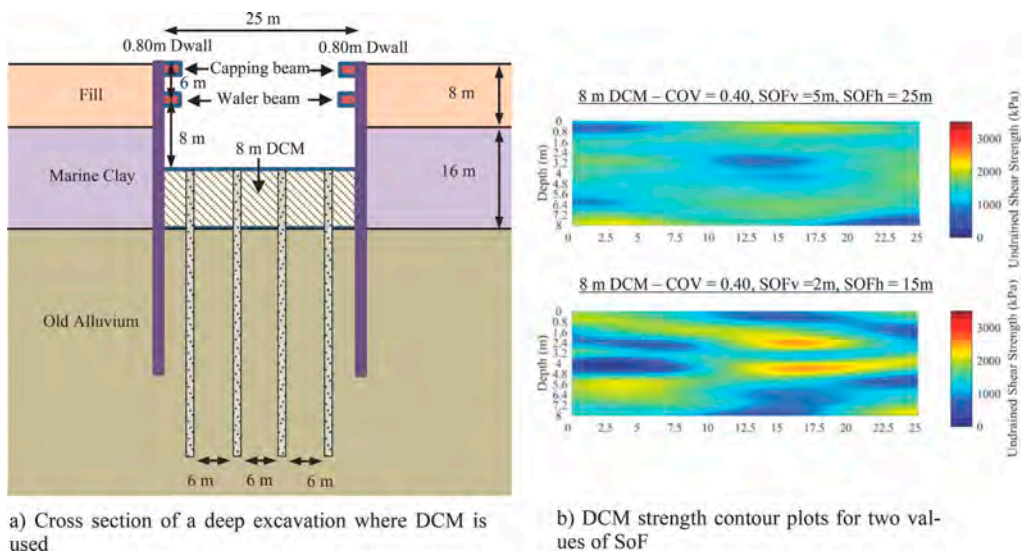


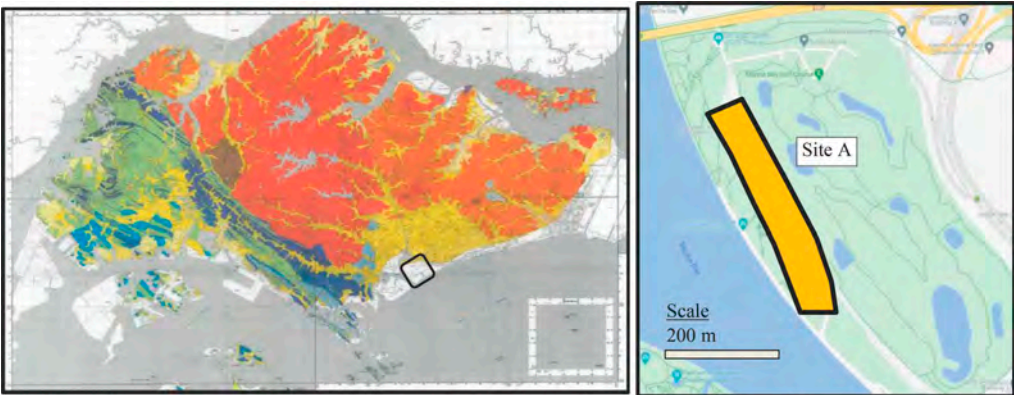
Figure 2. Example of a deep excavation where DCM is used below the formation level.

This paper presents results of SoF obtained from 5500 unconfined compressive tests obtained from over 700.000 m³ of in situ deep soil mixing (DSM) retrieved from a project in

Singapore. In this paper, DSM's horizontal and vertical SoF are obtained, and some recommendations are then drafted regarding the use of such values in design parameters selection.

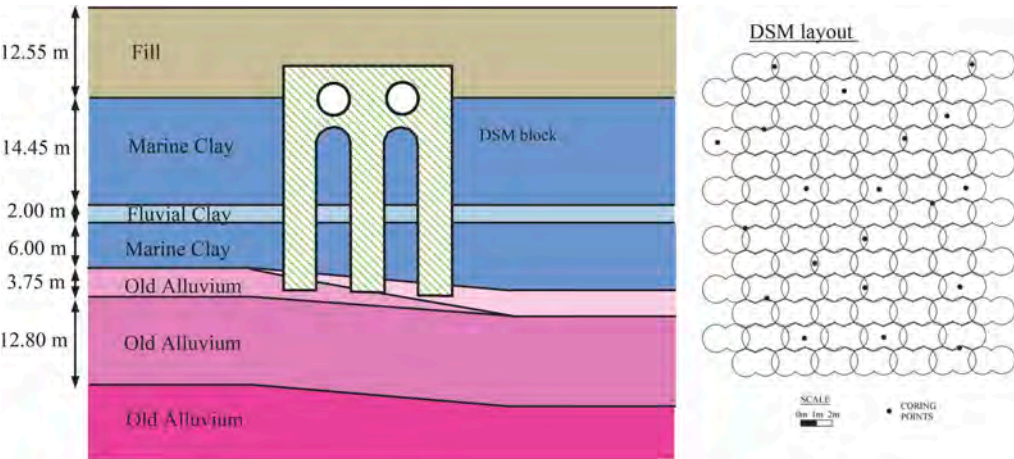
2 PROJECT IN THE SOUTH CENTRE AREA OF SINGAPORE

This section briefly describes a project in the south center area of Singapore, marked as site A in Figure 3, where DCM was used. Figure 3-b shows a close-up view of the locations and sizes of site A relative to the East Coast Parkway (ECP), Marina Coastal Expressway (MCP), Marina Bay Golf Course and the Marina East Development. In this project, circular tunnels were proposed in an underground area predominantly of soft clays of the marine clay where ongoing consolidation was occurring. DSM was then proposed to be installed as a mitigation measure to reduce unwanted consolidation settlement on the circular train tunnels. Moreover, the DSM block served as bearing layer for foundation piles of a future development at the ground level. Figure 4-a below shows the cross section of the DSM block which is embedded in soft clay and sit in stiff old alluvium. Figure 4-b shows a localized layout of the DSM with coring points which are used for sample retrieval.



a) Overview of the site locations superposed on the Singapore geological map b) Locations of the site A

Figure 3. Location of the site under study in this paper.



a) Cross section of DSM block and tunnels b) DSM layout with coring points

Figure 4. Typical geological profile at site A.

Figure 5 below presents the typical geological profile at the site A which comprises of extensive fill materials and reclaimed land deposits overlying a sequence of under-consolidated to normally consolidated, marine clays and fluvial sediments, collectively known as the Kallang Formation. Old alluvium (OA) formation, which is predominant of dense to very dense silty to clayey sand, is encountered below the Kallang formation as presented in Figure 5.

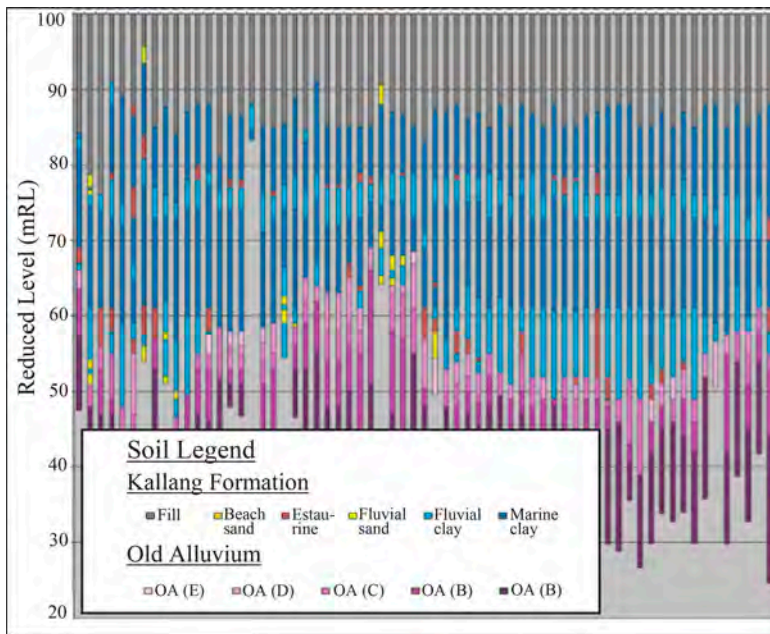


Figure 5. Typical geological profile at site A.

3 LABORATORY TESTING RESULTS AND SPATIAL VARIABILITY ANALYSES

In Site A, cement-treated soil formed by DSM was installed starting from the top of the Kallang formation to 1m embedment into the old alluvium formation. Over 1300 coring locations were drilled through the DSM columns to obtain cement-treated soil samples, from which 5500 UCS tests were carried out. For each coring points, at least 4 samples were subjected to unconfined compressive testing. Figure 6-a shows the UCS results vs sample depth, in this plot is clear that majority of the samples falls within a range between 1.8 MPa and 9.0 MPa with a sample average of 4.4 MPa.

The horizontal scale of fluctuation is evaluated separately for each of the 2m thick sublayers shown on Figure 6-a. In order to calculate the SoF, autocorrelation function fitting is used in this paper. The scale of fluctuation is estimated by fitting a theoretical autocorrelation function P to the sample autocorrelation coefficients. The single theoretical exponential model defined as follows is adopted:

$$P(\tau) = \exp(-2|\tau|/\theta) \quad (4)$$

where τ is the lag distance between two points and θ is the scale of fluctuation. The sample autocorrelation coefficient is calculated using:

$$P(\tau_j) = \frac{1}{\sigma^2 k} \sum_{i=1}^{k-j} (X_i - \mu)(X_{i+j} - \mu), \quad j = 0, \dots, k-1 \quad (5)$$

where $P(\tau_j)$ = sample correlation coefficient between two points separated by τ_j ; σ^2 = sample-variance of data; μ = sample mean of data; k = total number of measurement points; and i = total number of pairs of points separated by lag τ_j .

Figure 6-b depicts an example of the autocorrelation decay vs horizontal distance for the UCS results for one vertical layer (i.e. 70-72 mRL).

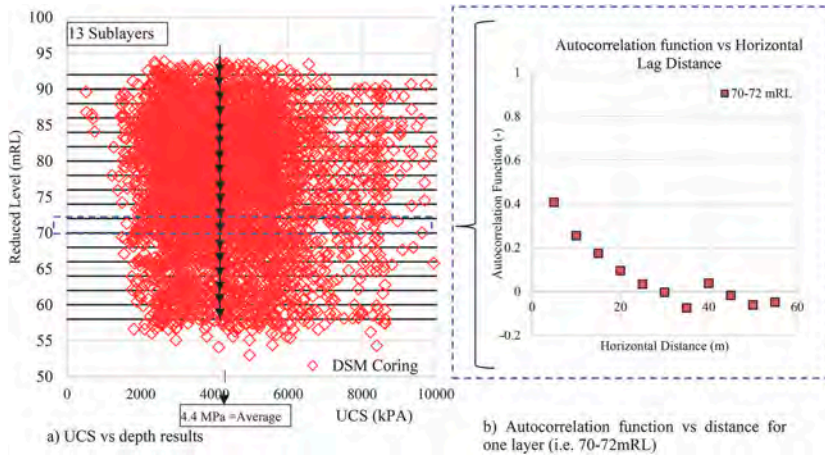


Figure 6. UCS testing results with one example of definition of autocorrelation function vs horizontal distance.

Moreover, to compute the vertical SoF, additional UCS were carried out from five full-cored 25m thick DSM. Samples every 1m vertical spacing were then obtained and tested for each coring point resulting in total of 125 additional tests (i.e. 25 tests per coring points time 5 coring points). A scheme of one coring point is shown on Figure 7. Within each one-meter core length, one sample was obtained and tested and therefore the vertical SoF was computed using 1m. vertical lag distance.

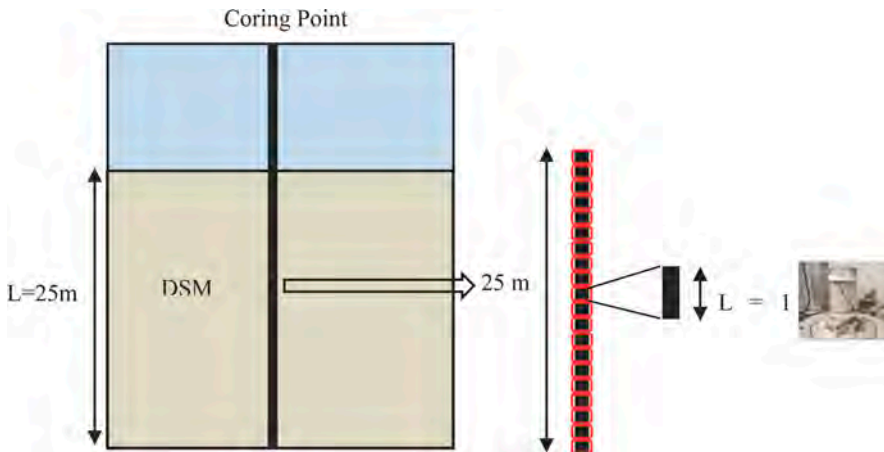


Figure 7. Sketch of coring, sampling and testing to obtain the vertical SoF.

Figure 8-a plots the UCS results vs reduced level of the five coring points while Figure 8-b shows the result of the autocorrelation function decay vs distance for one of the coring points.

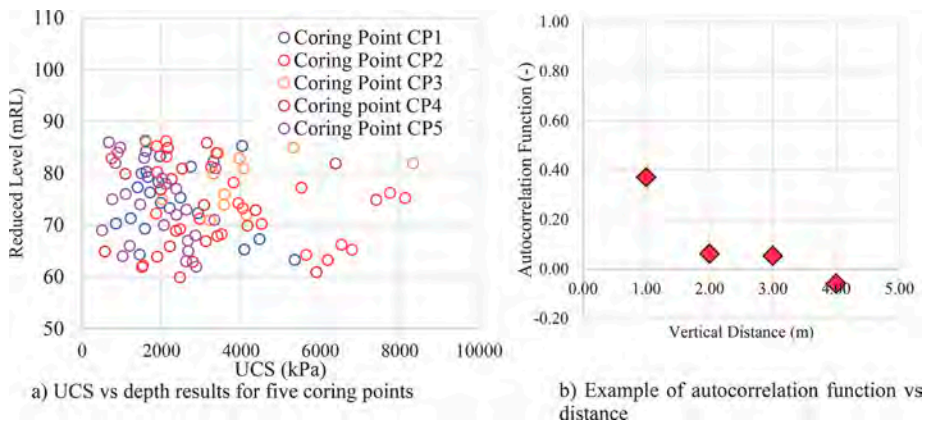


Figure 8. UCS testing results and one example of autocorrelation function decay.

Figure 9 summarizes the results presented previously. Figure 9-a plots the autocorrelation function results for all the 13 sublayers presented in Figure 6-a and are used to derive the range of horizontal scales of fluctuation which are representative of the horizontal spatial variability of Site A. The estimated minimum, mean and maximum estimated autocorrelation functions (marked as E.A.F lines) are plotted in Figure 9-a. Using the single autocorrelation function, the fitted horizontal scale of fluctuation ranges from 5m to 20m for Site A. The mean exponential autocorrelation function (E.A.F.) is obtained for a horizontal scale of fluctuation equal to 10m.

Similarly, Figure 9-b plots the autocorrelation function results for all the 5 vertical coring points. The results plotted are used to derive the range of vertical scales of fluctuation. The estimated minimum, mean and maximum estimated autocorrelation functions (marked as E.A.F lines) are plotted in Figure 9-b. Using the single autocorrelation function, the fitted vertical scale of fluctuation ranges from 0.5m to 3.5m for Site A. The mean exponential autocorrelation function (E.A.F.) is obtained for a horizontal scale of fluctuation equal to 1.5m.

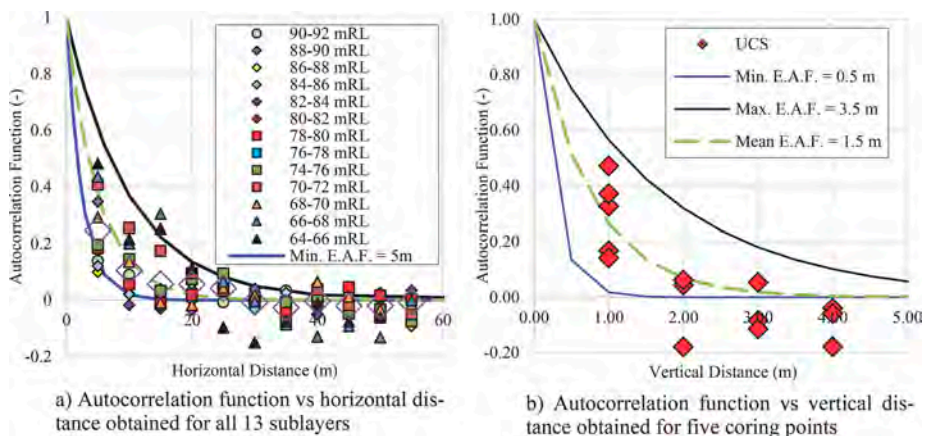


Figure 9. Autocorrelation function vs distance obtained in horizontal and vertical direction.

Information about the SoF of DCM from previous projects is generally limited, in the next paragraph some comparison with some available research is presented. The values obtained for the vertical SoF are within the range presented by Honjo (1982) for soil cement admixtures (i.e. between 0.80 and 8.0m). On the other hand, the horizontal SoF values are generally lower than the results obtained by Navin (2005) and He (2019) for DCM, which range from 24m to 40m.

Among the differences with the present study, Navin (2005) and He (2019)'s results are obtained for datasets with higher coefficient of variability and the SoF is obtained from samples with generally higher horizontal separation which might result in reduced precision in the calculation of the horizontal SoF. Honjo (1982), highlighted that the SoF depend on the nature of the soil and the construction techniques employed to install the cement treated soil, therefore different results are expected for DCM installed using different techniques in distinct in situ ground condition. To have a better understanding of the obtained results, Figure 10 below presents the average horizontal and vertical SoF obtained previously for randomly generated values of UCS.

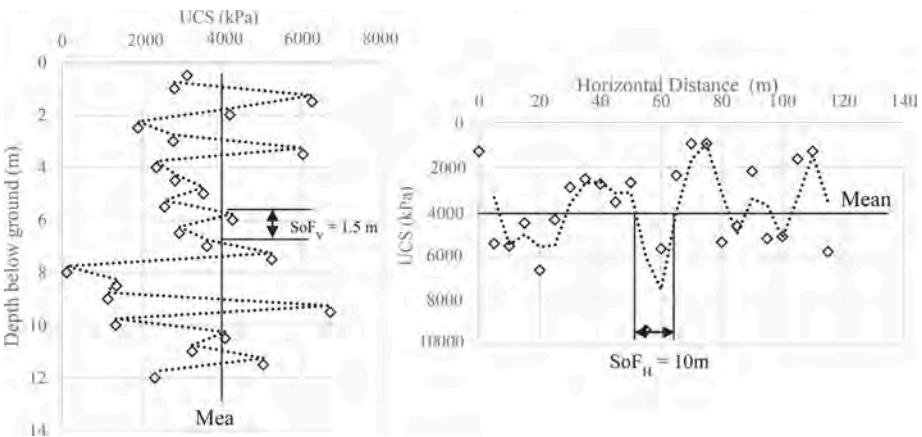


Figure 10. Random UCS values obtained using the average horizontal and vertical SoF.

4 USE OF SOF IN DESIGN AND MOVING FORWARD

Deep cement mixing has been used for over decades and information about its intrinsic variability (coefficient of variability) is widely available, however, information about the SoF is more limited in number. As presented in Equation 1, the variability of the soil and cemented treated soils can be defined a combination of the intrinsic variability and the spatial variability. Currently, available design codes do not specifically use the SoF of the ground to define design parameters, however some codes acknowledge the importance of the extent of the zone of failure. For example, Eurocodes (CEN, 2004) specify that, *if statistical methods are used, the characteristic value should be derived such that the calculated probability of a worse value governing the occurrence of the limit state under consideration is not greater than 5%. It also added that a cautious estimate of the mean value from a limited set of geotechnical parameter values should be based on a confidence level of 95%. Where local failure is concerned, the 5th fractile may be used as a cautious estimate.* Eurocodes, hence, acknowledges that, if local failure is concerned, a design value close to the minimum (i.e. 5th fractile) should be used, while if global failure is concerned, a value close to the mean (i.e. 50th fractile) should be selected. On this regard, by defining the parameters using a methodology that includes both the SoF and the failure mechanisms, engineers could account directly with the principle stated in Eurocode. In such case, lower l/SoF ratio will result in higher design parameters (where l is the failure length). This is because there will be more frequent fluctuations of the property around the mean on the length of failure. On the contrary, if higher values of l/SoF are obtained, the opposite occurs, i.e. lower values of design parameters should be obtained. This is more explicit in Equations 2 and 3 where higher values of Γ^2 (and therefore of CoV in equation 1) will be obtained for higher SoF.

The authors believe that considering the spatial variability in deep cement mixing will result in a parameters selection which is less onerous than current practice. This is true considering that the current practice for design parameters selection for cement treated ground usually

range between the 0 and 20th fractile (Pittaro, 2022). Figure 11 below presents a UCS histogram which is obtained from the data presented in Figure 6, where the values pertinent to the 0th and 50th fractile are highlighted. As previously mentioned, if the I/SoF ratio is considered on the parameter selection, the reduction of this ratio would imply an increment on the design parameters and vice versa. The histogram presented in Figure 11 depicts this principle.

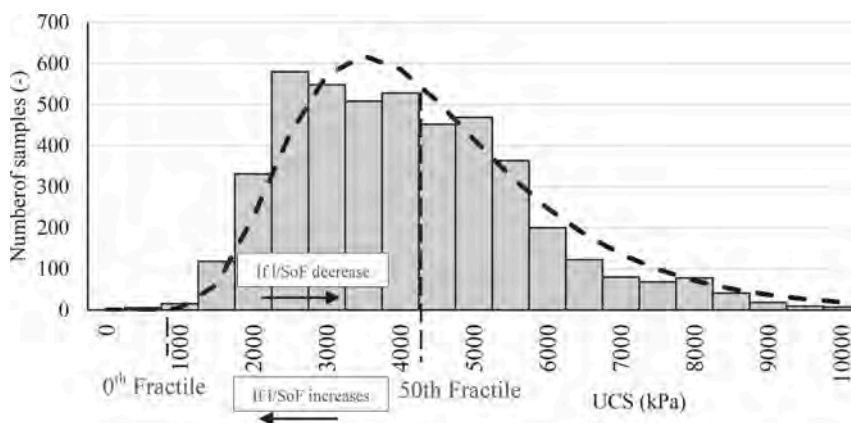


Figure 11. UCS histogram for site A.

5 CONCLUSION

Properties of Ground Improvement using Deep Cement Mixing (DCM) are commonly highly variable in intensity and in spatial distribution, this paper presents spatial variability results obtained from laboratory tests carried out from samples acquired from in situ DCM. Currently, there are not much information regarding DCM values of SoF therefore additional publications (such as this one) are needed to improve the state of knowledge of this parameter. Moreover, the use of SoF can help with the selection of design parameters of DCM leading to a more sustainable use of such material. On this regard some ideas were presented with the implications of the use of this parameter in a typical DCM's strength histogram.

REFERENCES

- Cami, B., Javankhoshdel, S., Phoon, K.-K., and Ching, J. (2020). Scale of Fluctuation for Spatially Varying Soils: Estimation Methods and Values. *ASCE-ASME Journal of Risk and Uncertainty in Engineering Systems, Part A: Civil Engineering*, 6(4), 03120002.
- Nie (2016). Scale of Fluctuation for Geotechnical Probabilistic Analysis
- Phoon, K. K., and Kulhawy, F. H. (1999). Characterization of geotechnical variability. *Canadian Geotechnical Journal*, National Research Council of Canada, 36(4), 612–624.
- Kasama, K., Whittle, A. J., and Zen, K. (2012). Effect of spatial variability on the bearing capacity of cement-treated ground. *Soils and Foundations*, Elsevier, 52(4), 600–619.
- Pittaro, G. (2022). A sustainable design framework incorporating the statistical and spatial variability of cement-treated soils for use in excavation support. Doctoral dissertation, National University of Singapore
- Pan, Y., Shi, G., Liu, Y., and Lee, F. H. (2018). Effect of spatial variability on performance of cement-treated soil slab during deep excavation. *Construction and Building Materials*, 188, 505–519.
- Honjo, Y. (1982). Probabilistic approach to evaluate shear strength of heterogeneous stabilized ground by deep mixing method. *Soils and Foundations*, Elsevier, 22(1), 2338.
- Navin, M. P., and Filz, G. M. (2005). Statistical Analysis of Strength Data from Ground Improved Columns. *Deep Mixing'05 International Conference on Deep Mixing Best Practice and Recent Advances*, 145–154.
- He, L. (2018). Spatial Variability in Deep Soil Mixing – Centrifuge Model and Field Data Study. NUS Thesis.
- CEN. (2004). Eurocode 7 geotechnical design.

Flow and filtration characteristics of bentonite slurry containing silt clay

S. Qin

College of Civil Engineering and Architecture, Xinjiang University, Urumqi, China
State Key Laboratory of Internet of Things for Smart City & Department of Civil and Environmental Engineering, University of Macau, China

Q.C. Lan

China Civil Engineering Construction Corporation, Beijing, China

W.H. Zhou

State Key Laboratory of Internet of Things for Smart City & Department of Civil and Environmental Engineering, University of Macau, China

ABSTRACT: Due to economic and environmental concerns, optimizing the reuse and minimizing disposal of used bentonite slurry are imperative in geotechnical engineering. Despite the desanding process, the slurry may retain silt clay-size soil particles that are difficult to eliminate. This presents a challenging problem in soil excavations. Hence, it is imperative to assess the adaptability of the slurry containing silt clay soils. In this study, water–bentonite–kaolin slurries with varying kaolin contents were first prepared. The rheological properties of these slurries were assessed using a concentric cylinder rheometer, and the hydraulic properties of the resulting cakes were tested through static pressure filtration. The results indicate that adding a small amount of kaolin did not notably alter the rheological properties. A significant increase in yield point and viscosity was observed only at high kaolin solid content. Higher-density slurries tend to form thicker filter cakes with a denser structure. Furthermore, the implications for engineering practice were also provided.

Keywords: bentonite slurry, kaolin, rheological property, filtration

1 INTRODUCTION

Bentonite slurry, a mixture of bentonite powder and water, finds extensive use for temporary support and cuttings transport in various construction applications, including diaphragm walls, boreholes, and mechanized tunnels (Morgenstern and Amir-Tahmasseeb 1965; Farmer and Attewell 1973; Qin et al. 2023c). Its application is particularly crucial in scenarios involving highly permeable ground with limited self-supporting capacity.

During excavation, bentonite slurry is injected into the natural soil and infiltrates the voids and channels between soil particles. A low-permeability barrier, often referred to as a “filter cake”, is intended to be formed at the liquid-soil interface. By establishing this barrier, the fluid pressure can effectively counter external pressures originating from both the soil and groundwater (Bezuijen et al. 2006; Min et al. 2013). The flow and filtration behavior are two important aspects that determine the adaptability of bentonite slurries (Nguyen et al. 2012; Qin et al. 2023a; Qin et al. 2023b). For example, the Bingham plastic model that features finite stress to initiate flow is normally used to describe the flow behavior of bentonite slurries (Choo and Bai 2015; Xu and Bezuijen 2019), as expressed in Equation (1).

$$\tau = YP + PV\dot{\gamma} \quad (1)$$

where τ = shear stress; $\dot{\gamma}$ = shear rate; YP = yield point; PV = plastic viscosity. An unavoidable reality is the inevitable mixing of bentonite slurry with soils, posing a challenge to its reusability. Despite undergoing desanding processes, the slurry may retain silt and clay-size soil particles (FPS 2006). This retention can alter the slurry's density and adaptability, particularly when excavating through soils with high clay content, as their particle size distribution may overlap with that of the bentonite.

This study experimentally assesses the flow and pressure filtration characteristics of bentonite slurry with varying silt clay content. The implications of the test results for excavation practices are discussed.

2 EXPERIMENTS

2.1 Slurry preparation

An activated sodium bentonite, IBECO[®] S, universally employed as a support medium for borehole and diaphragm wall constructions, was selected for this study. The powdered kaolin from IMERYS company was chosen as an additive for the bentonite slurry. The particle size distributions of bentonite and kaolin were analyzed using a laser particle size analyzer (MS3000, Malvern Instruments, UK) after dispersing them in water, as shown in Figure 1. It can be seen that most kaolin particles fall into the silt clay group.

The bentonite was initially added to tap water at a concentration of 50 g/l (50g bentonite in 1000 ml water). The resulting water-bentonite slurry underwent high-speed mixing at 11,000 rpm using a Hamilton Beach mixer for 20 min, followed by a 24-h hydration period (API 2003). Before application, the slurry underwent additional stirring at the same speed, incorporating a specific amount of kaolin to achieve the desired density. The component dosages for each element in the slurry are detailed in Table 1.

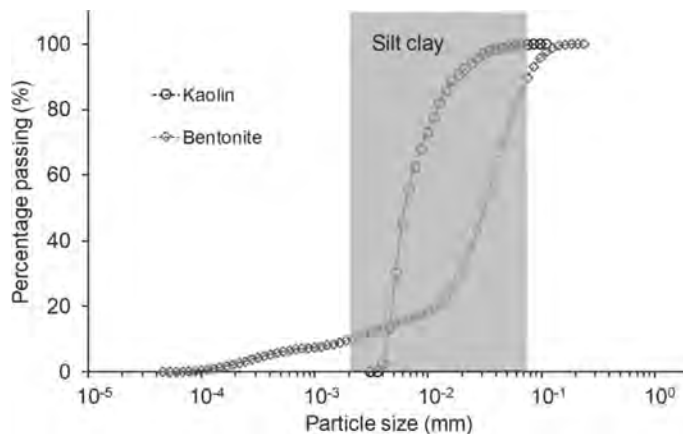


Figure 1. Particle size distributions of bentonite and kaolin used in the study.

Table 1. The component dosages for each element in the slurry.

Test no.	Bentonite (kg)	Kaolin (kg)	Water (kg)	Density (kg/m ³)
50-1031	50	0	1000	1031
50-1050	50	32	1000	1050
50-1100	50	119	1000	1100
50-1200	50	310	1000	1200

2.2 Rheological measurement

To characterize the flow behavior of the slurry, rheological measurements were implemented using a digital rheometer equipped with a concentric cylinder system from the Fann company (Figure 2(a)). The rheometer features a rotor with a smooth inner wall (diameter: 36.83 mm), a bob with an outer diameter of 34.49 mm, a torsion spring, and a stainless-steel sample cup.

Each measurement involved pouring about 350 ml of the slurry into the sample cup. The slurry's flow curve was established by applying six controlled shear rates $\dot{\gamma}$ (1021.38, 510.69, 340.46, 170.23, 10.21, and 5.11 s^{-1}) at around 20 \square . These shear rates correspond to the pre-programmed rotational speeds (600, 300, 200, 100, 6, and 3 rpm) in the used rheometer.

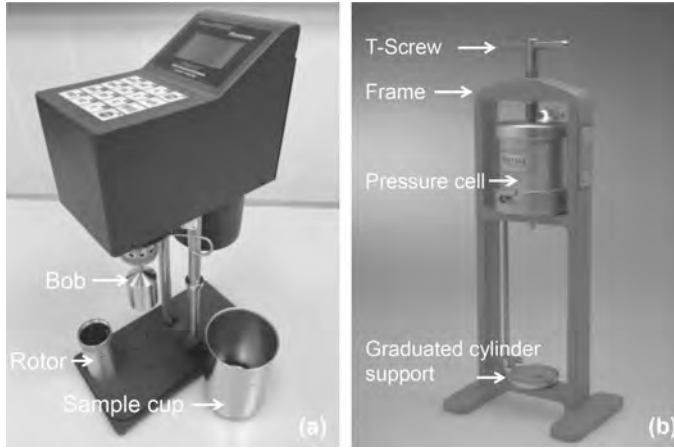


Figure 2. Setups used in the study: (a) Rheometer; (b) Filter press.

2.3 Modified fluid-loss test

The modified fluid-loss test, adapted from the standard API filter press test for assessing filtration behavior and filter cake-building characteristics of drilling fluid, utilized the Series 300 API LPLT Filter Press by Fann company. Comprising a cylindrical pressure cell, frame, filter paper as the medium, and a graduated cylinder for filtrate measurement (Figure 2(b)), this apparatus allows estimation of the filter cake's hydraulic conductivity k_c through the incorporation of cake filtration theory and Darcy's law (Chung and Daniel 2008):

$$k_c = \frac{\beta \gamma_w}{2A^2} \left(\frac{P_0 t}{V^2} \right)^{-1} \quad (2)$$

where γ_w = unit weight of water; A = filtration area (45.6 cm^2 in this study); P_0 the used pressure (100 kPa in this study); V = filtrate volume; β = constant of proportionality, which is calculated by:

$$\beta = \frac{AL_c}{V} = \frac{C_m \rho_w (1 + e_{ave})}{(1 - C_m) \rho_s - e_{ave} C_m \rho_w} \quad (3)$$

where L_c = thickness of the filter cake; C_m = mass fraction of bentonite and kaolin in the slurry; ρ_w = water density; ρ_s = density of bentonite and kaolin; e_{ave} = average void ratio of the filter cake.

For each test, 350 ml of the prepared slurry was added to the cell, and a constant pressure was applied. Filtrate volumes were recorded every 5 min. After 1 hour, the thickness of filter cake was measured. After that, water content and void ratio were calculated based on the cake's weights before and after drying.

3 RESULTS AND ANALYSIS

3.1 Rheological properties

Figure 3 illustrates the flow curves of tested slurries with different densities resulting from various clayey silt contents. In general, all slurries demonstrated non-Newtonian flow behavior under shearing conditions, with higher-density slurries exhibiting significantly increased shear stress. The shear-thinning behavior of slurries can be observed due to the presence of clay particles (bentonite and kaolin). After completely dispersed in water, the electrostatic forces between the negatively charged surfaces of clay platelets arrange the specific orientation. The shear forces cause the platelets to align in the direction of flow, allowing them to slide past each other more easily. Furthermore, the Bingham plastic model was found to be well-suited for fitting the measured data points, effectively capturing the flow behavior of bentonite and kaolin slurries to a considerable extent.

Two crucial rheological parameters—yield point and apparent viscosity—were calculated, as depicted in Figure 4. It is evident that the addition of a small amount of kaolin to the bentonite slurry in the 50-1050 test did not significantly alter the yield point and apparent viscosity. This can be attributed to the non-swelling nature of kaolin. The substantial increase in yield point and viscosity is only observed at high kaolin solid content. In practical applications, higher viscosity and yield point of drilling fluids can be advantageous for reducing soil permeability near the excavation and effectively suspending cuttings. However, it will lead to increased energy consumption during transport.

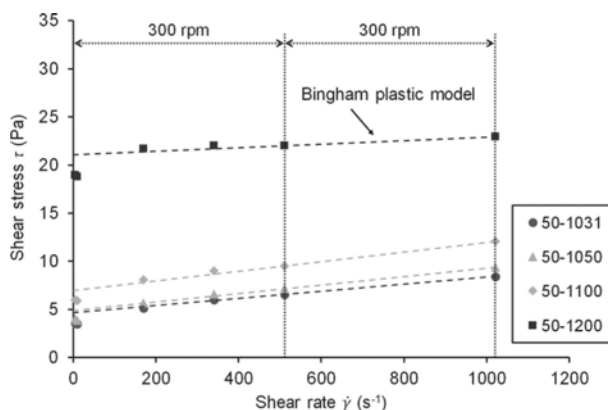


Figure 3. Flow curves of water-bentonite-kaolin slurries with varying densities.

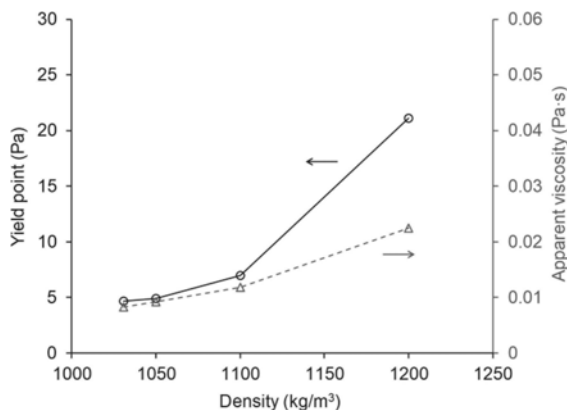


Figure 4. Rheological parameters of water-bentonite-kaolin slurries with varying densities.

3.2 Filtration characteristics

Under static pressure filtration, the slurry is dewatered as the soil particles were screened onto the filter paper, resulting in a cake of relatively low permeability. Figure 5 shows a plot of cumulative filtrate volume versus time. Each test exhibited two distinct stages characterized by fast and slow filtration velocities. The fast stage, often referred to as the mud spurt, is primarily attributed to the finer particles passing through the filter paper until its pores become plugged (Talmon et al. 2013). It can be seen that a higher silt clay content in the slurry has the potential to decrease the filtrate.

The validity of Equation (2) from Chung and Daniel (2008), which assumes the $P_{0t}/V-V$ graph passing through the origin, was assessed by plotting the data points of P_{0t}/V against V in each test, as shown in Figure 6. The strong linear relationship observed in each test confirms its validity.

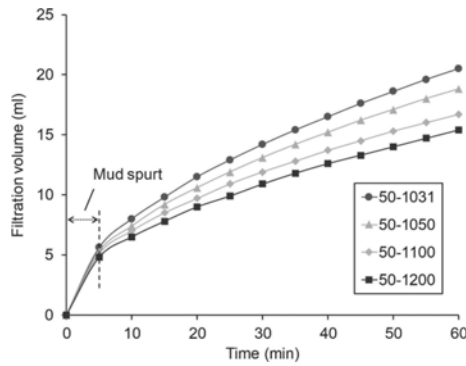


Figure 5. Filtrate volume variations of the slurries with time.

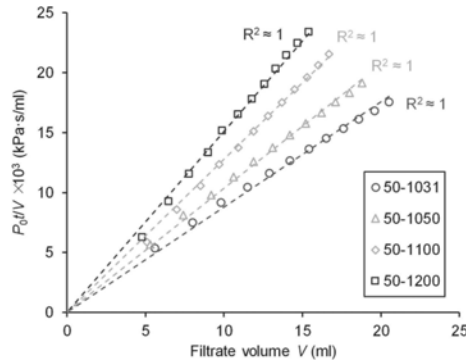


Figure 6. $P_{0t}/V-V$ graphs from the modified fluid-loss tests.

Table 2. Measured hydraulic properties of the filter cake in each test.

Test no.	Measured thickness (cm)	Average void ratio (-)	Hydraulic conductivity (m/s)
50-1031	2.0	18.0	6.5×10^{-9}
50-1050	2.6	10.3	5.1×10^{-9}
50-1100	3.0	6.5	6.6×10^{-9}
50-1200	3.9	3.4	7.8×10^{-9}

Table 2 summarizes the measured hydraulic properties of the filter cake from each modified fluid-loss test. The thickness increased with a higher silt clay content in the slurry, likely

attributed to the elevated density of solid particles in the mixture. In practice, thicker cakes could enhance safety during excavations by providing increased protection against potential damage from cutting tools. The reduction in the average void ratio suggests that higher-density slurries are prone to expelling water from the cake, leading to a densification of its inner structure. At the pressure of 50 kPa, the hydraulic conductivities did not exhibit significant variations among the tests; however, they consistently reached an extremely low level ($\sim 10^{-9}$ m/s).

4 CONCLUSIONS

In this study, we investigated the flow and filtration characteristics of bentonite slurries containing varying amounts of silt clay (kaolin) using rheometer tests and modified fluid-loss tests. From the test results, the following conclusions can be drawn: The addition of a small amount of kaolin to bentonite slurry, owing to kaolin's non-swelling nature, did not significantly alter the rheological properties. The notable increase in yield point and viscosity was observed only at high kaolin solid content, offering benefits in stabilizing unexcavated soils and suspending cuttings. However, it may be energy-consuming during transport. Higher-density slurries tend to form thicker filter cakes with a denser structure, enhancing safety during excavations by providing increased protection against potential damage from cutting tools.

ACKNOWLEDGEMENTS

The research work was funded by The Science and Technology Development Fund of Macau SAR (Grant No. 0035/2019/A1 and 001/2024/SKL), National Natural Science Foundation of China (Grant No. 52022001), and Guangdong Provincial Department of Science and Technology (Grant No. 2019B111106001).

REFERENCES

- API (American Petroleum Institute). 2003. Recommended practice standard procedure for field testing water-based drilling fluids, 13B-1, 3rd ed. American Petroleum Institute, Washington, DC, USA.
- Bezuijen, A., Pruiksma, J.P., van Meerten, H.H. 2006. Pore pressures in front of tunnel, measurements, calculations and consequences for stability of tunnel face. In: Bezuijen, A., van Lottum, H. (Ed.), *Tunnelling: A Decade of Progress*. Taylor & Francis, Leiden, pp. 27–33.
- Choo, K.Y. & Bai, K. 2015. Effects of bentonite concentration and solution pH on the rheological properties and long-term stabilities of bentonite suspensions. *Applied Clay Science*, 108: 182–190.
- Chung, J. & Daniel, D.E. 2008. Modified fluid loss test as an improved measure of hydraulic conductivity for bentonite. *Geotechnical Testing Journal*, 31: 243–251.
- Farmer, I.W. & Attewell, P.B. 1973. Ground movements caused by a bentonite-supported excavation in London Clay. *Géotechnique*, 23: 576–581.
- FPS (Federation of Piling Specialists). 2006. Bentonite support fluids in civil engineering, 2nd edn. Bromley, UK: Federation of Piling Specialists.
- Min, F., Zhu, W., Han, X. 2013. Filter cake formation for slurry shield tunneling in highly permeable sand. *Tunnelling and Underground Space Technology*, 38: 423–430.
- Morgenstern, N. & Amir-Tahmassebi, I. 1965. The stability of a slurry trench in cohesionless soils. *Géotechnique*, 15: 387–395.
- Nguyen, T.B., Lee, C., Lim, J., et al. 2012. Hydraulic characteristics of bentonite cake fabricated on cutoff walls. *Clays and Clay Minerals*, 60: 40–51.
- Qin, S., Cheng, Y., Huang H., et al. 2023a. Pressure infiltration behavior and fluid loss of bentonite slurry: A comparative study of two bentonite slurries. *Canadian Geotechnical Journal*, Just-in.
- Qin, S., Cheng, Y., Zhou, W.H. 2013b. State-of-the-art review on pressure infiltration behavior of bentonite slurry into saturated sand for TBM tunneling. *Smart Construction and Sustainable Cities*, 1:14.
- Qin, S., Xu, T., Zhou, W.H., et al. 2023c. Infiltration behaviour and microstructure of filter cake from sand-modified bentonite slurry. *Transportation Geotechnics*, 40: 100963.
- Talmon, A.M., Mastbergen, D.R. Huisman, M. 2013. Invasion of pressurized clay suspensions into granular soil. *Journal of Porous Media*, 16: 351–365.
- Xu, T. & Bezuijen, A. 2019. Pressure infiltration characteristics of bentonite slurry. *Géotechnique*, 69: 364–368.

Deformation of surrounding soil mass of subway tunnel subjected to traffic loads considering principal stress rotation

W. Wu & Y. Yang

Department of Civil Engineering, University of Nottingham, Ningbo, China

J. Wang

School of Highway, Chang'an University, Xi'an, Shanxi, PR China

ABSTRACT: Under complex loads such as traffic loads, the foundation soil of transportation infrastructure will bear Principal Stress Rotation (PSR) and ignoring PSR may underestimate the long-term deformation of the foundation soil. However, due to the loading limitations of experimental equipment, traditional experimental research mainly used triaxial apparatus without considering PSR. This article uses the finite element method to obtain stress paths in the soil element directly below the tunnel under subway traffic loads, considering PSR. Based on these paths, Hollow Cylinder Apparatus (HCA) tests on Fujian ISO standard sand are conducted. The axial and shear deformation are compared. PSR significantly impacts the axial deformation but has little effect on the shear deformation. The research results help to more accurately predict the long-term deformation of tunnel surrounding soil under subway traffic loads and improve the safety and economy of the project.

1 INTRODUCTION

Under the long-term cyclic traffic load, subways, highways, and railways built on the subsoil are prone to systematic permanent settlement during operation, significantly affecting this transportation infrastructure's design life and maintenance cost. There are numerous reports of damage to transportation infrastructure due to domestic and international long-term traffic loads. For example, the settlement of Line 1 of the Shanghai Metro has been continuous since its opening in 1994, and by 2007, the maximum settlement had reached 288mm (Ng et al. 2013). Therefore, an accurate prediction of traffic-load-induced deformation is important for traffic infrastructure (Zhang et al. 2013; Yaghoubi et al. 2021; Rogers et al. 2012).

The most widely used experimental equipment for foundation soil is triaxial testing machines, which assume the traffic loads to be a cyclic vertical load applied to the specimen (Fedakar et al. 2020; Zhang et al. 2022; Aursudkij et al. 2009). However, the traffic load generates a continuous principal stress rotation (PSR) in the subsoil element (Ishihara 1983), which is significantly different from the stress path in the conventional triaxial test. The hollow cylindrical torsional shear testing machine (HCA) is invented, which enables independent control of torque, axial load, internal pressure, and external pressure and can achieve continuous rotation of the principal stress axis. Specimens subjected to repeated loads with PSR require more loading cycles to reach a steady state, resulting in a larger permanent vertical strain compared to those under cyclic loads without PSR (Thevakumar et al. 2021; Pan et al. 2021; Guo et al. 2018).

Utilizing the Finite Element Method (FEM) in this research, the complete movement process of subway trains within a typical single-track tunnel with a single hole is simulated. By analyzing the FEM results, the stress path in the soil element directly below the tunnel was obtained when the train carriage passed through the midpoint section of the FEM model. Subsequently, the HCA tests are conducted using the simulated stress path to investigate the

impact of stress path types, normal stress amplitudes, shear stress amplitudes, and other parameters on soil deformation. The research findings contribute to a deeper comprehension of the long-term deformation behavior of tunnels surrounding rock and soil under traffic loads within the engineering community. These results offer more precise guidance for the design and execution of tunnel engineering projects, ultimately resulting in enhanced economic efficiency and improved safety measures.

2 STRESS PATH DETERMINED BY NUMERICAL SIMULATION

A dynamic finite–element (FE) analysis by ABAQUS is carried out to estimate the stress of soil below the subway tunnel. A typical subway tunnel in Ningbo City under traffic loading and the FE mesh of the model are plotted in Figure 1, all FEM parameter selections are based on actual engineering or slightly simplified. The entire numerical model and the locations of the elements used to observe stress paths are marked in Figure 2(a). The stress state of soil element in subgrade under traffic loads are shown in Figure 2(b). The corresponding materials described by linear elastic parameters (as shown in Table 1) are homogeneous. The rail, track bed, and lining in FEM simulations were represented by C3D8R elements which are eight–node linear bricks with reduced integration. The model is 50 meters wide, 50 meters high, and 100 meters long. Because only the stress path is obtained, to simplify the calculation, the constitutive model of the entire model is based on an elastic model.

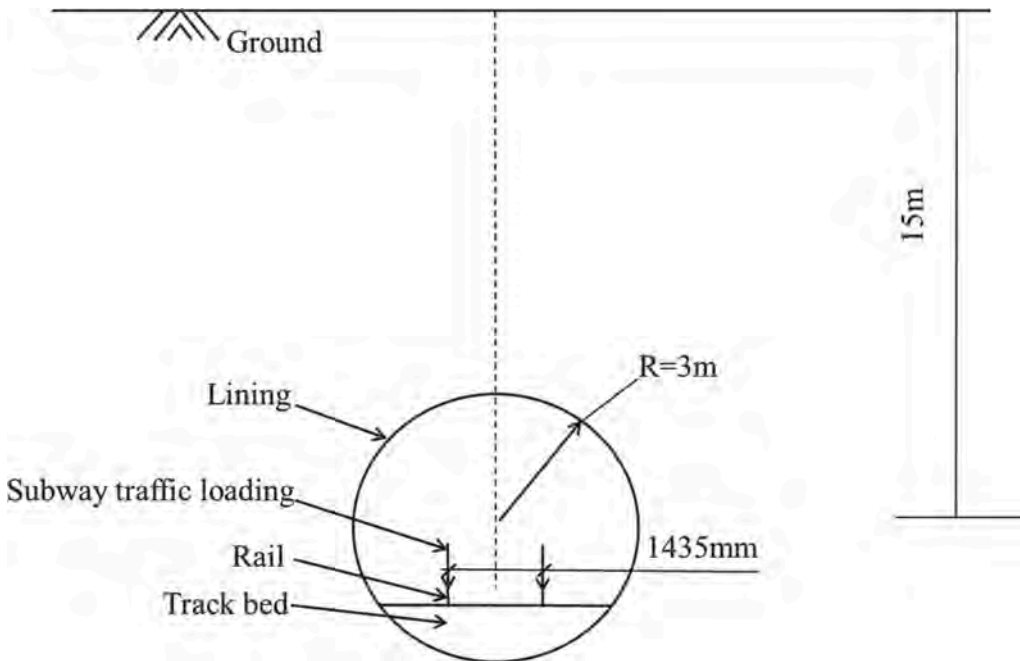


Figure 1. Typical cross-section of ningbo subway.

Four 14-ton axle loads are applied in the model based on the Ningbo subway lines. The wheel track is 2.2 m, and the fixed distance of each carriage is 12.6 m. The train speed is taken to be 80 km/h. The dynamic axle load impact factor was 1.2 when considering the irregularities of the rail or wheel. The stresses are calculated at depths of 0.5m to 3m below the subway tunnel. The simulation results are shown in Figure 3. The stress components of the subway traffic loading are shown in Figure 3(a). The calculated stresses in the $\tau_{zx} - (\sigma_z - \sigma_x)/2$ space and the rotation

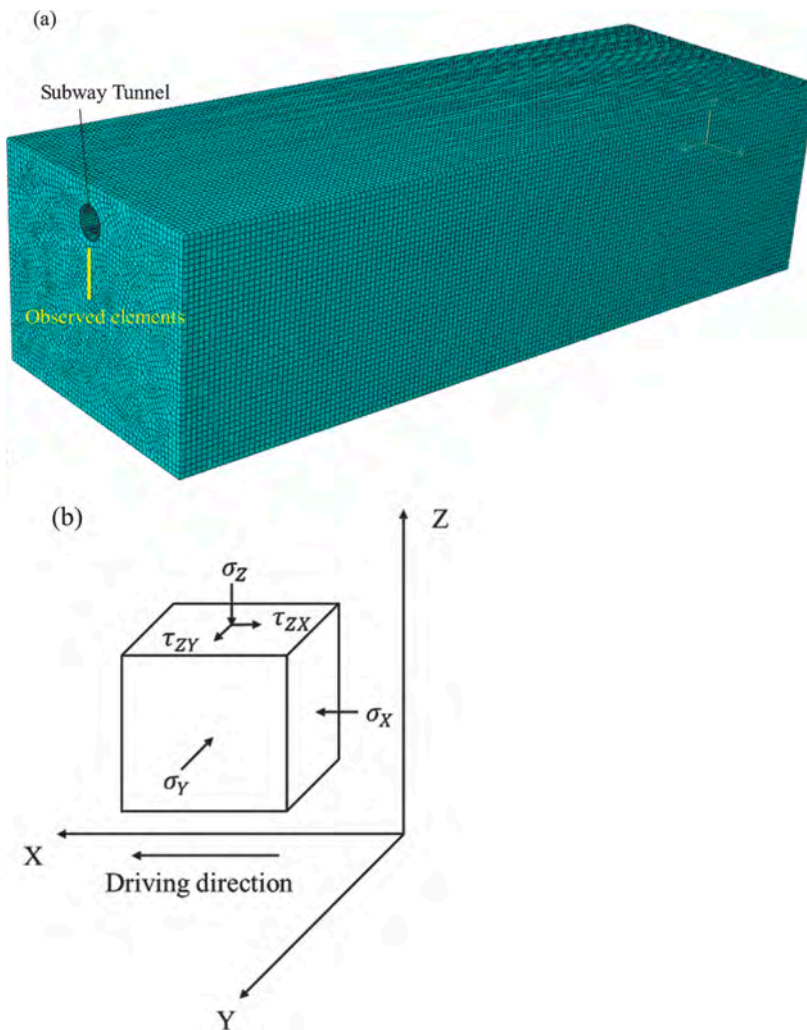


Figure 2. (a) FEM model of ningbo subway; (b) Stress state of soil element in subgrade under traffic loads.

angle of the principal stress are shown in Figure 3(b). Within one cycle, the direction of stress path movement starts from coordinate 0 and continues to move to the right along the X-axis until the end.

Table 1. Material properties in simulation.

Material	Elastic Modulus (MPa)	Density (kg/m^3)	Poisson Ratio
Sub-soil	30	2000	0.499
Rail	200000	7800	0.3
Tunnel and track bed	32500	2400	0.2

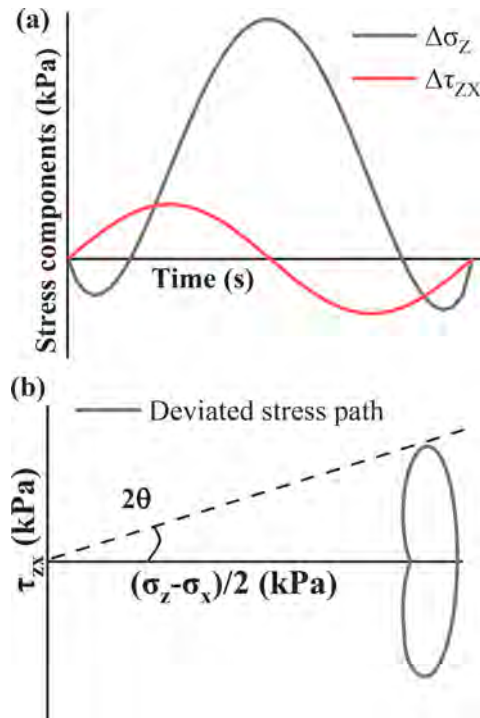


Figure 3. (a) Stress components of the subway traffic loading; (b) Deviated stress path of the subway traffic loading.

3 EXPERIMENTAL

The Hollow Cylinder Apparatus (HCA) developed by GCTS was used to conduct the tests. The apparatus used for the tests is shown in Figure 4 and consists of a triaxial cell, an axial-torsional loading system, pressure controllers, and an electronic system. The vertical loads and torques can be accurately applied independently or simultaneously using axial and rotating actuators. Three advanced digital pressure controllers are employed to apply internal pressure, external pressure, and back pressure through dewatering. This device can be used to generate multiple complicated stress paths and perform advanced Principal Stress Rotation (PSR) tests.

In this research, the Fujian ISO standard sand (ISO sand) which are produced by the Xiamen ISO Standard Sand Company of China was used. The particle sizes of ISO sands mainly range from 0.25 mm to 1 mm. And its maximum and minimum void ratios are 0.723 and 0.382, respectively. The Particle size distribution curve of the ISO sand is shown in Figure 5. All the tests are conducted at saturated state and the relative density of 68%.

Table 2 shows the cyclic test schemes. All stress values are selected from the observed elements in the numerical model as shown in Figure 2(a). As traffic loading frequencies are irregular, ranging from 0.5 to 5 Hz, 1 Hz is selected for all the tests.

4 RESULTS AND ANALYSIS

4.1 Axial strain development

Axial strain results of each test over 1,000 cycles (N) are presented in Figure. 10. From Figure 6, after 1000 cycles, the axial deformation of Test 1 and Test 2 is much smaller than



Figure 4. GCTS hollow cylinder apparatus.

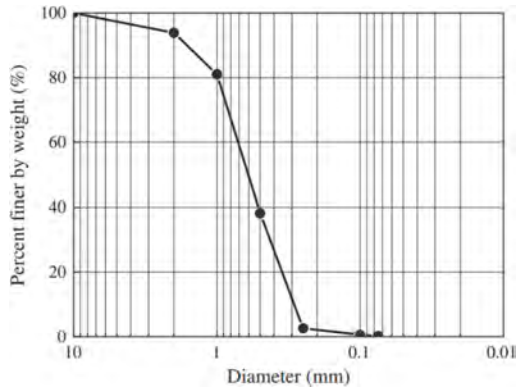


Figure 5. Particle size distribution curve of the ISO sample (Zhu et al., 2014).

Table 2. Cyclic test schemes.

Test No.	Confining pressure (kPa)	$\Delta\sigma_z$ (kPa)	$\Delta\tau_{zx}$ (kPa)
1	100	40	10
2	100	60	10
3	100	100	10
4	100	100	25

that of Test 3 and Test 4. This indicates that the amplitude of vertical stress is an important factor in the development of vertical deformation. Comparing Test 3 and Test 4, the final vertical strain of Test 4 is much greater than that of Test 3. Under the same vertical stress amplitude, the larger the rotation amplitude of the principal stress, the greater the vertical deformation.

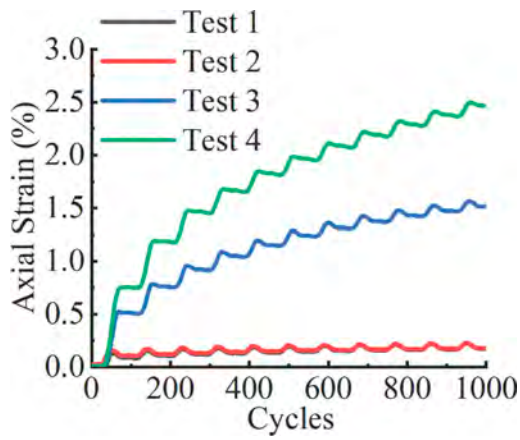


Figure 6. Axial strain development for each test.

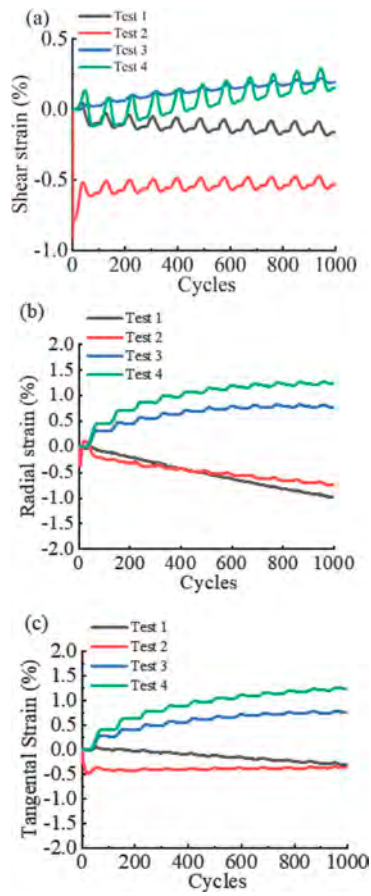


Figure 7. Strain components of the subway traffic loading: (a) Shear strain.

4.2 Strain components development

The shear strain, radial strain and tangential strain versus cycles are shown in Figure 7(a), (b), (c), respectively. Overall, compared to vertical strain, the other three strain components are generally smaller. The maximum strain is all within 1%. From Figure 7(a), it can be seen that the shear strain development curves of Test 3 and Test 4 are very close, indicating that the PSR amplitude has a relatively weak effect on the development of shear strain. From Figures 7(b) and (c), it can be seen that the radial strain and tangential strain development trends of Test 3 and Test 4 are very similar, indicating that the amplitude of PSR has an impact on the development of these two strains, and the larger the PSR, the greater the development of these two strains.

5 CONCLUSION

In this study, we used Abaqus to simulate the stress path below a typical tunnel section of Ningbo Metro when subway trains pass through the tunnel. And dynamic loading tests were conducted in HCA using the simulated stress path.

1. Directly below the tunnel, when the train passes through, the deviation stress path takes on a heart-shaped shape. The greater the rotation angle of the principal stress, the greater the vertical deformation.
2. Under the same vertical stress amplitude, the larger the rotation amplitude of the principal stress, the greater the vertical deformation.
3. The amplitude of PSR has little effect on the development of shear strain but has an impact on the development of radial and vertical strains, and the larger the PSR, the greater the development of these two strains.

ACKNOWLEDGEMENTS

This work is supported by National Natural Science Foundation of China (Project code 11872219), and Common Wealth project by Ningbo Bureau of Science and Technology (Project code 202002N3116). These supports are appreciated.

REFERENCES

- Aursudkij, B., McDowell, G.R. and Collop, A.C., 2009. Cyclic loading of railway ballast under triaxial conditions and in a railway test facility. *Granular Matter*, 11, pp.391–401.
- Fedakar, H.I., Cai, W., Rutherford, C.J. and Cetin, B., 2020, February. Evaluation of deformation behavior of sand-clay mixture under traffic loads. In *Geo-Congress 2020* (pp. 201–209). Reston, VA: American Society of Civil Engineers.
- Guo, L., Cai, Y., Jardine, R.J., Yang, Z. and Wang, J., 2018. Undrained behaviour of intact soft clay under cyclic paths that match vehicle loading conditions. *Canadian Geotechnical Journal*, 55(1), pp.90–106.
- Ishihara, K. and Towhata, I., 1983. Sand response to cyclic rotation of principal stress directions as induced by wave loads. *Soils and foundations*, 23(4), pp.11–26.
- Ng, C.W.W., Liu, G.B. and Li, Q., 2013. Investigation of the long-term tunnel settlement mechanisms of the first metro line in Shanghai. *Canadian Geotechnical Journal*, 50(6), pp.674–684.
- Pan, K., Liu, X.M., Yang, Z.X., Jardine, R.J. and Cai, Y.Q., 2021. Undrained Cyclic Response of K 0–Consolidated Stiff Cretaceous Clay under Wheel Loading Conditions. *Journal of Geotechnical and Geoenvironmental Engineering*, 147(8), p.04021078.
- Rogers, C.D.F., Hao, T., Costello, S.B., Burrow, M.P.N., Metje, N., Chapman, D.N., Parker, J., Armitage, R.J., Anspach, J.H., Muggleton, J.M. and Foo, K.Y., 2012. Condition assessment of the surface and buried infrastructure—A proposal for integration. *Tunnelling and Underground Space Technology*, 28, pp.202–211.

- Thevakumar, K., Indraratna, B., Ferreira, F.B., Carter, J. and Rujikiatkamjorn, C., 2021. The influence of cyclic loading on the response of soft subgrade soil in relation to heavy haul railways. *Transportation Geotechnics*, 29, p.100571.
- Zhang, J., Peng, J., Zhang, A. and Li, J., 2022. Prediction of permanent deformation for subgrade soils under traffic loading in Southern China. *International Journal of Pavement Engineering*, 23(3), pp.673–682.
- Zheng, L., Hai-lin, Y., Wan-ping, W. and Ping, C., 2012. Dynamic stress and deformation of a layered road structure under vehicle traffic loads: Experimental measurements and numerical calculations. *Soil Dynamics and Earthquake Engineering*, 39, pp.100–112.
- Zhu, J.F., Xu, R.Q. and Liu, G.B., 2014. Analytical prediction for tunnelling-induced ground movements in sands considering disturbance. *Tunnelling and underground space technology*, 41, pp.165–175.

Structural resilience assessment method for tunnels under seismic hazards

C.L. Zhang, D.M. Zhang & Z.K. Huang*

Department of Geotechnical Engineering, Key Laboratory of Geotechnical and Underground Engineering of Ministry of Education, Tongji University, Shanghai, China

ABSTRACT: The primary objective of this study is to provide a comprehensive resilience assessment framework aimed at evaluating the seismic resilience of tunnel engineering under earthquake disasters. The framework employs finite element software to establish numerical models tailored to specific tunnels. Subsequently, extensive numerical analyses are conducted using selected seismic inputs to develop a tunnel engineering vulnerability function concerning Peak Ground Acceleration (PGA). Ultimately, a comprehensive evaluation of the resilience is accomplished by integrating factors considering both the vulnerability and recoverability of tunnel engineering. The significance of this work lies in presenting an innovative assessment approach for the resilience of urban infrastructure, offering reliable technical support for addressing future seismic disasters.

Keywords: Tunnel, Resilience, Seismic, Fragility, Restoration

1 INSTRUCTIONS

With the continuous growth in urban demand, the construction and development of subway transportation systems are progressing more rapidly than ever before. In the past, engineers generally considered seismic design for underground structures as a non-essential step, as the damage to underground structures was thought to be relatively minor compared to aboveground structures (Hashash et al., 2001). However, severe seismic disasters shattered this confidence, rendering this perspective untenable. Taking the 1995 Great Hanshin Earthquake in Japan as an example, the earthquake caused severe damage to underground tunnels, with the Daikai station even collapsing entirely (Chen et al., 2023). In light of such incidents, conducting resilience assessments for critical hubs in urban underground transportation systems, such as subway tunnels, under seismic disasters has become crucial to prevent similar tragedies from recurring.

In the face of seismic disasters, predicting the overall reliability of subway transportation systems has become an increasingly challenging task (Chen et al., 2023). In recent years, seismic resilience theory has made significant progress, serving not only to enhance the safety of construction and operational services of subway transportation systems but also as a crucial component of seismic performance design (Psyrras et al., 2018). Seismic resilience is commonly defined as the ability of a structural system to withstand, respond to, and rapidly recover from seismic disasters (Cimellaro et al., 2010). In tunnel engineering, this concept is specifically manifested in the reduction of economic losses and infrastructure damage caused by disasters, aiming to achieve seismic design objectives that facilitate swift recovery in the aftermath. Various resilience assessment frameworks have been proposed for single or multiple disasters and have found extensive application across diverse types of infrastructure, including bridges (Argyroudis et al., 2022), transportation networks (Alipour et al., 2016), and other critical engineering structures (Panteli et al., 2016). However, as of the present literature, a resilience framework specifically tailored for tunnel engineering under seismic disasters has not considered the post-disaster recovery path. Additionally, there is an insufficient consideration of the influence of soil types on tunnel resilience.

To address the current gap between research and practical needs, this study introduces a pragmatic resilience assessment framework for tunnel engineering. The framework is

applied specifically to shallow-buried urban tunnel projects exposed to seismic disasters. In addition, the study assesses the robustness and rapid recovery capabilities of shallow-buried tunnel engineering under seismic events. It delves into an in-depth exploration of how different soil types influence the recovery capacity of tunnels and puts forth recommendations for further research. This research aims to bridge the existing disparities in the literature and meet the demands of practical applications in the field of tunnel engineering resilience.

2 TUNNELLING RESILIENCE ASSESSMENT FRAMEWORK

The resilience assessment framework for tunnel engineering proposed in this paper is primarily divided into three key components, as detailed in Figure 1. Firstly, by collecting geological and physical information related to tunnel engineering, a finite element numerical simulation is established to obtain the dynamic response results of tunnel structures under varying seismic loads. Secondly, based on the results of numerical analysis, a probabilistic relationship is established between seismic intensity indicators (IM) and the damage states of tunnel engineering. Finally, by constructing tunnel engineering loss and recovery functions, functional relationships are explicitly defined. A comprehensive evaluation of tunnel engineering resilience is achieved through the integration of these functional relationships. This resilience framework, utilizing vulnerability analysis and the establishment of functional relationships, can assess the absorptive capacity of tunnel engineering against seismic-induced damage as well as its potential for rapid recovery. These aspects will be thoroughly discussed in subsequent chapters.

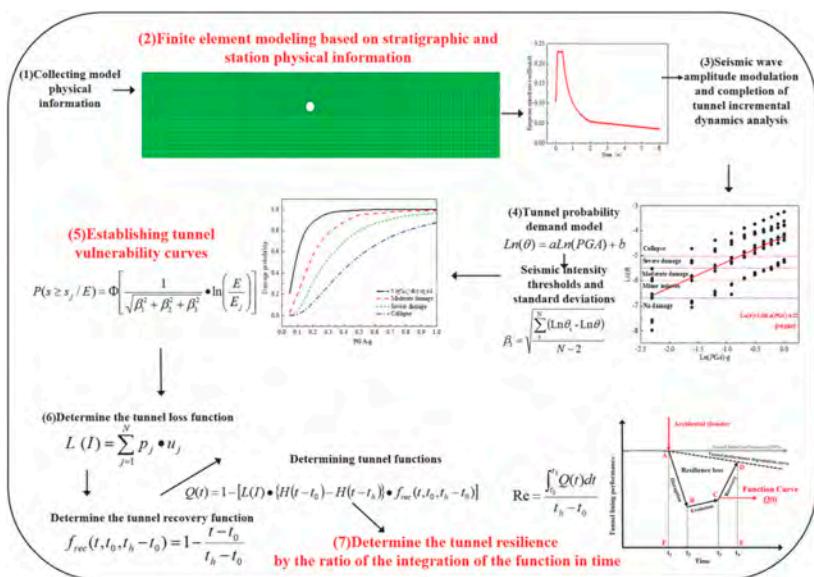


Figure 1. A framework for seismic resilience assessment of tunnels.

2.1 Vulnerability analysis

Under the seismic loading, tunnel engineering is primarily susceptible to radial convergence failure. Building upon the successful research and applications of predecessors, this paper adopts the radial convergence rate of the tunnel as a measure of damage and an engineering demand parameter. The calculation formula is expressed as follows:

$$\theta = \frac{d}{D} \tag{1}$$

In Equation (1): θ is the tunnel radial convergence rate, d is the maximum radial convergence value of the tunnel structure, and D is the tunnel diameter. Based on the previous research results, the threshold values of each damage state of the tunnel are shown in Table 1 (Wang et al., 2023).

Table 1. Damage status and radial convergence rate threshold of tunnel (Wang et al., 2023).

Damage state	No damaged	Minor damage	Moderate impairment	Serious damage
Radial convergence rate θ	$\theta < 0.6\%$	$0.6\% \leq \theta < 2.5\%$	$2.5\% \leq \theta < 4\%$	$4\% \leq \theta < 6\%$

This study also selects *PGA* as the seismic intensity indicator (Jiang et al., 2023). In seismic vulnerability analysis, it is commonly assumed that the structural dynamic response under seismic disasters follows a log-normal distribution (Hu et al., 2023). Hence, the seismic vulnerability function is formulated as follows:

$$P(s \geq s_j/IM) = \Phi \left[\frac{1}{\sqrt{\beta_1^2 + \beta_2^2 + \beta_3^2}} \cdot \ln \left(\frac{IM}{IM_j} \right) \right] \quad (2)$$

In Equation (2): P denotes the exceedance probability of a tunnel reaching a particular damage state for a given seismic intensity IM ; Φ is a standard normal distribution; IM_j is the average value of seismic intensity corresponding to different damage state thresholds of the tunnel; β_1 , β_2 and β_3 is the standard deviation characterizing the seismic uncertainty, construction quality and analysis model.

2.2 Resilience analysis

This paper adopts a widely used analytical definition to characterize this resilience, with its calculation formula as follows (Hu et al., 2023):

$$Re = \frac{\int_{T_0}^{T_2} Q(t) dt}{T_2 - T_0} \quad (3)$$

In Equation (3), R represents the tunnel resilience, $Q(t)$ represents the functionality of the tunnel during the seismic hazard restoration period, T_0 is the time of the seismic, and T_2 is the time of the end of the tunnel restoration.



Figure 2. Definition of resilience concept for tunnel.

2.2.1 Loss function

When assessing the functionality of structures under seismic disasters, Cimellaro (Cimellaro et al., 2010) suggest that the functionality of buildings can be determined based on the

calculation of direct economic losses. Drawing inspiration from this perspective, this paper formulates the structural loss function for tunnel engineering as follows:

$$L(I) = \sum_{j=1}^N p_j \bullet u_j \quad (4)$$

In Equation (4): $L(I)$ denotes the tunnel loss function; P_j represents the probability of the tunnel transitioning to damage state j and u_j denotes the repair coefficient required when the tunnel reaches the damage state j . The precise correlation coefficients for this calculation are delineated in Table 2.

Table 2. Repair coefficient of tunnel with different damage states (Huang et al., 2022).

Damage state (DS _{<i>j</i>})	S_1 -No	S_2 -Minor damage	S_3 -Moderate damage	S_4 -Severe damage	S_5 -Collapse
Repair coefficient(u_j)	0	0.10	0.25	0.75	1

2.2.2 Recovery function

The recovery function serves to characterize the restoration progress and speed of subway tunnels in the post-seismic phase, with its represented recovery duration and functionality being crucial for assessing seismic resilience (Hu et al., 2023). Consequently, this paper similarly adopts a linear recovery function to represent the tunnel recovery process, expressed as follows:

$$f_{rec}(t, T_0, T_2) = 1 - \frac{t - T_0}{T_2 - T_0} \quad (5)$$

In Equation (5), T_0 is the start time of tunnel rehabilitation and T_2 is the end time of tunnel rehabilitation. The total time required for the repair process is defined as shown in the following equation (Hu et al., 2023):

$$T_r = T_2 - T_1 = \sum_{j=1}^N t_j \bullet p_j \quad (6)$$

In Equation (6): t_j is the time required to repair the tunnel completely when its damage state is j . Detailed insights into the various tunnel damage states and their corresponding probabilities, denoted as P_j . Referring to the Chinese standard “RISN-TG041-2022 Guidelines for Seismic Resilience Assessment of Urban Engineering Systems” (2022), the required repair times for various damage states of the tunnel are determined, as presented in Table 3.

Table 3. Repair time of tunnel with different damage states.

Damage state	S_1 -No	S_2 -Minor damage	S_3 -Moderate damage	S_4 -Severe damage	S_5 -Collapse
Time (days)	0	0.5	2.4	45	210

2.2.3 Tunnel functions

When constructing the tunnel functionality function, it is commonly assumed that there is no performance loss before the occurrence of seismic disasters. Additionally, it is assumed that the tunnel performance will be fully restored after the completion of the restoration process. The tunnel functionality function can be calculated using the formula proposed by Cimellaro (Cimellaro et al., 2010), expressed as follows:

$$Q(t) = 1 - [L(I) \bullet f_{rec}(t, T_0, T_2 - T_0)] \quad (7)$$

In Equation (7): $L(I)$ and $f_{rec}(t, T_0, T_2-T_0)$ denote the tunnel loss function and recovery function, respectively.

Based on the tunnel engineering function formulated in Equation (7), a quantitative assessment of the tunnel engineering resilience index can be obtained by integrating over the time during which performance is impaired. In this study, actual structural parameters and geological parameters of a subway tunnel project will be employed. The dynamic response process of the tunnel under seismic disasters will be analyzed, applying the seismic resilience assessment framework proposed in this paper. This approach aims to accomplish a quantitative resilience analysis of the tunnel engineering system.

3 CASE STUDIES AND NUMERICAL MODELING ANALYSIS

The main structure of the tunnel is made of C50 grade concrete, and in this study, the CDP constitutive model is selected to simulate the lining. The relevant concrete material properties are set based on the Chinese Concrete Structure Design Code (GB50010-2010). The reinforcement within the tunnel structure primarily employs HRB335. Referencing the Chinese Concrete Structure Design Code (GB50010-2010) and relevant research findings, plastic constitutive models are employed to simulate the behavior of the reinforcement.

The surrounding geological layers are selected to represent the actual conditions adjacent to the tunnel construction site. Three types of soil conditions, labeled as Soil condition: I, II, and III, are identified. The Mohr-Coulomb constitutive model is employed to simulate the behavior of the soil. The layer thickness of each soil type is determined based on the average thickness obtained from geological surveys. Detailed variations in elastic modulus, density, cohesion, and friction angle with depth across the entire site are illustrated in Figure 3.

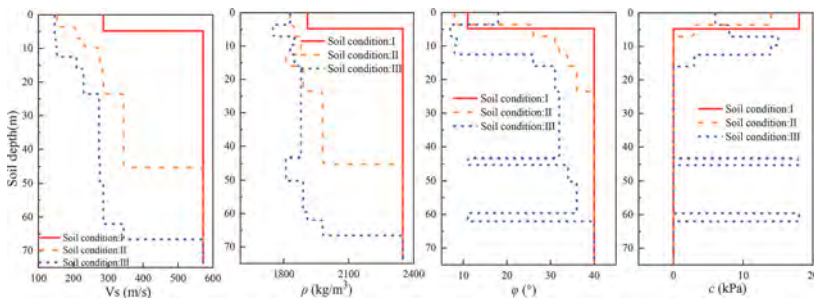


Figure 3. Relationship between soil material properties with depth.

This paper selects a tunnel engineering site in China for resilience assessment. The tunnel project represents a typical subway tunnel structure, with a diameter of 6.0 meters and a lining thickness of 0.35 meters. The reinforcement within the tunnel only considers the main bars and meets the relevant specifications, accounting for 0.6% of the total. A finite element numerical model (2D) considering the soil-tunnel coupling effects was established using ABAQUS software. The entire numerical model has a height of 74 meters and a width of 300 meters. By appropriately configuring dampers, the rock is simulated as an elastic foundation, and seismic loading is applied by subjecting the dampers to seismic oscillations. The lateral boundaries of the finite element model employ Motion-Periodic-Constraints (MPC) coupling to ensure simultaneous movement of both ends (Huang et al., 2022). The detailed dimensions of the model and boundary conditions are illustrated in Figure 4.

The finite element model employs plane strain elements for both the tunnel structure and the soil, utilizing the CPE4R element type. The reinforcement elements adopt a two-dimensional truss element, designated as T3D2. In the interaction setup, the reinforcement is embedded within the tunnel lining. The contact between the lining and the surrounding soil is categorized into normal and tangential behaviors. Normal behavior adopts a hard contact relation, while the tangential behavior employs a penalty function approach with a friction coefficient set at 0.6 (Huang et al., 2022). To

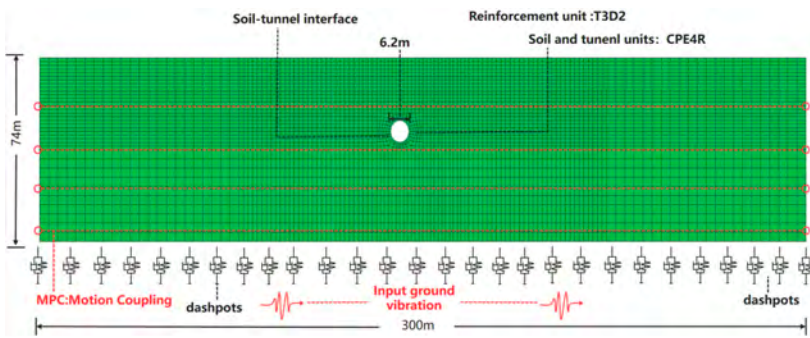


Figure 4. Numerical model dimensions and boundary conditions.

accurately conduct the seismic resilience assessment of tunnel structures, the selection of a sufficient and judicious number of seismic waves is crucial. Generally, choosing 10 seismic waves is considered adequate to fulfill the computational requirements. In this study, ten seismic waves meeting the response spectrum criteria were chosen from the Pacific Earthquake Engineering Research Center (PEER) database (<https://ngawest2.berkeley.edu/>). A scaling approach, incrementing in 0.1g increments from 0.1g to 1.0g, was applied to these waves. Subsequently, the resulting 100 scaled seismic waves were input into the finite element model to perform incremental dynamic analysis.

4 TUNNEL RESILIENCE ANALYSIS

4.1 Tunnel vulnerability analysis

When conducting seismic response calculations for Type I, II and III soil condition, we extracted the dynamic response of the interval tunnel finite element model, and the results are presented in the following Figure 5. As evident from Type I soil condition, the radial convergence of the interval tunnel shows an increasing trend with the gradual rise in peak ground acceleration (PGA). Under the influence of the EQ4 seismic wave, the radial convergence of the interval tunnel reaches its maximum value, measuring 18.5 mm. For the EQ5 seismic wave, the radial convergence is slightly lower, measuring 10.1 mm. Conversely, under the impact of the EQ7 seismic wave, the interval tunnel exhibits the smallest radial convergence, measuring 3.5 mm. Similar trends are observed in Type II and Type III soil condition, with the radial convergence of Type III soil condition tunnels being slightly larger than that of Type II soil condition.

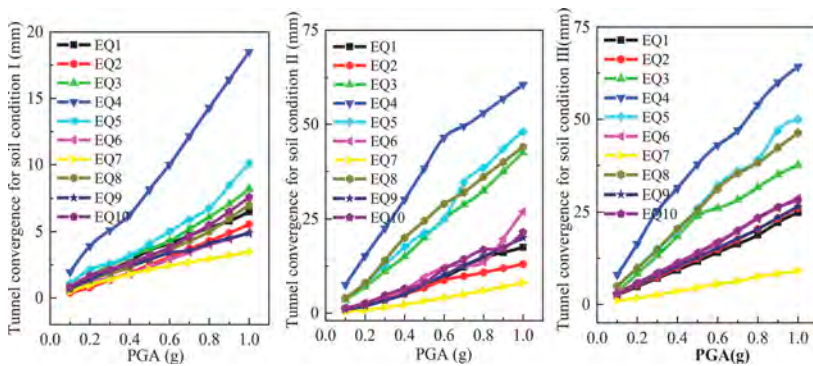


Figure 5. Radial convergence of the tunnel in soil condition I, II and III (mm).

The seismic dynamic response data of the interval tunnel were extracted for three distinct geological strata. The radial convergence rate of the tunnel was computed based on Formula

1, and a logarithmic relationship between PGA and the tunnel’s radial convergence rate was derived. Referring to the damage state thresholds provided in Table 1, the seismic demand models, logarithmic standard deviations, and other pertinent information for the interval tunnel under different geological conditions were organized, as presented in Table 4.

Table 4. Tunnel vulnerability database.

	Seismic Probability Demand Model	β_1	β_{tot}	IM ₁	IM ₂	IM ₃	IM ₄
Tunnel I	$LN(\theta)=0.901LN(PGA)-6.83$	0.373	0.518	0.518	2.548	4.304	6.766
Tunnel II	$LN(\theta)=1.256LN(PGA)-5.802$	0.809	0.886	0.274	0.859	1.251	1.731
Tunnel III	$LN(\theta)=0.993LN(PGA)-5.530$	0.584	0.686	0.147	0.626	1.008	1.520

Utilizing the data presented in Table 4, we constructed the damage probability curves for the interval tunnel in Type I, II and III soil condition, as illustrated in Figure 6. Upon close examination of the Type I soil condition, it is evident that the probabilities of various damage states for the interval tunnel exhibit a significant upward trend with the gradual increase in *PGA*. Starting from 0.1g, the probabilities of different damage states gradually increase from nearly zero. When the *PGA* reaches 1.0g, the probabilities for slight damage, moderate damage, severe damage, and collapse are 90%, 4%, 0.3%, and 0.1%, respectively. Similar results are observed in Type II and Type III soil condition, where the damage probabilities for Type III soil condition are slightly higher than those for Type II soil condition.

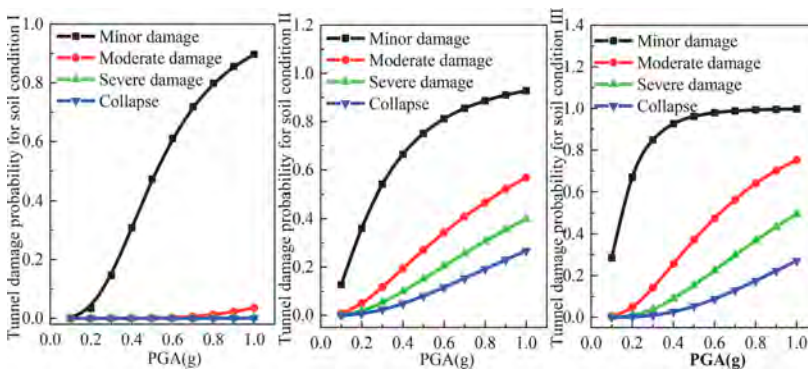


Figure 6. Damage probability of tunnels in soil condition I, II and III.

4.2 Tunneling resilience analysis

Referring to the resilience analysis in Section 2.2, the schematic representation of the tunnel engineering resilience under a seismic intensity of 1.0g is illustrated in Figure 7. From Figure 7, it is evident that as the soil conditions degrade, the seismic resilience of the tunnel engineering significantly decreases. This decline is primarily attributed to the fact that poorer soil conditions often exhibit larger ground deformations during earthquakes, making structures more susceptible to damage. This is further reflected in the robustness of the tunnel engineering, resulting in a reduction in seismic resilience. It is noteworthy that under a seismic intensity of 1.0g, the seismic resilience of tunnel engineering for all three types of ground conditions exceeds 0.7. According to the research by Huang (Huang et al., 2022), this indicates that the tunnel engineering demonstrates a moderate seismic resilience under such seismic intensity.

According to the seismic resilience assessment method established in Section 2.2, the seismic resilience values of a single-section tunnel are calculated under three soil conditions: Soil condition I, II, and III. The summarized results are depicted in Figure 8. From Figure 8, it is evident that the seismic resilience of the sectional tunnel significantly decreases with an increase

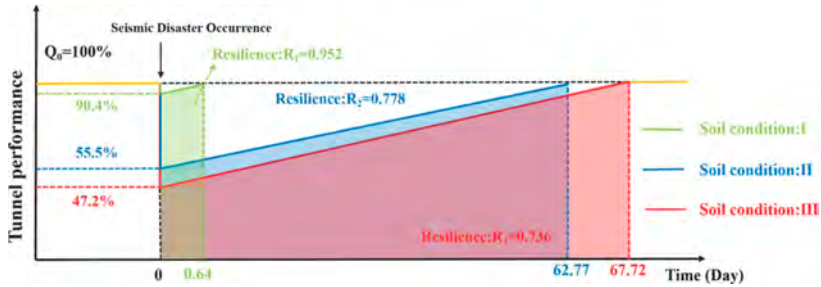


Figure 7. Results of resilience of tunnel under different soil condition.

in Peak Ground Acceleration (*PGA*). Additionally, the sectional tunnel exhibits the highest seismic resilience in Soil condition I, with the maximum seismic resilience values within this soil condition. For seismic intensities ranging from 0.1G to 1.0G, the seismic resilience assessment of the sectional tunnel consistently falls into the high resilience category. In Soil condition II, the sectional tunnel's seismic resilience is slightly lower, transitioning from high resilience to moderate resilience at a seismic intensity of 0.5G. Soil condition III, characterized by the poorest soil conditions, results in the lowest seismic resilience values for the sectional tunnel. At a seismic intensity of 0.5G, the seismic resilience assessment of the sectional tunnel shifts from high resilience to moderate resilience.

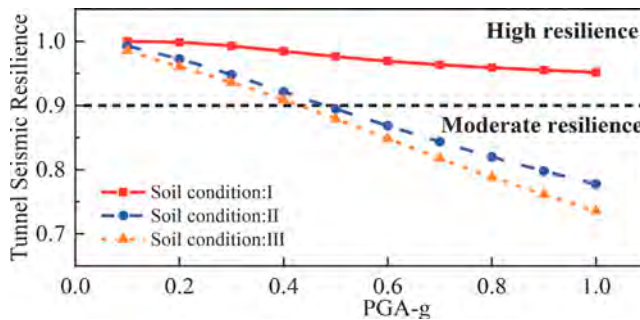


Figure 8. Seismic resilience results of tunnel under different soil conditions.

5 CONCLUSION

This paper introduces a feasible and practical resilience assessment framework designed to evaluate the robustness and rapid recovery capability of tunnel engineering under seismic disasters. The relevant analytical results indicate the following:

- (1) The magnitude of seismic intensity plays a crucial role in influencing the resilience indicators of tunnel engineering. As the seismic intensity increases, the resilience value of tunnel engineering decreases.
- (2) Soil conditions significantly impact the resilience indicators of tunnel engineering, with superior geological conditions associated with higher resilience values in tunnel engineering.
- (3) The resilience assessment framework for tunnel engineering underscores that a judiciously designed and seismic-resistant metro tunnel, coupled with rapid post-disaster recovery capabilities, is pivotal for maintaining high seismic resilience in tunnel systems.

ACKNOWLEDGMENTS

This work was supported by the Shanghai Science and Technology Committee Program (22dz1201202), the Damage Database for Urban Rail Transit Underground Structures and Resilience evaluation algorithm research (TSY2022QT161).

REFERENCES

- Argyroudis SA, 2022. Resilience metrics for transport networks: a review and practical examples for bridges. *Proceedings of the Institution of Civil Engineers-Bridge Engineering*. 175(3), 179–192.
- Alipour A, Shafei B, 2016. Seismic resilience of transportation networks with deteriorating components. *Journal of Structural Engineering*. 142(8), C4015015.
- Cimellaro GP, Reinhorn AM, Bruneau M, 2010a. Framework for analytical quantification of disaster resilience. *Engineering Structures*. 32, 3639–3649.
- Chen XS, Shen J, Bao XH, 2023 .A review of seismic resilience of shield tunnels. *Tunnelling and Underground Space Technology*. 136,105075.
- Hashash YM, Hook JJ, Schmidt B, John I, Yao C, 2001. Seismic design and analysis of underground structures. *Tunnelling and Underground Space Technology*. 16, 247–293.
- Hu J, Wen WP, Zhai CH, 2023. Seismic resilience assessment of buildings considering the effects of main-shock and multiple aftershocks. *Journal of Building Engineering*. 68, 106110.
- Huang ZK, 2022. Resilience Evaluation of Shallow Circular Tunnels Subjected to Earthquakes Using Fragility Functions. *Applied Sciences*. 12, 4728.
- Iida H, Hiroto T, Yoshida N, 1996. Damage to Daikai subway station. *Soils Found*. 36(Special), 283–300.
- Jiang JW, Nagggar MHE, Du XL, Xu CS, 2023. Seismic fragility curves for shallow buried subway station using pushover-based method. *Tunnelling and Underground Space Technology*. 135, 105059.
- Psyras NK, Sextos AG, 2018. Safety of buried steel natural gas pipelines under earthquake-induced ground shaking: A review. *Soil Dynamics and Earthquake Engineering*. 106, 254–277.
- Panteli M, Mancarella P, Trakas DN, Kyriakides E, Hatziaargyriou ND, 2017. Metrics and quantification of operational and infrastructure resilience in power systems. *IEEE Transactions on Power Systems*. 32(6), 4732–4742.
- Wang LJ, Geng P, Chen JB, 2023. Machine learning-based fragility analysis of tunnel structure under different impulsive seismic actions. *Tunnelling and Underground Space Technology*,133:104953.

An ArcGIS toolbox for the probabilistic performance-based assessment of surface building damage in large-scale urban excavations

J. Zhao

Department of Civil and Environmental Engineering, Berkeley, CA, USA

A.O.K. Lysdahl & E.W. Ånes

Norwegian Geotechnical Institute, Oslo, Norway

L. Piciullo & S. Ritter

Norwegian Geotechnical Institute & Oslo Metropolitan University, Oslo, Norway

M.J. DeJong

Department of Civil and Environmental Engineering, Berkeley, CA, USA

ABSTRACT: This paper presents an extension of the REMEDY_GIS_RiskTool (https://github.com/norwegian-geotechnical-institute/REMEDY_GIS_RiskTool), which is a Geographic Information System (GIS) geoprocessing toolbox. The toolbox was implemented in the software ArcGIS and was originally developed at the Norwegian Geotechnical Institute (NGI). This paper extended the toolbox by allowing Soil-Structure Interaction (SSI) modeling in the estimation of building response to excavation-induced short-term ground displacements. Another extension to the toolbox is a probabilistic performance-based assessment (PPBA) approach for quantifying building damage risks in large excavation projects. The PPBA approach enables quantifying the uncertainty caused by aleatoric ground deformation uncertainty and the epistemic uncertainty in SSI modeling. A case study of applying the presented toolbox to a foundation excavation project in Norway is presented to demonstrate how the toolbox can be used to facilitate engineering decision-making. Besides using ArcGIS, the backend Python program of the toolbox can also be adapted to other GIS software and environments.

1 INTRODUCTION

Tunneling and deep excavation (T&DE) in urban environments may cause significant ground and surface building movements. Due to congested urban environments, a number of surface buildings may be disturbed and may need assessment when planning urban excavation. The assessment of such ground and building movements may experience large uncertainty due to limited site characterization and lack of knowledge of underground conditions, complex construction activities, epistemic modeling uncertainty in the tunnel/excavation-soil-structure interaction process, etc. The uncertainties and the significant potential damage made T&DE-induced ground movements an important human-made hazard, and advanced modeling and assessment methods and tools are needed.

This paper presents a computational toolbox that facilitates the querying and modeling of spatially distributed excavation-soil-structure systems with Geographic Information System (GIS) models. The toolbox is developed based on the widely adopted three-stage assessment approach (Mair et al. 1996) in tunneling- and excavation-induced building damage

assessment. However, as discussed in Ritter (2018), the first two stages in the conventional three-stage approach are often too conservative. This is because an overly conservative prediction for ground deformation is often adopted to handle the uncertainty in predicting ground deformations. Additionally, the estimation of building response in the conventional method doesn't take into account the stiffness of the structure. To avoid overly conservative assessment due to ignoring building stiffness, the Timoshenko beam building model (Franza et al. 2020) and the elastoplastic soil-structure interface model (Franza & DeJong 2019) are adopted in the toolbox presented in this paper. Moreover, instead of adopting a usually overly conservative ground deformation, a probabilistic performance-based assessment (PPBA) approach (Zhao et al. 2021 & 2023) is implemented to formally quantify the uncertainty in the predicted ground deformation and other modeling parameters. The toolbox is developed based on the open-source ArcGIS toolbox REMEDY_GIS_RiskTool (Kahlstrøm et al. 2023) and may supplement the decision-making process in large T&DE projects. This paper first reviews the background of the REMEDY_GIS_RiskTool and the PPBA approach following a discussion of the development and extension to REMEDY_GIS_RiskTool. An application of the extended REMEDY_GIS_RiskTool is demonstrated with a case study, and some conclusions and future developments are discussed in the end.

2 BACKGROUND

2.1 *The GIBV method and the REMEDY_GIS_RiskTool toolbox*

Geographic Information System (GIS) models are usually adopted in large-scale T&DE projects to facilitate the querying and management of spatially distributed models. The open-source GIS-based toolbox REMEDY_GIS_RiskTool is one such model that is implemented in the software ArcGIS. REMEDY_GIS_RiskTool is based on the GIBV method (Piciullo et al. 2021), where the ground-work impact and the building vulnerability are estimated separately, and vulnerability versus impact matrices are used to provide an overall damage assessment. The ground-work impact includes both short-term ground displacements induced by the deflection of retaining walls and long-term ground displacements induced by pore water dissipating and soil consolidation. The short-term vertical ground displacements are predicted with empirical equations (Langford et al., 2021), and the long-term vertical ground displacements are estimated with empirical water dissipation models (Langford et al., 2016) and Janbu's consolidation model (Janbu, 1970). The ground movements are evaluated below each exposed building and classified into four impact levels according to the maximum settlement and maximum differential settlement. The buildings are classified into four vulnerability classes according to their materials, foundation systems, and conditions. A four-by-four risk matrix is then constructed, in which buildings with a higher impact level and higher vulnerability are assigned a higher damage state. Five damage classes, which are consistent with the ones defined by Burland et al. (1977), are used in REMEDY_GIS_RiskTool. The GIBV method was applied and validated in two case studies in Norway (Piciullo et al. 2021). However, the building vulnerability classification is not quantitative and can sometimes be rough and largely dependent on engineering judgments. As a result, this paper aims to improve the GIBV method and REMEDY_GIS_RiskTool toolbox with a quantitative SSI model in the PPBA approach.

2.2 *A probabilistic performance-based assessment approach for short-term assessment*

The probabilistic performance-based assessment (PPBA) approach adopted in this paper was first proposed by Zhao et al. (2021) for the assessment of tunneling-induced surface building damage and later modified and applied to deep-excavation assessments (Zhao et al. 2022 & 2023). Figure 1 is a summary of the PPBA approach, which is an extension of the widely used three-stage assessment approach (Mair et al. 1996) for short-term T&DE-induced building damage assessment. In contrast to the original three-stage approach, where deflection ratio and lateral strain estimated from the greenfield condition are used to determine building

damage in the second-stage assessment, the direct strain-based approach (Franza et al. 2020) is adopted to characterize building damage state. In the direct strain-based approach, the maximum strain in the Timoshenko beam model is first estimated from the elastoplastic SSI model and then used to determine the building damage state according to the correlation proposed by Boscardin and Cording (1989). Moreover, to quantify uncertainties, a probabilistic modeling approach is employed in all stages. In the preliminary assessment stage, the probability of the maximum settlement ($S_{v,max}$) less than 10 mm (i.e., probability of negligible impact) is estimated. If the probability is less than a limit probability (P_{lim}), the building is considered to suffer from non-negligible impact, and a second stage assessment is required. In the second stage, the probability that the maximum strain (ϵ_{max}) is below a safe limiting strain (ϵ_{lim}) is calculated. If the probability is less than P_{lim} , the building is considered likely to experience unacceptable damage, and a detailed evaluation is needed. In the end, a detailed evaluation of a full-scale soil-structure model (e.g., the ASRE3D model proposed by Zhao & DeJong (2023)) is used to estimate the probability of undesired damage. In the PPBA approach, the uncertainty of the greenfield ground displacement can be described by the random field models proposed by Zhao et al. (2023), where Equation 1a and 1b are used to describe the vertical and horizontal ground displacement profile, and the maximum vertical displacement ($d_{v,max}$) and profile width (η) are modeled with lognormal random fields estimated from case history data. The building stiffness, soil stiffness, and building weight are modeled with random variables with corresponding distribution types and statistical moments suggested by design guidelines and research literature (e.g., Ellingwood & Ellingwood, 1980, Beacher & Christian, 2005, Melcher & Beck, 2018, Cami et al., 2020). Compared to deterministic design methods, modeling the uncertainties in the PPBA approach may help identify building damages that are unpredictable in deterministic design methods. Furthermore, the PPBA approach may provide more confidence for engineering judgments and assumptions by allowing a clearer understanding of the range of possible outcomes and the associated

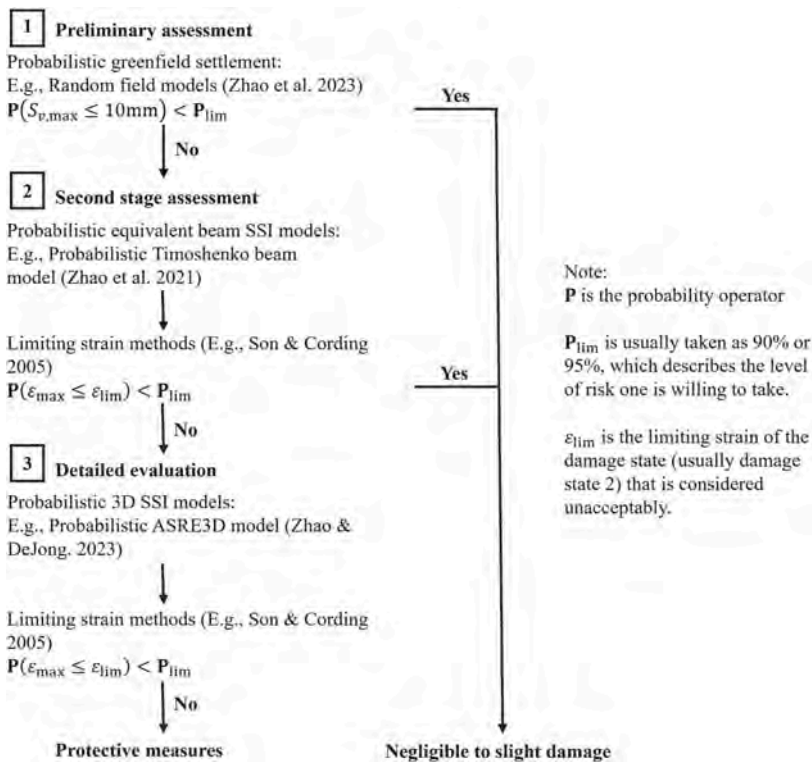


Figure 1. Three-stage probabilistic performance-based assessment (PPBA) approach.

probabilities. Such advantages of the PPBA approach are demonstrated with a case study in section 4 and more detailed discussions can be found in Zhao (2023).

$$\frac{\delta_v(d/H_e)}{\delta_{v,\max}} = \frac{1.14}{\frac{d}{H_e\eta} + 0.39} \frac{1}{0.46\sqrt{2\pi}} \exp\left(-\frac{(\ln(\frac{d}{H_e\eta} + 0.39) - 0.095)^2}{0.423}\right) \quad (1a)$$

$$\frac{\delta_l(d/H_e)}{\delta_{l,\max}} = \frac{2.14}{\frac{d}{H_e\eta} + 0.82} \frac{1}{0.44\sqrt{2\pi}} \exp\left(-\frac{(\ln(\frac{d}{H_e\eta} + 0.82) - 0.80)^2}{0.387}\right) \quad (1b)$$

3 THE EXTENDED REMEDY_GIS_RISKTOOL

3.1 *Preprocessing toolbox*

The adopted PPBA and SSI model uses equivalent beams to model surface buildings, and a preprocessing toolbox is created to generate the equivalent beams automatically for all buildings exposed to the excavation hazard. To generate the models, the building footprint polygons in the GIS database are first converted to raster. For each building raster, the second moment of area and product moment of area about two orthogonal axes are calculated for each polygon. By an eigen-decomposition of the 2 by 2 product moment of area matrix, two axes result in the largest second moment of area and zero product moment of area can be obtained. Because most building footprints are similar to parallelograms, the two axes with the largest second moment of area represent the two dominant spans of the building, which are considered the simplified beam geometry of the building. The preprocessing toolbox is a quick method to generate equivalent beam models for many buildings. The toolbox users may edit the equivalent beams as needed before sending the models to soil-structure interaction analysis. Other soil-structure interaction modeling parameters, such as beam dimensions, elastic stiffness, shear stiffness, and building-soil interface friction, are also set with the preprocessing toolbox.

3.2 *BegrensSkade toolbox*

The BegrensSkade (Damage Limitation in Norwegian) toolbox has two components, named the front end and the back end. The front end is a user interface that uses ArcGIS to manage and visualize the excavation extent, the building footprints, the bedrock depth, and the soil-structure interaction modeling parameters. The back end is a Python program that performs geospatial analysis of the excavation and the surrounding environments, creates ground impact maps, and traverses and performs building safety analysis for buildings around excavations.

In this paper, the first extension to the BegrensSkade tool is adding the greenfield ground displacement profile described in Equation 1a and Equation 1b to the front and back ends. The additional ground displacement profile allows the estimation of both vertical and horizontal surface ground displacement. Furthermore, the estimated ground displacements are continuous displacement fields in contrast to the discrete displacement profile in the existing BegrensSkade. The continuous displacement fields are necessary to enable soil-structure interaction analyses.

The second extension is adding the Timoshenko beam-based elastoplastic soil-structure interaction model, named ASRE, originally developed by Franza & DeJong (2020), to the toolbox's Python back end. ASRE, as shown in Figure 2, models the surface building with a Timoshenko beam and models the soil with an elastic semi-infinite space. The soil-structure interface is modeled with an elastoplastic interface, where Coulomb's friction law and a limited vertical tensile strength are modeled. ASRE was implemented in the Matlab environment when it was first developed, and it was converted to a C++ program by Zhao et al. (2021) to achieve a faster computational performance. To use ASRE in the BegrensSkade

tool, the C++ program is converted to a dynamic link library (DLL) and loaded to BegrensSkade's back end with a Python library "ctypes". The fast nature of ASRE is essential to achieve PPBA analyses of many buildings in large-scale excavation projects.

The third extension to the BegrensSkade tool is adding the PPBA approach. In the front end, features are developed to input and manage the uncertainty modeling parameters. The random field models for ground displacement analysis apply to all involved buildings and are managed with the geoprocessing interface. The building stiffness, building weight, and soil-structure interface friction are building-specific and are managed as attribute table entries of the building footprint feature layer. In the back end, the distances between each building node pair are calculated to compute the covariance matrix of ground displacements. Samples are then generated according to the covariance matrix and the user-specified mean and coefficient of variations. The samples are passed to ASRE, and the empirical probability density distribution of the maximum principal strain in each building is obtained by repetitive evaluation of the ASRE model with a Monte Carlo method. Currently, the Monte Carlo simulation is performed in sequence in the BegrensSkade tool. As demonstrated in the case study later, the computational time required for the multi-building PPBA analysis is believed to be affordable, and the computation time can be further reduced by applying a parallel computing scheme, as shown by Zhao et al. (2021).

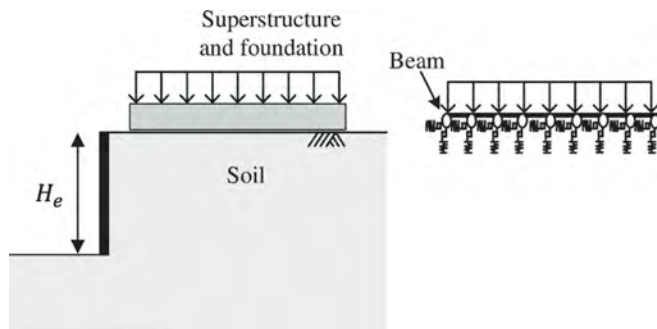


Figure 2. Sketch of the Timoshenko beam-based soil-structure interaction model in ASRE.

4 CASE STUDY

4.1 General information

The REMEDY_GIS_RiskTool was applied to assess the impact of the excavation of a building foundation on surrounding buildings in Oslo, Norway. The excavation pit is supported with sheet pile walls, and the excavation depth is around 5.5 m. The soil in the area consists mainly of marine clay, with some interspersed layers of silt and sand. The Norwegian marine clays were deposited about 10,000 years ago and are believed to be overconsolidated over the years. As a result, the soil is considered relatively stiff. In real engineering practice, both long-term ground settlements induced by pore water pressure reductions and soil consolidation and short-term displacement induced by horizontal displacements of the sheet pile walls were analyzed. Although the long-term ground settlements may affect a large area around the construction pit, the short-term settlement only affects the ground in the immediate vicinity behind the sheet pile walls, which is typically 2–3 times the excavation depth (in this case, around 10 – 15 m) from the sheet pile walls (Langford et al. 2021). Because this paper only presents extensions to the short-term assessment functions in the REMEDY_GIS_RiskTool, only short-term displacements and their effects on surrounding buildings are analyzed in this case study.

The buildings involved in this study are some small allotment buildings to the west of the excavation pit and one large commercial building located to the south side of the excavation. The small allotment buildings are mainly timber or masonry buildings with shallow foundations, while the large commercial building, which is located immediately to the south of the

excavation, was built with reinforced concrete. The building has two sections (labeled A and B in Figure 3), where section A is four stories tall and founded on concrete and steel core piles to rock, while section B is five stories tall and most likely sits on a shallow foundation. It is unclear how the two building sections are connected, and the two sections are analyzed independently in this paper. Section A, sitting on pile foundations, is not likely to settle, but the attached structures may deform and experience some damage from the differential settlements. To estimate such damage, section A is also analyzed with the Timoshenko beam model described in section 3.2, although the effect of the pile foundation system can not be modeled. Such analysis is considered conservative since buildings founded on piles are usually less impacted by settlements, but future research is needed to investigate the SSI effect of pile foundation buildings close to deep excavations. The construction is currently underway, and a comparison of the measured and predicted building damage will be studied in the future.

4.2 Analysis and results

A preliminary stage assessment was first performed with both the conventional deterministic method and the PPBA approach. In the conventional deterministic method, because the sheet pile walls are floating from bedrock and are unbraced, a maximum settlement ($\delta_{v,max}$) of 1% of excavation depth (H_e) was selected, as suggested by Langford et al. (2021). A width parameter of 1.0 is selected for Equation 1, which corresponds to the trough width suggested by Kung et al. (2007). In the PPBA approach, the coefficient of variation (CV), distribution type, and range of $S_{v,max}$ and (η) are described in section 2.2. The mean value of η is selected as 1.0, which is consistent with the deterministic method. Because the 1% maximum settlement suggested by Langford et al. (2021) is the upper bound of $\delta_{v,max}/H_e$ to achieve conservative assessment, a mean value of $\delta_{v,max}/H_e$ is selected as 0.8%. As a result, the marginal distribution of $\delta_{v,max}/H_e$ is $\text{LogN}(-0.29,0.37)$ which has a 90% coverage between 0.41% and 1.37%.

Figure 3 presents the results of the preliminary stage assessment. The deterministic assessment indicates that four buildings may experience non-negligible ground impact, and second-stage assessments are needed. In contrast, the PPBA approach suggests that 6 buildings need second-stage assessment if 90% confidence (i.e., $\mathbf{P}_{lim} = 90\%$) of $S_{v,max} < 10$ mm is desired. The different assessment result is because the possibility of non-negligible ground impact under two more buildings is identified by considering the possibility of $\delta_{v,max}/H_e$ greater than 1% and settlement trough (η) greater than 1 with the PPBA approach. In other words, the PPBA approach may help to detect potential damages that the deterministic approach can not identify.

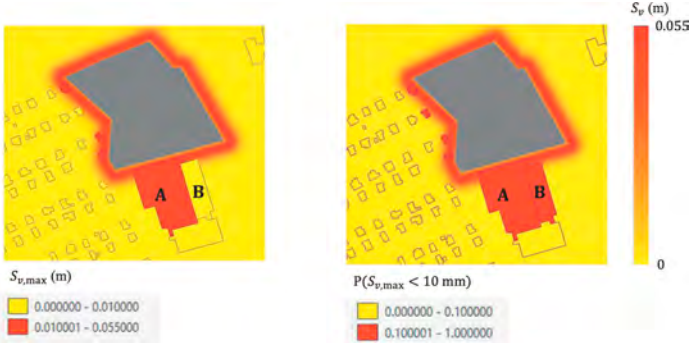


Figure 3. Preliminary assessment results. Left: The maximum settlement ($S_{v,max}$) predicted with the deterministic approach. Right: The probability of settlement ($\mathbf{P}(S_{v,max} < 10\text{mm})$) greater than 10 mm predicted with the PPBA approach.

To carry out the second-stage assessment, where a Timoshenko beam-based elastoplastic SSI model is employed, equivalent beam models for the non-negligibly impacted buildings are

constructed with the pre-processing toolbox. The locations of the equivalent beams are denoted as the crosses in each building footprint in Figure 4. The principal strain in each building is then calculated with the ASRE Timoshenko beam model embedded in the REMERY_GIS_RiskTool. In the deterministic assessment, the elastic modulus of the beams (E_b) is assumed as 3 GPa, and the soil stiffness (E_s) is estimated to be 20 MPa. Because this estimation of the beam stiffness is simple and may consist of relatively big uncertainty, a lognormal distribution with 3 GPa mean and 40% coefficient of variation is used in the PPBA approach to quantify the effect of the uncertainty. Dimmock and Mair (2008) suggested that the equivalent beam elastic over shear modulus ratio (E_b/G_b) can be selected as 2.6 for bearing-wall structures and 12.5 for frame structures. These values are selected for the deterministic assessment and used as the mean value in the PPBA assessment. The coefficient of variation of E_b/G_b is selected as 70% because the estimation of shear modulus is considered one of the major uncertainties in the Timoshenko beam-based SSI analysis, as argued by Zhao et al. (2021). The weight of buildings (L) is modeled as uniformly distributed loads with values of 10 kPa per story. The coefficient of variation of L is selected as 10%, as suggested by Ellingwood (1980). A random variable that follows a lognormal distribution with a coefficient of variation equal to 40% is selected to model E_s , which corresponds to a middle level of uncertainty for soil stiffness, as Phoon and Kulhawy (1999) suggested.

Figure 4 compares the results of the conventional and the PPBA approaches in the second-stage assessment. The deterministic analysis suggested that none of the buildings will experience category 1 ($\epsilon_{lim} = 0.05\%$) or above damage, as defined by Boscardin and Cording (1989). In the PPBA approach, the estimated mean maximum principal strain (ϵ_{max}) is almost identical to the principal strain estimated with the conventional method, which can be considered a sanity check of the PPBA approach. However, the PPBA approach also suggested that all the buildings have almost zero probability (less than 1%) of experiencing a ϵ_{max} greater than 0.05% (i.e., nonnegligible damage as defined by Boscardin and Cording (1989)), although the possibility of small beam stiffnesses and large ground impact is considered with the uncertainty models. This provides an extra assurance to the conventional deterministic methods in which the effect of the uncertainties in soil-structure interaction is unknown. Because the time required for the PPBA approach is only 15 min in the extended REMEDY_GIS_Risktool, the higher confidence level is achieved without significantly increasing the computational effort.



Figure 4. Second-stage assessment results. Left: The maximum principal strain (ϵ_{max}) predicted with the deterministic approach. Middle: The mean of maximum principal strain (ϵ_{max}) predicted with the PPBA approach. Right: The probability of maximum principal strain greater than 0.05% ($P(\epsilon_{max} > 0.05\%)$) predicted with the PPBA approach.

5 CONCLUSIONS AND FUTURE DEVELOPMENTS

The PPBA approach is not proposed to replace the conventional approach but to supplement it by allowing the quantification of uncertainties. The case study showed that the PPBA approach may detect potential damages that can not be identified with the conventional deterministic approach. At the same time, it can also provide an additional level of confidence for engineering decision-making.

The possible future developments of the REMEDY_GIS_Risktool include: 1. Automating the modeling procedure with the digital terrain/elevation models and Machine Learning-based building recognition algorithms. 2. Incorporating more accurate soil-structure interaction models that can capture different foundation systems with the toolbox. 3. Optimize the computational performance with parallel computing schemes. Parallel computing schemes are necessary when more computationally demanding third-stage assessments are performed. Zhao & DeJong (2023) demonstrated the PPBA approach can still be achieved in a practical amount of time with the aid of high-performance computers or cloud computing. The cloud computing service industry is developing quickly, and the cost of renting one cloud computation node with 1 GB of memory on Amazon's EC2 server is as low as 0.0116 USD per hour. With the aid of convenient and cheap cloud computing resources, the PPBA approach may become more practical in future T&DE projects in urban areas.

ACKNOWLEDGEMENT

The authors are grateful to the Peder Sather Centre for funding parts of this research. The authors are also grateful to Marit Skaug Løyland, Thomas Sandene, Einar John Lande, and other colleagues at NGI for providing valuable information on the case study.

REFERENCES

- Baecher, G.B. and Christian, J.T., 2005. *Reliability and statistics in geotechnical engineering*. John Wiley & Sons.
- Boscardin, M. D., and Cording, E. J., 1989. Building response to excavation-induced settlement. *Journal of Geotechnical Engineering*, 115(1), 1–21.
- Cami, B., Javankhoshdel, S., Phoon, K.K. and Ching, J., 2020. Scale of fluctuation for spatially varying soils: estimation methods and values. *ASCE-ASME Journal of Risk and Uncertainty in Engineering Systems, Part A: Civil Engineering*, 6(4), p.03120002.
- Cetiner, B., Wang, C., McKenna, F., Hornauer, S., and Gao, Y., 2022. NHERI-SimCenter/BRAILS: Release v3.0.0 (v3.0.0). Zenodo. <https://doi.org/10.5281/zenodo.7132010>
- Dimmock, P.S. and Mair, R.J., 2008. Effect of building stiffness on tunnelling-induced ground movement. *Tunnelling and Underground Space Technology*, 23(4), pp.438–450.
- Ellingwood, B. and Ellingwood, B.R., 1980. *Development of a probability based load criterion for American National Standard A58: Building code requirements for minimum design loads in buildings and other structures* (Vol. 577). Department of Commerce, National Bureau of Standards.
- Franza, A., Acikgoz, S. and DeJong, M.J., 2020. Timoshenko beam models for the coupled analysis of building response to tunnelling. *Tunnelling and Underground Space Technology*, 96, p.103160.
- Franza, A. and DeJong, M.J., 2019. Elastoplastic solutions to predict tunneling-induced load redistribution and deformation of surface structures. *Journal of Geotechnical and Geoenvironmental Engineering*, 145(4), p.04019007.
- Janbu, N., 1970. Grunnlag i geoteknikk. Trondheim: Tapir forlag
- Brinkgreve, R.B.J. 2002. PLAXIS 2D – version 8. A.A. Balkema Publishers. The Netherlands.
- Kahlstrøm, M., Lysdahl, A.O.K., Ånes, E.W. and Piciullo, L. 2023. REMEDY_GIS_RiskTool, GitHub repository, https://github.com/norwegian-geotechnical-institute/REMEDY_GIS_RiskTool.
- Kung, G.T., Juang, C.H., Hsiao, E.C. and Hashash, Y.M., 2007. Simplified model for wall deflection and ground-surface settlement caused by braced excavation in clays. *Journal of Geotechnical and Geoenvironmental Engineering*, 133(6), pp.731–747.
- Langford, J., Baardvik, G. and Karlsrud, K., 2016. Pore pressure reduction and settlements induced by deep supported excavations in soft clay. In *Proceedings of the 17th Nordic Geotechnical Meeting*.
- Langford, J., Lande, E. J., Sandene, T., Kahlstrøm, M., Nadim, F., Norén-Cosgriff, K., Piciullo, L., Ritter, S., Hauser, C., and Lysdahl, A., 2021. BegrensSkade II–REMEDY–Risk Reduction of Groundwork Damage: An Overview. In *IOP Conference Series: Earth and Environmental Science*. IOP Publishing.
- Mair, R.J., Taylor, R.N. and Burland, J.B., 1996. Prediction of ground movements and assessment of risk of building damage due to bored tunnelling. In *Geotechnical aspects of underground construction in soft ground* (pp. 713–718).
- Melchers, R. E., and Beck, A. T., 2018. *Structural reliability analysis and prediction*. John wiley & sons.

- Piciullo, L., Ritter, S., Lysdahl, A.O.K., Langford, J. and Nadim, F., 2021. Assessment of building damage due to excavation-induced displacements: The GIBV method. *Tunnelling and Underground Space Technology*, 108, p.103673.
- Phoon, K.K. and Kulhawy, F.H., 1999. Evaluation of geotechnical property variability. *Canadian Geotechnical Journal*, 36(4), pp.625–639.
- Ritter, S., 2018. Experiments in tunnel-soil-structure interaction (Doctoral dissertation, University of Cambridge).
- Son, M. and Cording, E.J., 2005. Estimation of building damage due to excavation-induced ground movements. *Journal of geotechnical and geoenvironmental engineering*, 131(2), pp.162–177.
- Zhang, W., Han, L., Gu, X., Wang, L., Chen, F. and Liu, H., 2022. Tunneling and deep excavations in spatially variable soil and rock masses: A short review. *Underground Space*, 7(3), pp.380–407.
- Zhao, J. and DeJong, M., 2023. Three-dimensional probabilistic assessment of tunneling induced structural damage using Monte-Carlo method and hybrid finite element model. *Computers and Geotechnics*, 154, p.105122.
- Zhao, J., Franza, A. and DeJong, M.J., 2021. Method for probabilistic assessment of tunneling-induced damage to surface structures considering soil-structure interaction effects. *ASCE-ASME Journal of Risk and Uncertainty in Engineering Systems, Part A: Civil Engineering*, 7(4), p.04021055.
- Zhao, J., Ritter, S. and DeJong, M.J., 2022. Early-stage assessment of structural damage caused by braced excavations: Uncertainty quantification and a probabilistic analysis approach. *Tunnelling and Underground Space Technology*, 125, p.104499.
- Zhao, J., Ritter, S. and DeJong, M.J., 2023. Framework to Enable Regional 3D Probabilistic Assessment of Excavation Induced Structural Damage Using a Monte-Carlo Method. In *Geo-Risk 2023* (pp. 33–41).
- Zhao, J., 2023. Numerical Modeling and Uncertainty Analysis of Tunneling-and Deep Excavation-Induced Structural Damage (Doctoral dissertation, University of California, Berkeley).



Taylor & Francis

Taylor & Francis Group

<http://taylorandfrancis.com>

Field case studies



Taylor & Francis

Taylor & Francis Group

<http://taylorandfrancis.com>

General report – field case studies

D. Boldini

DICMA, Sapienza University of Rome, Rome, Italy

ABSTRACT: This General Report presents an overview of the papers submitted for the Symposium session dedicated to “Field case studies”. These papers address case studies related to tunnelling and excavation projects carried out in Asia and Europe. The main focus is on the design and implementation of technical solutions to deal with anticipated challenges before construction, as well as on resolving unforeseen issues encountered during project execution. Many of the contributions cover the use of monitoring data, including new technologies, advanced interpretation, or real-time feedback during the excavation process.

1 OVERVIEW

A total of nine papers were submitted to the session dedicated to field case studies. Among these, seven contributions were authored by individuals from Asia, primarily from China (four), with additional representatives from Hong Kong, Dubai, and India, the latter with support from Singapore. Europe is represented by authors from the United Kingdom and a collaborative group from Italy and Spain. No contributions were received from other continents. In terms of affiliation, the submissions are equally distributed, with three from academia, three from industry, and three representing joint academia-industry cooperation.

The content of the papers predominantly focuses on tunnelling case histories using shield tunnel boring machines, with seven contributions dedicated to this topic. Only one paper addresses open excavation. Additionally, one paper describes a complex underground system excavated in rocks using drill-and-blast technology, which does not entirely align with the Symposium themes. Five out of nine papers present the results of numerical analyses to support discussions on design strategies and/or observed behaviour during construction.

The following discussion is organised into three sections. The first session provides an overview of papers primarily dedicated to designing and implementing technical solutions to address anticipated challenges before construction. The second session delves into contributions addressing unforeseen problems encountered during construction, along with the strategies employed to finalise solutions. Finally, the third section is dedicated to papers fully focused on monitoring, offering limited details on construction processes and explanations of soil-structure interaction phenomena.

2 ENGINEERING SOLUTIONS FOR PRE-CONSTRUCTION CHALLENGES

Different challenges and solutions identified before the construction are discussed in four papers.

In the paper by Lee et al. (2024), an innovative design was implemented to limit tunnel squat and long-term settlements along a stretch of the Tuen Mun-Check Lap Kok Link in Hong Kong. This stretch was excavated with a 14 m in diameter slurry shield in alluvium clays and sands, beneath recently reclaimed land and clayey marine deposits that were still

on-going to consolidation and creep settlements under the reclamation loading (Figure 1). The mitigation measure consisted of constructing a number of lower grade unforced barrettes at both sides of the tunnel springline using the diaphragm wall trenching method prior to the tunnel excavation (see geometrical details in Figure 2).

Finite Element analyses were carried out in both 2D and 3D conditions to evaluate the short- and long-term response to tunnelling, adopting an elasto-plastic creep model for the fine-grained strata. It was observed that the tunnelling-induced stresses concentrate in the barrettes and are transmitted to the stiffer alluvial sand below the tunnel invert (refer to Figure 2), thereby reducing excess pore pressure generation. The measured volume loss ratio of 0.3% was much smaller than the predicted 1.1%, partly due to the effectiveness of the barrettes.

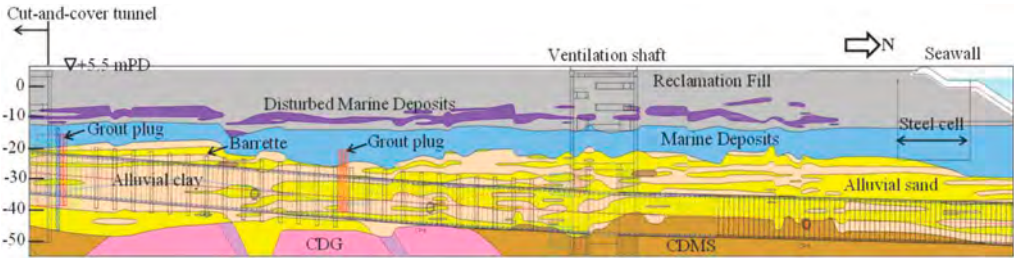


Figure 1. Geological profile at the tunnel site (Lee et al. 2024).

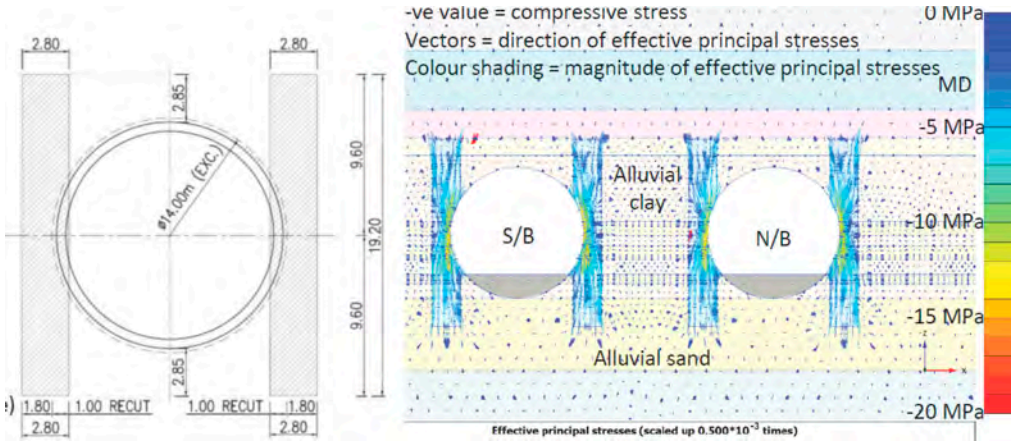


Figure 2. Details of the barrettes at the tunnel springline (dimensions are in metres) (left) and stress concentration in the barrettes obtained by numerical modelling (right) (Lee et al. 2024).

Sun et al. (2024) presented a case study involving a stretch of Line 6 of Suzhou Rail Transit, where two TBM-EPBs with a diameter of 6.84 m had to cut through reinforced concrete diaphragm walls and piles while traversing the Line 1 Lindun Road Station (Figure 3). The soil layers excavated by the machines outside the station were mainly silty clays. To facilitate consecutive excavation of soft soil strata over long-distance and reinforced concrete structures, a cutterhead incorporating rearing cutters and secondary rolling cutters was adopted (Figure 4). In addition, the front surface of the cutterhead was protected with wear-resistant plates and the main drive configuration was designed to handle the increasing torque expected during reinforced concrete cutting.

The risk associated with the structural safety of the station components was mitigated by reinforcing the soil around the tunnels before excavation with the Metro Jet System and by installing valve grouting pipes below the station floor for a possible compensation of settlements during construction.

During the reinforced concrete cutting, the total thrust force and the cutterhead torque displayed significant fluctuations. Additionally, significant cutter wear was observed, imposing cutter replacement. However, the project was successfully completed with very limited structural deformations.

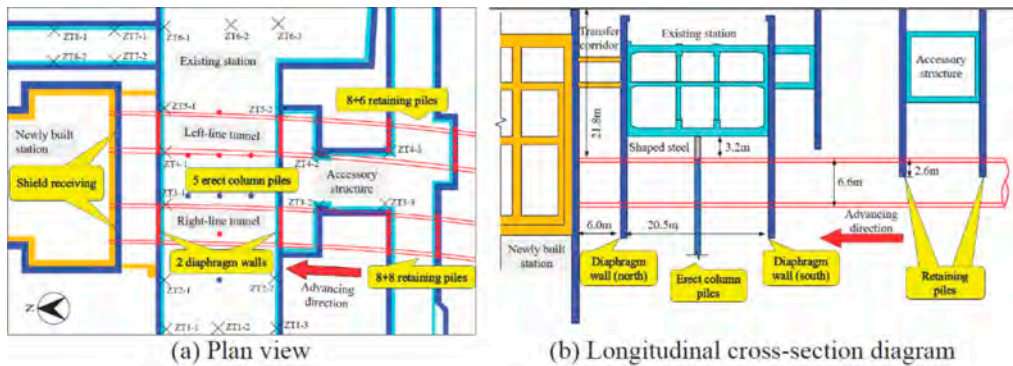


Figure 3. Layout of the project (Sun et al. 2024).

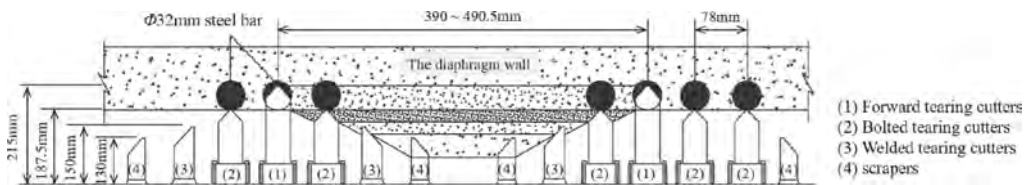


Figure 4. Arrangement of cutters (Sun et al. 2024).

3 ADDRESSING UNFORSEEN ISSUES DURING CONSTRUCTION

Two papers address issues that occurred during construction but were not unforeseen.

Another case-history related to problems affecting segmental lining is that described in Tellioğlu et al. (2024). Cracking, possibly leading to water leakage, were extensively observed after the installation of the lining during the excavation of the Dubai Metro Expo Line using a 9.66 m TBM-EPB. Most of the segments were made of steel fibre reinforced concrete and were affected by cracking mainly parallel to the tunnel axis, originating from the leading edge or trailing edge in almost equal percentages.

Careful investigation and analysis revealed that the main causes were likely found in the tail shield clearance (Figure 5), crew performance, segment handling and transportation, and the ring building process. A significant reduction in cracked segments was achieved after the implementation of mitigation measures, including TBM steering optimisation, increased time allocated to ring building, crew training, and transport route modification.

The paper by Mohanty et al. (2024) describes challenges related to rock wedge failure during the drill-and-blast construction of oil storage caverns. Stabilisation required the installation of remedial rock supports, such as rock bolts and steel fibre reinforced shotcrete, as well as partial excavation of one bench to provide additional support to the cavern sidewall.

4 UTILISATION OF MONITORING DATA AND TECHNOLOGIES

The two papers dedicated to monitoring data and technologies are those by Xue & Standing (2024) and Di Mariano et al. (2024).

In the paper of Xue & Standing, the evolution of tunnelling-induced settlements is discussed with reference to three instrumented greenfield sites in London, each representing different soil

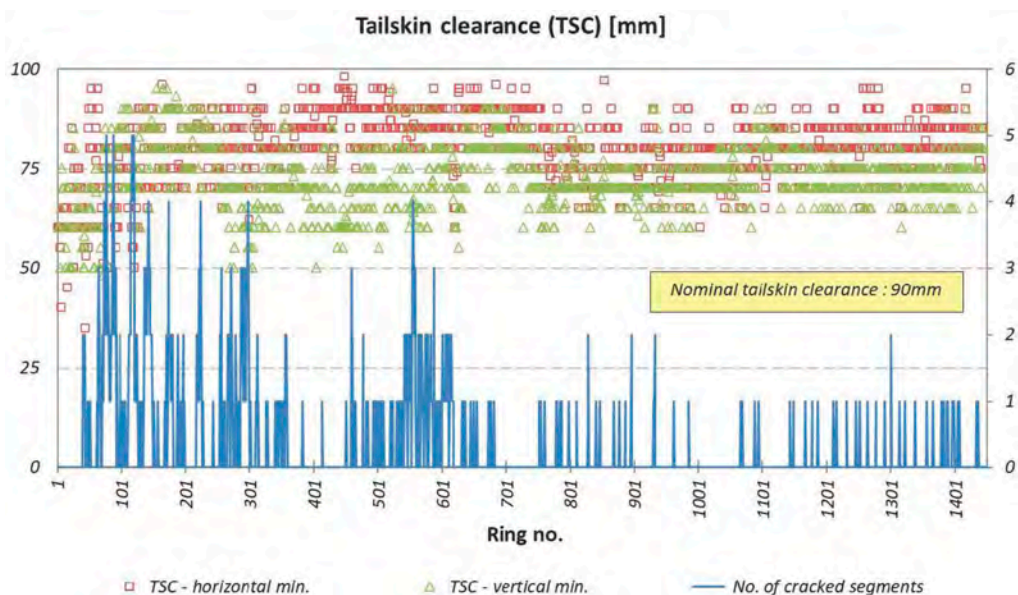


Figure 5. Correlation between tail shield clearance and cracked segments (Tellioglu et al. 2024).

conditions and TBM methods. At the instrumented sites of Hyde Park (HP) and St James's Park (SJP), the excavation of the westbound and eastbound tunnels was carried in London Clay, using an EPB machine and an open-faced shield, respectively. For the twin tunnels at Southwark Park (SP), an EPB machine was also used, but in Lambeth Group and partly in the Thanet Sand deposits. Additionally, the tunnels vary in diameter and depth, and in the case of St James's Park, they are not parallel.

The monitoring data are separated into three sets, representing different phases of excavation. For example, Figure 6(a) shows the transverse settlements recorded at the HP site during the westbound TBM drive. The first set (phase one, indicated by the black lines) collects measurements related to positions of the TBM shield face preceding the instrumented section (i.e., $x_f < 0$), while the second set (phase two, shown by the blue lines) includes those developing between $0 \leq x_f \leq 30$ m (or $3L$, with L representing the shield length). The last set (phase three, indicated by the orange lines) encompasses measurements from 30 to 60 m (or $6L$). Most settlements develop during phase two, which can be considered the limit of the short-term ground response to tunnelling, while the third phase is representative of the long-term effects. This is also evident when considering the longitudinal settlement profile in Figure 6(b), with the more pronounced increment corresponding to data above the tunnel axis (red curve). When normalising the single value of each monitoring point with respect to the corresponding maximum local settlements, it becomes evident that the shape of the settlement trough remains unchanged.

Similar trends were also observed for the other two sites, as summarised in Figure 7. However, during the westbound tunnelling at the SJP site, open-face excavation resulted in a significantly higher percentage of settlement at the end of phase 1 (51%) compared to that at the HP and SP sites (28% and 15%, respectively), due to the lack of face support. For the eastbound tunnel, the increased proportion of settlements in phase 1 at the HP site (38%) could be attributed to soil disturbance caused by the westbound tunnel operations, a behaviour not observed during the construction of the second tunnel at the SJP and SP locations, possibly do the different geometrical conditions.

In the paper of De Mariano et al., a comparison between conventional and innovative displacement measurements is carried out in the context of tunnel construction for a branch of metro Line 9 (now Line 10 South) in the city of Barcelona. The specific case study examines

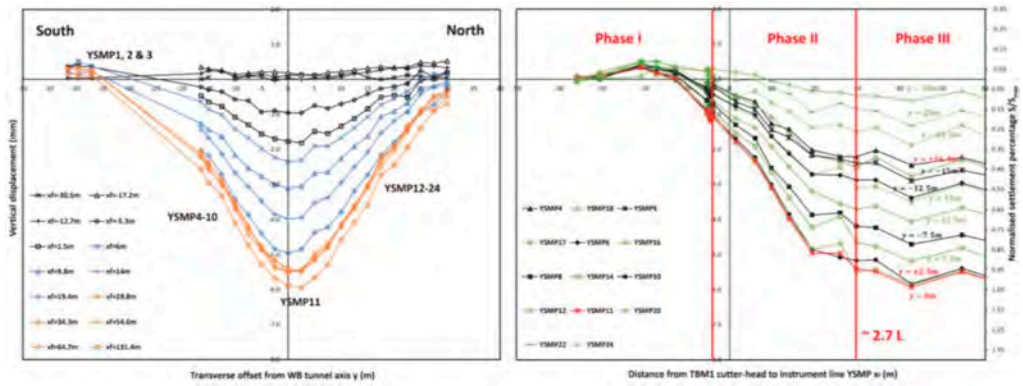


Figure 6. Settlement evolution at the Hyde Park site in the transverse (left) and longitudinal direction (right) during the west bound TBM drive (Xue & Standing 2024).

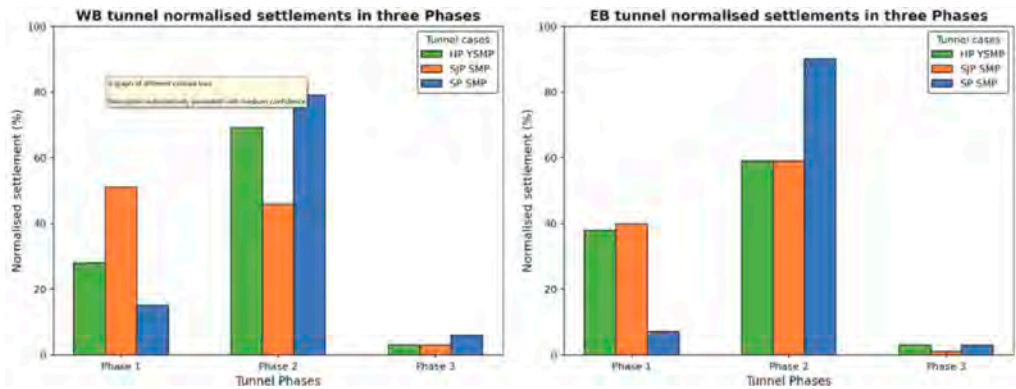


Figure 7. Normalised settlement evolution during west bound (left) and east bound (right) TBM advance in the three phases (Xue & Standing 2024).

the response of a rectangular, 31-meter-high, framed building to tunnel excavation. The tunnel was excavated in mixed ground conditions with a 12 m TBM-EPB, under a cover of 30-36 m. Conventional ground settlements were obtained by precision levelling and were compared with permanent scatter data obtained from multi-temporal synthetic aperture radar (SAR) images at a very high spatial resolution.

Figure 8 shows the comparison of measurements at two locations near the tunnel axis. Both datasets clearly recorded the TBM passage that occurred in March 2011. However, while in one case (point 2) the permanent scatter settlements matched well with the corresponding levelling point, in the other case (point 1) the satellite data were found to be associated with much lower values compared to the conventional measurements. The Authors explain this discrepancy as being due to the different distances of the two monitoring points from the tunnel axis, as well as the effect of phase unwrapping. In this case, the displacement is larger than half of the radar signal wavelength (i.e., 31.1 mm). Correction of this error (see the curve with grey dots) resulted in a significant shift in the settlement curve and a closer match with the conventional one.

The high density of permanent scatters also enables the evaluation of settlement profiles transverse to the tunnel axis. In Figure 9, data derived from two levelling monitoring sections are compared with values obtained from permanent scatters selected in a 10 m wide-band across the section itself, this second dataset being characterised by a larger amount of

measuring points. The fitted Gaussian curves are in discrete agreement in terms of maximum settlement, inflection point and related volume loss.

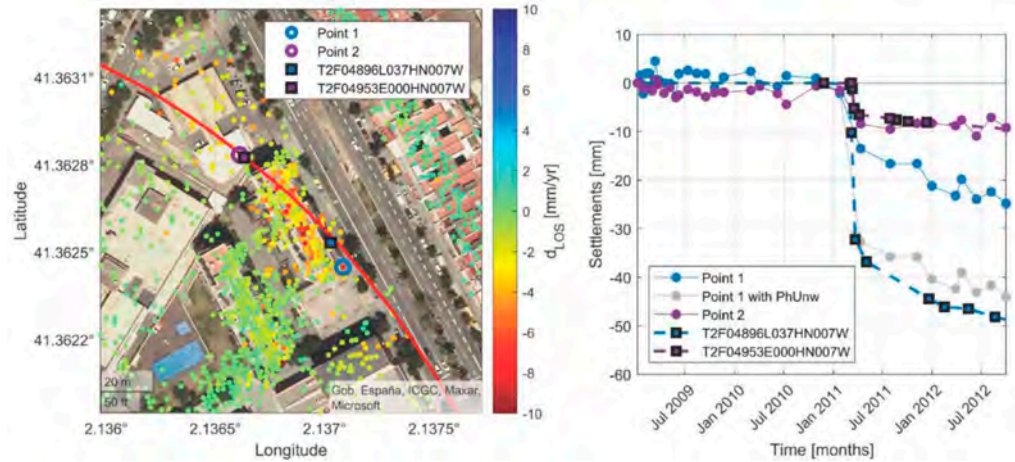


Figure 8. Comparison between levelling and satellite data for building displacements (Di Mariano et al. 2024).

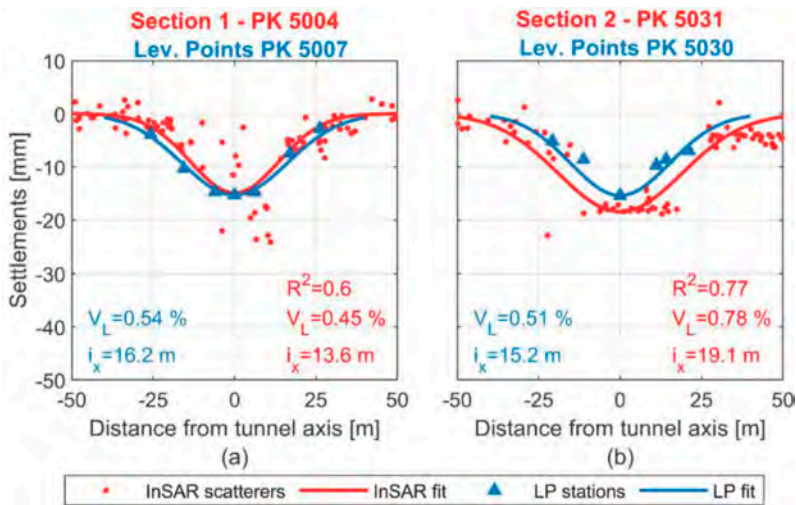


Figure 9. Comparison between levelling and satellite data for building displacements (Di Mariano et al. 2024).

5 CONCLUSIONS

This general report analysed nine papers dedicated to field case studies. Most of them were very interesting, presenting innovative applications in terms of design, construction techniques, and monitoring interpretation and approaches. It is evident that the contexts in which tunnels are built are becoming increasingly demanding over time, thus requiring new technologies as well as innovative engineering solutions. However, significant progress would also rely on an improvement of our understanding of the mechanical processes governing soil-structure interaction phenomena that go beyond mere observation of empirical data and phenomenological analysis. In

this respect, none of the manuscripts included numerical back-analyses, which would have provided a deeper interpretation of the evidence.

Unfortunately, no cases dedicated to deep open excavations were presented, despite the numerous constructions of this type occurring nowadays for railway and metro stations in the urban city centres.

REFERENCES

- Di Mariano, A., Gens, A., Della Ragione, G., Bilotta, E., Sanchez, J., Royo, B. & Cespa, S. 2024. Case study of soil-structure interaction during tunnelling for Barcelona Metro: a comparison between conventional and innovative displacement measurements. *Proceedings of 11th International Conference on Geotechnical Aspects of Underground Construction in Soft Ground, Macao SAR, 14-17 June 2024*.
- Lee, S.W., Leung, C.O., Cheung, K.F., Wijesooriya, T. & Schwob, A. 2024. Modelling of Large Diameter TBM Tunnelling Beneath New Reclamation. *Proceedings of 11th International Conference on Geotechnical Aspects of Underground Construction in Soft Ground, Macao SAR, 14-17 June 2024*.
- Mohanty, S.K., Krenn, F. & Sigl, O. 2024. Underground-unlined crude oil Strategic storage cavern project Visakhapatnam, Andhra Pradesh, India – concept, construction and challenges. *Proceedings of 11th International Conference on Geotechnical Aspects of Underground Construction in Soft Ground, Macao SAR, 14-17 June 2024*.
- Sun, J., Liao, S. & Wang, Z. 2024. A case study on shield cutting reinforced concrete diaphragm walls and piles directly: key technologies and field investigation. *Proceedings of 11th International Conference on Geotechnical Aspects of Underground Construction in Soft Ground, Macao SAR, 14-17 June 2024*.
- Tellioglu, V., Delikan, E., Ozturk, A., Haimoni, A.M. & Maghazy, M. 2024. Early Assessment and Mitigation of Cracking on Concrete Tunnel Segments – Dubai Metro Case Study. *Proceedings of 11th International Conference on Geotechnical Aspects of Underground Construction in Soft Ground, Macao SAR, 14-17 June 2024*.
- Xue, S. & Standing, J.R. 2024. Investigating transient tunnelling-induced ground surface responses. *Proceedings of 11th International Conference on Geotechnical Aspects of Underground Construction in Soft Ground, Macao SAR, 14-17 June 2024*.

Modelling of large diameter TBM tunnelling beneath new reclamation

S.W. Lee & C.O. Leung

Golder Associates (Hong Kong) Limited

K.F. Cheung, T. Wijesooriya & A. Schwob

Dragages Hong Kong Limited

ABSTRACT: The Tuen Mun-Chek Lap Kok Link successfully completed a 14 m diameter slurry mix-shield tunnel boring machine tunnelling in Alluvium, beneath a recently reclaimed land. The in situ clayey Marine Deposits and Alluvium were subject to on-going consolidation and creep settlements under the reclamation loading. This posed a challenge to the design of the tunnels which needed to achieve a limiting tunnel squat of 1% of tunnel diameter and a long-term settlement of 500 mm over an operational life of 120 years. An innovative design was conceived by installing barrettes at the tunnel springlines. The barrettes reduce the ground settlement and tunnel squat by sustaining the arching load around the tunnel. This paper presents the design methodology of tunnel construction by using finite element analysis. The predictions were compared to the field measurements of ground settlements. The strength gain in the clay layers due to consolidation and the barrettes were found to reduce the ground settlement caused by the tunnel excavation.

1 INTRODUCTION

The Tuen Mun–Chek Lap Kok Link (TMCLKL) consists of a 9 km dual two-lane carriageway between Tuen Mun and Lantau Island, Hong Kong, see Figure 1. The alignment commences in Tuen Mun and heads southeast to a new reclamation named as Northern Landfall (NL). It then heads south into a 4.2 km sub-sea tunnel passing beneath a busy navigation channel between Tuen Mun and Lantau Island. The deepest point of the subsea tunnel is 50 m below sea level. The alignment emerges into the Boundary Crossing Facilities reclamation named as Southern Landfall (SL), see Figure 2. The sub-sea tunnels and the 450 m approach tunnels at SL were excavated using two 14 m diameter slurry mix-shield tunnel boring machines (TBMs). This paper presents the background of the TMCLKL tunnel project, geotechnical design/analysis of TBM tunnelling, and comparison between predictions and measurements.

2 GROUND CONDITIONS AND RECLAMATION

The ground conditions at the SL are reclamation Fill, Marine Deposits (MD), Alluvium, completely decomposed granite (CGG) and completely decomposed metasiltstone (CDMS) formed by the weathering of in-situ rocks, see Figure 3. The tunnels were constructed predominantly in Alluvium underlying an area of land recently reclaimed between 2013 and 2016. The original seabed level of the reclamation varied between -3 and -11 metre above Principal Datum (mPD). The finished reclamation ground level is +5.5 mPD. The tunnel horizon is 25 m to 55 m below ground level (mbgl). The groundwater level is tidal and typically at 3 mbgl. When the TBM arrived at the SL in early 2017, the reclamation was still undergoing consolidation settlement at a rate of 1 to 2 mm/day. More details about the geological setting and reclamation can be found in Lee et al. (2023).

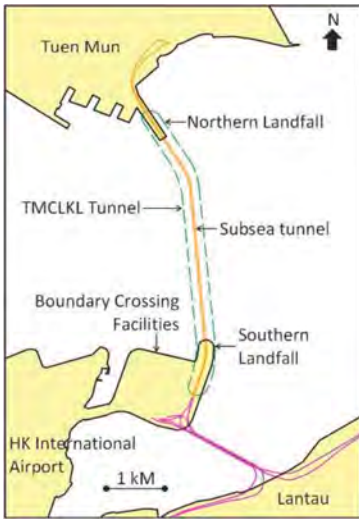


Figure 1. TMCLKL alignment.

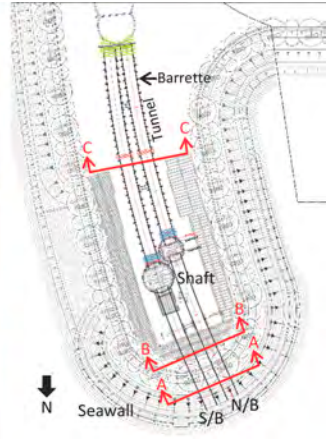


Figure 2. Southern Landfall reclamation and layout plan.

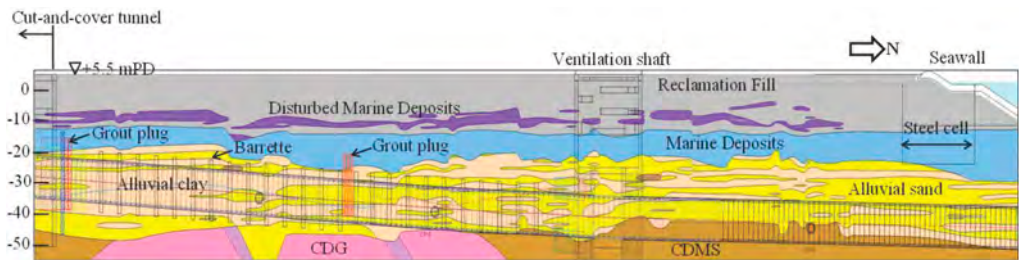


Figure 3. Geological profile at Southern Landfall.

3 SEGMENTAL TUNNEL LININGS AND BARRETTE SYSTEM

Two slurry mix-shield TBMs were deployed to construct the tunnels at the SL, see Figure 4. The segmental linings have an internal diameter of 12.4 m, lining thickness of 550 mm, ring width of 2.2 m, and comprise 6 standard segments, 2 counter keys and 1 large key made of Grade 55 pre-cast reinforced concrete. The ratio of soil cover to tunnel diameter ranged from 2 to 3.

As per the Contract requirement, the limiting tunnel squat (i.e. change of tunnel diameter) was 1% of the tunnel diameter. The squat limit of 130 mm needed to cater for the installation tolerance of linings, soil loadings, and tunnel internal structure loadings over the operational life of 120 years. The TBM would tunnel through the Alluvium layer, comprising interlayers of clay and sand, see Figure 3. The TBM excavation would generate excess pore water pressures in the alluvial clay and the MD layers. This would lead to consolidation settlement or compression in the clay layers, as well as secondary compression (creep) in the long term. This was further complicated by the on-going consolidation settlement caused by the loading of the reclamation itself. A barrette system was therefore designed as a mitigative measure to reduce the tunnel squat in both the short and long terms, see Figure 5.

The unreinforced barrettes were constructed at both sides of the tunnel springline by using the diaphragm wall trenching method prior to the tunnel excavation. The excavated trench sized 1.5 m x 2.8 m was tremie concreted without reinforcement. The excavated trench from the ground surface level to the top of barrette was backfilled with sand. A lower concrete

grade C20 was adopted to ensure that the TBM could excavate through the barrettes without difficulty. The barrettes extended from 2.85 m above the tunnel crown to 2.85 m below the invert, with a total height of 19.2 m. On plan, they were 2.8 m (breadth) x 1.5 m (width), and spaced at 8 m centre-to-centre.



Figure 4. 14m diameter TBMs.

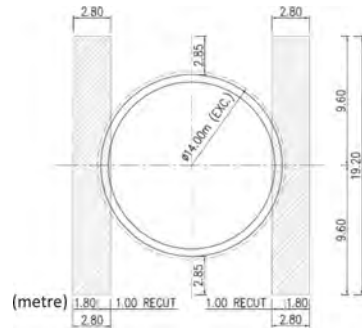


Figure 5. Barrettes at tunnel springline.

4 DESIGN ANALYSIS

A series of 2D and 3D finite element analyses were carried out to design and assess the TBM tunnelling, including TBM break-in and break-out of the ventilation shafts and adjacent cut-and-cover tunnel, stability of the tunnel face when TBM was parked in a grout plug, barrette-supported segmental tunnel linings, etc., see Figure 6. Where necessary, coupled consolidation analyses were conducted for a period of 120 years to model consolidation and creep settlements. The Convergence-Confinement method was adopted for modelling the TBM excavation (Aristaghes & Autuori, 1998), involving two stages, see Figure 7.

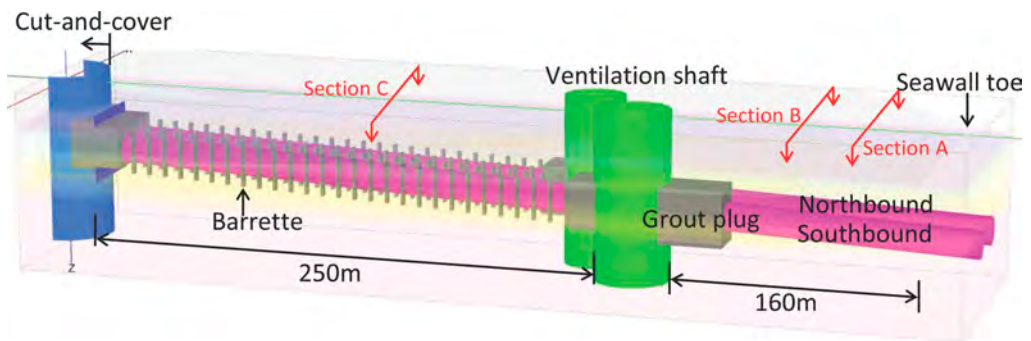


Figure 6. 3D numerical model.

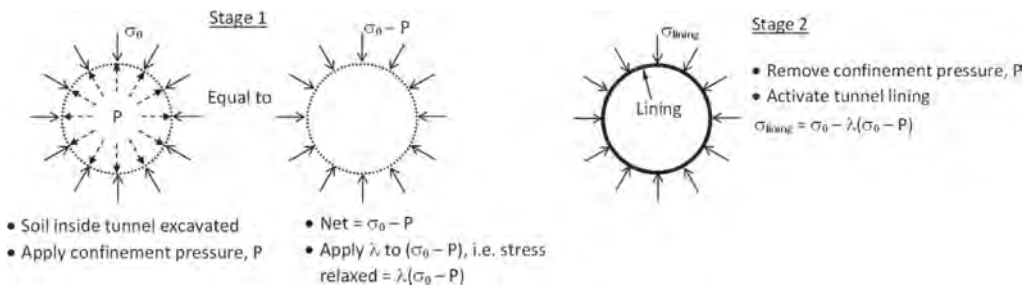


Figure 7. Convergence-confinement modelling of tunnel excavation in 2D.

Stage 1: Excavate soil elements inside tunnel, apply confinement pressure (P) from within tunnel, and apply a deconfinement ratio λ . This models the moment when the tunnel has been excavated and before installing the lining. Parameter P was determined from GEO Report 249, which checked for both ultimate limit state (ULS) for tunnel face stability and serviceability limit state (SLS) for ground deformation. Parameter λ is to consider the progression of the tunnel face relative to the monitored cross section, which is dependent on the ratio of TBM shield length (x) to excavated tunnel radius (R), see Figure 8. For the SL tunnels, $x/R = 13.2 \text{ m}/7 \text{ m} \approx 2$, hence $\lambda \approx 0.9$. The soil stress acting on the excavated tunnel perimeter = $\lambda(\sigma_0 - P) = 0.9(\sigma_0 - P)$, which is equal to ground stress relaxation before installing the linings, and σ_0 is the initial soil stress. The applied P increases with depth at a rate of 11 kPa/m, corresponding to the unit weight of slurry. To maintain the tunnel face stability, the P is at least equal to or greater than hydrostatic water pressure. Please note that the term ‘overpressure’ is defined as the confinement pressure (P) minus the hydrostatic water pressure. In the analysis, P and hydrostatic pressure are physically modelled.

Stage 2: Activate tunnel lining and remove P inside tunnel. This models the moment when the TBM is well past the monitored cross section after installing the lining. The soil stress acting on the lining, $\sigma_{\text{lining}} = \sigma_0 - \lambda(\sigma_0 - P)$. Stage 1 and Stage 2 were modelled for each tunnel. At the design stage, constructions for the 1st and 2nd tunnels were modelled back-to-back without interval.

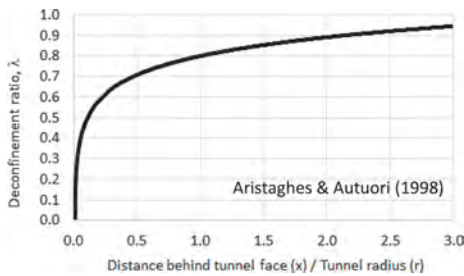


Figure 8. Deconfinement ratio, λ .

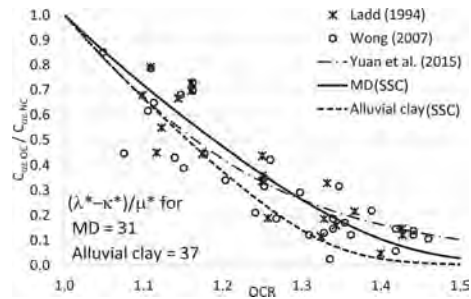


Figure 9. Ratio of C_{oe} in over consolidated state (OC) to normally consolidated state (NC) as a function of OCR.

Table 1 and Table 2 present the design parameters for the soils and the segmental tunnel linings, respectively. The linear elastic, perfectly plastic Mohr Coulomb model was adopted for the coarse-grained soils, whilst the Soft Soil Creep (SSC) model for the fine-grained soils (PLAXIS, V20). The coefficient of secondary compression (C_{ae}) and the over-consolidation ratio (OCR) were determined from cone penetration tests and oedometer tests. Figure 9 compares the relations of reducing C_{ae} with increasing OCR between the SSC predictions and the case histories. The Muir-Wood (1975) formula was adopted to consider the reduced moment of inertia (I_{eq}) of lining ring due to joints, i.e. $I_{eq} = I_{joint} + (4/n)^2 \cdot I_{segment}$, where $n =$ number of lining segments = 9, see Table 2. Figure 10 shows a truncated 3D finite element model, taking advantage of symmetrical planes that exist between the barrettes spaced at 8m c/c. The barrettes functioned by attracting soil arching load caused by the tunnel excavation, thereby sharing the soil overburden load and reducing the increase of stresses (excess pore pressures) in the clay layers. The concentrated stresses in the barrettes were transmitted down to the denser/stiffer stratum below the tunnel invert, e.g. alluvial sand.

Table 1a. Coarse-grained soils modelled by mohr coulomb model.

Soils	γ (kN/m ³)	ν' (-)	c' (kPa)	ϕ' (°)	k (m/s)	E'(MPa)
Fill	20	0.25	0	33	5×10^{-4}	15
Alluvial sand	19	0.25	0	35	1×10^{-6}	30–60
CDG	19	0.25	5	32	1×10^{-7}	> 60
CDMS	20	0.25	3	30	1×10^{-7}	> 80

γ = unit weight, ν' = Poisson's ratio, c' = effective cohesion, ϕ' = effective friction angle, k = permeability, E' = effective Young's modulus

Table 1b. Fine-grained soils modelled by soft soil creep model.

Soils	γ	ν'	c'	ϕ'	k	e_0	C_C	C_S	C_{α}	OCR
MD	16	0.3	0	28	5×10^{-9}	2.0	0.9	0.075	0.024	1.2
Alluvial clay	19	0.25	0	28	1×10^{-8}	1.1	0.25	0.045	0.0075	1.5

e_0 = initial void ratio, C_C = compression index, C_S = swelling index, C_{α} = secondary compression index, $C_{\alpha e} = C_{\alpha}/(1+e_0)$, $\lambda^* = C_C/[(2.3(1+e_0))]$, $\kappa^* \approx 2C_S/[(2.3(1+e_0))]$, $\mu^* = C_{\alpha}/[(2.3(1+e_0))]$

Table 2. Segmental tunnel linings modelled by plate elements with the linear elastic model.

γ (kN/m ³)	ν (-)	E (MPa)	I_{segment} (m ⁴ /m)	I_{joint} (m ⁴ /m)	I_{eq} (m ⁴ /m)	EA (MN/m)	EI (MNm ² /m)
25	0.2	28,900	0.0139	0.0042	0.0070	15,895	201

5 FIELD MEASUREMENTS

Figures 11(a), 11(b) and 11(c) compare the measured ground surface settlements with the design predictions at Sections A, B and C, respectively, see Figures 2 and 6. Legends “1st tun, 0m” and “1st tun, 14m” denote the 1st TBM face was right under the monitored section and went past the monitored section by 14m, respectively. The measured volume loss (VL), i.e. volume of the ground surface settlement curve per unit length, and the measured VL ratio, i.e. the VL divided by the cross-sectional area of the excavated tunnel(s), are summarised in Lee et al. (2023).

At Section A, the applied overpressure at the tunnel axis level was 77 kPa, similar to the design overpressure of 73 kPa (Lee et al., 2023). The difference in the measured settlements between stage “1st tunnel, 42m” and “2nd tunnel, 0m” represented the consolidation settlement that occurred over a period of three months from February to May 2017, when a consolidation settlement of 27 mm was measured above the 1st tunnel centreline. The design analysis did not model a consolidation period of three months to consider the different construction timing of the two tunnels, hence the predicted maximum settlement of 40 mm was smaller than the measured maximum of 62 mm. If the consolidation settlement that occurred between the construction of the two tunnels was excluded, the measured VL ratio reduced from 1.65% to 1.1%, which was still slightly larger than the predicted 0.9%.

At Section B, the applied overpressure at tunnel axis level was 110 kPa, compared to the design overpressure of 50 kPa (Lee et al., 2023). This could explain the measured maximum settlement of 43 mm being smaller than the predicted maximum of 65 mm, despite a consolidation settlement of 18 mm occurred between stage “1st tunnel, 42m” and “2nd tunnel, 0m” over a period of three months from February to May 2017. The measured VL ratio of 0.68% (or 0.52% excluding the intervening consolidation settlement) was smaller than the predicted 1.5%.

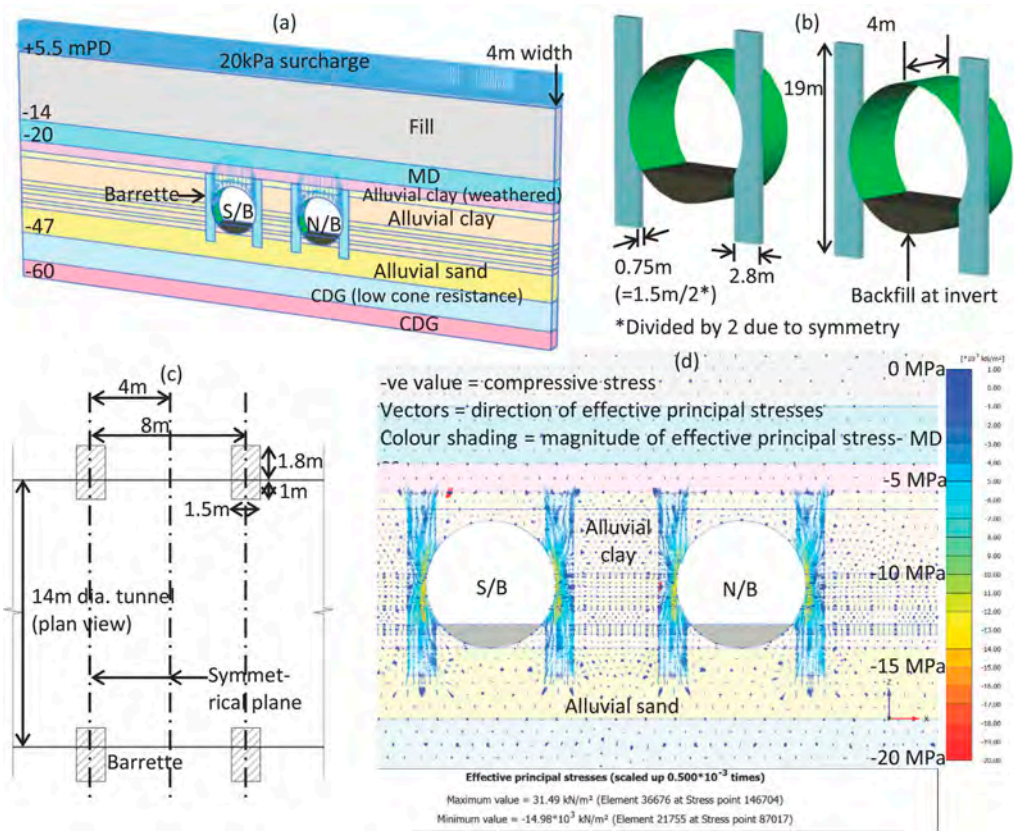


Figure 10. (a) And (b) truncated 3D model; (c) plan view of barrettes; (d) arching above barrettes and concentration of stresses in barrettes.

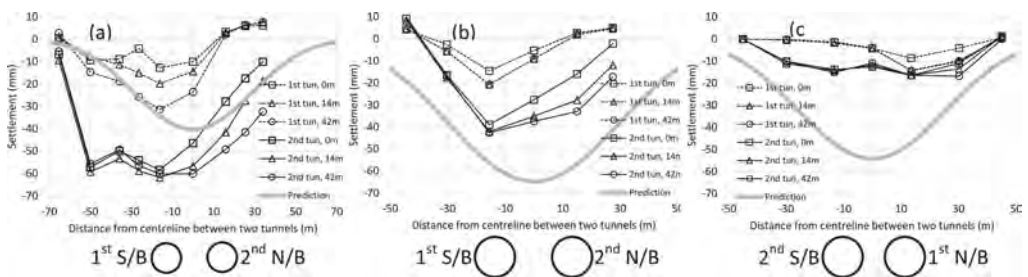


Figure 11. (a) Measured and predicted settlements at section A; (b) at section B; (c) at section C.

At Section C, the applied overpressure at the tunnel axis level was 128 kPa, compared to the design overpressure of 108 kPa (Lee et al., 2023). The difference of 20 kPa was not significant, as the design of confinement pressure typically allowed for a variation of +/- 20 kPa. The tunnelling at Section C was carried out from February to June 2018, which was one year later than Sections A and B. Much consolidation had occurred during the one-year period, and the MD and alluvial clay at Section C had gained strength. Only 2 mm consolidation settlement occurred between stage “1st tunnel, 42m” and “2nd tunnel, 0m” over a period of one and a half months above the 1st tunnel centreline. The stronger ground and the barrettes

at Section C had resulted in the measured maximum settlement of 17 mm being smaller than the predicted maximum of 54 mm. The measured VL ratio of 0.30% (or 0.25% excluding the intervening consolidation settlement) was much smaller than the predicted 1.1%.

6 CONCLUSIONS

The newly reclaimed land was still undergoing consolidation settlements when the tunnelling was carried out in Alluvium, overlain by soft Marine Deposits and sand fill. Barrettes were installed at the tunnel springlines for a section of the tunnel alignment to reduce the tunnel squat in both short and long terms. During tunnel excavation, soil arching above the tunnel crown transmitted the overburden soil loads to the barrettes which subsequently transmitted the loads down to the underlying denser/stiffer Alluvium. The measured volume loss ratio of 1.65% in the seawall area were higher than the predicted 0.9%, due to a higher rate of consolidation settlement when the TBM first arrived at the Southern Landfall (i.e. a relatively weak ground). In the barrette-supported area, the tunnelling was carried out one year later and much consolidation had occurred. The measured volume loss ratio of 0.3% was much smaller than the predicted 1.1%, partly due to the effectiveness of the barrettes.

At the completion of the tunnelling-induced settlements, there was no distress caused to the recent reclamation platform and seawalls. The TMCLKL tunnels provided a valuable case history for future large diameter tunnels to be constructed in heterogeneous ground conditions underlying new reclamations and soils developing consolidation and creep settlements.

REFERENCES

- Aristaghes, P. & Autuori, P. 1998. Slurry TBM in urban areas: connection between calculation and driving. In Negro Jr & Ferreira (eds), *Tunnels and Metropolis*: 841–847.
- Geotechnical Engineering Office 2009. *GEO Report 249 on Ground Control for Slurry TBM Tunnelling*. The Government of the Hong Kong SAR.
- Ladd, C.C. 1994. Soil behavior, class notes of MIT Course 1.322. <http://ocw.mit.edu/courses/civil-and-environmental-engineering/1-322-soil-behavior-spring-2005/lecture-notes/>.
- Lee, S.W., Leung, C.O., Cheung, C., Wijesooriya, T. & Schwob, A. 2023. Large diameter TBM tunnelling beneath new reclamation. *ISSMGE International Journal of Geoenvironment Case Histories* 7(3): 56–77.
- PLAXIS V20. *PLAXIS Material Models CONNECT Edition V20.02*.
- Wong, P.K. 2007. Preload design to reduce post construction creep settlement. Soft soils and ground improvement workshop, *Proc. 10th Australia New Zealand Conference on Geomechanics*: 23–31.
- Wood Muir, A.M. 1975. The circular tunnel in elastic ground. *Géotechnique* 25(1): 115–128.
- Yuan, Y., Whittle, A.J. & Nash, D.F.T. 2015. Model for predicting and controlling creep settlements with surcharge loading. *Proc. 6th International Symposium on Deformation Characteristics of Geomaterials*: 931–938.

Ground loss and settlement of shield tunnel in tail grouting

J. Liang

College of Civil Engineering, Taiyuan University of Technology, Taiyuan, China

W. Liu

School of Rail Transportation, Soochow University, Suzhou, China

Key Laboratory of Coastal Urban Resilient Infrastructures (Shenzhen University), Ministry of Education, China

T. Xu

School of Transportation, Southeast University, Nanjing, China

ABSTRACT: Tail grouting is regarded as an efficient method for reducing ground loss during shield tunnelling. The grout will inevitably be compressed under earth pressure, resulting in ground loss and surface settlement that have not been accurately estimated. In this paper, the compressed deformation of tail grouts subjected to earth pressure in different types of soils was investigated using a lab device. The lab test results reveal that compressed deformation rises with increased pressure and soil permeability. As the pressure increases, the increase rate of ultimate compressed deformation becomes smaller. Based on test results, analysis was conducted to determine how ground loss and surface settlement were affected by various parameters, including tail gap, tunnel radius, pressure, burial depth and soil permeability. The study could provide accurate predictions of ground loss and surface settlement considering grouting material properties.

1 INTRODUCTION

In shield construction, it is inevitable to induce ground loss and thereby cause surface settlement, as shown in Figure 1. Tail grouting is recognized as a useful approach in shield construction for controlling ground deformation (Kravitz et al., 2019; Shao et al., 2022; Mohammadzamani et al., 2023). This method involves filling the tail gap with specific grouting materials. As shown in Figure 2, tail grouts will inevitably be compressed under the earth pressure (Bezuijen & Talmon, 2006; Bezuijen et al., 2009; Liu et al., 2021; Liu et al., 2023). Unfortunately, the visualization of tail grout deformation during construction remains elusive, and direct measurement of the compressed deformation has proven challenging. The precise prediction of ground loss caused by grout deformation was inaccessible (Chen & Jia, 2019; Ren et al., 2023). It is crucial to examine the compressed deformation of tail grouts under earth pressure in order to improve the accuracy of tunneling-induced settlement estimations.

Tail grout consolidation is postulated to be the cause of the compressive deformation (Talmon & Bezuijen, 2009; Liu et al., 2021; Qin et al., 2021). Bezuijen et al. (2009) simulated the consolidation process of grouts using a pressure cell and noticed that the pressure on the grouts had a significant impact on their performance. Based on their field investigation, Talmon and Bezuijen (2009) identified that the consolidation of grouts was influenced by the permeability of the surrounding soil. Qin et al. (2021) used the oedometer test and column consolidation tests to explore the consolidation of the grouts. In contrast to the actual procedure of tail grouting, the impact of surrounding soil porosities is disregarded. Nazari et al. (2021) used the one-dimensional consolidation test to investigate the variation of void ratio after consolidation of the grout. Comparatively, the grouts injected into the tail tap measured between 1000 mm and 20,000 mm in height, whereas

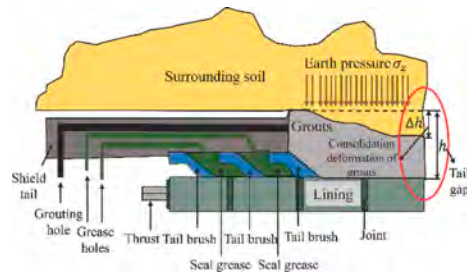


Figure 1. Tunnelling-induced ground settlement. Figure 2. Tail grouting (Liu et al., 2023).

the grout samples utilized in the experiments measured only 20 mm in height. Thus, in order to directly measure the compacted deformation of grouts, it is necessary to develop a test device that can effectively simulate various pressures on grouts while taking into consideration the permeability of the surrounding soils.

The ground loss is usually calculated by the gap parameter, which is considered induced by the deformation of tail grouts towards lining in analysis (Loganathan & Polous, 1998). The ground loss parameters and the surface settlement are usually adopted empirical values and vary for different construction conditions (Peck, 1969; Chi et al., 2001; Park, 2005; Zhang et al., 2016; Jin et al., 2022; Chen et al., 2022). The deformation of the tail grouts, however, could not be precisely calculated because it differs greatly depending on various construction parameters, including grouting pressure (Wu & Zhu, 2018; Ying et al., 2022; Lu et al., 2022), surrounding soil properties (Liang et al., 2022), and grouting volume (Ding et al., 2019; Mohammadzamani et al., 2023). The clarification of compressed deformation has great influence on the accuracy prediction of ground settlement. In this way, ground loss and surface settlement subjected to the compressed deformation of grouts should be explored.

In this paper, a test apparatus was devised to investigate the compressed deformation of tail grouts subjected to earth pressure in a variety of soils. With the test device, the compressed deformation could be real-time directly measured. Based on the test results, the ground loss and surface settlement were calculated and analyzed considering the influence of tail gap, tunnel radius, pressure, burial depth and soil permeability, which could provide references for optimization of construction parameters.

2 LAB TESTS

2.1 Test device

Figure 3 shows the lab test device that was developed to investigate the compressed deformation of grouts. The diameter of the test device was 20 cm, the soil materials had a height of 10 cm, and the grouts had a height of approximately 15 cm.

The grout was injected into the selected soil materials within the test column. Pressure was subsequently applied on the upper surface of a piston positioned above the grout. The resulting compressed deformation of the grout was then measured in real-time using a displacement sensor. The ground loss resulting from the compression of the grout can be defined as $\varepsilon = \Delta h/h$, where Δh represents the compressed deformation of the grouts, and h represents the original height of the grouts. The piston placed on the grout serves the purpose of maintaining uniform pressure on the grout and preventing air from infiltration. The pore pressure sensor in the test apparatus is utilised to observe the fluctuation of pore pressure in the grout. The consolidation of the grouts is thought to be complete when the pore pressure in the grout reaches a stable state. The ultimate deformation is considered to be the compressed deformation of the grout that corresponds to it.

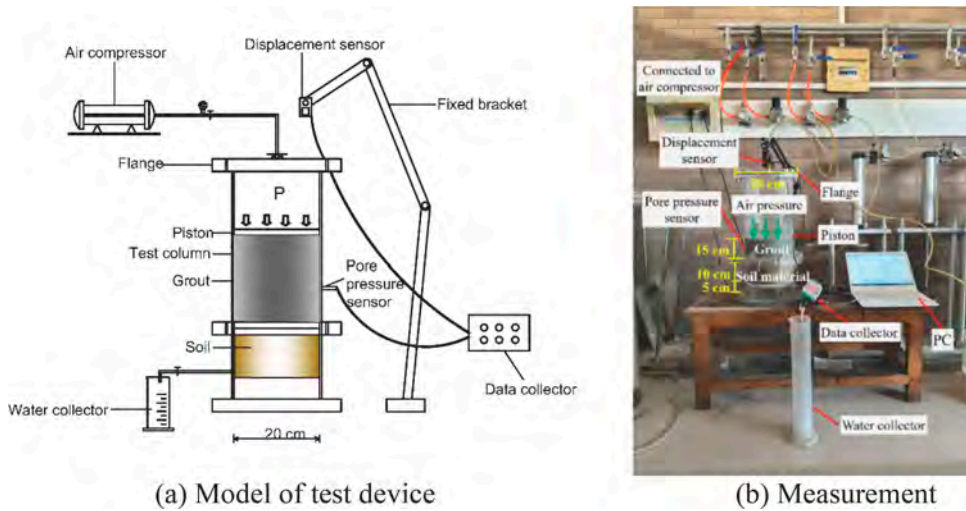


Figure 3. Test device.

2.2 Test materials

The grout used for the test is the concrete grout consisting of cement, fly ash, bentonite and sand, which is commonly used in shield tail grouting construction (Ding et al., 2019; Mao et al., 2020; Liang et al., 2022; Liu et al., 2023). Cement is the most essential component of the grouts to distinguish inert grouts and concrete grouts. In this research, the 42.5 Ordinary Portland cement was prepared according to ASTM C150/C150M-2012. The cement loss on ignition is 2.3%, the initial and final sets are 130 min and 255 min, the 3 d and 28 d compressive strength are 28.6 MPa and 56.8 MPa. According to ASTM C618-12, the Class F fly ash was selected to be used in the test. The loss on ignition of the selected fly ash is 3.5%, and the percent retained on 45 μm is 20%. The sodium bentonite was used in this research. Table 1 listed the major chemical composition of cement, fly ash and bentonite used in the tests. The ISO standard sand selected in this research was qualified for ISO 679-2009.

Table 1. Major chemical composition of raw materials.

Chemical composition	SiO ₂	Al ₂ O ₃	Fe ₂ O ₃	MgO	CaO	SO ₃	Na ₂ O	K ₂ O	P ₂ O ₅	TiO ₂
Cement (%)	23.50	7.60	4.80	2.50	57.20	2.40	/	/	/	/
Fly ash (%)	53.04	34.70	2.53	0.86	2.32	0.35	0.475	1.76	0.12	1.25
Bentonite (%)	64.10	16.39	4.67	3.22	3.16	0.03	4.10	2.12	0.20	0.91

The detailed proportion of the grout in the test is as follows: each kilogram of the grout contains 81 g of cement, 202 g of fly ash, 40 g of bentonite, 282 g of sand and 395 g of water. Three typical types of soil materials utilized in the tests are prepared according to ASTM D2487-00 as sand, silt and clay. The geotechnical parameters are shown in Table 2.

Table 2. Properties of soil materials.

Soil type	γ (kN/m ³)	c' (kPa)	φ' (deg)	k (cm/s)	d_{50} (mm)	C_u	C_c
Sand	17.6	1.4	31.4	4.6×10^{-2}	0.34	1.542	1.104
Silt	18.0	22.2	19.5	9.1×10^{-5}	/	/	/
Clay	17.9	11.0	9.5	4.0×10^{-7}	/	/	/

Note: γ is unit weight, c' is cohesion, φ' is internal friction angle, k is permeability coefficient, C_u is coefficient of uniformity, and C_c is coefficient of curvature.

3 TEST RESULTS

The basic performance of the grout was firstly tested to ensure that the grout is qualified for tail grouting. The grout is supposed to have certain stability and fluidity for transportation and injection in process of tail grouting. The detailed basic performance of the grout is as follows: the density is 1464 kg/m^3 , the fluidity is 350 mm , the bleeding rate is 18.85% , the consistency is 128 mm , the stone rate is 79.44% .

Figure 4 shows the compressed deformation of the grout under different pressure in sand, silt and clay, respectively. A nonlinear increase in time is observed in the compressed deformation of the grout. The compressed deformation first shows an almost linear increase, followed by a drop in the rate of growth. Eventually, the compressed deformation approaches the ultimate deformation (ε_0).

As shown in Figure 4, in the same soil, with the increase of the pressure, the compressed deformation increases as well. As the pressure rises from 100 kPa to 300 kPa , the amount of deformation increases from 31.47% to 39.46% in sand, from 25.37% to 29.30% in silt, and from 4.85% to 5.57% in clay. This is due to the fact that when the pressure increases, the grout is more prone to compaction, and the water in the grout is more likely to be expelled under high pressure, leading to an increase in compressed deformation. It is important to mention that when the pressure is below 300 kPa , the sand has a compressed deformation of approximately 10% at the start of the test, as shown in Figure 4a. The free water is compressed from the grout and discharged to the sand immediately. Thus, the deformation occurred instantaneously. When subjected to larger pressure, the consolidation of the grout can cause significant and immediate deformation in soil with high permeability. In such cases, additional reinforcements should be implemented.

When subjected to the same pressure, sand exhibits the greatest amount of compressed deformation, followed by silt, while clay has the least amount of deformation. As soil permeability decreases, the compressed strain also reduces. The grout's deformation decreases significantly in clays with very low permeability. Take the grout under 100 kPa as an example, the ε_0 in sand, silt and clay are 31.47% , 25.37% and 4.85% respectively. The compressed deformation grout in sand is close to that in silt, while it is rather small in clay. Compared Figure 4a and Figure 4c, the ε_0 value in clay is merely 15% of the value found in sand, and it exhibits a significant decline. The larger permeability of sand and silt compared to grout results in a higher drainage of water from the grout into the sand and silt, leading to increased compression deformation. The permeability of clay is similar to that of grout, resulting in limited drainage of water from the grout into the clay. This leads to a lower rate of compressive deformation in the grout compared to the bleeding rate. The similar variation could also be found in the grout under 200 kPa and 300 kPa .

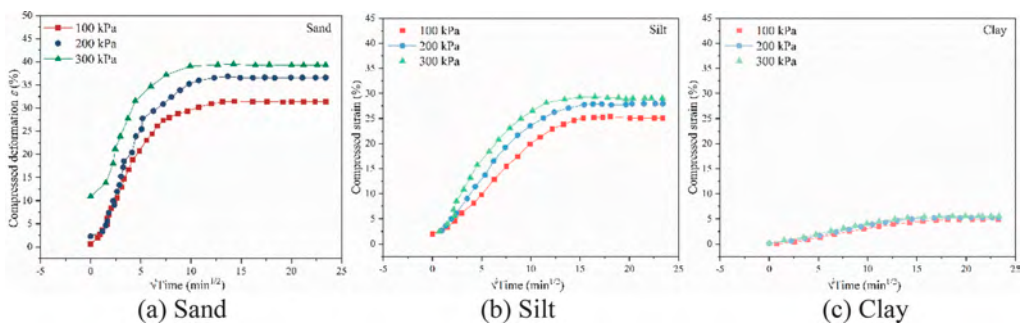


Figure 4. Time-varying deformation of the grout in different soils.

Figure 5 shows the ultimate compressed deformation (ε_0) of the grout under varying pressure in different soils. It could be found that the ε_0 will not increase indefinitely with the increase of pressure. As the pressure increases, the rate of increase of ε_0 decreases. The ε_0 is

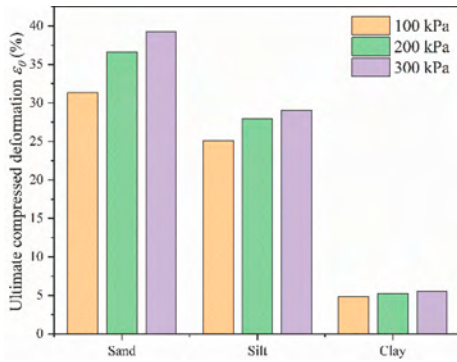


Figure 5. Ultimate compressed deformation.

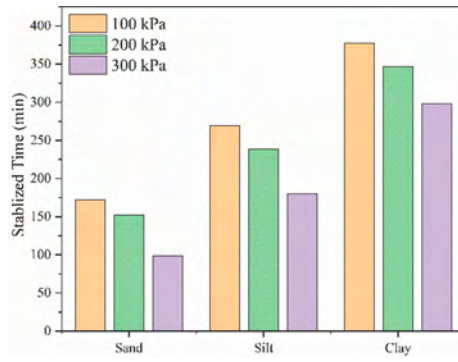


Figure 6. Stabilized time.

quite larger than bleeding rate in sand and silt, which indicates that the earth pressure could induce excessive deformation of the grout. Figure 6 illustrates that as the pressure rises from 100 kPa to 300 kPa, the time required for the grout's deformation to reach a stable state drops by around 50% in sand, but in clay it only decreases by 20%. Clay takes a significantly longer time to stabilize compared to sand and silt. Using the grout under 100 kPa as an example, the time it takes for the grout to reach a stable state is just 20% of the time it takes in clay when placed in sand. At higher pressures, the compressed deformation of the grout exhibits a quicker stabilization, particularly in soil with high permeability. When tunnelling in soil with high permeability, the consolidation of the grout may induce excess ground deformation, and grout with high performance should be utilized in tail grouting.

4 GROUND LOSS AND SETTLEMENT

According to Loganathan and Poulos (1998) and Peck (1969), the ground loss (V_{loss}) and ground surface settlement (S) could be calculated. The V_{loss} is calculated by the ground loss volume in plane. Take the grout in lab test as an example.

Figure 7 shows the variation of ground loss with different construction parameters. As shown in Figure 7a, as the tail gap increases, the V_{loss} increases linearly. The increase rate of V_{loss} is larger in soil with higher permeability. In Figure 7b, it could be found that with the increase of the tunnel lining radius (R_L), the V_{loss} increases correspondingly. The V_{loss} is more prominent when R_L increases in sand, in contrast to silt and clay. Figure 7c displays the V_{loss} at various pressures (P). The relationship between V_{loss} and pressure is nonlinear, with a more pronounced increase in V_{loss} observed at lower pressures. This is because the pores in the grout have a limited capacity to compress under increasing pressure. When the pressure decreases, the water in the grout can drain more freely, resulting in a higher increase in V_{loss} .

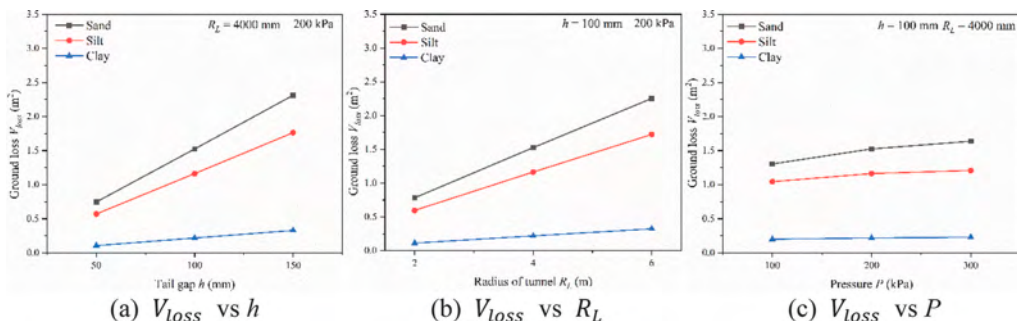


Figure 7. Variation of ground loss.

The ground loss has significant variation across different soils. As the soil's permeability decreases, the V_{loss} also decreases. The V_{loss} is significantly greater in sands compared to clay, with clays exhibiting only around 20% of the V_{loss} observed in sands.

Figure 8 shows the surface settlement distribution with different construction parameters. In Figure 8a, there is a significant rise in surface settlement as the tail gap grows. In sand, when the tail gap (h) increases from 50 mm to 200 mm, the maximum surface settlement increases about 300%. As shown in Figure 8b, the surface settlement exhibits a positive correlation with the increasing R_L . In sand, when the R_L increase from 2 m to 6 m, the maximum surface settlement increase about 200%. It indicates that construction of large-diameter shields can cause greater surface settlement. Figure 8c illustrates the impact of pressure on the surface settlement. When the pressure rises from 100 kPa to 300 kPa, the maximum surface settlement in sand increases by approximately 25%. Compared to the surface settlement in sand, the settlement in clay is rather small, which is only 5% of that in sand. For different construction conditions as shown Figure 8, the similar settlement trends could be found in silt and clay as in sand, while the increase rate for silt and clay is rather small. This indicates that grout with high performance should be adopted when excavation in soil with large permeability.

Figure 9 show the surface settlement with larger burial depth (C). Compared to Figures 8, it could be found in Figure 9 that the surface settlement decreases with the increase of C for the same V_{loss} . When the C increases from 12 m to 20 m, the maximum surface settlement decreases about 40%. This is due to that with the increasing of C the arching effect of the surrounding soils is enhanced, which results in the decrease of the surface settlement. It indicates that more reinforcement should be applied to in construction when tunnelling with shallow depth.

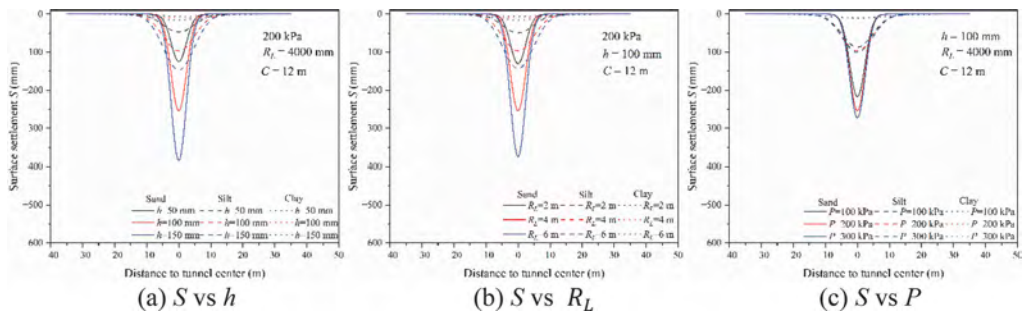


Figure 8. Surface settlement distribution at $C=12$ m.

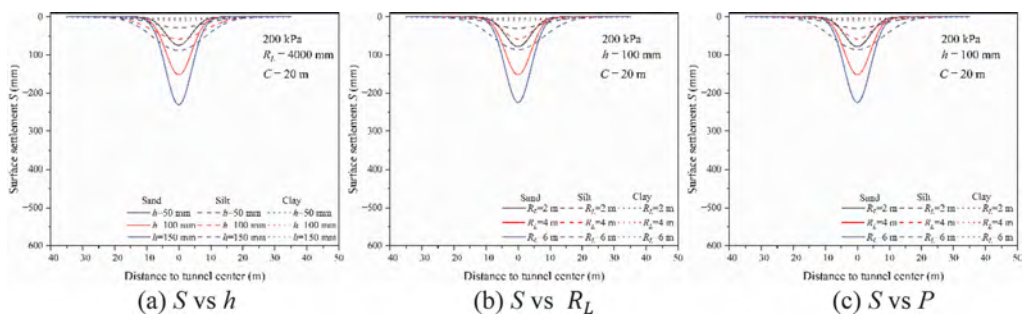


Figure 9. Surface settlement distribution at $C=20$ m.

As shown in Figures 8-9, the width of the settlement trough is greater in clay than in sand and silt. The consolidation of grouts will lead to wider range of settlement in soil with lower

permeability. It indicates that more attention needs to be paid to the deformation of surrounding structures when excavating in soft soils. When comparing Figure 9 with Figure 8, it is evident that the width of the settlement trough grows as the value of C increases. This finding indicates that tunnelling to greater depths induces a broader range of settlement, which is consistent with prior investigations (O'Reilly & New, 1982). When excavating in soil with low permeability such as silt and clay, more attention should be paid to settlement on a wider range and greater reinforcement should be applied in construction.

5 CONCLUSIONS

In this paper, the ground loss and surface settlement considering compressed deformation of tail grouts under earth pressure was investigated by a designed lab device. The compressed deformation could be real-time directly measured by the test device subjected to different pressure and soils permeabilities. Based on the test results, the ground loss and surface settlement could be accurately calculated, and the influence of various parameters were analyzed. The main conclusions are as follows:

1. With the lab test device, it was possible to precisely measure the real-time compressed deformation of the grout. The consolidation of the grout in different soils under different pressure could be explored.
2. As time increases, the compressed deformation grows nonlinearly, while the rate of growth falls. The compressed deformation increases with the increasing pressure and increasing soil permeability. The extent of deformation in clay grout is just 10%-15% compared to that in sand. The time required for the grout to reach a stable state of deformation in sand is only 15%-20% of the time it takes in clay. The value of ε_0 will not continue to rise indefinitely as pressure increases. As the pressure rises, the magnitude of ε_0 's increase decreases.
3. Based on the lab test results, the ground loss and surface settlement in different soils could be calculated. With the increase of tail gap, tunnel radius and pressure, the ground loss and maximum surface settlement increases. With the same ground loss, the increase of the burial depth will decrease the surface settlement. Soil permeability has great influence on the surface settlement, of which in clay is only 5% of that in sand. The settlement trough is much larger in clay than in silt and sand, wider reinforcement of grouting should be applied in tunnel construction.

ACKNOWLEDGEMENT

This research is supported by the National Natural Science Foundation of China (Grant No. 51978430), Natural Science Foundation of Jiangsu Province China (Grant No. BK20231318), and Open Research Fund of Key Laboratory of Coastal Urban Resilient Infrastructures (Shenzhen University), Ministry of Education (Grant No. CURI-G202304). These supports are gratefully appreciated.

REFERENCES

- Bezuijen, A., Sanders, M., & Den Hamer, D. 2009. Parameters that influence the pressure filtration characteristics of bentonite grouts. *Géotechnique*, 59(8): 717–721.
- Bezuijen, A., & Talmon, A. 2006. Grout pressures around a tunnel lining, influence of grout consolidation and loading on lining. In H. van Lottum & A. Bezuijen (Eds.), *Tunnelling. A Decade of Progress. GeoDelft 1995-2005*: 109–114. Taylor & Francis.
- Chen, R. P., Song, X., Meng, F. Y., Wu, H. N., & Lin, X. T. 2022. Analytical approach to predict tunneling-induced subsurface settlement in sand considering soil arching effect. *Computers and Geotechnics*, 141: 104492.
- Chen, Z., & Jia, P. 2019. Three-dimensional analysis of effects of ground loss on static and seismic response of shafts. *Tunnelling and Underground Space Technology*, 92: 103067.

- Chi, S. Y., Chern, J. C., & Lin, C. C. 2001. Optimized back-analysis for tunneling-induced ground movement using equivalent ground loss model. *Tunnelling and Underground Space Technology*, 16(3): 159–165.
- Ding, W., Chao, D., Zhu, Y., Zhao, T., Huang, D., & Li, P. 2019. The behavior of synchronous grouting in a quasi-rectangular shield tunnel based on a large visualized model test. *Tunnelling and Underground Space Technology*, 83(01): 409–424.
- Jin, H., Yuan, D., Zhou, S., & Zhao, D. 2022. Short-Term and Long-Term Displacement of Surface and Shield Tunnel in Soft Soil: Field Observations and Numerical Modeling. *Applied Sciences*, 12(7): 7.
- Kravitz, B., Mooney, M., Karlovsek, J., Danielson, I., & Hedayat, A. 2019. Void detection in two-component annulus grout behind a pre-cast segmental tunnel liner using Ground Penetrating Radar. *Tunnelling and Underground Space Technology*, 83: 381–392.
- Liang, J., Tang, X., Wang, T., Lin, W., Yan, J., & Fu, C. 2022. Analysis for Ground Deformation Induced by Undercrossed Shield Tunnels at a Small Proximity Based on Equivalent Layer Method. *Sustainability*, 14(16): 9972.
- Liang, X., Ying, K., Ye, F., Su, E., Xia, T., & Han, X. 2022. Selection of backfill grouting materials and ratios for shield tunnel considering stratum suitability. *Construction and Building Materials*, 314: 125431.
- Liu, W., Liang, J., & Xu, T. 2023. Tunneling-Induced Ground Deformation Subjected to the Behavior of Tail Grouting Materials. *Tunnelling and Underground Space Technology*, 140: 105253.
- Liu, X. X., Shen, S. L., Xu, Y. S., & Zhou, A. 2021. Non-linear spring model for backfill grout-consolidation behind shield tunnel lining. *Computers and Geotechnics*, 136: 104235.
- Lu, Z., Zhou, W. H., Yin, Z. Y., & Yang, J. 2022. Numerical modeling of viscous slurry infiltration in sand. *Computers and Geotechnics*, 146: 104745.
- Mao, J., Yuan, D., Jin, D., & Zeng, J. 2020. Optimization and application of backfill grouting material for submarine tunnel. *Construction and Building Materials*, 265: 120281.
- Mohammadzamani, D., Lavasan, A. A., & Wichtmann, T. 2023. Tail void grouting material: A parametric study on the role of hydro-mechanical characteristics in mechanized tunneling. *Tunnelling and Underground Space Technology*, 135: 105053.
- Nazari, Z., Tabarsa, A., & Latifi, N. 2021. Effect of compaction delay on the strength and consolidation properties of cement-stabilized subgrade soil. *Transportation Geotechnics*, 27: 100495.
- O'Reilly, M.P., New, B.M. 1982. Settlement above tunnels in the United Kingdom—Their magnitude and prediction. *Proceedings of Tunnelling*, 173–181.
- Park, K. H. 2005. Analytical solution for tunnelling-induced ground movement in clays. *Tunnelling and Underground Space Technology*, 20(3): 249–261.
- Peck, R. B. 1969. Deep excavations and tunneling in soft ground. Proceedings of the 7th International Conference on Soil Mechanics and Foundation Engineering. Mexico City: [s. n.], 225–290.
- Qin, J., Zheng, J., & Li, L. 2021. An analytical solution to estimate the settlement of tailings or backfill slurry by considering the sedimentation and consolidation. *International Journal of Mining Science and Technology*, 31(3): 463–471.
- Ren, Y., Zhang, C., Zhu, M., Chen, R., & Wang, J. 2023. Significance and formulation of ground loss in tunneling-induced settlement prediction: a data-driven study. *Acta Geotechnica*, 18(9): 4941–4956.
- Shao, X., Yang, Z., Jiang, Y., Yang, X., & Qi, W. 2022. Field test and numerical study of the effect of shield tail-grouting parameters on surface settlement. *Geomechanics and Engineering*, 29(5): 509–522.
- Talmon, A. M., & Bezuijen, A. 2009. Simulating the consolidation of TBM grout at Noordplaspolder. *Tunnelling and Underground Space Technology*, 24(5): 493–499.
- Wu, C., & Zhu, Z. 2018. Analytical Method for Evaluating the Ground Surface Settlement Caused by Tail Void Grouting Pressure in Shield Tunnel Construction. *Advances in Civil Engineering*, 2018: 1–10.
- Ying, K., Ye, F., Li, Y., Liang, X., Su, E., & Han, X. 2022. Backfill grouting diffusion law of shield tunnel considering porous media with nonuniform porosity. *Tunnelling and Underground Space Technology*, 127: 104607.
- Zhang, Z. X., Liu, C., Huang, X., Kwok, C. Y., & Teng, L. 2016. Three-dimensional finite-element analysis on ground responses during twin-tunnel construction using the URUP method. *Tunnelling and Underground Space Technology*, 58: 133–146.

Case study of soil-structure interaction during tunnelling for Barcelona Metro: A comparison between conventional and innovative displacement measurements

A.D. Mariano & A. Gens

Centre Internacional de Mètodes Numèrics a l'Enginyeria (CIMNE) & Department of Civil & Environmental Engineering, Universitat Politècnica de Catalunya · BarcelonaTech, Barcelona, Spain

G.D. Ragione & E. Bilotta

Department of Civil, Architectural and Environmental Engineering, University of Napoli Federico II, Napoli, Italy

J. Sanchez, B. Royo & S. Cespa

TRE ALTAMIRA S.L.U., Barcelona, Spain

ABSTRACT: The paper presents a case study on the response of an existing framed building founded on a deep basement to the construction of a 12 m diameter tunnel passing below it, in the city of Barcelona. Ground conditions on site involved a diverse range of soil materials, from very soft deposits to hard rock layers. The water table is located at a depth of about 10 m. The tunnel cover varies approximately from 30 to 36 m. Ground and building movements during tunnel construction were monitored. In the paper, the movements measured with conventional optical surveys are compared to those measured by multitemporal-InSAR analyses of satellite images. Hence, benefits and limitations of the latter technique in such complex Soil Structure Interaction (SSI) problem are discussed.

1 INTRODUCTION

Tunnelling under densely built urban areas is always a challenging task that may represent a risk for existing structures along the tunnel alignment. When tunnelling involves large diameter excavations, curved alignments and complex geological conditions, risks generally increase. In such scenarios, soil-structure interaction (SSI) problems are often difficult to analyse and even the most accurate prediction of tunnelling effects on buildings may be sometimes affected by large uncertainties. Monitoring tunnel construction is therefore a fundamental tool to control the performance of affected buildings and provide the necessary data to identify the need to undertake any mitigation action.

Due to the large number of buildings potentially affected by shallow tunnelling in urban areas, a preliminary screening of the most vulnerable ones is necessary to limit the scope of monitoring. This is generally based on established procedures, empirically accounting for the expected level of greenfield ground deformation (Peck, 1969; Attewell & Woodman, 1982; Rankin, 1988). Furthermore, historical buildings, heritage structures and public relevance infrastructures are of special interest.

Datasets gathered from monitoring are also an important source of information for the back-analysis of complex soil-structure interaction problems. This improves the potential of numerical modelling and calculations to capture several aspects of such interaction and enable better predictions to support the design of future projects. In this framework, the emerging

possibility to enrich ground movements databases by processing data from synthetic aperture radar (SAR) satellites cannot be neglected.

The recent development of high-resolution SAR satellites, such as the COSMO-SkyMed (CSK) or TerraSAR-X (TSX) constellations, along with recent advancement in data processing techniques, such as the multi-temporal interferometric synthetic aperture radar (MT-InSAR), has certainly improved in the last decade the capability to measure the field of displacements induced by tunnel excavations in urban areas (Ferretti et al., 2011; Perissin et al., 2012; Barla et al. 2016; Milillo et al, 2018; Giardina et al., 2018).

In this paper, ground movements measured with conventional optical survey nearby Foneria station during tunnel construction for a branch of metro Line 9 (now Line 10 South) in the city of Barcelona (Spain) are compared to those measured by multi-temporal InSAR analyses of satellite images. This allowed to validate this satellite monitoring technique, showing how it can be used during and after tunnel construction to expand the existing dataset from conventional survey and discussing its current limitations.

2 GROUND CONDITIONS AND WORKS

The paper presents a case study on the response of an existing framed building to the construction of a 12 m diameter tunnel passing below it (Di Mariano et al., 2021). The framed building object of this case study is part of a residential complex, consisting of two large twin reinforced concrete buildings founded on a two-level underground structure, excavated among diaphragm walls and used as parking garage (Figure 1). The building is 31 m high and has a rectangular horizontal cross-section of about 13.0 m \times 44.0 m (Figure 3b). The excavation process was executed from Foneria Station towards Ildefons Cerdà Station (Figure 1), with an Earth Pressure Balance (EPB) Tunnel Boring Machine (TBM) that proceeded in a closed mode of operation all throughout the alignment.

Geological conditions on site involved a diverse range of soil materials, from very soft deposits consisting of alluvial and detrital soils of Quaternary age to hard rock layers comprising Miocene siltstone and argillite (Figure 1). The excavation section along this part of the project was mostly through mixed ground conditions, involving alluvial and detrital deposits in the upper part of the tunnel face and hard Miocene materials in the lower part. The curved tunnel alignment in this area, the low cover to diameter ratios (C/D) below the building and the challenging geological conditions -owed to the presence of highly permeable Quaternary layers- conditioned the extensive monitoring plan on site. In order to gather detailed information about the excavation process and its effect on the surrounding ground and structures, a comprehensive instrumentation system was set in place. Surface and subsurface ground movements were monitored, as well as 3D movements of the framed building and its basement. Manual and automatic instruments were used. The first ones included topographic surveying, inclinometers, borehole extensometers, as well as strain gauges and load cells in structural elements. The second ones involved real-time robotic total stations, meteorological stations, as well as noise and vibration monitoring systems.

In the area of study, the tunnel ground cover varies approximately from 30 m to 36 m, with cover to diameter ratios (C/D) ranging from 2.5 to 3.0. The water table is roughly horizontal and always located above the tunnel crown, at a depth of about 10 m. Tunnelling below the framed building took place from the 7th to the 12th of March 2011, headed from its south to its north façade and led to ground movements that generated volume losses in the range 0.5-1.0%. The higher volume losses were observed as the EPB machine entered the south façade of the building (point 1 in Figure 3) due to the presence of gravelly soil layers, in the upper part of the tunnel section, through which face pressure escaped, causing loss of pressure in the head chamber: some overexcavation was experimented as a result. When the excavation proceeded from south to north, the ground cover increased and the tunnel section was almost exclusively characterised by the hard-Miocene materials. These new work conditions produced a gradual reduction in ground settlements (see point 2 in Figure 3). Volume losses reached values as low as about 0.5% once the EPB machine passed the building and arrived below the two monitoring sections at chainages PK 5007 and PK 5030 (Figure 1 and Figure 5).

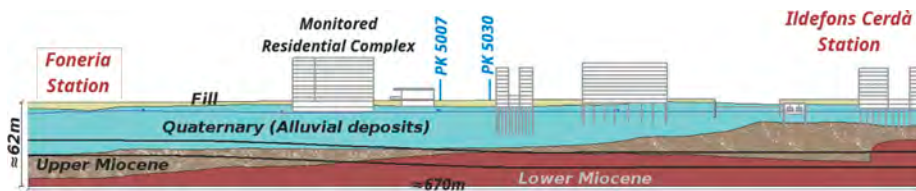


Figure 1. Geological profile of the tunnel alignment in the area of study.

3 METHODOLOGY

In this study, synthetic aperture radar (SAR) images were processed by TRE-Altamira as part of a research agreement with Universitat Politècnica de Catalunya (UPC).

SAR images were acquired by the TerraSAR-X full archive in Stripmap mode, that is as single or double polarized SAR images at a very high spatial resolution (3 m or lower), covering an area up to 1,500 km² (30 km × 50 km). 32 scenes have been processed, that were collected by satellite TSX1 (sensor SM009) in an ascending path direction from January 7th 2009 to October 2nd 2012: this time range covers completely the time window interested by tunnelling for Line 9 in that area. A total number of 30,883 measurement points over an area of

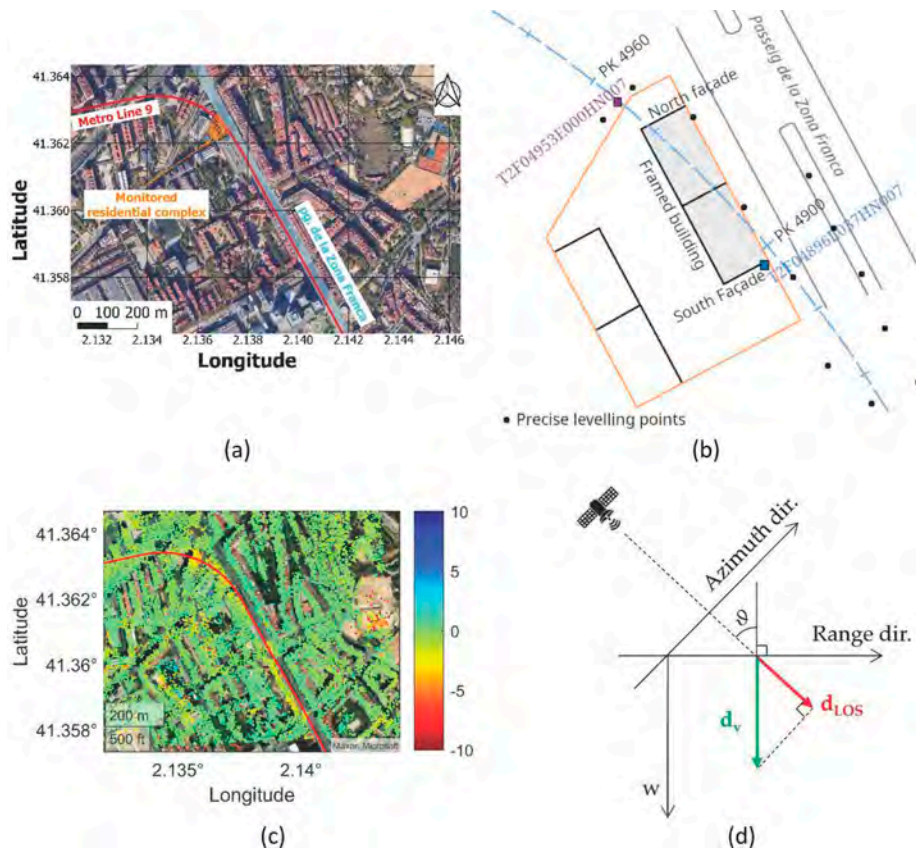


Figure 2. (a) Area of Interest (AoI) with the indication of the Metro Line 9 (red solid line) and the monitored residential complex (in orange solid texture); (b) Detail of the residential complex with respect to the tunnel alignment and layout of precise levelling points; (c) Velocity displacement map of the AoI from January 7th 2009 to October 2nd 2012 (mm/yr); (d) Transformation of Line of Sight (LoS) displacements in vertical ones.

10.9 km² have been considered (corresponding to 2,833.3 MP/km²) and referenced using the World Geodetic System (WGS) of 1984 in Microsoft Bing Maps. Figure 2a show a detail of the Area of Interest (AoI) along the “Passeig (pg.) de la Zona Franca” and Figure 2c the velocity displacement map of the AoI from January 7th 2009 to October 2nd 2012 as processed by SqueeSAR[®], an advanced algorithm for surface displacement detection developed by Ferretti et al. (2011).

A time history of displacements was hence generated for each radar target, or Permanent Scatterer (PS). As shown in Figure 2d, such displacements are the projection of a target motion onto the satellite Line of Sight (LoS). LoS displacements were then converted into vertical displacements (settlements) according to Equation 1:

$$d_v = d_{LoS} / \cos\vartheta \quad (1)$$

where d_{LoS} is the displacement in the direction of the satellite line of sight (LoS) and ϑ is the local incidence angle of the satellite LoS direction to the vertical.

Equation 1 assumes that the ground displacements due to tunnelling are predominantly vertical, that is theoretically true only along the tunnel vertical axis. Since in this case $\vartheta=35.35^\circ$, it has been demonstrated that for such a value this assumption leads to acceptable errors, lower than 5% on maximum settlements (Della Ragione et al., 2023).

4 RESULTS

Following the methodology described in section 3, the ground movements measured through multitemporal-InSAR in permanent scatterers of the AoI have been systematically compared with the closer precision levelling point measurements of the conventional survey.

Figure 3 shows the comparison of such measurements in two locations along the tunnel axis, in the area of the monitored residential complex (cf. Figure 2a and Figure 2b). The selected PS point 1 is located about 5 m away from the tunnel centreline and 12 m apart from the corresponding T2F04896L037HN007 Levelling Point (LP) that is located about 1 m away from the tunnel centreline. Point 2 and the corresponding LP T2F04953E000HN007 are located about 2 m apart from each other, just on the tunnel centreline (Figure 3a). The evolution of settlements starting from July 2009 is shown in Figure 3b. Both PSs and LPs clearly registered the TBM passing in March 2011. PS point 2 (purple markers) well matches the settlement measured by the corresponding LP. PS point 1 (blue markers) underestimates the settlement measured by the corresponding LP. This is partly justified by the different distance of the two points from the tunnel centreline: the out-of-alignment PS point 1 likely settles less than the corresponding levelling point, which is almost on the tunnel centreline. Another reason for such discrepancy can be the amount of movement that the ground surface has experienced: this is larger than half of the radar signal wavelength ($\lambda=31.1$ mm), therefore the PS InSAR measurements are very likely affected by phase unwrapping (Ferretti, 2014; Reinders et al., 2021). In fact, by shifting the measurements to correct this error, the curve with grey markers is obtained for point 1, which is much closer to the corresponding LP curve.

The high density of permanent scatterers in the area also allowed comparing settlement profiles along tunnel transverse sections. Several greenfield transverse alignments of permanent scatterers have been identified and compared with the closest monitoring points of conventional optical levelling. As an example, the location of two cross sections in chainages PK 5004 and PK 5031 (red dashed lines) is shown in Figure 4 together with the conventional monitoring sections at PK 5007 and PK 5030 (blue dashed lines).

To define a “InSAR” cross section, several PSs have been identified in a narrow band about 10 m wide across the tunnel section and the relevant measurements have been considered as belonging to that cross section. Therefore, monitoring sections do have a much larger number of measurements than what is common in conventional optical levelling cross sections. PS measurements have been fitted with the typical Gaussian curve (Peck, 1969) and compared in Figure 5 with the levelling point settlement profiles in the same corresponding cross sections.

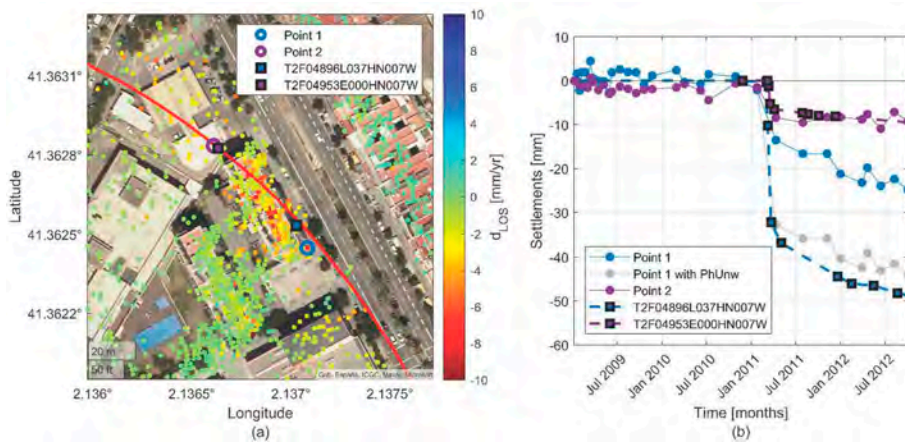


Figure 3. (a) Geographic location of traditional instrumentations (black markers) with the indication of the selected Permanent Scatterers for comparison; (b) history time series comparison between traditional monitoring stations (black lines) and InSAR scatterers (solid lines with circle markers).

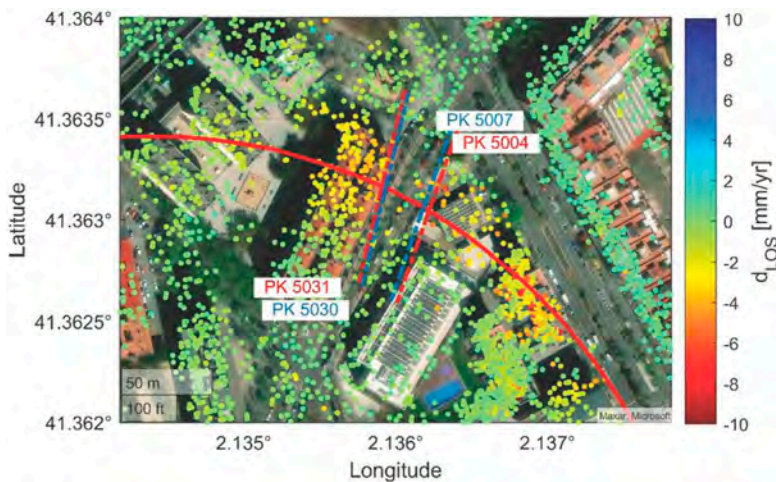


Figure 4. Location of cross section along tunnel alignment.

The comparison between corresponding InSAR and traditional monitoring profiles shows a rather good agreement. Despite curve fitting of PS measurements is affected by a large scatter, it indicates values of maximum settlement that are equal (Figure 5a) or very close to the optical measurements (Figure 5b). Moreover, curve fitting allowed estimating volume losses which are close to those measured on site and fully consistent with mechanised excavation. The distance of the settlement trough's inflection points from the tunnel centreline, i_{vs} , is also well bracketed by the satellite measurements, being slightly underestimated in one case and overestimated in the other (Figure 5a and Figure 5b respectively). It is worth noticing that the range of values is fully compatible with the tunnel depth and the ground condition at the tunnel face in the Area of Interest.

Figure 6 shows a comparison between the InSAR profile of the tunnelling-induced settlement of the block B of the building complex (Figure 6a) and the corresponding readings from the conventional survey of optical prisms on the building façade (Figure 6b). Both trend and magnitude of the displacement are very close, confirming the reliability of the Multi Temporal InSAR analysis.

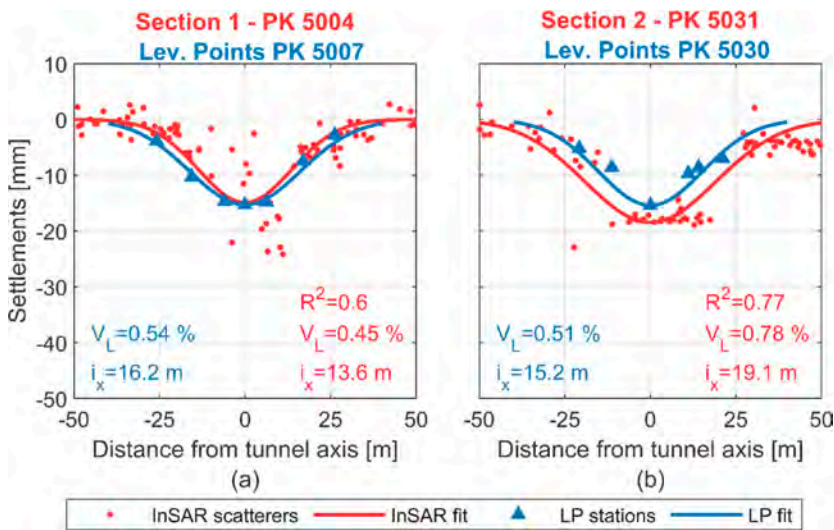


Figure 5. Induced settlement trough at two different locations. Comparison between Levelling Points (LP, blue markers and lines) data and satellite data (InSAR, red dots and lines).

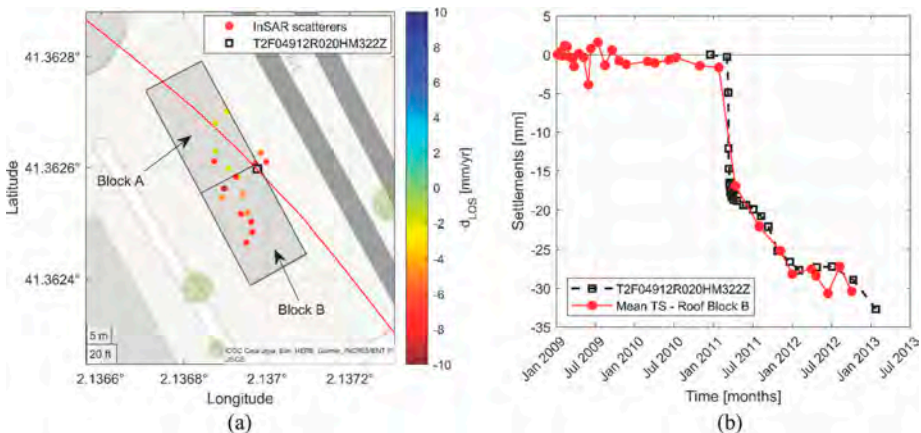


Figure 6. (a) Building displacements; (b) Comparison between Levelling Point (LP, black squared markers) data and satellite data (InSAR, circle markers).

5 CONCLUSIONS

In this work, tunnelling-induced ground and building displacements from conventional optical survey and multi-temporal interferometry of synthetic aperture radar (MT-InSAR) satellite image processing have been compared for the well documented case of Line 9 extension (now Line 10 south) of Barcelona metro.

MT-InSAR (SqueeSAR[®]) results do overall agree with the displacement evolution observed with optical surveys from the Earth's surface, as shown for ground settlements along the tunnel alignment and for building movements along the satellite Line of Sight.

Settlement profiles of Permanent Scatterers along tunnel transverse sections, after the excavation, also well agree with those of adjacent levelling points. Some inaccuracy is observed in the InSAR profiles that may be attributed to either difficult positioning or low backscattering properties at some locations. However, both volume losses, V_L , and distances of inflection

points from the tunnel centreline, i_x , assessed from satellite data are close to those obtained from conventional monitoring transverse sections.

A few assumptions were made when interpreting processed SAR image data to overcome limitations such as phase unwrapping, showing that MT-InSAR results are indeed useful to complement terrestrial monitoring but not to substitute it. The potential of satellite images processing in this field is clearly shown in the paper. It is also worth noticing that nowadays, more than one decade after the completion of Line 9 construction, SAR images datasets are increased. Therefore, by integrating datasets from different satellite constellations, the quality of monitoring tunnelling-induced movements may significantly improve. New constellations of SAR satellites aimed to high-resolution imaging of the earth surface are currently under production and this will very soon allow to further expand the ground deformation database, with clear benefits for the application of multitemporal-InSAR analysis, not only in the field of underground works but also in other areas.

ACKNOWLEDGEMENTS

The conventional optical survey data have been provided by Infrastructures de la Generalitat de Catalunya, S.A.U. that is kindly acknowledged.

REFERENCES

- Attewell, P.B. & Woodman, J.P. 1982. Predicting the dynamics of ground settlement and its derivatives caused by tunnelling in soil. *Ground Engineering* 15(7): 13–22.
- Barla, G., Tamburini, A., Del Conte, S. & Giannico, C. 2016. InSAR monitoring of tunnel induced ground movements. *Geomech. Tunn.* 9: 15–22, <https://doi.org/10.1002/geot.201500052>.
- Della Ragione, G., Rocca, A., Perissin, D. & Bilotta, E. 2023. Volume Loss Assessment with MT-InSAR during Tunnel Construction in the City of Naples (Italy). *Remote Sens.* 15, 2555, <https://doi.org/10.3390/rs15102555>.
- Di Mariano, A., Franza, A., Limatola, V., Gens, A. & Bilotta, E. 2021. Building Response to Line 9 EPB Tunnelling in Barcelona. A Case Study. M. Barla et al. (Eds.): *IACMAG 2021*, LNCE 126: 172–180, https://doi.org/10.1007/978-3-030-64518-2_21.
- Ferretti, A., Fumagalli, A., Novali, F., Prati, C., Rocca, F. & Rucci, A. 2011. A New Algorithm for Processing Interferometric Data-Stacks: SqueeSAR. In *IEEE Transactions on Geoscience and Remote Sensing* 49(9): pp. 3460–3470, <https://doi.org/10.1109/TGRS.2011.2124465>.
- Ferretti, A. 2014. *Satellite InSAR Data: reservoir monitoring from space (EET 9)*. EAGE Publications. ISBN: 978-90-73834-71-2, <https://doi.org/10.3997/9789073834712>.
- Giardina, G., Milillo, P., DeJong, M.J., Perissin, D. & Milillo, G. 2018. Evaluation of InSAR monitoring data for post-tunnelling settlement damage assessment. *Struct. Control. Health Monit.* 26(2), e2285, <https://doi.org/10.1002/stc.2285>.
- Milillo, P., Giardina, G., DeJong, M.J., Perissin, D. & Milillo, G. 2018. Multi-temporal InSAR structural damage assessment: The London Crossrail case study. *Remote Sens.* 10(2), 287, <https://doi.org/10.3390/rs10020287>.
- Peck, R.B. 1969. Deep excavations and tunnelling in soft ground. *Proc. 7th ICSMFE, Mexico City, State of the Art Volume*: 225–290.
- Perissin, D., Wang, Z. & Lin, H. 2012. Shanghai subway tunnels and highways monitoring through Cosmo-SkyMed Persistent Scatterers. *ISPRS J. Photogramm. Remote Sens* 73: 58–67, <https://doi.org/10.1016/j.isprsjprs.2012.07.002>.
- Rankin, W.J. 1988. Ground movements resulting from urban tunnelling: predictions and effects. Geological Society, London, *Engineering Geology Special Publications* 5: 79–92, <https://doi.org/10.1144/GSL.ENG.1988.005.01.06>.
- Reinders, K. J., Hanssen, R. F., van Leijen, F. J. & Korff, M. 2021. Augmented satellite InSAR for assessing short-term and long-term surface deformation due to shield tunnelling. *Tunnelling and Underground Space Technology* 110, 103745, ISSN 0886-7798, <https://doi.org/10.1016/j.tust.2020.103745>.

A case study on shield cutting reinforced concrete diaphragm walls and piles directly: Key technologies and field investigation

J. Sun & S. Liao

Department of Geotechnical Engineering, Tongji University, Shanghai, China

Z. Wang

Suzhou Rail Transit Corporation Ltd., Suzhou, China

ABSTRACT: In the absence of reserved transfer corridors at operating subway stations, the transfer nodes often necessitate the direct intersection of newly constructed tunnels with the Reinforced Concrete (RC) obstacles of the operating stations, which poses significant challenges to the existing stations and the construction of newly built tunnels. This paper presents a case study on the identification and management of main challenges during the construction of the shield cutting RC diaphragm walls and piles directly at a certain section of Line 6 of Suzhou Rail Transit. And the site observation on driving parameters, cutterhead performance and structural deformation was carried out after completion of the project. The results indicate employing a mixed cutter configuration consisting of tearing and rolling cutters, coupled with the soft soil foundation reinforcement and the optimization of driving parameters (a slow advance rate at 2~3 mm/min and intermediate rotation speed at 0.6~0.7 rpm), ensures the safe implementation of shield cutting RC diaphragm walls and piles directly and consecutively. Experiences obtained from this project can provide effective reference for analogous cases.

Keywords: shield tunnel, cutting directly and consecutively, RC diaphragm walls and piles, cutting parameters, shield type selection

1 INTRODUCTION

With the continuous increase in demand for urban rail transit construction in China and the rapid advancement of technology, the construction speed of urban rail transit far exceeds the early construction plans. The intermediate stations from early plans possibly upgrade to transfer stations as urban planning undergoes continuous updates. The construction of newly built subway lines faces significant challenges when passing through the existing subway stations in complex central urban environments without reserved transfer corridors. When facing conditions where the adjustment of tunnel alignment is not feasible, shield machine is inevitably confronted with RC obstacles in its forward progression (Wang et al., 2013).

Conventional shield machines lack the capability to directly cut RC structures. Typically, methods such as pile removing (Yang et al., 2012), pile underpinning (Xu et al., 2015), manual-cut borehole (Du, 2009) and freezing-mining (Zhao, 2023) were employed for pre-clearance construction. However, these approaches have drawbacks, including significant environmental impact and prolonged construction periods.

With the continuous development of shield tunneling technology and adaptive modifications to existing shield machine and cutters, several engineering cases in China have emerged in recent years where shields directly cut RC obstacles. The scale of the cut object continues to grow, and the construction difficulty increases (Wang, 2014, Wang et al., 2017, Wu et al.,

2018, Du et al., 2019, Li, 2020), accumulating rich engineering experience and yielding significant economic and social benefits.

However, research on the direct cutting of RC diaphragm walls using shield tunneling is still relatively scarce, and construction cases are limited. As the retaining structure for existing subway stations, diaphragm walls typically exhibit considerable depth, inevitably posing impediments to the construction of new subway lines. Diaphragm walls of newly planned transfer stations often use glass fiber reinforced polymer (GFRP) reinforcements instead of steel reinforcements to facilitate the conditions for shield cutting (Xiao et al., 2021, Zhou et al., 2023). While directly cutting of RC diaphragm walls may face several risks (Wang et al., 2022, Yu et al., 2022), such as wear of cutters, clogging of the cutterhead and blockage of the screw conveyor.

The shield tunnel of Suzhou Rail Transit Line 6, from Lindun Road to Suzhou University, was constructed by an earth pressure balanced (EPB) shield machine. The shield cut 2 rows of RC retaining piles and 2 sections of RC diaphragm walls directly and consecutively in a short distance. The amount of the cut objects in this project have not been reported in similar engineering cases. The feasibility of the shield direct cutting construction scheme has been a critical question that need urgent exploration. This paper, based on the engineering background in Suzhou, first summarizes the main engineering technical challenges and proposes targeted construction techniques. Subsequently, building on site observation, implementation outcome of the project is evaluated.

2 PROJECT BACKGROUND

2.1 Project overview

The newly constructed Lindun Road Station of Suzhou Rail Transit Line 6 is a three-level underground structure, located on the north side of the intersection of Lindun Road and Ganjiang East Road in Gusu District. The receiving wells for the shield tunnel of the Lindun Road to Suzhou University section (L-S section) are on its southern end, with a horizontal distance of 5.95 m to the existing Rail Transit Line 1 Lindun Road Station (a two-level underground structure with a width of 20.5 m), forming a “T”-shaped transfer configuration. The structural supports for the foundation pit of Line 1 Lindun Road Station are diaphragm walls on both north and south sides. Minimum distance between the bottom slab and the newly built shield tunnel is 3.2 m. The relative position between the newly constructed tunnel and the existing station in the crossing area is illustrated in Figure 1.

The tunnel segment of Line 6 at L-S section adopts a single-layer reinforced concrete lining segment structure, with an outer diameter of 6600 mm, an inner diameter of 5900 mm, a thickness of 350 mm, and a ring width of 1200 mm. A 6840 mm diameter EPB shield machine is utilized for tunnelling, equipped with a six-spoke hybrid cutterhead, achieving an overall opening ratio of 42%. The shield tunnels, both the right-line and left-line, commence excavation northward from Suzhou University Station. They cut through two rows of RC retaining piles, two sections of RC diaphragm walls, and several erect column piles. The tunnels then pass below the operational Lindun Road Station on Line 1 before reaching the receiving well.

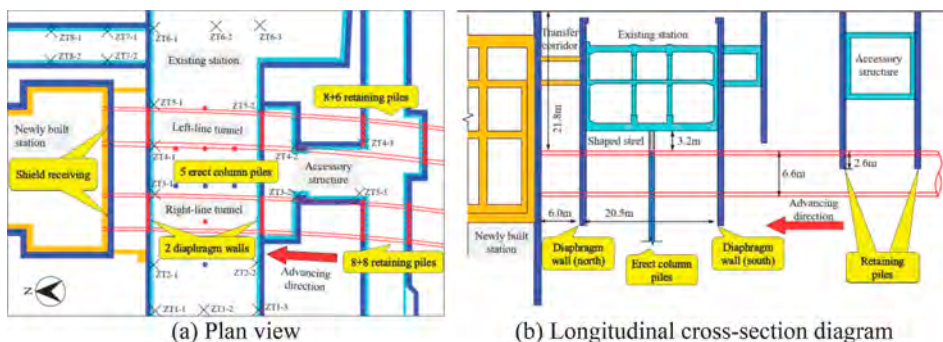


Figure 1. Layout of the project.

During this process, the right-line shield tunnel must directly cut two sections of 800 mm thick C35 diaphragm walls (dual-row main reinforcements with diameters of 32 mm and spaces of 150 mm, the same below) of Line 1 Lindun Road Station, 16 retaining piles with diameters of 800 mm and spaces of 1000 mm (eight main reinforcements with diameters of 25 mm, the same below) and one temporary erect column piles with diameters of 800 mm (16 main reinforcements with diameters of 20mm, the same below). The column pile also has a 3 m long latticed column inserted below the station floor, which does not intrude into the Line 6 tunnel area. The left-line shield tunnel, on the other hand, must directly cut two sections of diaphragm walls of Line 1 Lindun Road Station and 14 retaining piles, as well as four temporary erect column piles below the station floor.

2.2 Geological conditions

Geotechnical investigations were carried comprehensively to evaluate the subsurface geological conditions. Figure 2 presents typical strata profile along with soil properties at the project site.

Within the revealed depth, strata at the site of this project is composed of fill (①) in the depth range about 0-3.5 m, silty clay (③₁) in the depth range about 3.5-6.4 m, silty clay (③₂) in the depth range about 6.4-9.8 m, silty clay mixed with silt (⑤_{1a}) in the depth range about 9.8-16 m, silty clay (⑤₁) in the depth range about 16-22.8 m, silty clay (⑥₁) in the depth range about 22.8-26.4 m, sandy silt mixed with silty clay (⑥_t) in the depth range about 26.4-27 m, silty clay (⑥₂) in the depth range about 27-29.3 m, silty clay (⑦₁) in the depth range about 29.3-35.1 m, silt (⑦₂₋₁) in the depth range about 35.1-36 m, silt (⑦₂₋₂) in the depth range about 36-40 m. The observed long-term phreatic water level is about 1.15-3.86 m below the ground surface. It should be noted that strata crossed by the shield tunnel (ranging from 22 m to 28.6 m below ground surface) are mainly silty clay layers which possess the weakest strength and largest deformability. The ⑥_t layer has a pressurized water level of 1.43 m below the ground surface, which may cause inrush of water. Therefore, a cautious control of shield tunnelling and foundation reinforcement are of great importance.

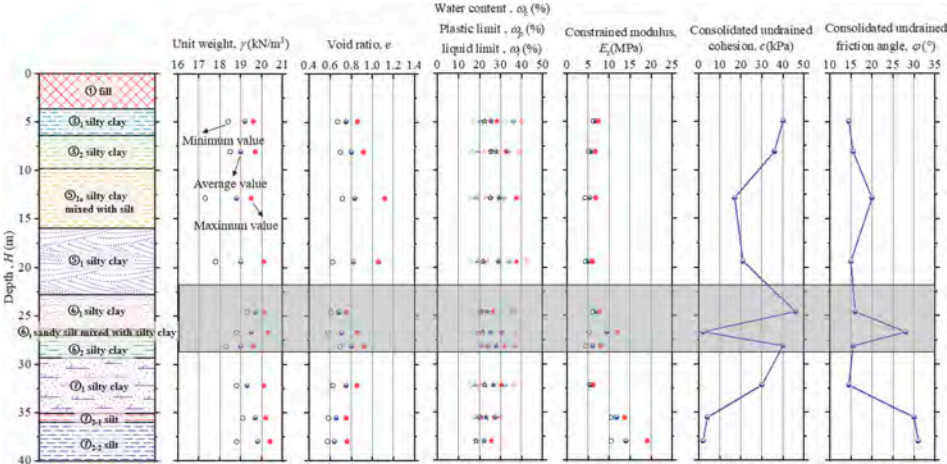


Figure 2. Strata information.

3 MAIN CHALLENGES

Subway construction safety risk can be divided into four main categories, including geological risks, construction technical risks, environmental risks and management risks (Zhang et al., 2019). In view of the scarcity of analogous construction projects and the proximity of the shield tunneling and existing stations, this section focuses on the direct impact of the new construction

technique (construction technical risks) and existing structures (environmental risks). These risks and challenges primarily arise from the shield direct cutting and crossing process.

3.1 *Construction technical risks*

Two primary risk sources can be associated with construction technical risk: (1) remove of obstacles, and (2) control of shield machine.

3.1.1 *Removing of RC diaphragm walls and piles*

One of the most challenging aspects during construction is removing of steel reinforcement. The quantity of steel reinforcements in diaphragm walls and piles is substantial. As an example, for the diaphragm wall within the range of shield cutting, the quantity of main reinforcement for a single wall section is approximately 434 m. With higher shear strength and relatively lower tensile strength compared with GFRP reinforcements (Mohamed et al., 2020), steel reinforcements are hard to be cut off. High elastic modulus will also result in wear of cutters and cutterhead. With the progress of tunnelling, the cutting performance of the shield machine may gradually decrease, and steel reinforcements could not be fully cut into short segments that are easy to be discharged from the screw conveyor. Long steel reinforcements with large radius of curvature enter into the soil chamber, elevating the risk of both cutterhead and screw conveyor jamming.

Another challenging aspect is removing of concrete. The process of cutting concrete material alone is quite similar to excavating in hard rock strata and has matured considerably as a tunneling construction technique. However, considering that this project requires long-distance excavation in soft soil and direct cutting of the diaphragm wall without changing cutters, a specialized cutterhead designed for cutting either soft soil or concrete may not meet the requirements for consecutive construction.

3.1.2 *Control of shield machine*

(1) tunnelling parameters

Strength of RC diaphragm walls and piles are much higher than that of soft soil. When the cutterhead and cutters interact with RC structures, contact force and torque increase as the shield advances. The tunnelling parameters employed during tunneling in soft soil are no longer applicable to cutting process. As steel reinforcements truncated and concrete crushed, significant fluctuations in tunnelling parameters occur, further increasing the difficulty of control.

(2) shield posture

Due to the gentle curve of tunnel alignment, there is a certain angle between existing structures and newly built tunnels when cutting south-side diaphragm wall (88°) and retaining piles (82°). The cutterhead only contacts with a partial section of obstacles at the beginning and end stages of the cutting process (as shown in Figure 3). The remaining part either cuts the original or reinforced soil. The cutting objects at the tunnel face exhibits variability throughout the cutting stage. Thus, the shield posture inclines to the softer side. Owing to substantial variations in the breakage difficulties among cutting objects, relying solely on uneven jacking force proves inadequate for shield posture adjustments. This limitation poses challenges in effectively controlling the shield posture, especially for horizontal deviation, vertical deviation and pitch attitude angle.

3.2 *Environmental risks*

There are two main construction stages with high-potential environmental risks: (1) cutting structures and, (2) crossing beneath structures.

3.2.1 *Deformation of RC diaphragm walls and piles*

At the cutting stage, except for the control of tunnelling parameters and shield posture, the deformation of structures should also be attached to great significance. In the example of shield cutting diaphragm walls, the deformation pattern of the wall during the cutting process is illustrated in Figure 4. The deformation of structures is influenced by both the total thrust force and

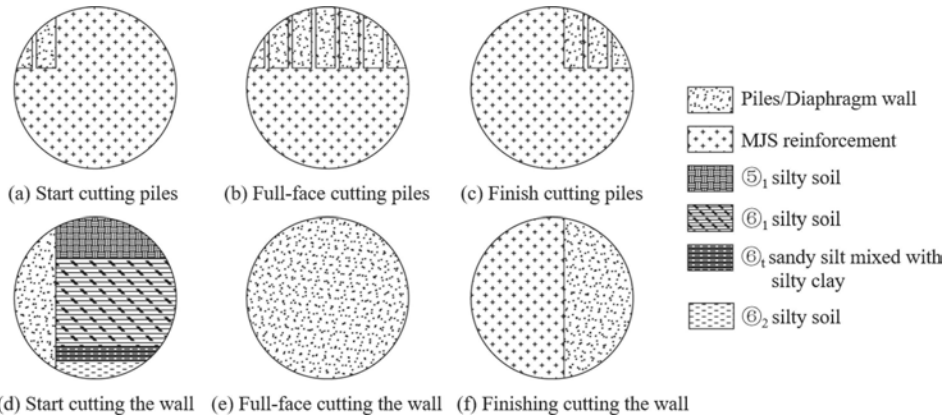


Figure 3. Cutting object at the tunnel face.

the rear support of the diaphragm wall. Shield advancing with high advance rate and low rotation speed may suffer considerable total thrust force. The counteracting force is applied to the wall, serving as the primary driving factor for the deformation of the diaphragm wall. And the soil behind the diaphragm wall imposes constraints on the deformation of the structure. The higher the strength of the soil behind the wall, the more pronounced its supporting effect on the wall. On the one hand, the deformation of the wall could be reduced, and on the other hand, removing of RC structures could be more effective. Moreover, distinct stress states characterize the junction between the existing station and the diaphragm wall during the cutting of the north-side and south-side walls. Specifically, the south-side wall experiences an inward push towards the station, whereas the north-side wall undergoes an outward push. This results in a tensile stress state at the junction between the north-side wall and the station, posing a potential risk of cracking.

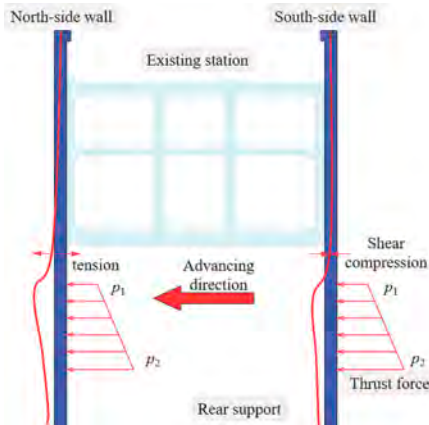


Figure 4. The deformation pattern of the diaphragm walls.

The deformation pattern of retaining piles is different from the diaphragm wall. The retaining piles are discontinuously distributed, taking the form of suspended footings. Cutting through the retaining piles may induce lateral oscillation or settlement deformation of piles.

3.2.2 Void stratum

When the shield closely crosses beneath the station floor, the displacement of the finite soil between the two retaining walls, beneath the station floor, is relatively sensitive to the pressure

exerted by the soil chamber of shield machine. Considering the overall stiffness of the subway station structure, the displacement of the finite soil has a limited impact on the heaving and settlement deformation of the station floor. However, insufficient pressure in the soil chamber may result in void stratum forming beneath the station floor, thereby impacting the long-term operational safety of the subway station structure.

4 MITIGATION MEASURES

To mitigate the severity of risks and challenges resulted from new construction technique and existing structures, several mitigation measures including shield type selection, foundation reinforcement technologies and tunnelling parameters control were adopted.

4.1 Shield type selection

To facilitate consecutive cutting through multiple RC diaphragm walls and piles within a short distance and long-distance crossing through soft soil, adaptive modifications were implemented for both the cutterhead, the cutters and the main drive system of the shield machine.

Addressing potential challenges such as mud cake formation and uneven wear of rolling cutters during the excavation through soft soil layers, a shield cutting tool configuration was chosen. This configuration primarily incorporates tearing cutters with secondary rolling cutters. To enhance the segmentation of steel reinforcement for efficient removal, a four-tiered cutter arrangement was devised (as shown in Figure 5):

- (1) The first tier consists of seven forward tearing cutters, with a height of 215 mm and a spacing of 390 mm. Their primary role is to pre-cut the RC structures with substantial spacing.
- (2) The second tier primarily features 28 bolted tearing cutters, with a height of 187.5 mm and a spacing of 78 mm. Additionally, 6 edge rolling cutters (18 inches), with a height of 187.5 mm, are used to cut and tear the steel reinforcements that was not sufficiently cut in the previous tier.
- (3) The third tier comprises 42 welded tearing cutters, with a height of 150 mm and a spacing of 78 mm. These are employed to ensure the shield machine's capability to cut RC structures, especially after the cutters in the first and second tiers experience wear.
- (4) The fourth tier consists of scrapers, including 30 front scrapers and 12 pairs of edge scrapers, with a height of 130 mm and a spacing of 220 mm. Their primary purpose is to gather the steel segments and concrete fragments produced during the cutting process.

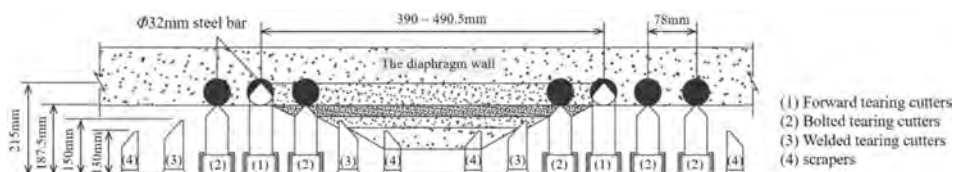


Figure 5. Arrangement of cutters.

The front surface of the cutterhead is protected by a 12.8 mm composite wear-resistant plate, while a 50 mm thick alloy wear-resistant plate is welded onto the outer periphery of the large circular ring. Additionally, the back and edge transition areas are reinforced with a dense wear-resistant grid to enhance the wear resistance of the cutterhead.

Additionally, the shield machine is equipped with an advanced main drive configuration. This configuration includes a main bearing with an outer diameter of 3.61 m and a total motor drive power of 1280 kW. The system can provide a rated torque of 8540 kN·m and a maximum torque of 9830 kN·m, specifically designed to manage the escalating torque demands during the cutting of the diaphragm wall. During the actual construction process, torque is controlled below 50% of

the rated torque to protect the cutting tools and prevent the cutterhead from jamming. Simultaneously, to avoid difficulties in restarting after a cutterhead jam, the interlocking parameters are set to shut down the propulsion mode when the torque reaches 80% of the rated torque.

4.2 Foundation reinforcement technologies

To ensure the structural safety of the existing subway station, the subway line, and the construction safety of the shield cutting through the diaphragm wall, the Metro Jet System (MJS) was employed to reinforce the soil within the excavation range of the shield tunnel (as shown in Figure 6(a)). Horizontal MJS full-section reinforcement (2000@1300×750 mm, as shown in Figure 6(b)) was applied beneath the existing station, with the reinforcement range extending from 1.2 m above the tunnel top to 2.7 m below the tunnel bottom. Vertical MJS reinforcement was used beneath the interchange area, with the reinforcement depth reaching 3 m below the tunnel bottom. Vertical MJS reinforcement was also implemented at the position of existing retaining piles, covering a range from 3 m above the tunnel top to 3 m below the tunnel bottom. The utilization of MJS reinforcement yields several advantageous outcomes, including the control of ground deformation beneath the station floor and lateral deformation of the diaphragm wall. It also offers efficient rear support for the cutting of RC structures, and provides favorable conditions for cutter replacement when needed.

In addition, two rows of sleeve valve grouting pipes were pre-embedded within the 2 m range below the station floor, with a horizontal spacing of approximately 1 m. Grouting was carried out based on monitored deformations of the existing station during the construction and operation period.

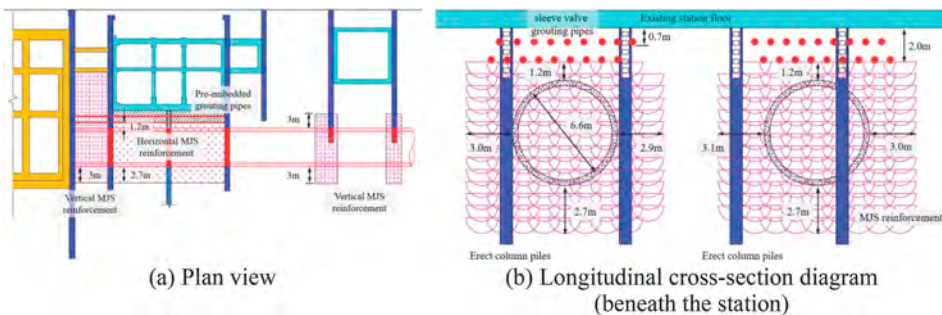


Figure 6. Layout of the foundation reinforcement.

4.3 Driving parameters control

The control of shield tunneling construction should rigorously follow the principles of slow advancing speed, moderate rotation speed, stable soil pressure and strict shield attitude (Wang, 2014). This methodology not only guarantees construction safety and minimizes environmental disturbance during cutting process but also ensures adequate cutting and crushing of steel reinforcement and concrete.

(1) control of advancing speed and rotation speed

When cutting through soil, the advancing speed is maintained at 40-50 mm/min, accompanied by a rotation speed set at 1 rpm, to reduce the abrasion of cutters. When cutting two rows of retaining piles, the targeted advancing speed is 10 mm/min, with the rotation speed held at 0.8 rpm. For cutting two diaphragm walls, the planned thrust speed is 2-3 mm/min, and the rotation speed is further reduced to 0.6-0.7 rpm. Because a slow advancing speed enhances the effectiveness of breaking the RC structures by grinding. Simultaneously, a moderate rotation speed addresses the dual requirements of protecting the cutters and managing cutterhead torque (Wang, 2014). When tunneling between two

underground continuous walls and passing beneath the station floor with a small clearance, the cutting objects shifts to reinforced soil, and the advancing speed can be restored to 40 mm/min, with the rotation speed returning to 1 rpm.

(2) control of face pressure

Before cutting the first diaphragm wall, the face pressure set value is determined based on the tunnel depth and the characteristics of the overlying soil layer, with a topsoil pressure setting of 1.8 bar. When tunneling beneath the main structure of the station, the face pressure setting depends on the weight of the overlying soil, the self-weight of the station structure, and the weight of the soil between the station floor and the top of newly built tunnel. Within this range, fluctuations in face pressure should be rigorously controlled to prevent void stratum beneath the station.

(3) control of shield posture

The main factor controlling the vertical and horizontal attitude of the shield machine is the thrust force of the jacks in each section. When the shield machine tilts to a certain direction, correction is achieved by increasing the jacking thrust force on that side of the shield machine. The correction process should control the correction speed, avoiding abrupt adjustments, and enhancing the monitoring and feedback control of the shield posture.

However, at the beginning and end stages of the cutting process, the shield posture incline to the softer side. Adjusting the jacking thrust force could hardly rectify the shield posture due to significant differences in the breakage difficulties among cutting objects. In this case, an inverse shield posture should be reserved for the potential deviation.

5 SITE OBSERVATION OF SHIELD CUTTING PERFORMANCE

The overall construction process of the shield cutting through diaphragm walls encountered several difficulties. However, there were no long-time shutdown of the shield machine or replacement of cutters before tunnel breakthrough. The mitigation measures ensured safety of the project. This section presents the cutting performance from various perspectives.

5.1 *Driving parameters*

To optimize the control of the shield tunnelling process, a measurement analysis of the dynamic variations in tunnelling parameters during the cutting process was conducted.

Taking the newly built right-line tunnel's tunnelling parameters during cutting stage as an example, before directly cutting the south-side diaphragm wall at ring 685, the average advancing speed was controlled in the range of 25 to 50 mm/min, with the total thrust fluctuating within the range of 12,000 to 15,000 kN. The corresponding cutterhead torque was maintained at around 1500 kN·m.

At ring 685, when the shield began cutting through the first diaphragm wall, the advancing speed decreased to 3.6 mm/min. The mean total thrust slightly increased to approximately 16,166 kN, and the mean cutterhead torque significantly increased to 2,864 kN·m, exceeding the planned torque for cutting the wall at 2,600 kN·m. The tunnelling parameters were accompanied by significant fluctuations, with the maximum thrust reaching 21,138 kN and the maximum torque reaching 3,818 kN·m. After cutting through the first diaphragm wall, the advancing speed returned to 10-40 mm/min. At this speed, the total thrust was maintained around 20,000 kN, and the cutterhead torque remained around 2,600 kN·m, indicating that the shield was in normal working condition. Compared to the parameters before cutting the wall, both thrust and torque increased when the advancing speed decreased, possibly due to ground reinforcement in this section.

At ring 703, when the shield began cutting the north-side diaphragm wall, the excavation speed decreased to 4 mm/min. The mean total thrust was 16,190 kN, with a further increased fluctuation range compared to cutting the south-side wall. The maximum thrust reached 30,021 kN, and the mean cutterhead torque was 2,767 kN·m, with a substantial fluctuation, and the maximum torque reached 4,130 kN·m. After cutting through the second wall, the

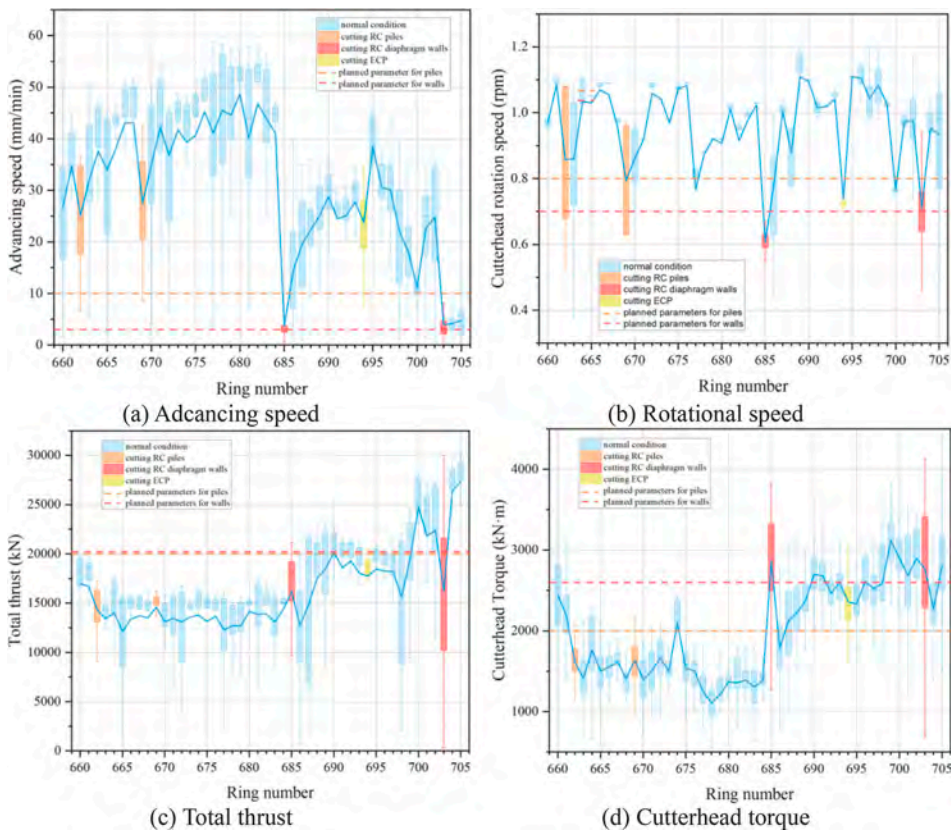


Figure 7. Variation of tunnelling parameters (right-line tunnel).

shield continued advancing at a speed of 10 mm/min or less. The mean total thrust increased to 27,000 kN, and the mean cutterhead torque remained around 2,600 kN·m, accompanied by frequent occurrences of the screw conveyor jamming. This indicated a decline in the cutting performance of the shield machine after completing the cutting of the second wall.

Comparing the actual construction parameters with the planned ones reveals the reasonableness of the plan. However, the planned values for the advancing speed while cutting the retaining piles are relatively conservative. Cutting through the retaining piles could be carried out at a speed of approximately 30 mm/min.

5.2 Cutting performance

The shield cutting performance can also be evaluated qualitatively based on the condition of the cutterhead and tools, as well as the cutting and discharge status of reinforcement bars.

5.2.1 Steel reinforcement blocking

During the shield tunneling process, destinations of the steel bar primarily include: (1) blocked at the screw conveyor outlet, (2) wrapped around the cutterhead, and (3) discharged along with muck (as shown in Figure 8). On-site collection was conducted for inadequately cut steel bars that blocked at the screw conveyor outlet. When the shield cut the first diaphragm wall on the right line, a total of 15 pieces of main bars, with diameters of 32 mm and lengths exceeding 30 cm, were collected at the outlet of the screw conveyor. Total length is 9.5 m, accounting for 2.2% of the theoretical quantity of main bars within the range of cutting. The reason for the relatively small proportion of collected steel bars may be attributed to the majority of steel bars undergoing sufficient cutting, being directly discharged through the belt

conveyor wrapped in the muck. Another portion of steel bars that were not adequately cut wrapped around the cutterhead and could not be discharged through the screw conveyor.

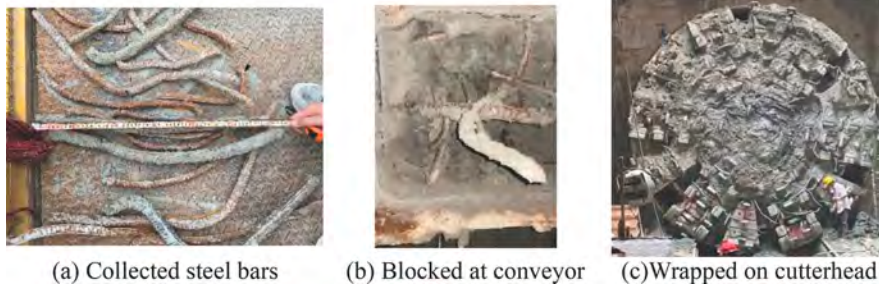


Figure 8. Distribution of reinforcement bars.

5.2.2 Mud cake clogging

During the shield receiving process, a severe mud caking phenomenon was observed in the cutterhead opening and the disc cutter box (Figure 9). In particular, the region at the center of cutterhead with a low opening rate (with a radius of 0.8 m) exhibited dense mud cakes, while the peripheral mud cakes were relatively loose and naturally fell off during the tunneling process or were easily removed manually. The analysis indicates that the significant mud caking on the cutterhead can be attributed to the following factors: (1) high-temperature and high-pressure environment in front of the cutterhead, (2) poor soil flowability resulted from the low cutting line speed at the center of the cutterhead, (3) incompletely hydrated components within the range of foundation reinforcement, and (4) extensive entanglement of steel bars around the cutterhead, further reducing the opening rate and increasing the adhesion area.



Figure 9. Mud cakes on the cutterhead.

5.2.3 Cutters wear

As shown in Figure 10, after the shield receiving stage of left-line tunnel, various degrees of cutters wear were observed. Eight tearing cutters located in the central region of the cutterhead exhibited overall abrasion and several tearing cutters in the edge region experienced cutter holder flipping and tool wear. Mud caking occurred in the rolling cutter boxes, causing obstruction in the rotation of the rolling cutters. The phenomenon indicated that, without cutters replacement, the cutting performance of the shield significantly deteriorated after cutting through two rows of RC retaining piles and two sections of RC diaphragm walls.

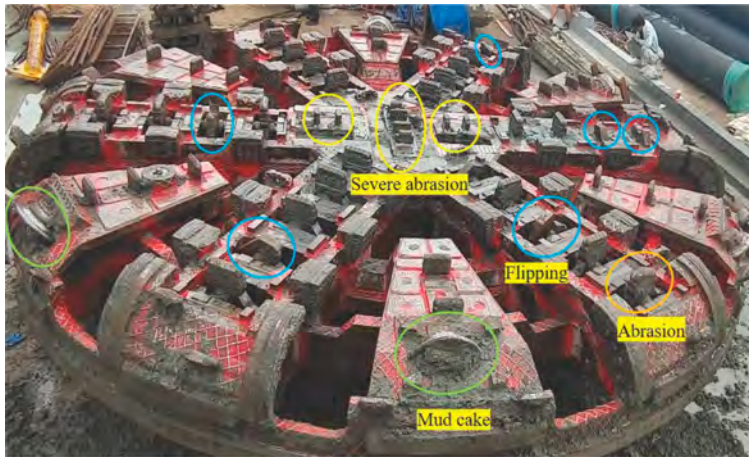


Figure 10. Status of cutters after the cutting process.

5.3 Structural deformation

The arrangement of vertical deformation monitoring points on the station hall is illustrated in Figure 1(a). The monitoring data indicates that, during the shield cutting phase of two tunnels (from 5/26/2023 to 8/20/2023), the maximum settlement occurred at monitoring point ZT4-3 and ZT3-3, located at the accessory structure, reaching -4.06 mm and -3.83 mm. Due to the substantial stiffness of the main station structure, the uplift and settlement deformations at various points during the shield cutting phase remained within 1.1mm. And the vertical deformation measured by the monitoring points at the platform floor shows that the platform floor of the existing station underwent overall uplift deformation, with the maximum uplift deformation reaching 1.3 mm on the upline and 2.5 mm on the downline. The monitoring data indicates the overall safety of the shield cutting process is under control.

6 CONCLUSIONS

In this paper, the main challenges, mitigation measures and implementation of shield cutting reinforced concrete diaphragm walls and piles directly were thoroughly investigated through a case study of the construction of newly build subway tunnels crossing an existing subway station in urban area of Suzhou. The main conclusions are as follows:

- (1) There are two major challenges for tunnelling under these conditions. The first stems from the new construction technique and the second results from the existing RC structures. To mitigate the severity of challenges, a mixed cutter configuration featuring tearing and rolling cutters and foundation reinforcement with Metro Jet System were adopted in the project.
- (2) The average total thrust force during the period in which the shield cut diaphragm walls of the right-line tunnel ranged from 16,166 to 16,190 kN, with an average cutterhead torque ranging from 2,767 to 2,864 kN·m. With the dynamic changes in concrete fragmentation, steel bar breakage, and the shield advancing state, both the total thrust force and cutterhead torque exhibited significant fluctuations. Therefore, it is advisable to rigorously control the tunnelling parameters, following the principles of slow advancing speed, moderate rotation speed, stable soil pressure and strict shield attitude.
- (3) According to the field measurements, maximum deformation of the existing station's main structure and accessory structure were controlled within 2.5 mm and 4.1 mm. The Safety of the structures and the operation subway was under control since deformation met the requirements for settlement control. It is feasible for the shield tunneling machine

to cut two sections of RC diaphragm walls and two rows of RC retaining piles directly and consecutively within a short distance.

ACKNOWLEDGEMENTS

The authors grateful acknowledge the engineers from Suzhou Rail Transit Co., Ltd and China Railway 16th Bureau Group Co., Ltd for their sincere help in provide relevant data and materials.

REFERENCES

- Du C. (2009) Technology of treatment of pile foundations intruding into shield tunnel by means of manual-cut borehole method. *Tunnel Construction*, 29, 222–226 (in Chinese).
- Du C., Zhang J. & Tang Z. (2019) Key technologies of shield direct cutting pile foundation. *Tunnel Construction*, 39, 1666–1677 (in Chinese).
- Li F. (2020) Key construction technology of shield cutting pile foundation group of cast-in-place piles: a case study on Qianhubeilu Station-Qiubi station section of Ningbo metro line no. 3. *Tunnel Construction*, 40, 569–574 (in Chinese).
- Mohamed H.M., Ali A.H., Hadhood A., Mousa S., Abdelazim W. & Benmokrane B. (2020) Testing, design, and field implementation of GFRP RC soft-eyes for tunnel construction. *Tunnelling and Underground Space Technology*, 106, 103626.
- Wang F., Yuan D., Dong C., Han B., Nan H. & Wang M. (2013) Study on cutter configuration for directly shield cutting of large-diameter piles. *China Civil Engineering Journal*, 46, 127–135 (in Chinese).
- Wang F. (2014) Study on shield cutting large diameter reinforced concrete piles directly. Beijing Jiaotong University (in Chinese).
- Wang Y., Li J. & Liao S. (2017) Numerical simulation and measured data analysis of pile group cutting by shield: a case study of running tunnel on line no.9 of Shenzhen metro. *Tunnel Construction*, 37, 192–199 (in Chinese).
- Wang Y., Wang X., Xiong Y., Yang Z. & Zhang J. (2022) Full-scale laboratory test of cutting large-diameter piles directly by shield cutterhead. *Advances in Civil Engineering*, 2022, e8780927.
- Wu G., Jia S., Chen W., Yang J. & Yuan J. (2018) Modelling analysis of the influence of shield crossing on deformation and force in a large diaphragm wall. *Tunnelling and Underground Space Technology*, 72, 154–161.
- Xiao C., Lu Y., Zhou Z., Fu X. & Wang S. (2021) Thrust calculation of earth pressure balance shield obliquely crossing diaphragm wall in composite strata: a case study of Nanning rail transit line 5 project. *Tunnel Construction*, 41, 1485–1491 (in Chinese).
- Xu Q., Zhu H., Ma X., Ma Z., Li X., Tang Z. & Zhuo K. (2015) A case history of shield tunnel crossing through group pile foundation of a road bridge with pile underpinning technologies in Shanghai. *Tunnelling and Underground Space Technology*, 45, 20–33.
- Yang Y., Kong X., Rong J., Fu X. & Liu J. (2012) Pile removing and retaining wall reestablishing technique of shield machine crossing through bridge. *Chinese Journal of Underground Space and Engineering*, 8, 370–374 (in Chinese).
- Yu H., Chen L. & Peng K. (2022) Adaptability of a reinforced concrete diaphragm wall cut by disc cutter. *Sustainability*, 14, 16154.
- Zhang S., Shang C., Wang C., Song R. & Wang X. (2019) Real-time safety risk identification model during metro construction adjacent to buildings. *Journal of Construction Engineering and Management*, 145, 04019034.
- Zhao P. (2023) Long distance horizontal freezing reinforcement and excavation obstacle removal technology. *Building Construction*, 45, 130–134 (in Chinese).
- Zhou Y., Xiao P., Feng Z., Liu A., Yang Z. & Wang S. (2023) Measurement and analysis of vibration of existing station caused by shield tunnel crossing underground diaphragm wall. *Forest Engineering*, 39, 161–171 (in Chinese).

Early assessment and mitigation of cracking on concrete tunnel segments – Dubai metro case study

V. Tellioglu

Jacobs, Tunnels and Ground Engineering, Dubai, UAE

E. Delikan

Jacobs (formerly with Expolink Consortium), Dubai, UAE

A. Ozturk

Expolink (Alstom-Acciona-Gulermak) Consortium, Dubai, UAE

A.M. Haimoni

RTA, Dubai Roads and Transport Authority, UAE

M. Maghazy

Jacobs (formerly with Systra), Tunnels and Ground Engineering, Dubai, UAE

ABSTRACT: This paper discusses the results of observations, analyses and mitigation measures on segment cracking occurred at various installation stages of concrete tunnel lining for Dubai Metro Expo Line. The study involved identification and ranking of various mechanical and geometric variables of ring installation that contribute to segment cracking. A total of 18 potential contributors were continuously monitored and evaluated daily. The crew performance, segment handling and transport, and the accuracy of geometry and surveying in ring building process exhibited the highest ranking of correlation to segment cracking. After deploying early mitigation actions, segment cracking decreased from 14.3% to 1.2% at the best performance. Cracking in Steel Fiber Reinforced Concrete (SFRC) segments is a complex and dynamic phenomenon and hence the term “contributor” rather than “root cause” is used to refer to the influencing factors in the subsequent sections of this paper.

1 INTRODUCTION

Dubai’s selection to host Expo 2020 was a significant factor in the development of the Route 2020 project – a new metro line extending from the existing Dubai Red Line to the Expo site located in the southern part of the city. The project consists of approximately 15km of metro track, including 12km of viaducts and 3.2km of tunnel and underground structures. The line features seven stations: one interchange station, three elevated stations, two underground stations, and an Iconic Station at the Expo site. Additionally, the project involves the procurement of 50 new trainsets, with 15 designated for the new line and 35 to enhance capacity on the existing network. The new line will establish a direct link connecting Dubai Airport, the City center and the Expo Site (Figure 1).

The passenger count was expected to reach 125,000 per day in 2020, rising to 275,000 by 2030. Dubai RTA (Roads and Transport Authority) awarded the design and build contract for the construction works to Expolink, a consortium led by Alstom (France) in collaboration with the Civil Works Joint Venture comprising Acciona (Spain) and Gulermak (Turkiye). Jacobs was entrusted with the detailed design of the civil works, commissioned by the Civil Works Joint Venture.

Tunnelling on the 2.5km bored tunnel between Discovery Gardens and Green Community was successfully completed in June 2018. An Earth Pressure Balance (EPB)-type Tunnel Boring Machine (TBM) was used with a bore diameter of 9.66 meters. A total of 10,150 segments were installed in 1450 rings. Each ring comprises six segments plus the key segment. The thickness of segmental lining was 400mm.

During the construction, some segments experienced cracking, however, early diagnosis and engagement of mitigation measures reduced cracking and resulted in a safe and cost-effective completion with minimal rectification. This paper presents the results of observations, analyses and mitigation measures on segment cracking experienced at different stages of lining installation. The method of assessment on segment cracking used in this case study is based on a generalized procedure for investigation proposed by the corresponding author [1].



Figure 1. General layout - Dubai Metro Expo2020 line.

2 RING BUILDING

The majority of segments installed are made of Steel Fiber Reinforced Concrete (SFRC), and some are conventionally rebar-reinforced concrete (R/C) due to either shallow cover or structural interfaces, i.e. tunnel to station, or tunnel to shaft connections. Table 1 lists down the ring numbers of R/C segments installed along the tunnel route.

Table 1. List of ring numbers with R/C segments with respect to locations.

Ring no.	Location on Tunnel Route
R1-R63	First 63 rings from Northern Cut & Cover – (TBM launching)
R200-R208	Nine rings inside Annex Shaft R72-A1
R619-R628	First 10 rings from R73 Station (TBM re-launching)
R1074-R1083	10 rings inside Annex Shaft R73-A1
R1436-R1450	Last 15 rings before R74 (TBM arrival)

A total of 107 R/C full rings were installed, 63 of these rings were located at the startup area due to structural reasons to facilitate TBM launching under shallow ground cover (R1 through R63). Additionally, nine R/C rings were installed as part of the R72-A1 annex structure (R200 through R208). The TBM was received at R73 underground station then transferred through the station box for re-launching. At the re-launch area, the first ten rings installed were R/C (R619 through R628). As the TBM passed through Annex shaft R73-A1, an additional 10 R/C rings were installed (rings R1074 through R1083). Finally, the last 15 R/C rings were installed before the R74 station headwall for tunnel breakthrough.

3 IDENTIFICATION & MAPPING OF CRACKS

During the construction of the tunnel, cracks began to appear on some of the segments. Expolink immediately commenced crack and leakage mapping inside the tunnel to collect data for a comprehensive analysis of the situation. The findings were analyzed and presented to the client regularly for joint decision-making. The crack mapping continued in the tunnel as the TBM progressed.

The complete mapping of the tunnel (R1 to R1450) was agreed through joint inspections made by both the Engineer and the Contractor (Expolink). The following definitions were mutually agreed upon and adopted for use in mappings.

3.1 Definitions

3.1.1 Initial drive

The “Initial Drive” for tunneling was considered as the installation of the first 200 rings, forming the tunnel from the permanent ring R1 to R200.

3.1.2 Bad zones

“Bad zones” refer to the zones of segments with multiple cracks over a minimum of three successive rings which appear to be usually wet (i.e. damp or flowing). Regardless of its width, any crack with detectable size, whether in wet or dry condition, was counted for labelling a bad zone.

3.1.3 Classification of leakage (infiltration)

The adopted classification of leakage is summarized in Table 2 below.

Table 2. Classification of leakage (infiltrations).

Class	Description
D – dry	No dampness, drip or flow of water
DP – damp	Minor leakage, discoloration of lining surface, moist to touch, damp patches, calcification
F – flowing	Major leakage, continuous dripping or stream of water reaching to tunnel invert

3.2 Distribution of cracked segments

The distribution of segment cracking for the entire tunnel, from R1 through R1450, is illustrated in Figure 2. It shows that the frequency and distribution of cracking gradually decreases from the start to the end along the tunnel. However, there was a noticeable increase in both the number and frequency of cracks as the tunnel approached the R73 underground station.

Between R1 and R1450, 486 segments experienced cracking. The vertical lines in orange color depict the identified ‘bad zones’. At the worst case, five out of seven segments in four rings experienced cracking. All were within the bad zones.

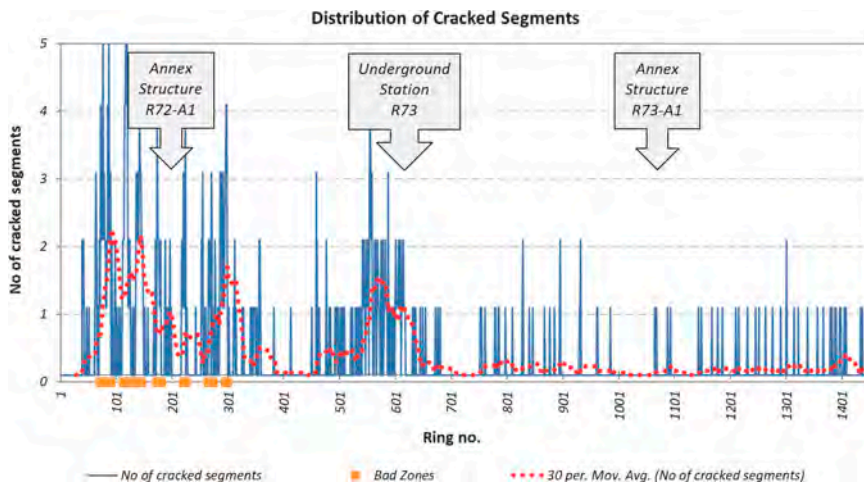


Figure 2. Distribution of segment cracking along the tunnel (R1 through R1450).

No bad zones were identified after R300. The number of segments cracked within the first 300 rings was found to be 269 which corresponds to 55% of the total cracked segments. A total of nine bad zones were identified which contained a total of 50 rings. Of these, in only three rings, the number of cracked segments reached to five. That was, one occasion in Bad Zone no.1, one occasion in Bad Zone no.2 and one occasion in Bad Zone no.3, respectively.

The outcomes of the crack mappings, assessment on potential influencers, and solution proposals have been presented to the Engineer and client (RTA) in weekly progress meetings. The details are summarized in Table 3.

Table 3. History of weekly status on segment cracking.

No.	From R1 to	Status	Bad Zones	Landmark
1	R90	Initial investigation	R72-80, R85-90	
2	R145	Interim update	R114-120, R137-139, R142-144	
3	R185	Interim update	R174-180	
4	R200	End of initial drive		
5	R275	Main drive	R222-225, R266-274	Passage through R72-A1
6	R390	Main drive	R297-299	All mitigation measures to control cracking in effect from R300
7	R425	Main drive	No bad zone observed	
8	R525	Main drive	No bad zone observed	
9	R560	Main drive	No bad zone observed	
10	R618	Main drive	No bad zone observed	Arrival at R73
11	R779	Main drive	No bad zone observed	Re-launching from R73
12	R819	Main drive	No bad zone observed	
13	R906	Main drive	No bad zone observed	
14	R994	Main drive	No bad zone observed	
15	R1265	Main drive	No bad zone observed	Passage through R73-A1
16	R1380	Main drive	No bad zone observed	
17	R1380	Main drive	No bad zone observed	
18	R1450	Main drive	No bad zone observed	Arrival at R74

3.3 Summary of initial findings

The following observations were made from the study:

- A great majority of cracks observed were less than or equal to 0.2mm wide. The majority were in damp condition, and some were flowing.
- The predominant orientation of the cracks was along the tunnel axis; no cracks were observed in a radial direction.
- Cracks appeared randomly both on the leading edge and trailing edge (approx. 50% on leading edge, 47% on trailing edge, and 3% segment-wide).
- Based on experience, it is noted that the hairline cracks (<0.2mm) tend to self-heal in 4 to 6 weeks' time. This was evident within the first 120 rings of the tunnel as the mapping continued. Similar observations have been reported in other case studies, referenced in [2] and [3].

4 TUNNEL BORING MACHINE (TBM) AND LINING INTERFACE

Cracking in concrete segmental linings, while undesirable, is not rare. Similar case story is reported in [1] and a research published can be found in [4]. Several potential mechanisms can lead to cracking in tunnel segments during construction. These include but not limited to:

- a) The contact of segment(s) with the tail brush and/or hardened backfill
- b) Insufficient tailskin clearance
- c) Excessive bending moment induced by thrust force due to uneven ring joint surface or birds-mouthing between segments. One of potential mechanisms of crack development in TBM tunnels is the combination of segment gap and thrust force. In such cases, bending moment is created in a segment then cracks take place on the tension face of the segment. Depending on the distorted support conditions, these cracks may appear on the leading edge or on the trailing edge of segments
- d) Eccentric loading onto segment due to the offset of thrust jack and spreader
- e) Excessive thrust force applied to the segments.

Notwithstanding the above, one should note that cracking in SFRC segments is a complex and dynamic phenomenon. This is why the term “contributor” instead of “root cause” to cracking is used in the subsequent sections of this paper.



Figure 3. Photo from a typical bad zone with multiple cracks & leakage.

5 REVIEW AND VERIFICATION OF SEGMENT DESIGN

In segmental lining design, the required design characteristic compressive strength of concrete cylinder (f_{ck}) was set to 50MPa at 28 days. The required design split tensile strength is 5.13MPa at 28 days. Steel fibers with dosage of 30kg/m^3 and yield strength of 1050 MPa was used in the concrete mix for both SFRC and R/C segments. In addition to steel fibers, a dosage of 2kg/m^3 of monofilament polypropylene fibers was added to the concrete mix to

retard spalling in case of a fire incident. For R/C segments, conventional weldable bar reinforcement with 500 MPa yield strength was used.

The observed cracks occurred during the tunnel boring process. The great majority of cracks were aligned along the tunnel axis; either on the leading edge or trailing edge of the ring joints. No radial cracking within the segment core along the tunnel profile was observed (Figure 3).

Therefore, as a first step in the analysis of segment cracking, the lining design under operational loads was revisited to make sure that the design assumptions and methodology were still valid and satisfactory under the actual loads that the lining ring experienced during TBM drive.

A total of 19 rams were considered in modelling the TBM advance in the design. Each ram had a pair of thrust cylinders and footprint dimensions of 800x290mm with 1457mm pad spacing. The nominal thrust force (unfactored) per ram shoe was 4926kN and 93,594kN per ring. The bursting stresses (segment splitting) under TBM ram loads were double-checked. An offset of 45mm between the ram centerline and segment centerline was considered towards extrados.

The SFRC characteristics have been investigated through the review of records on precast concrete testing. The actual strength values achieved on site were plotted in Figure 4 which demonstrated that the segment strengths were fully compliant with the design requirements except for a few values which were dealt with through Quality Control (QC) procedures.

It should be noted that the total thrust force over the first 300 rings did not exceed 40% of the total maximum loads applicable to the TBM rams. The analyses for determination of stress distribution under ram shoes showed that the induced tensile stresses remained within the tensile strength of SFRC. The design was validated under actual loads with no risk of bursting nor additional requirement for additional steel. In conclusion, no direct correlation could be established between the cracking and design deficiency.

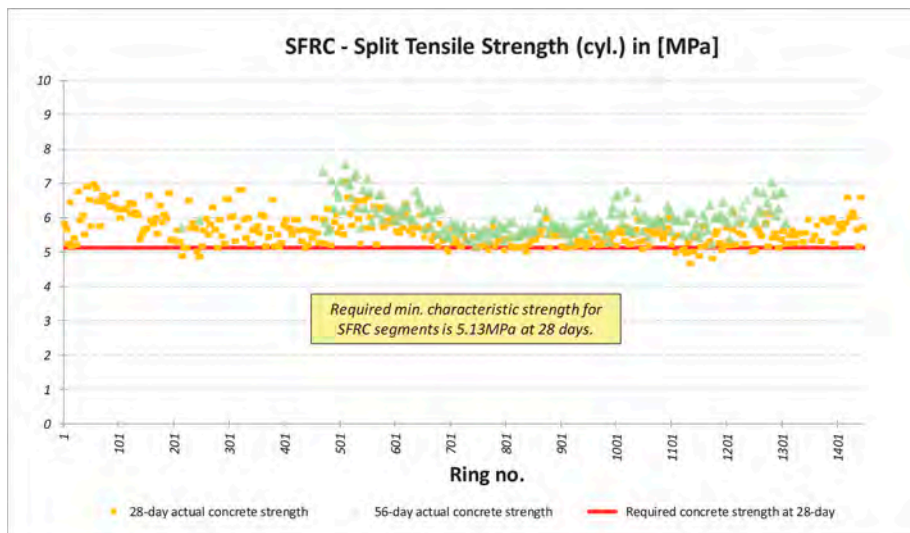


Figure 4. Split tensile strength of SFRC segments: Required vs Actual.

6 ANALYSIS OF SEGMENT CRACKING: MAIN CONTRIBUTORS

The initial observations were made looking at crack mappings and distribution. After the segment design was checked and verified, an assessment was undertaken in a step-by-step approach to analyze potential contributors to segment cracking as referenced in [1].

In TBM operations, various parameters and their combinations may affect ring building performance and result in segment cracking. In this assessment, 18 parameters (listed in Table 4) were considered as potential contributors to cracking, which were monitored over the time, analyzed daily and reported in weekly update meetings.

Table 4. List of parameters and data sources used in assessment.

Ring Reports -Electronic Guidance System	TBM Advance Reports	QC records	Site Observations
▪ Key position	▪ Thrust force (TF)	▪ Split tensile strength of concrete	▪ Shift in dowel markers
▪ Deviation of ring centroid (RC)	▪ Face pressure (FP)	▪ Crew performance	▪ Segment lifting & transport
▪ Tailskin clearance (TSC)	▪ Tailvoid injection pressure (GP)	▪ Segment type	▪ Position of cracks in segments (i.e. leading edge, trailing edge)
▪ Extension of tailskin articulation cylinders (TAC)	▪ Grout take (GT)	▪ Workshifts	
	▪ Extension of thrust cylinders (TC)	▪ Rate of segment erection	

The ring reports obtained from the electronic guidance system include geometric parameters whereas TBM advance reports cover mechanical parameters. Both reports are generated electronically by the guidance system and the TBM itself. In addition, shift reports and QC reports were analyzed along with the observations made at tunnel jobsite and at the segment factory.

All the quantitative and qualitative data were analyzed, i.e. the distribution of cracking was plotted against several variables to explore the characteristics of data and have a feel for apparent tendencies on visual outputs. Meaningful patterns in the data were identified and checked against physical meaning. The results were summarized in Table 5 below for potential contributors and their estimated weights to segment cracking.

Table 5. Potential contributors to segment cracking, their rankings, and mitigation measures.

No.	Description of Contributing Parameter	Ranking of Estimated Weight of Contribution to Cracking	Proposed Mitigative Action
1	Deviation of ring centroid (RC)	Low	-
2	Face pressure	Low	-
3	Tailvoid injection pressure	Low	-
4	Extension of thrust cylinders (TC)	Low	-
5	Key position	Low	-
6	Split tensile strength	Low	-
7	Rate of segment erection	Low	-
8	Extension of tailskin articulation cylinders (TAC)	Low	-
9	Grout take	Low	-
10	Workshifts	Low	-
11	Crack position	Low	-

(Continued)

Table 5. (Continued)

Description of Contributing No. Parameter	Ranking of Estimated Weight of Contribution to Cracking	Proposed Mitigative Action
12 EPDM gaskets and connectors (dowels)	Low	-
13 Segment type	Low	-
14 Thrust force	Low	-
15 Tailskin clearance (TSC)	Medium	More emphasis and diligence on steering. More care and time taken in ring building.
16 Crew performance	High	More training provided. Lessons learned identified and shared across crews. Communication enhanced among the three shifts. In effect from R300 approx.
17 Segment handling & transport	High	Complete review of handling. The route for transportation changed to eliminate effect of impact & vibration due to speed humps. In effect from R286 approx.
18 Geometry & surveying in ring building process including electronic guidance	High	Complete review undertaken. Accuracy and digital precision increased in the electronic guidance system. In effect from R300 approx.

None or negligibly weak correlation was observed between cracking and the parameters classified as “low” weight contribution (#1 through #14), therefore they were ruled out. The one which was marked as “medium” weight contribution (#15), “moderate correlation” was observed, the performance and data were examined more closely. Further evidence of correlation was sought. Parameters #16 through #18 exhibited the highest ranking of correlation to segment cracking. The details of assessment undertaken are summarized below for those parameters with moderate and strong correlation to cracking.

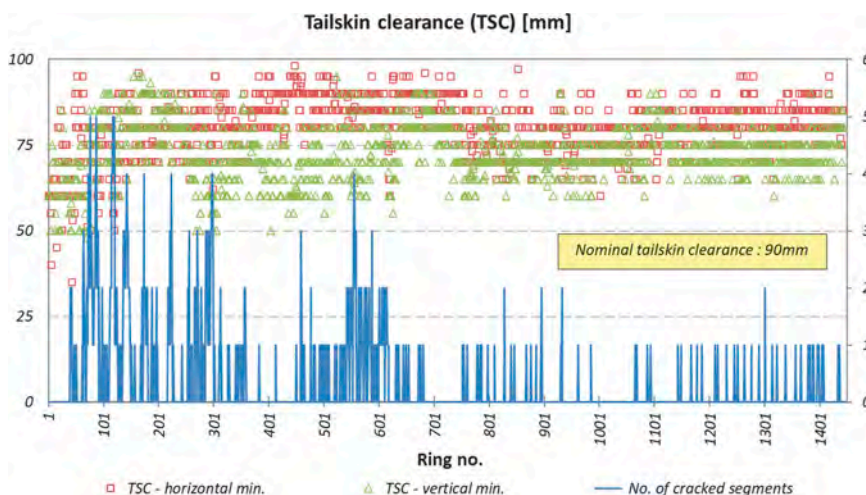


Figure 5. Tailskin clearance vs cracking.

6.1 Tailskin clearance

Insufficient tailskin clearance is recognized as a potential contributor to segment damage, as indicated above in TBM-ring interface. Tailskin clearance vs distribution of cracking is plotted in Figure 5. When the vertical or horizontal TSC dropped below 60mm, tendency to increase in cracking was recorded.

6.2 Crew performance

Figure 6 shows the performance up to R300 prior to improvements in ring building. Notable difference was observed in performance of Crew no.1 with respect to Crew no.2 and Crew no.3 over a certain length of tunnel, particularly between R1 and R275.

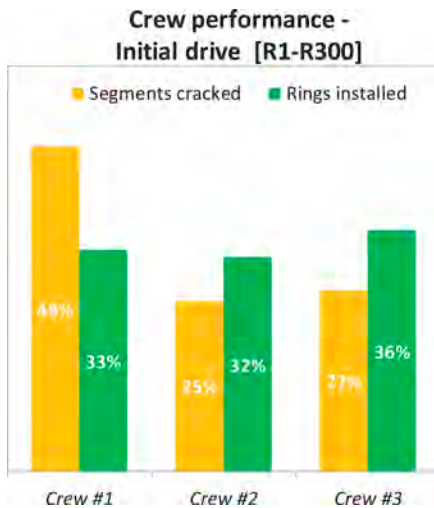


Figure 6. Crew performance vs cracking – first 300 rings.

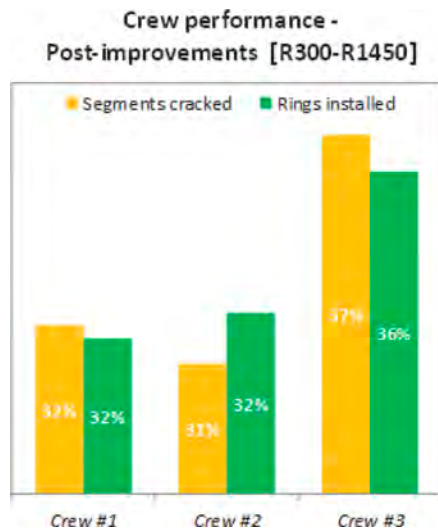


Figure 7. Crew performance vs cracking: overall post-improvements.

6.3 Segment handling & transport

Vibration or impact forces can induce tensile stresses and micro-cracking in matrix structure of segment concrete. Therefore, the sequence of operations in segment demoulding, handling, lifting, stacking and transport from the factory to the tunnel were suspected and jointly inspected by attendance of the Engineer and Designer.

- The entire life cycle of segments from the factory to installation at the site was inspected.
- The segment handling on site was inspected and reviewed. It was found that straps were used in lifting however maintaining the application points as per the design were not always consistent.
- A total of 14 speed humps on the road to TBM site (around the Discovery Gardens area) were identified.

6.4 Precision of navigation & ring installation

The precision of navigation and ring build was also found to be strongly correlated to risk of cracking. Complete review of the electronic guidance system was undertaken by the specialists.

7 MITIGATION ACTIONS

After identifying the moderate and strong correlation to segment cracking, the Contractor promptly initiated actions, and began to improve the ring building quality. The specifics of mitigation actions are summarized below.

7.1 *Main contributors*

In order to maintain TSC at/around nominal value, greater diligence and focus in TBM steering were implemented. More attention and time had to be taken in ring building. Continued improvement was observed in maintaining clearances close to nominal values (Figure 5).

Enhanced training was provided to the crews. Lessons learned were identified and shared after each shift. Communication and experience exchange were improved among the three shift crews. Following these measures, improvement was found to be significant. Figure 7 depicts the overall performance post-improvements (R300-R1450). The difference in crew performance became negligible. Crew no.1, who was the worst performer, improved its performance significantly.

At the segment factory, the lifting straps were replaced by a segment clamp. To eliminate the risk of potential premature cracking inside the segment core during transport due to impact loads, the Contractor diverted the segment transport to an alternative route with no speed humps. The timeline of events for investigation on segment handling and transport is recorded in Table 6 as below:

Table 6. Timeline of events for investigation on segment handling & transport.

Action	Relation to ring installation in time
1 Visit to the segment factory	around the installation of Ring R232
2 Changed transport route	around the installation of Ring R235
3 No. of rings stacked at TBM launching area	45 to 50 rings (R280 ~ R285 left the stacking yard when the stock was fully utilized)
4 First rings installed (via changed route)	from approximately Ring R286

Finally, the accuracy and digital precision of the electronic guidance system were enhanced to further improve ring building quality.

7.2 *Further mitigative actions on ring building quality*

In addition to the mitigative actions taken on the main contributors, further on-site actions were taken as followings:

- The differential between extension of thrust cylinders was set to a value close to diametral ring taper in the design which is 60mm to maintain plane ring joints.
- Double stage process for tightening of spear bolts was implemented (before and after ring left the shield) to maintain gasket compression hence avoid potential leakage.
- The gasket manufacturer was requested to perform an investigation on gasket and connector performance, the gasket lubrication was improved both in material and application workmanship.
- The segment erection crew focused on extra efforts to:
 - a) avoid eccentric or inclined loading of rams on the segments
 - b) ensure that ring joints remain planar
 - c) keep ram shoes and pads clean, free from grout
 - d) correct angles between contact surfaces to minimize birds-mouthing.

8 POST-IMPROVEMENT OBSERVATIONS ON RING BUILDING QUALITY

All the actions taken improved the ring building quality and aimed to eliminate potential sources of pre-installation cracking, ensuring segments remained intact until their final placement in the tunnel.

While it was impractical to conduct controlled experiments to individually measure the effectiveness of each mitigation measure on site, qualitative observations suggest that controlling the major contributors was crucial and led to significant improvements. In addition, consistent attention to workmanship helped maintain daily quality in ring installation.

As the implementation-correction cycle is a dynamic process, all technical findings were regularly shared with the Engineer and the Client on daily and weekly bases through presentations on segment cracking, attended by the Designer. In the weekly reviews, the proposed actions were identified and agreed for action. The TBM construction management implemented a series of actions to improve the quality and reduce the ratio of segment cracking. As a result, no bad zones of cracked rings were observed after R300, compared to the nine identified within the first 300 rings from launching.

The overall performance from R1 to R1450 showed remarkable improvement; the maximum ratio of cracked segments decreased from 14.3% down to 1.2% at the best performance (Figure 8). The implemented actions showed their effectiveness shortly after Week 5, around R300. No new bad zones were identified beyond R300.

The increase in cracking trends between Week 7 and Week 10 was attributed to partial damage to the tail brushes leading to ingress of groundwater and fines over a short length of tunnel. The tight deadline to meet for arrival of TBM at R73 station and proximity of R73 station made it impractical to stop the TBM to repair the damaged brushes. The flow of water and fines put severe pressure on the crew who were required to install some segments under water and in low visibility. After complete maintenance of the TBM which included the replacement of tail brushes, the TBM departed the R73 station and performed continuously better all the way to final breakthrough at R74 station headwall.

It is important to note that the first rings installed after the transportation route was changed to avoid speed humps were from R286 onwards, coinciding with the start of observable improvements and a decrease in segment cracking. It is likely that the segments might have been adversely affected by vibrations or impact loads during transport to the site.

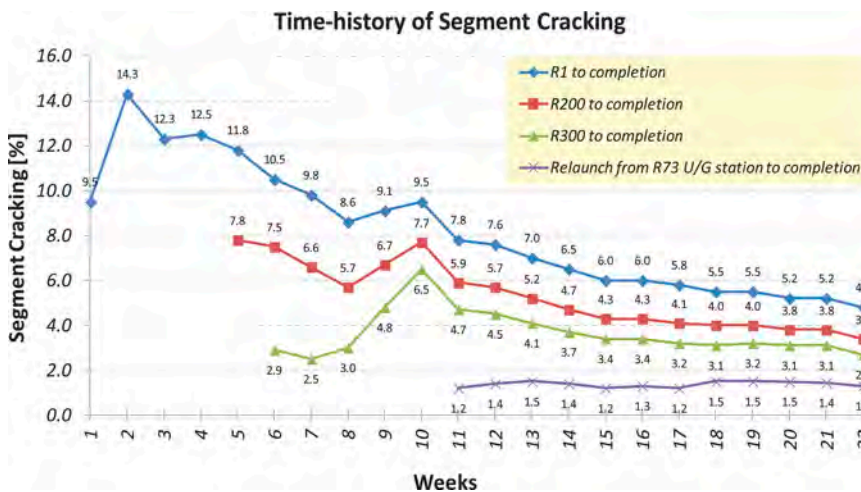


Figure 8. Overall performance.

9 SUMMARY OF CRACKS, LEAKAGE AND NEED FOR REPAIR WORKS

Table 7 summarizes the crack mapping data. It shows that a total of 10,150 segments were installed across 1450 rings. Out of these, 551 segments exhibited 773 cracks, resulting in an average cracking ratio of 5.4% across the tunnel's length. The progress and improvements in this aspect are further discussed in Section 10. The majority of these cracks were less than 0.2 mm in width. Notably, 61% of these cracks showed signs of self-healing, transitioning from a damp (DP) to a dry (D) state over time. This suggests a potential benefit of using SFRC linings under suitable conditions, with self-healing typically taking 4 to 6 weeks.

The final mapping shows that only 6% of all cracks were in a flowing/leaking condition (F), 27% were damp (DP), and the remaining 67% were dry (D). All cracks under the leakage category (F) were injected. This required a two-pass approach due to restricted access in certain cases of the tunnel such as behind the belt conveyor, ventilation bag and utility lines.

A minimal number of segment joints were found to be leaking. These were either sealed by injection in the lower half or caulked in the upper half of the tunnel cross-section. Additionally, 22 bolt holes that leaked during inspection were sealed using thixotropic high-strength repair mortars.

Table 7. Summary of cracks, leakage and need for repair (also refer Table 2 for leakage categorization).

Ring no.	Cracks								Joints			Bolt holes			
	Dry (D)		Damp (DP)		Flowing (F)		No. of Segments	No. of Cracks	To be repaired by	F changed to DP	DP changed to D	Flowing (F)	To be repaired	Flowing (F)	Repaired
	Initial	Final	Initial	Final	Initial	Final									
R1-100	38	107	79	17	8	1	79	125	1	7	69	1	1	3	3
R101-200	29	83	130	80	5	1	101	164	1	4	54	1	1	4	4
R201-300	11	88	105	30	11	9	90	127	9	2	76	8	8	2	2
R301-400	9	28	19	0	0	0	24	28	0	0	19	0	0	1	1
R401-500	16	25	16	9	2	0	28	34	0	2	9	0	0	3	3
R501-600	72	93	36	17	14	12	85	122	12	2	21	6	6	8	8
R601-700	31	40	14	5	0	0	28	45	0	0	9	-	-	1	1
R701-800	1	11	12	1	0	1	11	13	1	1	10	-	-	-	-
R801-900	0	9	13	5	5	4	14	18	4	1	9	2	2	-	-
R901-1000	0	3	11	8	0	0	8	11	0	0	3	-	-	-	-
R1001-1100	0	2	4	2	0	0	4	4	0	0	2	-	-	-	-
R1101-1200	0	9	8	3	8	4	15	16	4	4	6	-	-	-	-
R1201-1300	0	12	24	13	6	5	29	30	5	1	9	-	-	-	-
R1301-1400	0	9	19	14	13	9	31	32	9	4	5	-	-	-	-
R1401-1450	0	0	3	3	1	1	4	4	1	0	0	-	-	-	-
Totals	207	519	493	207	73	47	551	773	47	28	301	18	18	22	22

(* Either by injection or caulking as required)

Total no. of segments: **10,150**
 No. of DP cracks at initial mapping: **493**
 No. of cracks self-healed cracks (changed from DP to D at final inspection): **61%**

Abbreviations:

D: "Dry" state of a crack, joint or bolt hole

DP: "Damp" state of a crack, joint or bolt hole

F: "Flowing" state of a crack, joint or bolt hole

10 LESSONS LEARNED AND CONCLUDING REMARKS

The excavation of the R2020 was completed safely and on time. Ground surface settlements were effectively kept within 2mm with only one instance where it reached 5mm over a brief section, well below the Contract requirement of 10mm. Continuous and effective control of EPB face pressures played an important role in getting good results and preventing damage to the built environment.

Every TBM tunnelling operation typically starts with a learning curve. This phase is often linked to the tunneling crew acclimatizing to a new boring machine, new grout mixes, and site-specific geological and hydrogeological conditions. It is recommended for future projects that the Owner and the Contractor consider an allowance for this learning period and undertake together with their Designers and Consultants a thorough, early analysis of the results, to diagnose any deviation from the standard norms or deficiencies, in order to improve the construction outcomes from early stage. Lessons learned from prior projects, like this one, should be used to reduce the duration of this learning curve.

The tunnel builder should have the skill sets and resources to tackle potential problems at an early stage. Early detection, identification, mapping and response to segment damage (i.e. cracking and other), particularly over the first 200 rings (learning curve) is important to take control over repetitive damage in the tunnel lining.

From an overall performance standpoint (R1-R1450), a notable improvement in controlling segment cracking was observed from R300 onwards. The maximum ratio of cracked segments dropped from 14.3% down to 1.2% during the final tunnel drive. A maximum threshold value of 2 to 3% cracking in SFRC segments seems to be a reasonable and practicable range to target, although with proper controls and experience, it appears that 1 to 2% is possible.

Given the aggressive environmental exposure in the project area, self-healing was highly beneficial in maintaining durability in the long term with no detrimental repair works on tunnel linings. For this reason, SFRC linings is preferred as far as the conditions are suitable for SFRC design.

The design requirements and construction tolerances need to be closely followed not only in installation but also during segment handling and transportation. The segments should be prevented from exposure to excessive vibrations or impact stresses during handling and transportation.

Accuracy and precision of construction during tunnel advance are important and should be closely controlled to ensure accurate navigation and high-quality ring build, which combined should reduce cracking. The control shall include continuous surveying and plane checks on ring joints build quality. Further, the ram shoes should be kept clean, i.e. free from grout or similar impurities that might result in uneven support conditions for the subsequent ring.

TBM operation is usually a continuous three-shift process, with three separate crews. It has been evident that cross-communications to exchange experience amongst the crews is important to ensure consistent process and continues improvements are achieved throughout the tunnel advance. Analysis of the results from the various crews should be analyzed to identify trends at early stage and to ensure that the best practices are mirrored.

Preparedness for unfavorable conditions during tunneling is crucial. For example, the continuous ingress of water can be managed by using emergency seal grease. It is recommended to have enough quality materials available on hand and on-site for emergencies or unexpected situations. Additionally, for high quality work it is essential to ensure that the working conditions and environment are maintained at the highest level.

ACKNOWLEDGEMENTS

This paper reflects the views of the authors, who are solely responsible for reliability and accuracy of the information presented. The authors are grateful to Roads & Transport Authority (RTA) of Dubai Government for their kind permission to publish this paper. The encouragement and support of Dr. Abdussamie Himoni (RTA) is greatly appreciated.

REFERENCES

- Tellioglu V. 2019. Observations on Concrete Segment Cracking: An Assessment of Correlations. *Geomechanics & Tunneling Journal*, Vol.12, Issue 01/2019: 82–95., Salzburg: Ernst & Sohn (Wiley).
- Tellioglu V. 2015. Defect Identification and In-Tunnel Repair of Concrete Lining Segments in Highly Corrosive Environmental Conditions. *Underground Design and Construction Conference*. Hong Kong: The Institute of Materials, Minerals and Mining (IOM3) – UDCC 2015.
- Tellioglu V. & Lerpido S. 2014. Observations on Groundwater Leakage Through Cracks and Segment Joints in a Concrete Segmental Tunnel Lining. *ISSMGE International Symposium on Geotechnical Aspects of Underground Construction in Soft Ground*. Seoul: CRC & Balkema.
- Sugimoto M.2006. Causes of Shield Segment Damages During Construction. *International Symposium on Underground Excavation and Tunneling*. Bangkok.

Investigating transient tunnelling-induced ground surface responses

S. Xue & J.R. Standing

Imperial College London, London, UK

ABSTRACT: The assessment of tunnelling induced ground responses in the urban environment often focuses only on the final displacement profiles without considering their progressive development. Transient movements, especially in the longitudinal sense, can have relevance when assessing structural response and potential damage. Comprehensive field monitoring data from three instrumented research sites in London have been analysed (Hyde Park relating to the Elizabeth Line and St James's Park and Southwark Park to the Jubilee Line Extension Project), although the focus of this paper is on the responses observed at the Hyde Park site. Valuable insights into short-term transient surface ground responses to tunnelling have been gained. They are classified into three phases, based on the relative TBM position. Often there is uncertainty about where to define the end of short-term and start of long-term tunnelling-induced ground responses. The data analysed strongly suggest that the 'end of short term' be taken to be as the end of Phase 2, when $x_f \sim 30$ m (the distance of the TBM face from the monitoring line). Various normalisation approaches have been applied to the monitoring data to help unify them and provide overall generic ground responses to be developed and compared. For example, it was established that the shape of the developing transverse trough remains constant at all stages for both symmetric and asymmetric troughs.

1 INTRODUCTION

Tunnel construction in the urban environment has increased dramatically in recent decades. An essential component of any urban tunnelling project is the accurate prediction and monitoring of resulting ground and structural responses. Generally, predictions made only relate to the final 'short-term' condition (e.g. Peck 1969, Burland 1995, Mair & Taylor 1997). In this paper the transient deformations during the tunnelling advance are examined to investigate potential changes in developing displacement profiles, assess how readily they can be unified for typical London Basin ground conditions and tunnelling methods and to help understand the full ground surface response mechanisms. This in turn will help anticipate any potential adverse impacts on nearby surface structure.

In order to gain insights into the transient tunnelling-induced ground responses, field monitoring data from three greenfield 'control' sites have been compiled, analysed and compared (Xue, 2023). All three were set up by Imperial College as part of two major research projects: Hyde Park relating to Crossrail (subsequently renamed as Elizabeth Line), as described by Wan (2014) and Wan *et al.* (2017a & 2017b) and two Jubilee Line Extension (JLE) sites at St James's Park (Nyren 1998, Nyren *et al.* 2001, Xue 2023) and Southwark Park (Withers 2001). Tunnelling beneath Hyde Park (HP) was in London Clay using an Earth-Pressure Balance (EPB) Tunnel Boring Machine (TBM); at St James's Park (SJP) an open-faced shield was used also in London Clay, while at Southwark Park (SP) an EPB TBM was used in the Lambeth Group (with the invert just into the underlying Thanet Sands). The ground responses relating to the different ground conditions and tunnelling methods have been unified as far as possible, using various normalisation approaches, to explore overall generic ground responses,

compare them and provide guidance for future projects. This paper provides a brief summary of the study by Xue (2023), with its focus on the HP site although commentary is given about the responses observed at SJP and SP. Two far more comprehensive papers are in preparation covering surface and subsurface transient ground responses to tunnelling, comparing the responses at all three sites.

2 TYPICAL TUNNELLING-INDUCED GROUND DISPLACEMENT MECHANISMS

An idealised 3-D ‘greenfield’ surface soil displacements responses to tunnelling, modified from Attewell *et al.* (1986), is presented in Figure 1. Numerous field observations have demonstrated that in the transverse sense the settlement trough for a single tunnel has a Gaussian form and is symmetric. The magnitude of soil displacement increases as the tunnel approaches and passes beneath a given monitoring line. After the TBM has passed beyond the line, these generally undrained short-term movements can develop further in the long term due to influences such as consolidation, creep and construction of a second twin tunnel.

Normally, ground response to tunnelling is only assessed in the transverse sense. Equally, plane-strain conditions are usually assessed with field monitoring and small-scale physical or centrifuge model testing. The 3-D ground response is determined by compiling measurements from specific measurement times when the TBM is at different distances from the monitoring line. The red lines in Figure 1 represent developing transient transverse settlement troughs in y - z planes, corresponding to different tunnel positions, x_f , the distance between the TBM cutter-head (or front of the shield) and the monitoring line. The ‘short-term’ trough is reached shortly after the tunnel has passed the monitoring line. The blue lines in Figure 1 are transient longitudinal settlement troughs corresponding to x - z plane sections at different y -offset distances from the tunnel axis. There is an individual set of longitudinal troughs, relating to each specific x_f value when the tunnel face is at a given position.

The 3-D surface settlement trough can be expressed from the combined transverse and longitudinal profiles as they develop progressively with TBM advance (increasing x_f). ‘Short-term’ transverse troughs are usually predicted empirically using the Gaussian equation (e.g. Burland 1995), where the variables are volume loss, V_L , the horizontal distance to the inflection points from the tunnel central-axis, i_y , and the maximum settlement, S_{max} . When longitudinal trough predictions are made, they are usually modelled assuming that they can be represented by a cumulative probability curve (e.g. Attewell & Woodman 1982).

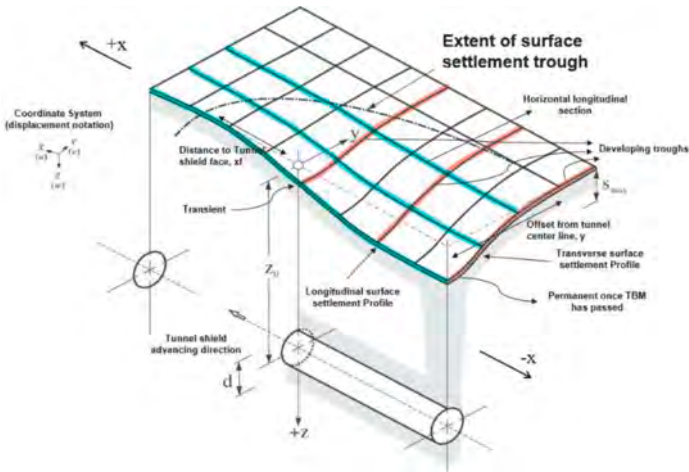


Figure 1. Typical tunnelling-induced ground deformations (after Attewell *et al.* 1986).

3 THREE TUNNELLING CASE STUDIES

Extensive field monitoring data were collected before, during and after tunnelling at the three Imperial College field instrumentation ‘control’ sites at HP, SJP and SP where comprehensive field instrumentation systems were installed.

Plan views of the monitoring layouts at the three sites are shown in Figures 2a-2c. Details of the TBMs used and tunnelling operations beneath the HP, SJP and SP sites are given by Wan *et al.* (2017), Nyren *et al.* (2001) and Mair & Jardine (2001) respectively. The twin tunnels beneath HP are parallel with their axis depths $z_0 = 34.6$ m and diameter $D = 7.1$ m. Also shown in Figure 2a are the existing Central Line tunnels, which are 3.8 m diameter, at a depth of 24 m and skew angle of 40° to the Crossrail tunnels. At SJP the axis levels of the westbound (WB) and eastbound (EB) tunnels are at depths of $z_0 = 31$ m and 20.5 m respectively and they are not parallel to each other. At SP the WB and EB tunnels are roughly parallel with their axes at depth $z_0 = 20.8$ m. The relative geometries of the tunnels and the ground conditions through which they were constructed, along with excavation rates are summarised in Figure 3.

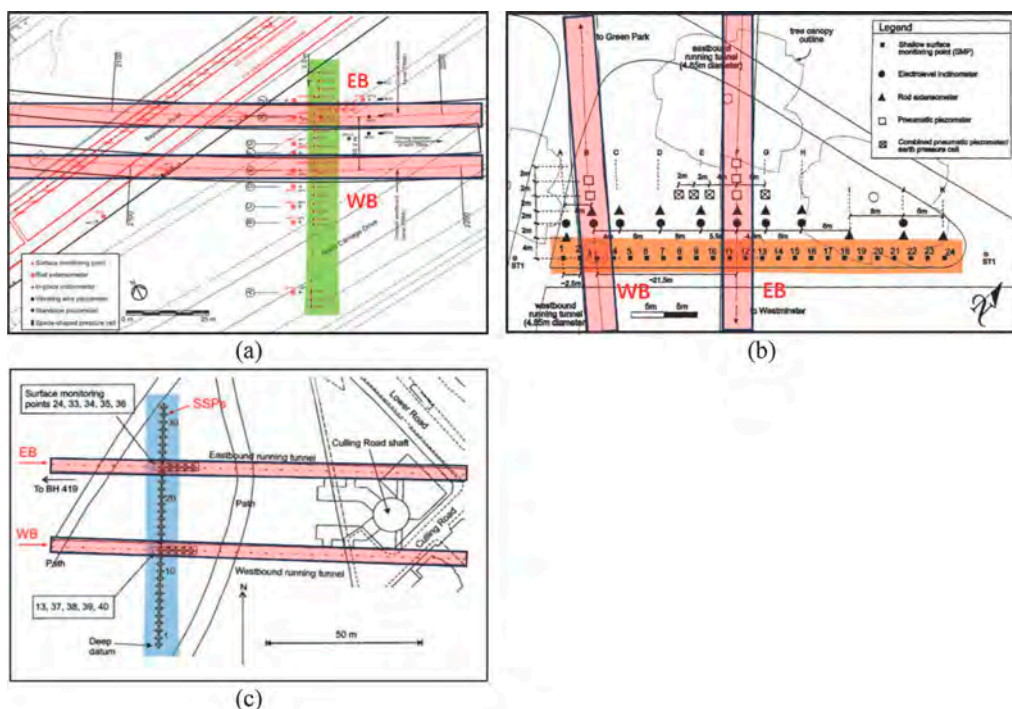


Figure 2. Plan views of the detailed instrumentation of three tunnelling cases in: (a) HP (b) SJP (c) SP.

4 CONCEPT OF UNIFICATION OF DATA

In order to make meaningful comparisons, given potential differences between the cases, such as tunnel: diameter; depth; excavation method; progress rate; location; ground conditions and monitoring instrument layouts, it is necessary to try to unify the data/differences when possible by normalisation or other means. Such unifications help when comparing the transient ground responses during tunnelling beneath the three sites.

To facilitate comparisons, the first tunnel (WB in all three cases) and its associated data are always presented in figures on the left-hand side, although this has the disadvantage that the

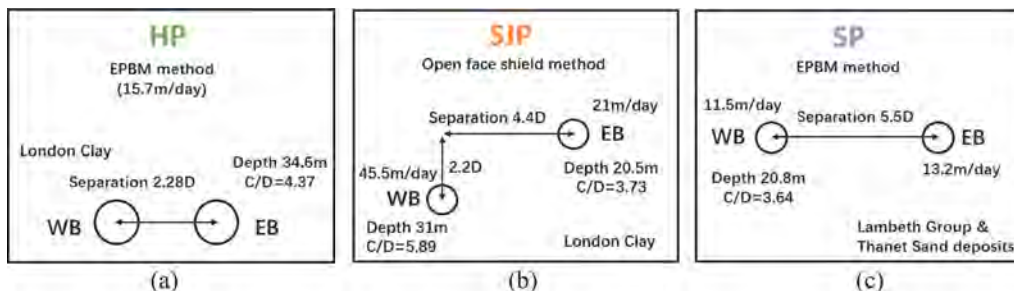


Figure 3. Schematic diagrams of three primary tunnelling case histories with relative tunnel positions and parameters in: (a) HP (b) SJP (c) SP.

view is only in the direction of tunnelling for the JLE TBM drives at SJP. In Figure 3, the separation distances between each pair of tunnels are normalised by tunnel diameter, D . In presenting the field monitoring data, to help recognition of data sets from the three sites, colour coding has been used: orange symbols relate to SJP; blue, SP; and green, HP, as also shown in Figure 2.

5 TRANSIENT GROUND SURFACE SETTLEMENTS DURING CROSSRAIL TUNNELLING

Surface settlement profiles from construction of the WB tunnel beneath HP are presented in Figure 4. The developing transverse settlement troughs are shown in Figure 4a. Each trough relates to a specific x_f distance: negative values are when the TBM is approaching the line and positive values when it is moving away from it. The transverse troughs develop almost symmetrically about the axis of the WB tunnel. The northern settlement half-troughs are slightly wider than those on the southern half, attributed by Wan *et al.* (2017) to ground disturbance from construction of the existing Central Line tunnels to the north of the WB tunnel. They also attribute the heave of the three monitoring points at the southern end of the line to rigid-body rotation of the adjacent North Carriage Drive (see Figure 2).

The data presented in Figure 4a have been divided into three phases corresponding to different stages in the development of the settlement troughs, the distance x_f and associated tunnelling processes. Note that the colours cited below only relate to the phases rather than the three sites.

Phase 1 (black lines): before the TBM shield face reaches the instrument line ($x_f < 0$).

Phase 2 (blue lines): when the TBM face has progressed to ~ 30 m or $3L$ ($L =$ TBM shield length in 11 m) beyond the monitoring line ($0 < x_f \leq 30$ m or $0 < x_f \leq 3L$).

Phase 3 (orange lines): once the TBM face is between ~ 30 m and ~ 60 m or $6L$ beyond the line ($30 < x_f < 60$ m or $3L < x_f < 6L$).

It is evident that the dominant settlement develops during Phase 2 as seen by the blue curves in Figure 4a. Normalised settlements, based on the maximum value at that time (or x_f value) are shown on the secondary left-hand axis in the figure: Phase 1 is between -0.03 to 0.3; Phase 2, between 0.3 to 0.9; and Phase 3, 0.9 to 1. There is often uncertainty about the ‘end’ of the short-term settlement development. As most of the settlement is complete at the end of Phase 2, it is deemed that the short-term ground response is complete at the start of Phase 3 when x_f is $+28.8$ m ($\sim 3L$), after which settlements tend to stabilise.

Longitudinal settlement profiles at different y -offset values are shown in Figure 4b. The most significant settlement occurs above the tunnel axis (red line). The longitudinal settlement profiles of equidistant surface monitoring points (SMPs) either side of the tunnel axis have similar magnitudes (same symbols but with different colours represent equidistant SMPs settlement curves).

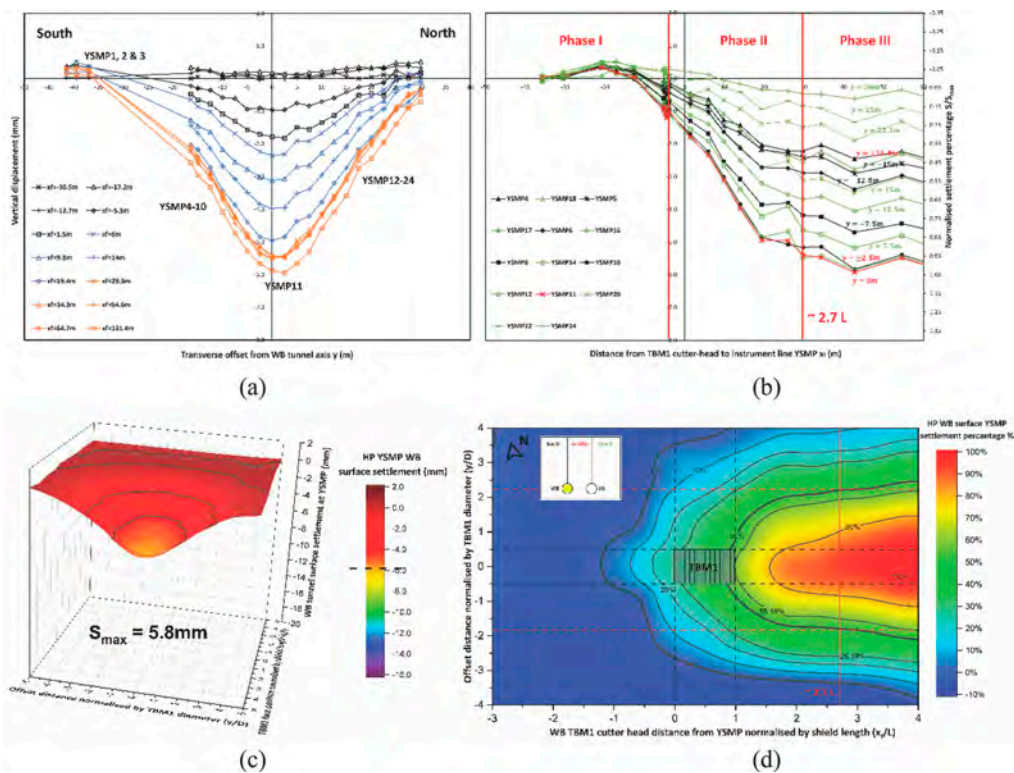


Figure 4. Development of incremental transient surface settlement profiles for WB drive at HP (Y-line) in (a) transverse (b) longitudinal (c) 3D views (d) horizontal plane.

The transient data shown in Figures 4a and 4b are combined to produce a three-dimensional (3-D) image of the surface settlement development in Figures 4c. This is very similar to the schematic given by Attewell *et al.* (1986) in Figure 1. The dashed line on the scale bar indicates the maximum settlement. A plan view (x - y plane) of the 3D trough is presented in Figure 4d, allowing the extent of the surface settlement to be assessed. The black dashed lines in the figure bound the first WB tunnel dimensions and positions and the red dashed lines define the offset position of the 50% normalised settlement contour either side of the progressing tunnel. Figure 4d confirms that the maximum settlement concentration occurs once the tunnel is roughly at $x_f = 3L$.

From both transverse and longitudinal HP WB tunnel surface settlement profiles, it can be surmised that they start developing (Phase 1) when $x_f \sim -12$ m ($\sim 1L$ ahead of the SMP-line) and are fully developed in the short term (end of Phase 2) and become more stable after the tunnel cutter-head passes $x_f = 30$ m ($x_f > 3L$). The ground response to the HP EB TBM followed a similar trend, although the trough was asymmetric because of the ground disturbance caused by the WB TBM, with settlement reaching a maximum of 9.9 mm when $x_f = 29$ m ($x_f \sim 3L$) during Phase 2, again confirming that this is an appropriate point to take as the ‘end’ of short-term ground response. Although greater settlements occurred at the shield face and tail, the combined settlement concentrations that developed were identical for both WB and EB drives, as evident in Figure 5.

In order to investigate in more detail, the development of vertical displacement at different SMP y -offsets, a term ‘ $S/S_{\max(\text{local})}$ ’ is introduced, where $S_{\max(\text{local})}$ is the local maximum short-term settlement at each SMP position. In this way settlement profiles, expressed in terms of each individual normalized SMP displacement, $S/S_{\max(\text{local})}$, can be generated as shown in Figure 6 for both transverse and longitudinal senses for the HP WB drive. Local normalised transverse settlement profiles for different tunnel advance positions (x_f values) are consistently

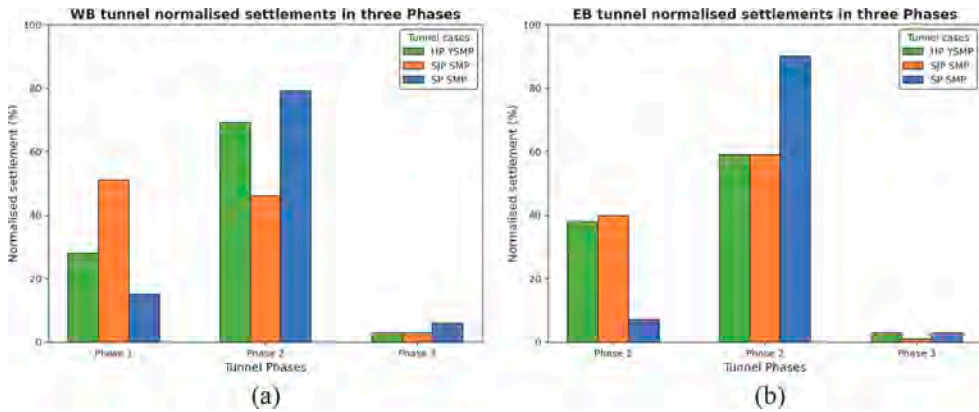


Figure 5. Development of transient surface settlement in three phases during (a) WB (b) EB TBM drives.

close to being constant (horizontal profiles) within the range of $y = \pm 15$ m in Figure 6a for the HP WB drive. This indicates that the shape of the settlement trough does not change, even from its very initial development, particularly in the proximity of tunnel axis. Deviations from these constant trends (outside the box marked in Figure 6a) reflect the accuracy of precise levelling at the extremes of the trough limbs where settlements are very small. The consistency of settlement development in the main central region of the YSMPs (within $y = \pm 15$ m) is also evident in the longitudinal sense (Figure 6b). Although not presented here, the same observation applies to the HP EB drive where the developing settlement trough was asymmetric.

In conclusion, plotting the field monitoring data in terms of local normalised settlement, $S/S_{\max(\text{local})}$, reveals that the shape of the settlement troughs is constant from the period that they start developing (Phase 1) to the end of the short-term (Phases 2) and into the longer term (Phase 3). This applies for both the symmetric (WB drive – first tunnel) and asymmetric (EB drive – second tunnel) settlement troughs and is demonstrated in both transverse and longitudinal senses.

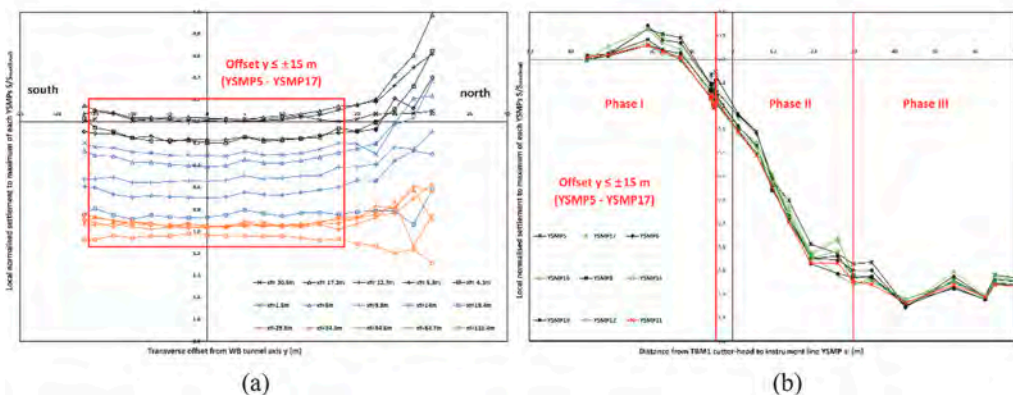


Figure 6. Local normalised settlement by the maximum for each SMP $S/S_{\max(\text{local})}$ for WB drive of HP WB drive in: (a) transverse (b) longitudinal.

6 TRANSIENT GROUND SURFACE SETTLEMENTS FOR THE THREE CASES

To investigate relationships of ground response for all three cases, the ground and tunnel position from different perspectives are normalised by corresponding tunnel variables: the transverse offset distance from tunnel axis, y , is normalised by the tunnel diameter, y/D ; and TBM advance position, x_f , is expressed in terms of the TBM shield length, x_f/L .

It is evident from the summarized data in Figure 5 that the majority of settlements have taken place by the end of Phase 2. In all three cases more than 90% of the overall settlement took place before Phase 3. This is the basis for assigning $x_f = 30$ m as the limit of Phase 2 to mark end of the short-term ground response. For the EPB TBMs at HP and SP, $x_f = 30$ m, corresponds to $2.7L$ to $4.3L$ and for open-face shield at SJP, this corresponds to around $6L$ due to the short shield length. The identification of the ‘end’ of short-term response is significant as it relates to the start of much slower ground displacements, which in the case of tunnels in clay strata, are associated with consolidation and creep.

Comparing the normalised surface settlements, S/S_{max} during the different tunnel phases summarised in Figures 5a & 5b, a number of marked differences are evident. In assessing the ‘green-field’ ground response to the first WB tunnels in Figure 5a, open-face shield tunnelling at SJP resulted in 51% of settlement occurring in Phase 1 due to the lack of face support, followed by 46% that developed during Phase 2. In contrast, for the EPB TBMs used beneath HP and SP only 28% and 15% respectively of the overall settlement occurred in Phase 1 followed by 69% and 79% in Phase 2. For the second EB tunnel at HP (Figure 5b), the increased proportion of settlement that developed during Phase 1 (38%) reflects the soil disturbance caused by the first tunnel. At SJP, despite the ground disturbance from the first tunnel, there is a decreased settlement magnitude during Phase 1. This is attributed to the shallower EB tunnel elevation (lower C/D), confirming the influence of the C/D ratio on the tunnelling-induced settlement development as well as the tunnelling method. At SP the $5.5D$ spacing between the tunnels is sufficiently large that the ground disturbance from the first TBM drive does not affect the second.

The development of transient surface settlement profiles for the WB drives of three tunnel cases in transverse and longitudinal senses is shown in Figure 7. The settlements induced by the tunnelling beneath SJP are greatest because of the use of an open-face shield

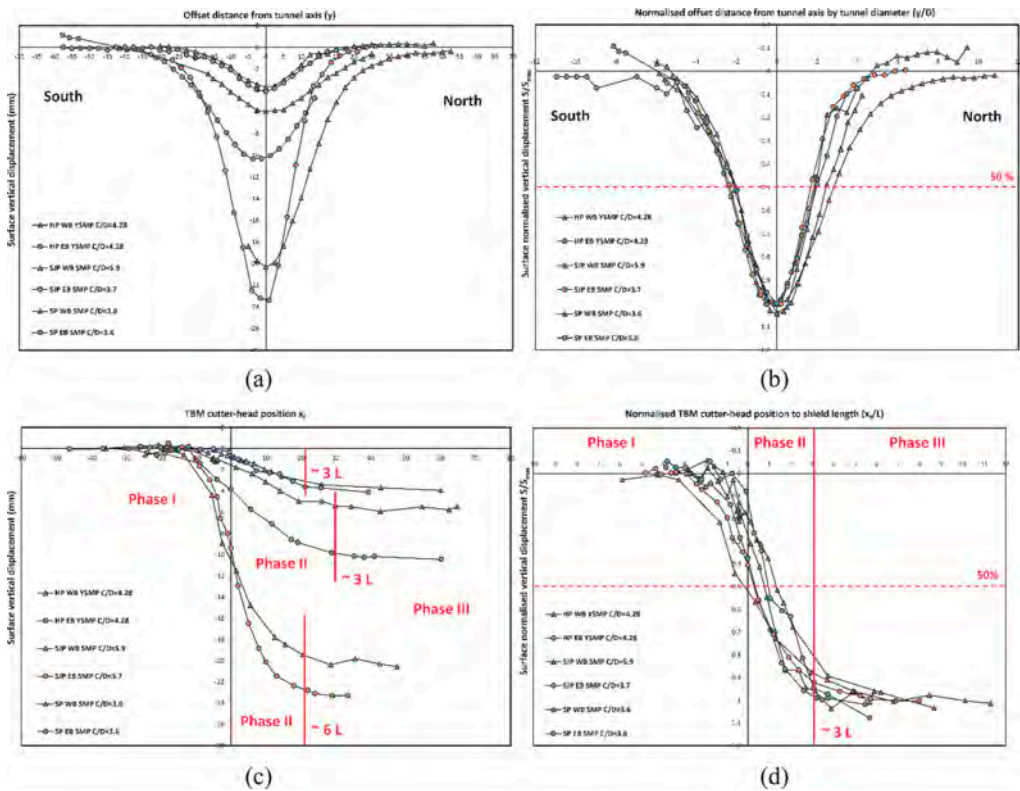


Figure 7. Transverse and longitudinal surface settlement profiles for the three greenfield sites, expressed in both absolute (a and c) and normalized forms (b and d).

(Figures 7a & 7c). The EB drive beneath SJP caused the most significant settlement due to its shallow depth, and the trough is slightly narrower than the WB one. The settlements induced from the WB and EB drives beneath SP are the smallest, being almost identical and symmetrical because of the $5.5D$ spacing between them, indicating that they can be treated as two individual tunnels. Regarding the twin tunnels at HP, settlements induced by the EB tunnelling are 1.7 times greater than the WB due to their close separation $2.28D$ and WB-induced ground disturbance.

The WB settlement troughs are mostly symmetric on either side of the tunnel axis, while for the EB tunnels at HP and SJP, the half-trough adjacent to the first tunnel is wider because of the resulting ground disturbance. This is very evident from the normalised transverse vertical displacement profiles presented in Figure 7b (note that normalised settlements at the tunnel axis are not unity as maximum settlement values are averaged from groups of data). The normalised settlement profiles are all identical on the undisturbed 'southern' side, the disturbed 'northern' side half-troughs becoming wider with increasing tunnel cover to diameter ratio (C/D) values. The width of the overall troughs is within $y = \pm 6D$, with that corresponding to the open-face shield at SJP being wider than others.

Longitudinal surface vertical displacement profiles for the three cases are shown in Figures 7c & 7d, expressed in terms of tunnel face position, x_f . As noted above, the open-face shields at SJP led to the greatest settlement magnitudes (Figures 7a & 7c), and this started at about $x_f = -10$ m. At HP and SP, settlement development started at $x_f = -20$ m and $x_f = -3$ m. The distance at which settlement starts is dependent on the tunnelling method (face support pressure) and C/D ratio. As C/D ratios reduced, there was a greater delay to the start of settlement development. At SJP, settlements were also exacerbated because it was possible excavate 1.9 m ahead of the shield, resulting in unsupported headings. Standing and Burland (2006) report that this did take place to some unquantified degree (and would have affected the settlement development pace).

7 CONCLUSIONS

Transient tunnelling-induced ground surface responses from three instrumented greenfield sites, with a main focus on one at Hyde Park, have been analysed and interrogated. Often there is uncertainty about when the 'end of short-term' response is complete and longer-term consolidation starts. To address this, the responses have been split into three phases according to the distance of the TBM face from the monitoring line, x_f . Assessment of the data suggests that it is appropriate to define the 'end of short-term' response at the end of Phase 2, where $x_f \sim 30$ m. At the end of Phase 2, when expressing x_f in terms of TBM shield length, L , the distance can be from $\sim 3L$ to $\sim 6L$, because of varying shield lengths. Further normalisation of the data, to try to unify the data/responses from the three sites has provided new insights into the transient responses. Introducing a new normalised term, ' $S/S_{\max(\text{local})}$ ', where $S_{\max(\text{local})}$ is the local maximum short-term settlement at each SMP position, reveals that the shape of the transverse and longitudinal settlement troughs is consistent throughout all phases of tunnelling, even from their very initiation. This is the case regardless of whether the trough shape is symmetrical or asymmetrical.

REFERENCES

- Attewell, P.B., Yeates, J., & Selby, A.R. 1986. *Soil movements induced by tunnelling and their effects on pipelines and structures*. Blackie, Glasgow.
- Attewell, P.B. & Woodman, J.P. 1982. Predicting the dynamics of ground settlement and its derivatives caused by tunnelling in soil. *Ground Engineering*, Vol. 15, No. 7, pp. 13–36.
- Burland, J.B. 1995. Assessment of risk of damage to buildings due to tunnelling and excavation. *Proc. Int. Conf. 1st Earthquake geotechnical engineering*. IS-Tokyo '95, 3, pp. 1189–1202
- Mair, R. J. & Taylor, R. N. 1997. Bored tunnelling in the urban environment: State-of-the-art report and theme lecture. *Proc. 14th Int. Conf. Soil Mech. Found. Eng.* Hamburg, Germany, Vol. 4, pp. 2353–2385.

- Mair, R. J. & Jardine, F.M. 2001. Tunnelling methods. In: Burland, J. B., Standing, J. R. & Jardine, F. M. (eds.). *Building response to tunnelling, case studies from construction of the Jubilee Line Extension, London, Volume 1, Projects and methods*. Ch. 10, pp. 127–134. London, Thomas Telford.
- Nyren, R.J. 1998. *Field measurements above twin tunnels in London Clay*. PhD thesis, Imperial College, University of London, London, UK.
- Nyren, R.J., Standing, J.R. & Burland, J.B. 2001. Surface displacements at St James's Park greenfield reference site above twin tunnels through the London Clay. In: Burland, J. B., Standing, J. R. & Jardine, F. M. (eds.). *Building response to tunnelling, case studies from construction of the Jubilee Line Extension, London, Volume 2, Case studies*. Ch. 25, pp. 387–400. London, Thomas Telford.
- Peck, R. B. 1969. Deep excavations and tunnelling in soft ground. *Proc. 7th Int. Conf. Soil Mech. Found. Eng.* Mexico City, State of the Art Volume, pp. 225–290.
- Standing, J. R. & Burland, J. B. 2006. Unexpected tunnelling volume losses in the Westminster area, London. *Géotechnique*. Vol. 56, No. 1, pp. 11–26.
- Wan, M. S. P. 2014. *Field monitoring of ground response to EPBM tunnelling close to existing tunnels in London Clay*. PhD thesis, Imperial College London, London, UK.
- Wan, M.S.P., Standing, J.R., Potts, D.M., & Burland, J.B. 2017a. Measured short-term ground surface response to EPBM tunnelling in London Clay. *Géotechnique*, Vol. 67, No. 5, pp. 420–445.
- Wan, M.S.P., Standing, J.R., Potts, D.M., & Burland, J.B. 2017b. Measured short-term subsurface ground response to EPBM tunnelling in London Clay. *Géotechnique*, Vol. 67, No. 9, pp. 748–779.
- Withers, A.D. 2001. Surface displacements at three surface reference sites above twin tunnels through the Lambeth Group. In: Burland, J. B., Standing, J. R. & Jardine, F. M. (eds.). *Building response to tunnelling, case studies from construction of the Jubilee Line Extension, London, Volume 2, Case studies*. Ch. 37, pp. 735–754. London, Thomas Telford.
- Xue, S. 2023. *Transient ground response during and after tunnelling*. PhD thesis, Imperial College London, London, UK.



Taylor & Francis

Taylor & Francis Group

<http://taylorandfrancis.com>

Author index

- Alagha, A.S.N. 206
An, H.L.C. 257
Ånes, E.W. 511
Ao, P.K. 279
- Bai, X.D. 357
Balamonica, K. 445
Bezuijen, A. 3, 231
Bilotta, E. 545
Boldini, D. 168, 523
Broere, W. 19
- Cao, W. 387
Cespa, S. 545
Chao, A. 396
Chen, C.J. 265
Chen, R.P. 30
Chen, T. 30
Chen, Y. 154
Chen, Y.L. 130
Chen, Y.N. 456
Chen, Y.Z. 93
Chen, Y.M. 287
Cheng, H.Z. 30
Cheng, S.H. 265
Cheng, W.C. 357
Cheng, Y. 464
Cheng, Y.X. 73
Cheung, K.F. 530
- DeJong, M.J. 511
Delikan, E. 564
Deng, X.M. 73
Ding, S. 130
Dong, S.S. 130
Dong, Y.P. 176
Dong, Q. 93
Dou, Z.Y. 182
- Elshafie, M.Z.E.B. 347
- Fan, C. 93
Fan, Z.C. 182
Feizi, S. 364
Feng, X. 116
- Franza, A. 206, 223, 439
Fuoco, S. 168
- Gan, Q. 99
Gao, H.D. 147
Gens, A. 545
Gu, W. 320
- Haimoni, A.M. 564
Hauser, L. 122
He, S.Y. 273, 310
Heron, C.M. 404
Hsiung, B.C.B. 396
Hsu, H.Y. 265
Huang, H. 371
Huang, H.W. 327, 456
Huang, J. 396
Huang, M. 190, 215
Huang, Z.K. 73, 502
- Ieong, K.P. 279
- Jiang, Q.H. 327
Jiang, Y. 99
Jie, A.L.J. 445
Jing, J. 378
Josefsen, J.M. 364
- Karenstuen, F. 364
Kristiansen, H.P. 364
- Laloui, L. 39
Lan, Q.C. 488
Lande, E.J. 122
Langford, J. 364
Lee, S.W. 530
Leung, C.F. 215
Leung, C.O. 530
Li, H. 215
Li, M.-Z. 287
Li, X. 116
Li, X.Y. 107
Li, Z. 293
Li, Y.Z. 287
Liang, J. 537
- Liao, S.M. 333
Liao, S. 552
Lim, J. 215
Lin, J. 471
Liu, J. 293
Liu, J.F. 387
Liu, J.Q. 130
Liu, W. 130, 537
Liu, X.Y. 147
Liu, Y.J. 182
Liu, Z.H. 182
Lok, T.M.H. 198, 429
Lusini, E. 168
Lysdahl, A.O.K. 511
- Ma, J.H. 387
Mace, N. 480
Maghazy, M. 564
Mariano, A.D. 545
Marshall, A.M. 223, 404
Marte, R. 122
Meng, F. 293
Meng, F.Y. 30
Monsås, E. 364
Mooney, M.A. 49
- Neves, L. 223
Ning, J. 190
- Oberhollenzer, S. 122
Ong, D.E.L. 357
Ozturk, A. 564
- Phan, K.H. 396
Piciullo, L. 511
Pittaro, G.A. 480
- Qin, S. 488
- Ragione, G.D. 545
Ravera, E. 39
Ritter, S. 511
Royo, B. 545

Sanchez, J. 545
 Sandene, T. 364
 Schweiger, H.F. 122
 Schwob, A. 530
 Selvaraj, S.P. 404
 Shao, H. 421
 Shen, D.Y. 320
 Shen, P. 413
 Shen, Y. 301
 Shi, Z.M. 320
 Skretting, E. 364
 Song, Y. 130
 Spaggiari, C. 168
 Standing, J.R. 577
 Stark, T.D. 471
 Stumpf, A.J. 471
 Sugimoto, M. 257
 Sun, J. 552
 Suzuki, T. 257

 Tan, Y.Y. 139
 Tang, C. 310, 404
 Tellioglu, V. 564
 Thi, H.N. 257
 Tian, Y. 287
 Ting, M.Z.Y. 139
 Tschuchnigg, F. 122

 Ung, W.L. 198

 Viggiani, G.M.B. 206

 Wang, Y.H. 198
 Wang, C. 116
 Wang, G. 147
 Wang, H.M. 371

 Wang, J. 301, 494
 Wang, S.Y. 85, 239
 Wang, T. 378
 Wang, X. 301
 Wang, Y. 293
 Wang, Z. 552
 Wei, J. 93
 Widjaja, M. 139
 Wijesooriya, T. 530
 Won, O.K. 445
 Wong, E.K.L. 206
 Wong, I.T.Y. 265
 Wong, R.K.N. 265
 Wu, B. 357
 Wu, H. 445
 Wu, K. 182
 Wu, S. 301
 Wu, W. 60, 494
 Wu, Y. 464

 Xia, Z. 301
 Xiao, F. 293
 Xiong, X. 320
 Xu, C. 99
 Xu, T. 251, 537
 Xu, Y.F. 107
 Xue, S. 577

 Yan, L. 147
 Yan, W. 413
 Yan, Y. 273
 Yang, C. 413
 Yang, Y. 494
 Ye, J.N. 287
 Ye, Z.W. 421
 Yi, Y. 139

 Yin, Z.Y. 161
 Yu, H. 49
 Yu, J. 190, 215
 Yu, Y. 223
 Yuan, L.J. 154
 Yuan, W.H. 154

 Zhang, C.L. 502
 Zhang, D.M. 73, 251
 Zhang, D.M. 327, 421, 456, 502
 Zhang, J. 327
 Zhang, J.Z. 421
 Zhang, Q. 231
 Zhang, Q.L. 182
 Zhang, X.W. 147
 Zhao, J. 511
 Zhao, L.S. 154
 Zhao, S. 333
 Zheng, D.Z. 231
 Zheng, H. 49
 Zhengxia, C. 445
 Zhong, J.Z. 239
 Zhou, J. 99
 Zhou, M.L. 421
 Zhou, Q. 421
 Zhou, W. 378
 Zhou, W.H. 107, 116, 273, 279, 310, 371, 413, 464, 488
 Zhou, Y. 293
 Zhou, Y.G. 287
 Zhou, Y.Z. 387
 Zhou, Z. 429
 Zhu, Z. 99